THE CHEMICAL PHYSICS OF SOLID SURFACES

EDITED BY

D.P. WOODRUFF

VOLUME 12

ATOMIC CLUSTERS
From Gas Phase to Deposited

THE CHEMICAL PHYSICS OF SOLID SURFACES

THE CHEMICAL PHYSICS OF SOLID SURFACES

Volume 1
CLEAN SOLID SURFACES

Volume 2
ADSORPTION AT SOLID SURFACES

Volume 3
CHEMISORPTION SYSTEMS

Volume 4
FUNDAMENTAL STUDIES OF HETEROGENEOUS CATALYSIS

Volume 5
SURFACE PROPERTIES OF ELECTRONIC MATERIALS

Volume 6
COADSORPTION, PROMOTERS AND POISONS

Volume 7
PHASE TRANSITIONS AND ADSORBATE RESTRUCTURING AT METAL SURFACES

Volume 8
GROWTH AND PROPERTIES OF ULTRATHIN EPITAXIAL LAYERS

Volume 9
OXIDE SURFACES

Volume 10
SURFACE ALLOYS AND ALLOY SURFACES

Volume 11
SURFACE DYNAMICS

Volume 12
ATOMIC CLUSTERS: FROM GAS PHASE TO DEPOSITED

THE CHEMICAL PHYSICS OF SOLID SURFACES

EDITED BY

D.P. WOODRUFF

B.Sc. (Bristol), Ph.D., D.Sc. (Warwick), FRS
Professor of Physics,
University of Warwick

VOLUME 12

ATOMIC CLUSTERS
From Gas Phase to Deposited

ELSEVIER

AMSTERDAM • BOSTON • HEIDELBERG • LONDON • NEW YORK
OXFORD • PARIS • SAN DIEGO • SAN FRANCISCO • SINGAPORE
SYDNEY • TOKYO

Elsevier
Radarweg 29, PO Box 211, 1000 AE Amsterdam, The Netherlands
Linacre House, Jordan Hill, Oxford OX2 8DP, UK

First edition 2007

Library of Congress Cataloging in Publication Data
A catalog record for this book is available from the Library of Congress.

British Library Cataloguing in Publication Data
A catalogue record for this book is available from the British Library.

ISBN: 978-0-444-52756-1
ISSN: 1571-0785

Printed and bound in The Netherlands
07 08 09 10 11 10 9 8 7 6 5 4 3 2 1

Contributors to Volume 12

P.H. ACIOLI — Chemistry Division, Argonne National Laboratory, Argonne, IL 60439, USA and Department of Physics, Northeastern Illinois University, Chicago, IL 60625, USA

M. ARENZ — Technische Universität München, Institut für Physikalische Chemie, 85748 Gärching, Germany

K.R. ASMIS — Fritz-Haber-Institut der Max-Planck-Gesellschaft, Faradayweg 4-6, D14195 Berlin, Germany

J.J. BELBRUNO — Department of Chemistry, Dartmouth College, Hanover, NH 03755, USA

L. BENZ — Department of Chemistry and Biochemistry, University of California, Santa Barbara, CA 93106, USA

T.M. BERNHARDT — Institut für Oberflächenchemie und Katalyse, Universität Ulm, D-89069 Ulm, Germany

C. BINNS — Department of Physics and Astronomy, University of Leicester, University Road, Leicester LE1 7RH, UK

M.T. BOWERS — Department of Chemistry and Biochemistry, University of California, Santa Barbara, CA 93106, USA

H. BRUNE
Institut de Physique des Nanostructures,
Ecole Polytechnique Fédérale de
Lausanne (EPFL),
CH-1015 Lausanne,
Switzerland

S.K. BURATTO
Department of Chemistry and Biochemistry,
University of California,
Santa Barbara,
CA 93106, USA

A.W. CASTLEMAN, JR.
Departments of Chemistry and Physics,
Pennsylvania State University,
University Park, PA 16802, USA

M. CHEN
Department of Chemistry,
Texas A&M University,
P.O. Box 30012, College Station,
TX 77842-3012, USA

S. CHRÉTIEN
Department of Chemistry and Biochemistry,
University of California,
Santa Barbara,
CA 93106, USA

J. DORANTES-DÁVILA
Instituto de Física,
Universidad Autónoma de San Luis Potosí,
Alvaro Obregón 64,
78000 San Luis Potosí,
Mexico

A. FIELICKE
Fritz-Haber-Institut der
Max-Planck-Gesellschaft,
Faradayweg 4-6,
D14195 Berlin, Germany

S. GILB
Technische Universität München,
Institut für Physikalische Chemie,
85748 Gärching,
Germany

D.W. GOODMAN
Department of Chemistry,
Texas A&M University,
P.O. Box 30012,
College Station,
TX 77842-3012, USA

U. HEIZ — Technische Universität München, Institut für Physikalische Chemie, 85748 Gärching, Germany

E. JANSSENS — Laboratorium voor Vaste-Stoffysica en Magnetisme & INPAC-Institute for Nanoscale Physics and Chemistry, Katholieke Universiteit Leuven, Celestijnenlaan 200D, B-3001 Leuven, Belgium

J. JELLINEK — Chemistry Division, Argonne National Laboratory, Argonne, IL 60439, USA

P. KEMPER — Department of Chemistry and Biochemistry, University of California, Santa Barbara, CA 93106, USA

S.D. KENNY — Department of Mathematical Sciences, Loughborough University, Loughborough, Leicestershire LE11 3TU, UK

S.N. KHANNA — Department of Physics, Virginia Commonwealth University, Richmond, VA 23284, USA

S.M. LANG — Institut für Oberflächenchemie und Katalyse, Universität Ulm, D-89069 Ulm, Germany

X. LI — Department of Physics, Washington State University, 2710 University Drive, Richland, WA 99354, USA
and
Chemical and Materials Sciences Division, Pacific Northwest National Laboratory, MS K8-88, P.O. Box 999, Richland, WA 99352, USA

P. LIEVENS — Laboratorium voor Vaste-Stoffysica en Magnetisme & INPAC-Institute for Nanoscale Physics and Chemistry, Katholieke Universiteit Leuven, Celestijnenlaan 200D, B-3001 Leuven, Belgium

M. MANARD
Department of Chemistry and Biochemistry,
University of California,
Santa Barbara,
CA 93106, USA

M. MARTINS
Universität Hamburg,
Institut für Experimentalphysik,
Luruper Chaussee 149,
D-22761 Hamburg,
Germany

G. MEIJER
Fritz-Haber-Institut der
Max-Planck-Gesellschaft,
Faradayweg 4-6,
D14195 Berlin,
Germany

H. METIU
Department of Chemistry and Biochemistry,
University of California,
Santa Barbara,
CA 93106, USA

S. NEUKERMANS
Laboratorium voor Vaste-Stoffysica en
Magnetisme & INPAC-Institute for
Nanoscale Physics and Chemistry,
Katholieke Universiteit Leuven,
Celestijnenlaan 200D,
B-3001 Leuven, Belgium

R.E. PALMER
Nanoscale Physics Research Laboratory,
School of Physics and Astronomy,
The University of Birmingham,
Edgbaston,
Birmingham B15 2TT, UK

J.H. PARKS
Rowland Institute at Harvard,
Cambridge,
MA 02142, USA

G.M. PASTOR
Institut für Theoretische Physik,
Universität Kassel Heinrich Plett Str. 40,
D-34132 Kassel,
Germany

D.M. POPOLAN
Institut für Oberflächenchemie und Katalyse,
Universität Ulm,
D-89069 Ulm, Germany

S. RUSPONI
Institut de Physique des Nanostructures,
Ecole Polytechnique
Fédérale de Lausanne (EPFL),
CH-1015 Lausanne,
Switzerland

R. SMITH
Department of Mathematical Sciences,
Loughborough University,
Loughborough,
Leicestershire LE11 3TU, UK

R.E. SILVERANS
Laboratorium voor Vaste-Stoffysica en
Magnetisme & INPAC-Institute for
Nanoscale Physics and Chemistry,
Katholieke Universiteit Leuven,
Celestijnenlaan 200D,
B-3001 Leuven, Belgium

X. TONG
Department of Chemistry and Biochemistry,
University of California,
Santa Barbara,
CA 93106, USA

G. vON HELDEN
Fritz-Haber-Institut der
Max-Planck-Gesellschaft,
Faradayweg 4-6,
D14195 Berlin,
Germany

L.-S. WANG
Department of Physics,
Washington State University,
2710 University Drive,
Richland, WA 99354, USA
and
Chemical and Materials Sciences Division,
Pacific Northwest National Laboratory,
MS K8-88, P.O. Box 999,
Richland, WA 99352, USA

W. WURTH
Universität Hamburg,
Institut für Experimentalphysik,
Luruper Chaussee 149,
D-22761 Hamburg,
Germany

X. XING
Rowland Institute at Harvard,
Cambridge, MA 02142, USA

H.-J. ZHAI

Department of Physics,
Washington State University,
2710 University Drive,
Richland, WA 99354, USA
and
Chemical and Materials Sciences Division,
Pacific Northwest National Laboratory,
MS K8-88, P.O. Box 999,
Richland, WA 99352, USA

Preface

During the late 1960s and 1970s, the commercial availability of ultra-high vacuum (UHV) systems allowed the development of a plethora of new techniques which were devised to probe materials in a surface-specific fashion, and this in turn led to the creation of modern surface science: the study of the structural, electronic and chemical properties of extremely well-characterised surfaces on an atomic scale. When David King and I first conceived this series of volumes in the later 1970s, our objective was to recognise the growing maturity of this new scientific discipline which was already starting to apply these techniques in a combined fashion to understand surface processes, and indeed we now see them being applied to problems of increasing complexity.

The present volume, at least in part, follows this trend. Clusters on surfaces certainly define a class of systems that are far more complex than traditional low-index single-crystal model surfaces, yet are highly relevant to practical applications in areas such as heterogeneous catalysis and magnetic materials. Of course, an important issue in investigating clusters on surfaces is the influence of the cluster/surface interaction, and for this reason studies of naked clusters in the gas phase are also of crucial importance. Indeed, clusters – aggregates of typically a few to a few thousand atoms – represent a distinct form of matter between atoms and molecules on the one hand and solids on the other, and are a fascinating subject for investigation in their own right. Of key importance is the influence of confinement on a scale of atomic dimensions, when physical and chemical properties may differ significantly from those of either the constituent atoms or the bulk solid. This has long been recognised as an issue in heterogeneous catalysis and represented an area of 'nanoscience' long before the word was invented. Perhaps the most striking example of this was the discovery that clusters of gold, a material known in its bulk form for its chemical passivity, can be highly chemically active and potentially form the basis of excellent catalysts. This specific system is addressed in several of the chapter in this volume. Another existing area of application of such clusters exploits their magnetic properties in recording media.

The objective of this volume is thus to bring together authoritative reviews of specific topics in both gas-phase and deposited clusters, covering the range of chemical, structural, electronic and magnetic properties that underpin their practical importance. The chemical reactivity of gas-phase clusters is the focus of the first three chapters by Arenz, Gilb and Heiz, by Lang, Popolan and Bernhardt and by Zhai, Li and Wang. In Chapters 4 and 5 Burratto, Bowers, Metiu, Manard, Tong, Benz, Kemper and Chrétien, and Chen and Goodman then describe studies of this chemical reactivity for deposited clusters. This is followed by two chapters concerned with the electronic structure of gas-phase clusters by Neukermans, Janssens, Silverans and Lievens, and by Jellinek and Acioli. One challenge in working with such small species, perhaps especially in the gas phase, is to obtain experimental information on the structure of the clusters. In Chapter 8 Asmis, Fielicke, von Helden and Meijer describe the results of investigations of the vibrational properties of these clusters, a rich source of structural information, albeit indirect, while in Chapter 9 Parks and Xing describe electron diffraction measurements on gas-phase clusters. In Chapter 10, Castleman and Khanna describe their novel ideas for understanding the relationship of the

electronic and chemical properties of gas-phase clusters and the idea of designing clusters with specific chemical properties, creating a kind of periodic table of clusters. Chapters 11–14, by Brune and Rusponi, by Wurth and Martins, by Binns, and by Pastor and Dávila, are concerned with the magnetic properties of clusters, covering both experimental and theoretical aspects and describing the different approaches associated with growing two-dimensional islands on substrates or depositing size-selected gas-phase clusters on, or in, surfaces. Finally, in Chapter 15, Smith, Kenny, Belbruno and Palmer describe the results of calculations that model the way clusters interact with a model substrate when deposited.

November 2006 D.P. Woodruff

Contents

Chapter 1

Size effects in the chemistry of small clusters

Matthias Arenz, Stefan Gilb and Ueli Heiz*

Technische Universität München, Institut für Physikalische Chemie, 85748 Gärching, Germany

1. INTRODUCTION

The playground of material science has been and continues to be the periodic table of elements, first introduced by D.I. Mendeleyev in the year 1869 at the Russian Chemical Society during his talk "On the relation of the properties to the atomic weights of the elements" [1]. Chemists, physicists, and material scientists have learned how to use the information summarized in the groups and periods of the periodic table to design new molecules and materials with specific properties and well-tuned functionalities. For about one to two decades now scientists have been exploring a third, new dimension of the periodic table, which is the size-dependent properties of material composed of a specific element (see Fig. 1). Many examples have demonstrated that chemical and physical properties of matter can be tuned by changing size, shape, and dimensionality.

Along this third, size-dependent dimension of the periodic table three distinct regimes can be identified. First, for matter larger than about 100 nm in diameter, the material properties are independent of size and many of these properties are summarized in periodic tables of solid-state physics. The second regime is the scalable size regime, defined by nanoparticles with sizes between about 1 and 100 nm. In this range, the properties of the nanoparticles as a function of size scale with those of the bulk (Fig. 2). As an example, the ionization potential (IP) of metal clusters in the scalable size regime can be expressed as a function of size (e.g., number of atoms, N, in the nanoparticle) and the work function, W, of the corresponding bulk material:

$$\mathrm{IP}(N) = W + aN^{-1/3} \tag{1}$$

with, e.g., $W = 2.3\,\mathrm{eV}$ and $a = 2.04\,\mathrm{eV}$ for potassium (Fig. 3). In another example, the melting point of gold nanoparticles in the scalable size regime as a function of the radius R is expressed by the following scaling law:

$$T_\mathrm{m}(R)/\mathrm{K} = 1336.15 - 5543.65(R/\mathrm{\AA})^{-1} \tag{2}$$

The Chemical Physics of Solid Surfaces, Volume 12
ISSN: 1571-0785
DOI: 10.1016/S1571-0785(07)12001-0

*Corresponding author.
E-mail: ulrich.heiz@mytum.de

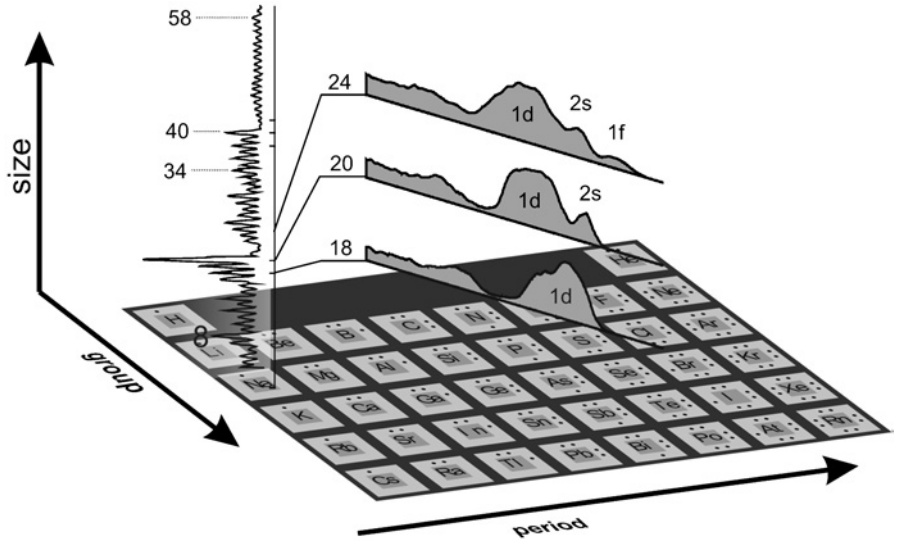

Figure 1: The chemical and physical properties can be summarized in the periodic table with its groups and periods of elements. A third coordinate along which the properties of matter are changing is the coordinate of size. Shown is the mass spectrum of sodium clusters with the magic numbers at Na_N ($N = 8$, 20, 34, 40, 58), which can be explained within the frame of the jellium model. The magic sizes correspond to electronic shell closings predicted at 2, 8, 18, 20, 34, 40, 58,.... As an example, PES for Na_{18}, Na_{20}, and Na_{24} are depicted, revealing the filling of subsequent shells (1d, 2 s, 1f) as a function of size. (Data taken from Refs. [9, 125].)

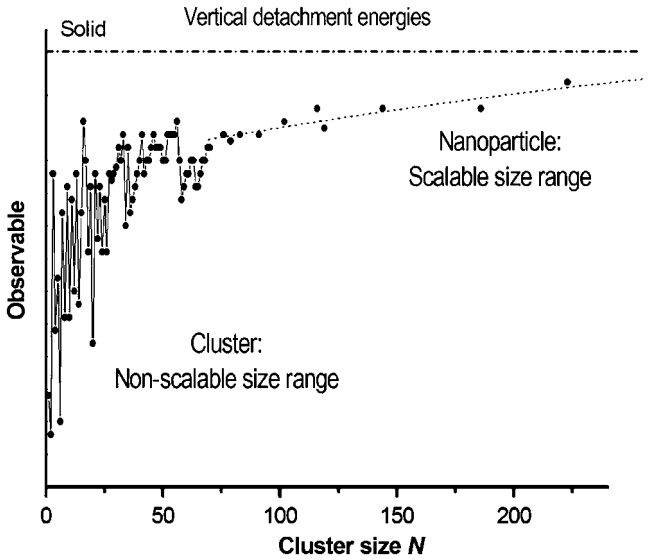

Figure 2: Physical properties observable as a function of cluster size. In this example the vertical detachment energies of Au_N^- are depicted from Ref. [126]. The corresponding value for the solid is the work function. It clearly can be distinguished between a non-scalable size regime and a scalable size regime. For metals this transition lies for many physical and chemical properties in the size range of about 100 atoms. The exact number of atoms for the transition is not sharp and depends on the property under consideration.

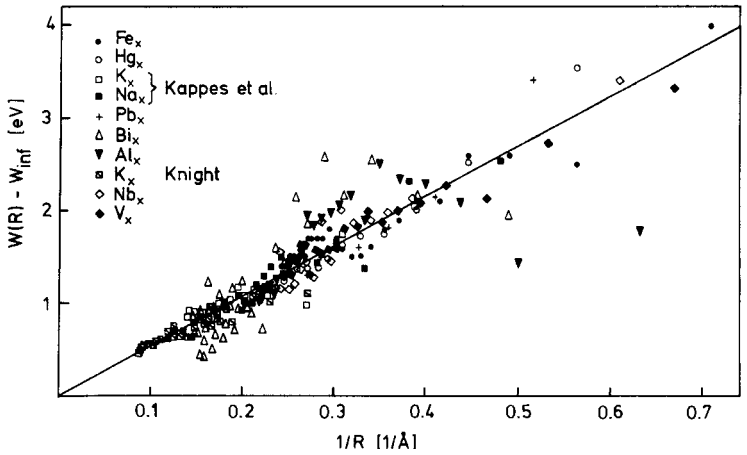

Figure 3: Shown are the changes of the ionization potentials (IP(R), here W(R)) with respect to the work function, W_{inf}, of the bulk as function of the inverse radius of the particles for several metals. For large radii the values $W(R) - W_{\text{inf}}$ lie on a straight line and can be expressed by a scaling law (see text); for small radii quantum size effects are responsible for the deviation.

where 1336.15 K is the melting point of solid gold. The scalable size range is certainly relevant for applications in nanotechnology as intrinsic properties of matter can be changed as a function of size; however, the effects are less drastic in the third regime, the non-scalable size regime.

The third regime involves going to even smaller sizes, where small clusters consisting of up to about 100 atoms characterize this non-scalable size regime. In this size domain, matter properties are controlled by quantum size effects. Systematic studies on size effects in the non-scalable size regime has already been performed for small sodium clusters by the group of Schumacher [2–5] and shortly thereafter by Knight's group [6–10] in the early 1980s. They discovered striking discontinuities in the mass spectra and ionization potentials at the magic numbers (of Na atoms per cluster) 8, 20, 34, and 40. With the jellium model, well known to nuclear physicists, the latter group achieved the first understanding of the abundant spectra [9, 11]. In this manner, the electronic shell structure of small alkaline clusters was established.

In a simplified picture, the size dependence of clusters can be described, in analogy to the classic periodic table, with an "electronic periodic table" simply by filling the electronic shells in different periods (Fig. 4). We find monovalent clusters, like Na_3, Na_9, and Na_{19}, or halide-like clusters, like Na_7 and Na_{17}, which reveal enhanced reactivities. More inert cluster sizes may be found for Na_8, Na_{18}, and Na_{20} with a closed-shell electronic structure. This simple analogy suggests that for small clusters, where the electronic structure is dominant in changing the cluster's properties, a new and exciting chemistry is waiting to be discovered. More recent studies on photoelectron spectra (PES) of sodium cluster anions Na_N^- ($4 \leqslant N \leqslant 19$) measured at room temperature and compared to the electronic density of states obtained from Born–Oppenheimer's local-spin-density Langevin molecular dynamics simulations [12] reveal considerable deviations from the jellium model occurring for Na_N ($N = 4$–7), where for instance Na_7^- clusters exhibit a triaxial deformation incompatible within the jellium approximations. At low temperatures and for transition metal clusters, the

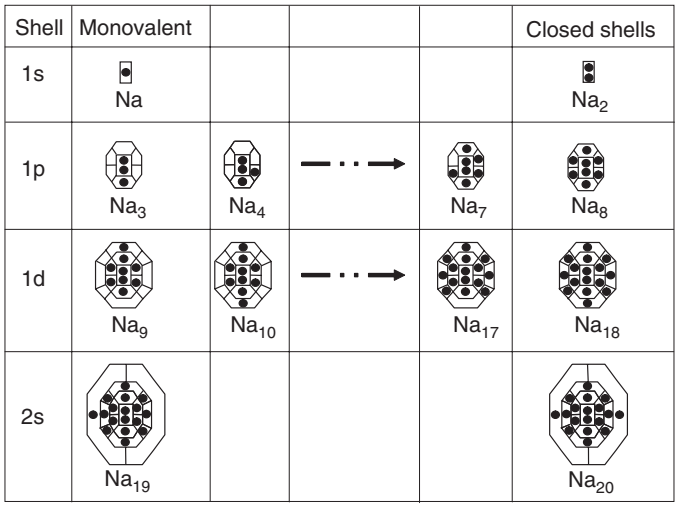

Figure 4: Electronic periodic table of small sodium clusters. According to the prediction of the jellium model, closed electronic shells exist for 2-, 8-, 18-, and 20-electron systems. For monovalent sodium magic numbers are observed as Na_2, Na_8, Na_{18}, Na_{20},.... These sizes thus reveal closed electronic shells similar to the rare gases. The sizes in between fill the periods of the electronic periodic table.

electronic structure only can be understood by using extensive ab initio calculations [13–15]. Furthermore, the geometric structure and symmetry of matter in the non-scalable size regime are considerably different from those of the solid. The most exciting example is the experimental discovery and theoretical description of planar structures for small gold clusters by the Kappes' group [16, 17]. Combined ion mobility measurements and ab initio calculations revealed planar structures for gold cations with up to seven atoms. Even more unexpected are the planar structures of gold anions observed for clusters up to Au_{12}^- and theoretically predicted even for Au_{13}^- [14, 17]. For other metals, the transition from two-dimensional to three-dimensional structures is observed at smaller sizes [18]. This unique behavior of gold has been shown to be an added manifestation of its strong relativistic effects [14]. Even more surprising is the appearance of magnetism for elements that are non-magnetic as bulk materials. Spin-density-functional calculations predict that unlike atomic and bulk Pd, both neutral and anionic Pd_N clusters ($2 \leqslant N \leqslant 7$ and $N = 13$) are magnetic, with relatively high local magnetic moments [19, 20]. Underlying this behavior is the hybridization of atomic s and d states when clusters are formed, which depletes local d contribution around each atom and leads to an open-shell-like behavior. It is predicted that an ensemble of Pd_7 clusters to exhibit an anomalous increase in the magnetic moment with temperature, as a close-lying spin isomer with a high magnetic moment is populated at higher temperatures.

These examples impressively illustrate the non-scalable size regime to be most important for new and exciting scientific discoveries. Understanding the fundamental concepts governing the non-scalable size regime will push nanotechnology beyond a simple continuation of miniaturization. In this contribution we focus on the chemistry of small clusters deposited on surfaces. Our aim is to present a concept for understanding surprising discoveries of the chemistry in the non-scalable size regime. In the

first section, we present size-dependent oxidation reactions on small gold clusters on MgO. We then discuss the chemistry of small Pd_N clusters and reveal that such small clusters are indeed catalytically active under multiple reaction cycles. Furthermore, we discuss cyclotrimerization and polymerization reactions on materials in the non-scalable size regime. Finally, we give a short outlook on how the non-scalable size regime may influence electrocatalytic reactions.

2. CO OXIDATION ON SMALL GOLD CLUSTERS

Perhaps the most prominent model surface reaction is the CO oxidation [21, 22]:

$$2CO + O_2 \rightarrow 2CO_2 \tag{3}$$

Although exothermic by 283 kJ/mol (2.93 eV) [23], the reaction does not take place in the gas phase due to a high reaction barrier. On a catalyst surface, the reaction is made possible by cleaving the O–O bond first, which can be achieved for instance by transition metals, in particular by the platinum group. For the reaction on such catalysts, a Langmuir–Hinshelwood (LH) mechanism is assumed in which both reactants are adsorbed on the surface before the reaction occurs. The O_2 dissociates spontaneously upon adsorption. Figure 5 shows the two-dimensional potential diagram of this reaction. The vertical axis depicts the O–CO reaction coordinate; the horizontal axis describes the surface–CO_2 distance. The reaction path is indicated by the broken line and starts in the upper left. Both reactants reside in a deep minimum well after adsorption. While the reaction proceeds, they have to overcome the transition state

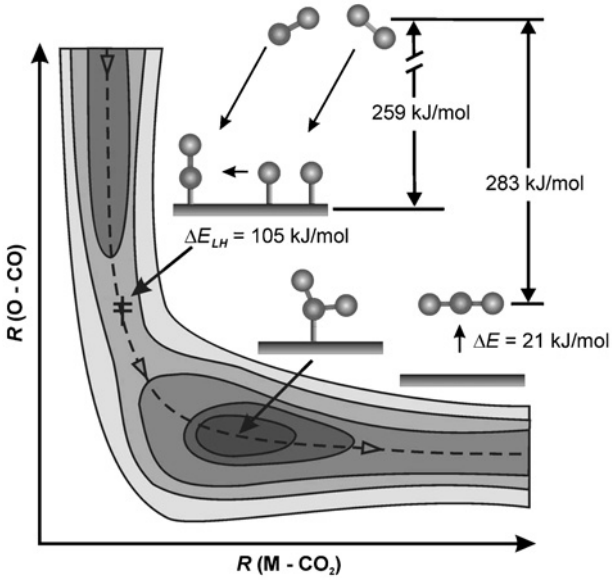

Figure 5: Two-dimensional potential energy diagram of the CO oxidation reaction on a platinum(1 1 1) surface with the corresponding energies indicated (see also text). The mutual O–CO distance of the unreacted system R(O–CO) is plotted vs. the CO_2–Pt distance R(M–CO_2). The reaction proceeds (at low coverages) as an LH mechanism. The reaction coordinate is marked by the broken line (adapted from Refs. [21, 127]). The CO is molecularly adsorbed, whereas the O_2 is dissociated upon adsorption.

(denoted by the symbol $\neq$) with an energy of 105 kJ/mol (1.09 eV). After traversing this energy maximum, the formed CO_2 molecule is only weakly bound by $\approx$20 kJ/mol (0.21 eV) and can easily escape.

Most prominent catalytic metals are those from the groups VIII and Ib of the periodic table [24]. Gold, a member of the group Ib and the noblest of all metals in bulk form, has long been considered as poor catalyst. The high ionization potential explains the low affinity toward molecules. Consequently, the gold surface shows no evidence of dissociative adsorption of H_2 or O_2. Nevertheless, in the early 1970s experiments suggested for the first time that gold could be interesting for catalyzing chemical reactions [25, 26]. But it took the work of Haruta et al. to establish that gold nanoparticles indeed possess some new exciting properties valuable for catalysis [24, 27, 28]. With the ability to prepare hemispherical gold nanoparticles on selected metal oxides, they were able to show that in this form gold is able to catalyze the oxidation of H_2 and CO [28]. Furthermore, these small gold nanoparticles show a surprisingly high catalytic activity at temperatures as low as 200 K [28, 29]. In an attempt to understand the special properties of gold nanoparticles in a size range above 1 nm in diameter, a vast number of papers have been published. For nanoparticles a few nanometers and larger in size, the change in reactivity can be explained by the existence of different crystalline facets and low-coordinated atoms on the particle [30–32]. For clusters consisting of only a few or few tens of atoms, the concept of crystal facets fails to explain the observed chemical reactivity. Here quantum size effects dominate the geometric and electronic structures. For example, the possible reaction sites for Au_8 are not necessarily present in Au_7 since the geometric and electronic structures can completely differ.

The expected strong size dependence of the catalytic properties of small gold clusters in the non-scalable size regime and the question whether reaction mechanisms for low-temperature catalysis also exist on clusters have stimulated the work on the chemical properties of mass-selected, supported Au cluster, which will be described here. In the course of investigations, it was also discovered that small mass-selected gold clusters are ideal model systems since they allow for a high level of theoretical characterization. We will review combined experimental and theoretical studies which revealed that even very basic mechanisms with the cleavage of the oxygen molecule do not occur in the non-scalable cluster size regime. In fact, on gold clusters the O_2 molecule is molecularly adsorbed but may be highly activated either in a superoxo- or peroxo-like state.

2.1. Preparation of the model catalysts

The preparation of size-selected clusters supported on different support materials is a challenging task. Only a brief overview will be given here; for a detailed description the reader is referred to the original publication [33]. In these studies, the metal clusters are produced by a laser vaporization source. From the generated cluster size distribution, a single size is mass-selected with a quadrupole mass spectrometer. Careful guiding of the metal cluster ion beam ensures that the ions do not gain too much kinetic energy. Thus, the mass-selected cluster beam with low kinetic energy can then be deposited on various support materials. In addition, the deposition is done at low temperatures, preventing diffusion and concomitant migration. The quality of the samples depends on two points: first, whether or not the substrate is modified by the incoming cluster;

and second, what is the fate of the cluster during and after deposition. To avoid modification of the substrate and fragmentation of the impinging cluster, the soft-landing condition has to be fulfilled, which means that the kinetic energy of the incoming cluster has to be held below 1 eV/atom. Molecular dynamics simulations, as well as several scanning tunneling microscope (STM) experiments, have shown that soft landing is indeed possible [34–37]. Recently, absorption measurements with cavity ring-down spectroscopy were also able to prove unambiguously the monodispersion of the samples prepared in this way [38]. The preparation of supported, monodispersed cluster samples was a milestone in the field, because it was a pre-requisite for studying the strongly size-dependent properties of small clusters. As we will show in this review, an atom-by-atom change indeed causes drastic changes in the chemical and catalytic properties of small clusters. This evolution could not have been observed when studying size-distributed cluster-assembled materials.

2.2. Experimental observation of the CO combustion on gold clusters

The first studies on the $^{18}O_2 + {}^{13}CO \rightarrow {}^{13}C^{18}O^{16}O$ reaction on size-selected gold clusters (Au_N with $1 \leqslant N \leqslant 20$) in the year 1999 led to surprising conclusions [39, 40]. In these experiments, the clusters were deposited on thin MgO films, grown in situ on Mo(1 0 0) single crystals. The thin films were prepared either as defect-rich film, characterized by a given density ($\approx 5\%$) of extended defects and point defects (F centers, FC), or as defect-poor films with a negligible density of F centers [40, 41]. The CO combustion was studied by temperature-programmed reaction (TPR) experiments. In a TPR experiment, the sample is saturated with both reactants (^{13}CO and $^{18}O_2$) at low temperatures (< 100 K). Subsequently, the sample is slowly heated up linearly and with a differentially pumped mass spectrometer the reaction products (e.g., $^{13}C^{18}O^{16}O$) are detected as function of the sample temperature. In this example, the desorption temperature of the product molecule CO_2 corresponds to the reaction temperature, as its binding energy to the cluster is very low ($\sim$0.2 eV), and thus desorbs from the cluster upon formation. The use of isotopically labeled $^{18}O_2$ allows distinguishing the combustion induced by oxygen from the gas phase or from the MgO support. Since in the TPR experiment both reactants have to be present on the surface before the reaction takes place, only product molecules from an LH-type mechanism can be observed. Reaction products formed in an Eley–Rideal mechanism cannot be observed because they are already formed during dosing. Figure 6a shows the results of TPR experiments of CO combustion on Au clusters on a defect-rich MgO film. For better comparison, the total $^{13}C^{18}O^{16}O$ yield is obtained by integrating the TPR spectra and it is shown as a function of cluster size (Fig. 6b). As expected, the bare MgO surface as well as the gold film shows no reactivity, the latter observation revealing the noble character of gold. Also, small clusters with less than eight atoms show no significant CO_2 production, but while starting with Au_8, CO_2 formation can be observed. The non-monotonic dependence between cluster size (surface) and CO_2 yield is not in agreement with the "classical" picture, which assumes the activity to be proportional to the surface area of the cluster. Furthermore, two distinct peaks observed below and above ≈ 250 K for Au_8 suggest that two different reaction mechanisms are responsible for the formation of CO_2. The role of the support for the reactivity of Au_8 is emphasized in Fig. 7, which shows the comparison of TPR experiments by changing the support from a defect-rich MgO film to a defect-poor MgO

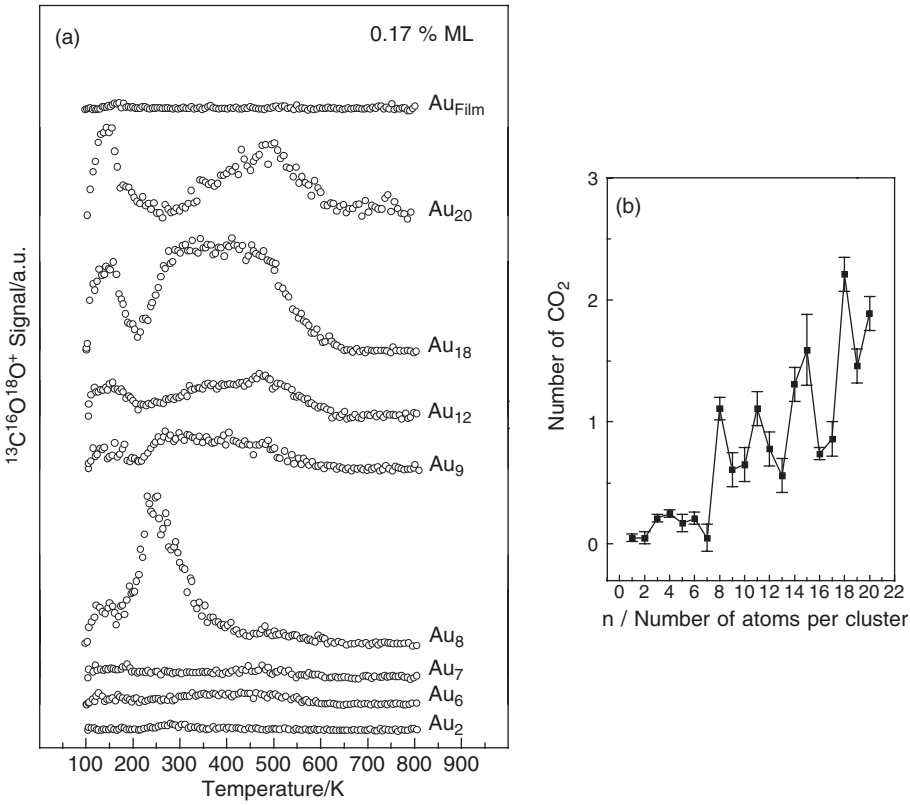

Figure 6: (a) TPR experiments for the CO-oxidation on selected Au_N clusters on defect-rich MgO(1 0 0) films. The model catalysts were saturated at 90 K with ^{13}CO and $^{18}O_2$ and the isotopomer $^{13}C^{18}O^{16}O$ was detected with a mass spectrometer, as a function of temperature. (b) The reactivities for Au_N expressed as the number of formed CO_2 per cluster.

film with a negligible amount of defects. Surprisingly, in the case of defect-poor films, the formation of CO_2 is drastically decreased. The important role of defect sites on the reactivity of Au_8 is further confirmed by preparing films with a high density of F centers by first evaporating Mg onto defect-poor MgO films and subsequently annealing the samples to 550 K [42]. Similar results for the defect-rich films also are obtained. The apparent difference in the CO_2 yield is a proof of the support–cluster interplay, which changes the cluster properties in a fundamental way. We will discuss this point in conjunction with the fundamental reaction mechanism.

2.3. Description of the reaction mechanism by DFT calculations

The experiments described in the previous section triggered the use of density functional theory (DFT) in order to shed light on the underlying reaction mechanisms. Figure 8 shows exemplarily the structure of Au_8 on the MgO(1 0 0) surface containing an oxygen vacancy (F center). The cluster is strongly anchored with 3.44 eV to the defect site. The fully optimized Au_8 structure bound to a defect-free MgO(1 0 0) surface is very similar, but exhibits a significantly smaller binding energy of only 1.22 eV.

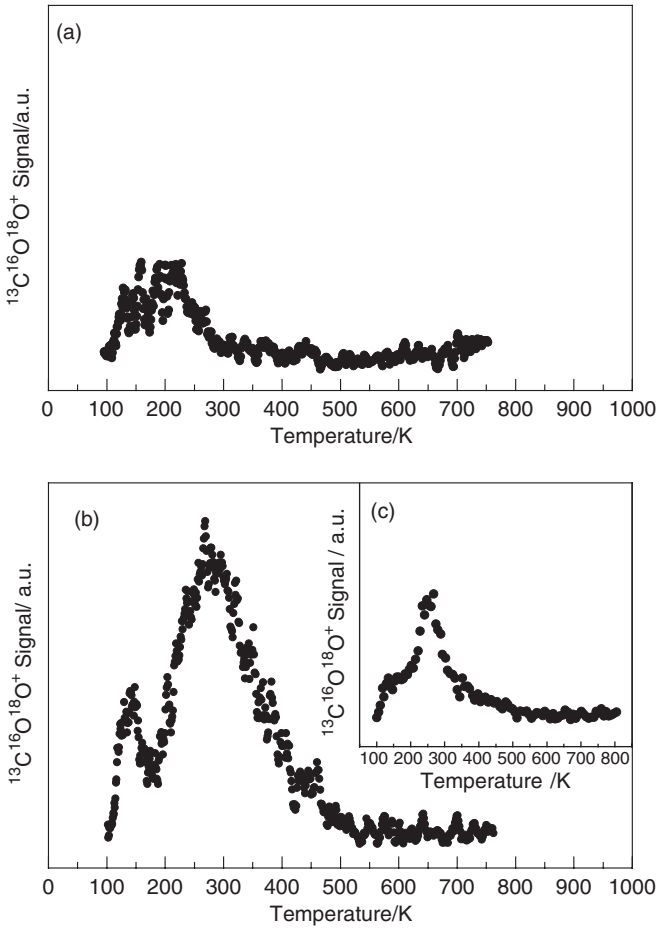

Figure 7: TPR experiments for the CO-oxidation on Au_8 clusters on (a) defect-poor and (b) defect-rich MgO(1 0 0) films; inset (c) shows the results after producing F centers on MgO(1 0 0) after the procedure of Pfnür et al. (see text). The model catalysts were saturated at 90 K with ^{13}CO and $^{18}O_2$ and the isotopomer $^{13}C^{18}O^{16}O$ was detected with a mass spectrometer, as a function of temperature.

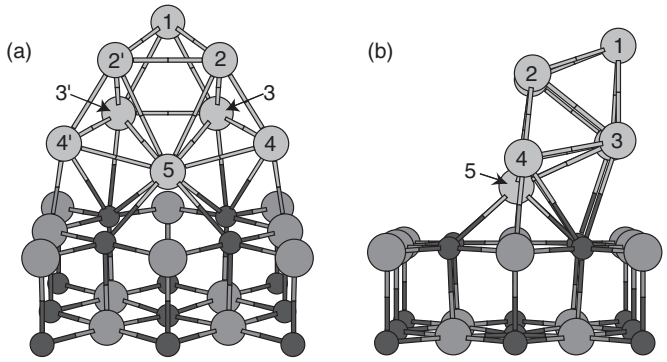

Figure 8: Front and top view of Au_8 on MgO. Au atom labeled with 5 is most strongly interacting with the F center of the MgO surface.

The structure of Au_8 is a piece of a hexagonal close-packed structure with a five (bottom) and three (top) atom layer. Both, for the defect-free and the F-center-bound cluster, a charge transfer from the bulk to the cluster is observed; however, the charge transfer is much stronger in the case of Au_8 bound to the F center. As we later discuss, this point is essential for understanding the reactivity of small, supported gold clusters. If the cluster is bound to the F center, one gold atom (No. 5 in the figure) is distorted toward the F center. With this structure as a starting point, three possible reaction paths for the $CO + O_2 \rightarrow CO_2$ reaction are found for Au_8. These paths are shown in Fig. 9. The first two describe LH (LHt and LHp)-type mechanisms, which can be observed in the TPR experiments, while the third is an Eley–Rideal mechanism not accessible for the TPR experiment. All three mechanisms share the fact that the O–O bond of the O_2 molecule is not cleaved prior to the reaction, a point that discriminates

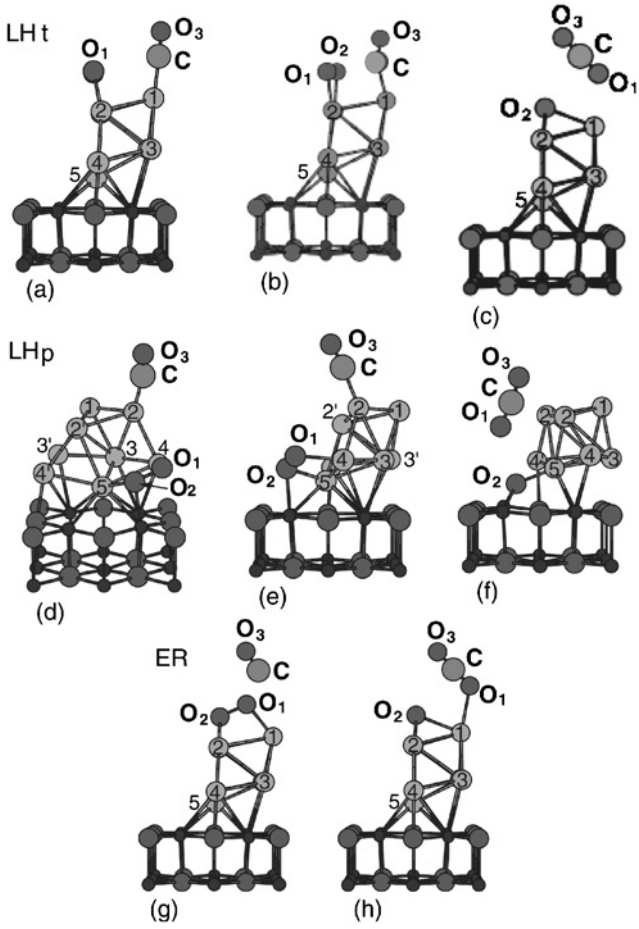

Figure 9: Reaction mechanisms of the CO oxidation on supported Au_8. Shown are two LH mechanisms, one occurring on the top facet of the cluster (LHt) and the other on the periphery (LHp). The third mechanism is of Eley–Rideal type (see text for details).

these mechanisms from the "classical" picture used for most conventional catalyst and even for small Pd_N clusters (see below).

2.3.1. LHt

In the first reaction path, both reactants O_2 and CO are coadsorbed on the top facet of the Au_8 cluster. In this configuration, the distance between the C atom and the reacting O atom is ≈ 3.1 Å. By mapping the reaction path, the barrier to form CO_2 is estimated to be ≈ 0.1 eV; the transition state is characterized by a C–O distance of ≈ 2 Å. The reaction $MgO(FC)/Au_8 + O_2(g) + CO(g) \rightarrow MgO(FC)/Au_8O + CO_2(a)$[1] is exothermic by about 5 eV. Note that the resulting CO_2 is only weakly bound by ≈ 0.2 eV and will leave the cluster spontaneously after formation. With the relatively low reaction barrier, this mechanism is possible even at low temperatures and can be associated with the low-temperature peak in the experiment at 140 K. Since the reaction takes place on a facet of the cluster, it is to expect that this mechanism (in contrast to the following) is insensitive to the cluster size. This is in line with the experimental data where both the height and the width of the first low-temperature peak is relatively unaffected by cluster size. This mechanism is also found with similar energetics if the Au_8 cluster is attached on top of a non-defective MgO(1 0 0) surface. This is also found in the experiment where a low-temperature peak is found for Au_8 on a defect-poor MgO(1 0 0) film.

2.3.2. LHp

The second LH mechanism found in the theoretical investigations takes place on the periphery of the Au_8 cluster. The O_2 molecule is bound at the interface between the cluster and the MgO surface, while the reacting CO is bound on the top facet. The distance between the reacting C and O atoms is ≈ 4.5 Å; mapping the potential along the reaction coordinate reveals a relatively broad barrier of ≈ 0.5 eV for the Au_8/Mg(FC) system, meaning that a higher temperature is required for this process. This reaction mechanism is assigned to the second higher temperature peak (280 K) observed in the measurements, which is not found on defect-poor substrates. As we will show later in more detail, in the case of the defect-free support, the O–O bond of the oxygen molecule is less activated compared to the defective support. Correspondingly, the energetics of this reaction changes significantly if the Au_8 is supported on a non-defective MgO(1 0 0) layer. In fact, the reaction barrier increases to 0.8 eV and is then comparable to the binding energy of CO. Thus, desorption of the CO molecule occurs before reaction. Consequently, the CO combustion is not observed in the experiment on a defect-poor MgO film.

2.3.3. Eley–Rideal

A third reaction found in DFT calculations is of Eley–Rideal type, where a CO molecule approaches the already adsorbed O_2 molecule from the gas phase and reacts without any barrier to CO_2 formation. With a missing reaction barrier, this reaction can take place even at temperatures as low as 90 K, and cannot be observed in TPR experiments because it already takes place during dosing in the early stage of the experiment [40].

One question arising in the comparison of theory and experiment is why the faster LHt process (with a rate one order of magnitude higher) is not dominating

the TPR spectrum. At first glance one expects the low-temperature LHt mechanism to deplete the CO while the LHp mechanism is still hindered. In fact, the theoretical studies as well as experiments in the gas phase reveal that small negatively charged cluster can adsorb only one O_2 molecule at a time. Thus, two ensembles of Au_8/O_2 complexes coexist, one with the O_2 bound at the facet and the second ensemble with the O_2 bound at the interface of Au_8 and MgO. The populations of the two ensembles are mainly governed by the adsorption mechanisms of CO. Whereas the on-top-bound O_2 originates by direct CO adsorption, the other ensemble is populated by the so-called reverse spillover, where CO adsorbs on the MgO substrate and then migrates to the cluster (see below). The found ratio of the two populations and the concomitant low- and high-temperature formation of CO_2 are in agreement with this explanation.

2.4. The role of the surface defects

In the following we turn our attention to the specific effects of the surface defects. To begin with, the discussed reaction mechanisms do not require cleavage of the O–O bond prior to reaction, the reaction barrier is lowered by the activation of the molecularly adsorbed O_2 molecule through population of the antibonding $2\pi^*$ orbital, the lowest unoccupied molecular orbital (LUMO) of the adsorbed oxygen molecule. In addition, the second ''high-temperature'' LHp mechanism is crucially dependent on surface defects with clusters deposited on defect-poor substrates forming only small amounts of CO_2 and with Au_8 adsorbed on oxygen vacancies turned active for the CO combustion at low temperature. Indeed, oxygen vacancies are an important class of point defects on MgO; their direct characterization, however, is not straightforward. Freund et al. recently succeeded in characterizing singly charged oxygen vacancies (F^+ centers) with electron paramagnetic resonance (EPR) measurements [43]. Neutral F centers, which are not susceptible to EPR, have been investigated by scanning tunneling microscopy and spectroscopy [44, 45].

In the studies reviewed here, the influence of the F center on the cluster is studied in more detail experimentally by using the probe molecule, CO, and Fourier transform infrared (FTIR) spectroscopy combined with extensive DFT calculations. The samples were prepared in the same manner as before with Au_8 deposited on defect-poor and defect-rich MgO films. After saturation of the samples with O_2 and CO molecules at 90 K, FTIR spectra were taken after annealing to various temperatures [46]. The spectra recorded at 90 K and after annealing to different temperatures are shown in Fig. 10. For both cluster samples, the vibrational bands around $2085\,cm^{-1}$ show that CO is indeed adsorbed molecularly and in on-top configuration; in addition, the observed vibrational frequency at $1300\,cm^{-1}$ is tentatively assigned to highly activated O_2. The vibrational bands disappear on increasing the temperature above 300 K consistently with the formation of CO_2 for $Au_8/MgO(FC)$ samples or with the desorption of CO and O_2 in the case of Au_8/MgO as monitored by mass spectroscopy.

Most important, CO adsorbed on an $Au_8/MgO(FC)$ complex shows a red-shift of ≈ 30–$50\,cm^{-1}$ compared to the CO adsorbed on the Au_8/MgO complex. It is well established that through electron transfer from metal surfaces the antibonding $2\pi^*$ orbital of CO may become occupied, weakening the CO bond and thus red-shifting the vibrational stretch frequency of the CO. This effect may be enhanced if the cluster is

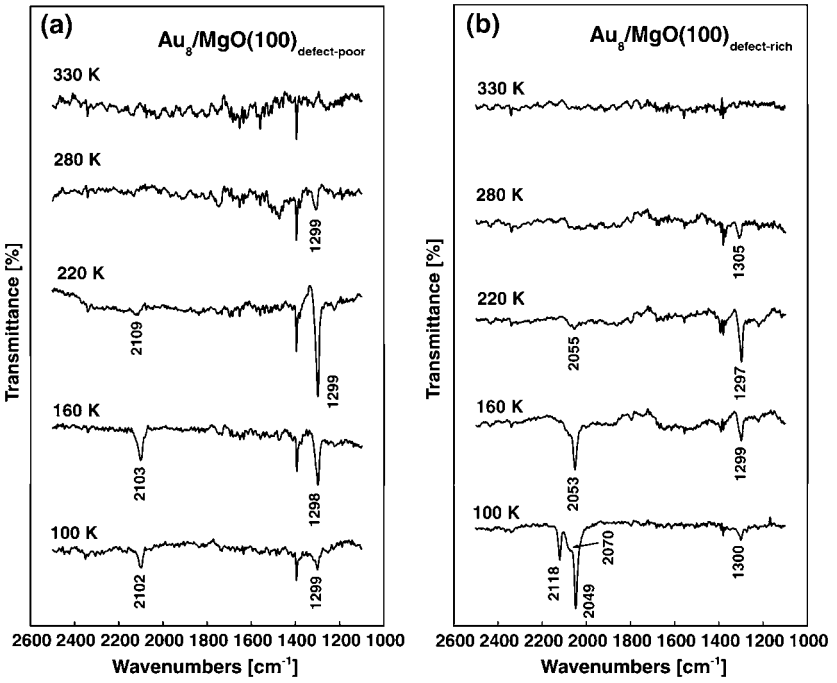

Figure 10: TIR spectra taken at 90 K after exposing the model catalysts (a) $Au_8/MgO(1\,0\,0)_{defect\text{-}poor}$ and (b) $Au_8/MgO(1\,0\,0)_{defect\text{-}rich}$ to ^{13}CO and O_2 and annealing the sample to the indicated temperature. The frequencies between 2050 and 2100 cm^{-1} are attributed to CO adsorbed on Au_8, whereas the band at 1300 cm^{-1} may originate from activated O_2 molecules. The band at 2118 cm^{-1} is assigned to CO adsorbed on MgO defects. Note the red-shift of the CO-stretch by 50 cm^{-1} on defect-rich films. This shift is consistent with the predicted charging of the cluster when deposited on an F center (c), where the difference of the charge densities of the isolated (Au_8, MgO_{5Fc}) and the model system (Au_8/MgO_{5Fc}) was calculated. The charging was estimated to be 0.5*e*.

charged and therefore the CO molecule acts as a tracer for the charge density on the metal cluster. The experimentally observed red-shift of $\approx 50\,cm^{-1}$ may thus be understood by an enhanced charge transfer to the cluster in $Au_8/MgO(FC)$ compared to Au_8/MgO. Recently, it has been shown for Au atoms on MgO surfaces that the CO molecule does not act as a tracer but induces the effect of charge transfer from the substrate to the cluster itself [47]. This effect, however, has only been observed for adsorbed atoms and does not occur on Au_2 or larger clusters [48]. In order to get a more detailed picture of the origin of the observed red-shift, extensive DFT calculations on the $Au_8O_2\,^{13}CO$ system have been carried out [46]. The main results are shown in Table 1, where the binding energies and vibrational frequencies for the $Au_8O_2\,^{13}CO$ complex are collected for different charge and spin states. Investigating the gas-phase (free) complex allows for separating charge effects from other possible effects due to the support. Concentrating on the spin 0 case, a red-shift of 30–50 cm^{-1}, corresponding to the one experimentally observed, is explained by a charging of the cluster by $\sim$0.5*e*. The total population of the antibonding $2\pi^*$ orbital of CO, $\Delta Q(^{13}CO)$, is calculated to be 0.34*e*. That charging is indeed responsible for part of the observed red-shift is also confirmed by electronic structure calculations for

Table 1: Vibrational frequencies of the Au_8O_2 ^{13}CO complex (gas phase) as function of charging.

ΔQ (Au_8O_2 ^{13}CO) (e)	Spin	ν (cm^{-1})	BE($O_2 + {}^{13}CO$) (eV)	d(^{13}CO) (Å)	ΔQ(^{13}CO) (e)	d(O_2) (Å)	ΔQ(O_2) (e)
0	1	2005	1.060	1.149	0.29	1.336	0.71
0.25	0.875	1987		1.150	0.32	1.344	0.75
0.5	0.75	1968		1.154	0.35	1.350	0.77
1.0	0.5	1926		1.160	0.43	1.364	0.86
0	0	2009	0.753	1.148	0.28	1.378	0.88
0.25	0	1990		1.150	0.31	1.381	0.89
0.5	0	1975		1.153	0.34	1.385	0.92
1.0	0	1920		1.158	0.41	1.398	1.00

Note: Results for free (Au_8O_2 ^{13}CO) complexes as a function of excess electron charge ΔQ. Results are shown for various values of the spin; for the neutral cluster we show triplet ($S = 1$) and singlet ($S = 0$) states. The quantities that we display are as follows: ν, the CO stretch frequency; BE($O_2 + {}^{13}CO$), the CO binding energy to the gold cluster with a pre-adsorbed oxygen molecule; the bond distances, d(^{13}CO) and d(O_2); and excess electronic charges, ΔQ(^{13}CO) and ΔQ(O_2), of the two adsorbed reactants CO and O_2, respectively. For reference we remark that the calculated vibrational frequency of gas-phase ^{13}CO is 2070 cm^{-1}, which is 25 cm^{-1} smaller than the experimental value of $\nu(^{13}CO) = 2095\,cm^{-1}$.

the $^{13}CO/O_2Au_8/MgO$ system (Fig. 11), where the population of electronic states with CO-2π^* character is calculated to be 1.27e in the case of Au_8 adsorbed on MgO(FC) in comparison to only 1.18e for Au_8 adsorbed on a regular site. As the observed red-shift and the concomitant charging of the Au_8 cluster correlate with the higher reactivity for the CO combustion, it can be concluded that charging of Au_8 is indeed a necessary ingredient for the activation of gold as a catalyst.

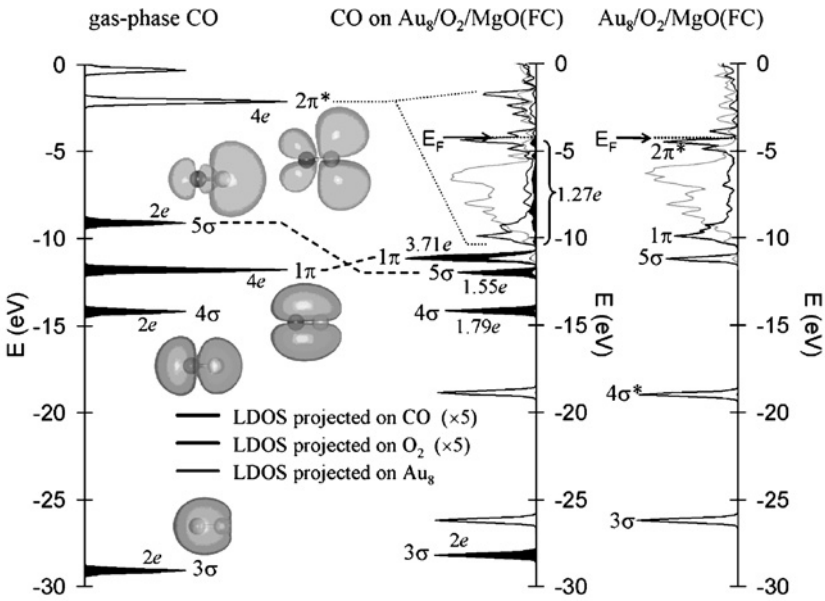

Figure 11: LDOS correlation diagram of free CO (left) and $Au_8/O_2/MgO(FC)$ (right) resulting upon adsorption of the CO molecule in the complex adsorbed on $Au_8/O_2/CO/MgO(FC)$ (middle). The assignments in the LDOS diagrams are given in the figure. The electron populations of the various levels are given as 2e, 4e, etc., and iso-surface images of the orbitals of the free CO molecules are also shown (left). Dashed lines indicate orbital shifts and redistribution caused by the adsorption of the CO molecule.

2.5. The role of the electronic structure

As important as the role of the substrate for tuning the chemistry of small supported clusters is the evolution of the electronic structure with cluster size. The experimental results clearly indicate that Au clusters with less than eight atoms are inert, even if they are deposited on defect-rich MgO surfaces. This can be explained by the fact that in the non-scalable size regime each cluster size has its own characteristic electronic structure. For a given cluster–surface complex, adsorbates can only be bound and activated if there are resonances between the electronic states of the cluster–surface complex and those of the adsorbate, e.g., resonances between the occupied states or bands of the cluster and the LUMO of the adsorbate. In the case of O_2 interacting with the cluster, the LUMO is the $2\pi^*$ state. Thus, the analysis of spectra of the local density of states (LDOS) of the $O_2/Au_8/MgO(FC)$ system is elucidative for understanding the bonding and activation of O_2 to the cluster [49]. The rightmost panel in Fig. 11 shows the LDOS of the $O_2/Au_8/MgO$ system, separated into the part located on the Au_8 cluster and the part centered on the O_2 molecule. The peaks in the LDOS of the O_2 molecule can clearly be assigned to the 5σ and 1π orbitals. The uppermost sd-band of the Au_8 shows metallic character, meaning that occupied states extend continuously up to the Fermi energy. The LUMO of the O_2 molecule lies below the Fermi level, and is thus in resonance with the sd-band of the Au_8 cluster. A charge transfer from the cluster to the antibonding $2\pi^*$ orbital occurs. This backdonation is responsible for the weakening and elongation of the O–O bond. In addition, this activation is accompanied by a change of the spin state of the O_2, from a triplet state in the gas phase to a peroxo-like state with zero net spin in the $O_2/Au_8/MgO(FC)$ complex. The calculation shows that, in accordance with the experiment, the presence of an F center amplifies this effect and the result is that the bonding of the O_2 molecule to the cluster is stronger (0.47 and 0.33 eV for the spin 0 and spin 1 states, respectively) compared to the case of a defect-free surface (0.33 and 0.30 eV for the spin 0 and the spin 1 states, respectively).

A similar situation is found when investigating the adsorption of the CO molecule to the Au_8/MgO complex. The LDOS of the corresponding complexes are shown on the left side of the correlation diagram in Fig. 11. As expected, the low-lying lone pairs of the CO, 3σ and 4σ, are relatively unaffected by the bonding to the $Au_8/O_2/MgO(FC)$ complex. In contrast, the 5σ and 1π orbitals hybridize with the sd-band of the cluster and the 5σ orbital gets strongly stabilized in energy (≈ 3 eV), whereas a small destabilization of the 1π orbital is observed. A donation of electron charge from the CO to the Au_8 takes place, which is responsible for only a part of the binding energy. The resonance and hybridization of the antibonding $2\pi^*$ orbital with the sd-band of the $Au_8/O_2/MgO(FC)$ complex spreads out the orbital over the respective energy range and pushes it partially below the Fermi level. As in the case of O_2, backdonation of electron charge into the LUMO of the CO strengthens the adsorption, but at the same time by occupying the antibonding $2\pi^*$ orbital the C–O bond gets weaker. Note that similar features are also observed on a defect-free surface but the backdonation is less pronounced, as observed in the experiment. As discussed above, the resulting redshift of the CO stretch frequency is less pronounced on the defect-free surface compared to the defective surface. The integration of the charge density over the respective energy range (taking only the charge projected onto the CO molecule into account) leads to a backdonation of 1.27*e* in the case of the MgO(FC) compared to 1.18*e* for the

regular MgO support. Note that due to the degeneracy of the $2\pi^*$ orbital in the gas phase, in principle there could be four electrons transferred, but only part of the orbitals are occupied by the charge transfer.

The dependence of the catalytic activity on the cluster size can also be explained by the analysis of the LDOS. Only if the electronic structure of the Au_N/MgO(FC) complex allows an overlap and hybridization with the molecular orbitals of the adsorbates can a charge transfer and a concomitant weakening and activation of the O–O and C–O bond occur, which is a pre-requisite for the discussed reactions paths. For comparison, a completely different scenario is found in the case of Au_4 [50] where the O_2 molecule binds with a single atom on top of the cluster. Since the antibonding $2\pi^*$ orbital of the oxygen stays above the Fermi level in energy and due to the narrower sd-band of the tetramer in comparison to the octamer, an overlap with the $2\pi^*$ orbital of the oxygen molecule does not occur. Consequently, the O–O bond length is nearly unperturbed and the binding energy is rather low (0.18 eV). The inactivated O_2 molecule remains inert toward the CO combustion in accordance with the experiment.

2.6. Structural dynamic fluxionality

It is one of the unique properties of clusters to have several isomers close in ground-state energy. Thus, in an experiment at finite temperature there always exists an ensemble of different isomers, and it has been shown in the gas phase that the lowest lying ground-state structure is not always the one observed in the experiment because of kinetic effects [16–18]. If the barrier for interconversion is lower than kT, the clusters will be fluxional and interconvert from one isomeric structure to the other [51]. As illustrated in Fig. 12a, b, e, and f, the existence of various isomers can also be true if the cluster is adsorbed on a surface. In the case of Au_8/MgO(FC), a quasi-planar

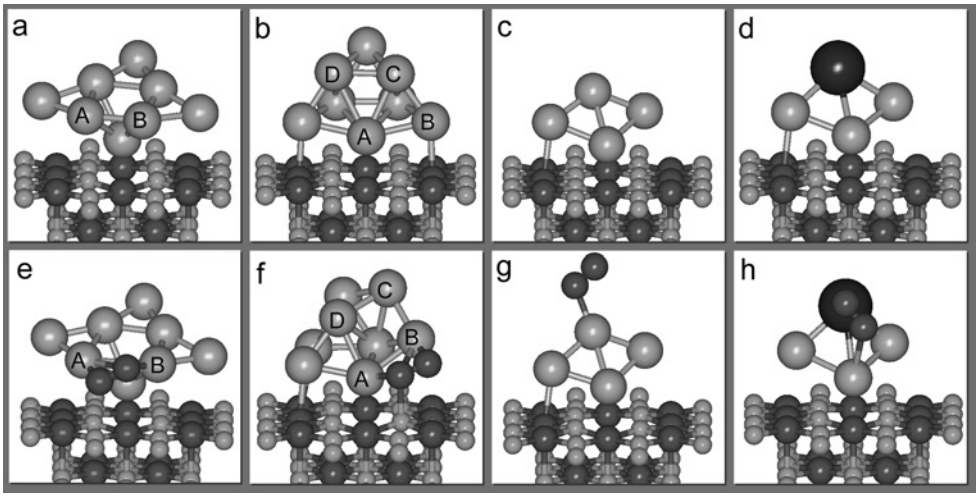

Figure 12: The optimized atomic structures of model catalysts comprising Au_8 (a and b), Au_4 (c), and Au_3Sr (d) clusters adsorbed at an F center of an MgO(1 0 0) surface. For Au_8 two relevant isomers are depicted, separated by an energy difference of 0.29 eV with the quasi-planar geometry being the ground state. The optimal geometries for the adsorption of the O_2 molecule on these model catalysts are shown in panels (e)–(h).

(Fig. 12a) and a three-dimensional isomer (Fig. 12b) with an energy separation of 0.29 eV coexist. Each of these isomers has its unique electronic structure and thus reveals a distinct chemical activity. While the three-dimensional structure is thermodynamically less stable, the binding energy gain upon oxygen absorption is higher in the three-dimensional case (0.28 eV in the quasi-planar case and 0.47 eV in the 3D case). Upon adsorption of oxygen the cluster is therefore adjusting its geometry to accommodate the adsorbate and changes its structure from a quasi-planar to a 3D one. In detail, the Au atom B in Fig. 12b and f moves away from the surface to open a pocket for the O_2 molecule. Interestingly, the adsorption is not possible if the structure of the Au_8 cluster is frozen, so the cluster's fluxionality is an important pre-requisite for the adsorption and activation of O_2. This example indeed reveals the essence of the so-called dynamic structural fluxionality of clusters. Furthermore, an analysis of the Au-cluster geometries along the reaction path of the CO oxidation (cf. Fig. 9) shows that the cluster is constantly adapting its structure and, in the course of a chemical reaction, the system has thus the possibility to find the most favorable free-energy reaction path by choosing the most suited isomeric structures.

2.7. Impurity doping

A logical expansion of the work discussed above is the tuning of the electronic structure of the metal catalyst by impurity doping to optimize the charging process and activation of the O_2 molecule. It is well known that combining gold with a less electronegative alkaline or alkaline earth metal can lead to an ionic core [52]. For experimental reasons, the system Au_NSr was chosen for these studies [50]. The formation of CO_2 in a TPR experiment was measured for different cluster sizes and Sr impurities. In these experiments, the samples were exposed to $^{18}O_2$ and CO_2 to saturate the clusters with the adsorbates. The CO_2 production as a function of the sample temperature is shown in Fig. 13. The onset for CO_2 production is clearly shifted to smaller cluster sizes by the Sr impurity doping. Whereas the pure gold tetramer is inert, the strontium-doped cluster Au_3Sr produces CO_2 at 250 and 500 K. As shown above, these clusters bind to the MgO(F5O) surface quite strongly (calculated binding energy of 2.65–4.06 eV) and their binding is significantly enhanced (typically by about 2 eV) due to the F center defects. These high binding energies and the "anchoring" effect by the F centers correlate well with the observed thermal stability of the supported clusters in the TPR experiments. This finding pertains to the charge state of the adsorbed clusters – in particular, calculations predict that the interaction with the surface is accompanied by charge transfer of 0.5*e*, 0.3*e*, and 0.3*e* to the adsorbed Au_8, Au_4, and Au_3Sr clusters, respectively. The early onset of the catalytic activity in the case of strontium-doped clusters can be easily explained by analyzing the LDOS spectra (Fig. 14). The spectra for O_2Au_4 are shown in Fig. 14c (the LDOS for the O_2) and d (for the Au_4). The overlap between the sd-band of the Au_4 cluster with the antibonding $2\pi^*$ orbital of the oxygen is only marginal and thus backdonation is not possible. The oxygen molecule is thus molecularly bound with a very weak interaction (0.18 eV) and remains in its triplet state. In the case of the Sr-doped cluster there are strong resonances between the electronic states located on the impurity atom and O_2, leading to substantial backdonation into the spin-down $2\pi^*_\perp$ orbital of oxygen. The binding energy with O_2 is therefore increased to 1.94 eV and accompanied by an activation of oxygen to a superoxo-like state with a O–O bond length of 1.37 Å. This is

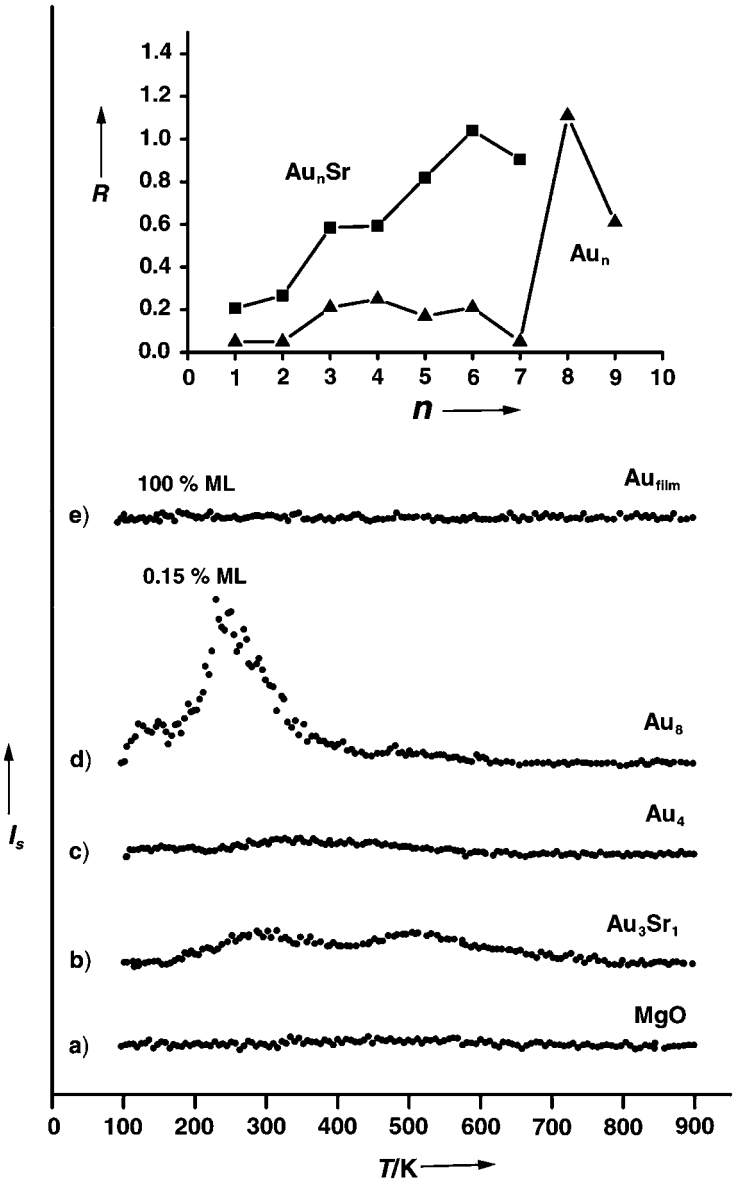

Figure 13: TPR spectra of CO_2 formation on (a) an MgO(1 0 0) film, (b) Au_3Sr/MgO(FC), (c) Au_4/MgO (FC), (d) Au_8/MgO(FC), and (e) a thick gold film grown on MgO(1 0 0). The Au_4/MgO(FC), pure MgO film, and the thick Au film are catalytically inert. The inset compares the chemical reactivity R of pure Au_N and doped Au_NSr clusters, with $1 \leqslant N \leqslant 9$, expressed by the number of product CO_2 molecules per deposited cluster. The TPR spectra are recorded after exposure of the model catalyst to isotopically labeled $^{18}O_2$ and $^{13}C^{16}O$ at 90 K. Only the production of the $^{13}C^{16}O^{18}O$ isotopomer is detected by measuring its ion current (I_s), which indicates that the oxidation of CO occurs only on the cluster and that no oxygen from the MgO substrate is involved.

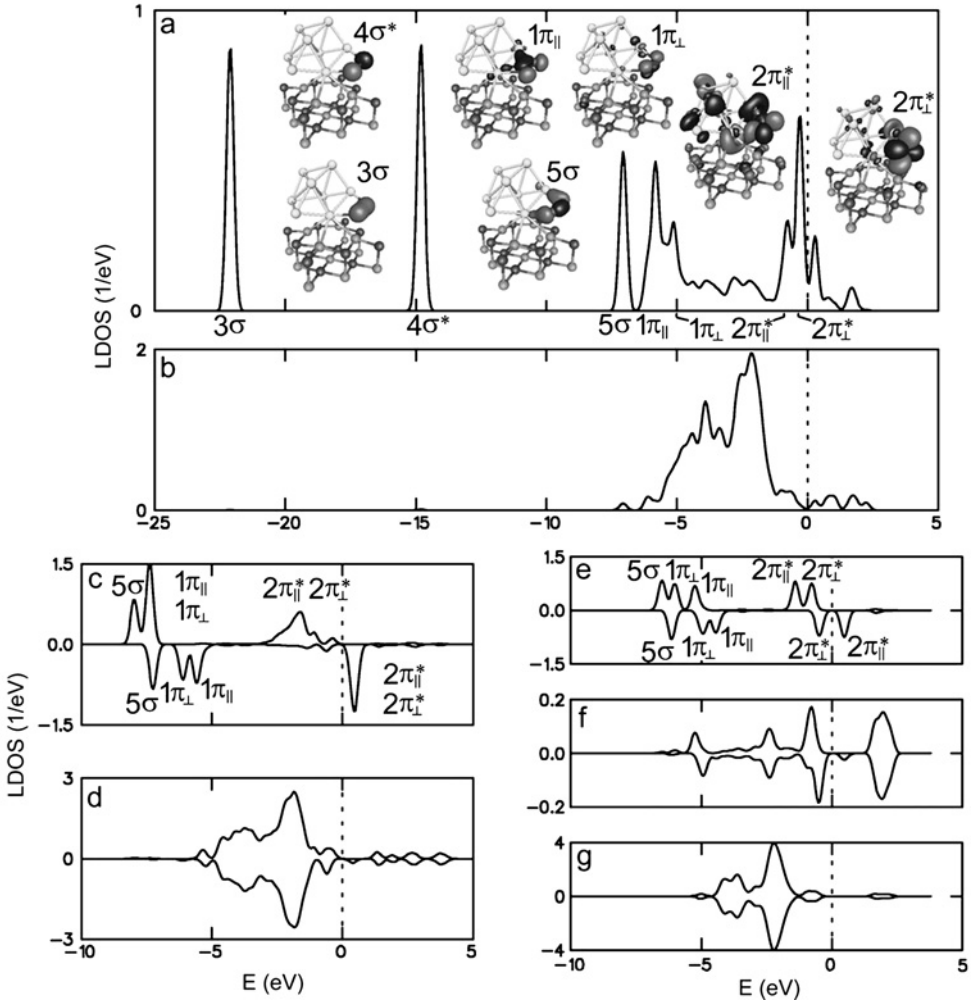

Figure 14: Local density of spin-up and spin-down electronic states (LDOS) of the model catalysts shown in Fig. 12(f–h) for oxygen (a, c, and e) and the metal part (b, d, f, and g). The prominent peaks of the oxygen LDOS are labeled following the conventional nomenclature for the molecular orbitals of the gas-phase O_2 molecule, with $\perp$ and $\parallel$ meaning perpendicular and parallel to the MgO surface, respectively. The Fermi energy E_F is at 0 eV. Note that here (in contrast to Fig. 11) the zero point of the energy was set to the Fermi level.

an illustrative example of how by changing cluster size and impurities the interaction of oxygen with the clusters can be tuned from molecular adsorption to a superoxo-like state and finally to the highly activated peroxo-like state. The experimental results clearly show that this has drastic influences on the CO combustion on these clusters.

2.8. Coadsorption of water

Early on, there was evidence for an enhancement of the activity of small gold nanoparticles by moisture [53]. Thus, the influence of water on the chemical activity of free and supported Au cluster was recently investigated by DFT calculations [54]. For details

Table 2: Energies (in eV) for the adsorption and coadsorption of O_2 and H_2O on free (Au_8 and Au_{30}) clusters and on a gold octamer supported on MgO(1 0 0), that is Au_8/MgO.

	O_2	H_2O	H_2O–O_2
Au_8	Unbound	~0.3	0.4–0.9
Au_{30}	⩽0.4	0.3–0.6	0.7–0.9
Au_8/MgO-T	⩽0.1	0.2–0.3	0.5–1.2
Au_8/MgO-P	0.3–0.8	0.4–0.6	1.3–2.1

Note: In the case of the Au_8/MgO system, results are given for both the adsorption on the top facet of the gold cluster (-T) and at the peripheral interface of the cluster with the substrate (-P).

of the calculations the reader may refer to the original publication. At first, the effects of coadsorption of water with O_2 manifest itself in the binding energy, as shown in Table 2. The calculations show that O_2 does not bind to free uncharged Au_8 and the adsorption energy on various adsorption sites on Au_{30} does not exceed 0.4 eV. The binding energy of H_2O is 0.3 eV for Au_8 and up to 0.6 eV for the different adsorption sites on Au_{30}. Coadsorption of water together with O_2 allows for binding with a combined binding energy (Au_8–H_2O–O_2) of 0.4–0.9 eV; thus, the binding of the two molecules is enhanced by cooperative adsorption on the octamer, which is unique for small clusters.

A similar behavior can be observed for the gold octamer supported on a defect-free MgO surface. Here two spatial adsorption regions have been treated separately: (1) the adsorption on the top facet (Au_8/MgO-T) and (2) the adsorption on the peripheral site of the gold cluster (Au_8/MgO-P). While on the top facet, the O_2 is bound very weakly with less than 0.1 eV, the peripheral site allows a binding of the O_2 molecule with up to 0.8 eV. The binding energy of coadsorption of H_2O and O_2 ranges up to 1.2 eV in the top facet case and up to 2.1 eV in the peripheral case. It is especially noteworthy to point out that cooperative adsorption is responsible for the increase in total binding energy for the coadsorbed case. Here the O_2 and the H_2O preferentially adsorb on neighboring sites. Moreover, O_2 may bind even at sites where the adsorption of O_2 without coadsorbed H_2O is energetically not possible.

In some cases of H_2O and O_2 coadsorbed on the top facet of Au_8/MgO both molecules share a proton and the distance between the proton-sharing oxygen atoms of O_2 and H_2O has values down to 2.5 Å. The H–O_2 bond length is as small as 1.1 Å, meaning that the proton actually is transferred to the O_2 and an $OH\cdots HO_2$ species is formed. This is accompanied with an increase in the O–O distance to a value of ≈1.48 Å (21% larger than the respective gas-phase value). In addition, a charge of ≈0.31*e* is transferred from the Au_8/MgO to the coadsorbed species. In summary, the coadsorption of H_2O with O_2 stabilizes the partially charged, highly activated state of the oxygen molecule. This is not the case for the exclusive adsorption of O_2 on the top facet of the supported gold octamer.

In the vicinity of the peripheral interfacial sites of the Au cluster, the calculations showed that the adsorption energy of H_2O increases by 0.1–0.2 eV depending on the particular site and adsorption configuration; thus, the gold cluster acts as an attractor for adsorbed water (reverse spillover). Hence, at the interface between the Au cluster and the MgO surface, peripheral sites show a high propensity to bind both H_2O and O_2 (Table 2). The markedly larger binding energies of the coadsorbed complex (compared to the individual adsorbates) reflect a synergetic effect, expressed through the occurrence of the aforementioned proton sharing and proton transfer processes.

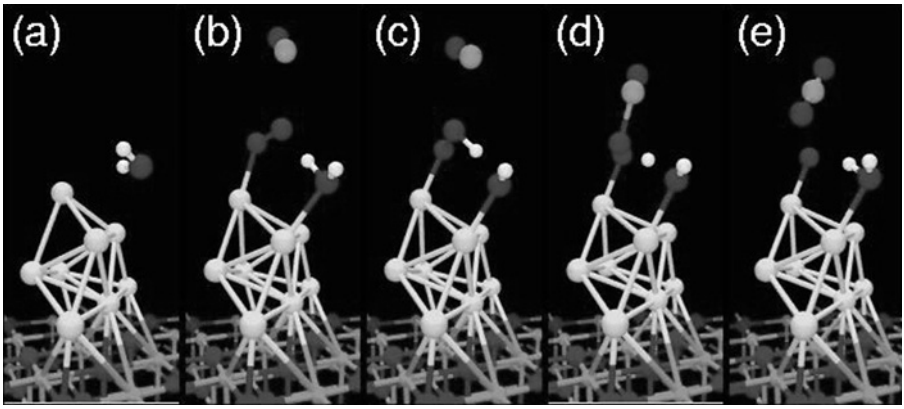

Figure 15: Relaxed atomic configurations displaying several stages in the simulation of the coadsorption of H_2O and O_2 on the top facet of an Au_8 cluster supported on MgO(1 0 0), and the subsequent reaction with gaseous CO to form CO_2. (a) The approach of an H_2O molecule to the cluster. (b) Coadsorbed H_2O (right) and O_2 (left) with an approaching CO. Note the preferential orientation of the H_2O and partial proton-sharing. (c) CO-induced proton transfer resulting in formation of a hydroperoxyl-like group (left) and a hydroxyl (right). (d) Transition state configuration with the CO binding to the activated species. The proton is about midway between one of the oxygen atoms of the transition-state complex (left) and the hydroxyl (right). (e) The proton shuttles back to re-form an adsorbed H_2O, and the CO_2 product desorbs from the surface, leaving an adsorbed oxygen atom that reacts in the next step with a CO molecule to yield a second CO_2.

A full adsorption and reaction cycle for the CO oxidation in the presence of H_2O is shown in Fig. 15, with the top facet as the reaction site. In the first step, H_2O is adsorbed on the bare supported Au_8 cluster (Fig. 16a). This is followed by adsorption of O_2 on a neighboring site. Fig. 16c shows the activated O_2 molecule, with the proton transferred to the oxygen. Subsequently, the CO is exposed to this highly activated configuration. Upon reaction of the CO molecule with the complex, the proton shuttles back toward the hydroxyl group (Fig. 8d), with the process culminating in the desorption of a CO_2 molecule and the re-formation of an adsorbed H_2O molecule that is preferentially oriented with respect to the remaining adsorbed oxygen atom (Fig. 8e). The above Eley–Rideal-like reaction mechanism involves relatively low barriers. It was found that the formation of the transition state (Fig. 8d) entails a readily accessible energy barrier of ~0.5 eV. An added CO molecule reacts readily (with a barrier of 0.1 eV) with the single adsorbed oxygen atom, and the (barrierless) desorption of the CO_2 product closes the catalytic cycle. For a peripherally adsorbed O_2 reacting with a CO molecule adsorbed in its vicinity, an LH reaction barrier of 0.4 eV was found (with or without a neighboring coadsorbed H_2O molecule). The barrier for desorption of the CO_2 product is 0.6 eV under dry conditions and 0.3 eV with coadsorbed H_2O.

3. THE CO CHEMISTRY OF SUPPORTED Pd_N CLUSTERS

In the following, the CO chemistry of supported Pd_N clusters is discussed based on the $CO + O_2$ oxidation reaction as well as on the $NO + CO$ reaction. The enormous attention these two reactions have drawn in the last decades is in part due to their

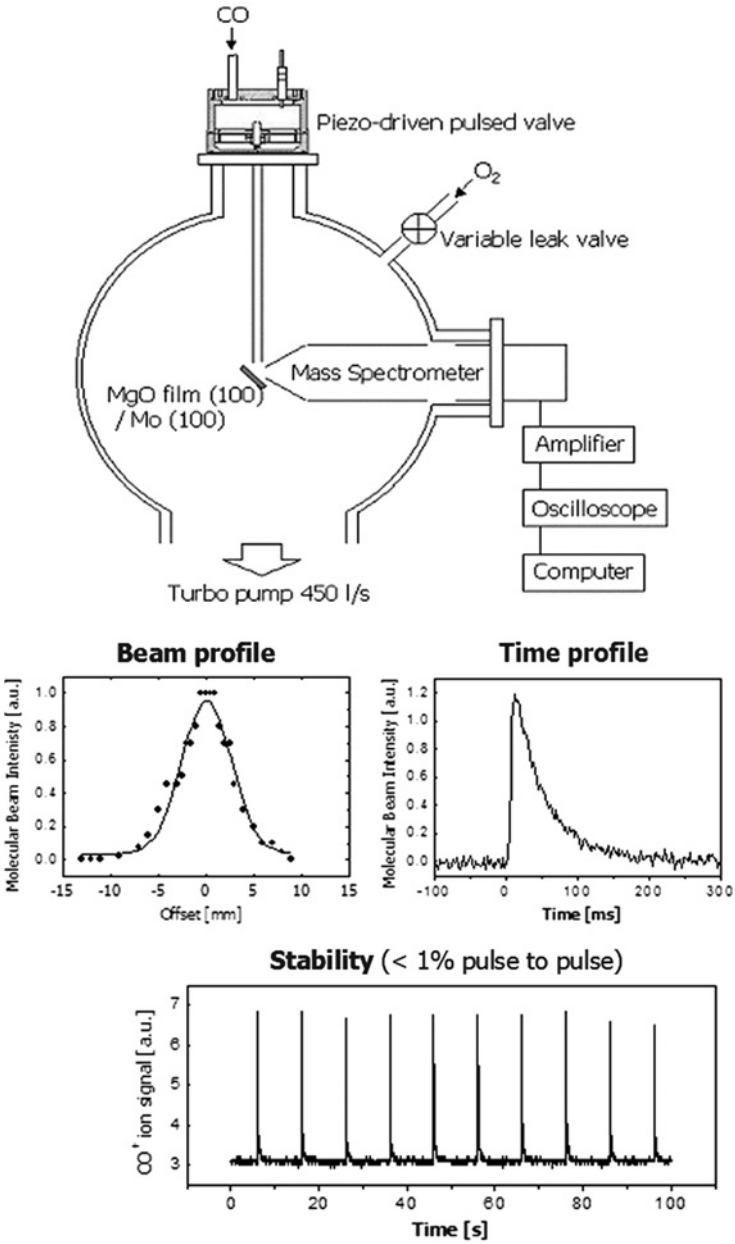

Figure 16: Experimental set-up for a pulsed molecular beam experiment for studying the catalytic properties of size-selected clusters on surfaces. It mainly consists of a pulsed valve for the generation of a pulsed molecular beam and a differentially pumped, absolutely calibrated quadrupole mass spectrometer. The length of the valve extension tube is adjusted to obtain a beam profile of similar dimensions as the sample under investigation. A typical time profile is also shown. It can be adjusted up to continuous operation.

industrial applications. For instance, in a commercial three-way automotive catalyst nitrous oxides NO_x and CO are removed by reduction/oxidation from the exhaust gases of an internal combustion engine. The active components of the catalyst are small platinum, rhodium as well as palladium particles. As discussed in the former section, the major role of the catalyst is thereby to weaken or break specific molecular bonds and to stabilize reactive intermediates [55], thus lowering the activation energies for the desired reactions. If the intermediates bind too strongly to the catalyst surface, the rates decline and eventually the intermediates poison the surface. This behavior leads to the so-called volcano curves when comparing the heats of formation of an intermediate in a specific reaction with the reaction rate for different elements [55], expressing that a good catalyst usually forms moderately strong bonds. In industrial catalysis, the overall catalytic reaction usually is the sum of several steps and not only the reaction rate (activity), but factors such as the stability of the particles and the selectivity of the reaction are crucial as well. The long-term stability of the catalyst, therefore, may be in conflict with its fluxionality, which, as shown for the example of supported gold clusters, may be decisive for its reactivity. As a result, applied catalysts are highly complex systems, and for example, 30 years after the first introduction of the automotive catalytic converter, it is still under development.

For this reason, often model catalysts are employed in order to disentangle different processes and to study single aspects of the complex properties of real catalysts in a well-defined and controlled manner. This field of research will be the focus of the next section. The $CO + O_2$ oxidation reaction and the $NO + CO$ reaction are especially attractive for such basic studies, since besides their applications they are considered to proceed through relative simple mechanisms, involving only a few steps. Furthermore, only diatomic molecules are part of the reaction. The exciting new field of supported cluster model catalysts thereby concentrates on the question of how the non-scalable change of the cluster properties with size alters the interaction with reacting molecules and thus may open new routes for designing tailor-made materials.

3.1. CO oxidation on Pd_N clusters supported on thin MgO films

As mentioned, the $CO + O_2$ reaction has been extensively studied on Pt-group metal model catalysts. Since it is beyond the scope of this chapter to give a complete overview about the existing literature, here we concentrate on a short summary of the most important results concerning the reaction mechanism and particle size effects, before we introduce studies of the non-scalable size regime. For the interested reader excellent reviews covering work on Pd single crystals [56] as well as oxide-supported Pd nanoparticles [57, 58] exist.

Since the pioneering work of Engel and Ertl [56] on Pd(1 1 1), it is well established for Pt-group metals that the CO oxidation reaction proceeds through an LH mechanism. In contrast to gold (see previous section), the adsorption of carbon monoxide is associative and reversible while oxygen chemisorption is dissociative and irreversible under the reaction conditions. Due to the strong interaction of carbon monoxide to palladium, an asymmetric behavior is observed in TPR measurements. That is, while pre-adsorbed CO inhibits the adsorption of oxygen, the reverse is not the case [56]. This observation is due to the ability of CO to compress pre-adsorbed oxygen layers. In such a compressed structure, the bond strengths of the adsorbates are lowered due to repulsive interactions, and consequently, different values are obtained for the LH

Table 3: LH activation energies of selected extended Pd surfaces and supported clusters.

Sample	E_{LH} (kJ/mol)	Conditions	Reference
Pd(1 1 1)	105	Low O_2 coverage, $T > 500$ K	[124]
	59	High O_2 coverage, $T < 420$ K	
Pd(1 1 1)	45–64	High O_2 coverage, $T < 500$ K	[60]
Pd[a] (27 nm)	32–45	High O_2 coverage, $T < 500$ K	[59]
Pd[b] (5–6 nm)	57 ± 8	CO rich regime, low T	[60]
	62 ± 9	O rich regime, low T	
Pd[a] (2.5 nm)	19–20	High O_2 coverage, $T < 500$ K	[59]
Pd_{30}[c]	36 ± 3	O saturated, $T < 400$ K	[63]
Pd_8[c]	25 ± 3	O saturated, $T < 400$ K	[63]

[a]On Al_2O_3 thin film.
[b]On Al_2O_3/NiAl(1 1 0).
[c]On MgO/Mo(1 0 0).

activation energy at low coverages (≈ 100 kJ/mol for Pd(1 1 1)) compared to high-coverage conditions (≈ 60 kJ/mol for Pd(1 1 1)) (see also Table 3) [56]. These processes outline the influence of coadsorbed molecules on the adsorption properties of reactants on the catalyst surface.

Compared to the relatively detailed understanding of the CO oxidation reaction on single crystals, less is known at the molecular level for supported Pd nanoparticles. Based on studies on different Pd single crystals, the CO oxidation reaction was considered to be insensitive to structure. Consequently, as discussed by Boudart et al. [58], the reaction rate should be independent of the size of supported Pd particles. However, Stara et al. [59] reported significant size effects by studying the transient CO_2 formation on Pd nanoparticles supported on Al_2O_3. Whereas LH activation energy determined for 2.5 nm sized Pd nanoparticles was ≈ 20 kJ/mol, for particles of 27 nm in diameter it was 30–45 kJ/mol [58]. Such significant effects, however, are not observed in recent work of Meusel et al. [60] on the same model systems. They found similar LH activation energies for 5–6 nm Pd particles and Pd(1 1 1), i.e., around 60 kJ/mol depending on the reaction conditions (see Table 3).

3.2. Molecular beam techniques

Before discussing the results obtained on supported Pd clusters, it is worth noting that an important experimental tool for such measurements on model catalysts proved to be the use of molecular beam techniques (e.g., molecular beam reactive scattering (MBRS)). While in the preceding section concerning the CO oxidation on supported gold clusters the catalytic properties were determined by comparing one-cycle TPR and FTIR experiments with ab initio calculations, most investigations on Pd clusters were performed by utilizing isothermal, transient molecular beams generated by piezoelectric-driven pulsed valves. Compared to TPR, the use of MBRS offers more realistic reaction conditions since the reactions take place at a constant temperature and multiple reaction cycles can be studied [57]. The latter aspect is especially important for catalytic reactions on small clusters, as it proves that the clusters are stable under reaction conditions (see below) [61]. Furthermore, in MBRS, reactions can be studied under steady-state as well as under transient conditions. The experimental set-up for pulsed MBRS used in the presented studies is shown in Fig. 16 [61]. As can be seen, the deposited clusters are exposed to the reactant gases (CO and O_2) by

two kinds of valves. A constant isotropic O_2 pressure is induced by a commercial variable leak valve, while the transient CO beam is generated by the home-made pulsed valve. The reaction products coming off the sample are detected by an absolutely calibrated quadrupole-mass spectrometer. A stainless steel tube attached to the pulsed nozzle collimates the molecular beam and guarantees that only the sample is exposed to the beam, thus minimizing the pressure increase in the UHV-chamber during the experiment. The pulse frequency and duration can be varied over a wide range; typical values are 0.1 Hz and a pulse width of 100 msec (resulting in a maximal effective pressure of 1×10^{-4} mbar at the surface). The excellent pulse-to-pulse stability, the beam profile, and the transient beam intensity at the sample position are shown in Fig. 16. Information on different set-ups for studying supported model catalysts by molecular beams, especially in combination with other experimental tools, such as FTIR spectroscopy, can be found in a recent review by Libuda and Freund [57].

The difference between the results obtained in TPR and MBRS experiments is exemplified in Fig. 17 for the CO oxidation of supported Pd atoms. Although Pd atoms form CO_2 in a one-heating cycle of a TPR experiment at around 280 K as depicted in the inset of Fig. 17b, no significant CO_2 signal is observed in pulsed MBRS experiments at the same temperature. In the pulsed MBRS measurements, the maximum reaction rate is observed around 450–500 K, where considerable amounts of CO_2 are formed on the surface (Fig. 17). There are two reasons for this observation: (1) in the TPR experiments the coverage of the reactants changes during the course of the measurement and (2) supported Pd atoms are not stable at 300 K after CO_2 formation and form larger clusters during the reaction. The second conclusion can be inferred from FTIR studies where the absorption bands of the probe molecule CO adsorbed on Pd atoms were monitored during the CO oxidation, i.e., with increasing temperature (Fig. 18). At 90 K for CO saturation coverage, a main absorption band between 2045 and 2005 cm^{-1} (Fig. 18a) is attributed to two on-top-bound CO molecules on the Pd atoms (Fig. 18b). In the presence of O_2, the high-frequency CO is efficiently oxidized as observed by the decrease of the corresponding band in the temperature range 180–250 K. At a temperature of 300 K, a new band at 1830 cm^{-1} grows in (Fig. 18a), which can be attributed to bridge-bonded CO. This binding mode, however, is only possible when larger clusters are formed via coalescence. In fact, the whole process has been described with ab initio calculations as well [62]: the low-temperature mechanism observed in the one-heating cycle experiment involves the perpendicularly bonded CO and a molecularly bonded, highly activated O_2 on the atom–substrate interface (Fig. 18b). Once the temperature of 300 K is reached and the first reaction cycle takes place, the trapped Pd atoms start to migrate and coalesce to larger clusters. This sudden migration is caused by the filling of the trapping center (oxygen vacancy) of the atom by the remaining oxygen atom after the formation of one CO_2 molecule, which strongly reduces the binding energy of the Pd atom with the substrate. Accepting this mechanism, it becomes evident that the catalytic formation at temperatures larger than 400 K and measured by pulsed molecular beams originates from larger Pd clusters. Thus, single Pd atoms do not withstand the first reaction cycle. As this example shows, studying catalysis on cluster model systems, TPR/FTIR and MBRS experiments can give complementary information on the reactivity and stability of the system.

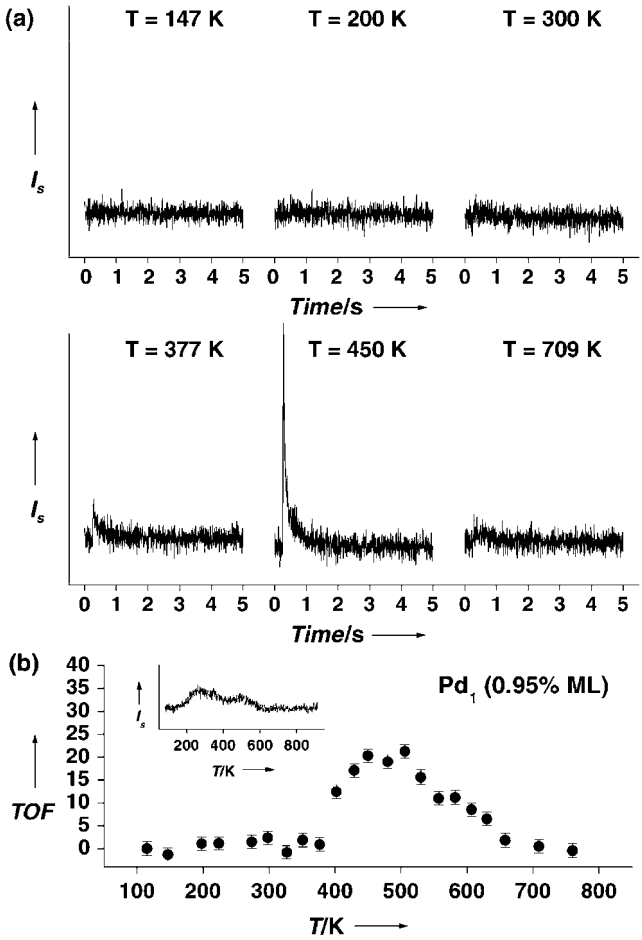

Figure 17: CO_2 transients for representative temperatures obtained in MBRS experiments on Pd_1/MgO (1 0 0) model catalysts at an isotropic pressure of O_2 of 5×10^{-7} mbar and an effective pressure of CO of 1×10^{-4} mbar. (b) Evolution of the absolute TOF as a function of temperature. The inset shows the CO_2 formation obtained by a one-heating cycle TPR experiment.

3.3. Activation energies

In the following we concentrate on the properties of stable Pd_N ($N = 8$ and 30) clusters studied by pulsed MBRS [63]. CO_2 transients obtained for Pd_8 (0.65% monolayer (ML)) soft-landed onto a well-defined MgO(1 0 0) thin oxide film are displayed in Fig. 19 for selected temperatures. Below 300 K no significant CO_2 evolution is observed, whereas with increasing temperature a CO_2 signal arises, reaching a maximum at around 450 K, before decreasing again at higher temperatures. At 709 K, CO_2 production is no longer observed. The transients are averaged over 30 cycles, showing that indeed Pd particles are stable under reaction conditions. Interestingly, in addition to the main peak, a small delayed contribution to the CO_2 formation is observed at 351 K between 1 and 2 sec (see enlarged transients in Fig. 19a). The delay time decreases with temperature, and at 450 K, the second peak merges with the main

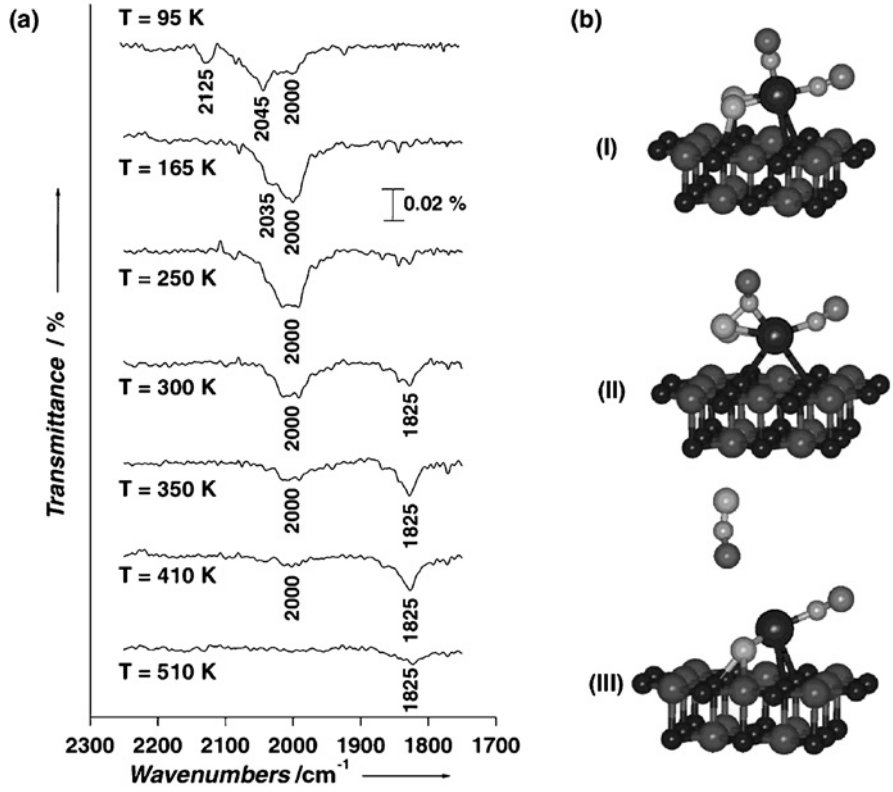

Figure 18: (a) Temperature-dependent CO absorption bands during the CO-oxidation on $Pd_1/MgO(1\,0\,0)$ model catalysts. In these experiments, the samples were annealed to the indicated temperatures and the IR spectra were recorded at 90 K. (b) Reaction mechanism of the CO-oxidation on a single Pd atom adsorbed on an F center, obtained by ab initio calculations (see text).

peak. Such a delayed contribution is also observed in MBRS investigations on supported Pd nanoparticles [58, 64–66]. Its origin can be explained by the competitive adsorption of the two reactants, CO and O_2. In the pulsed molecular beam experiments, upon opening the valve, the cluster experiences a high CO partial pressure, which rapidly decreases after closing the valve since at that moment CO is only supplied by diffusion from the substrate (see below). Consequently, the delayed CO_2 formation disappears at temperatures above 450 K, where CO readily desorbs from the substrate (see Fig. 19) and becomes enhanced by increasing the O_2 background pressure up to 2×10^{-6} mbar. This is due to the fact that the oxygen supply is the limiting factor.

Based on the change of produced CO_2 molecules with time, the reactivity of the clusters can be expressed as maximum turnover frequencies (TOF), calculated by dividing the maximum of the absolutely calibrated CO_2 signal by the number of deposited Pd atoms (Fig. 19). By this, three temperature regimes can be distinguished for the reactivity of Pd clusters for the CO oxidation reaction. The first temperature regime spans from 300 to about 350 K and is characterized by a rapid increase in the reaction rate with temperature. In this region, the apparent LH activation energy is

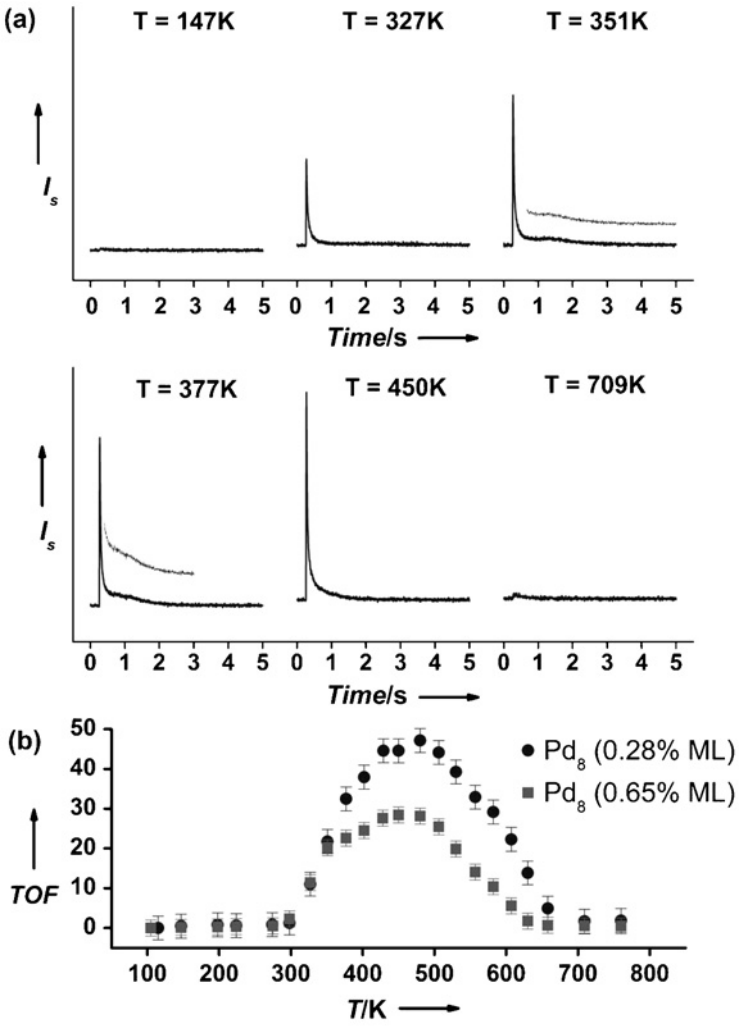

Figure 19: (a) CO_2 transients for representative temperatures obtained for $Pd_8/MgO(1\,0\,0)/Mo(1\,0\,0)$ model catalysts. The insets represent the enlarged transients. (b) Evolution of the maximum TOF as a function of temperature.

determined. For the Pd_8 system, a value of 25.3 ± 2.5 kJ/mol is obtained, compared to 36.5 ± 3.2 kJ/mol on supported Pd_{30} clusters under the same experimental conditions (Figs. 19 and 20), indicating size-dependent catalytic properties of supported Pd clusters. The LH activation energies for Pd nanoparticles are in a similar range (see Table 3), but no obvious correlation is seen by comparing supported Pd clusters and Pd nanoparticles. It is worth noting, however, that the apparent activation energies for the size-selected clusters are independent of the cluster coverage as can be seen by the same initial slope of the TOF with increasing temperature (Figs. 19 and 20). In this temperature region, the TOF is influenced only by the intrinsic properties of the specific cluster size since the total CO flux (see below) is constant.

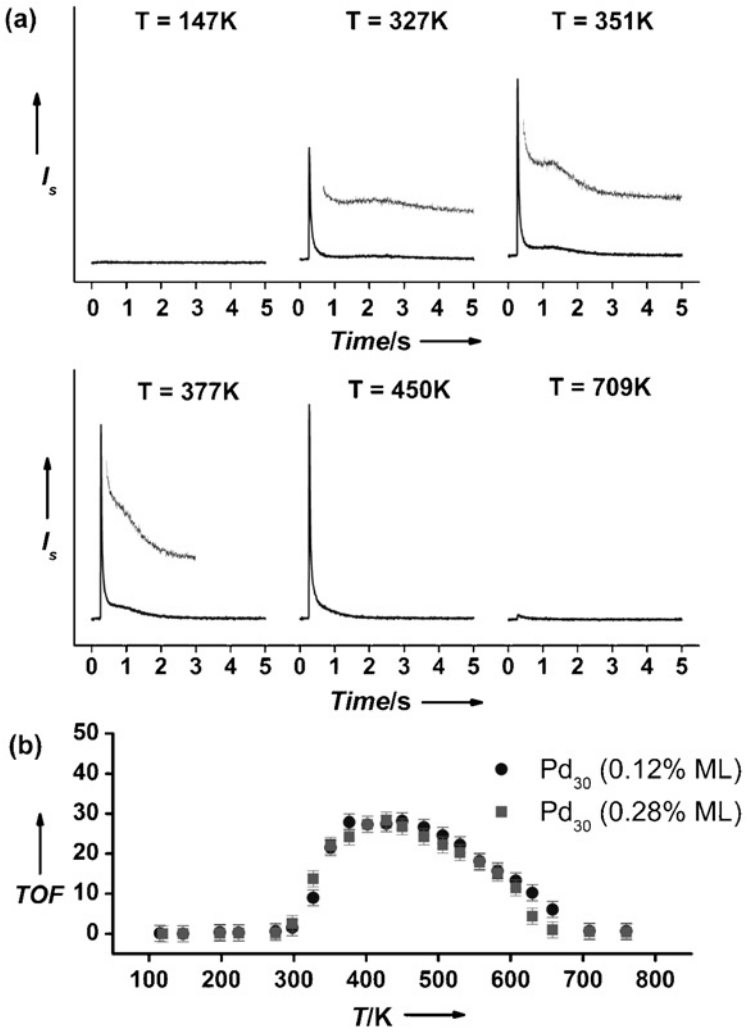

Figure 20: (a) CO_2 transients for representative temperatures obtained for Pd_{30}/MgO(1 0 0)/Mo(1 0 0) model catalysts. The insets represent the enlarged transients. (b) The evolution of the maximum TOF as a function of temperature.

3.4. Size effects

In contrast to the first temperature regime, a clear dependence of the cluster coverage on the reaction rate is observed in the second temperature regime, i.e., between $\approx$350 and $\approx$500 K and in the third temperature region above 500 K. Note that the third temperature region which is characterized by decreasing reaction rates with temperature due to possible cluster diffusion and agglomeration is not analyzed further. For the second regime, the temperature-dependent TOF of the CO oxidation reaction on Pd_8 and Pd_{30} are compared for two different coverages with identical covered surface areas of the support (see Figs. 19 and 20, respectively). This was possible due to the ability to vary the cluster coverage independently of the cluster size, which is an

important characteristic of size-selected cluster deposition and is in contrast to particles prepared by metal vapor deposition. As can be seen, quite a different dependence from the cluster coverage is observed, manifesting a clear cluster size effect. In detail, the obtained TOF for the Pd_8 system are ≈ 47 (CO_2/Pd atom $\times$ sec) at 480 K for 0.28% ML coverage and ≈ 28 (CO_2/Pd atom $\times$ sec) at 450 K for 0.65% ML, respectively [63]. For the Pd_{30} system (Fig. 20), the maximal TOF was about 28 (CO_2/Pd atom $\times$ sec) for both coverages (0.12% and 0.28% ML). More important than the absolute values of the TOF is their dependence on the cluster coverage and the particle size. This is due to the fact that the absolute values of the TOF depend on the experimental conditions, e.g., the effective pressure of reactants on the surface. This becomes clear when comparing the TOF obtained for the clusters to values obtained for Pd nanoparticles supported on MgO(1 0 0) given in the literature [64, 67]. For example, TOF of 0.12 are obtained for Pd particles in the range of 2.8–13 nm in diameter measured in molecular beam experiments under steady-state conditions. However, at higher pressures (Pd nanoparticles supported on SiO_2) values of 20–2000 were obtained.

An influence of the particle size on the reaction rate was also observed for Pd nanoparticles supported on MgO(1 0 0) by Henry et al. [64, 68]. By applying the so-called collection zone model, however, they concluded that the strong dependence on particle size and density is mainly due to the effect of the reverse spillover, i.e., the CO diffusion from the support to the particles. The basic idea of the collection zone model is displayed in Fig. 21. In short, CO molecules impinging on the surface can either be (1) adsorbed directly on the catalyst particle (direct flux, F_{dir}), (2) be reflected from, or (3) adsorbed on the substrate (diffusion flux, F_{diff}). For the latter it is assumed that all molecules will be captured by the catalyst particles by surface diffusion, which are adsorbed within the collection zone circularly surrounding the particle. This collection area is defined by the mean diffusion length of the CO molecule on MgO, which is a function of the residence time, the cluster size, and the cluster coverage. The diffusion area is maximal at low temperature, small cluster sizes, and low cluster coverage.

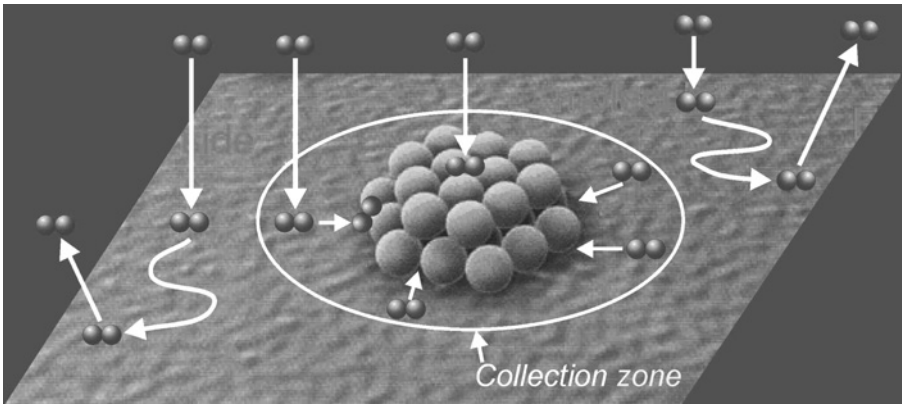

Figure 21: Collection zone model incorporates the diffusion flux onto a cluster beside the direct flux impinging directly from the gas phase. The amount of diffusive molecules reaching a cluster is defined through the collection zone, which is described by the mean diffusion length of the molecule on the support at the specific temperature.

Thus, by increasing the temperature, the cluster size, and/or the cluster coverage, the collection area will decrease. Under the boundary condition of overlapping adjacent zones, the total molecular flux to the catalyst particle (F_{tot}) is calculated by the impinging flux J_i and the so-called global sticking coefficient α_g:

$$F_{tot} = F_{dir} + F_{diff} = \alpha_g J_i \tag{4}$$

This equation is obtained from a solution of the differential diffusion equation and the cluster surface cross-section. For further details on the collection zone model see Refs. [58, 69].

From a fundamental point of view, it is therefore more appropriate to compare reaction probabilities (under identical conditions) rather than the different TOF. The reaction probability (RP) is given by $RP = TOF/F_{tot}$, defining the probability of transforming an impinging CO molecule, delivered either by direct or by diffusion flux (F_{diff}), into the product molecule CO_2. The reaction probabilities for the CO oxidation on Pd clusters obtained by applying the collection zone model are displayed in Fig. 22 [63]. As for the TOF, the properties of Pd_8 and Pd_{30} show a distinctively different behavior. While for both coverages of Pd_8 the RP is approximately the same, for Pd_{30} it clearly depends on the cluster coverage. As mentioned, the ratio of F_{diff}/F_{dir} is temperature dependent and it is higher for low cluster coverages, revealing an increased diffusion flux (insets in Fig. 22). As can be seen, a high diffusion flux results in a diminished reaction probability for Pd_{30}. This means that the conversion of CO to CO_2 is significantly less efficient for the CO molecules diffusing from the substrate than for CO molecules directly impinging from the gas phase onto the cluster. In the case of Pd_8, a higher efficiency of the diffusion flux is deduced compared to Pd_{30}. For this behavior two scenarios are possible: either the reaction takes place on the cluster or at the particle–support interface. In this case both pathways would have similar activation energies. Alternatively, only a small barrier for CO diffusion from the substrate onto the cluster exists. Unfortunately, these two scenarios cannot be distinguished by experimental means and additional information is required from ab initio DFT calculations. Recently, however, Huber et al. performed DFT calculations for the CO oxidation on Pd_N ($N = 4$–9) clusters [70]. They found that magnesia-supported Pd clusters form crystalline Pd_xO_y clusters upon reaction with oxygen. When exposing CO to the Pd_9O_y/MgO system, they observed different energy barriers for different reaction channels. The diffusion barriers of CO on the cluster, however, are low, preventing the experimental discrimination of the two reaction mechanisms.

3.5. NO reduction by CO on Pd single crystals and supported Pd nanoparticles: a short summary

As the CO oxidation reaction, the $NO + CO \rightarrow \frac{1}{2}N_2 + CO_2$ reaction has been extensively investigated on Pd single crystals as well as on supported nanoparticles [71–84]; only a short summary is given here. For our discussion, the most important result from single crystal studies is the structure sensitivity of the reaction. As the first step of the reaction, the adsorption of NO was investigated. It was found that while NO is molecularly adsorbed on the close-packed Pd(1 1 1) surface up to elevated temperatures, on more open surfaces NO readily dissociates upon adsorption. Somewhat surprisingly, however, the activity for NO reduction by coadsorbed CO increases in the order Pd(1 0 0) < Pd(1 1 0) < Pd(1 1 1) [78, 82, 83]. These results were explained by

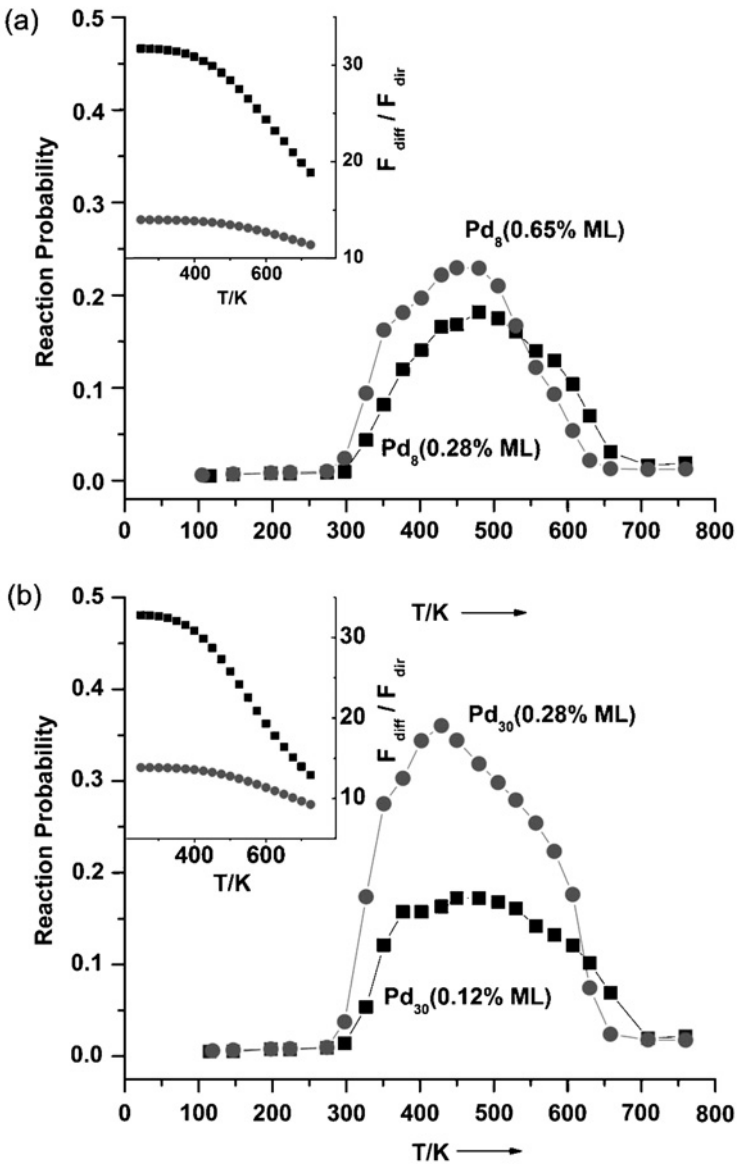

Figure 22: The reaction probabilities as a function of temperature for different surface coverages of the Pd_8 (a) and Pd_{30} (b) clusters. The insets depict the calculated ratio of F_{diff}/F_{dir} as a function of temperature.

the formation of a strongly bound nitrogen species upon dissociation, which effectively blocks the active sites and thus poisons open surfaces. Henry et al. systematically studied the NO + CO reaction on Pd nanoparticles supported on MgO(1 0 0) using MBRS. The main reaction product found was N_2, with only a small fraction of N_2O being formed. NO reduction was observed only at temperatures where NO dissociates upon adsorption and it was concluded that NO reduction exclusively occurs via dissociative NO adsorption. Two different types of adsorbed nitrogen atoms, N(a), were

proposed, with one type being more strongly bound to the surface than the other one. The more strongly bound N(a) poisons the active sites of the particle surface. Furthermore, it was found that the efficiency of the CO_2 formation depends on the structure and thus the size of Pd nanoparticles. Taking into account the capture zone effect (note that by metal vapor deposition the size of nanoparticles cannot be varied independently of the coverage), the authors concluded in accordance with the single crystal studies that particles with the highest density of close-packed facets are the most active.

3.6. NO reduction by CO on supported Pd_N clusters

The NO reduction by CO was studied on Pd_N clusters supported on thin MgO (1 0 0) films for $N<30$. As for the CO oxidation reaction utilizing pulsed molecular beams, it was shown that small Pd clusters indeed remain active during multiple (>100) catalytic cycles. In these experiments, molecular nitric oxide was pulsed onto the supported Pd clusters, whereas CO was introduced as a background pressure. The product molecules CO_2 and N_2 were detected as a function of cluster size, temperature, and CO background pressure. The catalytic formation of CO_2 on Pd_{30} and Pd_8 is shown in Fig. 23a and b for selected temperatures. CO was dosed at a partial pressure of 5×10^{-7} mbar, whereas NO was pulsed at the time $t = 0$ effecting a partial pressure

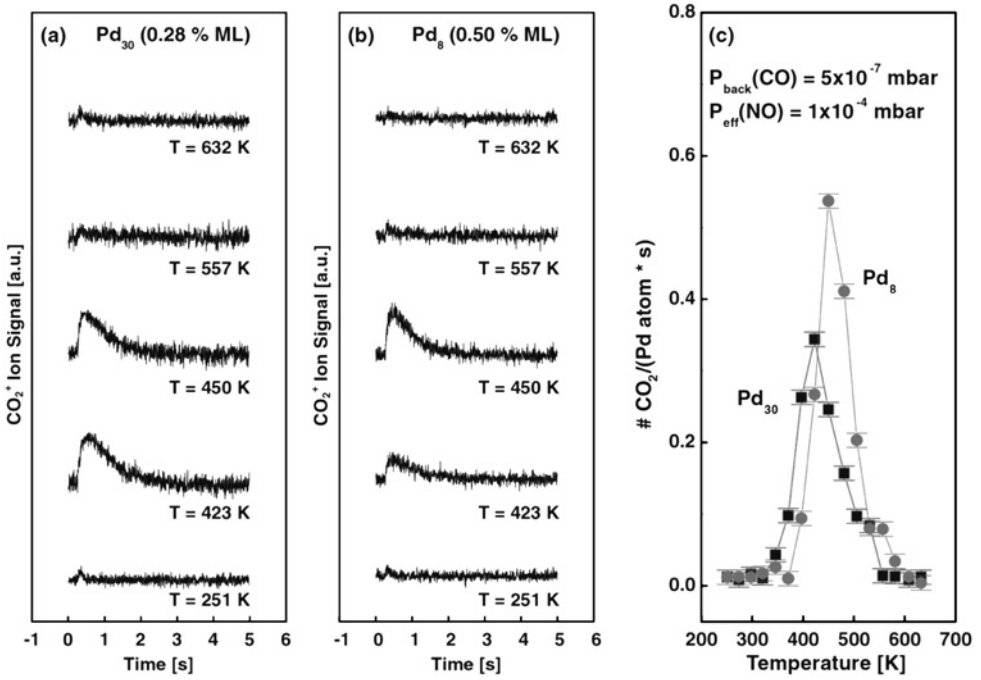

Figure 23: Transient CO_2 formation at selected temperatures measured in a pulsed molecular beam experiment on (a) Pd_{30} and (b) Pd_8. CO was dosed at an isotropic CO pressure of 5×10^{-7} mbar, whereas at the time $t = 0$ NO was pulsed effecting a partial pressure of 1×10^{-4} mbar. (c) Number of CO_2 molecules produced divided by the number of deposited Pd atoms times the pulse width (0.1 sec) plotted as a function of temperature.

of 1×10^{-4} mbar. The pulse duration was 0.1 sec. In Fig. 23c, the catalytic activity for both cluster sizes is summarized by plotting the number of produced CO_2 molecules per Pd atom divided by the pulse width as a function of temperature. As can be seen, for both cluster sizes, Pd_8 and Pd_{30}, up to a temperature of about 390 K almost no catalytic reactivity is observed. On Pd_{30} CO_2 formation starts at a temperature approximately 30 K lower than that for Pd_8; however, Pd_{30} is less reactive based on the maximum reactivity, which is 0.34 CO_2/atom × sec at 420 K and 0.54 CO_2/atom × sec at 450 K for Pd_{30} and Pd_8, respectively. As expected, at higher temperatures the formation of CO_2 decreases for both cluster sizes. Interestingly, Pd_4 (not shown) shows no measurable catalytic reactivity under any of these experimental conditions. In order to attribute these differences in catalytic activity to intrinsic electronic properties of the respective cluster size (quantum size effects), one has to assure that they cannot be explained by purely geometric effects, i.e., the size-dependent difference of the surface to bulk ratio of the Pd atoms of the respective clusters. For Pd_{30}, the exact ratio of surface to bulk atoms is not known, but we can estimate it based on a truncated octahedron of order 1, which contains 38 atoms. For such a configuration, the surface is composed of 32 atoms, representing 84% of the total number of atoms, whereas for Pd_8 all atoms are surface atoms. Thus, for a pure geometric effect, an increase in reactivity of about $\approx$19% would be expected when comparing Pd_8 with Pd_{30}. This is significantly smaller than the experimentally observed increase in reactivity by $\approx$59%, and the difference in catalytic activity between Pd_8 and Pd_{30} can be attributed in part to the size-dependent electronic properties of small supported clusters. This conclusion is supported by the fact that the catalytic activity of the clusters reaches its maximum at temperatures that are about 100 K lower than those for supported palladium nanoparticles [71, 72, 85]. Although care has to be taken when comparing data obtained under different experimental conditions (e.g., the reaction temperatures depend on the partial pressures of the reactant), this interesting trend is also observed in independent TPR experiments [86]. The influence of the mole fraction of the reactants, i.e., NO and CO, on the reactivity of supported Pd clusters was studied in a separate set of experiments. From Pd nanoparticles it is known that a shallow reactivity maximum is reached at a 0.5 mole fraction of the two reactants. Since with only one molecular beam it is not feasible to adjust a fixed mole fraction, the catalytic reactivity was measured for both cluster sizes at the optimum temperature as a function of increasing CO background pressure (see Fig. 24). As expected from the fact that at the time of the NO pulse, the CO mole fraction is always $\ll 0.5$, the reactivity increases with the CO background pressure showing that these experimental conditions are far from the optimum. Interestingly, for Pd_8 (Fig. 24a) as well as for Pd_{30} (Fig. 24b), the peak width of the CO_2 transients decreases with increasing isotropic CO pressure. Similar to the delayed peak in the CO oxidation experiment, this finding can be understood based on the competitive adsorption of the two reactants, i.e., on increasing the isotropic CO pressure, the NO molecules are replaced more efficiently on the cluster surface and the reaction can then take place. Thus, the reaction probability increases and narrower transients are observed.

3.7. Low-temperature catalysis: the reaction mechanism

In the following, the low-temperature reaction mechanism for NO reduction is discussed based on Pd_{30} clusters supported on MgO. As shown in the combined FTIR

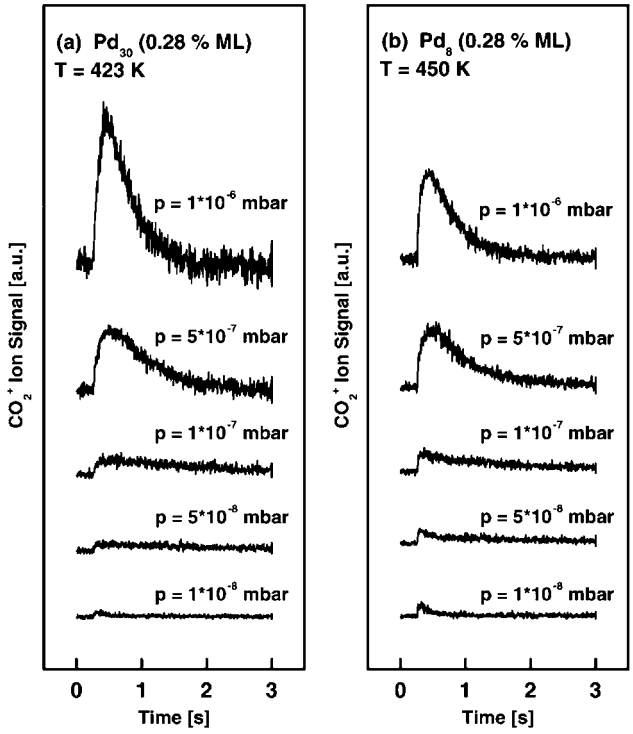

Figure 24: CO_2 formation measured in a pulsed molecular beam experiment as a function of the isotropic CO pressure (indicated in the figure) for (a) Pd_{30} and (b) Pd_8 supported on a thin MgO(1 0 0) film. The temperature was 423 and 450 K, respectively. NO was pulsed for 0.1 sec, resulting in an effective partial pressure of 1×10^{-4} mbar.

and TPR studies displayed in Fig. 25, the reactivity strongly depends on the reaction conditions, i.e., which of the two reactant gases was dosed first. Whereas bare MgO films are inert for this reaction (Fig. 25c), two CO_2 peaks are observed in the TPR spectrum for CO-rich conditions (CO dosed before NO), i.e., a small one at 145 K and the main peak at around 300 K. Note that N_2 is produced as a broad peak centered at around 450 K (not shown). The latter CO_2 peak is observed for all reactive cluster sizes Pd_N ($N > 4$), and is due to the reaction of molecularly adsorbed CO and an adsorbed oxygen atom resulting from the dissociation of NO [86]. This conclusion is supported by the presence of a strong CO absorption band at 2055 cm^{-1} (Fig. 25a, inset) and the fact that NO dissociates on the clusters (formation of N_2). The same reaction mechanism is also observed in the pulsed MBRS experiments. By contrast, the low-temperature mechanism observed at 145 K for Pd_{20}–Pd_{30} only [86, 87] has no corresponding CO_2 feature in the pulsed MBRS experiments and therefore is not relevant for continuous catalytic action. Nevertheless, the reaction mechanism is worth discussing, as it is unique to Pd clusters of a specific size. Also, such a low-temperature mechanism is not observed on Pd nanoparticles. The FTIR spectra indicate that the corresponding reaction mechanism can be ascribed to the direct reaction of molecularly bonded CO with an absorption band at 2055 cm^{-1} and a

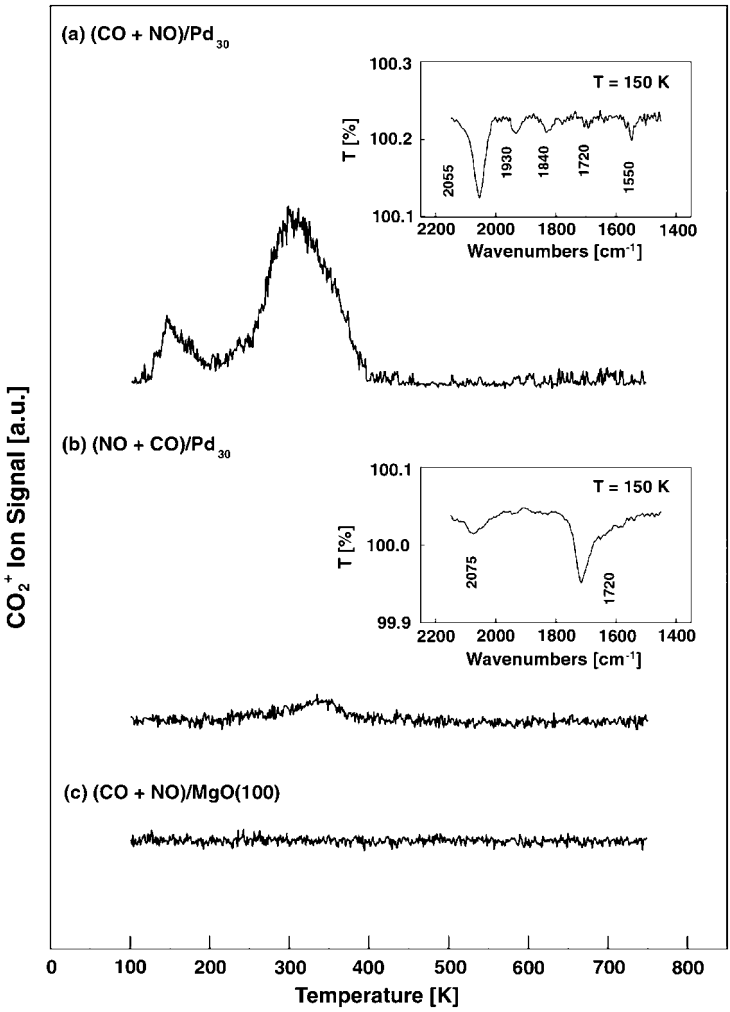

Figure 25: CO_2 formation on Pd_{30} deposited on a thin Mg(1 0 0) film obtained by a TPR experiment. (a) TPR spectra obtained if CO is dosed prior to NO. (b) TPR spectra obtained for the case if NO is dosed prior to CO. (c) TPR spectra for the bare MgO film (CO is predosed). The insets show the FTIR spectra for the corresponding conditions recorded at 150 K.

threefold-bound NO with an absorption band at 1550 cm^{-1} (Fig. 25a, inset) [88]. By contrast, under NO-rich conditions, the formation of CO_2 is largely inhibited (Fig. 25b), as the cluster is poisoned mainly by molecularly adsorbed NO with an absorption band at 1720 cm^{-1} (Fig. 25b, inset). Interestingly, the behavior of Pd_{30} clusters is much more similar to that of a Pd(1 1 1) surface than it is to Pd particles in the nanometer size range. In TPR experiments on Pd nanoparticles, nitrogen recombination is observed at 500 and 680 K, which is 50–230 K higher compared to the cluster model catalysts [80]. By contrast, on Pd(1 1 1) the high-temperature peak is almost absent and even disappears when the reactants are dosed at low temperature (as in the cluster TPR experiments). As discussed above, it was concluded that the

reactivity of Pd depends on the formation of a strongly bound N species upon dissociation of NO, which at steady-state conditions poisons the catalyst. The similarity between Pd(1 1 1) is also found in FTIR spectra. NO adsorbed on Pd(1 1 1) shows two bands near 1560 cm^{-1} (main peak above RT) and 1740 cm^{-1} (main peak below RT) corresponding to threefold and bridge sites, respectively. On Pd_{30} a strong absorption is observed at 1725 cm^{-1} at low temperature, while above RT an absorption band appears near 1590 cm^{-1}. By comparison, on Pd(1 0 0), NO gives only one absorption band that shifts from 1630 to 1672 cm^{-1} when the temperature decreases from 500 to 100 K. However, there are distinct differences between Pd_{30} and Pd(1 1 1). First, in TPR experiments, the low-temperature CO_2 peak at 145 K is observed on Pd_{30} but not on Pd(1 1 1). Furthermore, desorption of CO and NO from the small clusters is observed at much lower temperatures in comparison to the Pd(1 1 1) surface (Pd_{30}: $\approx$300 K for CO and 370 K for NO). This may either indicate smaller intrinsic binding energies of these molecules with the cluster or higher local densities of the adsorbates, where a larger repulsion leads to lower desorption temperatures. In addition, the energy of formation of N_2 on the cluster is distinctly smaller than that on extended surfaces and nanoparticles with crystalline facets. This may be due to a decreased interaction of atomic nitrogen atoms with the clusters and/or an increased dissociation probability of NO resulting in high local N_{ad} densities and a concomitant strong repulsion favoring N_2 formation. Thus, for small clusters poisoning through N_{ad} is neutralized at distinctly lower temperatures in comparison to surfaces of bulk palladium.

4. THE POLYMERIZATION OF ACETYLENE ON SUPPORTED CLUSTERS

One specific reaction of the polymerization of acetylene on palladium, the cyclotrimerization, is shown to occur only on an ensemble of at least seven atoms in the case of Pd(1 1 1) single crystals [89]. This indicates that this class of reaction is strongly dependent on the structure even for bulk materials. In the gas phase it has already been shown that atomic metal ions reveal a very interesting chemistry with respect to hydrocarbons (e.g., see in the reviews by Schwarz and Schröder [90, 91]). As an example, Kaldor and co-workers have studied palladium and platinum clusters interacting with a series of alkanes and aromatics [92–94]. In the case of CH_4 on Pt_N with up to $N = 24$ atoms, activation was realized for the first time on an unsupported metal cluster, and the reaction had a distinct cluster size dependence, with Pt_2 to Pt_5 being the most reactive. Charged $Pt_N^{+/-}$ clusters ($N = 1$–9) react with subsequent elimination of molecular hydrogen H_2, to form the final metal carbene complex $Pt_N^{+/-}CH_2$ [95]. In general, the cation cluster reactions were found to proceed more than one order of magnitude faster than the anionic cluster reactions. The platinum tetramer anion is unique in this respect, reacting more efficiently than the corresponding cation. Indications for a correlation of reactivity with the availability of low-coordination metal atoms were discussed by Trevor et al. [94]. Thus, it was speculated that low-coordination metal atoms activate CH_4 more readily than close-packed metal surface atoms [96]. The propensity of small Pd clusters to activate methane in a similar manner was also confirmed theoretically [97–99]. This indicates that in contrast to bulk materials already very small, free clusters in the non-scalable size regime reveal rich hydrocarbon chemistry. Indeed, we show in this section that already one metal

atom may be enough to catalyze the cyclotrimerization reaction of acetylene. Whether the reaction finally occurs or not depends not only on the type of atom or the support material and their defects, but also on the dynamics of the atom on the support. Further studies on small clusters revealed the possibility for tuning the branching ratio of the polymerization simply by changing the cluster size.

4.1. The trimerization reaction on single atoms

In contrast to both, Pd(1 1 1) [89], where an ensemble of seven atoms is needed for the reaction to occur, and solid Rh surfaces, which are inert, single Pd as well as single Rh atoms catalyze the cyclotrimerization reaction. In TPR experiments benzene is formed and desorbs at 300 and 430 K, respectively (Fig. 26). Furthermore, the reaction is very selective as no other product molecules of the polymerization reaction (e.g., C_4H_6, C_4H_8) are observed. However, similar to the bulk, single Ag atoms are found to hardly yield any benzene product (Fig. 26).

The electronic configurations of the various atoms and their change upon interaction with the support is one key factor for the element-specific reactivity [86]. Free Ag atoms do not adsorb C_2H_2 due to the presence of the partially filled 5 s level. This orbital does not hybridize with the filled 4d shell. As it is spatially expanded, it gives rise to a strong Pauli repulsion with the electronic states of the reactant in the entrance channel; thus, the reaction is not possible. A free Pd atom ($4d^{10}$) readily adsorbs two C_2H_2 molecules by an average binding energy of 1.35 eV/molecule and transforms them into the C_4H_4 intermediate with an energy gain of 3.9 eV. A third acetylene molecule, however, is only weakly bound and practically not activated. Therefore, a free Pd atom is also inert for the cyclotrimerization reaction. With the open d-shell configuration, however, Rh atoms become reactive and produce benzene at very low temperatures. The first two acetylene molecules adsorb with an energy gain of 1.57 and 1.23 eV, respectively, and transform with a very small barrier (0.04 eV) and an energy gain of 0.86 eV into the metallopentacycle, Rh(C_4H_4). The third acetylene molecule is readily adsorbed (0.76 eV) and activated as shown by a change from sp- to partly sp^2-hybridization. Finally, benzene is formed with a low barrier (0.24 eV) and an energy release of 2.1 eV.

Upon interaction with the MgO support there may be subtle changes in the electronic structure of the atoms, which can result in different reactivities. For Ag atoms, however, these changes are minor and Ag atoms remain inert when adsorbed on the oxide surface (Fig. 26). This is also confirmed theoretically. In fact, it is found that activation of Ag atoms would require depopulation of the 5 s orbital, which is not possible on basic oxides like MgO. Thus, the Ag/MgO(F) complex shows no ability to bind acetylene. In contrast to the inert character of Ag atoms, single Pd atoms are turned into active species when deposited on MgO films and benzene is detected in the TDS spectra at 300 K. This astonishing result can be rationalized by theoretically studying the Pd atom adsorbed on different MgO sites. First, a Pd atom on a five-coordinated oxygen ion on the MgO(0 0 1) terrace, O_{5c}, is bound by about 1 eV. It was found that the Pd(C_4H_4) complex is indeed formed but the third acetylene molecule is not bound to the complex and therefore this configuration remains catalytically inactive. On four-coordinated steps or three-coordinated corner oxygen sites, O_{4c} and O_{3c}, respectively, the Pd atom binds slightly more strongly with an energy of 1.2–1.5 eV. As a result, the atom becomes more reactive. However, on both O_{3c} and O_{4c}

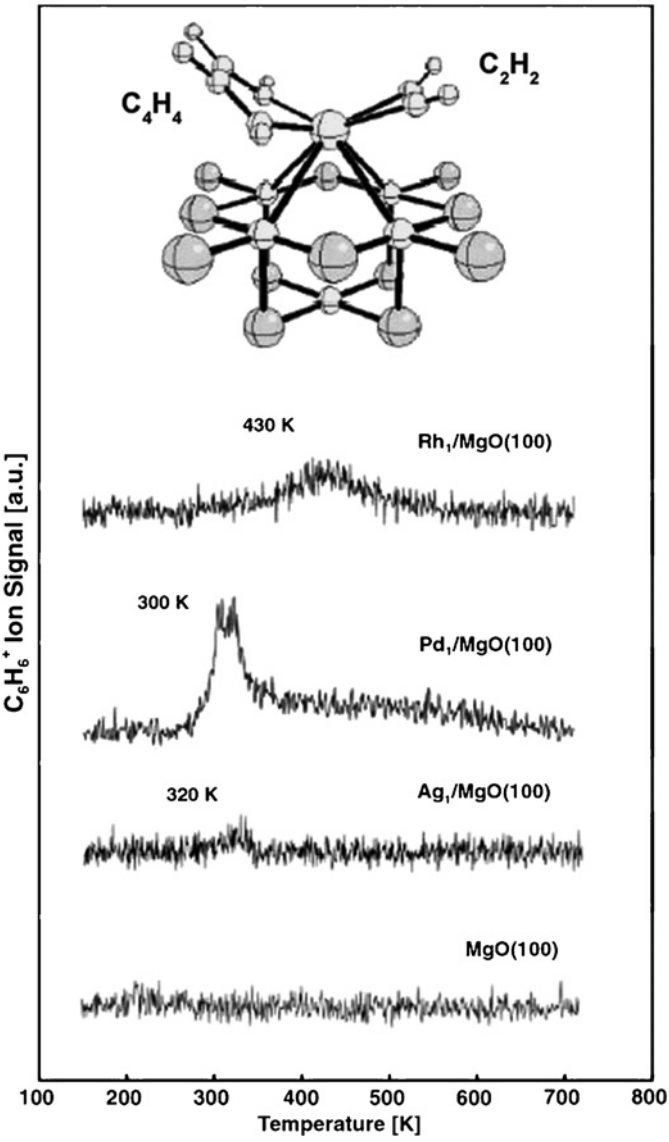

Figure 26: TPR spectra of C_6H_6 formed on Ag, Pd, and Rh atoms deposited on defect-rich MgO thin films grown on Mo(1 0 0) surfaces. For comparison, the same experiment was performed on a clean defect-rich MgO film. Shown is also the calculated $(C_4H_4)(C_2H_2)/Pd_1/F5c$ intermediate of the cyclotrimerization reaction on Pd atoms adsorbed on an F center of the MgO(1 0 0) surface. For Pd atoms the formation of benzene was also observed at 220 K.

sites, the third C_2H_2 molecule is only weakly bound or even unbound to the $Pd(C_4H_4)$ surface complex, with the binding energy being smaller than the activation energy of the formation of C_6H_6. The interaction of Pd atoms with F centers is much stronger, 3.4 eV. On F^+ centers, binding energies are about 2 eV smaller, but still enough to efficiently trap the metal atoms [100, 101]. Furthermore, the presence of trapped

electrons at the defect site results in a more efficient activation of the supported Pd atom. In fact, the complex $(C_4H_4)(C_2H_2)/Pd_1/F_{5c}$ (Fig. 26) shows a large distortion and a strong interaction with a third C_2H_2 molecule. These results indicate that F and F^+ centers can act as basic sites on the MgO surface and convert the inactive Pd atom into an active catalyst. Notice that the supported Pd atoms on defect sites not only activate the cyclization reaction, but also favor benzene desorption, as shown by the very small $(C_6H_6)/Pd_1/F_{5c}$ adsorption energy. The complete reaction path for this specific nanocatalyst has been calculated [102] and is shown in Fig. 27. The first barrier of the reaction path is the one for the formation of the intermediate $Pd(C_4H_4)$ and it is only 0.48 eV. The formation of the C_4H_4 intermediate is thermodynamically favored by 0.82 eV. On $(C_4H_4)/Pd_1/F_{5c}$, the addition of the third acetylene molecule is exothermic by 1.17 eV, leading to a very stable $(C_4H_4)(C_2H_2)/Pd_1/F_{5c}$ intermediate (Fig. 27). To transform this intermediate into benzene a barrier of 0.98 eV must be overcome. The corresponding energy gain is very large, 3.99 eV, and mainly related to the aromaticity of the benzene ring. Once formed, C_6H_6 is so weakly bound to the supported Pd atom that it immediately desorbs. Thus, the reaction on Pd/F_{5c} is rate limited in the last step, the conversion of $(C_4H_4)(C_2H_2)$ into C_6H_6. This differs from the Pd(1 1 1) surface where the rate-determining step for the reaction is the benzene desorption. The calculations are consistent with the experimental data. In fact, on Pd_1/F_{5c} the computed barrier of 0.98 eV corresponds to a desorption temperature of about 300 K, as is experimentally observed (Fig. 26). On Pd(1 1 1) surfaces, the binding energy of benzene is estimated to be $\approx$1.9 eV.This binding is consistent with a desorption temperature of 500 K as observed for a low coverage of C_6H_6 on Pd(1 1 1) [103]. Thus, this atom is activated on specific sites, F centers, of the MgO surface. From FTIR studies and using the CO molecule as a probe, it is known that Pd atoms

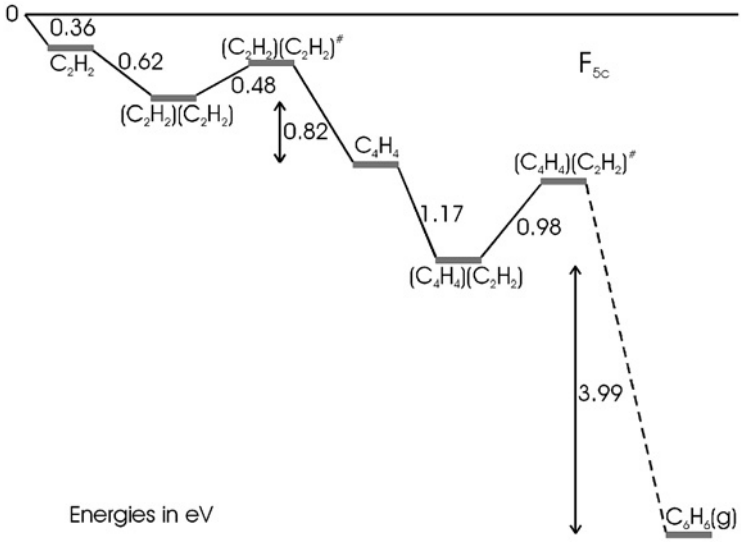

Figure 27: Computed reaction path for the formation of benzene starting from acetylene promoted by a Pd atom supported on a neutral oxygen vacancy at an MgO terrace, F5c (DFT BP results, see text).

already diffuse upon deposition to F centers and that it is this defect site which activates the Pd atom via a substantial amount of *charge transfer* [104].

A significant change in reactivity upon deposition is also observed for Rh. In this case, however, Rh atoms are *deactivated*, as the reaction occurs at higher temperature than predicted for the gas phase by DFT calculations. The product molecule, benzene, is found to desorb as a broad peak between 350 and 500 K (Fig. 26). The identification of the involved reaction mechanisms is more complex since Rh atoms are stabilized at two different trapping centers after deposition and migration on the MgO surface also occurs upon heating. This indicates that other key factors, such as the stability and diffusion properties of the deposited atoms, are relevant for the reactivity. In detail, after deposition and prior to acetylene exposure, the majority of the Rh atoms bind to step edges. Calculations show that these Rh atoms strongly interact with the first acetylene molecule by 1.76 eV. The reactant becomes highly activated as indicated by the long C–C distance (d(C–C) = 1.315 Å), and by the small HCC angle ($\angle$(H–C–C) = 140.2°). The $Rh(C_2H_2)$ complex is tightly bound (2.5 eV) to the surface. The high stability of the $Rh(C_2H_2)$ complex together with steric effects prevents adsorption of a second and third acetylene molecule to form the $Rh(C_2H_2)_2$ and the $Rh(C_2H_2)_3$ complexes essential for promoting the reaction. As a comparison, for free Rh atoms, the two acetylene molecules are bound at opposite sites, a configuration which is not possible when Rh is bound to step edges. Thus, in this configuration Rh atoms do not contribute to the observed formation of benzene. Heating up the model catalysts above room temperature induces migration of the $Rh(C_2H_2)$ complex to those F centers, which were not populated upon deposition of Rh atoms. On F centers, the $Rh(C_2H_2)$ complex is stably trapped with a binding of 2.8 eV. The computed diffusion barrier for $Rh(C_2H_2)$ from a step ($\approx$1 eV) is considerably lower than the binding energy of acetylene to Rh (1.76 eV), and consequently the entire $Rh(C_2H_2)$ complex detaches from the step edges and migrates on the surface. Interestingly, when Rh is bound at an F center, the binding (1.06 eV) and activation (d(C–C) = 1.274 Å; $\angle$(H–C–C) = 149°) of the acetylene molecule is considerably weakened with respect to the step case. This is one of the reasons why a second residual acetylene molecule from the vacuum chamber can then adsorb on Rh yielding an energy gain of 0.96 eV. At this stage of the process, the sample temperature is high enough ($>300\,K$) that the complex is immediately transformed into the metallopentacycle, $Rh(C_4H_4)$, with a gain of 0.91 eV and overcoming a barrier of 1.18 eV. This complex binds a third acetylene molecule with a binding energy of 1.07 eV and the product is subsequently formed in an exothermic process (3.2 eV). The activation energies involved in the formation of the metallopentacyle ($\Delta E^{\ddagger} = 1.18$ eV) and benzene ($\Delta E^{\ddagger} = 1.07$ eV) are of the same order but are about 20% higher than for Pd. This explains the higher reaction temperature for Rh. Notice that these are the rate-determining steps since, due to strong Pauli repulsion, benzene desorption requires very little energy (<0.2 eV) for both, Pd/MgO(F) and Rh/MgO(F). Assuming the Redhead equation with a pre-exponential factor of 10^{13}, the computed barriers correspond to a reaction temperature of about 300 K, which is lower than the temperature of maximal benzene formation at 420 K. In addition, the activation energy for benzene formation is similar to the barrier for detaching the $Rh(C_2H_2)$ complex from step edges. Thus, only Rh atoms initially trapped at F centers contribute to the initial formation of benzene at 350 K, and the main contribution at higher temperature originates from Rh atoms first trapped at

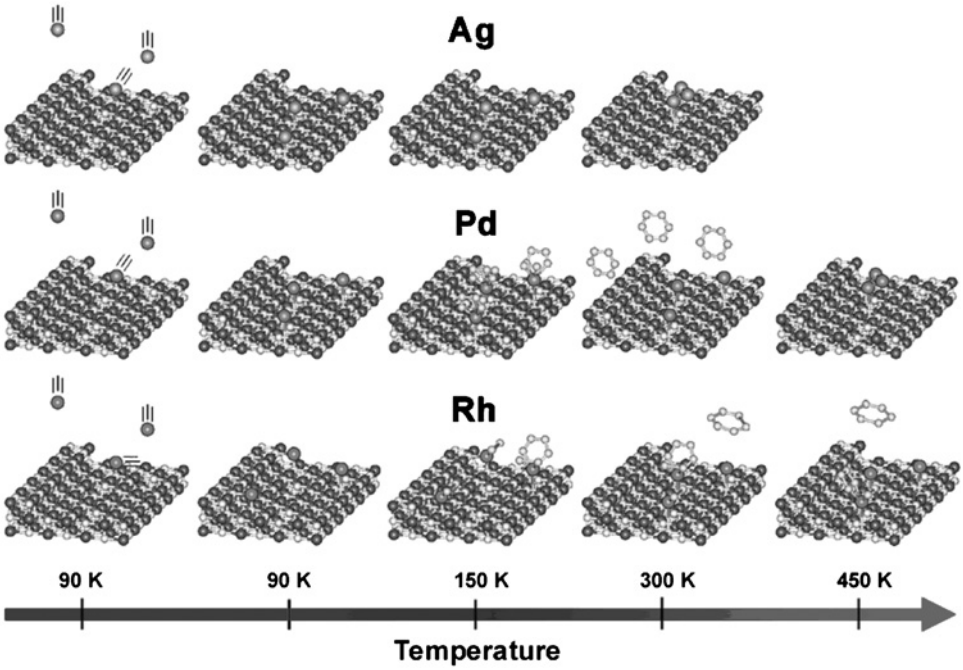

Figure 28: The proposed mechanisms are shown schematically for the three atoms. Ag and Pd atoms decorate exclusively F centers after deposition, whereas Rh is trapped at step edges and F centers at 90 K. Ag atoms do not adsorb acetylene and are therefore inert for the reaction. Pd and Rh form benzene only when trapped at F centers. Note that the relatively broad temperature range for the formation of C_6H_6 on Rh originates from the fact that Rh is trapped at two defect sites at 90 K and that the reaction occurs only after diffusion of the $Rh(C_2H_2)$ complexes from steps to F centers. For more details see text.

step edges and subsequently activated after diffusion to the F centers. The existence of a distribution of Rh atoms at F centers and at step edges prior to reaction therefore explains the rather broad desorption peak of benzene in contrast to the narrow peak observed for Pd, which populates only one kind of defect centers already at the deposition stage. The situation is even more complex as it could be shown that Rh can detach at around 450 K from the F centers and form larger clusters [105]. In this context, it is important to note that larger Rh_N clusters with $N>10$ are inert for the cyclotrimerization reaction.

The reaction mechanisms on the three atoms are summarized in Fig. 28. The specific electronic configuration of Ag renders these atoms inert for the polymerization of acetylene both as free and as supported atoms. The reactivity of Pd and Rh is strongly influenced by their adsorption and diffusion dynamics on the MgO surface. Pd atoms are converted into active catalysts for the cyclotrimerization reaction only when adsorbed on F centers as charge donation from the defect site to the atom occurs upon bonding. Finally, the low activation barriers present in free Rh atoms are substantially increased for Rh adsorbed on an MgO surface. The cyclotrimerization can only be catalyzed when Rh is trapped on F centers since steric effects, which are especially marked for supported atoms and small clusters, prevent the adsorption of a second or third acetylene molecules upon step edges.

4.2. The selectivity of acetylene polymerization on Pd_N clusters

Whereas single Pd atoms are very selective for the production of benzene, the polymerization of acetylene on larger Pd_N clusters reveals a remarkable pattern in the product formation (Fig. 29). Striking atom-by-atom size-dependent reactivity and selectivity are observed. Only three reaction products C_6H_6, C_4H_8, and C_4H_6 are detected. Interestingly enough, no C_3H_n, C_5H_n, and C_8H_n are formed, indicating the absence of C–C bond scission as already observed on Pd single crystals [106] and

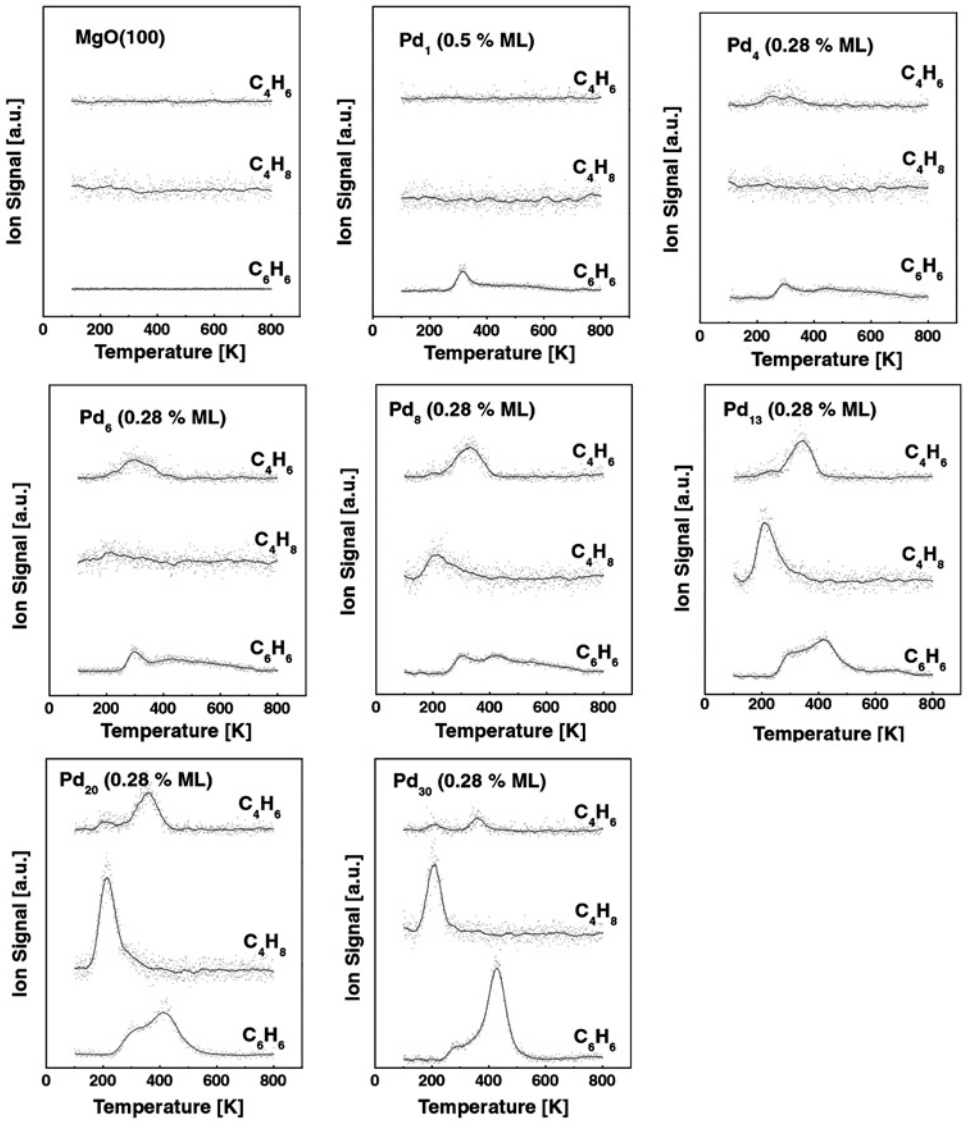

Figure 29: TPR spectra of the catalytic formation of C_6H_6, C_4H_6, and C_4H_8 for a defect-rich MgO thin film, Pd_1, Pd_4, Pd_6, Pd_8, Pd_{13}, Pd_{20}, and Pd_{30}. The relative ion intensities are corrected with the relative detection efficiencies of the experiment and scale with the number of formed product molecules per cluster.

Pd particles [107]. Up to Pd_3, only benzene is catalyzed reflecting a high selectivity for the cyclotrimerization of acetylene. Pd_N ($4 \leqslant N \leqslant 6$) clusters also reveal a second reaction channel by catalyzing the formation of C_4H_6, which desorbs at about 300 K. The third reaction product, C_4H_8, desorbing at a rather low temperature of 200 K, is clearly observed for Pd_8. For this cluster size, the amount of the three reaction products is found to be similar. For even larger clusters ($13 \leqslant N \leqslant 30$), the formation of C_6H_6 increases with cluster size, whereas the conversion of acetylene into C_4H_8 reaches a maximum for Pd_{20}. Note that Pd_{30} selectively suppresses the formation of C_4H_6 (the peak in the TPR spectrum of C_4H_6 at 200 K is part of the fragmentation pattern of C_4H_8). For Pd_{20}, the experiments were repeated in the presence of D_2 [108]. D_2 was exposed prior and after C_2H_2. The results clearly indicate that no product containing deuterium is formed. Consequently, D_2 is not involved in the polymerization reaction. However, the presence of D_2 opens a new reaction channel, the hydrogenation of acetylene. In addition, D_2 blocks the active sites on the palladium clusters needed for polymerization, as the formation of the products is slightly reduced when exposing D_2 prior to C_2H_2. On Pd(1 1 1), pre-dosing with H_2 completely suppresses the cyclotrimerization but enhances the hydrogenation of acetylene to form ethylene [103].

Assuming stoichiometric reactions, as indicated in Fig. 30c, and estimating the relative number of C_2H_2 from Fig. 30a, one observes a proportional increase of acetylene with the number of palladium atoms per cluster up to Pd_{13}. Surprisingly, at this

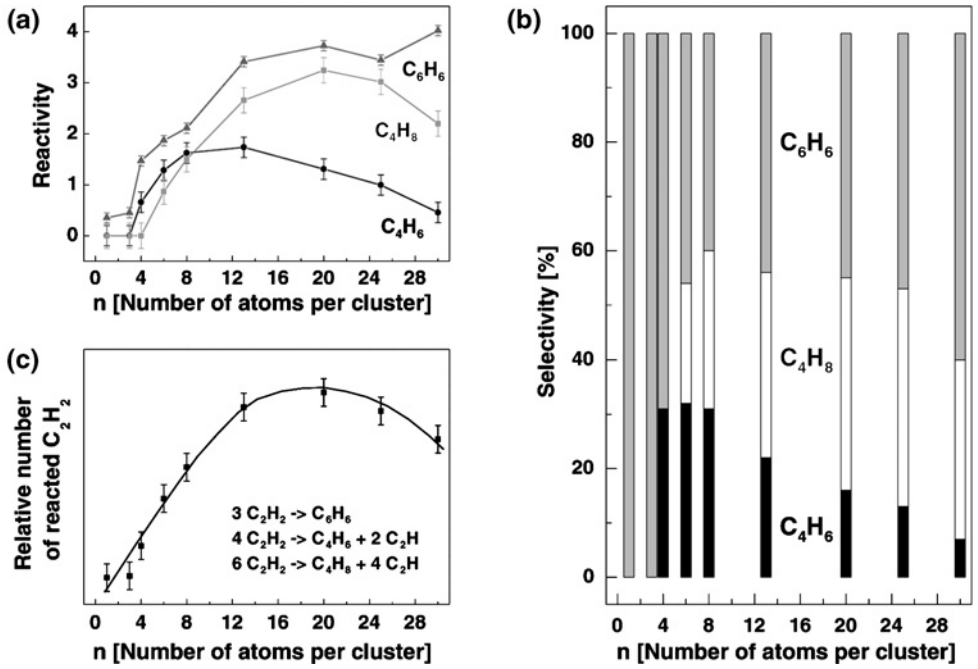

Figure 30: (a) Reactivity (expressed as the number of product molecules per cluster) and (b) selectivity (expressed as the relative amount in %) of the polymerization of C_2H_2 on size-selected Pd_N ($N = 1$–30) deposited on defect-rich MgO thin films. Also shown is the relative number of reacted C_2H_2 as function of cluster size (c).

cluster size the surface-to-bulk ratio as well as the coordination number of Pd in the cluster changes since at this size one Pd atom sits completely in the cluster. In addition, according to the free stoichiometric chemical reactions, each reaction requires a minimum number of Pd atoms, which are 3, 4, and 6. The experimental results are surprisingly consistent, that is C_4H_6 is formed for Pd_N with $N \geqslant 4$ and C_4H_8 for cluster sizes with $N \geqslant 6$.

Analysis of the products formed on small size-selected Pd_N ($1 \leqslant N \leqslant 30$) clusters deposited on MgO(1 0 0) thin films indicates that the surface intermediate C_4H_4 is produced efficiently on all cluster sizes. Thus, at least two acetylene molecules are adsorbed in a π-bonded configuration at the initial stage of the reaction [101]. The observed size-dependent selectivity may then be understood by regarding the influence of the cluster size to steer the reaction either toward the cyclotrimerization to form C_6H_6 or toward a direct hydrogen transfer from adsorbed C_2H_2 to the C_4H_4 intermediate to catalyze the formation of C_4H_6 or C_4H_8, respectively. Cyclotrimerization is generally observed when a third acetylene molecule is adsorbed in a π-bonded configuration, which results in a change from sp-hybridization toward sp^2-hybridization [109]. This bonding configuration leads to a weak activation of the C–H bond, analogous to ethylene [110]. The hydrogenation of the $Pd_N(C_4H_4)$ metallocycle, on the other hand, is favored by the adsorption of di-σ/π-bonded acetylene to three Pd atoms, effecting a more efficient activation of the C–H bond, in analogy to ethylene [110].

As shown above, for Pd atoms adsorbed on defect sites, the $Pd(C_4H_4)$ intermediate is readily formed as shown in Fig. 26. A third adsorbed C_2H_2 molecule is purely π-bonded and the activated acetylene molecule reacts with the intermediate to form benzene with a total exothermicity of about 7 eV (Fig. 27). The weakly bound C_6H_6 (0.3 eV) then desorbs at low temperature from the nanocatalyst [101]. A second reaction channel, the formation of butadiene, C_4H_6, opens for Pd_4. Pd_6 reveals the highest selectivity for this channel. In this case a third C_2H_2 molecule can bind in a di-σ/π bond configuration to three Pd atoms. The charge transfer from the substrate to the cluster further enhances the activation of the C–H bonds. For even larger cluster sizes, the adsorption of two di-σ/π-bonded C_2H_2 molecules becomes possible and opens up the third reaction path, the formation of C_4H_8. This is clearly observed for Pd_8 in our experiments. Purely geometric arguments (possible adsorption of two di-σ/π-bonded C_2H_2 molecules close to the C_4H_4 intermediate) suggest that this third channel is more pronounced for the larger clusters, and indeed our results show a maximal C_4H_8 formation for cluster sizes of 20–25 Pd atoms. For the largest clusters of the measured range, e.g., Pd_{30}, the increased number of metal–metal bonds and the concomitant delocalization of the charge transferred from the substrate to the cluster result in less charge density available for the activation of the C–H bond [111]. Consequently, the cyclotrimerization becomes again more efficient than the hydrogenation of the C_4H_4 intermediate. Going to even larger particles or to Pd(1 1 1) single crystals, the cyclotrimerization to benzene is selectively catalyzed.

5. SIZE-SELECTED, SUPPORTED CLUSTERS: EXCITING NEW MODEL SYSTEMS FOR ELECTROCATALYSIS

All of the examples of the size-dependent chemistry of supported clusters discussed so far involved gas-phase reactions. Another field of research where particle size-effects in

the scalable size regime have been proven to play a decisive role for applications is electrocatalysis [112]. The most prominent area of electrocatalysis certainly is research on fuel cell catalysts, especially for the polymer electrolyte fuel cell (PEMFC) and the direct methanol fuel cell (DMFC). Industrial catalysts of these low-temperature fuel cells consist of small platinum or platinum-alloy particles finely dispersed on a carbon support in order to maximize the active surface area. Current research focuses on reducing the Pt content of the catalyst as well as increasing the long-term stability of the catalyst and the membrane separating the anode from the cathode.

Previous studies of fuel cell electrocatalysts focused on the investigation of single crystal surfaces [113] or nanoparticles either in the form of industrial catalysts [114, 115] or produced in lab scale by wet-chemical methods, such as the synthesis of metal colloids by reduction of metal salts [116]. On these model systems, it was shown that important fuel cell reactions such as oxygen reduction and CO oxidation exhibit a distinguished structure sensitivity [117–119]. For example, Ross showed that for the oxygen reduction reaction, the specific activity of Pt (i.e., the reaction rate per Pt surface atom in units of $\mu A/cm^2$ Pt) decreases with the particle size [120]. This ''crystallite size effect'' was related to the blocking of adsorption sites due to specific anion adsorption from the electrolyte, which is different at different facets. Recent work in perchloric acid solution [112, 119] (an electrolyte presumably without specific anion adsorption), however, showed the same decrease in specific activity with decreasing particle size. The importance of this effect for application becomes clear in Gasteiger et al.'s excellent review concerning ''activity benchmarks and requirements'' for PEMFC in automotive applications. It was shown that the specific activity of industrial Pt catalysts is one order of magnitude lower than for bulk Pt [112]. For comparison, the PEMFC development targets require a fourfold increase in mass activity (i.e., A/mg Pt at 0.9 V_{RHE}).

Not only the oxygen reduction reaction but also the CO electro-oxidation reaction is found to exhibit particle size effects. Friedrich et al. [121] showed that the CO electro-oxidation on Pt nanoparticles is shifted to higher potentials compared to polycrystalline Pt. This effect was explained by an increased CO adsorption energy on small Pt particles concurrent with a decrease in CO diffusion [122]. Recent experiments on industrial carbon-supported Pt high surface area catalysts with different mean particle sizes confirmed that the CO oxidation potential depends on the average particle size. However, it was found that the oxidation potential could be reversibly influenced by the pretreatment of the electrode surface without changing the size of the particles [118]. The origin of this experimental observation was explained based on particle size-dependent defect structures, which serve as active centers for the dissociation of water. A conclusive description of the structural sensitivity of electrocatalytic reactions, however, is difficult to ascertain due to the generally (compared to UHV studies) ill-defined model systems. For example, the coexistence of very small particles on the surface is difficult to determine by electron microscopy (TEM), but may significantly influence the activity of the catalyst.

An exciting new approach for electrocatalysis entails the investigation of model catalysts consisting of size-selected clusters produced in UHV, as described in the previous section, and then transferred to an electrochemical cell. This procedure would allow for a yet unknown precision in the particle size and, for the first time in electrochemistry, the investigation of particle size effects in the non-scalable size regime. The

previous gas-phase examples showed that the defined electronic properties of supported clusters result in a new exciting chemistry, which can be expected to manifest in electrocatalytic reactions as well. Furthermore, it was shown how detailed ab initio calculations can help to understand certain detailed reaction mechanisms. In electrocatalysis, so far the development of suitable theoretical tools is hampered due to lack of comparison to experimental results due to ill-defined conditions [123]. Therefore, electrochemical experiments on size-selected clusters would be an important step toward a theoretical description of processes at the solid–liquid interface as well.

6. CONCLUSION

In conclusion, there is no question that a new catalytic chemistry emerges in the nonscalable size regime where every atom counts. This may have important implications for industrial catalysis with respect to low-temperature active catalytic materials and selectivity tuning by size selection. From a more fundamental point of view in particular the combination of gas-phase studies, clusters supported on surface, and ab initio theoretical simulation are fruitful in defining important nanocatalytic factors and concepts. The most important cluster-specific phenomena reviewed in this contribution are the tuning of the selectivity and activity by electronic quantum size effects and charging, the dynamic structural fluxionality, i.e., the self-selection of the low activation energy reaction path via interconversion of structural isomers, and especially for supported clusters, the tuning of activity through the design of the cluster–support interface and the size-dependent spill-over. Most of these factors are unique for small clusters and not observed for bulk catalytic systems or particles in the scalable size regime.

NOTE

1. (g) and (a) denote gas phase and adsorbed molecules, respectively.

REFERENCES

[1] Mendeleeff D.W., The Principle of Chemistry, 3rd edition, Longmans, Green and Co., London, 1905.
[2] Herrmann A., Leutwyler S., Schumacher E., Wöste L., Chem. Phys. Lett. 52 (1977) 418.
[3] Herrmann A., Schumacher E., Wöste L., J. Chem. Phys. 68 (1978) 2327.
[4] Herrmann A., Leutwyler S., Schumacher E., Wöste L., Helv. Chim. Acta 61 (1978) 453.
[5] Kappes M.M., Kunz R.W., Schumacher E., Chem. Phys. Lett. 91 (1982) 413.
[6] Knight W.D., Deheer W.A., Clemenger K., Saunders W.A., Solid State Commun. 53 (1985) 445.
[7] Knight W.D., Clemenger K., DeHeer W.A., Saunders W.A., Phys. Rev. B 31 (1985) 2539.
[8] Saunders W.A., Clemenger K., DeHeer W.A., Knight W.D., Phys. Rev. B 32 (1985) 1366.
[9] Knight W.D., Clemenger K., DeHeer W.A., Saunders W.A., Chou M.Y., Cohen M.L., Phys. Rev. Lett. 52 (1984) 2141.
[10] Knight W.D., Monot R., Dietz E.R., George A.R., Phys. Rev. Lett. 40 (1978) 1324.
[11] Dunphy J.C., Knight C., Sautet P., Ogletree D.F., Somorjai G.A., Salmeron M.B., Surf. Sci. 280 (1993) 313.

[12] Moseler M., Huber B., Häkkinen H., Landman U., Wrigge G., Hoffmann M.A., von Issendorff B., Phys. Rev. B 68 (2003) 165413.
[13] Häkkinen H., Landman U., Phys. Rev. B 62 (2000) R2287.
[14] Häkkinen H., Moseler M., Landman U., Phys. Rev. Lett. 89 (2002) 033401.
[15] Häkkinen H., Yoon B., Landman U., Li X., Zhai H.J., Wang L.S., J. Phys. Chem. A 107 (2003) 6168.
[16] Gilb S., Weis P., Furche F., Ahlrichs R., Kappes M.M., J. Chem. Phys. 116 (2002) 4094.
[17] Furche F., Ahlrichs R., Weis P., Jacob C., Gilb S., Bierweiler T., Kappes M.M., J. Chem. Phys. 117 (2002) 6982.
[18] Weis P., Bierweiler T., Gilb S., Kappes M.M., Chem. Phys. Lett. 355 (2002) 355.
[19] Moseler M., Häkkinen H., Barnett R.N., Landman U., Phys. Rev. Lett. 86 (2001) 2545.
[20] Moseler M., Häkkinen H., Landman U., Phys. Rev. Lett. 89 (2002) 176103.
[21] Christmann K., Introduction to Surface Physical Chemistry, Springer-Verlag, Berlin, 1991.
[22] Somorjai G.A., Introduction to Surface Chemistry and Catalysis, Wiley, New York, 1993.
[23] Holleman A.F., Wiberg E., Lehrbuch der Anorganischen Chemie, de Gruyter, Berlin, 1995.
[24] Haruta M., Cat. Tech. 6 (2002) 102.
[25] Cha D.Y., Parravan G., J. Catal. 18 (1970) 200.
[26] Bond G.C., Sermon P.A., Webb G., Buchanan D.A., Wells P.B., J. Chem. Soc. Chem. Commun. (1973) 444.
[27] Haruta M., Gold Bull 37 (2004) 27.
[28] Haruta M., Yamada N., Kobayashi T., Iijima S., J. Catal. 115 (1989) 301.
[29] Haruta M., Tsubota S., Kobayashi T., Kageyama H., Genet M.J., Delmon B., J. Catal. 144 (1993) 175.
[30] Meyer R., Lemire C., Shaikhutdinov S., Freund H.J., Gold Bull 37 (2004) 72.
[31] Lemire C., Meyer R., Shaikhutdinov S., Freund H.J., Angew. Chem. Int. Ed. 43 (2004) 118.
[32] Lemire C., Meyer R., Shaikhutdinov S.K., Freund H.J., Surf. Sci. 552 (2004) 27.
[33] Heiz U., Vanolli F., Trento L., Schneider W.D., Rev. Sci. Instrum. 68 (1997) 1986.
[34] Messerli S., Schintke S., Morgenstern K., Sanchez A., Heiz U., Schneider W.D., Surf. Sci. 465 (2000) 331.
[35] Abbet S., Judai K., Klinger L., Heiz U., Pure Appl. Chem. 74 (2002) 1527.
[36] Bromann K., Felix C., Brune H., Harbich W., Monot R., Buttet J., Kern K., Science 274 (1996) 956.
[37] Tong X., Benz L., Chrétien S., Kemper P., Kolmakov A., Metiu H., Bowers M.T., Buratto S.K., J. Chem. Phys. 123 (2005) 204701.
[38] Antonietti J.M., Michalski M., Heiz U., Jones H., Lim K.H., Rösch N., Del Vitto A., Pacchioni G., Phys. Rev. Lett. 94 (2005) 213402.
[39] Heiz U., Sanchez A., Abbet S., Schneider W.D., Eur. Phys. J. D 9 (1999) 35.
[40] Sanchez A., Abbet S., Heiz U., Schneider W.D., Häkkinen H., Barnett R.N., Landman U., J. Phys. Chem. A 103 (1999) 9573.
[41] Di Valentin C., Del Vitto A., Pacchioni G., Abbet S., Wörz A.S., Judai K., Heiz U., J. Phys. Chem. B 106 (2002) 11961.
[42] Peterka D., Tegenkamp C., Schröder K.M., Ernst W., Pfnür H., Surf. Sci. 431 (1999) 146.
[43] Sterrer M., Fischbach E., Risse T., Freund H.J., Phys. Rev. Lett. 94 (2005) 186101.
[44] Schintke S., Schneider W.D., J. Phys. Condens. Matter 16 (2004) R49.
[45] Sterrer M., Heyde M., Novicki M., Nilius N., Risse T., Rust H.P., Pacchioni G., Freund H.J., J. Phys. Chem. B 110 (2006) 46.
[46] Yoon B., Häkkinen H., Landman U., Wörz A.S., Antonietti J.M., Abbet S., Judai K., Heiz U., Science 307 (2005) 403.

[47] Sterrer M., Yulikov M., Risse T., Freund H.J., Carrasco J., Illas F., Di Valentin C., Giordano L., Pacchioni G., Angew. Chem. Int. Ed. 45 (2006) 2633.
[48] Pacchioni G., private communication.
[49] Bonn M., Funk S., Hess C., Denzler D.N., Stampfl C., Scheffler M., Wolf M., Ertl G., Science 285 (1999) 1042.
[50] Häkkinen H., Abbet W., Sanchez A., Heiz U., Landman U., Angew. Chem. Int. Ed. 42 (2003) 1297.
[51] Weis P., Bierweiler T., Vollmer E., Kappes M.M., J. Chem. Phys. 117 (2002) 9293.
[52] Knecht J., Fischer R., Overhof H., Hensel F., Chem. Soc. J., Chem. Commun. (1978) 905.
[53] Haruta M., Takase T., Kobayashi T., in: Catalytic Science and Technology, S. Yoshida, N. Takezawa, T. Ono (eds), VHC, Weinheim, 1991, p. XXV.
[54] Bongiorno A., Landman U., Phys. Rev. Lett. 95 (2005) 106102.
[55] Masel R.I., Principles of Adsorption and Reaction on Solid Surfaces, Wiley, New York, 1996.
[56] Engel T., Ertl G., Adv. Catal. 28 (1979) 1.
[57] Libuda J., Freund H.J., Surf. Sci. Rep. 57 (2005) 157.
[58] Henry C.R., Surf. Sci. Rep. 31 (1998) 231.
[59] Stara I., Nehasil V., Matolin V., Surf. Sci. 331–333 (1995) 173.
[60] Meusel I., Hoffmann J., Hartmann J., Heemeier M., Bäumer M., Libuda J., Freund H.J., Catal. Lett. 71 (2001) 5.
[61] Judai K., Abbet S., Wörz A.S., Röttgen M.A., Heiz U., Int. J. Mass Spectrom. 229 (2003) 99.
[62] Abbet S., Heiz U., Häkkinen H., Landman U., Phys. Rev. Lett. 86 (2001) 5950.
[63] Röttgen M.A., Abbet S., Judai K., Antonietti J.M., Wörz A., Arenz M., Henry C.R., Heiz U., submitted for publication.
[64] Becker C., Henry C.R., Surf. Sci. 352 (1996) 457.
[65] Hoffmann J., Meusel I., Hartmann J., Libuda J., Freund H.J., J. Catal. 204 (2001) 378.
[66] Becker C., Henry C.R., Catal. Lett. 43 (1997) 55.
[67] Santra A.K., Goodman D.W., Electrochim. Acta 47 (2002) 3595.
[68] Henry C.R., Appl. Surf. Sci. 164 (2000) 252.
[69] Piccolo L., Becker C., Henry C.R., Eur. Phys. J. D 9 (1999) 415.
[70] Huber B., Koskinen P., Häkkinen H., Moseler M., Nat. Mater. 5 (2006) 44.
[71] Piccolo L., Henry C.R., Appl. Surf. Sci. 670 (2000) 162.
[72] Piccolo L., Henry C.R., J. Mol. Catal. 181 (2001) 167.
[73] Daté M., Okuyama H., Takagi N., Nishijima M., Aruga T., Surf. Sci. 341 (1995) L1096.
[74] Daté M., Okuyama H., Takagi N., Nishijima M., Aruga T., Surf. Sci. 350 (1996) 79.
[75] Pisanu A.M., Gigola C.E., Appl. Catal. B 20 (1999) 179.
[76] Hirsimäki M., Suhonen S., Pere J., Valden M., Pessa M., Surf. Sci. 404 (1998) 187.
[77] Rainer D.R., Koranne M., Vesecky S.M., Goodman D.W., J. Phys. Chem. B 101 (1997) 10769.
[78] Vesecky S.M., Paul J., Goodman D.W., J. Phys. Chem. 100 (1996) 15242.
[79] Muraki H., Fujitani Y., Ind. Eng. Chem. Prod. Res. Dev. 15 (1986) 414.
[80] Xu X.P., Goodman D.W., Catal. Lett. 24 (1994) 31.
[81] Xu X., Chen P., Goodman D.W., J. Phys. Chem. B 98 (1994) 9242.
[82] Rainer D.R., Vesecky S.M., Koranne M., Oh W.S., Goodman D.W., J. Catal. 167 (1997) 234.
[83] Vesecky S.M., Chen P.J., Xu X.P., Goodman D.W., J. Vac. Sci. Technol. – Vac. Surf. Films 13 (1995) 1539.
[84] Honkala K., Pirilä P., Laasonen K., Surf. Sci. 489 (2001) 72.
[85] Rainer D.R., Xu C., Holmblad P.M., Goodman D.W., J. Vac. Sci. Technol. A 15 (1997) 1653.

[86] Wörz A., Abbet S., Judai K., Heiz U., J. Am. Chem. Soc. 125 (2003) 7964.
[87] Judai K., Abbet S., Wörz A.S., Heiz U., Henry C.R., J. Am. Chem. Soc. 126 (2004) 2732.
[88] Wörz A.S., Judai K., Abbet S., Heiz U., J. Am. Chem. Soc. 125 (2003) 7964.
[89] Ormerod R.M., Lambert R.M., J. Phys. Chem. 96 (1992) 8111.
[90] Schröder D., Schwarz H., Angew. Chem. Int. Ed. 34 (1995) 1973.
[91] Schwarz H., Schröder D., Pure Appl. Chem. 72 (2000) 2319.
[92] Fayet P., Kaldor A., Cox D.M., J. Chem. Phys. 92 (1990) 254.
[93] Trevor D.J., Whetten R.L., Cox D.M., Kaldor A., J. Am. Chem. Soc. 107 (1985) 518.
[94] Trevor D.J., Cox D.M., Kaldor A., J. Am. Chem. Soc. 112 (1990) 3749.
[95] Achatz U., Berg C., Joos S., Fox B.S., Beyer M.K., Niedner-Schattenburg G., Bondybey V.E., Chem. Phys. Lett. 320 (2000) 53.
[96] Klabunde K.J., Free Atoms, Clusters, and Nanoscale Particles, Academic Press, London, 1994.
[97] Blomberg M.R.A., Siegahn P.E.M., Svensson M., J. Phys. Chem. 96 (1992) 5783.
[98] Cui Q., Musaev D.G., Morokuma K., J. Chem. Phys. 108 (1998) 8418.
[99] Cui Q., Musaev D.G., Morokuma K., J. Phys. Chem. A 102 (1998) 6373.
[100] Abbet S., Heiz U., Ferrari A.M., Giordano L., Di Valentin C., Pacchioni G., Thin Solid Films 400 (2001) 37.
[101] Abbet S., Sanchez A., Heiz U., Schneider W.D., Ferrari A.M., Pacchioni G., Rösch N., J. Am. Chem. Soc. 122 (2000) 3453.
[102] Ferrari A.M., Giordano L., Pacchioni G., Abbet S., Heiz U., J. Phys. Chem. B 106 (2002) 3173.
[103] Tysoe W.T., Nyberg G.L., Lambert R.M., Chem. Soc. J., Chem. Commun. (1983) 623.
[104] Abbet S., Sanchez A., Heiz U., Schneider W.D., Ferrari A.M., Pacchioni G., Rösch N., 454 (2000) 984.
[105] Judai K., Abbet S., Wörz A.S., Heiz U., Giordano L., Pacchiono G., J. Phys. Chem. B 107 (2003) 9377.
[106] Patterson C.H., Lambert R.M., J. Phys. Chem. 92 (1988) 1266.
[107] Ormerod R.M., Lambert R.M., J. Chem. Soc., Chem. Commun. (1990) 1421.
[108] Abbet S., Sanchez A., Heiz U., Schneider W.D., Thin Solid Films 198 (2001) 122.
[109] Pacchioni G., Lambert R.M., Surf. Sci. 304 (1994) 208.
[110] Fahmi A., van Santen R.A., J. Phys. Chem. 100 (1996) 5676.
[111] Burkart S., Blessing N., Ganteför G., Phys. Rev. B 60 (1999) 15639.
[112] Gasteiger H.A., Kocha S.S., Sompalli B., Wagner F.T., Appl. Catal. BEnviron 56 (2005) 9.
[113] Markovic N.M., Ross P.N., Surf. Sci. Rep. 45 (2002) 121.
[114] Ralph T.R., Hogarth M.P., Platinum Metals Rev 46 (2002) 3.
[115] Ralph T.R., Hogarth M.P., Platinum Metals Rev 46 (2002) 117.
[116] Bonnemann H., Brinkmann R., Britz P., Endruschat U., Mortel R., Paulus U.A., Feldmeyer G.J., Schmidt T.J., Gasteiger H.A., Behm R.J., J. New Mater. Electrochem. Syst. 3 (2000) 199.
[117] Markovic N., Gasteiger H., Ross P.N., J. Electrochem. Soc. 144 (1997) 1591.
[118] Arenz M., Mayerhofer K.J.J., Stamenkovic V., Blizanac B., Tomoyuki T., Ross P.N., Markovic N.M., J. Am. Chem. Soc. 127 (2005) 6819.
[119] Mayrhofer K.J.J., Blizanac B.B., Arenz M., Stamenkovic V.R., Ross P.N., Markovic N.M., J. Phys. Chem. B 109 (2005) 14433.
[120] Ross P.N., Improvements in the utilization of Pt in fuel cells and batteries, Wiley-Interscience, New York, NY, 1997.
[121] Friedrich K.A., Henglein F., Stimming U., Unkauf W., Colloids Surf. Physicochem. Eng. Aspects 134 (1998) 193.

[122] Maillard F., Eikerling M., Cherstiouk O.V., Schreier S., Savinova E.R., Stimming U., Faraday Discuss. 357 (2004) 125.
[123] Wieckowski A., Spohr E., Workshop on Computational Electrochemistry; http://scs.uiuc.edu/workshops/, 2004.
[124] Engel T., Ertl G., J. Chem. Phys. 69 (1978) 1267.
[125] von Issendorff B., Cheshnovsky O., Annu. Rev. Phys. Chem. 56 (2005) 549.
[126] Taylor K.J., Pettiettehall C.L., Cheshnovsky O., Smalley R.E., J. Chem. Phys. 96 (1992) 3319.
[127] Meiwes-Broer K.-H. (ed.), Metal Clusters at Surfaces, Springer-Verlag, Berlin, 2000.

This page intentionally left blank

Chapter 2

Chemical reactivity and catalytic properties of size-selected gas-phase metal clusters

S.M. Lang, D.M. Popolan and T.M. Bernhardt*

Institut für Oberflächenchemie und Katalyse, Universität Ulm, D-89069 Ulm, Germany

1. INTRODUCTION

The fascination for metals in the cluster state of matter originates from the fact that the physical and chemical properties of clusters often change over orders of magnitude by the mere addition or removal of one single atom. Mass-selected gas-phase metal clusters are ideally suited to study these effects. By progressively reducing the dimension of a metal particle, the material properties start to change with size. However, if the cluster is still large enough, this change is smooth and often directly a simple function of the particle size. Figure 1 shows a physical property (vertical electron detachment energy, VDE) of free negatively charged gold clusters plotted as a function of cluster size. In this scalable size regime from thousands down to a few hundreds of atoms per aggregate, the small pieces of matter are termed nanoparticles and the VDEs of these gold nanoparticles already differ considerably from the bulk value (work function), but are decreasing gradually with cluster size with only minor deviations from an average monotonous function. However, if the particles become smaller than about 100 atoms, considerable, discontinuous variations in the VDEs are observed. This is the regime where the observable material properties become unpredictable and not scalable from bulk or atomic properties and where we speak of clusters rather than of nanoparticles.

Very characteristic for clusters with less than 30 atoms per particle (Fig. 1) is the drastic variation of the observable with the removal or addition of every single atom [2–4]. Moreover, in this non-scalable regime unanticipated physical and chemical properties might emerge which lead to completely new phenomena [3].

Recent experiments on nano-assembled model catalysts consisting of metal clusters in the non-scalable size regime supported on oxide surfaces revealed striking changes in the size-dependent efficiency and selectivity of catalytic processes [5]. These studies

The Chemical Physics of Solid Surfaces, Volume 12
ISSN: 1571-0785
DOI: 10.1016/S1571-0785(07)12002-2

*Corresponding author.
E-mail: thorsten.bernhardt@uni-ulm.de

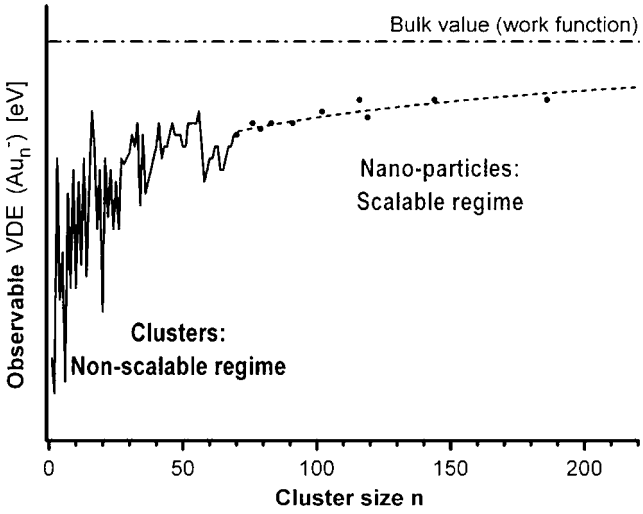

Figure 1: Scalable and non-scalable size regime in the case of negatively charged gas-phase gold clusters. The observable vertical electron detachment energy (VDE) is plotted as a function of the number *n* of atoms in the cluster [1].

also show that charging small clusters via charge transfer from the substrate is essential for turning clusters into active catalysts. Ion chemistry of small metal clusters is thus considered relevant for real catalysis. Although gas-phase studies of metal cluster reactivity might never account for the precise mechanisms in applied catalysis, such experiments complemented by computational investigations are extremely important [6]. Gas-phase studies can be performed under well-defined conditions and thus can play a key role for the more comprehensive analysis of the influence of charge state and cluster size on the catalytic activity and of the elementary steps in the reaction mechanisms. Furthermore, the finite size of the clusters enables a direct treatment by ab initio calculations which may support the quest for the origin of catalytic activity and for the details of reaction mechanisms.

Chemical reactions of gas-phase metal clusters are a very active field of research since the advent of intense cluster sources [7–9]. Adsorption and chemical reactions on free charged and neutral metal clusters were extensively studied and concepts for cluster reactivity were extracted from the large amount of experimental data. However, only a few full thermal catalytic cycles have been studied [10, 11]. All these investigations lead to the characterization of stable cluster complexes, the extraction of reaction probabilities, or even the measurement of absolute rate coefficients at a given temperature. Particular importance should be given to the temperature-dependent kinetics of metal cluster reactions, which are needed for obtaining reaction mechanisms of a chemical process at thermodynamically controlled conditions and for extracting kinetics data like absolute rate coefficients and activation energies [12].

To probe the catalytic activity of small noble metal clusters, the carbon monoxide combustion has been and still is often employed as a model-type catalytic reaction. In this review, one particular focus will be on the cluster charge state, size, and composition dependence of the catalytic activity in this particular reaction.

In the following section, the experimental schemes for studying chemical properties of free clusters will be introduced. Subsequently, important concepts to gas-phase cluster ion chemistry will be briefly summarized. Section 4 will present specific examples of gas-phase reactions catalyzed by size-selected free metal cluster ions. In this context, several results obtained by other groups on the reactivity and catalytic activity of metal cluster ions, in particular of iron and platinum monomers and clusters will be briefly reviewed. As gold nanoparticles and clusters currently attract considerable interest for their low-temperature catalytic activity in a variety of reactions, including the already mentioned CO combustion, a major part of the fourth section will concentrate on the reaction behavior of small free gold clusters. However, not only gold but also silver clusters indicate interesting size-dependent catalytic activity, which will be discussed. To complement these measurements, the last examples will deal with the reaction behavior of binary platinum–gold and silver–gold clusters.

2. EXPERIMENTAL TECHNIQUES IN CLUSTER ION CHEMISTRY

For almost two decades, isolated mass-selected metal clusters are considered important model systems for the understanding of chemical reactions, but in particular also as catalytically active particles [8]. The first catalytic cycle involving a free metal cluster was discovered by Irion and co-workers employing an ion cyclotron mass spectrometer (FT-ICR). This group reported the cyclopolymerization of ethylene to yield benzene catalyzed by free Fe_4^+ clusters [10]. The most important techniques presently utilized to investigate the chemical and, in particular, the catalytic activity of mass-selected free metal clusters will be summarized in the following together with a few selected reaction examples that aim to demonstrate the applications of the various experimental approaches. Besides these techniques, which directly yield kinetic and thermodynamic data of catalytic reactions such as reaction rates, binding properties, and activation energies, several other important gas-phase techniques strongly support these methods to obtain structural, electronic, and energetic data on the binding properties of molecules to small metal clusters, but will not be presented here. Two further techniques, photoelectron spectroscopy [13] and infrared multiphoton excitation spectroscopy [14] are presented in separate chapters of this volume.

2.1. Flow tube reactor

The flow tube reactor is the oldest method to investigate metal cluster reactions. In its most simple form, an extender is attached to a cluster source (e.g. to a laser vaporization or discharge cluster source), which permits the downstream addition of reactive gases. Different variations of this principle have been realized [7, 15–19]. Depending on the exact design, in a flow tube reactor relatively high reactant partial pressures might be reached. This means that (i) multiple-collision conditions prevail, (ii) thermal equilibration with the flow tube walls can be assumed, and (iii) saturation coverage of adsorbates are expected to be observed at the largest reactant concentrations. In Fig. 2 (top), a flow tube reactor attached to a pulsed arc cluster ion source (PACIS) [20] is shown. Metal clusters are generated during the electrical discharge through material ablation from the electrode followed by the flow through a cooled nozzle. The clusters are drawn by the buffer gas flow into the reactor where they

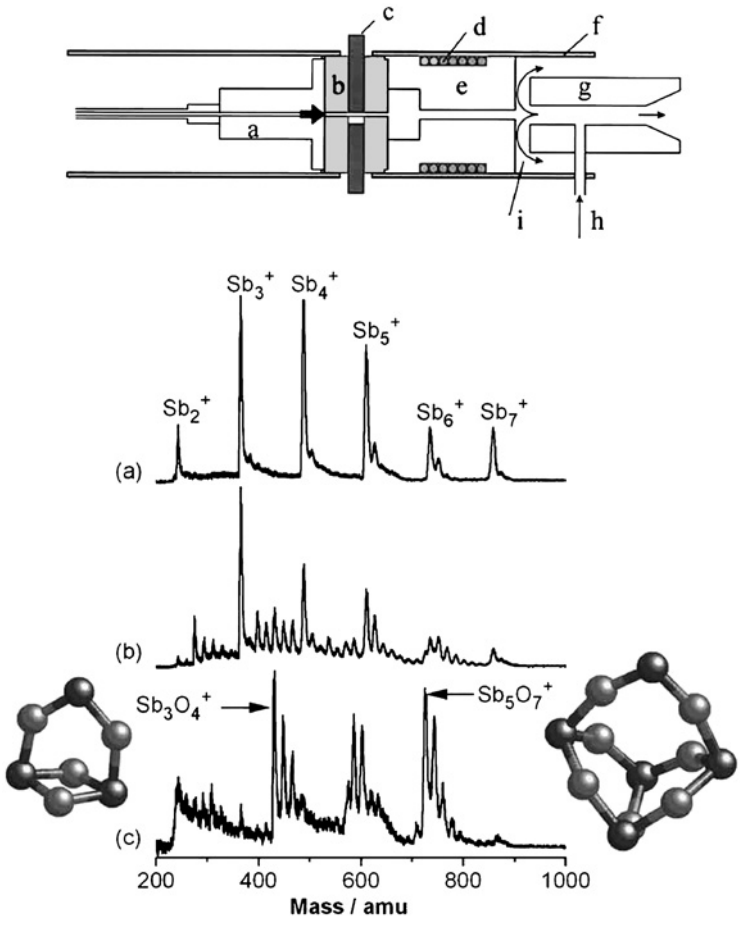

Figure 2: (Top) Schematics of the PACIS with flow tube reactor attached to the source nozzle. (a) Magnetic valve for buffer gas (He), (b) Macor insulator, (c) electrodes (the cluster material is contained in the cathode), (d) cooling coil, (e) nozzle, (f) source holder, (g) flow tube reactor, (h) reaction gas inlet, and (i) pumping channels. (Bottom) Mass spectra of antimony and antimony oxide cluster distributions at different oxygen partial pressures in the flow-tube reactor presented in the upper figure. (a) Oxygen traces only, (b) 4×10^2 Pa O_2, and (c) 4×10^3 Pa O_2. The calculated geometric structures are shown for the most prominent antimony oxide cluster species in the mass spectra (dark spheres: Sb atoms; light spheres: O atoms) [17, 18].

interact with reactive gases like oxygen. The extension of the desired reaction is controlled by adjusting the reactant partial pressure in the reactor channel.

Figure 2 (bottom) presents an example for a cluster reaction study employing this experimental arrangement [17, 18]. Antimony cluster ions are generated in the PACIS and react with molecular oxygen at different oxygen partial pressures in the subsequent flow tube reactor. With increasing oxygen pressure, oxide peaks appear in the mass spectra that are sampled after the clusters emerged from the flow tube reactor. At the highest oxygen pressure shown in Fig. 2c, the cluster distribution has changed completely and new prominent mass signals appear indicating the formation of particular stable reaction products. The stoichiometry of the observed products and

concurrent ab initio calculations suggest surprising structural arrangements for the stable antimony oxide clusters [18, 21–24] eventually converging toward the chain-like modification of bulk Sb_2O_3 [17].

2.2. Collision gas cell

In the previous fast flow reactor setup, the high reactant partial pressures and the addition of an unreactive buffer gas for thermalization lead to multiple collisions of the clusters before detection. In a different approach, *individual* collisions between clusters and reactive molecules are investigated to reveal the size-dependent cluster reactivity. This is achieved, e.g., in a collision gas cell experiment. In this case, a beam of neutral clusters passes through one or more cells filled with only low pressure of reactive gas. Under such single-collision-like conditions, the determination of absolute numbers of the reaction probability in a collision is possible [25]. The schematic layout of this experiment is shown in Fig. 3. A beam of clusters is produced by a laser vaporization source and is skimmed before passing two subsequent cells with reactive gas in which the clusters experience one or a few collisions with the gas molecules. Product detection is accomplished by time-of-flight mass spectrometry after photoionization [25]. The depletion of the pure metal clusters and the appearance of products may be evaluated by employing statistical rate theory to yield the reaction probability.

This method is claimed to be best suited for highly reactive systems, as the detection limit corresponds to a reaction probability of 0.01–0.05. For example, in oxidation reactions of large metal clusters, the reaction probability determination is rather accurate and the method represents a very valuable complement to other cluster reactivity experiments operating at different pressure levels. However, cluster fragmentation is likely for small clusters as the reactions often proceed with high probability, but are also highly exothermic. Thus, the excess energy cannot be abducted during the reaction causing the reaction product analysis ambiguous.

With this method, Andersson and Rosén recently investigated the adsorption of hydrogen or deuterium and oxygen on neutral platinum clusters and discovered the catalytic water formation on the free clusters [26]. Figure 3 (bottom) displays mass spectra obtained with different partial pressures of hydrogen and oxygen added in separate collision gas cells. Panel (a) in Fig. 3 shows a mass spectrum of pure Pt_n clusters with no reactive gas in the collision cell. The mass spectrum in panel (b) was sampled after the cluster ions passed reaction cell 1 filled with 0.14 Pa of O_2. The additional peaks in the mass spectrum correspond to clusters with one and, for $n > 12$, with two oxygen molecules adsorbed. If the oxygen pressure in reaction cell 1 is kept unchanged and deuterium is introduced in cell 2, the mass spectrum deviates significantly from a simple coadsorption spectrum, in which both molecules would add to the mass of the corresponding platinum cluster. Instead, it is apparent from panel (c) in Fig. 3 that the abundance of clusters with adsorbed oxygen molecules decreases and that the amount of clusters without adsorbed molecules increases. This observation is explained by the reaction of oxygen and deuterium atoms on the clusters to form water, which subsequently desorbs [26]. The catalytic water formation reaction is observed to proceed very efficiently on all investigated platinum cluster sizes with more than seven atoms displaying only moderate variations in the reaction probability with size.

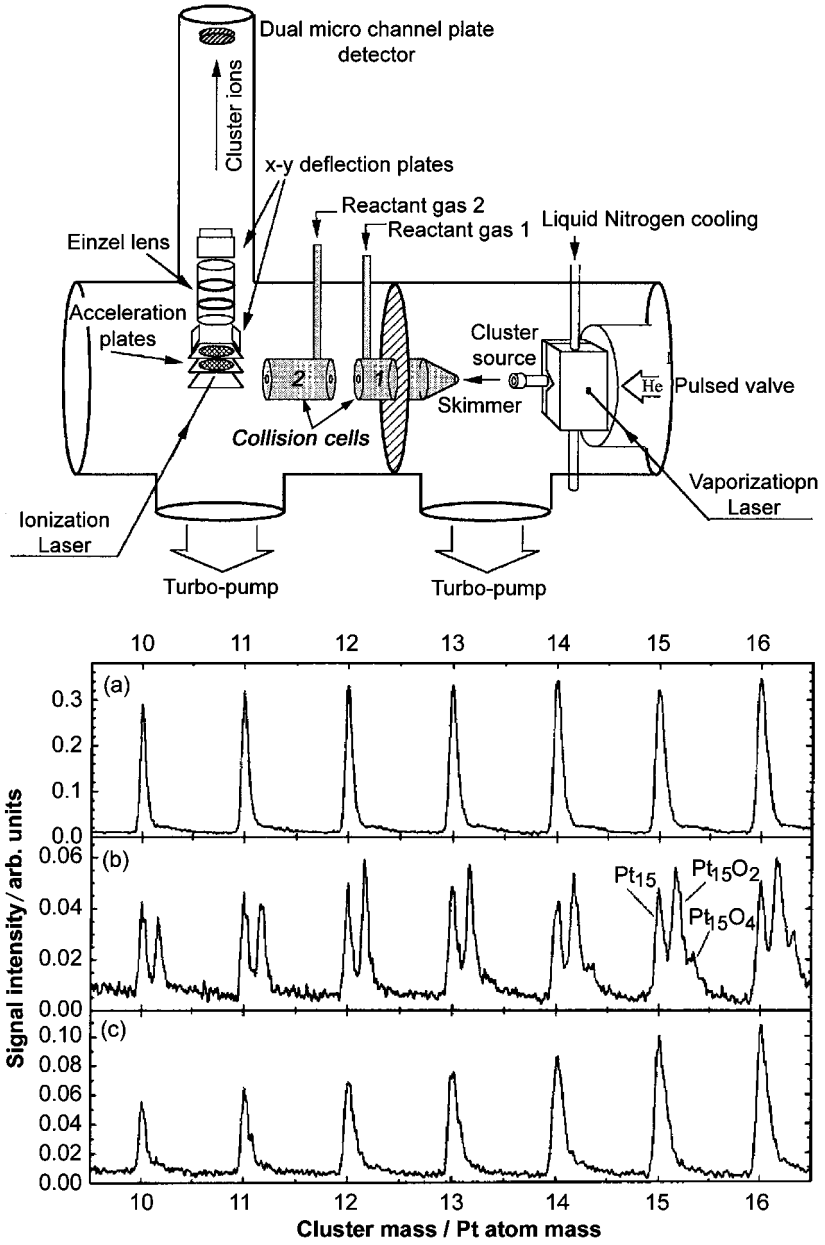

Figure 3: (Top) Schematic sketch of the collision cell method for the study of metal cluster reactivity. The supersonic laser vaporization source is depicted on the right hand side. The clusters subsequently pass two collision cells in which reactions can take place. Finally, laser ionization mass spectrometry serves to detect the neutral reaction products [25]. Reproduced with permission from American Institute of Physics. (Bottom) Mass spectra of platinum clusters Pt_n before and after reaction with O_2 and D_2. In the upper mass spectrum (a), no reaction gas was added to the collision gas cells. Spectrum (b) was obtained with 0.14 Pa O_2 in reaction cell 1 and no gas in reaction cell 2. Spectrum (c) was sampled after the metal cluster beam passed cell 1 with 0.14 Pa O_2 and cell 2 with a deuterium pressure of 0.95 Pa. Note that the mass peaks in (c) are slightly broader and exhibit a small shift with respect to mass spectrum (a). This is due to multiple deuterium adsorption onto the platinum clusters which can, however, not be resolved in the mass spectrum [26]. Reproduced with permission from American Chemical Society.

2.3. Low-energy ion guide

Molecular beam experiments are often strongly handicapped by fragmentation phenomena, which commonly occur during reactive collisions, electronic transitions, neutralization, or ionization processes. As a consequence, parent molecules and fragments can no longer be easily distinguished. In a typical low-energy guided ion beam experiment, this obstacle is circumvented by mass selection of the cluster ion beam in advance of the reactive encounter [27–32]. The reactions commonly take place in a radio frequency (rf) ion guide drift tube as shown in Fig. 4a. The cluster ions confined by the rf field inside the ion guide have a defined low kinetic energy and experience

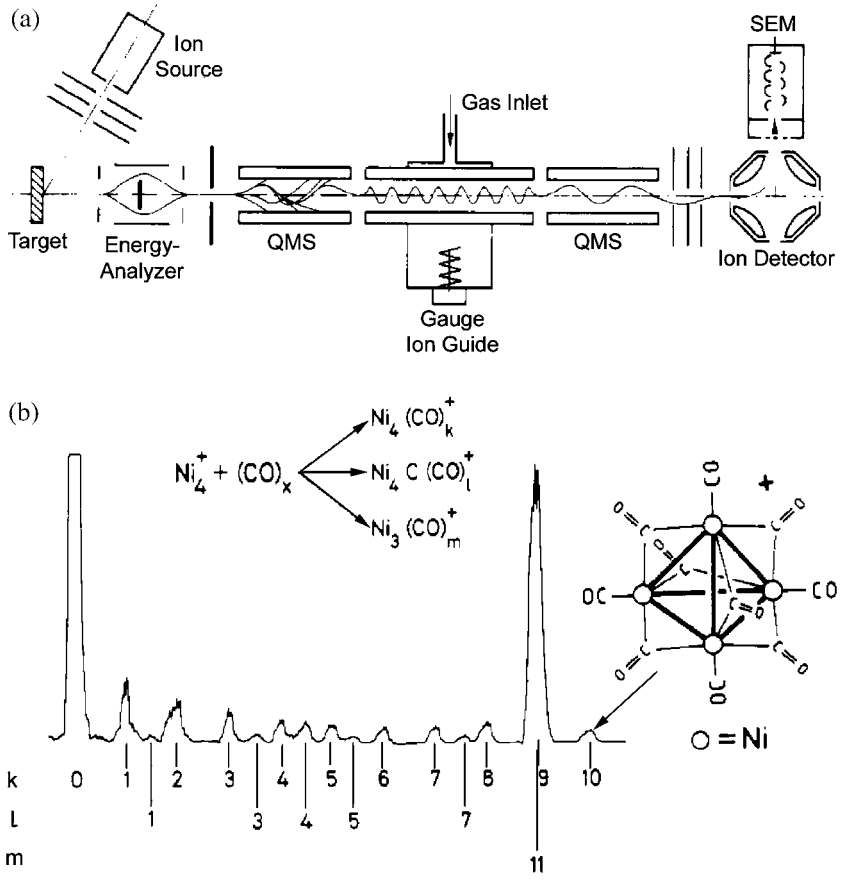

Figure 4: (a) Experimental setup employed by Wöste and co-workers to investigate the chemical reactivity of mass-selected low kinetic energy metal cluster ions with reactive gases like carbon monoxide. The metal clusters are generated by sputtering of a metal target with accelerated rare gas ions. The kinetic energy distribution of the resulting cluster ions is narrowed down during the passage through an energy analyzer. After mass selection with a first quadrupole mass filter (QMS), the ions subsequently enter the ion guide drift tube where they are exposed to reactant molecules. Product ion analysis is again accomplished by a quadrupole mass filter followed by ion detection and signal amplification [33]. (b) Product ion mass spectrum obtained after reaction of a mass-selected Ni_4^+ cluster with approximately 0.3 Pa of CO. The geometric structure of the saturated carbonyl cluster proposed on the basis of simple electron count–structure correlations is also displayed [33].

multiple collisions with the reactive gas added to the ion guide. Mass-selected detection of the product ions is accomplished by a quadrupole mass filter followed by signal amplification with a secondary electron multiplier (SEM).

An example for this method is depicted in Fig. 4b. Nickel clusters are initially produced in a broad size distribution but only Ni_4^+ cluster ions are selected via a first quadrupole mass spectrometer (QMS). Treatment of this beam of tetranuclear clusters with a defined pressure of carbon monoxide and subsequent mass spectrometric analysis of the products reveals the formation of a series of $Ni_4\ (CO)_k^+$ cluster ions. The mass spectrum in Fig. 4b was obtained by increasing the CO pressure gradually until no change in the product spectrum was observed anymore, i.e., when saturation of the cluster with carbon monoxide has occurred [33]. In this case, the highest molecular weight ion has the formula $Ni_4(CO)_{10}^+$. According to simple electron counting rules originally introduced by Wade and Mingos [34, 35] and extended later by Lauher to transition metal clusters [36–38], a four-atom metal cluster will assume tetrahedral symmetry and be maximally stabilized when the total number of cluster valence electrons is 60 [33]. This total is made up of the metal valence electrons augmented by those supplied by the ligands (two from each carbon monoxide). However, in the product ion mass spectrum in Fig. 4b, also the development of two more series of cluster ions can be identified: these are the tetranickel carbido carbonyls $Ni_4\ C(CO)_l^+$ and the trinickel carbonyl clusters $Ni_3\ C(CO)_m^+$, which appear as a consequence of fragmentation processes [33, 38].

2.4. Ion traps

Ion cyclotron resonance (ICR) mass spectrometry and also penning trap mass spectrometry have been demonstrated by several groups to be powerful tools to investigate metal cluster reactivity in the gas phase under single-collision conditions [39–46]. From the schematics in Fig. 5, it can be seen that the ICR cell is a small box or cylinder consisting of four isolated side plates and two isolated end plates. The cell is immersed in a homogeneous magnetic field. To investigate cluster reactions, the cluster ions are injected into the cell as depicted in the setup presented in Fig. 5. The cluster ion packets entering the cell are excited by an rf pulse applied to one plate. Due to the homogeneous magnetic field traversing the ICR cell, the ions are thus led to perform a circular motion in the cell. The cyclotron frequency of the circular motion depends on the ion mass and the magnetic field strength. The image current induced on two opposite plates of the cell is amplified and analyzed by Fourier transformation. Each ion of different mass gives rise to a sine function. From the obtained superposition of sine-waves, the Fourier analysis reveals the complete mass spectrum. This method has a particular high mass resolution and sensitivity. The ICR instruments operate under UHV conditions and reactions are investigated under strict single-collision conditions in this setup. Figure 5b shows an example to demonstrate the viability of an FT-ICR apparatus developed by Smalley and co-workers [47]. Because of the huge amount of germanium isotopes, the initial cluster distribution is simplified by selectively sweeping some masses out. This technique is known as SWIFT (stored waveform inverse Fourier transform). The bottom of Fig. 5b shows the result of exposure of the selected clusters to nitric oxide gas. For some clusters such as Ge_{43}^+ reaction products of the form $Ge_{43}(NO)^+$ and $Ge_{43}(NO)_2^+$ are clearly seen, whereas other clusters such as Ge_{39}^+ and Ge_{45}^+ show no evidence of reaction at all.

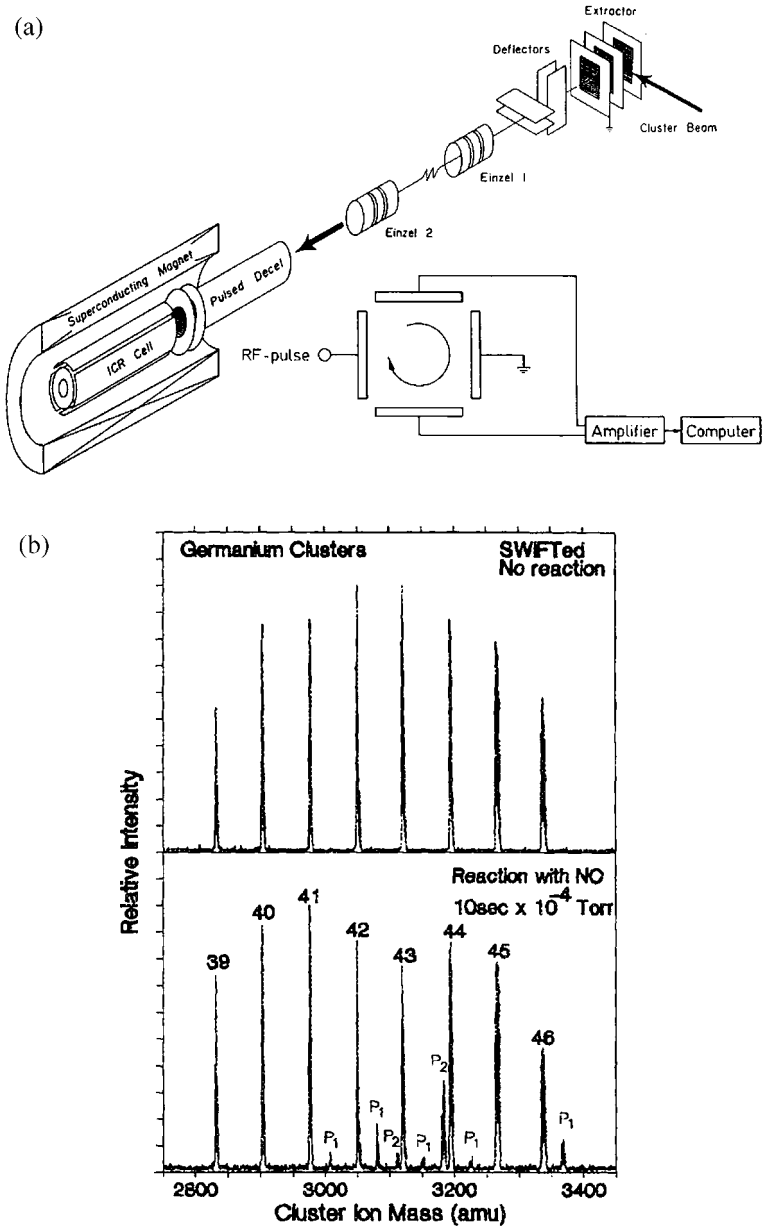

Figure 5: (a) Setup used by Smalley and co-workers to inject cluster ions into an ICR cell. The cluster beam is steered and focused by deflection plates and two Einzel lenses. Before entering the ICR cell, the cluster ions are decelerated. The inset shows the principle of an ICR mass spectrometer. Ions are excited by an rf pulse to propagate in circular orbits. The image currents induced in the electrode plates are amplified and analyzed through computer-based Fourier transformation. The magnetic field in this scheme is perpendicular to the drawing plane. The schemes have been adopted from Refs. [30, 37, 40]. Reproduced with permission from American Chemical Society. (b) Reaction study of Ge_n^+ clusters with nitric oxide. The top panel shows the FT-ICR mass spectrum after selective removal of some ions from the cell by "SWIFT" excitation. The bottom panel shows this spectrum after exposure of the clusters to 1×10^{-4} torr nitric oxide for 10 sec [47]. Reaction products of the form $Ge_x(NO)_y^+$ have been labeled P_y. Reproduced with permission from American Institute of Physics.

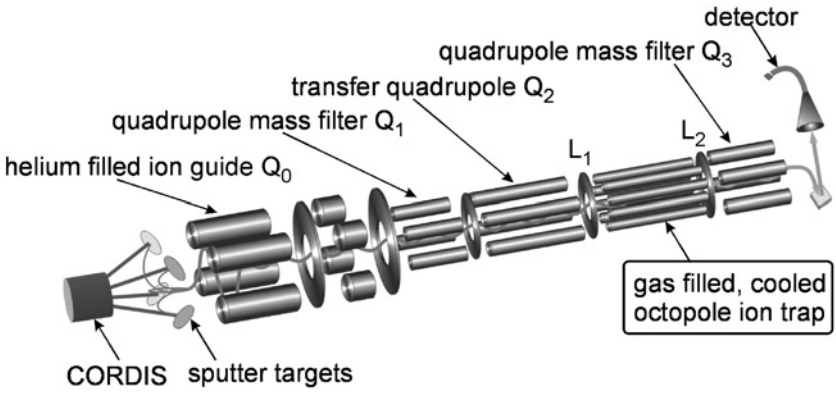

Figure 6: Experimental setup for the investigation of gas-phase catalytic activity of mass-selected metal clusters. The cluster ions are sputtered from solid targets with a cold reflex discharge ion source (CORDIS), mass selected (Q_1), and guided at low energies (Q_0 and Q_2) into the temperature controllable octopole ion trap. By means of appropriate switching of the lenses L_1 and L_2, the reaction products are extracted and subsequently mass-analyzed by another quadrupole mass filter (Q_3) [12, 52].

A rather new approach to investigate metal cluster reactivity and catalysis consists in storing the mass-selected cluster ions in a temperature variable rf octopole ion trap filled with helium buffer gas and small partial pressures of reactant gases under multi-collision conditions. The major advantages of this approach for the investigation of gas-phase reactions is the precise control over reaction time, reactant concentrations, and reaction temperature inside the ion trap. The trap acts like a test tube for gas-phase reaction kinetics studies. It is inserted into a standard guided ion beam apparatus [9, 28, 48]. The schematic layout of the experimental setup is displayed in Fig. 6. Metal clusters are prepared by a sputter source based on the cold reflex discharge ion source (CORDIS [49]). The charged clusters are steered into a first helium filled quadrupole Q_0 to collimate and thermalize the cluster ions. The ion beam is further guided into a mass-selective quadrupole filter Q_1 to select one particular cluster size. Subsequently, the cluster ions are transferred with a third quadrupole Q_2 into the home-built octopole ion trap [12, 45], which is filled with metal cluster ions up to the space charge limit. The trap is prefilled with a helium partial pressure on the order of 1 Pa. A closed cycle helium cryostat attached to the trap allows temperature adjustment in the range between 40 and 350 K. Time-resolved kinetic measurements on the timescale of seconds are performed with small, well-defined partial pressures of the reactants like O_2 and CO present in the trap. For this purpose, all ions are extracted from the trap after a defined storage time by means of a pulsed electrostatic field (lenses L_1 and L_2) and are subsequently mass-analyzed by a final quadrupole mass filter (Q_3). By recording all ion concentrations as a function of the reaction time, the kinetics of the reaction may be obtained. The concentrations of the reactive gases in the octopole trap are orders of magnitude larger than the metal cluster ion concentration. Hence, all the proposed reaction steps are assumed to follow pseudo first-order kinetics. Possible reaction mechanisms are evaluated by fitting the integrated rate equations to the experimental kinetic data to obtain reaction rate constants k [50, 51]. A simple statement on the activation energy of a given system can be made

considering Arrehenius' classical empirical equation for the temperature dependence of reaction rates:

$$k(T) = v \exp\left(\frac{-E_a}{RT}\right) \tag{1}$$

with v being the frequency factor, T the temperature, R the gas constant, and E_a the activation energy of the reaction.

The total pressure inside the ion trap is on the order of 1 Pa, which means that the experiment is operating in the kinetic low-pressure regime. Therefore, a Lindemann-type mechanism has to be considered for each reaction step and the reaction rates depend on the buffer gas pressure [50, 51]. As a consequence, the obtained pseudo first-order rate constant k contains the termolecular rate constant $k^{(3)}$ as well as the concentrations of the helium buffer gas and of the reactants. Considering the following equation as a generalized reaction of the metal anion M^- with the neutral reactant X in the presence of helium as buffer gas:

$$M^- + X \rightarrow MX^- \tag{2}$$

the first-order rate constant k is given by

$$k = k^{(3)}[He][X] \tag{3}$$

The details of the reaction are described by the Lindemann energy transfer model for association reactions, which is represented by the following equations [50, 51, 53]:

$$M^- + X \underset{k_d}{\overset{k_a}{\rightleftarrows}} MX^{-*} \tag{4a}$$

$$MX^{-*} + He \xrightarrow{k_s} MX^- + He^* \tag{4b}$$

The reaction model includes the elementary steps of the initial formation of an energized complex MX^{-*} (rate constant k_a) and its possible unimolecular decomposition back to the reactants (k_d) in competition with a stabilizing energy transfer collision with helium buffer gas (k_s). Assuming all these elementary reaction steps to be again of pseudo first order and employing steady-state assumption for the intermediate, the overall third-order rate expression is obtained to be [54]

$$k^{(3)} = \frac{k_a \times k_s}{k_d + k_s[He]} \tag{5}$$

As the experiment is operating in the kinetic low-pressure regime, the decomposition rate constant can consequently be considered to be much larger than the stabilization rate constant term: $k_d \gg k_s[He]$. This leads to a simplified expression for the termolecular rate constant, which can be applied to the experimental conditions in the rf ion trap experiment:

$$k^{(3)} = \frac{k_a \times k_s}{k_d} \tag{6}$$

The ion–molecule association rate constant k_a as well as the final stabilization rate constant k_s are well represented by ion–molecule collision rate coefficients as specified by Langevin theory [54]. According to this theory, ion–molecule reactions

are basically charge-induced dipole interactions and exhibit no activation barrier, i.e., no temperature dependence [55]. In order to estimate k_d, statistical rate theory such as Rice–Ramsperger–Kassel (RRK)-theory or Rice–Ramsperger–Kassel–Markus (RRKM)-theory may be employed [50, 51].

3. CONCEPTS IN CLUSTER ION CHEMISTRY

The aim of this section is to present some aspects unique to the study of gas-phase metal cluster ions and to introduce concepts that are important to cluster ion chemistry, in particular, with respect to the analysis of catalytic reaction mechanisms. These aspects and concepts summarized here will be illustrated by examples in the following sections of this chapter.

3.1. Particle size-dependent reactivity

Gas-phase investigations allow to employ mass spectrometric techniques to define the exact number of atoms that constitute the metal particles of interest. This is particularly important as in the non-scalable size regime below about 100 atoms per particle each atom is important to the catalytic reaction behavior and the chemical and physical properties of the particles often change by orders of magnitude when adding or removing a single atom (cf. Fig. 1). Whereas small free metal clusters present fascinating new catalytic materials by themselves, mass-selective gas-phase methods also enable the study of size-dependent reaction behavior starting from isolated atomic ions over small clusters and eventually reaching the regime of nanoparticles employed in condensed-phase heterogeneous catalysis.

3.2. Charge state-dependent reactivity

In particular, in noble metal catalysis, charging of supported metal particles has been found to decisively determine the catalytic activity of the model catalyst materials [56, 57]. However, the analysis of the influence and the extent of the charge transfer is difficult to evaluate experimentally in supported systems. In gas-phase systems, the charge state is exactly defined and the investigation of the chemical reaction behavior as a function of the charge state can provide important insight into electronic effects in catalytic reactions on small metal clusters like the O_2 activation.

3.3. Composition-dependent reactivity

With respect to the influence of the electronic structure on catalytic activity, the elemental composition of the metal cluster presents a second important aspect [56]. By changing the constituents of a cluster atom by atom, reactive behavior and important catalytic properties such as the reaction selectivity might be tuned to a maximum for a specific reaction system. In the majority of cases, mass spectrometric gas-phase techniques enable precise control over the metal particle composition, which is in turn widely tunable with modern cluster sources. This versatile access to the influence of particle composition on catalytic behavior should provide important basic information for systematic catalyst material design.

3.4. Cooperative coadsorption effects

Coadsorption phenomena in heterogeneous catalysis and surface chemistry quite commonly consider competitive effects between two reactants on a metal surface [58, 59]. Also, cooperative mutual interaction in the adsorption behavior of two molecules has been reported [58]. Recently, this latter phenomenon was found to be very pronounced on small gas-phase metal cluster ions, too [60–63]. This is assigned to the above-mentioned fact that the metal cluster reactivity is often strongly charge state dependent and that an adsorbed molecule can effectively influence the electronic structure of the metal cluster by, e.g., charge transfer effects. This changed electronic complex structure in term might foster (or also inhibit) adsorption and reaction of further reactant molecules that would otherwise not be possible. Specific examples of cooperative adsorption effects on gas-phase gold and silver clusters will be presented in the following section.

3.5. Ultimate "single site" catalysts

In a recent review, Böhme and Schwarz convincingly present gas-phase studies on "isolated" reactants as an ideal arena for detailed experiments leading to a profound understanding of energetics and kinetics of catalytic reactions on a strictly molecular level. In concluding, these authors state that "… after all, ions in the gas phase provide the 'single sites' that are active in surface catalysis" [6]. Nevertheless, on the basis of the investigations conducted so far, it becomes already clear that ion and cluster catalysis in the gas phase must be regarded most instructive in the comprehension of important fundamental aspects of practical catalysis in the condensed phase.

4. CATALYTIC ACTIVITY OF GAS-PHASE CLUSTERS

In this section, the focus will be on some prominent examples for the reactivity and, in particular, the catalytic behavior of small clusters of iron, platinum, gold, and silver. Surprisingly, for both, iron and platinum, already the monomer shows strong reactivity. The understanding of platinum clusters especially in the CO combustion reaction is extremely important as platinum besides palladium and rhodium is a central material used in heterogeneous catalysis. The catalytic activity of gold and silver clusters in the CO oxidation reaction has been discovered only recently and a large part of this section will be devoted to gas-phase studies on gold, silver, and binary cluster ions, trying to illustrate the concepts outlined in Section 3.

4.1. Review of free transition metal cluster catalysis

4.1.1. Iron clusters

Kappes and Staley reported the first catalytic cycles involving transition-metal cations and their oxides in the gas phase. In 1981, using ICR mass spectrometry, the oxidation of CO catalyzed by iron cations was reported [39]. Fe^+ exposed solely to CO does not react. However, about 80% of the iron ions react to yield the oxide FeO^+ when Fe^+ is exposed to 5×10^{-4} Pa of N_2O. The addition of CO to this reaction system increases the Fe^+ ion signal while the FeO^+ ion signal decreases. This is evidence that the oxygen atom is transferred to the CO molecule forming the neutral CO_2 while the catalyst Fe^+ is recovered and can undergo further reaction cycles. Analogue catalytic cycles were observed for Fe^+ exposed to mixtures of N_2O with ethylene, propylene,

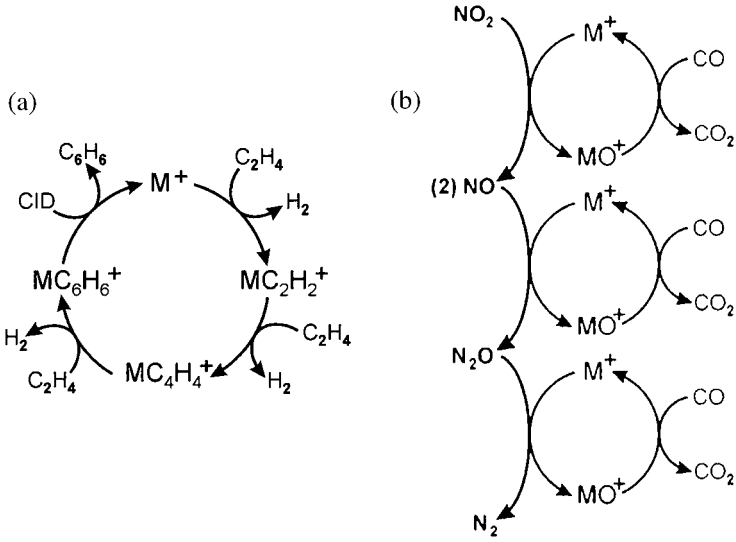

Figure 7: (a) General schema for the trimerization reaction of ethylene to yield benzene in a final collisionally activated reaction step (CID). This reaction has been shown to proceed with the iron tetramer cluster Fe_4^+ as a catalyst [10]. (b) Catalytic cycles for the homogeneous reduction of nitrogen oxides by carbon monoxide, mediated by atomic transition metal cations [68].

allene, ethane, and propane [39], and rate constants for the reaction of Fe^+ and FeO^+ with a variety of neutral inorganic and organic molecules (e.g., CO, N_2O, H_2O, CH_4) were measured later also by other groups [64, 65].

Interestingly, not only the monomer cation but also the cluster Fe_4^+ is catalytically active. Fe_4^+ is able to facilitate the cyclization reaction of ethylene C_2H_4 to benzene C_6H_6 [10]. Figure 7a shows the gas-phase trimerization of ethylene which was observed to proceed, in addition to Fe_4^+, also for the ions W^+ and U^+ [10, 66, 67]. The reaction cycle starts with the formation of a cationic metal–ethyne complex via dehydrogenation of ethylene by the metal (cluster) ion M^+. The next step is often rate determining and yields $MC_4H_4^+$ by dehydrogenation of a further ethylene molecule. Upon the third addition of ethylene, benzene complexes are formed again via loss of molecular hydrogen. Although the latter reaction step is exothermic, the heat of reaction liberated is usually not enough to overcome the large bond dissociation energy of the metal–benzene complex. Using collision-induced dissociation (CID) with xenon to act on the above-described system, two fragmentation patterns are observed. Products with less than three acetylene lead to the formation of carbides while CID of adducts with three or more ligands leads to the loss of all C and H atoms. Bare M^+ ions are the result. The kinetic behavior of the adducts suggests that benzene C_6H_6 is liberated. From these results, the conclusion can be drawn that Fe_4^+ catalyzes the formation of benzene from ethylene; however, in an ideal catalytic system under thermal conditions, the catalytically active species should be regenerated without an additional supply of energy.

As already mentioned, the oxidation of carbon monoxide has always been a prominent reaction to show catalytic activity of metal clusters. Böhme and co-workers published a comprehensive thermodynamic and kinetic study of the catalytic activity

of 29 transition metal cations toward the reduction of the nitrogen oxides NO_2, NO, and N_2O in combination with the oxidation of CO [68]. The three catalytic cycles shown in Fig. 7b reflect the results of the investigation using an inductively coupled plasma/selected-ion flow tube (ICP/SIFT) tandem mass spectrometer. Among Os^+ and Ir^+, the iron cation Fe^+ was most effective in all three complete cycles. In each of the three cycles, the iron cation is first oxidized by a nitrogen oxide, which is the necessary source for further CO oxidation. The bare iron cation is then regenerated. The combination of the three cycles shown in Fig. 7b leads to the conversion of N_2O and CO to N_2 and CO_2:

$$2NO_2 + 4CO \rightarrow N_2 + 4CO_2 \tag{7}$$

While the combination of only the second and third cycle leads to the overall reaction

$$2NO + 2CO \rightarrow N_2 + CO_2 \tag{8}$$

This is the resulting reaction taking place in automotive catalytic converters to annihilate toxic gases produced in the fossil-fuel combustion.

4.1.2. Platinum clusters

The first catalytic *cluster ion* reaction cycle under thermal conditions was observed by Ervin and co-workers [11]. A "full thermal catalytic cycle" means a reaction cycle in which a bare metal cluster adsorbs reactant molecules, desorbs product molecules, and regenerates the intact cluster, all at thermal energies. Ervin demonstrated that the gas-phase cluster anions Pt_n^- ($n = 3$–7) efficiently catalyze the oxidation of CO to CO_2 by N_2O or O_2 near room temperature in a combined flow tube and gas cell reactor instrument under multi-collision conditions. The observed catalytic reaction cycles are summarized in Fig. 8a. In previous experiments, it was shown that the addition of O_2 or N_2O to the Pt_n^- clusters leads to a rapid exothermic reaction, in which Pt_nO^- and $Pt_nO_2^-$ ions are formed [69]. The only observed reaction with N_2O is the addition of oxygen atoms to the intact cluster under liberation of N_2. With the introduction of CO into the reaction gas cell of the instrument containing mass-selected Pt_nO^- complexes ($n = 4$–6), the only product ion observed with mass spectrometry is Pt_n^-. Only

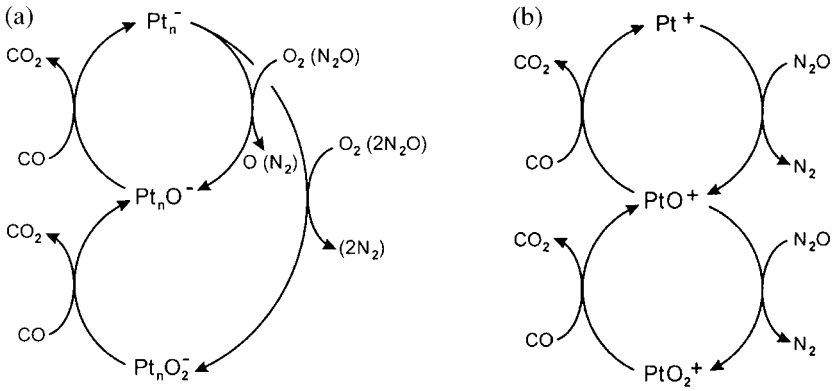

Figure 8: (a) Reaction cycles for the oxidation of CO catalyzed by gas-phase platinum cluster anions as formulated by Shi and Ervin [11]. (b) Observed reaction cycles for the oxidation of carbon monoxide by nitrous oxide catalyzed by gas-phase atomic platinum cations [70].

for smaller cluster sizes, negligible fragmentation of the metal cluster occurs. It was concluded that the sole exothermic product channel is the oxidation of CO to form neutral CO_2.

The introduction of CO into the reaction cell containing $Pt_nO_2^-$ shows two reaction channels, yielding Pt_nO^- and Pt_n^-. CO pressure dependence studies reveal that the bare Pt_n^- cluster is regenerated by sequential oxidation of two CO molecules. Collisional stabilization of the cluster oxides in the presence of buffer gas was pointed out as an important factor for the observation of catalytic activity, because under single-collision conditions in the guided beam, extensive fragmentation would prohibit the re-formation of the initial metal clusters. The regeneration of Pt_n^- ions at low energies proves that a full catalytic oxidation cycle can be completed at near room temperature, in either a single-step or a two-step process as indicated in Fig. 8a.

The activity of Pt^+ ions in the catalytic conversion of CO to CO_2 has been investigated by Schwarz and co-workers in an FT-ICR mass spectrometer [70]. As atomic platinum cations do not react with molecular oxygen [46], the oxygen-atom transfer reaction with nitrous oxide has to be used for the generation of the active intermediates PtO^+ and PtO_2^+ (Fig. 8b). Isotopic exchange reactions with $H_2^{18}O$ and $^{18}O_2$ suggest that the structure of PtO_2^+ is rather described as a dioxide ($OPtO^+$) than as a peroxide ($PtOO^+$) or as a dioxygen complex ($Pt(O_2)^+$). The absence of an O–O bond in this ion is confirmed by calculations using correlated ab initio methods at the CASPT2 level of theory [70]. In the presence of carbon monoxide, both oxide ions readily react releasing carbon dioxide. Upon treating PtO_2^+ with a mixture of CO and N_2O, quasistationary concentrations of Pt^+, PtO^+, and PtO_2^+ are obtained in the FT-ICR experiment after only a few seconds of reaction time. Identical stationary concentrations of these ions evolve when starting from Pt^+ or PtO^+, respectively. Thus, reaction cycles as depicted in Fig. 8b can be formulated, describing the effective catalysis of the conversion $CO + N_2O \rightarrow CO_2 + N_2$ by the gaseous platinum species.

Figure 8 also shows that the catalytic cycles for negatively and positively charged platinum atoms and clusters are very similar and that there is no obvious charge state dependence in the mechanism of small platinum cluster CO combustion catalysis. The only difference results from the fact that, in contrast to Pt^+, Pt_n^- clusters react with O_2 leading to a direct formation of the intermediate dioxide $Pt_nO_2^-$ without previous formation of the monoxide Pt_nO^- as it is the case for the oxidation reaction involving nitrous oxide.

A gas-phase catalytic reaction similar to the one described for Pt^+ in Fig. 8b was recently observed also for Pt_n^+ clusters in reaction with CO and N_2O in an FT-ICR experiment [71]. Most interestingly, a strong size dependence not only in the reactivity but also in the catalytic activity of the clusters is obvious. Catalytic activity was observed for platinum cluster cations with five to eight atoms, whereas Pt_9^+ and particularly Pt_{10}^+ were found to predominantly merely adsorb carbon monoxide instead of oxidizing CO. Detailed investigations of the Pt_7^+ reaction (cf. Fig. 9) revealed that efficient catalytic oxidation of CO to CO_2 is achieved in three different ways: (i) CO collision with Pt_7O^+, formed by oxidation of Pt_7^+ through N_2O; (ii) CO collision with $Pt_7O_2^+$, formed by a two-step oxidation of Pt_7^+ through N_2O; (iii) N_2O oxidation of preadsorbed CO on Pt_7CO^+. Evidently, by addition of multiple CO molecules, some bare Pt_7^+ clusters were removed from the catalytic cycle. To further investigate this observation, the experiments were run at high CO partial pressures in the ICR cell.

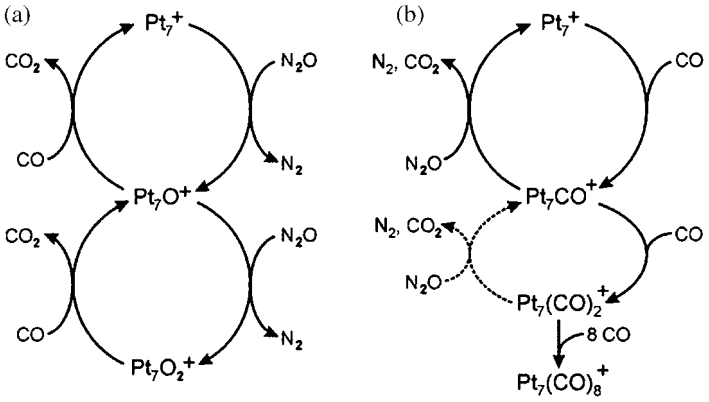

Figure 9: (a) Catalytic cycles of the Pt_7^+ ion in a 1:6 mixture of CO and N_2O. The experiment was carried out under single-collision conditions in an FT-ICR instrument. (a) The catalytic cycles involving Pt_7O^+ and $Pt_7O_2^+$ are identical to the Pt^+ cycles in Fig. 8b. (b) In addition, a cycle involving the initial formation of Pt_7CO^+ is observed. Additional CO molecules, however, increasingly poison the cluster. The conversion of $Pt_7(CO)_2^+$ back to Pt_7CO^+ might contribute to a minor extent to the catalytic activity [71].

The previously mass-selected Pt_7CO^+ complexes were either converted back to Pt_7^+ under liberation of N_2 and CO_2 or they adsorbed another CO molecule to form $Pt_7(CO)_2^+$. $Pt_7(CO)_2^+$, in turn, was found to eagerly adsorb further CO molecules and only a very minor part could be oxidized back to the bare metal cluster. In this way, platinum clusters are CO poisoned and are increasingly removed from the catalytic reaction cycles at enhanced CO partial pressures. With regard to the other cluster sizes, it was observed that the catalytic activity with respect to CO oxidation by N_2O is largely determined by the reactivity of the bare cluster with N_2O: A high reactivity toward N_2O apparently shifts the cluster intensities in favor of the oxide species, effectively hindering the poisoning reaction by sequential CO adsorption on the bare cluster [71].

4.2. Gold cluster catalysis

A very prominent recent example for the importance of size effects on the properties of matter is the catalytic activity of highly dispersed supported gold nanoparticles and clusters. Nanometer-sized gold particles on metal oxide support efficiently oxidized carbon monoxide even at low temperatures, where the activity of common catalyst materials is marginal [72–77]. Since gold is known as noble, hence inert material [78], this counterintuitive observation fostered numerous experimental and theoretical investigations on the chemical reactivity of small gold particles and clusters. Most strikingly, in the non-scalable cluster size regime, mass-selected gold clusters on magnesia with eight atoms actively facilitate the oxidation of CO whereas seven-atom gold clusters are completely inert [79]. The reason for this strong size dependence and the mechanism of the oxidation reaction is still unresolved. The charge state of the atomic gold clusters was identified in these investigations as one important factor for the catalytic activity. Electron transfer from surface defect centers to the cluster–adsorbate complex has been found to be essential to activate catalytic properties

[57, 79]. These findings were one of the starting points for the gas-phase reactivity investigations with mass-selected gold cluster ions, which will be presented and discussed in this section.

4.2.1. Electronic structure and chemical properties of free gold clusters

The interesting charge state-dependent reactivity of free gold clusters was recognized already in 1991 by Cox et al. [80, 81]: Small positively charged gold clusters do not react with molecular oxygen, whereas negatively charged gold clusters exhibit a pronounced odd–even alternation in their reaction behavior with O_2. This remarkable size and charge state dependence was confirmed by several groups later on [61, 82, 83]. Recently, Castleman and co-workers, however, were able to show the oxidation of CO molecules on atomic gold anions and cationic gold clusters with *atomic* oxygen [84, 85]. Due to oxygen introduction in a laser evaporation source, they were able to produce preoxidized gold cluster cations in which oxygen is bound in both the molecular and atomized forms to Au^+ and Au_2^+. All these oxides were observed to react with CO molecules at the reactant gas inlet. Yet, these processes are not thermal catalytic cycles and therefore will not be further discussed here. Thus, the focus of this section will be on the size-dependent electronic and the corresponding chemical properties of *negatively charged* gold clusters in particular with respect to the activation of *molecular* oxygen, which is considered decisive to the understanding of catalytic activity in the CO oxidation reaction.

Gold cluster anions show a strong odd–even alternation in VDE values with cluster size, which can be attributed largely to the s^1 valence electron structure of group Ia transition metal elements. Electronic closed shell (paired electron) cluster sizes are generally more stable and exhibit higher VDEs than open shell systems [1, 86, 87]. Compared with the other coinage metal clusters silver and copper, the VDE values of the gold cluster anions (with the exception of Au_6^-) are in general roughly about 1 eV higher. It has been discussed by several authors that, although silver and copper belong to the same group in the periodic system as gold and the atomic electronic structure of all of them exhibit a filled d shell and a singly occupied s shell ($nd^{10}(n+1)s^1$, with $n = 3$, 4, and 5 for copper, silver, and gold, respectively), the bonding in gold compounds and clusters is substantially different from that of copper and silver due to relativistic effects only occurring in gold clusters. This phenomenon is referred to as "gold anomaly" [88, 89]. The main relativistic effect in gold is the stabilization of the $6s^1$ orbital and the destabilization of the $5d^{10}$ orbitals, thus bringing them energetically closer [90]. The result is a hybridization of atomic s and d states in the case of gold, which has important implications not only on the chemistry of gold clusters but also on their geometrical structure. Gold cluster anions, e.g., are planar in structure up to sizes of about 12 atoms [87, 90, 91], whereas silver and copper clusters are three-dimensional from Ag_6^- and Cu_6^- on [90, 92, 93].

Gold anions also show the above-mentioned pronounced odd–even alternation with cluster size in their reactivity toward O_2, in contrast to positive and neutral gold clusters. Figure 10a presents a compilation of the results on Au_n^- reactivity toward O_2. Small gold cluster anions only adsorb one or none oxygen molecule depending on the cluster size. The reactions of gold cluster anions with carbon monoxide have also been reported [63, 82, 94–96]. However, although strong size effects in reactivity are apparent, no odd–even alternations are observed in this case as can be seen from

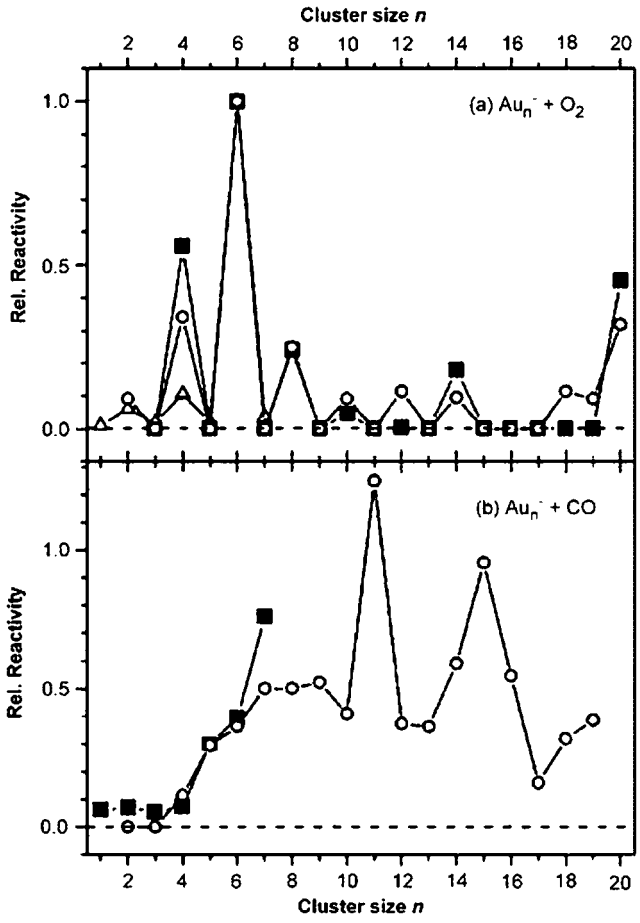

Figure 10: Compilation of experimental results from the literature on the relative reactivity of gold cluster anions in the adsorption reaction of one O_2 or one CO molecule, respectively, as a function of the cluster size *n*. (a) Reactions of Au_n^- with O_2: (-■-) data from Ref. [80, 81], (-□-) data from Ref. [82], (-○-) data from Ref. [83]. For comparison, all data are normalized to the reactivity of Au_6^-. (b) Reactions of Au_n^- with CO: (-■-) data from Ref. [82], (-○-) data from Ref. [63]. Again, the data shown have been normalized to the reactivity of Au_6^- toward O_2.

Fig. 10b, which is based on results of Lee and Ervin [82], as well as of Wallace and Whetten [63].

The observed odd–even alternations in reactivity of Au_n^- toward O_2 with the cluster size (Fig. 10a) can be rationalized qualitatively by considering the frontier orbital interactions: The degenerate 2p π_g^* anti-bonding orbitals of oxygen are each occupied by an unpaired electron. This triplet open-shell electronic ground state structure is rather unusual for stable molecules and leads to an electron acceptor behavior similar to the one found in the NO_x family of free radicals [83]. Oxidative addition to the cluster requires interaction of an O_2 π_g^* orbital with the highest occupied molecular orbital (HOMO) of the noble metal cluster which has σ-type symmetry. In the case of even *n* clusters, the Au_n^- HOMO has an unpaired electron with relatively low binding

energy. In the bound complex $Au_nO_2^-$, this electron is easily paired with the single electron in one O_2 π_g^* orbital. The combination of the two orbitals results in an attractive interaction and a partial electron transfer to the O_2 adsorbate. In contrast, for odd n clusters, the Au_n^- HOMO is doubly occupied leading to higher VDEs. Consequently, the electron transfer to the adsorbate is considerably weaker, meaning that the interaction with the O_2 π_g^* is much less attractive, because the additional electron must be placed in the anti-bonding orbital of the $Au_nO_2^-$ complex. As a result, the reactivity of even n gold cluster anions toward molecular oxygen is by far superior to that of odd n clusters [82, 83, 97].

The consequences for the O_2 adsorbate structure, deduced from the frontier orbital picture, are an O–O bond elongation resulting from the electron transfer into the O_2 π_g^* anti-bonding orbitals. This effect evidently depends on the amount of charge transfer and generates a superoxide, or superoxo (O_2^-)-type adsorbate species. In the case of negatively charged gold clusters, the molecular superoxo structure of the adsorbed oxygen could be confirmed by UV photoelectron spectroscopy (UPS) experiments [98–100]. Figure 11 shows UPS spectra of different small gold cluster anions with adsorbed O_2 molecules. The vibrational fine structures with spacings of about 150–180 meV measured for $Au_nO_2^-$ with $n = 2, 4$ correspond to the O–O stretching frequencies, which are indicative of the non-dissociative adsorption of O_2 [98]. In contrast, the observed vibrational frequency of the $Au_1O_2^-$ complex (98 meV) is more likely to be assigned to atomic Au–O stretching, as also indicated by the calculated structure in Fig. 11 [98]. For a better understanding of the chemisorption mechanism of O_2, further UPS spectra of the bare clusters Au_2^- and Au_4^- in comparison with their oxides $Au_nO_2^-$ were performed. It was observed that upon the adsorption of an O_2 molecule, the valence band structure of the gold cluster is completely changed, indicating a large interaction

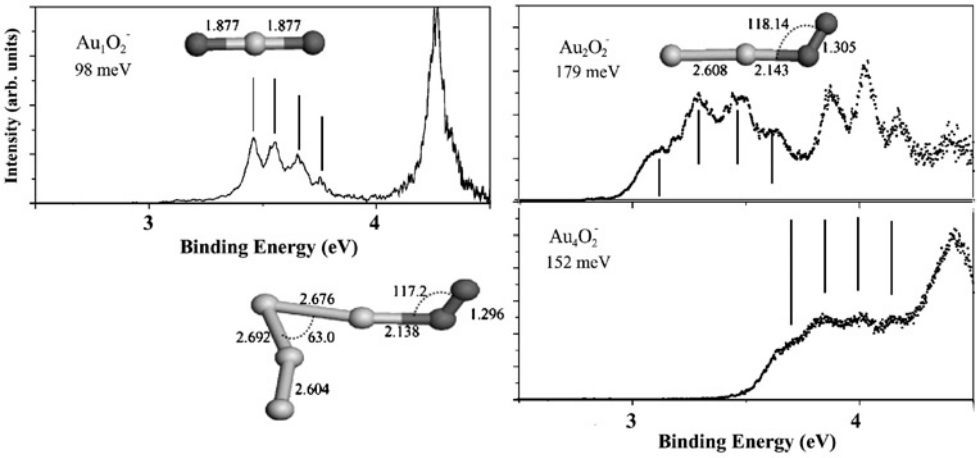

Figure 11: Mass-selected negative ion photoelectron spectra for $Au_nO_2^-$ clusters ($n = 1, 2, 4$). The fine structures in the spectra correspond to the vibrational frequencies of the neutral state in the geometry of the anion. Indicated are also the geometric equilibrium structures of the cluster complexes obtained from DFT calculations [98]. Reproduced with permission from American Institute of Physics.

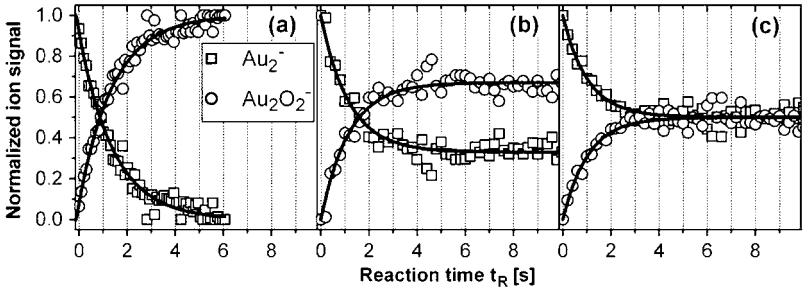

Figure 12: Kinetic traces for the reaction of Au_2^- clusters with (a) O_2 only; (b) and (c) with O_2 and CO in the rf octopole ion trap at 300 K [53]. The reaction parameters are (a) $p(He) = 1.00$ Pa, $p(O_2) = 0.30$ Pa, $p(CO) = 0$ Pa; (b) $p(He) = 0.99$ Pa, $p(O_2) = 0.13$ Pa, $p(CO) = 0.16$ Pa; (c) $p(He) = 1.01$ Pa, $p(O_2) = 0.11$ Pa, $p(CO) = 0.25$ Pa.

between O_2 and the Au cluster anions [98] which leads to a highly activated adsorbed oxygen molecule.

In gas-phase kinetic experiments employing a temperature variable rf octopole ion trap, it was also found that $Au_2O_2^-$ is the only product in the reaction of Au_2^- with molecular oxygen [97, 101]. The kinetic data of this reaction are displayed in Fig. 12a. The reaction proceeds in a straightforward association mechanism:

$$Au_2^- + O_2 \rightarrow Au_2O_2^- \tag{9}$$

which is supported by the excellent fit of the integrated rate equation of this mechanism represented by the solid line in Fig. 12a. However, most notably, the deduced reaction rate appears to increase with decreasing reaction temperature. According to Arrhenius law (Eq. (1)), this inverse temperature dependence would yield a negative activation energy that is indicative for barrierless adsorption pathways in the framework of the Lindemann mechanism discussed in Section 2.4.

In the following section, we will discuss the CO oxidation reaction catalyzed by the negatively charged gold dimer. Indications for catalytic activity in the CO combustion reaction have been reported also for larger gold cluster anions [63]; however, through combination of kinetic, temperature-dependent ion trap measurements with ab initio calculations, a detailed molecular mechanistic understanding could be obtained for the catalysis by free Au_2^- [53].

4.2.2. Catalytic CO oxidation by Au_2^-

CO also reacts with Au_2^- in the ion trap experiment, however, with a reaction rate which is about one order of magnitude slower than that of the O_2 reaction. As a consequence, carbonyls of Au_2^- are only observed at temperatures below 250 K [102]. Accordingly, when the octopole ion trap is filled with similar partial pressures of both reactive gases, O_2 adsorption will most likely precede CO adsorption [53]. Figure 12b and c shows the product ion concentration of Au_2^- and $Au_2O_2^-$ as the only observed reaction product at 300 K as a function of reaction time while *both, O_2 and CO*, are present in the trap. In contrast to Fig. 12a where solely oxygen was present in the trap, surprisingly enough, Au_2^- is no longer completely transformed into oxide, but an offset appears in the gold cluster concentration at long reaction times. The most

simple reaction mechanism that fits these data is the equilibrium reaction in which oxide is formed but the bare gold dimer is re-formed to a certain extent.

$$Au_2^- + O_2 \underset{k_{-1}}{\overset{k_1}{\rightleftarrows}} Au_2O_2^- \tag{10}$$

Note that the Au_2^- offset is only observed when CO is present in the ion trap, although this is not reflected in Eq. (10). Further insight into the reaction mechanism can be obtained from partial pressure-dependent measurements shown in Fig. 12b and c. Correlated with the ratio $p(CO)/p(O_2)$, the rate constant k_{-1} doubles in Fig. 12c compared with that in Fig. 12b. Hence, increasing the CO partial pressure enhances the backward reaction step. Consequently, Eq. (10) fails to provide a complete description of the reaction and an appropriate description involves more complex reaction steps. To reveal the complete reaction mechanism, the reaction was investigated at lower temperatures.

Product ion distributions at two different temperatures for the case when O_2 and CO are present in the trap are depicted in the left hand side of Fig. 13. As can be seen from these mass spectra, the dimer Au_2^- forms the dioxide $Au_2O_2^-$ as the only reaction product observable at 300 K, but a new, additional peak at the mass of $Au_2(CO)O_2^-$ appears at a temperature of 100 K (hatched peak in Fig. 13). This is a final major reaction product which shows that Au_2^- clearly favors the simultaneous coadsorption of both, oxygen and carbon monoxide, over adsorption of just one sort of reactive molecules [53, 97].

This kind of cooperative effect was also found for Au_3^- in the ion trap experiments [97] and for larger gold cluster anions in a flow tube reactor study [63]. Furthermore, under the conditions of the ion trap experiment at 100 K, small amounts of $Au_2O_2^-$ are present, too (Fig. 13 (left)). But most interestingly, no Au_2CO^- or $Au_2(CO)_2^-$ carbonyls are observed at any temperature or reaction time, although these complexes are stable products at cryogenic temperatures [102]. The absence of carbonyl complexes can be rationalized by the above-mentioned observation that the reaction of Au_2^- with oxygen appears to be considerably faster than with carbon monoxide.

The product ion mass spectra recorded at low temperatures with O_2 and CO in the ion trap (Fig. 13 (left) [53]) show the appearance of the coadsorption complex $Au_2(CO)O_2^-$ as discussed above. This complex represents a key intermediate in the reaction mechanism of the catalytic oxidation of CO to CO_2 as has been predicted in an earlier theoretical study [103]. The experimental evidence obtained so far demonstrates that O_2 adsorption is likely to be the first step in the observed reaction mechanism. Subsequent CO coadsorption yields the observed intermediate and finally the bare gold dimer ion must be re-formed. The objective then was to find one reaction mechanism that is able to fit all experimental kinetic data obtained under the various reaction conditions (see right hand side of Fig. 13). This kinetic evaluation method results in the simplest mechanism that is able to fit the experimental data. In this way, it is possible to rule out all but one possible reaction mechanism that is represented by the following reaction equations:

$$Au_2^- + O_2 \rightarrow Au_2O_2^- \tag{11a}$$

$$Au_2O_2^- + CO \rightleftarrows Au_2(CO)O_2^- \tag{11b}$$

$$Au_2^- + 2CO_2 \rightarrow Au_2^- + 2CO_2 \tag{11c}$$

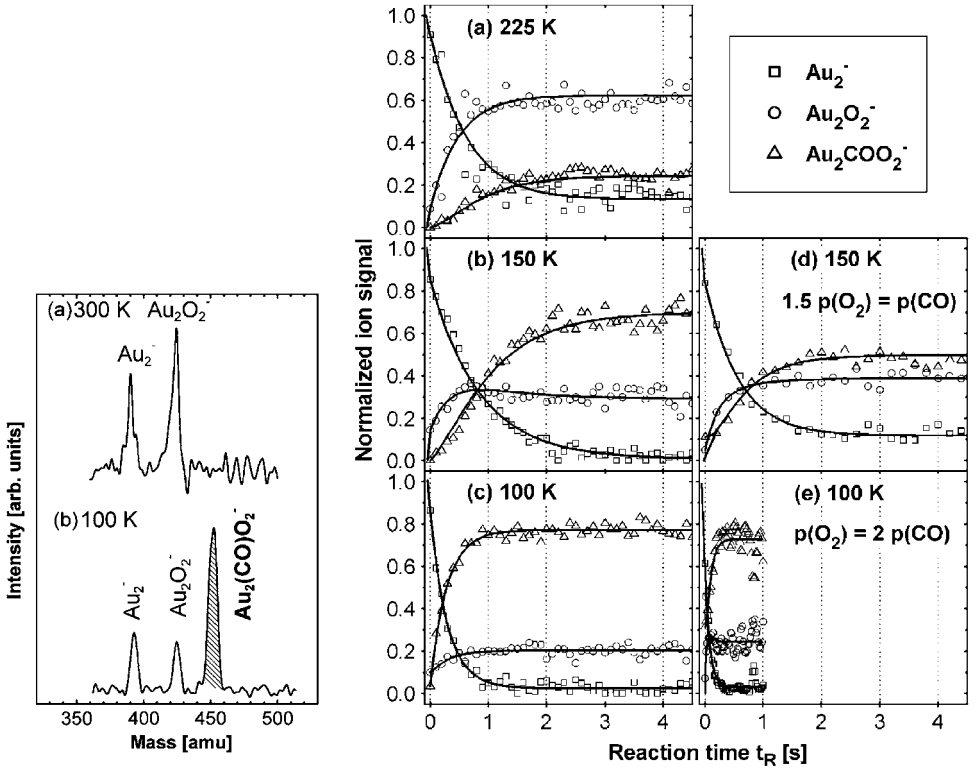

Figure 13: (Left) Mass spectra of product ion distributions analyzed after trapping Au_2^- for 500 msec inside the octopole ion trap filled with 0.02 Pa O_2, 0.05 Pa CO, and 1.23 Pa He at two different temperatures. (Right) Product ion concentrations as a function of the reaction time for three different reaction temperatures and different reactant gas concentrations. (a) $T_{Octopole} = 225$ K, $p(O_2) = 0.09$ Pa, $p(CO) = 0.10$ Pa, $p(He) = 1.07$ Pa. (b) $T_{Octopole} = 150$ K, $p(O_2) = 0.04$ Pa, $p(CO) = 0.04$ Pa, $p(He) = 1.0$ Pa. (c) $T_{Octopole} = 100$ K, $p(O_2) = 0.02$ Pa, $p(CO) = 0.03$ Pa, $p(He) = 1.0$ Pa. (d) $T_{Octopole} = 150$ K, $p(O_2) = 0.04$ Pa, $p(CO) = 0.06$ Pa, $p(He) = 1.01$ Pa. (e) $T_{Octopole} = 100$ K, $p(O_2) = 0.08$ Pa, $p(CO) = 0.04$ Pa, $p(He) = 1.03$ Pa. Open symbols represent the normalized experimental data. The solid lines are obtained by fitting the integrated rate equations of the catalytic reaction cycle (Eq. (11)) to the experimental data.

The solid lines in Fig. 13 (right) represent the fit of this mechanism to the experimental kinetic data. It equally well fits all obtained kinetic data [53]. In this catalytic reaction cycle, $Au_2O_2^-$ reacts with CO to form $Au_2(CO)O_2^-$ which will either re-dissociate to the oxide or further react with a second CO molecule to re-form Au_2^- while liberating two CO_2 molecules. It should be noted that the quality of the fit is very sensitive to the postulated reaction steps and that the kinetic evaluation procedure is clearly able to discriminate against alternative mechanisms. The replacement of the equilibrium in Eq. (11b), e.g., by a simple forward reaction will lead to a mechanism that yields an inadequate fit to the experimental data. The $Au_2O_2^-$ signal will then disappear at long reaction times, which is not the case as can be seen from Fig. 13 (right). As the postulation of an equilibrium in reaction step (11b) is essential to the mechanism, this in turn has implications on the possible structure of the intermediate species $Au_2(CO)O_2^-$ in the catalytic cycle (Eqs. (11a–c)) which might be a simple

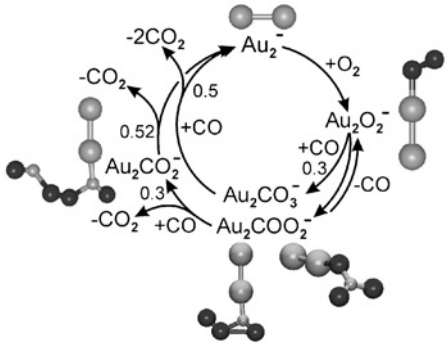

Figure 14: Schematic representation of the gas-phase catalytic cycle for oxidation of carbon monoxide by gold dimer anions, based on the reaction mechanism determined by kinetic measurements in conjunction with first-principle simulations. The numbers denote calculated energy barriers in eV. Also displayed are geometrical structures of reactants and intermediate products according to the calculations (large gray spheres: Au; small gray spheres: C; dark spheres: O) [53].

coadsorption of the two molecules, e.g., on different sides of Au_2^-, or already a reacted carbonate (CO_3)-like species adsorbed onto the gold dimer. Apparently, the observed intermediate can have different isomers and one of them is formed by molecular coadsorption of CO and O_2, because otherwise the possible CO loss required by Eq. (11b) would not be feasible. Therefore, several possible structures of $Au_2(CO)O_2^-$ have been calculated by Häkkinen and Landman [53].

The detailed catalytic reaction cycle emerging from experimental and theoretical evidence for the CO oxidation by gas-phase Au_2^- clusters is depicted in Fig. 14. Also included are the calculated energy barriers for the different reaction steps and the simulated intermediate structures. Five structures corresponding to the mass of the complex $Au_2(CO)O_2^-$ were studied theoretically, while the ones shown in Fig. 14 are the those pertinent to the observed reaction steps (Eqs. (11a–c)).

The left hand structure for the complex $Au_2(CO)O_2^-$ in Fig. 14 contains a reacted O–O–C–O group that is attached through the carbon atom to the gold dimer anion. The O–O bond is activated to a superoxo state, and this species bears some resemblance to the gold–peroxyformate complex identified in the early experiments of gold atoms in cryogenic CO/O_2 matrices [104]. Most notably, the adsorption of O_2 as well as the coadsorption of CO leading to the peroxyformate structure is barrierless according to the calculations. This is in excellent agreement with the experimental observation that all but one step of the reaction cycle show a negative dependence of the corresponding termolecular rate constants on the reaction temperature. As discussed above, within the Lindemann model for low-pressure gas-phase kinetics, this negative temperature dependence is indicative of a barrierless reaction step. Only the last reaction step (Eq. (11c)) representing the re-formation of Au_2^- and the liberation of CO_2 displays a positive temperature dependence of the rate constant [53] demonstrating the presence of an activation barrier in this particular reaction step. This experimental information on the reaction energetics is again in accord with theoretical modeling of the reaction pathway. The formation of CO_2 from the reaction between CO(g) and the peroxyformate structure involves a low barrier of 0.3 eV, resulting in the formation of a metastable $Au_2CO_2^-$ complex, where CO_2 is bound to Au_2^- via the

carbon atom. However, the heat of reaction (4.75 eV) evolving from the formation of the first CO_2 molecule is large enough in order to overcome the binding energy (0.52 eV) of the remaining CO_2 to Au_2^-, thus facilitating its desorption from the metal cluster.

The right hand structure for the complex $Au_2(CO)O_2^-$ in Fig. 14 is one of the most stable structures proposed by Häkkinen and Landman earlier [103]. The formation of this structure by insertion of CO(g) into the O–O bond in $Au_2O_2^-$ (where the O_2 molecule is end-on bonded to the gold dimer anion) requires a barrier of only 0.3 eV, which is easily overcome under the experimental conditions. The production of CO_2 then involves a modest barrier of 0.5 eV, it releases readily two CO_2 molecules, since the remaining $Au_2CO_2^-$ species, where CO_2 is bound to Au_2^- via one of the oxygen atoms, is unstable under the experimental conditions (100–300 K) [53]. All observed reaction steps of the catalytic cycle proceed via Eley–Rideal mechanisms where the detailed collision geometry of the CO reaction partner is crucial to the outcome of the reaction and no adsorbate diffusion on the metal cluster contributes to the catalysis on the small gold clusters.

In addition to a comprehensive molecular mechanistic understanding based on experiment and theory, the efficiency of the catalytic reaction can be estimated from the experimental kinetic data. From the kinetic fit, it is possible to simulate the CO_2 formation rate and thus to obtain the turn-over-frequency (TOF) of the catalytic reaction. The deduced TOF amounts to 0.4 CO_2 molecules per gold cluster per second. This value is in the same order of magnitude as the catalytic activity of oxide supported gold cluster particles with a size of a few nanometers, which ranges between 0.2 sec^{-1} per Au atom (~2 nm diameter particles at 273 K) and 4 sec^{-1} per Au atom (3.5 nm particles at 350 K) [72–74].

4.3. Silver cluster catalysis

In contrast to gold, very few is known so far about the capabilities of atomic silver clusters to act as oxidation catalysts. Supported silver catalysts with μm particle size are employed commercially in large scale in the important selective oxidation of ethylene involving molecular oxygen [105, 106]. But although a great deal of information about the catalytic activity of silver is available, the details of the oxidation reaction mechanism remain elusive. Apparently, the rate-determining step involves some form of oxygen bound to the silver particle surface [106, 107]. The approach to employ well-defined gas-phase metal clusters as reaction centers in interaction with molecular oxygen therefore might aim to add to an understanding of elementary catalytic reaction steps. Also in this case again, the experimental techniques of modern gas-phase cluster science provide two major advantages: First, the reaction system, i.e., the number of atoms in the cluster and the charge state, can be defined exactly in a controlled environment. Second, due to the finite size of clusters a direct treatment by ab initio theoretical approaches is amenable and can strongly enhance the insight provided by the experimental data. This fact has been very important for a large part of the work presented in this chapter. In the following, before discussing the catalytic activity of silver clusters in the CO oxidation reaction, the interesting charge- and size-dependent reaction behavior of silver clusters with molecular oxygen will be presented.

4.3.1. Reactivity of silver clusters toward molecular oxygen

The charge state-dependent reaction of O_2 will be discussed for the case of the silver dimer, where detailed information is available for all three charge states [12, 60, 82, 108–112]. Neutral Ag_2 has been found to be unreactive toward O_2 in a fast flow reactor at ambient temperature [108], which is not surprising considering the paired valence electron structure of Ag_2. The anionic dimer adsorbs one O_2 molecule in a straightforward association reaction similar to the mechanism discussed earlier for the case of Au_2^- (Eq. (9)). No further reaction products are detected at any reaction temperature or partial pressure conditions in the rf ion trap [60]. This result is also in agreement with previous flow-tube reactor measurements [82], and the molecular superoxo-type bonding of the adsorbate has been confirmed spectroscopically [112].

In contrast, the positively charged silver dimer adsorbs at most two oxygen molecules at very low reaction temperatures of 50 K [12]. Adsorption of up to three O_2 ligands has been observed recently in a guided ion beam experiment [113]. The O_2 binding energies determined from these experiments amount to 0.20, 0.18, and 0.15 eV for the first, second, and third O_2, respectively [113]. In the rf ion trap measurements, no reaction products $Ag_2O_n^+$ with $n>4$ are observed for temperatures between 50 and 300 K [12]. However, the distribution of the reaction products reveals a strong temperature dependence: Whereas at 50 K the exclusive oxidation products $Ag_2O_2^+$ and $Ag_2O_4^+$ point toward molecular adsorption, at 95 K the new product Ag_2O^+ appears and no $Ag_2O_4^+$ is observed anymore. At even higher temperatures (130 K), $Ag_2O_3^+$ is detected as the largest product. These results indicate a strongly temperature-dependent reaction mechanism. In order to extract possible reaction schemes, the reactant and product concentrations have been measured as a function of the reaction time in the rf ion trap. The evolution of the Ag_2^+ concentration with reaction time shows a multi-exponential decay at all temperatures. $Ag_2O_2^+$ is identified as an intermediate product with maximum concentration at very short reaction times and increasing amplitude for higher reaction temperatures. The final product at 95 and 110 K is Ag_2O^+, whereas at 130 K the new product $Ag_2O_3^+$ appears with a delay of about 2 sec.

These experimental findings suggest the following reaction mechanism:

$$Ag_2^+ + O_2 \rightleftarrows Ag_2O_2^+ \tag{12a}$$

$$Ag_2O_2^+ \rightarrow Ag_2O^+ + O \tag{12b}$$

$$Ag_2O^+ + O_2 \rightleftarrows Ag_2O_3^+ \tag{12c}$$

$Ag_2O_2^+$ is unambiguously identified as an intermediate and is formed in a first elementary step by molecular adsorption of O_2 onto Ag_2^+. Molecular adsorption of up to two O_2 molecules is also observed at 50 K. $Ag_2O_4^+$ is, however, not a stable product at higher temperatures. In a second elementary step, Ag_2O^+ is formed by dissociation of the adsorbed O_2 molecule. The dissociation of O_2 is not observed at 50 K, as the corresponding activation energy is thermally not reached. Increasing the temperature to 130 K results in a further product, $Ag_2O_3^+$. This third elementary step is observed at delayed reaction times and consists of molecular adsorption of O_2 to Ag_2O^+.

Most interestingly, the described temperature dependence of the product ion mass spectra and reaction kinetics clearly show that, in contrast to the O_2 adsorption on negatively charged silver and gold clusters, the molecular adsorption and the

dissociation of O_2 on Ag_2^+ are activated processes. This has been confirmed recently also for the case of larger positively charged silver clusters [109, 110, 114]. In this particular case of positively charged silver clusters, it is interesting to consider for comparison the O_2 adsorption on single crystal surfaces. For the highly reactive Ag(110) surface oxygen adsorbs in four different states, depending on the surface temperature: below 40 K O_2 is bound in a physisorbed state; in the range between 40 and 170 K it is molecularly chemisorbed, and at higher temperatures the molecules dissociate on the surface and chemisorb atomically [12, 110, 115].

The reactivity of the larger silver cluster anions toward O_2, measured in an rf ion trap experiment, presents an illustrative example for cooperative adsorption effects on small cluster ions. This reaction behavior of free Ag_n^- with O_2 is in marked contrast to the reaction behavior of free Au_n^- clusters with oxygen as presented in Section 4.2.1. Whereas Ag_n^- with even n adsorb only one O_2, similar to even n Au_n^-, silver clusters with odd number n of silver atoms adsorb at maximum two oxygen molecules, in contrast to odd size Au_n^- which do not react with O_2 at all [80, 83, 97]. Ag_4^- even first forms $Ag_4O_2^-$, but then reacts with additional two O_2 molecules at long reaction time and low temperature. No products with an odd number of oxygen atoms are detected. The corresponding adsorption kinetics data are best fitted by a sequential adsorption reaction mechanism with the reaction rate constants k_1 and k_2:

$$Ag_n^- + 2O_2 \xrightarrow{k_1} Ag_nO_2^- + O_2 \xrightarrow{k_2} Ag_nO_4^- \tag{13}$$

In combination with a systematic theoretical study [60], an understanding of the measured rate constant evolution with cluster size depicted in Fig. 15 emerges, and reasons for the distinct behavior of silver cluster anions can be given [60].

The obtained rate constants are termolecular under the low-pressure multi-collision conditions of the ion trap experiment (Lindemann model for gas-phase association reactions, cf. Section 2.4 [50, 53]). They include the elementary steps of the initial formation of an energized complex (rate constant k_a) and its possible unimolecular

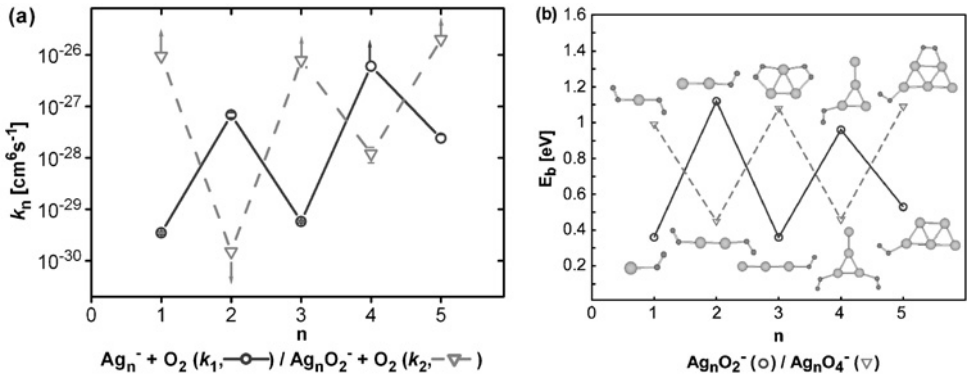

Figure 15: (a) Experimental rate constants k_n obtained for the adsorption of the first and second O_2 molecule onto gas-phase Ag_n^- at 300 K reaction temperature in an rf ion trap experiment. (b) Theoretical binding energies E_b and lowest energy structures (light gray spheres: silver atoms; dark spheres: oxygen atoms). Note that the lowest energy structures of AgO_2^- and $Ag_3O_4^-$ contain dissociated oxygen (not shown), which however requires considerable activation energy not available under the experimental conditions [60].

decomposition back to the educts (k_d) in competition with a stabilizing energy transfer collision with helium buffer gas (k_s). As the ion–molecule reaction rate constants k_a ($\approx 5.5 \times 10^{-10}\,cm^3\,sec^{-1}$) and k_s ($\approx 5.3 \times 10^{-10}\,cm^3\,sec^{-1}$) show no significant cluster size dependence [55], the observed strong size effects must be contained in k_d. The experimentally obtained reaction rate constants (Fig. 15a) compare particularly well with the trend in the calculated O_2 binding energies E_b (Fig. 15b), because, according to statistical rate theory, E_b largely determines the rate of unimolecular decomposition of the initially formed energized complex (k_d).

The results concerning multiple adsorption of O_2 onto the anionic sliver clusters according to Eq. (13) can be assessed by qualitative frontier orbital considerations for the binding of molecular oxygen. The oxygen molecule, as a one-electron acceptor, binds strongly to the anionic silver clusters with odd number of electrons (even n) and low VDE values leading to a small k_d and hence to a fast reaction rate k_1. In contrast, it binds only weakly to silver clusters with even number of electrons (odd n) and closed shell electronic structure resulting in low reaction rates k_1 in these cases as can be seen from Fig. 15a.

However, recent work on the reactivity of hydrated anionic gold clusters with molecular oxygen has shown that this behavior can be inverted by binding of a strong electron acceptor such as the OH group [116]. Due to the electron withdrawing effect, electron transfer from the cluster occurs leaving an unpaired electron on the clusters with even number of electrons and inducing subsequent stronger binding of the molecular oxygen to hydrated clusters.

An analogous mechanism is proposed for the activation of molecular oxygen and the cooperative binding of two oxygen molecules on the anionic silver clusters in which the first adsorbed O_2 serves as an activator [60]. Since anionic silver clusters have generally lower VDE values than gold clusters, weaker electron acceptors such as O_2 can already induce electron transfer and activate them which is not possible in the case of Au_n^-. The first oxygen molecule is bound to the silver clusters with even number of electrons by 0.36, 0.36, and 0.53 eV for Ag^-, Ag_3^- and Ag_5^-, respectively [60]. The mechanism of the bonding involves the electron transfer from the metal cluster into the π^*-MO of O_2. The binding of the first O_2 molecule changes the electronic structure of the cluster and induces a stronger cooperative binding with the second O_2. This results in the case of Ag_3^- and Ag_5^- in new oxide species with doubly bound, superoxo-like O_2 subunits as can be seen from the calculated structures in Fig. 15b. The cooperative effect is reflected in larger binding energies as shown also in Fig. 15b. Moreover, the binding of the second molecular oxygen shows a reversed pattern being stronger for clusters with odd number of atoms and weaker for the ones with even number of atoms. The latter ones with one unpaired electron bind strongly only one oxygen molecule since the electron transfer leaves them with a closed shell electronic structure.

Hence, experimental rate constant measurements in combination with theoretical simulations show a pronounced size- and structure-selective activity of anionic silver clusters toward molecular oxygen due to cooperative effects. In particular, for Ag_n^- clusters with odd n, a weakly bound first O_2 promotes the adsorption of a second O_2 molecule which is then (for $n = 3, 5$) differently bound with the O_2 bond elongated to 1.32 Å and thus potentially activated for further oxidation reactions such as CO combustion which have indeed been observed for larger cluster sizes [111] as will be discussed in the following section.

4.3.2. Catalytic CO oxidation by Ag_n^-

Strongly size-dependent reactions of $Ag_nO_4^-$ with CO were revealed in the rf ion trap experiment [111]. Whereas the smallest cluster sizes with $n = 1$ and 3 did not exhibit any reactivity toward CO, in the case of Ag_5^-, the reaction of CO with the $Ag_5O_4^-$ complex leads to the formation of the fragment ion $Ag_3CO_2^-$ pointing toward a reaction between CO and O_2 involved with the metal cluster decomposition. The observed strong fragmentation is probably due to the fact that the small cluster is not able to accommodate the excess energy liberated in the formation of the intermediate energized complex which then is likely to decompose.

For the larger sizes Ag_n^- ($n = 7$–13), the most surprising behavior was observed [111]: Filling the trap with CO in addition to O_2 resulted in a partial reduction or even a complete depletion of $Ag_nO_4^-$ signals and an analogous increase of the bare Ag_n^- cluster signals for odd n, while the $Ag_nO_2^-$ peaks (n even) and Ag_{13}^- remained unaffected by CO addition. Figure 16 (left) shows the corresponding product ion mass spectra at 100 K and equal reaction times, but under different reaction conditions: (a) When only trace amounts of oxygen are present in the trap, odd size clusters Ag_7^-, Ag_9^-, and Ag_{13}^- do not react, Ag_{11}^- yields some product $Ag_{11}O_4^-$, while even size clusters completely react to $Ag_nO_2^-$ products. (b) If the oxygen partial pressure is raised to

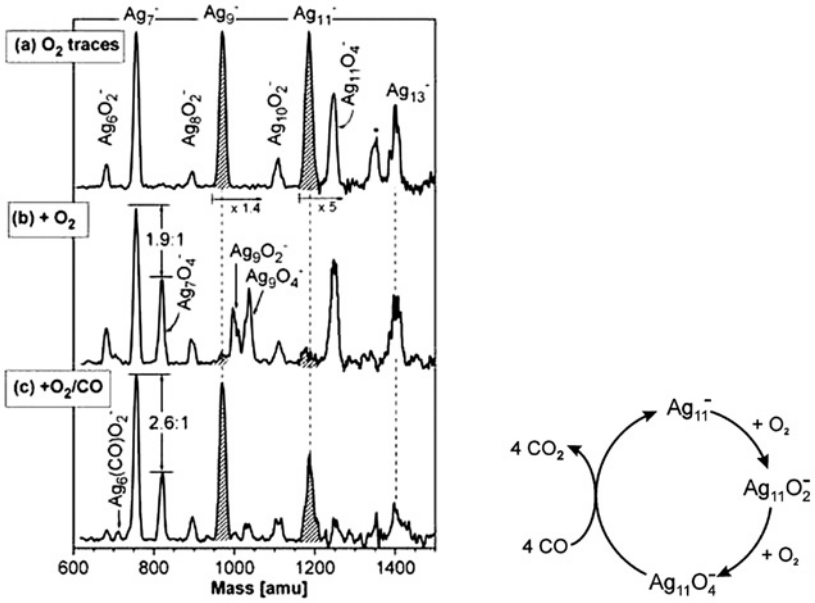

Figure 16: (Left) Product ion mass spectra of silver clusters Ag_{7-13}^- obtained at reaction temperature $T = 100$ K and reaction time $t_R = 0.1$ sec with different reactant concentrations in the rf ion trap experiment. (a) Reaction with trace amounts of oxygen. $p(He) = 1.2$ Pa. (b) Reaction with oxygen. $p(O_2) = 0.01$ Pa, $p(He) = 1.17$ Pa. (c) Reaction with oxygen and carbon monoxide. $p(O_2 = 0.01$ Pa, $p(CO) = 0.03$ Pa, $p(He) = 1.17$ Pa. In the case of Ag_7^-, the bare to oxide cluster signal ratio is indicated in (b) and (c). The Ag_9^- and Ag_{11}^- mass peaks (hatched) disappear almost completely after reaction with oxygen and reappear when CO is added. The peak in (a) labeled by an asterisk would correspond to the mass of $Ag_{12}O_4^-$, but is only observed at extremely low oxygen partial pressures (traces) and does not appear at measurable O_2 content [111]. (Right) Tentative catalytic reaction cycle for the oxidation of CO on free Ag_{11}^- clusters.

0.01 Pa, Ag_7^- reacts and forms the oxide $Ag_7O_4^-$, Ag_9^- almost completely disappears and the products $Ag_9O_2^-$ and $Ag_9O_4^-$ are observed, also the Ag_{11}^- signal almost vanishes and $Ag_{11}O_4^-$ remains. The product ion mass spectrum (c) in Fig. 16 was obtained under conditions where partial pressures of both reactants, O_2 and CO, are present in the trap. Unexpectedly, the bare silver cluster signals Ag_9^- and Ag_{11}^- reappear, while the corresponding oxide product intensities decrease considerably. Also, in the case of Ag_7^-, the bare to oxide cluster ratio shifts in favor of the bare Ag_7^-.

Considering the fact that the pure metal clusters do not react with carbon monoxide, the conclusion can be drawn that CO reacts with the oxides of Ag_7^-, Ag_9^-, and Ag_{11}^-. The observed complexes $Ag_nO_4^-$ are then the decisive intermediates in the reaction with CO. These data thus provide evidence that, in contrast to other cluster sizes, silver cluster anions with $n = 7$, 9, and 11 activate the adsorbed oxygen to be able to react with CO under our reaction conditions. In this process, CO_2 is likely to be liberated and the metal clusters are re-formed to complete a catalytic reaction cycle (illustrated in Fig. 16 (right)), although the experimental evidence obtained so far does not yet reveal the complete details of the reaction mechanism and more investigations are needed to solve this task.

4.3.3. Catalytic NO reduction with CO on Ag_n^-

Nitric oxide (NO) plays an important role in many biological and chemical processes. For instance, it is known to be a key physiological regulator in biological processes [117]. At the same time, NO and the higher oxides of nitrogen NO_x are toxic gases liberated during combustion processes in power plants and automobile engines. In atmospheric environment, these molecules are very reactive and responsible for the ozone production in urbanities and the generation of acid rain [118]. Modern catalysts, like the three-way catalyst in automotive exhaust converters, aim to eliminate NO_x. During the catalytic process, NO is reduced via the catalytically active material and at the same time CO, which is another toxic side product of hydrocarbon combustion, is oxidized:

$$2NO + 2CO \rightarrow N_2 + 2CO_2 \tag{14}$$

This reaction is highly exothermic releasing 343.9 kJ mol^{-1} [119]. The most efficient catalyst material known so far is rhodium, but the high cost of this noble metal has stimulated efforts to replace it by a less expensive material. One possible alternative process is the reduction of NO on an alumina-supported silver catalyst in the presence of oxygen containing hydrocarbons like ethanol and acetone [120]. Molecular oxygen adsorbed and activated on the catalyst is responsible for this reaction. Both, bulk silver and supported silver catalysts have been characterized with respect to their reactivity toward NO and O_2 [121]; the catalytic reaction mechanism itself, however, is still unclear. Also, in this case, studies of small clusters in the gas phase may support the quest for the elementary reaction steps of chemical and catalytic reactions and for the identification of the active sites.

Reactive cluster fragmentation is found to be the main reaction channel for the clusters Ag_2^-, Ag_3^-, Ag_4^-, and for Ag_5^- in reaction with NO at 300 K under the multi-collision reaction conditions in the rf ion trap experiment [122]. The mass spectra obtained at longer reaction times reveal the particular stability of product peaks assigned to $AgN_2O_4^-$ and Ag_3NO^-. A size-dependent charge transfer mechanism

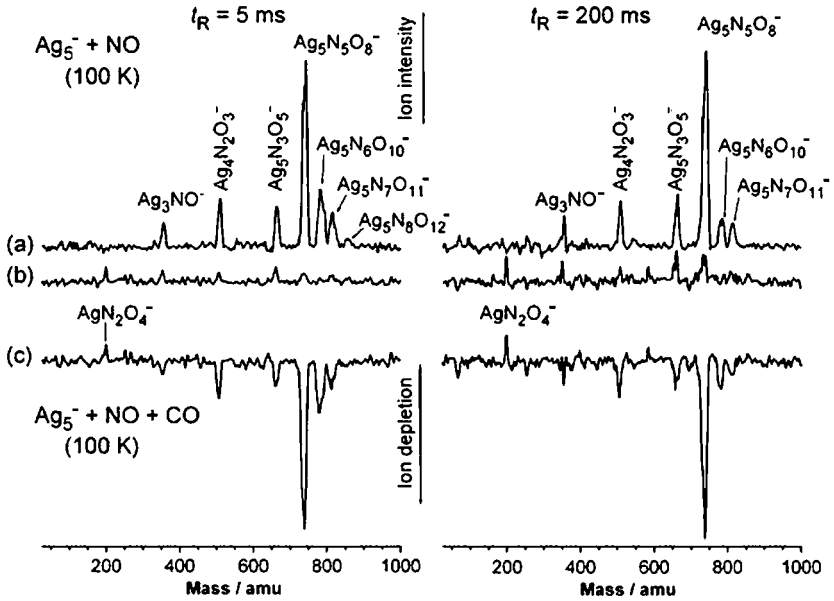

Figure 17: (a) Product ion mass spectra obtained after reaction of Ag_5^- with NO at 100 K for $t_R = 5$ msec (left mass spectrum) and $t_R = 200$ msec (right mass spectrum) in the rf ion trap experiment. Partial pressures: $p(NO) = 0.01$ Pa; $p(He) = 1.0$ Pa. (b) Product ion mass spectra obtained after reaction of Ag_5^- with a mixture of NO and CO under otherwise identical conditions ($p(CO) = 0.16$ Pa). (c) Difference, i.e., reaction depletion mass spectra for the reaction of Ag_5^- with NO and CO at $t_R = 5$ msec (left) and $t_R = 200$ msec (right). The mass spectra for the reaction of Ag_5^- with solely NO (a) have been subtracted from the product mass spectra obtained after reaction of Ag_5^- with a mixture of NO and CO (b).

between the metal clusters, Ag_n^-, and the NO ligands leads to the formation of $Ag_nN_xO_y^-$ ($x<y$) compounds and of NO_2^-. At low temperatures, a non-dissociative reaction pathway opens for Ag_5^- with multiple adsorption of NO molecules onto the cluster, followed by disproportionation reactions yielding N_2O and NO_2 and producing product species of the stoichiometry $Ag_5N_xO_y^-$ ($x<y$). The reactivity measurements of Ag_n^- in the presence of NO and CO clearly demonstrate that the latter gas strongly reacts with the N_xO_y ($x<y$) entities adsorbed on Ag_5^- (see Fig. 17). In contrast, one stable product of reactive fragmentation, Ag_3NO^-, is only depleted to a minor extent and the other, $AgN_2O_4^-$, is even generated in the course of the reaction with carbon monoxide. These results present a first insight into the reduction of NO in the presence of CO on the small silver clusters.

4.4. Catalytic activity of bimetallic clusters

The possibility to change the composition of a small metal cluster atom by atom presents a further intriguing aspect of gas-phase cluster chemistry. Surprisingly enough, often chemical properties are not proportional to the chemical composition, but change rather discontinuously as illustrated by the first example in this section, the activation of molecular oxygen by binary silver–gold clusters [101]. In the second example, platinum–gold clusters, the platinum content is found to be decisive for the reactivity of the mixed clusters in the same reaction [61].

Table 1: Composition and size dependence of the termolecular reaction rate constants $k^{(3)}$ for the reactions of silver, gold, and binary silver–gold cluster anions with O_2 obtained in an rf ion trap mass spectrometer.

Monomer		Dimer		Trimer	
Ion	$k^{(3)}$	Ion	$k^{(3)}$	Ion	$k^{(3)}$
Ag^-	0.51	Ag_2^-	100	Ag_3^-	0.85
Au^-	0	$AgAu^-$	79	Ag_2Au^-	0
		Au_2^-	12	$AgAu_2^-$	0
				Au_3^-	0

The rate constants have been normalized to $6.8 \times 10^{-28}\,cm^6\,sec^{-1} \equiv 100$. The estimated rate constant errors are between 5% and 9%. Reaction temperature $T = 300\,K$ in all experiments [101].

4.4.1. Bimetallic silver–gold clusters

In Table 1, reaction rate constants $k^{(3)}$ for the reactions of $Ag_nAu_m^-$ ($n+m = 1, 2, 3$) with O_2 at $T = 300\,K$ obtained in an rf ion trap experiment are listed. For the atomic ions, only Ag^- reacts with O_2 displaying the lowest rate constant observed for all investigated reacting ions. However, as described in Section 4.3.1, the formed AgO_2^- reacts very fast with a second oxygen molecule to form the final product AgO_4^- [60]. The dimer anions Ag_2^-, $AgAu^-$, and Au_2^- each adsorb only one oxygen molecule. Due to the open shell electronic structure of the dimer anions, with one unpaired electron, the bonding to O_2 is strong compared with closed shell even size cluster anions [60, 82]. O_2 acts as an electron acceptor through one of its degenerate singly occupied $2\pi^*$ antibonding orbitals which interacts with the highest (also singly) occupied molecular orbital (HOMO) of the metal dimer anion leading to considerable stabilization of the oxide complex [60]. This in turn results in a low unimolecular decomposition rate constant k_d of the metastable intermediate complex, e.g., $Au_2O_2^-$*, and according to Eq. (6) in a large termolecular rate constant $k^{(3)}$. The oxygen molecule is still expected to be molecularly adsorbed on the noble metal dimers, which is confirmed by recent photoelectron spectroscopic measurements on $Ag_2O_2^-$ and $Au_2O_2^-$ [98, 112] and also by several theoretical contributions [103, 123–129].

In theoretical calculations, Au_2^- always shows a larger binding energy to O_2 (1.06–1.39 eV [103, 116, 124, 127, 128]) than $AgAu^-$ (0.94 eV [126]) and a binding energy value similar to Ag_2^- (1.12 eV [97]). This is in marked contradiction to the experimental kinetic data (Table 1), which display only a small difference between the reaction rates of the dimers Ag_2^- and $AgAu^-$ with oxygen, but Au_2^- reacts considerably slower, indicating a much smaller O_2 binding energy according to simple statistical rate theory considerations [50, 51]. This non-linear change in chemical reactivity toward O_2 with composition yet is in accord with measured VDEs of the dimer anions. The VDE of $AgAu^-$ (1.43 eV [130]) is closer to the VDE value of Ag_2^- (1.06 eV [86]) than to that of Au_2^- (2.01 eV [86]). The VDE basically relates to the energy of the cluster HOMO. Thus, a comparably low VDE facilitates electron transfer to the O_2 $2\pi^*$ orbital resulting in a stronger bonding as confirmed by our measurements.

Due to the relatively strong bonding of O_2 to the silver containing dimers, the CO oxidation catalysis is not necessarily expected to proceed under thermal condition. In addition, in contrast to Au_2^-, Ag_2^- and $AgAu^-$ do not show any reactive behavior toward CO. Consequently, in experiments with O_2 and CO in the ion trap reactor, no

indications for the prevalence of a catalytic reaction cycle could be identified. This is again in contrast to theoretical simulations that predict a catalytic CO oxidation cycle involving $AgAu^-$ [126]. The unanticipated and discontinuous change of reactivity with the composition of the small clusters is even more pronounced for the trimer anions, because both, Ag_2Au^- and $AgAu_2^-$, do not react with O_2 at all in the rf ion trap experiment, similar to Au_3^- [97]. Au_3^- reacts with up to two CO molecules only at cryogenic temperatures. However, after adsorption of a first CO, the cluster complex structure is changed and conditioned for the subsequent cooperative adsorption of up to two O_2 molecules [97]. The formed complexes $Au_3CO(O_2)_{1,2}^-$ do not further react and no indications for CO_2 release were observed. All other trimer anions do not react with CO at all and no coadsorption complex formation or catalytic CO oxidation are detected in these cases.

4.4.2. Bimetallic platinum–gold clusters

The experimental values for the rate constants of pure platinum and gold cluster cations together with those of the bimetallic clusters measured in an FT-ICR mass spectrometer by Schwarz and coworkers are presented in Table 2 [61]. As in case of bimetallic silver–gold cluster anions, the reactions of binary platinum–gold cluster cations with O_2 exhibit a marked dependence on cluster composition. The smallest bimetallic cluster ion $PtAu^+$ presents no reactivity toward O_2, cluster degradation occurs only if the cluster contains a second platinum atom as in Pt_2Au^+ according to

$$Pt_2Au^+ + O_2 \rightarrow PtAu^+ + PtO_2 \tag{15}$$

In the case of tetrameric binary clusters, three different compositions are possible, but only Pt_3Au^+ and $Pt_2Au_2^+$ react with O_2, with loss of a PtO_2 unit, if no stabilizing buffer gas collisions are possible. This behavior is similar to the reactions of the pure platinum clusters. No reaction at all was observed in the case of the gold-rich tetramer ion $PtAu_4^+$. The trends in the reactivity observed for the $Pt_mAu_n^+$ clusters resemble those predicted by theory for the analogous neutral dimer and trimer clusters and, most interestingly, apparently mimic the observed poisoning of heterogeneous catalysts by gold [131].

Table 2: Composition and size dependence of the bimolecular reaction rate constants k for the reactions of platinum, gold, and binary platinum–gold cluster cations with O_2 obtained with an FT-ICR mass spectrometer.

Monomer		Dimer		Trimer		Tetramer	
Ion	$k^{(3)}$	Ion	$k^{(3)}$	Ion	$k^{(3)}$	Ion	$k^{(3)}$
Pt^+	0	Pt_2^+	54	Pt_3^+	0.6	Pt_4^+	58
Au^+	0	$PtAu^+$	0	Pt_2Au^+	16	Pt_3Au^+	100
		Au_2^+	0	$PtAu_2^+$	0	$Pt_2Au_2^+$	100
				Au_3^+	0	$PtAu_3^+$	0
						Au_4^+	0

The rate constants have been normalized to $2.4 \times 10^{-10}\,cm^3\,sec^{-1} \equiv 100$. The estimated rate constant errors are at $\pm 30\%$. A combined value is given for Pt_3Au^+ and $Pt_2Au_2^+$ [61].

The reaction of bimetallic $Pt_mAu_n^+$ ($m+n \leqslant 4$) cluster ions with O_2 thus exhibits a strong dependence on cluster composition in the way that clusters with a predominant fraction of platinum atoms undergo reactions similar to those of pure Pt_m^+ clusters. In contrast, clusters with a higher fraction of gold atoms are unreactive toward O_2. This behavior corresponds to that of pure Au_m^+ clusters [61, 80, 81]. In the case of cluster ions containing equal amounts of gold and platinum, two situation can be distinguished: first $PtAu^+$, which does not react with O_2, and second $Pt_2Au_2^+$, which undergoes reaction with molecular oxygen supporting that platinum apparently determines the overall reactivity of the cluster. For the explanation of these findings, a comparison between pure Pt_n^+ and Au_n^+ is elucidating. The metal cluster acts as an electron donor with respect to adsorbed oxygen, thus an electropositive support or the addition of an electron to the gaseous clusters is necessary to enable charge transfer to O_2, whereas the cationic clusters Au_n^+ do not react. In contrast, Pt_n^+ clusters are oxidized by O_2 despite their positive charge because of the ability of platinum to adopt higher oxidation states than gold [61]. Therefore, it is expected that the bimetallic clusters show a monotonic decrease of reactivity as a function of gold contents, but this trend is only partly observed in Table 2. Whereas the reaction rate of the dimer clusters meet the anticipation, Pt_2Au^+ reacts faster with O_2 than Pt_3^+ does, and also Pt_3Au^+ and $Pt_2Au_2^+$ react slightly faster than the monometallic Pt_4^+. Interestingly, the reaction of Pt_3^+ with O_2 is extremely inefficient compared with the analogous process for the other sizes of Pt_n^+ ion clusters [46]. Hence, the anomaly is suggested not to lie on the side of the bimetallic clusters, but on that of the monometallic Pt_n^+, with Pt_3^+ and Pt_4^+ exhibiting both possibly particular electronic or geometric features. Considering this particular situation, it is concluded that the composite reactivities of the binary platinum–gold clusters do indeed appear to arise from the individual reactivities of the components in an additive manner [61].

5. CONCLUDING REMARKS

Having been in the focus of interest now for several decades with respect to their fascinating size-dependent chemical reactivity, mass-selected gas-phase metal clusters provide unique well-defined model systems for the study of thermal catalytic reactions and the elucidation of detailed catalytic reaction mechanism. In addition, there is no doubt that a new catalytic chemistry emerges in the non-scalable size regime where reactivity and selectivity can be influenced in a distinct way by adding or removing single atoms and by changing the electronic charge state and the composition of the cluster. Furthermore, the combination with ab initio theoretical simulations is invaluable for defining and evaluating important nanocatalytic factors and concepts. The emphasis of this chapter has been on the activation of molecular oxygen and the combustion reaction of carbon monoxide. Besides the well-known catalytic activity of highly dispersed transition metals like iron and platinum, the newly discovered reactivity of clusters of the noble metals, gold and silver, offers most intriguing perspectives to influence and optimize catalytic activity with respect to this reaction and potentially other related chemical reactions like the selective oxidation of short-chain hydrocarbons.

REFERENCES

[1] Taylor K.J., Pettiette-Hall C.L., Cheshnovsky O., Smalley R.E., J. Chem. Phys. 96 (1992) 3319.
[2] Bonačić-Koutecký V., Fantucci P., Koutecký J., Chem. Rev. 91 (1991) 1035.
[3] Landman U., Int. J. Mod. Phys. B 6 (1992) 3623.
[4] Jortner J., Z. Phys. D 24 (1992) 247.
[5] Heiz U., Schneider W.-D., J. Phys. D 33 (2000) R85.
[6] Böhme D.K., Schwarz H., Angew. Chem. Int. Ed. 44 (2005) 2336.
[7] Ervin K.M., Int. Rev. Phys. Chem. 20 (2001) 127.
[8] Kaldor A., Cox D.M., Zakin M.R., Adv. Chem. Phys. 70 (1988) 211.
[9] Parent D.C., Anderson S.L., Chem. Rev. 92 (1992) 1541.
[10] Schnabel P., Weil K.G., Irion M.P., Angew. Chem. Int. Ed. Engl. 31 (1992) 636.
[11] Shi Y., Ervin K.M., J. Chem. Phys. 108 (1998) 1757.
[12] Socaciu L.D., Hagen J., Heiz U., Bernhardt T.M., Leisner T., Wöste L., Chem. Phys. Lett. 340 (2001) 282.
[13] Ganteför G., Schulze Icking-Konert G., Handschuh H., Eberhardt W., Int. J. Mass Spectrom. Ion Proc. 159 (1996) 81.
[14] von Helden G., van Heijnsbergen D., Meijer G., J. Phys. Chem. A 107 (2003) 1671.
[15] Parks E.K., Nieman G.C., Kerns K.P., Riley S.J., J. Chem. Phys. 107 (1997) 1861.
[16] Leuchtner R.E., Harms A.C., Castleman A.W., Jr., J. Chem. Phys. 92 (1990) 6527.
[17] Kaiser B., Bernhardt T.M., Kinne M., Rademann K., Heidenreich A., J. Chem. Phys. 110 (1999) 1437.
[18] Kinne M., Bernhardt T.M., Kaiser B., Rademann K., Z. Phys. D 40 (1997) 105.
[19] Riley S.J., Nanostruct. Mater. 1 (1992) 155.
[20] Ganteför G., Siekmann H.R., Lutz H.O., Meiwes-Broer K.H., Chem. Phys. Lett. 165 (1990) 293.
[21] Kaiser B., Bernhardt T.M., Kinne M., Rademann K., Int. J. Mass Spectrom. Ion Proc. 177 (1998) L5.
[22] Kinne M., Bernhardt T.M., Kaiser B., Rademann K., Int. J. Mass Spectrom. Ion Proc. 167/168 (1997) 161.
[23] France M.R., Buchanan J.W., Robinson J.C., Pullins S.H., Tucker J.L., King R.B., Duncan M.A., J. Phys. Chem. 101 (1997) 6214.
[24] Reddy B.V., Jena P., Chem. Phys. Lett. 288 (1998) 253.
[25] Andersson M., Persson J.L., Rosén A., J. Phys. Chem. 100 (1996) 12222.
[26] Andersson M., Rosén A., J. Chem. Phys. 117 (2002) 7051.
[27] Jarrold M., Bower J.E., J. Chem. Phys. 85 (1986) 5373.
[28] Gerlich D., in: State-Selected and State-to-State Ion-Molecule Reaction Dynamics, Part 1: Experiment, C.-Y. Ng, M. Baer (eds), Wiley, New York, 1992.
[29] Scoles G. (ed.), Atomic and Molecular Beam Methods, Oxford University Press, New York, 1988 and 1992.
[30] Haberland H. (ed.), Clusters of Atoms and Molecules, Springer Series in Chemical Physics, Vols. 52 and 56, Springer, Berlin, 1994.
[31] Hanley L., Ruatta S.A., Anderson S.L., J. Chem. Phys. 87 (1987) 260.
[32] Guo B.C., Kerns K.P., Castleman A.W., Jr., J. Phys. Chem. 96 (1992) 6931.
[33] Fayet P., McGlinchey M.J., Wöste L.H., J. Am. Chem. Soc. 109 (1987) 1733.
[34] Wade K., Adv. Inorg. Chem. Radiochem. 18 (1976) 1.
[35] Mingos D.M.P., Slee T., Zhenyang L., Chem. Rev. 90 (1990) 383.
[36] Lauher J.W., J. Am. Chem. Soc. 100 (1978) 5305.
[37] Alford J.M., Weiss F.D., Laaksonen R.T., Smalley R.E., J. Phys. Chem. 90 (1986) 4480.

[38] Vajda S., Wolf S., Leisner T., Busolt U., Wöste L.H., Wales D.J., J. Chem. Phys. 107 (1997) 3492.
[39] Kappes M.M., Staley R.H., J. Am. Chem. Soc. 103 (1981) 1286.
[40] Elkind J.L., Weiss F.D., Alford J.M., Laaksonen R.T., Smalley R.E., J. Chem. Phys. 88 (1988) 5215.
[41] Irion M.P., Selinger A., Chem. Phys. Lett. 158 (1989) 145.
[42] Irion M.P., Selinger A., Wendel R., Int. J. Mass Spectrom. Ion Proc. 96 (1990) 27.
[43] Berg C., Schindler T., Niedner-Schatteburg G., Bondybey V.E., J. Chem. Phys. 102 (1995) 4870.
[44] Dietrich G., Krückenberg S., Lützenkirchen K., Schweikhard L., Walther C., J. Chem. Phys. 112 (2000) 752.
[45] Hess H., Kwiet S., Socaciu L., Wolf S., Leisner T., Wöste L., Appl. Phys. B 71 (2000) 337.
[46] Koszinowski K., Schröder D., Schwarz H., J. Chem. Phys. A 107 (2003) 4999.
[47] Maruyama Y., Anderson L.R., Smalley R.E., Rev. Sci. Instrum. 61 (1990) 3686.
[48] Fayet P., Wöste L., Surf. Sci. 156 (1985) 135.
[49] Keller R., Nöhmeier F., Spädtke P., Schönenberg M.H., Vacuum 34 (1984) 31.
[50] Laidler K.J., Chemical kinetics, HarperCollins, New York, 1987.
[51] Steinfeld J.I., Francisco J.S., Hase W.L., Chemical Kinetics and Dynamics, Prentice Hall, Upper Saddle River, NJ, 1999.
[52] Bernhardt T.M., Int. J. Mass Spectrom. 243 (2005) 1.
[53] Socaciu L.D., Hagen J., Bernhardt T.M., Wöste L., Heiz U., Häkkinen H., Landman U., J. Am. Chem. Soc. 125 (2003) 10437.
[54] Castleman A.W., Jr., Weil K.G., Sigsworth S.W., Leuchtner R.E., Keesee R.G., J. Chem. Phys. 86 (1987) 3829.
[55] Gioumousis G., Stevenson D.P., J. Chem. Phys. 29 (1958) 294.
[56] Häkkinen H., Abbet S., Sanchez A., Heiz U., Landman U., Angew. Chem. Int. Ed. Engl. 42 (2003) 1297.
[57] Yoon B., Häkkinen H., Landman U., Wörz A.S., Antonietti J.-M., Abbet S., Judai K., Heiz U., Science 307 (2005) 403.
[58] Christmann K., Introduction to Surface Physical Chemistry, Topics in Physical Chemistry, Springer-Verlag, Berlin, 1991.
[59] Somorjai G.A., Introduction to Surface Chemistry and Catalysis, Wiley, New York, 1994.
[60] Hagen J., Socaciu L.D., Le Roux J., Popolan D., Bernhardt T.M., Wöste L., Mitrić R., Noack H., Bonačić-Koutecký V., J. Am. Chem. Soc. 126 (2004) 3442.
[61] Koszinowski K., Schröder D., Schwarz H., ChemPhysChem 4 (2003) 1233.
[62] Koszinowski K., Schröder D., Schwarz H., J. Am. Chem. Soc. 125 (2003) 3676.
[63] Wallace W.T., Whetten R.L., J. Am. Chem. Soc. 124 (2002) 7499.
[64] Baranov V., Javahery G., Hopkinson A.C., Böhme D.K., J. Am. Chem. Soc. 117 (1995) 12801.
[65] Schröder D., Schwarz H., Clemmer D.E., Chen Y., Armentrout P.B., Baranov V.I., Böhme D.K., Int. J. Mass Spectrom. 161 (1997) 175.
[66] Berg C., Kaiser S., Schindler T., Kronseder C., Niedner-Schattenburg G., Bondybey V.E., Chem. Phys. Lett. 231 (1994) 139.
[67] Heinemann C., Cornehl H.H., Schwarz H., J. Organomet. Chem. 501 (1995) 201.
[68] Blagojevic V., Jarvis M.J.Y., Flaim E., Koyanagi G.K., Lavrov V., Böhme D.K., Angew. Chem. Int. Ed. 42 (2004) 4923.
[69] Hintz P.A., Ervin K.M., J. Chem. Phys. 103 (1995) 7897.
[70] Brönstrup M., Schröder D., Kretzschmar I., Schwarz H., Harvey J.N., J. Am. Chem. Soc. 123 (2001) 142.
[71] Balaj O.P., Balteanu I., Roßteuscher T.T.J., Beyer M.K., Bondybey V.E., Angew. Chem. Int. Ed. 43 (2004) 6519.

[72] Haruta M., Catal. Today 36 (1997) 153.
[73] Haruta M., Daté M., Appl. Catal. A 222 (2001) 427.
[74] Valden M., Lai X., Goodman D.W., Science 281 (1998) 1647.
[75] Bond G.C., Thompson D.T., Catal. Rev.-Sci. Eng. 41 (1999) 319.
[76] Abelson P.H., Science 288 (2000) 269.
[77] Meyer R., Lemire C., Shaikhutdinov S.K., Freund H.-J., Gold Bull. 37 (2004) 72.
[78] Hammer B., Norskov J.K., Nature 376 (1995) 238.
[79] Sanchez A., Abbet S., Heiz U., Schneider W.-D., Häkkinen H., Barnett R.N., Landmann U., J. Phys. Chem. A 103 (1999) 9573.
[80] Cox D.M., Brickman R., Creegan K., Kaldor A., Z. Phys. D 19 (1991) 353.
[81] Cox D.M., Brickman R.O., Creegan K., Kaldor A., Mater. Res. Soc. Symp. Proc. 206 (1991) 43.
[82] Lee T.H., Ervin K.M., J. Phys. Chem. 98 (1994) 10023.
[83] Salisbury B.E., Wallace W.T., Whetten R.L., Chem. Phys. 262 (2000) 131.
[84] Kimble M.L., Castleman A.W., Jr., Int. J. Mass Spectrom. 233 (2004) 99.
[85] Kimble M.L., Castleman A.W., Jr., Mitrić R., Bürgel C., Bonačić-Koutecký V., J. Am. Chem. Soc. 126 (2004) 2526.
[86] Ho J., Ervin K.M., Lineberger W.C., J. Chem. Phys. 93 (1990) 6987.
[87] Häkkinen H., Yoon B., Landman U., Li X.L., Zahi H.-J., Wang L.-S., J. Phys. Chem. A 107 (2003) 6168.
[88] Balasubramanian K., Relativistic Effects in Chemistry, Wiley, New York, 1997.
[89] Schwarz H., Angew. Chem. Int. Ed. 42 (2003) 4442.
[90] Häkkinen H., Moseler M., Landman U., Phys. Rev. Lett. 89 (2002) 033401.
[91] Furche F., Ahlrichs R., Weis P., Jacob C., Gilb S., Bierweiler T., Kappes M.M., J. Chem. Phys. 117 (2002) 6982.
[92] Bonačić-Koutecký V., Cespiva L., Fantucci P., Pittner J., Koutecký J., J. Chem. Phys. 100 (1994) 490.
[93] Bonačić-Koutecký V., Veyret V., Mitrić R., J. Chem. Phys. 115 (2001) 10450.
[94] Nygren M.A., Siegahn P.E.M., Jin C., Guo T., Smalley R.E., J. Chem. Phys. 95 (1991) 6181.
[95] Wallace W.T., Whetten R.L., J. Phys. Chem. B 104 (2000) 10964.
[96] Wallace W.T., Whetten R.L., Eur. J. Phys. D 16 (2001) 123.
[97] Hagen J., Socaciu L.D., Elijazyfer M., Heiz U., Bernhardt T.M., Wöste L., Phys. Chem. Chem. Phys. 4 (2002) 1707.
[98] Sun Q., Jena P., Kim Y.D., Fischer M., Ganteför G., J. Chem. Phys. 120 (2004) 6510.
[99] Kim Y.D., Int. J. Mass Spectrom. 238 (2004) 17.
[100] Stolcic D., Fischer M., Ganteför G., Kim Y.D., Sun Q., Jena P., J. Am. Chem. Soc. 125 (2003) 2848.
[101] Bernhardt T.M., Socaciu-Siebert L.D., Hagen J., Wöste L., Appl. Catal. A 291 (2005) 170.
[102] Hagen J., Socaciu L.D., Heiz U., Bernhardt T.M., Wöste L., Eur. J. Phys. D 24 (2003) 327.
[103] Häkkinen H., Landman U., J. Am. Chem. Soc. 123 (2001) 9704.
[104] Huber H., McIntosh D., Ozin G.A., Inorg. Chem. 16 (1977) 975.
[105] Lefort T.E., FR 729 925, 1931; 739 562, 1931, France, 1931.
[106] Gates B.C., Catalytic Chemistry, Wiley, New York, 1992.
[107] Madix R.J. and Roberts J.T., in: Surface Reactions, R.J. Madix (ed.), Springer-Verlag, Berlin, 1994.
[108] Lian L., Hackett P.A., Rayner D.M., J. Chem. Phys. 99 (1993) 2583.
[109] Schmidt M., Cahuzac P., Bréchignac C., Cheng H.-P., J. Chem. Phys. 118 (2003) 10956.
[110] Schmidt M., Masson A., Bréchignac C., Phys. Rev. Lett. 91 (2003) 243401.

[111] Socaciu L.D., Hagen J., Le Roux J., Popolan D., Bernhardt T.M., Wöste L., Vajda S., J. Chem. Phys. 120 (2004) 2078.
[112] Kim Y.D., Ganteför G., Chem. Phys. Lett. 383 (2004) 80.
[113] Manard M.J., Kemper P.R., Bowers M.T., Int. J. Mass Spectrom. 228 (2003) 865.
[114] Chen Y.-M., Armentrout P.B., J. Chem. Phys. 103 (1995) 618.
[115] Besenbacher F., Nørskov J.K., Prog. Surf. Sci. 44 (1993) 5.
[116] Wallace W.T., Wyrwas R.B., Whetten R.L., Mitrić R., Bonačić-Koutecký V., J. Am. Chem. Soc. 125 (2003) 8408.
[117] Richter-Addo G.B., Legzdins P., Burstyn J., Chem. Rev. 102 (2002) 857.
[118] Seinfeld J.H., Pandis S.N., Atmospheric Chemistry and Physics, Wiley, New York, 1998.
[119] Ford P.C., Lorkovic I.M., Chem. Rev. 102 (2002) 993.
[120] Shimizu K., Shibata J., Satsuma A., Hattori T., Phys. Chem. Chem. Phys. 3 (2001) 880.
[121] Zemlyanov D.Y., Nagy A., Schlögl R., Appl. Surf. Sci. 133 (1998) 171.
[122] Hagen J., Socaciu-Siebert L.D., Le Roux J., Popolan D., Vajda S., Bernhardt T.M., Wöste L., Int. J. Mass Spectrom. (2007) in press.
[123] Okumura M., Kitagawa Y., Haruta M., Yamaguchi K., Chem. Phys. Lett. 346 (2001) 163.
[124] Mills G., Gordon M.S., Metiu H., Chem. Phys. Lett. 359 (2002) 493.
[125] Wells D.H., Jr., Delgass W.N., Kendall T.T., J. Chem. Phys. 117 (2002) 10597.
[126] Mitrić R., Bürgel C., Burda J., Bonačić-Koutecký V., Fantucci P., Eur. J. Phys. D 24 (2003) 41.
[127] Yoon B., Häkkinen H., Landman U., J. Phys. Chem. A 107 (2003) 4066.
[128] Ding X., Li Z., Yang J., Hou J.G., Zhu Q., J. Chem. Phys. 120 (2004) 9594.
[129] Yuan D.W., Zeng Z., J. Chem. Phys. 120 (2004) 6574.
[130] Negeshi Y., Nakamura Y., Nakajima A., Kaya K., J. Chem. Phys. 115 (2001) 3657.
[131] Sinfelt J.H., Bimetallic Catalysts, Wiley, New York, 1985.

Chapter 3

Probing the unique size-dependent properties of small Au clusters, Au alloy clusters, and CO-chemisorbed Au clusters in the gas phase

Hua-Jin Zhai[a,b], Xi Li[a,b] and Lai-Sheng Wang[a,b,*]

[a]Department of Physics, Washington State University, 2710 University Drive, Richland, WA 99354, USA

[b]Chemical and Materials Sciences Division, Pacific Northwest National Laboratory, MS K8-88, P.O. Box 999, Richland, WA 99352, USA

1. INTRODUCTION

When materials are reduced in size to the nanometer scale, their physical and chemical properties undergo major changes and become size-dependent, forming the foundation for nanoscience and nanotechnology. Gold nanoparticles and small gold clusters have been the focus of intensive research activities lately. The modern ''gold-rush'' is largely motivated by the recent discoveries that (i) nanogold shows unexpected catalytic properties for a wide spectrum of chemical reactions [1], (ii) nanogold enables selective binding to biomolecules such as DNA and thus can serve as biosensors [2], (iii) gold has important potential applications in nanoelectronics [3, 4], and (iv) gold clusters and gold-containing compounds possess unique chemical properties [5]. All these golden discoveries have made gold a surprising and rewarding subject of investigation in nanoscience and cluster science. Indeed, some of our oldest notions regarding gold, such as its inertness, are being changed dramatically by the recent findings in nanogold.

The properties of gold are dominated by strong relativistic effects [6] and the so-called aurophilic interactions [7]. The nobleness and the ever-lasting luster of gold are entirely due to relativity, as is its golden color. In 1979 Pyykkö and Desclaux [8] first showed that gold exhibits an unusually large relativistic 6s-orbital contraction as compared to its neighboring elements in the periodic table, which is now known as the ''gold maximum of relativity''. Since then, our understanding of gold on the basis of the relativistic effects has expanded vastly, as documented in several recent reviews [5, 6]. The main effects of relativity on the atomic orbitals are the relativistic radial contraction and energetic stabilization of the s and p shells (*direct relativistic effect*), the relativistic radial

The Chemical Physics of Solid Surfaces, Volume 12
ISSN: 1571-0785
DOI: 10.1016/S1571-0785(07)12003-4

*Corresponding author.
E-mail: ls.wang@pnl.gov

expansion and energetic destabilization of the (outer) d and all f shells (*indirect relativistic effect*, due to the increased screening of the nuclear attraction by the contracted s and p shells), and the *spin–orbit splitting*. All these effects are of the same order of magnitude and scale roughly as the square of the nuclear charge (Z^2).

Aurophilic interactions in gold compounds had not been recognized until the late 1980s when Schmidbaur first coined this term [9], despite the fact that a large body of gold compounds were synthesized and characterized in the past half a century [10]. The aurophilic interactions are due to closed-shell–closed-shell interactions between two Au(I) d^{10} units. Such interactions are of dispersive nature, but they are substantially enhanced in gold (up to 30 kJ/mol) due to strong relativistic effects and hence the reduced Au–Au distances. Aurophilic interactions have thus been called ''super van der Waals interactions'' [11], and they are roughly comparable in strength with typical hydrogen bonds. Aurophilicity greatly enhances the intramolecular and intermolecular Au–Au interactions and leads to unusual structural chemistry in gold compounds. Today, the concept of aurophilicity has proved highly useful not only in the rationalization of unique crystalline structures in gold compounds, but also in the prediction and design of new compounds [7]. For a comprehensive review on closed-shell interactions in inorganic chemistry, the readers are referred to Ref. [11].

We have been interested in the electronic structure and chemical bonding of novel atomic clusters and utilizing the clusters as molecular models for solid-state materials, interfaces, and surfaces over the past decade. In particular, we have shown that photoelectron spectroscopy (PES) in combination with accurate computational studies provides a powerful approach to elucidate the complex structures and chemical bonding of atomic clusters. Upon confirmation of cluster structures from the comparison of well-resolved PES spectra – which provide electronic fingerprints of the underlying clusters – with theoretical calculations, we can further analyze the detailed chemical bonding in the clusters and the factors that control their structures. The combined PES and computational studies have resulted in unexpected discoveries [12, 13]. We should point out that structural determination of atomic clusters in the gas phase has been a grand challenge in experimental physical chemistry and a number of other methods have also been utilized to obtain cluster structural information, including ion mobility [14], electron diffraction [15], infrared vibrational spectroscopy [16], and chemisorption [17].

In this chapter, we will review recent studies in our laboratory on the structural and electronic properties, and chemical bonding in elemental gold clusters, gold alloy clusters, and CO-chemisorbed gold clusters in the gas phase [18–30], which represent further examples to demonstrate the diverse and expanding chemistry of gold. Topics to be covered include the planarity in small elemental Au cluster anions [18]; the tetrahedral Au_{20} cluster [19, 20]; icosahedral gold cage clusters $M@Au_{12}$ (M = W, Mo) and $M@Au_{12}^-$ (M = V, Nb, Ta) [24, 25]; gold as hydrogen in $SiAu_n$ ($n = 2$–4), Si_2Au_2, Si_2Au_4, and $B_7Au_2^-$ [26–28]; and CO chemisorption on Au clusters as molecular models for mechanistic understanding of nanogold catalysts [29, 30]. The findings are not only fundamental in cluster science and physical chemistry, but may also have important potential applications. For example, the observation of Au_2H^- impurity in pure gold clusters provides strong, albeit indirect, evidence that H is the ''invisible'' atom that gives the anomalous Au–Au distance in atomic-thick Au nanowires [22]; the series of $M@Au_{12}$ (M = W, Mo) and $M@Au_{12}^-$ (M = V, Nb, Ta) cage

clusters demonstrates the potential of fine-tuning electronic properties of gold by doping with impurity atoms [24, 25]; the discovery of the Au/H analogy has added a new dimension to gold chemistry [26–28]; and the electronic evolution of the Au cluster CO complexes provides key insight into the CO chemisorption sites on Au, the activation of Au by CO chemisorption, and the cooperative coadsorption of CO and O_2 on gold clusters, and may be important to elucidate the catalytic mechanisms of nanogold for CO oxidation at low temperatures [29, 30].

There is a large body of recent literature on gold clusters that is not attempted to be reviewed here. However, relevant literature will be discussed in each subtopic throughout this chapter.

ABBREVIATIONS

2c-2e	two-center two-electron bond
2D	two-dimensional
3D	three-dimensional
ADE	adiabatic detachment energy
B3LYP	a hybrid method, a mixture of Hartree–Fock exchange with density functional exchange correlation
BE	binding energy
CCSD(T)	coupled-cluster method with all single and double excitations with noniterative inclusion of triple excitations
CID	collision-induced dissociation
DFT	density functional theory
DOS	density of states
EA	electron affinity
ESI	electrospray ionization
FWHM	full width at half maximum
GGA	generalized gradient approximation
HOMO	highest occupied molecular orbital
KE	kinetic energy
LUMO	lowest unoccupied molecular orbital
MD	molecular dynamics
MO	molecular orbital
NBO	natural bond orbital
PES	photoelectron spectroscopy
TD-DFT	time-dependent DFT
TEM	transmission electron microscopy
VDE	vertical detachment energy

2. EXPERIMENTAL METHOD

Experiments on atomic clusters in our laboratory were carried out using a state-of-the-art magnetic-bottle time-of-flight photoelectron spectrometer coupled with a laser vaporization supersonic cluster source. Details of the experimental setup have been published

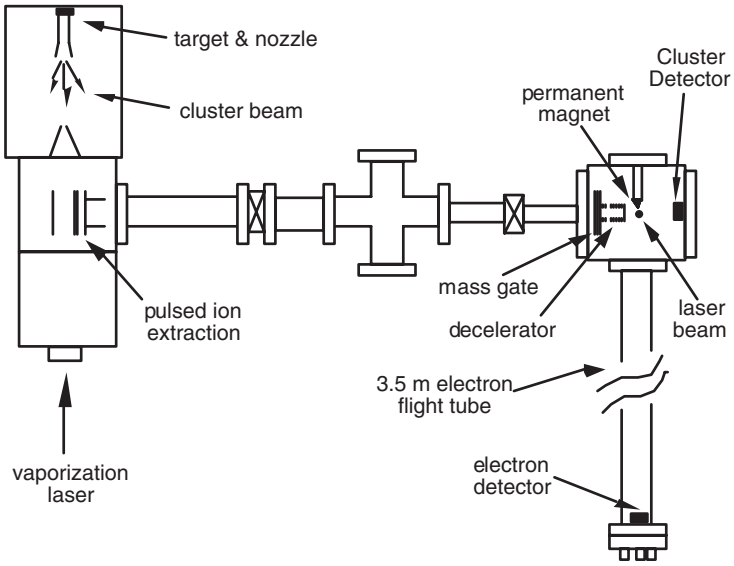

Figure 1: Schematic view of the magnetic-bottle time-of-flight photoelectron spectroscopic apparatus coupled with a laser vaporization supersonic cluster source and a time-of-flight mass spectrometer.

previously [31]. Figure 1 shows a schematic view of our experimental apparatus. Briefly, disk targets containing the appropriate atoms required to synthesize the desired clusters are vaporized by an intense pulsed vaporization laser beam. The laser-induced plasma is cooled by a high-pressure helium carrier gas, initiating nucleation and formation of clusters. The different types of cluster species discussed in this chapter are each produced using slightly different approaches: elemental Au clusters and Au alloy clusters are produced using a pure Au target and appropriate M/Au mixed targets, respectively, in the presence of a pure helium carrier gas, whereas the CO-chemisorbed $Au_m(CO)_n^-$ species are produced with a pure Au target in the presence of a helium carrier gas seeded with 2% CO.

The nascent clusters are entrained in the helium carrier gas and undergo a supersonic expansion to form a collimated cluster beam. Negatively charged species are extracted from the cluster beam perpendicularly and are analyzed by time-of-flight mass spectrometry. A mass-gate is used to select the desired clusters to enter the interaction zone of the magnetic-bottle photoelectron analyzer. The selected clusters are decelerated before being photodetached by a laser beam. A variety of detachment laser photon energies are utilized in the PES experiments (532, 355, 266, and 193 nm). Photoemitted electrons are collected by the magnetic-bottle at nearly 100% efficiency and analyzed in a 3.5 m long electron time-of-flight tube. The photoelectron time-of-flight spectra are calibrated using the known spectra of Rh^- and Au^- and converted to kinetic energy (KE) spectra. The reported binding energy (BE) spectra are obtained by subtracting the KE spectra from the photon energy ($h\nu$) using the Einstein's photoelectric equation: $BE = h\nu - KE$. High-photon-energy spectra are particularly important because they reveal more electronic transitions, which are essential to facilitate comparisons with theoretical calculations. Low photon energies in general yield better-resolved spectra

for the ground-state transitions, allowing more accurate determination of adiabatic detachment energies (ADEs) and vibrational resolution for the neutral species in favorable cases. The energy resolution of the apparatus is $\Delta KE/KE \sim 2.5\%$, i.e., ~25 meV for 1 eV electrons.

3. ELECTRONIC AND STRUCTURAL PROPERTIES OF ELEMENTAL GOLD CLUSTERS

3.1. Small Au cluster anions Au_n^- ($n = 1$–14): planarity and 2D-to-3D transition

Our interest in small Au cluster anions was stimulated by the theoretical [32, 33] and experimental [33] discoveries of planarity in small Au_n^- clusters (n up to about 12 atoms). The occurrence of planar metal clusters in this size range is unprecedented because metal clusters are expected to form compact three-dimensional (3D) structures. Stability of the planar Au clusters was explained by the strong relativistic effects in gold that reduce the 6s–5d energy gap and enhance s–d hybridization. In order to uncover electronic signatures for the planar Au clusters, we performed a combined PES and density functional theory (DFT) study on Au_n^- ($n = 1$–14) [18]. PES of size-selected Au_n^- clusters has been performed by several groups previously [34]. However, the prior data were either of poor resolution [34b] or limited size range [34a, 34c].

Figure 2 shows our 193 nm PES spectra for Au_n^- ($n = 1$–14). Better-resolved spectra at 266 nm were also obtained. The spectra were all highly resolved with numerous discrete electronic transitions up to the highest photon energy used (6.424 eV). The most significant observation in the spectra is the even–odd alternation, where the even clusters show lower electron binding energies and sizable energy gaps, indicating that the neutral even-sized clusters are closed-shell electronic systems. However, the spectrum of Au_{10}^- represents a clear exception to the even–odd pattern. The weak signals in the lower binding energy range between 2.8 and 3.8 eV of the Au_{10}^- spectrum were actually due to weakly populated isomers. In fact, the vertical detachment energy (VDE) of the main isomer of Au_{10}^- was measured to be 3.92 eV, which is higher than that of either Au_9^- (3.84 eV) or Au_{11}^- (3.80 eV). Minor isomers were also observed for other clusters, notably in the spectrum of Au_4^-, where two weak features were observed in the HOMO–LUMO gap region at VDEs of 3.41 and 3.76 eV. A very weak peak at 2.49 eV in the Au_4^- spectrum should also come from an isomer. In the spectra of Au_8^- and Au_{12}^-, the first peak showed a splitting, each with a shoulder on the higher binding energy side. The splitting is too large to be attributed to vibrational excitations, and it is likely due to the presence of isomers with similar VDEs as the main isomers. The weak feature at the lowest-binding-energy side (3.76 eV) in the spectrum of Au_{13}^- is also indicative of a contribution from a minor isomer.

A number of optimized low-energy structures for Au_n^- ($n = 4$–14) are shown in Fig. 3, a striking feature being the occurrence of energetically favorable planar structures up to Au_{14}^-. For clusters larger than Au_{10}^-, many low-lying 3D isomers exist, but the ground states predicted by DFT are planar, in agreement with the finding by Furche et al. [33]. Figure 4 compares the calculated and measured VDEs. For most clusters, the theoretical VDEs for the lowest-energy clusters (filled dots) agree well with the experimental result. For Au_{13}^-, the calculated VDEs for both the 2D and 3D structures seem to agree with the experimental data. However, for Au_{14}^-, only the

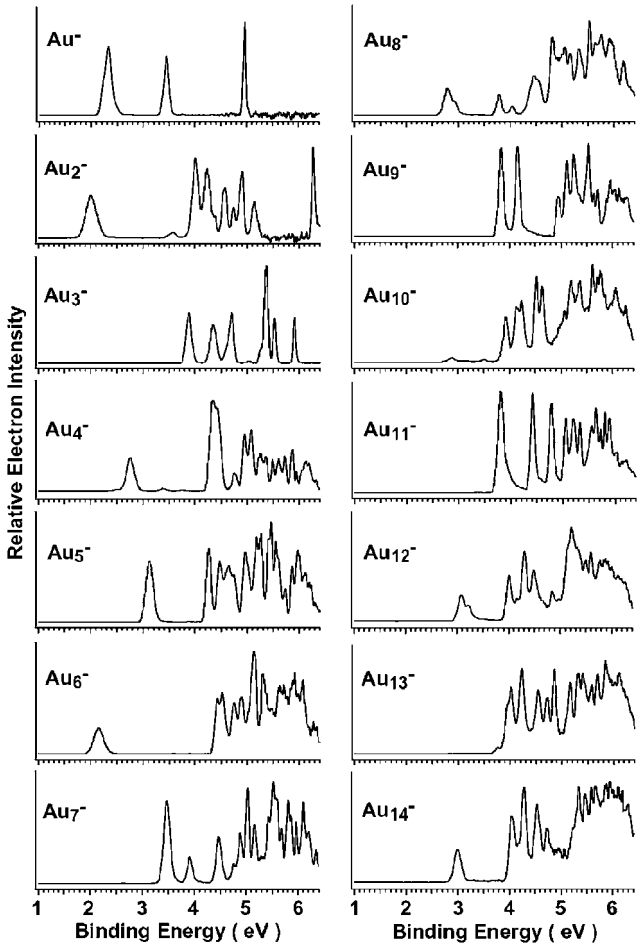

Figure 2: Photoelectron spectra of Au_n^- ($n = 1$–14) measured at 193 nm. Reproduced from Ref. [18].

3D isomer agrees with the experiment, suggesting that 3D Au_n^- clusters become energetically favorable for $n > 13$.

3.1.1. Au_4^- and Au_5^-

The DFT calculations reveal four structures (4A–4D) very close in energy (within 0.1 eV) for Au_4^-. All four structures may be present in the PES experiment, as evidenced by the weak features in the HOMO–LUMO gap region in the spectrum of Au_4^- (Fig. 2). The first main PES peak at 2.75 eV agrees with the calculated VDE value (2.78 eV) of isomer 4B. The calculated density of states (DOS) of isomer 4B exhibits a large HOMO–LUMO gap, also consistent with the measured PES data. Thus, the "Y"-shaped isomer 4B should be the dominating anion in the Au_4^- cluster beam. The very weak features at 2.5 and 3.4 eV are consistent with the calculated DOS of isomer 4D (rhombus).

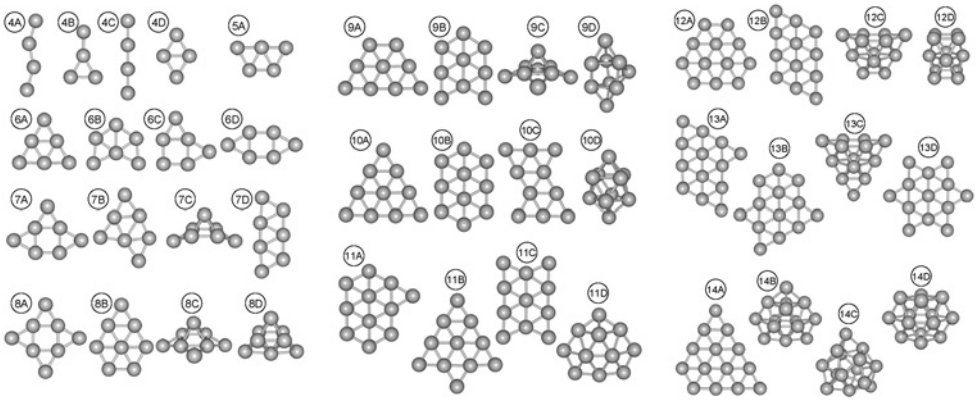

Figure 3: Optimized low-energy structures for Au_n^- ($n = 4$–14). Several isomers are shown for each size, and the ground state is labeled by "A" in each case. Reproduced from Ref. [18].

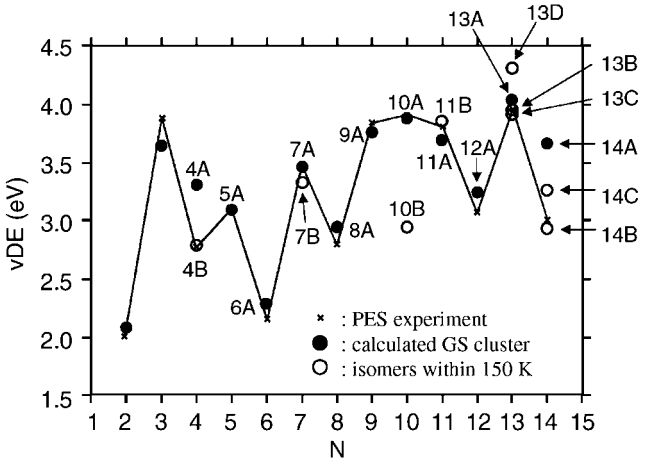

Figure 4: Comparison of theoretical and experimental VDEs for Au_n^-. All theoretical isomers are labeled as in Fig. 3, and "GS" stands for the ground state. Reproduced from Ref. [18].

Structure 5A is clearly the ground state for Au_5^- and the next isomer is 0.3 eV higher in energy. The calculated DOS of 5A agrees well with the measured PES spectrum.

3.1.2. Au_6^-

The Au hexamer anion has been studied extensively; it was shown early on that its PES spectrum exhibits a very large gap of 2.3 eV between the first two peaks [34b]. Furthermore, the first PES band has been resolved vibrationally with a spacing of 108 cm^{-1} [35], indicating that the cluster has a high symmetry. A D_{6h} ring structure was proposed initially [35]. However, the D_{3h} triangular structure 6A (Fig. 3) has been found to be the ground state from the DFT calculations. Ab initio molecular dynamics (MD) simulations show that electron detachment from the ground state of Au_6^- to that of the Au_6 neutral induces a symmetric vibration with a frequency of 114 cm^{-1}, compared

well to the experimental value of 108 cm^{-1}. The calculated energy gap (1.94 eV) and VDE (2.29 eV) of structure 6A are also in good agreement with the experiment (energy gap: 2.30 eV and VDE: 2.13 eV).

3.1.3. Au_7^- and Au_8^-

The ground state 7A and the first isomer 7B (Fig. 3) for Au_7^- are separated by only 0.04 eV, followed by a larger separation of 0.4 eV from the first 3D isomer (7C). Based on this result, the coexistence of 7A and 7B isomers in the Au_7^- beam is likely. Both structures give theoretical VDEs (7A: 3.46 eV and 7B: 3.32 eV) that are consistent with the experimental value (3.46 eV). Additionally, ab initio MD simulations show interconversions between structures 7A and 7B at 350 K, which is probably comparable to the cluster temperature in the beam.

Isomers 8A and 8B (Fig. 3) for Au_8^- are energetically close to each other (within 0.16 eV) and both should be considered in interpreting the PES data. Indeed, the two features visible in the low binding energy side of the PES spectrum (Fig. 2) could come from the two isomers. The calculated VDEs for isomers 8A and 8B are 2.94 and 3.02 eV, respectively, in good agreement with the PES spectral pattern.

3.1.4. Au_9^-, Au_{11}^-, and Au_{13}^-

The calculated VDEs of the ground-state structures 9A (3.75 eV) for Au_9^-, 11A (3.69 eV) for Au_{11}^-, and 13A (4.03 eV) for Au_{13}^- agree reasonably well with the experimental values of 3.83, 3.80, and 3.94 eV, respectively. The calculations predict the existence of several low-lying isomers particularly for Au_{11}^- and Au_{13}^- (Fig. 3), which may contribute to the observed PES spectra.

3.1.5. Au_{10}^-

The PES spectrum of Au_{10}^- (Fig. 2) differs qualitatively from all the other spectra of even-sized clusters. It does not show an energy gap, suggesting that the Au_{10} neutral either has a very small HOMO–LUMO gap or is open-shell. The binding energy of Au_{10}^- is also unusually high; its first VDE is at 3.91 eV. In addition, there are weak features in the low binding energy range (at 2.9 and 3.5 eV), indicating the presence of low-lying isomers. The planar D_{3h} 10A structure (Fig. 3) is calculated to be the ground state, separated by 0.12 eV from the planar D_{2h} isomer 10B. The calculated VDE of 10A is 3.86 eV, in good agreement with the first strong PES peak at 3.91 eV. The VDE of the D_{2h} isomer, 2.94 eV, matches the first weak PES feature at ~2.9 eV.

3.1.6. Au_{12}^-

For Au_{12}^-, DFT calculations predict the planar D_{3h} structure 12A (Fig. 3) to be the ground state, followed by a planar C_{2h} structure 12B and a 3D C_{2v} structure 12C, which are 0.32 and 0.54 eV higher in energy, respectively. The DOS spectra of all these isomers show a clear HOMO–LUMO gap (~0.8 eV), in good agreement with the experimental PES spectra that revealed a HOMO–LUMO gap of about 0.9 eV. Based on ion mobility data, Furche et al. [33] concluded that $n = 12$ is the critical size for 2D–3D transition, namely isomers of both dimensionality (12A and 12C) are present in the Au_{12}^- anion beam, and clusters with $n > 12$ are 3D. The calculated VDE values for the first three isomers (12A, 3.24 eV; 12B, 3.25 eV; and 12C, 3.10 eV) all agree well with the measured value of 3.06 eV. Additionally, the contributions from all these

clusters would give a double feature in the first photodetachment peak, as is indeed observed experimentally. Thus, our work gives further support for the conclusion of Ref. [33] that both planar and 3D structures are present in the beam of Au_{12}^-.

3.1.7. Au_{14}^-

For Au_{14}^-, two structures (14A and 14B) were found within an energy interval of 0.1 eV. Comparison of the experimental VDE (3.00 eV) with calculated VDE (14A: 3.66 eV and 14B: 2.93 eV) indicated that the 3D flat cage-like structure 14B agrees with the experimental data. Furthermore, the calculated HOMO–LUMO gap for 14B (1.05 eV) also reproduces well the observation (1 eV), whereas 14A shows a much smaller energy gap (<0.4 eV). It is therefore safe to conclude that the experimental PES spectrum for $n = 14$ comes from the 3D cluster, and the most likely candidate is structure 14B. This conclusion is also consistent with that from the ion mobility experiment – that above $n = 12$, the 3D gold cluster anions become favorable [33].

In summary, the combined PES and theoretical investigation on Au_n^- ($n = 4$–14) allows us to gain insight into the structural characteristics and growth patterns of the Au cluster anions. We also found that the most likely structural candidates for Au cluster anions up to $n = 12$ are planar, confirming the findings of Furche et al. [33] using ion mobility. For $n = 13$, a definite structural assignment cannot be done on the basis of the PES data due to the existence of many low-lying 2D and 3D isomers. For $n = 14$, a 3D flat cage-like structure has been clearly identified. Isomeric effects are recognizable in the experimental PES data for several cluster sizes, most notably for $n = 4$, 7, 8, 10, and 12. The 2D–3D transition seems to take place via cage-like structures, but for $n = 13$ the commonly considered icosahedral or cuboctahedral structures are not energetically favorable. Also, we note that theoretical calculations indicate that, for most cluster sizes, the energetic ordering of the Au_n neutrals does not follow that of the corresponding anions. However, the planar structures are energetically very competitive with respect to 3D structures also in neutral gold clusters; indeed, only for the largest size considered, Au_{14}, a 3D ground-state structure has been found. Nevertheless, experimental verification for the 2D–3D transition in neutral clusters is challenging because the cluster beam experiment usually observes properties of charged clusters. Moreover, the critical size for 2D–3D transition in the Au_n neutrals has turned out to be very controversial even for state-of-the-art computational methods [36]. For positively charged clusters, Au_n^+, the 2D–3D transition size has been deduced to be $n = 8$ from the ion mobility experiment [37].

3.2. Au_{20}: a tetrahedral cluster and an ideal molecular model for nanogold catalysis

During our experiment on small Au clusters, we found that the 20–atom gold cluster exhibits an extremely large HOMO–LUMO gap, as shown in Fig. 5. The 193 nm spectrum displays a weak peak around 2.7 eV (labeled *X*), followed by a large energy gap and more discrete transitions at higher binding energies (*A*, *B*, *C*,…). This spectral pattern suggests that neutral Au_{20} is a closed-shell molecule with a HOMO–LUMO gap of 1.77 eV, as measured from the *X*–*A* separation. This energy gap in Au_{20} is very large, about 0.15 eV greater than that in C_{60} (1.62 eV) [38]. Electron signals observed in the HOMO–LUMO gap region in the 266 nm spectrum (Fig. 5b) were owing to autodetachment as a result of a photoexcited Au_{20}^{-*} upon absorption of a 266 nm

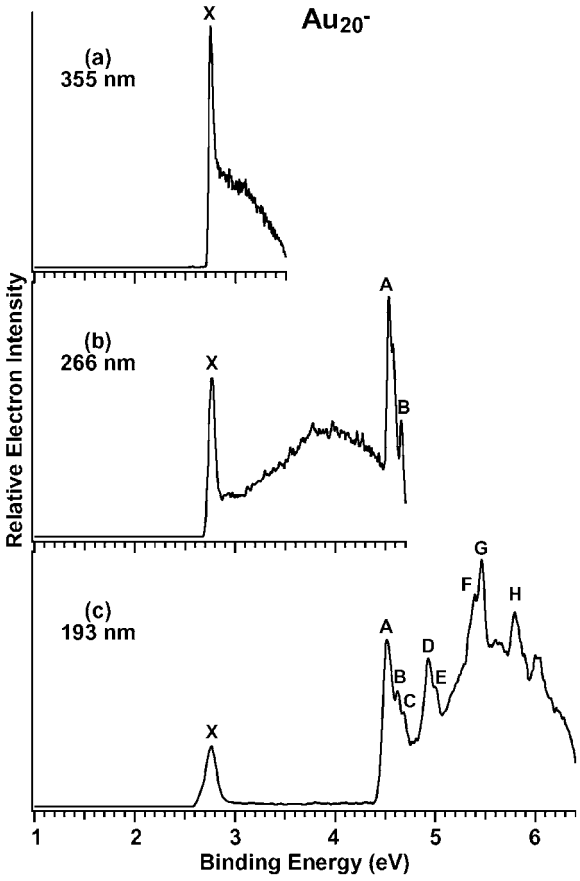

Figure 5: Photoelectron spectra of Au_{20}^- at (a) 355 nm, (b) 266 nm, and (c) 193 nm. Reproduced from Ref. [19].

photon. Similar autodetachment signals were also observed previously in C_{60}^- [38]. The 355 nm spectrum of Au_{20}^- (Fig. 5a) revealed a very sharp peak for the ground-state transition (autodetachment signals were also observed at this detachment energy), suggesting that there is very little geometry change between the ground states of the Au_{20}^- anion and the Au_{20} neutral. This is different from C_{60}^-, whose PES spectra exhibit vibrational features due to structural distortions of the anion ground state [39]. The 355 nm spectrum yielded a VDE of 2.751 ± 0.010 eV and an ADE of 2.745 ± 0.015 eV for Au_{20}^-. The latter is the electron affinity (EA) of Au_{20}: a measure of how tightly the cluster can bind an electron. The EA of Au_{20} is higher than that of C_{60} (2.683 ± 0.008 eV) [38], thus Au_{20} is even more electronegative than C_{60}. According to the electron shell model, Au_{20} with 20 valence electrons should represent a major shell closing. What is surprising is the magnitude of the HOMO–LUMO gap. With the exception of Au_2 and Au_6, the HOMO–LUMO gap observed for Au_{20} is the largest among all known coinage metal clusters.

An extensive structural search for neutral and negatively charged Au_{20} was carried out using relativistic DFT calculations, as shown in Fig. 6. The structural search starts

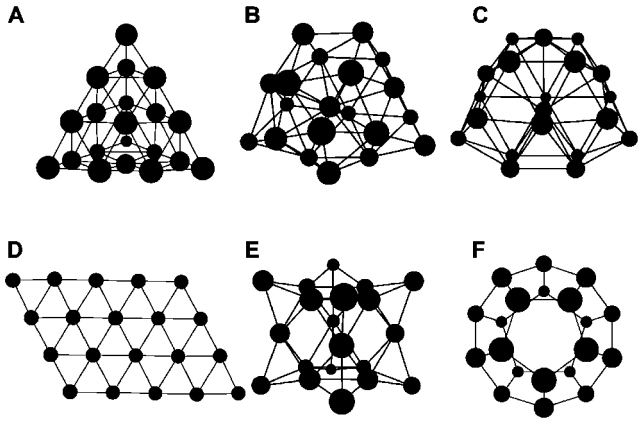

Figure 6: Selected optimized Au_{20} structures: (A) tetrahedral structure (T_d), (B) amorphous structure (C_1), (C) capped decahedron (C_{2v}), (D) planar structure (C_{2h}), (E) octahedral structure (O_h), and (F) dodecahedral structure (I_h). Reproduced from Ref. [19].

from the highest symmetry possible (the Platonic dodecahedron with icosahedral (I_h) symmetry and octahedron with octahedral (O_h) symmetry) to their various important subgroups, as well as the ring and bowl structures known for C_{20}. Also tested are a capped decahedron (C_{2v}) structure and an amorphous (C_1) structure, which were found as "global minima" in previous calculations [40]. The I_h and O_h Au_{20} structures are open-shell and would be subject to Jahn–Teller instability; a string-bag-like cage, a bowl, and a ring structure are closed-shell but are highly unstable, with small HOMO–LUMO gaps. Because smaller Au_n^- ($n < 13$) clusters prefer planar geometries (Fig. 3) [18, 32, 33], a planar Au_{20} structure was also calculated, as well as a linear Au_{20} chain, which has recently been formed on an NiAl surface and studied with scanning tunneling microscopy (STM) [41]. Although less stable than the tetrahedral structure (Fig. 6A), the planar structure (Fig. 6D) was found to be more stable than any other isomers except the amorphous cluster (Fig. 6B) and the capped decahedron (Fig. 6C). The linear chain is highly unstable, with almost no HOMO–LUMO gap, which is consistent with its metallic behavior observed by STM. The calculated molecular properties are summarized in Table 1.

The most stable structure identified is the ideal tetrahedral (T_d) structure (Fig. 6A), which is more stable than the previously suggested "global minima" C_1 and C_{2v} structures [40] by 1.4 and 1.8 eV, respectively. The T_d Au_{20} structure is closed-shell with a HOMO–LUMO gap of 1.8 eV, in excellent agreement with the experiment. The Au–Au distances (0.268, 0.271, 0.283, 0.297, and 0.312 nm) in the calculated T_d Au_{20} structure are close to those in bulk gold (0.288 nm), yielding a tetrahedral edge around 1 nm. Frequency calculations for T_d Au_{20} confirmed it is a minimum on the potential energy surface.

To facilitate comparison with experimental results, the geometries of the anions for all the isomers were also optimized. Consistent with the experiment, very little structural change was observed upon electron addition to T_d Au_{20}: the Jahn–Teller distortion energy (~0.02 to 0.04 eV for distortion to the D_{2d} and C_{3v} symmetries) is much smaller than the spin–orbit coupling energy (0.16 eV), so that the geometry distortion

Table 1: Optimized molecular structures, point group symmetries, electronic configurations, HOMO–LUMO energy gaps (ΔE_{HL}), relative scalar-relativistic energies (E_{SR}), and electron affinities (EA) of Au_{20} (Ref. [19])[a].

Structure	Symmetry	Configuration	ΔE_{HL}	E_{SR}	E_{SR} (anion)	EA
Tetrahedral pyramid	T_d	$(t_2)^6(e)^4(t_2)^0$	1.818	0	−2.612	2.612
No symmetry	C_1	$(a)^2(a)^2(a)^0$	0.495	1.395	−1.767	3.162
Capped decahedron	C_{2v}	$(a_1)^2(a_1)^2(b_2)^0$	0.204	1.779	−1.616	3.395
Planar	C_{2h}	$(a_g)^2(b_u)^2(b_u)^0$	0.689	2.063	−1.636	3.699
Octahedron	O_h	$(a_{1g})^2(e_g)^2(t_{1u})^0$	0	2.509	−0.484	2.993
String-bag cage	D_{2h}	$(a_{1g})^2(b_{2u})^2(b_{3g})^0$	0.170	2.898	−0.729	3.627
Dodecahedron	I_h	$(h_g)^{10}(g_u)^2(t_{2u})^0$	0	8.466	4.842	3.624
Bowl	C_{5v}	$(e_2)^4(e_1)^4(e_1)^0$	0.087	10.504	6.176	4.328
Ring	D_{5h}	$(e_1')^4(a_2')^2(a_1')^0$	0.737	11.520	7.249	4.271
Chain	$C_{\infty v}$	$(\sigma)^2(\pi)^4(\pi)^4(\sigma)^0$	0.003	17.625	12.101	5.524

[a]The relative scalar-relativistic energies of the optimized anions are also listed, E_{SR} (anion). All energies are in eV. The total energies of the various isomers of Au_{20} and Au_{20}^- are relative to those of the neutral tetrahedral Au_{20}.

is quenched. The total energy difference between the anion and the neutral defines the theoretical EA. The calculated EA for T_d Au_{20} is 2.61 eV. However, when spin–orbit coupling is included, a theoretical EA of 2.741 eV is obtained, which is in excellent agreement with the experimental value of 2.745 ± 0.015 eV, whereas the calculated EAs for all other structures deviate considerably from the experimental measurement (Table 1). Because the *X–A* gap represents the excitation energy of the lowest triplet excited state, this quantity for T_d Au_{20} was also calculated. The calculated excitation energy for the lowest triplet state ($^3A_1$) is 1.777 eV, in close agreement with the experimentally determined value of 1.77 eV.

The tetrahedral Au_{20} can be viewed as a small piece of bulk gold with a small relaxation. Each of the four faces represents a (1 1 1) surface of face-centered cubic (fcc) gold. It has a very high surface area (all the atoms are on the cluster surface) and a large fraction of corner sites with low coordination. The three different kinds of atoms in the T_d structure, 4 at the apexes, 4 at the center of each face, and 12 along the edges, have different coordination environments and may provide ideal surface sites to bind different molecules for catalysis (such as CO, O_2, and CO_2). Preliminary calculations of four CO absorbed on the apex and face-center sites reveal a HOMO–LUMO gap of 1.43 and 1.50 eV for the $Au_{20}(CO)_4$ clusters and a binding energy of 0.84 and 0.15 eV per CO, respectively. The large HOMO–LUMO gaps in the naked and CO-adsorbed clusters indicate that the T_d Au_{20} is highly chemically inert, and will maintain its structural integrity during catalysis.

The tetrahedral Au_{20} cluster has been confirmed by numerous follow-up works [42–48]. Wang et al. [42] conducted a comparative DFT–GGA study of Au_{20}, Ag_{20}, and Cu_{20}, and showed that Au_{20} indeed possesses a highly symmetric T_d structure (0.675 eV lower than the low-symmetry C_s compact structure). More interestingly, Cu_{20} was found to possess a low-symmetry C_s structure (0.579 eV lower than the T_d structure), whereas for Ag_{20} the T_d and C_s structures are virtually isoenergetic. In a closely relevant quasi-relativistic DFT study [49], Johansson et al. showed surprising stability of a series of tetrahedral pyramidal Cd_n clusters (including Cd_{20}), and suggested that relativistic effects play vital roles in stabilizing the T_d clusters. de Bas et al. [43] reported combined first principles and empirical potentials calculations of gold clusters from

3 to 38 atoms, and confirmed the T_d structure for Au_{20}. These authors further investigated the melting behaviors of Au_{20} through MD calculations [44], and found that, in contrast to other Au clusters, the Au_{20} tetrahedron does not undergo any structural isomerization prior to melting and shows a sharp transition between solid-like and liquid-like phases at about 1200 K (comparable to the melting point of bulk gold), indicating that the tetrahedron sits at the bottom of a deep, isolated energy well. King et al. [45] proposed that the tetrahedral Au_{20} cluster can be generated from a regular dodecahedron by forming two transannular Au–Au bonds across each face (through aurophilic interactions) while preserving T symmetry. Wu et al. [46] recently studied the dipole polarizability, static first hyperpolarizability, and UV–Vis spectrum of Au_{20} using time-dependent DFT (TD-DFT) calculations, and showed remarkable second-order optical nonlinearity in Au_{20}, which may be used as novel molecular optoelectronic devices. Neumaier et al. [47] studied the chemical reactivity of Au_n^+ ($n = 1$–65) with CO and found a local minimum at Au_{20}^+ in the first CO adsorption rate constant, indicative of a stable Au_{20}^+ cluster. Furthermore, it was also characteristic that the first four CO molecules adsorb on Au_{20}^+ with very similar rate constants, consistent with a symmetric structure with four equivalent sites. Molina and Hammer [48] studied the catalytic activity of Au_{20} using DFT simulations, and found that Au_{20} is extremely robust against distortion on oxide surface and is highly catalytically active.

3.3. Toward solution synthesis of the tetrahedral Au_{20} cluster

Bulk synthetic effort has also been devoted in our lab to the Au_{20} cluster, and recently we successfully observed the tetrahedral Au_{20} cluster in solution, ligated with triphenyl phosphine (PPh_3) ligands [20]. Theoretical calculations (Fig. 7A–C) revealed that the

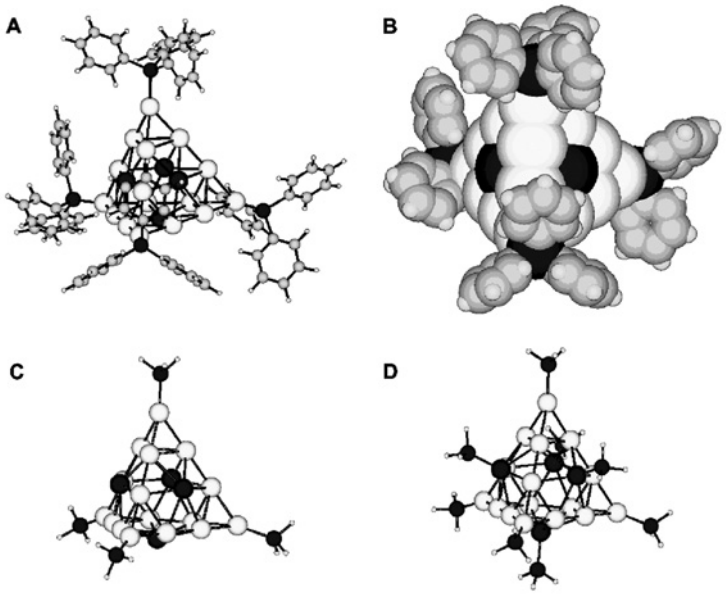

Figure 7: Computed structures of Au_{20} and its phosphine complexes: (A) $Au_{20}(PPh_3)_4$, (B) van der Waals surface of $Au_{20}(PPh_3)_4$, (C) $Au_{20}(PH_3)_4$, and (D) $Au_{20}(PH_3)_8$. Reproduced from Ref. [20].

$Au_{20}(PR_3)_4$ (R = H, Ph) complexes indeed possess high stability. Figure 7A shows the optimized structure of Au_{20} coordinated with four PPh_3 ligands; its van der Waals surface is shown in Fig. 7B. Expecting that the effect of PH_3 on the Au_{20} core would be similar to that of PPh_3, the $Au_{20}(PH_3)_4$ complex was also calculated for computational simplicity (Fig. 7C). Indeed, the only effect the phosphine ligands have on the Au_{20} core is that the four face-centered Au atoms tend to be pushed outward from the four Au_{10} faces: the calculated distance between the face-centered atoms is increased from 3.1 Å in Au_{20} to 3.4 Å (4.0 Å) in $Au_{20}(PPh_3)_4$ ($Au_{20}(PH_3)_4$). But the ligated complexes still maintain a large HOMO–LUMO energy gap: 1.44 eV in $Au_{20}(PPh_3)_4$ and 1.82 eV in $Au_{20}(PH_3)_4$, compared to 1.77 eV in the parent Au_{20} (Fig. 5) [19]. Thus, the Au_{20} complexes should have beautiful color and interesting optical properties.

High-resolution transmission electron microscopy (TEM) images showed that the soluble as-synthesized samples contained gold nanoparticles with diameters as large as 3 nm, as well as many particles with diameters less than 1 nm. Each edge of the bare Au_{20} was calculated to be 0.81 nm and was not changed in the PH_3-capped complex. Thus, the T_d Au_{20} core is expected to give a triangular image with an overall dimension slightly less than 1 nm. Indeed, numerous triangular particles with dimensions of less than 1 nm were found in the TEM images [20], consistent with the anticipated PPh_3-capped Au_{20}.

The solution sample containing Au nanoparticles was further characterized using a high-resolution Fourier transform ion cyclotron resonance (FTICR) mass spectrometer, which was accurately calibrated and equipped with an electrospray ionization (ESI) source. We carefully searched the m/z range around $Au_{20}(PPh_3)_4^+$ (m/z = 4987.695) but did not observe any singly charged ions in this mass range. All of the mass peaks observed in this m/z range and in higher m/z ranges appeared to be doubly charged ions, which could be easily recognized from the 1/2 m/z difference in the isotopic patterns. We then searched the lower m/z range corresponding to $Au_{20}(PPh_3)_4^{2+}$ (m/z = 2493.848), as shown in Fig. 8A (left column). Prominent singly charged ions were observed, corresponding to five- and six-atom gold clusters, but no doubly charged ions at m/z = 2493.848 were observed. However, a careful examination of the mass spectrum revealed that doubly charged ions corresponding to Au_{20} clusters with eight and seven PPh_3 ligands were observed at m/z = 3018.030 and 2886.984, respectively. We also observed mass peaks corresponding to Au_{10} complexes, but familiar clusters such as the undecanuclear Au_{11} species were not observed under our experimental conditions.

Figure 8B (left column) shows the observed isotopic pattern of the $Au_{20}(PPh_3)_8^{2+}$ cation primarily due to the ^{13}C isotope, compared to the simulated isotopic pattern (Fig. 8C, left column). The perfect agreement between experimental and simulated isotopic patterns, as well as the accurate m/z measurement, unequivocally confirmed the correct identification of the $Au_{20}(PPh_3)_8^{2+}$ composition. Such good agreement was also obtained for the observed $Au_{20}(PPh_3)_7^{2+}$ ions.

To obtain structural information for $Au_{20}(PPh_3)_8^{2+}$, we conducted collision-induced dissociation (CID) experiments in the FTICR cell, which revealed that four PPh_3 ligands can be readily dissociated from $Au_{20}(PPh_3)_8^{2+}$, resulting in a highly stable $Au_{20}(PPh_3)_4^{2+}$ ion, which could not be dissociated further under our experimental conditions (Fig. 8, right column). The CID results suggested that the tetrahedral core of Au_{20} is intact in the PPh_3-coordinated clusters.

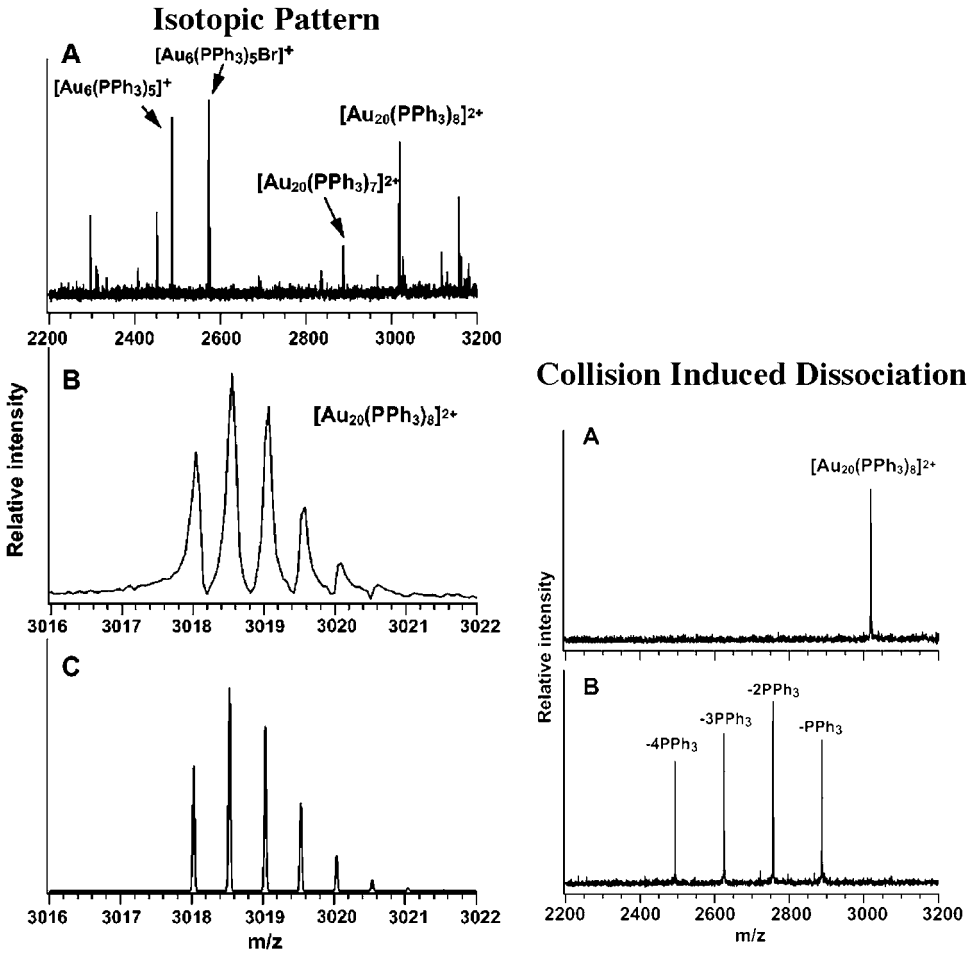

Figure 8: (Left column) High-resolution mass spectrometric characterization of Au–PPh_3 complexes: (A) mass spectrum containing the $Au_{20}(PPh_3)_8^{2+}$ and $Au_{20}(PPh_3)_7^{2+}$ doubly charged clusters, (B) isotopic pattern of the $Au_{20}(PPh_3)_8^{2+}$ mass peak, and (C) simulated isotopic pattern using the natural isotopic abundances of Au, P, C, and H. (Right column) CID of $Au_{20}(PPh_3)_8^{2+}$: (A) $Au_{20}(PPh_3)_8^{2+}$ peak after mass isolation, (B) CID products of $Au_{20}(PPh_3)_8^{2+}$ terminated at the lose of the maximum of four PPh_3 units, and no more PPh_3 could be removed under the current CID condition. Reproduced from Ref. [20].

To elucidate this observation, further calculations were performed on an Au_{20} cluster coordinated by eight PH_3 (Fig. 7D), with the four additional PH_3 ligands coordinated to the face-centered sites. The calculations indeed showed that the T_d Au_{20} core is intact in $Au_{20}(PH_3)_8$, which also has a large energy gap (1.55 eV) that is only slightly smaller than that of Au_{20}. The edge length of the T_d Au_{20} was not influenced by the PH_3 coordination; the only structural change is the outward move of the face-centered atoms. The four face-centered atoms in Au_{20} form a smaller tetrahedron, with an Au–Au distance of 3.1 Å being increased to 4.0 Å in $Au_{20}(PH_3)_4$ and 4.7 Å in $Au_{20}(PH_3)_8$. The average binding energy of PH_3 to the face-centered sites was calculated to be 16 kcal/mol, which is still sizable but smaller than that of the apex

sites. It should be pointed out that the Au–PPh_3 binding energy is expected to be larger for the apex sites and smaller for the face-centered sites because of steric repulsion between the bulkier PPh_3 ligands compared to the PH_3 ligands used in the calculations. Thus, the theoretical results were completely consistent with the CID experiment and confirmed that the T_d Au_{20} core is a robust cluster building block.

The phosphine ligands are electron donors, causing the increase in the HOMO energies of Au_{20} from –5.60 eV in the bare cluster to –4.51 eV in $Au_{20}(PH_3)_4$ and −3.89 eV in $Au_{20}(PH_3)_8$. This result suggests that the latter has a relatively low ionization energy and may exist as doubly charged closed-shell cations in solution. This explains why we were not able to observe singly charged $Au_{20}(PPh_3)_8^+$ from the ESI source. It also explains why we did not observe negatively charged $Au_{20}(PPh_3)_8^-$ ions when the negative mode was used in the ESI mass spectrometry. The weaker $Au_{20}(PPh_3)_7^{2+}$ ion signals may be produced from the dissociation of the parent $Au_{20}(PPh_3)_8^{2+}$ in the ESI source. The current experimental and theoretical results suggest that the T_d Au_{20} cluster coordinated with phosphine ligands may be obtained in bulk quantity. It is expected that by increasing the size of the ligands one can synthesize the T_d Au_{20} clusters with only the four apex sites coordinated.

3.4. Au_{32}: a golden fullerene cage cluster?

A recent theoretical surprise in Au clusters is the prediction of a highly stable Au_{32} cage cluster [50], which was found to have the same icosahedral (I_h) symmetry as C_{60} and can be viewed as decorating one atom to each of the 32 faces of C_{60}. Such a high-symmetry structure with a hollow core is intriguing but completely unexpected for a metal cluster. However, this structure has not been confirmed experimentally. Among even larger Au clusters, Gao and Zeng [51] studied a closed-shell I_h symmetrical model Au_{42} fullerene cluster using DFT calculations. The Au_{42} cluster can be constructed from the carbon fullerene C_{80} (I_h symmetry) as a template. It is a local minimum on the potential energy surface, being ~0.7 eV higher in energy than two compact structures previously identified. Very recently, Wang et al. [52] in their DFT calculations found a hollow cage Au_{50} structure, which is slightly more stable than its alternative space-filling isomeric structures.

We combined PES and DFT calculations to elucidate the electronic and geometrical structures of Au_{32} and Au_{32}^- [21]. The PES spectra of Au_{32}^- (Fig. 9) were measured at two photon energies, 266 and 193 nm. A total of seven discrete bands were resolved (labeled as *X* and *A*–*F*). The well-resolved bands in this spectral range make it possible to compare with theoretical calculations and to determine the geometric structure of the observed Au_{32}^- cluster. The *X* band yielded an EA for Au_{32} to be 3.96 ± 0.02 eV. The PES spectral pattern indicates that Au_{32} has a closed-shell electronic structure with a relatively small energy gap of 0.30 eV as defined by the *X*–*A* separation.

The previous theoretical search showed that for neutral Au_{32}, the I_h cage is the most stable structure, with the closest isomer (D_{6h}) being 0.94 eV higher in energy [50b]. The current DFT calculations are focused on the Au_{32}^- anion. It was found that the I_h cluster with a slight Jahn–Teller distortion (D_{3d}) remains to be the lowest-energy structure for Au_{32}^- (Fig. 10a and Table 2), but the closest noncage isomer C_1-I (Fig. 10b) is only 0.40 eV higher in energy based on the ADF calculations. Because of the Jahn–Teller effect, several lower symmetry species were considered for the cage

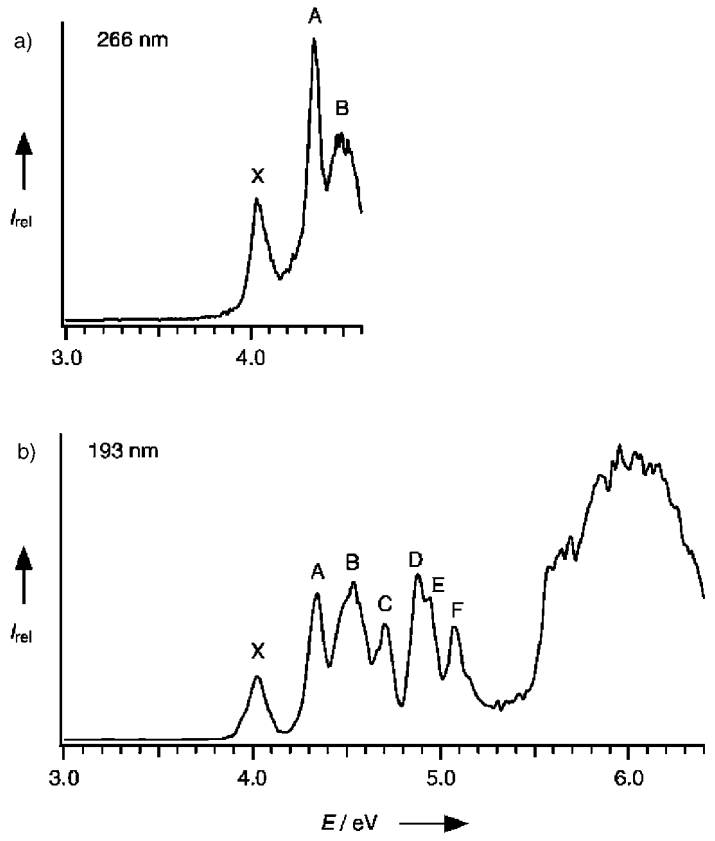

Figure 9: Photoelectron spectra of Au_{32}^- at (a) 266 nm and (b) 193 nm. Reproduced from Ref. [21].

structure of Au_{32}^-. The structural distortions are all very minor and the four lower symmetry structures are close in energy (Table 2). Except the planar structure, the other four low-lying isomers of Au_{32}^- as shown in Fig. 10 (C_1-I, D_{6h}, C_2, and C_1-II) are also close in energy. The two C_1 isomers have no symmetry and can be characterized as being amorphous. These two structures and the C_2 isomer are 3D, whereas the I_h and D_{6h} structures are cages, which can be considered to be quasi-2D. The three low-symmetry 3D structures are more compact and can be viewed essentially as distorted cages with two to four atoms inside.

Due to its high symmetry, the I_h Au_{32} has been shown to possess a very large HOMO–LUMO gap. A gap of 1.7 and 2.5 eV was evaluated in DFT calculations using the BP86 and PBE0 functionals, respectively [50a], whereas a gap of 1.5 eV was obtained using the VASP code [50b]. These values are considerably larger than the 0.30 eV gap measured in the PES spectra of Au_{32}^- (Fig. 9), suggesting that the experimentally observed Au_{32}^- cannot be the I_h cluster. To help determine the structure of Au_{32}^-, the ADE and VDE of all the six low-lying isomers were computed for comparison with the experimental PES spectra. The calculated ADEs for the C_1-I isomer (3.96 eV) and the C_2 isomer (3.94 eV) are both in perfect agreement with

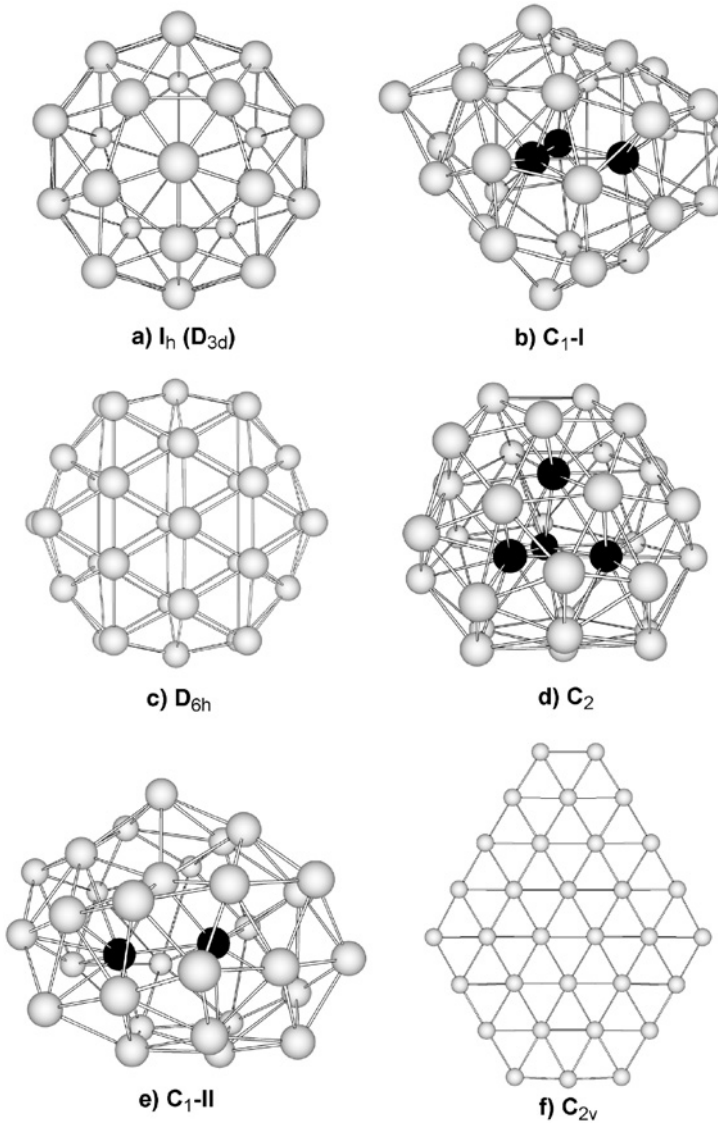

Figure 10: Selected optimized structures of Au_{32}^-: (a) the global minimum icosahedral cage structure (I_h), (b) first isomer with C_1 symmetry (C_1-I), (c) isomer with D_{6h} symmetry, (d) isomer with C_2 symmetry, (e) second isomer with C_1 symmetry (C_1-II), and (f) planar structure with C_{2v} symmetry. Reproduced from Ref. [21].

the experimental value (3.96 ± 0.02 eV), whereas that of the I_h structure is considerably smaller. The calculated ADEs of other isomers are also in poor agreement with the experimental value. The computed VDE spectra are shown in Fig. 11 in comparison with the experimental spectrum at 193 nm (dotted curve). The simulated spectrum of the I_h isomer (Fig. 11a) is very simple with its large HOMO–LUMO gap due to the high symmetry of this cage structure. The simulated spectra of the

Table 2: Optimized structures and electron configurations for Au_{32} and Au_{32}^-, HOMO–LUMO energy gaps (ΔE_{HL}) for Au_{32}, relative total energies (ΔE_{tot}), and ADEs and VDEs for Au_{32}^-, all calculated by the ADF PW91/TZ2P method (Ref. [21])[a].

Neutral			Anion				
Symmetry	Configuration	ΔE_{HL}	Symmetry	Configuration	ΔE_{tot}	ADE	VDE
C_{2v}	$(b_2)^2(a_1)^0$	≈ 0	C_{2v}	$(b_2)^2(a_1)^1$	2.50	4.28	4.32
C_1	$(a)^2(a)^0$	0.44	C_1-II	$(a)^2(a)^1$	0.81	3.74	3.79
C_2	$(b)^2(a)^0$	0.39	C_2	$(b)^2(a)^1$	0.46	3.94	4.11
D_{6h}	$(e_{1u})^4(e_{2g})^0$	0.84	D_{2h}[b]	$(b_{3u})^2(b_{1g})^1$	0.41	3.63	3.68
C_1	$(a)^2(a)^0$	0.22	C_1-I	$(a)^2(a)^1$	0.40	3.96	4.03
I_h	$(g_u)^8(g_g)^0$	1.56	D_{5d}	$(e_{2u})^4(a_{1g})^1$	0.16	2.90	3.02
			D_{2h}	$(a_{1u})^2(a_{1g})^1$	0.02	3.05	3.10
			C_{2h}	$(b_u)^2(b_g)^1$	0.01	3.06	3.16
			D_{3d}	$(a_{1u})^2(a_{1g})^1$	0.00	3.06	3.15

[a]All energies are in eV. The HOMO–LUMO energy gaps are for the optimized neutral species.
[b]Structural distortion in the anion is very small and the anion symmetry is very close to the neutral D_{6h} structure.

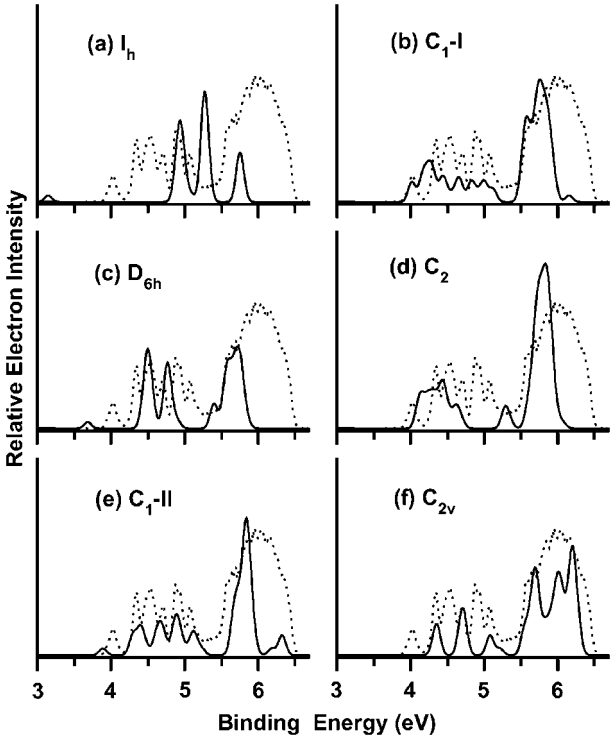

Figure 11: Simulated photoelectron spectra of Au_{32}^- for different isomers shown in Fig. 10, overlaid with the experimental spectrum at 193 nm (dotted curve) for comparison. The simulated spectra were constructed by fitting each of the calculated VDEs with a Gaussian of 0.05 eV width. Reproduced from Ref. [21].

D_{6h} cage and the C_{2v} planar structures are also quite simple due to their relatively high symmetries. These spectra (Fig. 11c and f) clearly disagree with the experimental PES data.

The simulated spectra of the three low-symmetry structures display some similarities (Fig. 11b, d, and e), all with an intense band above 5.5 eV derived from the high DOS of the 5d electrons. However, the lower binding energy parts of the simulated spectra are highly structured and exhibit clear differences, which seem to be quite sensitive to the detailed cluster structures. The simulated spectrum of the C_2 structure (Fig. 11d) is very congested near the threshold region between 4.0 and 4.8 eV, followed by a gap and another band at 5.3 eV. This simulated pattern is clearly inconsistent with the observed PES spectra (Fig. 9). On the first glance, the simulated spectrum of the C_1-II structure (Fig. 11e) seemed to display some similarity to the experimental spectra. However, the first peak of this structure at 3.74 eV is considerably lower compared with the experimental data. The number of bands between 4.2 and 5.1 eV is also inconsistent with the experimentally observed bands. In addition, the total energy of the C_1-II structure is 0.81 eV higher above the ground state, making it unlikely to be populated under our experimental conditions. On the other hand, the calculated ADE of the C_1-I structure (3.96 eV) is in excellent agreement with the experimental data (3.96 ± 0.02 eV), so that the first peak of the simulated spectrum of the C_1-I structure (Fig. 11b) coincides with the first experimental peak. The calculated HOMO–LUMO gap (0.22 eV) for the C_1-I structure seems to be slightly smaller than the measured gap of 0.3 eV.The number of bands and their spacings in the low binding energy part of Fig. 11b (except the HOMO–LUMO gap) are in excellent agreement with the observed PES spectra for Au_{32}^-. Overall, the simulated spectrum of the C_1-I structure agrees best with the PES spectra.

The C_1-I isomer is energetically the closest-lying isomer above the I_h structure, but it is still 0.4 eV higher based on the DFT calculations. Why was this isomer observed experimentally whereas the energetically more favorable Au_{32}^- cage was not? To understand this apparent paradox, the relative stabilities of the various isomers as a function of temperature were considered by taking into account the entropy contributions, i.e., the free energy. It was found that, although at zero temperature the I_h cage structure is the most stable, the relative stability of the C_1-I isomer increases rapidly with temperature due to contributions from the vibrational entropy. Significantly, it was observed that the C_1-I isomer becomes the most stable cluster above ~300 K. Although the actual cluster temperature in the experiment is not known, our previous experience shows that for medium-sized Al clusters a vibrational temperature of room temperature or slightly below can be achieved [53]. Because of the large size of Au_{32}^- and the ineffectiveness of the supersonic cooling, the best estimate for its vibrational temperature even under the relatively cold source conditions is probably around or slightly below room temperature. Considering the approximate nature of the free energy calculations, it is concluded that the formation of amorphous C_1-I Au_{32}^- in the experiment was indeed controlled by the vibrational entropy. Note that the C_1-II isomer is higher in energy than the lowest-energy C_1-I isomer at room temperature by 0.5 eV, making it very unlikely to be significantly populated under our experimental conditions. This is reinforced by the observation that the C_2 and D_{6h} isomers, which are both more stable than the C_1-II isomer, do not seem to have any contributions to the observed spectra.

4. NOVEL GOLD ALLOY CLUSTERS

4.1. Observation of Au_2H^- impurity in pure gold clusters and implications for the anomalous Au–Au distances in gold nanowires

One of the recent exciting developments in nanoelectronics is the fabrication of gold nanowires one-atom thick, which are the thinnest nanocontacts [3, 54]. Atomic-thick nanowires were exclusively observed for 5d metals [55], and strong relativistic effects were believed to play vital roles. These monoatomic gold nanowires were observed to be exceptionally stable, reaching interatomic distances as large as 3.6 Å [3, 54], a value significantly larger than the equilibrium Au–Au distances in gold dimer (2.48 Å) and in bulk fcc gold (2.88 Å). Several proposals have been put forth to interpret the abnormally high Au–Au distances [56–60]. Among the previous proposals is the existence of undetected impurity atoms [59, 60], such as H, B, C, CC, N, O, and S. All the impurities except H have been shown to give Au–Au distances much larger than 3.6 Å. Two recent theoretical works [59] concluded that H is the best and only candidate for the 3.6 Å Au–Au distance. Nevertheless, a further debate on the computational simulations is still ongoing [60], primarily because there has been no direct experimental observation of any hydrogen impurity atoms in the monoatomic gold nanowires.

During our experiment on Au_2^-, we noticed a mysterious PES band (*X*) at ~3.6 eV (Fig. 12), which appeared in the HOMO–LUMO gap region of Au_2. Upon examination of the literature, we found that the same feature was also present in several previous PES studies on Au_2^- [34b, 34c]. No convincing explanations for this feature have been put forth, despite extensive efforts [34c]. Recently, Gantefor and co-workers have reported PES spectra for a series of small gold hydride clusters [61]. We noted that the binding energy of the leading PES feature of Au_2H^- was very close to the mysterious band present in the Au_2^- PES spectra. This led to our suspicion that the origin of the mysterious band in the Au_2^- spectrum might be due to contamination from Au_2H^-.

We carefully re-examined the PES spectra of Au_2^-. We first repeated the Au_2^- experiment using a pure Au target and pure He carrier gas, as we did before [18]. The spectra at 193 and 266 nm are shown in Fig. 12a and b. Nine main spectral features were observed and are labeled with the lower case letters, *x* and *a–h*. The weak mysterious peak at ~3.6 eV was labeled as *X*. To test if there would be any contamination due to Au_2H^- in the Au_2^- peak, we delayed the mass gate slightly to select the later part of the Au_2^- peak (because our mass spectrometer cannot resolve Au_2^- from Au_2H^-) and took the data again, as shown in Fig. 12c and d. We noted that the relative intensity of the 3.6 eV peak increased slightly. We then delayed the mass gate further to choose the tail part of the Au_2^- peak on the high-mass side and obtained the spectra displayed in Fig. 12e and f. To our surprise, the relative intensity of the 3.6 eV peak increased dramatically, accompanied by the appearance of a very weak feature (*X'*) at ~2.8 eV and two features (E and F) at the high-binding-energy side. At the same time, the relative intensities of features *d* and *f* were also enhanced, suggesting that there were Au_2H^- contributions. We noted that the binding energy of the 3.6 eV peak (*X*) was the same as that reported recently for Au_2H^- [61]. Thus, the additional features in Fig. 12e should all be due to Au_2H^-. This observation clearly showed that there was a small amount of contamination from the Au_2H^- in the Au_2^- mass peak. Our mass resolution was about 350, which was barely enough to resolve the Au_2H^- peak from

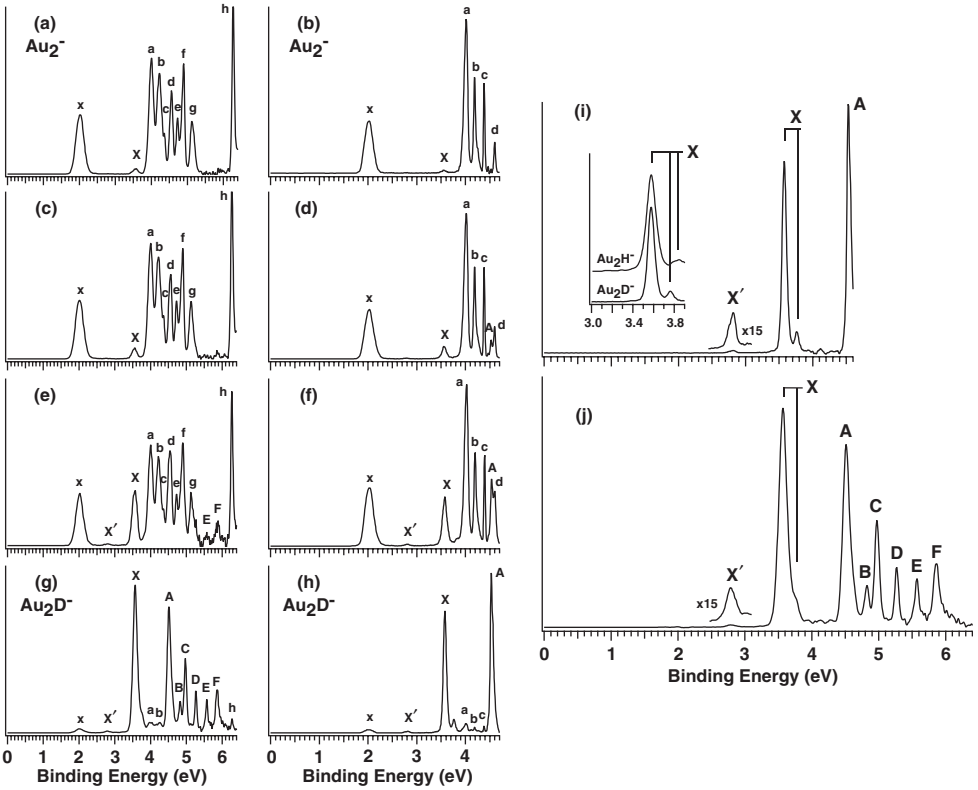

Figure 12: Photoelectron spectra of Au_2^- (a–f) and Au_2D^- (g and h) at 193 and 266 nm. Also shown are spectra of pure Au_2D^- at (i) 266 nm and (j) 193 nm after weighted subtraction of the Au_2^- components. The inset in (i) shows the vibrational structures of Au_2H^- vs. Au_2D^-. Reproduced from Ref. [22].

that of Au_2^-. Since ultra-pure He carrier gas (99.9999%) was used and no contamination was ever observed in other cluster experiments with this carrier gas, we suspect the hydrogen contamination came from trace amount of hydrogen impurity in the gold target, which has a specified purity of 99.99%.

To verify the above observation, we produced Au_2H^- using a H_2-seeded He carrier gas. We obtained spectra similar to those shown in Fig. 12e and f because the Au_2^- mass peak was always dominating and the Au_2H^- peak could not be cleanly mass selected, as discussed above. To further confirm the observation of Au_2H^-, we performed experiments using a D_2-seeded He carrier gas, as shown in Fig. 12g and h. Because of the 2 amu mass separation between Au_2D^- and Au_2^-, it could be mass-selected more cleanly, although a small amount of Au_2^- was still discernible in the spectra of Au_2D^-. But the main spectral features in Fig. 12g and h are due to Au_2D^- and they are identical to those observed for Au_2H^-. (The isotope shift on the electron binding energy is expected to be much smaller than our instrumental resolution.) In addition to the three strong features (*X*, *E*, and *F*) observed in Fig. 12e for Au_2H^-, four more features (*A–D*) were identified in Fig. 12g. These features were overlapped with those from Au_2^- in the case of Au_2H^- (Fig. 12e). A very weak band *X′* was also observed in the spectra of Au_2D^-, identical to that in the spectra of Au_2H^-

(Fig. 12e and f). The X' feature was extremely weak for both Au_2H^- and Au_2D^-, but was always present. It was attributed to a minor isomer of Au_2H^-/Au_2D^- and was born out from the theoretical calculations, as shown below.

We obtained "clean" spectra for Au_2D^- (Fig. 12i and j) by subtracting the respective Au_2^- contaminations. The ground-state transition (X) of Au_2D^- was clearly vibrationally resolved with a frequency of $1470 \pm 50\,cm^{-1}$. Such a high frequency is likely due to the Au–D stretching vibration. In the inset of Fig. 12i, we compared the vibrational structures of Au_2D^- and Au_2H^-. There is a clear isotope shift, and the vibrational frequency estimated for Au_2H is $2050 \pm 100\,cm^{-1}$ from our data. Our obtained vibrational frequencies for Au_2D and Au_2H compare well with those for the diatomics, AuD ($1635.0\,cm^{-1}$) and AuH ($2305.0\,cm^{-1}$) [62], and the isotope shift factor (v_D/v_H) is identical for both systems. In Fig. 12i and j, the weak feature X' is expanded and is more clearly shown. Despite its weak intensity, good signal-to-noise ratio was obtained due to the high count rates. The ADE and VDE for the X' band were measured to be 2.73 and 2.81 eV, respectively.

The optimized structures for Au_2H^- and Au_2H from DFT calculations are summarized in Fig. 13. The anion ground state turned out to be linear $[Au–Au–H]^-$ (Fig. 13a, $C_{\infty v}$, $^1A_1$). A linear isomer $[Au–H–Au]^-$ (Fig. 13b, $D_{\infty h}$, $^1A_1$) was found to be 0.60 eV higher in energy. These results are in agreement with a previous DFT study on Au_2H^- [61]. The neutral Au_2H ground state was triangular (Fig. 13c, C_{2v}, $^2B_2$), in which the H atom bridges the Au–Au atoms. The linear Au–Au–H and Au–H–Au neutral species were located 0.10 and 0.17 eV higher, respectively. Frequency analyses showed that the linear $[Au–Au–H]^-$ and $[Au–H–Au]^-$ anions and the triangular Au_2H neutral were all true minima on the potential energy surfaces, whereas the neutral Au–Au–H and Au–H–Au species were second-order saddle points, each with two imaginary frequencies. The calculated ADE for the ground-state anion is 3.20 eV, compared with the experimental value of 3.55 eV. The calculated ADE for the low-lying isomer is 2.56 eV, much lower than that of the ground-state anion, in good agreement with the measured ADE of 2.73 eV for feature X'.

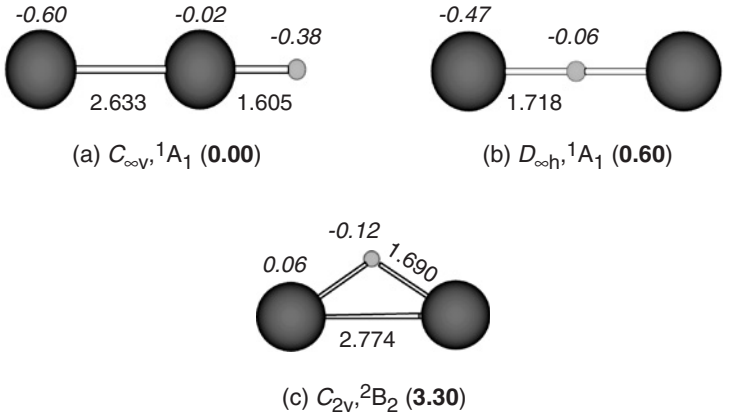

Figure 13: (a) Optimized ground-state structure and (b) a low-lying isomer for Au_2H^-, and (c) the ground-state structure for Au_2H. Bond lengths are in Å, and the relative energies in eV are given in parentheses. Shown in italics is the Mulliken charge distribution. Reproduced from Ref. [22].

The observation of the impurity Au_2H^- cluster in our PES experiment using a highly pure Au target was totally unexpected. It should be noted that this was an exception among many studies on transition metal clusters in our laboratory. We confirmed that the hydrogen source comes from the Au target itself, i.e., the trace amount of H impurity in the Au target. This observation suggests that it should not be too surprising that H may appear as an impurity in the atomic-thick gold nanowires. The calculated Au–Au distance in the $[Au–H–Au]^-$ isomer is 3.44 Å, very close to the anomalous Au–Au distance (3.6 Å) observed in gold nanowires. Considering that abnormal Au–Au distance is observed for atomic Au nanowires under tension, this would bring the gas-phase Au–H–Au distance (3.44 Å) even closer to the observations in atomic nanowires (3.6 Å). Both the observation of the Au_2H^- impurity from a pure gold target and the correct Au–Au distance in the $[Au–H–Au]^-$ cluster provide strong, albeit indirect, evidence that H is the ''invisible'' atom that gives the anomalous Au–Au distance in gold nanowires [3, 54].

4.2. Atomic-like magnetism in transition-metal-doped gold clusters: MAu_6 (M = Ti, V, Cr)

Although transition metal atoms with a partially filled d shell are magnetic, their magnetism is quenched or significantly reduced in the bulk due to chemical bonding that gives rise to crystal cohesion. For transition metal impurities in nonmagnetic host, the hybridization of the impurity d states with the host metal plays a crucial role in determining the local magnetic moments, which is sensitive to both the local structure and the electronic nature of the host. Atomic clusters provide a unique medium to explore magnetism because the cluster size, the local structure, and the atomic compositions can be readily controlled and varied. Generally, the reduced coordination number and higher symmetry in clusters lead to narrower electronic bands and enhanced magnetization. Transition-metal-doped gold clusters have been actively pursued to tailor the desired structural, electronic, and chemical properties for potential applications. We recently investigated a series of transition-metal-doped gold clusters, MAu_6^- (M = Ti, V, Cr), and found that the magnetic moments of the impurity transition metal atoms are not quenched by the nonmagnetic gold host in the MAu_6 clusters, which possess total magnetic moments corresponding to the number of d electrons localized in atomic-like unhybridized 3d orbitals of the dopants [23].

Figure 14 shows the photoelectron spectra of MAu_6^- (M = Ti, V, Cr) at 193 nm with numerous well-resolved features. The spectra for all three species are very similar and all have nearly identical electron binding energies. The spectra can be divided into two spectral regions: region I displays the only differences among the three species: more transitions are observed from M = Ti → V → Cr. Remarkably, region II is almost identical in all three species. These observations suggest that the spectral features in region I are from detachment of dopant-dominated orbitals, whereas region II is from the Au_6 motif of the bimetallic clusters. The similarity of the PES spectra of the three MAu_6^- species implies that these bimetallic clusters must have the same geometrical structure. The observation of the clear separation between spectral features of the dopant and the Au_6 motif in the MAu_6^- bimetallic clusters suggests a unique chemical interaction between the dopant and the host. The inset of Fig. 14A displays the 355 nm spectrum of $TiAu_6^-$, which was vibrationally resolved with a frequency of $160 \pm 20\,cm^{-1}$. The observation of a single short vibrational progression suggested that there is very little

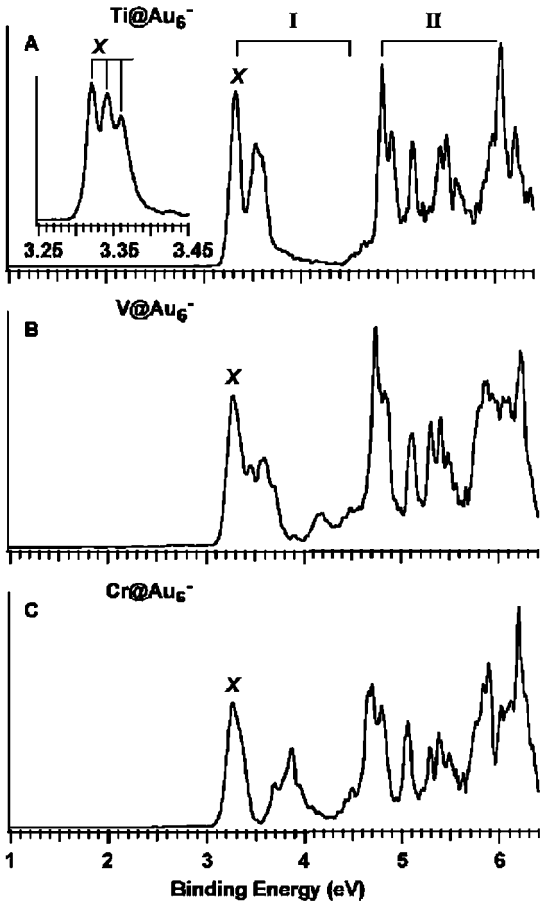

Figure 14: Photoelectron spectra of MAu_6^- (M = Ti, V, Cr) at 193 nm. The inset in (A) shows the 355 nm spectrum of $TiAu_6^-$ with a vibrational progression. Reproduced from Ref. [23].

geometrical change between the ground states of $TiAu_6^-$ and $TiAu_6$ and that they both have very high symmetry. Quantum calculations were performed to identify the most stable structures of MAu_6^- and MAu_6 and to obtain insight into the nature of bonding between the transition metal guest and the nonmagnetic host. Among the numerous possible structural isomers, two types of structures are important (Fig. 15). First, since small gold clusters have been shown to be planar, various 2D structures were considered. Second, 3D structures with six Au atoms surrounding a central impurity atom analogous to the icosahedral $M@Au_{12}$ and $M@Au_{12}^-$ clusters [24, 25] were considered.

The most stable structure for MAu_6^- and MAu_6 is the 2D structure, an Au_6 ring with a central transition metal atom (Fig. 15A). The high-symmetry 3D octahedral arrangement is not a stable structure and geometry optimization led to a distorted isomer (Fig. 15B), which is much higher in energy than the 2D ring structure. It should be noted that all the ground-state 2D structures of MAu_6^- have high spins, whereas the 3D structures tend to have low spins (Fig. 15). The doublet $TiAu_6^-$ and quartet $CrAu_6^-$ form perfectly symmetrical D_{6h} structures. However, due to the Jahn–Teller effect, the

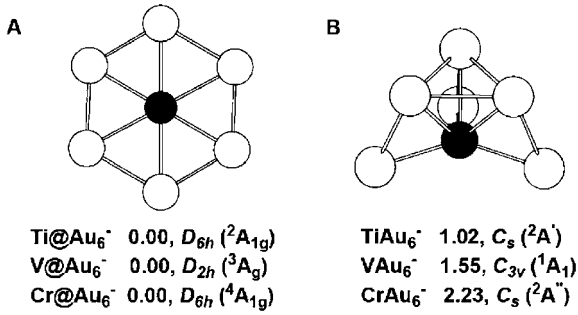

Figure 15: Optimized structures for MAu_6^- (M = Ti, V, Cr) using DFT at the PW91-SDD level. Relative energies are given in eV. Reproduced from Ref. [23].

triplet VAu_6^- has a very slight in-plane distortion to a lower symmetry D_{2h} structure with very minor bond length changes. Although the most stable isomer for neutral MAu_6 is also the Au_6 ring with the dopant at the center, for $TiAu_6$ the 2D structure is only more stable than the 3D one by 0.15 eV. However, for VAu_6 and $CrAu_6$ the 2D structure is overwhelmingly favored (0.75 and 2.72 eV in favor of the 2D structure for VAu_6 and $CrAu_6$, respectively). The neutral ground-state structures all have marginally distorted geometries from the perfect D_{6h} molecular wheels. Due to the very flat potential energy surfaces, these distortions have negligible effect on the energies from the corresponding planar forms, consistent with the sharp ground-state PES transitions. More interestingly, all the neutral structures were found to prefer higher spin multiplicities (S = 3, 4, and 5 for $TiAu_6$, VAu_6, and $CrAu_6$, respectively) compared to the corresponding anions. All the computed detachment energies agree very well with the experimental results (Table 3). The calculated vibration frequency for the totally symmetric mode for the ground state of $TiAu_6$ is 137 cm^{-1}, which also compares well to the observed value ($160 \pm 20\,cm^{-1}$). The closeness of the calculated ADEs and VDEs for each species is consistent with the negligible geometry change between the anion and neutral ground-state structures.

Figure 16 displays a schematic molecular orbital (MO) correlation diagram for the three 2D MAu_6^- clusters and their valence orbital pictures, which provide insight into the observed spectral features and the nature of bonding between the dopant and the Au_6 ring. The energy levels for all these clusters separate into two distinct regions with a considerable energy gap. The frontier orbitals consist of almost pure d orbitals from the central dopant, whereas all the occupied levels derived from the Au_6 ring lie

Table 3: Experimental ADEs and VDEs of MAu_6^- (M = Ti, V, Cr) compared with those calculated for the lowest-energy isomers (Ref. [23]) (all energies are in eV).

Species	ADE		VDE	
	Experimental	Theoretical	Experimental	Theoretical
$TiAu_6^-$	3.32 ± 0.02	3.28	3.32 ± 0.02	3.29
VAu_6^-	3.23 ± 0.02	3.20	3.25 ± 0.02	3.23
$CrAu_6^-$	3.23 ± 0.02	3.20	3.25 ± 0.02	3.23

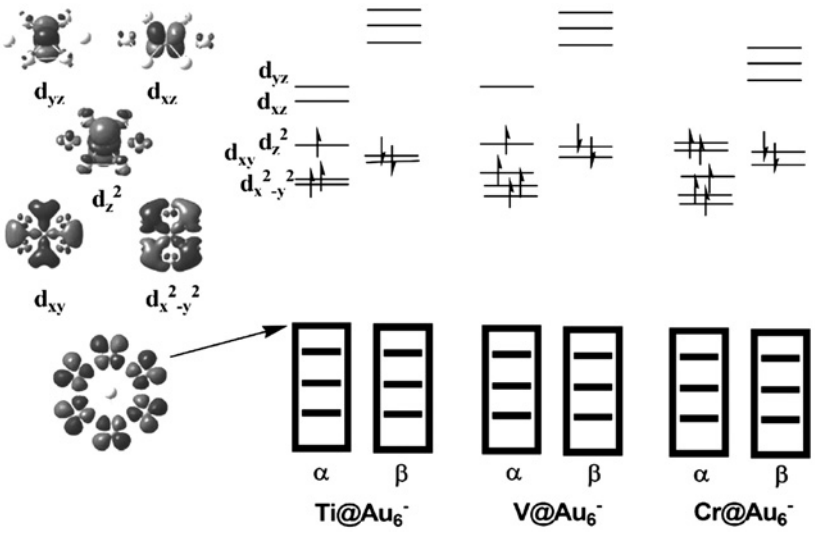

Figure 16: Molecular orbitals (MOs) and MO energy level diagrams for MAu_6^- (M = Ti, V, and Cr). Mainly M 3d orbitals (denoted by discrete lines) are well separated from the Au-derived orbitals (represented by boxes). Reproduced from Ref. [23].

significantly deeper. These orbital level schemes are in exact agreement with the PES spectra (Fig. 14). The bonding interactions between the dopant and the Au_6 ring come by symmetry from the overlaps between the in-plane d_{xy} and $d_{x^2-y^2}$ orbitals with the antibonding 6s orbitals of the Au_6 ring. The first detachment channel, common for all three MAu_6^- clusters, is the removal of the $d_{xy}\beta$ electron. This explains why the first ADEs for all three MAu_6^- clusters are remarkably similar and also explains the observation of the single vibrational progression in the 355 nm spectrum of $TiAu_6^-$ (Fig. 14) due to the ring breathing mode. As the dopant changes from Ti to Cr, the extra d electrons fill the nonbonding, atomic-like d orbitals, whose binding energies gradually increase. Consequently, extra detachment bands appear to fill the gap between the two main regions in the PES spectra of VAu_6^- and $CrAu_6^-$ (Fig. 14).

Thus, the bonding in the MAu_6^- bimetallic clusters can be viewed as an Au_6 ring interacting with an M^-, which possesses the d^5, d^6, and d^7 valence configuration for M = Ti, V, and Cr, respectively (i.e., the 4s electrons are promoted to the 3d orbitals). Four of these electrons (two α and two β) are involved in the bonding between M^- and Au_6, leaving one, two, and three unpaired spins in the MAu_6^- anions for M = Ti, V, and Cr, respectively. In the neutral cluster, one of the bonding electrons ($d_{xy}\beta$) is detached, resulting in two, three, and four unpaired spins in MAu_6 for M = Ti, V, and Cr, respectively. These unpaired spins occupy atomic-like d orbitals and the number of spins corresponds exactly to the number of unpaired d electrons in the atoms (except for Cr, which has a d^5s^1 ground-state configuration). Thus, the MAu_6 bimetallic clusters possess atomic-like magnetism, carrying magnetic moments of 2, 3, and $4\mu_B$ for M = Ti, V, and Cr, respectively. Although there is considerable chemical bonding between the impurity atom and the Au_6 ring, the atomic magnetism is maintained in the bimetallic clusters.

4.3. Icosahedral gold cage clusters: M@Au_{12} (M = W, Mo) and M@Au_{12}^- (M = V, Nb, Ta)

Despite the fact that the bare 13–atom gold cluster anion has been shown not to possess a high-symmetry icosahedral structure [33], Pyykkö and Runeberg [63] recently predicted a series of highly stable gold clusters containing an icosahedral Au_{12} cage and a central heteroatom, M@Au_{12} (M = Ta^-, W, Re^+), which is valent isoelectronic to the known I_h Au_{13}^{5+} cage [10]. These remarkable M@Au_{12} clusters were shown to attain their stabilities from the strong relativistic effects, the aurophilic attraction, and the perfect 18–electron counting. Shortly after, we reported the first experimental observation and characterization of a series of icosahedral cage clusters, M@Au_{12} (M = W, Mo) and M@Au_{12}^- (M = V, Nb, Ta) [24, 25].

Figure 17 (left column) shows the PES spectra of $MoAu_{12}^-$ and WAu_{12}^- at two photon energies (193 and 532 nm). The spectra of the two species are nearly identical, each with a sharp and weak peak (*X*) around 2 eV, followed by a large energy gap and a high density of electronic transitions at higher binding energies. The threshold peak *X* was very sharp, as shown by the 532 nm spectra, which has a width of ~36 meV (FWHM), very close to the instrumental resolution. The sharp threshold peak suggests that there is little geometry change between the MAu_{12}^- anion and its corresponding neutral ground state. The threshold peak defined an EA of 2.17 ± 0.02 eV for $MoAu_{12}$ and 2.08 ± 0.02 eV for WAu_{12}. The energy difference between the *X* and *A* features yielded an energy gap of 1.48 eV for $MoAu_{12}^-$ and 1.68 eV for WAu_{12}^-. This large energy gap is consistent with the previous prediction [63] of a large HOMO–LUMO

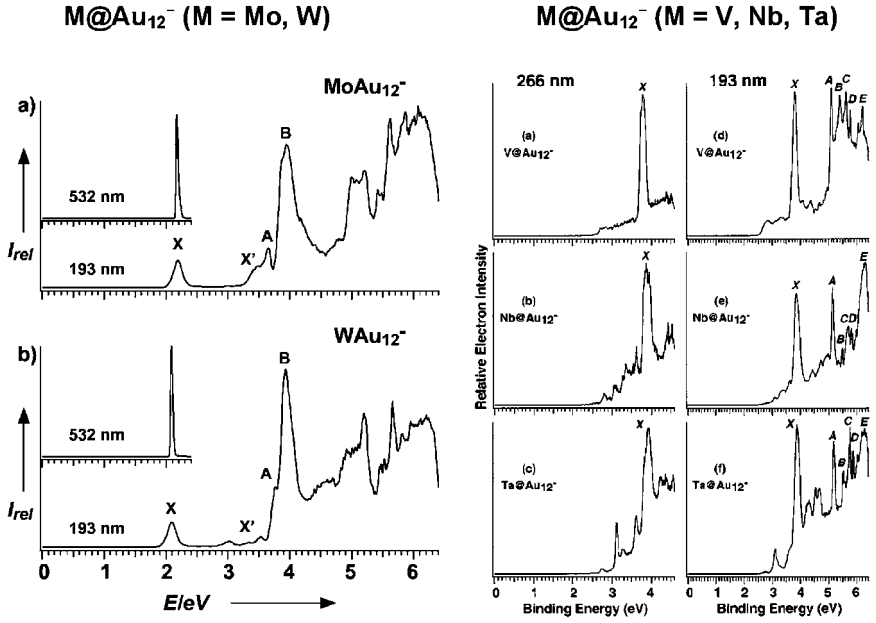

Figure 17: (Left column) Photoelectron spectra of $MoAu_{12}^-$ and WAu_{12}^- at 532 and 193 nm. Reproduced from Ref. [24]. (Right column) Photoelectron spectra of MAu_{12}^- (M = V, Nb, Ta) at 266 and 193 nm. Reproduced from Ref. [25].

Table 4: Observed ADEs and VDEs in eV from anion photoelectron spectra of MAu_{12}^- (M = V, Nb, Ta) (Ref. [25]).

Species	ADE[a,b]	VDE[a]					
		X	*A*	*B*	*C*	*D*	*E*
VAu_{12}^-	3.70 (3)	3.79 (2)	5.08 (4)	5.39 (3)	5.63 (3)	5.77 (3)	6.21 (3)
$NbAu_{12}^-$	3.77 (3)	3.88 (2)	5.14 (4)	5.48 (3)	5.71 (3)	5.82 (3)	~6.28
$TaAu_{12}^-$	3.76 (3)	3.90 (2)	5.19 (4)	5.53 (3)	5.76 (3)	5.87 (3)	~6.25

[a]The numbers in parentheses represent the experimental uncertainties in the last digit.
[b]The ADE of an anion also represents the EA of the corresponding neutral species.

gap for $W@Au_{12}$. The similarity of the spectra of $MoAu_{12}^-$ and WAu_{12}^- indicates that they have the same electronic and geometrical structures.

The PES spectra of MAu_{12}^- (M = V, Nb, Ta) at 193 and 266 nm are shown in Fig. 17 (right column). Extremely high electron binding energies were observed for these three species. The 266 nm spectrum of VAu_{12}^- revealed one intense band (labeled *X*) with a VDE of 3.79 eV. A similar intense peak was also observed for $NbAu_{12}^-$ and $TaAu_{12}^-$ at slightly higher VDEs (Table 4). The 193 nm spectrum of VAu_{12}^- revealed numerous bands at higher binding energies (labeled as *A*–*E*), which are well separated from the ground-state transition (*X*). The *A* band at a VDE of 5.08 eV represents the first excited state of neutral VAu_{12} and the other features correspond to higher excited states. Similar higher binding energy features were also observed for $NbAu_{12}^-$ and $TaAu_{12}^-$. In fact, all the observed PES features for the three systems have a one-to-one correspondence to each other and they also have very similar VDEs, as given in Table 4. The ground-state ADEs, i.e., the EAs for MAu_{12} (M = V, Nb, and Ta), were measured to be 3.70, 3.77, and 3.76 eV, respectively, all higher than those of the halogens.

One of the most important questions we want to address here is to confirm the lowest-energy structures of the MAu_{12} (M = W, Mo) and MAu_{12}^- (M = V, Nb, Ta) clusters. While exohedral structures are obviously less stable, the endohedral structures can adopt several different geometries, including those with I_h, O_h, and D_{5h} symmetries, as shown in Fig. 18. The computational results for $M@Au_{12}$ (M = Mo, W) and $M@Au_{12}^-$ (M = V, Nb, Ta) are summarized in Tables 5 and 6, respectively.

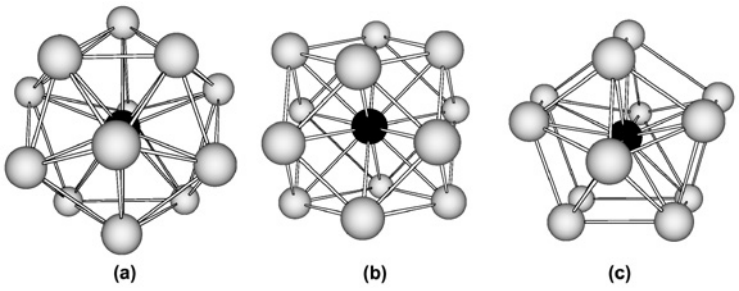

Figure 18: Optimized geometric structures of $M@Au_{12}$ (M = Mo, W) and $M@Au_{12}^-$ (M = V, Nb, Ta). (a) I_h, (b) O_h, and (c) D_{5h}. Reproduced from Refs. [24, 25].

Table 5: Relative energies (kJ/mol), EAs (eV), and bond lengths (pm) of $Mo@Au_{12}$ and $W@Au_{12}$ (Ref. [24]).

Species	Symmetry	State	Energy	EA	R(M–Au)	R(Au–Au)
$Mo@Au_{12}$	I_h	$^1A_{1g}$	0.0	2.25	275.7×12	289.8×30
	O_h	$^1A_{1g}$	0.3	2.32	280.6×12	280.6×24
	D_{5h}	$^1A_1'$	18.4	2.48	279.5×10, 283.2×2	286.3×10, 283.9×10, 274.3×5
$W@Au_{12}$	I_h	$^1A_{1g}$	0.0	2.02	275.5×12	289.7×30
	O_h	$^1A_{1g}$	9.8	2.11	280.6×12	280.6×24
	D_{5h}	$^1A_1'$	20.4	2.26	279.4×10, 283.0×2	286.4×10, 284.2×10, 273.3×5

For $M@Au_{12}$ (M = Mo, W), even though the calculations for the I_h cluster were performed in its D_{5d} subgroup, the geometry optimizations still led to the I_h structure, confirming the finding of Pyykkö and Runeberg [63]. Additionally, two low-lying isomers with O_h and D_{5h} symmetries were found. The O_h isomer is very close in energy with the I_h ground state, whereas the D_{5h} isomer is considerably higher in energy. The computed EAs are 2.25 and 2.02 eV for I_h $Mo@Au_{12}$ and $W@Au_{12}$, respectively, in excellent agreement with the experimental values. The calculated EA for the O_h isomer of $MoAu_{12}$ is 2.32 eV, 0.15 eV higher than the experimental value. However, the calculated EA for the O_h isomer of WAu_{12} (2.11 eV) is too close to the experimental value to be distinguished from the I_h isomer. However, the computed PES pattern for $M@Au_{12}^-$ (M = Mo, W) (not shown) indicates that the observed species were the I_h clusters, whereas the observed weak features (X') may contain contribution from the O_h isomers.

For $M@Au_{12}^-$ (M = V, Nb, Ta), all-electron DFT calculations were performed with different endohedral structures to search for the global minima (Fig. 18). It was found that the icosahedral structures are always favored even without symmetry restrictions during the geometry optimizations, with the energies of the O_h and D_{5h} structures being higher (Table 6). With the increase in the central atom size, the energy difference between the O_h and the I_h structures tends to diminish, consistent with the enhanced M–Au interaction in the O_h structure. However, this trend is clearly offset by the increased relativistic and aurophilic effects, which favor the I_h structure with its

Table 6: PW91 total energies and relative energies of $M@Au_{12}^-$ (M = V, Nb, Ta) anions calculated using ADF with all-electron TZ2P basis sets (Ref. [25])[a,b].

Species	Symmetry	E_{tot}(SR)	ΔE(SR)	E_{tot}(SO)	ΔE(SO)
$V@Au_{12}^-$	I_h	−39.8091	0.00	−10564.3068	0.00
	O_h	−39.5963	20.53	−10563.9801	31.52
	D_{5h}	−39.4019	39.29	−10563.8084	48.09
$Nb@Au_{12}^-$	I_h	−42.3900	0.00	−10575.2088	0.00
	O_h	−42.3427	4.56	−10575.0822	12.21
	D_{5h}	−42.2422	14.25	−10574.9830	21.78
$Ta@Au_{12}^-$	I_h	−42.0502	0.00	−11084.5739	0.00
	O_h	−41.9281	11.78	−11084.3948	17.28
	D_{5h}	−41.8724	17.16	−11084.3335	23.19

[a]The scalar-relativistic (SR) and spin–orbit (SO) coupling calculations were both performed with ZORA approximation.
[b]The total energies (in eV) are relative to the restricted atomic fragments, and the relative energies (in kJ/mol) are those relative to the respective total energies of the icosahedral structure (I_h).

favorable Au–Au interactions. Interestingly, the spin–orbit coupling effects tend to stabilize the I_h structure relative to the O_h and D_{5h} structures. The calculated ADEs and VDEs agree well with the experiment, in particular for those of I_h Nb@Au_{12}^- and Ta@Au_{12}^-. The calculated values for I_h V@Au_{12}^- are slightly lower than the experimental data.

It is instructive to compare the PES spectra of M@Au_{12}^- (M = V, Nb, Ta) with those of M@Au_{12}^- (M = Mo, W) and Au_{13}^-. The similarities and differences between the spectra of the M = Mo, W species and the M = V, Nb, Ta species can be immediately revealed: except for the very low binding energy band at ~2.1 eV for the M = Mo, W species (Fig. 17), its higher binding energy features show obvious similarity to those of the M = V, Nb, Ta species. The M = V, Nb, Ta anions and the M = Mo, W neutrals are valent isoelectronic, both are closed-shell with 18 valence electrons. The low binding energy band in the M = Mo, W species is due to the extra electron that occupies its neutral LUMO. The similarity of the higher binding energy part of all M@Au_{12}^- (M = V, Nb, Ta, Mo, W) species suggests that they have similar MO energy levels, i.e., similar symmetry and geometrical structures. On the other hand, the spectrum of Au_{13}^- (Fig. 2) is much more complicated with many more features, which display no resemblance to either the spectra of the M = V, Nb, Ta species or the M = Mo, W species. Ion mobility experiment [33] has ruled out either a planar or an I_h structure for Au_{13}^-, which is likely to have a low-symmetry 3D structure, commensurate with its complicated PES spectrum.

As an example, Fig. 19 displays an energy-level correlation diagram for the atomic orbitals of W and Au and the MOs of I_h W@Au_{12} and its Au_{12} fragment. Since the Au 6s orbitals span $a_g + t_{1u} + h_g + t_{2u}$ ligand group orbitals, the major orbital interactions in W@Au_{12} occur between the W 5d and Au_{12} ligand group orbitals, yielding the bonding h_g HOMO and antibonding h_g^* LUMO, which is consistent with the slight expansion of the Au_{12} cage upon electron addition in the anion. The HOMO is composed mainly of Au 6s and 5d (77% Au and 23% W), whereas the LUMO is composed primarily of W 5d orbitals. Due to relativistic effects, the Au 6s and 5d orbitals are stabilized and destabilized by 1.60 and 1.17 eV, respectively, resulting in strong 6s–5d hybridization in the W@Au_{12} molecule. Spin–orbit coupling splits the Au 5d orbitals into $5d_{3/2}$ and $5d_{5/2}$ spinors by 1.24 eV, which cause the split of the 5d bands into two separated $5d_{3/2}$ and $5d_{5/2}$ bands. Moreover, the $6s_{1/2}$–$5d_{5/2}$ energy gap (0.75 eV) is much smaller than the scalar relativistic 6s–5d gap (1.22 eV), again favoring strong 6s–5d hybridization. The spin–orbit splitting of the h_g HOMO is only 0.04 eV, while that of the LUMO is as large as 0.43 eV, in agreement with the atomic spin–orbit splitting of W 5d orbital (0.56 eV).

Heretofore we have confirmed and characterized two of the three M@Au_{12} (M = Ta^-, W, Re^+) cage clusters originally predicted by Pyykkö and Runeberg [63]. Furthermore, we have extended this family of clusters to include 4d and 3d heteroatoms, thus demonstrating that the Au_{12} cage is highly flexible to accommodate a central heteroatom. As commented by Schwerdtfeger [64], the discovery of the series icosahedral gold cage clusters demonstrated the potential of fine-tuning electronic properties of gold with the central "impurity" atom. For example, while the M@Au_{12} (M = Mo, W) species are stable closed-shell molecules with large HOMO–LUMO gaps and should be chemically inert, the M@Au_{12} (M = V, Nb, Ta) species – by simply switching the heteroatom from group VIB to group VB – possess remarkably

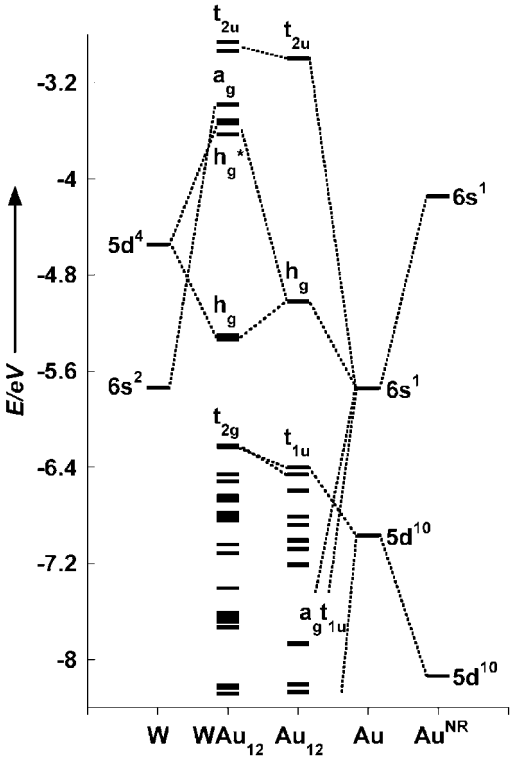

Figure 19: Energy-level correlation diagrams of W, Au, Au_{12}, and I_h W@Au_{12}. All energies are calculated at the scalar-relativistic level, except for Au^{NR}, which is calculated at the nonrelativistic level. The HOMO and LUMO of I_h W@Au_{12} are h_g and h_g^*, respectively. Reproduced from Ref. [24].

high electron affinities (>3.7 eV) and should clearly be classified as superhalogen molecules [65], because their EAs are higher than those of halogens. Interestingly, the 12 Au atoms forming the icosahedral cage appear to be rather fluxional [66] despite the high stabilities of the I_h M@Au_{12} (M = Mo, W) and M@Au_{12}^- (M = V, Nb, Ta) cage clusters, as evidenced by the closely-lying O_h and D_{5h} structures (only for VAu_{12}^- the I_h cage structure is significantly more stable than either the O_h or the D_{5h} structure). The O_h isomer involves a slight rearrangement of the 12 Au atoms on the cage, whereas the D_{5h} structure involves a rotation of a hemisphere of the I_h Au_{12} cage against each other. The corresponding h_u vibrational mode for W@Au_{12} is predicted to have a very low frequency around 30 cm^{-1} [66]. The frequencies for the corresponding vibrational modes in M@Au_{12}^- (M = V, Nb, Ta) were calculated to be 37, 27, and 27 cm^{-1}, respectively [25].

5. GOLD AS HYDROGEN IN Si−Au AND B−Au CLUSTERS

The strong relativistic effects in gold result in its unique physical chemistry, which differs substantially from the lighter coinage metals. The relativistic stabilization of Au

6s orbital gives rise to its anomalously high EA, which is comparable to the halogens. The gold–halogen analogy was extensively demonstrated in an entire class of auride (Au^-) compounds [6b]. A prototypical example is the ionic cesium auride compound (Cs^+Au^-), analogous to Cs^+Cl^-. Recently, tetraaurides MAu_4 (M = Ti, Zr, Th) were also predicted [67], in which the Au atoms were compared to the halogens. The most remarkable chemistry of gold is the isolobal analogy between a gold phosphine unit $AuPR_3$ and a hydrogen atom, which has been exploited to bring out tetra- and hypercoordination in compounds such as $[C(AuPR_3)_4]$ and $[C(AuPR_3)_5]^+$ [10, 68]. However, the analogy between a single gold atom and a hydrogen atom in gold complexes was not discovered until our own recent works [26–28].

5.1. $SiAu_4$: aurosilane

During experiments aimed at understanding the electronic structure of Si–Au binary clusters, we observed an extremely large energy gap in the PES spectra of $SiAu_4^-$, as shown in Fig. 20 [26]. This result suggested that $SiAu_4$ is a highly stable neutral

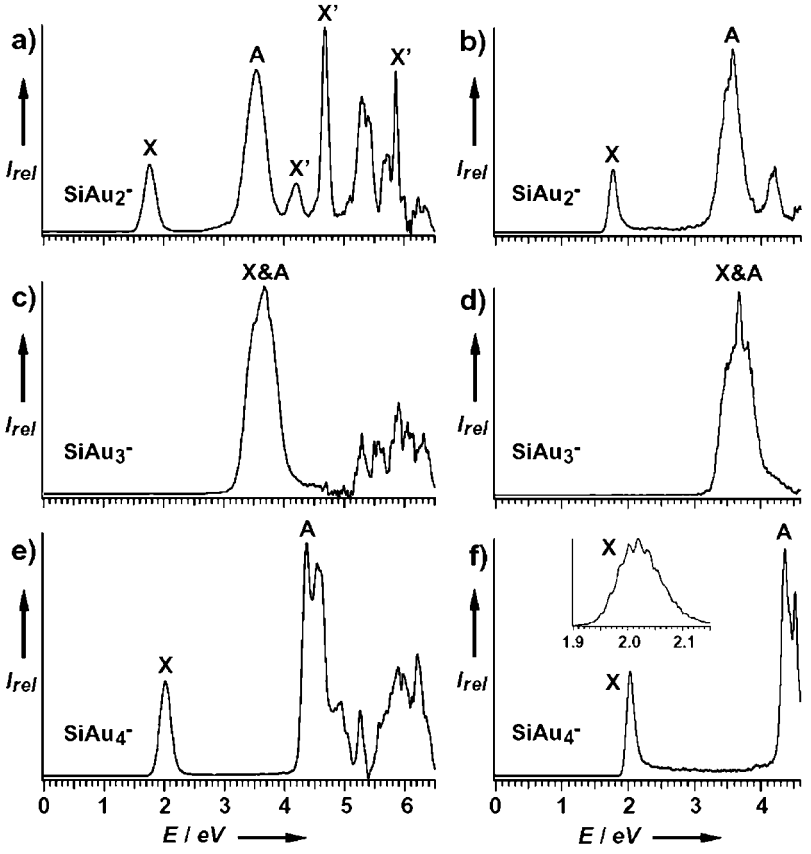

Figure 20: Photoelectron spectra of $SiAu_2^-$ (a and b), $SiAu_3^-$ (c and d), and $SiAu_4^-$ (e and f) at 193 nm (left) and 266 nm (right). The inset in (f) shows the spectrum of $SiAu_4^-$ taken at 532 nm. Reproduced from Ref. [26].

molecule with a large HOMO–LUMO gap (2.36 eV as measured by the binding energy difference between the *X* and *A* bands). The inset of Fig. 20f shows a high-resolution spectrum of the *X* band of $SiAu_4^-$ at 532 nm, revealing a partially resolved vibrational progression with an average spacing of $140 \pm 30\,cm^{-1}$, which indicated that both $SiAu_4$ and $SiAu_4^-$ must be highly symmetric and there is little geometry change between them.

The Si–Au clusters were further studied computationally at DFT and CCSD(T) levels. The two lowest-energy structures for $SiAu_n$ and $SiAu_n^-$ ($n = 2$–4) are given in Fig. 21, along with their geometrical parameters. At all levels of theory, the most stable $SiAu_2^-$ structure has C_{2v} symmetry with a doublet $^2B_1$ state (Fig. 21a). A quasi-linear C_s isomer (Fig. 21b) is much higher in energy. The most stable neutral $SiAu_2$ is $^1A_1$ of C_{2v} symmetry with a very similar structure as the anion. The most stable structure of $SiAu_3^-$ has C_{3v} symmetry (Fig. 21c). The second-lowest isomer (Fig. 21d) is 0.78 eV higher in energy. The D_{3h} isomer, which is a transition state (a first-order

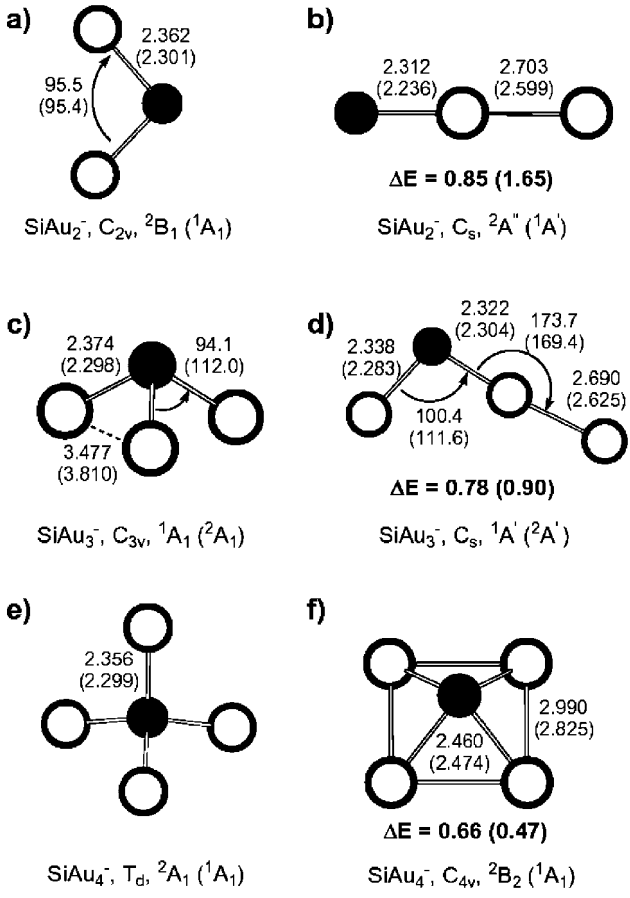

Figure 21: Optimized structures at B3LYP level for the two low-lying isomers of $SiAu_n^-$ and $SiAu_n$. All bond lengths are given in Å and angles in degrees. The relative energies are in eV for the higher energy isomer. The values and the symmetry labels given in the parentheses correspond to the neutral structures. Reproduced from Ref. [26].

saddle point) for the umbrella inversion of the C_{3v} $SiAu_3^-$, is 0.96 eV higher in energy. The ground state of $SiAu_3$ has the same C_{3v} symmetry as the anion, but there is a large geometry change upon electron detachment. The Si–Au bond length is decreased by 0.07 Å and the $\angle$ SiAuSi bond angle increased considerably by 18° in $SiAu_3$ relative to $SiAu_3^-$ (Fig. 21c). For $SiAu_4^-$, several isomers were calculated and the most stable structure is tetrahedral (Fig. 21e) with a pyramidal low-lying isomer (Fig. 21f) at both the DFT and CCSD(T) levels of theory. Neutral $SiAu_4$ is found to be a closed-shell singlet also with T_d symmetry and there is only a slight shortening of the Si–Au bond length (by 0.05 Å) compared to the anion. The relative energy difference between the two isomers is 0.47 eV for the neutral and 0.66 eV for the anion at the DFT level, and 0.39 eV for the neutral and 1.13 eV for the anion at the CCSD(T) level. Clearly, at the CCSD(T) level, the tetrahedral $SiAu_4^-$ is much more stable than the pyramidal isomer.

The geometry changes between the ground states of $SiAu_n^-$ and $SiAu_n$ (Fig. 21) are consistent with the nature of the first PES band (*X*, Fig. 20). The sharp threshold peaks in $SiAu_2^-$ and $SiAu_4^-$ and the broad band in $SiAu_3^-$ were all born out in the calculated structural changes from the anions to the neutrals. The ADEs and VDEs were further calculated for the ground-state structures of $SiAu_n^-$ at both DFT and CCSD(T) levels of theory (Table 7). At the CCSD(T) level, the ADE of $SiAu_2^-$ and the VDEs of $SiAu_2^-$ and $SiAu_3^-$ are in quantitative agreement with the experimental values. The calculated ADE for $SiAu_3^-$ (2.93 eV) is much smaller than the experimentally estimated threshold value (3.22 eV). This difference is due to the large geometry change between the ground states of $SiAu_3^-$ and $SiAu_3$ such that there is negligible Franck–Condon factor for the 0–0 transition. In this case, the detachment threshold estimated from the PES spectra can only be viewed as an upper limit for the true ADE. For $SiAu_4^-$, the calculated VDE and ADE at both DFT and CCSD(T) agree well with the experimental values, but are off by about 0.16 eV in different directions at the two levels of theory. The vibrational frequencies were also calculated for $SiAu_4$ at the B3LYP level and an unscaled value of 127 cm^{-1} was obtained for the totally symmetric mode, in excellent agreement with the experimental value of 140 ± 30 cm^{-1}. The simulated PES spectra (not shown) are also in excellent agreement with the experimental data, thus firmly confirming the ground-state structures for the $SiAu_n^-$ and $SiAu_n$ ($n = 2$–4) clusters.

Table 7: Experimental ADEs and VDEs of $SiAu_n^-$ ($n = 2$–4) compared to those calculated from the lowest-energy isomers (Ref. [26]) (all energies are in eV).

Species	Feature	Experimental		DFT (CCSD(T))[a]	
		ADE	VDE	ADE	VDE
$SiAu_2^-$	*X*	1.68 ± 0.03	1.72 ± 0.03	1.77 (1.67)	1.81 (1.71)
	A		3.48 ± 0.05		3.19
$SiAu_3^-$	*X*	3.22 ± 0.03[b]	3.48 ± 0.02	2.74 (2.93)	3.22 (3.46)
	A		3.67 ± 0.06		3.66
$SiAu_4^-$	*X*	1.96 ± 0.02	2.00 ± 0.01	2.08 (1.79)	2.15 (1.84)
	A		4.36 ± 0.02		4.23

[a]DFT calculations using hybrid B3LYP functional and CCSD(T) values are given in parentheses. Aug-cc-pVTZ basis set for Si and stutgaurd-19-electron effective core potentials augmented with two f (0.498 and 1.461) polarization functions were used for both R(U)B3LYP and R(U)CCSD(T) calculations.
[b]Estimated detachment threshold.

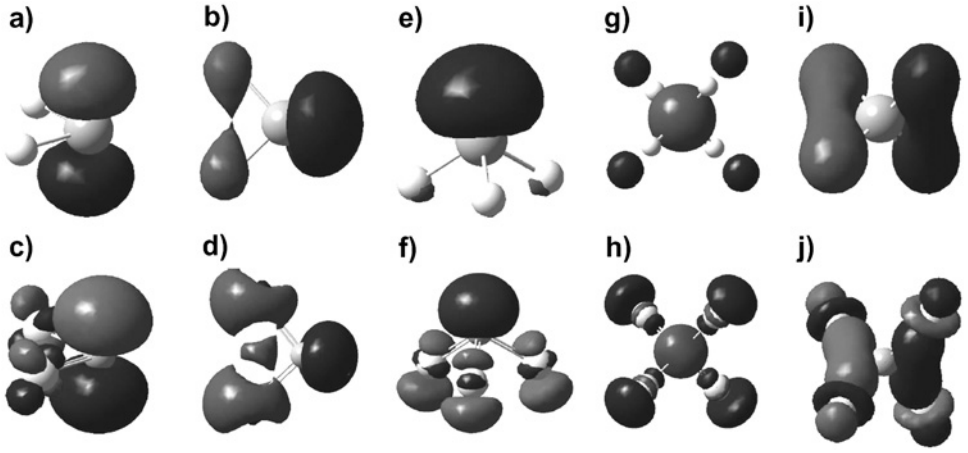

Figure 22: Comparison of the relevant frontier MOs between SiH_n (top panel) and $SiAu_n$ (bottom panel). (a) LUMO (b_1) of SiH_2, (b) HOMO (a_1) of SiH_2, (c) LUMO (b_1) of $SiAu_2$, (d) HOMO (a_1) of $SiAu_2$, (e) HOMO (a_1) of SiH_3, (f) HOMO (a_1) of $SiAu_3$, (g) LUMO (a_1) of SiH_4, (h) LUMO (a_1) of $SiAu_4$, (i) one of the three Si–H bonding orbitals of SiH_4 (t_2), and (j) one of the three Si–Au bonding orbitals of $SiAu_4$ (t_2). Reproduced from Ref. [26].

We note that the structures of the $SiAu_n$ clusters are nearly identical to the silicon hydride (SiH_n) molecules. The geometry changes between the $SiAu_n^-$ anions and the $SiAu_n$ neutrals also exactly parallel those between SiH_n^- and SiH_n, that is, very little geometry change exists between SiH_2^- and SiH_2, and between SiH_4^- and SiH_4, whereas a large bond angle change occurs between SiH_3^- and SiH_3. To further understand the chemical bonding in the Si–Au clusters, the MOs of $SiAu_n$ were analyzed and compared to those of the SiH_n counterparts (Fig. 22). Except for the s–d hybridization in Au, the valence MOs that involve the Si–Au bonding in $SiAu_n$ ($n = 2$–4) are nearly identical to those of the corresponding SiH_n species. Like silylene, the HOMO of $SiAu_2$ (aurosilylene) is mainly an Si lone-pair and LUMO is a pure silicon p orbital. The HOMO of both $SiAu_3^-$ and SiH_3^- is an Si lone-pair, which is one of the Si sp^3 hybrid MOs. Removal of an electron from this MO produces the doublet ground state for both $SiAu_3$ and SiH_3 and significantly flattens the neutral molecules in both cases. Similarly, the silane counterpart, $SiAu_4$, brings out sp^3 hybridization in silicon, analogous to that in SiH_4. The LUMO and the four Si–Au bonding orbitals are very similar to those in SiH_4. Charge analysis by using the natural-bond-orbital theory revealed that the interaction between Si and Au in all $SiAu_n$ species is covalent with negligible charge transfer. Thus, a complete isolobal analogy is observed between Au and H in the $SiAu_n$ series of molecules. This analogy is further supported by the similar electronegativity of gold (2.5) and hydrogen (2.1). Lastly, the calculated single Si–Au bond energies (at CCSD(T) level) in $SiAu_2$ (67.1 kcal/mol), $SiAu_3$ (60.6 kcal/mol), and $SiAu_4$ (62.7 kcal/mol) are amazingly similar to those in the corresponding Si–H molecules, SiH_2 (75.2 kcal/mol), SiH_3 (74.4 kcal/mol), and SiH_4 (79.6 kcal/mol). These relatively high atomization energies and the strong Si–Au bonds reflect both the covalent nature of the Si–Au bonds and the high stability of the $SiAu_n$ silicon auride molecules.

Au and Si do not form any stable alloys, but the Au–Si interfaces have been studied extensively owing to their importance in microelectronics. It has been shown that despite that Au is a very stable and unreactive noble metal, it is very reactive on Si surfaces even at room temperature [69]. Several metastable Si–Au alloys, including an $SiAu_4$ phase, have been observed to form in the Si–Au interfaces [70]. However, the nature of the chemical interactions between Au and Si in the Si–Au interfaces is still not well understood [71]. The current finding of the Au/H analogy, the strong Si–Au covalent bonding, and the highly stable gaseous silicon auride species are consistent with the high reactivity of Au on Si surfaces and should provide further insight into the nature of the chemical interactions in the Si–Au interfaces.

5.2. Structures and bonding in $Si_2Au_n^-$ and Si_2Au_n ($n = 2$ and 4) and comparisons to Si_2H_2 and Si_2H_4

To test the generality of the Au/H analogy in Si–Au alloy clusters, we further produced disilicon–Au clusters, $Si_2Au_n^-$ ($n = 2$ and 4), and investigated their structure and bonding [27]. The photoelectron spectra of $Si_2Au_n^-$ ($n = 2$ and 4), as shown in Fig. 23, revealed a HOMO–LUMO gap (the X–A separation) for both species: 0.8 eV for Si_2Au_2 and 0.6 eV for Si_2Au_4, suggesting that both neutral species should be closed-shell systems. The feature next to the first triplet A band, labeled as A', in both spectra

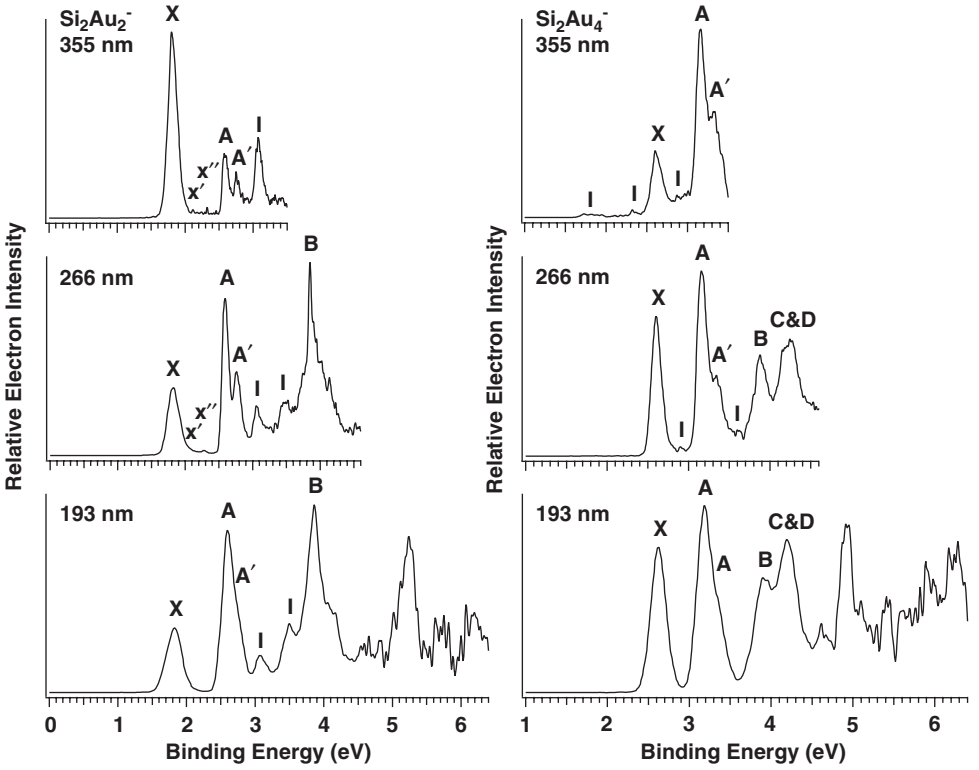

Figure 23: Photoelectron spectra of $Si_2Au_2^-$ (left column) and $Si_2Au_4^-$ (right column) at 355, 266, and 193 nm. Reproduced from Ref. [27].

is most likely due to detachment transition to the lowest singlet excited state of the neutral species, judging by their relatively lower intensity compared to that of the *A* band. The *A*–*A*′ separation thus represents the singlet–triplet splitting from detachment of the filled HOMO orbital of the neutral species. The *A*–*A*′ separation (~0.17 eV) is identical for both species. This is a relatively small value, suggesting that the HOMO of Si_2Au_2 and Si_2Au_4 should be primarily Si-based orbitals.

The PES data of $Si_2Au_2^-$ (Fig. 23, left column) revealed that the next major peak (*B*) is around 4 eV, with two relatively weak bands (labeled *I*) between the *A* and *B* bands. Except for an intense band around 5.2 eV, the spectral features beyond 4.5 eV had poor signal-to-noise ratios and were not well defined. Photodetachment from Au 5d-derived MOs occurs in the higher binding energy region [18], consistent with the more congested spectral features. The peaks labeled I were mainly due to contamination of Si_9Au^- as a result of a near-mass degeneracy between seven Si atoms (major isotopmers at mass 196, 197, 198, etc.) and one Au atom (mass 197). The extremely weak features (labeled *x*′ and *x*″) were not related to those features labeled *I*, which were due to potential minor isomers as born out in the theoretical results.

Beyond band *A*, the spectra of $Si_2Au_4^-$ (Fig. 23, right column) are more complicated with three intense bands around 4 eV (*B*–*D*). The higher energy part of the $Si_2Au_4^-$ spectra is similar to that of $Si_2Au_2^-$. Except for an intense band at 5.0 eV, this part of the spectra is congested and not very well defined, again likely due to photodetachment from the Au 5d-derived orbitals. Numerous weak signals (labeled *I*) were tentatively assigned to be from $Si_9Au_3^-$ contamination, similar to the Si_9Au^- contamination in the $Si_2Au_2^-$ spectra.

Optimized ground-state and low-lying geometries for $Si_2Au_2^-$, $Si_2Au_4^-$, and their neutrals are shown in Fig. 24. At both B3LYP and CCSD(T) levels, the most stable isomer for $Si_2Au_2^-$ is the dibridged structure (**1**). Note that the nonbonding Au···Au distance, 4.04 Å at the B3LYP level and 3.93 Å at the CCSD(T) level, indicates weak aurophilic interaction [7]. The second isomer, the *trans*-monobridged structure (**2**), is nearly isoenergetic (0.01 eV) to the ground state at the B3LYP level. However, the relative energy difference is marginally increased in favor of **1** by 0.14 eV at the CCSD(T) level. Closely following in energy is the *cis*-monobridged isomer (**3**), which is only 0.15 eV higher in energy than **1** at B3LYP. The nonbonding Au···Au distance in the *cis*-isomer falls within the range of aurophilic interaction [7]. As expected, the Au···Au distance at the CCSD(T) level (3.10 Å) is much shorter than the corresponding value (3.64 Å) at the B3LYP level. Consequently, the *trans*–*cis* relative energy difference was also reduced: 0.06 eV at the CCSD(T) level compared to 0.14 eV at the B3LYP level. Nevertheless, B3LYP correctly predicts the relative energy ordering of the isomers and differs quantitatively by 0.1–0.2 eV from the coupled-cluster method. Finally, the auro-disilavinylidene (**4**) with classical bonding features is also a stable isomer higher in energy only by 0.19 eV than the dibridged global minimum at B3LYP. It is interesting to note that for $Si_2H_2^-$ the relative energy ordering between structures **1** and **4** is exactly in reverse order, i.e., the disilavinylidene is more stable than the dibridged isomer [72f]. This indicates that gold has more propensity to form bridges compared to hydrogen.

Unlike $Si_2Au_2^-$, only two minima (**5** and **6**, Fig. 24) could be located on the neutral Si_2Au_2 potential energy surface. Several other isomers were tested and they were either high-order stationary points or collapsed to one of the two minima. The dibridged

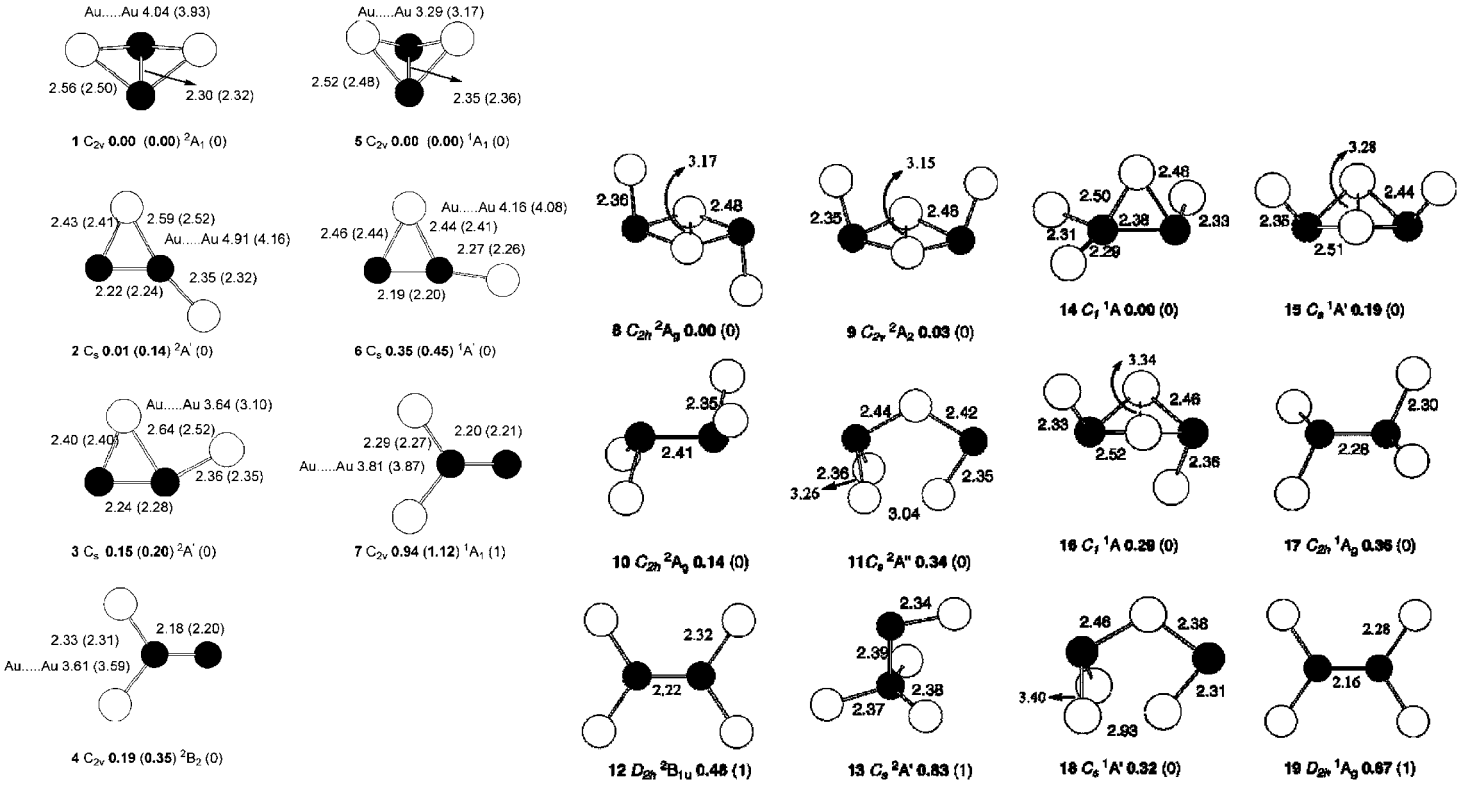

Figure 24: Optimized geometries for $Si_2Au_2^-$ (**1**–**4**), Si_2Au_2 (**5**–**7**), $Si_2Au_4^-$ (**8**–**13**), and Si_2Au_4 (**14**–**19**) at B3LYP and CCSD(T) (in parentheses) levels. Bond lengths are in Å, and the numbers in bold are energies in eV relative to the corresponding ground state. Reproduced from Ref. [27].

isomer (**5**) is the global minimum for Si_2Au_2, similar to that for the $Si_2Au_2^-$ anion, except that the folding angle is significantly reduced in the neutral from 124.3° to 95.4° (at B3LYP) and from 125.3° to 92.9° (at CCSD(T)). Similar but less dramatic changes in the folding angle have been observed for the Si_2H_2 systems [72f]. Removal of the negative charge enhances folding of the unit and brings gold atoms closer to within the range of significant aurophilic interaction. The only other stable isomer for Si_2Au_2 is the monobridged structure (**6**), which is higher in energy by 0.35 (0.45) eV at B3LYP (CCSD(T)). Unlike the anion, there are no *cis*- and *trans*-isomers for neutral Si_2Au_2. Upon geometry optimization, both structures collapse to the single monobridged structure, in which the $Si–Si–Au_{edge}$ angle is nearly linear (171.8° at B3LYP). The neutral auro-disilavinylidene (**7**) is a transition state with a barrier height of 0.58 (0.67) eV at B3LYP (CCSD(T)) for the scrambling of the gold atoms from the bridge to the edge position, resulting in the single monobridged isomer **6**.

The $Si_2Au_4^-$ and Si_2Au_4 stoichiometry corresponds to that of ethylene. However, it is well known that the corresponding silicon hydride, Si_2H_4, does not possess the classical ethylene structure [72]. Here it will be shown that Si_2Au_4 and its anions also do not assume the conventional structures. These species have much richer potential energy surfaces compared to the carbon analogues. Many possible isomers (**8**–**13**, Fig. 24) were considered in order to locate the lowest-energy structure for $Si_2Au_4^-$. Most of these structures have direct resemblance to the silicon–hydrogen counterparts [72f, 72g]. However, some of the structures have more "cluster-like" geometries. The most stable isomer is the *trans*-dibridged structure (**8**), and the *cis*-isomer (**9**) is almost degenerate with the *trans*-isomer. These two structures can be constructed by adding two gold atoms to the opposite (*trans*-) or the same side (*cis*-) of the most stable isomer of $Si_2Au_2^-$ (**1**) with one major change, that is, there is no Si–Si bonding in **8** and **9**. Instead, the relatively short $Au_{bridge}\cdots Au_{bridge}$ distances, 3.17 Å (**8**) and 3.15 Å (**9**), indicate stronger Au–Au interactions across the four-membered ring.

The *trans*-bent auro-disilene (**10**), which is the global minimum for Si_2H_4 [72g], is only 0.14 eV higher in energy than **8**. The planar, D_{2h} ethylene analogue (**12**) is a transition state (i151.7 cm^{-1}) with a barrier height of 0.31 eV, connecting the flipping motion of the silicon atoms in disilene to the global minimum (**8**). An isomer with a cluster-like geometry (**11**) is also found, in which three Au atoms seem to cluster on one side of the structure. This structure is 0.34 eV higher in energy than **8** and does not have an Si_2H_4 counterpart. Another important isomer is auro-silylsilylene (**13**). The corresponding silicon hydride, silylsilylene, is higher in energy than disilene by 0.28 eV and is also a minimum [72f]. However, the current B3LYP result suggests that structure **13** lies 0.69 eV above the auro-disilene (**10**) and has one imaginary frequency (i113.2 cm^{-1}) corresponding to the transfer of a gold atom between the two silicon atoms.

For neutral Si_2Au_4 (**14**–**19**, Fig. 24), the most stable isomer was found to be a monobridged structure (**14**) without any symmetry. This is a very interesting structure: except for the bridging atom, the rest of the atoms are nearly planar. It can be constructed by rearranging an edge gold atom from the disilene (**19**) to the bridging position. There is no anionic state for this structure. Optimization by adding an electron to **14** led to the *trans*-bent disilene structure (**10**). The neutral counterparts of the *cis*- and *trans*-dibridged structures became low-lying isomers, C_s (**15**) and C_1 (**16**), with reduced symmetries. The neutral *trans*-bent auro-disilene (**17**) is 0.36 eV above **14**. The

planar auro-disilene (**19**) is 0.67 eV higher in energy than the lowest-energy structure and is again a transition state (i190.2 cm^{-1}). Finally, the cluster-like isomer with C_s symmetry (**18**) is 0.32 eV above the ground state with enhanced Au–Au interactions.

Theoretical studies on the potential energy surface of Si_2H_4 span nearly two decades [72]. Most of the studies have focused on two isomers: disilene and silylsilylene. All studies agree that disilene is the most stable isomer followed by silylsilylene and the *trans*- and *cis*-dibridged structures. Recently, using highly correlated ab initio calculations and the experimental rotational spectrum from microwave spectroscopy, Sari et al. [72g] identified a new monobridged isomer, similar to **14**, which is 0.31 eV above disilene. No such minimum had been observed at SCF [72h]. Very expensive but highly desirable CCSD(T) geometry optimizations were needed to locate the C_1 monobridged minimum. The Si_2H_4 structures were checked using B3LYP with the aug-cc-pVTZ basis set, and it was found that the monobridged isomer is a minimum and is 0.28 eV above disilene. Like the corresponding Au analogue, there is no anionic state for the monobridged isomer of Si_2H_4 at B3LYP, which collapses to the disilene upon optimization.

The potential energy surfaces of the gold and hydrogen analogues of the disilicon species are shown to be indeed very similar. However, the relative energy differences between the various isomers for $Si_2Au_n^-$ and Si_2Au_n ($n = 2$ and 4) are very closely distributed. Detailed comparison of the computational detachment energies with the PES data (Fig. 23) allows firm establishment of the ground-state structure **1** for $Si_2Au_2^-$ as the main species (X) being observed experimentally, whereas the *trans*-isomer (**2**) and *cis*-isomer (**3**) are likely weakly populated in the $Si_2Au_2^-$ beam and are responsible for the very weak features x' and x'', respectively. As for $Si_2Au_4^-$, there are at least two isomers competing for the ground state: the dibridged *trans*-isomer (**8**) and *cis*-isomer (**9**) are nearly isoenergetic. Based on both the energetics and the simulated PES spectra, we cannot rule out isomer **9** and should conclude that both isomers **8** and **9** may exist in the cluster beam. The calculated VDEs from the auro-disilene isomer (**10**) clearly disagree with the PES pattern and can be ruled out from the experimental observation.

The Au/H analogy in disilicon gold clusters can be further understood via MO analysis. Bonding in the Si_2Au_2 dibridged structure (**5**) is quite similar to that of the corresponding hydride system (Fig. 25a). Basically, there are one Si–Si σ-bond, two 3c-2e (Si–Au–Si) bonds, and two lone-pairs on each of the silicon atoms. This simple valance bond picture captures the essential bonding features in **5**. There is clearly a one-to-one correspondence between the Si_2H_2 and Si_2Au_2 systems in both their structure and bonding. The six bonding MOs for the global minimum monobridged Si_2Au_4 (**14**) are also compared to those of the monobridged Si_2H_4 (Fig. 25b), whose bonding can be represented as an Si–Si σ-bond and an Si–Au(H)–Si 3c-2e bond with three Si–Au(H) σ-bonds and a lone-pair on one of the silicon atoms. By virtue of the lack of symmetry, the corresponding canonical MOs are heavily mixed, but the similarity between their MOs is clearly revealed. Analogously, the bonding and MOs in the *trans* (**16**)- and *cis* (**15**)-dibridged isomers and the *trans*-bent double-bonded system (**17**) have also been analyzed and they are also identical with the corresponding Si_2H_4 systems.

5.3. $B_7Au_2^-$ vs. $B_7H_2^-$

Despite its proximity to carbon in the periodic table and its richness of chemistry second only to carbon, pure boron clusters have received surprisingly limited

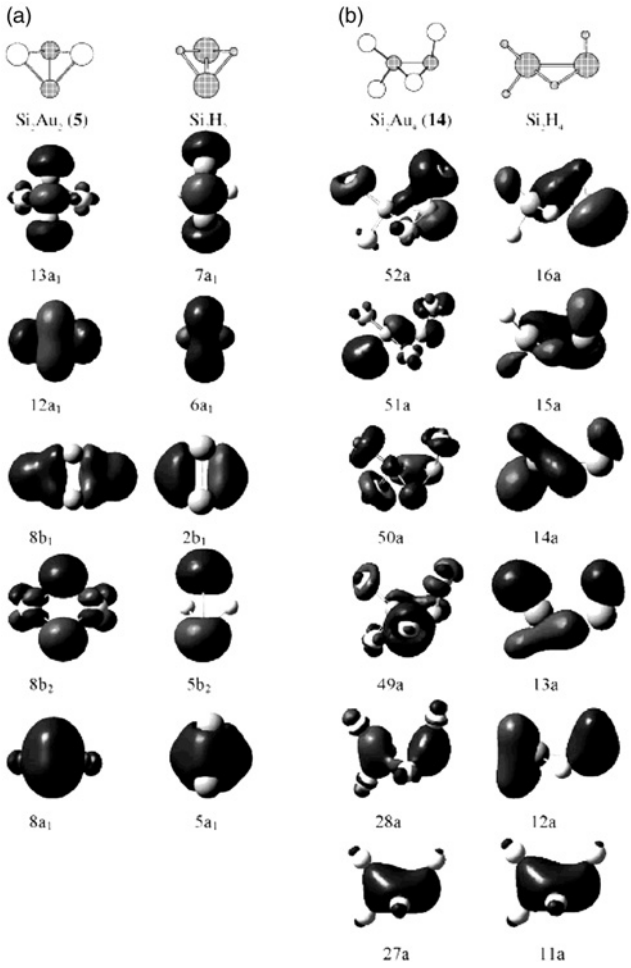

Figure 25: Comparison of bonding MOs of global minimum structures of (a) Si_2Au_2 (**5**) and (b) Si_2Au_4 (**14**) and the corresponding structures of Si_2H_2 and Si_2H_4, respectively. Reproduced from Ref. [27].

experimental attention in the literature over the past couple of decades [73, 74]. A major breakthrough has resulted from a series of recent joint experimental and theoretical studies that have established that all the small boron clusters are planar or quasi-planar, which can be understood on the basis of π and σ aromaticity/antiaromaticity [12c, 13d, 13e, 13f, 75]. Among the small boron clusters, the B_7^- cluster is a particularly interesting and complex system, because we observed the presence of three quite different isomers in its PES spectra [75e]: (1) a wheel-type quasi-planar doubly (σ and π) aromatic triplet C_{6v} ($^3A_1$) global minimum (structure I in Fig. 26), (2) a σ-aromatic and π-antiaromatic singlet C_{2v} ($^1A_1$) isomer with a quasi-planar shape (structure II, only 0.7 kcal/mol above the global minimum), and (3) an elongated planar doubly (σ and π) antiaromatic C_{2v} ($^1A_1$) isomer (structure III, 7.8 kcal/mol above the global minimum). Upon addition of two hydrogen atoms to the B_7^- cluster, it is found very recently using ab initio calculations that an inversion in stability occurs

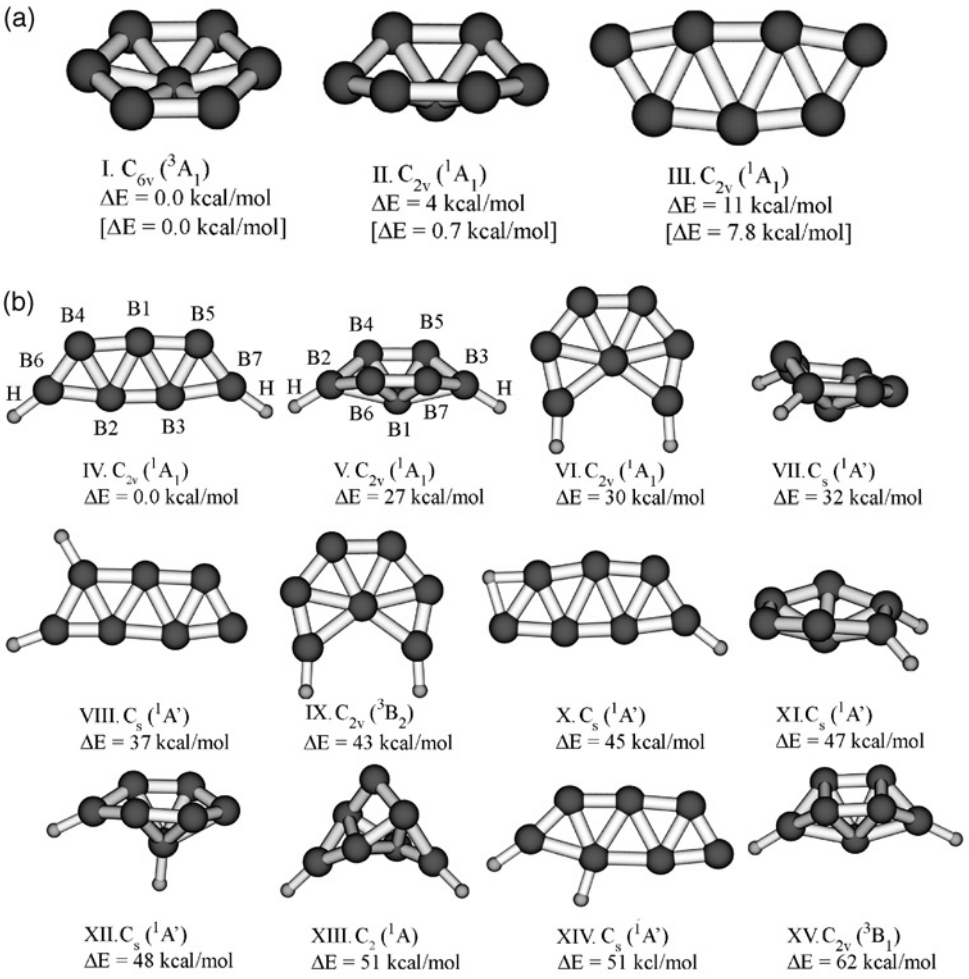

Figure 26: (a) Low-energy isomers of the B_7^- cluster at B3LYP/6–311 + G* level (relative energies at CCSD(T)/6–311 + G(2df) level are shown in square brackets) (from Ref. [75e]). (b) The global minimum and low-lying isomers of $B_7H_2^-$ at B3LYP/6–311 + G* level (from Ref. [76]).

(Fig. 26b) [76]. The planar $B_7H_2^-$ (C_{2v}, $^1A_1$) isomer (structure IV), formed by the addition of two hydrogen atoms to the doubly antiaromatic C_{2v} ($^1A_1$) B_7^- isomer III, is overwhelmingly favored as the global minimum structure. It is 27 kcal/mol more stable than the lowest high-energy isomer V of $B_7H_2^-$, originated from the addition of two hydrogen atoms to the global minimum of B_7^-.

Our recent discovery of Au–H analogy in Au–Si clusters [26, 27] has motivated us to conjecture that Au may also form B–Au clusters similar to the corresponding valence isoelectronic B–H clusters, because of the similar electronegativity between B (2.0) and Si (1.9). If this is true, the $B_7Au_2^-$ cluster would behave similarly to $B_7H_2^-$, thus yielding a predominantly stable $B_7Au_2^-$ cluster similar to the global minimum of $B_7H_2^-$ (IV in Fig. 26).

The PES spectra of $B_7Au_2^-$ at 266 and 193 nm photon energies are shown in Fig. 27 [28], compared with that of B_7^-. Indeed, the PES data of $B_7Au_2^-$ are substantially simpler and better resolved than that of B_7^-, despite its larger size. Most surprisingly, despite the addition of two heavy atoms, the ground-state transition (X) of $B_7Au_2^-$ is completely vibrationally resolved at 266 nm (Fig. 27a) with two vibrational modes, a low-frequency mode of $790 \pm 40\,cm^{-1}$ and a high-frequency mode of $1380 \pm 40\,cm^{-1}$. The vibrationally resolved ground-state transition yielded an accurate EA of 3.52 ± 0.02 eV for B_7Au_2. Interestingly, the EA of B_7Au_2 is very close to that of isomer III for B_7 (3.44 ± 0.02 eV) corresponding to feature X' in the spectrum of B_7^-

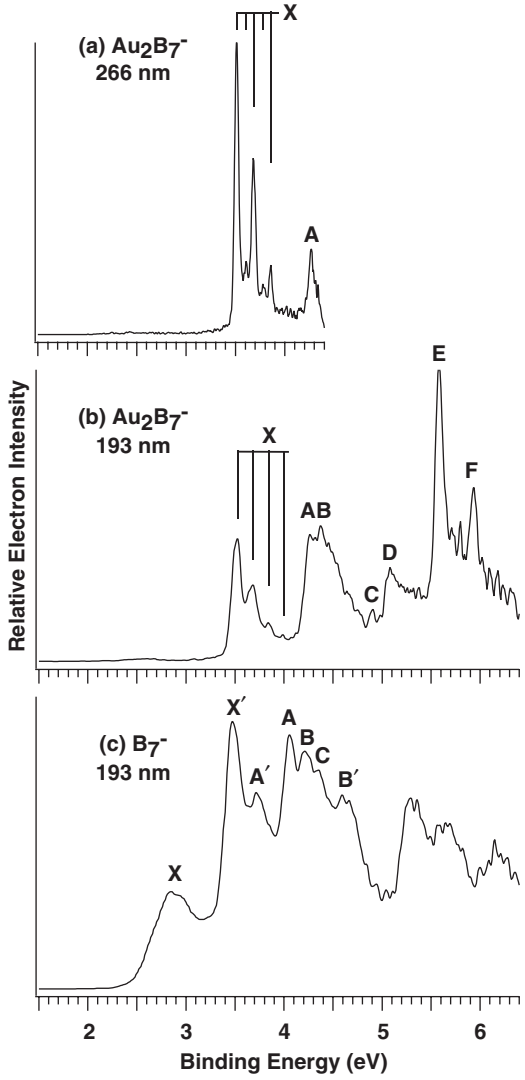

Figure 27: Vibrationally resolved photoelectron spectra of $B_7Au_2^-$ at (a) 266 nm and (b) 193 nm (from Ref. [28]). (c) The 193 nm spectrum of B_7^- is also included for comparison (from Ref. [75e]).

Table 8: Experimental VDEs of $B_7Au_2^-$ from the photoelectron spectra, compared with theoretical calculations (Ref. [28]).

Feature	VDE (experimental) (eV)[a]	MO	VDE (theoretical) (eV)[b]
X[c,d]	3.52 (2)	$3a_2$	3.46
A	4.27 (2)	$9a_1$	4.21
B	4.38 (3)	$8a_1$	4.36
C	4.90 (2)	$7b_2$	4.92
D	5.08 (3)	$6b_2$	5.19
E	5.58 (2)	$7a_1$	5.31
F	5.93 (2)	$3b_1$	5.75

[a]Numbers in parentheses represent experimental uncertainties in the last digit.
[b]At TD-B3LYP/B/aug-cc-pvTZ/Au/Stuttgart_rsc_1997_ecp level of theory.
[c]EA of B_7Au_2: 3.52 ± 0.02 eV.
[d]Ground-state vibrational frequencies for the Au_2B_7 neutral are measured to be 790 ± 40 and $1380 \pm 40\,cm^{-1}$.

(Fig. 27c). Clearly, only one dominant isomer was present in the $B_7Au_2^-$ beam. The observed detachment energies for the various detachment channels are summarized in Table 8. The observed $B_7Au_2^-$ cluster is likely to correspond to the isomer III of B_7^- by adding two Au atoms to its two terminal B atoms similar to the ground-state structure of $B_7H_2^-$, as we expected.

To prove our hypothesis and confirm the observed $B_7Au_2^-$ structure, quantum chemical calculations were performed for a variety of $B_7Au_2^-$ structures (XVI–XXI, Fig. 28), which were derived from the low-lying structures of $B_7H_2^-$. The geometries were initially optimized at the B3LYP/B/cc-pvDZ/Au/LANL2DZ level of theory, and it was found that the structure XVI of $B_7Au_2^-$ (C_{2v}, $^1A_1$) (Fig. 28), nearly identical to the ground state of $B_7H_2^-$, is indeed substantially more stable than the other structures.

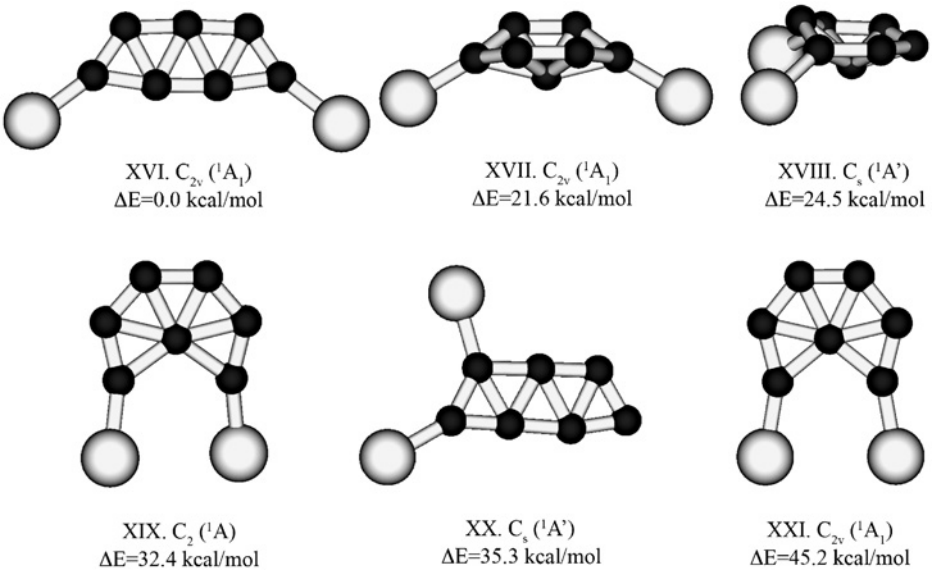

Figure 28: The global minimum and low-lying isomers of $B_7Au_2^-$ at B3LYP/B/cc-pvDZ/AuLANL2DZ level. Reproduced from Ref. [28].

The geometry of the $B_7Au_2^-$ global minimum structure XVI was then reoptimized at the B3LYP/B/aug-cc-pvTZ/Au/Stuttgart_rsc_1997_ecp + 2f1g (a(f) = 0.448, a(f) = 1.464, a(g) = 1.218) level of theory, and it was found that the two levels of theory give nearly identical structures. The geometry for the neutral B_7Au_2 cluster was also optimized and the obtained ground-state structure is similar to that of the anion. The VDEs from the $B_7Au_2^-$ global minimum structure were computed using the TD-B3LYP/aug-cc-pvTZ/Au/Stuttgart_rsc_1997_ecp + 2f1g level of theory, and they are compared with the experimental data in Table 8.

The ground-state transition in the spectra of $B_7Au_2^-$ (*X*, Fig. 27) involves electron detachment from the $3a_2$-HOMO, which is a π-bonding/antibonding orbital over the B_7 moiety with some small contributions from the Au 5d orbitals (Fig. 29). The calculated VDE of 3.46 eV agrees well with the experimental VDE (3.52 eV) of the *X* band (Table 8). Because both $B_7Au_2^-$ and B_7Au_2 have the same symmetry in their ground states, only the totally symmetric modes (a_1) can be active in the

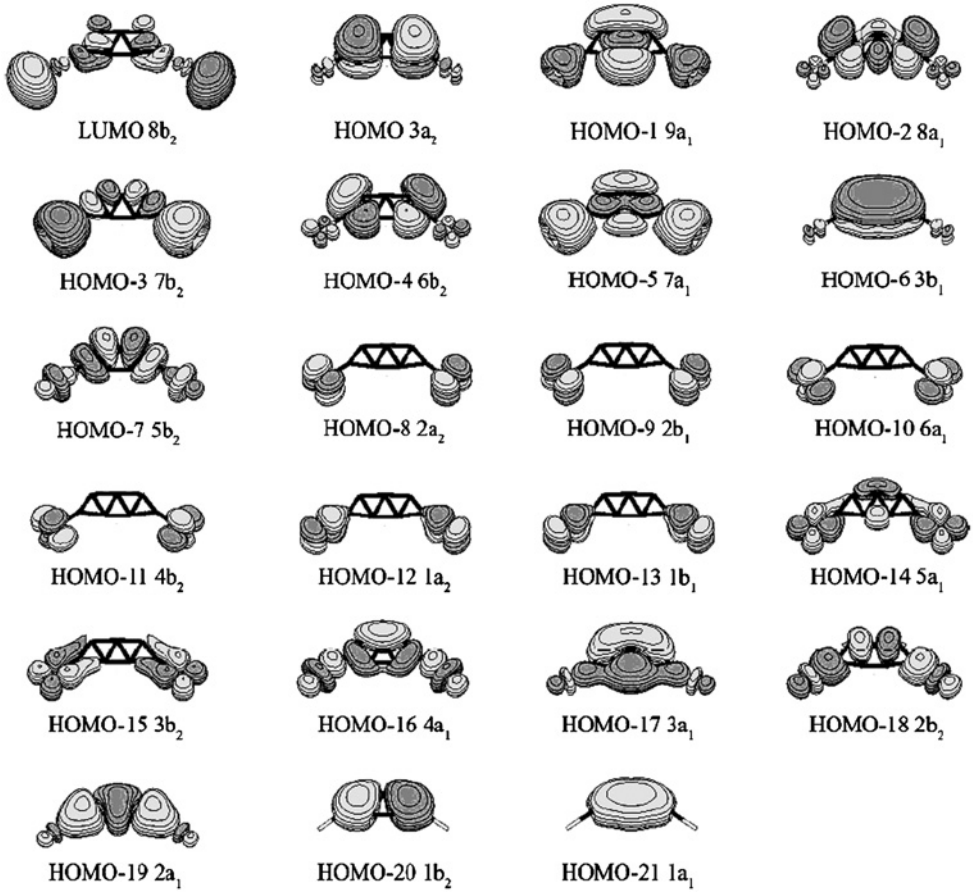

Figure 29: Molecular orbitals of $B_7Au_2^-$ (XVI, C_{2v}, $^1A_1$) at the B3LYP/B/cc-pvDZ/Au/LANL2DZ level. MOs are ordered according to the TD-B3LYP/B/aug-cc-pvTZ/Au/Stuttgart_rsc_1997_ecp + 2f1g level of theory. Reproduced from Ref. [28].

photodetachment transition. The C_{2v} B_7Au_2 possesses eight symmetric modes, among which the ω_1 (B–B in-plane stretching) and ω_3 (B–Au stretching) modes with frequencies of 1358 and 828 cm^{-1} are in good agreement with the two observed vibrational modes (1380 ± 40 and 790 ± 40 cm^{-1}). The geometry changes between the anion and neutral ground states are very small, consistent with the short vibrational progressions observed. The calculated ADE is 3.35 eV (B3LYP/aug-cc-pvTZ/Au/Stuttgart_rsc_1997_ecp + 2f1g), and it agrees well with the experimental value of 3.52 ± 0.02 eV. The next six detachment channels are due to electron removal from HOMO−1 to HOMO−6 (Fig. 29), respectively, and the computed VDEs for these detachment channels are also in good agreement with the experimental data (Table 8).

The good agreement between the experimental and theoretical VDEs confirmed the theoretical prediction of the global minimum structure XVI for $B_7Au_2^-$, which is the same as that of $B_7H_2^-$. Why the structure IV is the most stable for $B_7H_2^-$ has been discussed in detail in Ref. [76]. The same applies to $B_7Au_2^-$ and can be understood from the MO pictures depicted in Fig. 29. Among the 22 occupied valence MOs, 10 can be approximately assigned due the Au 5d orbitals (HOMO−8 to HOMO−16 plus HOMO−18), although a few of the lower-lying orbitals have significant mixing with the B_7 backbone, seven are primarily responsible for the formation of seven 2c-2e (two-center two-electron bond) peripheral B–B bonds (HOMO−2, HOMO−4, HOMO−7, HOMO−17, and HOMO−19 to HOMO−21; see Ref. [76] for more details) and two are primarily responsible for the B–Au bonding (HOMO−3 and HOMO−5). This leaves two delocalized π orbitals (HOMO and HOMO−6) and one delocalized σ orbital HOMO−1 ($9a_1$), which are responsible for the global bonding over the five boron atoms that are not bonded to Au. Thus, $B_7Au_2^-$ is π-antiaromatic (four delocalized π electrons) and σ-aromatic (two delocalized σ electrons) with all other MOs representing the two 2c-2e B–Au bonds and the seven 2c-2e B–B peripheral bonds. The planar $B_7Au_2^-$ structure can then be viewed as originating from the mixing of the Au hybrid 6s–5d orbitals with one of the delocalized σ orbitals in the B_7^- isomer III, thus transforming the doubly (σ- and π-) antiaromatic B_7^- into a σ-aromatic but still π-antiaromatic $B_7Au_2^-$. Essentially, a delocalized σ orbital, forming the original σ-antiaromatic pair of orbitals, is transformed to two B–Au localized bonds, providing major stabilization to the structure XVI for $B_7Au_2^-$. The second most stable isomer for $B_7Au_2^-$ (XVII), originating from the quasi-planar doubly aromatic isomer I of B_7^-, becomes doubly (σ and π) antiaromatic and thus significantly less stable. The stability of the planar structure XVI of $B_7Au_2^-$ is also reinforced by the two strong B–Au bonds formed. The calculated dissociation energy for the $Au_2B_7^-$ (C_{2v}, $^1A_1$, structure XVI) → Au_2 ($^1\Sigma_g^+$) + B_7^- (C_{2v}, $^1A_1$, structure III) reaction is +119 kcal/mol at B3LYP/B/aug-cc-pvTZ/Au/Stuttgart_rsc_1997_ecp + 2f1g level.

The similarity in stability, structure, and bonding in the global minima of $B_7Au_2^-$ and $B_7H_2^-$ is analogous to the previous discovery of the Au/H analogy in Si–Au clusters. Similar to the Si–Au bond, which is highly covalent, it was found that the B–Au bonds in $B_7Au_2^-$ are also highly covalent with very little charge transfer from Au to B (NBO charges at B3LYP/B/cc-pvDZ/Au/LANL2DZ are $Q(Au) = -0.007e^-$ and $Q(B) = -0.251e^-$). This is again due to the close electronegativity between B and Au, as a result of the strong relativistic effects in Au. This study demonstrates that the Au/H analogy may be a more general phenomenon and may exist in many systems involving Au. The Au/H analogy will not only extend our understanding of the

chemistry of Au, but will also be highly valuable in predicting the structures and bonding of many Au alloy clusters.

6. CO CHEMISORPTION ON Au CLUSTERS: IMPLICATIONS FOR NANOGOLD CATALYSIS

Gold is the noblest of all metals in the periodic table. Therefore, the discovery of catalytic activity in gold nanoparticles [1] is quite remarkable and has attracted significant research attention [77]. In particular, gold nanoparticles are able to catalyze low-temperature CO oxidation, whose mechanisms have been the focus of extensive investigations lately [77]. Different models have been proposed, but the exact mechanisms that govern this highly useful catalytic reaction are still under debate [1, 78]. Size-selected cluster deposition studies [79] and gas-phase experimental [80, 81] and theoretical [82, 83] studies represent alternative approaches to model this reaction in a well-controlled manner and provide fundamental understanding at the molecular level. Recent experimental and theoretical studies established that O_2 adsorbs molecularly on gold clusters and nanoparticles [80, 82]. Coadsorption of CO and O_2 on small gold clusters was also revealed in mass-spectrometry-based experiments [81]. Importantly, they were shown to adsorb cooperatively, rather than competitively. However, relatively little experimental information is available on how CO interacts with small gold clusters and nanoparticles, particularly regarding the electronic and structural properties of the CO-chemisorbed gold clusters. A number of chemical reaction studies of gold clusters with CO have been reported and size dependence and saturation were observed [84]. But definitive experimental structural information is still elusive [85]. We will show that Au–CO cluster complexes in the gas phase provide insightful molecular models for mechanistic understanding of nanogold catalysis [29, 30].

6.1. Chemisorption sites of CO on small gold clusters and transitions from chemisorption to physisorption: $Au_m(CO)_n^-$ ($m = 2$–5, $n = 0$–7)

The 193 nm PES spectra of $Au_2(CO)_n^-$ and $Au_3(CO)_n^-$ with n up to 3 and $Au_4(CO)_n^-$ and $Au_5(CO)_n^-$ with n up to 5 are shown in Fig. 30 [29]. Data were obtained for $Au_3(CO)_n^-$ up to $n = 5$ and for $Au_4(CO)_n^-$ and $Au_5(CO)_n^-$ up to $n = 7$. But the additional spectra do not show significant spectral changes and are not shown. The obtained ADEs are plotted in Fig. 31 as a function of CO numbers. PES data of Au_2^- (Fig. 30a) revealed a large HOMO–LUMO gap (2.0 eV) for the closed-shell Au_2 neutral. Upon CO adsorption, the spectral features are similar to those of Au_2^-, but the lowest-binding-energy feature (X) is significantly red-shifted by 0.69 eV for the first CO and by 0.56 eV for the second CO. However, the third CO does not produce a red-shift, but rather induces a slight blue-shift by 0.17 eV. For Au_3^-, we also observed that the first two CO induce significant red-shifts (0.68 and 0.47 eV, respectively) to the PES spectra (Fig. 30b), whereas the third CO appears to have very little effect. It produces a very slight blue-shift (0.04 eV), but the spectral pattern of $Au_3(CO)_3^-$ is nearly identical to that of $Au_3(CO)_2^-$. We have PES data up to $n = 5$, but the spectra of $Au_3(CO)_4^-$ and $Au_3(CO)_5^-$ (not shown) are identical to that of $Au_3(CO)_3^-$, each with a very small blue-shift. The CO adsorption behavior of Au_4^- is similar, but here the first three CO each induces a significant red-shift, 0.58, 0.35, and 0.45 eV, respectively, to the PES spectra

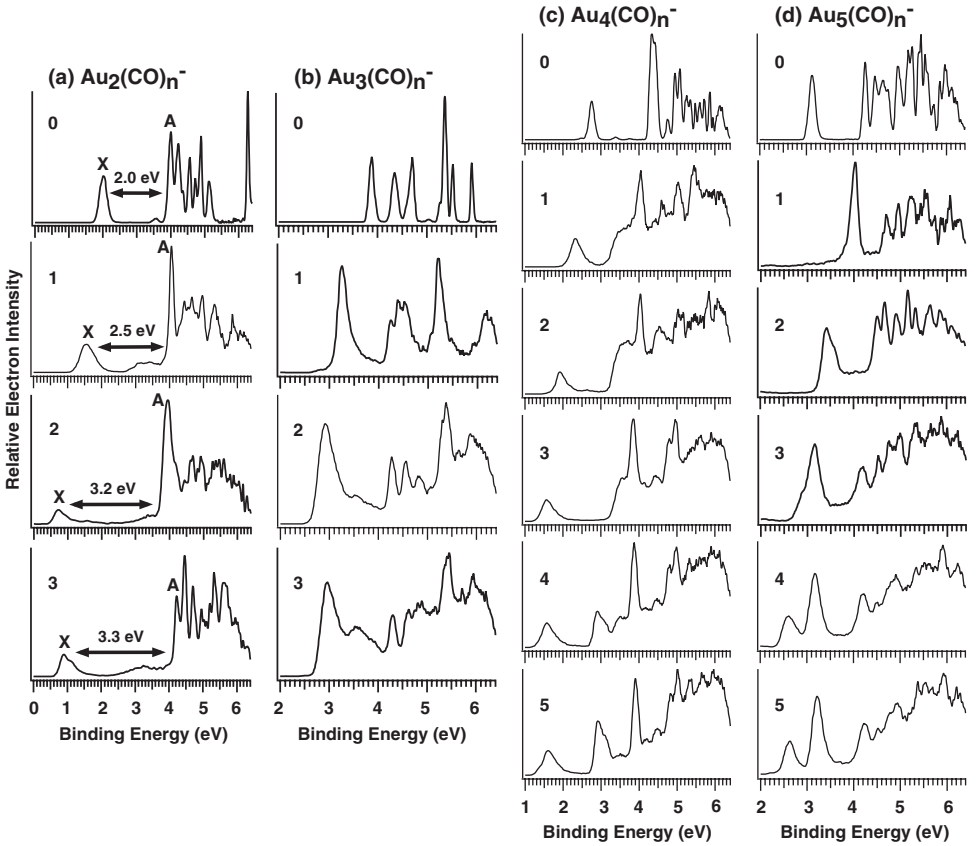

Figure 30: Photoelectron spectra of (a) $Au_2(CO)_n^-$, (b) $Au_3(CO)_n^-$, (c) $Au_4(CO)_n^-$, and (d) $Au_5(CO)_n^-$ at 193 nm. Energy gaps between features *X* and *A* are labeled for $Au_2(CO)_n^-$. Reproduced from Ref. [29].

(Fig. 30c). The fourth CO only produces a tiny red-shift of 0.02 eV. Additional CO up to $n = 7$ yielded PES spectra identical to that of $Au_4(CO)_4^-$ except that each additional CO induces a tiny blue-shift of 0.02–0.03 eV, as can be seen by the similarity between the spectra of $n = 4$ and 5 in Fig. 30c. The CO adsorption behavior of Au_5^- is slightly different, only because the first CO induces a huge blue-shift of 0.85 eV (Fig. 30d). This is due to the special electronic structure of $Au_5(CO)^-$, which can be considered to be an eight-electron system (a major shell closing in the electron shell model) [84]. However, each subsequent CO adsorption produces a red-shift up to $n = 4$ (by 0.59, 0.64, and 0.26 eV, respectively), beyond which both the electron binding energies and the spectral pattern change little between $n = 5$ and 7. Starting at $Au_5(CO)_3^-$, the first PES band seemed to show a splitting, which can be seen more clearly in $Au_5(CO)_4^-$ and all the larger clusters for $n = 5$–7.

Our experimental observation suggests that the first few CO interact more strongly with the Au clusters, inducing significant red-shifts to the electron binding energy and representing chemisorption. Once the available sites on the Au clusters are used up, further CO adsorption has relatively little effect on the electronic structure of the

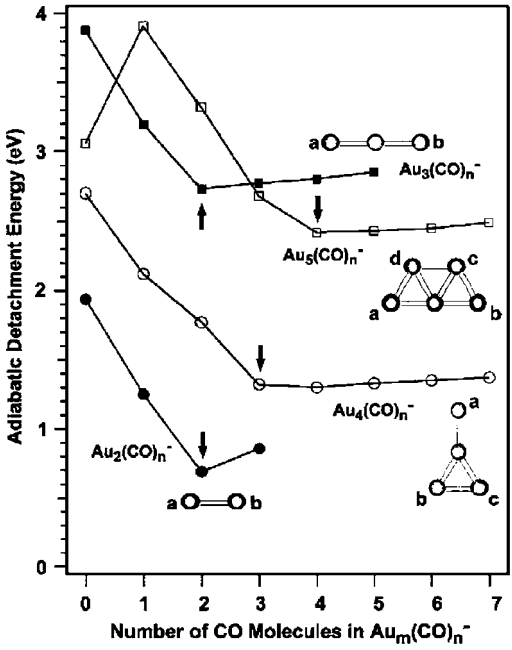

Figure 31: Adiabatic electron detachment energies of the $Au_m(CO)_n^-$ complexes vs. the number of CO. The arrows indicate the transitions from chemisorption to physisorption. Schematic structures of Au_m^- ($m = 2$–5) are also shown, where the letters a–d label the active sites for CO chemisorption. Reproduced from Ref. [29].

chemisorbed $Au_m(CO)_n^-$ clusters, indicating the physisorption regime. Thus, the PES spectra (Fig. 30a–d) reveal vividly a transition from chemisorption to physisorption of CO on Au clusters. Importantly, the maximum numbers of chemisorbed CO correspond precisely to the available low-coordination apex sites on each Au cluster (Fig. 3) [18, 33], as can be seen from the structures of the bare Au clusters given in Fig. 31. The letters (a–d) indicate the CO chemisorption sites. For Au_2^- and Au_3^-, the two terminal Au atoms (a and b) should be the natural sites for CO chemisorption. For Au_4^-, there are two low-lying isomers, a linear one and a Y-shaped one. The maximum of three chemisorbed CO suggests that the Au_4^- cluster possesses the Y-shaped structure, which has three peripheral low-coordination sites. The most likely chemisorption sites for the W-shaped Au_5^- are also labeled in Fig. 31. It is interesting to note that the fifth Au atom with a coordination number of only 4 is not a chemisorption site. The current experimental observation is consistent with recent experimental and theoretical evidence that shows that the active sites for CO adsorption on supported Au nanoparticles are in fact low-coordination Au atoms [77e, 78b].

The PES data also provide insight into the mechanisms for the cooperative coadsorption of CO and O_2 on gold cluster anions [81]. The interactions of Au clusters with CO and O_2 are fundamentally different. CO interacts with Au as an electron donor, whereas O_2 is an electron acceptor. We note that the CO chemisorption induces significant lowering of the electron binding energies to the chemisorbed $Au_m(CO)_n^-$ clusters, making them better electron donors and enhancing their interaction with O_2. The chemisorption of O_2 withdraws electron density from Au clusters and increases

their electron binding energies, making them better electron acceptors and enhancing their interactions with CO. Thus, CO and O_2 are chemisorption promoters to each other, naturally leading to cooperative adsorption on Au clusters. The same mechanism should work in real gold catalysts and may hold the key for understanding why gold nanoparticles are capable of catalyzing CO oxidation at low temperatures.

6.2. Unique CO chemisorption properties of gold hexamer: $Au_6(CO)_n^-$ ($n = 0$–3)

Bare gold hexamer has unique electronic and structural properties. Structurally, Au_6 and Au_6^- are well characterized to possess a close-packed planar triangular structure with D_{3h} symmetry (Fig. 3) [18, 32, 33]. This highly symmetric structure may be viewed as a small piece of Au(1 1 1) surface or an ideal model catalytic surface composed of apex and edge sites only. Electronically, Au_6 is known to possess the largest HOMO–LUMO gap among gold clusters (Fig. 2) [18, 34b] and has been proposed to be a six-electron magic cluster within a 2D electronic shell model [86]. Upon CO chemisorption, we observed surprisingly that the first three CO chemisorptions do not significantly change the electron binding energies of the first PES band in $Au_6(CO)_n^-$ ($n = 1$–3), in direct contrast to our previous study on the smaller $Au_m(CO)_n^-$ ($m = 2$–5) complexes (Fig. 30). Only the binding energies of the second PES band in $Au_6(CO)_n^-$ were observed to be red-shifted, resulting in a closing of the HOMO–LUMO gaps upon CO chemisorption.

The PES spectra of $Au_m(CO)_n^-$ ($n = 0$–3) were obtained at three detachment photon energies (532, 266, and 193 nm) [30]. Figure 32 compares the 193 nm spectra of all the species. The ADE and VDE of the ground-state X of Au_6^- (Fig. 32a) were measured to be 2.06 and 2.13 eV, respectively, where the ADE is in good agreement with a previous ZEKE measurement (2.05 eV) [34]. The VDE of band A at 4.43 eV defines an extremely large HOMO–LUMO gap of 2.30 eV for neutral Au_6, which is the largest among all gold clusters [18, 34]. Upon adsorption of the first CO, the ground-state feature X broadened (Fig. 32b), but its binding energies (ADE: 2.04 eV and VDE: 2.20 eV) showed very little change relative to that of the bare cluster. This is completely different from the chemisorption behavior of the smaller gold clusters, where a red-shift of as much as 0.6–0.7 eV was observed upon the first CO chemisorption for Au_n^- ($n = 2$–5) (Figs. 30 and 31). However, the second VDE, corresponding to electron detachment transition from the anion ground state to the first neutral excited state (A), was measured to be 3.92 eV, significantly red-shifted by 0.51 eV with respect to that of Au_6^- and resulting in a much smaller X–A energy gap (1.72 eV).

Upon further CO adsorption, the overall spectral patterns of $Au_6(CO)_2^-$ (Fig. 32c) and $Au_6(CO)_3^-$ (Fig. 32d) appeared similar to that of $Au_6(CO)^-$: the first PES band X showed very little dependence on the number of CO ligands, whereas the higher-binding-energy features displayed continued red-shifts (by 0.32 and 0.28 eV, respectively), resulting in smaller and smaller X–A energy gaps: 1.45 eV for $Au_6(CO)_2^-$ and 1.17 eV for $Au_6(CO)_3^-$. Very weak signals were observed in the X–A gap region in the spectra of the CO-chemisorbed species. These weak signals were likely due to minor structural isomers in the CO-chemisorbed complexes [30].

Extensive computational searches identified the ground-state structures of $Au_6(CO)_n^-$ ($n = 0$–3) as shown in Fig. 33, which were confirmed from comparison with experimental data (Table 9). The bonding in Au_6 can be understood by mainly considering the orbital interactions of the Au $6s^1$ electrons; the Au $5d^{10}$ manifold can

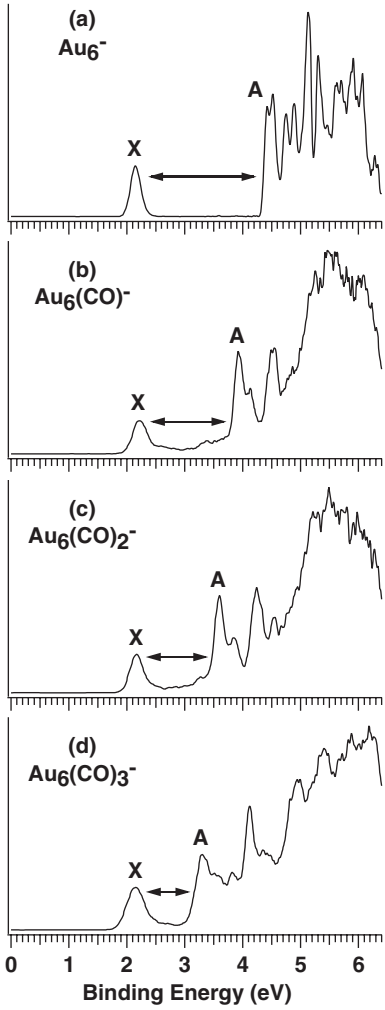

Figure 32: Photoelectron spectra of $Au_6(CO)_n^-$ ($n = 0$–3) at 193 nm.The arrows indicate the observed energy gaps. Reproduced from Ref. [30].

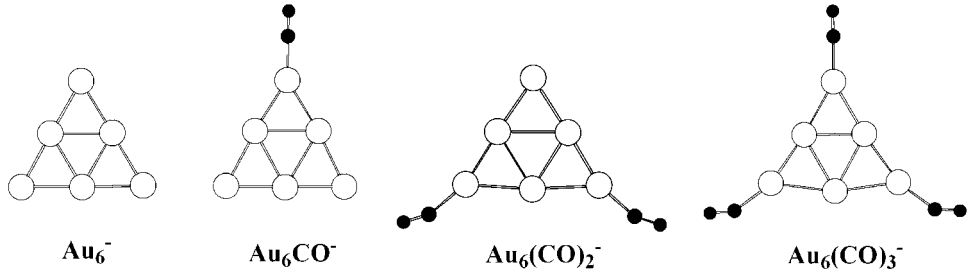

Figure 33: Ground-state structures of $Au_m(CO)_n^-$ ($n = 0$–3) from B3LYP calculations. Reproduced from Ref. [30].

Table 9: Observed ADEs and VDEs from the photoelectron spectra of $Au_6(CO)_n^-$ ($n = 0$–3) and comparison with theoretical detachment energies (Ref. [30]).

Species	Expermental[a,b]			Theoretical[a,c]		
	Feature	ADE	VDE	ADE	State (MO)	VDE
Au_6^-	*X*	2.06 (2)	2.13 (2)	2.02	$^1A_1'$ ($6a_1'$)	2.12
	A		4.43 (2)		$^3E'$ ($7e'$)	4.43
$Au_6(CO)^-$	*X*	2.04 (5)	2.20 (3)	2.10	$^1A_1$ ($11b_2$)	2.26
	A		3.92 (2)		$^3B_2$ ($15a_1$)	3.91
$Au_6(CO)_2^-$	*X*	2.03 (5)	2.15 (3)	2.16	$^1A_1$ ($17a_1$)	2.30
	A		3.60 (2)		$^3B_2$ ($13b_2$)	3.75
$Au_6(CO)_3^-$	*X*	1.95 (5)	2.15 (3)	1.86	$^1A_1$ ($20a_1$)	2.15
	A		3.32 (3)		$^3B_2$ ($14b_2$)	3.53

[a]All detachment energies are in eV.
[b]The ground-state ADE also represents the EA of the corresponding neutral species.
[c]"State (MO)" denotes the final neutral triplet and singlet states upon electron detachment from the corresponding MO of the anion.

be qualitatively viewed as being simply broadened upon orbital overlap. Specifically, the 6s orbitals of the inner and outer triangles in Au_6 both form $a_1' + e'$ representations. The orbital interaction between the inner and outer Au_3 fragments leads to the formation of a bonding and antibonding pair of $a_1' + e'$. The six $6s^1$ electrons fully occupy the $a_1' + e'$ bonding orbitals, giving rise to the $(a_1')^2(e')^4(a_1')^0(e')^0$ electron configuration, which is analogous to the delocalized π electrons in benzene. The antibonding $a_1' + e'$ orbitals, which are nearly degenerate, are unoccupied and become LUMO and LUMO + 1, respectively. This unique electron configuration and the delocalized nature of the $a_1' + e'$ orbitals render Au_6 a highly σ-aromatic system, explaining its special stability and its extremely large HOMO–LUMO gap. As shown in Fig. 34, the a_1' LUMO of Au_6 is mainly from the outer Au_3 fragment, whereas the e' LUMO + 1 orbitals ($8e'$) are mainly from the inner Au_3 fragment. The different spatial distributions of these orbitals and their near degeneracy turn out to be the key in understanding the interaction of Au_6 and CO.

The schematic MO level diagram of $Au_6(CO)_n^-$ is depicted in Fig. 34. The HOMO of Au_6 is the degenerate $7e'$ orbitals, which involve strong s–d hybridization and are highly delocalized. The LUMO of Au_6 is $6a_1'$, which is mainly distributed on the three apex atoms (outer triangle). In the Au_6^- anion, the extra electron enters the $6a_1'$ orbital and the charge is distributed on the outer triangle. What is unique to Au_6 is that its LUMO + 1 ($8e'$), which is mainly concentrated on the inner triangle, is very close in energy to the LUMO. The consequence of this energetic proximity between the LUMO and LUMO + 1 in Au_6 will become clear when CO is adsorbed. When one CO is coordinated to an apex atom of Au_6, the symmetry of the molecule is lowered from D_{3h} to C_{2v}, and the degenerate LUMO + 1 ($8e'$) of Au_6 is split into a_1 and b_2 orbitals. The a_1 component of the $8e'$ orbital strongly mixes with the $6a_1'$ orbital, which are both destabilized (Fig. 34). On the other hand, the b_2 component of the $8e'$ orbital interacting with the CO 2π orbitals becomes the LUMO, into which the extra electron enters in $Au_6(CO)^-$. Consequently, the CO chemisorption to Au_6^- induces an internal electron transfer from the outer triangle to the inner triangle. Since the b_2 LUMO of Au_6CO ($11b_2$) does not change much energetically relative to that in the bare Au_6 species, similar electron binding energies are expected for the two systems. In

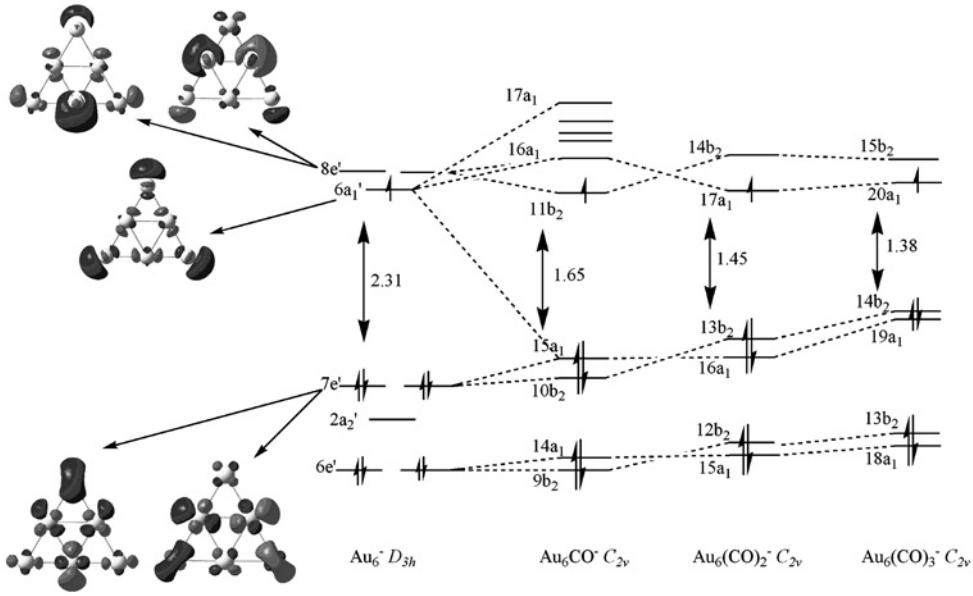

Figure 34: Energy level diagrams of $Au_6(CO)_n^-$ ($n = 0$–3) based on TD-DFT calculations. Reproduced from Ref. [30].

$Au_6(CO)_2^-$ and $Au_6(CO)_3^-$, the a_1 component of the 8e′ orbital becomes the LUMO, which is again localized on the inner triangle (Fig. 34) and whose binding energy is not expected to change significantly relative to that of Au_6^-. This situation is unique to the D_{3h} Au_6 structure, where there exist two spatially distinct but energetically similar regions in the molecule. Thus, in the anions, the extra electron shuttles from the outer triangle to the inner triangle upon chemisorption, resulting in a relatively constant electron binding energy for the singly occupied molecular orbital (SOMO) in both Au_6^- and $Au_6(CO)_n^-$ ($n = 1$–3) (Fig. 34). In other words, since the extra electron in $Au_6(CO)_n^-$ ($n = 1$–3) is localized on the inner Au atoms, it is not sensitive to the CO chemisorption, which only involves the outer Au atoms.

The CO chemisorption also lifts the degeneracy of the 7e′ HOMO of the D_{3h} Au_6, forming a_1 and b_2 orbitals under the C_{2v} symmetry in $Au_6(CO)_n$. The a_1 or b_2 orbital from the HOMO mixes with the corresponding orbital from the LUMO, pushing up the HOMO level in the chemisorbed complexes, $15a_1$ for $n = 1$, $13b_2$ for $n = 2$, and $14b_2$ for $n = 3$ (Fig. 34). The destabilization of the HOMO in the chemisorbed species is further enhanced by the CO 5σ-donation, which is repulsive due to closed-shell–closed-shell interactions. The relatively constant LUMO level plus the destabilization of the HOMO level in $Au_6(CO)_n$ gives rise to the decreasing HOMO–LUMO gaps as observed in the PES data of the chemisorbed $Au_6(CO)_n^-$ anion complexes (*X*–*A* gaps, Fig. 32).

The large HOMO–LUMO gap in Au_6 arises from the σ-aromaticity of the Au_6 6s manifold. Accordingly, the Au_6 cluster is quite inert chemically, and it is not expected to be reactive to O_2. However, the destabilization of its HOMO upon CO chemisorption provides an important activation mechanism. Thus, it is expected that neutral

chemisorbed $Au_6(CO)_n$ complexes should be reactive toward O_2. This cooperative chemisorption behavior seems to be an essential feature in considering the catalytic mechanisms of nanogold for CO oxidation.

7. CONCLUDING REMARKS

We have reviewed recent studies in our laboratory about elemental Au anion clusters, novel gold alloy clusters, and CO-chemisorbed Au clusters. This body of work represents a rather broad spectrum of distinct chemical species, demonstrating that PES is a highly powerful and versatile technique in exploring the novel structure, bonding, and chemistry of gold clusters. The main results are summarized as follows: (i) The PES data confirmed that Au_n^- cluster anions prefer planar structures up to Au_{12}^-, in accord with a previous ion mobility study. Evidence for coexisting isomers was also presented for several cluster sizes, most notably for Au_4^-, Au_7^-, Au_8^-, Au_{10}^-, and Au_{12}^-. (ii) It was revealed that the Au_{20} cluster is highly special and has an extremely large HOMO–LUMO gap, which suggests Au_{20} should be highly stable and chemically inert. Relativistic DFT calculations showed Au_{20} possesses a tetrahedral structure – a fragment of the fcc lattice of bulk gold with a small relaxation. Au_{20} is thus a unique molecule with atomic packing similar to bulk gold but with very different properties, and can be synthesized in solution with ligand protections. (iii) Combined PES and DFT study showed that the Au_{32}^- anion likely possesses a low-symmetry structure controlled by vibrational entropy, in contrast to the Au_{32} neutral that was predicted to be a highly symmetric icosahedral cage. (iv) The Au_2H^- impurity was observed unexpectedly in pure gold clusters and the hydrogen source was shown to be from trace H impurities from the bulk gold target, thus providing strong, albeit indirect, evidence that H is the "invisible" atom that gives the mysterious 3.6 Å Au–Au distance in atomic-thick gold nanowires. (v) Atomic-like magnetism was revealed in transition-metal-doped gold clusters MAu_6 (M = Ti, V, Cr). (vi) Icosahedral cage clusters $M@Au_{12}^-$ (M = Mo, W, V, Nb, Ta) were observed and characterized in the gas phase, which confirmed the earlier theoretical prediction of $M@Au_{12}$ ($M = Ta^-$, W, Re^+) by Pyykkö et al. and also extended this family of clusters to include 4d and 3d heteroatoms. This series of stable cage clusters demonstrated the potential of fine-tuning electronic properties of gold with the central heteroatom. (vii) Au/H analogy was discovered in Si–Au and B–Au binary clusters. This new concept will not only extend our understanding of Au chemistry but will also be highly valuable in predicting the structures and chemical bonding in many Au alloy clusters. (viii) Several extensive series of Au–CO complexes were produced and characterized in the gas phase. These complexes were utilized as molecular models for mechanistic understanding of nanogold catalysis for CO oxidation. Spectroscopic evidence was obtained for CO chemisorption sites on small Au clusters and transitions from chemisorption to physisorption. The PES data also revealed important activation mechanisms of Au clusters by CO chemisorption and provided a natural interpretation for cooperative coadsorption of CO and O_2 on Au clusters, which may hold the key for understanding nanogold catalytic CO oxidation at low temperatures. Gold, the noblest metal in the periodic table, seems to hold many surprises in the nano regime. It is anticipated that many more secrets of nanogold are still waiting to be discovered.

NOTE ADDED IN PROOF

Since submission of this review, we have completed two highly relevant studies [87, 88]. We have discovered and confirmed the first and the smallest empty golden cages in Au_{16}^- and Au_{17}^- [87], which possess enough inner spaces to host a foreign atom to form endohedral golden cages. In another recent study, we have extended the Au/H analogy to Si_3Au_3 [88].

ACKNOWLEDGMENTS

We thank Professor Alexander I. Boldyrev (Utah State University), Dr Jun Li (Pacific Northwest National Laboratory), Professor Uzi Landman and Dr Hannu Häkkinen (Georgia Institute of Technology), Professor Xingao Gong (Fudan University, Shanghai), Professor X. C. Zeng (University of Nebraska-Lincoln) and Dr Boggavarapu Kiran for fruitful theoretical collaborations. We also enjoyed many valuable discussions with Professors Pekka Pyykkö and Manfred M. Kappes. This work was supported by the U.S. National Science Foundation (CHE-0349426 and DMR-0503383) and performed at the W. R. Wiley Environmental Molecular Sciences Laboratory, a national scientific user facility sponsored by the U.S. Department of Energy's Office of Biological and Environmental Research and located at the Pacific Northwest National Laboratory, operated for DOE by Battelle.

REFERENCES

[1] (a) Haruta M., Catal. Today 36 (1997) 153; (b) Haruta M., Chem. Rec. 3 (2003) 75; (c) Bond G.C., Thompson D.T., Catal. Rev. – Sci. Eng. 41 (1999) 319.
[2] (a) Thaxton C.S., Rosi N.L., Mirkin C.A., MRS Bull. 30 (2005) 376; (b) Daniel M.C., Astruc D., Chem. Rev. 104 (2004) 293.
[3] (a) Ohnishi H., Kondo Y., Takayanagi K., Nature 395 (1998) 780; (b) Yanson A.I., Bollinger G.R., van den Brom H.E., Agrait N., van Ruitenbeek J.M., Nature 395 (1998) 783.
[4] (a) Kondo Y., Takayanagi K., Science 289 (2000) 606; (b) Wu B., Heidelberg A., Boland J.J., Nat. Mater. 4 (2005) 525.
[5] (a) Pyykkö P., Angew. Chem. Int. Ed. 43 (2004) 4412; (b) Pyykkö P., Inorg. Chim. Acta 358 (2005) 4113.
[6] (a) Pyykkö P., Chem. Rev. 88 (1988) 563; (b) Pyykkö P., Angew. Chem. Int. Ed. 41 (2002) 3573; (c) Bartlett N., Gold Bull. 31 (1998) 22; (d) Schwerdtfeger P., Heteroatom Chem. 13 (2002) 578; (e) Schwarz H., Angew. Chem. Int. Ed. 42 (2003) 4442.
[7] (a) Schmidbaur H., Chem. Soc. Rev. 24 (1995) 391; (b) Schmidbaur H., Gold Bull. 33 (2000) 3; (c) Schmidbaur H., Nature 413 (2001) 31.
[8] Pyykkö P., Desclaux J.P., Acc. Chem. Res. 12 (1979) 276.
[9] Scherbaum F., Grohmann A., Huber B., Kruger C., Schmidbaur H., Angew. Chem. Int. Ed. 27 (1988) 1544.
[10] For selected reviews, see: (a) Hall K.P., Mingos D.M.P., Prog. Inorg. Chem. 32 (1984) 237; (b) Jones P.G., Gold Bull. 14 (1981) 102, 14 (1981) 159, 16 (1983) 114, 19 (1986) 46; (c) Whetten R.L., Shafigullin M.N., Khoury J.T., Schaaff T.G., Vezmar I., Alvarez M.M., Wilkinson A., Acc. Chem. Res. 32 (1999) 397.

[11] Pyykkö P., Chem. Rev. 97 (1997) 597.
[12] (a) For a feature article on experiment and theory of nonstoichiometric molecules and clusters, see: Boldyrev A.I., Wang L.S., J. Phys. Chem. A 105 (2001) 10759; (b) For a recent review on all-metal aromaticity and antiaromaticity, see: Boldyrev A.I., Wang L.S., Chem. Rev. 105 (2005) 3716; (c) For a recent review on the structures and bonding in small boron clusters, see: Alexandrova A.N., Boldyrev A.I., Zhai H.J., Wang L.S., Coord. Chem. Rev. 250 (2006) 2811.
[13] (a) Wang L.S., Boldyrev A.I., Li X., Simons J., J. Am. Chem. Soc. 122 (2000) 7681; (b) Li X., Kuznestov A.E., Zhang H.F., Boldyrev A.I., Wang L.S., Science 291 (2001) 859; (c) Kuznestov A.E., Birch K.A., Boldyrev A.I., Li X., Zhai H.J., Wang L.S., Science 300 (2003) 622; (d) Zhai H.J., Alexandrova A.N., Birch K.A., Boldyrev A.I., Wang L.S., Angew. Chem. Int. Ed. 42 (2003) 6004; (e) Zhai H.J., Kiran B., Li J., Wang L.S., Nat. Mater. 2 (2003) 827; (f) Kiran B., Bulusu S., Zhai H.J., Yoo S., Zeng X.C., Wang L.S., Proc. Natl. Acad. Sci. USA 102 (2005) 961.
[14] (a) Kemper P.R., Bowers M.T., J. Phys. Chem. 95 (1991) 5134; (b) Jarrold M.F., J. Phys. Chem. 99 (1995) 11; (c) Weis P., Gilb S., Gerhardt P., Kappes M.M., Int. J. Mass Spectrom. 216 (2002) 59.
[15] (a) Kruckeberg S., Schooss D., Maier-Borst M., Parks J.H., Phys. Rev. Lett. 85 (2000) 4494; (b) Schooss D., Blom M.N., Parks J.H., Issendorff B.v., Haberland H., Kappes M.M., Nano Lett. 5 (2005) 1972.
[16] (a) van Heijnsbergen D., von Helden G., Duncan M.A., van Roji A.J.A., Meijer G., Phys. Rev. Lett. 83 (1999) 4983; (b) von Helden G., Tielens A.G.G.M., van Heijnsbergen D., Duncan M.A., Hony S., Waters L.B.F.M., Meijer G., Science 288 (2000) 313; (c) von Helden G., van Heijnsbergen D., Meijer G., J. Phys. Chem. A 107 (2003) 1671.
[17] (a) Park E.K., Weiller B.H., Bechthold P.S., Hoffman W.F., Nieman G.C., Pobo L.G., Riley S.J., J. Chem. Phys. 88 (1988) 1622; (b) Parks E.K., Winter B.J., Klots T.D., Riley S.J., J. Chem. Phys. 94 (1991) 1882.
[18] Häkkinen H., Yoon B., Landman U., Li X., Zhai H.J., Wang L.S., J. Phys. Chem. A 107 (2003) 6168.
[19] Li J., Li X., Zhai H.J., Wang L.S., Science 299 (2003) 864.
[20] Zhang H.F., Stender M., Zhang R., Wang C.M., Li J., Wang L.S., J. Phys. Chem. B 108 (2004) 12260.
[21] Ji M., Gu X., Li X., Gong X.G., Li J., Wang L.S., Angew. Chem. Int. Ed. 44 (2005) 7119.
[22] Zhai H.J., Kiran B., Wang L.S., J. Chem. Phys. 121 (2004) 8231.
[23] Li X., Kiran B., Cui L.F., Wang L.S., Phys. Rev. Lett. 95 (2005) 253401.
[24] Li X., Kiran B., Li J., Zhai H.J., Wang L.S., Angew. Chem. Int. Ed. 41 (2002) 4786.
[25] Zhai H.J., Li J., Wang L.S., J. Chem. Phys. 121 (2004) 8369.
[26] Kiran B., Li X., Zhai H.J., Cui L.F., Wang L.S., Angew. Chem. Int. Ed. 43 (2004) 2125.
[27] Li X., Kiran B., Wang L.S., J. Phys. Chem. A 109 (2005) 4366.
[28] Zhai H.J., Wang L.S., Yu. Zubarev D., Boldyrev A.I., J. Phys. Chem. A 110 (2006) 1689.
[29] Zhai H.J., Wang L.S., J. Chem. Phys. 122 (2005) 051101.
[30] Zhai H.J., Kiran B., Dai B., Li J., Wang L.S., J. Am. Chem. Soc. 127 (2005) 12098.
[31] (a) Wang L.S., Cheng H.S., Fan J., J Chem. Phys. 102 (1995) 9480; (b) Wang L.S., Wu H., in: Advances in Metal and Semiconductor Clusters, Vol. 4, Cluster Materials, M.A. Duncan (ed.), JAI Press, Greenwich, CT, 1998, pp. 299–343; (c) Wang L.S., Li X., in: Cluster and Nanostructure Interfaces, P. Jena, S.N. Khanna, B.K. Rao (eds), World Scientific, Singapore, 2000, pp. 293–300.
[32] (a) Häkkinen H., Moseler M., Landman U., Phys. Rev. Lett. 89 (2002) 033401; (b) Häkkinen H., Landman U., Phys. Rev. B 62 (2000) R2287; (c) Bravo-Perez G., Garzon I.L., Novaro O., J. Mol. Struct. (Theochem.) 493 (1999) 225; (d) Lee H.M., Ge M., Sahu B.R., Tarakeshwar P., Kim K.S., J. Phys. Chem. B 107 (2003) 9994.

[33] Furche F., Ahlrichs R., Weis P., Jacob C., Gilb S., Bierweiler T., Kappes M.M., J. Chem. Phys. 117 (2002) 6982.
[34] For previous PES studies on Au clusters, see: (a) Ho J., Ervin K.M., Lineberger W.C., J. Chem. Phys. 93 (1990) 6987; (b) Taylor K.J., Pettiette-Hall C.L., Cheshnovsky O., Smalley R.E., J. Chem. Phys. 96 (1992) 3319; (c) Handschuh H., Gantefor G., Bechthold P.S., Eberhardt W., J. Chem. Phys. 100 (1994) 7093.
[35] Taylor K.J., Jin C., Conceicao J., Wang L.S., Cheshnovsky O., Johnson B.R., Nordlander P.J., Smalley R.E., J. Chem. Phys. 93 (1990) 7515.
[36] (a) Xiao L., Wang L., Chem. Phys. Lett. 392 (2004) 452; (b) Fernandez E.M., Soler J.M., Garzon I.L., Balbas L.C., Phys. Rev. B 70 (2004) 165403; (c) Gronbeck H., Broqvist P., Phys. Rev. B 71 (2005) 073408; (d) Olson R.M., Varganov S., Gordon M.S., Metiu H., Chretien S., Piecuch P., Kowalski K., Kucharski S.A., Musial M., J. Am. Chem. Soc. 127 (2005) 1049; (e) Remacle F., Kryachko E.S., J. Chem. Phys. 122 (2005) 044304; (f) Walker A.V., J. Chem. Phys. 122 (2005) 094310; (g) Han Y.K., J. Chem. Phys. 124 (2006) 024316.
[37] Gilb S., Weis P., Furche F., Ahlrichs R., Kappes M.M., J. Chem. Phys. 116 (2002) 4094.
[38] (a) Wang X.B., Woo H.K., Wang L.S., J. Chem. Phys. 123 (2005) 051106; (b) Wang X.B., Ding C.F., Wang L.S., J. Chem. Phys. 110 (1999) 8217.
[39] Gunnarsson O., Handschuh H., Bechthold P.S., Kressler B., Gantefor G., Eberhardt W., Phys. Rev. Lett. 74 (1995) 1875.
[40] (a) Wilson N.T., Johnston R.L., Eur. Phys. J. D 12 (2000) 161; (b) Wang J., Wang G., Zhao J., Phys. Rev. B 66 (2002) 035418.
[41] Nilius N., Wallis T.M., Ho W., Science 297 (2002) 1853.
[42] Wang J., Wang G., Zhao J., Chem. Phys. Lett. 380 (2003) 716.
[43] de Bas B.S., Ford M.J., Cortie M.B., J. Mol. Struct.: Theochem. 686 (2004) 193.
[44] de Bas B.S., Ford M.J., Cortie M.B., J. Phys. Condens. Matter 18 (2006) 55.
[45] King R.B., Chen Z., Schleyer P.v.R., Inorg. Chem. 43 (2004) 4564.
[46] Wu K., Li J., Lin C., Chem. Phys. Lett. 388 (2004) 353.
[47] Neumaier M., Weigend F., Hampe O., Kappes M.M., J. Chem. Phys. 122 (2005) 104702.
[48] Molina L.M., Hammer B., J. Catal. 233 (2005) 399.
[49] Johansson M.P., Pyykkö P., Phys. Chem. Chem. Phys. 6 (2004) 2907.
[50] (a) Johansson M.P., Sundholm D., Vaara J., Angew. Chem. Int. Ed. 43 (2004) 2678; (b) Gu X., Ji M., Wei S.H., Gong X.G., Phys. Rev. B 70 (2004) 205401.
[51] Gao Y., Zeng X.C., J. Am. Chem. Soc. 127 (2005) 3698.
[52] Wang J., Jellinek J., Zhao J., Chen Z., King R.B., Schleyer P.v.R., J. Phys. Chem. A 109 (2005) 9265.
[53] Akola J., Manninen M., Häkkinen H., Landman U., Li X., Wang L.S., Phys. Rev. B 60 (1999) R11297.
[54] (a) Untiedt C., Yanson A.I., Grande R., Rubio-Bollinger G., Agrait N., Vieira S., van Ruitenbeek J.M., Phys. Rev. B 66 (2002) 085418; (b) Rodrigues V., Ugarte D., Phys. Rev. B 63 (2001) 073405; (c) Legoas S.B., Galvao D.S., Rodrigues V., Ugarte D., Phys. Rev. Lett. 88 (2002) 076105; (d) Takai Y., Kawasaki T., Kimura Y., Ikuta T., Shimizu R., Phys. Rev. Lett. 87 (2001) 106105.
[55] (a) Smit R.H.M., Untiedt C., Yanson A.I., van Ruitenbeek J.M., Phys. Rev. Lett. 87 (2001) 266102; (b) Bahn S.R., Jacobsen K.W., Phys. Rev. Lett. 87 (2001) 266101.
[56] (a) Okamoto M., Takayanagi K., Phys. Rev. B 60 (1999) 7808; (b) Häkkinen H., Barnett R.N., Landman U., J. Phys. Chem. B 103 (1999) 8814; (c) Häkkinen H., Barnett R.N., Scherbakov A.G., Landman U., J. Phys. Chem. B 104 (2000) 9063; (d) De Maria L., Springborg M., Chem. Phys. Lett. 323 (2000) 293; (e) Skorodumova N.V., Simak S.I., Comput. Mater. Sci. 17 (2000) 178.
[57] (a) Sanchez-Portal D., Artacho E., Junquera J., Ordejon P., Garcia A., Soler J.M., Phys. Rev. Lett. 83 (1999) 3884; (b) Torres J.A., Tosatti E., Dal Corso A.,

Ercolessi F., Kohanoff J.J., Di Tolla F.D., Soler J.M., Surf. Sci. 426 (1999) L441; (c) Stepanov I.A., Surf. Sci. 463 (2000) 211; (d) Torres J.A., Tosatti E., Dal Corso A., Ercolessi F., Kohanoff J.J., Di Tolla F.D., Soler J.M., Surf. Sci. 463 (2000) 213.

[58] Bahn S.R., Lopez N., Norskov J.K., Jacobsen K.W., Phys. Rev. B 66 (2002) R081405.

[59] (a) Skorodumova N.V., Simak S.I., Phys. Rev. B 67 (2003) R121404; (b) Novaes F.D., da Silva A.J.R., da Silva E.Z., Fazzio A., Phys. Rev. Lett. 90 (2003) 036101.

[60] (a) Legoas S.B., Rodrigues V., Ugarte D., Galvao D.S., Phys. Rev. Lett. 93 (2004) 216103; (b) Hobi E., Jr., da Silva A.J.R., Novaes F.D., da Silva E.Z., Fazzio A., Phys. Rev. Lett. 95 (2005) 169601; (c) Legoas S.B., Rodrigues V., Ugarte D., Galvao D.S., Phys. Rev. Lett. 95 (2005) 169602.

[61] Fischer D., Andreoni W., Curioni A., Gronbeck H., Burkart S., Gantefor G., Chem. Phys. Lett. 361 (2002) 389.

[62] Huber K.P., Herzberg G., Molecular Spectra and Molecular Structure. IV. Constants of Diatomic Molecules, Van Nostrand Reinhold Company, New York, 1979.

[63] Pyykkö P., Runeberg N., Angew. Chem. Int. Ed. 41 (2002) 2174.

[64] Schwerdtfeger P., Angew. Chem. Int. Ed. 42 (2003) 1892.

[65] (a) Gutsev G.L., Boldyrev A.I., Adv. Chem. Phys. 61 (1985) 169; (b) Wang X.B., Ding C.F., Wang L.S., Boldyrev A.I., Simons J., J. Chem. Phys. 110 (1999) 4763.

[66] Autschbach J., Hess B.A., Johansson M.P., Neugebauer J., Patzschke M., Pyykkö P., Reiher M., Sundholm D., Phys. Chem. Chem. Phys. 6 (2004) 11.

[67] Gagliardi L., J. Am. Chem. Soc. 125 (2003) 7504.

[68] (a) Lauher J.W., Wald K., J. Am. Chem. Soc. 103 (1981) 7648; (b) Burdett J.K., Eisenstein O., Schweizer W.B., Inorg. Chem. 33 (1994) 3261.

[69] Yeh J.J., Hwang H., Bertness K., Friedman D.J., Cao R., Lindau I., Phys. Rev. Lett. 70 (1993) 3768.

[70] Ma Z., Allen L.H., Phys. Rev. B 48 (1993) 15484.

[71] Ivanco J., Kobayashi H., Almeida J., Margaritondo G., Pincik E., J. Appl. Phys. 90 (2001) 345.

[72] (a) Lischka H., Kohler H.J., J. Am. Chem. Soc. 105 (1983) 6646; (b) Bogey M., Bolvin H., Demuynck C., Destombes J.L., Phys. Rev. Lett. 66 (1991) 413; (c) Grev R.S., Schaefer H.F., J. Chem. Phys. 97 (1992) 7990; (d) West R., Fink M.J., Michl J., Science 214 (1981) 1343; (e) Andrews L., Wang X., J. Phys. Chem. A 106 (2002) 7696; (f) Pak C., Rienstra-Kiracofe J.C., Schaefer H.F., J. Phys. Chem. A 104 (2000) 11232; (g) Sari L., McCarthy M.C., Schaefer H.F., Thaddeus P., J. Am. Chem. Soc. 125 (2003) 11409; (h) Trinquier G., J. Am. Chem. Soc. 113 (1991) 144.

[73] (a) Hanley L., Anderson S.L., J. Phys. Chem. 91 (1987) 5161; (b) Hanley L., Whitten J.L., Anderson S.L., J. Phys. Chem. 92 (1988) 5803; (c) Ruatta S.A., Hintz P.A., Anderson S.L., J. Chem. Phys. 94 (1991) 2833; (d) Sowa-Resat M.B., Smolanoff J., Lapicki A., Anderson S.L., J. Chem. Phys. 106 (1997) 9511; (e) Wyss M., Riaplov E., Batalov A., Maier J.P., Weber T., Meyer W., Rosmus P., J. Chem. Phys. 119 (2003) 9703; (f) Cias P., Araki M., Denisov A., Maier J.P., J. Chem. Phys. 121 (2004) 6776; (g) Batalov A., Fulara J., Shnitko I., Maier J.P., Chem. Phys. Lett. 404 (2005) 315.

[74] For selected previous theoretical work, see: (a) Kato H., Tanaka E., J. Comput. Chem. 12 (1991) 1097; (b) Kato H., Yamashita K., Morokuma K., Chem. Phys. Lett. 190 (1992) 361; (c) Boustani I., Int. J. Quantum Chem. 52 (1994) 1081; (d) Boustani I., Surf. Sci. 370 (1997) 355; (e) Boustani I., Phys. Rev. B 55 (1997) 16426; (f) Ricca A., Bauschlicher C.W., Chem. Phys. 208 (1996) 233; (g) Ricca A., Bauschlicher C.W., J. Chem. Phys. 106 (1997) 2317; (h) Gu F.L., Yang X., Tang A.C., Jiao H., Schleyer P.v.R., J. Comput. Chem. 19 (1998) 203; (i) Fowler J.E., Ugalde J.M., J. Phys. Chem. A 104 (2000) 397; (j) Aihara J., J. Phys. Chem. A 105 (2001) 5486; (k) Ma J., Li Z.H., Fan K.H., Zhou M.F., Chem. Phys.

Lett. 372 (2003) 708; (l) Jin H.W., Li Q.S., Phys. Chem. Chem. Phys. 5 (2003) 1110; (m) Li Q.S., Jin Q., J. Phys. Chem. A 107 (2003) 7869.

[75] (a) Ritter S.K., Chem. Eng. News 82 (9) (2004) 28; (b) Zhai H.J., Wang L.S., Alexandrova A.N., Boldyrev A.I., Zakrzewski V.G., J. Phys. Chem. A 107 (2003) 9319; (c) Zhai H.J., Wang L.S., Alexandrova A.N., Boldyrev A.I., J. Chem. Phys. 117 (2002) 7917; (d) Alexandrova A.N., Boldyrev A.I., Zhai H.J., Wang L.S., Steiner E., Fowler P.W., J. Phys. Chem. A 107 (2003) 1359; (e) Alexandrova A.N., Boldyrev A.I., Zhai H.J., Wang L.S., J. Phys. Chem. A 108 (2004) 3509; (f) Alexandrova A.N., Zhai H.J., Wang L.S., Boldyrev A.I., Inorg. Chem. 43 (2004) 3552; (g) Alexandrova A.N., Boldyrev A.I., Zhai H.J., Wang L.S., J. Chem. Phys. 122 (2005) 054313.

[76] Alexandrova A.N., Koyle E., Boldyrev A.I., J. Mol. Model. 12 (2006) 569.

[77] For selected surface studies, see: (a) Valden M., Lai X., Goodman D.W., Science 281 (1998) 1647; (b) Chen M.S., Goodman D.W., Science 306 (2004) 252; (c) Kim T.S., Stiehl J.D., Reeves C.T., Meyer R.J., Mullins C.B., J. Am. Chem. Soc. 125 (2003) 2018; (d) Guzman J., Gates B.C., J. Am. Chem. Soc. 126 (2004) 2672; (e) Lemire C., Meyer R., Shaikhutdinov S., Freund H.J., Angew. Chem. Int. Ed. 43 (2004) 118; (f) Date M., Okumura M., Tsubota S., Haruta M., Angew. Chem. Int. Ed. 43 (2004) 2129.

[78] (a) Cho A., Science 299 (2003) 1684; (b) Lopez N., Janssens T.V.W., Clausen B.S., Xu Y., Mavrikakis M., Bligaard T., Norskov J.K., J. Catal. 223 (2004) 232.

[79] (a) Sanchez A., Abbet S., Heiz U., Schneider W.D., Häkkinen H., Barnett R.N., Landman U., J. Phys. Chem. A 103 (1999) 9573; (b) Yoon B., Häkkinen H., Landman U., Wirz A.S., Antonietti J.M., Abbet S., Heiz U., Science 307 (2005) 403; (c) Lee S., Fan C., Wu T., Anderson S.L., J. Am. Chem. Soc. 126 (2004) 5682.

[80] (a) Stolcic D., Fischer M., Gantefor G., Kim Y.D., Sun Q., Jena P., J. Am. Chem. Soc. 125 (2003) 2848; (b) Kim Y.D., Fischer M., Gantefor G., Chem. Phys. Lett. 377 (2003) 170; (c) Sun Q., Jena P., Kim Y.D., Fischer M., Gantefor G., J. Chem. Phys. 120 (2004) 6510.

[81] (a) Hagen J., Socaciu L.D., Elijazyfer M., Heiz U., Bernhardt T.M., Woste L., Phys. Chem. Chem. Phys. 4 (2002) 1707; (b) Wallace W.T., Whetten R.L., J. Am. Chem. Soc. 124 (2002) 7499.

[82] (a) Yoon B., Häkkinen H., Landman U., J. Phys. Chem. A 107 (2003) 4066; (b) Varganov S.A., Olson R.M., Gordon M.S., Meitu H., J. Chem. Phys. 119 (2003) 2531; (c) Molina L.M., Hammer B., J. Chem. Phys. 123 (2005) 161104.

[83] (a) Häkkinen H., Landman U., J. Am. Chem. Soc. 123 (2001) 9704; (b) Liu Z.P., Hu P., Alavi A., J. Am. Chem. Soc. 124 (2002) 14770; (c) Wu X., Senapati L., Nayak S.K., Selloni A., Hajaligol M., J. Chem. Phys. 117 (2002) 4010; (d) Molina L.M., Hammer B., Phys. Rev. Lett. 90 (2003) 206102; (e) Yuan D.W., Zeng Z., J. Chem. Phys. 120 (2004) 6574; (f) Bongiorno A., Landman U., Phys. Rev. Lett. 95 (2005) 106102.

[84] (a) Nygren M.A., Siegbahn P.E.M., Jin C., Guo T., Smalley R.E., J. Chem. Phys. 95 (1991) 6181; (b) Lee T.H., Ervin K.M., J. Phys. Chem. 98 (1994) 10023; (c) Wallace W.T., Whetten R.L., J. Phys. Chem. B 104 (2000) 10964; (d) Balteanu I., Balaj O.P., Fox B.S., Beyer M.K., Bastl Z., Bondybey V.E., Phys. Chem. Chem. Phys. 5 (2003) 1213.

[85] (a) Fielicke A., von Helden G., Meijer G., Pedersen D.B., Simard B., Rayner D.M., J. Am. Chem. Soc. 127 (2005) 8146; (b) Fielicke A., von Helden G., Meijer G., Simard B., Rayner D.M., J. Phys. Chem. B 109 (2005) 23935.

[86] (a) Tanaka H., Neukermans S., Janssens E., Silverans R.E., Lievens P., J. Am. Chem. Soc. 125 (2003) 2862; (b) Janssens E., Tanaka H., Neukermans S., Silverans R.E., Lievens P., New J. Phys. 5 (2003) 46.

[87] Bulusu S., Li X., Wang L.S., Zeng X.C., Proc. Natl. Acad. Sci. USA 103 (2006) 8326.

[88] Kiran B., Li X., Zhai H.J., Wang L.S., J. Chem. Phys. 125 (2006) 133204.

Chapter 4

Au_n and Ag_n ($n = 1$–8) nanocluster catalysts: gas-phase reactivity to deposited structures

S.K. Buratto, M.T. Bowers*, H. Metiu, M. Manard, X. Tong, L. Benz, P. Kemper and S. Chrétien

Department of Chemistry and Biochemistry, University of California, Santa Barbara, CA 93106, USA

1. INTRODUCTION

The chemistry of small metal clusters has received considerable attention over the last several years [1–3], due primarily to the fact that the intrinsic properties of clusters are intermediate to those of atoms and the bulk phase [4]. This region is of particular interest for coinage metals because it is has been shown to be important in a number of catalytic reactions [5]. Few materials provide a more compelling example of the inherent differences between the bulk and "nano" scales than gold. Known to be chemically inert in the bulk phase [6], the experimental results of Haruta first showed that highly disperse gold clusters are catalytically active when supported on metal-oxide surfaces [7]. A mixture of H_2, O_2, and $CH_3CH{=}CH_2$ passing over very small clusters of Au on TiO_2 will produce propylene oxide with high selectivity (~90%). Passed over slightly smaller clusters, the same mixture reacts to make propane. A further increase in size renders the Au useless: no catalysis takes place on it. Silver clusters have similar catalytic activity. They too serve as epoxidation catalysts for ethene and propene when supported on semiconductor surfaces [8].

The discovery of the catalytic properties of noble metal nanoclusters has prompted a sizable experimental and theoretical research effort aimed at characterizing the catalytic activity [9–13]. Particular attention has been focused on trying to understand the size-dependent catalytic activity [14] of these clusters and to develop robust theoretical models that are independent of both the metal (Ag, Au) and substrate. We have made considerable progress in this area and our results are summarized in this chapter. We have approached our goal of understanding the size-dependent chemistry of metal clusters on two fronts: by probing the reactivity of mass-selected Au_n^+ and Ag_n^+ nanoclusters in the gas phase, and by studying the properties of mass-selected Au_n^+

The Chemical Physics of Solid Surfaces, Volume 12
ISSN: 1571-0785
DOI: 10.1016/S1571-0785(07)12004-6

*Corresponding author.
E-mail: bowers@chem.ucsb.edu

and Ag_n^+ nanoclusters deposited on $TiO_2(1\,1\,0)$ surfaces under ultrahigh vacuum (UHV) conditions. Detailed results on gas-phase clusters provide important thermodynamic information, both as data for testing theoretical models and to establish structural, energetic, and reactive properties for size-selected clusters. Depositing size-selected clusters provides a platform for studying model nanocluster catalysts with a well-defined size. Surface structures, binding sites, and binding energies are determined by combining atomic-resolution scanning tunneling microscopy (STM) and density functional theory (DFT).

2. EXPERIMENTAL METHODS

2.1. Ion mobility mass spectrometry

2.1.1. Instrumentation

All of the ion–molecule reactions described in this work were carried out on a home-built dual-quadrupole mass spectrometer equipped with a high-pressure drift/reaction cell located between the two quadrupole mass filters (Fig. 1) [15]. Transition metal cluster ions are generated from pulsed laser vaporization [16] of a translating/rotating metal rod in a high-pressure Ar bath gas. The laser used in these experiments is a 308-nm XeCl excimer. It is typically operated at 20 Hz with a power output of approximately 300 mJ/pulse. The desorbed metal plasma is then entrained in a high-pressure pulse of Ar that collisionally cools the plasma and induces cluster formation. The timing of the Ar pulse is synchronized with the laser using a home-built delay generator. The typical Ar pulse width is on the order of 500 μsec with a backing pressure of 75 psi. Metal clusters exiting the source are then mass selected by the first quadrupole mass filter and injected into the drift/reaction cell.

The drift/reaction cell is a Cu block that is 4 cm in length with an entrance and exit orifice measuring 0.5 mm in diameter. The cell can be filled with both inert and reactive gases. These gases are flowed through the cell so that a constant pressure can be maintained. For the majority of the work presented in this chapter, a mixture of reactive gases and He was used to fill the cell. The typical composition of the gas mixture is 4.5 Torr of He combined with 0.001–0.5 Torr of reactant gas. Pressures in the cell are measured using a capacitance manometer. For gas mixtures, a residual gas analyzer (RGA) can also be used to monitor the presence of the reactive component.

The experimental temperature range of the cell can be varied from 80 to 800 K. Temperatures greater than 300 K are achieved by resistive heating of Ta resistors embedded in the cell body while temperatures below 300 K are reached by flowing N_2

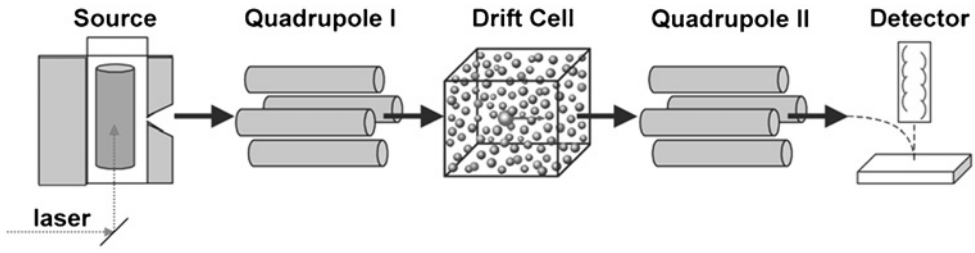

Figure 1: A schematic view of the quadrupole–cell–quadrupole mass spectrometer.

gas cooled in liquid nitrogen through channels that are also present in the cell body. The temperature is monitored by three thermocouples placed at various locations on the cell. This is a means of determining if significant temperature gradients across the cell exist and if errors in the temperature reading are present.

Ions are drawn through the cell under the influence of a weak electric field. The field is weak enough so that the thermal energy of the ions is not significantly perturbed. Ions exiting the cell are mass selected by a second quadrupole mass filter and detected using a Venetian-blind electron multiplier. A conversion dynode is used to allow for both positive and negative ion operation.

2.1.2. Equilibrium reactions

Equilibria are rapidly established in the cell for successive association reactions of neutral ligands to the transition metal cluster ions (Eq. (1)).

Integrated peak areas of the various $M_m^{+/-}L_n$ ions are recorded and these values,

$$M_m^{+/-}L_{n-1} + L \rightleftarrows M_m^{+/-}L_n \tag{1}$$

along with the pressure of the ligating gas (P_L) in Torr, are used to determine an equilibrium constant (K_P°) for each reaction using the following equation:

$$K_P^\circ = \frac{[M_m^{+/-}(L)_n]}{[M_m^{+/-}(L)_{n-1}]} \times \frac{760}{P_L} \tag{2}$$

The equilibrium constants can then be used to calculate the standard Gibbs free energies for the reactions,

$$\Delta G_T^\circ = -RT \ln(K_P^\circ) \tag{3}$$

and the values obtained for ΔG_T° plotted vs. the temperature, to obtain ΔS_T° and ΔH_T° for each reaction using the following equation:

$$\Delta G_T^\circ = \Delta H_T^\circ - T\Delta S_T^\circ \tag{4}$$

The resulting plots are linear over the experimental temperature range for all systems reported here. A least-squares fitting procedure is used to obtain slopes and intercepts of each line. The slopes are used to determine the association entropy for Eq. (1) (ΔS_T°) and the intercepts give the corresponding ΔH_T° values. The reported uncertainty in these values is a measure of variance in the data from the fit.

For some of the systems discussed here, 0 K bond dissociation energies (BDE) have been determined by fitting the experimental data using statistical thermodynamics and extrapolating to 0 K [17, 18]. To accomplish this task, ΔG_T° is calculated (Eq. (4)) using the total clustering entropy, given in the following equation:

$$\Delta S_{TOT} = \Delta S_{TRANS} + \Delta S_{ROT} + \Delta S_{VIB} + \Delta S_{EL} \tag{5}$$

The observed slope is $\Delta S_{TOT} + R$ ln(mass discrimination), where "mass discrimination" is the ratio of collection efficiencies for parent and product ions. The enthalpy is obtained from the following equation:

$$\Delta H_{TOT} = \Delta H_0^\circ + \int_0^T \Delta C_{P(TRANS)} + \Delta C_{ROT} + \Delta C_{VIB} dT \tag{6}$$

The necessary vibrational frequencies and rotational constants are taken from DFT [19, 20] calculations (see Section 2.13). In all cases, molecular parameters that are not well fixed by theoretical calculations or comparisons with known systems, such as the theoretical vibrational frequencies and the mass discrimination, are varied over a wide range of physically reasonable values until the calculated ΔG°_{T} vs. T line matches the experimental data points. It should be stressed that uncertainties in these parameters have little effect on the final values of ΔH°_{0}. Thus, we expected only small uncertainties in the derived bond energies. This is confirmed for each cluster equilibrium by determining the range of ΔH°_{0} values resulting from a wide range of vibrational frequencies. It should also be noted that the translational entropies and heat capacities are precisely known for all the clusters. Therefore, since $\Delta S_{\mathrm{TRANS}}$ is the largest component of ΔS_{TOT}, even substantial errors in the calculated ΔS_{ROT} or ΔS_{VIB} will only have a small effect on the calculated value of ΔS_{TOT}.

2.1.3. Theory

The product ions of interest were examined theoretically to determine the molecular parameters needed to analyze the experimental data and to identify factors important in the bonding. DFT calculations were carried out using the B3LYP hybrid functional [21–23] and the Gaussian 03 package [24]. For all of the calculations reported here, carbon and hydrogen were described using the standard 6-31 + G** basis set [25]. The basis set for the silver cationic clusters is a (5s6p4d)/[3s3p2d] contraction of the Hay–Wadt ($n+1$) effective core potential (ECP) valence double zeta basis proposed by Hay [26, 27]. Here, the outermost core orbitals are not replaced by the ECP, but are instead treated equally with the valence orbitals. This allows for increased accuracy in the calculations without a substantial increase in computation time. The ECP for silver incorporates the Darwin and mass–velocity relativistic effects into the potential. The Stuttgart/Dresden relativistic ECP and (8s7p6d)/[6s5p3d] valence basis set were used to treat both the silver anionic clusters and the gold cationic clusters [27, 28]. Nineteen valence electrons are explicitly treated by the basis set.

Geometry optimizations of metal ion/alkene clusters of interest were performed over a wide variety of conceivable geometries in order to obtain minimum energy cluster conformations and to ensure that no alternate theoretical geometries exist that significantly differ from those reported here. All confirmed minima consist of largely unperturbed C_2H_4 and C_3H_6 ligands bound to a metal core ion.

2.2. Ion soft landing of mass-selected Au_n^+ and Ag_n^+ on TiO_2

The creation and investigation of mass-selected clusters takes place in a home-built, laser ablation source [29] coupled with several surface science probes including STM, as shown in Fig. 2.

2.2.1. The ion cluster source

The operating principles of ablation sources have been discussed elsewhere and only the details relevant to the present design are presented here.

The sample format is a rotating translating metal rod, mounted vertically in the "waiting room" ($\sim$1 cm^3) directly in front of a pulsed valve orifice. A pulse of argon fires prior to a laser pulse, inducing nucleation of the ablated plasma into a variety of cluster sizes. Positively charged ions exit through an expansion nozzle insert. Argon is used as

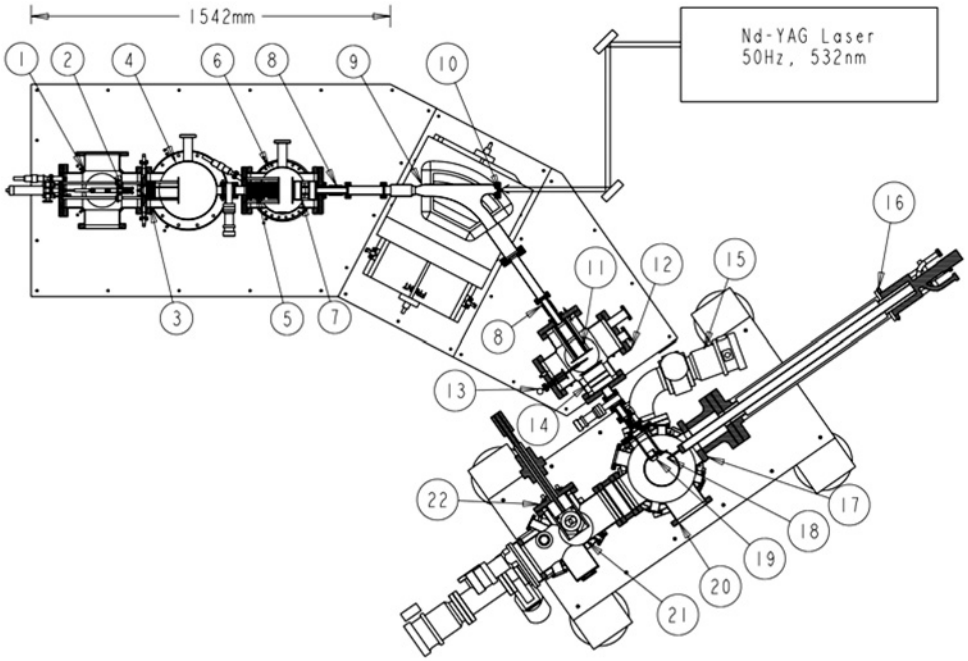

Figure 2: Overall view of instrument (drawn to scale). The absolute dimension of the laser vaporization source and associated pumping/expansion region is indicated. (1) Source chamber; (2) cluster source; (3) first einzel/steering lens; (4) diffusion pump chamber; (5) second einzel/steering lens; (6) acceleration chamber; (7) acceleration/focus lens; (8) ceramic break; (9) magnet flight tube; (10) laser entrance window; (11) deceleration/y focus lens; (12) deceleration/collector chamber; (13) moveable detector; (14) z focus/steering lens; (15) turbo pump; (16) cryo-manipulator; (17) deposition chamber; (18) sample holder stage; (19) final focus lens; (20) Auger; (21) microscope chamber; and (22) microscope.

the expansion gas (rather than the more commonly used helium) as it seems to result in significantly greater clustering. The green line (532 nm) of an Nd-YAG laser is focused on the sample through the nozzle orifice. Positively charged clusters are extracted using ion optics. The ion beam exits the source vacuum chamber through a skimmer. The source/nozzle assembly is electrically biased (~150 V) with respect to the skimmer (0 V), therefore the ions have ~150 eV kinetic energy. Clusters of a particular mass are selected in a magnetic sector, focused, and finally guided into a deposition chamber. A movable detector can be placed in the path of the beam to measure a mass spectrum of the available clusters, as well as the kinetic energy distribution of the incoming clusters.

Figure 3 shows an extended mass scan of gold clusters from 0 to 8500 amu. Intensities for Au^+_{1-4} range from 0.4 to 1.6 nA while those for Au^+_{5-40} are roughly 30 pA. From this scan, the mass resolution ($M/\Delta M$) is seen to be $\geqslant 40$ at 8500 amu, allowing selection of individual clusters up to Au_{40}. The present cluster intensities of 0.1–1 nA for Ag^+_n and Au^+_n correspond to deposition times of ~10–100 min (for ~0.02 ML).

In the absence of collisions, the cluster ion deposition energy is given by the difference between source and substrate potentials. When gas is present, energy is added in the expansion and subtracted by collisions in the acceleration region between the nozzle and skimmer. The velocity added in the expansion is fairly uniform while a

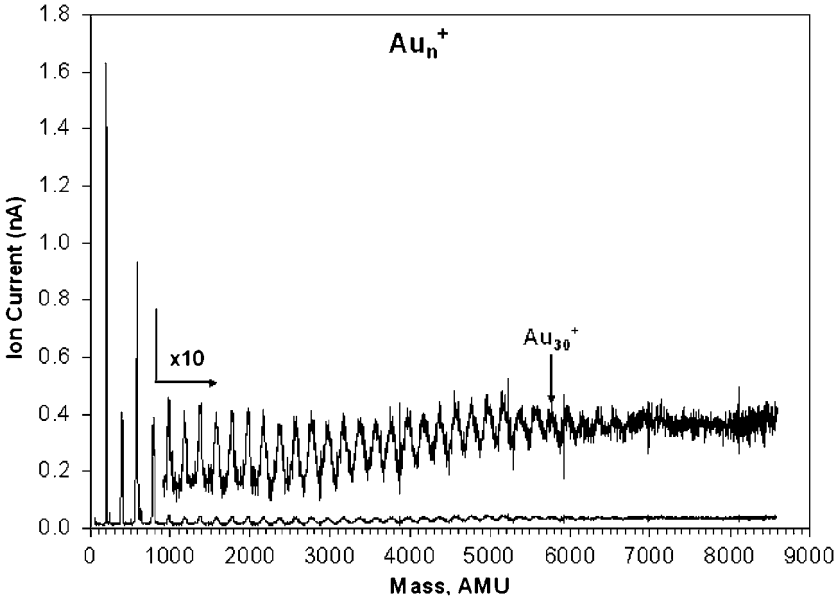

Figure 3: Au_n^+ mass spectrum; 0–8500 amu.

Poisson distribution of collision numbers (ranging from 0 to several) governs the energy lost. The expected result is a KE distribution with some fraction of clusters having a uniform maximal energy equal to the acceleration potential (i.e., source to ground potential, ~150–200 eV) with the energies of the remainder of the ions tailing off to lower values. This is in fact what is found. Figure 4 shows a plot of Ag^+ ion current vs. detector stopping potential for an acceleration potential of ~180 V. Superimposed on the data is an integrated normal distribution (fit to the high energy side of the data) as well as its derivative. Note that the high energy half of the distribution is quite sharp (~1–2 eV wide) with an energy corresponding to the source acceleration potential. This narrow distribution is critical because it is the high energy side of the distribution which is deposited after retardation to 50% ion loss. The low energy part of the distribution – although broad – is lost when the cluster ions are decelerated before deposition. We can thus deposit ions with <2–3 eV/cluster. The KE range does increase with cluster size but the maximum KE/atom is roughly constant.

The coverage is estimated by measuring the current on a movable target positioned ~2 mm in front of the sample to be approximately 0.01–0.02 ML in all cases relative to Ag or Au(1 1 1), both of which have a surface atom density of 1.39×10^{15} atoms/cm^2.

2.2.2. Sample preparation and STM

The clusters reach the sample in the deposition chamber, which has a base pressure of $<2 \times 10^{-10}$ Torr, rising somewhat to $<1 \times 10^{-9}$ during deposition due to residual argon gas. The rutile titania (1 1 0)-(1 × 1) samples (Commercial Crystal Laboratories or Princeton Scientific Corp.) were prepared in UHV by multiple cycles of Ar^+ bombardment (1–2 kV, 20 min) and annealing to 860–1100 K prior to use, causing the crystals to change from transparent to blue in color due to the creation of oxygen

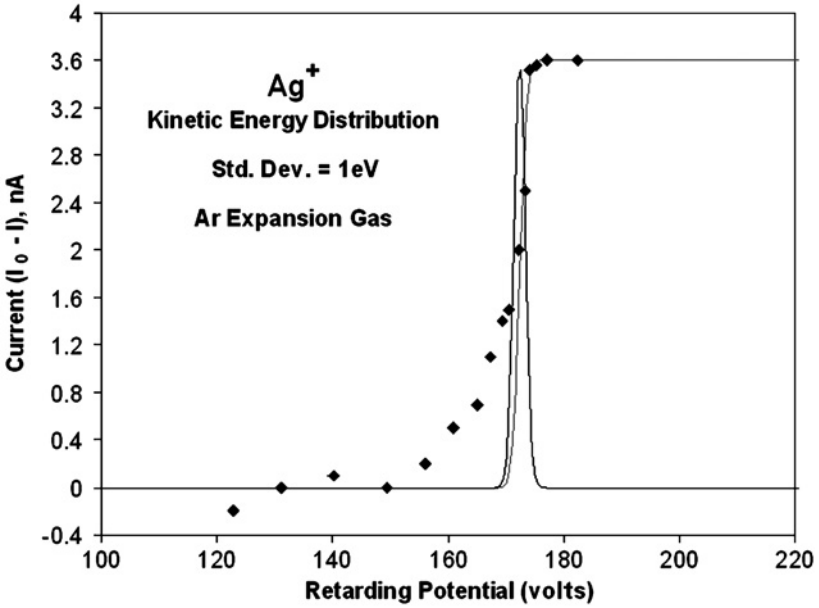

Figure 4: Kinetic energy distribution of Ag^+ at the collector.

vacancies. For temperatures below 900 K, longer annealing times of 10–20 min were typical, while higher temperatures were used in a flash preparation method during which the temperature was held for only 10–20 sec. Once clusters have been deposited, the sample is shuttled into the UHV STM chamber (RHK-SPM 100, base pressure $< 2 \times 10^{-10}$ Torr) and scanned with electrochemically etched tungsten tips, which are electron bombarded in vacuum prior to use. Feature heights are reported here as measured, while feature diameters are reported as full-width half-max values, and are uncorrected for tip convolution effects. Height and width ranges given represent one standard deviation. Typical scanning parameters of $+1$ to $+2$ V and 0.1 to 0.2 nA were used, therefore empty states are probed. High resolution, UHV STM can be used to determine cluster size, shape, and position on the surface.

2.3. Density functional theory calculations of clusters on TiO_2(1 1 0) surfaces

Once the clusters have been investigated using STM, we perform DFT calculations in order to compare our experimental results to theory. We have performed periodic Kohn–Sham DFT calculations using the Perdew and Wang 1991 (PW91) exchange-correlation functional [30, 31] and the VASP program [32–35]. The ionic cores were described by scalar relativistic ultrasoft pseudopotentials [36] allowing 6, 10, and 11 "valence" electrons for O, Ti, and Au atoms, respectively. Two pseudopotentials were used to describe oxygen atoms. We denote them soft- and hard-oxygen pseudopotentials. The cutoff in the plane wave expansion was 270 eV in calculations involving the soft-oxygen pseudopotential and 396 eV in the other case. Differences less than 0.1 eV are generally observed between the relative and desorption energies computed with the two oxygen pseudopotentials. This difference is negligible compared with the accuracy of DFT. However, the computational time is significantly reduced

when the soft-oxygen is used. Relativistic effects were partially taken into account through the use of a relativistic scalar pseudopotential. We have neglected the effect of spin–orbit coupling. All calculations aimed at understanding the catalytic activity or the surface science of gold, performed so far, have used this approximation without producing manifestly unreasonable results. Moreover, it has been shown recently that spin–orbit coupling has negligible effect on the atomization energy and the orbital energies of the frontier orbital small Au clusters [37].

The Brillouin zone was sampled at the Γ-point only. Monopole, dipole, and quadrupole corrections to the energy were taken into account using a modified version of the method proposed by Makov and Payne [38]. We allowed fractional occupancies of the bands by using a window of 0.05 eV and the Gaussian smearing method. A Harris–Foulkes like correction to the forces was included. The Kohn–Sham matrix was diagonalized iteratively using the residual minimization method-direct inversion in the iterative subspace [33, 39].

Many starting structures (more than 30 for all clusters larger than the dimer), corresponding to the adsorption of Au/Ag clusters on a stoichiometric and on a reduced rutile TiO_2(1 1 0) surface, have been fully optimized without symmetry constraints by using a conjugated gradient algorithm [40]. Both surfaces are considered since the cluster, if immobile, can encounter local areas which are both stoichiometric and reduced. Various configurations for a given cluster were considered, including 3-dimensional (3-D) and metastable structures located up to 2 eV above the ground state based on calculations performed for the unsupported (gas phase) neutral, cationic, and anionic clusters, i.e. Au_p^q ($n = 1$–7, $q = 0, +1, -1$). We removed one of the protruding bridging oxygen atoms to model the defective (reduced) surface. This corresponds to a concentration of 17% oxygen atom vacancies, which is slightly larger than the experimental value (~10%).

We use the term desorption energy (D_e), as is common in surface science, to describe the binding strength between the clusters and the rutile TiO_2(1 1 0) surface. For example, the desorption energy of Au_2 adsorbed on a stoichiometric surface, $D_e[Au_2]$, is

$$D_e[Au_2] = E[TiO_2(\text{perfect})] + E[Au_2] - E[Au_2/TiO_2(\text{perfect})] \tag{7}$$

$E[TiO_2(\text{perfect})]$ and $E[Au_2/TiO_2(\text{perfect})]$ are the total energies of the stoichiometric TiO_2(1 1 0) surface without and with a Au cluster while $E[Au_2]$ is the total energy of Au_2 in the gas phase.

The dissociative adsorption of Au clusters was studied on a [5 × 2] supercell. In these calculations, the fragments occupy their respective equilibrium positions and the separation between the fragments is more than 6.5 Å except in very few cases. The fragmentation energies, $\Delta E_{frag}[Au_n/TiO_2]$, were obtained using the formula:

$$\Delta E_{frag}[Au_n/TiO_2] = E[Au_n/TiO_2] - E[(Au_x + Au_{n-x})/TiO_2] \tag{8}$$

$E[Au_n/TiO_2]$ is the total energy of the lowest energy structure of the intact cluster and $E[(Au_x + Au_{n-x})/TiO_2]$ the total energy of the fragmented cluster in which both fragments occupy their equilibrium position on the surface. On the reduced surface, only one of the fragments occupies the defect site (missing bridging oxygen). The other one is located at its equilibrium position on a stoichiometric area of the surface.

3. INTERACTIONS BETWEEN Au_n AND Ag_n CLUSTER IONS AND SMALL ALKENES

3.1. Introduction

An initial step that must be made to further our understanding of the properties of coinage metal clusters is the determination of their gas-phase conformations. Toward these ends, Kappes and co-workers have reported the gas-phase conformations of both positively and negatively charged Au_m ($m<14$) clusters [41, 42] and the conformations of positively charged Ag_m^+ ($m<12$) clusters [43] using ion mobility methods combined with DFT calculations. Additionally, a host of theoretical studies have been conducted that report the geometries of silver and gold clusters in this size range [44–47].

The interactions between transition metals and small, catalytically relevant molecules have also been the source of extensive study [48–51]. Systematic experiments have examined the properties of an assortment of gas-phase metal ion $M_y^{+/-}$-X_n clusters with $X = H_2$ [18, 52, 53], CO [54–56], and O_2 [57–60] along with a variety of other ligands [61–63]. These experiments, coupled with theoretical calculations, have broadened our understanding of the nature of transition metal ion bonding and have provided some of the fundamental information that is necessary to elucidate the complex factors involved with many catalytic processes.

Small alkenes have been the focus of many studies because of their ability to serve as effective prototypes for other unsaturated hydrocarbons [64–67]. Dewar first proposed an interaction model to interpret the structure of metal–olefin complexes [68]. This model suggests that bonding consists mainly of electron density donated from the π orbitals of the ligand to the unoccupied s orbital of the metal coupled with back-donation from the filled d orbitals of the metal to the unoccupied π^* orbitals of the ligand. Subsequent studies have used this model to explain the bonding of small alkenes to group 11 transition metal cations [64–66]. Furthermore, it has been shown that back-donation plays a more significant role in the bonding of first row transition metals and is less important for the second and third row counterparts [66, 67, 69].

In this work, temperature-dependent equilibrium measurements in conjunction with ab initio calculations were used to determine the interactions of Ag_m^+ ($m<14$) clusters with C_2H_4 and C_3H_6 and the interactions of Au_m^+ ($m = 1$, 3–9) clusters with C_2H_4. Some of these systems have been previously investigated in other laboratories. Guo and Castleman [64] measured the binding energies of one and two C_2H_4 ligands to Ag^+. Chen and Armentrout [70] examined reactions of Ag^+ with a variety of small hydrocarbons and reported a lower limit for the BDE of the $Ag^+(C_2H_4)$ ion. Little information could be found in the literature pertaining to the interactions of C_2H_4 or C_3H_6 with the larger Ag or Au clusters studied here.

In addition to thermodynamic information, many other properties of coinage metal clusters have been examined. Rate constants for the dissociation of Ag_2^+ via association of both ethene and propene have been measured [71]. DFT calculations were performed to generate potential transition state structures for the dissociation reactions and phase space theory (PST) was used to model the experimental rate data.

Structural information for the metal cationic clusters has also been obtained from thermodynamic measurements of sequential ligand additions to a bare cluster. Ligand addition to metal clusters has been formerly used to imply structure [70,72,73]. In these studies, saturation experiments are performed and a set of empirical rules used to

interpret the data. Here, recent theoretical work has indicated that the lowest unoccupied molecular orbital (LUMO) on Ag and Au clusters is primarily located on "corner" atoms in the cluster [74–76]. The position of the LUMO strongly affects the charge distribution of the metal clusters. Binding energies at a particular cluster site should correlate with the charge distribution for an electron donating ligand. Therefore, measured bond energies will correlate with charge distributions and allow us to identify equivalent, or near equivalent, "corners" of the metal clusters.

3.2. $Ag_m^+(C_2H_4)_n$ and $Ag_m^+(C_3H_6)_n$ ($m = 1$–9) association reactions

Examples of the kind of data we obtain from our experiments are presented in Fig. 5 and the resultant values of ΔH and ΔS derived from the data are given in Tables 1–4.

Several trends in the experimental data were observed. With the exception of Ag_5^+ and Ag_{10}^+, the strongest silver–alkene bond results from the addition of the first ligand to the transition metal core ion, although the decrease in the binding energies of successive ligand additions vary substantially and are unique to each silver cluster.

Additionally, the BDEs of the Ag_m^+/C_3H_6 systems are systematically larger than those of the Ag_m^+/C_2H_4 systems for a given value of m.

Trends in the association entropies for the systems studied can also be seen. Typical ΔS_T° values ranged from approximately –20 to –30 cal/(mol K). All association reactions where the value of $n > m$ result in values of ΔS_T° that are approximately 10 entropy units "less negative" than those of the first m ligands. Some association reactions give rise to values of ΔS_T° that are much more negative than –30 cal/(mol K). The reasons for these large negative values of ΔS_T° are unique to the system in which it occurs and several cases will be discussed in detail in the following sections.

A trend concerning the BDEs of the first alkene ligand additions to the Ag_m^+ clusters is also observed. With the exception of the Ag_6^+ and Ag_7^+ clusters, the binding energies of the first alkene ligands systematically decrease as the size of the Ag_m^+ clusters increase, as shown in Fig. 6. Figure 6 also shows that the BDEs appear to be asymptotically approaching the binding energy of C_2H_4 and C_3H_6 to the bulk silver surface.

The energies and geometries of ligated silver cluster ions were calculated using DFT. DFT calculations provide binding energies in good quantitative agreement with experiment for the early ligand additions to the smaller Ag_m^+ ($m = 1$–5) clusters. The quantitative agreement worsens for the larger clusters with more ligands attached, but the experimental trends in binding energies are nicely duplicated. The geometries of $Ag_4^+(C_2H_4)_{1-5}$, $Ag_4^+(C_3H_6)_{1-5}$, and $Ag_6^+(C_2H_4)_{1-6}$ are shown here as examples of ligated structures. Theoretical molecular geometries and electronic population analysis provided information necessary to identify factors important in the binding interactions of the various clusters.

A detailed understanding of the interactions between silver cluster ions and their alkene ligands can be achieved by examining the valence electronic configurations of each species separately. Recently, Weis et al. used ion mobility spectrometry along with DFT to investigate bare silver cluster cations [43]. Using this combination of theory and experiment, they were able to determine cluster geometries. We have used their results as a basis for our own DFT calculations to determine NBO populations. These results are given in Table 5 along with the bare silver cluster geometries. NBO

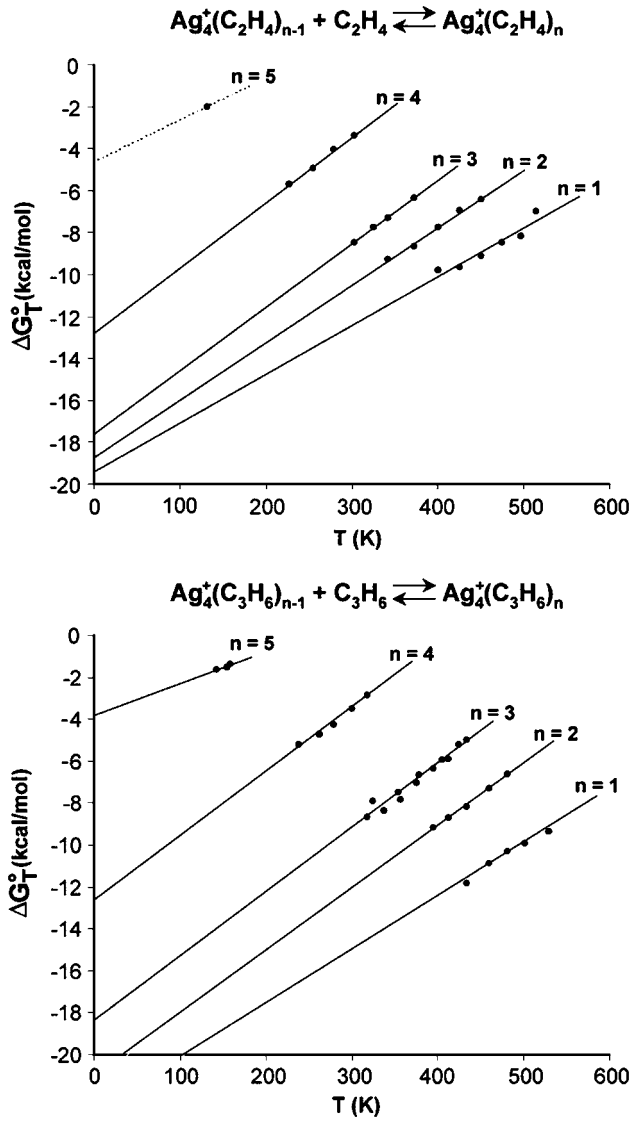

Figure 5: Plot of experimental ΔG_T° vs. temperature data for the association reactions: $Ag_4^+(L)_{n-1} + L \rightleftarrows Ag_4^+(L)_n$ (L = either C_2H_4 or C_3H_6). For $n = 5$ of the C_2H_4 system, the slope of the line is 10 cal/(mol K) more positive than the $n = 4$ line (see text for details).

analysis shows that the highest occupied molecular orbitals (HOMO) of the Ag_m^+ clusters are created by overlap of the 5s orbitals of each Ag atom in a given cluster. For each Ag_m^+ cluster, one of these 5s orbitals is initially unoccupied, giving rise to the positive charge of the cluster. The remaining $m - 1$ 5s orbitals are singly occupied. In most cases, the electron density is delocalized about the cluster. Equivalent amounts of electron density located on two or more atoms of a cluster (see Table 5) are found for metal clusters having highly symmetric geometries.

Table 1: $Ag_m^+(C_2H_4)_{n-1} + C_2H_4 \rightleftarrows Ag_m^+(C_2H_4)_n$ bond dissociation energies $(-\Delta H_0^\circ)$[a].

m	n							
	1	2	3	4	5	6	7	8
3	21.5±0.8	19.7±0.9	17.1±0.6	5.5±0.6				
4	19.2±1.8	18.6±0.9	17.4±0.5	12.5±0.7	~4.6[b]			
5	18.7±1.1	18.2±1.2	25.2±0.9	8.9±0.6	6.7±0.6	4.5±0.6		
6	25.7±1.0	22.0±0.6	14.6±0.7	11.2±0.6	8.5±0.6	6.9±0.8		
7	26.4±0.7	22.1±1.0	12.7±0.6	9.9±0.5	7.9±0.7	6.3±0.7	5.2±0.8	
8	17.5±1.0	15.3±0.6	11.0±0.5	10.5±0.6	9.7±0.6[c]	7.2±0.4[c]	6.2±0.6[c]	~5.6[c,d]
9	16.3±0.8	14.8±0.9	12.4±0.7	10.8±0.5	9.6±0.4	8.1±0.4[c]	6.7±0.4[c]	
10	14.7±0.9	15.7±0.7						
11	14.7±0.7	13.7±1.0						
12	16.5±0.8	13.4±0.9						
13	16.2±0.6							

[a]In units of kcal/mol.
[b]Estimated by assuming that the association entropy was 10 cal/(mol K) more positive than the previous ligand addition.
[c]ΔH_T° value, no ΔH_0° value was generated.
[d]Estimated by assuming the same association entropy as the previous ligand addition.

Table 2: $Ag_m^+(C_2H_4)_{n-1} + C_2H_4 \rightleftarrows Ag_m^+(C_2H_4)_n$ association entropies $(-\Delta S_T^\circ)$[a].

m	n						
	1	2	3	4	5	6	7
3	23.1±1	26.0±1	28.5±1	19.7±3			
4	23.3±4	27.4±2	30.2±1	31.1±2			
5	24.3±2	27.8±2	45.3±1	23.3±2	21.1±2	12.6±2	
6	35.8±2	38.5±1	28.8±1	25.1±1	20.3±2	20.7±3	
7	38.7±1	36.6±2	26.3±1	21.3±1	18.6±2	16.9±3	18.6±3
8	30.0±3	29.5±1	23.1±1	26.4±2	27.3±3	20.8±2	20.4±3
9	26.9±2	29.8±3	28.6±2	27.3±1	27.9±2	25.1±2	24.6±2
10	25.8±2	30.7±2					
11	28.5±1	26.9±3					
12	31.3±2	25.7±2					
13	32.3±1						

[a]In units of cal/(mol K).

Table 3: $Ag_m^+(C_3H_6)_{n-1} + C_3H_6 \rightleftarrows Ag_m^+(C_3H_6)_n$ bond dissociation energies $(-\Delta H_0^\circ)$[a].

M	N							
	1	2	3	4	5	6	7	8
3	26.1±1.0	21.3±1.5	18.7±0.9	4.9±0.4	4.2±0.8			
4	22.8±1.5	21.0±0.9	18.3±1.1	12.5±0.9	3.8±0.6[b]			
5	21.6±0.7	19.8±1.0	25.0±1.0	11.3±0.9	9.4±1.0	6.0±0.7[b]		
6	25.8±1.2	19.8±1.1	14.9±1.4	13.9±1.4	11.1±0.6[b]	9.8±0.5[b]		
7	25.1±1.3	20.8±1.3	14.3±0.9	13.1±1.1	12.0±0.3[b]	10.8±0.3[b]	8.5±0.2[b]	
8	19.7±1.0	16.9±0.8	15.2±0.6	12.9±0.6[b]	11.6±0.3[b]	10.6±0.5[b]	~8.3[b,c]	
9	19.2±0.8	16.2±0.7	14.5±1.1	13.0±0.8[b]	11.2±0.4[b]	10.2±0.2[b]	8.5±0.2[b]	~7.0[b,c]

[a]In units of kcal/mol.
[b]ΔH_T° value, no ΔH_0° value was generated.
[c]Estimate, values obtained from two data points.

Table 4: $Ag_m^+(C_3H_6)_{n-1} + C_3H_6 \rightleftarrows Ag_m^+(C_3H_6)_n$ association entropies $(-\Delta S_T^\circ)$[a].

m	*n*							
	1	2	3	4	5	6	7	8
3	27.5±2	26.4±2	31.1±1	15.0±1	18.1±3			
4	25.7±3	29.9±1	30.7±2	29.8±2	15.1±3			
5	27.3±1	29.6±2	44.3±1	28.4±2	30.6±3	21.4±3		
6	33.3±2	30.3±2	26.5±3	30.9±3	27.8±2	31.5±2		
7	33.4±2	31.5±2	27.2±2	29.2±3	30.8±1	32.7±1	30.5±1	
8	29.9±2	29.5±1	32.6±1	30.6±2	31.3±1	32.6±2	~31.0[b]	
9	29.6±2	28.7±2	30.7±3	31.2±3	30.6±2	32.6±1	28.9±1	~28.5[b]

[a]In units of cal/(mol K).
[b]Estimate, values obtained from two data points.

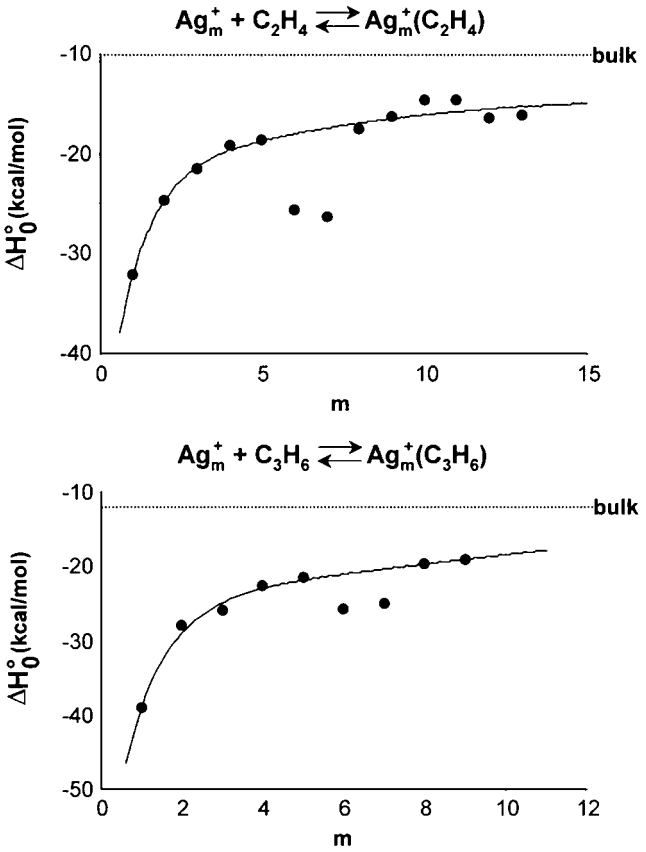

Figure 6: Plot of ΔH_0° vs. cluster size (m) for the association reactions $Ag_m^+ + L \rightleftarrows Ag_m^+(L)$ (m = 3–13, L = C_2H_4; m = 3–9, L = C_3H_6). The curve through the data points is provided to guide the eye. Dashed lines indicate the binding energy of the respective alkene ligands to an Ag(1 1 0) surface.

Table 5: Natural bond order populations and charges of the Ag_m^+ clusters ($m = 2$–13).

m	Structure[a]	Symmetry	5s Populations[b]	5s Charges[b]
2		$D_{\infty h}$	0.500	0.500
3		D_{3h}	0.666	0.333
4		D_{2h}	0.722 0.759	0.254 0.245
5	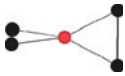	D_{2d}	0.744 1.005	0.258 −0.030
6		C_{2v}	0.585 0.899 0.952	0.354 0.091 0.056
7		D_{5h}	0.522 0.953	0.378 0.049
8[c]		C_s	0.823	0.184
9		D_{3h}	0.856 0.876	0.137 0.098
10		C_s	0.857 0.953	0.113 0.048
11		D_{3h}	0.807 0.906 1.060	0.136 0.093 −0.047
12[c]		C_{2v}	0.844	0.130
13[c]		C_{2v}	0.823	0.121

[a]Cluster geometries obtained from ion mobility data [43] and DFT calculations. Ag atoms of a given cluster having equal charge distributions are identically colored.
[b]Populations for the 5 s atomic orbitals of the Ag atoms of each cluster and the corresponding partial atomic charge. Text color corresponds to analogously colored atoms of a given structure.
[c]Only populations and charges of atoms having the greatest amount of partial positive charge (shown in black) are given for these clusters.

To understand the binding interactions of a silver–alkene cluster, we must also consider the valence electronic configurations of C_2H_4 and C_3H_6. These species are well characterized. The HOMOs of C_2H_4 and C_3H_6 are the $\pi(2p_y)^2$ bonding orbitals that make up the C–C double bond in both molecules.

A series of DFT calculations performed by Chrétien et al. [74–76] indicate that absorption of an electron donating ligand to a coinage metal cluster preferentially occurs at the location where the LUMO of the metal clusters protrudes most into the vacuum. This location is found on atoms located at "corners" of the metal clusters. Additionally, for the entire series of positively charged cluster ions studied here, our DFT calculations indicate that the position of the LUMO directly correlates with the location of highest partial-positive charge of a cluster. This implies that alkene ligand additions to the Ag_m^+ clusters occur at the Ag atom carrying the most partial-positive charge.

NBO analysis shows that for the addition of the first m ligands to the Ag_m^+ clusters, a substantial amount of electron density is transferred from the ligand to the transition metal cluster. The exact amount of electron density donated varies with cluster size and with the alkene ligand (either C_2H_4 or C_3H_6). This electron density originates from the $\pi(2p_y)^2$ bonding orbitals of C_2H_4 and C_3H_6 and is donated to the LUMO of the Ag_m^+ clusters, and suggests that the primary silver–alkene binding interaction is covalent in nature.

The interaction of C_3H_6 with the Ag_m^+ clusters is systematically stronger than that of C_2H_4. NBO shows that electron donation from C_3H_6 to the Ag_m^+ clusters is slightly larger than for C_2H_4 for a given value of m. This result suggests the larger BDEs of the silver–propene clusters are a result of a slightly stronger covalent interaction. However, it should also be noted that C_3H_6 has both a larger polarizability than C_2H_4 (6.3 vs. 4.3 $Å^3$) [77] and dipole moment (0.44 vs. 0.0 D according to DFT) indicating electrostatic forces also contribute to the differences in the observed binding energies.

From the theoretical silver–alkene molecular geometries given in Figs. 7 and 8, it is apparent that both types of alkene ligands adsorb side-on to the Ag_m^+ clusters, perpendicular to the silver–alkene bond axis. This orientation allows for optimum molecular orbital overlap between the Ag_m^+ clusters and the alkene ligands. Additionally, the calculated C–C double bond distances for ligands of an $Ag_m^+(L)_n$ cluster, where $n \leqslant m$, are increased slightly compared with that of the free molecules, consistent with electron transfer out of a bonding orbital.

Plots of ΔG_T° vs. T provide information as to the manner in which sequential C_2H_4 and C_3H_6 additions to the Ag_m^+ clusters occur. Plots generated from each system were found to fall into one of the two groups. The first group accounts for ligand additions to a silver cluster in which all the atoms of the cluster have equal or nearly equal charge distributions. For the purposes of this discussion, the Ag_4^+ cluster will serve as the example for these types of systems. The second group accounts for ligand additions to a silver cluster in which the charge is unequally distributed about the atoms of the metal cluster. The Ag_6^+ cluster will serve as the example for these types of systems.

Five ligand additions are observed for the Ag_4^+ system (Fig. 7). The first four additions have similar BDEs and association entropies (Tables 1–4). However, the BDEs do slightly decrease as the number of ligands bound to the cluster increase. The fifth ligand BDE is significantly smaller than the first four. From the structure of Ag_4^+ and the partial atom charges shown in Table 5, it appears that Ag_4^+ has four equivalent

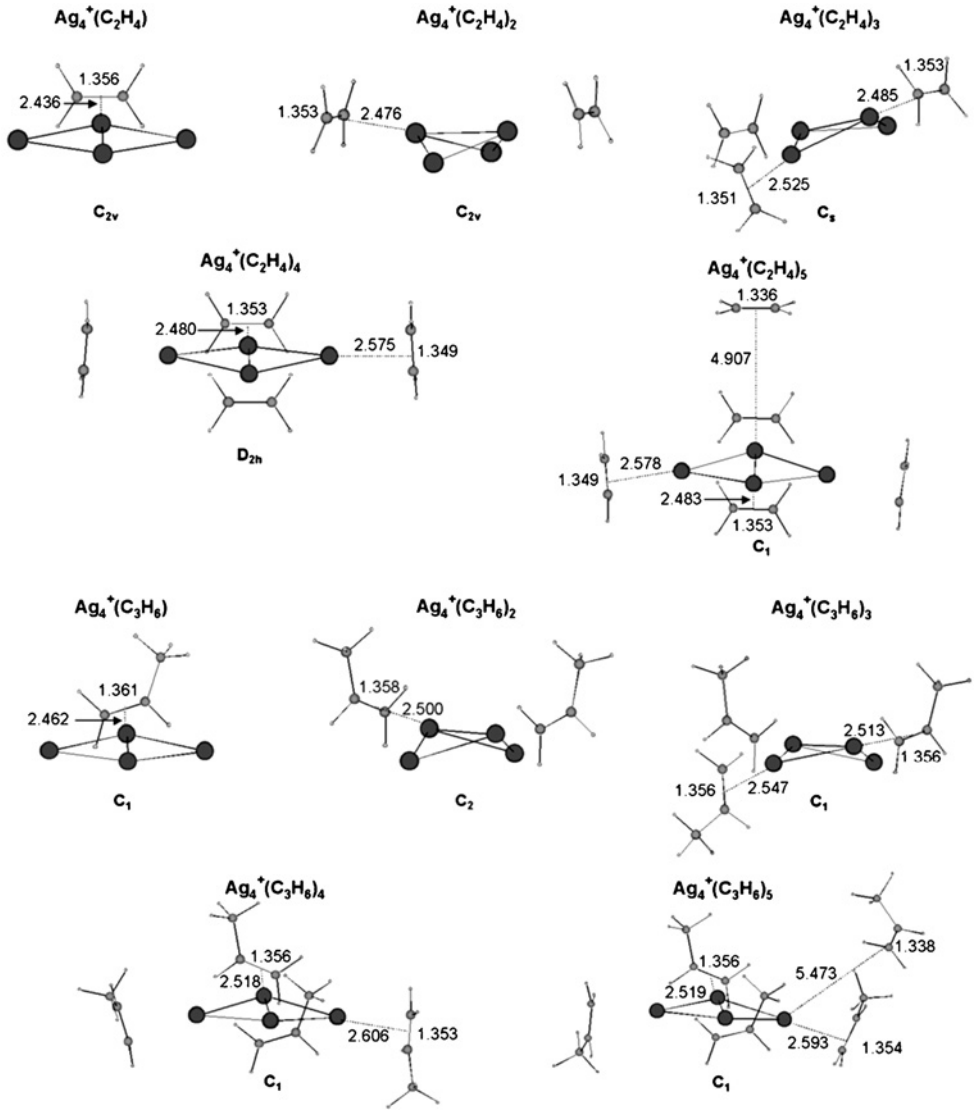

Figure 7: Theoretical geometries of the $Ag_4^+(L)_n$ clusters (L = either C_2H_4 or C_3H_6) calculated at the DFT B3LYP level. Distances are in angstroms. All $Ag_4^+ - L$ bond distances are measured from the bonding atom of the Ag_4^+ ion to the center of the C–C double bond.

corners. The first four ligands bind to individual corners of the Ag_4^+ cluster until none remain. Since the four corners of Ag_4^+ have similar partial-positive charges, each ligand donates similar amounts of electron density to the transition metal cluster, although the amount does slightly decrease as the number of ligands bound to the metal cluster increases. This decrease is due to increased Pauli repulsion caused by the increase in the amount of electron density present on the metal cluster and can be observed experimentally by small decreases in the BDEs of the $Ag_4^+(L)_n$ systems as n goes from 1 to 4.

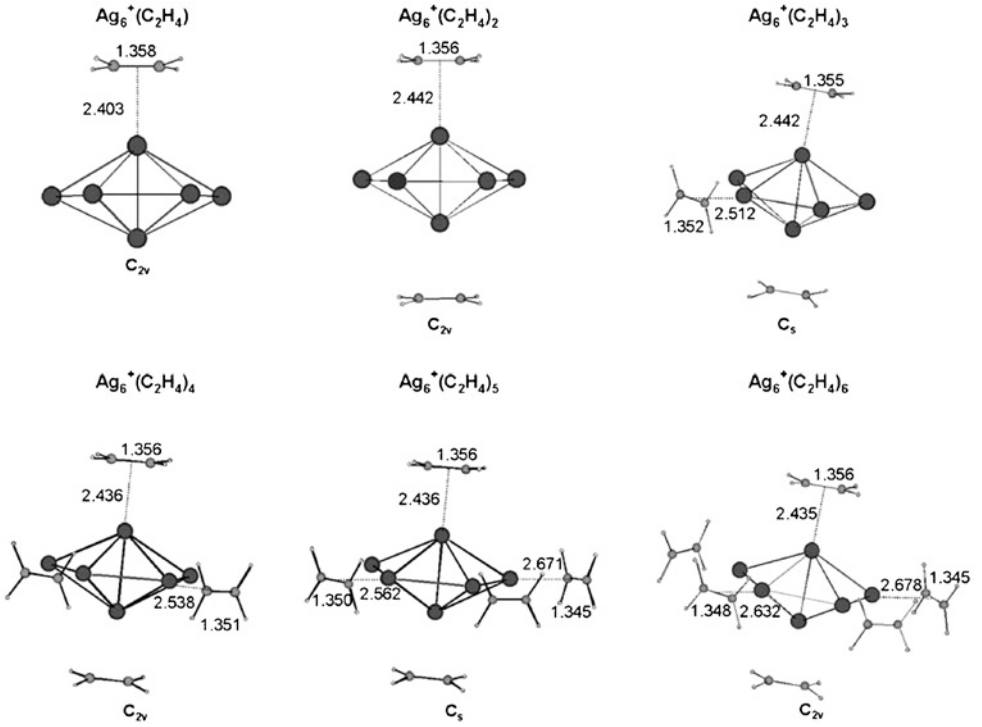

Figure 8: Theoretical geometries of $Ag_6^+(C_2H_4)_n$ clusters calculated at the DFT B3LYP level. Distances are in angstroms. All $Ag_6^+ - C_2H_4$ bond distances are measured from the bonding atom of the Ag_6^+ ion to the center of the C–C double bond. C_3H_6 additions to Ag_6^+ are analogous to the C_2H_4 system.

A slightly larger reduction in the BDE of the fourth alkene ligand addition to Ag_4^+ relative to the initial three is observed. This indicates that the $Ag_4^+(L)_3$ clusters may be unusually stable structures. The theoretical geometries given in Fig. 7 show that the Ag_4^+ core ion takes on a slightly bent conformation when the second ligand binds and remains that way until addition of a fourth ligand when the metal cluster returns to the original planar geometry. DFT indicates that an alternative $Ag_4^+(L)_3$ conformer exists that is energetically degenerate with the structure shown in Fig. 7 in which the Ag_4^+ core forms a tetrahedral structure with three ligands bound. The tetrahedral geometry of Ag_4^+ is only found to be stable when three ligands are attached and spontaneously reverts back to the structure of $Ag_4^+(L)_4$ shown in Fig. 7 when the fourth ligand adds. The increased stability of the tetrahedral geometry of Ag_4^+ when three ligands are bound may cause the addition of the fourth ligand to be energetically less favorable than would be the case if the Ag_4^+ core remained in a quasi-planar conformation.

The data for the fifth ligand addition to Ag_4^+ could only be taken over a limited temperature range for the C_3H_6 system (145–160 K) and for the C_2H_4 system only a single data point could be obtained. For all association reactions in which $n > m$ (Tables 1–4), an increase in association entropy occurs by approximately 10 cal/(mol K) relative to the $n = m$ association reaction. This increase indicates that the terminal ligand is much more mobile than the previous additions and hence occupies the second

solvation shell. Since all the coordination sites on the metal cluster are occupied, the ligand is essentially unbound.

The geometry and valence electron density of bare Ag_6^+ is given in Table 5. Six ligand additions are observed for the Ag_6^+ system (Fig. 8). The first two ligand additions to Ag_6^+ are very strongly bound (Tables 1–4). The association entropies, especially for the C_2H_4 system, are also outside the range of typical silver–alkene ligand additions (–20 to –30 cal/(mol K)). The reasons for the large BDEs and association entropies of these additions will be discussed in a subsequent section. The BDEs of the next four ligand additions to Ag_6^+ are significantly reduced compared with the initial two. However, the third and the fourth ligands add with similar BDEs as do the fifth and sixth ligands. In essence, the six alkene ligands bind to Ag_6^+ in a "pairwise" manner.

NBO analysis indicates that there is a large amount of positive charge located on the atoms of Ag_6^+ where the first two ligands bind. This allows the two ligands to donate relatively large amounts of electron density to the metal cluster. There is a large drop in the amount of positive charge located on the four remaining Ag atoms of the cluster. This gives rise to the reduced BDEs of the final four ligand additions to Ag_6^+. These ligands bind to the cluster in a region of relatively high electron density and the increased Pauli repulsion results in a reduction in the covalent interactions of the ligands with Ag_6^+. However, the positive charge found in this region is also unequally distributed, with the Ag atoms where the third and fourth ligands bind being slightly more positively charged than Ag atoms where the fifth and sixth ligands add to the cluster. We believe this pairwise distribution of charge is responsible for the manner in which alkene ligands add to Ag_6^+.

3.2.1. Cluster structures from ligand binding energies

In the interest of brevity, only the results for the silver/ethene system will be shown here. However, all results for the silver/propene system are analogous to the ethene system. Others have used ligand attachment to infer metal cluster structure. Usually "saturation" experiments are performed and a set of empirical rules used to interpret the data [72, 73]. Here, we take a different approach. We have stated that recent theoretical work indicates the LUMO on Ag and Au clusters is primarily located on "corner" atoms in the cluster [74–76] and that the LUMO location strongly affects the charge distribution in Ag_m^+. We have also shown that for electron donating ligands like C_2H_4, the binding energy at a particular cluster site correlates with the charge distribution. Thus, our hypothesis is that measured bond energies will allow us to identify equivalent, or near equivalent, "corners" in the clusters and therefore can be used to deduce structural information about the cluster.

A plot of ΔG_T° vs. T for the first four C_2H_4 ligand additions to Ag_3^+ is shown in Fig. 9. The first three additions form a family, having similar values of ΔH_T° and ΔS_T°. The fourth ligand is much less strongly bound with a more positive value for ΔS_T°. These data suggest three similar binding sites for the first three ethene ligands with the fourth C_2H_4 occupying a second solvation shell. The data are consistent with the triangular lowest energy theoretical structure shown in Table 5.

There is little ambiguity with the Ag_3^+ and Ag_4^+ systems. This changes with Ag_5^+. The ΔG_T° vs. T data are shown in Fig. 10. Six ligand additions are observed. The first two yield similar thermodynamic quantities. The third addition gives values of $-\Delta H_T^\circ$ and $-\Delta S_T^\circ$ that are substantially larger than the previous two additions. The fourth and

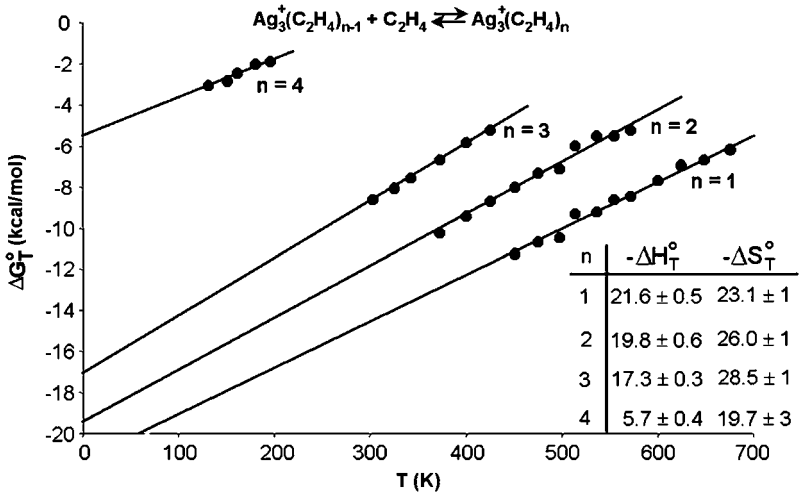

Figure 9: Plot of ΔG_T° vs. temperature data for the Ag_3^+/C_2H_4 system. ΔH_T° (kcal/mol) and ΔS_T° (cal/(mol K) in insert.

fifth additions form a family of less strongly bound ligands and the sixth ligand appears to add in the second solvation shell. Thus, experiment indicates two equivalent "strong" sites, a third even stronger site not originally available, two weaker sites, and then the second solvation shell.

Two Ag_5^+ cluster geometries are shown in Fig. 11. The lowest energy structure has four equivalent corners carrying the positive charge and a central atom with essentially no charge. The first two additions are consistent with this structure.

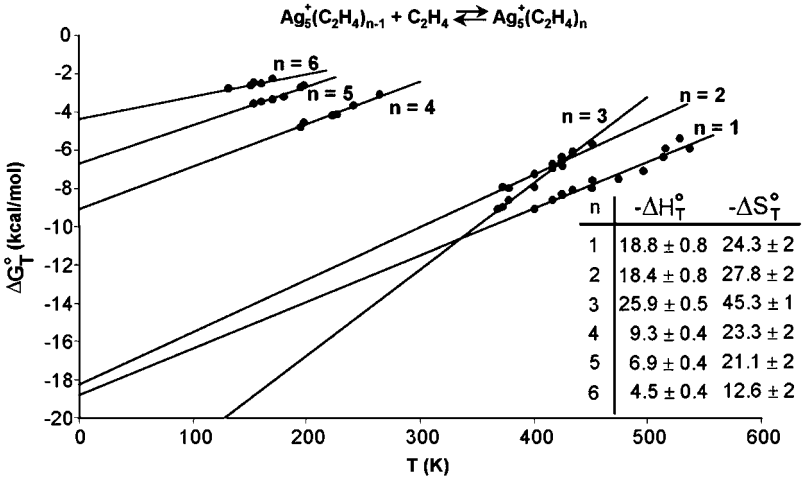

Figure 10: Plot of ΔG_T° vs. temperature data for the Ag_5^+/C_2H_4 system. The $n = 3$ data points are shown in gray for clarity. ΔH_T° (kcal/mol) and ΔS_T° (cal/(mol K) in insert.

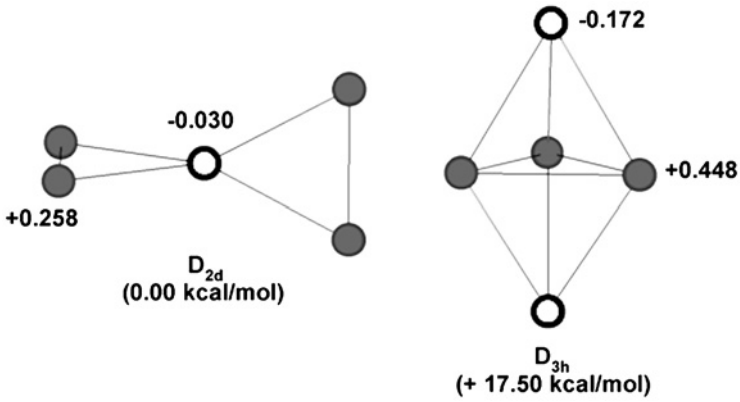

Figure 11: Calculated Ag_5^+ structures obtained from DFT. Ag atoms with equal charge distributions are colored identically for a given cluster. Charges are taken from NBO population analysis. Energies reported for the Ag_5^+ cluster are relative to the D_{2d} conformer (DFT).

However, the next three additions are not. The second Ag_5^+ structure, 17.5 kcal/mol higher in energy, is consistent with three strong additions followed by two weak additions. The data suggest a structural change upon addition of the third ligand from the D_{2d} lowest energy structure to the D_{3h} higher energy structure. Based on the measured binding energies, this process becomes exoergic on addition of the third C_2H_4 ligand. DFT also indicates that the D_{3h} conformation of Ag_5^+ becomes the minimum energy structure of Ag_5^+ when the third ligand binds (by 1.19 kcal/mol for C_2H_4 and approximately degenerate for C_3H_6). The three atoms of the D_{3h} conformer, shown in gray (Fig. 11), are highly positively charged. The structural rearrangement of Ag_5^+ allows for greatly increased covalent interactions with these three ligands.

NBO indicates that some back-donation from Ag_5^+ to the unoccupied $\pi^*(2p_y)$ orbitals of the alkene ligands takes place. Additionally, calculations show the loss of low frequency vibrational modes that are found for most of the other $Ag_m^+(L)_n$ clusters indicating tighter, more ordered bonds. The strengthening and tightening of all three ligand bonds is responsible for the highly negative value of ΔS_T° and the large BDE for loss of the third ligand. Note that the D_{3h} structure cannot be the initial gas-phase structure since we would have seen a family of three similar additions for the first three ligands.

In order to test this interpretation, Ag_5^+ was ligated with CH_4, a more weakly binding ligand than C_2H_4. In this case, the first four ligands have similar binding energies and entropies while the fifth occupies the second solvation shell. These results are entirely consistent with the lowest energy D_{2d} Ag_5^+ structure, which has four equivalent binding sites and with the fact that CH_4 ligation energies are too weak to induce structural isomerization of Ag_5^+.

For Ag_6^+ and Ag_7^+, the number of observed C_2H_4 additions equals the number of atoms in the two clusters, respectively. In both systems, the first two C_2H_4 ligands are strongly bound. For Ag_7^+, the final five additions yield similar ΔH_T° and ΔS_T° values. As previously mentioned for Ag_6^+, the final four ligands bind to the cluster in a pairwise manner. Hence, the experiment predicts that there are three sets of two equivalent binding sites for Ag_6^+ and a set of two and a set of five equivalent sites for

Ag_7^+. For both Ag_6^+ and Ag_7^+ (Table 5), DFT indicates that the two atoms that lie above and below the planar region of the clusters have relatively high partial-positive charge. The planar region of Ag_7^+ is a pentagon, consistent with five equivalent additions of C_2H_4. In Ag_6^+, the four planar Ag atoms of the cluster are not equivalent. The electron density is asymmetrically distributed giving rise to two, distinguishable pairs of Ag atoms. The experiment is again in excellent agreement with the DFT calculations indicating that the planar region of Ag_6^+ does not comprise four equivalent atoms.

The BDEs of the first alkene ligand additions to the Ag_m^+ clusters ($m = 1$–13 for C_2H_4 and $m = 1$–9 for C_3H_6) are plotted as a function of silver cluster size (m) in Fig. 6. The BDEs of the first ligand additions decrease as m increases. The Ag_6^+ and Ag_7^+ systems are exceptions to this trend. The BDEs for the loss of a ligand from $Ag_{6,7}^+(L)$ are comparable to those for the $Ag_{2,3}^+$ systems. Some deviation from the trend is also observed for C_2H_4 additions to the larger silver clusters. The BDEs for loss of a ligand from $Ag_{12,13}^+(C_2H_4)$ are slightly larger than for the $Ag_{10,11}^+$ systems. However, the differences in the BDEs of these systems are quite small (<2 kcal/mol).

In order to understand the observed bonding trend, the electron distributions of the Ag_m^+ clusters must be examined (Table 5). The strongest silver–alkene bond formed is observed for the monomer systems. Here, the $\pi(2p_y)^2$ electron density is donated from the alkene ligand to the unoccupied 5s orbital of Ag^+. The amount of positive charge the first ligand encounters at the binding site is $+1$. For the dimer, a single electron occupies the $\sigma(5s)$ orbital of the cluster. The amount of positive charge that the first ligand encounters at a binding site is reduced to $+0.5$ due to symmetry. Each additional increase in the size of a silver cluster (by adding on Ag atom) results in one additional electron that is distributed in some manner about the atoms that comprise the cluster. The additional electron density usually reduces the amount of positive charge at the atomic center encountered by a ligand attempting to bind to the cluster. The result is a systematic decrease in the covalent interactions of the Ag_m^+ clusters with the alkene ligands as the cluster size (m) increases.

The explanation for why the Ag_6^+ and Ag_7^+ systems break from the trend can be found by examination of Table 5. Ag_6^+ and Ag_7^+ are the first bare silver clusters to have 3-D geometries. The onset of 3-D conformations brings about an interesting shift in the electron configuration. NBO indicates that the valence electron density is mainly distributed about the four atoms shown in red and green for Ag_6^+ and about atoms shown in red for Ag_7^+. This leaves the two remaining Ag atom of both clusters highly positively charged. The amount of positive charge encountered by a ligand binding to one these sites is intermediate between the Ag_2^+ and Ag_3^+ systems and leads to the relatively large BDEs of the first (and second) ligand additions to Ag_6^+ and Ag_7^+. As with the $Ag_5^+(L)_3$ clusters, calculations indicate that back-donation from Ag_6^+ and Ag_7^+ to the unoccupied $\pi^*(2p_y)$ orbitals of the alkene ligands also plays a role in the bonding. This contributes to the highly negative ΔS_T° values of these association reactions.

Although the structures of the larger Ag_m^+ clusters ($8 \leqslant m \leqslant 13$) are also 3-D, no large concentration of positive charge is found on the atoms of these clusters. Instead, the electron density of these clusters is distributed somewhat evenly about all the atoms leading to the observed decline in the BDEs of the first ligand additions.

Information about the approach to bulk-phase properties of silver can also be extracted from the plot in Fig. 6. It is clear from the graph that the BDEs of the first

ligand additions to the clusters are asymptotically approaching some value. The energy required to remove a C_3H_6 and a C_2H_4 ligand from an Ag(1 1 0) surface has been measured to be approximately 12 kcal/mol [78] and 10 kcal/mol [79], respectively. For Ag_9^+, the BDE for loss of the C_3H_6 ligand is still larger than the value for propene desorption from bulk silver and the BDE for Ag_{13}^+ for loss of C_2H_4 is also larger than the value for ethene desorption. However, the Ag_m^+ systems are rapidly nearing these values by the time the ninth (thirteenth) cluster is reached. This implies that the Ag_m^+ clusters may arrive at their bulk-phase properties fairly quickly, most likely at sizes of tens of atoms rather than at sizes of hundreds or thousands of atoms. However, deviations from the trend shown in Fig. 6 cannot be ruled out at some larger Ag_m^+ cluster size.

3.3. $Au_m^+(C_2H_4)_n$ ($m = 1$–9) association reactions

The results for the gold clusters will be discussed more briefly since there are many similarities with the silver clusters. Only results for the ethane addition will be given here.

Binding energies (ΔH_T°) and association entropies (ΔS_T°) were measured for each sequential ligand addition. These values are given in Tables 6 and 7, respectively. The structures consist of an Au_m^+ core ion surrounded by largely unperturbed C_2H_4 ligands (Fig. 12).

3.3.1. Polyatomic gold cations

Au_3^+ is the first gold cluster where multiple conformations are possible. As such, the Au_3^+ system serves as a prototype for the analysis of the larger Au_m^+ clusters. First, the transition metal core ion geometries must be determined to correctly characterize their interactions with any ligating species. Second, the binding interactions of Au_3^+ with C_2H_4 establish a pattern that is essentially followed by the larger Au_m^+ clusters discussed below. Both aspects were investigated using the measured thermodynamic values in combination with ab initio calculation for each of the Au_m^+ ($m = 3$–9) clusters. Five C_2H_4 ligand additions are observed to bind to Au_3^+. The first three ligands

Table 6: $Au_m^+(C_2H_4)_{n-1} + C_2H_4 \rightleftarrows Au_m^+(C_2H_4)_n$ binding energies $(-\Delta H_T^\circ)$[a].

m	n						
	1	2	3	4	5	6	7
1	60[b]						
	71.2±2.5[c]	59.6±2.8	13.4±0.5	3.7±0.8			
3	41.6±2.7	44.0±1.0	31.3±0.5	6.5±0.6	~3.0[d]		
4	41.1±4.0	42.6±1.4	32.1±0.7	21.8±0.7	8.9±0.7	6.2±0.7	
5	39.6±2.8	36.4±1.3	31.4±1.0	26.2±1.0	20.0±1.0		
6	36.4±2.0	31.5±0.7	27.3±1.0	24.4±0.7	20.4±1.0	18.8±0.6	~4.5[d]
7	41.4±1.5	31.8±1.1	30.0±1.5	22.9±1.5	19.2±1.0	20.2±0.8	~4.5[d]
8	30.7±0.7	31.5±1.1	29.4±0.9	23.3±1.0	20.9±1.0	~14.1	~13.5
9	28.0±0.7						

[a]In units of kcal/mol.
[b]Estimated lower limit.
[c]Estimated upper limit.
[d]Estimate, values obtained from two data points.

Table 7: $Au_m^+(C_2H_4)_{n-1} + C_2H_4 \rightleftarrows Au_m^+(C_2H_4)_n$ association entropies $(-\Delta S_T^\circ)$[a].

m	N						
	1	2	3	4	5	6	7
1	–	45.2±4	26.2±2	14.9±3			
3	26.5±3	36.0±2	34.9±1	16.0±3	~8.5[b]		
4	31.0±5	37.2±2	37.6±2	32.3±2	26.4±4	21.0±4	
5	29.2±4	30.1±2	35.9±2	37.9±2	43.1±3		
6	28.2±3	32.1±2	31.8±2	35.0±1	36.3±3	38.0±2	~15.0[b]
7	33.9±3	36.2±2	37.6±3	36.7±4	32.6±3	40.0±2	~15.0[b]
8	29.9±1	36.7±1	38.1±2	32.2±2	34.7±3	~28.6	~29.0
9	29.7±1						

[a]In units of cal/(mol K).
[b]Estimate, values obtained from two data points.

bind with similar strength and association entropies to Au_3^+. A large drop in binding energy is observed for the relatively weakly bound fourth and fifth C_2H_4 additions along with more positive values of ΔS_T°. Therefore, the experimental data suggest that Au_3^+ comprises three equivalent binding sites.

The bare Au_3^+ geometry has been reported to be an equilateral triangle by Kappes and co-workers [42]. DFT predicts that the "corners" of Au_3^+ are electronically equivalent, meaning here that they carry equal amounts of partial positive charge. This is in agreement with the thermodynamic data reported here. The weak binding energies and relatively positive association entropies of the fourth and fifth ligand additions indicate that bonding occurs in the second solvation shell of Au_3^+. These findings are also in agreement with the work of Fielicke et al. [56] in which Au_3^+ is found to be saturated by the addition of three CO ligands at relatively high CO partial pressures. The results of the Kappes group were used as the basis for our own DFT calculations to determine NBO populations for all the Au_m^+ ($m = 3$–9) clusters. These results are given in Table 8 along with the bare gold cluster geometries.

The interpretation of the binding energy trends for ligand addition to Au_3^+ and Au_4^+ is similar to Ag_3^+ and Ag_4^+. However, five strong ligand additions to Au_5^+ are observed (Table 6). All of the C_2H_4 ligands bind with roughly similar values of ΔS_T° (Table 7) and a systematic decrease of approximately 5 kcal/mol in binding energy is observed for each sequential C_2H_4 addition after the second.

The bare cluster geometry of Au_5^+ is a "bow tie" (Table 8). DFT calculations predict that the cluster has four, electronically equivalent corners. The fifth "central atom" of Au_5^+ is essentially neutral and not considered to be a binding site. Thus, four equivalent C_2H_4 additions are expected for this conformation of Au_5^+. Clearly, this is not consistent with the thermodynamic data.

In order to resolve this disagreement, a series of DFT calculation was performed in which multiple conformation of Au_5^+ were ligated with C_2H_4 to determine the minimum energy $Au_5^+(C_2H_4)_n$ ($n = 1$–5) cluster geometries. The results indicate that the first four ligands do, in fact, add to the corner atoms of the D_{2d} structure reported by the Kappes group (Fig. 12). When a fifth ligand adds to the D_{2d} Au_5^+ conformer, DFT suggests that it coordinates in the second solvation shell. This second solvation shell addition of the fifth ligand is not consistent with the experimental data, which in turn

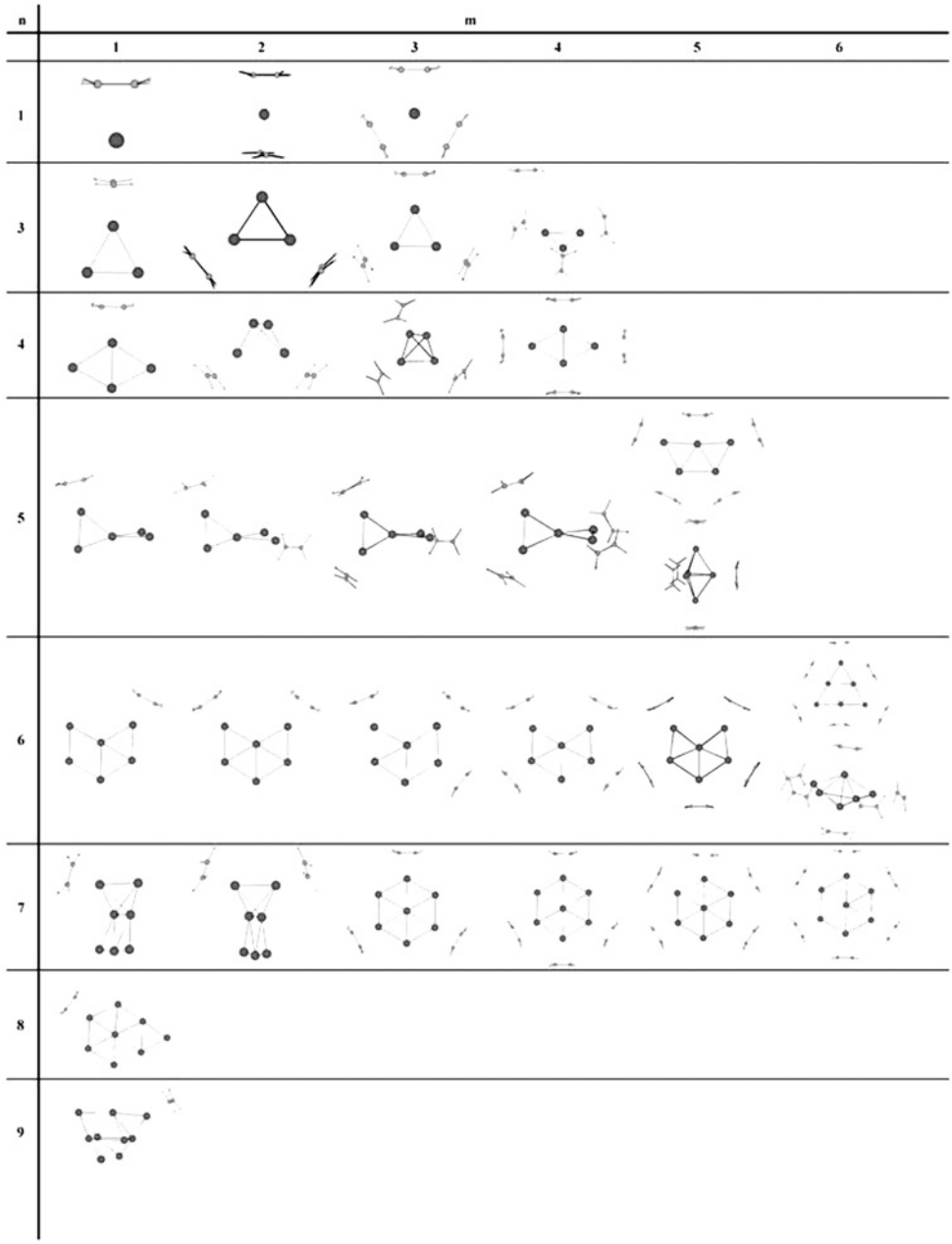

Figure 12: Theoretical geometries of $Au_m^+(C_2H_4)_n$ clusters calculated at the DFT B3LYP level.

suggests that the structure of Au_5^+ changes when the fifth ligand adds in order to accommodate this ligand in the first solvation shell. Figure 12 shows two possible, energetically degenerate conformations of the $Au_5^+(C_2H_4)_5$ cluster. Both structural rearrangements of the Au_5^+ core allow the fifth atom of the cluster to be accessed as a binding site for a C_2H_4 ligand. However, it should be noted that the DFT energies of

Table 8: Natural bond order populations and charges of the Au_m^+ clusters ($m = 3$–9).

m	Structure[a]	Symmetry	Populations[b]	Charges[b]
3		D_{3h}	0.707	0.333
4	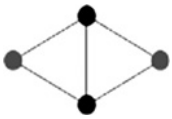	D_{2h}	0.753 0.843	0.29 0.21
5		D_{2h}	0.744 1.005	0.246 0.015
6(a)		C_{2v}	0.839 0.804 0.910 0.981	0.218 0.200 0.147 0.071
6(b)	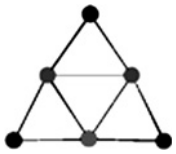	C_{2v}	0.788 0.856 0.944 0.967	0.270 0.259 0.124 0.112
7	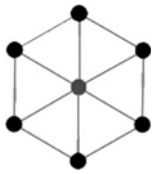	D_{6h}	0.888 0.948	0.152 0.090
8(a)		C_{2v}	0.862 0.905 0.937 0.952 0.997	0.180 0.143 0.128 0.097 0.064
8(b)	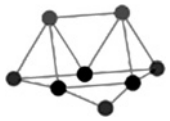	C_s	0.833 0.892 0.914 0.981	0.204 0.147 0.128 0.080
9	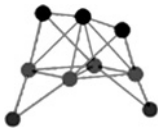	C_{2v}	0.814 0.900 1.005 1.016	0.211 0.140 0.067 0.048

[a]Au_m^+ ($m = 3$–9) cluster geometries obtained from ion mobility data [42] and DFT calculations. Au atoms of a given cluster having equal charge distributions are identically colored.
[b]Populations for the 6 s atomic orbitals of the Au atoms of each cluster and the corresponding partial atomic charge. Text color corresponds to analogously colored atoms of a given structure.

both of these $Au_5^+(C_2H_4)_5$ conformers are similar to that of the fifth C_2H_4 addition to the second solvation shell of the D_{2d} Au_5^+ isomer. All three $Au_5^+(C_2H_4)_5$ structures differ in energy by approximately 3 kcal/mol.

In order to test our interpretation of the data, Au_5^+ was ligated with CH_4. The experiment was conducted at very low temperatures and high CH_4 pressures to determine the saturation number for Au_5^+ with a weakly binding ligand such that the ligation energetics would not be sufficient to facilitate structural rearrangement of the transition metal core. The experiment did, in fact, show that four ligand additions to Au_5^+ was the dominant peak in the mass spectrum, as expected from the structure of Au_5^+ reported by the Kappes group. All these results are also consistent with those reported by Fielicke and co-workers where a saturation number of four was rapidly obtained for CO ligands adding to Au_5^+ [56]. However, the system did go on to add a fifth ligand more slowly at higher CO pressures. This result was also interpreted as a possible structural rearrangement of Au_5^+.

A summary of the results for the Au_6^+/C_2H_4 system is given in Tables 6 and 7. Seven ligand additions to Au_6^+ were observed. The first six C_2H_4 ligands bind with roughly similar values of ΔS_T°, and a systematic decrease of approximately 4 kcal/mol in binding energy is seen for each sequential addition. The seventh ligand binds significantly more weakly to Au_6^+ and has a much more positive association entropy.

The Au_6^+ cluster is especially interesting because its bare gas-phase conformation could not be unambiguously determined by ion mobility and DFT. The Kappes group reported two possible structures for Au_6^+ whose cross-sections are essentially the same and that are energetically degenerate according to DFT. Both structures are shown in Table 8.

Initially, the thermodynamic data for the Au_6^+/C_2H_4 system seem to support the triangular conformation of Au_6^+. However, upon closer inspection, this turns out not to be entirely true. A series of DFT calculations were carried out in which C_2H_4 ligands were sequentially added to both Au_6^+ conformers and indicated that the first five C_2H_4 additions to conformer Au_6^+(a) are lowest in energy. The sixth ligand was added to conformer Au_6^+(a) in the second solvation shell, inconsistent with the experimental data. The sixth ligand addition to the triangular conformation of Au_6^+ does form a bond in the first solvation shell; however, this conformation of $Au_6^+(C_2H_4)_6$ is considerably higher in energy (16.58 kcal/mol) than the alternate, 3-D Au_6^+ geometry with six bonded C_2H_4 ligands also shown in Fig. 12. This 3-D conformation of Au_6^+ is similar to the structure that has been reported for Ag_6^+ [43]. These results indicate that conformer Au_6^+(a) (Table 5) may well be the nascent geometry of Au_6^+ but that the cluster probably undergoes a conformational shift to the 3-D structure driven by the ligation energetics of the sixth C_2H_4 addition.

To test this, CH_4 saturation experiments were again performed with Au_6^+. A saturation number of five CH_4 additions to Au_6^+ was observed, consistent with our interpretation of the Au_6^+/C_2H_4 data. These findings are again in agreement with what has been reported by Fielicke et al. [56] where a saturation number of five is rapidly obtained for CO ligands adding to Au_6^+ and a sixth ligand adds more slowly at higher CO pressures indicating a possible structural rearrangement of Au_6^+.

Seven C_2H_4 additions to Au_7^+ are observed. The binding energies form an interesting pattern. The first addition binds relatively strongly to Au_7^+. The second and third additions bind with similar ΔH_T° and ΔS_T° values. There is a drop in binding energy of

approximately 11 kcal/mol for the second addition compared with the first. The fourth, fifth, and sixth ligands addition bind more weakly to Au_7^+ with similar thermodynamic values and the seventh ligand binds even weaker than the previous three with a more positive value of ΔS_T°.

The ion mobility/DFT structure of Au_7^+ is shown in Table 8. Au_7^+ is a hexagon with one Au atom coordinated at the center of the six-member ring. The thermodynamic data suggest that six ligands bind to Au_7^+ in the first solvation shell and that the seventh ligand begins the second shell. This is consistent with the symmetric geometry shown in Table 8. However, the data also show that the first six C_2H_4 additions can be separated into three distinguishable families and this is not in agreement with the highly symmetric geometry of Au_7^+.

The nonequivalent bonding of the six C_2H_4 ligands suggests that the structure of the Au_7^+ cluster may change as a result of ligand addition. Consequently, DFT calculations were carried out in which C_2H_4 ligands were added to multiple conformations of Au_7^+, including the unligated gas-phase structure, in order to determine a series of minimum energy structures. The minimum energy conformation of the $Au_7^+(C_2H_4)$ cluster (Fig. 12) is obtained by geometric rearrangement of the transition metal core ion into a 3-D structure. This structure is predicted by DFT to be 1.91 kcal/mol higher in energy than the D_{6h} isomer when no ligands are bound to either conformer. The 3-D conformation of Au_7^+ has also been reported to be the minimum energy theoretical geometry of the $Au_7^+(CO)$ cluster [80]. Thus, DFT indicates that a change in the structure of Au_7^+ occurs when the first C_2H_4 ligand binds.

Although the structural rearrangement of Au_7^+ can be used to rationalize the nonequivalent bonding of the system, a new problem arises. Namely, the 3-D conformations of Au_7^+ contains seven binding sites for C_2H_4 addition. This is not in agreement with the experimental data that indicate six ligand-binding sites and a seventh ligand addition in the second solvation shell. To address this issue, calculations of $Au_7^+(C_2H_4)_n$ clusters using multiple Au_7^+ geometries were continued for ligand additions beyond the first C_2H_4. These DFT results indicate that when the third C_2H_4 ligand binds, the original bare cluster geometry of Au_7^+ re-emerges as the minimum energy conformation. This implies that a second structural rearrangement occurs that shifts Au_7^+ back to its original geometry when the third ligand adds. Furthermore, subsequent ligands seem to bind to this conformation of Au_7^+.

The multiple ligation-induced conformational shifts of Au_7^+ are consistent with the families of ligand additions observed in the thermodynamic data. DFT indicates that the first C_2H_4 ligand binds strongly to the minimum energy 3-D Au_7^+ isomer. The subsequent drop in binding energy observed for the second ligand addition is quantitatively reproduced by theory. When Au_7^+ returns to its original geometry, DFT reproduces the drop in the binding energy of the fourth ligand addition and indicates that the fifth and sixth ligand binding energy will be similar to the fourth.

Seven C_2H_4 ligand additions are observed to Au_8^+ and form a 3:2:2 pattern. The last two ligands are bound much more weakly than the first five but still appear to be in the first solvation sphere from analysis of the experimental ΔS_T° values associated with each of the two additions.

The Au_8^+ system is obviously complex and the most we can say is that the present data are consistent with the planar form of the Au_8^+ core (Table 8). Seven ligands should add. NBO predicts two strong C_2H_4 bonds, three somewhat weaker bonds, and finally two

quite weak bonds. This agrees well with the observed experimental binding energies. We were unable to fully saturate Au_8^+ with CH_4 to test for the nascent 3-D structure nor were calculations with serial C_2H_4 additions successful. Multiple C_2H_4 coordination sites gave essentially degenerate ligation energies for later additions and identifications of a preferred structure became impossible. In the case of $Au_8^+(C_2H_4)_2$, for example, three structures were found that differed in energy by approximately 1 kcal/mol. Consequently, only the minimum energy $Au_8^+(C_2H_4)$ structure is shown in Fig. 12.

3.4. Conclusions

Here, we have sought to demonstrate the rich chemistry inherent to coinage metal clusters (Ag, Au) in the gas phase. Systematic investigation into the interactions of these clusters with small catalytically relevant ligands, including but not limited to ethene and propene, has revealed some of the underlying information necessary to elucidate the nature of their catalytic properties. Specifically, some of these findings include the binding energies and association entropies for sequential clustering of alkene ligands to $M_m^{+/-}$ ($m<14$) clusters (M = Ag, Au). The ligand binding is unique to each metal cluster of a given size (m) and is governed by the electronic environment of the transition metal core ion. The primary binding interaction of the metal/alkene clusters is electron donation from the $\pi(2p_y)^2$ orbital of the ligands into the LUMO of the $M_m^{+/-}$ clusters. In all systems studied, the location of the LUMO of a given $M_m^{+/-}$ cluster directly correlates with the position of the metal atom of the cluster having the highest partial positive charge. Additions of alkene ligands to $M_m^+(L)_n$ clusters where $n>m$ and to some of the smaller anionic clusters ($m<9$) yield bonds that are essentially purely electrostatic (second solvation shell).

Global structures of gas-phase silver and gold cationic clusters can be obtained from sequential addition of ligands. These structures are consistent with theory. The method is also sensitive to ligand-induced changes in bare cluster conformations and results can be fine tuned by changing ligands and hence, ligand binding energies.

The binding energies of the first alkene ligand additions to Ag_m^+ were plotted as a function of cluster size. With the exception of the $Ag_{6,7}^+$ clusters, the BDEs for loss of the ligand from the Ag_m^+ clusters decrease as the size of the cationic silver clusters increase. These trends are attributed to a reduction of the affect of the charge of the metal clusters. The trends suggest that the binding energies of the Ag_m^+ clusters approach their bulk-phase values for m = 10's of atoms rather than 100's of atoms.

A similar trend was observed for the anionic clusters Ag_m^- where the binding energy of the first ligand addition increased with cluster size (data not shown). Both trends ($Ag_m^{+/-}$) approach the binding energies of C_2H_4 and C_3H_6 to the bulk silver surface.

4. Au_n^+ AND Ag_n^+ DEPOSITED ON TiO_2(1 1 0) SURFACES UNDER SOFT-LANDING CONDITIONS

4.1. Introduction

The catalytic activity of supported Au is currently explained in the literature from various positions ranging from strong interaction with the support to unique properties of the Au related to its nanoscale size [9, 81–83]. The most common method for studying the size dependence involves the use of model catalysts under UHV

conditions where Au nanoclusters are formed by vapor deposition from a gold source [9, 84–86]. Gold deposited in this way is known to sinter into large clusters of tens of atoms, and the less gold deposited, the smaller the resulting cluster size [87–91]. By controlling the amount of gold deposited, one can have some control over the size of the resulting cluster, but this is far from atom-by-atom control. Studying reactions occurring on these model catalysts having such a wide size distribution makes an atomistic model of the catalysis difficult.

A considerable improvement was made by the work of Heiz et al. [92] who prepared a model catalyst containing mass-selected clusters (all clusters in the system had the same number of atoms). This methodology has been used by Schneider, Heiz, and co-workers [14, 92–95] to do beautiful work on several systems. Heiz and co-workers showed that the activity in CO oxidation for Au_n clusters ($n < 20$) on MgO increases dramatically for Au_8 and peaks around Au_{18} [14]. Anderson and co-workers have performed room temperature CO oxidation over mass-selected Au clusters on titania, and found oscillations in activity, with activity occurring for clusters as small as three atoms in size, with a sharp increase in the catalytic activity for clusters of >5 atoms [96, 97]. In these few existing studies, using mass-selected clusters, an important piece of information is missing. No direct measurement of the size and shape of the nanoclusters were performed before or after the reaction. This information is critical to the development of an atomistic model of the catalysis, and is possible using atomic-resolution STM. Cluster size, shape, and binding site are probed directly by the STM.

4.2. Scanning tunneling microscopy of TiO_2

The clean titania surface appears in STM on a large scale (Fig. 13a) to consist of terraces a few hundred angstroms wide, and steps measuring ~3 Å in height, the latter of which is in agreement with the expected step height for the rutile titania (1 1 0)-(1 × 1) surface [98]. On a smaller scale (Fig. 13b), alternating bright and dark rows are visible, separated by ~6.5 Å. The consensus in the literature is that the bright rows are

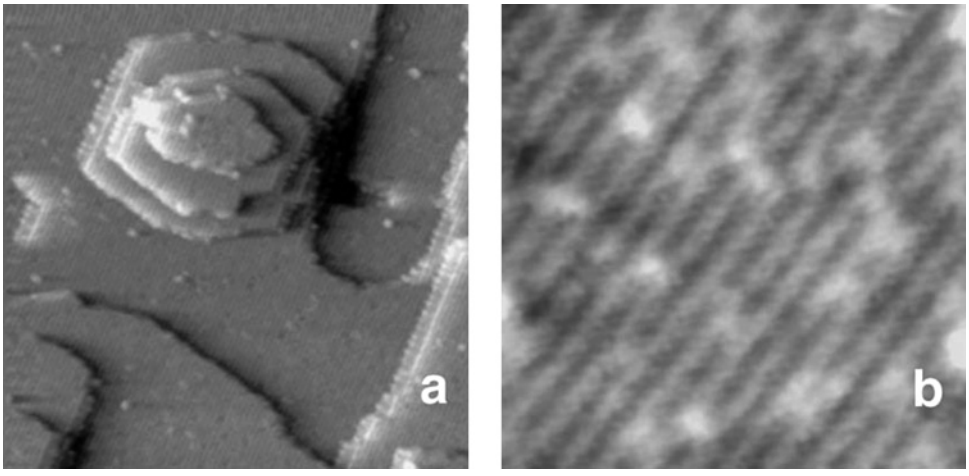

Figure 13: STM images of the clean surface: (a) on a larger scale (500 Å × 500 Å) terraces and step edges are visible, (b) on a smaller scale (90 Å × 90 Å) fivefold-coordinated Ti atom rows and bridging O atom rows are visible, as well as bright defect features between Ti atom rows.

fivefold coordinated titanium (5c-Ti) atom rows, while the dark rows are bridging oxygen atom rows [99]. The surface of titania following annealing in UHV also contains defect sites. The most discussed and most prevalent defects appear as bright spots between the 5c-Ti rows. Typically, these features have been assigned as bridging oxygen vacancies [99]; however, work by Suzuki et al. [100], and most recently by Wendt et al. [101], suggests that oxygen vacancies can convert to hydroxylated sites even in UHV due to the partial pressure of water present. The assignment of the bright features between the titanium atom rows using STM alone can be difficult due to the subtle differences between the two features. Previously reported by Schaub et al. [102], the features that were assigned to vacancies were thought to be slightly brighter than the features assigned to hydroxyls, though recently this assignment has been reversed [101], as the brighter features are now assigned to hydroxyl groups. Since the background of water in UHV is believed to cause the formation of hydroxyls, it is reasonable to assume that the exact percentage of hydroxyls on the surface is expected to change over time. It is important to note, however, that immediately prior to cluster deposition, the surfaces discussed here are briefly flashed to ~1000 K, therefore any hydroxyls on the surface at this point will be at least temporarily removed, as the desorption temperature of these species has been shown via thermal desorption to be ~500 K [103]. Interpretation of the bright features apparent between titanium atom rows after cluster deposition becomes even more difficult, since the clusters may alter the electronic nature of the surface. In our experiments, we assume that all OH groups are desorbed prior to metal deposition. In addition, STM experiments are performed within 3 h of the exposure to metal in vacuum in the 10^{-10} Torr region. We believe that under these conditions, the number of OH groups bound to vacancies is small.

4.3. Au_n^+ ($n = 1$–8) on TiO_2(1 1 0)

Figure 14 shows the results of the deposition of Au_n^+ on TiO_2(1 1 0). Figure 14A shows large clusters on the surface resulting from the deposition of Au_1^+. A magnified region of this image, shown in Fig. 14a, reveals that there are no small clusters on surface. These observations indicate that Au_1 monomers are highly mobile on the rutile surface, leading to aggregation into larger clusters. Figure 15a shows a broad height distribution for the deposition of Au atoms with an average value of 4.3 Å (Fig. 16) and a standard deviation of 1.7 Å. This result is similar to that observed from Au vapor deposition in the coverage region of 0.013–0.08 ML [87]. These sintered clusters have an average lateral diameter of 14.8 ± 3.9 Å, which indicates that an average cluster contains tens of atoms.

Figure 14B–H shows STM images taken after the deposition of Au_2^+ to Au_8^+, respectively. In contrast to the monomer deposition, large, sintered clusters are rarely observed. Instead, a high density of very small clusters is seen (Fig. 14b–h), implying limited mobility on the surface. The amount of metal on the surface was calculated from the incident flux and compared with that determined from the STM images, giving reasonable agreement. The height distributions of Au_n^+ ($n = 2$–8) are much narrower relative to that found in the case of the Au_1 deposition, as shown in Fig. 15.

The nearly uniform height and the preference for certain adsorption sites suggest that the dominant adsorbed Au_n^+ ($n = 2$–8) clusters remain intact during landing. As shown in Fig. 16, the average heights for Au_2, Au_3, and Au_4 clusters are 1.6 ± 0.5, 1.5 ± 0.2, and 1.7 ± 0.2 Å, respectively, suggesting that adsorbed Au_2, Au_3, and Au_4

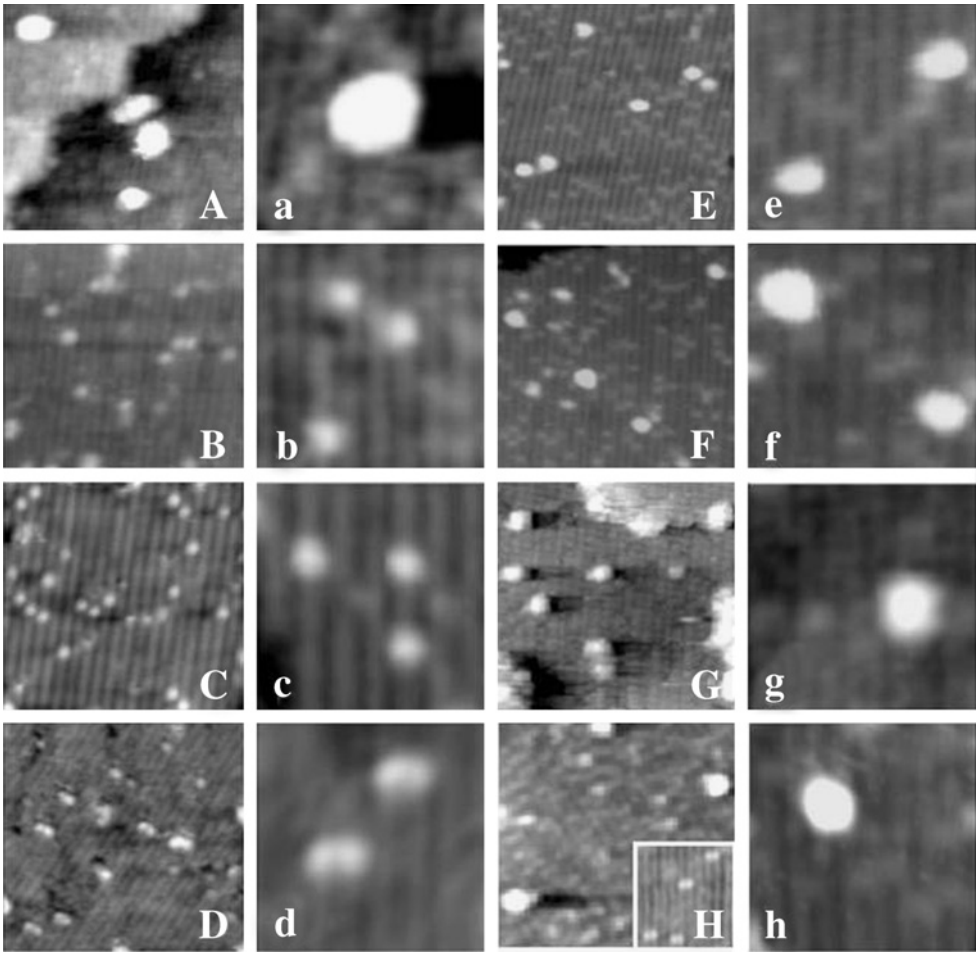

Figure 14: STM images 150 Å × 150 Å (uppercase letters) and 50 Å × 50 Å (lowercase letters) of the same surfaces, respectively. The bright spots are the clusters. The bright stripes in each image are the fivefold-coordinated Ti atom (5c-Ti) rows separated by the bridging oxygen rows which are dark [104]. The dim spots that appear on the bridging oxygen rows are bridging-oxygen vacancies [100, 105–107]. (A/a) The TiO_2 surface after the deposition of Au_1; (B/b) the same for Au_2; (C/c) the same for Au_3; (D/d) the same for Au_4; (E/e) the same for Au_5; (F/f) the same for Au_6; (G/g) the same for Au_7; and (H/h) the same for Au_8.

lay flat on the surface. In contrast, the clusters of Au_5, Au_6, Au_7, and Au_8 have an average height of 2.6 ± 0.6, 2.3 ± 0.7, 2.8 ± 0.7, and 2.7 ± 0.9 Å, respectively. This suggests that these clusters bind to the surface such that some of the atoms in the cluster are away from the surface. This is indicative of a tilted or bi-layer structure for these clusters.

Insight into the binding site and detailed structure of the adsorbed cluster can be gleaned by comparing the atomically resolved STM image of an isolated cluster with structures obtained from DFT calculations. In STM, we obtain the position of the cluster relative to the 5c-Ti rows and the bridging O rows, the height of the cluster, and the lateral size of the cluster including any asymmetry. It is worth noting that the

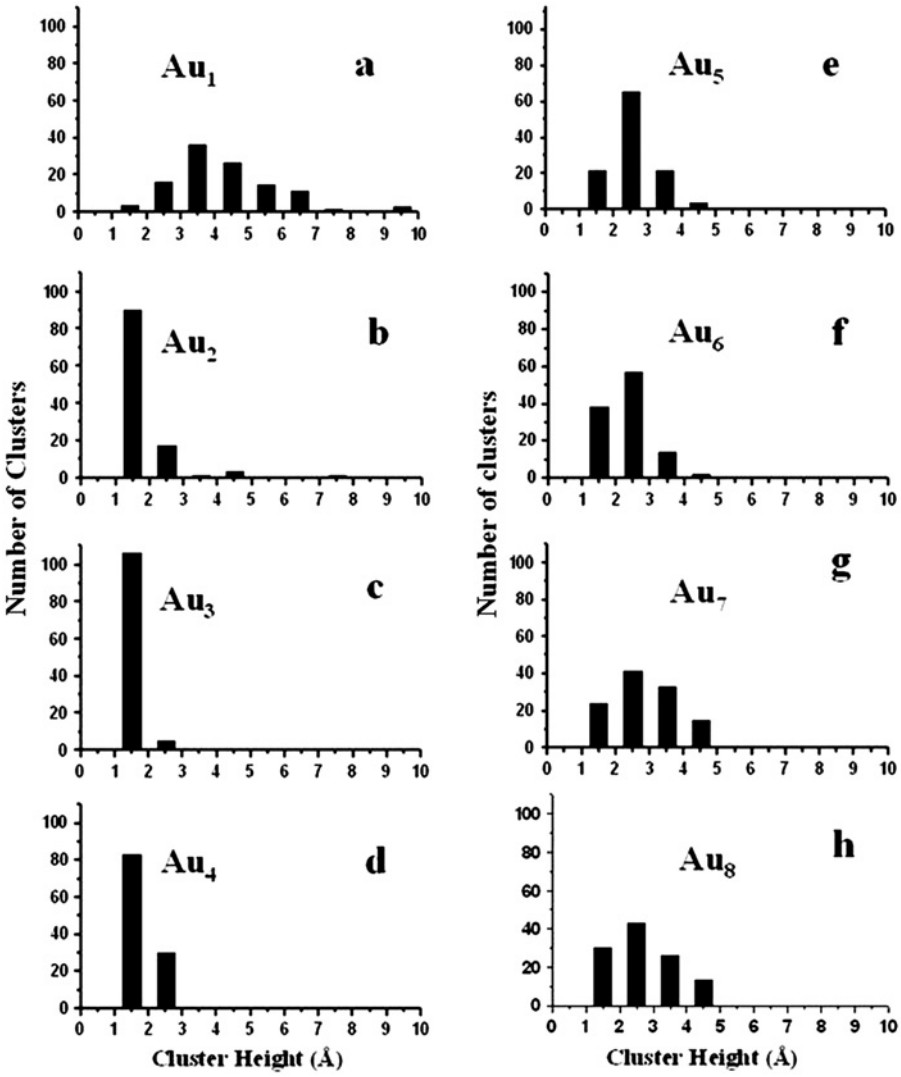

Figure 15: The cluster height distributions of deposited Au_n ($n = 1$–8) on TiO_2(1 1 0) surface.

position and height for each cluster is measured with high precision. The lateral size, however, is a convolution of the tip diameter and the cluster size. For very small clusters ($n < 5$), the tip diameter dominates and the lateral size of the spot in the STM image does not adequately represent the size of the cluster. For larger clusters ($n > 4$), it is possible to observe relative changes in the lateral size from one cluster to the next.

4.3.1. Structures of Au_n ($n = 1$–7) on TiO_2: comparing DFT structures with STM

In the DFT calculations, the desorption energy is maximized for all possible isomers of a given cluster on both the stoichiometric and reduced surfaces as described in

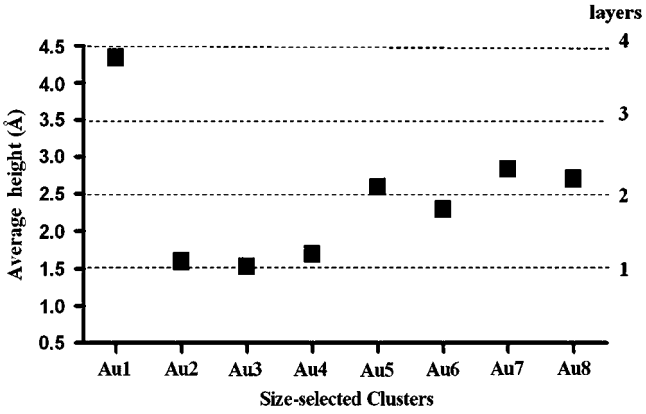

Figure 16: The average cluster heights of Au_n ($n = 1$–8) on $TiO_2(1\,1\,0)$-(1×1) surface. The dashed lines indicate heights expected for various gold layers in the cluster.

Section 2. The desorption energy (D_e) is displayed in the figures as a positive value. The desorption energy is numerically equal to the surface binding energy with opposite sign. To understand the trends in our data, it is important to remember that the larger the desorption energy, the more stable the structure on the surface.

Figure 17a and b shows STM images of the two types of Au_2 clusters bound to the surface. As mentioned above, all of the Au_2 clusters measured 1.6 ± 0.5 Å in height, indicating that they lay flat on the surface. The cluster shown in Fig. 17a is centered over the 5c-Ti row. This cluster is indicative of 78% of the more than 100 clusters observed in our experiments. The remaining 22% of the clusters appear centered over the bridging O rows (as seen in the image of Fig. 17b). The difference between the clusters of Fig. 17a and b suggests at least two different binding sites for Au_2 on the surface.

Detailed insight into the binding of Au_2 clusters on the surface is obtained from DFT. The lowest energy structures for Au_2 bound to the stoichiometric and reduced surfaces are shown in Fig. 17c and d, respectively. The cluster bound to the stoichiometric surface shows the gold dimer bound to the bridging oxygen atoms in adjacent rows with the center of the cluster over the 5c-Ti atom row. The STM of this cluster would be one layer of atoms tall and would be centered over the 5c-Ti rows, similar to the image of Fig. 17a. The lowest energy DFT structure for the reduced surface (Fig. 17d) shows the gold dimer bound over the vacancy, flat on the surface, and centered over the bridging O row. This structure is consistent with the STM image of Fig. 17b. Of the two DFT structures, the dimer bound to the vacancy has a binding energy 0.27 eV higher than the dimer bound to the stoichiometric surface. Based on this difference, one expects that if the Au_2 clusters are free to diffuse on the surface then all of these clusters would be bound to vacancies and exhibit an STM image centered over the bridging O rows. Based on our experimental data, however, most of the Au_2 clusters are centered over the 5c-Ti rows, this suggests that the Au_2 clusters are not mobile on the surface and that most are bound to the stoichiometric surface. Furthermore, the fraction of clusters bound to the reduced surface is close to the amount one expects from a statistical distribution. The fraction of clusters bound to vacancies is approximately equal to the probability of landing near a vacancy

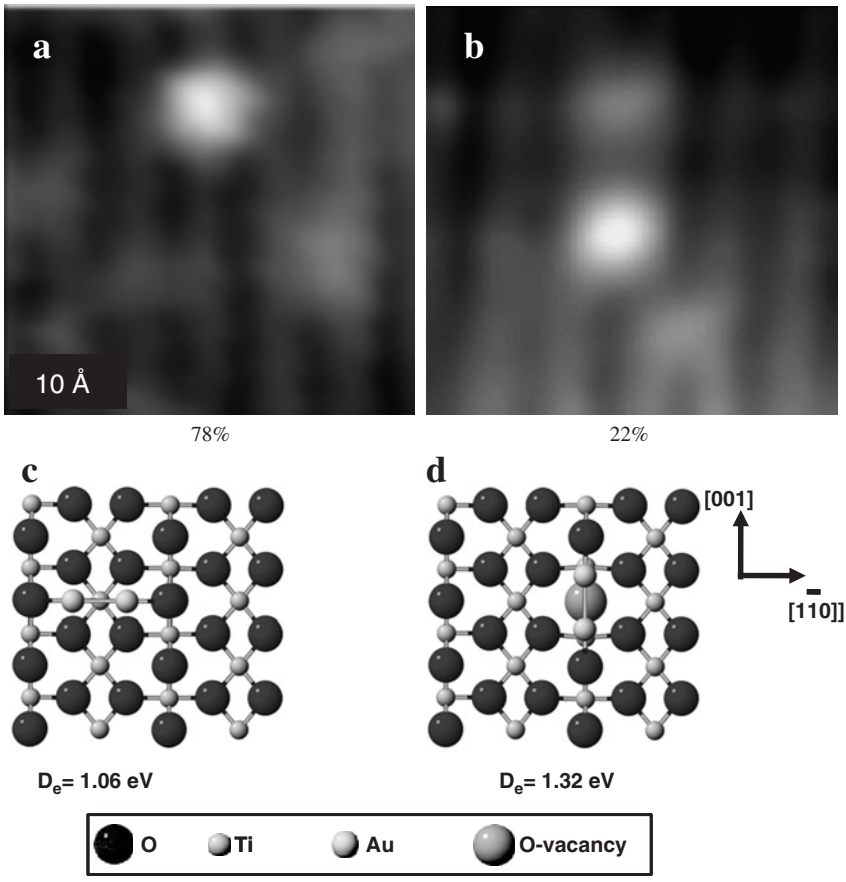

Figure 17: Comparison of STM images ($4 \times 4\,nm^2$) and the lowest energy structures predicted by DFT for adsorption structures of Au_2.

suggesting that the Au_2 clusters have very limited mobility on the surface and bind close to where they land.

In the case of the deposition of Au_3^+, only small, identical features are observed in the STM images as shown in Fig. 18. These features are predominantly (~95%) centered above the 5c-Ti rows (Fig. 18a). Only 3% of the features are observed over bridging O rows. An example of one of these clusters is shown in the STM image of Fig. 18c.

We also observe a very small fraction (2%) of the clusters centered between the 5c-Ti and bridging O rows. An example of this type of STM spot is given in Fig. 18b. The lowest energy structure on the stoichiometric surface determined via DFT (shown in Fig. 18d) shows ligation to two bridging O atoms on adjacent rows with the center Au atom in between. An STM image of this structure would be centered over the 5c-Ti row, similar to the image of Fig. 18a. It should be noted that the DFT structure is not linear, but slightly buckled. This center atom has a bond angle slightly larger than 120°. All of the STM images of Au_3 clusters on the $TiO_2(1\,1\,0)$ surface are the same height and attributed to a cluster that is flat on the surface. It is possible that the slight

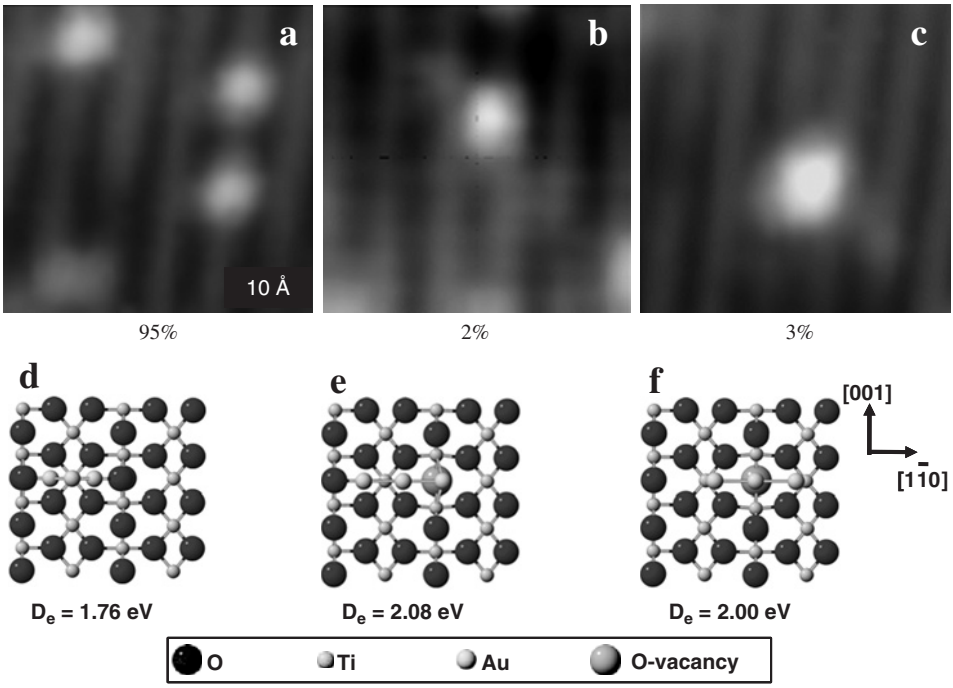

Figure 18: Comparison of STM images ($4 \times 4\,nm^2$) and the lowest energy structures predicted by DFT for adsorption structures of Au_3.

buckling of the center atom is not observed because the large electronic contrast in the STM dominates the small height difference.

The lowest energy structure for an Au_3 cluster on the reduced surface is linear and has either one of the end atoms bound to the vacancy (see Fig. 18e) or the center atom bound to the vacancy (see Fig. 18f). An STM image of the structure of Fig. 18e would be centered between the 5c-Ti and bridging O rows, similar to the image of Fig. 18b. An STM image of the structure of Fig. 18f would be centered over the bridging O row, similar to the image of Fig. 18c. The desorption energy for either structure on the reduced surface is higher than that for the stoichiometric surface by a minimum of 0.21 eV implying that the Au_3 clusters should all be bound to the O vacancies. Just as the case of Au_2 clusters bound to the surface, we do not observe the majority of clusters bound to vacancies. STM images attributed to Au_3 clusters bound to the stoichiometric surface (Fig. 18a) dominate the statistics. In addition, the fraction of Au_3 clusters bound to vacancies (Fig. 18b and c) is much smaller than the probability that a gas-phase Au_3^+ lands near a vacancy. This suggests some additional driving force for binding to the stoichiometric surface other than simple probability.

An important point to note regarding the deposition of Au_3^+ is that the shape of the trimers bound to the surface is different than the gas-phase structure of the trimer cation, which is an equilateral triangle as described in Section 3. The cluster shape is thus modified by binding to the surface, especially in the case of binding to an O vacancy, and the ultimate shape of the cluster is determined by surface ligation either to the bridging O atoms or to an O vacancy.

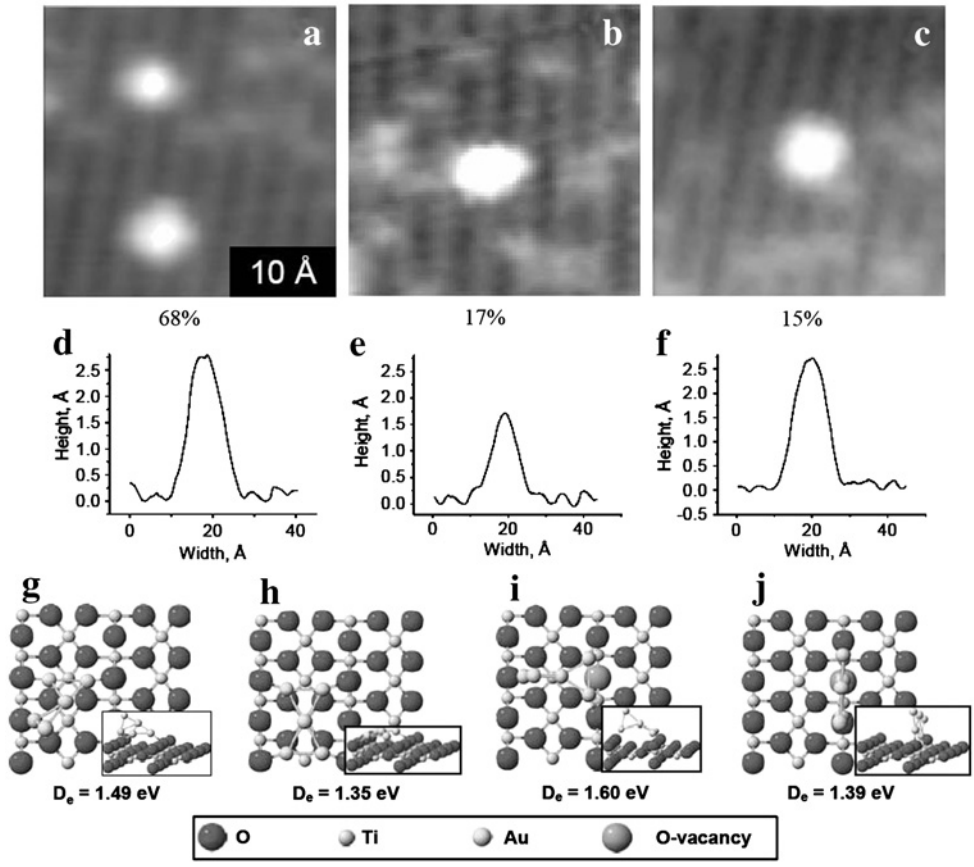

Figure 19: Comparison of STM images ($5 \times 5\,nm^2$) and the lowest energy structures predicted by DFT for adsorption structures of Au_5.

The effect of surface ligation on the cluster shape is most dramatic for Au_5 clusters. Figure 19 shows the three types of STM images observed following the deposition of Au_5^+.

Figure 19a shows two clusters centered over the 5c-Ti rows, each with a height of ~2.5 Å. These images are taller than any of the images observed for Au_2, Au_3, and Au_4 by more than 1 Å (see the line trace through the center of bottom cluster in Fig. 19d). The largest percentage of the clusters (68%) are similar to the clusters of Fig. 19a. Clusters of this type have an image centered over the 5c-Ti atom rows and are 2.6 ± 0.6 Å in height. Figure 19b shows an example of a cluster centered over the 5c-Ti row with a height of ~1.5 Å. This image is representative of approximately 17% of the clusters on the surface. Clusters of this type have an image centered over the 5c-Ti atom rows and are 1.7 ± 0.5 Å in height (see the line trace through the center of this cluster in Fig. 19e). Finally, we also observe tall clusters (~2.5 Å) centered over the bridging O rows. An example of this type of cluster is shown in Fig. 19c. This cluster is representative of the remaining 15% of the clusters on the surface. Clusters of this type

have an image centered over the 5c-Ti atom rows and are 2.6 ± 0.8 Å in height (see the line trace through the center of this cluster in Fig. 19f).

The multiple types of STM images seen for Au_5 clusters on the $TiO_2(1\,1\,0)$ surface implies that there are multiple structures adopted by the bound Au_5 clusters. Insight into these structures can be obtained from DFT. For Au_5 clusters bound to the stoichiometric surface, two low energy structures are obtained. The lowest energy structure is shown in Fig. 19g. The geometry of this structure, while it is quite distorted, is reminiscent of the gas-phase structure of Au_5^+. In the gas phase, Au_5^+ has a bow tie shape as seen in Table 8. Rotation of an Au dimer about the central Au atom has a small barrier of 0.03 eV [42]. The surface structure of Fig. 19g is derived from a 90° rotation of an Au dimer about the central atom in the bow tie, a structure similar to the structure of Ag_5 in the gas phase as seen in Table 5 (heretofore known as the 3-D bow tie structure). In Fig. 19g, the 3-D bow tie Au_5 cluster is bound to the stoichiometric surface such that three of the four corner Au atoms are bound to bridging O atoms: two on the same bridging O row and the other on an adjacent row. Three of the four ligation sites of the Au_4 cluster are occupied in binding this cluster and the fourth corner Au atom is oriented out of the plane of the surface and in the second layer of atoms. This cluster is centered mostly over the 5c-Ti rows and has a height larger than a planar structure by a single Au atom. This structure is consistent with the STM image of Fig. 19a and the line trace of Fig. 19d. An additional low energy structure is observed for Au_5 bound to the stoichiometric surface. This structure is shown in Fig. 19h. This structure has all four ligation sites occupied by binding to O atoms on adjacent rows. As is seen in the structure of Fig. 19h, the gold isomer is the planar bow tie conformation and the cluster lies flat on the surface. An STM image of this cluster would be a single layer of atoms tall and would be centered over the 5c-Ti row. This is consistent with the STM image of Fig. 19b and the line trace of Fig. 19e. Despite the occupation of four ligation sites, which should stabilize the bound cluster, the Au–O bond lengths are optimum. The planar bow tie conformer is too small for the binding pocket, which accounts for the lower binding energy of this cluster relative to the 3-D cluster of Fig. 19g.

The lowest energy structure for Au_5 on the reduced surface, according to DFT, is shown in Fig. 19i. This structure is derived from the 3-D bow tie structure described above where one of the Au dimers is bound to the O vacancy in a manner similar to Au_2 (see Fig. 17d). A corner atom of the opposite Au dimer is bound to a bridging O atom in the adjacent row and the fourth corner Au atom is oriented out of the plane of the surface and in the second layer of atoms. This cluster is centered mostly over the 5c-Ti rows and has a height larger than a planar structure by a single Au atom. This structure is also consistent with the STM image of Fig. 19a and the line trace of Fig. 19d. Thus, it is not possible for us to distinguish between Au_5 clusters with either the structure of Fig. 19i bound to the reduced surface or the structure of Fig. 19g bound to the stoichiometric surface in our STM images. It is possible that a portion of the 68% of the clusters with the STM image of Fig. 19a and the line trace of 19d are bound to the reduced surface. An additional low energy structure of Au_5 bound to the reduced surface is observed in DFT and is presented in Fig. 19j. This cluster is bound to the O vacancy with a single Au atom. The cluster itself is planar (see Fig. 12 for the planar shape) and tilted 90° to the plane of the surface resulting in two rows of atoms: a bottom row with two atoms and a top row with three atoms. Either atom of the

bottom row is bound to the vacancy. Orientation of this cluster is parallel to the bridging O row (as shown in Fig. 19j). This structure is centered over the bridging O row and is consistent with the STM image of Fig. 19c and the line trace of Fig. 19f. An interesting point to note regarding Au_5 clusters is that this is the only case we have seen where the binding energy to the stoichiometric surface is nearly equal to the binding energy to the reduced surface. We attribute this to the optimized surface ligation of the structure of Fig. 19g. In the case of Au_5, the cluster is able to efficiently bind to the stoichiometric surface with at least three ligation sites. In order to bind to the vacancy, the cluster must give up at least one of these ligation sites (as seen in Fig. 19i). The increased stability gained by binding to the vacancy is just barely able to account for this loss.

We have performed the same comparison between the STM images and DFT structures described in the preceding paragraphs to Au_6 and Au_7 clusters on $TiO_2(1\,1\,0)$. For clusters larger than Au_5, we see a number of structures with binding energy close to the maximum binding energy. In most cases, the differences in the DFT structures are subtle. In our comparison between the STM images and DFT structures for Au_6 clusters (Fig. 20) and Au_7 clusters (Fig. 21), we show only DFT structures for the stoichiometric and reduced surfaces with the highest binding energy.

In the case of Au_6 clusters, the STM images and DFT structures for both the stoichiometric and reduced surfaces are shown in Fig. 20. The highest percentage of the features (80%) in the STM images appear centered over the 5c-Ti atom row (Fig. 20a).

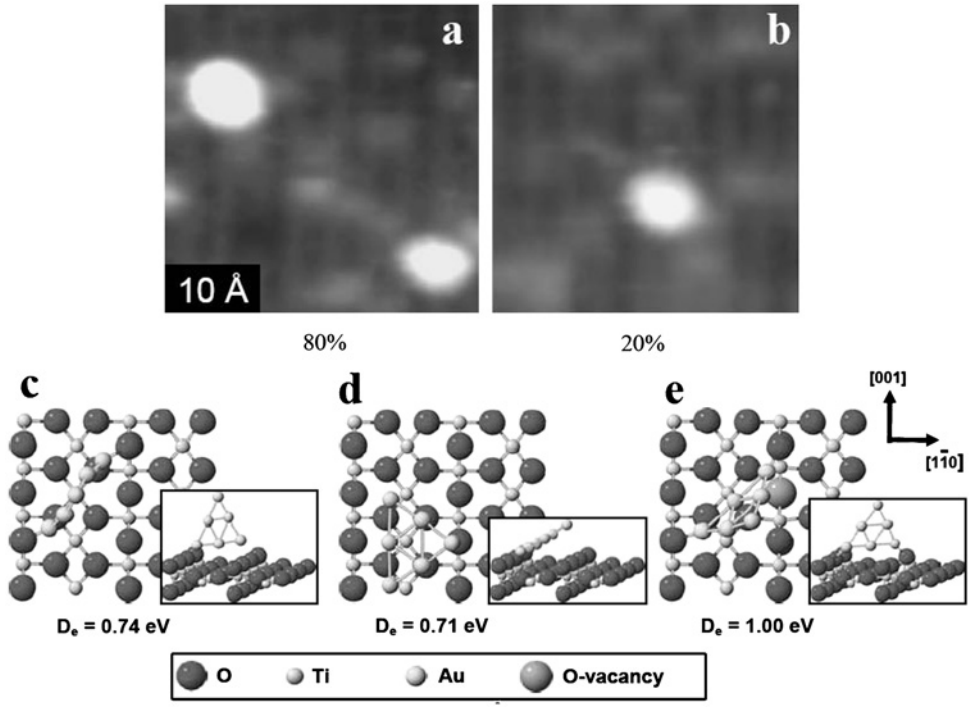

Figure 20: Comparison of STM images ($5 \times 5\,nm^2$) and the lowest energy structures predicted by DFT for adsorption structures of Au_6.

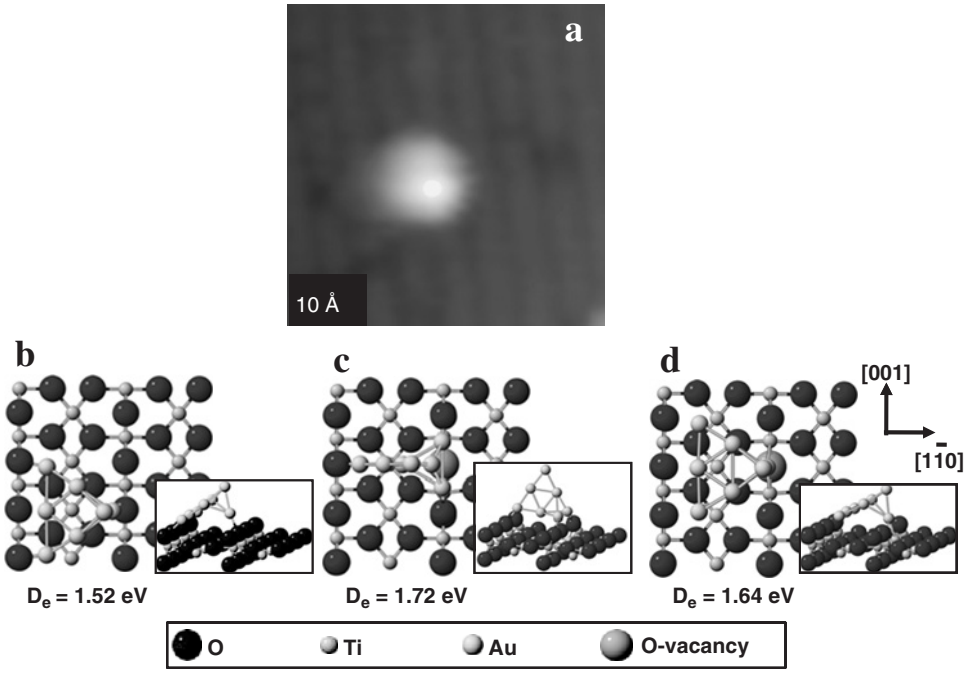

Figure 21: Comparison of STM image ($5 \times 5\,nm^2$) and the lowest energy structures predicted by DFT for adsorption structures of Au_7.

The remaining 20% of the features appear centered over the bridging O rows (Fig. 20b). The DFT calculations for Au_6 clusters bound to TiO_2(1 1 0) resulted in a number of isomers with binding energy between 0.7 and 1.0 eV. The three isomers shown in Fig. 20c–e represent structures that have a binding energy in this range and exhibit shapes that are consistent with the STM images. One trend that is easily deduced from the structures is that only two ligation sites are occupied on this cluster instead of the three seen in the case of Au_5 clusters. The reason for this is the stability of the planar Au_6 structures (see Fig. 12). The two planar isomers of Au_6 can only bind to the surface in such a way that two ligation sites are occupied. This results in tilting of the cluster relative to the surface of the TiO_2. The structures of Fig. 20c and d differ only in the angle of the tilt relative to the plane of the surface. Other tilt angles of this Au_6 isomer on the surface are also observed in DFT (not shown) with binding energy varying to 0.7 eV. It is very likely that all of these isomers are observed in our data and this accounts for the distribution in height (Fig. 15f). The structure of Fig. 20e shows the structure with the highest binding energy to the reduced surface. This structure is also a planar structure oriented at an angle to the TiO_2 surface. It is curious that this structure is not bound directly to the O vacancy but prefers to bind to bridging O atoms on adjacent rows and tilt toward the vacancy. This is the only cluster where the highest binding energy is not observed for a cluster bound directly to the vacancy. Isomers bound directly to the O vacancy (not shown) have binding energies in the 0.7–0.9 eV range and are much less stable according to theory than the structure of Fig. 20e.

The result from the deposition of Au_7^+ is shown in Fig. 21. The average height for these clusters is 2.8 ± 0.7 Å, which is similar to that obtained for both Au_5 and Au_6. The STM images for these large clusters span more than two adjacent bridging O rows (and two adjacent 5c-Ti rows), and it is difficult to determine the center of the spot relative to the bridging O row. A representative STM image for an Au_7 cluster on TiO_2 is shown in Fig. 21a. DFT reveals three high binding energy structures (shown in Fig. 21b–d) in the 1.50–1.75 eV range: one bound to the stoichiometric surface and two bound to the reduced surface.

Each of these structures is 3-D on the surface with at least one apex atom. All three of these clusters have binding sites on the surface that are reminiscent of the other Au clusters. The most stable structure is the structure bound to the reduced surface as seen in Fig. 21c. In this structure, two Au atoms (a dimer) are bound to the O vacancy similar to that observed for Au_2 (Fig. 17d) and Au_5 (Fig. 19i). Another Au atom is bound to a bridging O atom on an adjacent row. The structures of Fig. 21b (bound to the stoichiometric surface) and Fig. 21d (bound to the reduced surface) are identical. In Fig. 21b, the cluster is formed via four bridging O atoms: three in one row and one in an adjacent row. In the structure of Fig. 21d, the O vacancy replaces the single bridging O atom as the fourth ligation site.

The comparison between DFT-derived structures and the STM images for the case of gold tetramers is different from all other Au clusters we have studied. Figure 22 shows the three types of STM images observed for Au_4 clusters. Small clusters were observed in all cases with a height of 1.7 ± 0.2 Å suggesting that adsorbed Au_4 lays flat on the surface. The majority of the Au_4 clusters (61%) exhibit the interesting two-lobed shape observed in the image of Fig. 22a. Each lobe of the two-lobed feature is centered over a 5c-Ti row and has the same height. The remaining 39% of observed features are single, round spots, which are slightly bigger in appearance than the features observed following the deposition of Au_2 and Au_3. Roughly 28% of these features are centered over 5c-Ti rows (Fig. 22b), and 11% are centered over the bridging O rows (Fig. 22c).

The highest binding energy structures determined via DFT for the stoichiometric and the reduced surfaces are shown in Fig. 23a and b, respectively. The structure of Fig. 23b is the structure with the highest binding energy. It lies flat on the reduced surface with three of the four gold atoms positioned over the bridging O row, similar

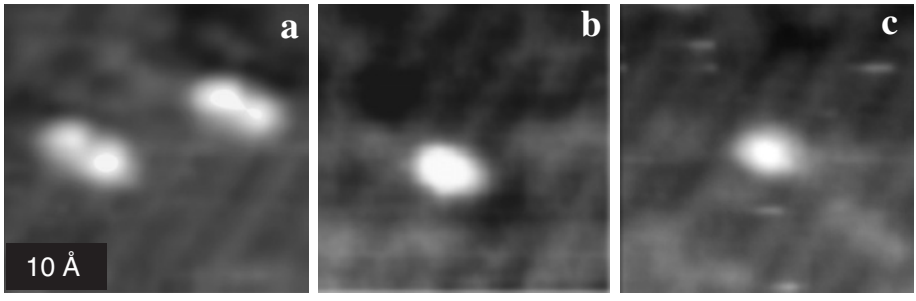

Figure 22: STM images ($4 \times 4\,nm^2$) for adsorption of Au_4.

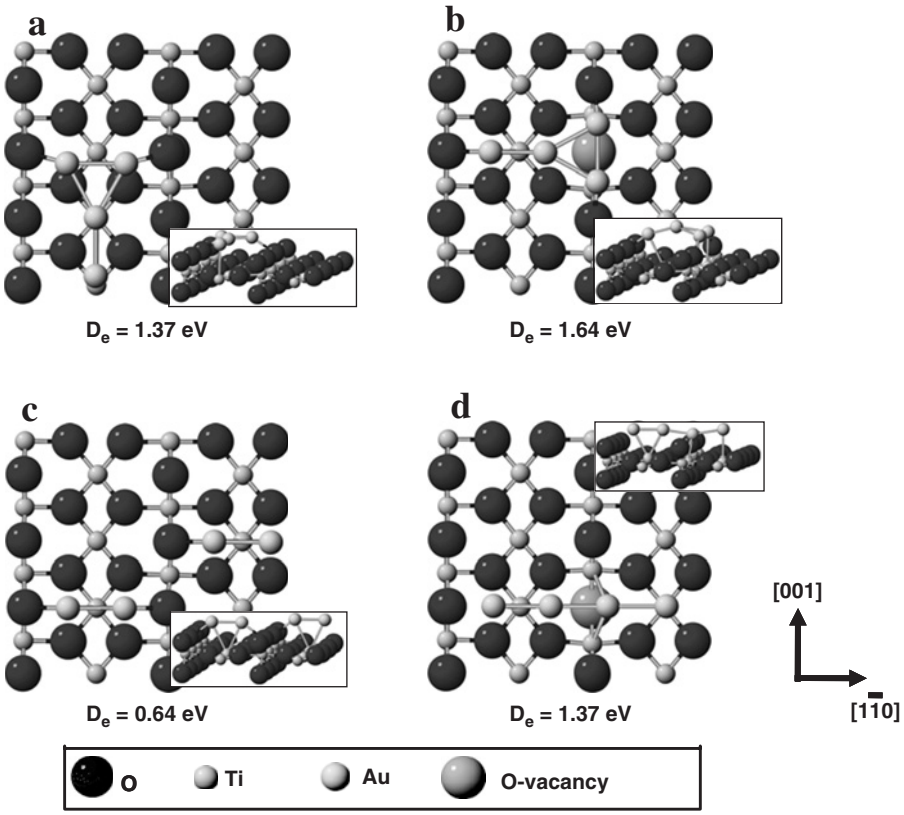

Figure 23: The lowest energy structures predicted by DFT for adsorption structures of Au_4, and the structures that most closely correspond to the STM feature of Fig. 22a.

to the image of Fig. 22c. Figure 23a is the structure with the highest binding energy to the stoichiometric surface. It lies flat on the surface and is centered over the 5c-Ti row, similar to the image of Fig. 22b.

None of the DFT structures we calculated with binding energy >1.00 eV would result in a feature similar to the two-lobed feature in Fig. 22a. The structures of Fig. 23c and d (for the stoichiometric and reduced surfaces, respectively) are the only structures that result in a flat cluster with two lobes. The linear structure of Fig. 23d bound to the reduced surface should not result in two lobes centered over adjacent 5c-Ti rows as observed experimentally in Fig. 22a. The structure that best corresponds to the STM image of Fig. 22a is shown in Fig. 23c, which shows a four-atom Au cluster that consists of adjacent gold dimers, i.e., a dissociated cluster. While this structure would result in a two-lobed image of the type observed in Fig. 22a, the binding energy of the pair of gold dimers is much smaller than either of the two highest binding energy structures of Fig. 23a and b, and theory strongly suggests that this structure would not be possible. The gold tetramer is the only system where the most abundant STM shape does not correspond to the highest binding energy cluster in DFT for either the stoichiometric or reduced surface.

4.3.2. Summary of Au_n clusters on TiO_2

In all cases of deposition of Au_1 to Au_7, the density of oxygen vacancies is larger or comparable to the density of the clusters, providing sufficient opportunity for oxygen vacancies to be occupied by clusters. The small cluster size, multiple conformations (adsorption sites), and relatively low probability of cluster adsorption to a site involving an oxygen vacancy suggest the clusters have low mobility.

The results presented here are consistent with a number of earlier studies and provide some new, unexpected, and important information. Soft-landing gold atoms lead to rapid sintering and formation of globules with an average height consistent with four atomic layers. Earlier STM studies on titania with larger coverages from evaporative gold sources indicated significant sintering and formation of very large globules. Our low coverage, single atom depositions thus confirm the high mobility of Au atoms on titania and their tendency to sinter.

There is no direct evidence that defects are required for binding the clusters. In fact, the lack of mobility of clusters as small as the dimer indicates strong binding occurs with the stoichiometric surface. This is shown by the DFT calculation in Fig. 17, and also supported by the fact that the STM images observed were stable over several days and did not change with repeated scans by the STM tip. The multiple conformations predicted by DFT, particularly for larger clusters such as

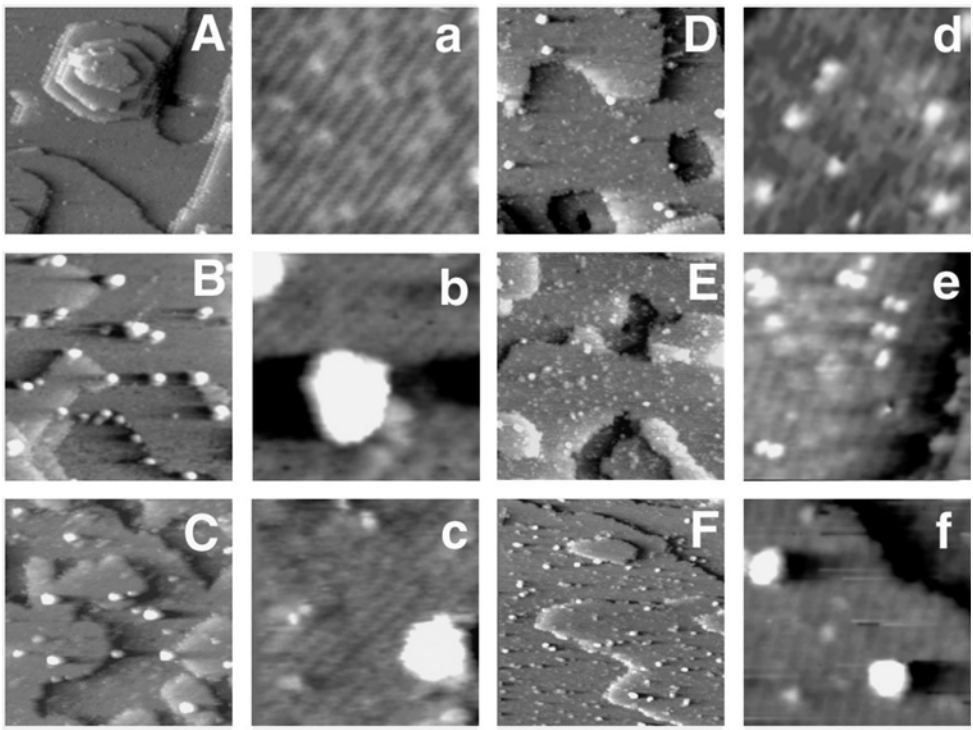

Figure 24: STM images following the deposition of Ag_z^+ ($n = 1$–5) on the surface of $TiO_2(1\,1\,0) \times (1\,1\,1)$. Images marked with capital letters are 500 Å × 500 Å, while lower case images are 90 Å × 90 Å. Images: (A/a) clean surface; (B/b) surface after depositing Ag_1; (C/c) Ag_2; (D/d) Ag_3; (E/e) Ag_4; and (F/f) Ag_5.

Au_n ($n = 5$–8), seem likely given the height distributions of the surface bound clusters as shown in Fig. 14.

These results imply that Au clusters have low mobility under soft-landing condition because small fragments are unstable compared with larger ones. Clusters are resistant to sintering upon annealing for a few seconds at 600 K. We exclude sintering also because deposition of Au clusters results in different average height. For example, deposition of Au_2 (1.6 ± 0.5 Å) is different from Au_7 (2.8 ± 0.7 Å).

The surface can have two effects on the gold cluster. First, electron transfer can occur from the surface to the cluster. This effect would favor planar structures based on gas-phase results [41, 42]. Second, the surface can specifically ligate the cluster. The primary ligation sites are the bridging oxygen atoms, separated by 6.5 Å between rows. The tetramer is the smallest cluster able to coordinate with two oxygen atoms on adjacent rows, and then only if a quasi-linear structure is invoked. This result suggests surface ligation is driving cluster structure since the linear form of Au_4 is not favored by theory [41]. We know from the gas-phase experiments on both silver [108] and gold [109] cluster cations (Section 3) that ligation can induce structural changes and our surface experiments are consistent with this observation. The fact that the 2-D to 3-D transition occurs at Au_5 reflects the strong driving force of ligation. The 3-D structure for Au_5 is a direct result of surface ligation.

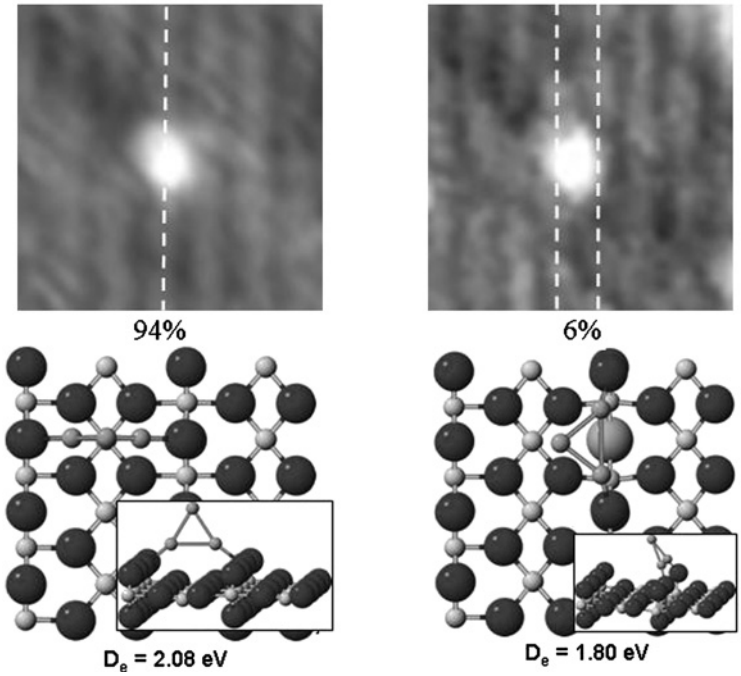

Figure 25: Specific binding locations for Ag_3. The clusters appear predominantly above 5c-Ti atom rows. White dotted lines are drawn over the 5c-Ti atom rows to guide the eye. The lowest energy DFT structure predicted for a stoichiometric surface confirms this, as the bridging O atoms in neighboring rows act as ligation sites, resulting in the appearance of the cluster above the 5c-Ti atom rows. The structure on the right is representative of a cluster interacting with a vacancy.

4.4. Ag_n^+ ($n = 1$–5) on TiO_2(1 1 0)

STM images shown in Fig. 24 give an overview of the deposition of Ag_n^+ ($n = 1$–5), a titanium dioxide substrate. The images of Fig. 24B/b were taken following the depositions of Ag_1. The predominant features after deposition consist of sintered islands containing ~100 atoms, indicating that similar to Au_1, Ag_1 is also mobile on the surface of titania. This result matches what is observed following deposition of Ag from an evaporative source [87, 110, 111]. The Ag clusters are somewhat larger than the clusters observed following the deposition of Au_1 as described in the previous section, averaging 7.5 ± 1.5 Å in height and in 23.3 ± 4.7 Å diameter. The differences in the observed heights and diameters here are not relevant given that the coverage was predicted to be approximately a factor of 2 lower for the deposition of Au_1 from the integrated ion current measurement. In examining the nucleation sites of the clusters, it is notable that in the image of Au clusters (previous section), in the limit of low coverage and low flux, nucleation takes place on the terraces and at step edge sites. In the case of Ag, however, almost all clusters visible are nucleated at step edges sites. It is important to note that beam flux, step-edge density, and oxygen vacancy density is similar in both cases shown here. These observations suggest that Au_1 is less mobile on the terraces of titania than Ag_1, which has therefore a longer diffusion length, and is able to reach step sites more frequently than Au. High-resolution image 24b reveals clean 5c-Ti and bridging O rows between the Ag clusters.

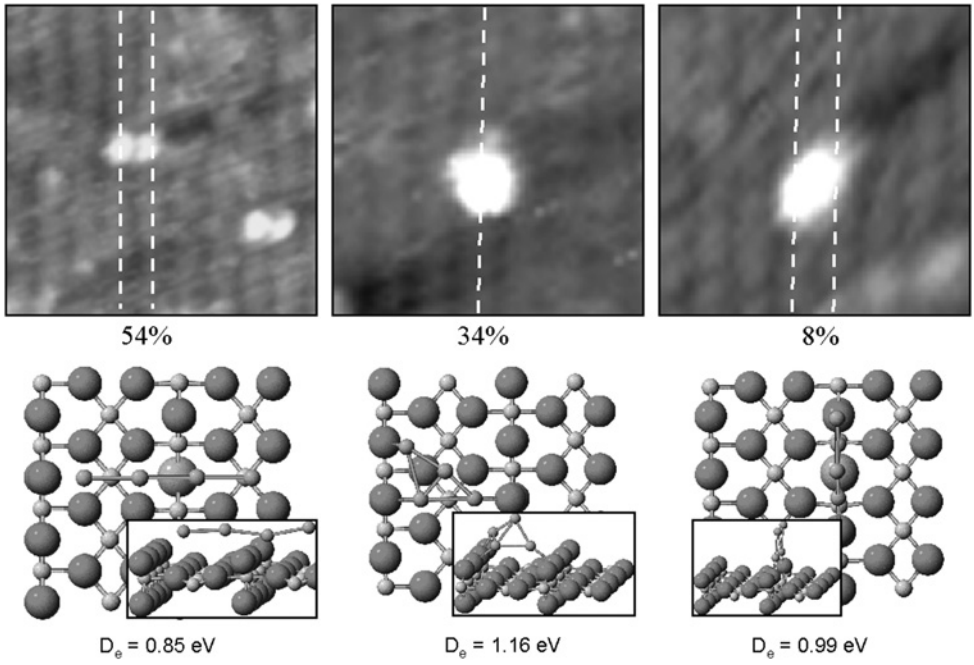

Figure 26: STM images of the various structures and binding locations observed for Au_4 clusters. The predominant two-lobed structure is shown on the left, each lobe centered above a 5c-Ti row, accounting for 54% of all observed features. 34% of the features appear above a 5c-Ti atom row (single feature), and the remainder above bridging O atom rows.

Following the deposition of Ag_2, STM images shown in Fig. 24C/c reveal that once again large, agglomerated clusters are present on the surface, measuring 6.2 ± 1.4 Å in height and 17.2 ± 3.1 Å in diameter. These clusters appear mainly bound at terrace sites, although a few of them are found at step sites. We note here that we previously concluded that Ag_2 is in fact less mobile than Ag_1, as more clusters appear to form at terrace sites than at step sites, since steps are known nucleation sites [112]. Between clusters, the titania surface appears fairly clean, as shown in Fig. 24c. This result is in clear contrast with that observed for Au_2, which as described above results in intact, immobile clusters. It is evident from these observations that Ag_2 is in fact more mobile than Au_2.

STM images shown in Fig. 24D/d reveal that the predominant features following the deposition of Ag_3 are small, measuring 1.5 ± 0.3 Å high and 5.6 ± 0.7 Å wide. We conclude that the clusters have limited mobility on the surface, given the small size and predominant binding at terrace sites. The features appear above 5c-Ti rows 94% of the time, as shown in high-resolution image of Fig. 25a. The remainder of the features appear to bind above the bridging O rows. This result is very similar to the result obtained for Au_3.

Interesting feature shapes become apparent on the surface following the deposition of Ag_4. As shown in Fig. 24E/e, there are few large clusters on the surface, and a high density of smaller features. Once again, most of the features are found at terrace sites, suggesting limited mobility, averaging 1.5 ± 0.6 Å in height and 6.6 ± 1.7 Å in

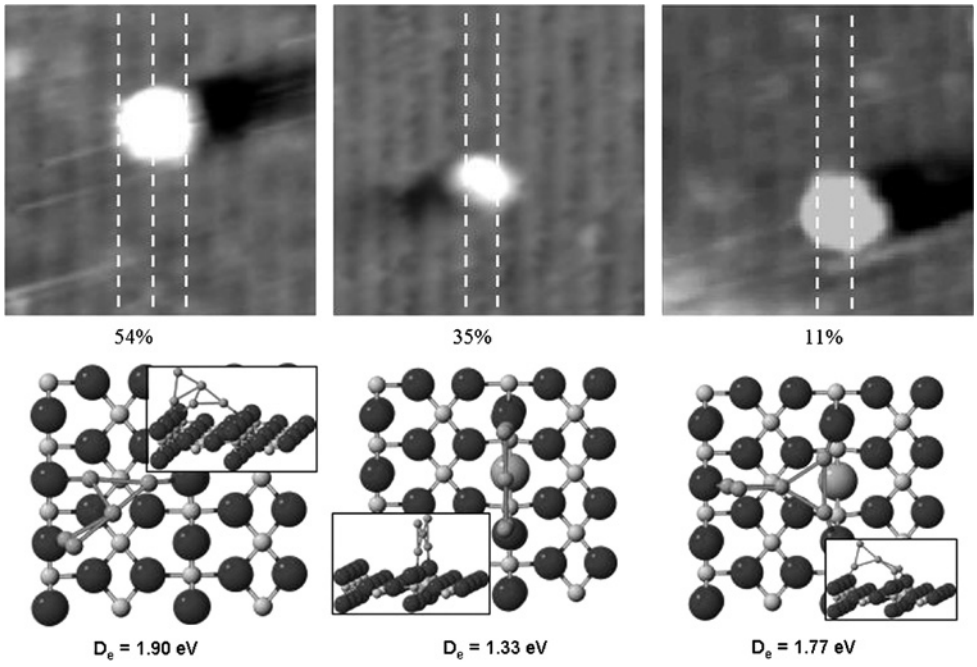

Figure 27: STM images following the deposition of Ag_5. The predominant feature appears centered over the titanium atom rows, as shown at the left, in agreement with the lowest energy DFT structure predicted for the stoichiometric surface. The remaining features appear above bridging O atom rows (35%) and in between rows (11%), which we attribute to cluster interaction with vacant sites.

diameter. Among these features, as shown in high-resolution images in Fig. 26, 54% exhibit the same type of two-lobed structure observed in the case of Au_4 adsorption (Fig. 22a).

These features are nearly identical in appearance to those appearing following the deposition of Au_4. The similarity of these features suggests that Au and Ag adopt the same major structure on the surface. Each of the lobes appears above a 5c-Ti row, while the center of the structure is a node, appearing over a bridging O row. Of all features observed, 34% appeared above 5c-Ti sites, while only 8% and 4%, not shown were found above bridging O rows and between bridging O and 5c-Ti rows, respectively, as shown in Fig. 26.

Features found on the surface of titania following the deposition of Ag_5, as shown in Fig. 27, measure on average 2.4 ± 0.9 Å in height and 9.3 ± 2.0 Å in diameter. With the exception of those clusters that sintered (Ag_1, Ag_2), the cluster heights measured here are approximately 1 Å higher than the heights of Ag_3 and Ag_4.

We believe this is due to an increase in the average number of layers in the structures, or a higher overall degree of protrusion above the surface. A similar transition was noted in the above section for Au in going from Au_4 to Au_5. Once again, the clusters appear predominantly bound above 5c-Ti atom sites, as 54% of all features following Ag_5 deposition appear above the 5c-Ti rows. For the remaining features, 35% appear over bridging O rows, and 11% appear between bridging O and 5c-Ti rows.

4.5. Conclusions

STM images and DFT calculations reveal that Au_1 and Ag_1 atoms are highly mobile on the titania surface and sinter to large islands with a broad height distribution due to the weak binding energy of Au_1 and Ag_1 with the stoichiometric surface. Au interacts more strongly with vacant sites than Ag, as a result, nucleation is observed more frequently at terrace sites in comparison to Ag. Ag dimers are also surprisingly mobile on the surface of titania, nucleating into large clusters. This can be explained by the relatively small increase in binding energy in going from Ag_1 to Ag_2 vs. that for Au_1 to Au_2 on the stoichiometric surface, as predicted by DFT. Depositions of small clusters of Au_n ($n = 2$–8) and Ag_n ($3 \leqslant n \leqslant 5$) result in fairly immobile, intact clusters on the surface, with relatively narrow height distributions. The immobile clusters adapt specific conformations and binding sites according to STM results and DFT calculations. Overall, most of the features observed after the deposition of mass-selected clusters (Au_2, Au_3, Au_5, Au_6 and Ag_3, Ag_5) appear above 5c-Ti rows in STM images. This suggests that oxygen vacancies play a lesser role in the interaction of these clusters with the titania substrate. DFT predicts that the clusters bind preferentially to the bridging O atom rows, and are ligated by at least two O atoms in neighboring rows such that the appearance of the cluster itself is generally above the 5c-Ti atom rows. In the event that a cluster should land in the immediate vicinity of a vacancy, interaction with a vacancy can occur, resulting in the appearance of a cluster over a bridging O atom row or between 5c-Ti atom and bridging O atom rows. Interestingly, Au_7 are the first truly 3-D structures (according to DFT and supported by our STM data), often containing highly uncoordinated peak atoms, perhaps responsible for their relatively high catalytic activity in comparison to other cluster sizes.

REFERENCES

[1] O'Hair R.A.J., Khairallah G.N., J. Cluster Sci. 15 (2004) 331.
[2] Kappes M.M., Chem. Rev. 88 (1988) 369.
[3] Moskovits M., Metal Clusters, Wiley, New York, 1986.
[4] Castleman A.W., Keesee R.G., Acc. Chem. Res. 19 (1986) 413.
[5] Lee S.S., Fan C.Y., Wu T.P., Anderson S.L., J. Am. Chem. Soc. 126 (2004) 5682.
[6] Hammer B., Norskov J.K., Nature 376 (1995) 238.
[7] Haruta M., Catal. Today 36 (1997) 153.
[8] Serafin J.G., Liu A.C., Seyedmonir S.R., J. Mol. Catal. A 131 (1998) 157.
[9] Valden M., Lai X., Goodman D.W., Science 281 (1998) 1647.
[10] Lopez N., Janssens T.V.W., Clausen B.S., Xu Y., Mavrikakis M., Bligaard T., Norskov J.K., J. Catal. 223 (2004) 232.
[11] Lopez N., Norskov J.K., J. Am. Chem. Soc. 124 (2002) 11262.
[12] Haruta M., Date M., Appl. Catal. A 222 (2001) 427.
[13] Meyer R., Lemire C., Shaikhutdinov S.K., Freund H., Gold Bull. 37 (2004) 72.
[14] Sanchez A., Abbet S., Heiz U., Schneider W.D., Hakkinen H., Barnett R.N., Landman U., J. Phys. Chem. A 103 (1999) 9573.
[15] Kemper P.R., Weis P., Bowers M.T., Int. J. Mass. Spectrom. 160 (1997) 17.
[16] Hopkins J.B., Langridgesmith P.R.R., Morse M.D., Smalley R.E., J. Chem. Phys. 78 (1983) 1627.
[17] Kemper P.R., Bushnell J., Vankoppen P., Bowers M.T., J. Phys. Chem. 97 (1993) 1810.
[18] Kemper P.R., Bushnell J., Vonhelden G., Bowers M.T., J. Phys. Chem. 97 (1993) 52.
[19] Hohenberg P., Kohn W., Phys. Rev. B 136 (1964) B864.
[20] Kohn W., Sham L.J., Phys. Rev. 140 (1965) 1133.
[21] Stephens P.J., Devlin F.J., Chabalowski C.F., Frisch M.J., J. Phys. Chem. 98 (1994) 11623.
[22] Becke A.D., Phys. Rev. A 38 (1988) 3098.
[23] Becke A.D., J. Chem. Phys. 98 (1993) 5648.
[24] Frisch M.J., Trucks G.W., Schlegel H.B. et al., Gaussian 03, Gaussian Inc., Pittsburgh, 2003.
[25] Francl M.M., Pietro W.J., Hehre W.J., Binkley J.S., Gordon M.S., Defrees D.J., Pople J.A., J. Chem. Phys. 77 (1982) 3654.
[26] Clark T., Chandrasekhar J., Spitznagel G.W., Schleyer P.V., J. Comput. Chem. 4 (1983) 294.
[27] Krishnan R., Binkley J.S., Seeger R., Pople J.A., J. Chem. Phys. 72 (1980) 650.
[28] Gill P.M.W., Johnson B.G., Pople J.A., Frisch M.J., Chem. Phys. Lett. 197 (1992) 499.
[29] Kemper P., Kolmakov A., Tong X., Lilach Y., Benz L., Manard M., Metiu H., Buratto S.K., Bowers M.T. 254 (2006) 202.
[30] Perdew J.P., Burke K., Phys. Rev. B 54 (1996) 16533.
[31] Perdew J.P., Chevary J.A., Vosko S.H., Jackson K.A., Pederson M.R., Singh D.J., Fiolhais C., Phys. Rev. B 46 (1992) 6671.
[32] Kresse G., Furthmuller J., Comput. Mater. Sci. 6 (1996) 15.
[33] Kresse G., Furthmuller J., Phys. Rev. B 54 (1996) 11169.
[34] Kresse G., Hafner J., Phys. Rev. B 47 (1993) 558.
[35] Kresse G., Hafner J., Phys. Rev. B 49 (1994) 14251.
[36] Vanderbilt D., Phys. Rev. B 41 (1990) 7892.
[37] Xiao L., Wang L.C., Chem. Phys. Lett. 392 (2004) 452.
[38] Makov G., Payne M.C., Phys. Rev. B 51 (1995) 4014.
[39] Pulay P., Chem. Phys. Lett. 73 (1980) 393.

[40] Press W.H., Teukolsky S.A., Flannery W.T., Vetterling B.P., Numerical Recipes in Fortran: The Art of Scientific Computing, Cambridge University Press, Cambridge, 1992.
[41] Furche F., Ahlrichs R., Weis P., Jacob C., Gilb S., Bierweiler T., Kappes M.M., J. Chem. Phys. 117 (2002) 6982.
[42] Gilb S., Weis P., Furche F., Ahlrichs R., Kappes M.M., J. Chem. Phys. 116 (2002) 4094.
[43] Weis P., Bierweiler T., Gilb S., Kappes M.M., Chem. Phys. Lett. 355 (2002) 355.
[44] Bonacickoutecky V., Cespiva L., Fantucci P., Pittner J., Koutecky J., J. Chem. Phys. 100 (1994) 490.
[45] Matulis V.E., Ivashkevich O.A., Gurin V.S., J. Mol. Struct. 664 (2003) 291.
[46] Bonacickoutecky V., Cespiva L., Fantucci P., Koutecky J., J. Chem. Phys. 98 (1993) 7981.
[47] Hakkinen H., Landman U., Phys. Rev. B 62 (2000) R2287.
[48] Eller K., Schwarz H., Chem. Rev. 91 (1991) 1121.
[49] Knickelbein M.B., Annu. Rev. Phys. Chem. 50 (1999) 79.
[50] Freiser B.S., Organometallic Ion Chemistry, Kluwer Academic Publishers, Dordrecht, The Netherlands, 1996.
[51] Russel D.H., Gas Phase Inorganic Chemistry, Plenum, New York, 1989.
[52] Manard M.J., Bushnell J.E., Bernstein S.L., Bowers M.T., J. Phys. Chem. A 106 (2002) 10027.
[53] Bushnell J.E., Kemper P.R., Bowers M.T., J. Phys. Chem. 97 (1993) 11628.
[54] Sievers M.R., Armentrout P.B., J. Phys. Chem. 99 (1995) 8135.
[55] Schultz R.H., Crellin K.C., Armentrout P.B., J. Am. Chem. Soc. 113 (1991) 8590.
[56] Fielicke A., von Helden G., Meijer G., Pedersen D.B., Simard B., Rayner D.M., J. Am. Chem. Soc. 127 (2005) 8416.
[57] Zhang X.G., Armentrout P.B., J. Phys. Chem. A 107 (2003) 8904.
[58] Manard M.J., Kemper P.R., Bowers M.T., Int. J. Mass Spectrom. 228 (2003) 865.
[59] Vardhan D., Liyanage R., Armentrout P.B., J. Chem. Phys. 119 (2003) 4166.
[60] Salisbury B.E., Wallace W.T., Whetten R.L., Chem. Phys. 262 (2000) 131.
[61] Vankoppen P.A.M., Bowers M.T., Fisher E.R., Armentrout P.B., J. Am. Chem. Soc. 116 (1994) 3780.
[62] Weis P., Kemper P.R., Bowers M.T., J. Phys. Chem. A 101 (1997) 8207.
[63] Carpenter C.J., van Koppen P.A.M., Kemper P.R., Bushnell J.E., Weis P., Perry J.K., Bowers M.T., Int. J. Mass Spectrom. 230 (2003) 161.
[64] Guo B.C., Castleman A.W., Chem. Phys. Lett. 181 (1991) 16.
[65] Kaneti J., de Smet L.C.P.M, Boom R., Zuilhof H., Sudholter E.J.R., J. Phys. Chem. A 106 (2002) 11197.
[66] Hertwig R.H., Koch W., Schroder D., Schwarz H., Hrusak J., Schwerdtfeger P., J. Phys. Chem. 100 (1996) 12253.
[67] Ma N.L., Chem. Phys. Lett. 297 (1998) 230.
[68] Dewar J.S., Bull. Soc. Chim. Fr. 18 (1951) C71.
[69] Ziegler T., Rauk A., Inorg. Chem. 18 (1979) 1558.
[70] Chen Y.M., Armentrout P.B., J. Phys. Chem. 99 (1995) 11424.
[71] Manard M.J., Kemper P.R., Carpenter C.J., Bowers M.T., Int. J. Mass Spectrom. 241 (2005) 99.
[72] Kerns K.P., Parks E.K., Riley S.J., J. Chem. Phys. 112 (2000) 3394.
[73] Hintz P.A., Ervin K.M., J. Chem. Phys. 100 (1994) 5715.
[74] Chrétien S., Gordon M.S., Metiu H., J. Chem. Phys. 121 (2004) 3756.
[75] Chrétien S., Gordon M.S., Metiu H., J. Chem. Phys. 121 (2004) 9931.
[76] Chrétien S., Gordon M.S., Metiu H., J. Chem. Phys. 121 (2004) 9925.
[77] Nishimura H., Tawara H., J. Phys. B: At., Mol. Opt. Phys. 27 (1994) 2063.
[78] PawelaCrew J., Madix R.J., J. Chem. Phys. 104 (1996) 1699.
[79] Backx C., Degroot C.P.M., Biloen P., Sachtler W.M.H., Surf. Sci. 128 (1983) 81.

[80] Neumaier M., Weigend F., Hampe O., Kappes M.M., J. Chem. Phys. 122 (2005) 104702.
[81] Goodman D.W., Catal. Lett. 99 (2005) 1.
[82] Chen M.S., Goodman D.W., Science 306 (2004) 252.
[83] Rodriguez J.A., Dekker Encyclopedia of Nanoscience and Technology, Marcel Dekker, New York, NY, 2004.
[84] Bondzie V.A., Parker S.C., Campbell C.T., Catal. Lett. 63 (1999) 143.
[85] Ajo H.M., Bondzie V.A., Campbell C.T., Catal. Lett. 78 (2002) 359.
[86] Shaikhutdinov S.K., Meyer R., Naschitzki M., Baumer M., Freund H.J., Catal. Lett. 86 (2003) 211.
[87] Spiridis N., Haber J., Korecki J., Vacuum 63 (2001) 99.
[88] Wallace W.T., Min B.K., Goodman D.W., Top. Catal. 34 (2005) 17.
[89] Kolmakov A., Goodman D.W., Chem. Rec. 2 (2002) 446.
[90] Benz L., Tong X., Kemper P., Metiu H., Bowers M.T., Buratto S.K., J. Phys. Chem. B (2005).
[91] Tong X., Benz L., Kemper P., Metiu H., Bowers M.T., Buratto S.K., J. Am. Chem. Soc. 127 (2005) 13516.
[92] Heiz U., Sherwood R., Cox D.M., Kaldor A., Yates J.T., J. Phys. Chem. 99 (1995) 8730.
[93] Schaffner M.H., Patthey F., Heiz U., Schneider W.D., Kuffer O., Roy H.V., Fayet P., Gimzewski J.K., Berndt R., Eur. Phys. J. D 2 (1998) 79.
[94] Heiz U., Sanchez A., Abbet S., Schneider W.D., J. Am. Chem. Soc. 121 (1999) 3214.
[95] Heiz U., Sanchez A., Abbet S., Schneider W.D., Eur. Phys. J. D 9 (1999) 35.
[96] Lee S., Fan C., Wu T., Anderson S.L., J. Chem. Phys. 123 (2005) 124710.
[97] Lee S., Fan C.Y., Wu T.P., Anderson S.L., Surf. Sci. 578 (2005) 5.
[98] Onishi H., Iwasawa Y., Surf. Sci. 313 (1994) L783.
[99] Diebold U., Anderson J.F., Ng K.O., Vanderbilt D., Phys. Rev. Lett. 77 (1996) 1322.
[100] Suzuki S., Fukui K., Onishi H., Iwasawa Y., Phys. Rev. Lett. 84 (2000) 2156.
[101] Wendt S., Schaub R., Matthiesen J., Vestergaard E.K., Wahlström E., Rasmussen M.D., Thostrup P., Molina L.M., Lægsgaard E., Stensgaard I., Hammer B., Besenbacher F., Surf. Sci. 598 (2005) 226.
[102] Schaub R., Thostrup P., Lopez N., Laegsgaard E., Stensgaard I., Norskov J.K., Besenbacher F., Phys. Rev. Lett. 87 (2001) 266104.
[103] Hugenschmidt M.B., Gamble L., Campbell C.T., Surf. Sci. 302 (1994) 329.
[104] Diebold U., Surf. Sci. Rep. 48 (2003) 53.
[105] Diebold U., Lehman J., Mahmoud T., Kuhn M., Leonardelli G., Hebenstreit W., Schmid M., Varga P., Surf. Sci. 411 (1998) 137.
[106] Schaub R., Thostrup R., Lopez N., Laegsgaard E., Stensgaard I., Norskov J.K., Besenbacher F., Phys. Rev. Lett. 87 (2001) 266104.
[107] Tong X., Benz L., Kolmakov A., Chrétien S., Metiu H., Buratto S.K., Surf. Sci. 575 (2005) 60.
[108] Manuel M., Kemper P., Bowers M.T., J. Am. Chem. Soc. (Submitted for publication).
[109] Kemper P., Manuel M., Bowers M.T. (Manuscript in preparation).
[110] Lai X., St. Clair T.P., Valden M., Goodman D.W., Prog. Surf. Sci. 59 (1998) 25.
[111] Chen D.A., Bartelt M.C., Seutter S.M., McCarty K.F., Surf. Sci. 464 (2000) L708.
[112] Benz L., Tong X., Kemper P., Lilach Y., Kolmakov A., Metiu H., Bowers M.T., Buratto S.K., J. Chem. Phys. 122 (2005) 081102.

This page intentionally left blank

Chapter 5

Oxide-supported metal clusters

Mingshu Chen and D. Wayne Goodman*

Department of Chemistry, Texas A&M University, P.O. Box 30012, College Station, TX 77842-3012, USA

1. INTRODUCTION

Oxides are fundamentally important in heterogeneous catalysis as an active catalyst and as a support for metal clusters [1]. Many of the traditional techniques used to study heterogeneous catalysts are limited with respect to resolving atomic details of metal-supported catalysts. Work over the last two decades has demonstrated that atomic-level surface science techniques can provide fundamental insights into the physics and chemistry of oxide surfaces by enabling the synthesis of metal clusters on oxide films [2–14]. Furthermore, correlation among structure, electronic properties, and reactivity of these model catalysts can now be studied in situ with newly developed surface science techniques. These specially prepared model systems offer advantages typically found for single crystals, while addressing important issues of supported catalysts such as metal cluster size effects and the role of the support. Representative oxide thin films have been shown to mimic the chemical and physical properties of the corresponding bulk oxides, yet are electrically conductive [11]. The conductivity and planarity of these model catalysts allow study with various charged particle spectroscopies that comprise the core of modern surface science while being suitable for study with scanning tunneling and atomic force microscopies. The structural, electronic, and chemical properties of metal overlayers on oxide supports have been extensively reviewed [1–33]. Here, we focus on recent developments in the investigations of metal clusters supported on well-defined, thin oxide films. Four prototype oxide supports are addressed: Al_2O_3, MgO, SiO_2, and TiO_x. The chapter is organized as follows: the preparation, structure, and properties of the oxide supports are first addressed followed by a description of metal clusters supported on these oxide surfaces. Discussion of the interaction of these composite systems with molecular reactants is included.

The Chemical Physics of Solid Surfaces, Volume 12
ISSN: 1571-0785
DOI: 10.1016/S1571-0785(07)12005-8

*Corresponding author.
E-mail: goodman@mail.chem.tamu.edu

ABBREVIATIONS

AES	Auger electron spectroscopy
AFM	atomic force microscopy
AREELS	angle resolved electron energy loss spectroscopy
ARUPS	angle resolved ultraviolet photoelectron spectroscopy
DFT	density function theory
EELS	electron energy loss spectroscopy
ESR	electron spin resonance
EXAFS	extended X-ray absorption fine structure
FTIRS	Fourier transform infrared spectroscopy
HAADF	high-angle annular dark-field microscopy
HREELS	high resolution electron energy loss spectroscopy
HRSEM	high resolution scanning electron microscopy
HRTEM	high resolution transmission electron microscopy
IR	infrared
LEED	low energy electron diffraction
LEIS	low energy ion scattering spectroscopy
MIES	metastable impact electron spectroscopy
ML	monolayers
NC-AFM	non-contact atomic force microscopy
PM-RAIRS	polarization modulation reflectance absorption infrared spectroscopy
RAIRS	reflectance absorption infrared spectroscopy
RHEED	reflectance high energy electron diffraction
SFVS	sum-frequency vibrational spectroscopy
SPA-LEED	spot profile analysis low energy electron diffraction
SPM	scanning probe microscopy
STEM	scanning transmission electron microscopy
STM	scanning tunneling microscopy
STS	scanning tunneling spectroscopy
TEM	transmission electron microscopy
TDS	thermal desorption spectrometry
TPD	temperature programmed desorption
UHV	ultrahigh vacuum
WBDF	weak beam dark field
XAFS	X-ray absorption fine structure
XAS	X-ray absorption spectroscopy
XMCD	X-ray magnetic circular dichroism
XPD	X-ray photoelectron diffraction
XPS	X-ray photoelectron spectroscopy
XRD	X-ray diffraction

2. ALUMINA-SUPPORTED METAL CLUSTERS

Aluminum oxide (Al_2O_3) is a widely used support for heterogeneous catalysts. Ultrathin Al_2O_3 ordered layers on alloys are used as templates for model catalysts,

tunneling barriers in electronic devices, or corrosion-resistant layers. While aluminum oxide crystallizes in various structures depending on conditions and the precursors used in its preparation, alumina is thermodynamically the most stable compound over a wide temperature range. The physical and chemical properties of the hydrated α-Al_2O_3(0 0 0 1) surface are important for understanding the reactivity of natural and synthetic aluminum-containing oxides. The structure of this surface has been determined in the presence of water vapor at 300 K by crystal truncation rod diffraction [34]. The fully hydrated surface is oxygen terminated with a 53% contracted double Al layer directly below. The structure is intermediate between α-Al_2O_3 and γ-$Al(OH)_3$, a fully hydroxylated form of alumina. A partially ordered oxygen layer ~0.23 nm above the terminal oxygen layer is believed to be adsorbed water. The clean α-Al_2O_3(0 0 0 1) surface, in contrast, is Al terminated and significantly relaxed relative to the bulk structure. These differences have been used to explain the different reactivities of the clean and hydroxylated surfaces.

2.1. Preparation of Al_2O_3 on a metal or alloy surface

A thin, well-ordered alumina film 0.4–0.5 nm in thickness can be grown on low-index terminations of NiAl alloy like NiAl(1 1 0) [35, 36] and Ni_3Al(1 1 1) [37–39]. However, films grown on NiAl(1 1 1) and NiAl(1 0 0) are not highly ordered or conformal [40, 41]. Epitaxial Al_2O_3 grown on NiAl(1 1 0) has been studied using LEED, EELS, HREELS, XPS, ARUPS, and STM [22, 35, 42, 43]. The film exhibits a 2D band structure measured by ARUPS [35]. The highly ordered crystalline films can be prepared at temperatures between 620 and 670 K as indicated by LEED. Stoichiometry of O–Al bonds during oxygen absorption and realignment during annealing is important in epitaxial growth of well-ordered crystalline films [44]. NC-AFM reveals atomic rows with a 0.9-nm periodicity [45].

The complex atomic structure of well-ordered Al_2O_3/NiAl(1 1 0) films has been resolved using XRD [46]. The oxide layer is composed of a double layer of strongly distorted hexagonal oxygen ions with aluminum ions in octahedral and tetrahedral sites with equal probability. The alumina overlayer exhibits a domain structure related to defects formed by the growth of a hexagonally ordered overlayer (Al_2O_3) on a body-centered cubic (1 1 0) substrate (NiAl). Using high-resolution soft XPS, the relative populations of tetrahedrally and octahedrally coordinated Al^{3+} have been determined to be ~27/73 [47]. The band structure along two azimuths (1 1 0) and (1 0 0) has been compared with values theoretically determined [35].

DFT calculations were also used to model the structure shown in Fig. 1 [48]. This model reproduces the essential experimental data including the detailed phonon spectrum (Fig. 2; [48, 49]). The surface of the alumina film is characterized by an almost coplanar Al–O layer, as predicted for terminated bulk single crystal alumina surfaces. The film structure is characterized by Al ions in different coordinative environments and compares with the structure believed to exist on an oxygen deficient corundum surface. The oxide layer contains domain boundaries, both regular and antiphase-domain boundaries, which play an important role in the reactivity of the film toward molecules and metal deposits. The stoichiometry of the film is estimated to be $Al_{10}O_{13}$, i.e. an oxygen deficient alumina.

A smooth, continuous alumina film can also be grown on an Ni_3Al(1 1 1) surface with a thickness comparable to that on NiAl(1 1 0) [37–39, 50, 51]. A conclusive and

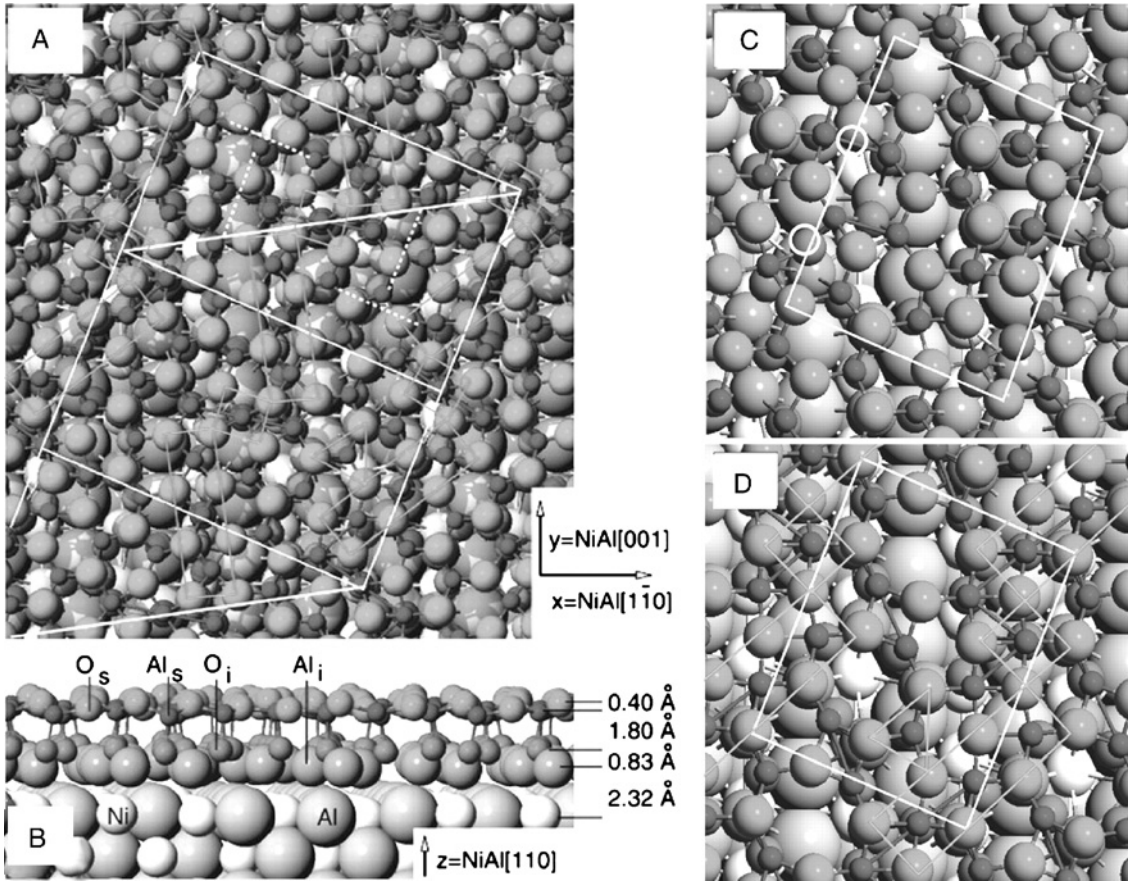

Figure 1: (A) Top and (B) side view of the DFT- and STM-based model for the ultrathin aluminum oxide film on NiAl(1 1 0). (C, D) Energetically favorable models for smaller oxide unit cells with stoichiometries (C) $2(Al_4O_6Al_6O_6)$ and (D) $2(Al_4O_6Al_6O_7)$ on an NiAl unit cell (white rectangle) [48].

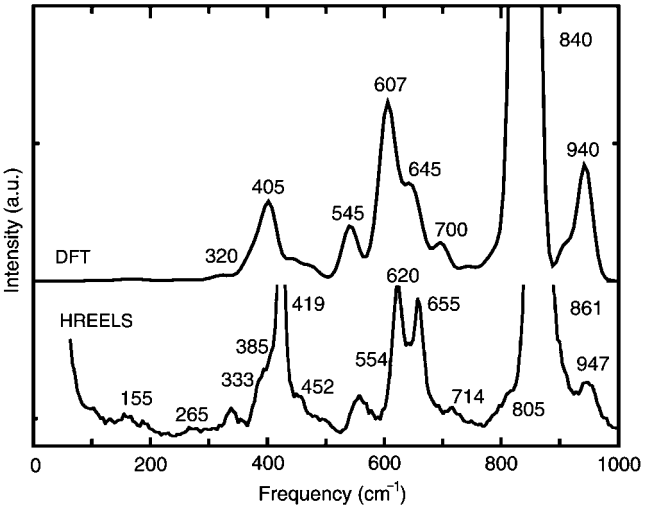

Figure 2: Infrared-active modes as calculated by DFT (broadened by a Gaussian with a width of 20 cm^{-1}) [48] and HREELS data from Ref. [49].

detailed structure of $Al_2O_3/Ni_3Al(1\,1\,1)$ has not yet been obtained. Attempts have been made to hydroxylate the film under UHV as well at ambient conditions [52–55]. STM data suggest that at elevated water pressures, the film is hydroxylated and becomes rough. A remarkable property of $Al_2O_3/Ni_3Al(1\,1\,1)$ is its ability to nucleate various metal clusters in an almost regular hexagonal array [56].

The heteroepitaxial growth of thin $Al_2O_3(1\,1\,1)$ films on Ta(1 1 0) has been studied using LEIS and LEED, and the initial film growth found to be largely 2D clusters [57]. The LEED results indicate formation of a long-range, ordered epitaxial Al_2O_3 film with a slightly distorted ($\beta = 117.9^\circ$) hexagonal lattice. Detailed structural analysis has shown that the hexagonal lattice is due to an ordered, close-packed oxygen anion layer associated with either the (0 0 0 1) face of α-Al_2O_3 or the (1 1 1) face of α-Al_2O_3. Chemically, the $Al_2O_3(1\,1\,1)/Ta(1\,1\,0)$ film is very inert toward a variety of gas molecules, indicating no unsaturated surface bonds.

Thin Al_2O_3 films with various thicknesses have been prepared on an Mo(1 1 0) surface [58]. Film growth, carried out in an oxygen background pressure of 10^{-6} Torr, was studied by AES, LEED, and HREELS. The AES results show formation of a stoichiometric Al_2O_3 film with no indication of metallic Al. LEED studies of very thin Al_2O_3 films (<0.8 nm) show a hexagonal pattern corresponding to the structure described above for $Al_2O_3/Ta(1\,1\,0)$. Thin Al_2O_3 films have also been synthesized on Mo(1 0 0) and their surface chemical activity examined with AES, XPS, and RAIRS [59]. Surface hydroxyls were formed by reaction with D_2O and monitored by the presence of a RAIRS feature at 2700 cm^{-1}. Ammonia adsorption on a dehydroxylated surface yields a single peak at 1260 cm^{-1} due to ammonia adsorbed at a surface Lewis site where the principle symmetry axis of ammonia is oriented perpendicular to the surface plane. Ammonia also adsorbs at Lewis sites on a hydroxylated surface with a slightly different adsorption geometry from that on a dehydroxylated surface [59]. A single-crystal film of α-Al_2O_3 with a thickness of 0.65–3.0 nm is reported to have

been grown on Ru(0 0 0 1) [60]. The dispersion relation as a function of the wavevector parallel to the surface, $q_{||}$, was observed to have a negative gradient in the $(\Gamma - \overline{M})$ direction using AREELS.

Most molecules interact rather weakly with the alumina surface. For example, the adsorption of CO on alumina has been studied with EELS [61]. The vibrational fine structure of the energy loss features due to electronic transitions of adsorbed CO has been clearly resolved. The EELS results for CO on a monolayer film show broader vibrational line widths and a higher excitation energy than for CO on multilayer alumina. The half-widths of the loss features have been used to estimate the lifetime of the excited states. NO, on the other hand, interacts with the alumina film at room temperature and at higher exposures by forming compounds such as nitrites and nitrates [62]. The reaction appears to occur exclusively at the domain boundaries in the film as this reactivity may be completely suppressed by selective decoration of the defects by Pd metal deposition [63].

2.2. Pt-group metals on Al_2O_3

Pt clusters supported on Al_2O_3/NiAl(1 1 0) and CO adsorption on the supported clusters have been characterized using STM, SPA-LEED, ARUPS, HREELS, EELS, TPD, XPS, and TEM [18, 64–70]. The Al_2O_3 film has been shown to be strongly modified by deposition of Pt where the Pt is incorporated into the oxide layer. To a large extent, this process can be suppressed by deposition at low temperature (100 K), whereas heating to temperatures >800 K leads to diffusion of Pt through the oxide into the substrate followed by recovery of the oxide superstructure. Deposition of several monolayers of Pt at 500 K results in the formation of a polycrystalline film with a ⟨1 1 1⟩ orientation and a preferred azimuthal orientation with respect to the substrate. In addition to CO desorption from metallic-like Pt, a low-temperature CO desorption state has been attributed to $A1_2O_3$ modified by Pt. HREELS results show that CO is adsorbed at the on-top site at low to intermediate CO coverages. At higher CO coverages, the bridging site is also populated. XPS results at 300 K show a feature at 284.8 eV, typical for adsorbed carbon, in addition to a feature corresponding to molecularly adsorbed CO. These results indicate that dissociative CO adsorption occurs on small Pt clusters even at room temperature. The first HREELS observation of the ethylidyne species on alumina-supported catalysts was reported by Hensley and Kesmodel [70], where π and di-σ species of C_2H_4 are identified for adsorption at 165 K; ethylidyne is observed only for relatively large Pt clusters upon warming to 325 K.

Ab initio methods have been used to study the electronic structure of Pt on Al- and O-terminated α-Al_2O_3 [71]. A coexistence of charge-transfer valence-band states and band-like metallic states is predicted to lead to significant changes in the surface chemistry. Pd and Rh show similar modifications of the electronic structure, indicating that these changes may be general for transition metals on both electronegative and electropositive surfaces. These results demonstrate the importance of metal-support charge transfer in defining the properties of a supported metal [33, 72, 73]. Increased activity at the perimeter of metal clusters with diameters <5 nm may be partially attributed to the strong metal–oxide interaction at the metal–oxide interface.

By carefully controlling the growth conditions, Rh clusters with varying cluster sizes have been deposited on Al_2O_3/NiAl(1 1 0) [74] and the size distributions characterized with STM [18, 75]. It is known from metal single crystal studies that CO

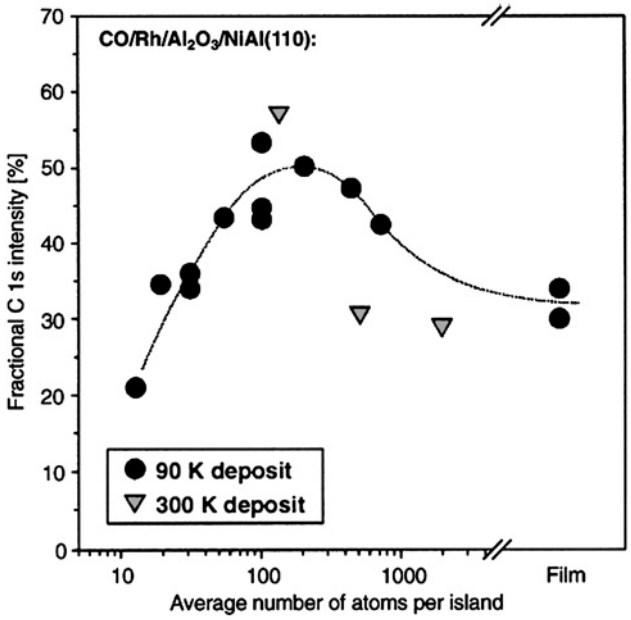

Figure 3: CO dissociation activity on alumina-supported Rh clusters as determined by XPS. Note that the behavior of the clusters grown at 300 K (triangles) is not fully identical to the behavior of 90 K deposits (circles) [80].

adsorbs/desorbs molecularly on clean low-index Rh surfaces [76]. On the other hand there is conflicting evidence in the literature with respect to the onset of CO dissociation as a function of Rh cluster size [77–79]. Some reports claim that CO dissociation increases with increasing cluster size while others report the reverse. Figure 3 shows the CO dissociation probability as a function of Rh cluster size on alumina films [80, 81]. The dissociation probability decreases to zero for very small Rh clusters, a result consistent with the existent of stable molecular Rh carbonyl complexes. The dissociation probability also decreases for large clusters, asymptotically approaching a value similar to stepped Rh single crystal surfaces [82, 83]. In an intermediate regime of cluster size, the dissociation goes through a maximum that correlates with the formation of irregular clusters as indicated by their aspect ratio. This result rationalizes the observation of both decreasing and increasing CO dissociation probabilities on technical powder catalysts where the precise cluster size is not well defined.

A large data set has been assembled for Pd deposition on alumina films [22, 25, 28, 30, 84–87]. Figure 4 shows an STM image of 6 nm average size Pd clusters with well-resolved facets [85]. The adhesion energy for Pd on Al_2O_3 has been determined to be $(2.8 \pm 0.2)\,J/m^2$ [85]. SFVS has been used for the first time to monitor CO stretching vibrations on alumina-supported Pd clusters in the pressure range from 10^{-7} to 200 Torr. Two adsorption sites (twofold bridging and on-top) have been identified on Pd aggregates 3 and 6 nm mean size with a high density of surface defects. The CO adsorption site occupancy on Pd clusters is primarily governed by the CO pressure as well as the structure of the clusters and their temperature [86]. In this respect, clusters down to a size containing only a few atoms have been studied. In fact, single Pd atoms

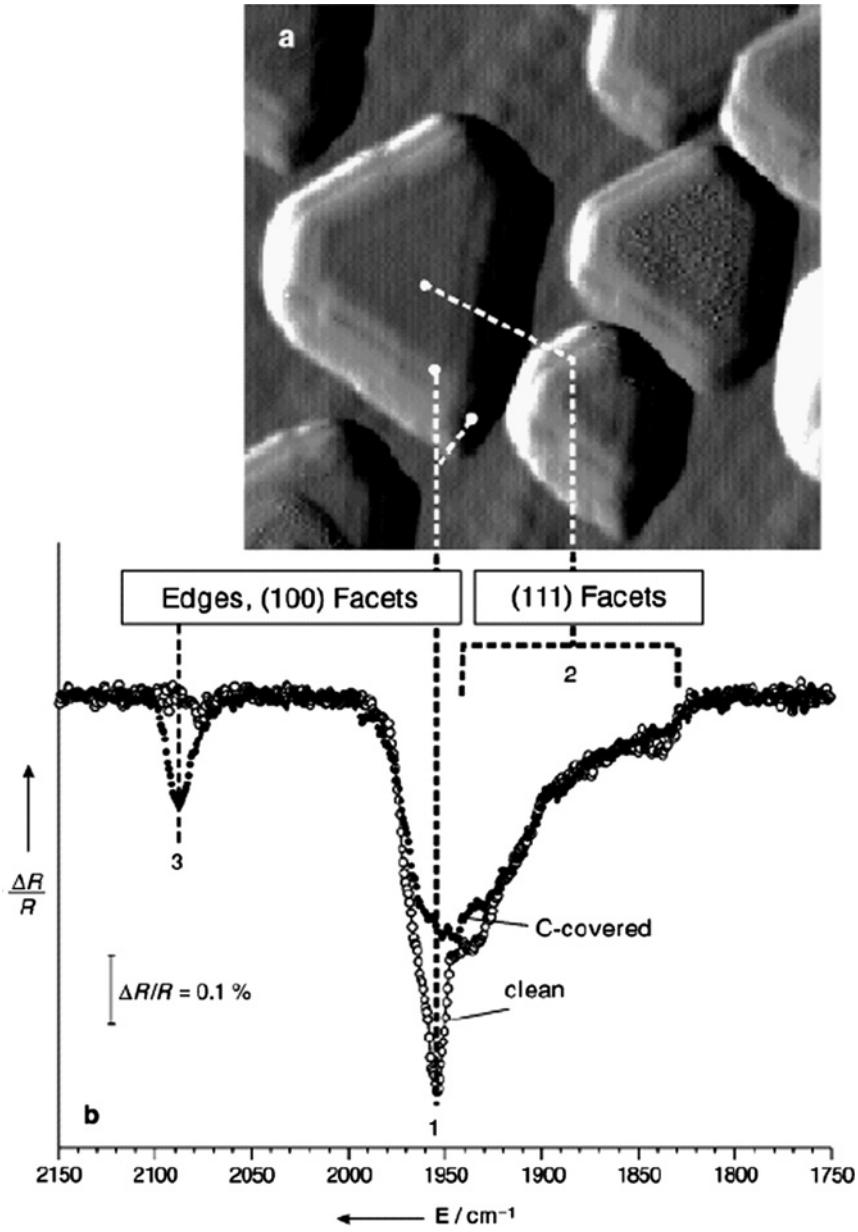

Figure 4: (a) STM image of the Pd clusters grown at 300 K on Al_2O_3/NiAl(1 1 0) (20 × 20 nm). (b) RAIR spectra for NCO adsorption on Pd/Al_2O_3/NiAl(1 1 0) (sample temperature 100 K, after CO exposure at 300 K); R = reflectivity; open symbols: immediately after preparation; solid symbols: after prolonged exposure to methanol at 440 K [85].

have been imaged on an Al_2O_3 film [87]. Bimetallic alloy clusters (Pd–Co and Pd–Ag) have also been prepared, characterized, and studied with respect to reactivity [88–93].

Adsorption and reaction of a variety of molecules have been studied in detail at UHV conditions and at elevated pressures [86, 94–104]. The most frequently studied molecules are CO, NO, CH_3OH, and C_2H_4 with respect to oxidation, hydrogenation, and oxidative dehydrogenation reactions. CO dissociation has not been observed for Pd/alumina model systems [105, 106]. On the other hand, for the corresponding technical catalysts, dissociation has been reported [107, 108]. In any case, CO bond cleavage has been seen for CH_3OH dehydrogenation on Pd/alumina [105]. Detailed molecular beam experiments have shown C–O bond cleavage before the methanol molecule has been fully dehydrogenated. The reaction occurs very rapidly at the edges and corners of Pd clusters. Figure 5 shows CO infrared spectra acquired before and after reaction with CH_3OH [109]. CO probes the available sites at the surface (shown schematically in Fig. 5) and indicates that the deposited carbon blocks the edge and Pd(1 0 0) sites. Similar results indicative of the influence of step edges on dissociation have been found for NO [109]. Data show that dissociation products enhance the chemical reactivity of steps.

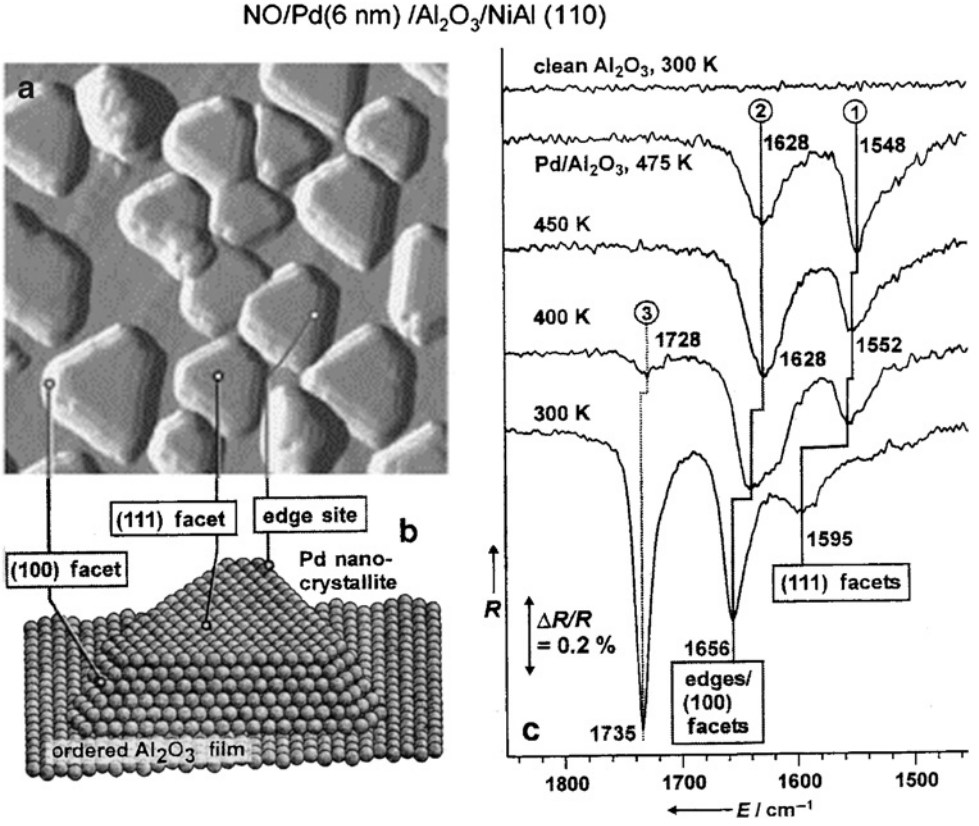

Figure 5: (a) 40 nm × 40 nm STM image for Pd clusters deposited on Al_2O_3/NiAl(1 1 0) planar oxide support (top) schematic depicting the geometry of Pd clusters of diameter 6 nm (bottom). (b) Low-pressure RAIR spectra for NO adsorption on Pd(6 nm)/Al_2O_3/NiAl(1 1 0) [109].

The adsorption, decomposition, and oxidation of methanol on $Pd/Al_2O_3/NiAl(1\,1\,0)$ model catalysts have also been investigated utilizing a combination of molecular beams, RAIRS, and TPD [110]. On Al_2O_3, two molecular adsorption states of methanol are distinguished by RAIRS and TPD where the features for methanol adsorbed on Pd clusters can be differentiated from methanol adsorbed on Al_2O_3. Preadsorbed CO suppresses methanol adsorption on the Pd clusters whereas preadsorbed oxygen reduces the reaction probability. A methoxy intermediate species was identified and shown to be stable up to 200 K. The dominant pathway is dehydrogenation to CO, followed by CO_2 formation in the presence of oxygen. Adsorbed oxygen has a pronounced inhibiting effect on the rate of decomposition.

Changes in the site of adsorbed CO induced by femtosecond (fsec) laser irradiation has been investigated on Pd clusters containing 100–6000 atoms supported on epitaxial $Al_2O_3/NiAl(1\,1\,0)$ using laser light at $\lambda = 400$ nm and pulse lengths of 70 fsec [111]. The laser-induced processes correlate with the presence of higher local adsorbate densities and a substantial population of edge sites. The interaction of oxygen with $Pd/Al_2O_3/NiAl(1\,1\,0)$ was studied by STM, AES, LEED, XPS, TPD, and molecular beam techniques [112]. The results show that O_2 exposure at 400–500 K strongly influences the oxide support, probably due to the fact that oxygen atoms formed by dissociation on the Pd surface can diffuse through the alumina film and react with the NiAl substrate beneath the Pd clusters. The surface oxygen inhibits hydrogen adsorption and readily reacts with CO at 300–500 K. At low coverage, CO adsorbs 5–7 kJ/mol more strongly on the smaller Pd clusters compared with the larger clusters.

Hydrazine decomposition was carried out on mass-selected deposited $Ir_n^+/Al_2O_3/NiAl(1\,1\,0)$ [113, 114]. Small Ir_n ($n \leqslant 15$) clusters promote hydrazine decomposition at temperatures well below room temperature with significant activity first appearing at Ir_7. Both activity and product branching are strongly dependent on the cluster size, with smaller clusters showing only dehydrogenation and N_2 desorption at low temperatures, and H_2 recombinative desorption at temperatures above 300 K. For Ir_{15}, ammonia production appears signaling the onset of a transition to clusters able to facilitate more complex chemistry. $Ir_n^+/Al_2O_3/NiAl(1\,1\,0)$ model catalysts were found to exhibit hydrazine decomposition properties qualitatively similar to those observed for single-crystal Ir and polycrystalline Rh. At 800 K, sintering of the clusters occurs with a significant fraction of the nitrogen contained in the hydrazine being converted to aluminum nitride (or mixed $Al_xO_yN_z$).

TPD was used to study the interaction of oxygen with both large (~10 nm) and small (<2 nm) Rh, Pt, and Pd clusters supported on α-$Al_2O_3(0\,0\,0\,1)$ [115]. The results of this study indicate that O_2 desorption from large clusters of Rh, Pt, and Pd is similar to that from low-index planes of the respective metal single crystals. Additionally, O_2 desorption from small Rh clusters is similar to that from the close-packed planes of bulk Ph. In contrast, O_2 desorption from small clusters of Pt and Pd occurs at a significantly higher temperature than that from the respective, low-index single crystal surfaces despite a significantly higher saturation oxygen coverage on the small clusters.

Ethene hydrogenation has been used as a probe reaction to show that the reactivity of clusters is very different from single crystals [99, 116–119]. While ethene is not hydrogenated on Pd(1 1 1) under UHV conditions, this reaction readily occurs on (1 1 1)-terminated Pd/alumina clusters. The rationale is the subsurface hydrogen whose nature and quantity varies with the reaction temperatures. On a bulk single crystal

subsurface hydrogen can diffuse into the bulk, whereas in a nanocluster, subsurface hydrogen is confined near the surface. This example clearly shows that single crystal surface studies are not always good models for understanding processes on metal clusters. However, divergence of reactive properties from single crystal surfaces can be probed with metal clusters of varying size. Silvestre-Albero et al. [102, 120] have recently studied butadiene hydrogenation on Pd/alumina model systems as a function of cluster size. The kinetics show pronounced, characteristic differences between smaller (<5 nm) and significantly larger clusters. While the larger clusters show a close correspondence to Pd(1 1 1) single crystal surfaces, the smaller clusters exhibit very different kinetics. These results show that extrapolation of data from single crystals to data for facetted clusters is possible and establishes a limiting size for similar behavior.

Thin alumina films can be chemically modified by hydroxylation [121, 122]. The influence of chemical modification on nucleation, growth, and thermal stability of metal deposits is substantial as indicated by studies on Rh and Pd clusters. In the case of Rh, the metal appears to be oxidized by the OH groups, releasing hydrogen in the process. The metal dispersion increases with the extent of hydroxylation. In addition, the temperature at which cluster sintering becomes appreciable is increased with an increase in hydroxylation by $\sim$100 K [123].

Thin film oxide supports are generally well suited as model supports for heterogeneous model catalysts. However, it has recently been predicted by Pacchioni et al. [124] that for particular metals on thin oxide films, a strong interaction can occur between the deposited metal cluster and the supporting oxide film. This prediction is in line with a suggestion by Mott [125] that electrons tunneling from the metal lead to oxidization of the metal [125] and that growth at the oxide interface may be rate limiting. Kulawik et al. [126] recently demonstrated that Au atoms evaporated onto thin alumina films on NiAl(1 1 0) nucleate at Al rather than oxygen sites, which are the preferred sites for Au adsorption on bulk alumina. Bonding of Pd atoms on the film, on the other hand, is influenced very little by the underlying metal support as predicted theoretically. Furthermore, due to interaction between Au and the underlying metal, Au on alumina grows in a linear arrangement of atoms with no strong direct Au–Au interaction. The formation of the chains is also mediated by the substrate.

Well-faceted Rh nanocrystals with mean cluster sizes of 7.8, 13.3, and 16.7 nm have been synthesized on Al_2O_3 and TiO_2 [127]. Wetting of the support and coalescence of Rh clusters were observed upon high-temperature reduction ($\sim$620 K on titania and $\sim$720 K on alumina) of large (>10 nm) and closely spaced Rh clusters. Catalysts with smaller Rh clusters did not exhibit such pronounced changes. Rh/Al_2O_3 after reduction at 523 K exhibits maximum activity for ring opening of methylcyclobutane at 373 K due to the formation of low-coordinated sites as shown by TEM. The activity of Rh/TiO_2 peaks after reduction at 373 K decreases exponentially with reduction temperatures to 673 K. For Rh/TiO_2, the changes in cluster size and microstructure as observed by TEM account for only a portion of the kinetic behavior. The sharp activity decrease for Rh clusters supported on TiO_2 with increasing anneal temperatures parallels the increase in the number of oxygen vacancies and low-valent Ti cations on the TiO_2 surface. The latter may affect the electric field at the metal–support boundary and thereby reduce the catalytic activity for hydrocarbon reactions. In addition, the decoration of Rh clusters by migrating Ti suboxide could account for the diminished activity subsequent to high-temperature reduction.

2.3. IB group metals on Al_2O_3

Numerous studies have addressed the morphology and structure of Ag [69, 128, 129], Au [130–133], and alloy clusters on alumina. It is noteworthy that Au at room temperature shows a higher degree of dispersion in comparison with Ag. The electronic structure of the coinage metal clusters has been investigated using a photon-scanning tunneling microscopy [69], and the dependence of the plasmon on metal, size, and alloying has been determined.

It is worth noting that IR spectra of CO adsorbed on Pd supported on alumina compares very closely to equivalent data for deposited Pd clusters synthesized by wet impregnation of precursor salts on high-surface-area powder catalysts [116]. The IR spectra of Pd/alumina model systems also compare closely with powder catalysts prepared with Pd deposits from the decomposition of $Pd(N_3)_2$, i.e. with no precursor residues. Dellwig et al. [86] have reported vibrational data of CO at room temperature on Pd clusters deposited on alumina films as a function of pressure from 10^{-10} to 600 Torr. While there are differences between the CO spectra acquired at varying pressures for the Pd clusters and equivalent data acquired for Pd(1 1 1) (the orientation of the most abundant facet of the Pd clusters in question), there is no indication for any additional "high-pressure species." Also, the spectra acquired for the Pd clusters are fully reversible as a function of pressure [106].

The growth of Cu deposits on Al_2O_3 films has been investigated in the 80–800 K substrate temperature range [58]. The films used for supporting the Cu clusters were typically 2 nm thick and exhibited excellent thermal stability and chemical inertness toward adsorption. Although Cu clusters prepared at relatively low substrate temperatures exhibit smaller average cluster sizes and higher cluster densities than those prepared at higher temperatures [134–136], the low temperature preparations are unstable and undergo a major change in morphology and size upon annealing or following CO chemisorption. It was shown that in order to prepare thermally and chemically stable clusters of catalytic interest, it is imperative to carry out the metal deposition at elevated substrate temperatures [58].

TPD spectra of Cu deposited onto an Al_2O_3 film at various substrate temperatures, T_s, show a shift of the peak maxima to higher temperatures and a narrowing of the TPD peak as T_s is increased. It was suggested that the broad TPD peaks observed at low substrate temperatures is due to heterogeneity reflecting a broader size distribution of the Cu clusters. AES measurements show that Cu clusters prepared at $T_s = 600$ K are thermally stable up to an annealing temperature of 850 K, whereas a decrease in Cu AES intensity was observed upon annealing of Cu clusters prepared at $T_s = 80$ K. A family of TPD spectra of Cu deposited at $T_s = 600$ K is plotted in Fig. 6 as a function of the Cu coverage in equivalent monolayers, θ_{Cu}. The leading edge of the TPD peak shifts continuously toward higher temperatures as θ_{Cu} is increased. At the same time, the TPD peak width remains essentially unchanged as θ_{Cu} is varied over many Cu multilayers. The inset in Fig. 6 shows that the heat of sublimation of Cu clusters decreases rapidly from its bulk value of (334.4 ± 12) kJ/mol at $\theta_{Cu} \approx 1.2$–205 kJ/mol at $\theta_{Cu} \approx 0.2$. This has been attributed to a decrease in the number of neighboring Cu atoms as the Cu clusters become smaller. The average size of the Cu clusters estimated from the AES measurements compares favorably with direct measurements by TEM.

The reaction of NO and CO has been studied by exposing the surface with varying Cu deposits supported on Al_2O_3 films to a $^{15}NO/CO$ (1:1) mixture using TPD and

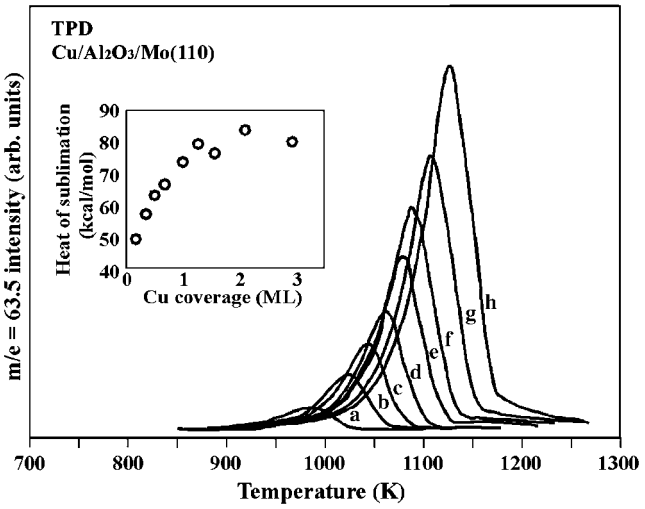

Figure 6: A family of TPD spectra of Cu deposited at $T_s = 600$ K as a function of equivalent monolayers, θ_{Cu}: (a–h) 0.16, 0.33, 0.50, 0.67, 0.98, 1.25, 1.55, and 2.09 ML, respectively. The inset shows the heat of sublimation, derived from the leading edge analysis of the spectra, as a function of Cu coverage in equivalent monolayers. A linear heating rate of 10 K/sec was used [58].

HREELS [58]. At $\theta_{Cu} = 2.7$, corresponding to a cluster size of ≈ 10.5 nm, desorptions of the parent molecules of ^{15}NO and CO and the gaseous products $^{15}N_2$ and $^{15}N_2O$, due to ^{15}NO decomposition, were observed in TPD. A small CO_2 desorption peak is also observed at temperatures between approximately 150 and 250 K, indicating reaction between CO and ^{15}NO on the supported Cu clusters. For small Cu coverages, i.e. $\theta_{Cu} \leqslant 0.67$, a CO_2 desorption peak was not observed. However, since the CO_2 yield is relatively small, the effect of cluster size on CO_2 production is unclear. Exposure of the clean surface to the $^{15}N_2$/CO gas mixture gives rise to several adsorbate HREELS features in the 1000–2500 cm^{-1} frequency range, the losses at 1255 and 1465 cm^{-1} attributed to the $\nu(^{15}NO)$ mode of adsorbed ^{15}NO and $^{15}N_2O$, respectively, and 2110 cm^{-1} to ν(CO) of adsorbed CO.

Both Cu and Au form 3D clusters on Al_2O_3/Mo(1 1 0) regardless of thickness (2–5 ML). At a very low coverage (<0.4 ML), Cu deposited on the oxide strongly interacts with the surface oxygen forming a species resembling Cu oxide(s); higher Cu coverages have metallic character. On the other hand, Au behaves very differently in that no evidence for the formation of Au–O bonds was found at room temperature. Annealing of Au and Cu deposits on an Al_2O_3 film results in metal/oxide intermixing and chemical reaction [137]. The desorption behavior of Ag from Al_2O_3/Ru(0 0 0 1) and α-Al_2O_3 surfaces is identical, indicating that thin-film Al_2O_3 is a viable model for an α-Al_2O_3 support. The activation energy for Ag desorption from Al_2O_3 is smaller than the Ag bulk sublimation heat [138].

Size-selected Au clusters, Au_n^+ ($n = 1, 3, 4$), deposited on an ordered Al_2O_3/NiAl(1 1 0), have been investigated by XPS and LEIS [139]. Changes in morphology and electronic properties with deposition/annealing temperature and in cluster size via extensive agglomeration were observed by LEIS for annealing temperatures above 300 K. These changes were accompanied by large shifts in the Au XPS binding energy.

Agglomeration is more extensive following room-temperature deposition compared with samples prepared by low-temperature deposition and very dependent on the cluster size. CO adsorption was studied by LEIS and TPD. No activity for CO oxidation was observed for Au_n/Al_2O_3 whereas, under similar conditions, substantial activity was seen for Au_n/TiO_2.

3. MAGNESIUM OXIDE-SUPPORTED METAL CLUSTERS

Magnesium oxide (MgO) is a commonly used oxide support for metal catalysts. Well-ordered surfaces of MgO relatively free of defects can be created by cleaving bulk single crystals. MgO(1 0 0) surfaces are stoichiometric and show practically no surface relaxation [140, 141].

3.1. Preparation of MgO films

MgO(1 0 0) films have been prepared mainly on Mo(1 0 0) and Ag(1 0 0) substrates. Mo is used because of its high melting point; Ag is used as a substrate because of the close match of its lattice constant with MgO. Epitaxial MgO(1 0 0) with a thickness ranging from 2 to 100 ML can be grown by evaporating Mg onto Mo(1 0 0) at 300 K in 10^{-6} Torr of oxygen. Stoichiometric MgO(1 0 0) thin films have been characterized using LEED, AES, XPS, HREELS, EELS, UPS/MIES, and TPD [142–152]. The films, stable up to 1300 K, are reduced at higher temperatures by the Mo substrate, forming MoO_3 and Mg vapor. The electronic and vibrational structures of thin MgO films are very similar to those of the bulk oxide; EELS and UPS/MIES have shown that these MgO films are nearly free of point defects [153–160]. MgO films with a thickness of 2 nm can be grown on W(1 1 0) [161].

LEED indicates the growth of MgO(1 0 0) films with the MgO(1 1 0) oriented along ⟨1 0 0⟩ directions of the Mo(0 0 1) substrate [162–164]. Despite the insulating nature of bulk MgO, films up to 2.5 nm thick are sufficiently conducting to perform STM measurements. STM reveals Mg deposition in an oxygen ambient at substrate temperatures from 300 to 900 K producing uniform films. Films as thick as eight atomic layers typically have only three layers exposed, and consist of small domains between 2.0 and 6.0 nm in diameter. The domain shapes are random and the perimeters show no preferential orientation. In contrast, films grown at temperatures in excess of 1000 K exhibit much larger 3D MgO islands. Steps on these high-temperature films orient preferentially along thermodynamically favored MgO(1 0 0) directions. The dimensions and symmetry of this pattern are consistent with the coincidence arising from the mismatch of the MgO(1 0 0) and Mo(0 0 1) lattice. Annealing room temperature deposited films results in island coalescence and produces uniform films with domains in excess of 10.0 nm. The perimeters of these domains are oriented along MgO(1 0 0) directions.

MgO(1 0 0)/Ag(1 0 0) systems were prepared by evaporating metallic Mg from an alumina crucible in an oxygen background of 5×10^{-7} Torr at 350 K followed by annealing to 500 K [165–176]. As in the case of MgO(1 0 0)/Mo(1 0 0) [136–146], the as-prepared film appears to be free of point defects (color centers). By dosing electrons to the surface, color centers can be produced and detected by EELS. Exposure to oxygen quenches these defects indicative of their location within the surface layer.

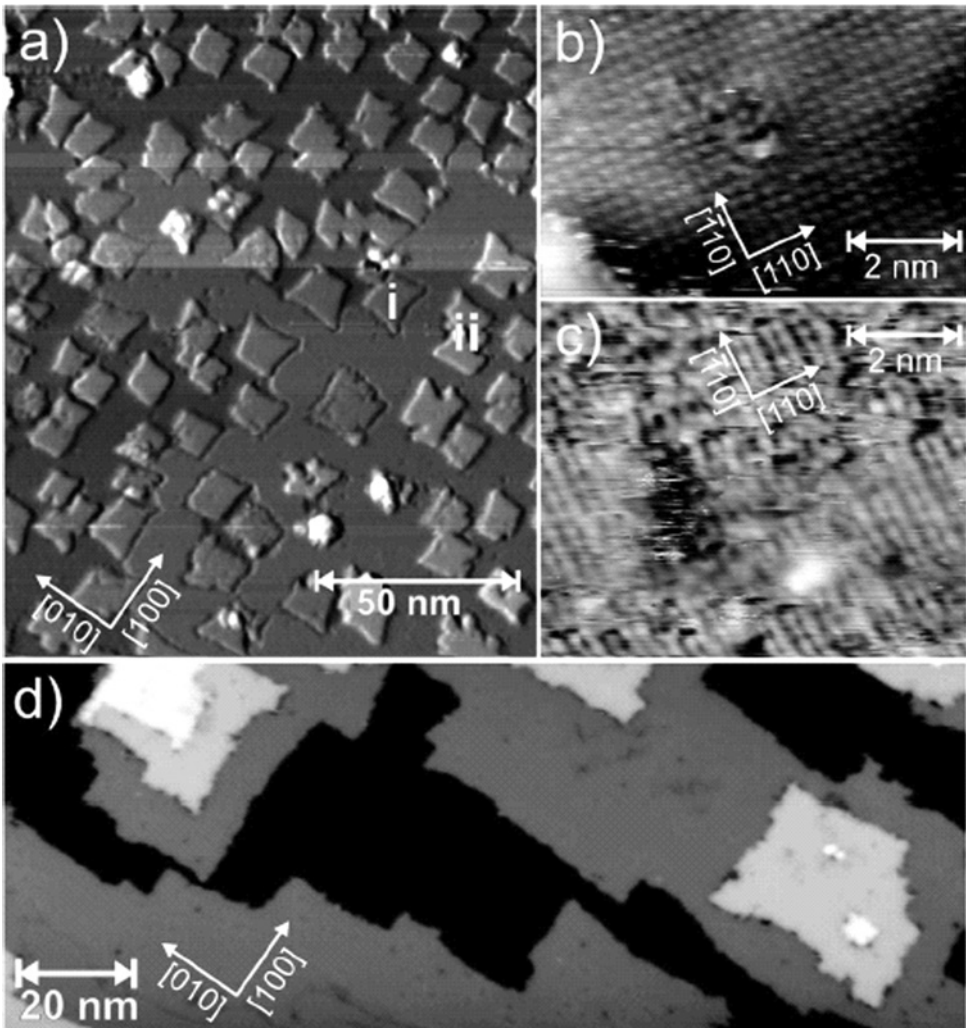

Figure 7: STM images of (a) 0.3 ML MgO/Ag(0 0 1), $U = 5.0$ V, $I = 1.0$ nA; (b) Ag(0 0 1) atomic resolution through an MgO island, $U = 30$ mV, $I = 2$ pA; (c) atomic resolution of the MgO layer (one type of ion is resolved, $U = 2.5$ V, $I = 50$ pA; (d) 2.0 ML MgO/Ag(0 0 1), $U = 3.0$ V, $I = 1.0$ nA [171].

Low-temperature STM has been used to image the growth of the MgO(1 0 0) film on Ag(1 0 0) and the creation of color centers [167, 168, 171]; a series of images is shown in Fig. 7. Layer-resolved differential conductance (dI/dU) measurements show that a three monolayer film has a band gap of ~6 eV, comparable to an MgO(0 0 1) single crystal, as shown in Fig. 8. Layer-resolved DFT calculations corroborate this finding [171]. The MgO film exhibits line defects by LEED profile analysis; point defects only become apparent by STS with electron bombardment, after which, paramagnetic surface colors centers are detectable by ESR spectroscopy [167]. These results can be directly compared with studies on powder samples [177–179]. On mono- and bi-layer domains of MgO/Ag(0 0 1), the edges are mainly oriented along the (1 1 0) oxide

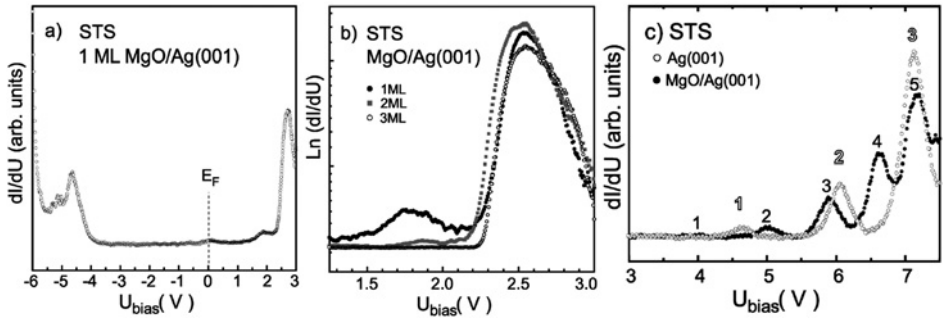

Figure 8: STS of ultrathin MgO/Ag(0 0 1) films (U-sweep interval, tunneling parameters before opening the feedback loop, linear tip–sample distance variation: (a) tip placed above a 1-ML MgO island: −6.0 to 0 V, $U_0 = -6.0$ V, $I_0 = 0.2$ nA, $dz/dU = -0.16$ nm/V; (b) film thickness-dependent dI/dU spectra; 3.0–1.0 V, $U_0 = 3.0$ V, $I_0 = 0.2$ nA, $dz/dU = 0.25$ nm/V; (c) Ag(0 0 1) field resonance states: (o) tip above Ag(0 0 1), (•) tip above 1 ML MgO island: 7.5–3.0 V, $U_0 = -7.5$ V, $I_0 = 0.2$ nA, $dz/dU = -0.2$ nm/V [171].

direction, corresponding to polar perimeters, while on multi-layer domains non-polar perimeters appear, corresponding to the (1 0 0) orientation [180].

Thin MgO films (1–20 ML) synthesized by evaporating metallic Mg in an oxygen atmosphere onto Ag(1 0 0) exhibit a relative small lattice misfit (3.1%) between the (1 0 0) surface unit of the Ag fcc and MgO rock salt structures that facilitates epitaxial growth of MgO layers with the (0 0 1)MgO parallel to (0 0 1)Ag and (1 0 0)MgO parallel to (1 0 0)Ag [181]. In spite of the weak interaction between the oxide overlayer and the substrate, there is a significant tetragonal distortion of the MgO structure. STM data indicate that the substrate is essentially covered after 3 ML of MgO. Thin film growth of MgO on Ag(1 0 0) as a model oxide/metal interface system was studied using RHEED, AES, EELS, and UPS [182]. At a substrate temperature of 450 K, a single-domain MgO film ([1 0 0] (film)//[1 0 0] (substrate)) grows heteroepitaxially on Ag(1 0 0). The in-plane lattice constant of the film changes continuously from the substrate value to that of the film. MgO adsorbs preferentially with the oxygen atom over the Ag atom and the Mg atom over the hollow site. EELS results show that the MgO band gap does not change for thicknesses from 1 to 20 ML, indicating that the band gap of a 1-ML thick MgO film on a metal substrate is essentially that of bulk MgO. The UPS results, on the other hand, show a destabilizing shift of the valence band with decreasing film thickness. These UPS results are explained as due to image charge screening of a hole created by photoionization in the near metal vicinity. The lattice constant increases gradually from bulk Ag(1 0 0) to that of bulk MgO(1 0 0). The lattice constant of the film is nearly equal to that of bulk MgO for films thicker than 20 ML.

Surface sites can also be identified via adsorption and desorption of probe molecules such as CO. The interaction of CO with the MgO(1 0 0) surface is considered as a prototype system for studying properties of ionic surfaces experimentally and theoretically [143, 172–174, 183–189]. From theoretical, it has been concluded that CO binds weakly with its carbon end down to MgO terrace sites in an almost purely electrostatic manner [186]. Adsorption at low-coordinated sites, e.g. at steps, edges, or corners, leads to an increase of the polarization of the molecule, i.e. a blue shift of the CO stretching frequency, with an increase in the binding energy compared with CO

adsorbed on regular terrace sites [143–146]. The magnitude of the CO binding energy has been discussed and debated in the literature [186]; however, CO-TDS of vacuum-cleaved MgO single crystals resolved the controversy [183]. Very similar results have been obtained for MgO thin films [190]. The TDS data compare very favorably with infrared data on micro-crystalline MgO samples. The acid–base properties of MgO(1 0 0)/Mo(1 0 0) have been characterized using HREELS and TPD [144, 145, 147]. Various probe molecules with increasing acid strength from alkanes and alkenes, to water and alcohols, to carboxylic acids were employed in these studies. The use of a high-energy electron beam (50 eV) and off-specular geometry allowed the suppression of the strong surface optical phonons of substrate. Multiple phonon losses are attenuated as the electron beam energy is increased. The HREELS results show that acetic acid, formic acid, methanol, and water undergo heterolytic dissociation, with the acidic proton adsorbed on the basic oxygen anion sites and the conjugate base anions adsorbed on the cationic surface sites. Ethylene and ethane, however, are found to adsorb associatively on the MgO(1 0 0)/Mo(1 0 0) surface. Water and methanol each show a similar desorption behavior. A sharp peak near 150 K is attributed to condensation (of water or methanol) while a broad peak near 300 K is assigned to recombinative desorption.

The partial oxidation of methane to ethane on Li-promoted MgO(1 0 0)/Mo(1 0 0) has been studied by Wu et al. [148–150] using surface analysis and kinetic measurements at elevated pressures. The peaks at 1.6, 3.6, and 5.33 eV in EELS spectra have been attributed to $[Li^+O^-]$ centers, F-aggregates, and F-centers, respectively. It has been found that the ethane formation rate from methane coupling correlates with the F-center concentration but not with the concentration of $[Li^+O^-]$ centers. The role of Li is to promote F-center formation. These results indicate that $[Li^+O^-]$ centers are not likely to be directly involved in the methane activation step, but rather promote the production of color centers in the near-surface region.

The interface of MgO/Ag(0 0 1) has been studied with DFT calculations applied to slabs [191]. Stoichiometric MgO films show limited adhesion to the Ag substrate whereas the adhesion strength can be increased for non-stoichiometric films, either by the presence of O vacancies at the oxide film or by a small excess of O atoms at the interface between the MgO and Ag. For defect-free deposits containing 1 or 2 ML and at low voltages, tunneling occurs from the surface Ag substrate; at large positive voltages, Mg atoms are imaged. Oxygen vacancy defects facilitate tunneling resulting in large apparent protrusions in the image. The additional O, stored at the interface, can be detected for very thin films.

The local atomic structure of MgO epilayers on Ag(0 0 1) has been determined by polarization-dependent XAS at the Mg(K) and O(K) edges [192]. In the ultrathin limit, the local structure of the films is rocksalt. An in-plane compressive strain, due to lattice mismatch with the Ag substrate, is present for the 3 ML film. The out-of-plane lattice constant is found to expand, in agreement with the expected behavior for a tetragonal distortion of the unit cell. This growth-induced strain is gradually released with increasing thickness and it is almost completely relaxed at 20 ML. Any significant intermixing with the Ag substrate was ruled out.

The growth of epitaxial and stoichiometric MgO(1 1 1) thin films on an Mo(1 1 0) surface has been demonstrated using LEED, XPS, AES, and LEIS [193, 194]. The MgO(1 1 1)/Mo(1 1 0) film is stable up to 1400 K, and is reduced by the Mo substrate

at higher temperature, forming MoO_3 and Mg vapor. The adsorption of $[Re_2(CO)_{10}]$ and $[HRe(CO)_5]$ onto this thin film has been studied using TPD and RAIRS. Both molecules decarbonylate upon adsorption to form various surface-bound rhenium carbonyls depending upon the surface temperature.

The geometric structure of MgO deposited on Fe(0 0 1) in UHV by electron evaporation was determined in detail using surface XRD [195]. In contrast to the common belief that MgO grows in direct contact to the Fe(0 0 1) substrate, a FeO interface layer between the substrate and the growing MgO structure has been proposed. This result opens new avenues for addressing and understanding the Fe/MgO/Fe(0 0 1) interface.

3.2. Pt-group metals on MgO(1 0 0)

Pd clusters, 1.5–12 nm, have been epitaxially grown on UHV-cleaved MgO(1 0 0) surfaces, and their crystalline structure and morphology studied by various TEM techniques [196]. At high deposition temperatures, homogeneous distributions of clusters, with a shape of a half octahedron truncated on the top by a (1 0 0) plane, have been obtained. At low deposition temperature, the Pd clusters were flatter with mainly ⟨1 0 0⟩ facets. At high temperatures, on clean air-cleaved substrates, homogeneous distributions of very small clusters (1.5–2 nm) with a high number density and a narrow size distribution were obtained. Pd clusters prepared at UHV conditions on MgO single crystals were in situ annealed under various pressures of O_2 at high temperature, then observed by ex situ HRTEM and WBDF [197]. Annealing induces extension of the ⟨1 0 0⟩ faces and cluster flattening. These morphological variations are reversible after reduction in H_2 and their experimental shapes close to the equilibrium shapes. After oxygen adsorption, the evolution of the cluster shapes is in good agreement with the calculated shapes from thermodynamic considerations.

The growth of Pd on an atomically flat MgO(0 0 1) surface at room temperature has been investigated by grazing incidence X-ray scattering [198]. The structure and morphology of deposits in the range of 0.2–183 ML were analyzed in situ in UHV. The growth proceeds by nucleation, growth, and coalescence of islands. Pd grows cube-on-cube epitaxially on MgO(0 0 1) with an average lattice parameter between that of bulk Pd and MgO. Neither stacking faults nor twins were found. As growth proceeds, Pd is increasingly relaxed; however, most of the Pd in the first one or two atomic planes is fully lattice matched with the substrate. The islands are coherent with the substrate up to 4–5 ML of Pd. Above 5 ML, interfacial misfit dislocations are introduced at the edges. These dislocations reorder to form a square network above 35 ML. The epitaxial site of the Pd is above the substrate oxygen ions with a bonding distance of 0.222 ± 0.003 nm. Pd interacts rather weakly with the acidic sites, but with a moderately large interaction with the basic sites [199]. The general trend is that the interaction energy increases from Ni, Pd to Pt [199]. The adsorption energy of a single Pd atom is considerably enhanced by oxygen defects on MgO(1 0 0). Electron transfer from the substrate toward the adsorbed Pd atom occurs as predicted using ab initio full-potential linearized augmented-plane-wave calculations [200]. The vacancy-induced modification of the deposit is likely limited to those metal atoms at the cluster edges that adsorb directly at the vacancies. The reactivity change from pure Pd surfaces to Pd thin films supported on MgO can be assigned to an electronic effect [201]. The reactivity changes at Au surfaces, e.g. Au thin films (including Au edges) and at the Au/MgO interface, are altered in analogous fashion. The reactivity

enhancement at atomic step-sites can be attributed to electronic/structural contributions for NO dissociation at Ru, Rh, and Pd surfaces. In contrast, the enhancement of the CO oxidation reactivity of PtO_2 oxide island edges on Pt(1 1 1) compared with CO + O coadsorbed on Pt(1 1 1) is mainly due to a structural effect. CO adsorption on Pd atoms deposited on MgO(1 0 0) thin films has been studied by TDS and RAIRS [202]. CO desorbs from Pd atoms at ~250 K, corresponding to a binding energy, E_b, of approximately (0.7 ± 0.1) eV. FTIR spectra suggest that at saturation, two different sites for CO exist on a single Pd atom. The vibrational frequency of the most stable, singly adsorbed CO molecule is 2055 cm^{-1}. CO/Pd complexes located at regular or low-coordinated O anions of the surface are predicted to bind considerably stronger (2–2.5 eV) with a larger vibrational shift than observed experimentally. CO/Pd complexes located at oxygen vacancies (F− or F+ centers) are characterized by much smaller binding energies, (0.5 ± 0.2) and (0.7 ± 0.2) eV, respectively, in agreement with experimental observations. CO/Pd complexes located at paramagnetic F+ centers show vibrational frequencies in close agreement with experiment. These comparisons therefore suggest that the Pd atoms are mainly adsorbed at oxygen vacancies.

A high-surface-area Pd/MgO catalyst was characterized by Pd K-edge XAFS, TPD, and FTIR of adsorbed NO [203]. At 25 °C, the spectrum shows one principal band at 1722 cm^{-1} due to an on-top Pd nitrosyl species. In situ XAFS of the Pd/MgO catalyst indicates that neither Pd oxidation nor cluster sintering occurs while heating at 300 °C in flowing 1% NO/He. Steady-state catalytic decomposition of NO to N_2 and O_2 occurs at 600 °C [203]. Pd interacts weakly with acidic sites, but is moderately enhanced as predicted in interacting with basic sites. The general trend is that the interaction energy increases from Ni, Pd to Pt [199].

Gradient corrected DFT calculations for Pd tetramers and pentamers deposited on MgO(0 0 1) as well as for the chemisorption of CO molecules on Pd clusters have also been carried out [204]. Perturbation of the metal cluster due to interaction with the support, although not large, has two important consequences: (i) a weakening of the metal–metal bonds which results in an elongation of the Pd–Pd distances within the cluster, and (ii) a change in the preferred CO adsorption site. On the other hand, the geometrical and vibrational properties of the adsorption complexes CO–Pd/MgO and CO–Pd do not differ significantly. The interaction of Ni and Cu atoms as well as Ni_4 and Cu_4 clusters with cationic and anionic sites of the MgO(1 0 0) surface has been studied by means of gradient-corrected DFT calculations using cluster models [205]. The cationic surface atoms and the fourfold hollow sites were found to be essentially inert while Ni and Cu atoms as well as Ni and Cu clusters are weakly oxidized by the surface oxygens. The adhesion energy is 0.62 eV/atom for Ni_4 and 0.36 eV/atom for Cu_4, reflecting the stronger bonding of a surface oxygen with an Ni atom, 1.24 eV, compared with a Cu atom, 0.28 eV. The reason for the stronger bonding of Ni is the presence of the incomplete 3D shell. In fact, the mixing of the 3D orbitals with the O 2p band leads to the formation of a covalent polar bond of moderate strength. Cu binds mainly via the 4s electrons with a weaker interaction. An important conclusion from these studies is that the metal–metal bonds in clusters are stronger than metal–substrate bonds.

Nanoclusters offer a variety of opportunities for tuning properties since quantum size effects in limited-dimensional clusters can significantly influence catalytic, optical, electronic, and magnetic properties. The use of low-energy, high-flux monodispersed

cluster beams facilitates the systematic study of cluster reactivity following deposition onto a chemically inert substrate [206]. The catalytic activity for CO oxidation on monodispersed Pt clusters shows a distinct atom-by-atom size dependency when deposited on thin MgO(1 0 0) films. These results demonstrate that the efficiency of a heterogeneous catalytic reaction can be tuned by the judicious choice of cluster size. Simple geometric and molecular orbital arguments are sufficient to describe the general trend of the observed catalytic activity with cluster size. The prospect of tuning catalytic processes as a function of cluster size, a long-sought goal in heterogeneous catalysis, is a plausible extension of these studies.

3.3. IB group metals on MgO

In situ XAS measurements as a function of Cu coverage on MgO(1 0 0) indicate a Cu–Cu distance close to that of the bulk metal, a result of a weak film–substrate interaction independent of the Cu thickness. Oxidation of Cu on the MgO surface is not observed [207]. An isolated Cu atom adsorbed on the oxygen sites of MgO(0 0 1) is believed to bind to oxygen centers of MgO(0 0 1) relatively weakly [208]. MgO films with a thickness of 2 nm were grown on W(1 1 0) while MIES and UPS spectra were collected in situ. Apart from valence-band emission, no additional spectral features were detected [161]. The MgO surface was exposed to metal atoms, Cu or Pd, at 300 K. For Cu, but not for Pd, a characteristic initial decrease of the surface work function by $\sim$0.4 eV was observed for small exposures. The metal-induced intensity developed at the top of the O 2p valence band in UPS as a result of 3D Cu (4dPd) emission. The emission seen for Cu/MgO in the MIES spectra above the O 2p valence band is attributed to ionization of Cu 4s states of neutrally adsorbed Cu species; the shape of the MIES spectra suggests island growth even at the lowest exposures. For Cu/MgO, the critical coverage for the transition from 2D to 3D island growth, as determined with MIES, is estimated to be 0.15 ML.

Calorimetrically measured heats of adsorption of Cu, Ag, and Pb on MgO(1 0 0) have been correlated with the bulk properties of the metals, their relative sticking probabilities, and the film morphologies (see Fig. 9) [209, 210]. The low-coverage heats of adsorption (when the metals are mainly in 2D islands) were used to estimate metal–MgO(1 0 0) bond energies within a pairwise bond additivity model. These values correlate well with the observed initial sticking probabilities and saturation island densities of the metals. These results support a transient mobile precursor model for adsorption. The values also correlate with their bulk sublimation energies suggesting that covalent metal–Mg bonding dominates the interaction at low coverage, probably due to very strong bonding at defects. The heats of adsorption integrated to multilayer coverages provide the metal–MgO(1 0 0) adhesion energies and metal–MgO(1 0 0) bond energies for metals in 3D films. These values correlate with the sum of magnitudes of the metal bulk sublimation energy plus the heat of formation of the bulk oxide of the metal per mole of metal atoms. This suggests that local chemical bonds, both metal–oxygen and covalent metal–Mg, dominate the interfacial bonding for 3D films. Calorimetric measurements of metal adsorption energies directly provide the energies of metal atoms in supported metal clusters. As the metal coverage increases, the clusters grow, revealing the dependence of this energy on cluster size, which is found to be much stronger than predicted with the usual Gibbs–Thompson relation.

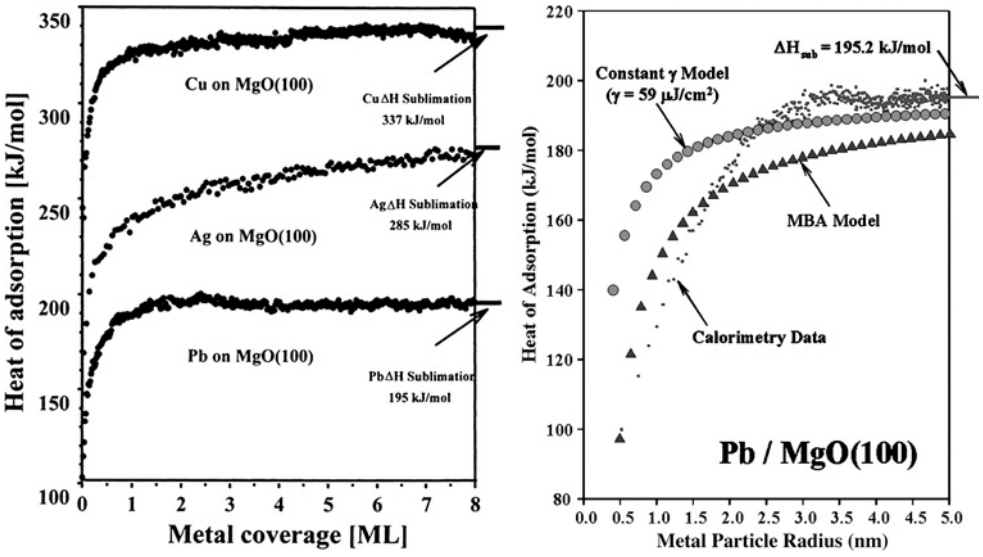

Figure 9: (Left panel) Standard enthalpies of adsorption of Cu, Ag, and Pb on MgO(1 0 0) at 300 K. Also shown are the literature values for the bulk sublimation enthalpies at 300 K. (Right panel) Measured differential heat of adsorption versus coverage of Pb onto MgO(1 0 0), replotted as a function of the average Pb cluster radius, to which the Pb atom adds upon adsorption. For comparison, also shown are the results predicted by Eq. (1) assuming that the surface energy is constant at its value for bulk solid Pb, and by an MBA model [209, 210].

These studies provide information crucial for accurately modeling long-term sintering rates of metal clusters in catalysts.

Cu on MgO(1 0 0) [211–214] grows as 2D islands initially to approximately 0.3 ML then switches to 3D island growth. The initial heat of adsorption for Cu on MgO(1 0 0) in the first 2–4% of a monolayer is 240 kJ/mol and increases rapidly to the bulk sublimation heat of Cu. At the transition from 2D to 3D growth, the heat of adsorption of Cu reaches approximately 92% of the bulk heat of sublimation. The sticking probability of Cu on MgO at room temperature was determined to be >0.99. For the Pb/MgO(1 0 0) system, the initial heat of absorption is 103 kJ/mol with an initial sticking probability of 0.70 at 300 K. The heat of adsorption and sticking probability are affected by pre-decorated surface hydroxyl groups. The presence of OH increases the low-coverage heats of adsorption of both Pb and Cu, and leads to a steady increase in these heats with metal coverage as the metal cluster size increases. The initial sticking probability is lower on the OH-dosed surface. Ag on MgO(1 0 0) grows as 3D islands from submonolayer coverages [215]. The initial adsorption energy of Ag is 176 kJ/mol and rapidly increases with coverage as does the sticking probability. At the lowest coverages, the sticking probability of Ag is 0.94 and approaches 1.0 with increasing coverage. DFT calculations show that small clusters of Pd atoms (up four atoms) are highly mobile on the MgO(1 0 0) surface [216, 217]. Neutral oxygen vacancy sites bind Pd monomers 2.63 eV stronger than does terrace sites; these neutral oxygen vacancy sites also bind larger clusters strongly enough to trap them.

The structural and electronic properties of Cu_n ($n = 1$–13)/MgO(1 0 0) have been addressed with DFT calculations [218, 219]. The preferred adsorption site for a

Cu adatom is the oxygen site with an adsorption energy and bond length of 0.99 eV and 0.204 nm, respectively. Binding occurs through Cu(3D-4 s)–O(2p) band overlap. The adsorption energy per Cu atom decreases with increasing cluster size, while the Cu–Cu cohesive energy rapidly becomes dominant for cluster stabilization. For Cu cluster sizes equal to or greater than 5, 3D cluster formation is preferred to 2D metal decoration of the surface.

Layer-by-layer growth was found for Ag on a carbon- and defect-free MgO(1 0 0) surface. The presence of either of these chemical defects precludes such a growth mode [220]. Ag forms a 2D layer on MgO(1 0 0) at low coverage and at room temperature [221]. EXAFS data demonstrate that the lattice parameter of the Ag overlayer is expanded to fit the MgO parameter giving rise to an interface having orientations (1 0 0)(Ag) parallel to (1 0 0)(MgO) and [1 0 0] (Ag) parallel to [1 0 0] (MgO). Interface Ag atoms are on-top the oxygen atoms of the MgO(1 0 0) surface at a distance of (0.253 ± 0.005) nm. The structure and morphology of Ag deposits grown at room temperature on high-quality MgO(0 0 1) surfaces have been investigated in situ, from 0.2 to 300 equivalent ML of Ag [222]. Surface XRD and grazing incidence small angle X-ray scattering parallel and perpendicular to the surface indicate nucleation, growth, and coalescence of islands from 0.2 ML. Ag grows in cube-on-cube epitaxy with respect to the MgO(0 0 1) substrate. The small Ag islands (<9 nm) are coherent with the MgO below 4–6 ML, while islands formed below 1 ML (<3.5 nm islands) have the bulk lattice parameter. Quantitative measurements and analysis of the MgO crystal truncation rods during growth show structural parameters of the interface consistent with epitaxial growth, with the oxygen atoms above the substrate atoms at an interfacial distance of (0.252 ± 0.01) nm. EELS, HREELS, UPS, and XPS indicate 3D growth of Ag on MgO(1 0 0)/Mo(1 0 0) at room temperature [223].

The atomic and electronic structure of Ag/MgO(1 0 0) have been calculated using ab initio Hartree–Fock methods combined with a supercell model [224]. These calculations show that the Ag adhesion energy is mainly due to an electrostatic interaction with the substrate atoms and to a complex charge redistribution in the metal layer(s). This interaction is characterized by large quadrupole moments as well as electron density redistribution toward bridging and hollow positions between the nearest and next-nearest Ag atoms.

An electronic-structure total-energy investigation of Ag/MgO(0 0 1) shows that the preferred adsorption site for the Ag atom is above the O site of the clean MgO(0 0 1) surface [225]. The binding energy of the overlayer Ag atom on the MgO(0 0 1) surface is 0.3 eV/atom ($0.64\,J/m^2$). No significant charge transfer is found between the overlayer Ag and the MgO(0 0 1) substrate, and the influence of the MgO(0 0 1) on Ag is limited to the interface layer. The Ag overlayer shows typical metal features in the electronic band structure as well as in the charge distributions. The interface O atom is slightly metallized, i.e. the occupied states at the E_f have hybridized O–Ag character. Compared with O, the Mg is less influenced by the Ag.

The heats of adsorption of metal atoms on single crystalline surfaces can be measured directly as a function of coverage using a specially built microcalorimeter [215, 226]. Heats of adsorption have been measured for pulses of atoms containing a few percent of a monolayer with a pulse-to-pulse standard deviation as low as 1.5 kJ/mol. The adhesion energy of multilayer metal films can be estimated from the integral enthalpy of adsorption. The adsorption energy and the sticking probability of Ag on

MgO(1 0 0) thin films grown on Mo(1 0 0) have been measured as a function of Ag coverage at room temperature. The initial heat of Ag adsorption is 176 kJ/mol and increases rapidly with coverage, reaching the bulk Ag heat of sublimation of 285 kJ/mol by 8 ML. At the lowest coverages, the sticking probability of Ag is ~0.94 and approaches 1.0 with increasing coverage. AES indicates that Ag grows as 3D islands from submonolayer coverages. From the integral heat of adsorption, the adhesion energy of Ag to MgO is estimated to be $(0.3 \pm 0.3)\,J/m^2$. The Ag–MgO(1 0 0) bond energy is estimated to be 110 kJ/mol for Ag atoms in small 2D clusters (probably nucleated at defects) and 15 kJ/mol for large 3D Ag particles.

Nonrelativistic and relativistic gradient-corrected DFT calculations have been used to study the interaction of Cr, Mo, W; Ni, Pd, Pt; Cu, Ag, and Au, with the oxygen sites of MgO(0 0 1) [227]. On-top adsorption is found to be energetically preferred compared with bridge adsorption. These adsorbates can be classified into two groups depending on the strength of the bond with the surface. Cu, Ag, Au, Cr, and Mo exhibit relatively weak bonds (on the order of 0.3 eV) whose interactions are due to polarization and dispersion with little mixing with the substrate orbitals. Ni, Pd, Pt, and W, on the other hand, form relatively strong bonds (on the order of 1 eV) with the oxide anions. These bonds are covalent-polar with little charge transfer from the metal to the oxide, consistent with the fact that MgO is a very weak oxidant and a wide band gap insulator.

The interaction of transition metals of the group Pt–Pd–Ni and the period Ni–Cu–Zn, with an F-center of the MgO(1 0 0) surface has been investigated using DFT calculations [228]. The maximum values of the electron localization function confirm that two electrons are largely localized in the F-center vacancy. These electrons can delocalize over an adsorbed metal atom and can stabilize surface complexes. Molecular orbital analysis shows that the filling and the symmetry of the highest occupied orbitals of the complex M–F center/MgO depends on the particular metal. For Ni and Pt, the highest occupied molecular orbital (HOMO) and the next three highest lying orbitals (HOMO-2–HOMO-4) are d orbitals and the interaction orbital is the HOMO-5, while for Pd the interaction orbital is the HOMO and the orbitals HOMO-1–HOMO-5 are of d character. The chemical activity of the metal is shown to strongly depend on the particular metal support.

DFT plane-wave calculations have been used to study the adsorption properties of ultrathin MgO films grown on Mo(1 0 0) as function of the thickness of the oxide film. These results compared with those of unsupported slabs representing a single-crystal MgO(1 0 0) surface show that the presence of a metal substrate at the interface with the MgO film results in charging of adsorbed atoms with high electron affinity, e.g. Ag and Au, while Pd is basically unperturbed [229]. As a consequence, while the properties of Pd are identical on MgO(1 0 0) or MgO/Mo(1 0 0), for Ag and Au, substantial differences are obvious. On MgO/Mo(1 0 0) films, the Ag(5s) and the Au(6s) levels fall below the E_f of Mo, leading to negative charging of the metal atom and to a change in the bonding mechanism; the 5s level of Pd, on the other hand, is just above the E_f of Mo, thus no charge transfer occurs. The effect tends to decrease for thicker MgO films and is closely related to the change in work function of the Mo(1 0 0) surface. Upon deposition of a thin MgO film, metal-induced gap states appear at the metal–insulator interface. This charging effect is absent on single-crystal or polycrystalline MgO surfaces.

The interaction of Au with MgO(1 0 0) may be regarded as a prototype for a number of metal–oxide combinations [14, 209, 230–232]. The heats of adsorption for metals (Cu, Ag, Pb) on MgO allow estimation of metal–MgO(1 0 0) adhesion energies and metal–MgO(1 0 0) bond energies for metals in 3D films (see Fig. 9). These results suggest that local chemical bonds, both metal–oxygen and covalent metal–Mg, dominate the interfacial bonding for 3D films. Single atom adsorption has been imaged for Au on MgO(1 0 0) [232]. At the lowest temperatures (8 K), Au adsorbs at terrace sites. At higher temperatures (above 30 K), the atoms diffuse to step and edge sites as shown by SPM measurements. The Au atoms reside on oxygen atoms in accord with theoretical predictions. The experimental proof comes from ESR spectra through an analysis of the ^{197}Au hyperfine coupling on single crystal thin films. It is noteworthy that a neutral Au atom (according to calculations and in line with the experiments) is strongly distorted in the 6s electron distribution such that CO, adsorbed on the Au atoms, becomes negatively charged and tilts with respect to the CO–Au bonding axis, consistent with CO being isoelectronic with NO [233, 234]. In addition to single neutral Au atoms, neutral Au clusters are also formed depending on the amount of deposited metal. Neutral Au clusters exhibit a CO stretching frequency close to metallic Au. Partially, negatively charged Au atoms and small clusters can be produced by evaporating Au onto an electron bombarded MgO(1 0 0) surface which contains paramagnetic charged and non-paramagnetic color centers [233]. Using full potential linearized augmented plane wave calculations, the adsorption of Au on the ideal MgO(0 0 1) surface is found to be very weak with an Au–O bond length of 0.216 nm and an adsorption energy of −0.13 eV/adatom. On the defective MgO(0 0 1) surface, Au adatoms prefer the vacancy sites with a strongly enhanced adsorption energy of −1.93 eV/adatom [235].

Gas-phase mass-selected clusters have been deposited onto MgO(1 0 0) surfaces and their reactivity investigated [236–240]. There is a clear increase in reactivity at Au_8 and a marked decrease in reactivity with an increase in cluster size above Au_8. This trend has been explained by Au_8 clusters decorating surface color centers. Presumably, the color centers are formed during thermal annealing pretreatments as has been shown previously [149]. Molecular beams have been used to directly probe the fraction of methane molecules that dissociate at Pd sites as a function of the molecular beam energy and incident angle. This approach has been used to investigate the desorption kinetics and dissociative sticking probability of methane on Pd clusters supported on MgO(1 0 0) compared with Pd(1 1 1) [241]. Sticking measurements on supported Pd clusters (3 nm) with a methane beam directed normal to the MgO(1 0 0) surface results in a large fraction of the methane/Pd collisions occurring on regions of the clusters where the beam direction is far from the local cluster surface normal, resulting in lower sticking probability. The sticking probability on similar Pd clusters surfaces is approximately twice as large as on Pd(1 1 1). TPD of physisorbed (undissociated) methane reveals that Pd clusters bind methane more strongly than does Pd(1 1 1). Oxygen adsorbs on the Pd clusters via a mobile, molecular O_2 precursor state which is transiently adsorbed on the MgO(1 0 0) surface. An induction period is observed for the titration of adsorbed O by CO on Pd clusters but not on Pd(1 1 1).

Ab initio calculations show that the CO adsorption energy is reduced on Ag/MgO compared with unsupported Ag films providing evidence for a direct electronic effect of the oxide on supported Ag [242]. The oxidation of CO on MgO-supported Au

clusters has been studied by DFT calculations [243]. In addition to serving as a structural promoter of Au clusters, the supporting oxide also influences the bonding and activation of adsorbates bound to Au. The oxide stabilizes a peroxo-like reaction intermediate, CO–O_2, and causes steric repulsion between CO. The most reactive site at Au/MgO is that where Au screens MgO creating a cavity allowing several low-coordinated Au atoms and Mg^{2+} cations to interact simultaneously with an adsorbate. The activity for CO catalytic oxidation on Au/MgO has been found to correlate closely with the density of surface F-centers [244].

2D assemblies of octahedral-shaped FePt clusters embedded in an MgO matrix have been synthesized by alternate deposition of FePt and MgO layers on MgO(0 0 1) single-crystal substrates with a thermal cycling process [245]. The detail structural, chemical, and magnetic properties of Fe at the MgO interface have been investigated by molecular-beam epitaxy and analyzed using RHEED, STM, AES, XPS, XAS, and XMCD measurements [246]. XPS and XAS-XMCD analyses indicate hybridization between Fe or Co with MgO with relatively little charge transfer, and that the magnetization at the interface is larger than in bulk Fe (3 μB/atom).

4. SILICA-SUPPORTED METAL CLUSTERS

Silica (SiO_2) is an important support material used in many commercial catalyst systems [1]. The synthesis of well-defined thin films SiO_2 is a pre-requisite for the preparation of model-supported metal catalysts on this important oxide.

4.1. Preparation of SiO_2 thin films

Thin SiO_2 films may be synthesized on an Mo(1 1 0) [247, 248] and Mo(1 0 0) [249] substrates by evaporating silicon at a rate of 0.12 nm/min onto the respective substrate at room temperature in $<\sim 2 \times 10^{-5}$ Torr O_2 background followed by an anneal at $<\sim$1300 K. The gas-phase precursor for the SiO_2 film is SiO, produced by oxidative etching of silicon. Such thin SiO_2 films have been studied with AES, EELS, XPS, and RAIRS. The as-prepared film is predominantly silicon dioxide with a small fraction of suboxides (SiO) as shown in Fig. 10. Annealing to approximately 1300 K yields a stoichiometric film of SiO_2 (Fig. 10). The suboxides are believed to react further with oxygen to form SiO_2 at elevated temperatures. The silicon oxide films prepared at room temperature exhibit additional low energy electron loss features at ~5 and 7 eV. These features are attributed to a local structure with broken Si–O bonds in tetrahedra of [SiO_4] and the presence of some suboxide. After annealing at ~1200 K, these features disappear, yielding EELS features essentially identical to those of vitreous silica. These results are consistent with the formation of defect-free vitreous silica consisting of [SiO_4] tetrahedra connected by an oxygen bridge to form a long-range 3D network. RAIRS further illustrates that such structural changes occur when the silicon dioxide films are annealed. The asymmetric stretching mode of the Si–O bonds appears as a broad asymmetric peak centered at 1178 cm^{-1} in the RAIRS spectrum for the film prepared at a substrate temperature of 323 K. This peak gradually shifts to higher frequency upon heating and reaches a maximum of 1252 cm^{-1} as the silicon dioxide film is annealed to $>\sim$1300 K. Furthermore, the line shapes, the peak energies of the AES electrons, and the EELS spectra are consistent with those of silicon dioxide.

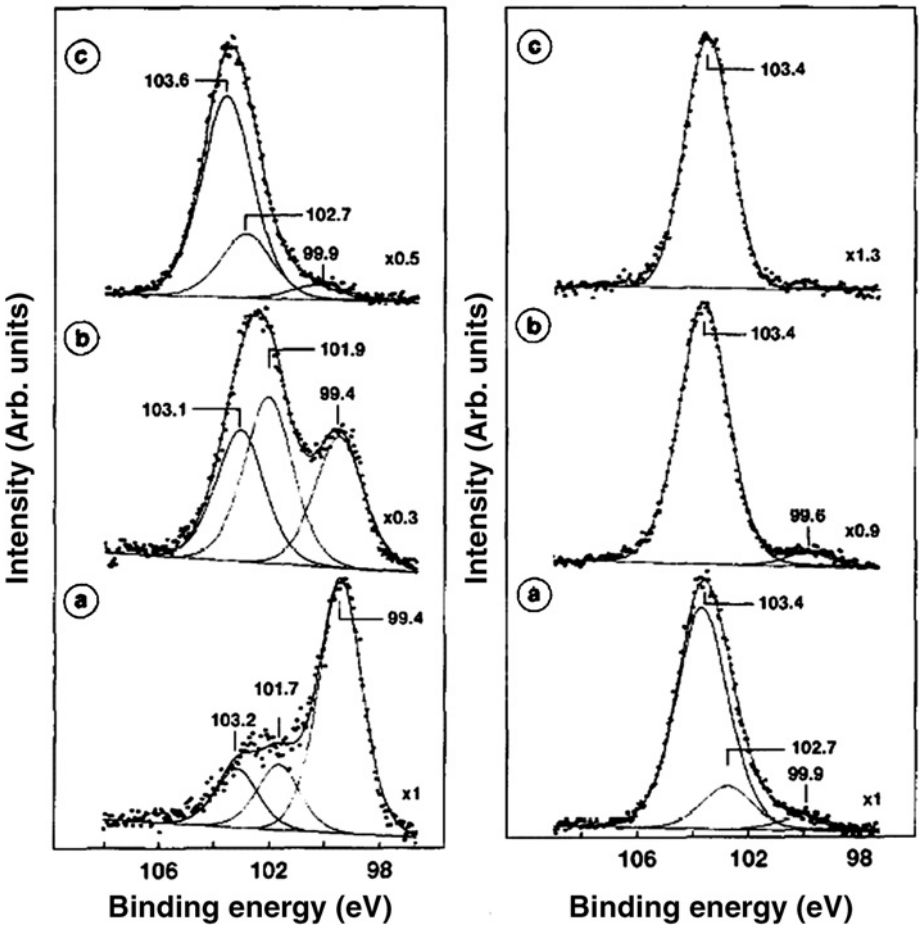

Figure 10: The Si(2p) XPS spectra of SiO_2 films (3.6 nm) on an Mo(1 0 0) surface. (Left panel) The films were prepared by evaporating Si in an O_2 pressure of (a) 1×10^{-8} Torr, (b) 5×10^{-8} Torr, and (c) 2×10^{-5} Torr. The substrate temperature during the film preparation was ~350 K. (Right panel) The films were prepared by evaporating Si in an O_2 pressure of 2×10^{-5} Torr at ~350 K, then annealed at (a) 393 K, (b) 1023 K, and (c) 1373 K [249].

The SiO_2 films are thermally stable up to 1600 K with the stability increasing with film thickness. At high temperatures, silicon dioxide is reduced by the Mo substrate to form volatile SiO and MoO_3.

An ordered silica film can be grown on Mo(1 1 2) as has been described by Schröder et al. [250–253]. This film, which exhibits a sharp $c(2 \times 2)$ LEED pattern, was shown to have a thickness of 1 ML as estimated from AES intensity attenuation of the Mo(MNN) feature (187 eV) and to exhibit self-limited growth properties [254–256]. The orientation and growth of benzene and pyridine were used to characterize the quality of the SiO_2 films via HREELS, AES, and LEED [257]. A single vibrational mode corresponding to the Si–O asymmetric vibration (assigned to an Si–O–Mo) led to the proposal of a structure consisting of isolated $[SiO_4]$ units as shown in

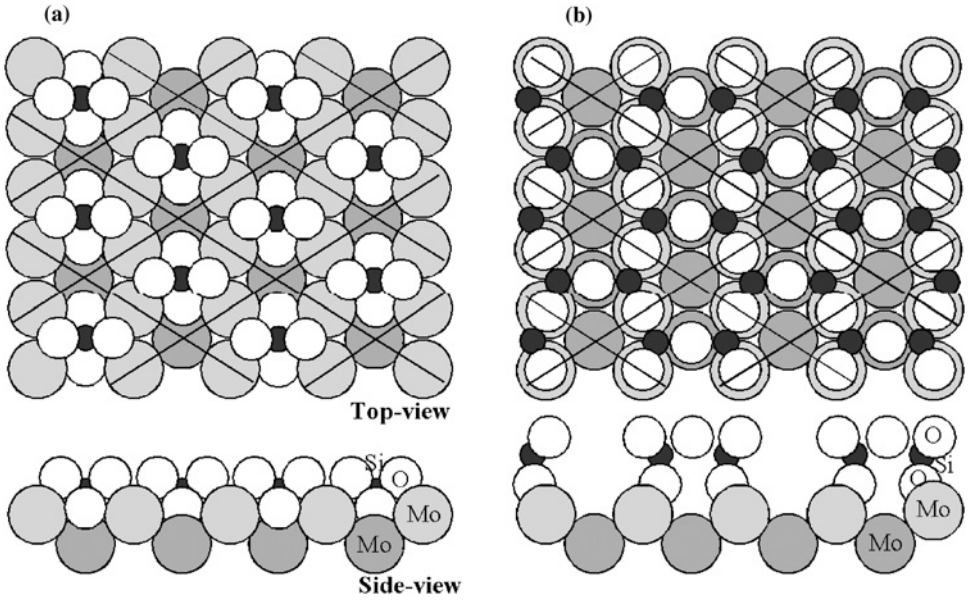

Figure 11: (a) and (b) Top- and side view of the structural models of (a) isolated [SiO_4], and (b) 2D network for SiO_2(1 ML)/Mo(1 1 2) [254].

Fig. 11a [254], a conclusion supported by DFT calculations [258]. Based on more recent studies of the phonon spectrum and electronic calculations [259, 260], the structure has been proposed to be that shown in Fig. 11b. This structure, in contrast to that of Fig. 11a consists of a 2D network of SiO_4 tetrahedra where one oxygen is bound to the metal substrate and the other three form a hexagonal honeycomb structure [259, 260]. Resolution of the precise structure of monolayer SiO_2/Mo(1 1 2) is a subject of ongoing experimental and theoretical studies. H_2O molecularly absorbs on low- and high-defect SiO_2/Mo(1 1 2) forming 3D water clusters even at low coverage. No evidence for dissociation of water was found [261, 262]. Various defect sites on SiO_2/Mo(1 1 2) have been characterized with MIES, and the interaction between deposited Ag and these defects sites investigated with MIES/UPS [160, 263, 264]. MIES/UPS data for low- and high-defect SiO_2 surfaces acquired as a function of Ag exposure are consistent with 2D Ag growth at low coverage and 3D growth at higher Ag coverages. With increasing defect density on the SiO_2 surfaces, no significant change is observed in the behavior of the work function with respect to the Ag coverage, suggesting that the interaction between Ag and SiO_2 is not influenced significantly by the presence of defects.

4.2. IB group metals on SiO_2

Model silica-supported Cu [265–268] catalysts have been prepared by evaporating Cu onto a silica thin film grown on Mo(1 1 0). The preparation conditions control the corresponding metal cluster dispersions, i.e. average size. The Cu sticking probability depends markedly on the surface temperature, varying from (0.6 ± 0.1) at 90 K to <0.1 above 400 K. Upon covering the silica surface with multilayer water, the

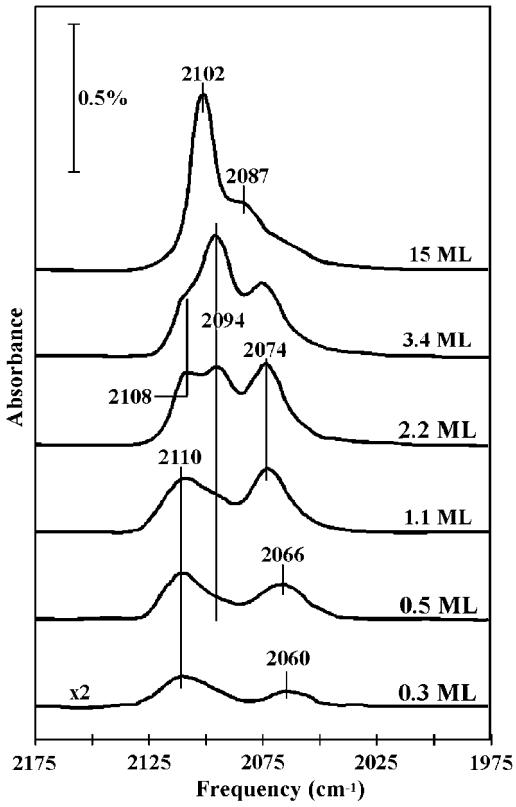

Figure 12: RAIRS spectra for carbon monoxide adsorbed on $Cu/SiO_2(100)/Mo(1\,1\,0)$. The Cu coverages are 0.3, 0.5, 1.1, 2.2, 3.4, and 15 ML, respectively. The Cu films were deposited at 90 K and annealed to 900 K. CO was adsorbed at 90 K to saturation. The spectra were taken at 90 K with a resolution of 4 cm^{-1} [265].

sticking probability of Cu increases to approximately 1.0. The structure of model silica-supported Cu catalysts has been investigated with RAIRS (see Fig. 12) and STM (see Fig. 13). RAIRS data indicate that there are several types of Cu clusters with surface structures similar to (1 1 1), (1 1 0), and other high-index planes of single-crystal Cu. The STM studies show several types of Cu clusters on silica and reveal images of metal clusters on an amorphous oxide support with atomic resolution. When deposited at 100 K, Cu initially forms a 2D structure on silica; however, annealing induces the ultrathin Cu films (<3 ML) to form small clusters. The unannealed Cu films have a significant density of low-coordinated Cu sites, whereas the annealed films consist of Cu clusters with structures similar to low-index [(1 1 1), (1 1 0)] and high-index Cu planes [(2 1 1) or (3 1 1)]. The distribution of the facets depends upon the initial Cu coverage. The desorption energy of Cu from the SiO_2 is found to depend markedly on Cu coverage (cluster size) as shown in Fig. 14. A small amount of Cu (<0.1 ML) is partially oxidized at the Cu/SiO_2 interface with the remainder forming 3D clusters. Carbon monoxide desorbs in a single peak centered at approximately 210 K from the unannealed Cu film, but in several peaks between 150 and 220 K from the annealed film. The CO adsorption energy also strongly depends on

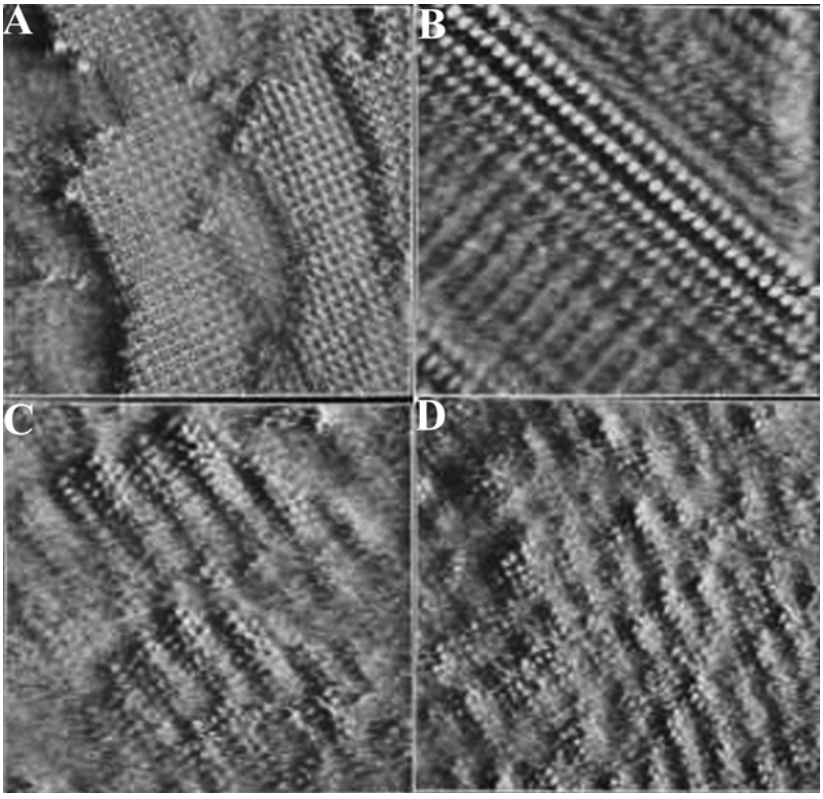

Figure 13: STM images of four area of 0.6 ML $Cu/SiO_2(100)/Mo(1\,1\,0)$. (A) 17.0×17.0 nm image of a near square lattice with Cu–Cu spacing of 0.60×0.54 nm. (B) 8.0×8.0 nm image of a near square lattice with Cu–Cu spacing of 0.54×0.29 nm. (C) 11.0×11.0 nm and (D) 12.0×12.0 nm image of disordered Cu clusters with interatomic spacing of 0.28–0.38 nm. These images were acquired after the sample was immersed in water and dried air [265].

the CO coverage, varying from approximately 71 kJ/mol at the low coverage limit to approximately 42 kJ/mol near CO saturation. Both NO and H_2O were found to dissociate on the Cu/SiO_2 to yield surface oxygen during TDS [269]. The Cu structure, the dispersion, the cluster size distribution, and the heats of CO adsorption for the model systems are remarkably similar to the corresponding values for silica-supported Cu catalysts prepared by the ion-exchange method. These similarities demonstrate that UHV-prepared metal clusters on an oxide film is an excellent model for the corresponding supported metal catalyst.

Ag clusters grow 2D on SiO_2(1 ML)/Mo(1 1 2) with a preferred orientation and sinter with a bimodal size distribution upon exposure (60 min) to elevated pressures (160 Torr) of oxygen. Annealing the as-deposited Ag clusters at elevated temperatures (>600 K) in UHV also leads to sintering [270]. Adsorption of the $[Au(en)_2]^{3+}$ cationic complex has been successfully employed for the deposition of Au clusters (1.5–3 nm) onto SiO_2 with high metal loading and excellent dispersion, i.e. small Au cluster sizes [271]. The Au loading in Au/SiO_2 samples increases proportionally (from 0.2 to 5.5 wt.%) as the solution pH is increased (from 3.8 to 10.5), with a corresponding

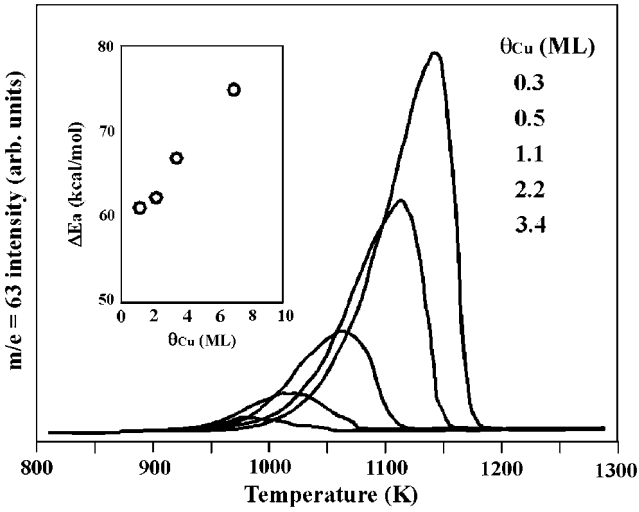

Figure 14: Metallic Cu desorption as a function of Cu coverage on SiO_2/Mo(1 1 0). The SiO_2 film is ~10 nm thick and the total Cu coverage is 0.3, 0.5, 1.1, 2.2, and 3.4 ML, respectively. The inset shows Cu desorption energy as a function of coverage. The vaporization energy for Cu is 331.5 kJ/mol [266].

increase in the average Au cluster size (from 1.5 to 2.4 nm). Clusters with a size of 3–5 nm show highly defective structures, while clusters with an average size of ~2 nm exhibit defect-free structures with well-distinguishable ⟨1 1 1⟩ planes. TEM and HAADF observations show no metal cluster agglomeration on the SiO_2 support and that Au is present on the surface of SiO_2 as small clusters.

The nucleation and growth of Au clusters supported on SiO_2/Mo(1 1 0) have been studied by XPS, LEIS, and TPD [272]. At 300 K, the growth mode of Au at fractional monolayer coverages is quasi-2D; at higher coverages, 3D growth was found with no evidence of a significant chemical interaction between Au and silica. Annealing Au/SiO_2/Mo(1 1 0) to 1000 K leads to sintering of the Au clusters. The desorption activation energies for Au coverages <0.2 ML equivalents were determined by TPD to be significantly lower than the sublimation energies found for higher coverages of Au clusters and for bulk Au.

Au clusters formed by deposition of Au onto a well-ordered SiO_2 film on Mo(1 1 2) are very prone to sintering [31, 273–276]. This effect can be suppressed by replacing Si atoms in the SiO_2 network by Ti atoms, prepared by evaporating Ti onto the SiO_2 film followed by an anneal. STM images acquired subsequently (Fig. 15a) show Ti atoms as bright spots. Au evaporated onto this Ti–SiO_2 surface form clusters that reside on top of the Ti defect sites (Fig. 15a). Further evaporation of Ti onto the surface of Fig. 15a leads to the formation of needle-like islands of TiO_x on the silica network (see Fig. 15b). Au evaporated onto this surface decorates exclusively as clusters at the termini of the titania islands as shown in Fig. 15b and is extremely resistant to thermal sintering. The origin of the unusual stability of the Au clusters is not fully understood but is thought to relate to the unusual strong interaction between Au and the TiO_x structures arising from the enhanced defect density at their termini.

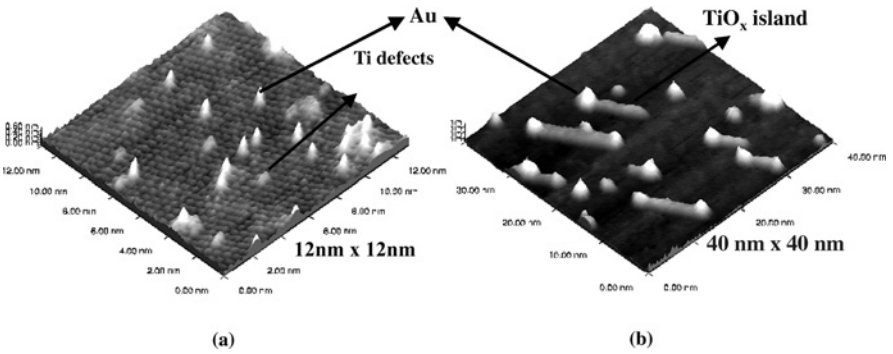

Figure 15: 3D STM images of (a) Au(0.04 ML)/TiO$_x$(8%)–SiO$_2$ and (b) Au(0.08 ML)/TiO$_x$(17%)–SiO$_2$ showing that both Ti defects and TiO$_x$ islands play a role as nucleation sites for Au nanoclusters [273].

4.3. Pt-group metals on SiO_2

The adsorption and reaction of CO on silica-supported Pd catalysts over a wide range of temperatures and pressures have demonstrated parallels between catalysis on Pd single crystals and on Pd small clusters [277, 278]. The kinetics of CO oxidation at low and high pressures on Pd clusters and Pd single crystals has been shown to be comparable [279–282]. The structural and catalytic properties of model Pd/SiO$_2$ were investigated by TPD, RAIRS-CO, STM, AFM, and CO oxidation at both low pressure and elevated pressures. By evaporating Pd onto silica thin films (10 nm), followed by an anneal to 900 K, the size of the Pd clusters can be controlled within the range 3.0–50.0 nm. The surface of the Pd clusters consists mainly of ⟨1 1 1⟩ and ⟨1 0 0⟩ facets, and exhibit catalytic activity similar to Pd single crystals for CO oxidation at low- (10^{-8}–10^{-6} Torr) and high-pressure (15 Torr) conditions. At low pressures, the rate of CO oxidation increases with temperature, reaches a maximum at 500–600 K, and then declines. At high pressures, the activation energy and turnover frequency for the CO oxidation reaction on the model catalysts compare favorable with analogous results from single crystal and high-surface-area catalysts. Therefore, metal clusters supported on a silica thin film are an excellent means of bridging between single crystals and high-surface-area catalysts. The CO oxidation reactions on Pd(1 1 1), Pd(1 1 0), and Pd(1 0 0) have similar, but distinctive activation energies ((117.5 ± 1.6), (128.3 ± 2.1), and (122.9 ± 1.2) kJ/mol, respectively) and turnover frequencies, indicating a subtle structure sensitivity for CO oxidation on different crystal planes of Pd.

The IR spectra of adsorbed CO on model silica-supported Pd catalysts are shown in Fig. 16 for Pd coverages of 1.0, 7.0, and 15 ML. The Pd cluster size was determined by chemisorption methods and verified using scanning probe techniques [279, 280]. For different Pd coverages, three distinct absorption features corresponding to CO adsorbed onto threefold hollow (1880 cm^{-1}), bridging (1990 cm^{-1}), and a-top (2110 cm^{-1}) configurations are observed. At $\theta_{Pd} = 1.0$ ML, the dominant absorption feature corresponds to CO adsorbed onto an a-top position, while the peaks originating from threefold hollow and bridging CO are broad, suggesting a non-homogeneous distribution of these adsorption sites. Increasing the Pd coverage to 7.0 ML

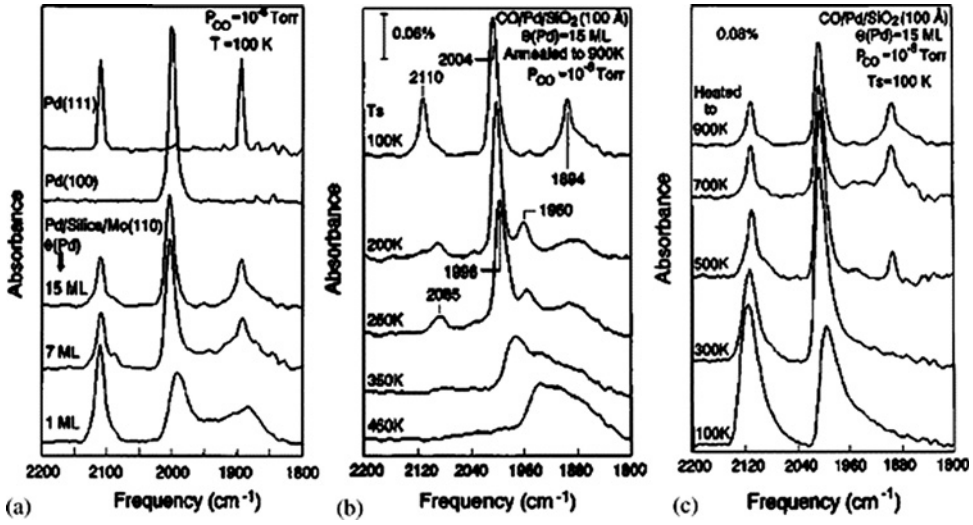

Figure 16: (a) RAIR spectra for CO adsorption on $Pd/SiO_2/Mo(1\,1\,0)$ surface at 100 K with varying Pd coverages of 1, 7, 15 ML in comparison with Pd(1 1 1) Pd(1 0 0) surface (Pd clusters were ordered by pre-annealing to 900 K prior to CO adsorption) [281]. (b) Effect of temperature on the CO adsorption on $Pd(Pd = 15\,ML)/SiO_2/Mo(1\,1\,0)$ [281]. (c) RAIRS for CO adsorption on $Pd(Pd = 15\,ML)/SiO_2/Mo(1\,1\,0)$ acquired at 100 K after pre-annealing the Pd clusters to the given temperatures [279]. All of the spectra in (a)–(c) were obtained in the presence of $P_{CO} = 1 \times 10^{-6}$ Torr.

and then to 15 ML results in the sharpening of the absorption features and the dominance of CO adsorbed in the bridging positions. These results demonstrate that the large clusters have well-defined crystal orientations, whereas the smaller clusters have a wide distribution of adsorption sites. A comparison of the IR spectra of equilibrated CO overlayers obtained from $Pd_{15\,ML}/SiO_2$ and from the Pd(1 0 0) and Pd(1 1 1) single crystals reveal striking similarities. The stretching frequencies of adsorbed CO on the model Pd/SiO_2 catalyst (Fig. 16) exhibit comparable features observed for Pd(1 0 0) and Pd(1 1 1). The agreement among the IR spectra of the model-supported catalysts and the metal single crystals suggests that the metal clusters formed on the thin SiO_2 film have facets consisting primarily of ⟨1 0 0⟩ and ⟨1 1 1⟩ orientations.

The specific activities of single crystal and supported catalysts for CO oxidation are essentially identical [279]. The apparent activation energies for the relatively large clusters (>2 ML) are similar (~113 kJ/mol), but somewhat lower (~104 kJ/mol) for the smaller clusters (0.6 and 0.3 ML). The apparent activation energies for three Pd single crystals with different orientations are similar [277–280] but distinct: (122.9 ± 1.2) kJ/mol for Pd(1 0 0), (117.5 ± 1.7) kJ/mol for Pd(1 1 1), and (128.3 ± 2.1) kJ/mol for Pd(1 1 0). The effect of Pd cluster size on the catalytic properties was investigated utilizing the decomposition of chemisorbed NO and reactions of NO with CO in flowing conditions. ^{15}NO was used to differentiate N_2 from CO and N_2O from CO_2 via mass spectrometry. Following a saturation ^{15}NO exposure on the large clusters, ^{15}NO desorbs in three peaks centered at 315, 515, and 595 K, while $^{15}N_2$ is produced in peaks at 545, 595, and 690 K; $^{15}N_2O$ is evolved in a peak at 545 K. The 545 K N_2 peak is attributed to the fragmentation of N_2O. On small Pd clusters ($\approx$5.0 nm), $^{15}N_2O$ is not produced whereas ^{15}NO desorbs in two peaks at 310 and 515 K, and N_2 is evolved at 530 and 670 K.

The relative yield of N_2 with respect to ^{15}NO desorption (above 400 K) decreases as the cluster size grows (from $\approx$50% for 3.0 nm to $\approx$20% for 25.0 nm clusters), suggesting less NO decomposition on the larger clusters. In addition, the formation of N_2O on the larger clusters correlates with the appearance of the NO desorption peak at 595 K. There is no detectable O_2 evolution below 1000 K for all sizes of Pd clusters. However, O_2 desorption is observed in a peak centered at $\approx$1250 K, desorbing concurrent with Pd. Therefore, the oxygen from nitric oxide decomposition is apparently dissolved into the bulk of the Pd clusters.

The reaction of CO with NO under flowing conditions further demonstrates a cluster size effect. The relative rate of product evolution was monitored with a quadrupole mass spectrometer during reaction with flowing ^{15}NO and CO (1:1) at 10^{-6} mbar. The reaction rate increases with increasing catalyst temperature, reaches a maximum at 580 K, and then declines. On the large Pd clusters, the maximum rate of $^{15}N_2O$ evolution occurs at 570 K, 10 K lower than the maxima for both CO_2 and N_2 production. On the small clusters ($<$5.0 nm), $^{15}N_2O$ is not produced during the steady-state reaction of a 1:1 mixture of ^{15}NO and CO. N_2 is produced by NO dissociation and atomic nitrogen recombination, and CO_2 is produced from the oxidation of carbon monoxide. The residence time for CO and NO decreases with temperature, whereas the reaction rates increase with temperature leading to an optimum at approximately 580 K where the product formation rate is maximized.

Both the decomposition of NO and the reaction of NO with CO show that the reaction channel for N_2O formation is not available on the small cluster ($<$5.0 nm). The formation of N_2O requires the simultaneous presence of adsorbed NO and atomic nitrogen at sufficiently high coverages. TDS spectra show that the dissociation of NO occurs along the trailing edge of the main NO desorption peak at 515 K. The formation of N_2O correlates with the appearance of the NO desorption peak at 595 K. The higher adsorption energy of the 595 K state increases the NO surface residence time and thus enhances the probability of N_2O formation by NO combination with atomic nitrogen. On extended single crystal surfaces, N_2O is also formed during the decomposition of NO [283–287]. However, the decomposition of NO and the formation of N_2O correlates with the presence of step/defect (low-coordination sites) on the single crystal surfaces [283–285, 288]. On the perfect (1 1 1) and (1 0 0) facets, NO desorbs below 520 K [285, 288] whereas on clusters with a variety of low-coordinated sites, NO decomposes to atomic nitrogen and oxygen on a fraction of the sites and adsorbs more strongly (595 K desorption state) on other sites. The presence of multiple sites on the large Pd clusters, e.g. one binding NO strongly and a second that promotes decomposition, provides a mechanism for the formation of N_2O. The absence of N_2O on the small Pd clusters can be explained by the absence of the high-temperature NO adsorption state (595 K) which correlates with the relative site reactivity. The surface of the small clusters is more reactive, as indicated by an increase in NO dissociation ($\approx$50% for 3.0 nm and $\approx$20% for 25.0 nm clusters); essentially all the NO on the low-coordinated sites decompose to atomic oxygen and nitrogen at lower temperatures. The presence of atomic oxygen and nitrogen in the near surface region is believed to decrease the NO adsorption energy.

Pd clusters grown on SiO_2/Mo(1 1 2) at room temperature are hemispherical and disordered by STM, suggesting a strong interaction between the Pd clusters and the silica support [289]. The same general CO adsorption sites are observed by RAIRS for

the $Pd/SiO_2/Mo(1\,1\,2)$ as have been observed for crystalline Pd/Al_2O_3. However, a larger fraction of on-top sites observed on silica-supported Pd is indicative of smaller and more disordered clusters. The kinetics of CO oxidation on a nanolithographically prepared planar Pd/SiO_2 model catalyst was studied by molecular-beam methods [290]. Under conditions of limited oxygen mobility, the switching between kinetic regimes is largely driven by the surface mobility of CO.

The PM-RAIRS technique was used to study oxide-supported metal clusters (specifically silica-supported Pd nanoclusters) at elevated pressures for the first time [291]. PM-RAIRS data for CO adsorption on $SiO_2/Mo(1\,1\,2)$-supported Pd clusters with an average diameter of 3.5 nm at 185 Torr is shown in Fig. 17a and compared with CO adsorption at 133 mbar on Pd(1 1 1) (Fig. 17b) [291, 292]. The identical features observed on supported clusters and Pd(1 1 1) indicate that the silica-supported Pd clusters studied here exhibit mostly ⟨1 1 1⟩ facets. In addition to these adsorption bands, a small feature located at 2009 cm^{-1} in the uppermost spectrum of Fig. 18a is also visible and corresponds to CO adsorbed at bridging sites of ⟨1 0 0⟩ facets. Temperature-dependent reversibility of CO adsorption on SiO_2-supported Pd clusters at elevated pressures has also been investigated (Fig. 18a) [291]. Annealing Pd clusters in the presence of high-pressure CO ($P_{CO} = 185$ mbar) and cooling to 300 K lead to irreversible changes in the PM-RAIR spectra. Contrary to crystalline SiO_2-supported Pd clusters, CO adsorption on Pd(1 1 1) at $P_{CO} = 133$ mbar is totally reversible (Fig. 18b).

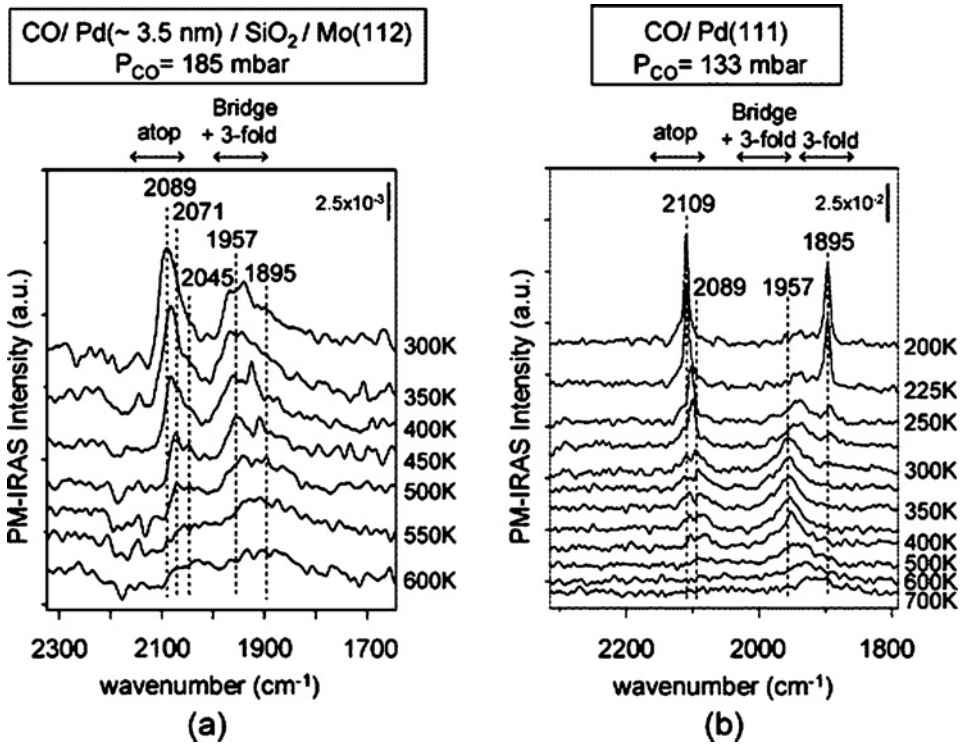

Figure 17: (a) PM-RAIRS for CO adsorption on Pd (3.5 nm)/SiO_2/Mo(1 1 2) at 185 mbar (140 Torr) [292]. (b) PM-RAIRS for CO adsorption on Pd(1 1 1) at 133 mbar (100 Torr) [291].

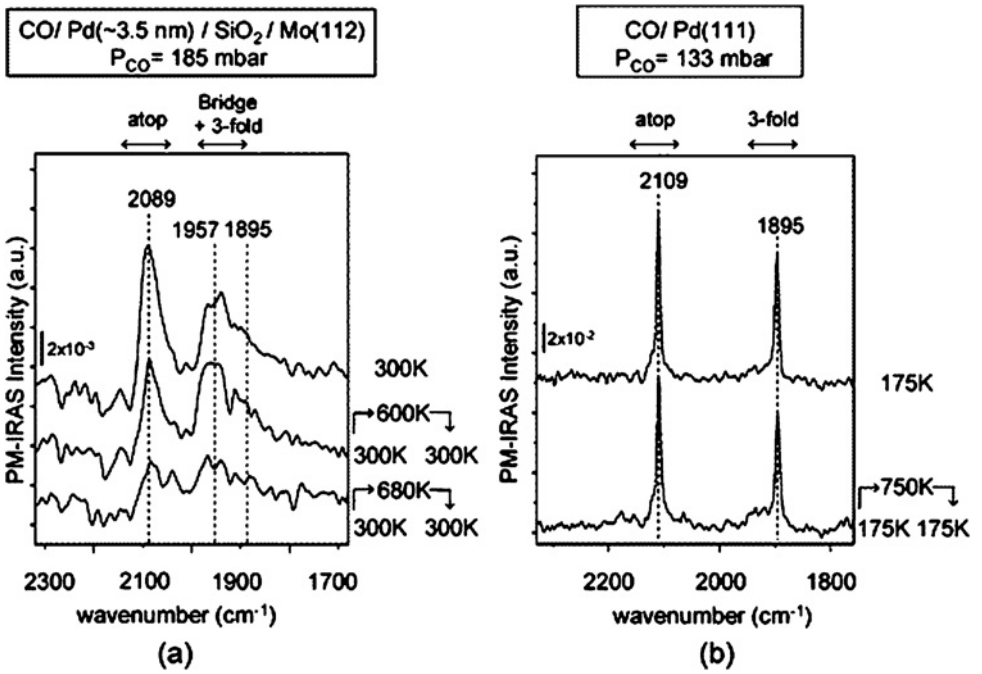

Figure 18: Reversibility/irreversibility of the CO adsorption bands at elevated pressures for (a) Pd(3.5 nm)/SiO_2/Mo(1 1 2) and (b) Pd(1 1 1). Initial adsorption was performed at a low temperature (300 K for (a), 175 K for (b)). Pd surfaces were annealed to the given temperatures in the presence of CO subsequently cooled down to the initial adsorption temperatures where PM-RAIRS data were acquired [292].

It should be noted that the temperature-dependent STM experiments show that Pd cluster morphology is invariant to annealing between 300 and 700 K. The changes observed in the PM-RAIRS data cannot be attributed to reconstruction of the Pd clusters but rather has been shown to be caused by carbon deposition on the Pd clusters after annealing. Subsequent AES data (see inset of Fig. 18a) confirm that CO dissociation takes place on the small Pd clusters at elevated pressures and temperatures ($T > 600$ K) and leads to poisoning of the CO adsorption sites on supported Pd clusters. CO dissociation on small oxide-supported Pd clusters has also been reported for Pd/SiO_2 high-surface-area powder catalyst [293] and $Pd/Al_2O_3/Ta(1\,1\,0)$ planar model catalysts [294]. On the other hand, reversibility of the CO adsorption with temperature on a Pd(1 1 1) single crystal surface reveals that C–O bond scission does not occur on atomically flat Pd(1 1 1), therefore the active sites for CO dissociation are likely the defect/edge sites on Pd nanoclusters.

The thermal stability of facetted Pt nanocrystals on amorphous silica support films was investigated using in situ TEM in a temperature range between 25 and 800 °C [295]. Changes in the cluster shapes begin at 350 °C. Above 500 °C, the clusters spread on the support film with increasing temperature, rather than becoming more spherical. Such temperature-induced wetting of Pt clusters on silica surface can be attributed to the interfacial mixing of Pt and SiO_2.

Au–Pd bimetallic model catalysts were synthesized as alloy clusters on SiO_2 ultrathin films (2–5 nm) [296]. The surface composition and morphology were characterized

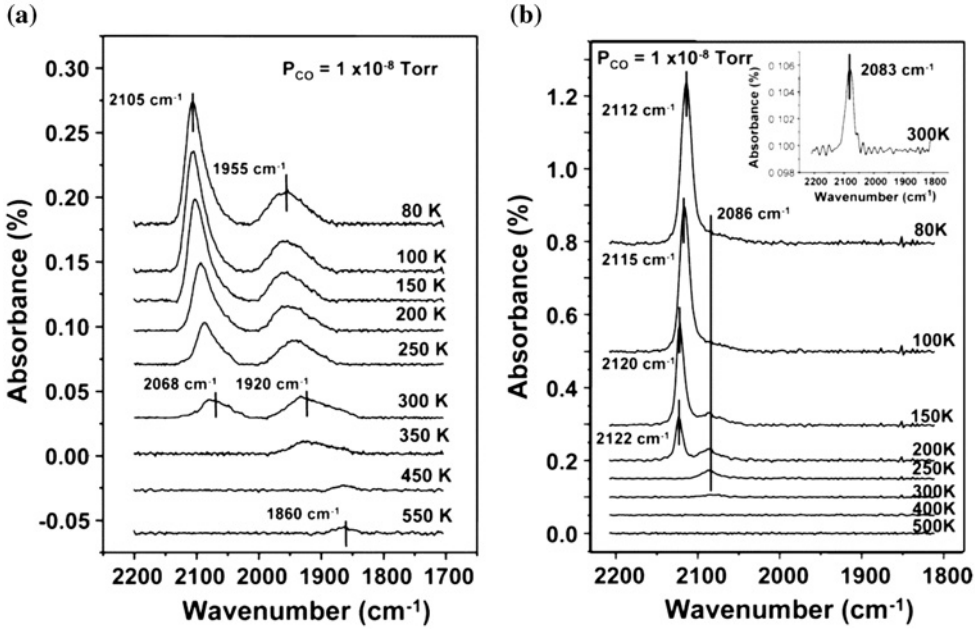

Figure 19: RAIRS spectra of CO adsorption as a function of temperature: (a) on 1.0 ML $Pd/SiO_2/Mo(1\,1\,0)$; (b) on 1.0 ML Au/1.0 ML $Pd/SiO_2/Mo(1\,1\,0)$ [296].

with LEIS, RAIRS, and TPD. The surface of the clusters is shown by LEIS to be Au-rich compared with the bulk of the cluster. However, the extent of Au enrichment is less than that observed for a planar Pd–Au bimetal system [297]. With CO as a probe using RAIRS and TPD, isolated Pd sites were identified as a unique surface ensemble, as shown in Fig. 19. CO adsorption on 1.0 ML Pd/SiO_2 leads to a relatively narrow feature at $\sim$2105 cm^{-1} and a broad feature extending from 2000 to 1875 cm^{-1} corresponding to CO on Pd atop sites and on bridge/threefold hollow sites, respectively (Fig. 19a). On 1.0 ML Au/1.0 ML $Pd/SiO_2/Mo(1\,1\,0)$ (Fig. 19b), only a sharp feature at 2112 cm^{-1}, assigned to CO atop on Au, with a small shoulder at lower frequency side is apparent, with no features corresponding to CO adsorbed on Pd in bridging or threefold hollow sites. The shoulder observed on the low-frequency side at 80 K is clearly evident at 150 K with a stretching frequency at 2086 cm^{-1} and distinctly resolved from the Au atop sites at 200 K. This feature is assigned to CO atop on isolated Pd sites. Such isolated Pd sites have been proposed as an active site for vinyl acetate synthesis by acetoxylation of ethylene [298]. Ethylene adsorption and dehydrogenation show a clear structure–reactivity correlation with respect to the structure/composition of these Au–Pd model catalysts. The TPD spectrum for C_2D_4 on 1.0 ML $Pd/SiO_2/Mo(1\,1\,2)$ (Fig. 20) is broad with a desorption maximum at 250 K, assigned to π- and di-σ-bonded C_2D_4. Upon adding Au to the 1.0 ML Pd/SiO_2, the intensity of the C_2D_4 TPD decreases and shifts to lower temperature. These changes are attributed to dilution of Pd by Au, thus reducing the di-σ-bonded species on two contiguous Pd sites. D_2 formation from ethylene dehydrogenation was also monitored with TPD (Fig. 20b). On Pd/SiO_2, two D_2 features appear with desorption maxima at 310 and 470 K. With the addition of 0.1, 0.2, and 0.4 ML Au to 1.0 ML Pd/SiO_2, the

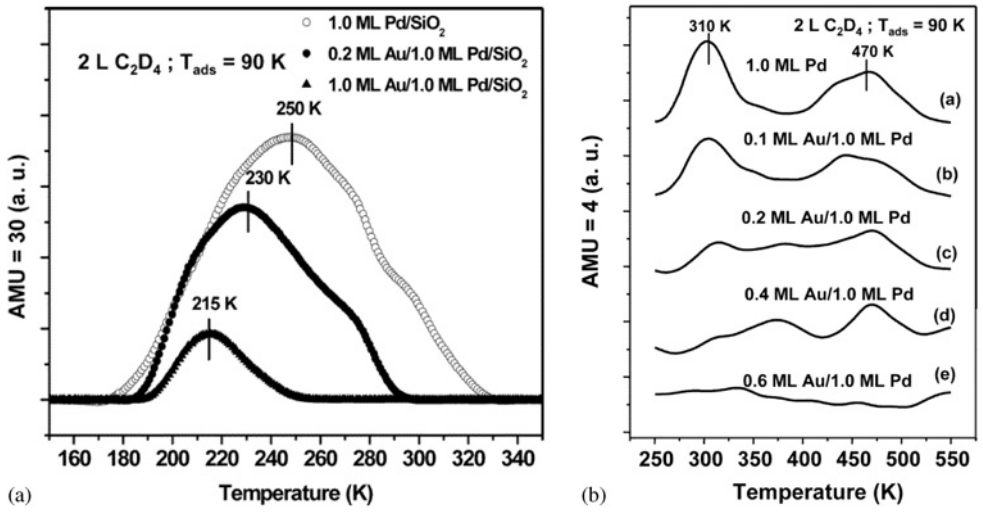

Figure 20: (a) TPD of C_2D_4 with 2.0 L C_2D_4 exposure at 90 K on 1.0 ML Pd/SiO_2 (upper); 0.2 ML $Au/1.0$ ML Pd/SiO_2 (middle); and 1.0 ML $Au/1.0$ ML Pd/SiO_2 (lower). (b) D_2 signals collected from C_2D_4 TPD with 2.0 L C_2D_4 exposure at 90 K on $Au/1.0$ ML Pd/SiO_2 surfaces [296].

production of D_2 gradually disappears. These data demonstrate that contiguous Pd sites are required for ethylene decomposition.

5. TITANIA-SUPPORTED METAL CLUSTERS

5.1. TiO_2 single crystals

Titanium dioxide (TiO_2) is the most investigated single-crystalline oxide studied by surface science techniques. Rutile (1 1 0), (1 0 0), (0 0 1), and anatase surfaces have been reported to be investigated. Among them, rutile (1 1 0) has been studied most extensively. Since TiO_2 is important for a wide range of technical uses, the bulk structure, defects, and electronic structure have been extensively studied and summarized [299]. The photochemistry of TiO_2 surfaces has also been reviewed, including the production and characterization of surface defects, the role of nitrogen doping on the photothreshold of TiO_2, charge transfer between excited TiO_2 and adsorbates, and mechanisms of photocatalysis [300, 301]. Diffusion of oxygen molecules on transition metal oxide surfaces plays a vital role in catalysis and photocatalysis on these materials. Time-resolved STM provides evidence for a charge transfer-induced diffusion mechanism for O_2 molecules adsorbed on rutile TiO_2(1 1 0) [302]. Adsorbed oxygen molecules mediate vacancy diffusion via the loss of an oxygen atom to a vacancy and the sequential capture of an oxygen atom from a neighboring bridging oxygen row, leading to an anisotropic oxygen vacancy diffusion pathway perpendicular to the bridging oxygen rows. The O_2 hopping rate has been shown to depend on the number of surface oxygen vacancies [302, 303]. A high-resolution STM image and schematic structure model of TiO_2(1 1 0) is shown in Fig. 21 [33].

The electronic properties, defect formation, and surface structure of rutile TiO_2(1 1 0) and anatase TiO(1 0 1) single crystals as a function of N-doping have

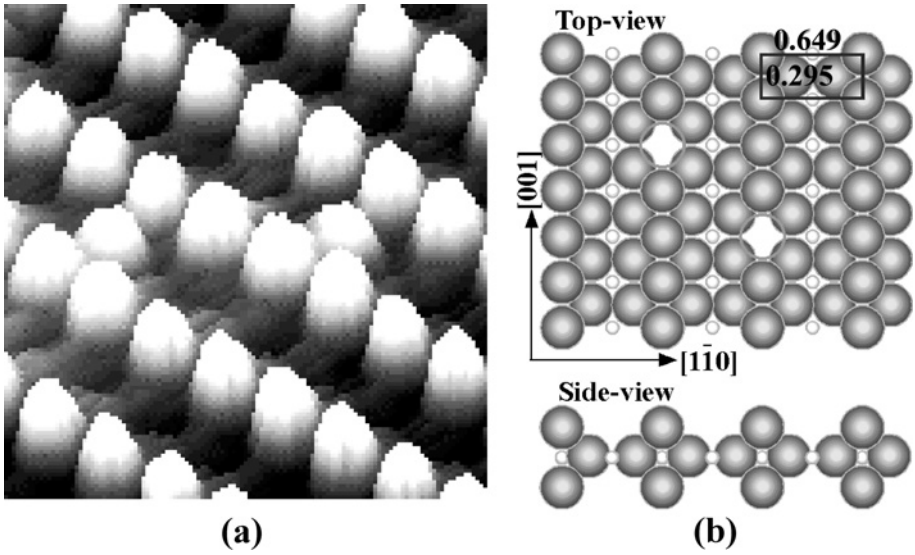

Figure 21: (a) A high-resolution STM image of TiO_2(1 1 0), (b) a schematic structural model of TiO_2(1 1 0) with empty circles indicating the surface oxygen vacancies [33].

been investigated [304]. Although no band gap narrowing was observed, N-doping induces localized N 2p states within the band gap just above the valence band. N is present in an N(III) valence state, which facilitates the formation of oxygen vacancies and Ti 3D band gap states at elevated temperatures. The increased O vacancy formation facilitates the 1×2 reconstruction of the rutile (1 1 0) surface. Recent STM studies of TiO_2(1 1 0) reveal three types of configurations of adsorbed formates, i.e. bridge formate on a fivefold coordinated Ti^{4+} row, bridge formate with one oxygen of the formate on an oxygen vacancy site and the other bonded to a fivefold coordinated Ti^{4+} ion, and a monodentate formate bonded by an oxygen atom to the oxygen vacancy site [305]. Oxygen vacancies produced by dehydration of two hydroxyls under catalytic reaction conditions are essential for reaction. On the stoichiometric TiO_2(1 1 0) surface, the adsorption and desorption of C_4H_4S is completely reversible [306]. On a defective TiO_2(1 1 0) surface, a small fraction of adsorbed thiophene molecules (<0.05 ML) decompose.

On a nearly perfect TiO_2(1 1 0) surface, a H_2O desorption peak is observed at 250–300 K and has been attributed to molecularly adsorbed H_2O at Ti^{4+} sites based on the O(1s) peak position and the change in work function [307]. The coverage of water in this state is estimated from O(1s) signals to be approximately one per unit cell or one for every Ti^{4+} site. A tail of the feature that extends to 375 K is attributed to disproportionation of surface hydroxyl groups present in low concentrations. Higher coverages of water give rise to a TPD peak at 170 K, and is attributed to water bound to bridging oxygen anion sites. Finally, multilayer water desorbs in a feature at 160 K. Surface hydroxyls bound to thermally induced oxygen vacancies of approximately 1% concentration disproportionate to give a water TPD peak at approximately 500 K. A recent combination of high-resolution STM and DFT has been used to study the interaction of water with a reduced TiO_2(1 1 0)-(1×1) surface. This study shows that

water dissociates at oxygen vacancies to form paired hydroxyl groups [308–310]. The features observed by STM have been assigned to bridging oxygen vacancies, oxygen atoms on surface Ti atoms, and single as well as pairs of hydroxyls on bridging oxygen rows. These hydroxyl pairs are immobile and stable unless they interact with adsorbed water molecules. As a result of these interactions, protons are transferred to adjacent oxygen rows, thereby forming single hydroxyl groups. Additionally, it has been shown that hydroxyl groups facilitate the diffusion of water molecules over the oxygen rows.

The decomposition and protonation of surface ethoxy groups on TiO_2(1 1 0) indicate two different types of adsorbed ethoxy species: (1) an ethoxy species that can readily be removed by combination with surface hydroxyl groups and desorption as ethanol between 250 and 400 K; these ethoxy groups are bound to surface Ti atoms (Ti-OEt) and are protonated by neighboring hydroxyl groups to form a ''bridging oxygen'' atom of the surface lattice; and (2) an ethoxy species that cannot react with surface water or hydroxyls below 450 K in TPD; this species is attributed to an ethoxy group bound at ''bridging oxygen'' vacancies in the surface lattice [311]. This latter species is removed at ~650 K by decomposition via β-hydrogen elimination to form ethylene and ethanol in a 1:1 ratio. Methanol on the vacuum-annealed, reduced TiO_2 surface produces ethylene as the main desorption product [312]. Reoxidation of the TiO_2 surface quenches the production of ethylene and promotes the formation of formaldehyde [312]. Propene adsorbed on Ti sites at the edges of Au islands is bonded more strongly than on bare Ti sites [313].

The anatase TiO_2(1 0 1) surface is stable in a (1×1) configuration and exhibits twofold coordinated (bridging) oxygen atoms and fivefold coordinated Ti atoms with a density comparable to that found on rutile TiO_2(1 1 0) [314, 315]. Step edges are terminated by fourfold coordinated Ti sites. In contrast to rutile TiO_2(1 1 0), anatase TiO_2(1 0 1) does not show a strong tendency to lose twofold coordinated oxygen atoms upon annealing in UHV. The anatase TiO_2(1 0 0) surface has the second-lowest surface energy and tends to form a (1×2) reconstruction. A model with (1 0 1)-oriented microfacets agrees with the observed features in atomically resolved STM images. The TiO_2(0 0 1) surface forms a (1×4) reconstruction that is well explained by an ''ad-molecule'' model predicted from density functional calculations. A (1×3) reconstruction is observed for the anatase TiO_2(1 0 3) surface.

5.2. Metal clusters on TiO_2(1 1 0)

5.2.1. Pt-group metals

One of the most interesting phenomena related to metals supported on TiO_2 is the so-called strong metal–support interaction (SMSI). The SMSI effect, first described in 1978 by Tauster et al. [316, 317], is manifested by a strong inhibition of CO and H_2 chemisorption following a high-temperature calcination (above ~700 K) and a sharp reduction in reactivity for alkane hydrogenolysis. Concomitantly, CO–H_2 reactions are strongly promoted [318, 319]. Two explanations have been offered: (1) the effect is due to an electronic perturbation of the metal, e.g. via charge transfer; and (2) the effect is due to encapsulation by TiO_x species which acts as a site blocker. Work has shown that encapsulation does indeed occur on supported catalysts and on single crystals [320, 321].

Considerable work has addressed the SMSI effect and much has been surmised about the molecular-level details of this phenomenon; however, most explanations are

based on global kinetic measurements. One of the very few investigations at the nanoscale is the study of Diebold and co-workers [322] who examined model $Pt/TiO_2(1\,1\,0)$ catalysts. LEIS and STM showed that relatively large Pt clusters were covered by a layer of partially reduced titania (Figs. 22 and 23). Nanosized Pt clusters grown on a $TiO_2(1\,1\,0)$ surface, which showed an SMSI state following an anneal in UHV at high temperatures, were also found to be completely encapsulated with a reduced titanium oxide layer [323].

Annealing Rh clusters (1–3 nm) on $TiO_2(1\,1\,0)$-(1×2) system produces one of the three results [324]: (i) encapsulation of the clusters in the temperature range 500–700 K as indicated by a decrease in the relative AES signal of Rh by 40%; (ii) an increase in the size of clusters between 700 and 900 K, indicating coalescence; and (iii) separation of the 3–5 nm diameter and 3–5 atomic layers thick Rh crystallites (with their (1 1 1) planes parallel to the substrate) from titania above 1100 K, with the substrate exhibiting a well-ordered (1×2) terrace structure.

A combination of Z-contrast imaging and EELS in STEM shows evidence for a strong interaction between the Pt clusters and TiO_2. This interaction is found to be dependent on the Pt cluster size and is manifested either as an encapsulation of the Pt clusters by the support or a distortion of the structure of the Pt clusters [325]. For clusters only a few atoms in size, there is a direct evidence for epitaxial nucleation of Pt on titania. Pt clusters were found to exhibit preferential nucleation on rutile rather than anatase [325]. The surface structure and stoichiometry of TiO_2 have profound effects on the formation and growth of nanosized Pt clusters on $TiO_2(1\,1\,0)$ [326]. On the (1×1) surface, Pt forms randomly distributed 3D nanoclusters that coalesce and are encapsulated when thermally annealed. In contrast, smaller Pt clusters adsorb on top of the titanium atomic rows on the (1×2) surface and exhibit higher thermal stability. This is presumed to arise from charge transfer from Ti to Pt. Using vicinal $TiO_2(1\,1\,0)$ surfaces with alternating (1×1) and (1×2) domains, the different interactions of Pt with the two domains were verified. An array of self-organized Pt nanoclusters was formed on the (1×2) surface. CO dissociation, possibly due to the reduction by Ti^{3+}, was observed on the $Pt–TiO_2(1\,1\,0)$-(1×2) [327]. On the reduced (1×2)-reconstructed surface, CO desorbs between 140 and 170 K, whereas on the stoichiometric (1×1) surface, desorption occurs at 140 K. CO adsorption/desorption was found to strongly depend on the size of Pt nanoclusters. With a decrease in cluster size, CO was found to desorb at higher temperatures. This unusual desorption chemistry of the Pt nanoclusters was attributed to quantum size effects. STS revealed that clusters below 2 nm in diameter exhibited non-metallic behavior, while those above 4 nm were metallic. This transition in the properties of Pt nanoclusters from metallic to non-metallic with a decrease in the cluster size correlates with the observed increase in the binding energy of CO.

By growing metal clusters at high temperature (1100 K), arrays of Rh and Ir clusters have been fabricated with specific mean distances and narrow size-distributions [328, 329]. Dulub et al. [322] have recently reported an ordered, self-limiting $TiO_{1.1}$ overlayer on Pt clusters supported on $TiO_2(1\,1\,0)$. The $TiO_{1.1}$ overlayer decoration has no effect on the ordered growth of Pt nanocrystallites [330]. The I–V spectra recorded above the mid-point of the Pt clusters show that an increase in the average diameter of the clusters does not lead to greater metallic character [331]. Moreover, the characteristic line shape of the tunneling spectra is that of an insulator

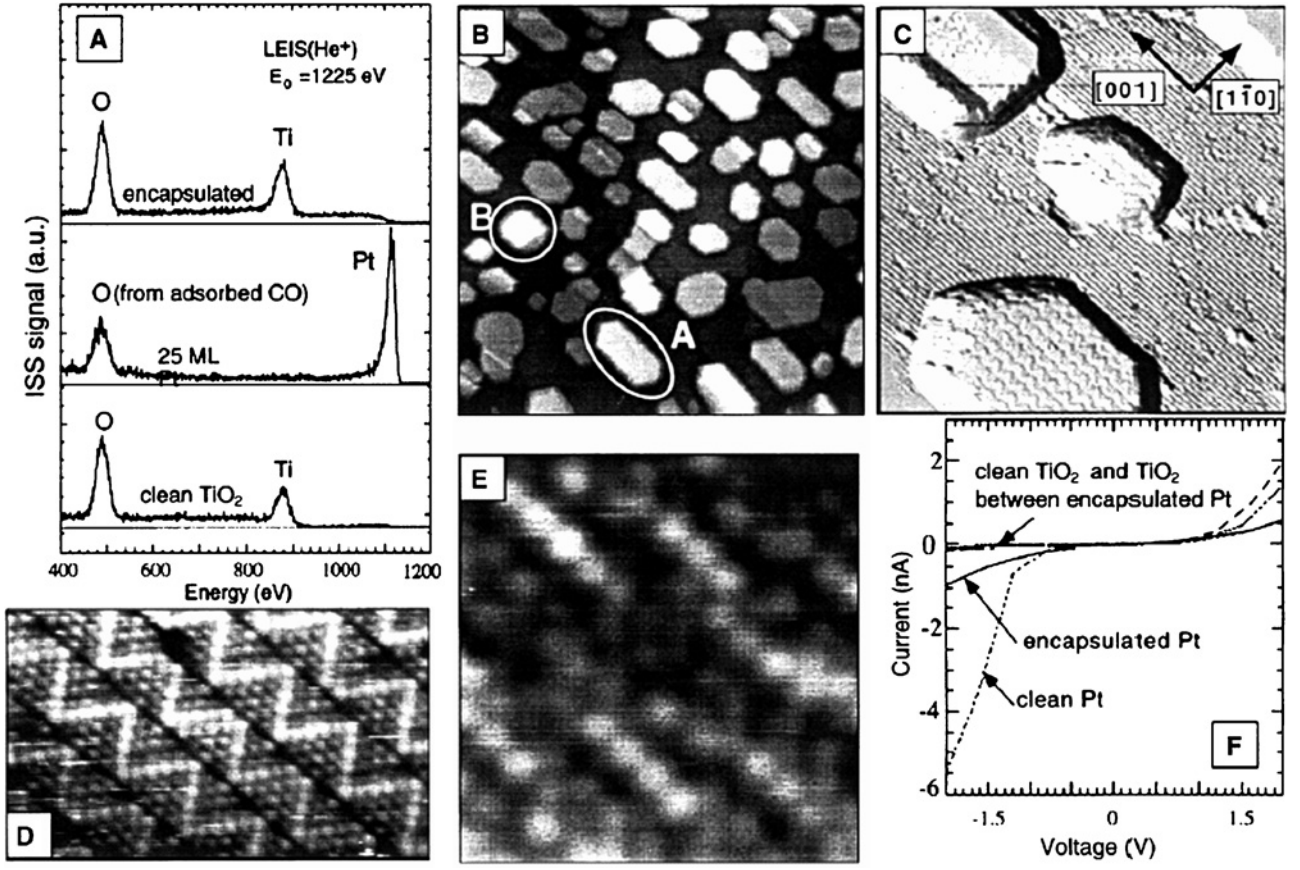

Figure 22: (A) LEIS spectra of the clean TiO_2(1 1 0) surface (bottom), after evaporation of 25 ML Pt at room temperature (center), and after the high-temperature treatment leading to encapsulation (top). (B)–(E) STM results after the high-temperature treatments; (B) overview (200 × 200 nm). Clusters are approximately 20 nm wide and 4 nm high. Most clusters show hexagonal shapes elongated along the substrate [0 0 1] direction (type A). A few square clusters (type B) are seen; (C) small scale image (50 nm × 50 nm), filtered to show the structure of the encapsulation layer on type A clusters; (D) atomic-resolution image of an encapsulated (type A) cluster; (E) atomic-resolution image (type B) cluster, showing an amorphous overlayer; (F) STS of the different surfaces [322].

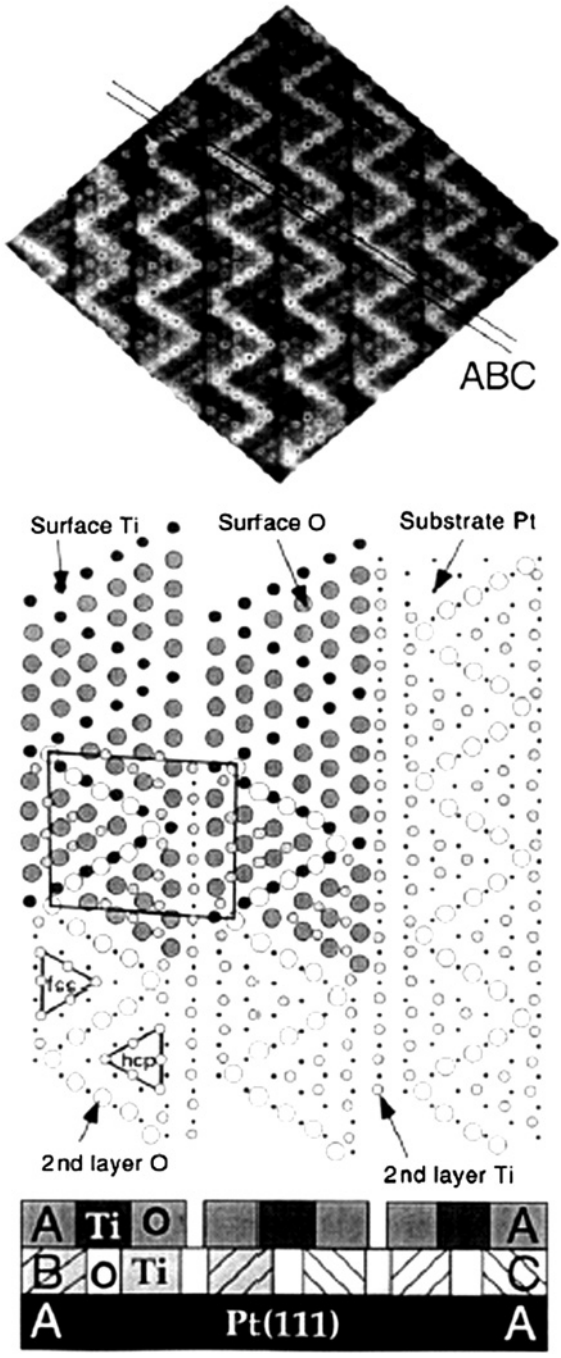

Figure 23: (Top) Atomically resolved STM image (10 nm × 10 nm) of an encapsulated hexagonal cluster. The image is compensated for distortion. Atomic positions are indicated. (Bottom) Top and side view of the proposed atomic model for the encapsulation layer on type-A clusters [322].

even for relative large clusters (> 5 nm). This behavior was attributed to the formation of a TiO_x decoration on the top facets of the Pt clusters [331]. The influence of a surfactant on the growth and chemisorption of Pt ultrathin films on TiO_2(1 1 0) has been studied [332]. Continuous hot electron generation was detected for Pt/TiO_2, Pd/TiO_2, and Pt/GaN during catalytic CO oxidation between 80 and 150 °C [333, 334]. These observations are consistent with the Schottky diode model of oxide-supported metal catalysis proposed by Schwab, Solymosi, and others beginning in 1960s. Hot electrons may influence the chemistry at oxide–metal interfaces and contribute to metal cluster size-dependent catalytic activity/selectivity.

The nucleation and growth of Pd on the TiO_2(1 1 0) surface have been studied with atomically resolved STM [335, 336]. Both dimer and tetramer Pd clusters have been observed; however, no single Pd atoms were detected. These results support the "classical" nucleation model which assumes that only monomers are mobile, whereas dimers are stable entities. A marked preferential nucleation and growth of Pd clusters at step edges have also been observed. For Pd clusters (3.5 nm in diameter and 0.8 nm in height) on TiO_2(1 0 0)-(1 × 3), it has been demonstrated that STM is capable of imaging individual atoms [337]. Low coverages of Pd (< 3 ML) deposited on TiO_2(1 1 0) at 300 K adsorb CO exclusively in a bridged-site configuration with a band at 1990 cm^{-1} characteristic of CO adsorption on Pd(1 1 0) and Pd(1 0 0) surfaces [338]. When annealed to 500 K, XPS and LEED indicate the nucleation of Pd clusters onto which CO adsorbs predominantly as a strongly bound linear species at 2085 cm^{-1} assigned to edge sites on Pd clusters. Pd overlayers with coverages of 10–20 ML undergo some nucleation during growth at 300 K. These clusters adsorb CO with bands at 1990 and 1940 cm^{-1}, the latter of which is associated with the formation of Pd(1 1 1) facets. LEED indicates that at Pd coverages above 10 ML, the clusters exhibit (1 1 1) facets parallel to the substrate and aligned with the TiO_2(1 1 0) unit cell.

For Pd clusters supported on TiO_2(1 1 0)-(1 − 1), adsorption of CO has been measured using a thermal molecular beam [339]. The adsorption is dominated by weakly held "precursor" states, populated mainly via reverse spillover of CO from the support (where it only exists with a relatively short lifetime) to the Pd clusters where it is trapped into a long-lived adsorbed state. The heat of adsorption of the weakly held species on the support is approximately 38 kJ/mol. CO appears to be more weakly bound to Pd clusters with an initial heat of adsorption of 110 kJ/mol compared with 135 kJ/mol for a Pd single crystal; there is zero net sticking of CO above 400 K. Annealing of the model catalyst above 573 K leads to a significant reduction in CO uptake and in the sticking probability, probably due to a combination of sintering and an SMSI-like effect and/or alloying of the Pd with Ti. Pd clusters enhance the rate of re-oxidation of a sub-stoichiometric TiO_2(1 1 0) surface [340]. O_2 is believed to dissociatively adsorb at 673 K on Pd, then "spills over" onto the support upon further reaction. Formic acid was found to dehydrogenate on Pd nanoclusters on TiO_2(1 1 2) [341]. The reaction rate is lower compared with bulk Pd metal, probably due to alloying with Ti originating from interstitial Ti^{3+} cations that attenuate electron density at the Fermi level of the clusters. On a clean TiO_2 surface, only the dehydration reaction is apparent and proceeds at steady state with a very high reaction probability above 500 K; no evidence for a dehydrogenation pathway is evident. In any case, the adsorption probability of formic acid with Pd is higher than expected due to diffusion of formic acid, via a weakly bound state, from the support to the metal clusters.

Molecular beam measurements show that Pd clusters on $TiO_2(1\,1\,0)$ are active for CO adsorption, with a global sticking probability of 0.25. These clusters are deactivated by annealing above 600 K, an effect indicative of SMSI [342]. The Pd clusters are single crystals oriented with their $\langle 1\,1\,1\rangle$ planes parallel to the surface plane of titania [343]. Analysis of the surface by atomically resolved STM shows the formation of two structures at the surface of the Pd clusters for films annealed above 800 K. Atomically resolved STM shows a "pinwheel" superstructure with one domain having a ((7 2)(5 7)) unit cell with respect to Pd(1 1 1) and a second domain with a ((7 5)(2 7)) unit cell. Coexisting with this phase is a structure consisting of zigzag rows that run along the close-packed directions of the Pd(1 1 1) islands, as shown in Fig. 24. This structure has a rectangular unit cell incommensurate with both the substrate $TiO_2(1\,1\,0)$ and the Pd(1 1 1) islands. The two structures merge with no noticeable domain barriers or steps, suggesting a close relationship between the two domains. LEED shows several distinct, overlapping patterns that can be identified with the structures, $TiO_2(1\,1\,0)$-(1×2), Pd(1 1 1)-(1×1), the hexagonal pinwheel structure, and the rectangular zigzag unit cell. XPS at normal and grazing emission show the encapsulating layer to be composed of TiO_x with Ti predominantly in 2^+ or 3^+ oxidation states, having stoichiometries of TiO and $TiO_{1.4}$. The STM images of the zigzags bear a strong similarity to structures seen for annealed Pt islands on $TiO_2(1\,1\,0)$-(1×1) and TiO_x supported on Pt(1 1 1). The pinwheel structure is similar to that for annealed Cr on Pt(1 1 1) [343]. In similar fashion, encapsulation of the metal clusters on an oxide layer was observed on nanostructured $SrTiO_3(0\,0\,1)$ [344]. The presence of these new structures consisting of a mixed alloy overlayer of Pd and Ti within a reduced titania overlayer on Pd clusters after annealing is proposed to give rise to the SMSI effect. These alloy structures consist of two discrete ratios of atoms: Pd/Ti of 1:1 (pinwheel) and 1:2 (zigzag), as shown in Fig. 25 [342]. It is interesting to note that Nuzzo and Dubois have proposed that the SMSI effect could result from the formation of intermetallic compounds such as Pt_3Ti or Ni_3Ti [345]. Encapsulation of Pd clusters by TiO_x was observed to depend on the electronic structure of TiO_2, reduced by heavy Ar^+ sputtering, Nb-doping, or annealing in vacuum [346]. In addition, encapsulation of Fe or Pt clusters by Ti suboxides TiO_x on $TiO_2(1\,1\,0)$ after thermal annealing in UHV at 773–979 K was evidenced by LEIS and XPS [320, 321, 347]. The oxide adlayer of $TiO_{1.36}$ or $TiO_{1.37}$ on the Pd(1 1 1) cluster surface also reveals two superstructures with different lattice parameters and crystallographic rotations. Figure 24 shows STM images of the (1 1 1) surface of Pd clusters. A superstructure, labeled as structure A, consisting of bright spots connected by lines is evident (see Fig. 24a–c). This superstructure has been previously termed the "wag 2D" structure. The atoms are aligned along the line connecting the bright spots of the wagon wheel structure. A second superstructure was observed on the surface of other clusters. This superstructure is perfectly hexagonal with a lattice of (1.05 ± 0.02) nm.

A method was developed by which supported Ir clusters can be fabricated in desired uniform sizes in the range of 1.5–20 nm with constant intercluster distances [329]. $Ir_n/TiO_2(1\,1\,0)$ ($n = 1, 2, 5, 10, 15$) samples were prepared by size and energy-selected deposition at room temperature [348]. The Ir clusters are found to be formally in the zero oxidation state, with no significant shifts in the Ir 4f binding energy with cluster size. Over a wide range of impact energies, both the Ir XPS intensities and peak positions are constant, indicating a constant sticking coefficient and no impact-driven

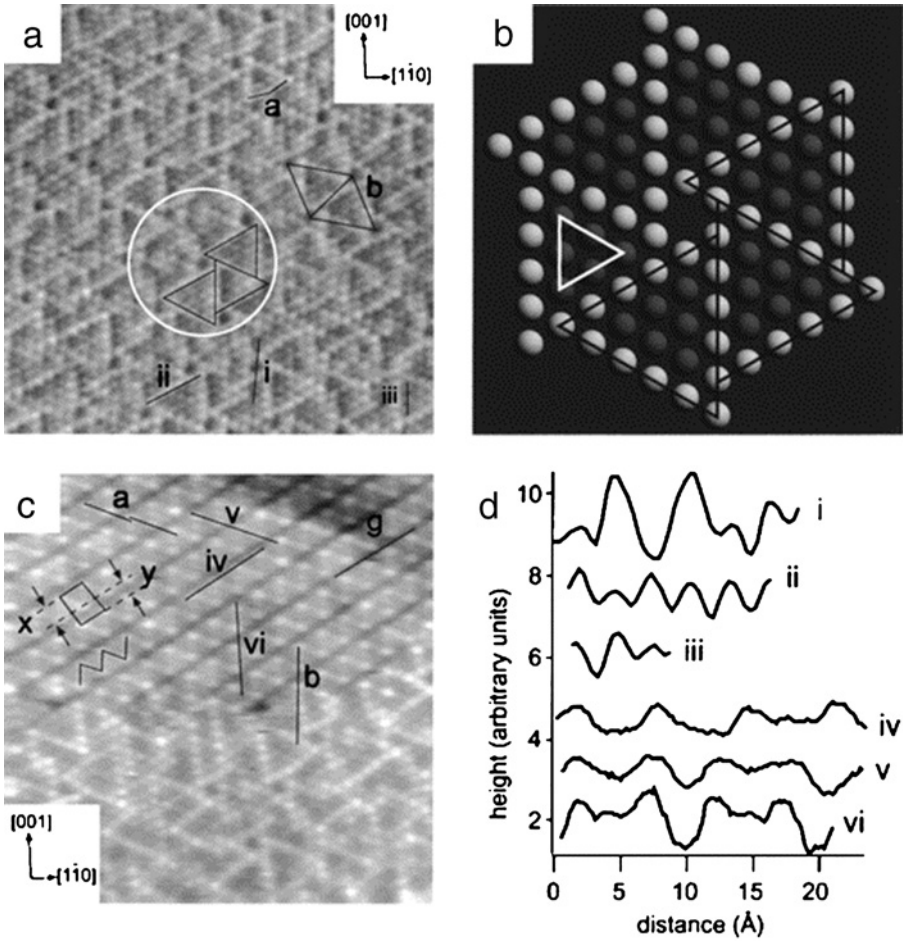

Figure 24: (a) 10.5×10.5 nm STM images of the pinwheel structure. The circle highlights a pinwheel and the three triangles mark out part of the ideal pinwheel structure. The line, *a*, indicate a bend in a spoke, and *b* indicates the superstructure. The lines *i*, *ii*, and *iii* indicate image of an area showing the pinwheel structure (bottom) and zigzag structure (top). The unit cell marked that of the zigzag structure. The central spot in the unit cell is off-center as indicated by the ratio $x{:}y = 27{:}23$. *a* marks two lines drawn along the zigzag diagonals; these indicate the phase shift as one goes across the troughs. *g* marks a glide-plane. *b* marks the rotation as one goes from the spokes of the pinwheel to the diagonal of the zigzag. (b) Schematic arrangement of surface atoms for the area indicated by the circle in (a). (c) The lines *iv*, *v*, and *vi* indicate line profiles shown in (d). (d) Line profiles along the lines marked in (c). Profiles shown are taken from a processed image for clarity; height information is not retained, although the measurements are presented in the text [342].

redox chemistry. LEIS suggests that the deposited Ir clusters remain largely intact, neither fragmenting nor agglomerating, and retain 3D structures for the larger sizes. For impact energies above 10 eV/atom, comparison of LEIS and XPS data show that the Ir clusters penetrate into the TiO_2 surface, with the extent of the penetration increasing with an increase in the energy per atom and the cluster size. TPD of CO has been used to further characterize the deposited Ir_n. This system shows pronounced substrate-mediated adsorption (SMA) at low CO exposures, with a strong cluster size

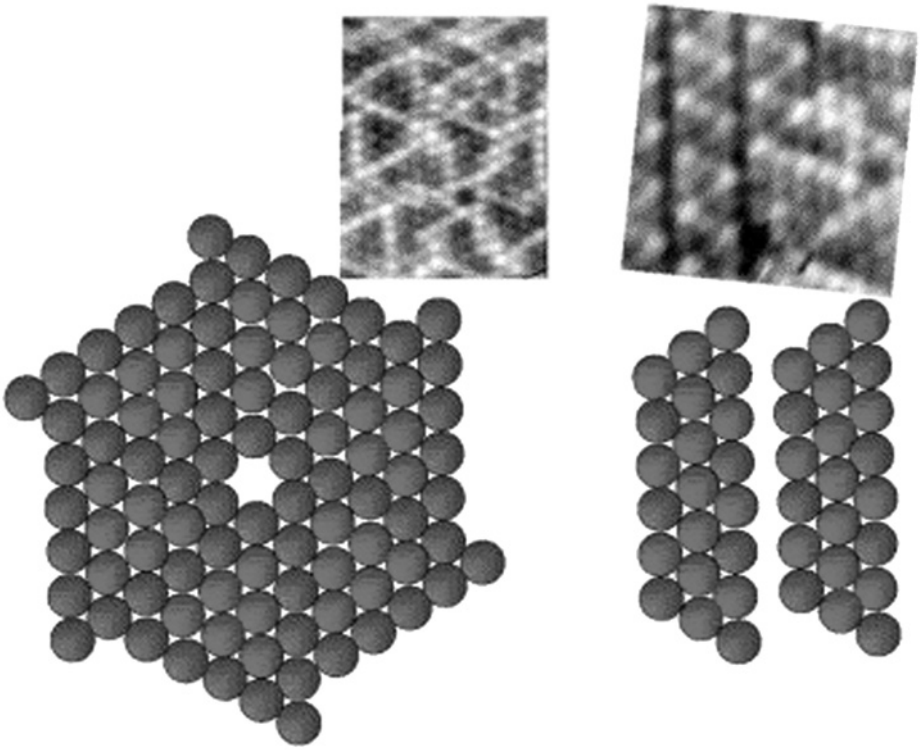

Figure 25: Idealized surface structural models for Pd/TiO_2, together with the related high-resolution STM images [342].

dependence. LEIS and sputtering experiments indicate that CO adsorbed via SMA is bound differently compared with CO adsorbed at high exposures. The cycle of CO adsorption and heating comprising a TPD experiment has a dramatic effect on the sample morphology, leading to encapsulation of Ir by a thin TiO_x layer.

The structure of low coverage Ni atoms on the $TiO_2(1\,1\,0)$ surface was studied using polarization-dependent EXAFS [349–351]. Ni atoms interacted with oxygen atoms at the step edges, where atomically dispersed Ni species were found with Ni–O distances at (0.199 ± 0.002) and (0.204 ± 0.003) nm along the parallel and perpendicular directions to the $TiO_2(1\,1\,0)$ surface, respectively. The bonding position corresponds to the virtual Ti site of the next TiO_2 layer on the TiO_2 surface. The Ni location was mainly determined by the directions of the surface oxygen dangling bond at the surface [349–351]. The electronic states of Fe, Ni, and Cu overlayers on $TiO_2(1\,1\,0)$ surfaces have been investigated using normal-emission and resonant UPS using synchrotron radiation [352, 353]. It was found that Fe grows in a Stranski–Krastanov mode. At low coverages, Fe deposition on $TiO_2(1\,1\,0)$ creates surface Ti^{3+} ions leading to identical in-gap emission as that produced by surface oxygen vacancies on TiO_2. At high coverages, Fe-induced in-gap emission evolves into a bulk Fe spectrum. However, initially, an E_f is not observed, indicating that small non-metallic Fe clusters are formed. A sharp E_f edge is present at higher coverages, indicating that with an increase in size, the

clusters become metallic. For Ni on TiO_2(0 0 1), an in-gap emission from the reduced Ti^{3+} state appears at 1.2 eV with the initial deposition of Ni with no apparent E_f, suggesting the formation of small Ni clusters on TiO_2(0 0 1). Upon further deposition, the emission grows and evolves into a spectrum of bulk Ni. For the Cu/TiO_2(1 1 0) system, Cu grows in a Stranski–Krastanov mode. Two in-gap emissions from the reduced Ti^{3+} state and oxidized Cu^{+} or Cu^{2+} states are observed at 0.8 and 2.8 eV below the E_f, respectively, for initial Cu deposition, providing convincing evidence that there is significant charge transfer between Cu and the substrate. Upon further deposition, the emission in the band-gap region evolves into a spectrum of Cu metal, although with a delayed formation of E_f, assumed to relate to finite cluster size effects.

5.2.2. IB group metals

Cu was found to form 3D islands on TiO_2(1 1 0) at all the coverages indicating the relatively high mobility of Cu atoms on TiO_2 at room temperature and a weak Cu–TiO_2 bond compared with the Cu–Cu bond [354]. At low coverages (<0.5 ML), Cu islands exhibit self-limiting growth, i.e. with increasing coverage, the average island size remains almost constant whereas the island density increases. At higher coverages (>0.5 ML), the average island size scales with coverage. However, the increase in island size is primarily due to an increase in height, not diameter. Although larger islands can be formed by annealing, the average size of the islands is nearly independent of coverage for any given annealing temperature. Ni also forms 3D clusters on TiO_2(1 1 0) at room temperature with an average height of $\sim$0.65 nm and a diameter of $\sim$3.0 nm [355]. Although the Ni–TiO_2 interfacial energy is estimated to be greater than that of Cu–TiO_2, Ni does not appear to wet the surface to a greater extent than does Cu. The higher surface free energy for Ni relative to Cu apparently dominates over its greater interfacial energy, resulting in Cu and Ni islands with similar aspect ratios [355–357]. Small 3D Cu clusters on TiO_2(1 1 0) were found to dissociate into 2D clusters upon exposure to O_2 at room temperature. Oxygen-induced dissociation of Ni clusters is much slower than that of Cu for similar oxygen exposures. The formation of 2D clusters is thermodynamically favorable for Cu and Ni with consideration of the lower surface energy of the oxygen-covered metal compared with the pure metal [358, 359]. Cu nanoclusters on TiO_2(1 1 0) are more active for methanol decomposition than bulk single-crystal Cu surfaces, but with no apparent cluster size effects [312]. Thermal decomposition of dimethylmethylphosphonate was carried out on Cu/TiO_2(1 1 0) and Ni/TiO_2(1 1 0) surfaces [360, 361].

Small 3D Ag islands with a narrow diameter distribution are formed on TiO_2(1 1 0)-(1 × 1) at room temperature with Ag deposition of 0.05–1 ML [362]. This behavior is qualitatively similar to the "self-limiting" growth previously reported for Cu. That is, above $\sim$0.5 ML, the average Ag island diameter is nearly independent of coverage whereas island nucleation continues up to 1 ML in coverage. The Ag islands are remarkably stable under thermal annealing; long-term or high-temperature annealing increases the island diameter by less than a factor of two [362]. Ag grows 3D on TiO_2(1 1 0)-(1 × 1) and (1 × 2) surfaces; no strong chemical interaction between Ag and TiO_2 was detected [363]. At 0.05 ML Ag exposure, the Ag 3D core level binding energy shifts to 1.2 eV higher than that for metallic Ag. In addition, the Ag 3D peak width increases with decreasing cluster size. The binding energy shifts and peak broadenings are attributed to initial and final state effects. The valence band as a function of Ag

exposure suggests that a metal-to-nonmetal transition occurs for Ag clusters between 0.5 and 1 ML (3.5–4.4 nm) [363]. An oxygen-induced cluster ripening was observed by STM after Ag/TiO_2(1 1 0) was exposed to 10 Torr O_2 for 2 h in an elevated-pressure reactor [364]. The Ag clusters exhibit a clear bimodal size distribution after O_2 exposure due to Ostwald ripening, i.e. some clusters increase in size while other clusters decrease in size. The cluster density also increases 5–15% after O_2 exposure, indicating redispersion simultaneously occurs with ripening. It is shown that intercluster transport likely takes place via the formation of Ag_2O [364].

Au on TiO_2(1 1 0) has recently become one of the most extensive studied system because of its extraordinary catalytic properties [14, 27, 32, 33, 72, 73, 365–387]. The size of the Au clusters and the support properties have been shown to be critical to their unique catalytic activity, as shown in Fig. 26. Isolated Au atoms can be prepared by mass-selected Au^+ ions deposited front the gas phase at room temperature with kinetic energies from <3 to 190 eV [386]. For substrate temperatures of 160 and 300 K and for fractional monolayer Au coverages, 2D Au islands are initially formed up to a certain average critical coverage (θ) [387–390]. At coverages above θ, added Au mainly goes on top of these to form 3D islands. The 1D, 2D, and 3D growth of Au clusters on TiO_2(1 1 0) was clearly evident in STM, as shown in Fig. 27 together with possible structural models. Even though thermodynamically the islands would prefer to form 3D islands from the onset of growth, kinetic limitations constrain the growth initially to 2D islands. The critical coverage is found to decrease with temperature (see Fig. 28), but is not dependent on the Au flux or the defect density of the TiO_2 surface. The 3D clusters are oriented with their (1 1 1) orientations parallel to the surface. The coverage at which 3D islands become apparent in LEIS data decreases as the surface temperature increases. No evidence of significant chemical interactions has been found between the Au and TiO_2 substrate. By annealing Au/TiO_2 to 775 K, the Au islands continue to grow; encapsulation of the Au islands by Ti suboxides is not observed. There is little or no CO adsorption on small Au clusters at 300 K (0.05 ML) based on

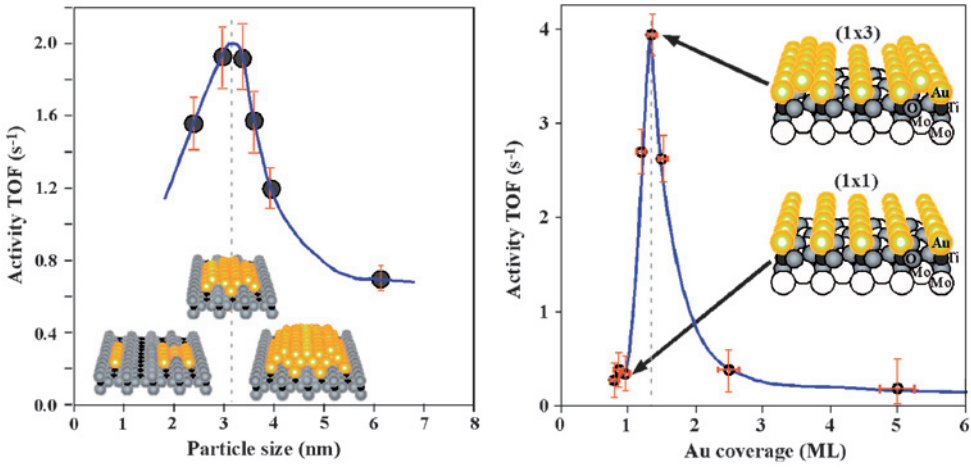

Figure 26: Catalytic activity for CO oxidation as a function of (a) cluster size on the TiO_2(1 1 0) at 353 K, (b) Au coverage on the Mo(1 1 2)-(8 × 2)-TiO_x at room temperature [33].

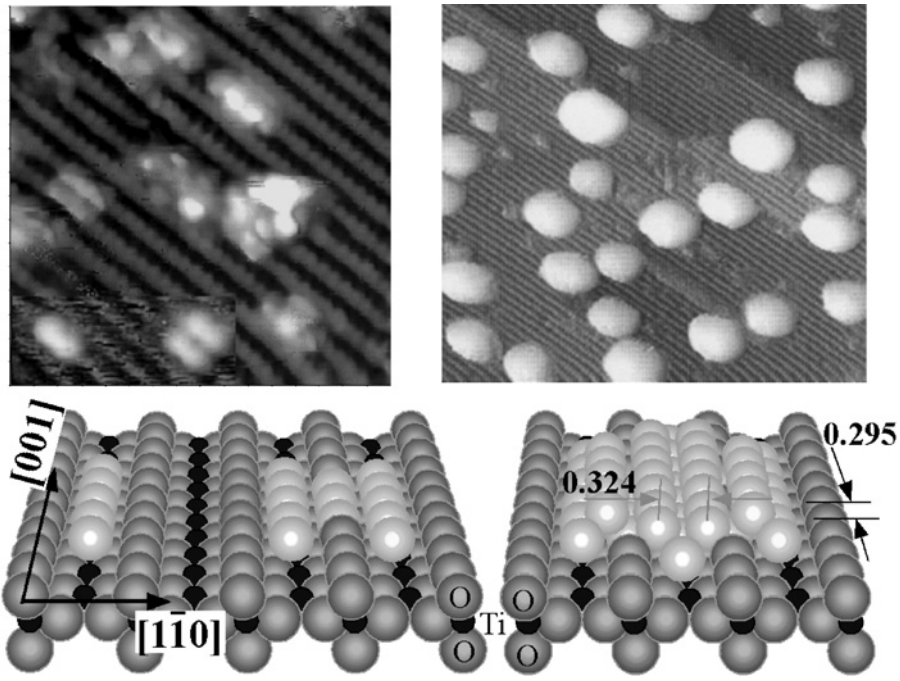

Figure 27: (a) and (b) STM images of Au on TiO_2(1 1 0), (c) 1D and 2D Au clusters on TiO_2(1 1 0), and (d) a 3D Au cluster with a thickness of two atomic layers on TiO_2(1 1 0) [33, 366].

LEIS measurements [387–390]. The effects of substrate temperature on the epitaxial growth of Au on TiO_2(1 1 0) surface have been studied by HRSEM and electron backscatter diffraction [391–393]. Au on TiO_2(1 1 0)-(1 × 1) forms highly faceted islands with hexagonal shapes. The epitaxial orientation relationship is (1 1 1)Au//(1 1 0)TiO_2 with (1 1 0)Au//[0 0 1] TiO_2 at room temperature deposition and annealing at 775 K; the structure is (1 1 2)Au//(1 1 0)TiO_2 with (1 1 0)Au//(0 0 1)TiO_2 for direct deposition at 775 K. For both orientations, two epitaxial variants are observed which are rotated with respect to each other by 180° about the TiO_2(1 1 0) surface normal. These two variants are in a twin orientation relationship. For high-temperature deposition, extensive (1 1 1) twinning of the Au islands is observed with boundaries separating the two orientation variants.

Comparison of 1–3 nm clusters of both Au and Mo on TiO_2(1 1 0) shows that clusters are not stable to even short anneals at 700 K, resulting in significant growth of the clusters and reduction in their number [394]. Mo clusters show remarkable resistance to sintering during short durations of annealing at 700 K. The differences are attributed to a stronger cluster–surface interaction for Mo than for Au, due to partial oxidation of Mo at the interface.

The importance of surface defects on TiO_2(1 1 0) has been more directly revealed by highly atomic-resolved STM and DFT calculations [395]. Surface bridging oxygen vacancies (see Fig. 21) are the active nucleation sites for Au clusters on the rutile TiO_2(1 1 0) surface. A direct correlation exists between a decrease in density of vacancies and the amount of Au deposited. Confirmed by DFT calculations, the

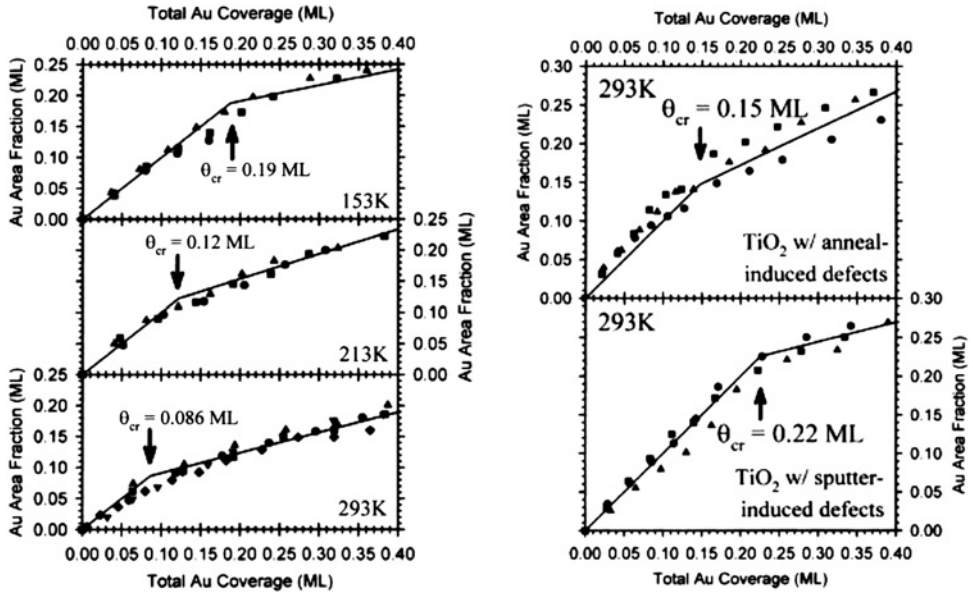

Figure 28: The area fraction of Au islands on $TiO_2(1\,1\,0)$ as a function of total Au coverage for Au deposition at ~0.3 ML/min at three different substrate temperatures: (a) 153 K; (b) 213 K; and (c) 293 K. Au growth on differently treated initial TiO_2 substrates at 293 K, followed by LEIS: (a) with anneal-induced defects; and (b) with Ar^+ sputtered defects. The anneal-induced defected surface was prepared by UHV anneals at 900 K, followed by a final anneal in 3×10^{-6} mbar O_2 for 10 min. The sputter-induced defected surface was prepared by annealing the surface in 3×10^{-6} mbar O_2 for 10 min, followed by a 30-sec 1 keV Ar^+ sputter at 5×10^{-6} mbar Ar pressure to create defect sites on the surface [389].

oxygen vacancy is indeed the strongest Au binding site. Both experimentally and theoretically, a single oxygen vacancy can bind three Au atoms on average. Valence level and shallow core states of Au nanoclusters on $TiO_2(1\,1\,0)$ have been studied by synchrotron photoemission [396]. The shift to high binding energy and broadening of the Au 4f peaks with decreasing Au surface coverage can be understood in terms of decreasing cluster size and the associated effects of charge on the cluster in the final state. Shifts in the photoemission onset are much more pronounced than the core level shifts and show a strong dependence on the degree of reduction of the $TiO_2(1\,1\,0)$ substrate. These observations suggest that the photoemission onset is influenced by an initial state effect involving charge transfer from defect states into cluster states.

The morphology changes of Au clusters on $TiO_2(1\,1\,0)$ under CO catalytic oxidation conditions (elevated temperatures) were investigated by in situ STM [384, 397, 398]. Au clusters (2.5–4 nm diameter) on fully stoichiometric $TiO_2(1\,1\,0)$ rutile substrates were studied by AFM and XPS over a wide range of pressures of O_2 and air. Under UHV conditions, the clusters are stable even after annealing at 400 °C, and only minor changes in the cluster size are detected after annealing at 773 K. In 50 Torr O_2, the clusters are relatively stable at room temperature but grow significantly after annealing to 673 K. In air, cluster growth begins at room temperature and is accompanied by the formation of Au–OH species.

Li^+ neutralization studies of Ag and Au clusters and thin films supported on TiO_2 show very efficient neutralization on small clusters with a decrease for the smallest clusters [399]. These results closely follow the size effects observed in the reactivity of these systems. The energy dependence of the neutralization was studied for the larger clusters (>4 nm) and observed to be similar to the trend observed on films and bulk (1 1 1) crystals. The highest neutralization efficiency corresponds to that clusters size for which a metal to non-metal transition occurs. The relative position of the Li level and the HOMO in the molecular cluster is expected to strongly affect the electron transfer process.

DFT calculations reveal that Cu and Ag interact strongly with the bridging oxygens of TiO_2 and transfer outer $(n+1)$s electron density to the Ti 3D states; Au forms weaker bonds at these sites via formation of a covalent polar bond [400]. The origin of the different behavior of Cu and Ag from that of Au can be understood in terms of the higher ionization potential of Au. A relative weak interaction with little charge transfer is found for all three metals bonded to Ti sites. The bonding at Ti sites is due to metal polarization and results in relatively long metal–surface distances. Accordingly, the Ti rows are channels where rapid diffusion of the metal atoms is expected. The electronic structure of a reduced TiO_2(1 1 0) surface, the interactions between oxygen vacancies, the dynamics of oxygen molecules on the reduced surface, the role of oxygen vacancies, and the oxygen adspecies in the nucleation of Au, Ag, and Cu clusters have been addressed [401]. On the non-reducible oxide support, MgO(1 0 0), CO oxidation occurs via CO first adsorbing on Au clusters then CO-promoted O_2 capture followed by formation of a CO–O_2 reaction intermediate complex. On the reducible oxide support, TiO_2(1 1 0), O_2 adsorbs independently of the CO. However, on this support, the reaction still proceeds via a CO–O_2 intermediate rather than via O_2 dissociation [402].

In situ STM using a tip shadowing technique has been used to follow the growth kinetics of Au on clean TiO_2(1 1 0) and an Ag pre-deposited TiO_2(1 1 0) surface on a cluster-by-cluster basis [403]. The growth of Au on step-sites can be isolated from that on terrace sites; the rates for the growth rate of clusters on step-sites are shown to be much faster. Growth on Ag pre-covered surfaces suggests that competitive nucleation and growth on empty step-sites and on pre-nucleated Ag clusters depend upon the availability of empty step-sites. However, the overall growth closely resembles that of Ag on TiO_2(1 1 0) suggesting that the pre-deposited Ag clusters are determining the growth mode. Spontaneous formation of Ag–Au clusters are evident from the STM images acquired as a function of Au coverage. These binary clusters are believed to be of the "alloy" type rather than the "core-shell" type.

5.3. Preparation of titania thin films

Ultrathin (<10.0 nm) titanium oxide films can be synthesized on an Mo(1 0 0) surface [404]. Epitaxial growth with varying film thickness studied by LEIS, XPS, AES, and LEED showed a $(2\sqrt{2}\times\sqrt{2})R45^\circ$ diffraction pattern, whereas STM images showed that the TiO_2 films were ordered along the [0 1 0] and [0 0 1] directions of the Mo(1 0 0) substrate. XPS data revealed that unannealed titanium oxide films exhibit only a Ti^{4+} valence state, whereas annealed titanium oxide films are partially reduced and exhibit Ti^{3+} and Ti^{2+} states. Ultrasmall Au clusters on TiO_2 show excellent activity and selectivity toward a number of oxidation reactions [405, 406]. Oxygen adsorption on

Au islands on TiO_2(1 1 0) with controlled thicknesses from one to several monolayers show higher O_2 desorption temperatures (741 K) compared with ultrathin Au clusters or thicker clusters on TiO_2(1 1 0). This implies that O bonds much more strongly to ultrathin islands of Au, a result rationalized using a Bronsted argument, given that Au clusters should dissociatively adsorb O_2 more readily than thick Au clusters. Studies of the titration reaction of oxygen adatoms with CO (to produce CO_2) show that this reaction is extremely rapid at room temperature, with the rate being slightly slower for the thinnest Au islands. Thus, the association reaction ($CO(g) + O(a) \rightarrow CO_2(g)$) becomes faster as the oxygen adsorption strength decreases, again as expected from Bronsted considerations. For islands of about two atomic layers thickness, the rate increases slowly with temperature, with an apparent activation energy of (11.4 ± 2.8) kJ/mol, and shows a first-order rate in CO pressure and oxygen coverage, similar to bulk Au(1 1 0).

Ordered titanium oxide films can also be epitaxially grown on an Mo(1 1 0) substrate [407, 408]. Using various synthetic methods, TiO_2(1 0 0) or Ti_2O_3(0 0 0 1) were synthesized, as evidenced by (1×1) rectangular and (1×1) hexagonal LEED patterns, respectively, with supporting data from AES and XPS. STM indicates layer-by-layer growth at 900 K with the presence of flat terraces with three different orientations. The spacings between the neighboring atomic rows for all terraces were similar (0.65 nm), suggesting epitaxial growth of TiO_2(1 1 0)-(1×1). TiO_2 films have also been grown on Ni(1 1 0) [409, 410] and W(1 0 0) [411].

Titanium oxide thin films can also be grown on Pt(1 1 1) by vapor-phase deposition of titanium metal followed by oxidation in 10^{-6} Torr O_2 [412, 413]. A threefold symmetric structure with a unit cell of 1.82×1.82 nm is observed at coverages ranging from 1.0 to 5.0 ML. XPS measurements of this phase show stoichiometric TiO_2. Heating in vacuum at 650–850 °C leads to a new structure with a unit cell of 1.82×1.39 nm which is shown by XPS to have the stoichiometry of Ti_4O_7. Angle-resolved XPS measurements indicate that reduced Ti^{3+} is concentrated at the oxide/Pt(1 1 1) interface. By varying the Ti dose and the annealing conditions, six different long-range ordered phases of TiO_x are obtained. XPS binding energy and XPD data indicate that all the phases, except one (the stoichiometric rect-TiO_2), are one monolayer thick and composed of a Ti–O bilayer with interfacial Ti. Atomically resolved STM images confirm that these TiO_x phases wet the Pt surface, in contrast to rect-TiO_2.

Surface structures formed by titanium oxide thin films at a Pt(1 0 0) surface have been studied by STM, LEED, AES, XPS, XRD, and LEIS to explore and elucidate stable high-temperature structures that form at titania–Pt interfaces and provide a basis for characterizing the chemistry of titania thin films on Pt(1 0 0) [414, 415]. Titanium oxide films were produced by two different methods, the first via oxidation of a Pt_3Ti surface alloy at 300 K using ozone (O_3) and annealing at 1000 K. Smooth thin films with a (3×5) structure were observed at 1 ML (monolayer) using this procedure. This (3×5) structure is one layer of a Ti_2O_3 film that is similar to the (1×2) strands formed on reduced TiO_2(1 1 0) surfaces. Structures prepared by this method show particularly "flat" terraces without islands. A second method of synthesis is by Ti evaporation and deposition on Pt(1 0 0) in 6.7×10^{-5} Pa O_2 and annealing the substrate above 750 K in vacuum. A (3×5) structure was also produced for these films below 1 ML. A $(4 \times 3\sqrt{5})$R60° structure was observed after deposition of 2 ML and annealing at 850–1000 K. A model for this structure composed of TiO_2

tetragonal nets with some O atoms in the second layer was proposed. The $(4 \times 3\sqrt{5})R60^\circ$ film changed to a (3×5) structure after annealing above 960 K in vacuum. TiO_2 clusters decomposed to form a $(2\sqrt{2} \times 2\sqrt{2})R45^\circ$ structure, proposed to be Ti_5O_8, and (3×5) domains after annealing at 1300 K. Assuming this model, the composition of all titanium oxide ultrathin films on a Pt(1 0 0) surface is $TiO_{2-1.5}$ after annealing at 850–1300 K. Chemical changes occurring during annealing of titanium oxide films include Ti dissolution (alloying) into the bulk of the Pt(1 0 0) crystal. O_3 or NO_2 (nitrogen dioxide) oxidation of the (3×5)-Ti_2O_3 film at 600 K and subsequent annealing to 700–950 K in vacuum produces ordered oxide regions and domains of a (4×13) structure that are attributed to a TiO_2 film with a square –Ti–O– net. This film is transformed further after annealing at 1000–1100 K to (3×5)-Ti_2O_3 to domains exhibiting a $(2\sqrt{2} \times 2\sqrt{2})R45^\circ$ structure. Further heating of this film to 1200 K leads to a (3×5)-Ti_2O_3 oxide film. Initial oxidation of a "flat" (3×5) oxide film at 600 K reconstructs this surface to form a multilayer, porous oxide film, and more extensive oxidation eventually forms a much less porous oxide film with pyramidal oxide crystallites. The titanium oxide films on Pt(1 0 0) described above block adsorption of CO at Pt sites at temperatures above 210 K; these surfaces also do not oxidize CO.

A well-ordered monolayer titanium oxide film, Mo(1 1 2)-(8×2)-TiO_x, can be synthesized on the Mo(1 1 2) surface [72, 416, 417]. A TiO_x/Mo(1 1 2) film was synthesized

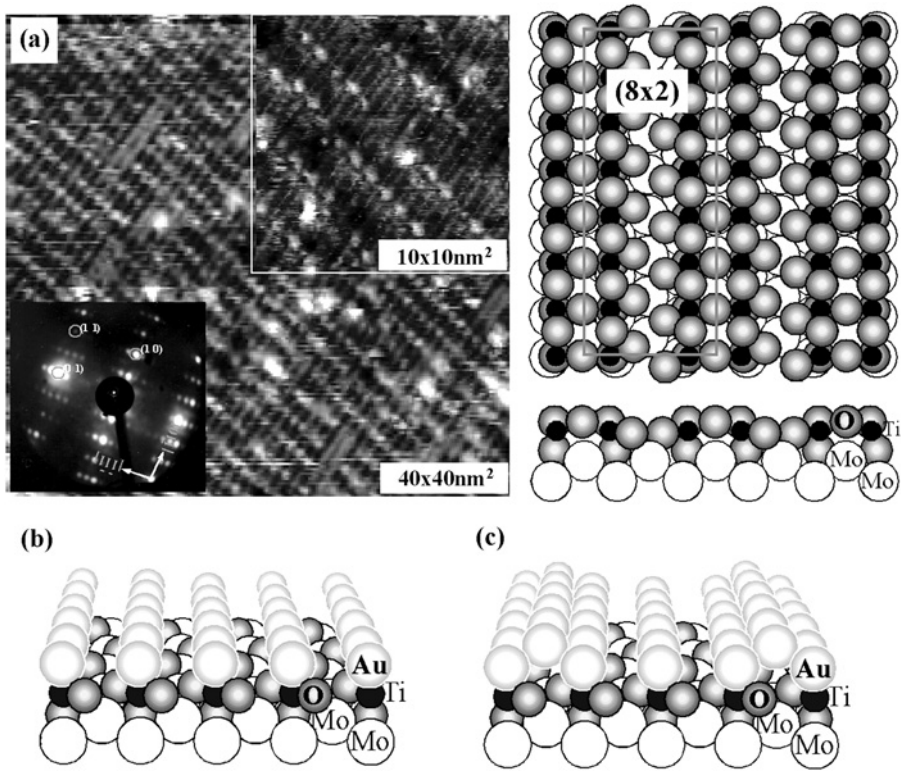

Figure 29: Structural model and atomic-resolved STM image of (a) Mo(1 1 2)-(8×2)-TiO_x, (b) Mo(1 1 2)-(1×1)-(Au,TiO_x), and (c) Mo(1 1 2)-(1×3)-(Au, TiO_x) [33, 72].

by depositing ~1 ML Ti onto an SiO_2(ML)/Mo(1 1 2) followed by oxidation/annealing. A final anneal at 1400 K completely removes the SiO_2 film and any residual Si. The TiO_x film so formed exhibits a very sharp (8 × 2) LEED pattern (Fig. 29) and a very smooth and well-ordered surface that exhibits relatively large terraces as seen by STM images (Fig. 29). The thickness of this TiO_x film is estimated to be one monolayer based on the attenuation of the AES intensity of the Mo MNN (187 eV) feature. The (8 × 2)-TiO_x film can also be synthesized by the step-wise deposition of Ti onto an oxygen-covered Mo(1 1 2) surface followed by oxidation-annealing cycles. However, the quality and reproducibility of the film derived from the direct deposition method are not comparable to that grown on an SiO_2 film. A single phonon feature at 84 meV, related to the Ti–O stretching mode, was observed for the (8 × 2) structure. This feature was assigned to Ti^{3+}–O–Mo and/or Ti^{3+}–O–Ti^{3+} based on HREELS and XPS data [72, 416, 417]. A row spacing of 0.9 nm, corresponding to two rows of the Mo(1 1 2) trough along the [−1 1 0] direction, is seen by STM (Fig. 29), consistent with the observed (8 × 2) LEED pattern. A high-resolution STM image shows a double-row feature with a spacing of 0.9 nm. A possible structural model for the Mo(1 1 2)-(8 × 2)-TiO_x

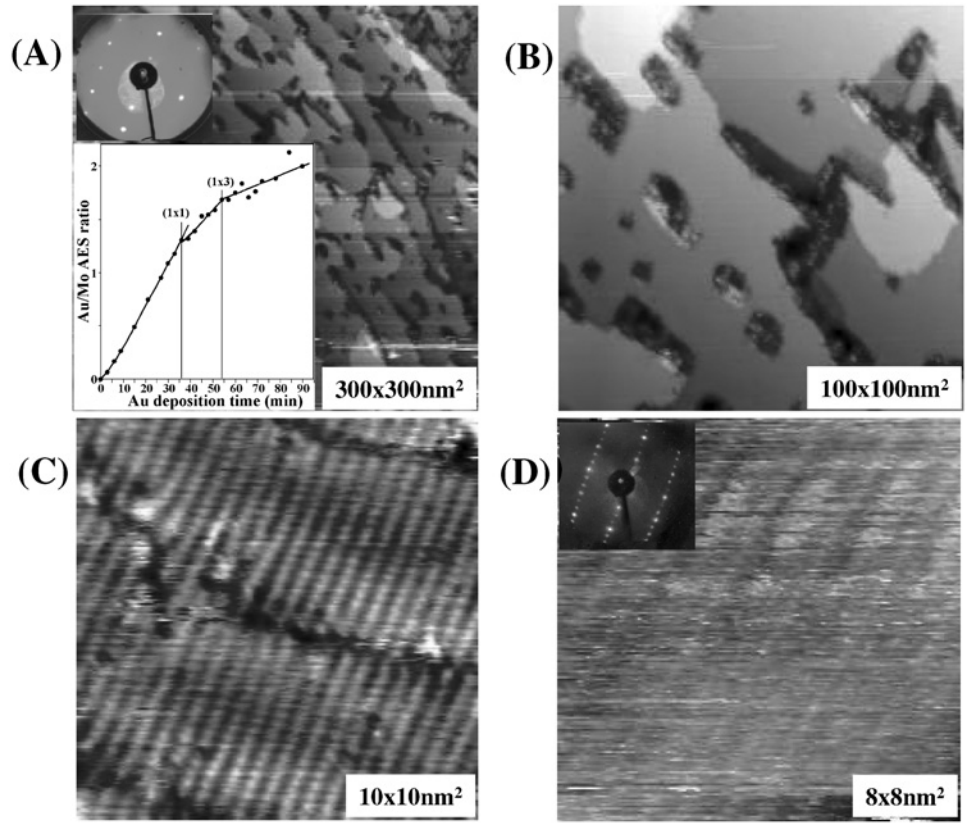

Figure 30: STM images of (A–C) the (1 × 1)-Au/TiO_x/Mo(1 1 2) with Au coverage of ~1 ML, $U_S = +1.0$ V, $I = 0.5$ nA; and (D) the (1 × 3)-Au/TiO_x/Mo(1 1 2), $U_S = +1.0$ V, $I = 0.5$ nA [417].

surface is shown in Fig. 29 in which seven Ti atoms decorate every eight Mo atoms along the Mo(1 1 2) trough (the [−1 −1 1] direction). The Ti atoms are bound to the surface via Ti–O–Mo bonds and to each other via Ti–O–Ti linkages [72, 73, 416, 417].

5.4. Au on TiO_x/Mo(1 1 2)

On the rutile TiO_2(1 1 0) surface, the two Ti atoms nearest to an oxygen vacancy are reduced to Ti^{3+}, whereas for the (8 × 2)-TiO_x surface, there is a full monolayer of reduced Ti^{3+} sites [72, 416, 417]. Accordingly, strong binding between deposited Au and the TiO_x surface is anticipated. Indeed, upon deposition of Au onto this (8 × 2)-TiO_x surface followed by an anneal at 900 K, well-ordered Au monolayer and bilayer structures form with Au completely wetting the surface [72, 73, 416, 417]. The two ordered structures, designated as (1 × 1) Au-TiO_x mono- and (1 × 3) Au-TiO_x bi-layer, respectively, are shown schematically in Fig. 29b and c [72, 73, 416, 417]. Wetting was confirmed by AES, LEED, LEIS, and STM, as shown in the atomically resolved STM images of Fig. 30. A flat surface with large terraces is apparent with the presence of atomically resolved (1 × 1) and (1 × 3) structures. The electronic properties of the ordered Au films were probed by CO adsorption using RAIRS. As shown in Fig. 31, the ν(CO) frequency for CO adsorption on the (1 × 1)-Au/TiO_x/Mo(1 1 2) is lower than that on bulk Au but higher than that on a (1 × 1)-Au/Mo(1 1 2). This is an evidence that the Au film is negatively charged with ~0.08 electrons per Au [73]. TPD indicates that the Au–TiO_x interaction is much stronger compared with the Au–Au interaction,

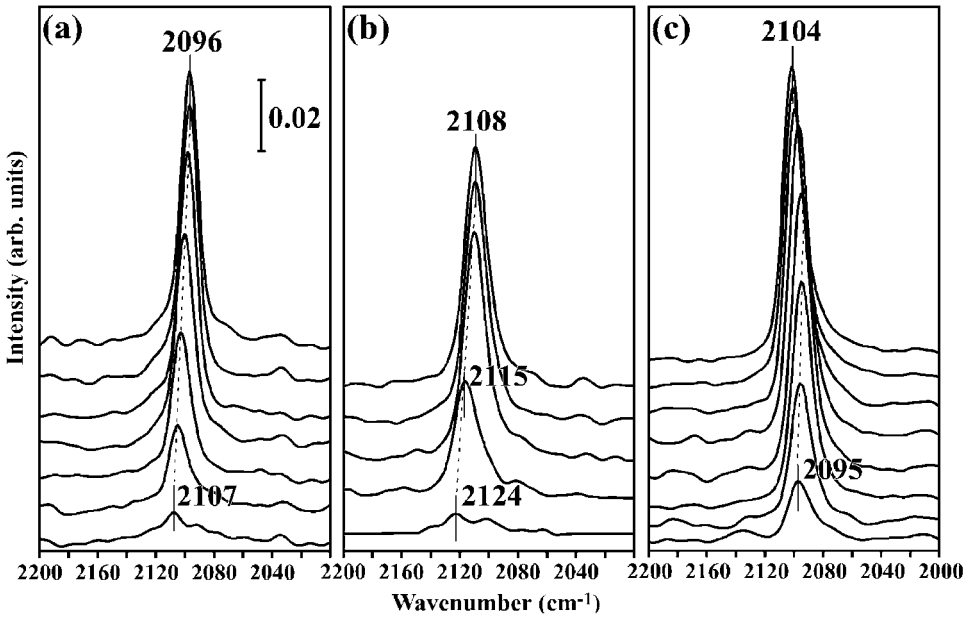

Figure 31: CO RAIRS spectra on (a) (1 × 1)-Au/TiO_x/Mo(1 1 2), (b) Au(8 ML)/Mo(1 1 2) and (c) (1 × 1)-Au/Mo(1 1 2) as a function of CO exposure at 90 K [73].

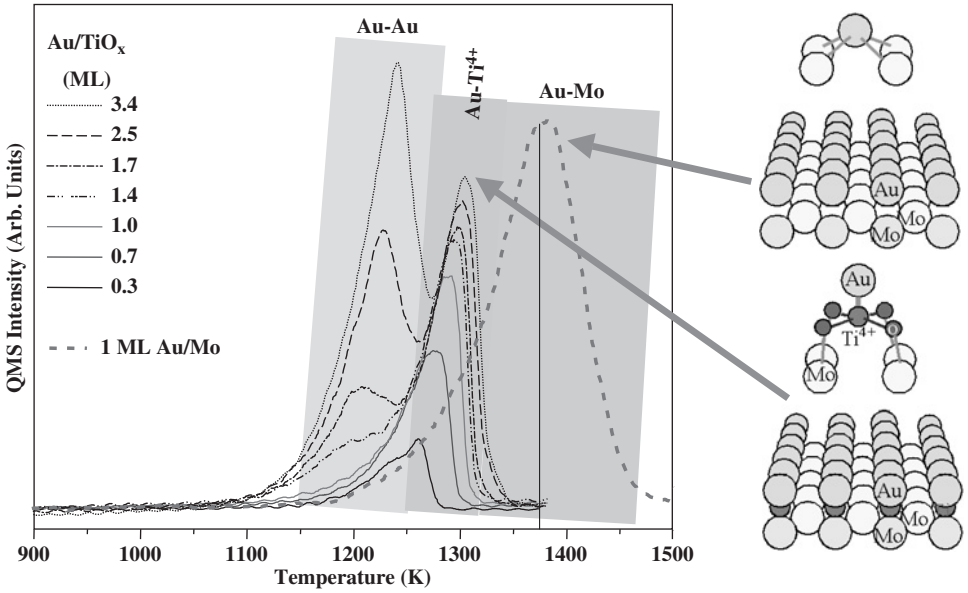

Figure 32: TPD spectra of Au on Mo(1 1 2) with coverage of ~1 ML and on TiO_x/Mo(1 1 2) with various Au coverages [417].

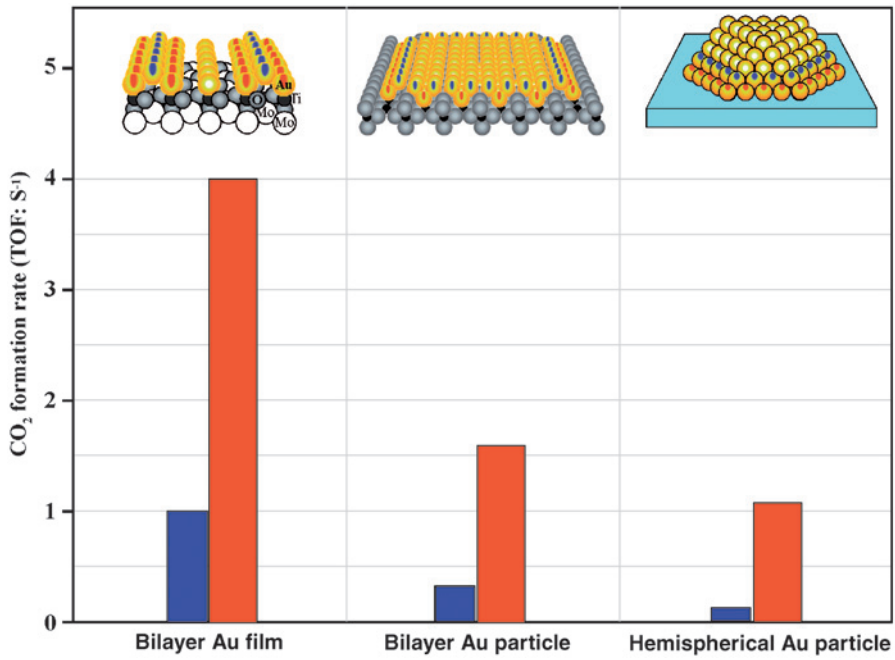

Figure 33: Comparison of catalytic activities for CO oxidation on the Mo(1 1 2)-(1 × 3)-(Au,TiO_x), Au/TiO_2(1 1 0) and Au supported on high-surface-area TiO_2 with a mean particle size of ~3 nm. The insets show structural models using marks to indicate the active sites [33].

as shown in Fig. 32. Kinetic measurements for the catalytic oxidation of carbon monoxide show that the (1×3)-Au–TiO_x bilayer is significantly more active (by more than an order of magnitude) than the monolayer (see Fig. 26), and is about 45 times more active than that reported for the most active high-surface-area Au/TiO_2 catalyst [33, 72].

This is the first report of Au completely wetting an oxide surface and demonstrates that ultrathin Au films on an oxide surface have exceptionally high catalytic activity, comparable to the activity observed for Au clusters [33, 73]. This discovery is a key to understanding the nature of the active site of supported Au catalysts, in which a bilayer Au structure has been shown to be a critical feature for catalytically active Au clusters. As shown by the histogram in Fig. 33, the rates for ordered bilayers, model nanoparticles with two atomic layers in thickness, and the very best high-surface-area-supported catalysts are compared. The blue bars of the histogram are the computed rates based on total Au. The rates obtained for the ordered bilayers are approximately one order of magnitude higher than the rates for the high-surface-area-supported catalysts. Assuming that a combination of the first and second layer Au atoms is the active site (see the insets of Fig. 33), the rates, computed on a per active site basis from the corresponding particle structure, become comparable as shown by the red bars of the Fig. 33 histogram. Low-coordinated Au sites, support-to-cluster charge effects, and quantum size effects are key contributing factors to the unique catalytic activity for supported Au catalysts [33, 73, 74, 371].

6. CONCLUSIONS

An abundance of recent studies has demonstrated that the synthesis of model oxide surfaces enables their exploration with a wide assortment of charged particle surface techniques. These model oxide surfaces offer unprecedented opportunities to address the details of the structure, electronic properties, and chemistry of oxide-supported metal clusters at the atomic/molecular level. With such model catalysts, a convenient method is now available to study important aspects of supported metal catalysts such as cluster size effects, cluster morphology, and support–cluster interactions.

With the recent advent of operando techniques such as polarization modulation RAIRS, sum frequency vibrational spectroscopy, and synchrotron-based X-ray spectral/diffraction probes, model catalysts so prepared allow bridging of the pressure and material gaps of catalysis. Accordingly, new avenues are now accessible to directly connect studies of single crystals and ordered thin films under UHV environments with analogous investigations of catalytic processes of complex technical catalysts at realistic conditions. These advances will unquestionably lead to new insights into the optimization of existing catalysts and to the design of novel, new catalysts.

ACKNOWLEDGMENTS

We acknowledge with pleasure the financial support of this work by the Department of Energy, Office of Basic Energy, Division of Chemical Sciences, the Robert A. Welch Foundation, and the National Science Foundation under Grant No. INT-0136194.

REFERENCES

[1] Ertl G., Knözinger H., Weikamp J.T. (eds), Handbook of Heterogeneous Catalysis, Wiley-VCH, Weinheim, 1997.
[2] Freund H.-J., Kuhlenbeck H., Neumann M., in: Adsorption on Ordered Surfaces of Ionic Solids and Thin Films, E. Umbach, H.-J. Freund (eds), Vol. 33, Springer-Verlag, Berlin, 1993, p. 136.
[3] Henrich V.E., Cox P.A., The Surface Science of Metal Oxides, Cambridge University Press, Cambridge, 1994.
[4] Goodman D.W., Chem. Rev. 95 (1995) 523.
[5] Freund H.-J., Kuhlenbeck H., Staemmler V., Rep. Prog. Phys. 59 (1996) 283.
[6] Campbell C.T., J. Chem. Soc. Faraday Trans. 92 (1996) 1435.
[7] Goodman D.W., J. Phys. Chem. 100 (1996) 13090.
[8] Campbell C.T., Surf. Sci. Rep. 27 (1997) 1.
[9] Gunter P.L.J., Niemantsverdriet J.W., Ribeiro F.H., Somorjai G.A., Catal. Rev. Sci. Eng. 39 (1997) 77.
[10] Henry C.R., Surf. Sci. Rep. 31 (1998) 235.
[11] Rainer D.R., Goodman D.W., J. Mol. Catal. A 131 (1998) 259.
[12] Chambers S.A., Surf. Sci. Rep. 39 (2000) 105.
[13] Franchy R., Surf. Sci. Rep. 38 (2000) 195.
[14] Campbell C.T., Grant A.W., Starr D.E., Parker S.C., Bondzie V.A., Top. Catal. 14 (2001) 43.
[15] Goodman D.W., Surf. Rev. Lett. 2 (1995) 9.
[16] Goodman D.W., J. Vac. Sci. Technol. A 14 (1996) 1526.
[17] Freund H.-J., Angew. Chem. Int. Ed. Engl. 36 (1997) 452.
[18] Bäumer M., Libuda J., Freund H.-J., in: Chemisorption and Reactivity on Supported Clusters and Thin Films, R.M. Lambert, G. Pacchioni (eds), Vol. 331, Kluwer, Dordrecht, 1997, p. 61.
[19] Kuhlenbeck H., Freund H.-J., in: Growth and Properties of Ultrathin Epitaxial Layers, The Chemical Physics of Solid Surfaces, D.A. King, D.P. Woodruff (eds), Vol. 8, Elsevier, New York, 1997, p. 340.
[20] Street S.C., Xu C., Goodman D.W., Annu. Rev. Phys. Chem. 48 (1997) 43.
[21] Ertl G., Freund H.-J., Phys. Today 52 (1999) 32.
[22] Bäumer M., Freund H.-J., Prog. Surf. Sci. 61 (1999) 127.
[23] Freund H.-J., Bäumer M., Kuhlenbeck H., Adv. Catal. 45 (2000) 333.
[24] Freund H.-J., Surf. Sci. 500 (2002) 271.
[25] Freund H.-J., Libuda J., Bäumer M., Risse T., Carlsson A.F., Chem. Rec. 3 (2003) 181.
[26] Santra A.K., Goodman D.W., J. Phys. C 15 (2003) R31.
[27] Meyer R., Lemire C., Shaikhutdinov Sh.K., Freund H.J., Au Bull. 37 (2004) 72.
[28] Ozensoy E., Goodman D.W., Phys. Chem. Chem. Phys. 6 (2004) 3765.
[29] Freund H.-J., Catal. Today 100 (2005) 3.
[30] Libuda J., Freund H.-J., Surf. Sci. Rep. 57 (2005) 157.
[31] Wallace W.T., Min B.K., Goodman D.W., Top. Catal. 34 (2005) 17.
[32] Chen M.S., Goodman D.W., Catal. Today 111 (2006) 22.
[33] Chen M.S., Goodman D.W., Acc. Chem. Res. Published on line: 29-Jun-2006; (Article) DOI: 10.1021/ar040309d.
[34] Eng P.J., Trainor T.P., Brown G.E., Waychunas G.A., Newville M., Sutton S.R., Rivers M.L., Science 288 (2000) 1029.
[35] Jaeger R.M., Kuhlenbeck H., Freund H.-J., Wuttig M., Hoffmann W., Franchy R., Ibach H., Surf. Sci. 259 (1991) 235.

[36] Libuda J., Winkelmann F., Bäumer M., Freund H.-J., Bertrams T., Neddermeyer H., Müller K., Surf. Sci. 318 (1994) 61.
[37] Becker C., Kandler J., Raaf H., Linke R., Pelster T., Dräger M., Tanemura M., Wandelt K., J. Vac. Sci. Technol. A 16 (1998) 1000.
[38] Rosenhahn A., Schneider J., Becker C., Wandelt K., J. Vac. Sci. Technol. A 18 (2000) 1923.
[39] Rosenhahn A., Schneider J., Kandler J., Becker C., Wandelt K., Surf. Sci. 433–435 (1999) 705.
[40] Niehus H., Nucl. Instrum. Methods Phys. Res. Sect. B 33 (1988) 876.
[41] Blum R.-P., Ahlbehrendt D., Niehus H., Surf. Sci. 396 (1998) 176.
[42] Ceballos G., Song Z., Pascual J.I., Rust H.P., Conrad H., Bäumer M., Freund H.J., Chem. Phys. Lett. 359 (2002) 41.
[43] Kulawik M., Nilius N., Rust H.-P., Freund H.-J., Phys. Rev. Lett. 91 (2003) 256101.
[44] Lay T.T., Yoshitake M., Mebarki B., J. Vac. Sci. Technol. A 20 (2002) 2027.
[45] Pang C.L., Raza H., Haycock S.A., Thornton G., Phys. Rev. B 65 (2002) 201401.
[46] Stierle A., Renner F., Streitel R., Dosch H., Drube W., Cowie B.C., Science 303 (2004) 1652.
[47] Mulligan A., Dhanak V., Kadodwala M., Langmuir 21 (2005) 8312.
[48] Kresse G., Schmid M., Napetschnig E., Shishkin M., Köhler L., Varga P., Science 308 (2005) 1440.
[49] Frank M., Wolter K., Magg N., Heemeier M., Kuhnemuth R., Baumer M., Freund H.J., Surf. Sci. 492 (2001) 270.
[50] Kurnosikov O., Flipse C.F.J., Swagten H.J.M., Koopmans B., De Jonge W.J.M., Jpn. J. Appl. Phys. Part I 45 (2006) 2215.
[51] Degen S., Krupski A., Kraj M., Langner A., Becker C., Sokolowski M., Wandelt K., Surf. Sci. 576 (2005) L57.
[52] Addepalli S.G., Ekstrom B., Magtoto N.P., Lin J.S., Kelber J.A., Surf. Sci. 442 (1999) 385.
[53] Magtoto N.P., Niu C., Anzaldua M., Kelber J.A., Jennison D.R., Surf. Sci. 472 (2001) L157.
[54] Niu C., Shepherd K., Martini D., Tong J., Kelber J.A., Jennison D.R., Bogicevic A., Surf. Sci. 465 (2000) 163.
[55] Garza M., Magtoto N.P., Kelber J.A., Surf. Sci. 519 (2002) 259.
[56] Becker C., Rosenhahn A., Wiltner A., von Bergmann K., Schneider J., Pervan P., Milun M., Wandelt K., New J. Phys. 4 (2002) 75.
[57] Chen P.J., Goodman D.W., Surf. Sci. 312 (1994) L767.
[58] Wu M.C., Goodman D.W., J. Phys. Chem. 98 (1994) 9874.
[59] Kaltchev M., Tysoe W.T., Surf. Sci. 430 (1999) 29.
[60] Nagata K., Yamada C., Takahashi T., Murata Y., J. Phys. Condens Matter 15 (2003) 8165.
[61] Jaeger R.M., Homann K., Kuhlenbeck H., Freund H.-J., Chem. Phys. Lett. 203 (1993) 41.
[62] Schauermann S., Johanek V., Laurin M., Libuda J., Freund H.J., Chem. Phys. Lett. 381 (2003) 298.
[63] Schauermann S., Johanek V., Laurin M., Libuda J., Freund H.J., Phys. Chem. Chem. Phys. 5 (2003) 5139.
[64] Winkelmann F., Wohlrab S., Libuda J., Bäumer M., Cappus D., Menges M., Al-Shamery K., Kuhlenbeck H., Freund H.J., Surf. Sci. 307–309 (1994) 1148.
[65] Bäumer M., Libuda J., Sandell A., Freund H.-J., Graw G., Bertrams T., Neddermeyer H., Ber. Bunsenges. Phys. Chem. 99 (1995) 1381.
[66] Klimenkov M., Nepijko S., Kuhlenbeck H., Freund H.-J., Surf. Sci. 385 (1997) 66.

[67] Klimenkov M., Nepijko S., Kuhlenbeck H., Bäumer M., Schlögl R., Freund H.-J., Surf. Sci. 391 (1997) 27.
[68] Nepijko S.A., Klimenkov M., Kuhlenbeck H., Freund H.-J., J. Vac. Sci. Technol. A 17 (1999) 577.
[69] Freund H.J., Dillmann B., Ehrlich D., Hassel M., Jaeger R.M., Kuhlenbeck H., Ventrice C.A., Jr., Winkelmann F., Wohlrab S., Xu C., Bertrams T., Brodde A., Neddermeyer H., J. Mol. Catal. 82 (1993) 143.
[70] Hensley D.A., Kesmodel L.L., J. Phys. Chem. 95 (1991) 1368.
[71] Cooper V.R., Kolpak A.M., Yourdshahyan Y., Rappe A.M., Phys. Rev. B 72 (2005) 081409.
[72] Chen M.S., Goodman D.W., Science 306 (2004) 252.
[73] Chen M.S., Cai Y., Yan Z., Goodman D.W., J. Am. Chem. Soc. 128 (2006) 6341.
[74] Libuda J., Frank M., Sandell A., Andersson S., Brühwiler P.A., Baeumer M., Martensson N., Freund H.J., in: Elementary Processes in Excitations and Reactions on Solid Surfaces, A. Okiji, H. Kasai, K. Makoshi (eds), Vol. 121, Springer, Berlin, 1996, p. 210.
[75] Stempel S., Bäumer M., Freund H.J., Surf. Sci. 402–404 (1998) 424.
[76] Yates J.T., Williams E.D., Weinberg W.H., Surf. Sci. 91 (1980) 562.
[77] Matolin V., Elyakhloufi M.H., Maek K.S., Gillet E., Catal. Lett. 21 (1993) 175.
[78] Matolin V., Maek K.S., Elyakhloufi M.H., Gillet E., J. Catal. 143 (1993) 492.
[79] Nehasil V., Stara I., Matolin V., Surf. Sci. 331–333 (1995) 105.
[80] Frank M., Andersson S., Libuda J., Stempel S., Sandell A., Brena B., Giertz A., Bruhwiler P.A., Bäumer M., Martensson N., Freund H.J., Chem. Phys. Lett. 279 (1997) 92.
[81] Frank M., Andersson S., Libuda J., Stempel S., Sandell A., Brena B., Giertz A., Brühwiler P.A., Baeumer M., Martensson N., Freund H.J., Chem. Phys. Lett. 310 (1999) 229.
[82] Marbrow R.A., Lambert R.M., Surf. Sci. 67 (1977) 489.
[83] Rebholz M., Prins R., Kruse N., Surf. Sci. 259 (1991) L797.
[84] Freund H.J., Ernst N., Baeumer M., Rupprechter G., Libuda J., Kuhlenbeck H., Risse T., Drachsel W., Al-Shamery, K., Hamann H., in: Surface Chemistry and Catalysis, A.F. Carley, P.R. Davies, G.J. Hutchings, M.S. Spencer (eds), Kluwer, New York, 2002, p. 103.
[85] Hansen K.H., Worren T., Stempel S., Lægsgaard E., Baeumer M., Freund H.J., Besenbacher F., Stensgaard I., Phys. Rev. Lett. 83 (1999) 4120.
[86] Dellwig T., Rupprechter G., Unterhalt H., Freund H.-J., Phys. Rev. Lett. 85 (2000) 776.
[87] Nilius N., Wallis T.M., Ho W., Phys. Rev. Lett. 90 (2003) 046808.
[88] Heemeier M., Carlsson A.F., Naschitzki M., Schmal M., Baeumer M., Freund H.J., Angew. Chem. Int. Ed. 41 (2002) 4073.
[89] Carlsson A.F., Naschitzki M., Bäumer M., Freund H.J., J. Phys. Chem. B. 107 (2003) 778.
[90] Risse T., Carlsson A., Baeumer M., Klüner T., Freund H.J., Surf. Sci. 546 (2003) L829.
[91] Carlsson A.F., Bäumer M., Risse T., Freund H.J., J. Chem. Phys. 119 (2003) 10885.
[92] Khan N.A., Uhl A., Shaikhutdinov S., Freund H.J., Surf. Sci. 600 (2006) 1849.
[93] Khan N.A., Shaikhutdinov S., Freund H., Catal. Lett. 108 (2006) 159.
[94] Rupprechter G., Freund H.J., Top. Catal. 14 (2000) 3.
[95] Rupprechter G., Dellwig T., Unterhalt H., Freund H.-J., J. Phys. Chem. B 105 (2001) 3797.
[96] Dellwig T., Hartmann J., Libuda J., Meusel I., Rupprechter G., Unterhalt H., Freund H.-J., J. Mol. Catal. A 162 (2000) 51.
[97] Rupprechter G., Dellwig T., Unterhalt H., Freund H.-J., Top. Catal. 15 (2001) 19.
[98] Unterhalt H., Rupprechter G., Freund H.J., J. Phys. Chem. B 106 (2002) 356.
[99] Freund H.-J., Bäumer M., Libuda J., Risse T., Rupprechter G., Shaikhutdinov S., J. Catal. 216 (2003) 223.

[100] Yudanov I.V., Sahnoun R., Neyman K.M., Rosch N., Hoffmann J., Schauermann S., Johanek V., Unterhalt H., Rupprechter G., Libuda J., Freund H.J., J. Phys. Chem. B 107 (2003) 255.
[101] Morkel M., Rupprechter G., Freund H.-J., Surf. Sci. 588 (2005) L209.
[102] Silvestre-Albero J., Rupprechter G., Freund H.J., Chem. Commun. 1 (2006) 80.
[103] Borasio M., Rodrigez de la Fuente O., Rupprechter G., Freund H.J., J. Phys. Chem. B 109 (2005) 17791.
[104] Rodriguez de la Fuente O., Borasio M., Galletto P., Rupprechter G., Freund H.J., Surf. Sci. 566–568 (2004) 740.
[105] Schauermann S., Hoffmann J., Johanek V., Hartmann J., Libuda J., Freund H.-J., Angew. Chem. Int. Ed. 41 (2002) 2532.
[106] Kaichev V.V., Prosvirin I.P., Bukhtiyarov V.I., Unterhalt H., Rupprechter G., Freund H.J., J. Phys. Chem. B 107 (2003) 3522.
[107] Doering D.L., Poppa H., Dickinson J.T., J. Catal. 73 (1982) 104.
[108] Rainer D.R., Xu C., Holmblad P.M., Goodman D.W., J. Vac. Sci. Technol. A 15 (1997) 1653.
[109] Johanek V., Schauermann S., Laurin M., Libuda J., Freund H.-J., Angew. Chem. Int. Ed. 42 (2003) 3035.
[110] Schauermann S., Hoffmann J., Johanek V., Hartmann J., Libuda J., Phys. Chem. Chem. Phys. 4 (2002) 3909.
[111] Wille A., Buchwald R., Al-Shamery K., Appl. Phys. A 78 (2004) 205.
[112] Shaikhutdinov S., Heemeier M., Hoffmann J., Meusel I., Richter B., Baumer M., Kuhlenbeck H., Libuda J., Freund H.J., Oldman R., Jackson S.D., Konvicka C., Schmid M., Varga P., Surf. Sci. 501 (2002) 270.
[113] Fan C.Y., Wu T.P., Kaden W.E., Anderson S.L., Surf. Sci. 600 (2006) 461.
[114] Lee S., Fan C.Y., Wu T.P., Anderson S.L., J. Phys. Chem. B 109 (2005) 381.
[115] Putna E.S., Vohs J.M., Gorte R.J., Surf. Sci. 391 (1997) L1178.
[116] Doyle A.M., Shaikhutdinov S., Freund H.-J., J. Catal. 223 (2004) 444.
[117] Shaikhutdinov S., Frank M., Bäumer M., Jackson S.D., Oldman R.J., Hemminger J.C., Freund H.-J., Catal. Lett. 80 (2002) 125.
[118] Doyle A.M., Shaikhutdinov S., Jackson S.D., Freund H.-J., Angew. Chem. Int. Ed. 42 (2003) 5240.
[119] Doyle A.M., Shaikhutdinov S., Freund H.J., Angew. Chem. Int. Ed. 44 (2005) 629.
[120] Silvestre-Albero J., Rupprechter G., Freund H.J., J. Catal. 235 (2005) 52.
[121] Libuda J., Frank M., Sandell A., Andersson S., Brühwiler P.A., Bäumer M., Mårtensson N., Freund H.-J., Surf. Sci. 384 (1997) 106.
[122] Heemeier M., Frank M., Libuda J., Wolter K., Kuhlenbeck H., Bäumer M., Freund H.-J., Catal. Lett. 68 (2000) 19.
[123] Heemeier M., Stempel S., Shaikhutdinov S.K., Libuda J., Bäumer M., Oldman R.J., Jackson S.D., Freund H.-J., Surf. Sci. 523 (2003) 103.
[124] Pacchioni G., Giordano L., Baistrocchi M., Phys. Rev. Lett. 94 (2005) 226104.
[125] Mott N.F., Trans. Faraday Soc. 43 (1947) 429.
[126] Kulawik M., Nilius N., Freund H.J., Phys. Rev. Lett. 96 (2006) 036103.
[127] Rupprechter G., Seeber G., Goller H., Hayek K., J. Catal. 186 (1999) 201.
[128] Nilius N., Ernst N., Freund H.-J., Phys. Rev. Lett. 84 (2000) 3994.
[129] Benten W., Nilius N., Ernst N., Freund H.J., Phys. Rev. B 72 (2005) 045403.
[130] Nilius N., Ernst N., Freund H.J., Surf. Sci. 478 (2001) L327.
[131] Winkler C., Carew A., Raval R., Ledieu J., McGrath R., Surf. Rev. Lett. 8 (2001) 693.
[132] Nilius N., Ernst N., Freund H.J., Phys. Rev. B 65 (2002) 115421.
[133] Shaikhutdinov S.K., Meyer R., Naschitzki M., Baeumer M., Freund H.J., Catal. Lett. 86 (2003) 211.

[134] Poppa H., Catal. Rev. Sci. Eng. 35 (1993) 359.
[135] Poppa H., Vacuum 34 (1984) 1081.
[136] Poppa H., Ultramicroscopy 11 (1983) 105.
[137] Magkoev T.T., Christmann K., Moutinho A.M.C., Murata Y., Surf. Sci. 515 (2002) 538.
[138] Vancampen D.G., Hrbek J., J. Phys. Chem. 99 (1995) 16389.
[139] Lee S., Fan C.Y., Wu T.P., Anderson S.L., J. Phys. Chem. B 109 (2005) 11340.
[140] He J.W., Møller P.J., Chem. Phys. Lett. 129 (1986) 13.
[141] Duriez C., Chapon C., Henry C.R., Rickard J.M., Surf. Sci. 230 (1990) 123.
[142] Wu M.C., Corneille J.S., Estrada C.A., He J.-W., Goodman D.W., Chem. Phys. Lett. 182 (1991) 472.
[143] He J.-W., Estrada C.A., Corneille J.S., Wu M.-C., Goodman D.W., Surf. Sci. 261 (1992) 164.
[144] Wu M.C., Estrada C.A., Goodman D.W., Phys. Rev. Lett. 67 (1991) 2910.
[145] Wu M.C., Estrada C.A., Corneille J.S., Goodman D.W., J. Chem. Phys. 96 (1992) 3892.
[146] He J.-W., Corneille J.S., Estrada C.A., Wu M.C., Goodman D.W., J. Vac. Sci. Technol. A 10 (1992) 2248.
[147] Wu M.C., Goodman D.W., Catal. Lett. 15 (1992) 1.
[148] Wu M.C., Truong C.M., Coulter K., Goodman D.W., J. Am. Chem. Soc. 114 (1992) 7565.
[149] Wu M.C., Truong C.M., Goodman D.W., Phys. Rev. B 46 (1992) 12688.
[150] Wu M.C., Truong C.M., Coulter K., Goodman D.W., J. Vac. Sci. Technol. A 11 (1993) 2174.
[151] Corneille J.S., He J.-W., Goodman D.W., Surf. Sci. 306 (1994) 269.
[152] Xu X., Oh W.S., Goodman D.W., Langmuir 12 (1996) 4877.
[153] Gunster J., Liu G., Kempter V., Goodman D.W., Surf. Sci. 415 (1998) 303.
[154] Kolmakov A., Stultz J., Goodman D.W., J. Chem. Phys. 113 (2000) 7564.
[155] Kim Y.D., Stultz J., Wei T., Goodman D.W., J. Phys. Chem. B 106 (2002) 6827.
[156] Kim Y.D., Stultz J., Goodman D.W., Langmuir 18 (2002) 3999.
[157] Kim Y.D., Stultz J., Goodman D.W., Surf. Sci. 506 (2002) 228.
[158] Yang Z.X., Wu R.Q., Zhang Q.M., Goodman D.W., Phys. Rev. B 65 (2002) 155407.
[159] Kim Y.D., Stultz J., Wei T., Goodman D.W., J. Phys. Chem. B 107 (2003) 592.
[160] Wendt S., Kim Y.D., Goodman D.W., Prog. Surf. Sci. 74 (2003) 141.
[161] Krischok S., Stracke P., Kempter V., Appl. Phys. A 82 (2006) 167.
[162] Gallagher M.C., Fyfield M.S., Cowin J.P., Joyce S.A., Surf. Sci. 339 (1995) L909.
[163] Gallagher M.C., Fyfield M.S., Joyce S.A., Phys. Rev. B 59 (1999) 2346.
[164] Gallagher M.C., Fyfield M.S., Bumm L.A., Cowin J.P., Joyce S.A., Thin Solid Films 445 (2003) 90.
[165] Tegenkamp C., Pfnuer H., Ernst W., Malaske U., Wollschlaeger J., Peterka D., Schröder K.M., Zielasek V., Henzler M., J. Phys. Condens. Matter 11 (1999) 9943.
[166] Kramer J., Ernst W., Tegenkamp C., Pfnuer H., Surf. Sci. 517 (2002) 87.
[167] Sterrer M., Fischbach E., Risse T., Freund H.-J., Phys. Rev. Lett. 94 (2005) 186101.
[168] Sterrer M., Fischbach E., Heyde M., Nilius N., Rust H.-P., Risse T., Freund H.J., J. Phys. Chem. B 110 (2006) 8665.
[169] Giovanardi C., di Bona A., Moia T.S., Valeri S., Pisani C., Sgroi M., Busso M., Surf. Sci. 505 (2002) L209.
[170] Valeri S., Altieri S., del Pennino U., di Bona A., Luches P., Rota A., Phys. Rev. B 65 (2002) 245410.
[171] Schintke S., Messerli S., Pivetta M., Patthey F., Libioulle L., Stengel M., De Vita A., Schneider W.-D., Phys. Rev. Lett. 87 (2001) 276801.
[172] Audibert P., Sidoumou M., Suzanne J., Surf. Sci. 273 (1992) L467.

[173] Gerlach R., Glebov A., Lange G., Toennies J.P., Weiss H., Surf. Sci. 331–333 (1995) 1490.
[174] Heidberg J., Kandel M., Meine D., Wildt U., Surf. Sci. 331–333 (1995) 1467.
[175] Wichtendahl R., Rodrigez-Rodrigo M., Härtel U., Kuhlenbeck H., Freund H.J., Phys. Stat. Sol. A 173 (1999) 93.
[176] Pacchioni G., Chemphyschem 4 (2003) 1041.
[177] Giamello E., Paganini M.C., Murphy D.M., Ferrari A.M., Pacchioni G., J. Phys. Chem. B 101 (1997) 971.
[178] Chiesa M., Paganini M.C., Spoto G., Del Vitto A., Di Valentin C., Pacchioni G., Giamello E., J. Phys. Chem. B 109 (2005) 7314.
[179] Berger T., Sterrer M., Diwald O., Knoezinger E., J. Phys. Chem. B 108 (2004) 7280.
[180] Ferrari A.M., Casassa S., Pisani C., Altieri S., Rota A., Valeri S., Surf. Sci. 588 (2005) 160.
[181] Valeri S., Altieri S., di Bona A., Luches P., Giovanardi C., Moia T.S., Surf. Sci. 507 (2002) 311.
[182] Kiguchi M., Goto T., Saiki K., Sasaki T., Iwasawa Y., Koma A., Surf. Sci. 512 (2002) 97.
[183] Wichtendahl R., Rodriguez-Rodrigo M., Härtel U., Kuhlenbeck H., Freund H.-J., Surf. Sci. 423 (1999) 90.
[184] Spoto G., Gribov E.N., Ricchiardi G., Damin A., Scarano D., Bordiga S., Lamberti C., Zecchina A., Prog. Surf. Sci. 76 (2004) 71.
[185] Dohnalek Z., Kimmel G.A., Joyce S.A., Ayotte P., Smith R.S., Kay B.D., J. Phys. Chem. B 105 (2001) 3747.
[186] Pacchioni G., Surf. Rev. Lett. 7 (2000) 277.
[187] Pacchioni G., Cogliandro G., Bagus P.S., Surf. Sci. 255 (1991) 344.
[188] Pacchioni G., Minerva T., Bagus P.S., Surf. Sci. 275 (1992) 450.
[189] Spoto G., Gribov E., Damin A., Ricchiardi G., Zecchina A., Surf. Sci. 540 (2003) L605.
[190] Sterrer M., Risse T., Freund H.-J., Surf. Sci. 596 (2005) 222.
[191] Lopez N., Valeri S., Phys. Rev. B 70 (2004) 125428.
[192] Luches P., D'Addato S., Valeri S., Groppo E., Prestipino C., Lamberti C., Boscherini F., Phys. Rev. B 69 (2004) 045412.
[193] Purnell S.K., Xu X., Goodman D.W., Gates B.C., J. Phys. Chem. 98 (1994) 4076.
[194] Purnell S.K., Xu X., Goodman D.W., Gates B.C., Langmuir 10 (1994) 3057.
[195] Meyerheim H.L., Popescu R., Kirschner J., Jedrecy N., Sauvage-Simkin M., Heinrich B., Pinchaux R., Phys. Rev. Lett. 87 (2001) 076102.
[196] Henry C.R., Chapon C., Duriez C., Giorgio S., Surf. Sci. 253 (1991) 177.
[197] Graoui H., Giorgio S., Henry C.R., Surf. Sci. 417 (1998) 350.
[198] Renaud G., Barbier A., Robach O., Phys. Rev. B 60 (1999) 5872.
[199] Lopez N., Illas F., J. Phys. Chem. B 102 (1998) 1430.
[200] Giordano L., Goniakowski J., Pacchioni G., Phys. Rev. B 64 (2001) 075417.
[201] Hammer B., Top. Catal. 37 (2006) 3–16.
[202] Abbet S., Riedo E., Brune H., Heiz U., Ferrari A.M., Giordano L., Pacchioni G., J. Am. Chem. Soc. 123 (2001) 6172.
[203] Wang X.Q., Spivey J.J., Lamb H.H., Appl. Catal. B 56 (2005) 261.
[204] Neyman K.M., Rosch N., Pacchioni G., Appl. Catal. A 191 (2000) 3.
[205] Pacchioni G., Rosch N., J. Chem. Phys. 104 (1996) 7329.
[206] Heiz U., Sanchez A., Abbet S., Schneider W.D., J. Am. Chem. Soc. 121 (1999) 3214.
[207] Colonna S., Arciprete F., Balzarotti A., Fanfoni M., De Crescenzi M., Mobilio S., Surf. Sci. 512 (2002) L341.
[208] Lopez N., Illas F., Rosch N., Pacchioni G., J. Chem. Phys. 110 (1999) 4873.
[209] Campbell C.T., Starr D.E., J. Am. Chem. Soc. 124 (2002) 9212.
[210] Campbell C.T., Parker S.C., Starr D.E., Science 298 (2002) 811.

[211] Ranney J.T., Starr D.E., Musgrove J.E., Bald D.J., Campbell C.T., Faraday Discuss 114 (1999) 195.
[212] Starr D.E., Bald D.J., Musgrove J.E., Ranney J.T., Campbell C.T., J. Chem. Phys. 114 (2001) 3752.
[213] Starr D.E., Campbell C.T., J. Phys. Chem. B 105 (2001) 3776.
[214] Starr D.E., Diaz S.F., Musgrove J.E., Ranney J.T., Bald D.J., Nelen L., Ihm H., Campbell C.T., Surf. Sci. 515 (2002) 13.
[215] Larsen J.H., Ranney J.T., Starr D.E., Musgrove J.E., Campbell C.T., Phys. Rev. B 63 (2001) 195410.
[216] Xu L.J., Henkelman G., Campbell C.T., Jonsson H., Surf. Sci. 600 (2006) 1351.
[217] Xu L.J., Henkelman G., Campbell C.T., Jonsson H., Phys. Rev. Lett. 95 (2005) 146103.
[218] Musolino V., Selloni A., Car R., J. Chem. Phys. 108 (1998) 5044.
[219] Musolino V., Selloni A., Car R., Surf. Sci. 402 (1998) 413.
[220] Didier F., Jupille J., Surf. Sci. 307 (1994) 587.
[221] Flank A.M., Delaunay R., Lagarde P., Pompa M., Jupille J., Phys. Rev. B 53 (1996) R1737.
[222] Robach O., Renaud G., Barbier A., Phys. Rev. B 60 (1999) 5858.
[223] Schaffner M.H., Patthey F., Schneider W.D., Surf. Sci. 417 (1998) 159.
[224] Heifets E., Zhukovskii Y.F., Kotomin E.A., Causa M., Chem. Phys. Lett. 283 (1998) 395.
[225] Li C., Wu R.Q., Freeman A.J., Fu C.L., Phys. Rev. B 48 (1993) 8317.
[226] Larsen J.H., Starr D.E., Campbell C.T., J. Chem. Therm. 33 (2001) 333.
[227] Yudanov I., Pacchioni G., Neyman K., Rosch N., J. Phys. Chem. B 101 (1997) 2786.
[228] Florez E., Mondragon F., Truong T.N., Fuentealba P., Phys. Rev. B 73 (2006) 115423.
[229] Giordano L., Baistrocchi M., Pacchioni G., Phys. Rev. B 72 (2005) 115403.
[230] Campbell C.T., Curr. Opin. Solid State Mater. Sci. 3 (1998) 439.
[231] Xu C., Goodman D.W., Chem. Phys. Lett. 263 (1996) 13.
[232] Yulikov M., Sterrer M., Heyde M., Rust H.P., Risse T., Freund H.J., Pacchioni G., Scagnelli A., Phys. Rev. Lett. 96 (2006) 146804.
[233] Sterrer M., Yulikov M., Fischbach E., Heyde M., Rust H.-P., Pacchioni G., Risse T., Freund H.J., Angew. Chem. Int. Ed. 45 (2006) 2630.
[234] Sterrer M., Yulikov M., Risse T., Freund H.J., Carrasco J., Illas F., Di Valentin C., Giordano L., Pacchioni G., Angew. Chem. Int. Ed. 45 (2006) 2633.
[235] Yang Z.X., Wu R.Q., Zhang Q.M., Goodman D.W., Phys. Rev. B 65 (2002) 155407.
[236] Abbet S., Sanchez A., Heiz U., Schneider W.D., Ferrari A.M., Pacchioni G., Rosch N., J. Am. Chem. Soc. 122 (2000) 3453.
[237] Judai K., Worz A.S., Abbet S., Antonietti J.M., Heiz U., Del Vitto A., Giordano L., Pacchioni G., Phys. Chem. Chem. Phys. 7 (2005) 955.
[238] Abbet S., Heiz U., Hakkinen H., Landman U., Phys. Rev. Lett. 86 (2001) 5950.
[239] Antonietti J.M., Michalski M., Heiz U., Jones H., Lim K.H., Rosch N., Del Vitto A., Pacchioni G., Phys. Rev. Lett. 94 (2005) 213402.
[240] Heiz U., Schneider W.-D., J. Phys. D: Appl. Phys. 33 (2000) R85.
[241] Tait S.L., Dohnalek Z., Campbell C.T., Kay B.D., Surf. Sci. 591 (2005) 90.
[242] Qin C.Y., Sremaniak L.S., Whitten J.L., J. Phys. Chem. B 110 (2006) 11272.
[243] Molina L.M., Hammer B., Phys. Rev. Lett. 90 (2003) 206102.
[244] Yan Z., Chinta S., Mohamed A.A., Fackler J.P., Jr., Goodman D.W., J. Am. Chem. Soc. 127 (2005) 1604.
[245] Shima T., Takanashi K., Takahashi Y.K., Hono K., Appl. Phys. Lett. 88 (2006) 063117.
[246] Sicot M., Andrieu S., Tiusan C., Montaigne F., Bertran F., J. Appl. Phys. 99 (2006) 08D301.
[247] Xu X., Goodman D.W., Appl. Phys. Lett. 61 (1992) 774.
[248] Xu X., Goodman D.W., Surf. Sci. 282 (1993) 323.

[249] He J.W., Xu X.P., Corneille J.S., Goodman D.W., Surf. Sci. 279 (1992) 119.
[250] Schröder T., Adelt M., Richter B., Naschitzki M., Bäumer M., Freund H.-J., Surf. Rev. Lett. 7 (2000) 7.
[251] Schröder T., Adelt M., Richter B., Naschitzki M., Bäumer M., Freund H.J., Microelectron. Reliab. 40 (2000) 841.
[252] Schröder T., Hammoudeh A., Pykavy M., Magg N., Adelt M., Bäumer M., Freund H.-J., Solid-State Electron 45 (2001) 1471.
[253] Schröder T., Giorgi J., Bäumer M., Freund H.-J., Phys. Rev. B 66 (2002) 165422.
[254] Chen M.S., Santra A.K., Goodman D.W., Phys. Rev. B 69 (2004) 155404.
[255] Wendt S., Ozensoy E., Wei T., Frerichs M., Cai Y., Chen M.S., Goodman D.W., Phys. Rev. B 72 (2005) 115409.
[256] Chen M.S., Goodman D.W., Surf. Sci. 600 (2006) L255.
[257] Chen M.S., Santra A.K., Goodman D.W., J. Phys. Chem. B 108 (2004) 17940.
[258] Yakovkin I.N., Surf. Rev. Lett. 12 (2005) 449.
[259] Weissenrieder J., Kaya S., Lu J.-L., Gao H.-J., Shaikhutdinov S., Freund H.-J., Sierka M., Todorova T.K., Sauer J., Phys. Rev. Lett. 95 (2005) 076103.
[260] Todorova T.K., Sierka M., Sauer J., Kaya S., Weissenrieder J., Lu J.L., Gao H.J., Shaikhutdinov S., Freund H.J., Phys. Rev. B 73 (2006) 165414.
[261] Wendt S., Frerichs M., Wei T., Chen M.S., Kempter V., Goodman D.W., Surf. Sci. 565 (2004) 107.
[262] Yates J.T., Surf. Sci. 565 (2004) 103.
[263] Kim Y.D., Wei T., Wendt S., Goodman D.W., Langmuir 19 (2003) 7929.
[264] Kim Y.D., Wei T., Goodman D.W., Langmuir 19 (2003) 354.
[265] Xu X.P., Vesecky S.M., Goodman D.W., Science 258 (1992) 788.
[266] Xu X., He J.-W., Goodman D.W., Surf. Sci. 284 (1993) 103.
[267] Xu X., Goodman D.W., J. Phys. Chem. 97 (1993) 683.
[268] Xu X.P., Goodman D.W., Appl. Phys. Lett. 61 (1992) 1799.
[269] Xu X.P., Vesecky S.M., He J.W., Goodman D.W., J. Vac. Sci. Technol. A 11 (1993) 1930.
[270] Santra A.K., Min B.K., Goodman D.W., Surf. Sci. 515 (2002) L475.
[271] Zanella R., Sandoval A., Santiago P., Basiuk V.A., Saniger J.M., J. Phys. Chem. B 110 (2006) 8559.
[272] Luo K., Kim D.Y., Goodman D.W., J. Mol. Catal. A 167 (2001) 191.
[273] Min B.K., Wallace W.T., Goodman D.W., J. Phys. Chem. B 108 (2004) 14609.
[274] Chen M.S., Goodman D.W., Surf. Sci. 574 (2005) 259.
[275] Wallace W.T., Min B.K., Goodman D.W., J. Mol. Catal. A 228 (2005) 3.
[276] Min B.K., Wallace W.T., Goodman D.W., Surf. Sci. 600 (2006) L7.
[277] Szanyi J., Kuhn W.K., Goodman D.W., J. Phys. Chem. 98 (1994) 2978.
[278] Szanyi J., Goodman D.W., J. Phys. Chem. 98 (1994) 2972.
[279] Xu X., Goodman D.W., J. Phys. Chem. 97 (1993) 7711.
[280] Xu X., Goodman D.W., Catal. Lett. 24 (1994) 31.
[281] Xu X.P., Szany J., Xu Q., Goodman D.W., Catal. Today 21 (1994) 57.
[282] Goodman D.W., Surf. Sci. 299 (1994) 837.
[283] Davies P.W., Lambert R.M., Surf. Sci. 110 (1981) 227.
[284] Schmick H.D., Wassmuth H.W., Surf. Sci. 123 (1982) 471.
[285] Jorgensen S.W., Canning N.D.S., Madix R.J., Surf. Sci. 179 (1987) 322.
[286] Ma Y.S., Matsushima T., Shobatake K., Kokalj A., J. Chem. Phys. 124 (2006) 144711.
[287] Ma Y.S., Matsushima T., Catal. Today 111 (2006) 302.
[288] Wickham D.T., Banse B.A., Koel B.E., Surf. Sci. 243 (1991) 83.
[289] Giorgi J.B., Schroeder T., Baumer M., Freund H.J., Surf. Sci. 498 (2002) L71.

[290] Laurin M., Johanek V., Grant A.W., Kasemo B., Libuda J., Freund H.J., J. Chem. Phys. 123 (2005) 054701.
[291] Ozensoy E., Meier D.C., Goodman D.W., J. Phys. Chem. B 106 (2002) 9367.
[292] Ozensoy E., Min B.K., Santra A.K., Goodman D.W., J. Phys. Chem. B 108 (2004) 4351.
[293] Ichikawa S., Poppa H., Boudart M., J. Catal. 91 (1985) 1.
[294] Rainer D.R., Wu M.C., Mahon D.I., Goodman D.W., J. Vac. Sci. Technol. A 14 (1996) 1184.
[295] Yu R., Song H., Zhang X.F., Yang P.D., J. Phys. Chem. B 109 (2005) 6940.
[296] Luo K., Wei T., Yi C.-W., Axnanda S., Goodman D.W., J. Phys. Chem. B 109 (2005) 23517.
[297] Yi C.W., Luo K., Wei T., Goodman D.W., J. Phys. Chem. B 109 (2005) 18535.
[298] Chen M.S., Kumar D., Yi C.-W., Goodman D.W., Science 310 (2005) 291.
[299] Diebold U., Surf. Sci. Rep. 48 (2003) 53.
[300] Linsebigler A.L., Lu G.Q., Yates J.T., Chem. Rev. 95 (1995) 735.
[301] Thompson T.L., Yates J.T., Top. Catal. 35 (2005) 197.
[302] Wahlstrom E., Vestergaard E.K., Schaub R., Ronnau A., Vestergaard M., Laegsgaard E., Stensgaard I., Besenbacher F., Science 303 (2004) 511.
[303] Schaub R., Wahlstrom E., Ronnau A., Laegsgaard E., Stensgaard I., Besenbacher F., Science 299 (2003) 377.
[304] Batzill M., Morales E.H., Diebold U., Phys. Rev. Lett. 96 (2006) 026103.
[305] Aizawa M., Morikawa Y., Namai Y., Morikawa H., Iwasawa Y., J. Phys. Chem. B 109 (2005) 18831.
[306] Liu G., Rodriguez J.A., Hrbek J., Long B.T., Chen D.A., J. Mol. Catal. A 202 (2003) 215.
[307] Hugenschmidt M.B., Gamble L., Campbell C.T., Surf. Sci. 302 (1994) 329.
[308] Schaub R., Thostrup R., Lopez N., Laegsgaard E., Stensgaard I., Norskov J.K., Besenbacher F., Phys. Rev. Lett. 87 (2001) 266104.
[309] Wendt S., Matthiesen J., Schaub R., Vestergaard E.K., Laegsgaard E., Besenbacher F., Hammer B., Phys. Rev. Lett. 96 (2006) 066107.
[310] Wendt S., Schaub R., Matthiesen J., Vestergaard E.K., Wahlstrom E., Rasmussen M.D., Thostrup P., Molina L.M., Laegsgaard E., Stensgaard I., Hammer B., Besenbacher F., Surf. Sci. 598 (2005) 226.
[311] Gamble L., Jung L.S., Campbell C.T., Surf. Sci. 348 (1996) 1.
[312] Varazo K., Parsons F.W., Ma S., Chen D.A., J. Phys. Chem. B 108 (2004) 18274.
[313] Ajo H.M., Bondzie V.A., Campbell C.T., Catal. Lett. 78 (2002) 359.
[314] Hebenstreit W., Ruzycki N., Herman G.S., Gao Y., Diebold U., Phys. Rev. B 62 (2000) R16334.
[315] Diebold U., Ruzycki N., Herman G.S., Selloni A., Catal. Today 85 (2003) 93.
[316] Tauster S.J., Fung S.C., Garten R.L., J. Am. Chem. Soc. 100 (1978) 170.
[317] Tauster S.J., Acc. Chem. Res. 20 (1987) 389.
[318] Ko E.I., Garten R.L., J. Catal. 68 (1981) 223.
[319] Resasco D.E., Haller G.L., Stud. Surf. Sci. Catal. 11 (1982) 105.
[320] Pesty F., Steinruck H.-P., Madey T.E., Surf. Sci. 339 (1995) 83.
[321] Poirer G., Hance B., White J.M., J. Phys. Chem. 97 (1998) 5965.
[322] Dulub O., Hebenstreit W., Diebold U., Phys. Rev. Lett. 84 (2000) 3646.
[323] Jennison D.R., Dulub O., Hebenstreit W., Diebold U., Surf. Sci. 492 (2001) L677.
[324] Berko A., Menesi G., Solymosi F., Surf. Sci. 372 (1997) 202.
[325] Iddir H., Disko M.M., Ogut S., Browning N.D., Micron 36 (2005) 233.
[326] Gan S., Liang Y., Baer D.R., Grant A.W., Surf. Sci. 475 (2001) 159.
[327] Gan S., Liang Y., Baer D.R., Sievers M.R., Herman G.S., Peden C.H.F., J. Phys. Chem. B 105 (2001) 2412.

[328] Berko A., Solymosi F., Surf. Sci. 400 (1998) 281.
[329] Berko A., Klivenyi G., Solymosi F., J. Catal. 182 (1999) 511.
[330] Berko A., Szoko J., Solymosi F., Surf. Sci. 532 (2003) 390.
[331] Szoko J., Berko A., Vacuum 71 (2003) 193.
[332] Steinruck H.P., Pesty F., Zhang L., Madey T.E., Phys. Rev. B 51 (1995) 2427.
[333] Ji X.Z., Somorjai G.A., J. Phys. Chem. B 109 (2005) 22530.
[334] Somorjai G.A., Catal. Lett. 101 (2005) 1.
[335] Xu C., Lai X., Zajac G.W., Goodman D.W., Phys. Rev. B 56 (1997) 13464.
[336] Lai X., St Clair T.P., Valden M., Goodman D.W., Prog. Surf. Sci. 59 (1998) 25.
[337] Murray P.W., Shen J., Condon N.G., Pang S.J., Thornton G., Surf. Sci. 380 (1997) L455.
[338] Evans J., Hayden B.E., Lu G., Surf. Sci. 360 (1996) 61.
[339] Bowker M., Stone P., Bennett R., Perkins N., Surf. Sci. 497 (2002) 155.
[340] Ramirez-Cuesta A.J., Bennett R., Stone P., Mitchell P.C.H., Bowker M., J. Mol. Catal. A 167 (2001) 171.
[341] Bowker M., Stone P., Bennett R., Perkins N., Surf. Sci. 511 (2002) 435.
[342] Bowker M., Stone P., Morrall P., Smith R., Bennett R., Perkins N., Kvon R., Pang C., Fourre E., Hall M., J. Catal. 234 (2005) 172.
[343] BennettA R., Pang C.L., Perkins N., Smith R., Morrall P., Kvon R.I., Bowker M., J. Phys. Chem. B 106 (2002) 4688.
[344] Silly F., Castell M.R., J. Phys. Chem. B 109 (2005) 12316.
[345] Nuzzo R., Dubois L.H., in: Strong Metal-Support Interactions, ACS Symp. Ser. Vol. 298, R. Baker, S. Tauster, J. Dumesic (eds), ACS, Washington, DC, 1986, p. 136.
[346] Fu Q., Wagner T., Olliges S., Carstanjen H.D., J. Phys. Chem. B 109 (2005) 944.
[347] Pan J.M., Madey T.E., Catal. Lett. 20 (1993) 269.
[348] Aizawa M., Lee S., Anderson S.L., Surf. Sci. 542 (2003) 253.
[349] Iwasawa Y., Surf. Sci. 402 (1998) 8.
[350] Tero R., Fukui K., Iwasawa Y., J. Phys. Chem. B 107 (2003) 3207.
[351] Koike Y., Ijima K., Chun W.J., Ashima H., Yamamoto T., Fujikawa K., Suzuki S., Iwasawa Y., Nomura S., Maakura K., Chem. Phys. Lett. 421 (2006) 27.
[352] Nakajima N., Kato H., Okazaki T., Sakisaka Y., Surf. Sci. 561 (2004) 79.
[353] Nakajima N., Kato H., Okazaki T., Sakisaka Y., Surf. Sci. 561 (2004) 93.
[354] Chen D.A., Bartelt M.C., Hwang R.Q., McCarty K.F., Surf. Sci. 450 (2000) 78.
[355] Reddic J.E., Zhou J., Chen D.A., Surf. Sci. 494 (2001) L767.
[356] Zhou J., Chen D.A., Surf. Sci. 527 (2003) 183.
[357] Zhou J., Kang Y.C., Chen D.A., Surf. Sci. 537 (2003) L429.
[358] Zhou J., Kang Y.C., Chen D.A., J. Phys. Chem. B 107 (2003) 6664.
[359] Zhou J., Kang Y.C., Ma S., Chen D.A., Surf. Sci. 562 (2004) 113.
[360] Ma S., Zhou J., Kang Y.C., Reddic J.E., Chen D.A., Langmuir 20 (2004) 9686.
[361] Zhou J., Ma S., Kang Y.C., Chen D.A., J. Phys. Chem. B 108 (2004) 11633.
[362] Chen D.A., Bartelt M.C., Seutter S.M., McCarty K.F., Surf. Sci. 464 (2000) L708.
[363] Luo K., St Clair T.P., Lai X., Goodman D.W., J. Phys. Chem. B 104 (2000) 3050.
[364] Lai X.F., St Clair T.P., Goodman D.W., Faraday Discuss 114 (1999) 279.
[365] Haruta M., Yamada N., Kobayashi T., Iijima S., J. Catal. 115 (1989) 301.
[366] Valden M., Lai X., Goodman D.W., Science 281 (1998) 1647.
[367] Bell A.T., Science 299 (2003) 1688.
[368] Bond G.C., Thompson D.T., Catal. Rev. Sci. Eng. 41 (1999) 319.
[369] Goodman D.W., J. Catal. 216 (2003) 213.
[370] Kung H.H., Kung M.C., Costello C.K., J. Catal. 216 (2003) 425.
[371] Campbell C.T., Science 306 (2004) 234.

[372] Goodman D.W., Catal. Lett. 99 (2005) 1.
[373] Deng X.Y., Min B.K., Guloy A., Friend C.M., J. Am. Chem. Soc. 127 (2005) 9267.
[374] Valden M., Pak S., Lai X., Goodman D.W., Catal. Lett. 56 (1998) 7.
[375] Hayashi T., Tanaka K., Haruta M., J. Catal. 178 (1998) 566.
[376] Fu Q., Saltsburg H., Flytzani-Stephanopoulos M., Science 301 (2003) 935.
[377] Rodriguez J.A., Liu G., Jirsak T., Hrbek J., Chang Z.P., Dvorak J., Maiti A., J. Am. Chem. Soc. 124 (2002) 5242.
[378] Daniel M.C., Astruc D., Chem. Rev. 104 (2004) 293.
[379] Lopez N., Janssens T.V.W., Clausen B.S., Xu Y., Mavrikakis M., Bligaard T., Norskov J.K., J. Catal. 223 (2004) 232.
[380] Lim D.C., Lopez-Salido I., Dietsche R., Bubek M., Kim Y.D., Angew. Chem. Int. Ed. 45 (2006) 2413.
[381] Guzman J., Gates B.C., J. Am. Chem. Soc. 126 (2004) 2672.
[382] Schwartz V., Mullins D.R., Yan W.F., Chen B., Dai S., Overbury S.H., J. Chem. Phys. B 108 (2004) 15782.
[383] Liu L.M., McAllister B., Ye H.Q., Hu P., J. Am. Chem. Soc. 128 (2006) 4017.
[384] Kielbassa S., Kinne M., Behm R.J., J. Phys. Chem. B 108 (2004) 19184.
[385] Maennig A., Zhao Z., Rosenthal D., Christmann K., Hoster H., Rauscher H., Behm R.J., Surf. Sci. 576 (2005) 29.
[386] Benz L., Tong X., Kemper P., Metiu H., Bowers M.T., Buratto S.K., J. Phys. Chem. B 110 (2006) 663.
[387] Diebold U., Pan J.M., Madey T.E., Phys. Rev. B 47 (1993) 3868.
[388] Zhang L., Persaud R., Madey T.E., Phys. Rev. B 56 (1997) 10549.
[389] Parker S.C., Grant A.W., Bondzie V.A., Campbell C.T., Surf. Sci. 441 (1999) 10.
[390] Chusuei C.C., Lai X., Luo K., Goodman D.W., Top. Catal. 14 (2001) 71.
[391] Zhang L., Cosandey F., Persaud R., Madey T.E., Surf. Sci. 439 (1999) 73.
[392] Cosandey F., Zhang L., Madey T.E., Surf. Sci. 474 (2001) 1.
[393] Cosandey F., Madey T.E., Surf. Rev. Lett. 8 (2001) 73.
[394] Kitchin J.R., Barteau M.A., Chen J.G.G., Surf. Sci. 526 (2003) 323.
[395] Wahlstrom E., Lopez N., Schaub R., Thostrup P., Ronnau A., Africh C., Laegsgaard E., Norskov J.K., Besenbacher F., Phys. Rev. Lett. 90 (2003) 026101.
[396] Howard A., Clark D.N.S., Mitchell C.E.J., Egdell R.G., Dhanak V.R., Surf. Sci. 518 (2002) 210.
[397] Kolmakov A., Goodman D.W., Surf. Sci. 490 (2001) L597.
[398] Mitchell C.E.J., Howard A., Carney M., Egdell R.G., Surf. Sci. 490 (2001) 196.
[399] Canario A.R., Esaulov V.A., J. Chem. Phys. 124 (2006) 224710.
[400] Giordano L., Pacchioni G., Bredow T., Sanz J.F., Surf. Sci. 471 (2001) 21.
[401] Pillay D., Wang Y., Hwang G.S., Catal. Today 105 (2005) 78.
[402] Molina L.M., Hammer B., Appl. Catal. A 291 (2005) 21.
[403] Santra A.K., Yang F., Goodman D.W., Surf. Sci. 548 (2004) 324.
[404] Oh W.S., Xu C., Kim D.Y., Goodman D.W., J. Vac. Sci. Technol. A 15 (1997) 1710.
[405] Bondzie V.A., Parker S.C., Campbell C.T., Catal. Lett. 63 (1999) 143.
[406] Bondzie V.A., Parker S.C., Campbell C.T., J. Vac. Sci. Technol. A 17 (1999) 1717.
[407] Guo Q., Oh W.S., Goodman D.W., Surf. Sci. 437 (1999) 49.
[408] Lai X., Guo Q., Min B.K., Goodman D.W., Surf. Sci. 487 (2001) 1.
[409] Ashworth T.V., Thornton G., Thin Solid Films 400 (2001) 43.
[410] Chang Z., Thornton G., Surf. Sci. 462 (2000) 68.
[411] McCavish N.D., Bennett R.A., Surf. Sci. 546 (2003) 47.
[412] Boffa A.B., Galloway H.C., Jacobs P.W., Benitez J.J., Batteas J.D., Salmeron M., Bell A.T., Somorjai G.A., Surf. Sci. 326 (1995) 80.

[413] Sedona F., Rizzi G.A., Agnoli S., Xamena F.X.L.I., Papageorgiou A., Ostermann D., Sambi M., Finetti P., Schierbaum K., Granozzi G., J. Phys. Chem. B 109 (2005) 24411.
[414] Matsumoto T., Batzill M., Hsieh S., Koel B.E., Surf. Sci. 572 (2004) 127.
[415] Matsumoto T., Batzill M., Hsieh S., Koel B.E., Surf. Sci. 572 (2004) 146.
[416] Chen M.S., Wallace W.T., Kumar D., Zhen Y., Gath K.K., Cai Y., Kuroda Y., Goodman D.W., Surf. Sci. 581 (2005) L115.
[417] Chen M.S., Luo K., Yi C.W., Goodman D.W., Surf. Sci. (Submitted for publication).

This page intentionally left blank

Chapter 6

Magic numbers for shells of electrons and shells of atoms in binary clusters

S. Neukermans, E. Janssens, R.E. Silverans and P. Lievens*

Laboratorium voor Vaste-Stoffysica en Magnetisme & INPAC-Institute for Nanoscale Physics and Chemistry, Katholieke Universiteit Leuven, Celestijnenlaan 200D, B-3001 Leuven, Belgium

1. INTRODUCTION

The human interest in cluster physics may be a few hundred or thousand years older than what we generally assume. At least, several of the highly symmetric structures often encountered in clusters already intrigued human beings as early as the New Stone Age (Neolithicum) [1]. Hundreds of carved stones with lines corresponding to the edges of regular polyhedra were found in Scotland and believed to date back to around 2000 BC [2]. The icosahedron and dodecahedron were known to the ancient Greeks and described by Plato as two of the five Platonic solids, besides the tetrahedron, cube, and octahedron. Dating back to the Roman time (second to fourth century), dozens of hollow bronze dodecahedra (Fig. 1) have been found in Austria, Belgium, France, Germany, Great Britain, Hungary, Luxembourg, the Netherlands, and Switzerland. Artmann also reports a Roman icosahedron, which, misclassified as a dodecahedron, was stored in a museum's basement for 40 years before it got recognized as an icosahedron [3]. But, as is the case for the carved stones found in Scotland, their function remains mysterious.

Even if it seems quite unlikely that people in ancient times had atomic clusters in mind, the possible existence of highly symmetric species constitutes a major issue in current atomic cluster physics. Although governed by the same fundamental laws, the physics of clusters is very different from their analogues on a macroscopic scale. Nanometer-sized pieces of matter show magnetic, optical, chemical, catalytic, etc. properties different and often superior to their bulk counterparts. In this respect, in particular clusters composed of two types of atoms are considered to be very attractive study objects, as one can flexibly tune the unique physico-chemical properties of clusters by controlling their composition. After all, binary clusters composed of elements with

The Chemical Physics of Solid Surfaces, Volume 12
ISSN: 1571-0785
DOI: 10.1016/S1571-0785(07)12006-X

*Corresponding author.
E-mail: Peter.Lievens@fys.kuleuven.be

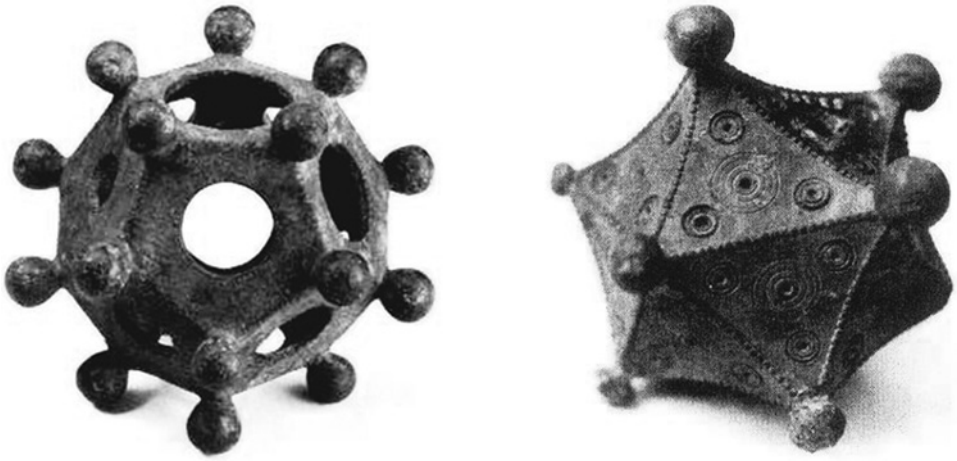

Figure 1: Highly symmetric bronze objects dating back to the Gallo-Roman time, dodecahedron (left) and icosahedron (right) of which a few tens have been retrieved all over Europe [1].

different valences allow to vary the total number of electrons independently of the number of constituent atoms.

Playing around with the number and type of building blocks (nuclei and electrons) in atomic clusters was not arbitrarily invented merely to extend the range of cluster systems to be investigated. Pioneering mass spectrometric observations immediately revealed the influence of the number of atoms or the number of electrons, depending on the type of its constituent atoms, on the stability of clusters. The physical origin of the importance of the exact number of atoms or electrons, compared to bulk matter, relates to the large surface-to-volume ratio on one hand, and to the finite spacing between electronic energy levels or *energy quantization* in small clusters on the other hand.

In clusters composed of rare gas atoms, the interatomic interactions are weak and isotropic. These aggregates are observed to form close-packed structures as was discovered in 1981 in a mass spectrum of xenon clusters by Echt and co-workers, which showed pronounced peaks or steps in abundances for clusters containing a 'magic number' of 13, 55, 147… atoms [4]. The intervals between these numbers correspond to the completion of an additional layer of xenon atoms, consisting of 20 regular triangular faces arranged concentrically around the central atom forming the symmetric icosahedral structures described by Mackay [5]. As such, the origin of these magic numbers is related to the geometric packing, or to *shells of atoms* in the clusters.

On the other hand, clusters composed of alkali metal atoms feature metallic bonds provided by the itinerant valence electrons of the constituent atoms. The identification of magic numbers (2, 8, 20, 40, 58…) and their interpretation in terms of an electronic shell structure in small clusters of sodium in 1984 by Knight and co-workers [6] in one stroke inspired numerous research groups to embark on the line of cluster research.

Where the packing in rare gases is interesting but more of a 'fait-divers', the study of metals is much more central to the subject of condensed matter physics and chemistry in general. The shell structure identified in alkali metal clusters has nothing to do with the packing of atoms. It is attributed to a delocalization behavior of valence electrons

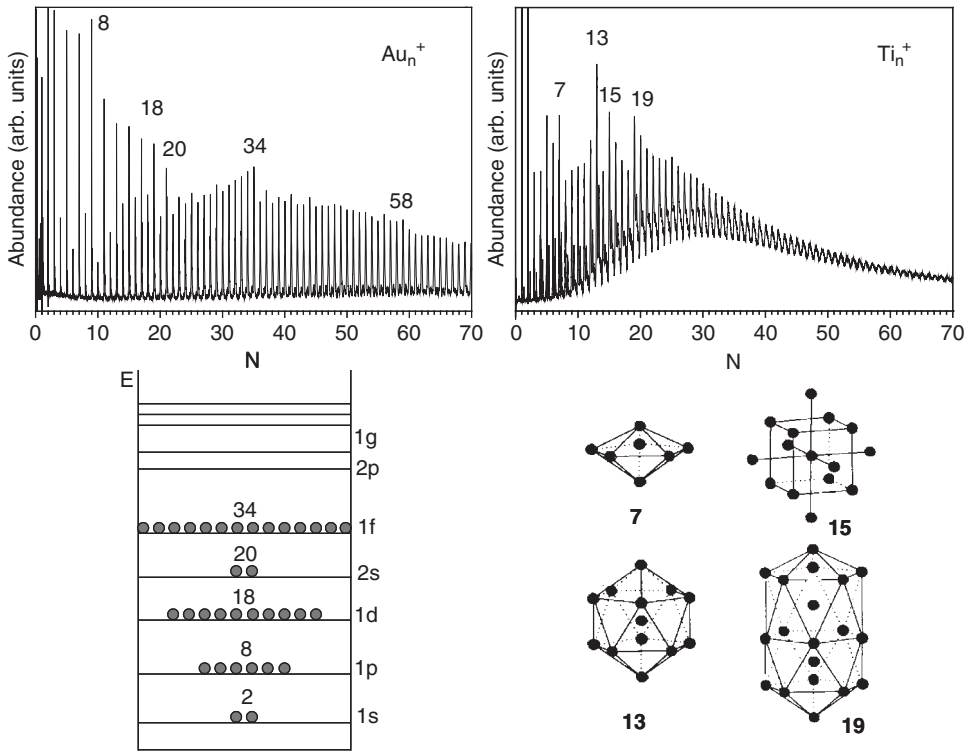

Figure 2: Mass-abundance spectra of gold (left) and titanium (right) clusters, showing electronic and geometric magic numbers, respectively. The lower panel shows a schematic representation of the sequence of spherical electronic shells, as it applies to gold clusters, and a number of small symmetric geometric structures, which apply to titanium clusters.

of the constituent atoms. Each conduction electron is delocalized over the entire cluster volume and occupies a one-particle state in a centro-symmetric potential well. Clusters in which the number of delocalized electrons corresponds to the number of electrons required to fill an electronic shell are more stable and as such observed more abundantly. This is illustrated in Fig. 2 (left) for the case of pure gold cluster cations after photofragmentation. In the mass spectrum, steps are observed in abundance for cluster sizes containing 2, 8, 18, 20, 34… valence electrons. These numbers correspond to electronic shell filling numbers in the sequence of spherical shells 1s/1p/1d/2s/1f/…. Contrary to simple (alkali, noble) metal clusters, in the case of transition metal clusters such as titanium (Fig. 2, right), enhanced stabilities are observed for cluster sizes 7, 13, 15, 19… corresponding to symmetric geometric structures.

Ever since, the quest for both geometrically and electronically closed shell, and consequently very stable *magic* species is a leading thread in current cluster research. Highly symmetric clusters, presenting special structural, as well as electronic and thermodynamic stability, with tailored physical and chemical properties look very attractive as building blocks for nanostructured materials. And as mentioned above, aside from highly symmetric systems like C_{60} [7], binary or doped clusters are well suited for this purpose, since they inherently offer the possibility of altering cluster

properties nearly at will by varying the number of atoms independently of the number of itinerant electrons.

The study of (binary) clusters is interdisciplinary by definition. In inorganic chemistry and solid-state chemistry, a traditional quest has been to understand how materials are built up by combining different atoms, similarly, condensed matter physics has been aiming to understand the fundamentals of bulk properties by investigating small-scale precursors. Evidently, the complexity of this interdisciplinary field cannot be covered in a short review. Here, we will restrict the discussion to sets of mixed clusters where the interpretation of their properties strongly relies on shell structure descriptions, both shells of electrons and shells of atoms. This chapter reviews recent studies of small binary clusters, with less than 100 atoms per clusters. Because of these small sizes, many of the species can be considered as molecules, implying the use of molecular language when describing their structure. In this review, we will combine this with terminology borrowed from condensed matter physics.

Two introductory sections give a concise description of how binary clusters are produced and a summary of relevant cluster models, respectively. In the bulk of the fourth section, three types of binary cluster systems will be reviewed: electronegatively doped main group metals, transition-metal-doped noble metals, and metal-doped semi-metal clusters. In all three cases, special attention will be given to binary systems in which the interplay between electronic shell closing and specific geometries gives rise to pronounced or exceptional physico-chemical (stability, reactivity, magnetic, etc.) properties.

2. PRODUCTION OF BINARY CLUSTERS

A general overview of the different types of single-element cluster sources is given in Ref. [8]. Several cluster sources for producing binary clusters in a controlled way have been reported. Nearly all types of single-element cluster sources can be used to produce binary clusters, which contain one element that is available as a gas (component), through the addition of (small amounts of) that reactant gas to the inert carrier gas of the source. The cluster composition can be tuned by controlling the partial pressure of the reactant gas. Typical examples of dopant gasses added to the carrier gas are O_2, Cl_2, H_2O, etc. [9]. Although this technique is important and widely applied in particular for the study of metal cluster oxides, the variety of binary systems that can be produced is rather limited.

Bimetallic clusters have been produced by a single mixed-cartridge [10, 11] or dual cartridge [9] hot oven source. In the former, the relative abundance of the constituent elements can be adjusted by changing the mixing ratio in the cartridge, but is limited to a single evaporation temperature for both elements, and thus to fixed relative vapor pressures. The latter improves this concept by including separate temperature control for the two metals, allowing a larger range of mixing ratios. Applications of hot oven sources or thermal cluster sources are restricted to low boiling point metals and usually produce relatively hot clusters. The first use of both a single mixed-cartridge [10] and dual cartridge [9] oven source was reported by Martin to produce arsenic sulfide clusters and cesium sulfide clusters, respectively.

Laser vaporization sources [12] are an alternative to hot oven sources for the production of bimetallic clusters. Although the thermodynamical properties of this

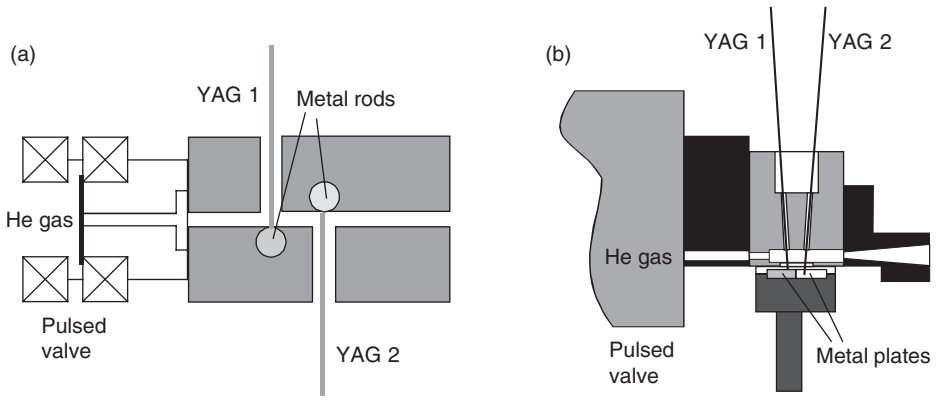

Figure 3: (a) Schematic diagram of the original binary laser vaporization source developed by Kaya and co-workers using two separate metal rods [18]. (b) Schematic diagram of the binary laser vaporization source constructed by Lievens and co-workers using two different metal plates [19]. In both cases, the metal targets are vaporized by the second harmonics (532 nm) of two Nd^{3+}:YAG lasers and the He carrier gas (5–10 atm, 99.9999% purity) enters the source through a pulsed gas valve. The plumes of evaporated material are mixed with the inert carrier gas, collisions occur and cluster formation starts. The mixture of gas, atoms, and clusters expands adiabatically into the vacuum through the nozzle opening on the right. Hereby, the clusters are further cooled and cluster formation stops because of the rapidly decreasing density.

kind of source are not as well described, it allows for cluster production of a greater variety of materials and produces colder clusters ($T \leqslant 300$ K). Binary metallic clusters have been produced by a variety of laser vaporization sources: single target sources using binary alloy targets [13, 14], pressed mixed powders [15], or coated rods [16], and dual-rod target sources using a split vaporization laser beam [17] or two vaporization lasers [18, 19]. The latter type, using two separate lasers for two separate targets, originally developed by Kaya and co-workers, has demonstrated to be the most versatile technique [20–22]. In Fig. 3, a schematic overview is given of two types of dual-target dual-laser vaporization sources, developed by Kaya and co-workers [18] and Lievens and co-workers [19], respectively. The use of two independent lasers allows varying vaporization energy and timing independently. The amount of introduced helium can be controlled through the gas valve. Cluster formation in a laser vaporization source is strongly dependent on the amount of three body collisions and the particle temperature, which is determined by collisions with the carrier gas atoms. This implies that the densities of the constituent elements and the carrier gas in the formation chamber are governing the aggregation process. The composition of the bimetallic clusters can be controlled by varying the partial pressures of the two metal vapors and the helium gas. The metal vapor pressures depend on the vaporization laser energies and on the time delays of the laser pulses with respect to the gas pulse. Furthermore, the cluster formation is influenced by the source geometry, in particular by the volume of the formation chamber and by the shape of the nozzle.

To our knowledge, the use of other types of cluster sources for the production of bimetallic species is very rare. An example is the production of Au_nAg_m clusters from a sputtering source with silver–gold alloy targets [23].

3. PHENOMENOLOGICAL MODELLING OF THE MANY BODY PROBLEM FOR DOPED METAL CLUSTERS

Binary clusters impose an additional degree of complexity not only on experiments but also on theoretical models. In nearly all first-principles calculational approaches to the many-particle problem of a cluster, replacing one or more atoms (X) in a homoatomic cluster (X_n) by one or more atoms of a different element (Y) drastically increases the number of possible structural isomers that have to be probed for optimization. Pioneering ab initio quantum chemical studies on different binary cluster systems already started in the late 1980s [24–28]. Although computational resources are rapidly evolving, quantum chemical computational studies of binary cluster systems still remain restricted to the smaller sizes (typically less than about 15–20 atoms) or high symmetries. Larger systems have been studied using molecular dynamics [29, 30].

Luckily, several (size-dependent) properties of simple metal (alkali, noble) clusters are not drastically influenced by the details of the ionic structure. In a *jellium* model, a significant simplification of the quantum mechanical many-particle problem is achieved, at the expense of computational accuracy, by introducing a constant potential replacing the effect of the ions and core electrons in the cluster. Only the many-body problem of the valence electrons confined by the interaction with this homogeneous distribution of positive charges is treated self-consistently with density functional theory [31]. *Phenomenological shell models*, inspired by the nuclear shell model, simplify the computational problem of a cluster even further and consider only the possible states of a single electron confined in a potential well of a given shape [8]. Nevertheless, the shell model is able to explain qualitative electronic shell effects in size-dependent properties of simple (alkali, noble) metal clusters, where the valence electrons of the constituent atoms can be considered itinerant. However, it is not a priori clear if this behavior can be extrapolated to heterogeneous clusters composed of two different (simple) metals. The different electron density, electron affinity, and ionization energy of the dopant atom perturbs the effective potential experienced by the valence electrons. The electronic energy level sequence and the electron delocalization behavior are also affected by this modified potential.

If the valence electrons are itinerant, completely occupied electron states are responsible for enhanced stability and abundance maxima are expected to occur at electron numbers 2, 8, 20, 34, 40… for spherical shapes. This should be the case irrespective of the number of cores contributing to the effective potential and in spite of the heterogeneous ionic structure. Experimental studies on doped alkaline [32–38], aluminum [39, 40], and coinage [41–43] metal clusters indeed showed that the free-electron picture remains valid, at least to a certain extent. More stable clusters correspond to systems where the total amount of valence electrons equals one of the known spherical magic numbers.

However, a number of stable heterogeneous clusters were found, which correspond to electron numbers that are not observed for single element clusters. Evidence for a magic number corresponding to 10 electrons was found in clusters doped with electronegative elements, such as K_8Zn, Na_9Au, Na_6Pb, K_8Mg, and Na_8Zn [33, 36–38], while 18 was found to be a pronounced magic number in species doped with electropositive elements, such as $Au_{18}Cu^+$, $Au_{16}Al^+$, and $Au_{16}In^+$ [41, 42]. These novel magic numbers were related to dopant-induced changes in the energy level sequence.

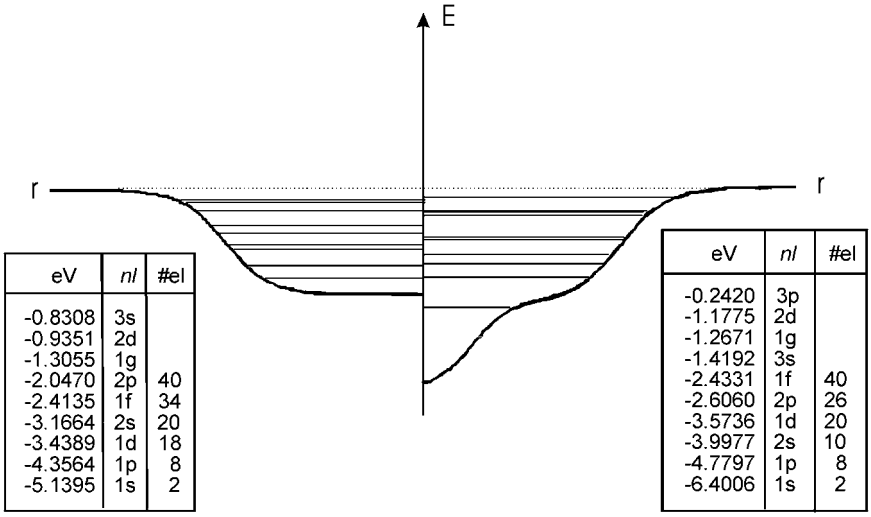

Figure 4: Wood–Saxon potential for Na_{40} and a modified Wood–Saxon potential for $Na_{38}Mg$ (both clusters have a total of 40 valence electrons). Their respective eigenstates are compared with identical energy scale to illustrate the modification of the potential due to the incorporated heteroatom. The heteroatom induces a depression at the center of the well. This leads mainly to a selective stabilization of *n*s states (states with angular momentum zero) and in a weaker fashion for p > d > f.... In the tables, the energy, principal and angular momentum quantum numbers (*n* and *l*), and the sum of valence electrons for the calculated eigenstates are listed for Na_{40} and $Na_{38}Mg$, respectively. The difference in the level order is due to a 1d/2s level inversion. (Reproduced with permission from Ref. 36.)

The standard *jellium model* is inadequate to explain these changes, since it assumes a uniformly charged background. A *two-step spherical jellium model* was introduced to deal with this shortcoming. Host and impurity atoms are both characterized by a uniform but different positively charged background [44–46]. Similarly, a *modified phenomenological* (Wood–Saxon) potential was used to account for the 'new' magic numbers observed in doped alkali cluster systems [36]. The latter is illustrated in Fig. 4. In both approaches, two situations can be distinguished [47], as illustrated schematically in Fig. 5.

(i) If the central heteroatom is more electronegative than the host atoms, the effective potential is more attractive at the center of the cluster. Orbitals that have (most of) their density in the center (i.e., s, and to a lesser extent p levels) will energetically be favored, while orbitals that have several nodal planes crossing the origin (d and f levels) remain relatively unaffected. The deeper the depression, the more the *n*s states are pulled down. A small depression results in a shift of the energy levels and fades electronic shell closings for 18 and 34 electrons. A stronger depression results in 1d/2s and 1f/2p level inversions and the new magic numbers 10 and 26, while the 18 and 34 electron shell closures disappear. The level sequence becomes 1s/1p/2s/1d/2p/1f/... with corresponding magic numbers 2, 8, 10, 20, 26, 40... (see Fig. 5b).

(ii) If the central heteroatom is less electronegative than the host atoms, it causes a hump in the center of the potential. This leads to an upward shift of the *n*s levels

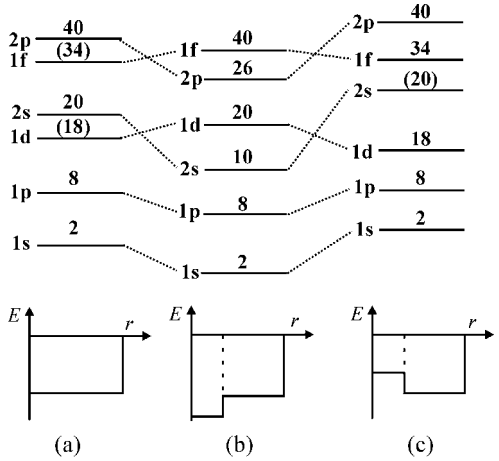

Figure 5: Schematic representation of the single particle energy levels in the standard jellium model (a) and in the two-step jellium model with a depression (b) and an increase (c) in the central part of the background potential. Note the lowering of the 2s and the 2p levels in (b) causing the magic numbers 10 and 26, and the lifting of the 2s level in (c) enhancing the magic number 18. (Reproduced with permission from Ref. [47].)

relative to the levels with non-zero angular momentum. Regardless of the exact shape of the potential this again will cause level shifts, e.g., enlarge the gap between the 1d and 2s levels, and decrease the spacing between the 2s and 1f levels. The magic number 20 disappears in favor of the magic number 18, resulting in a 1s/1p/1d/2s/1f/2p/… level sequence with magic numbers 2, 8, 18, 34, 40… (see Fig. 5c).

It should be noted that modified jellium or phenomenological models only hold for (centro-symmetrically) singly doped species or segregated binary clusters, since a spherical symmetry is assumed and both models naively incorporate the ionic structure. For clusters with a reduced symmetry, for example if the heteroatom is in an off-center position, one may no longer be able to assign electron shells and energy levels using a simple spherical phenomenological potential. Also, in multiply doped species (*alloy* clusters) or doped metal clusters composed of atoms with a large difference in electronegativity, the manifestation of electronic shell effects in their physico-chemical properties can be strongly suppressed because of the formation of covalent/directional and/or ionic bonds.

Size-dependent features in the properties of certain types of clusters cannot be explained using simplified electronic shell models. The magic behavior in their properties depends more on the atomic packing or the optimization of d–d interactions and is governed by symmetric geometric structures, often termed *shells of atoms* [48]. This is, in general, the case for larger clusters of nearly all materials, since the band of electronic states broadens and the highest occupied–lowest unoccupied molecular orbital (HOMO–LUMO) gap, which is a measure for the electronic shell closing effect, becomes small. However, for certain clusters, atomic shells or close-packed structures also are important in the small size range. Transition metal clusters, due to the presence of partially occupied d states, feature magic numbers of atoms that correspond to symmetric close-packed structures, for example, 7 (bicapped pentagon or half

icosahedron), 13 (icosahedron), 15 (bcc unit), 19 (double icosahedron), etc. Also clusters of covalently bound non-metals usually have more open geometries that satisfy the specific highly directional bonding requirements of these elements [49]. Carbon species may adopt geometries as diverse as chains, rings, graphene sheets, fullerenes, and nanotubes. Silicon and germanium clusters, up to $n \approx 25$–35, form prolate structures that are built by stacking exceptionally stable Si_9 and Ge_9 tricapped trigonal prism units [50, 51], and rearrange to more spherical morphologies for larger sizes.

Important is the fact that the stability of several of these geometries can be further enhanced by proper doping. The stability of a 13-atom icosahedron can be enhanced by substituting the central atom by a suitable heteroatom. This arises due to the fact that the vertex–vertex bonds (a) are about 5% longer than center–vertex bonds (R):

$$R = \frac{5^{1/4}}{2}\sqrt{\phi}a$$

where $\phi = (1+\sqrt{5})/2 = 1.618\ldots$ is the golden ratio or divine proportion. For example, symmetric Si_n and Ge_n cages are known to be stabilized by transition metal encapsulation. Hereby the open d-band of the transition metal dopant is crucial to host the dangling bond electrons of the surrounding Si_n or Ge_n cages [52, 53].

4. A SELECTION OF DOPED METAL CLUSTER SYSTEMS

4.1. Electronegatively doped group I, II, and III metal clusters

Metallic clusters doped with electronegative elements ((C), O, S, F, Cl, I, etc.) probably are the oldest type of binary cluster systems that have been investigated. No dual cluster source is required to study these systems because the dopants can be added in gaseous form to the carrier gas of the source. Depicting a single pioneering study on metal clusters doped with electronegative elements is very difficult. Nevertheless, the identification of Li_3O, by Wu and co-workers [54] in 1979, as a very stable molecule in a mass spectrometric analysis of the vapor from Knudsen effusion of solid lithium oxide, can be regarded as an important step in the onset of binary metal cluster physics and chemistry. Despite the fact that the normal octet rule in traditional chemical bonding is violated, its dissociation energy toward the corresponding octet molecule Li_2O was found to be very high (2.45 ± 0.50 eV) [54].

About 4 years later, the origin of the unusual stability observed for Li_3O was revealed by Schleyer and co-workers, who computationally investigated a large number of stable M_nX molecules having polycoordinated central atoms (X), which suggests violation of the octet rule [26]. In these species, excess electrons (beyond the usual octet) populate an orbital with a highly delocalized character. Such an orbital, usually the HOMO, are antibonding with respect to M–X, but bonding with respect to M–M.

Species with this behavior have been termed hypermetallated, and numerous examples exist. They all exhibit an exceptional stability although formally the octet rule in the chemical bonding is violated. For example, Li_4O, Li_5O, Li_5C, and Li_6C are found to be thermodynamically stable toward all possible dissociation modes [26, 27, 55–58]. In Fig. 6, a mass-abundance spectrum of lithium–carbon clusters is shown featuring the exceptional stability of Li_6C [55, 59]. The energy level scheme and corresponding molecular orbitals show a 10-electron closed-shell structure ($1s^2/1p^6/2s^2$) and a HOMO

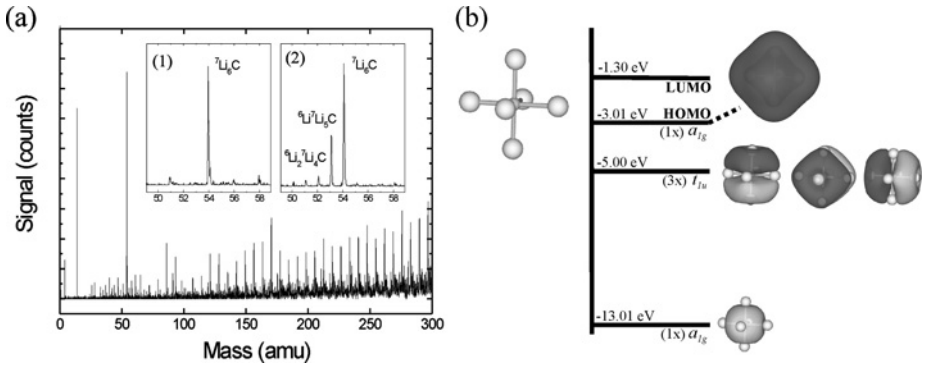

Figure 6: (a) Mass-abundance spectra of doped Li clusters ionized with photons of 6.4 eV, employing isotopically enriched ^{7}Li as a vaporization target. Insets: (1) selected mass region around Li_6C, and (2) same mass region as (1) employing natural ^{6,7}Li metal. (b) Ground-state geometry, energy level scheme, and orbitals of the octahedral Li_6C from a density functional theory calculation. The 10 valence electrons of Li_6C occupy the five depicted molecular orbitals. The two lowest energy electrons are located around the central C atom in an orbital with a_{1g} symmetry (1s type). The ionic bonds of all Li atoms to the C atom consume six electrons, located in triple degenerate t_{1u} orbitals (1p type). The HOMO of a_{1g} symmetry (2s type) contains the two remaining electrons that are located on a far extended orbit that is Li–Li bonding and Li–C antibonding.

orbital that is antibonding with respect to Li–C but strongly Li–Li bonding. Many examples have been studied computationally [26, 27, 56, 60, 61] and identified experimentally [55, 58, 62–64]. In general, hypermetallic species (M_nX) consist of an electronegative main group element (X = O, C, N, B, F, Cl, S, P, Be, etc.) surrounded by a shell of metal atoms (M = Li, Na, K, Mg, Al, In, Si, etc.). Notice that Li_3O can be considered as a sort of *cluster precursor* since the classical chemical bonding in *normal* molecules (directional and fully saturated bonds) is violated. Instead, an excess electron in an orbital delocalized over the entire system provides extra bonding. This delocalized electronic bonding is a typical characteristic for metal clusters compared to regular molecules.

Along with the development of cluster sources, larger clusters composed of mixtures of electronegative and metal atoms could also be studied. One particular example is a class of molecular clusters, the so-called Met-Cars (short for metallo-carbohedrenes), where for a number of mixed carbon and transition metal clusters, specific stoichiometries and sizes with enhanced stability were discovered [65]. Another subset is formed by alkali metals with electronegative elements. In several cases, such systems, e.g., Cs_nO_m, Li_nO_m, Li_nC, Na_nO_m, Li_nH_m, Na_nF_m [59, 66–71], showed segregation between an ionically bound bulk-like crystallite and a metallic part with properties very similar to bare metal clusters. In the case of oxygen-doped clusters, segregation or alloy formation strongly depends on the dopant concentration. In a threshold photoionization study of (monovalent) cesium oxide clusters, peculiarly high ionization energy values were found for $Cs_{z+2n}O_n$ species with $z = 8, 18, 34, 58, 92\ldots$; sizes that correspond to magic numbers resulting from a simple spherical shell model [68]. Most probably, segregation occurs between an ionically bound $Cs_{2n}O_n$ unit and a shell of z surrounding cesium atoms, which leads to the unexpected spherically symmetric potential well in which z delocalized valence electrons are confined. In oxygen- or

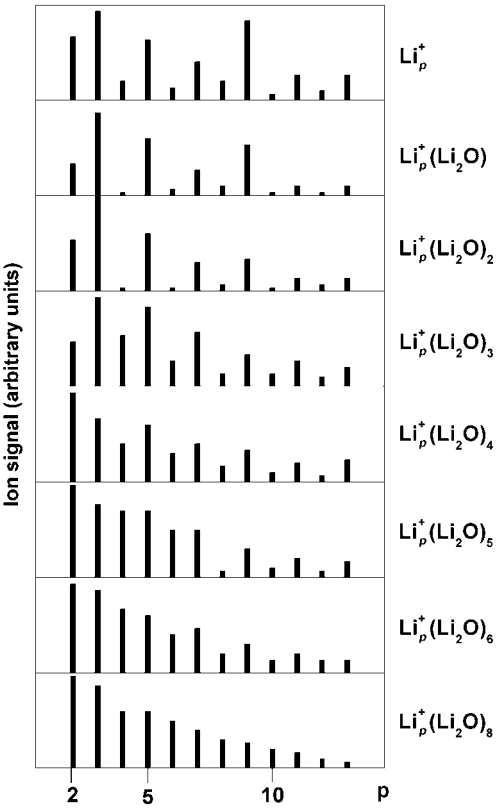

Figure 7: Mass spectra of evaporative sub-ensembles of $Li_p^+(Li_2O)_n$ versus p for several sizes of the ionic component $(Li_2O)_n$. Mixed lithium–lithium oxide aggregates are experimentally obtained from unimolecular evaporative cascades starting from metal rich $Li_p^+(Li_2O)_n$. The results provide evidence that the properties of the quantum metallic droplet, i.e., shell-closing and odd–even alternation, are vanishing with increasing size of the oxide component. Note, for example, the gradual disappearance of the enhanced abundance of the $p = 9$ species, which corresponds to the electronic shell closing for eight delocalized valence electrons, with increasing ionic component n. (Reproduced with permission from Ref. [72].)

carbon-doped lithium clusters, electronic shell closings could be identified in the size-dependent ionization energies [59, 66, 67]. In a photofragmentation study, of metal-rich lithium oxide clusters $Li_p^+(Li_2O)_n$, loss of metallicity was observed for increasing size (n) of the oxide component [72]. As illustrated in Fig. 7, the results show vanishing of the odd–even alternation and the disappearance of an electronic shell closing for 8 itinerant electrons. Another example is a unimolecular evaporation study of lithium-rich $Li_nH_m^+$ cluster ions, which indicated a clear separation between a metallic Li_{n-m}^+ part and an insulating $(LiH)_m$ part [71].

The picture appears to be completely different in the case of divalent metal oxide clusters, e.g., $(MgO)_n^+$, $(MgO)_nMg^+$, Ca_nO, Ba_nO_m [73–76]. High peak intensities in mass-abundance spectra or variations in ionization energies cannot be related to electronic shell closing but rather to structural or geometric effects. In particular, the segregation model, which holds relatively well for doped alkali clusters, does not seem to be valid for alkaline-earth oxides. Studies on the third main group metal oxide

clusters, i.e., Al_nO_m, Ga_nO_m, In_nO_m [77], report an enhanced stability for cluster ions containing an even number of electrons, even for the oxygen-rich ones. Nevertheless, as for their pure metal counterparts, their size-dependent properties seem to be governed by the interplay between electronic and geometric factors. Among the species doped with a single electronegative atom, enhanced stabilities or electronic shell closing effects in their electronic properties (ionization energies, photoelectron spectra) have been reported for Al_7N, Al_7C^-, In_7O^+, $Al_{12}C$, and $Al_{12}B^-$ [78–81], which can be related to electronic shell closing numbers 26 and 40 that show up in electronic shell models modified for electronegative central dopant atoms, as discussed above. Moreover, the enhanced stabilities of the 13-atom species $Al_{12}C$ and $Al_{12}B^-$ are due to the combined effect of a closed electronic structure and a highly symmetric dopant-encapsulated icosahedral structure [82]. As an example of the eight-atom species, the electronic structure resulting from quantum chemical calculations of the endohedral In_7O^+ C_{3v}-isomer is shown in Fig. 8. The pattern shows a closed electronic shell structure with a large HOMO–LUMO gap of 2.3 eV and 26 electrons in 13 delocalized

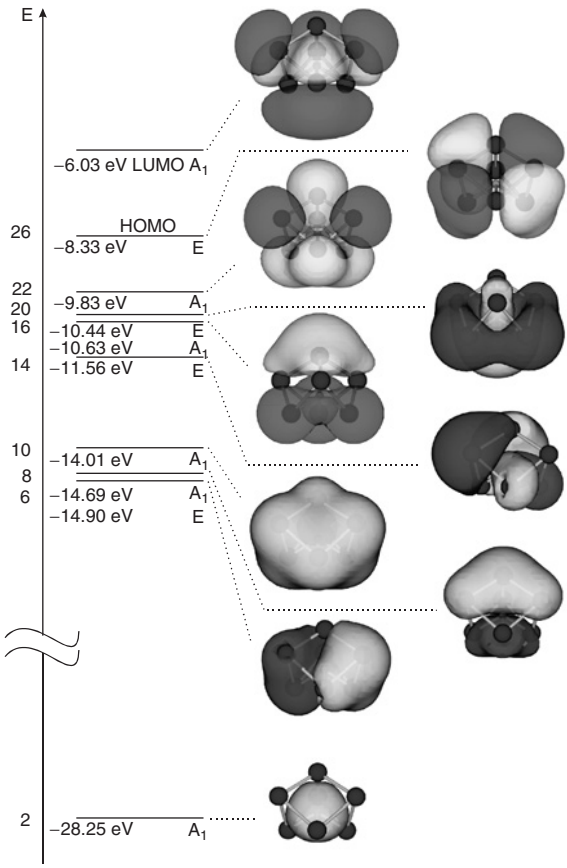

Figure 8: Energy level sequence and corresponding orbitals of the C_{3v} ground-state isomer of In_7O^+, computed using density functional theory [81], showing 26 electrons in 13 delocalized orbitals and a large HOMO–LUMO gap of 2.3 eV confirming its magic electronic character.

orbitals. Because of the rather spherical shape of the C_{3v}-isomer, the orbitals, to a certain extent, resemble the s, p, and d type spherical harmonics. Notice that both the energy gaps (shell closings) at 10 and 26 electrons are present in the modified two-step jellium model (Fig. 5) discussed above for a central depression of the potential due to a central electronegative dopant. The latter example illustrates how valuable simple spherical shell models are in predicting the basic electronic properties of a large variety of clusters and, the other way round, how these basic features remain present in the output of more sophisticated quantum chemical computations.

More recently, iodized aluminum clusters attracted a lot of attention in the quest for clusters with coincident closures of their electronic and geometric shells that can act as superatoms. The observation of the very stable $Al_{13}I^-$ cluster evidences the super-halogen character of Al_{13}, lacking one electron to form a 40-electron closed-shell structure [83]. The stability and reactivity of the $Al_{13}I_x^-$ and $Al_{14}I_x^-$ series also are interpreted in terms of a simple spherical shell model, and their potential use in superatom chemistry is addressed [84].

It should be noted that, apart form the doped main group metal clusters, numerous studies are available on transition metal oxide clusters. Because of the open d shell of the transition metal atoms, size-dependent properties of such clusters are governed by a complex interplay between electronic and structural aspects and are impossible to describe using simple electronic and geometric shell models.

4.2. Transition-metal-doped coinage metal clusters

Size-dependent properties, e.g., stability patterns in mass-abundance spectra, ionization energies, dissociation energies, etc., of coinage metal (Cu, Ag, and Au) clusters can be described by theoretical models based on the dominating role of the number of delocalized valence electrons as in the case of, for example, simple alkali metal clusters, because they have a completely filled d shell and one valence s electron in the atomic ground state. On the other hand, a simple electronic shell model cannot be applied for clusters comprised of more complex atoms, such as open d shell transition metals. The d electrons of transition metals engage in more localized, directional bonding than the outermost s and p electrons of simple metals. With the study of transition-metal-doped noble metal clusters, the interaction between localized bonds and free electrons can be examined.

The radial extent of the open d shell is an important parameter. The extent decreases along a row (e.g., from Sc to Ni) and increases with the increasing row number (e.g., from Sc to Ac). Large dopant d orbitals can hybridize strongly with host s or d electrons. This increases the tendency toward itinerant d behaviour, in such a way that the d electrons should be considered as free electrons. On the other hand, smaller d orbitals do not interact strongly with the host electrons.

A photofragmentation mass spectrometry study of Au_n clusters doped with 3d transition metal atoms demonstrated that the light dopants (Sc, Ti) contribute both their 4s and 3d electrons to the cloud of itinerant electrons, while for the heavier elements (Cr, Mn, Fe, Co, Ni) only the 4s electrons are delocalized [85, 86]. The interpretation was supported by the shapes of the HOMOs found in density functional theory calculations [87, 88]. The difference between the light and heavy dopants is related to the different size of d electron wave functions resulting in a stronger or weaker hybridization with the gold valence electrons. Moreover, if only the dopant s

electrons are itinerant, the energetic competition between $3d^x4s^2$ and $3d^{x+1}4s^1$ dopant configurations is crucial. Most often, the monovalent or divalent character agrees with the atomic ground-state configuration of the free atom. However, the host environment may alter energetic preferences, e.g., Cr ($3d^54s^1$) is divalent in Au_n, Ni ($3d^84s^2$) is monovalent in Na_n, Cu_n, and Au_n [85, 89], and Co ($3d^74s^2$) acts monovalent in Al_n, while it is divalent in Au_n [85, 90].

The stability patterns of the doped Au_n clusters mentioned above were discussed on the basis of a simple phenomenological shell model, taking into account only the electronic structure of the dopant atom. In several doped systems, e.g., $Au_{16}Sc^+$, $Au_{15}Ti^+$, $Au_{17}X^+$ (X = Cr, Mn, Fe, Co), $Au_{18}Ni^+$, or $Au_{16}Y^+$, the magic number 18 manifests itself as a strong shell-closing, at the cost of 20, which is observed for pure Au_n clusters. As an example, the photofragmentation spectrum of cationic Au_nY^+ clusters is given in Fig. 9 [42]. The most pronounced feature in this mass spectrum is the intense signal recorded for $Au_{16}Y^+$, which is a direct fingerprint of the high stability of this species relative to neighboring cluster sizes and relates to the closed electronic shell structure formed by the 18 valence electrons.

Besides a dopant dependence of the electronic structure, this study also indicates how the cluster shape can be modified by proper doping, resulting in new magic numbers that correspond to planar cluster species. While Au_9^+ is observed as a magic cluster containing eight delocalized electrons in the case of pure gold cationic clusters, the mass-abundance spectra of Au_nX^+ (X = Cr, Mn, Fe, Co, Zn) feature enhanced stability for Au_5X^+ systems, which is ascribed to a planar triangular ground-state structure in combination with six delocalized electrons being a magic number for 2D systems [86, 91, 92]. The experiments showed very little evidence for an enhanced

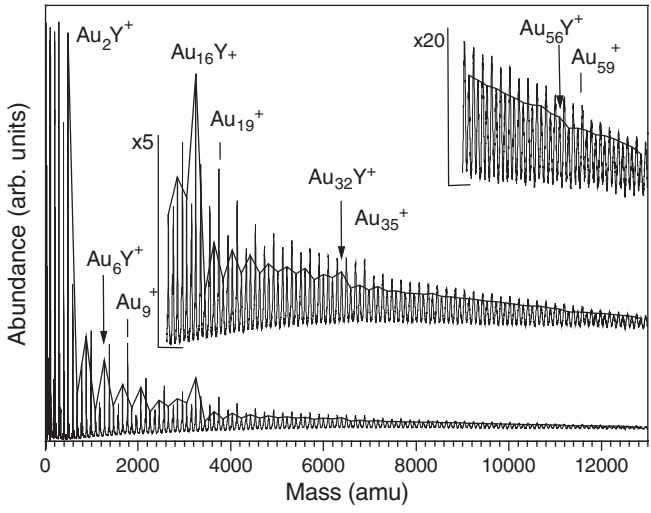

Figure 9: Mass-abundance spectrum of $Au_nY_m^+$ clusters after photofragmentation. The solid line connects the Au_nY^+ species. Steps in abundance are observed at $n = 2$, 6, 16, 32, and 56. The pronounced pattern results from cooling by fragmentation and can be explained by the enhanced stability related to electronic shell closings for 2, 8, 18, 34, and 58 delocalized valence electrons [42]. Recent computational studies predict stable endohedral fullerene-like structures for $Au_{15}Y$ and $Au_{15}Sc$ clusters, which are isoelectronic with $Au_{16}Y^+$ [112]. (Reproduced with permission from Ref. [42].)

stability of Au_7X^+ species, which should contain eight valence electrons. The electronic structure and magnetic properties of Au_6M^- (M = Ti, V, Cr) have been investigated experimentally using photoelectron spectroscopy and density functional theory calculations [93]. It is found that all Au_6M^- and Au_6M clusters possess a planar structure, in which the transition metal atom is located in the center of an Au_6 ring and carries large magnetic moments. Meanwhile, also homogeneous gold clusters are known to be planar up to fairly large sizes, depending on their charge state, due to relativistically enhanced s–d hybridization [94–96].

Transition-metal-doped gold clusters not only have been studied because of the fundamental interest in the interplay between geometric and electronic effects in bimetallic clusters. At the same time, the peculiar optical and catalytic properties observed for pure gold clusters [97] triggered the search for highly stable transition-metal-doped gold clusters, since the additional degree of freedom inherent to bimetallic clusters can enhance the chemical versatility for tuning the electronic and geometric properties of gold-based clusters and related potential applications.

The pioneering example in this respect is the icosahedral $Au_{12}W$ cluster [98–101]. In the latter, the W dopant atom has large d orbitals and delocalizes both its two 6s and four 5d electrons. This cluster has a compact geometry with the tungsten atom in the center of a cage and a closed-shell electronic structure with a large HOMO–LUMO gap, confirmed experimentally by photoelectron spectroscopy [99]. $Au_{12}W$ is stabilized for three complementary reasons: (i) relativistic effects that strengthen the radial W–Au and the covalent Au–Au bonds, (ii) aurophilic attraction in the periphery, and (iii) a closed electronic structure with 18 valence electrons [98]. The electrons occupy orbitals with a_g, t_{1u}, and h_g symmetries that show similarities to the 1s, 1p, and 1d spherical levels, although the orbital shapes are somewhat more complex because of strong gold s–d hybridization). Meanwhile, the isoelectronic species $Au_{12}Mo$, $Au_{12}V^-$, $Au_{12}Nb^-$, and $Au_{12}Ta^-$ have been produced and characterized experimentally by photoelectron spectroscopy, while the theoretically predicted isoelectronic cation $Au_{12}Re^+$, however, has not. It should be noted that icosahedral $Au_{12}Pd$ has been prepared chemically in solution [102] and characterized computationally [103] before $Au_{12}W$; however, this is not a magic closed electronic shell cluster.

Although $Au_{12}W$ was originally thought to be stiff, a careful study of its vibrational properties [100] actually showed it to be very soft in the angular motions of the W–Au bonds, a property shared by many systems with Au–Au bonds [96]. Another indication of this softness is that $Au_{12}W$ completely deforms when placed inside a Si_{60} cage [104]. As can be seen in Fig. 10, the magic $Au_{12}W$ cluster interacts strongly with Si_{60} and stabilizes the caged structure. This interaction completely destroys the icosahedral geometry of $Au_{12}W$ and the symmetry of the Si_{60} cage.

A number of fullerene-like pure gold cages of different sizes, e.g., Au_{26} [105], Au_{32} [106], Au_{42} [107], Au_{50} [108], have been predicted. More recently, experimental evidence for the existence of hollow Au_n (n = 16–18, 20) cages was deduced from PES data [109, 110]. Calculations suggest that these hollow Au_n (n = 16–18) cages can easily accommodate a guest atom with very little structural distortion to the host cages. Indeed, a number of highly stable gold-covered bimetallic clusters, $M@Au_n$ (n = 9–17) obeying the 18-electron rule, were predicted computationally [111, 112]. It is found that starting from $n = 9$, the heteroatom (M) prefers to be entirely surrounded by gold atoms to attain the lowest-energy structure. In particular, WAu_{12},

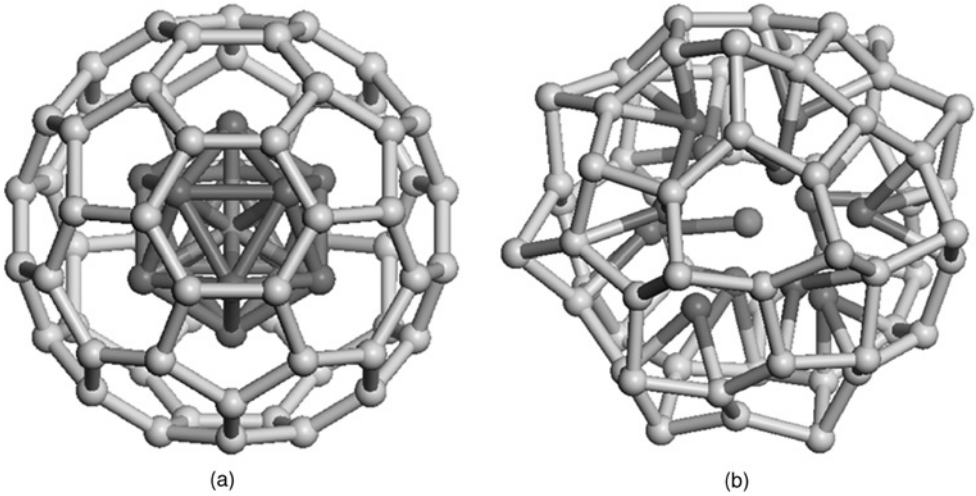

Figure 10: The initial (a) and optimized (b) geometries of $Au_{12}W$ in Si_{60}. The magic $Au_{12}W$ cluster is chemically active in Si_{60} and strongly interacts with the cage, resulting in a large energy gain, stabilization, and major deformation of both the doped gold cluster and the Si_{60} cage. (Reproduced with permission from Ref. [104].)

$Au_{14}Zr$, $Au_{15}Sc$, and $Au_{15}Y$ would stand out in stability, as concluded by their high binding energy per atom ($>2.40\,eV$) as well as a large HOMO–LUMO gap ($>1.70\,eV$). The latter may explain the very large abundances observed experimentally for the isoelectronic cations $Au_{16}Y^+$ and $Au_{16}Sc^+$ in the photofragmentation studies mentioned above [42, 85]. Note that the endohedral geometry of these clusters confirms the shell model interpretation based on a hump at the center of the phenomenological potential.

In another theoretical study, $Au_{16}Si$ is found to be a stable dopant-encapsulated tetrahedral, geometrically robust cage, satisfying the 20-electron shell closing of the conventional jellium model [113].

To end the overview of gold-based binary systems, we want to mention a recently reported 'eccentric' computational example of a molecular gold-plated diamond C_5Au_{12} cluster [114]. A tetrahedral C_5 radical (unit of the diamond crystal lattice) is encapsulated in an Au_{12} layer of matching geometry, with the gold atoms in positions correlating to the pattern of bonds of the sp^3-hybridized carbon atoms, resulting in nearly isoenergetic distorted icosahedral and octahedral geometries.

To our knowledge, studies on binary silver-based clusters are much less numerous compared to gold. However, the 3d transition-metal-doped gold clusters' study mentioned above has been extended to silver clusters [115–118]. The stability patterns of Ag_nX^+ (X = Sc, Ti, V, Cr, Mn, Ni, Cu) reflect an electronic shell structure with dopant-dependent magic numbers. The open 3d shell transition metal dopant is considered to contribute its 4s electrons (for Cr up to Ni) or its 3d and 4s electrons (Sc and selected sizes for Ti and V) to a cloud of itinerant electrons. Among the clusters containing 18 valence electrons, remarkable stabilities are observed for $Ag_{16}Sc^+$, $Ag_{15}Ti^+$, $Ag_{14}V^+$, similar to doped gold. The size-dependent electron delocalization is attributed to the small energy difference between $3d^x4s^2$ and $3d^{x+1}4s^1$ atomic

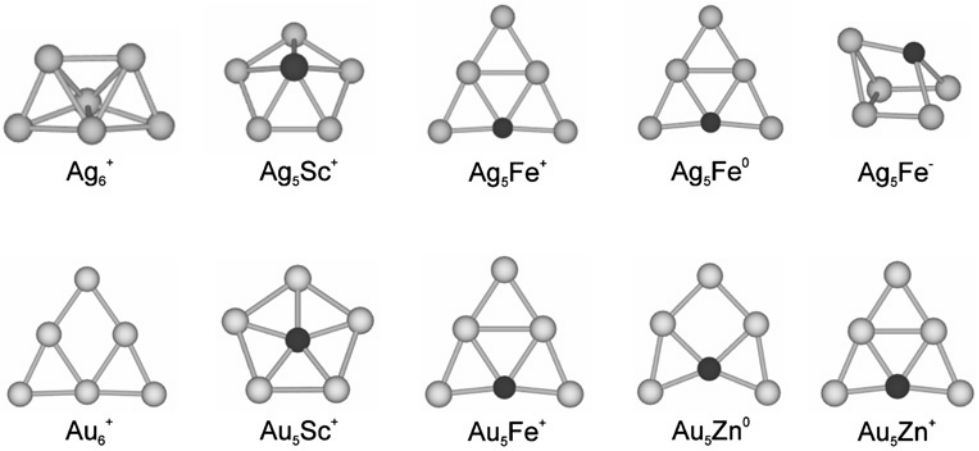

Figure 11: Ground-state geometries of Ag_6^+ [117], Ag_5Sc^+ [117], Ag_5Fe^+ [117], Ag_5Fe^0 [119], Ag_5Fe^- [119], Au_6^+, Au_5Sc^+ [92], Au_5Fe^+ [92], Au_5Zn^0 [91], and Au_5Zn^+ [91] clusters obtained with density functional theory.

configurations of the dopant atoms. Contrary to doped gold clusters, Ag_5X^+ (X = V, Cr, Mn, Fe, Co) species do not show up as particularly stable and as such no evidence is found for the existence of 2D electronic shell closures in doped silver clusters [116]. Nevertheless, a density functional theory study revealed that the Ag_5X^+ (X = Sc, Ti, V, Cr, Mn, Fe, Co, and Ni) clusters prefer planar or semi-planar C_{5v} symmetries, significantly flattened compared to the 3D tripyramidal geometry found for pure Ag_6^+, indicating that the transition metal dopant enhances the planar character of the clusters [117]. In all low-energy isomers, the dopant occupies a highly coordinated site. Also, a high spin magnetic moment is found on the dopant atoms, only slightly lower than the free-atom value, which is a signature for limited silver 5s dopant 3d hybridization. These results were recently extended toward neutral and anionic $Ag_5X^{0,-}$ (X = Sc, Ti, V, Cr, Mn, Fe, Co, and Ni) clusters [119]. In Fig. 11, the ground-state geometries of a few doped $Ag_5X^{+,0,-}$ and $Au_5X^{+,0}$ are compared with the geometries of Ag_6^+ and Au_6^+. Where both the bare gold and the doped gold clusters are planar, several three-dimensional geometries are found for the doped silver clusters. However, most $Ag_5X^{0,+,-}$ clusters are seriously flattened compared to the bare $Ag_6^{+,0,-}$ geometries [119]. A comparison of the cationic Ag_5Fe^+, the neutral Ag_5Fe^0, and the anionic Ag_5Fe^- shows that the charge state can also have an important influence on the structure.

The most astonishing observation for 3d transition-metal-doped silver clusters is the strong stability of $Ag_{11}Fe^+$, $Ag_{10}Co^+$, and Ag_9Ni^+ [115]. Enhanced stabilities for the corresponding sizes were not observed for doped gold clusters. These stabilities could be explained by an itinerant behavior of both the 4s and 3d dopant atom electrons. In that case, the Fe, Co, and Ni atoms in $Ag_{11}Fe^+$, $Ag_{10}Co^+$, and Ag_9Ni^+ would delocalize 8, 9, and 10 valence electrons, respectively, yielding a total of 18 electrons, a magic number in the spherical shell model. Although unrealistic at first sight, this argumentation was confirmed by detailed quantum chemical calculations of the electronic and geometric structure of $Ag_{10}Co^+$ [115]. The latter was found to have a

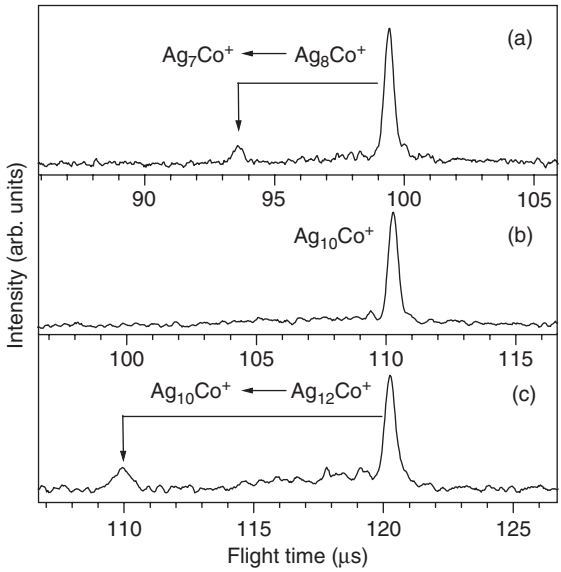

Figure 12: Delayed fragmentation spectra of (a) Ag_8Co^+, (b) $Ag_{10}Co^+$, and (c) $Ag_{12}Co^+$. The main fragmentation channel is labeled and appears to be size dependent. Ag_8Co^+ decays mainly by neutral silver evaporation. This is also the main dissociation channel for most other cluster sizes (see Ref. [118] for more details). However, $Ag_{10}Co^+$ does not show any delayed fragmentation, which is consistent with the high stability of this cluster [115]. For $Ag_{12}Co^+$, the main dissociation channel is the evaporation of a silver dimer, to create the stable $Ag_{10}Co^+$. The successive evaporation of two silver monomers is not very likely, since this would require the presence of a significant amount of $Ag_{11}Co^+$ fragments.

symmetric endohedral geometry (only slightly distorted from D_{4d}) with a closed 18-electron singlet electronic shell structure, implying that the magnetic moment on the cobalt atom is completely quenched. Hybridization of the atomic silver 5s levels with the cobalt 3d levels leads to the formation of delocalized molecular orbitals that resemble the spherical harmonic 1s, 1p, and 1d functions. This specific size and composition dependent behavior is analogous to the screening electron cloud formation in magnetic-element-doped bulk metals and therefore can be interpreted as a finite-size precursor of a Kondo system. It should be noted that a similar behavior has been predicted in a number of highly symmetric transition-metal-doped noble metal clusters: $Cu_{12}Cr$ [120], $Ag_{12}Cr$ [121], $Au_{12}Cr$ [122], and $Au_{12}W$.

By investigating the preferable dissociation channel after laser heating and subsequent fragmentation of mixed silver–cobalt particles, it was recently shown that in clusters containing mainly silver, the cobalt sits at the cluster center and fragmentation proceeds by the evaporation of silver surface atoms [118]. In clusters containing mainly cobalt, silver atoms also locate at the periphery and are more weakly bound to the cluster than the cobalt surface atoms. Moreover, the special stability of $Ag_{10}Co^+$ was demonstrated in these delayed fragmentation studies, as is shown in Fig. 12.

4.3. Transition-metal/metal-doped group IV

Silicon is one of the most important materials used in microelectronics industry. Stimulated by the discovery of carbon fullerenes and, later on, carbon nanotubes,

many efforts are made to search for similar silicon cage structures. However, although silicon shares the diamond structure with carbon, both elements behave differently in clusters. Carbon prefers sp^2 bonding, which appears in the structure of graphite, while silicon prefers sp^3 bonding. The latter makes it difficult to form stable hollow cage structures such as C_{60}. A possible approach to stabilize hollow silicon cage structures was proposed by Jackson and Nellermoe [123]. Inspired by small C_{28} fullerenes that were stabilized by a central guest atom as, for example, in UC_{28} [124], applying the same idea, a strikingly large binding energy (15.2 eV) is obtained for the icosahedral Si_{20} cage, which is not a stable isomer for the bare cage, by putting a zirconium atom inside.

About 10 years earlier, Beck had already discovered stable silicon cluster–metal atom compounds of remarkable but identical stoichiometries for three different transition metal dopants, namely chromium, molybdenum, and tungsten: $Si_{15}M$ and $Si_{16}M$ (M = Cr, Mo, and W) [125]. However, despite a valuable attempt based on a topological model [126], the magic behavior of these structures remained unexplained for more than a decade until Kumar and Kawazoe computationally attributed the strong stability to dopant-encapsulated cage-like structures with large values of binding energy, HOMO–LUMO gap, and embedding energy of the dopant atom [127]. The magnetic moment of the dopants is completely quenched. An interesting property of these metal-encapsulated silicon clusters lies in the tunability of the band gap depending on the dopant atom. Metal dopants can enhance the symmetry of the host cluster or enlarge the HOMO–LUMO gap into the region of visible light.

Experiments on endohedral complexes involving metal atoms and non-metallic Si_n cages have demonstrated that $Si_{14}Hf$, $Si_{13}Ta$, $Si_{12}W$, and $Si_{11}Re$ clusters are magic [128]. Calculations on $Si_{10}Fe$, $Si_{12}Cr$, and $Si_{12}W$ predict endohedral geometries (no icosahedra) with interesting electronic structures [128–130]. The central dopant atom in the Si_nX clusters has a $md^{18-n-2}(m+1)s^2$ electron configuration and interacts with all n silicon atoms. If each silicon atom is singly bonded to the central atom, this atom gets 18 electrons ($18 - n - 2$ from d orbitals, 2 from s orbitals, and n from the silicon neighbors) in total. The transition metal dopant obtains a closed electronic structure, in accordance with the 18-electron rule for d-block organometallic complexes. This rule states that the number of non-bonded electrons at the metal plus the number of electrons in the metal–ligand bonds should be 18 [131]. At the same time, three valence electrons are left for each silicon atom, making it possible to form a silicon polyhedron without dangling bonds [128, 130]. So, these clusters are not stabilized by the formation of closed jellium states but by the 18-electron rule for the metal dopant in combination with a covalently bonded silicon cage.

Most recently, Nakajima and co-workers [132] reported the selective formation of highly stable $Si_{16}M$ (M = Sc, Ti, and V) clusters by fine-tuning the laser vaporization source conditions (Fig. 13). $Si_{16}V^+$, $Si_{16}Ti$, and $Si_{16}Sc^-$ are closed electronic shell systems. Similar to Al_{13} discussed above, the reactivity of $Si_{16}M$ toward F_2 was examined. The formation of $Si_{16}VF$ suggests that $Si_{16}V$ is an alkali atom-like species and $Si_{16}Sc^-$ is suggested to behave like a superhalogen, similar to Al_{13}^- [83, 84].

The initial interest in doped silicon systems [133–148] rapidly extended to its higher mass congeners [52, 149–153]. Notable examples, computationally predicted, are metal-encapsulated icosahedral superatoms of germanium and tin, $Ge_{12}Zn$ and $Sn_{12}Cd$, with large HOMO–LUMO gaps, or $Ge_{12}Mn$ and $Sn_{12}Mn$, with high magnetic

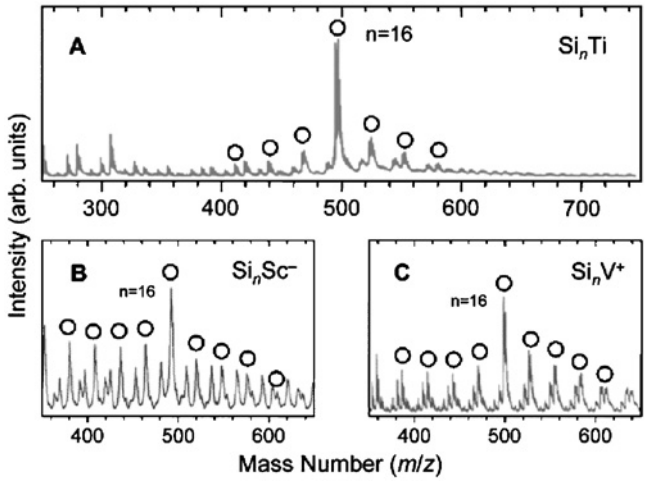

Figure 13: Mass spectra showing size-selective formation of (A) $TiSi_{16}$ neutrals, (B) $ScSi_{16}$ anions, and (C) VSi_{16}. (Reproduced with permission from Ref. [132].)

moments. A number of typical endohedral close-packed structures for metal-encapsulated group IV clusters $X@M_n$ in the size range $n = 10$, 12, 14–16 are shown in Fig. 14 [154]. Experimental studies, however, are far more scarce than for doped silicon species [53, 125, 132, 155–158]. A mass spectrometric study on $Ge_nCo_x^-$, Sn_nCo^-, and Pb_nCo^- anions reports an enhanced stability for $Pb_{10,12}Co^-$ [159].

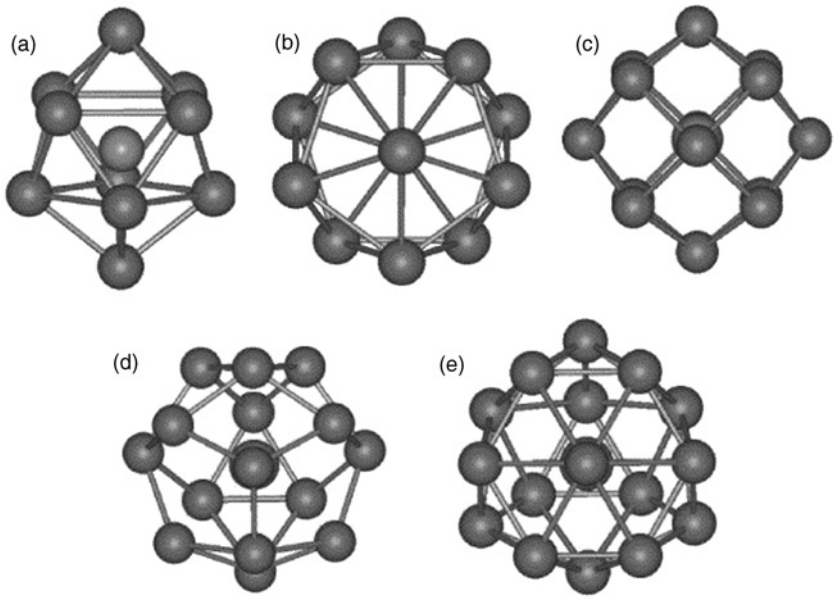

Figure 14: Close-packed structures of M-encapsulated clusters of X atoms: (a) bicapped tetragonal antiprism for $Be@Si_{10}$, $Ni@Ge_{10}$, and $Pt@Sn_{10}$; (b) icosahedral $Be@X_{12}$, $Mn@X_{12}$ (X = Ge and Sn), $Al^+@Pb_{12}$, $Pt^{-2}@Pb_{12}$, $M@Au_{12}$ (M = Mo and W), $Cu@Al_{12}$, and $Si@Al_{12}$; (c) cubic $M@Si_{14}$ (M = Fe, Ru, and Os); (d) Frank–Kasper (FK) $M@Si_{15}$ (M = Cr, Mo, W); and (e) FK $Ti@Si_{16}$ and $Zr@Ge_{16}$. The M atom is inside the cage. (Reproduced with permission from Ref. [154].)

Mass spectrometric characterization of Pb_nAl^+ clusters produced in a laser vaporization source showed an extremely large abundance for $Pb_{12}Al^+$ species and to a lesser extent for $Pb_{10}Al^+$ [160] (Fig. 15). Structural analysis with density functional theory revealed an icosahedral ground state for $Pb_{12}Al^+$. A large HOMO–LUMO gap (3.1 eV) and a large energy difference relative to the second most favorable isomer (1.96 eV) were further evidence for the particular stability of this system. The 50 valence electrons occupy 25 molecular orbitals, which are delocalized over the entire cluster. The orbitals resemble spherical shell model states, but the level ordering is different. The 50-electron shell closing originates from the crystal-field splitting of the high angular momentum levels according to the icosahedral symmetry of the cluster.

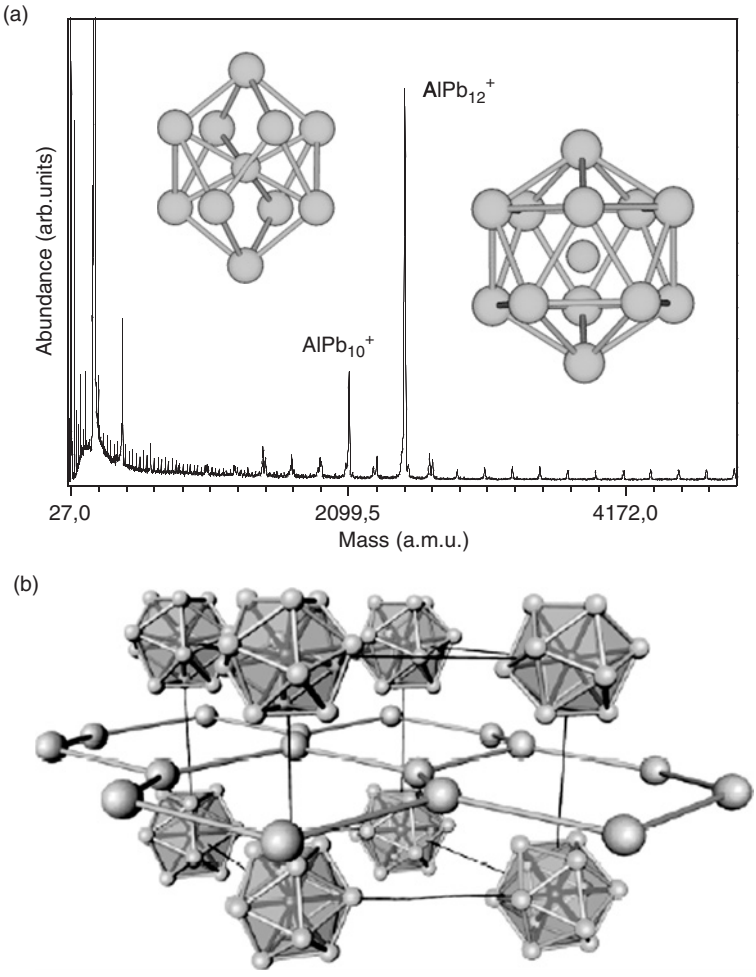

Figure 15: (a) Mass-abundance spectrum of Pb_nAl^+ clusters featuring the exceptional stability observed for $Pb_{12}Al^+$ and, to a lesser extent, $Pb_{10}Al^+$. Their respective highly symmetric dopant-encapsulated structures are shown. (b) Schematic illustration of $Pb_{12}M^{2-}$ ions (M = Ni, Pd, Pt) that are chemically produced in solutions in high yield as crystallized $[K(2,2,2\text{-crypt})]_2[M@Pb_{12}]$ salts. These crystallized salts form superlattices of cations and anions and are prototypes for assembled cluster materials. (Reproduced with permission from Ref. [163].)

The radial orbitals that point toward the positively charged lead atom centers are lower in energy, while tangential molecular orbitals with maximum density in between the atoms are less favorable. The splitting of the 1 g level results in a very pronounced HOMO–LUMO gap at the 50-electron occupancy. Almost at the same time $Pb_{12}Pt^{2-}$ clusters, which are isoelectronic with $Pb_{12}Al^{+}$, were prepared chemically in high yield (60%) [161]. Meanwhile, also the size-dependent stability and electronic and geometric properties of the lower mass congeners X_nAl^{+} (X = Si, Ge, Sn) have been investigated [162] and related species like $Pb_{10,12}M^{2-}$ (M = Ni, Pt, Pd) as well as Pb_{12}^{2-} and Sn_{12}^{2-} have been identified experimentally [163–165]. Recently, the superalkali character of the neutral $Pb_{12}M$ (M = B, Al, Ga, In, and Tl) was studied computationally [166].

A more extended experimental study of the size-, host-, and dopant-dependent stability of metal-doped semi-metal clusters S_nM (M = Cr, Mn, Cu, Zn; S = Si, Ge, Sn, Pb) partly covers the large variety of metal dopant–group IVA host combinations that have been accessed theoretically in literature [167]. Enhanced stabilities are observed for $Si_{15,16}M$ and $Ge_{14–16}M$ with M = Cr, Mn but not for Cu- and Zn-doped clusters, which seems to confirm that the possibility of d band filling of the dopant atom with dangling bond electrons from the surrounding Si_n and Ge_n cages is crucial in obtaining stable endohedral cage structures. Similar to the examples discussed above, relatively enhanced abundances are found for $Pb_{12}M$ species, which probably relate to close-packed icosahedral structures. The situation is less straightforward for doped Sn_n clusters, but the reported data experimentally confirm the theoretically predicted special stability of the metal-doped magic magnetic superatom $MnSn_{12}$.

Finally, a general principle for designing stable highly symmetrical clusters was proposed [162]. The approach takes advantage of both the extra stability provided by an optimal electronic configuration of the cage and the good geometrical balance between the outer cage and the endohedral atom, as schematically represented in Fig. 16. In this case, the optimal character of the electronic configuration of the cluster

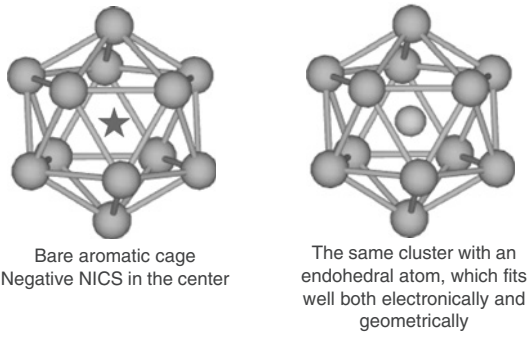

Figure 16: Schematic representation of the procedure to design a stable spherical cluster [162]. At first, the character of the electronic structure of a bare cage is probed through its aromatic properties [168]. Hereby, the number of electrons is adjusted by the appropriate choice of atoms and charges to achieve a closed electronic structure (significant aromatic character). The cage does not necessarily have to be a local minimum structure. Subsequently, the cage is filled with a dopant atom of suitable size and electronic structure (to maintain the electron count). Electron transfer and a degree of covalent bonding between the endohedral atom and the outer cage can further enhance the binding energy. The endohedral complex should be a local minimum with no imaginary vibrational frequencies.

is probed through its aromatic properties [168]. The applicability of this design principle was confirmed by gas-phase experimental observations on group IV element cages with endohedral aluminium atoms and also was illustrated by many literature examples of diverse systems.

5. SUMMARY AND OUTLOOK

Proper choice of the constituent atoms provides a handle to tune the properties of mixed clusters. Indeed, physical (optical, electronic, magnetic, etc.) and chemical (reactivity, catalytic activity, etc.) properties not only depend on the cluster size, but they obviously are determined by the choice of constituent atoms. Moreover, several recent examples outlined in this review have demonstrated that tuning the atomic building blocks allows forming specific clusters with strongly enhanced stability. Shell model concepts developed now 20 years ago based on shells of electrons and shells of atoms are playing a key role in this context. If highly symmetric structures with a well-defined geometry coincide with closed shells of delocalized valence electrons of properly chosen constituent atoms, doubly magic species are demonstrated to exist. With still a large number of binary and even more ternary cluster systems to explore, many more sizes and compositions may result in clusters with enhanced stability.

Since in several cases these species were shown to have atom-like characteristics, their use as building blocks for new materials can be envisaged. Therefore, one can expect that engineering the properties of these clusters building blocks by size and composition will lead to the creation of new materials structured on a nanometer scale with tailor-made properties.

REFERENCES

[1] Hart G.W., Encyclopedia of Polyhedra, http://www.georgehart.com.
[2] Marshall D.N., Proc. Soc. Antiq. Scot. 180 (1976/1977) 40.
[3] Artmann B., Am. Math. Monthly 103 (1996) 132–133.
[4] Echt O., Sattler K., Recknagel E., Phys. Rev. Lett. 47 (1981) 1121–1124.
[5] Mackay A.L., Acta Crystallogr. 15 (1962) 916–918.
[6] Knight W.D., Clemenger K., de Heer W.A., Saunders W.A., Chou M.Y., Cohen M.L., Phys. Rev. Lett. 52 (1984) 2141–2143.
[7] Kroto H.W., Heath J.R., O'Brien S.C., Curl R.F., Smalley R.E., Nature 318 (1985) 162–163.
[8] de Heer W.A., Rev. Mod. Phys. 65 (1993) 611–676.
[9] Martin T.P., J. Chem. Phys. 81 (1984) 4426–4432.
[10] Martin T.P., J. Chem. Phys. 80 (1984) 170–175.
[11] Bréchignac C., Cahuzac P., Pflaum R., Roux J.P., J. Chem. Phys. 88 (1988) 3732–3735.
[12] Dietz T.G., Duncan M.A., Powers D.E., Smalley R.E., J. Chem. Phys. 74 (1981) 6511–6512.
[13] Rousset J.L., Cadrot A.M., Aires F.J.C.S., Renouprez A., Mélinon P., Perez A., Pellarin M., Vialle J.L., Broyer M., J. Chem. Phys. 102 (1995) 8574–8585.
[14] Menezes W.J.C., Knickelbein M.B., Chem. Phys. Lett. 183 (1991) 357–362.
[15] Deng H.T., Guo B.C., Kerns K.P., Castleman A.W., Jr., Int. J. Mass Spectrom. Ion Processes 138 (1994) 275–281.
[16] Brock L.R., Knight A.M., Reddic J.E., Pilgrim J.S., Duncan M.A., J. Chem. Phys. 106 (1997) 6268–6278.

[17] Wagner R.L., Vann W.D., Castleman A.W., Rev. Sci. Instrum. 68 (1997) 3010–3013.
[18] Nonose S., Sone Y., Onodera K., Sudo S., Kaya K., J. Phys. Chem. 94 (1990) 2744–2746.
[19] Bouwen W., Thoen P., Vanhoutte F., Bouckaert S., Despa F., Weidele H., Silverans R.E., Lievens P., Rev. Sci. Instrum. 71 (2000) 54–58.
[20] Nakajima A., Hoshino K., Naganuma T., Sone Y., Kaya K., J. Chem. Phys. 95 (1991) 7061–7066.
[21] Hoshino K., Naganuma T., Watanabe K., Konishi Y., Nakajima A., Kaya K., Chem. Phys. Lett. 239 (1995) 369–372.
[22] Koyasu K., Mitsui M., Nakajima A., Kaya K., Chem. Phys. Lett. 358 (2002) 224–230.
[23] Rosche C., Wolf S., Leisner T., Granzer F., Wöste L., IS&T 48th Annual Conference Proceedings, The Society for Imaging Science and Technology, Springfield, Va, USA, 1994, pp. 325–327.
[24] Pewestdorf W., Bonačić-Koutecký V., Koutecký J., J. Chem. Phys. 89 (1988) 5794–5802.
[25] Fantucci P., Bonačić-Koutecký V., Pewestdorf W., Koutecký J., J. Chem. Phys. 91 (1989) 4229–4241.
[26] Schleyer P.v.R., Würthwein E.U., Pople J.A., J. Am. Chem. Soc. 104 (1982) 5839–5841.
[27] Schleyer P.v.R., in: New Horizons of Quantum Chemistry, P.O. Löwdin, B. Pullman (eds), D. Reidel Publishing Company, Dordrecht, Holland, 1983, pp. 95–109.
[28] Röthlisberger U., Andreoni W., Chem. Phys. Lett. 198 (1992) 478–482.
[29] Rapallo A., Rossi G., Ferrando R., Fortunelli A., Curley B.C., Lloyd L.D., Tarbuck G.M., Johnston R.L., J. Chem. Phys. 122 (2006) 194308 (and references therein).
[30] van Hoof T., Hou M., Eur. Phys. J. D 29 (2004) 33–38 (and references therein).
[31] Brack M., Rev. Mod. Phys. 65 (1993) 677–732.
[32] Knight W.D., de Heer W.A., Clemenger K., Saunders W.A., Solid State Commun. 53 (1985) 445–446.
[33] Kappes M.M., Radi P., Schär M., Schumacher E., Chem. Phys. Lett. 119 (1985) 11–16.
[34] Martin T.P., Angew. Chem. 98 (1996) 197–212.
[35] Bréchignac C., Cahuzac P., Roux J.P., Chem. Phys. Lett. 127 (1996) 445–451.
[36] Yeretzian C., J. Phys. Chem. 99 (1995) 123–130.
[37] Yeretzian C., Röthlisberger U., Schumacher E., Chem. Phys. Lett. 237 (1995) 334–338.
[38] Heiz U., Vayloyan A., Schumacher E., Yeretzian C., Stener M., Gisdakis P., Rösch N., J. Chem. Phys. 106 (1996) 5574–5585.
[39] Hoshino K., Watanabe K., Konishi Y., Taguwa T., Nakajima A., Kaya K., Chem. Phys. Lett. 231 (1994) 499–503.
[40] Thomas O.C., Zheng W., Bowen K.H., J. Chem. Phys. 111 (2001) 5514–5519.
[41] Heinebrodt M., Malinowski N., Tast F., Branz W., Billas I.M.L., Martin T.P., J. Chem. Phys. 110 (1999) 9915–9921.
[42] Bouwen W., Vanhoutte F., Despa F., Bouckaert S., Neukermans S., Kuhn L.T., Weidele H., Lievens P., Silverans R.E., Chem. Phys. Lett. 314 (1999) 227–233.
[43] Xing X.P., Tian Z.X., Liu H.T., Tang Z.C., Rapid Commun. Mass Spectrom. 17 (2003) 1411–1415.
[44] Yannouleas C., Jena P., Khanna S.N., Phys. Rev. B 46 (1992) 9751–9760.
[45] Zhang S.B., Cohen M.L., Chou M.Y., Phys. Rev. B 36 (1987) 3455–3458.
[46] Baladron C., Alonso J.A., Physica B 154 (1988) 73–81.
[47] Janssens E., Neukermans S., Lievens P., Curr. Opin. Solid State Mater. Sci. 8 (2004) 185–193.
[48] Martin T.P., Phys. Rep. 273 (1996) 199–241.
[49] Shvartsburg A.A., Jarrold M.F., Chem. Phys. Lett. 317 (2000) 615–618.
[50] Ho K.M., Shvartsburg A.A., Pan B., Lu Z.Y., Wang C.Z., Wacker J.G., Fye J.L., Jarrold M.F., Nature 392 (1998) 582–585.
[51] Wang J., Wang G., Zhao J., Phys. Rev. B 64 (2001) 205411.

[52] Lu J., Nagase S., Chem. Phys. Lett. 372 (2003) 394–398.
[53] Zheng W., Nilles J.M., Radisic D., Bowen K.H., J. Chem. Phys. 122 (2005) 071101.
[54] Kudo H., Wu C.H., Ihle H.R., J. Nucl. Mater. 78 (1978) 380–389.
[55] Kudo H., Nature 355 (1992) 432–434.
[56] Schleyer P.v.R., Würthwein E.U., Kaufmann E., Clark T., J. Am. Chem. Soc. 105 (1983) 5930–5932.
[57] Wu C.H., Chem. Phys. Lett. 139 (1987) 357–359.
[58] Kudo H., Wu C.H., J. Nucl. Mater. 201 (1993) 261–266.
[59] Lievens P., Thoen P., Bouckaert S., Bouwen W., Vanhoutte F., Weidele H., Silverans R., Chem. Phys. Lett. 302 (1999) 571–576.
[60] Würthwein E.U., Schleyer P.v.R., Pople J.A., J. Am. Chem. Soc. 106 (1984) 6973–6978.
[61] Boldyrev A.I., Schleyer P.v.R., J. Am. Chem. Soc. 113 (1991) 9045–9054.
[62] Kudo H., Zmbov K.F., Chem. Phys. Lett. 187 (1991) 77–80.
[63] Hampe O., Koretsky G.M., Gegenheimer M., Huber C., Kappes M.M., Gauss J., J. Chem. Phys. 107 (1997) 7085–7095.
[64] Neukermans S., Janssens E., Tanaka H., Silverans R.E., Lievens P., Yokoyama K., Kudo H., J. Chem. Phys. 119 (2003) 7206–7213.
[65] Guo B.C., Kerns K.P., Castleman A.W., Jr., Science 255 (1991) 1411.
[66] Lievens P., Thoen P., Bouckaert S., Bouwen W., Vanhoutte F., Weidele H., Silverans R., Navarro-Vázquez A., Schleyer P., J. Chem. Phys. 110 (1999) 10316–10329.
[67] Lievens P., Thoen P., Bouckaert S., Bouwen W., Vanhoutte F., Weidele H., Silverans R., Navarro-Vázquez A., Schleyer P., Eur. Phys. J. D 9 (1999) 289–295.
[68] Bergmann T., Limberger H., Martin T.P., Phys. Rev. Lett. 60 (1988) 1767–1770.
[69] Limberger H., Martin T., J. Chem. Phys. 90 (1989) 2979–2991.
[70] Bergmann T., Martin T.P., J. Chem. Phys. 90 (1989) 2848–2855.
[71] Antoine R., Dugourd P., Rayane D., Benichou E., Broyer M., J. Chem. Phys. 107 (1997) 2664–2672.
[72] Brechignac C., Cahuzac P., de Frutos M., Garnier P., Z. Phys. D 42 (1997) 303–307.
[73] Boutou V., Lebault M., Allouche A., Bordas C., Paulig F., Viallon J., Chevaleyre J., Phys. Rev. Lett. 80 (1998) 2817–2820.
[74] Boutou V., Lebault M., Allouche A., Bordas C., Paulig F., Viallon J., Chevaleyre J., J. Chem. Phys. 112 (2000) 6228–6236.
[75] Ziemann P.J., Castleman A.W., J. Chem. Phys. 94 (1991) 718–728.
[76] Martin T.P., Bergmann T., J. Chem. Phys. 90 (1989) 6664–6667.
[77] King F.L., Dunlap B.I., Parent D.C., J. Chem. Phys. 94 (1991) 2578–2587.
[78] Li X., Wang L.S., Phys. Rev. B 65 (2002) 153404.
[79] Kawamata H., Negishi Y., Nakajima A., Kaya K., Chem. Phys. Lett. 337 (2001) 255–262.
[80] Leskiw B.D., Castleman A.W., Chem. Phys. Lett. 316 (2000) 31–36.
[81] Janssens E., Neukermans S., Vanhoutte F., Silverans R.E., Lievens P., Navarro-Vázquez A., Schleyer P.v.R., J. Chem. Phys. 118 (2003) 5862–5871.
[82] Charkin O.P., Charkin D.O., Klimenko N.M., Mebel A.M., Chem. Phys. Lett. 365 (2002) 494–504.
[83] Bergeron D.E., Castleman A.W., Jr., Morisato T., Khanna S.N., Science 304 (2004) 84–87.
[84] Bergeron D.E., Roach P.J., Castleman A.W., Jr., Jones N.O., Khanna S.N., Science 307 (2005) 231–235.
[85] Neukermans S., Janssens E., Tanaka H., Silverans R.E., Lievens P., Phys. Rev. Lett. 90 (2003) 033401.
[86] Janssens E., Tanaka H., Neukermans S., Silverans R.E., Lievens P., New J. Phys. 5 (2003) 46.1–46.10.
[87] Janssens E., Tanaka H., Neukermans S., Silverans R.E., Lievens P., Phys. Rev. B 69 (2004) 085402.

[88] Tanaka H., Neukermans S., Janssens E., Silverans R.E., Lievens P., J. Am. Chem. Soc. 125 (2003) 2862–2863.
[89] Dennler S., Ricardo-Chavez J.L., Morillo J., Pastor G.M., Eur. Phys. J. D 24 (2003) 237–240.
[90] Menezes W.J.C., Knickelbein M.B., Z. Phys. D 26 (1993) 322–324.
[91] Tanaka H., Neukermans S., Janssens E., Silverans R.E., Lievens P., J. Chem. Phys. 119 (2003) 7115–7123.
[92] Torres M.B., Fernandez E.M., Balbas L.C., Phys. Rev. B 71 (2005) 155412.
[93] Li X., Kiran B., Cui L.F., Wang L.S., Phys. Rev. Lett. 95 (2005) 253401.
[94] Furche F., Ahlrichs R., Weis P., Jacob C., Gilb S., Bierweiler T., Kappes M.M., J. Chem. Phys. 117 (2002) 6892–6990.
[95] Häkkinen H., Yoon B., Landman U., Li X., Zhai H.J., Wang L.S., J. Phys. Chem. A 107 (2003) 6168–6175.
[96] Pyykkö P., Angew. Chem. Int. Ed. 43 (2004) 4412–4456.
[97] Corti C.W., Gold Bull. 37 (2004) 12–19.
[98] Pyykkö P., Runeberg N., Angew. Chem. Int. Ed. 41 (2002) 2174–2176.
[99] Li X., Kiran B., Li J., Zhai H.J., Wang L.S., Angew. Chem. Int. Ed. 41 (2002) 4786–4789.
[100] Autschbach J., Hess B.A., Johansson M.P., Neugebauer J., Patzschke M., Pyykkö P., Reiher M., Sundholm D., Phys. Chem. Chem. Phys. 6 (2004) 11–22.
[101] Manninen K., Pyykkö P., Hakkinnen H., Phys. Chem. Chem. Phys. 7 (2005) 2208–2211.
[102] Laupp M., Strähle J., Angew. Chem. Int. Ed. 33 (1994) 207–209.
[103] Arratia-Pérez R., Hernández-Acevedo L., Chem. Phys. Lett. 303 (1999) 641–648.
[104] Sun Q., Wang Q., Kawazoe Y., Jena P., Eur. Phys. J. D 29 (2004) 231–234.
[105] Fa W., Dong J., J. Chem. Phys. 124 (2006) 114310.
[106] Johansson M.P., Sundholm D., Vaara J., Angew. Chem. Int. Ed. 43 (2004) 2678–2681.
[107] Gao Y., Zeng X.C., J. Am. Chem. Soc. 127 (2005) 3698–3699.
[108] Wang J., Jellinek J., Zhao J., Chen Z., King R.B., Schleyer P.v.R., J. Phys. Chem. A 109 (2005) 9265–9269.
[109] Bulusu S., Li X., Wang L.S., Zeng X.C., Proc. Natl. Acad. Sci. 103 (2006) 8326–8330.
[110] Li J., Li X., Zhai H.J., Wang L.S., Science 299 (2003) 864–867.
[111] Gao Y., Bulusu S., Zeng X.C., J. Am. Chem. Soc. 127 (2005) 15680–15681.
[112] Gao Y., Bulusu S., Zeng X.C., Chem. Phys. Chem. 7 (2006) 2275–2278.
[113] Walter M., Häkkinen. H., Phys. Chem. Chem. Phys. 8 (2006) 5408–5411.
[114] Naumkin F., Phys. Chem. Chem. Phys. 8 (2006) 2539–2545.
[115] Janssens E., Neukermans S., Nguyen H.M.T., Nguyen M.T., Lievens P., Phys. Rev. Lett. 94 (2005) 113401.
[116] Janssens E., Neukermans S., Wang X., Veldeman N., Silverans R.E., Lievens P., Eur. Phys. J. D 34 (2005) 23–27.
[117] Janssens E., Hou X.J., Nguyen M.T., Lievens P., J. Chem. Phys. 124 (2006) 184319.
[118] Janssens E., van Hoof T., Veldeman N., Neukermans S., Hou M., Lievens P., Int. J. Mass Spectrom. 252 (2006) 38–46.
[119] Hou X.J., Janssen E., Lievens P., Nguyen M.T., Chem. Phys. 330 (2006) 365–379.
[120] Sun Q., Gong X.G., Zheng Q.Q., Sun D.Y., Wang G.H., Phys. Rev. B 54 (1996) 10896–10904.
[121] Sun Q., Wang Q., Yu J.Z., Li Z.Q., Wang J.T., Kawazoe Y., J. Phys. I 7 (1997) 1233–1244.
[122] Wang S.Y., Yu J.Z., Mizuseki H., Sun Q., Wang C.Y., Kawazoe Y., Phys. Rev. B 70 (2004) 165413.
[123] Jackson K., Nellermoe B., Chem. Phys. Lett. 254 (1996) 249–256.
[124] Jackson K., Kaxiras E., Pederson M.R., J. Phys. Chem. 98 (1994) 7805–7810.
[125] Beck S.M., J. Chem. Phys. 87 (1987) 4233–4234.
[126] King R.B., Z. Phys. D 18 (1991) 189–191.
[127] Kumar V., Kawazoe Y., Phys. Rev. B 65 (2002) 073404.

[128] Hiura H., Miyazaki T., Kanayama T., Phys. Rev. Lett. 86 (2001) 1733–1736.
[129] Khanna S.N., Rao B.K., Jena P., Nayak S.K., Chem. Phys. Lett. 373 (2003) 433–438.
[130] Khanna S.N., Rao B.K., Jena P., Phys. Rev. Lett. 89 (2002) 016803.
[131] Crabtree R.H., The Organometallic Chemistry of the Transition Metals, 3rd edition, Wiley, New York, 2001.
[132] Koyasu K., Akutsu M., Mitsui M., Nakajima A., J. Am. Chem. Soc. 127 (2005) 4998–4999.
[133] Jackson K., Nellermoe B., Chem. Phys. Lett. 254 (1996) 249–256.
[134] Hagelberg F., Yanov I., Leszczynski J., J. Mol. Struct. 487 (1999) 183–192.
[135] Kumar V., Kawazoe Y., Phys. Rev. Lett. 87 (2001) 045503.
[136] Xiao C., Hagelberg F., Lester W.A., Phys. Rev. B 66 (2002) 075425.
[137] Hagelberg F., Xiao C., Lester W.A., Phys. Rev. B 67 (2003) 035426.
[138] Sen P., Mitas L., Phys. Rev. B 68 (2003) 155404.
[139] Miyazaki T., Hiura H., Kanayama T., Phys. Rev. B 66 (2002) 121403.
[140] Kumar V., Majumder C., Kawazoe Y., Chem. Phys. Lett. 363 (2002) 319–322.
[141] Khanna S.N., Rao B.K., Jena P., Phys. Rev. Lett. 89 (2002) 016803.
[142] Lu J., Nagase S., Phys. Rev. Lett. 90 (2003) 115506.
[143] Kumar V., Briere T.M., Kawazoe Y., Phys. Rev. B 68 (2003) 155412.
[144] Kumar V., Comp. Mat. Sci. 30 (2004) 260–268.
[145] Majumder C., Kulshreshtha S.K., Phys. Rev. B 70 (2004) 245426.
[146] Kawamura H., Kumar V., Kawazoe Y., Phys. Rev. B 70 (2004) 245433.
[147] Kawamura H., Kumar V., Kawazoe Y., Phys. Rev. B 71 (2005) 075423.
[148] Singh A.K., Kumar V., Kawazoe Y., Phys. Rev. B 71 (2005) 115429.
[149] Kumar V., Kawazoe Y., Appl. Phys. Lett. 80 (2002) 859–861.
[150] Kumar V., Kawazoe Y., Phys. Rev. Lett. 88 (2002) 235504.
[151] Kumar V., Kawazoe Y., Appl. Phys. Lett. 83 (2003) 2677–2679.
[152] Kumar V., Eur. Phys. J. D 24 (2003) 227–232.
[153] Kumar V., Singh A.K., Kawazoe Y., Nano Lett. 4 (2004) 677–681.
[154] Kumar V., Comp. Mat. Sci. 36 (2006) 1–11.
[155] Beck S.M., J. Chem. Phys. 90 (1989) 6306–6312.
[156] Hiura H., Miyazaki T., Kanayama T., Phys. Rev. Lett. 86 (2001) 1733–1736.
[157] Ohara M., Koyasu K., Nakajima A., Kaya K., Chem. Phys. Lett. 371 (2003) 490–497.
[158] Zhang X., Tang Z., Gao Z., Rapid Commun. Mass Spectrom. 17 (2003) 621–626.
[159] Zhang G. Li X., Xing X., Zhao X., Tang Z., Gao Z., Rapid Commun. Mass Spectrom. 15 (2001) 2399–2403.
[160] Neukermans S., Janssens E., Chen Z.F., Silverans R.E., Schleyer P.v.R., Lievens P., Phys. Rev. Lett. 92 (2004) 163401.
[161] Esenturk E.N., Fettinger J., Lam Y.F., Eichhorn B., Angew. Chem. Int. Ed. 43 (2004) 2132–2134.
[162] Chen Z., Neukermans S., Wang X., Janssens E., Zhou Z., Silverans R.E., King R.B., Schleyer P.v.R., Lievens P., J. Am. Chem. Soc. 128 (2006) 12829–12834.
[163] Esenturk E.N., Fettinger J., Eichhorn B., J. Am. Chem. Soc. 128 (2006) 9178–9186.
[164] Cui L.F., Huang X., Wang L.M., Li J., Wang L.S., J. Phys. Chem. A 110 (2006) 10169–10172.
[165] Cui L.F., Huang X., Wang L.M., Zubarev D.Y., Boldyrev A.I., Li J., Wang L.S., J. Am. Chem. Soc. 128 (2006) 8390–8391.
[166] Chen D.L., Tian W.Q., Lu W.C., Sun C.C., J. Chem. Phys. 124 (2006) 154313.
[167] Neukermans S., Wang X., Veldeman N., Janssens E., Silverans R.E., Lievens P., Int. J. Mass Spectrom. 252 (2006) 145–150.
[168] Chen Z., Wannere C.S., Corminboeuf C., Puchta R., Schleyer P.v.R., Chem. Rev. 105 (2005) 3842–3888.

This page intentionally left blank

Chapter 7

Computational electron spectroscopy of gas-phase metal clusters

Julius Jellinek* **and Paulo H. Acioli†**

Chemistry Division, Argonne National Laboratory, Argonne, IL 60439, USA

1. INTRODUCTION

The emergence of the field of atomic and molecular clusters about three decades ago can be traced to the desire to understand fundamental properties of the condensed phase of matter at atomic and/or molecular level. Clusters of atoms and molecules were initially viewed and used as convenient paradigmatic systems for microscopic explorations of surface and bulk properties of solids and liquids. This initial stage, however, soon gave way to the realization that clusters, even those of larger sizes, may possess features and properties that are very different from the attributes of either their constituent atoms and molecules or the corresponding bulk matter. Often these properties are quite unique, and they change with the size of the clusters in a non-monotonic and unexpected manner. For example, clusters of nominally metallic elements may not possess metallic attributes at all. These attributes then grow in as the clusters grow in size. The chemical reactivity of clusters may change orders of magnitude as a consequence of changing the number of atoms in them just by one. Clusters of elements that are chemically inert in bulk quantities (e.g., gold) may exhibit unprecedented low-temperature chemical activity and selectivity. Clusters of nonmagnetic materials may possess unusual magnetic features, which show strong size variations. The optical properties of clusters are also quite unique and distinctly size specific.

Because of their applied potential, clusters became of central interest to many technologies. The expectation was (and is) that they will open new avenues not only for optimization of existing technologies, but also for formulation of principally new, even revolutionary ones. The current developments in various areas of nanoscience and nanotechnology represent, at least in part, realization of the anticipated revolution. The continued role of cluster science in this revolution is to provide the microscopic

†Permanent address: Department of Physics, Northeastern Illinois University, Chicago, IL 60625, USA

The Chemical Physics of Solid Surfaces, Volume 12
ISSN: 1571-0785
DOI: 10.1016/S1571-0785(07)12007-1

*Corresponding author.
E-mail: jellinek@anl.gov

foundation and the fundamental understanding underlying the broad field of nanosystems and nanophenomena.

The main objective of cluster studies is to furnish an understanding and characterization of various physical and chemical properties of finite systems as a function of their size and composition. The properties of central interest include electron energy spectra and electronic densities of states. These play a particularly important role as they define many other fundamental characteristics (e.g., structural, dielectric, magnetic, optical, and chemical) of any system, be it an atom, molecule, cluster, or extended object. Therefore, providing an understanding and a description of how the electronic properties of an element, or mixture of elements, evolve from those of its (their) atom(s) to those of the corresponding bulk matter is a task of paramount importance. Clusters are the natural ''laboratories'' to undertake this task.

Because of their broad technological relevance and extra cognitive interest, which stems from their particularly complex nature, metal clusters constitute an area of their own [1]. The goal of understanding and characterizing the size-evolution of the electronic features of metal clusters and the nature of bonding in them is both tantalizing and challenging. Experimentally, photoelectron spectroscopy (PES) emerged [2] as a particularly powerful tool for interrogation of electronic properties as a function of cluster size. PES yields spectra of electron binding energies (EBEs), which contain a wealth of information on the size, structure, composition, and charge state of systems. Most of this information, however, cannot be extracted from the measurements alone. For example, questions such as – what is the correlation between a structure of a cluster and its measured EBE spectrum?; why do the spectra change with the cluster size the way they do?; and what are the fundamental mechanisms underlying the size-variability of the spectra? – cannot be answered (at least not at present) by the experiments. These questions can be addressed through theoretical analyses. A prerequisite of such analyses is the ability to compute accurately and efficiently EBE spectra of systems of interest. In principle, one could compute these spectra using various techniques of quantum chemistry. For metallic systems, however, these techniques, especially those of higher accuracy, become impractical, except possibly for the smallest clusters of simple metals. An alternative approach that emerged as the tool of choice in studies of metallic (and many other) systems, both finite and extended, is the density functional theory (DFT). DFT proved powerful in characterizing total energies, structural features, and a host of other properties. However, it is not appropriate, at least not in its most commonly used Kohn–Sham (KS) formulation, for description of single-electron properties (a possible exception is the case of the highest occupied molecular orbital (HOMO)). The main reason for this is that the KS single-particle characteristics (eigenenergies and eigenfunctions) correspond to auxiliary quasiparticles, rather than real electrons. As a consequence, the binding energies of these quasiparticles have to be corrected to convert them into the binding energies of the corresponding electrons.

In this article we give a brief description of a DFT-based computational electron spectroscopy scheme, which incorporates a new correction technique we have formulated recently. We present results of the application of this scheme to metal clusters of different elements and sizes and show how the analyses of these results allow one to unravel the true meaning of and the reasons for the size-driven changes in EBE spectra observed in PES experiments. We also illustrate how by combining results of

high-quality computations with data obtained in high-accuracy measurements one can use EBE spectra as a rich source of information on properties of systems and phenomena they exhibit.

The scheme for conversion of the KS eigenenergies into EBEs is outlined in the next section. The details of the computational methodology are sketched in Section 3. In Section 4, we present and analyze results for magnesium clusters. The analysis includes size, structure, and charge-state effects, as well as a discussion of the phenomenon of size-induced transition to metallicity. Results on structural and electronic properties of aluminum clusters are presented in Section 5. The discussion here includes a new analysis that allows for identification of the separate roles of the size-driven changes in the structure and symmetry of a cluster, on the one hand, and in its number of electrons, on the other, as parameters responsible for the size-evolution of its EBE spectrum (or, more precisely, spectra). We conclude with a summary in Section 6.

2. CONVERTING KOHN–SHAM EIGENENERGIES INTO ELECTRON BINDING ENERGIES

As mentioned above, in order to use the computationally efficient DFT (we restrict our consideration here to the time-independent formalism) in studies of EBE spectra, one has to have a procedure for converting the KS single-particle eigenenergies into EBEs. A variety of such procedures have been formulated in the past, however they either are specific to a given implementation of DFT (e.g., the local density approximation), use an a priori orbital-independent recipe, or involve elements incompatible with DFT as a ground-state theory (see Ref. [3] for a brief critical review). Here we outline the main elements of a new scheme we have formulated recently [3], which is free from the mentioned deficiencies (cf. also Ref. [4]).

The main idea behind this scheme is that the binding energy of an arbitrary Mth electron of a nominally N-electron system, $1 \leqslant M \leqslant N$, can be computed rigorously within any version of DFT when this electron is the most external one; any electron can be made the most external by removing all the electrons "above" it. The binding energy $\mathrm{BE}_{\mathrm{HOMO}}(M) \equiv \mathrm{BE}_M(M)$ of the "top" ("HOMO") Mth electron can be computed as

$$\mathrm{BE}_{\mathrm{HOMO}}(M) = E(M-1) - E(M) \tag{1}$$

where $E(K)$ is the DFT-defined ground-state total energy of the system with K electrons. The correction $\Delta_{\mathrm{HOMO}}(M) \equiv \Delta_M(M)$ that converts the negative of the top (HOMO), Mth KS eigenenergy $\varepsilon_{\mathrm{HOMO}}(M) \equiv \varepsilon_M(M)$ of the M-electron system into the binding energy of the Mth electron is then defined as

$$\Delta_{\mathrm{HOMO}}(M) = \mathrm{BE}_{\mathrm{HOMO}}(M) - (-\varepsilon_{\mathrm{HOMO}}(M)) \tag{2}$$

Our ultimate objective is the correction term $\Delta_M(N)$ that converts the negative of an arbitrary Mth KS eigenenergy $\varepsilon_M(N)$ of an N-electron system into the binding energy of the Mth electron in the N-electron system. The recipe for computing $\Delta_M(N)$ should take into account the shift in the value of the Mth KS eigenenergy from $\varepsilon_M(M)$, for which the correction term is defined by Eq. (2), to $\varepsilon_M(N)$ as the total charge of the system is increased from M to N.

Assume that the values of $\Delta_K(K) = \Delta_{\mathrm{HOMO}}(K)$ have been obtained as defined by Eqs. (1) and (2) for all $K = M, M+1, \ldots, N$. Our prescription for computation of the correction $\Delta_M(M+1)$ that converts the negative of $\varepsilon_M(M+1)$ into the binding energy of the Mth electron in the $M+1$-electron system,

$$\mathrm{BE}_M(M+1) = -\varepsilon_M(M+1) + \Delta_M(M+1) \tag{3}$$

is

$$\Delta_M(M+1) = \Delta_M(M) + [\Delta_{M+1}(M+1) - \Delta_M(M)]\alpha_M(M+1) \tag{4}$$

where

$$\alpha_M(M+1) = \frac{\varepsilon_M(M+1) - \varepsilon_M(M)}{\varepsilon_{M+1}(M+1) - \varepsilon_M(M)} \tag{5}$$

The meaning of Eqs. (4) and (5) is transparent. If an increase of the total charge of the system from M to $M+1$ does not shift the value of $\varepsilon_M(M)$, i.e., $\varepsilon_M(M+1) = \varepsilon_M(M)$, then $\Delta_M(M+1) = \Delta_M(M)$. If, on the other hand, $\varepsilon_M(M+1) = \varepsilon_{M+1}(M+1)$, i.e., the Mth and the $M+1$th KS eigenenergies of the $M+1$-electron system are degenerate, then $\Delta_M(M+1) = \Delta_{M+1}(M+1)$. Typically, the value of $\varepsilon_M(M+1)$ is between those of $\varepsilon_M(M)$ and $\varepsilon_{M+1}(M+1)$. In this case, the correction $\Delta_M(M+1)$ is defined by Eq. (4) as a linear in $\alpha_M(M+1)$ interpolation between $\Delta_M(M)$ and $\Delta_{M+1}(M+1)$, where $\alpha_M(M+1)$ is given by Eq. (5).

As one adds one more electron to the system, the additive correction $\Delta_{M+1}(M+2)$ that converts the negative of the KS eigenenergy $\varepsilon_{M+1}(M+2)$ into the binding energy of the $M+1$th electron in the $M+2$-electron system is obtained by applying again Eqs. (4) and (5) with the values of all the subscripts and the arguments in the parentheses incremented by 1. The knowledge of $\Delta_M(M+1)$ and $\Delta_{M+1}(M+2)$ allows for computation of the correction $\Delta_M(M+2)$, which is to be added to the negative of the KS eigenenergy $\varepsilon_M(M+2)$ in order to convert it into the binding energy of the Mth electron in the $M+2$-electron system. The correction $\Delta_M(M+2)$ is defined as

$$\Delta_M(M+2) = \Delta_M(M+1) + [\Delta_{M+1}(M+2) - \Delta_M(M+1)]\alpha_M(M+2) \tag{6}$$

where

$$\alpha_M(M+2) = \frac{\varepsilon_M(M+2) - \varepsilon_M(M+1)}{\varepsilon_{M+1}(M+2) - \varepsilon_M(M+1)} \tag{7}$$

Adding successively one electron at a time and repeating each time the procedure described above, one eventually arrives at the sought value of $\Delta_M(N)$.

The general prescription for computation of $\Delta_M(N)$ can be summarized as

$$\Delta_M(N) = \Delta_M(N-1) + [\Delta_{M+1}(N) - \Delta_M(N-1)]\alpha_M(N) \tag{8}$$

where

$$\alpha_M(N) = \frac{\varepsilon_M(N) - \varepsilon_M(N-1)}{\varepsilon_{M+1}(N) - \varepsilon_M(N-1)} \tag{9}$$

The corrections $\Delta_M(N-1)$ and $\Delta_{M+1}(N)$ in the r.h.s. of Eq. (8) are themselves obtained through recursive application of Eqs. (8) and (9), until they are reduced to $\Delta_{\mathrm{HOMO}}(K)$ with $K = M, M+1, \ldots, N$. The corrections $\Delta_{\mathrm{HOMO}}(K)$ are computed using Eq. (2). The KS eigenenergies $\varepsilon_{\mathrm{HOMO}}(K)$ are to be used in Eq. (9) in conjunction with the

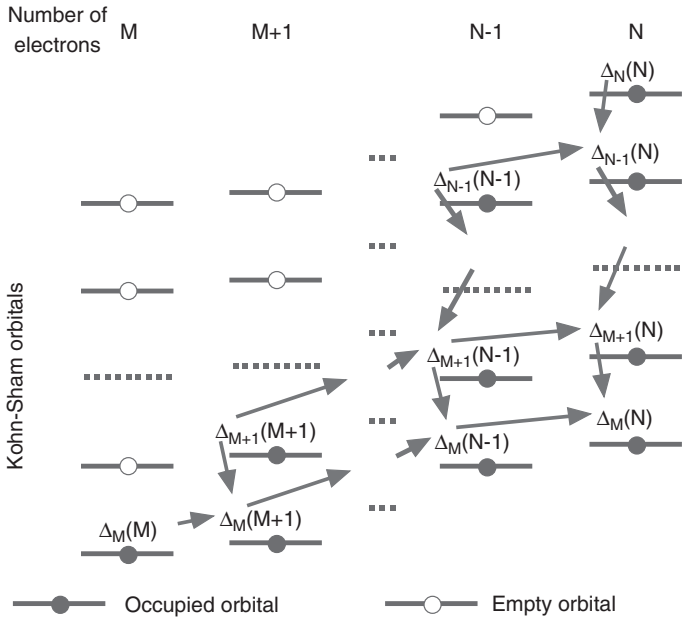

Figure 1: Schematic of the interpolation procedure for computing the corrections $\Delta_K(N)$ (see the text for details).

corrections $\Delta_{\mathrm{HOMO}}(K)$ in the r.h.s. of Eq. (8). As a byproduct, the procedure also yields the values of $\Delta_{M+1}(N)$, $\Delta_{M+2}(N),\ldots,$ $\Delta_{N-1}(N)$. The schematic for the computation of the corrections $\Delta_K(N)$, $K = M,\ M+1,\ldots,\ N$, is shown in Fig. 1. A natural question one can pose with regard to the linear interpolation defined by Eqs. (8) and (9) is how accurate is it on a grid of integer charges. To answer this question, one can consider the total electronic charge of the system as a real-valued continuous variable and replace the grid of integer charges by a more refined grid of real-valued charges. An interpolation of the type of Eqs. (8) and (9) can then be performed on this more refined grid. The quantities necessary for interpolation between noninteger charges can be obtained by performing DFT computations at these charges (DFT formally allows for noninteger total charges). Alternatively, to avoid extra computations, one can generate the necessary quantities at noninteger charges from those computed for integer charges through use of appropriate models; for details see Ref. [3]. If the grid of the real-valued charges is refined enough, the linear interpolation between two neighboring points is justified. In fact, through an appropriate refinement of the grid one can obtain values of the corrections $\Delta_K(N)$, $K = M,\ M+1,\ldots,\ N$, converged within any predefined degree of accuracy. Table 1 lists the degree of convergence of the correction terms for different spin-orbital states of atoms of ten elements as obtained on the grid of integer charges, as well as the number of extra grid points that have to be added between each pair of integer charges to arrive at values of the correction terms converged to 99% or better. As is clear from the table, the use of integer-valued grids is more than adequate taking into account the inaccuracies inherent in practical implementations of DFT due to the approximate nature of the exchange-correlation functionals and other approximations. Table 2 lists the corrections to the eigenenergies

Table 1: Convergence characteristics of the correction terms $\Delta_i(N)$ (see the text for details).

Atom	Spin-orbital State i	Convergence on the Grid of Integer Charges (%)	Number of Extra Grid Points Needed for 99% Convergence
	2s (α)	100	0
Li	1s (β)	92.5	8
	1s (α)	92.5	8
	2s (α,β)	100	0
Be	1s (α,β)	94.2	8
	2p (α)	100	0
	2s (β)	98	1
B	2s (α)	97.7	2
	1s (β)	95.3	4
	1s (α)	95.3	4
	2p (α,α)	100	0
	2s (β)	99.5	0
C	2s (α)	99.8	0
	1s (β)	96.2	4
	1s (α)	96.2	4
	2p (α,α,α)	100	0
	2s (β)	98.8	1
N	2s (α)	99.7	0
	1s (β)	96.8	4
	1s (α)	96.8	4
	2p (β)	100	0
	2p (α)	98	1
	2p (α,α)	95.5	4
O	2s (β)	97.2	2
	2s (α)	98.6	1
	1s (β)	97.2	2
	1s (α)	97.3	2
	2p (β,β)	100	0
	2p (α,α)	99.2	0
	2p (α)	97.3	4
F	2s (β)	97.3	1
	2s (α)	97.9	1
	1s (β)	97.6	2
	1s (α)	97.6	2
	2p (α,β,α,β,α,β)	100	0
Ne	2s (α,β)	98.4	1
	1s (α,β)	97.8	2
	3s (α,β)	100	0
	2p	90.7	8
Mg	(α,β,α,β,α,β)		
	2s (α,β)	97.5	1
	1s (α,β)	98.4	1
	3p (α,β,α,β,α,β)	100	0
	3s (α,β)	98.9	1
Ar	2p	96.0	4
	(α,β,α,β,α,β)		
	2s (α,β)	96.7	4
	1s (α,β)	98.8	1

Table 2: The (negative) KS eigenenergies $\varepsilon_i(N)$, correction terms $\Delta_i(N)$, and electron binding energies $\mathrm{EBE}_{i(j)}$ (all in eV) for ten atoms (see the text for details). The experimental EBE (Exp) are from Ref. [7].

Atom	Spin-Orbital State i				Shell j		Exp
	i	$-\varepsilon_i$	Δ_i	EBE_i	j	EBE_j	
Li	2s (α)	3.27	2.30	5.57	$2s^1$	5.57	5.39
	1s (β)	52.12	13.30	65.42	$1s^2$	65.54	64.84
	1s (α)	52.30	13.35	65.65			
Be	2s (α,β)	5.71	3.43	9.14	$2s^2$	9.14	9.32
	1s (α,β)	106.91	17.59	124.50	$1s^2$	124.50	119.3
B	2p (α)	4.24	4.54	8.78	$2p^1$	8.78	8.30
	2s (β)	8.81	4.66	13.47	$2s^2$	13.94	14.05
	2s (α)	9.73	4.67	14.40			
	1s (β)	180.91	22.15	203.07	$1s^2$	203.21	194
	1s (α)	181.17	22.18	203.35			
C	2p (α,α)	6.13	5.50	11.63	$2p^2$	11.63	11.26
	2s (β)	12.04	5.93	17.97	$2s^2$	19.26	19.39
	2s (α)	14.46	6.08	20.54			
	1s (β)	273.01	26.64	299.65	$1s^2$	300.08	
	1s (α)	273.79	26.71	300.50			
N	2p (α,α,α)	8.29	6.51	14.80	$2p^3$	14.80	14.55
	2s (β)	15.45	7.02	22.47	$2s^2$	24.83	25.41
	2s (α)	19.82	7.37	27.19			
	1s (β)	383.28	31.15	414.43	$1s^2$	415.25	409.93
	1s (α)	384.82	31.25	416.07			
O	2p (β)	7.57	6.63	14.20			
	2p (α)	8.78	6.72	15.50	$2p^4$	16.23	16.53
	2p (α,α)	10.82	6.79	17.61			
	2s (β)	21.63	7.91	29.54	$2s^2$	31.44	32.31
	2s (α)	25.08	8.26	33.34			
	1s (β)	513.88	35.88	549.76	$1s^2$	550.47	543.10
	1s (α)	515.21	35.96	551.17			
F	2p (β,β)	10.26	7.56	17.82			
	2p (α,α)	11.00	7.63	18.63	$2p^5$	18.80	18.67
	2p (α)	13.38	7.70	21.08			
	2s (β)	28.60	8.98	37.58	$2s^2$	38.62	40.19
	2s (α)	30.52	9.14	39.66			
	1s (β)	663.01	40.47	703.48	$1s^2$	703.90	696.71
	1s (α)	663.81	40.51	704.32			
Ne	2p (α,β,α,β,α,β)	13.27	8.56	21.83	$2p^6$	21.83	21.56[a]
	2s (α,β)	36.19	10.09	46.28	$2s^2$	46.28	48.47
	1s (α,β)	830.63	45.04	875.67	$1s^2$	875.67	870.1
Mg	3s (α,β)	4.81	2.91	7.72	$3s^2$	7.72	7.65
	2p (α,β,α,β,α,β)	46.86	9.30	56.16	$2p^6$	56.16	(57.54, 54.8)[a]
	2s (α,β)	79.73	13.26	92.99	$2s^2$	92.99	96.5, 94.0
	1s (α,β)	1258.66	55.89	1314.56	$1s^2$	1314.56	1311.2
Ar	3p (α,β,α,β,α,β)	10.34	5.54	15.88	$3p^6$	15.88	15.57[a]
	3s (α,β)	24.10	6.12	30.22	$3s^2$	30.22	29.24
	2p (α,β,α,β,α,β)	230.16	16.99	247.15	$2p^6$	247.15	248.50[a]
	2s (α,β)	294.94	20.58	315.52	$2s^2$	315.52	326.0
	1s (α,β)	3108.86	88.07	3196.93	$1s^2$	3196.93	3202.9

[a]Binding energy of the $sp_{3/2}$ subshell.

of the KS spin-orbital states computed for the ten atoms using the Becke–Perdew (BP86) [5, 6] exchange-correlation functional and DZVP basis sets. It also illustrates the accuracy of the computed shell EBEs as evaluated against the experimental data. The shells are defined by the principal and orbital angular momentum quantum numbers. The EBEs of the shells are computed as spin-multiplicity-weighted averages of the EBEs corresponding to the different spin states of a given shell. Further details on the computation of quantities presented in Tables 1 and 2, as well as on more general technical points such as how to treat cases when the KS eigenenergies cross as the total electronic charge of the system is increased, can be found Ref. [3]. Here we mention only that the new scheme is general in that it is applicable to any implementation of DFT. It is rigorous as it uses only quantities well defined within DFT as a ground-state theory. It yields orbital-specific corrections to the KS eigenenergies, and finally, it furnishes highly accurate EBEs. The scheme uses as input binding energies of electrons when they occupy the HOMO state. These energies can come either from DFT computations (cf. Eq. (1)), when the chosen version of DFT yields them with sufficient accuracy, or from experiments (see Ref. [3] for further discussion).

3. COMPUTATIONAL METHODOLOGY

The computations were performed using gradient-corrected versions of DFT as implemented in the Gaussian-98 package [8]. The systems studied included magnesium and aluminum clusters. The choice of the exchange-correlation functionals and the basis sets/pseudopotentials was guided by extensive tests. For magnesium, these were performed on Mg_n, $n = 1$–4, using available quantum chemistry and experimental results as benchmark data. A variety of functionals (BP86, BPW91, B3LYP, and MPW1PW91) were tested in all-electron computations with the 6-31G* basis set [8]. The results of these tests together with the benchmark data are listed in Table 3. As is clear from the table, the BP86 functional is the best choice for magnesium. To make the

Table 3: Comparison of all-electron DFT (BP86, BPW91, and B3LYP) results with those of earlier ab initio (CCSD(T) and MP2-R12) and experimental (Exp) studies (see the text for details). The MPW1PW91 functional yields results similar to those of BPW91. IP is the ionization potential, EA is the electron affinity, r_e is the equilibrium interatomic distance, and D_e is the dissociation energy.

System	Property	BP86	BPW91	B3LYP	CCSD(T)	MP2-R12	Exp
Mg	*IP (eV)*	7.731	7.529	7.751			7.646[d]
	EA (eV)	<0	<0	<0			Unstable
Mg_2	R_e (Å)	3.562	3.527	3.919		3.891[c]	3.891[e]
	D_e (eV)	0.091	0.099	0.016		0.057[c]	0.049[e]
Mg_3 (D_{3h})	r_e (Å)	3.295	3.275	3.480	3.387[a]	3.387[c]	
	D_e (eV)	0.41	0.46	0.13	0.25[a]	0.33[c]	
Mg_4 (T_d)	R_e (Å)	3.103	3.094	3.180	3.110[a] 3.103[b]	3.110[c]	
	D_e (eV)	1.21	1.33	0.55	1.04[a] 1.14[b]	1.37[c]	

[a]Ref. [11].
[b]Ref. [12].
[c]Ref. [13].
[d]Ref. [7].
[e]Ref. [14].

computations more efficient, the [Ne] cores of the Mg atoms were represented by the Wadt–Hay (WH) pseudopotential [9]. The remaining two 3s electrons of each atom, as well as the extra electron in the case of the anionic clusters (see below), were described by a (21|21) contracted Gaussian basis set. Of the two pseudopotentials tested with the BP86 functional, the WH and the "Stuttgart" [10], the former was selected based on its slightly better performance as judged by comparison with data obtained in the all-electron treatments. For aluminum, we used the BPW91 exchange-correlation functional and a DFT-optimized all-electron contracted Gaussian basis set of the type (73111/6111/1). The BPW91 functional was chosen based on tests performed on Al and Al_2.

The restricted and unrestricted formalisms were utilized in the cases of closed-shell and open-shell systems, respectively. The equilibrium structures of the clusters were obtained using gradient-based techniques. A variety of initial guess configurations were considered for each cluster size. The optimizations were carried out over all the degrees of freedom. Normal mode analysis was applied to every stationary configuration obtained to separate structures that are in stable equilibria from those that correspond to saddle points of the corresponding potential energy surfaces. The correction scheme of Section 2 implemented on the grid of integer charges was applied to the KS eigenenergies to convert them into the EBE spectra of the clusters. These spectra were then analyzed as a function of cluster size, structure, and charge state.

4. MAGNESIUM CLUSTERS: RESULTS AND DISCUSSION

The computations for Mg_n covered the size range of $n = 2$–22 and were performed for both the neutral and the anionic charge states of the clusters.

4.1. Structures

The most stable structural forms of Mg_n and Mg_n^- as obtained in our computations [15, 16] are shown in Figs. 2 and 3, respectively. For the most part, the lowest energy isomers of the neutral Mg_n agree with, or are close to, those found in earlier computational studies [17–20]. Mg_{15} and Mg_{16} are exceptions: their most stable forms shown in Fig. 2 appear to be new. The different lowest energy structures of these clusters identified in Ref. [19] emerge in our computations as well, but as the second isomer (see below). With the exception of Mg_{18}, the preferred spin-multiplicity state of Mg_n, $n = 2$–22, is a singlet. For Mg_{18} it is a triplet.

Only small anionic Mg_n^-, $n = 1$–7, clusters have been considered in earlier theoretical studies [21] (cf. also Ref. [20]). In agreement with the available computational [21] and experimental evidence [22], we find that Mg^- is not a stable species. Our most stable forms of Mg_6^- and Mg_7^- shown in Fig. 3 are different from those found in Ref. [21] – an octahedron for Mg_6^- and a distorted pentagonal bipyramid for Mg_7^-.

These latter structures emerge in our computations as well, but as the second isomer. With the exception of Mg_{18}^-, the preferred spin-multiplicity state of Mg_n^-, $n = 2$–22, is a doublet. For Mg_{18}^- it is a quartet.

Inspection of Figs. 2 and 3 shows that the preferred structural forms of clusters may depend on their charge state: the lowest energy isomers of Mg_n differ from those of Mg_n^- for $n = 6$, 7, 8, 11, 12, 18, and 21. As discussed in the next section, this has an important implication regarding the interpretation of the PES data measured on anionic species [15, 16].

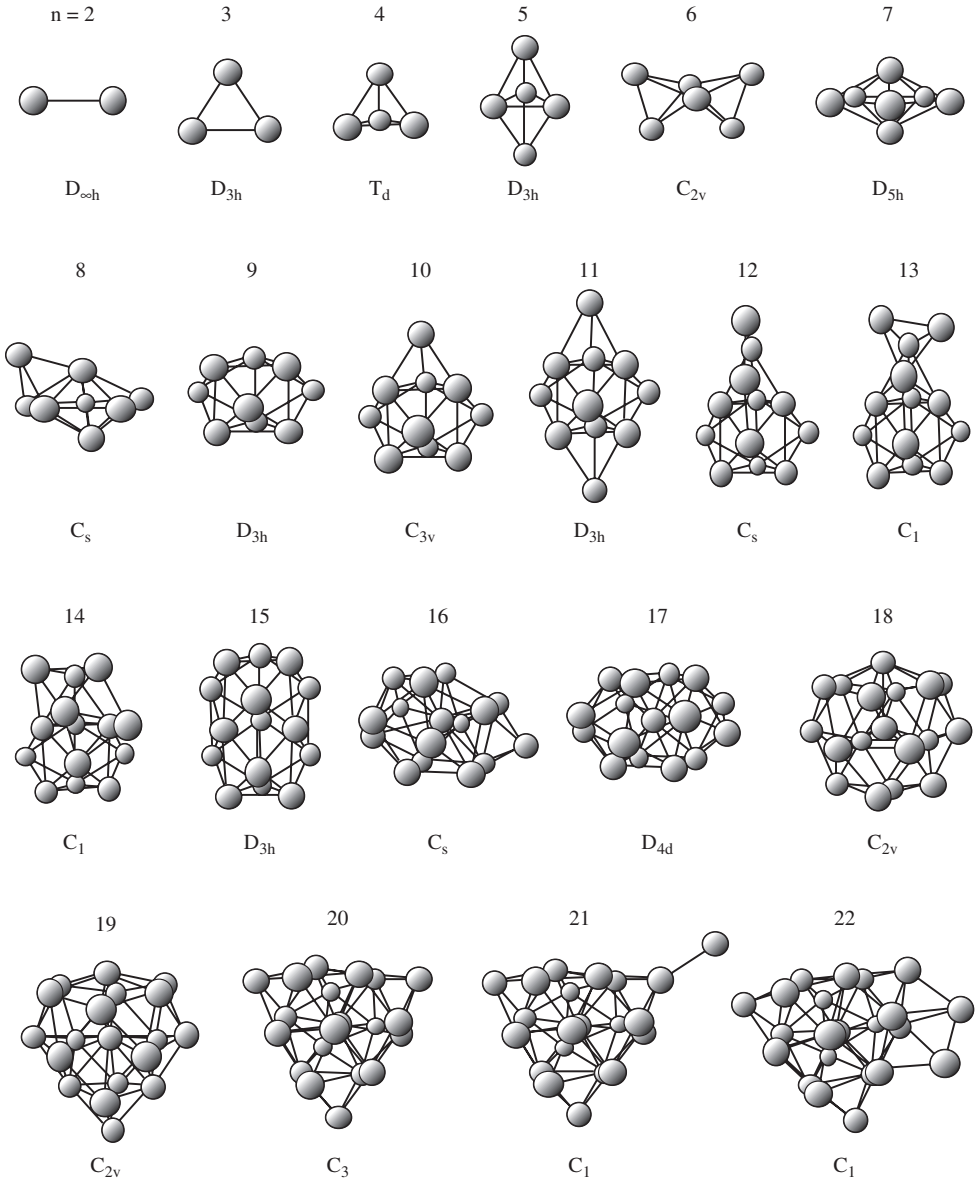

Figure 2: The most stable structures and their symmetries for the neutral Mg_n, $n = 2$–22, clusters.

The charge state of a cluster may affect not only the energy ordering of its structural forms, but also the energy gaps between them. Figure 4 shows the first two fully relaxed isomers of the neutral and anionic Mg_{11}. The most stable conformation of the neutral becomes the second most preferred structure in the case of the anion. The energy gap between the first two isomers of the neutral is twice that between the first two isomers of the anion.

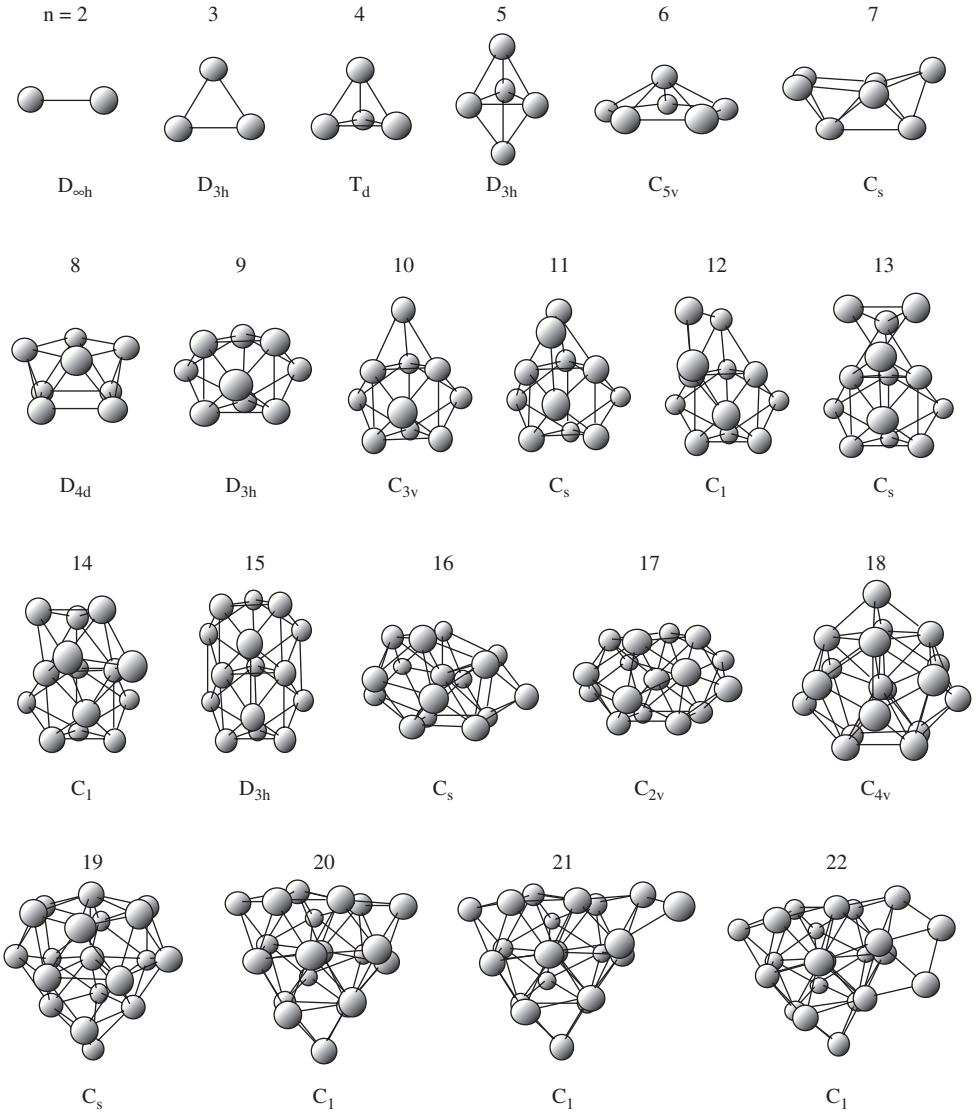

Figure 3: The most stable structures and their symmetries for the anionic Mg_n^-, $n = 2$–22, clusters.

The first three isomers of the neutral and anionic Mg_{16} are shown in Fig. 5. One notices that the ordering of the second (C_{3v}) and the third (C_s) isomers of the neutral is reversed in the case of the anion, and for this cluster the energy gaps between the anionic isomers are larger than those between the neutral isomers. Fig. 6 displays the situation for the first three lowest energy structures of the neutral and anionic Mg_{18}. Here, all three isomers of the anion are very close in energy, whereas in the case of the neutral the second and the third isomers are separated from the most stable structure by large energy gaps. It is the structural form of the third (C_{4v}) isomer of Mg_{18} that is the energetically most preferred conformation of Mg_{18}^-.

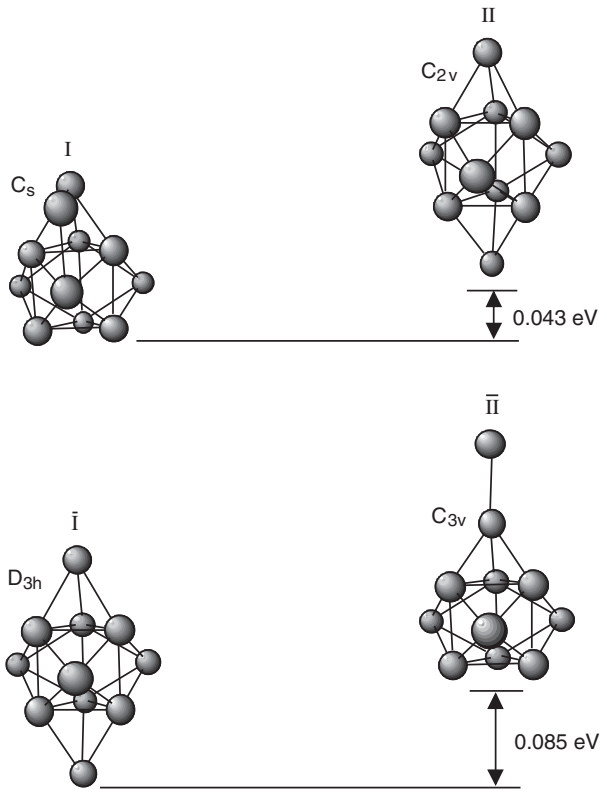

Figure 4: The first two isomers of the anionic Mg_{11}^{-} (Roman numerals) and neutral Mg_{11} (Roman numerals with bars).

The energy changes accompanying the structural relaxations caused by an addition of an electron to isomeric forms of a neutral Mg_n cluster can be assessed from Figs. 7–9. The figures show the configurational energies of the anionic Mg_{11}^{-}, Mg_{16}^{-}, and Mg_{18}^{-}, respectively, computed in the fixed equilibrium structures of both the anionic and the neutral clusters and referred to the energy of the most stable isomer of the anion (of course, the equilibrium structures of the neutrals are nonequilibrium structures in the anionic state). In the case of Mg_{11}^{-}, the relaxation of the nonequilibrium structure $\overline{\text{I}}$ into the equilibrium structure II involves an energy change of 0.112 eV, whereas the seemingly more dramatic relaxation of $\overline{\text{II}}$ into I is accompanied by an energy change of only 0.021 eV. For Mg_{16}^{-}, Fig. 8, the relaxation energies are 0.032 eV (relaxation of $\overline{\text{I}}$ into I), 0.111 eV ($\overline{\text{III}}$ into II), and 0.101 eV ($\overline{\text{II}}$ into III). For Mg_{18}^{-}, Fig. 9, they are 0.078 eV ($\overline{\text{III}}$ into I), 0.056 eV ($\overline{\text{I}}$ into II), and 0.039 eV ($\overline{\text{II}}$ into III).

4.2. Electronic features

Here we present and analyze results on electronic features of magnesium clusters with an emphasis on the effects of the cluster size, structure, and charge state [15, 16, 23]. These results are obtained using the correction scheme described in Section 2. An illustration of the genuine need for corrections and an indication of their magnitude in the case of magnesium clusters are given by the data shown in Table 4. One notices

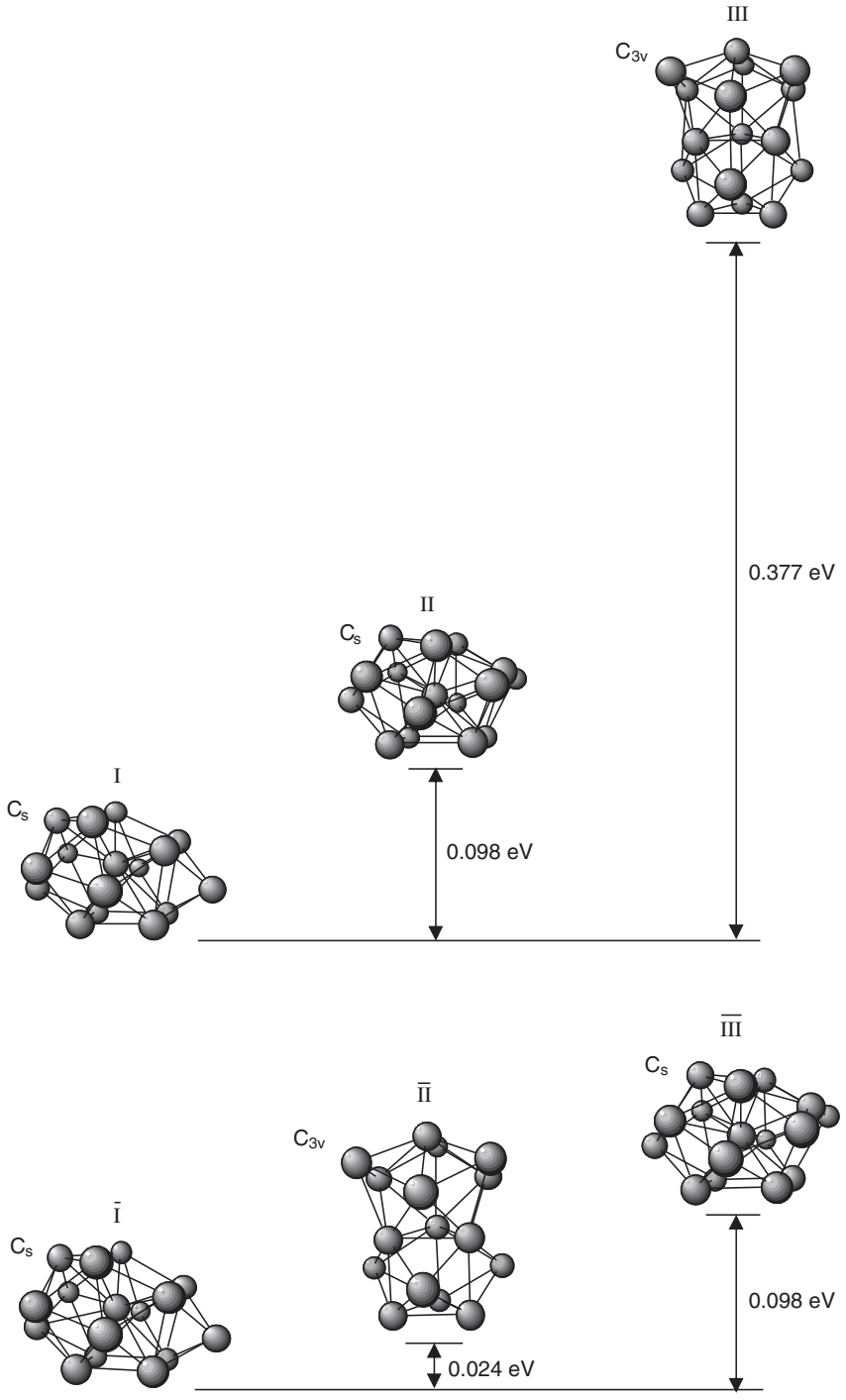

Figure 5: The first two isomers of the anionic Mg_{16}^{-} (Roman numerals) and neutral Mg_{16} (Roman numerals with bars).

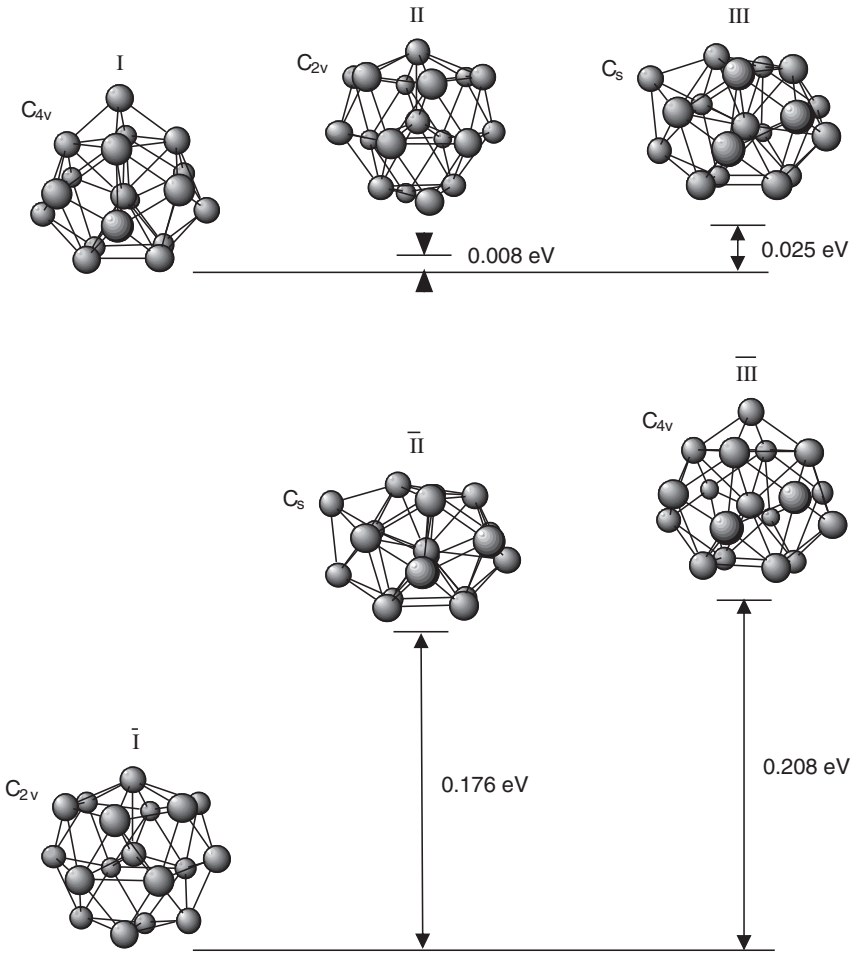

Figure 6: The first two isomers of the anionic Mg_{18}^{-} (Roman numerals) and neutral Mg_{18} (Roman numerals with bars).

that without the correction the KS eigenenergy of the HOMO of the Mg_4^- cluster is positive, which could be misinterpreted as inability of Mg_4 to bind an electron. The corrections represent a substantial fraction of the EBEs, especially for electrons occupying frontier orbitals. The magnitudes of the corrections are orbital-dependent, although the dependence is weak. The corrections presented in the table are converged to within 99% or better; addition of a single extra point between pairs of integers in the interpolation procedure (cf. Section 2) is sufficient for achieving this. The integer grid interpolation used to obtain the results presented below yields corrections converged to within 98% or better.

4.2.1. Role of size and structure

Figure 10 shows the spectrum of the EBEs of Mg_4^- as obtained in our computations [23] together with the experimental PES [24] of this cluster. Our computations predict

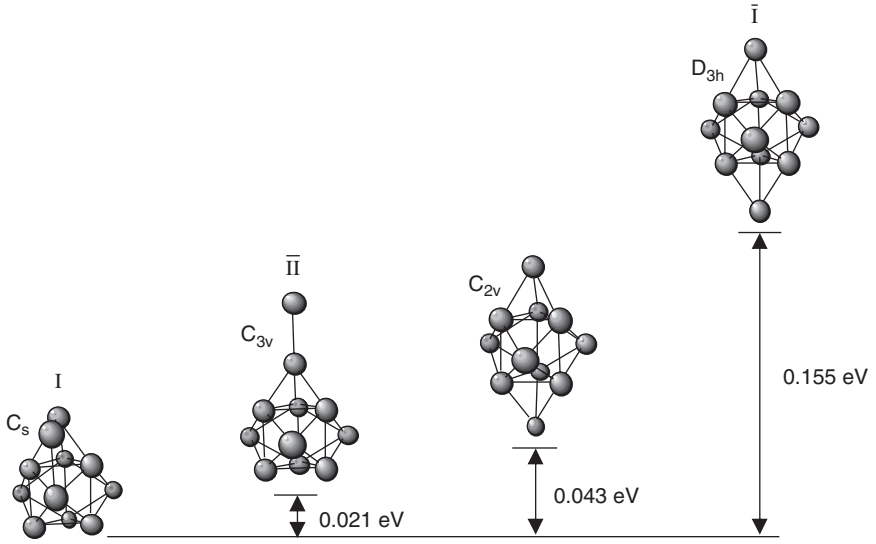

Figure 7: Energy ordering of Mg_{11}^{-} in different structures shown in Fig. 4.

that Mg_4^- forms a single, tetrahedral isomer. The remarkable agreement between the measured and computed data serves as an experimental corroboration of the predicted T_d structure of this cluster.

The spectra of EBE computed for Mg_{11}^{-} in the four configurations shown in Fig. 7 are displayed together with the measured spectrum of this cluster in Fig. 11. Comparison of the computed and measured results leads to the following observations: (1) The pattern of the spectrum computed for the most stable isomer I is in excellent agreement with the shape of the measured spectrum; (2) the computed binding energy of the least bound electron in isomer II falls outside the range of the measured

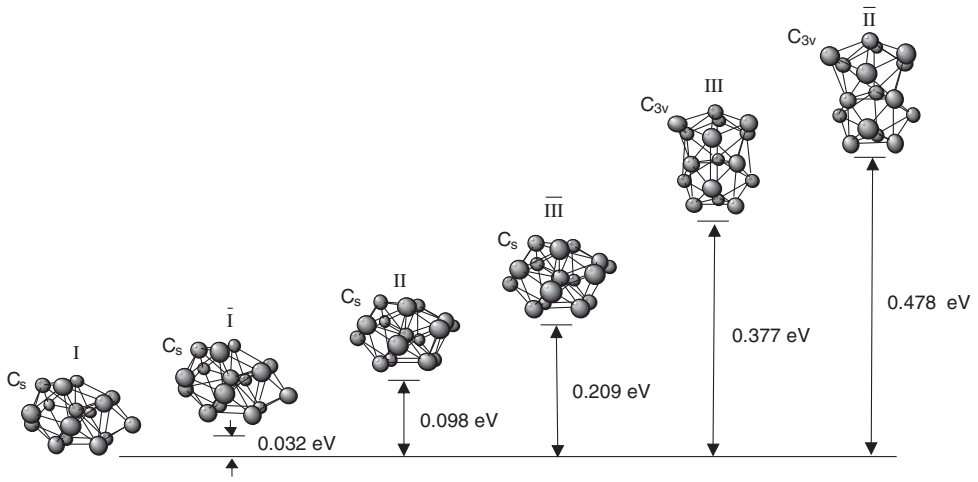

Figure 8: Energy ordering of Mg_{16}^{-} in different structures shown in Fig. 5.

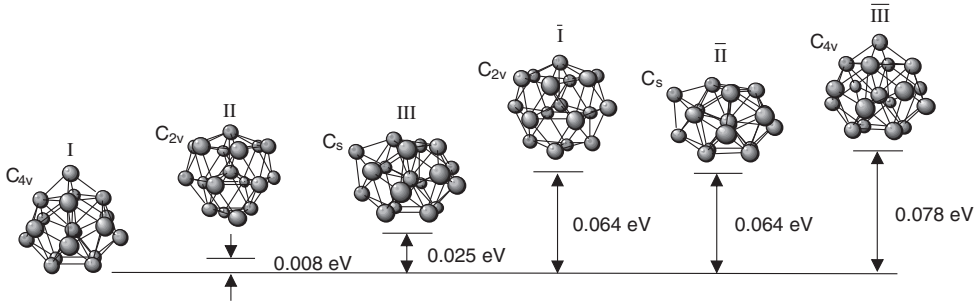

Figure 9: Energy ordering of Mg_{18}^{-} in different structures shown in Fig. 6.

spectrum; (3) the same is true for the structures $\bar{\mathrm{I}}$ and $\overline{\mathrm{II}}$, which are isomeric configurations of the neutral Mg_{11} (Fig. 4). Observation (1) serves as an experimental evidence for the correctness of the predicted most stable structure of Mg_{11}^{-}. Observation (2) indicates that the measured spectrum was taken under conditions that do not support the presence in the beam of the anionic isomer II, at least not in quantities sufficient for detection. An important implication of observation (3) is that photodetachment experiments on anionic species interrogate, in general, electronic properties of the anionic species themselves as defined by their characteristic structure(s), rather than those of their neutral counterparts (see further discussion below). Comparison of spectra computed for structures I and II with those obtained for configurations $\bar{\mathrm{I}}$ and $\overline{\mathrm{II}}$ allows one to assess the differences in EBE patterns of Mg_{11}^{-} when it is considered in its native isomeric structures vs. those that are isomeric forms of the neutral Mg_{11}. Relaxation from structure $\bar{\mathrm{I}}$ to structure II is accompanied only by moderate changes in the spectrum. These changes are considerably more substantial when structure $\overline{\mathrm{II}}$ converts into structure I.

The EBE spectra computed for Mg_{16}^{-} in its different configurations shown in Fig. 8 are displayed together with the experimental spectrum of this cluster in Fig. 12. As in the case of Mg_{11}^{-}, the pattern obtained for the most stable isomer I (three groups of lines) fits the shape of the measured spectrum very well. The pattern for isomer II is different from that of isomer I, but it falls entirely under the measured spectrum. The broad nature of the latter is an indication that the experiment probes both isomers I

Table 4: The (negative) KS eigenenergies ε, correction terms Δ, and electron binding energies EBE (all in eV) for the top five levels of Mg_4^{-}. The numbers in brackets indicate the number of electrons (the occupancy) in the levels. The results of the all-electron treatment are shown to allow for benchmarking of the pseudopotential-based computations.

Level	Pseudopotential			All-electron		
	$-\varepsilon$	Δ	EBE	$-\varepsilon$	Δ	BE
$a_1(\alpha)$ [1]	−0.603	1.614	1.012	−0.663	1.608	0.945
$t_2(\beta)$ [3]	0.841	1.664	2.505	0.877	1.661	2.538
$t_2(\beta)$ [3]	0.984	1.670	2.654	1.012	1.666	2.678
$a_1(\beta)$ [1]	3.612	1.816	5.428	3.465	1.804	5.269
$a_1(\alpha)$ [1]	3.723	1.821	5.544	3.674	1.814	5.488

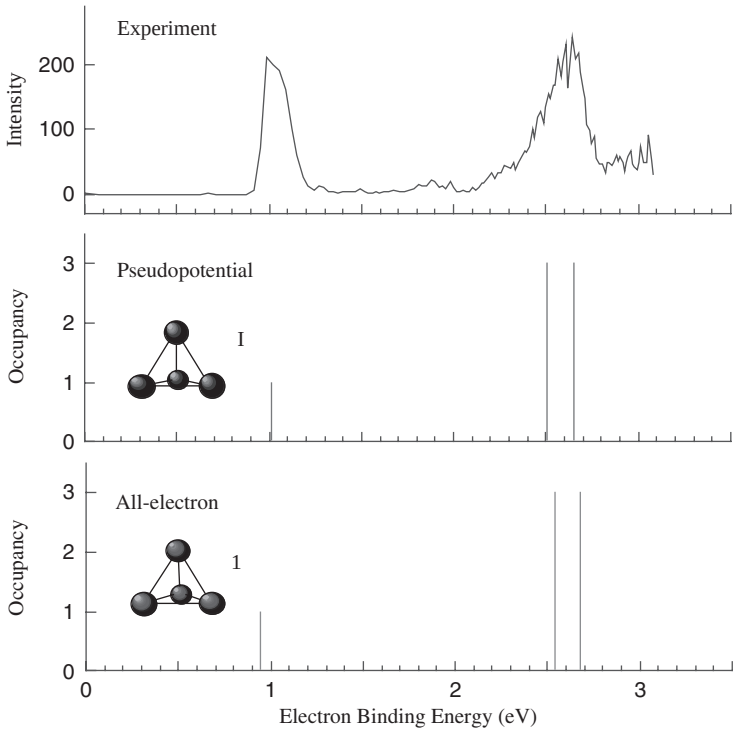

Figure 10: Computed electron binding energies and the occupancy of the corresponding orbitals (vertical bars) in Mg_4^- [23]. The experimental spectrum [24] of the binding energies is also shown (the intensity is in arbitrary units). The accuracy of the pseudopotential-based computations can be assessed through comparison with the results of the all-electron treatment.

and II. This, however, is not the case for isomer III. It can be excluded as a contributor to the measured spectrum because the binding energy of its most external electron is not represented in this spectrum. The changes in the EBEs of Mg_{16}^- that accompany the relaxation of structure $\overline{\text{I}}$ into isomer I are only minor. Relaxations of structure $\overline{\text{III}}$ into isomer II and of structure $\overline{\text{II}}$ into isomer III have more noticeable effects on the corresponding EBE patterns.

Data similar to those in Figs. 11 and 12, but for Mg_{18}^-, are shown in Fig. 13. The spectra computed for the three isomers (I, II, and III; Figs. 6 and 9) of this cluster fall under the measured spectrum, and most probably all three contribute to it. The shifts in the EBEs of Mg_{18}^- accompanying the relaxations of structure $\overline{\text{III}}$ into isomer I and of $\overline{\text{II}}$ into III are moderate. Relaxation of $\overline{\text{I}}$ into II causes a more substantial change in the EBE pattern.

Figures 10–13 illustrate how results of high-accuracy computations provide the tools necessary to explain the features of the measured PES and to correlate these features with size-specific structural characteristics of clusters. A comparative analysis of the EBEs computed for different isomeric forms of an anionic cluster, on the one hand, and its measured spectrum, on the other, allows for identification of and discrimination between the structural forms that have actually been generated under the conditions of the experiment. A quantitative evaluation of the degree of participation

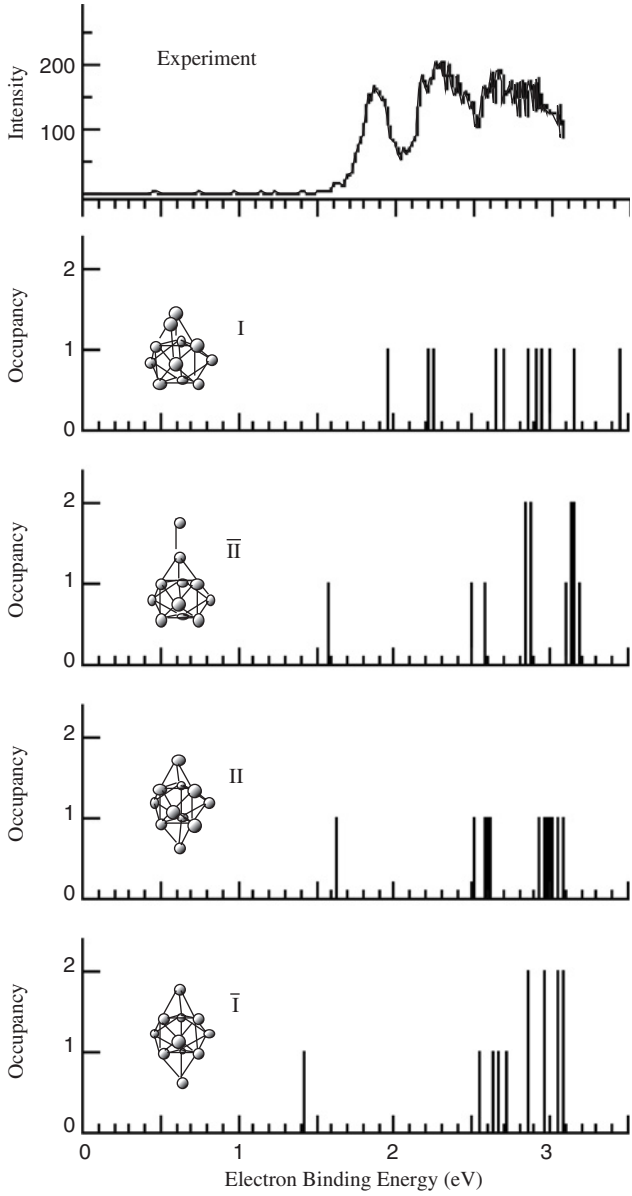

Figure 11: Computed electron binding energies and the occupancy of the corresponding orbitals (vertical bars) in different structures of $Mg_{\bar{1}1}$ shown in Fig. 7 [23]. The experimental spectrum [24] of the binding energies is also shown (the intensity is in arbitrary units).

of different isomers in a spectrum measured at a given temperature requires inclusion of the entropic effect. Computationally, this can be accomplished through evaluation of the densities of states, although such an evaluation remains a nontrivial challenge for anharmonic systems. On the experimental side, the task is to achieve a better calibration of and control over the temperature.

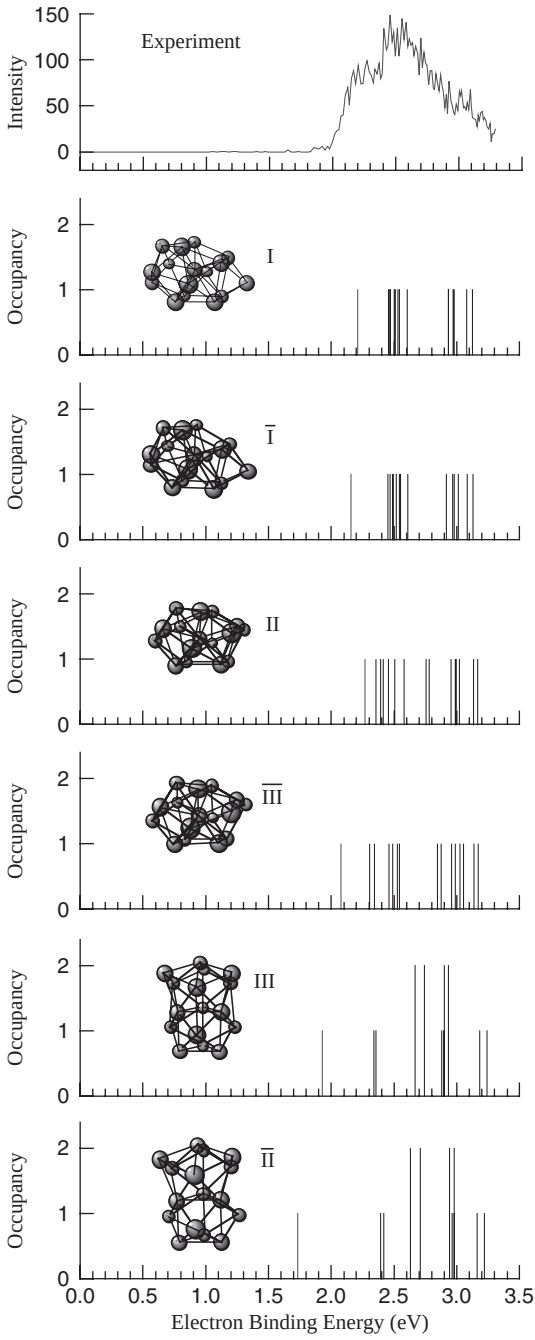

Figure 12: Computed electron binding energies and the occupancy of the corresponding orbitals (vertical bars) in different structures of Mg_{16}^{-} shown in Fig. 8 [23]. The experimental spectrum [24] of the binding energies is also shown (the intensity is in arbitrary units).

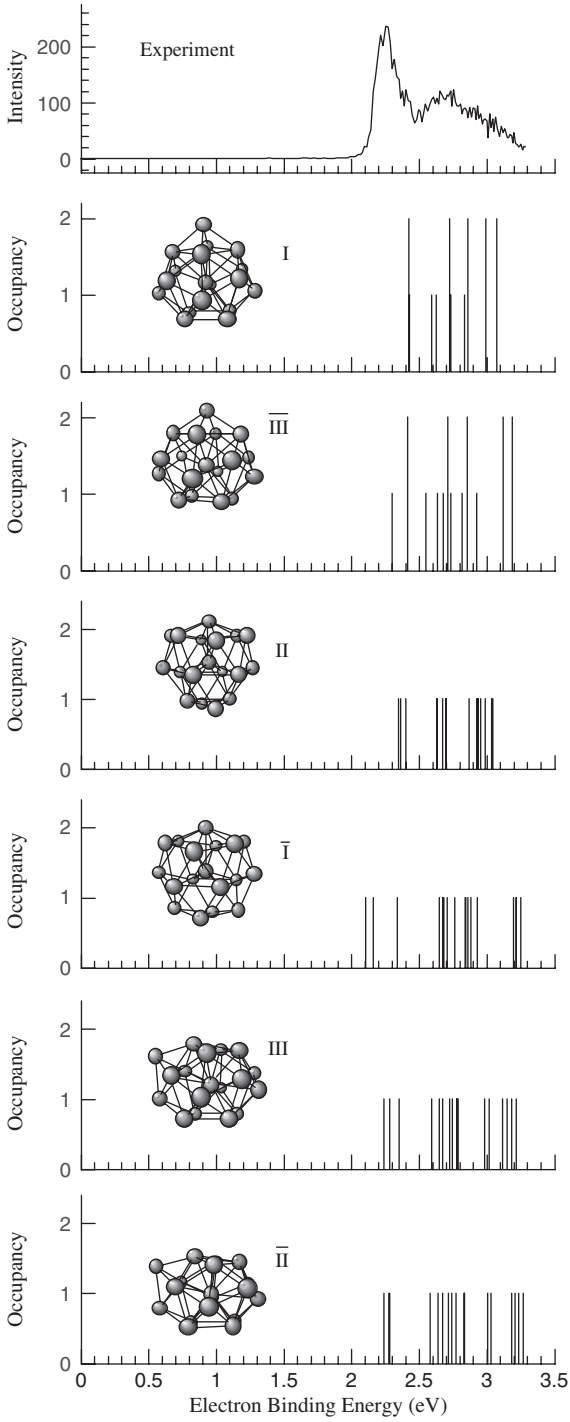

Figure 13: Computed electron binding energies and the occupancy of the corresponding orbitals (vertical bars) in different structures of Mg_{18}^{-} shown in Fig. 9 [23]. The experimental spectrum [24] of the binding energies is also shown (the intensity is in arbitrary units).

4.2.2. Size-induced transition to metallicity: role of the charge state

The size-evolution of cluster properties gives rise to size-driven phenomena. One of the most intriguing among these is the size-induced transition to metallicity exhibited by clusters of elements that are metals in bulk quantities. As mentioned above, small clusters of metallic elements may lack metallic attributes altogether. These attributes then grow in as the clusters grow in size (see, e.g., Ref. [25]). Is the transition to metallicity gradual or abrupt? Are the changes in different properties accompanying the transition monotonic or not? At which size, or size range, does the transition take place? What is (are) the indicator(s) of finite-size metallicity and the transition to it? The answers to these questions are largely unknown. Yet they are central not only from the fundamental but also applied point of view (e.g., in establishing limits of miniaturization in electronic devices).

The transition to metallicity may be gauged by different physical processes and properties, which include electron transport, spectrum of single-electron energy levels, dielectric characteristics, and others. The picture of size-induced transition to metallicity and the size, or size range, at which it takes place will depend on the property chosen to gauge the transition, as different properties evolve with cluster size at different rate. Because of experimental considerations, the property that has been used most often is the spectrum of electron energy levels. It can be probed accurately both experimentally and computationally, as illustrated in the preceding section (the binding energies of electrons are fingerprints of the single-electron energy levels).

The conceptual picture behind the electron energy spectrum of a finite system as an indicator of a metallic or nonmetallic state is based on the following considerations. Bulk metals are systems with a zero gap between the conduction and the valence bands. In finite systems, the energy bands are replaced by discrete energy levels, and the difference between the HOMO and the lowest unoccupied molecular orbital (LUMO) plays the role of the band gap. A finite system with a large HOMO–LUMO gap (as gauged by an appropriate measure, e.g., the value of kT, where k is the Boltzmann constant and T is the temperature) is qualified as nonmetallic. A system with a small (i.e., comparable to or smaller than kT) HOMO–LUMO gap is viewed as metallic. Thus, one can monitor how the HOMO–LUMO gap of a finite system changes with its size and anticipate an effective closure of this gap in metal clusters as their size increases.

The line of thought that underlies the experimental PES studies, which are performed on anionic clusters, proceeds as follows. The extra electron in an anionic species occupies the LUMO of its neutral counterpart. Thus, measuring the binding energies of the two most external electrons in an anionic cluster and evaluating the difference between them one can, neglecting the shifts in the energy levels due to the presence of the extra electron, determine the HOMO–LUMO gap of the neutral cluster (we will see below that, in fact, this may not be the case).

The two elements, for which the size-induced transition to metallicity has been explored most, are mercury [26–31] and magnesium [15–17, 20, 24, 32–34]. Here we present the picture that emerges for magnesium based on the analysis of the EBE spectra computed [15, 16] and measured [24] for its clusters. Figure 14 displays the difference in the binding energies of the two most external electrons in anionic Mg_n^-, $n = 2$–22, as computed in their most stable structures and evaluated from the results of PES measurements (cf. Figs. 10–13). The figure also shows the HOMO–LUMO gap computed for the lowest energy isomers of the neutral Mg_n clusters.

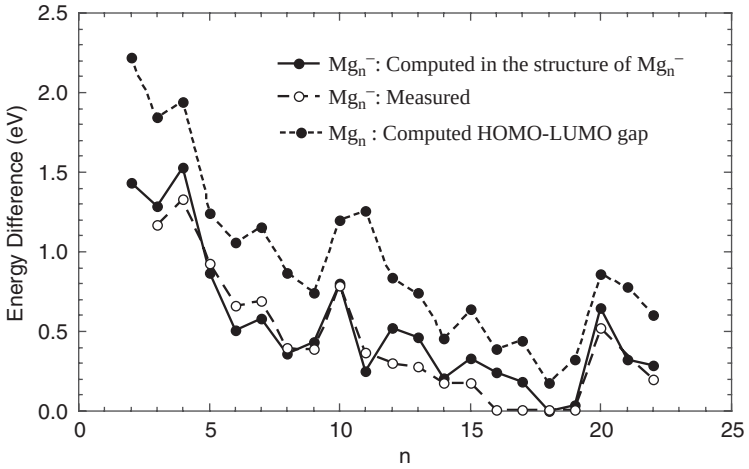

Figure 14: Computed [15, 16] and measured [24] difference in the binding energies of the two most external electrons in anionic Mg_n^- clusters. The HOMO–LUMO gap of the neutral Mg_n [16] is also shown. The computed results correspond to the most stable structures of the clusters.

All three sets of data display an overall, albeit nonmonotonic, decrease in their values as the cluster size increases. The energy differences computed and measured for the anionic clusters are in an essentially quantitative agreement. This, however, is not the case for the HOMO–LUMO gap of the neutral clusters. Not only are its values systematically larger, but they also show peculiar local trends. For example, in going from $n = 10$ to $n = 11$, the graph of the HOMO–LUMO gap turns upward, whereas the two graphs for the anionic clusters turn downward. The clear message of the data in Fig. 14 is that contrary to the line of thought presented above, PES experiments on anionic clusters (more generally, finite anionic systems) probe, in general, the properties of the anionic species themselves and not those of their neutral counterparts. The main issue here is not the shift in the energy levels caused by the extra electron in anionic systems. This is clear from Fig. 15, which shows the graphs of the HOMO–LUMO gap of the neutral Mg_n and the difference in the binding energies of the two most external electrons computed for anionic Mg_n^- frozen in the most stable structures of their neutral counterparts. The two quantities follow the same trend over the entire size range of $n = 2$–22, and the differences in their values are indeed only minor, except for the smallest clusters.

As discussed above, the central reason for the possible major differences in the electronic properties of a cluster in its different charge states is that addition (or withdrawal) of an electron to (from) it may cause a major change in its energetically preferred geometric form. This change, in turn, triggers a restructuring of the electronic energy levels. The geometric and electronic properties are coupled in any system, finite or infinite, and they are both the cause and the consequence of each other. The added sensitivity to this coupling in clusters stems from the fact that they possess many isomeric conformations, which often are energetically competitive. The preferred conformation, therefore, may (and often does) change with the charge state. This has to be taken into account in analyses and interpretation of PES data acquired on anionic clusters.

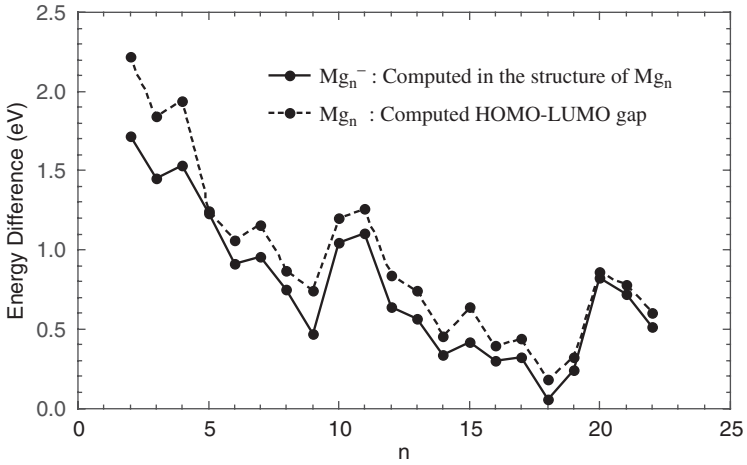

Figure 15: Computed difference in the binding energies of the two most external electrons in anionic Mg_n^- clusters frozen in the most stable structures of their neutral counterparts. The HOMO–LUMO gap of the latter is also shown.

Does the fact that negative photodetachment experiments may not provide information on the HOMO–LUMO gap of finite systems diminish the role of these experiments in studies of the phenomenon of size-induced transition to metallicity? The answer to this question is "no". The source for this answer is in the realization that the size-induced transition to metallicity has many "faces", including the one exhibited by anionic species. The difference in the binding energies of the two most external electrons in anionic systems (which can be measured as a function of size) is as a legitimate finite-size analog of the bulk band gap as the HOMO–LUMO gap of their neutral counterparts. The two quantities approach each other as the systems grow in size and both converge to the bulk band gap in the limit of large sizes.

Although equally legitimate, the neutral and the anionic finite-size analogs of the band gap are different, and they may converge to the bulk limit with different rates. A comprehensive characterization of the size-induced transition to metallicity will have to include all its complementary manifestations, including those presented by different charge states. The computed and measured results for Mg_n^- shown in Fig. 14 display the anionic picture. The overall decrease of the difference between the binding energies of the top two electrons in Mg_n^-, as the cluster grows in size, and the disappearance of this difference at $n = 18$ are consistent with evolution toward a metallic state. It is clear however that what is shown in Fig. 14 is only a stage in this evolution. In fact, the figure indicates that for $n > 18$ the difference between the binding energies becomes nonzero again (see also Ref. [24]). The studies will have to be extended into the range of larger sizes. The central task, however, is to develop a true understanding of what constitutes the finite-size analog (or analogs) of the bulk metallic state. Such an understanding is a pre-requisite for fundamental studies of size-induced transition to metallicity, a phenomenon that is considerably more multifaceted and more complex than the bulk nonmetal-to-metal transition.

5. ALUMINUM CLUSTERS: RESULTS AND DISCUSSION

In this section we present and discuss results on the structure and EBE spectra of Al_n^-, $n = 12$–15. The analysis focuses on the understanding and explanation of the changes in the spectra as a function of cluster size.

The most stable isomers of Al_n^-, $n = 12$–15, as obtained in our computations, are shown in Fig. 16. These are in qualitative agreement with the lowest energy structures found for these clusters in earlier studies [35, 36]. The EBE spectra computed for the configurations of Fig. 16 are displayed together with the measured spectra of Al_n^-, $n = 12$–15, in Fig. 17. The agreement between the two is excellent for all four sizes.

The fact that all the features of the measured spectra are fully reproduced by the patterns of EBEs computed for the most stable isomers of the clusters is a consequence of the low temperature of the experiments [36, 37]. The EBEs computed in Ref. [36] applying a constant shift correction to the KS eigenenergies are close to our results (Fig. 17), which are obtained using the correction scheme of Section 2 [38]. The reason for this is that, as in the case of Mg_n^-, the corrections to the KS eigenenergies of Al_n^- are only weakly orbital-dependent; this weak orbital dependence, however, is not a general rule for clusters – see, for example, Ref. [39].

Perhaps the most striking feature of Fig. 17 is the dramatic changes in the spectra as a function of cluster size. Clusters that differ by only one atom display qualitatively different EBE patterns. For example, the three prominent humps in the spectrum of Al_{12}^- evolve into a single hump with a shoulder in the spectrum of Al_{13}^-. What drives the size-dependent changes in the EBE patterns? Can one correlate these changes with the size-driven variations in the structure, symmetry, and number of electrons of a cluster?

As indicated in Fig. 16, addition of an Al atom changes the C_s symmetry of the lowest energy structure of Al_{12}^- into the I_h symmetry of the most stable isomer of Al_{13}^-. The 13th atom is naturally added to the surface of the C_s Al_{12}^-. In order to analyze the separate roles of the structure and symmetry changes, on the one hand, and of the change in the number of electrons, on the other, one can consider an alternative path from C_s Al_{12}^- to I_h Al_{13}^-. This alternative path is depicted in Fig. 18, which shows the correlation between the KS eigenenergies of Al_{12}^-, Al, and Al_{13}^-. Because of the

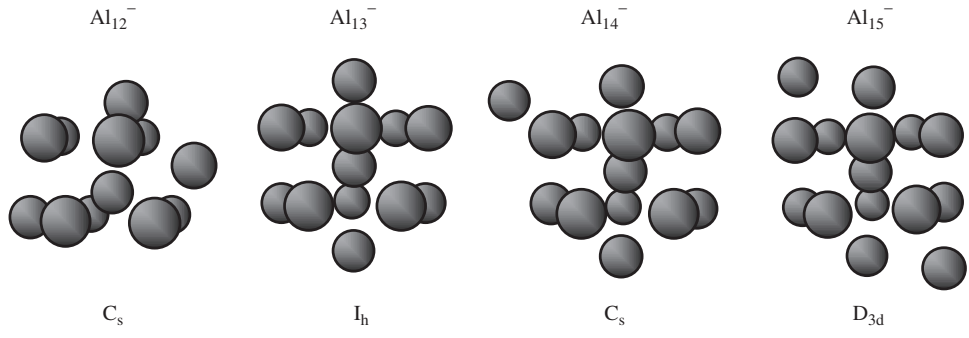

Figure 16: Structure and symmetry of the most stable isomers of Al_n^-, $n = 12$–15, clusters.

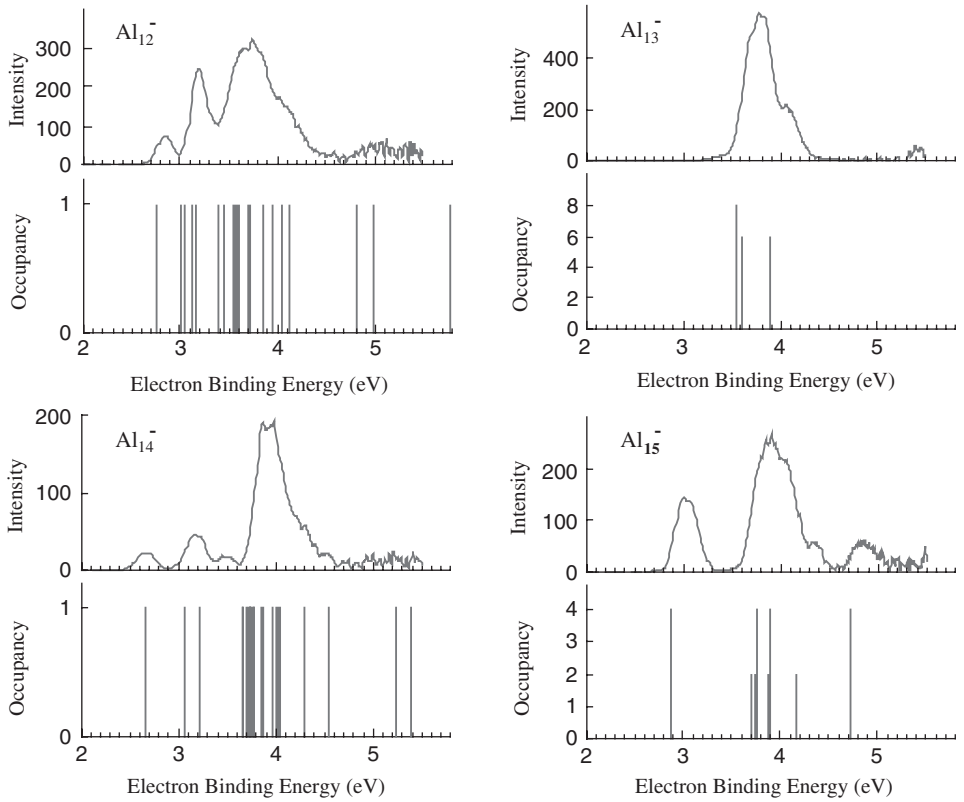

Figure 17: Computed electron binding energies and the occupancy of the corresponding orbitals (vertical bars) for the most stable isomers of Al_n^-, $n = 12$–15 [37]. The experimental spectra (continuous line graphs) [36, 38] are also shown (the intensity is in arbitrary units).

weak orbital dependence of the correction terms for these systems, the patterns of their KS eigenenergies and EBEs mimic each other.

Along the alternative path, one first considers the transformation of the C_s isomer of Al_{12}^- into an I_h cage structure, which is obtained from the I_h isomer of Al_{13}^- by removing its central atom (upon relaxation, the hollow cage with 12 surface Al atoms becomes a genuine, higher energy I_h isomer of Al_{12}^-). As is clear from Fig. 18, this transformation leads to the loss of the second hump in the spectrum of the C_s Al_{12}^-. Next, one considers the consequences of adding an Al atom in the center of the I_h structure of Al_{12}^-. These consequences can be assessed by correlating the eigenenergies of the added atom, computed under the constraints of I_h symmetry, and those of the I_h structure of Al_{12}^- with the eigenenergies of the I_h Al_{13}^-. As exhibited by the figure, the effect of the added electrons brought in by the central atom in the energy range of interest is twofold. First, the HOMO eigenenergy of the I_h Al_{13}^-, which traces the first hump in the spectrum of the C_s Al_{12}^-, shifts downward and joins the manifold of eigenenergies that traces the third hump in the spectrum of the C_s Al_{12}^-. Second, some eigenenergies in this latter manifold shift to deeper levels. The cumulative

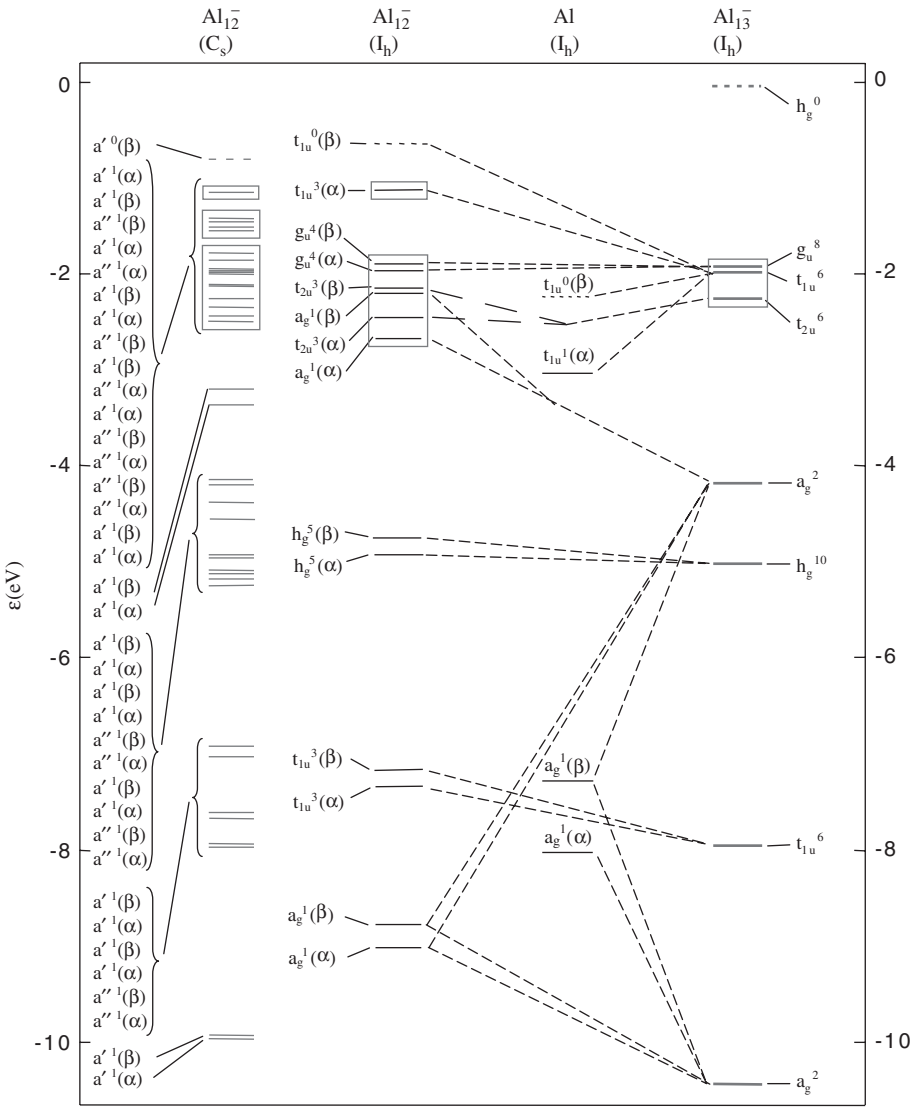

Figure 18: Correlation diagram for the KS eigenenergies of Al_{12}^-, Al, and Al_{13}^-. The eigenenergies for the I_h Al_{12}^- correspond to the unrelaxed structure (see the text for details). The boxes group eigenenergies corresponding to (or tracing) the humps in the measured EBE spectra displayed in Fig. 17.

effect of all the changes in the pattern of the eigenenergies that accompany the described stepwise transformation of a C_s Al_{12}^- into an I_h Al_{13}^- is that the spectrum of the latter exhibits a single, relatively narrow hump in the range of measured energies. Similar arguments can be invoked to explain the evolution of the spectrum of Al_{13}^- into that of Al_{14}^- and, subsequently, Al_{15}^-. The above analysis explains the size-driven changes in EBE spectra in terms of the effects of the changes in the structure, symmetry, and number of electrons of the system. It is general and applicable to any cluster.

6. SUMMARY

In this article we reviewed our recent work on methodology and applications of computational electron spectroscopy. The methodology is based on the DFT of electronic structure combined with a new correction scheme for conversion of the KS eigenenergies into EBEs. The scheme is rigorous in that it uses only ground-state properties that are well defined within DFT. It is robust in that it is applicable to any implementation of DFT. It defines orbital-specific corrections to the (negatives of the) KS eigenenergies. And it yields highly accurate EBEs, provided the (input) binding energies of the individual electrons, when they occupy the HOMO (i.e., the most exposed), are reproduced by the chosen implementation of DFT with sufficient accuracy. One can use the correction scheme even when the latter is not the case utilizing as input measured data on the binding energies of the most exposed electrons in different oxidation states of the system.

The applications are given for gas-phase magnesium and aluminum clusters. We show that the spectra of EBEs computed for the anions of these clusters are in excellent correlation with the corresponding experimental PES data. We demonstrate that these data carry a wealth of information on the material, size, structure, and charge state of clusters (or, more generally, finite systems) and illustrate the role and power of computational electron spectroscopy as a tool for unraveling this information.

We show that the size-driven changes in the EBEs of a system can be correlated with and understood in terms of the effects of the changes in its geometry, symmetry, and number of electrons. We illustrate how the size-dependent peculiarities in the spectra (e.g., the closure of the gap between the EBEs corresponding to frontier orbitals) can be used to study novel and complex size-driven phenomena (e.g., the size-induced transition to metallicity). An important role of computational electron spectroscopy is to identify subtleties in the descriptors of these phenomena that are central for correct understanding and interpretation of the results of measurements. The examples we discussed include the realization that the picture of size-induced transition to metallicity may, and indeed does, depend on the charge state of the system, and that the manifestation of this transition, as probed in PES experiments on anions, represents the anionic, rather than the neutral species, picture.

ACKNOWLEDGMENTS

This work was supported by the Office of Basic Energy Sciences, Division of Chemical Sciences, Geosciences, and Biosciences, U.S. Department of Energy under Contract number DE-AC-02-06CH11357. We thank K.H. Bowen and L.-S. Wang for providing us measured PES data.

REFERENCES

[1] See, e.g., Moskovits M., Annu. Rev. Phys. Chem. 42 (1991) 465; H. Haberland (ed.), Clusters of Atoms and Molecules, Vols. 1 and 2, Springer, Heidelberg, 1994; J. Jellinek (ed.), Theory of Atomic and Molecular Clusters with a Glimpse at Experiments, Springer, Heidelberg, 1999; W. Ekardt (ed.), Metal Clusters, Wiley, New York, 1999; and references therein.

[2] Ng C.-Y. (ed.), Photoionization and Photodetachment, Parts I and II, World Scientific, Singapore, 2000, and references therein.
[3] Jellinek J., Acioli P.H., J. Chem. Phys. 118 (2003) 7783.
[4] Mercero J.M., Matxain J.M., Lopez X., York D.M., Largo A., Erikson L.A., Ugalde J.M., Int. J. Mass Spectrom. 240 (2005) 37.
[5] Becke A.D., Phys. Rev. A 38 (1988) 3098.
[6] Perdew J.P., Phys. Rev. B 33 (1986) 8822.
[7] Lide D.R. (ed.), CRC Handbook of Chemistry and Physics, 82nd edition, CRC, Boca Raton, FL, 2001.
[8] Frisch M.J., Trucks G.W., Schlegel H.B. et al., Gaussian 98, Gaussian Inc, Pittsburgh, 1998.
[9] Wadt W.R., Hay P.J., J. Chem. Phys. 82 (1985) 284.
[10] Fuentealba P., Szentpaly L.V., Preuss H., Stoll H., J. Phys. B 18 (1985) 1287.
[11] Lee T.J., Rendell A.P., Taylor P.R., J. Chem. Phys. 93 (1990) 6636.
[12] Bauschlicher C.W., Jr., Partridge H., Chem. Phys. Lett. 300 (1999) 364.
[13] Klopper W., Almlof J., J. Chem. Phys. 99 (1993) 5167.
[14] Balfour W.J., Douglas A.E., Can. J. Phys. 48 (1970) 901.
[15] Acioli P.H., Jellinek J., Phys. Rev. Lett. 89 (2002) 213402.
[16] Jellinek J., Acioli P.H., J. Phys. Chem. A 106 (2002) 10919; Jellinek J., Acioli P.H., J. Phys. Chem. A 107 (2003) 1610.
[17] Kumar V., Car R., Phys. Rev. B 44 (1991) 8243.
[18] Rothlisberger U., Andreoni W., Giannozzi P., J. Chem. Phys. 96 (1992) 1248.
[19] Köhn A., Weigend F., Alrichs R., Phys. Chem. Chem. Phys. 3 (2001) 711.
[20] Akola J., Rytkonen K., Manninen M., Eur. Phys. J. D 16 (2001) 21.
[21] Reuse F., Khanna S.N., de Coulon V., Buttet J., Phys. Rev. B 41 (1990) 11743.
[22] Hotop H., Lineberger W.C., J. Phys. Chem. Ref. Data 14 (1985) 731.
[23] Acioli P.H., Jellinek J., Eur. Phys. J. D 24 (2003) 27.
[24] Thomas O.C., Zheng W., Xu S., Bowen K.H., Jr., Phys. Rev. Lett. 89 (2002) 213403.
[25] von Issendorff B., Cheshnovsky O., Annu. Rev. Phys. Chem. 56 (2005) 549 and references therein.
[26] Brechignac C., Broyer M., Cahuzac Ph., Delacretaz G., Labastie P., Wöste L., Chem. Phys. Lett. 120 (1985) 559.
[27] Rademann K., Kaiser B., Even U., Hensel F., Phys. Rev. Lett. 59 (1987) 2319.
[28] Brechignac C., Broyer M., Cahuzac P., Delacretaz G., Labastie P., Wolf J.P., Wöste L., Phys. Rev. Lett. 60 (1988) 275.
[29] Garcia M.E., Pastor G.M., Bennemann K.H., Phys. Rev. Lett. 67 (1991) 1142.
[30] Haberland H., von Issendorf B., Yufeng J., Kolar T., Phys. Rev. Lett. 69 (1992) 3212.
[31] Busani R., Folkers M., Cheshnovsky O., Phys. Rev. Lett. 81 (1998) 3836.
[32] Delaly P., Ballone P., Buttet J., Phys. Rev. B 45 (1992) 3838.
[33] Gong X.G., Zheng Q.Q., He Y.Z., Phys. Lett. A 181 (1993) 459.
[34] Diederich T., Döppner T., Braune J., Tiggesbaunker J., Meiwes-Broer K.-H., Phys. Rev. Lett. 86 (2001) 4807.
[35] Khanna S.N., Jena P., Phys. Rev. Lett. 69 (1992) 1664.
[36] Akola J., Manninen M., Hakkinen H., Landman U., Li X., Wang L.-S., Phys. Rev. B 60 (1999) R11297.
[37] Acioli P.H., Jellinek J., to be published.
[38] Li X., Wu H., Wang X.-B., Wang L.-S., Phys. Rev. Lett. 81 (1998) 1909.
[39] Li S., Alemany M.M.G., Chelikowsky J.R., Phys. Rev. B 71 (2005) 165433.

Chapter 8

Vibrational spectroscopy of gas-phase clusters and complexes

Knut R. Asmis, André Fielicke, Gert von Helden and Gerard Meijer*

Fritz-Haber-Institut der Max-Planck-Gesellschaft, Faradayweg 4-6 D14195 Berlin, Germany

1. INTRODUCTION

The successful application of infrared (IR) free electron lasers (FEL) to the vibrational spectroscopy of gas-phase particles during the last decade has had a major impact on the field of cluster science. Here we present an overview of IR experiments utilizing FEL radiation, which are performed at the Free Electron Laser for Infrared eXperiments (FELIX)[1], focusing on size-selected metal-containing clusters. The motivation for performing IR experiments on metal-containing clusters is manifold, ranging from their appearance in the interstellar medium to understanding and improving the production of tailored nanoparticles. In recent years the largest stimulus has come from the field of catalysis, in which the potential to tune the properties of nanoparticles as a function of cluster size and composition has stimulated a comprehensive characterization of these species.

The central goal of performing IR experiments on gas-phase clusters lies in the unraveling of their geometric structure, which is otherwise difficult to experimentally probe. Understanding and assigning vibrational spectra of gas-phase clusters requires both sensitive experimental techniques to deal with the low number densities as well as reliable quantum mechanical calculations in order to assign the spectral features. Metal-containing clusters, and in particular transition metal clusters with open d-shells, can yield a wealth of geometric isomers. This makes both the prediction of the cluster structure solely based on quantum mechanical calculations, on one hand, and the assignment of an experimental vibrational spectrum without calculated vibrational frequencies, on the other hand, a difficult and in many cases unreliable endeavor. As we will describe in the following sections, often only the combination of the two methods can yield an unambiguous structural characterization of the particular cluster structure.

The systems studied and some of their characteristic IR absorption regions probed in our experiments are summarized in Fig. 1. Four different types of metal-containing clusters are presented in more detail, namely pure metal, metal oxide, and metal

The Chemical Physics of Solid Surfaces, Volume 12
ISSN: 1571-0785
DOI: 10.1016/S1571-0785(07)12008-3

*Corresponding author.
E-mail: meijer@fhi-berlin.mpg.de

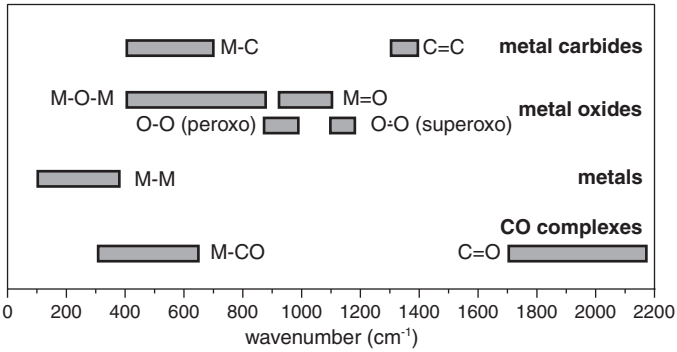

Figure 1: Overview of the spectral ranges for observed vibrational fundamentals (mainly stretching modes) in the different types of metal-containing cluster systems discussed in Section 4.

carbide clusters, as well as pure metal cluster–CO complexes. Typical vibrational modes of pure metal clusters are generally found below 400 cm^{-1}. Metal oxide and metal carbide modes involving predominantly single bonds absorb in-between 400 and 900 cm^{-1}. The characteristic M=O and C=C stretching modes are located in relatively narrow regions at higher energy, around 1000 and 1400 cm^{-1}, respectively. The absorption region of dioxygen units bound to metal oxide clusters depends on their formal oxidation state, with peroxo groups absorbing roughly 150–300 cm^{-1} below superoxo groups, which are found around 1150 cm^{-1}. For metal cluster–CO complexes the C=O stretching mode is found in-between 1700 and 2150 cm^{-1}, while the M–CO stretch lies below 650 cm^{-1}.

This chapter is structured as follows. We start with a description of the experimental methods in Section 2, beginning with the mechanism of IR multiple photon excitation (MPE) in Section 2.1, followed by a short discussion of the processes that can follow MPE and are used within our work to detect resonant IR-MPE, namely IR resonance enhanced multiple photon ionization (REMPI) and IR multiple photon dissociation (MPD) in Section 2.2. The section ends with the description of an alternative photodissociation (PD) technique in Section 2.3. This technique is based on the formation of cluster–messenger atom complexes and is particularly suited for the measurement of IR-PD spectra at longer wavelength and/or of smaller clusters. Details of the IR light source FELIX and of the experimental setups are given in Section 3. Section 4 gives an overview on our studies on metal-containing clusters and is divided into four parts: metal carbide clusters (Section 4.1), metal oxide clusters (Section 4.2), transition metal clusters (Section 4.3), and complexes of transition metal complexes (Section 4.4). The chapter ends with an outlook summarizing potential future developments in the field.

2. METHODS

Vibrational spectroscopy paired with quantum chemistry currently offers a direct and generally applicable approach to structural investigation of neutral and charged clusters in the gas-phase [1–3]. Direct absorption measurements based on, for instance, discharge modulation methods [4, 5] can yield high-resolution spectra of small molecules and molecular ions. However, these types of experiments become increasingly difficult

for larger and heavier species, owing to lower gas-phase number densities and the presence of other absorbing species. Therefore, alternative techniques have been developed in which the absorption of photons can be measured indirectly. These techniques make use of the measurement of the response of the molecule or ion after photon absorption and hence are referred to as different types of action spectroscopy. The responses that can be detected are (a) a change in a quantum state, monitored via ion or fluorescence dip methods, (b) the emission of photons, (c) a change in mass, and (d) a change in charge. Here, we will only report on the latter two, i.e., on systems where one or more IR photons are utilized to induce fragmentation, or where many photons are used to induce the thermal evaporation of an electron from a neutral cluster.

For weakly bound complexes, one absorbed IR photon can be sufficient to bring the complex above the dissociation barrier such that it can undergo vibrational predissociation. Monitoring the fragmentation yield as a function of wavelength can then give directly the linear absorption spectrum of the complex. In the IR, such experiments have first been performed by Lee and co-workers [6–9] on weakly bound hydrogen cluster ions. In Section 2.3, we will give more details on IR-PD experiments using the messenger atom technique and in Sections 4.2 and 4.3, we will show how this technique can be applied to the study of pure as well as oxygen-containing transition metal clusters.

More strongly bound clusters and complexes can be more difficult to fragment. With typical dissociation energies of 1–6 eV for a covalent bond, many IR photons need to be absorbed in order to induce fragmentation. High-fluence lasers are needed in such experiments. Since the 1970s, powerful CO_2 lasers have been used in IR-MPD experiments [10], initially mainly with the goal of isotope selective MPD for the purpose of isotope separation. Line-tunable CO_2 lasers can, however, also be used to perform spectroscopic studies on, for example, size-selected gas-phase neutral [11] and ionic species [12–14]. The use of an FEL to this end has greatly enhanced the possibilities, as suitable FELs [15] make a large region in the IR available for IR-MPD experiments [16–18]. In Section 2.2, we will give more detailed information on the physical principles of IR-MPD, and in Sections 4.2–4.4, results from experiments on metal oxide, pure metal clusters, as well as metal cluster complexes will be presented.

Most highly vibrationally excited neutral species in the gas-phase will cool via the emission of photons or small neutral fragments. However, some highly vibrationally excited molecules and clusters have an alternative cooling channel available: the thermal evaporation of an electron. For gas-phase species, this was first observed for fullerenes [19–21] as well as for metallic clusters [22]. This process will only occur for very stable species with a low ionization potential (IP) and – in zeroth order – the IP should be lower than the fragmentation barrier. The initial experiments used UV or visible lasers to indirectly populate highly excited vibrational states. The direct excitation of vibrational modes using an FEL was first performed for C_{60} [23] and later for metal carbide [24] and metal oxide clusters [25]. In those experiments, the resonant absorption of several hundreds of IR photons in a single molecule or cluster is necessary to reach the required internal energy levels. Recording the ionization yield as a function of IR frequency then gives the IR-REMPI spectrum of the species. While such a spectrum is not equal to the linear IR absorption spectrum, it can be surprisingly close to it and can give a good idea about IR resonances in the molecule or cluster. In Section 2.2, the mechanism will be discussed, and in Sections 4.1 and 4.2.1, the application of IR-REMPI to metal carbide and metal oxide clusters will be presented.

2.1. Mechanism of infrared multiple photon excitation (IR-MPE)

The mechanisms and efficiency of the IR-MPE process depend strongly on the size and properties of the absorber, its initial internal energy, and the properties of the light source. The details and modeling of the excitation process can be found elsewhere [10, 18, 26] and only a qualitative outline will be given here. An important role is played by anharmonicities. They prevent the absorption of more than a few photons in a single mode, as the anharmonicity will usually shift the resonance out of the excitation range of the laser ("anharmonic bottleneck").

The mechanism of the resonant absorption of many photons will thus not be a coherent multiphoton absorption process in one vibrational ladder, but rather the non-coherent, sequential absorption of multiple single photons. Anharmonicities also introduce a coupling mechanism between different modes, which allows an internal vibrational redistribution (IVR) of the energy, which in turn can cause line broadening. In the case of fast IVR, each photon absorption event can then be followed by redistribution of the energy, effectively "de-exciting" the IR-excited vibrational mode. The rate of photon absorption is then limited by the IVR rate, the properties of the light source, as well as the anharmonicities and cross-anharmonicities, which still can shift the resonance out of the excitation profile of the laser. For the value of the IVR rate, an important parameter is the internal energy at which the line broadening, caused by IVR, is approximately equal to the average mode spacing, given by the density of states. At low internal energies, IVR is slow and anharmonicities can limit the rate of photon absorption. At high internal energies, there is a quasi-continuum of vibrational states, IVR is fast and rapid absorption of photons can take place. Typical timescales for intramolecular relaxation of highly excited polyatomic molecules in this quasi-continuum regime are 10^{-11}–10^{-12} sec.

The IVR rate and the density of vibrational states are extremely important numbers for the IR-MPE process and are determined by several properties of the molecule. The density of states is determined by the size of the molecule or cluster and the values of the vibrational frequencies of the fundamental modes and scales roughly with $E^{(3n-7)}$ ($n =$ number of atoms, $n \geqslant 3$, $E =$ internal energy). This density of states quickly reaches values of many states/cm^{-1} for systems containing only a few atoms at internal energies of $> 1000\,\mathrm{cm}^{-1}$ and can reach extremely high values for larger systems at higher internal energies.

C_{60} at a temperature of 800 K, for example, has a vibrational state density of 10^{48} states/cm^{-1} [27] – clearly a quasi-continuum of states. Although the name quasi-continuum suggests that photons of any wavelength can be absorbed, this region is characterized by semi-resonant absorption in zones near the original fundamental transition [10]. These zones represent the background vibrational states that borrow intensity from the bright state via (indirect) anharmonic coupling. For C_{60} at a temperature of 1790 K with $> 10^{100}$ states/cm^{-1}, still well-resolved resonances are observed which are not broader than $50\,\mathrm{cm}^{-1}$ [27]. The often found statement that only the first photons are absorbed on discrete resonances and then, photons of any color can be absorbed is thus not generally true.

IR-MPE can be efficiently performed on polyatomic molecules that are not too cold, such that the density of states is high enough to allow for fast IVR. On the other hand, the spectral resolution deteriorates with increasing internal temperature and therefore a compromise for the cluster temperature has to be found, which strongly depends on the

particular system of interest. For small and/or colder molecules, in particular in triatomic systems, higher peak intensities may be necessary to reach the quasi-continuum.

2.2. Infrared resonance enhanced multiple photon dissociation and ionization

The IR-excited molecules or clusters can cool themselves via the emission of photons, neutral fragments or the emission of an electron. The rate of emission of photons rises with the fourth power of the internal energy (Stefan–Boltzmann law) and is dominant at lower excitation energies. The rate constants for the emission of neutral fragments or electrons grow exponentially with internal energy and will thus dominate at higher energies. The branching between those three processes depends on the internal energy and the properties of the species. For most molecules or clusters, the emission of neutral fragments will be much faster than the emission of electrons, as typical bond dissociation energies are lower than typical values for IPs.

With the exception of the dissociation of a rare gas atom from a cluster, all processes described here require significant energy at which the densities of states are high and the system is in a quasi-continuum of states. Under such conditions, statistical theories often give a good description of the observed kinetics. Those theories are built on the assumptions such that each energetically allowed quantum state has the same a priori probability to be occupied and that there is a free flow of energy in the system. Then, the rate constant for dissociation or ionization is just given by

$$k(E) = \frac{\sigma N''(E - E_0)}{h\rho(E)} \tag{1}$$

where σ is a reaction symmetry factor, $N''(E-E_0)$ the sum of the available states above the transition state (at energy E_0) leading to products, h Planck's constant, and $\rho(E)$ the density of states at energy E. Details can be found elsewhere [28]. A dissociation or ionization process becomes energetically allowed when the internal energy is equal the reaction energy (dissociation of ionization energy). However, the rate constant for this process can be extremely small at low energies, and for the rate constant to reach a value such that the process becomes observable in the experimental time window, the internal energy often needs to be considerable above the reaction energy.

In addition, it has to be considered that the IR-MPE process creates an ensemble of molecules with a distribution of energies. This distribution not only depends on the mechanism of IR-MPE, but also needs to be convoluted over the spatial profile of the excitation laser. The process of IR-MPE followed by dissociation [26] and ionization [18] has been modeled, taking the above points into consideration. Both the IR-MPD and the IR-REMPI processes require the absorption of many photons and, when monitored as a function of IR wavelength, give IR spectra that are not necessarily the same as a regular linear absorption spectrum. However, it has been shown previously that, very often, they are close to the linear absorption spectrum [18, 26] and give a good idea about the IR active modes.

2.3. Messenger atom technique

A method that can avoid having to excite a cluster by many photons and that enables the measurement of IR-PD spectra in the linear regime is the messenger atom

technique [6], which can be schematically depicted as

$$AB^+ \cdot M \xrightarrow{h\nu} (AB^+ \cdot M)^* \xrightarrow{\text{vib. predissociation}} AB^+ + M \tag{2}$$

Here, the experiment is not performed on the bare ion of interest (AB^+), but rather on the weakly bound complex $AB^+ \cdot M$. If the binding energy of the messenger species M is small enough, absorption of a single photon will be followed by vibrational predissociation and can be detected by monitoring either the depletion of the complex or the formation of the bare ion. Ideally, the perturbation of the geometric and electronic structure of the AB^+ moiety in the complex by the messenger species M is negligible, such that the IR spectrum of the complex reflects the IR spectrum of the bare ion. The use of He atoms as messenger species approaches this ideal situation quite well. When heavier species like Ar atoms are used, complications can arise and we discuss a few such examples in Sections 4.2.3 and 4.3.2. We note here already that binding energies of more than $1000\,cm^{-1}$ for cluster ion–Ar atom complexes are not unusual. Thus at longer IR wavelengths, e.g., in the absorption region of pure metal clusters, this binding energy surpasses the photon energy again and the absorption of several photons is required, which may lead to complications related to the anharmonic bottleneck. The MPD approach (without rare gas atom) remains attractive for systems, in which the perturbation of the messenger atom cannot be neglected or for systems where rare gas attachment is difficult.

The messenger atom technique is not restricted to ionic species, and can be applied to neutral clusters as well, if soft ionization without fragmentation of the rare gas complex is possible to allow for mass spectrometric characterization. An example for neutral metal clusters will be given in Section 4.3.3.

3. EXPERIMENTAL SECTION

3.1. Infrared free electron laser (IR-FEL)

In an FEL, electromagnetic radiation is generated from a beam of relativistic electrons. The central part of an FEL is the undulator (Fig. 2), a periodically alternating static magnetic field. The peak emission wavelength depends on the undulator period L, the strength of the magnetic field, expressed by a dimensionless parameter K, and the electron energy:

$$\lambda \propto \frac{L}{2\gamma^2}(1 + K^2) \tag{3}$$

where γ is the relativistic factor and corresponds to the kinetic energy of the electrons along the axis of the FEL in units of the electron rest energy m_0c^2. In the moving electron frame the electrons see not only an oscillating magnetic field, but also an oscillating electric field in the perpendicular direction – in short, they see an electromagnetic wave with wavelength L/γ. Upon interaction with this wave the electrons emit (first-harmonic) light of the same wavelength. The corresponding wavelength in the laboratory frame is subject to the Doppler effect. Thus, for MeV electrons the peak emission wavelength is shortened relative to the macroscopic undulator period

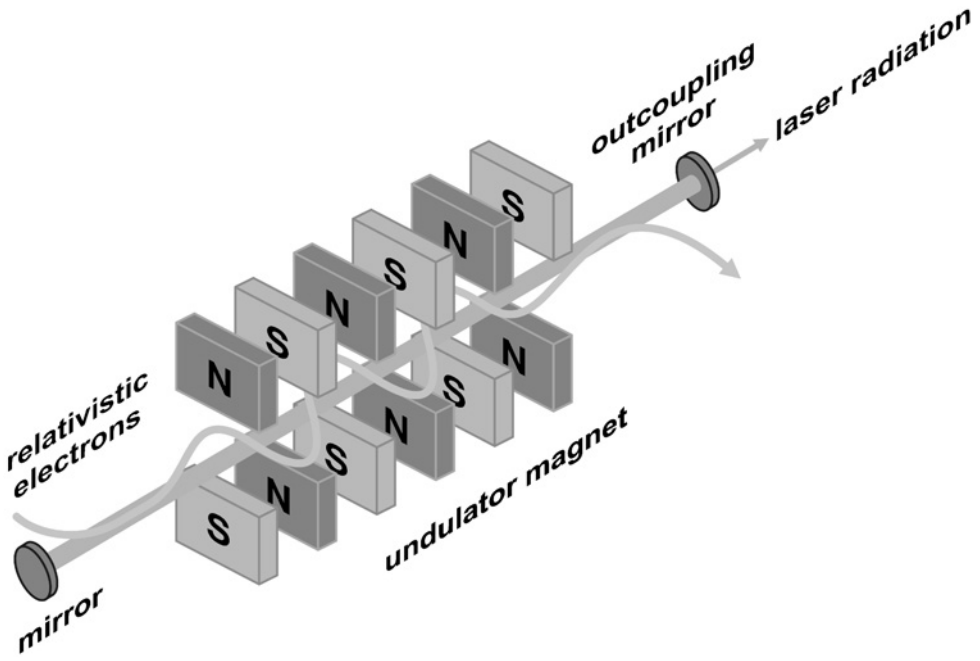

Figure 2: Scheme of an FEL undulator and optical cavity.

($L \approx 1\,\mathrm{cm}$) by the Lorentz contraction ($1/\gamma$) and the Doppler shift ($1/2\gamma$) into the micrometer wavelength region.

The amount of power radiated spontaneously by a very energetic beam of electrons is not large. If the electrons were spaced uniformly along the beam, there would be no power emitted at all due to negative interference. Only the fluctuations in particle current would lead to a net radiation, which scales linearly with n, the number of electrons. The spectrum of the spontaneous radiation is determined by the finite undulator length $l = N \cdot L$, resulting in a finite transit time and a fractional width of the spontaneous or noise radiation of $1/N$.

The ponderomotive force acting between the axial electron velocity and the magnetic component of the electromagnetic wave is the origin of the stimulated emission of (highly coherent) photons. It couples the electron motion to the electromagnetic field and is phase dependent. Electrons that are in phase with the electromagnetic wave are retarded, while the ones with opposite phase gain energy. Through this exchange of energy a longitudinal density modulation on the scale of the wavelength is created, the so-called micro-bunching. More and more electrons begin to radiate in phase, which results in an increasingly coherent superposition of the radiation emitted from the micro-bunched electrons. The more intense the electromagnetic field gets, the more pronounced the longitudinal density modulation of the electron bunch and vice versa. With complete micro-bunching, all electrons radiate in phase and this leads to a radiation power, which is proportional to N^2 and amplified many orders of magnitude with respect to the spontaneous emission of the undulator.

The temporal structure of the optical output pulse is determined by the incoming electron beam. The linear radio frequency (RF) accelerators of FELIX [29, 30] typically generate 7 μs long pulse trains of 1 ps long electron bunches at a repetition rate of up to 10 Hz. The micropulse repetition rate is either 25 MHz or 1 GHz, the latter corresponding to 40 optical pulses circulating in the 6 m long cavity. The micropulse duration of the optical pulses can be varied in-between 300 fs to several picoseconds and their bandwidth is near-transform limited, ranging from less than 0.5% to several percent full width at half maximum (FWHM) of the central wavelength.

The output wavelength of FELIX depends on the electron beam energy and the magnetic field strength. Generally, the wavelength is scanned by mechanically adjusting the distance of the undulator magnetic poles for a fixed beam energy. A factor of three in wavelength can be covered using a single electron beam setting. In total, a wavelength range from 4.5 to 250 μm is covered by FELIX. Typically, macropulse energies at narrow bandwidth and 1 GHz micropulse repetition rate are 30–50 mJ. The IR radiation is guided via an evacuated transport system to a user station (roughly 30 m away).

3.2. Molecular beam spectrometer

The experiments on cluster beams (all IR-REMPI experiments as well as the IR-PD experiments described in Sections 4.2.2, 4.3, and 4.4) are performed in a molecular beam setup that is coupled to the beam-line of FELIX. A scheme of the experimental setup is shown in Fig. 3. The clusters are produced by ablating a metal rod using the second-harmonic output of a pulsed Nd:YAG laser. After subsequent injection of a short pulse of helium, cooling of the plasma and condensation into clusters occurs within the 3 mm diameter wide clustering channel. This channel is extended by a flow

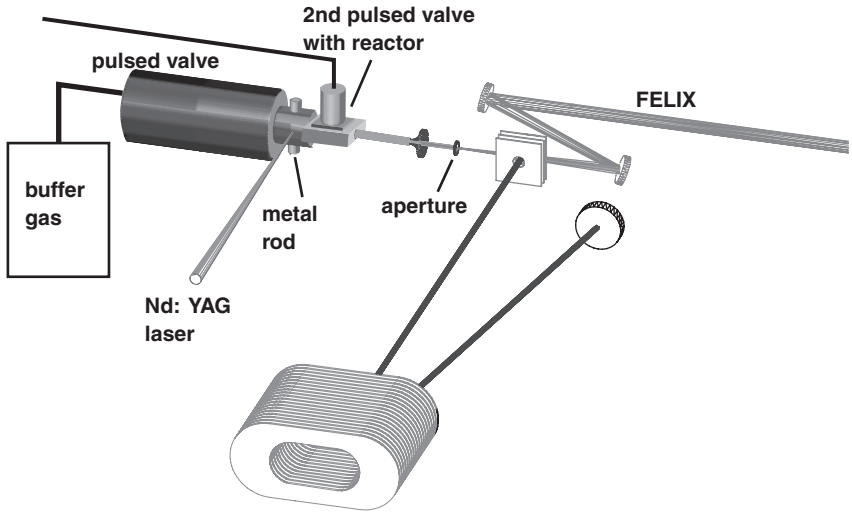

Figure 3: Molecular beam setup that is used for fragmentation and ionization spectroscopy of cluster complexes. The second pulsed valve with the reactor operating at room temperature can be replaced by a copper channel that is cooled to 80 K to form rare gas complexes of the clusters.

reactor channel of 5 mm diameter and 35 mm length in which reaction gases can be injected by a second pulsed valve. The composition of the reaction products can be controlled via the flow of the reaction gas through the pulsed valve.

After expansion into vacuum, the molecular beam is shaped by a skimmer followed by an aperture of 0.8 mm diameter. The cluster distribution in the molecular beam is analyzed using a reflectron time-of-flight mass spectrometer (ToF-MS). When studying neutral clusters, the charged clusters are deflected out of the molecular beam and the remaining neutrals are ionized using an excimer laser (ArF, 6.4 eV/photon or F_2, 7.9 eV/photon) or using the frequency-doubled output of a dye laser. The molecular beam is overlapped with the counter-propagating IR laser beam, delivered by FELIX. The IR beam is focused onto the aperture in the molecular beam and is timed to irradiate the pulsed cluster beam when this is near the focus. When the frequency of the IR radiation is resonant with an IR-active mode of the cluster, one or more photons can be absorbed by the cluster. The excitation occurs typically 50 μs before the clusters arrive in the ion extraction region of the mass spectrometer. The resulting heating of the clusters may induce fragmentation of the complexes, leading to their depletion in the beam. IR depletion spectra are constructed by recording the ion intensities of the complexes as function of the FELIX frequency. As the detection is mass selective, the simultaneous measurement of IR spectra for different cluster sizes is possible. To correct for long-term intensity fluctuations of the cluster source, the experiments are performed in a toggle mode with the cluster beam source running at 10 Hz and FELIX at 5 Hz. Using two different channels of a digital storage oscilloscope, mass spectra are recorded and averaged alternatingly, transferred to a computer, and analyzed to obtain the IR spectra.

Vibrational spectra of metal clusters in the far-IR can be obtained by PD of their weakly bound complexes with rare gas atoms. In these experiments, a copper channel that is thermally isolated from the main body of the cluster source and that is cooled by direct contact to a liquid nitrogen filled reservoir replaces the reaction channel. The helium carrier gas is blended with a minor amount of a heavier rare gas, e.g., Ar, and when this gas mixture contains a sufficient concentration of Ar and when the copper channel is maintained at ~80 K, complexes of the metal clusters with Ar atoms can be observed. Examples for the far-IR PD spectroscopy on these metal cluster rare gas complexes are discussed in Section 4.3.3.

For the measurements of IR-REMPI spectra the aforementioned setup is only slightly modified. Clusters of metal oxides or carbides are formed by laser vaporization using methane or oxygen mixed into the carrier gas and the reactor extension of the cluster source is replaced by a conical nozzle. To achieve high photon flux in the overlap region with the molecular beam, the IR beam is tightly focused onto the molecular beam between the extraction plates of the ToF-MS. Details of the IR-REMPI experiments have been described elsewhere [18].

3.3. Guided ion beam tandem-mass spectrometer

The experiments on the vanadium oxide cluster ions described in Section 4.2.3 are performed in a guided ion beam tandem-mass spectrometer [31] that was temporarily installed at the FELIX facility. A schematic view of the experimental setup is given in Fig. 4.

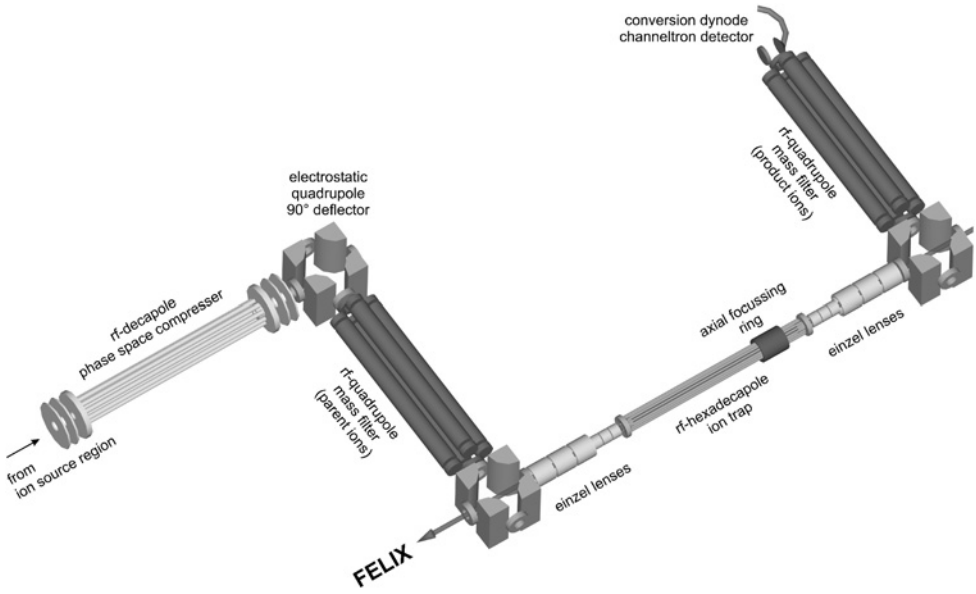

Figure 4: Schematic view of the guided ion beam tandem-mass spectrometer used in the present studies [31]. The instrument is housed in a five-stage differentially pumped vacuum chamber. The FEL radiation is applied collinearly to the axis of the ion trap.

Gas-phase vanadium oxide ions are produced by laser vaporization in a Smalley-type [32] source. The second harmonic of a Q-switched Nd:YAG laser is focused on a rotating and translating vanadium rod. The nanosecond laser pulse impinges on the metallic target and the metal vapor produced by the early portion of the laser pulse forms a dense cloud near the metal surface. This cloud is quickly ionized and the resulting plasma is entrained in an He carrier gas pulse and allowed to thermalize through collisions in the expansion channel. Cluster formation occurs here through three-body collisions. Adding small amounts of a reactive gas to the carrier gas allows tailoring the cluster composition. The average oxygen content per cluster, e.g., can be tuned by the amount of oxygen added to the He gas. The gas pulse then expands into the vacuum, cooling mainly rotational and translational degrees of freedom. The vibrational temperature of the ions is determined mainly by the temperature of the expansion channel.

The ion beam, containing a distribution of cluster ions of different size exits the source region, is collimated and compressed in phase space in a gas-filled RF ion guide and directed into the first quadrupole mass filter. Mass-selected ions are then guided into a temperature-adjustable RF ion trap. The trap consists of a linear RF ion guide and two electrostatic ion lenses contained in a cylindrical housing, which is connected to the cold head of a closed-cycle He cryostat. The cylinder is continuously filled with He. The use of a buffer gas has several advantages. (i) The trap can be operated in a continuous ion-fill-mode. (ii) Trapped ions are collisionally cooled to the ambient temperature (approximately within a few milliseconds). (iii) At low trap temperatures ion–messenger atom complexes can be formed. (iv) Experiments can be performed at a defined, variable ion temperature, currently in-between 14 and 350 K.

IR-PD spectra are obtained by photoexcitation of the trapped ions with the pulsed FEL radiation and subsequent monitoring of the fragment ion signal. A new measurement cycle is triggered by the previous FEL macropulse. First, the ion trap is filled with mass-selected ions. The trap is then closed and the ions are allowed to thermalize. Directly after FELIX fires, all ions are extracted and the mass-selected ion yield is monitored. This cycle is repeated multiple times, the signal is summed, and then the FEL is set to the next wavelength. The accuracy of the determined vibrational frequencies is generally within 1% of the central wavelength. The accuracy of the relative intensities is less well defined, mainly due to the non-monotonic variation of the FELIX beam intensity, bandwidth, and waist size with wavelength. We try to minimize these variations and do not correct for them in our spectra.

4. RESULTS

4.1. Metal carbide clusters

Metal carbides are promising systems for applications in heterogeneous catalysis, not only as support materials, but also as catalytically active phases. They are thought of having the potential of being future economic replacements of noble metals in methane reforming, in the treatment of auto exhausts or for other (electro) oxidation reactions [33–35]. Several bulk transition metal carbides are metallic in character. The structure of, for example, TiC and similar metal carbides can be thought of as a regular cubic metal lattice in which the octahedral holes are intercalated by carbon atoms. When the size of the octahedral hole is large enough to accommodate a carbon atom without distorting the metal lattice, the intercalation is energetically favored and very stable metal carbides result, which have a metal to carbon ratio of 1:1 and a face centered cubic (fcc) crystal structure. This is the case for metals in which the atom radius is above about 1.3 Å, like Ti, Zr, Hf, V, Nb, Ta, Mo, and W. Their carbides are characterized by very high melting points (3000–4000 K), high hardness (between topaz and diamond), and high electrical conductivity [36]. Those special properties make it interesting to investigate finite systems, clusters, of such materials in the gas-phase as a function of size and composition. In early experiments, the main focus was on intensity distributions in mass spectra. Those distributions are determined in a complicated way by the stabilities and reactivities of the clusters. For several metal carbides it is found that clusters of the composition M_8C_{12} are very abundant and a spherical shape was proposed [37], which later could be supported by ion mobility measurements [38]. Another group of clusters with compositions such as, for example, $M_{14}C_{13}$ are also found to be very abundant and they are thought to have structures that resemble small pieces of the cubic bulk material, so-called nanocrystals [39]. We study the IR properties of such species by measuring their IR-REMPI spectra [18] (see Section 2.2). Systems investigated so far include TiC [24, 40], VC [41], NbC, and TaC [42]. To some extent, the properties of those carbides are similar and we will focus here on the TiC clusters.

4.1.1. IR-REMPI of titanium carbide clusters

Metal carbide clusters can be generated using the setup described in Section 3.2 by vaporization of the corresponding metal in a gas mixture of 95% argon and 5% CH_4.

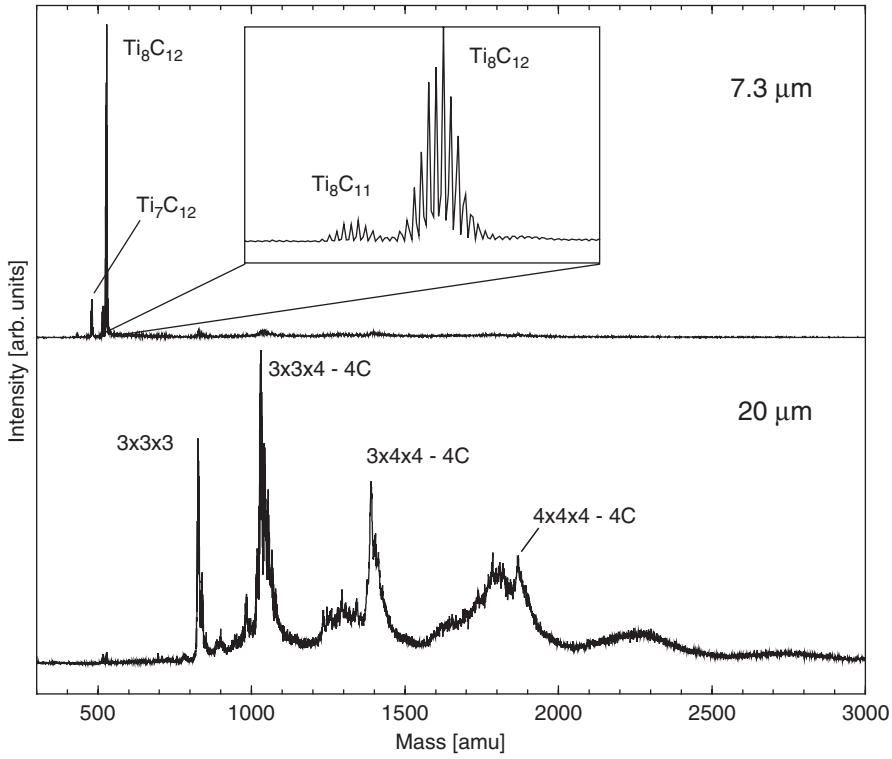

Figure 5: Mass spectra of titanium carbide cluster ions when exciting at 7.3 μm (top trace) and at 20 μm (bottom trace). In the inset shown in the top trace, the titanium isotope distribution can be seen. At higher masses (bottom trace), the mass resolution is no longer sufficient to separate isotopic peaks.

Mass spectra of titanium carbide clusters when exciting at two different wavelengths are shown in Fig. 5. All mass peaks result from neutral cluster precursors that have absorbed enough IR photons in order to enable the evaporation of an electron. As mentioned previously, molecules and clusters of most materials will emit neutral atoms or fragments rather than electrons when being highly vibrationally excited. The evaporation of an electron is the prerogative of very strongly bound species with low IP. When exciting at a wavelength of 7.3 μm (top trace), several small clusters are observed. The largest peak (or better group of peaks) results from clusters having the composition Ti_8C_{12}. $Ti_8C_{12}^+$ has previously been observed to be abundant (''magic'') in mass spectra [37]. Less intense peaks are observed for Ti_8C_{11} as well as for Ti_7C_{12}. In the inset, an expanded view of the region around Ti_8C_{12} and Ti_8C_{11} is shown. Clearly, fine structure can be observed that arises from the natural isotope distribution of titanium. The observed isotope distribution is virtually indistinguishable from a simulated distribution, giving evidence for the stoichiometries indicated in the figures.

In the lower trace, a mass spectrum after excitation at 20 μm is shown. Clearly, the mass distribution is very different from the one observed after 7.3 μm excitation. Hardly any $Ti_8C_{12}^+$ is found and all mass peaks result from larger clusters. The lowest mass peak with significant intensity results from $Ti_{14}C_{13}^+$ and is assigned to a cubic cluster consisting of $3 \times 3 \times 3$ atoms having a structure similar to that of bulk TiC,

which has an fcc (NaCl-like) structure. For the larger clusters, prominent peaks are observed at masses that correspond to those of ideal or near ideal cubes of atoms. In the presented mass spectrum the isotopic distribution of Ti and the limited mass resolution of the mass spectrometer of ≈ 1500 result in a not fully resolved mass spectrum. Nonetheless, distinct groups of peaks are observed having rather sharp maxima. These maxima appear at masses corresponding to cubes of $3 \times 3 \times 4$, $3 \times 4 \times 4$, and $4 \times 4 \times 4$ atoms, all however, shifted 48 amu toward lower masses. They thus could correspond to clusters having one titanium atom less than the ideal clusters. They could, however, also correspond to clusters having four carbon atoms less than the ideal cluster. While a $Ti_{14}C_{13}$ cluster with the dimension of $3 \times 3 \times 3$ atoms will have all eight corners occupied by metal atoms, this is no longer possible if one or more sides have an even number of atoms. In this case, four corner atoms will be occupied by metal atoms and four by carbon atoms. In experiments on vanadium carbide clusters, clusters with carbon atom vacancies, presumably at the corners, are observed [41]. For those clusters, it is also observed that other cubic structures, such as $3 \times 3 \times 5$ or $3 \times 4 \times 5$ atom clusters, are present. There, the $3 \times 4 \times 5$ structure shows again a tendency to form clusters that lack four carbon atoms. The $3 \times 3 \times 5$ structure on the other hand can have all corners occupied with metal atoms and the cluster prefers to form the ideal structure [41]. In the case of TiC, the complicated isotope distribution of titanium prevents us from deducing similarly detailed information from the mass spectrum. Nonetheless, it is clear that the mass distribution when exciting at 20 μm is compatible with (defective) cubic cluster structures.

For each mass peak, its wavelength dependence can be monitored and an IR spectrum can be obtained. In Fig. 6, the IR-REMPI spectra for Ti_8C_{12} and Ti_8C_{11} as well as for V_8C_{12} and V_8C_{11} are shown. The spectra are dominated by a strong resonance, centered around 1400 cm^{-1} (7.3 μm).

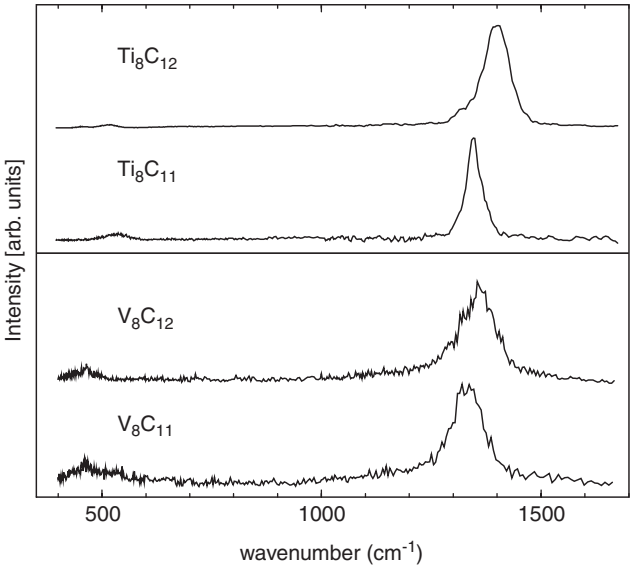

Figure 6: IR-REMPI spectra for M_8C_{12} and M_8C_{11} clusters, with M=Ti and V.

Ion signal for those clusters is also found at around 500 cm^{-1} (20 μm); its relative intensity there is however significantly less than at 1400 cm^{-1}. As described above, in order for clusters to undergo thermionic electron emission, they need to be very stable as neutrals, i.e., they need to possess high dissociation thresholds and relatively low IPs. While this is somewhat expected for Ti_8C_{12} and V_8C_{12}, it comes as a surprise for Ti_8C_{11} and V_8C_{11}. These clusters have not previously been observed to be special ("magic"), nor did anybody propose a special structure for them. The spectra of the (8,11) clusters can be compared to their (8,12) counterparts. Clearly, the spectra are very similar but it is important to note that they are not the same. If they would be the same, one could not exclude the possibility that the (8,11) clusters are formed during or after the excitation/ionization process by fragmentation of (8,12) clusters. The peaks in the spectra of the (8,11) clusters are somewhat red-shifted compared to the (8,12) clusters and, at least for Ti_8C_{11}, the resonance is clearly narrower. The spectrum of the (8,12) and (8,11) clusters look very different than the spectra of the other larger titanium carbide clusters (Fig. 7). This is in line with the large differences in proposed structure of Ti_8C_{12} to the structures of the larger titanium carbide clusters. While there is some uncertainty on the details of the structure, all proposed structures for (8,12) clusters involve C_2 units that coordinate to the metal atoms [43–47]. The intense modes around 1400 cm^{-1} can be related to C=C stretching vibrations in these dimers. The IR spectra of the (8,11) clusters in Fig. 6 are similar to those of Ti_8C_{12} and V_8C_{12}, indicating that the main structural motives are similar as well.

4.1.2. IR spectra of titanium carbide nanocrystals

In Fig. 7, IR spectra for Ti_xC_y clusters in the frequency range between 400 and 1000 cm^{-1} are shown. The mass spectra recorded when exciting in this spectral range are dominated by clusters with a very different stoichiometry than the (8,12) or (8,11) clusters. These clusters have a near 1:1 ratio of Ti/C and, as is discussed in the previous section, the distributions observed in the mass spectra that are recorded when exciting at around 500 cm^{-1} point to nanocrystalline structures. The IR spectra of all clusters are dominated by a strong resonance at 485 cm^{-1}. When going from $Ti_{14}C_{13}$ ($3 \times 3 \times 3$ atom cluster) to clusters of sizes in the range $Ti_{63}C_{62}$ ($5 \times 5 \times 5$ atoms cluster), the position of this peak does not shift within experimental uncertainty. For $Ti_{14}C_{13}$, an additional peak at 630 cm^{-1} is observed. For larger clusters, this peak becomes weak and broad and melts into an almost constant background that persists up to 1000 cm^{-1} and beyond.

Since it is claimed that the TiC nanoparticles have a structure that is very similar to the structure of bulk TiC, their IR spectra should be compared to spectra of bulk TiC. As is mentioned before, bulk TiC is a conductor (metallic). When irradiating bulk TiC with (IR) light, the light will interact with the conduction electrons, leading to the reflection of the incoming electromagnetic wave. This effect will effectively shield the lattice vibrations and a phonon spectrum is thus difficult to measure using IR light. An alternative method to get information on (surface) phonons of bulk samples is electron energy loss spectroscopy (EELS). Using this technique, the entire phonon dispersion curve can be measured, including the $k = 0$ optically active phonons. The group of Oshima has done so for most of the refractory metal carbides, including TiC [48]. In Fig. 7, the positions of the two optically active phonon modes of the TiC (100) surface [48] are indicated

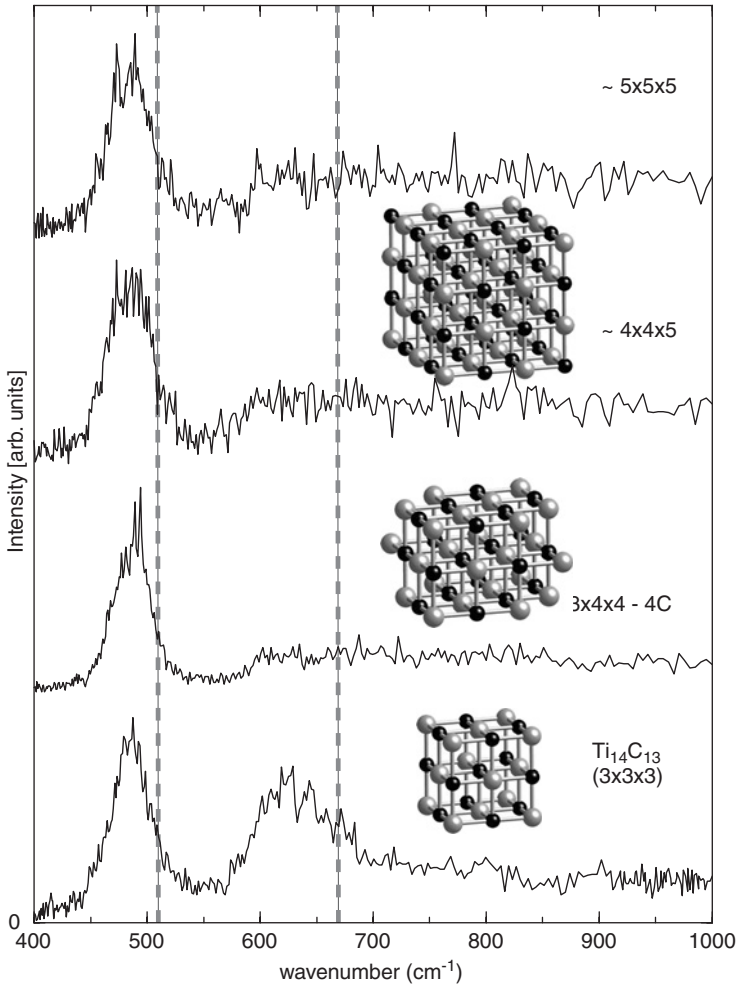

Figure 7: IR-REMPI spectra for TiC clusters with compositions that correspond to cubic clusters of sizes $3 \times 3 \times 3$ to $5 \times 5 \times 5$ atoms. Shown as dashed lines are the frequencies of IR active surface phonon modes of bulk TiC.

as dashed lines. Surprisingly, the peak positions observed in the spectra of TiC nanocrystals are very close to the surface phonons observed for the bulk in the EELS experiment. In the EELS experiment, it can be argued that the lower frequency line at $504\,cm^{-1}$ corresponds to motion of the surface carbon atoms perpendicular to the surface, while the higher frequency mode at $653\,cm^{-1}$ corresponds to motion of carbon atoms parallel to the surface. It is of course not clear how such a mode description can be applied to the small nanocrystals that are studied here, as many carbon atoms will be located on edges or corners. Nonetheless, it is striking how close the here observed resonances are to the bulk and it is surprising that clusters as small as $3 \times 3 \times 3$ atoms seem to have already "bridged the gap" to the bulk, at least as far as their vibrational properties are concerned.

At $Ti_{14}C_{13}$ or $V_{14}C_{13}$, the vibrational properties seem already converged to the bulk. It would thus be interesting to investigate smaller nanocrystalline clusters. Unfortunately, for titanium [24] and vanadium [41], no ion signal for smaller nanocrystalline clusters is observed. This can have several reasons. First, it might be that there are no smaller neutral nanocrystalline clusters in the beam. This seems unlikely, as they are expected to be intermediates in the growth of the (observed) larger clusters. Another reason might be that the clusters are not excited high enough using FELIX. This could be caused by either resonances being weaker or significantly shifted from those of the bigger clusters. Or, alternatively, their anharmonicities might be significantly larger and their resonances could thus quickly shift out of the excitation profile of FELIX. The most likely explanation is, however, that when the small clusters are excited, they evaporate neutral atoms and not electrons. When particles get smaller, their IPs usually increase and their dissociation thresholds decrease. It thus might be the case that small TiC or VC nanocrystals are just not stable enough to undergo thermionic emission in the IR-REMPI experiment. In experiments on tantalum and niobium carbide clusters, IR-REMPI signal was observed for clusters as small as M_4C_4 [42]. In those experiments, it is observed that the very small clusters from M_4C_4 to M_9C_9 have an IR spectrum that is significantly different from that of larger clusters and the bulk. Starting from $M_{10}C_{11}$, the low-frequency mode appears and, as for TiC and VC clusters, becomes the dominant mode for larger clusters.

4.2. Metal oxide clusters

Over the last ten years great progress has been made in the study of the size-dependent properties of isolated metal oxide clusters. These studies are motivated not only by the interest in this peculiar state of matter, but also, for example, to aid in the design of functional building blocks for nanostructured materials, to identify nanoparticles in diverse astrophysical environments, to gain a better understanding of the elementary steps in heterogeneous catalysis, or to deliver crucial benchmark data for higher level quantum mechanical calculations, on the basis of which efficient models applicable to the computationally more demanding cluster/surface systems can be developed. A corner stone in these studies is the experimental characterization of the cluster structure using gas-phase vibrational spectroscopy. Here we present a chronological overview of recent IR studies on neutral and charged metal oxide clusters performed at the FELIX facility.

The first IR studies performed on metal oxide clusters were IR-REMPI experiments [25, 49–51] and these are summarized in Section 4.2.1. Neutral metal oxide cluster distributions were irradiated with tunable and intense IR radiation and the so produced ions were mass-selectively detected. Cluster ionization, dissociation, and ionization followed by dissociation are all feasible channels and require comparable energies in these particular systems, complicating the interpretation of the experimental spectra and making a detailed structural assignment to individual cluster structures very difficult. Nonetheless, these experiments provided an overview of the IR absorption properties of metal oxide clusters over a large size distribution and over a broad spectral range, yielding a first glimpse at the size dependence of characteristic structural motifs in these clusters.

The IR-REMPI scheme requires that the cluster of interest has an IP that is lower than its barrier for fragmentation, and therefore this method is not applicable to

oxides containing a transition metal in a high formal oxidation state. These clusters usually have IPs larger than 10 eV and considerably lower fragmentation barriers. In these cases IR-PD studies need to be applied, which generally require charged species for pre- and/or post-mass selection and thus have mainly been applied to charged clusters. IR-PD studies have been performed on metal oxide clusters using two experimental setups. Measurements using the molecular beam ToF-MS machine (see Section 3.2) have the advantage that IR spectra of all ions can be measured simultaneously, reducing the acquisition time considerably and making them particularly interesting for overview studies. Such experiments on niobium oxide cations [52] are described in Section 4.2.2. However, these experiments lack mass selection of the cluster ions prior to the interaction with the IR beam and thus the absorbing species is not uniquely identified when parent ions of different mass produce fragment ions of identical mass. In these cases it becomes advantageous to use a tandem-mass spectrometer setup (see Section 3.3), which allows mass selection of both the parent and the fragment ion. These experiments combined with the messenger atom technique produce the most detailed IR spectra, and examples of such studies on vanadium oxide cations [31, 53, 54] and anions [55, 56] are described in Section 4.2.3.

4.2.1. Zr, Mg, Al, and Ti oxide clusters

The initial IR-REMPI studies focused on the size-dependent structural characterization of neutral zirconium oxide clusters [25]. IR spectra of distributions of ZrO clusters with sizes up to $Zr_{32}O_{63}$ were measured (see Fig. 8). High ionization energies of ~6–8 eV as well as comparable dissociation energies complicate the interpretation of the IR-REMPI spectra, because the efficiency of the photoionization process is strongly intensity dependent and it is accompanied by PD. All spectra reveal an absorption feature in the 500–800 cm^{-1} region, which is assigned to the absorption of vibrations involving Zr–O–Zr single bonds. In particular, B3LYP calculations predict the formation of Zr–O–Zr–O four-membered rings in all calculated structures, which have active modes between 600 and 800 cm^{-1}. Stretching vibrations of terminal Zr–O groups are calculated to be around 900 cm^{-1}; however, there are no corresponding bands in the experimental spectra.

The subsequent studies on magnesium and aluminum oxides confirmed the characteristic and size-dependent absorption of neutral metal oxide clusters between 400 and 800 cm^{-1}, but difficulties with identifying individual cluster structures remained. IR-REMPI spectra were obtained for magnesium oxide clusters in the size range from 30 to 300 atoms [49]. For the smaller clusters, enhanced abundances were observed for stoichiometries corresponding to $(MgO)_{3n}$ species, while for the larger clusters the prominent peaks in the mass spectra are consistent with cubic nanocrystal structures. All clusters, independent of closed cubic structure or an incomplete lattice fragment, were found to have essentially the same IR spectra: two broad resonances at 625 and 450 cm^{-1}, correlating well with the perpendicular and parallel bulk phonon modes.

Mass spectra of neutral aluminum oxide clusters produced by laser vaporization and then ionized by irradiation with FELIX at 11 μm are dominated by peaks corresponding to cluster ions with $AlO(Al_2O_3)_n$ stoichiometries [50]. Their abundance in the mass spectra is attributed to the open-shell nature of neutral $AlO(Al_2O_3)_n$ clusters compared to the closed-shell nature of the $(Al_2O_3)_n$ clusters. On ionization, $AlO(Al_2O_3)_n$ clusters can form closed-shell $AlO(Al_2O_3)_n$ ions and thus should be

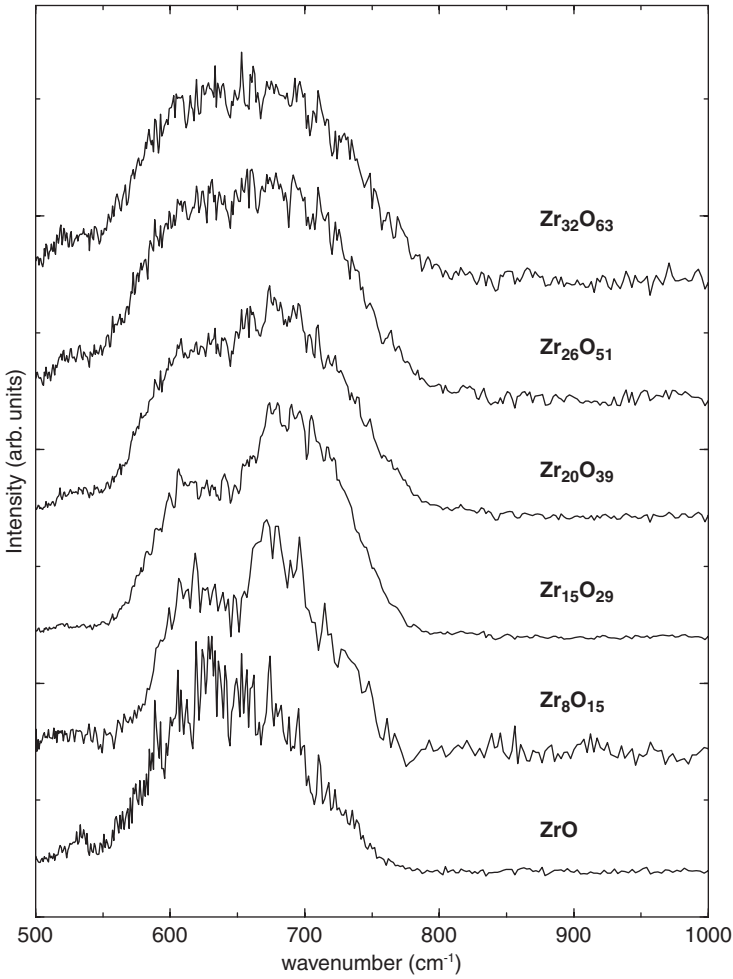

Figure 8: IR-REMPI spectra for ZrO clusters. The lowest trace corresponds to the signal of ZrO^+, which is formed as a fragment.

characterized by lower ionization energies than $(Al_2O_3)_n$ clusters, where the situation is reversed. The IR-REMPI spectra of $AlO(Al_2O_3)_n$ clusters with $n = 11$–71 show absorption in the 475–1100 cm^{-1} region. The smaller clusters show two absorption bands, which are assigned to integrated "lattice-like" structures resembling γ-Al_2O_3 rather than α-Al_2O_3, which is the thermodynamically stable form of the bulk. These absorption features change with cluster size leading to one broad band for $n > 34$, suggesting a transition to an amorphous phase of Al_2O_3 [51].

IR-REMPI spectra of titanium oxide clusters [18, 51] were measured for three cluster sizes, corresponding to the following clusters: $(Ti_2O_3)_2(TiO_2)_5$, $(Ti_2O_3)_3(TiO_2)_9$, and $(Ti_2O_3)_5(TiO_2)_{15}$. The spectra are similar for all cluster sizes, containing a single peak in the region from 333 to 2000 cm^{-1}. With increasing cluster size, the peak shifts from 725 to 740 cm^{-1} and the FWHW increases from 80 to 210 cm^{-1}. The strong

absorption around $\sim$730 cm^{-1} suggests a cluster structure, which is close to the rutile bulk phase of TiO_2.

4.2.2. Niobium oxide cluster cations

Using the molecular beam setup described in Section 3.2, IR-MPD spectra of niobium oxide cluster cations were measured in the range of 400–1650 cm^{-1} by irradiation of a pulsed molecular beam, followed by mass-selective detection of the ions. IR-MPD leads to a change in the ion signal; signal depletion indicates fragmentation of the monitored ion, while an increase in signal indicates heavier clusters fragmenting into this mass channel. The method favors detection of cluster ions with low dissociation energies and therefore IR-MPD spectra of mainly the stoichiometric clusters $(Nb_2O_5)_n^+$, $(Nb_2O_5)_nNbO^+$, and oxygen richer species are measured. The spectra of most clusters show two features: a narrow band around 990 cm^{-1}, which is assigned to stretching vibrations involving Nb=O double bonds, and a broader band in the 700–900 cm^{-1} range, which is attributed to stretching vibrations of Nb–O–Nb bridges. For several clusters a unique structural assignment based on a comparison between experimental and calculated spectrum is possible. An example is shown in Fig. 9 for $Nb_2O_6^+$, which is found to form a four-membered Nb–O–Nb–O ring, characteristic for smaller transition metal oxide clusters, and to contain a dioxo (η^1-superoxo) unit.

4.2.3. Vanadium oxide ions

The most comprehensive study on metal oxide ions has focused on vanadium oxide ions and these studies are described here in more detail. These experiments employ the tandem-mass spectrometer/ion trap setup described in Section 3.3 and deliver IR spectra with high detail. We discuss various aspects relating to the assignment of the spectra, the size dependence of the structure, both geometric as well as electronic, and the influence of the messenger atom on the cluster energetics and spectroscopy. Recent advances, in particular with respect to cluster preparation, are highlighted at the end of this section and point to possible future developments in this still increasingly active research field.

An overview of IR-MPD spectra of vanadium oxide cations and anions is presented in Figs. 10 and 11, respectively [53–59]. The experimental spectra (left) are shown together with the simulated spectra of the assigned isomers, which in most cases correspond to the lowest energy structures. Exceptions are discussed further down in the text. The geometric structures of the assigned isomers are shown in Figs. 12 and 13.

Three types of vibrational normal modes are IR active in vanadium oxide cluster ions. (i) The vanadyl stretching region is located in-between 910 and 1070 cm^{-1}. Typically, the vanadyl stretch modes lie below 1000 cm^{-1} in the anions and above 1000 cm^{-1} in the cations. (ii) Separated from, and energetically below, this region is the V–O–V stretching region, ranging from below 600 to 870 cm^{-1} and mainly involving vibrational motion of the V–O single bonds comprising the ring and backbone structure of the cluster ions. Modes delocalized over larger parts of the ion are generally found at lower wavenumber. (iii) In oxygen-rich compounds various types of oxo-species can be observed, which range from associated O_2 molecules, over superoxo (O_2^-) to peroxo $(O_2)^{2-}$ species (the charges specified are formal charges). Due to an increasing occupation of antibonding π-orbitals, the bond order decreases with increasing formal negative charge. As a result, the O–O distance increases and the

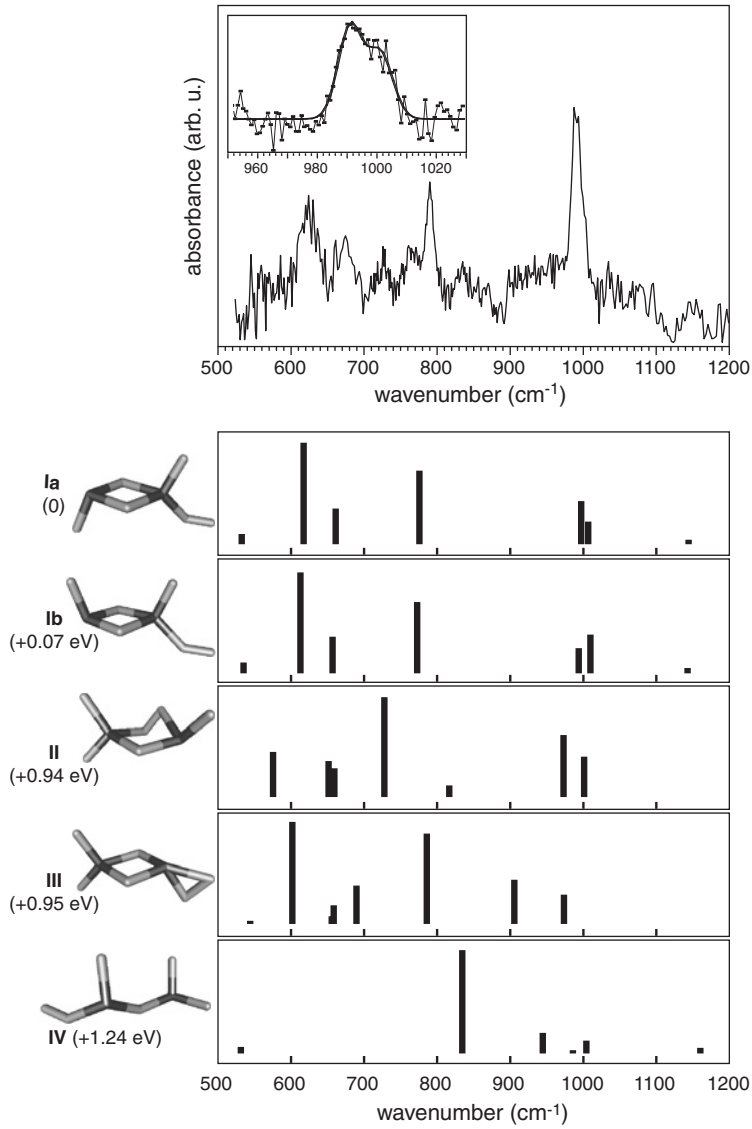

Figure 9: Top: Experimental IR spectrum of $Nb_2O_6^+$ as obtained by IR multiple photon dissociation spectroscopy. The inset shows the band around 990 cm^{-1} with higher resolution. The fitted line is the envelope of two separate peaks at 989 and 999 cm^{-1} (10 cm^{-1} FWHM). Bottom: Calculated IR spectra for five different isomers, whose geometric structure is schematically indicated on the left-hand side.

originally dipole-forbidden vibrational transition (1580 cm^{-1} in O_2) is red-shifted and gains in intensity.

The intensities of the IR active modes range from weak, e.g., ~50 km/mol for the superoxo-mode in $V_2O_7^-$, to very strong (>2000 km/mol) for individual O–V–O modes in the largest cluster anions studied. In general, the intensity of the V–O–V modes is comparable to those of the V=O modes; however, since the latter often

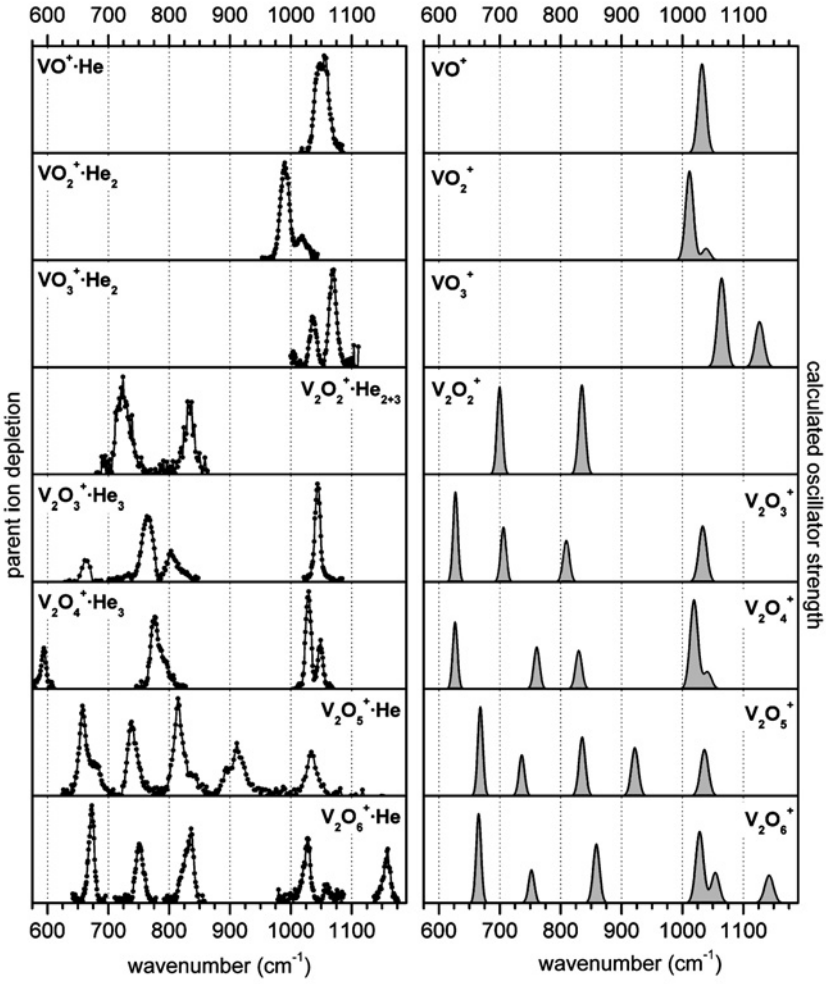

Figure 10: Overview of experimental messenger atom IR-PD spectra (left column) and simulated IR absorption spectra (right column), based on scaled B3LYP/TZVP frequencies and oscillator strengths of the lowest energy isomer in its electronic ground state for vanadium oxide cluster cations ranging from VO^+ to $V_2O_6^+$ (from top to bottom).

overlap in a narrower region the vanadyl band is generally the most intense feature in the spectrum. An exception is $V_4O_{10}^-$, where as a result of the high symmetry of the cluster anion only a comparably weak and red-shifted O–V–O band is observed.

4.2.3.1. Assignment of vibrational spectra The identification of the electronic state and structure of a particular vanadium oxide cluster ion is based on the comparison between the experimental PD spectra and simulated IR spectra of possible structural and electronic isomers. The simulated spectra are convoluted stick spectra, representing the scaled harmonic frequencies from B3LYP/TZVP calculations. Different scaling factors were used for the vanadyl modes (0.9167) and for the V–O–V modes as well as other modes below 900 cm^{-1} (0.9832) [53]. An assignment based exclusively on the

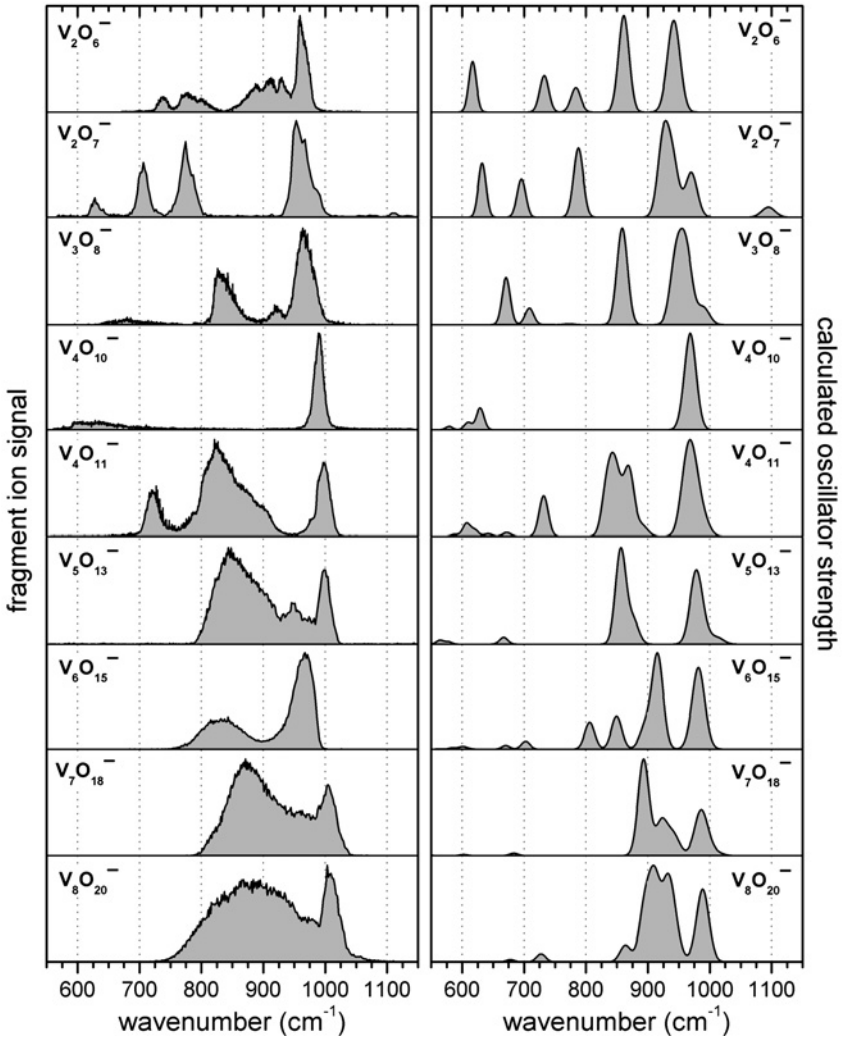

Figure 11: Overview of experimental IR-MPD spectra (left column) and simulated IR absorption spectra (right column), based on scaled B3LYP/TZVP frequencies and oscillator strengths of the lowest energy isomer in its electronic ground state of vanadium oxide cluster anions ranging from $V_2O_6^-$ to $V_8O_{20}^-$ (from top to bottom).

experiment or theory is nearly impossible for the vanadium oxides ions because of the wealth of possible electronic and structural isomers. Two examples are shown in Fig. 14. For $V_2O_5^+$ the lowest two isomers are nearly identical with respect to their geometry, but differ in their electronic symmetry, $^2A'$ vs. $^2A''$. Interestingly, their vibrational spectra are markedly different: five bands for the $^2A'$ isomer vs. four bands for the $^2A''$ isomer. Comparison with the experiment nicely confirms the $^2A'$ isomer as the lowest in energy [53], resolving a discrepancy in the literature concerning the nature of the electronic ground state of $V_2O_5^+$ [60, 61].

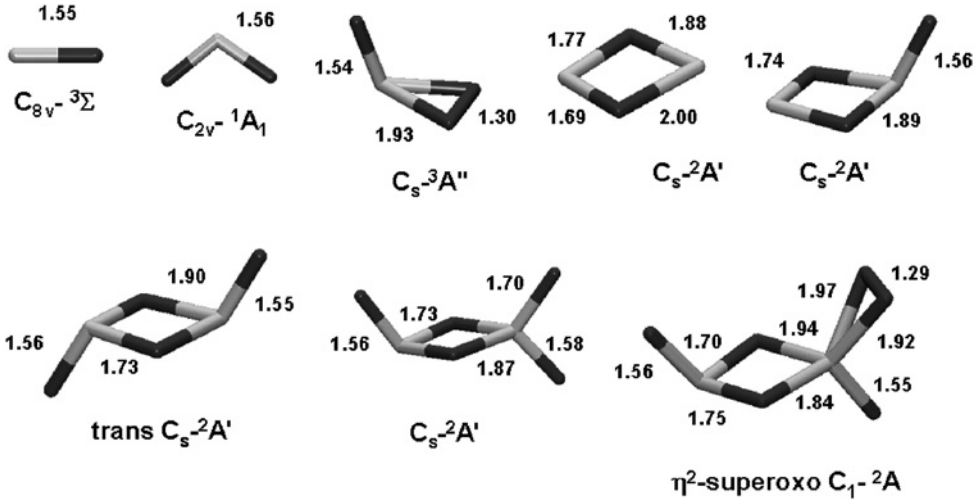

Figure 12: B3LYP/TZVP structures of small cationic vanadium oxide clusters.

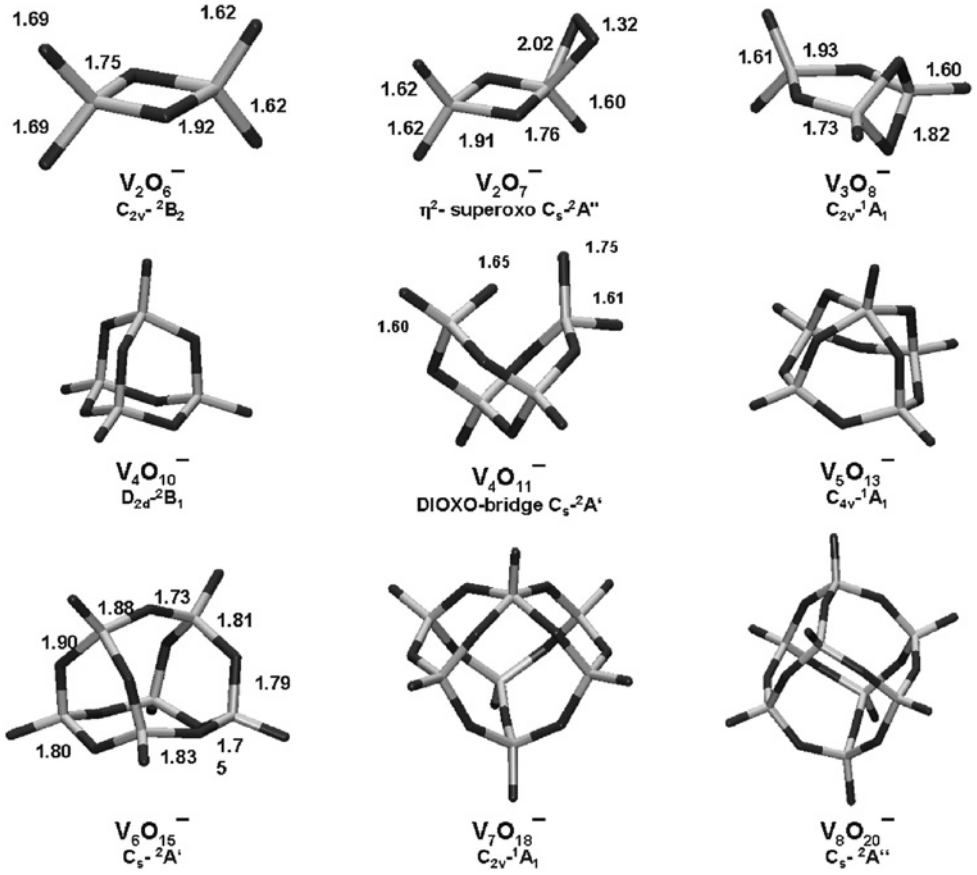

Figure 13: B3LYP/TZVP structures of anionic vanadium oxide clusters.

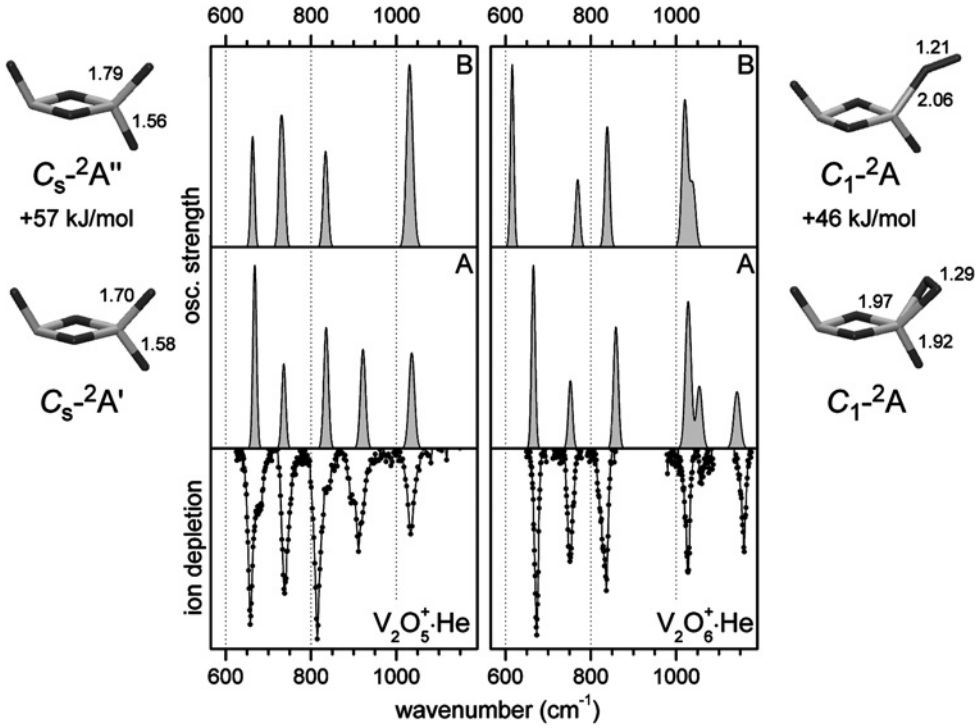

Figure 14: Assignment of the experimental vibrational spectra based on comparison with simulated IR spectra. The experimental messenger atom IR-PD spectra of $V_2O_5^+$ (bottom left) and $V_2O_6^+ \cdot He$ (bottom right) are shown together with the lowest (A) and second lowest energy isomers of $V_2O_5^+$ (left) and $V_2O_6^+$ (right).

The $V_2O_6^+$ spectra (right side in Fig. 14) demonstrate the sensitivity of the vibrational spectra to the interaction strength with oxo-groups in oxygen-rich vanadium oxide ions. Isomer B had been suggested to be the ground state of $V_2O_6^+$ [61]. Its vibrational spectrum, however, lacks a band observed in the experiment. This stimulated a further search, which came up with isomer A. The two calculated isomers consist of a nearly identical trans-V_2O_4 unit, but differ in the way they bind the dioxygen group. Isomer A forms a η^2-superoxo structure, while isomer B only weakly binds the O_2 unit, forming an O_2-complex with formally no charge. The different types of binding are reflected in the scaled vibrational frequencies involving the O_2-unit: 1142 cm^{-1} in the superoxo structure vs. 1404 cm^{-1} in the O_2 complex [53]. The experiment yields 1160 cm^{-1}, supporting the superoxo structure.

4.2.3.2. Change in structural motifs with cluster size Several structural motifs are found as a function of size. A characteristic four-membered planar V–O–V–O ring is found in divanadium oxide cations [53] and anions [56]. Its spectral signature consists of three in-plane deformation bands of comparable intensity in the 550–870 cm^{-1} region. Only two of these bands are observed for $V_2O_2^+$, because the third, predicted at 565 cm^{-1}, lies outside of the measurement window. An M–O–M–O (M = metal atom) ring was originally predicted for small neutral scandium oxide clusters [62] and

experimentally observed, in the form of a broad, unstructured band in-between 600 and 800 cm^{-1}, in the IR-REMPI spectra of neutral zirconium oxide clusters [25] (see Section 4.2.1 and Fig. 8). The latter study was not able to resolve the individual vibrational ring modes, mainly due to lack of mass selection of the absorbing (parent) species. Vanadium oxide cluster ions with three vanadium atoms represent an intermediate cluster class; they show a 3D backbone structure, but still contain one vanadium atom that contributes only two bonds to the cage backbone. $V_4O_{10}^-$ is the first cage structure, in which each vanadium atom forms three V–O–V bonds and only a single terminal vanadyl bond. All larger clusters follow this trend, making this structural element a general criterion for particular stable structure in $V_xO_y^{+/-}$ ions with $x \geqslant 4$.

Figure 15 compares the gas-phase IR-MPD spectrum of $V_8O_{20}^-$ with the electron energy loss spectrum of a V_2O_5 surface [63], which also probes vibrational states. The spectra are surprisingly similar in the region above 740 cm^{-1}, both displaying two bands of similar width and relative intensity. Their assignment is identical, i.e., to vibrational modes of singly and doubly coordinated oxygen atoms. The third broadband of the surface spectrum is not observed in the gas-phase. This can easily be rationalized because this band is assigned [64, 65] to triply coordinated oxygen sites, which do not exist in the $V_8O_{20}^-$ cluster anion. Hence, the vibrational spectra reflect clearly the common (V=O and V–O–V bonds) and the discriminating (triply coordinated O) structural features of gas-phase clusters and solid surfaces.

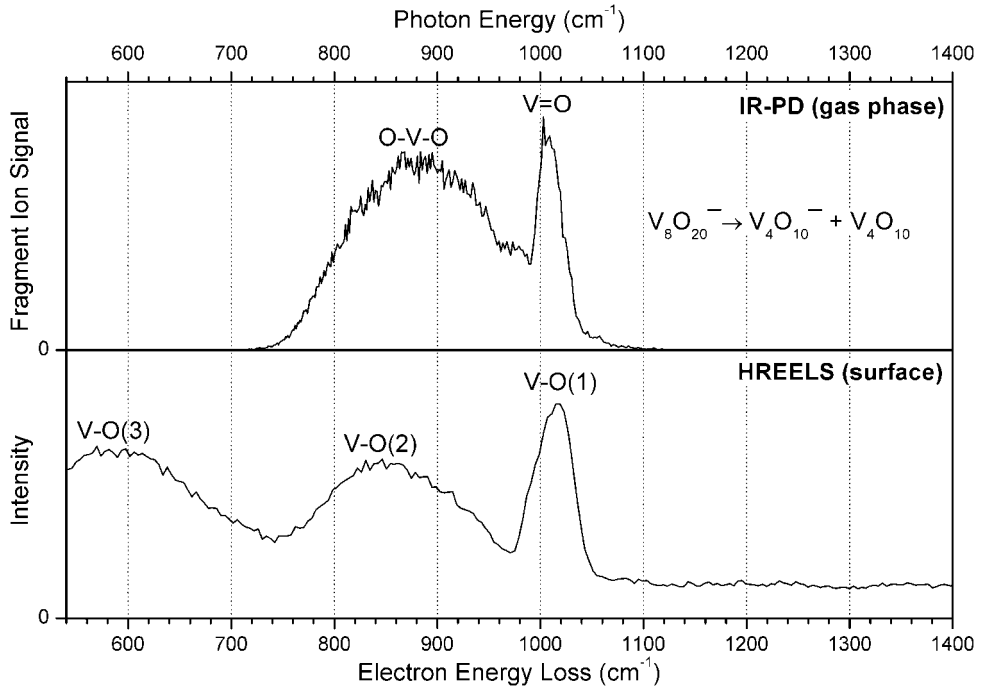

Figure 15: Vibrational spectra of different forms of vanadium oxide. The IR-MPD spectrum of the gas-phase cluster anion $V_8O_{20}^-$ (top) is shown together with the spectrum of a freshly cleaved (001) surface of V_2O_5 (bottom), measured using high-resolution electron energy loss spectroscopy.

4.2.3.3. Influence of the messenger atom For the IR-PD measurements we generally assume that if He is used as a messenger atom, its influence on the cluster ion energetics and dynamics is negligible. Ar can also be used, but its eight times larger polarizability leads to a considerably stronger charge-induced dipole interaction with the ion and may cause complications. This is supported by experiments [54] and high-level calculations [58, 66] that we performed on VO^+ complexes with various messenger atoms/molecules. Experimentally, we find ν(VO) to be $1053 \pm 5\,cm^{-1}$ for the He-containing messenger complex, and the small relative shifts ($\pm 1\,cm^{-1}$) for the $VO^+ \cdot He_n$ ($n > 1$) and $VO^+ \cdot H_2$ complexes indicate only a minimal influence of the lighter ligands (H_2, He) on the vibrational frequency of VO^+. This is supported by CASPT2/cc-pVQZ calculations, which predict a shift of $+2\,cm^{-1}$ for He and place the harmonic vibrational frequencies of VO^+ and $VO^+ \cdot He$ at 1052 and $1054\,cm^{-1}$, respectively. For Ar, the experimental shift is $+8\,cm^{-1}$, significantly larger, but still on the order of the experimental accuracy. That Ar may be more problematic in this particular case is also indicated by its more than four times larger binding energy to VO^+ ($D_e = 3535\,cm^{-1}$) compared to $VO^+ \cdot He$ ($D_e = 788\,cm^{-1}$), requiring the absorption of several (≥ 4) photons to overcome the dissociation threshold.

The IR-MPD spectrum of $V_3O_6^+ \cdot Ar_2$ (bottom spectrum in Fig. 16) is a good example for how Ar, in contrast to He, messenger atoms can affect the vibrational spectrum of vanadium oxide cations. The lowest energy structure found for $V_3O_6^+$ is the chain-like structure shown in Fig. 16. Its scaled harmonic frequencies (spectrum C) match the experimentally observed bands rather well, considerably better than, e.g., the frequencies of the energetically second lowest isomer (spectrum D) with a ribbon-like structure and 31.8 kJ/mol higher in energy. However, the experimental spectrum clearly has additional bands in the V–O–V stretch region compared to spectrum C and does not reproduce the relative intensity of the vanadyl band at $1044\,cm^{-1}$. Both of these effects can be attributed to the presence of the Ar atoms. Calculations on the Ar-complexes of $V_3O_6^+$ confirm that the additional bands are, at least in part, due to a splitting of the vibrational modes as a result of the asymmetric solvation of $V_3O_6^+$ by the Ar atoms. The discrepancies with respect to the relative intensities are a result of the relatively high sequential binding energies for the first and second Ar atom of 28.3 and 21.3 kJ/mol, respectively. Consequently, the absorption of at least two and, in the region below $\sim 900\,cm^{-1}$, three IR photons are required to pump sufficient energy into the complex in order to break the bond to one of the messenger atoms in $V_3O_6^+ \cdot Ar_2$.

A different example of how the Ar messenger atom can lead to an apparent discrepancy between experiment and theory is found for $V_3O_7^+$ (see Fig. 16). Here the calculations on bare $V_3O_7^+$ find a caged structure lowest in energy, but its IR spectrum disagrees with the experimental spectrum of $V_3O_7^+ \cdot Ar$ (Fig. 16). Interestingly, the simulated IR spectra of the (bare) ring isomer, found 17.4 kJ/mol above the (bare) caged isomer, match much better. Calculations on the respective Ar complexes yield almost IR spectra identical to those of the bare clusters (e.g., spectrum A and B in Fig. 16), but, surprisingly, change the energetic ordering of the isomers. While the Ar complex of the cage isomer is only stabilized by 15.6 kJ/mol relative to the bare ion, the ring isomer is found to drop by 50.1 kJ/mol in energy, placing it 17.1 kJ/mol below (!) the Ar complex of the cage isomer. This behavior is exceptional, but emphasizes the importance of taking the influence of the messenger atom into account.

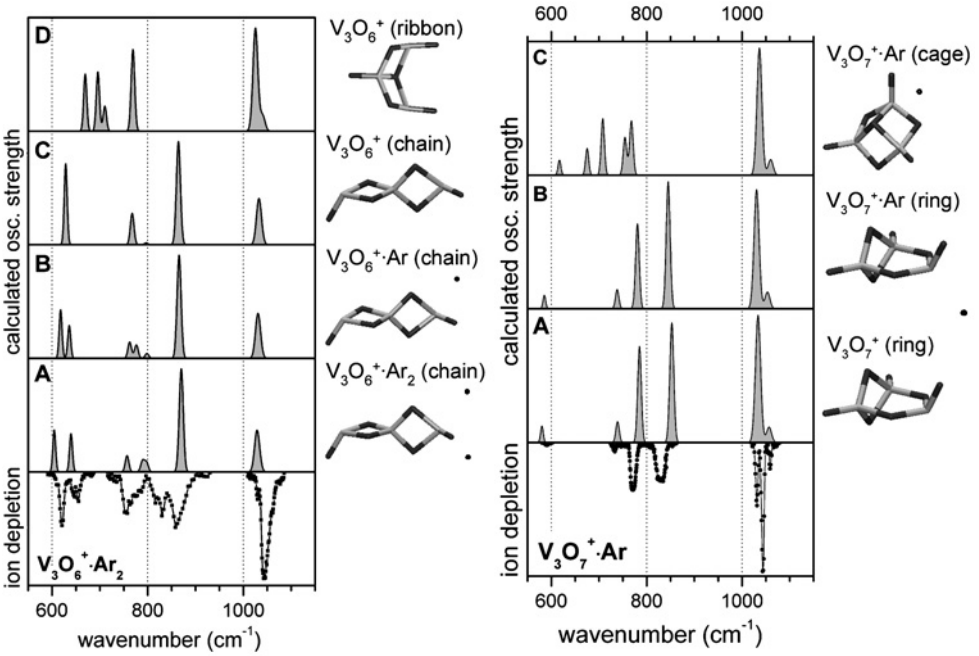

Figure 16: Left: The experimental messenger atom IR-PD spectrum of $V_3O_6^+ \cdot Ar_2$ (bottom) is shown together with the simulated IR spectra of the two lowest energy isomers, which have a chain-like (spectrum C) and a ribbon-like structure (spectrum D), respectively. For the chain-like isomer structure we also calculated the IR spectra of the corresponding messenger atom complexes with one (spectrum B) and two Ar atoms (spectrum A). Right: The experimental messenger atom IR-PD spectrum of $V_3O_7^+ \cdot Ar$ (bottom) is shown together with the simulated IR spectra of the Ar messenger atom complexes of the two lowest energy isomers, which have a ring-like (spectrum B) and a cage-like structure (spectrum C), respectively. The IR spectrum of the bare ring-like isomer is also shown (spectrum A).

Without considering the interaction with Ar, the spectrum seemed to indicate that it is not due to the lowest energy isomer.

4.2.3.4. Electron localization Symmetry-breaking electron or hole localization is observed in many chemical systems and its proper description by density functional theory (DFT) depends on the functional used. For example, the electron hole created in quartz when doped with Al is not delocalized over all four oxygen sites of the AlO_4 defect site, but localized at one oxygen only [67, 68]. We use the measured IR-MPD spectra of $(V_2O_5)_n^-$ with $n = 2$, 3, and 4 as criterion for selecting the proper functional and find that only B3LYP has the right admixture of Fock exchange to reproduce the size-dependent change from delocalized to localized d-electron states in vanadium oxide cages correctly [55].

For $V_4O_{10}^-$ we find a tetragonal D_{2d} structure, which is minimally Jahn-Teller distorted from the T_d structure. The unpaired electron is completely delocalized over d-states of all four vanadium sites as illustrated by its singly occupied natural orbital SONO(1) (Fig. 17). In contrast, in the larger anions the unpaired electron localizes at a single vanadium site, which lowers the symmetry of their structures to C_s. For $V_6O_{15}^-$ and $V_8O_{20}^-$ we find the distorted trigonal prism and cube structures (Fig. 13). Their

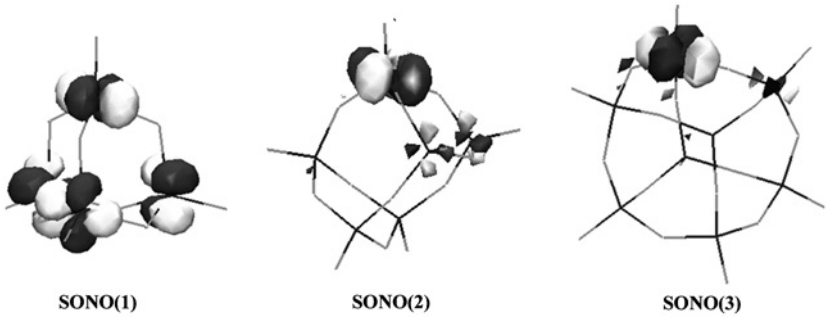

Figure 17: Singly occupied natural orbitals for (from left to right) $V_4O_{10}^-$, $V_6O_{15}^-$, and $V_8O_{20}^-$.

singly occupied natural orbitals, SONO(2) and SONO(3), reflect the localization of the unpaired electron. Unlike the closed-shell neutral parent compounds, the D_{3h} structure (trigonal prism) of $V_6O_{15}^-$ and the D_{2d} structure (cube) of $V_8O_{20}^-$ are higher order saddle points. For both $V_6O_{15}^-$ and $V_8O_{20}^-$ first order saddle points with C_{2v} symmetry are found, which represent transition structures for the interconversion of two equivalent C_s-minimum structures and have the additional electron delocalized over two sites.

The effects of symmetry breaking are directly observed in the vibrational spectra of these species, indicated by the gray-shaded area in Fig. 18. On localization of the unpaired electron, intense V–O–V stretch transitions appear $\sim$100–200 cm^{-1} below the strong vanadyl band, which replace the weak V–O–V feature more than $\sim$350 cm^{-1} below the vanadyl band in the spectrum of the delocalized case ($V_4O_{10}^-$). The vanadyl modes are not affected by the electron localization and therefore their position and width remain nearly unchanged. Comparison with the experimental IR spectra confirms the general predictions of the B3LYP model, in particular the pronounced, qualitative changes on electron localization when the size of the cluster is increased.

Figure 18 shows not only the B3LYP results discussed so far, but also results of DFT calculations that employ the BLYP [69, 70] and BHLYP [70, 71] functionals. The increasing admixture of Fock exchange (0%, 20%, and 50%) in BLYP, B3LYP, and BHLYP, respectively, leads to an increasing tendency for symmetry-breaking [67, 68, 72, 73]. BHLYP (right column in Fig. 18) yields localization of the unpaired electron for all three cage-type anions, also for $V_4O_{10}^-$. Consequently, the BHLYP spectrum of $V_4O_{10}^-$ shows additional bands between 800 and 900 cm^{-1} that are absent in the experimental spectrum. In contrast, BLYP predicts delocalization of the unpaired electron for all three cage-type anions studied and C_{2v} and D_{2d} structures become the ground states of $V_6O_{15}^-$ and $V_8O_{20}^-$, respectively. All three BLYP spectra do not show any band between 750 and 950 cm^{-1}, which is in clear contrast with the experimental spectra of $V_6O_{15}^-$ and $V_8O_{20}^-$. In summary, Fig. 18 shows that only B3LYP reproduces correctly the transition from symmetric (delocalized) to broken-symmetry (localized) structures when passing from $V_4O_{10}^-$ to $V_6O_{15}^-$ in this series of $(V_2O_5)_n^-$ cluster anions.

This conclusion is further supported by single point CCSD(T) calculations that have been made on the BHLYP optimized structures [56]. They confirm that for $V_4O_{10}^-$ the

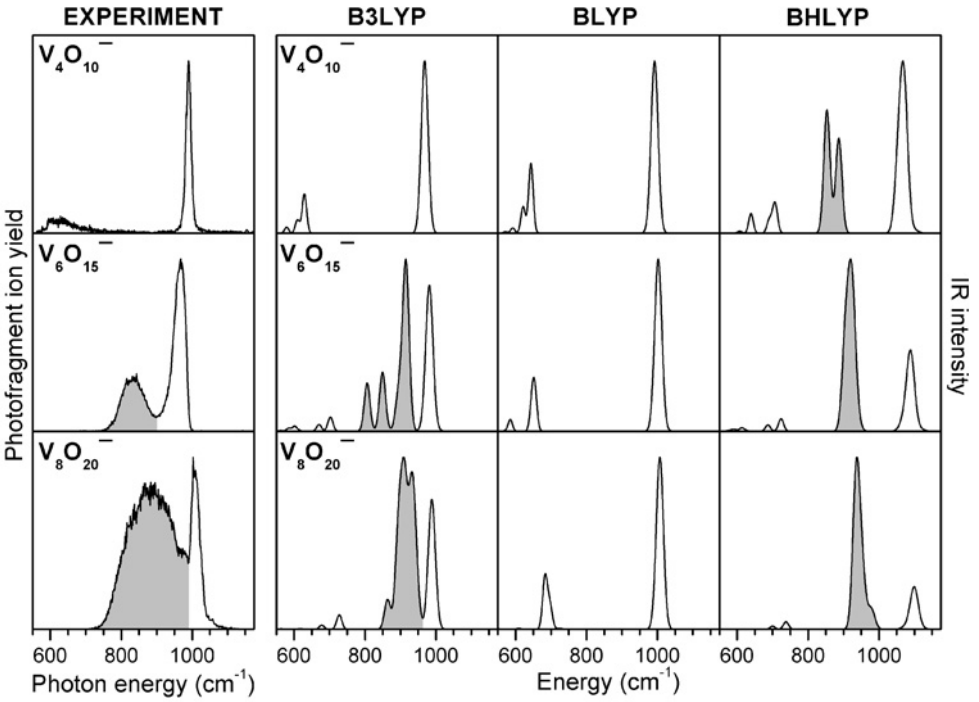

Figure 18: Experimental and simulated vibrational spectra of vanadium oxide cluster anions in the region of the V–O single and double bond stretch modes. IR-MPD spectra (left) of $V_4O_{10}^-$ (top), $V_6O_{15}^-$ (center), and $V_8O_{20}^-$ (bottom) were measured from 550 to 1175 cm^{-1} monitoring the dominant fragmentation channel, leading to formation of $V_3O_8^-$, $V_4O_{10}^-$, and $V_4O_{10}^-$, respectively. Simulated spectra (right) were obtained from scaled harmonic frequencies and oscillator strengths employing the B3LYP, BLYP, and BHLYP functionals. The calculated stick spectra were convoluted with a Gaussian line function for better comparison with the experiment. Gray shaded peaks indicate localization of the unpaired d-electron (see text).

D_{2d} structure has a lower energy than the C_s structure (33 kJ/mol compared to 7 kJ/mol with B3LYP), while for $V_6O_{15}^-$ the C_{2v} structure has a higher energy than the C_s structure (9 kJ/mol compared to 10 kJ/mol with B3LYP).

4.2.3.5. Mixed metal oxide clusters Advances with respect to cluster ion sources are aimed at a greater flexibility in producing the metal oxide species. Recently, the first IR-MPD spectra of mixed metal oxide clusters were measured (Fig. 19), using a dual laser dual metal target laser vaporization source [74]. Adding a second metal to clusters allows tailoring both the electronic and geometric structure of the cluster ion. The singly substituted $TiV_{y-1}O_z^-$ cluster anions, for example, can be used as models for the isoelectronic neutral, pure V_yO_z clusters. These experiments are aimed at eventually producing model systems in the gas-phase that simulate the metal oxide cluster-metal oxide support interaction. Another promising approach is the application of ion spray techniques to the production of gas-phase metal oxide ions from an aqueous solution of synthesized, complex metal oxide species, which opens the door to the efficient gas-phase production of a whole new series of metal oxide-containing species [75].

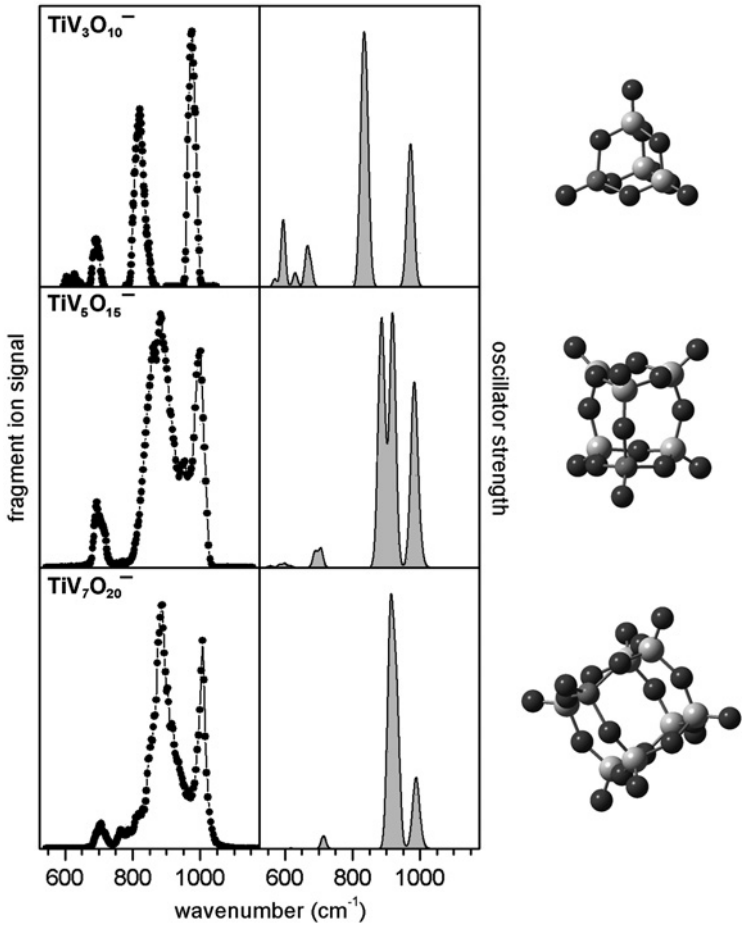

Figure 19: Experimental IR-MPD spectra (left) and simulated IR spectra (right) of the mixed metal oxide cluster anions $TiV_3O_{10}^-$, $TiV_5O_{15}^-$, and $TiV_7O_{20}^-$.

4.3. Transition metal clusters

Structural characterization of metallic clusters and of their complexes with small ligand molecules has greatly benefited from the introduction of the FEL as IR light source as well. Here, in particular, the far-IR spectroscopy has profited from the intensity of FELIX radiation in the long wavelength range, providing access to modes of low IR intensity, as for instance M–M vibrations. Additionally, the spectroscopy in the gas-phase allowed for the detection of low-frequency modes that in case of deposited or embedded clusters are often covered by vibrational bands related to the substrate.

4.3.1. Geometric structure and vibrational spectroscopy

Until recently the determination of geometric structures of isolated transition metal clusters relied on rather indirect methods like the counting of adsorption sites on the surfaces of the clusters [76] or the interpretation of photoelectron spectra [77–79].

Far-IR-PD spectroscopy together with the measurement of cluster ion mobilities [80] and electron diffraction of trapped cluster ions [81] has been developed and applied more recently to obtain direct structural information of transition metal clusters. Here the focus is on the IR spectroscopy of bare transition metal clusters containing typically less than 30 atoms in the gas-phase. Such small clusters have a discrete electronic level structure, but with growing size, a transition from molecular and insulator-like to the metallic behavior occurs [82]. The extended metals do not have a structured IR absorption spectrum due to the shielding of the incident electromagnetic field by the free electron gas. As an alternative, collective vibrations, e.g., the optical active phonon modes, can be experimentally determined via inelastic neutron scattering [83].

In the past, vibrational properties of ligand-free metal clusters larger than the dimers have nearly exclusively been obtained via Raman spectroscopy on clusters deposited in low-temperature matrices. Small metal clusters have been grown directly in the matrix by co-deposition of atomic metal vapor and neon or argon atoms. However, this technique does not yield cluster size-specific spectra. The more recent development of mass-selective deposition of clusters into the matrix allows a more direct assignment of the size-specific vibrational spectrum. A comprehensive review on the vibrational properties of small metal clusters obtained by these and further methods, e.g., optical or photoelectron spectroscopy, has been given in 2002 by Lombardi and Davis [84]. At that time, vibrational properties were known for about 20 transition metal trimers; Ta_4, Ag_5, Ag_7, and Ag_9 were the only larger clusters sizes that had been characterized with mass selection.

Even for stabilized forms of transition metal clusters, data for the far-IR and in particular data on the metal–metal vibrational modes are rather limited. There have been reports on the growth of metal clusters in zeolites detected via the appearance of bands in the far-IR that are assigned to metal cluster modes [85]. The field of the vibrational spectroscopy of ligand stabilized transition metal clusters in the range of the metal–metal vibrations has been reviewed in the past and will not be discussed here, and it is noted that, in any case, most of the available information is only on small dimeric systems [86, 87].

The introduction of the FEL for the spectroscopy of clusters in the mid- and far-IR spectral range has noticeably increased the number of transition metal clusters that has been studied and gives the possibility to obtain size-selective IR spectra of isolated clusters in the gas-phase. Furthermore, the gas-phase experiments permit the investigations of species in different charge states (including neutral clusters), whereas, e.g., matrix isolation studies have been limited so far to the study of neutral metal clusters.

4.3.2. Photodissociation using messenger atoms

Similar to the studies on the vibrational properties of charged metal oxide clusters (see Sections 4.2.2 and 4.2.3), we obtain the IR spectra of free metal clusters in the gas-phase by resonance enhanced MPD spectroscopy. PD techniques have been extensively used before in the spectroscopy of metal clusters in the UV and visible spectral range. Direct PD of bare metal clusters has been applied to probe their electronic absorption spectra. However, only a few examples of the spectroscopy of transition metal clusters have been reported, e.g., for small copper clusters [88–90]. Direct PD

has found more application for the less strongly bound s^1 or s^2p^1 metals [91–93]. Obviously, this method is limited by the height of the barrier for cluster dissociation with respect to the photon energy, at least as long as only single photon absorption processes are concerned. Transition metal clusters have rather high binding energies of typically 3–5 eV per atom [94]. In this case, the introduction of weakly bound spectator ligands that are vaporized off the cluster on excitation allows to study the absorption spectra of these more strongly bound systems and to extend the spectral range into the IR. The sensitivity toward thermal excitation of the cluster is particularly high when using physisorbed messengers, e.g., N_2 molecules or rare gas atoms that have low binding energies toward the cluster. So far, UV, optical, and near-IR absorption spectra of neutral and charged transition metal clusters have been measured via the dissociation of such weakly bound complexes, but the unavailability of intense and tunable light sources in the far-IR prohibited an extension into the spectral range of the vibrational fundamentals of metal clusters. With an FEL as an intense light source, PD of rare gas complexes has been demonstrated to be possible down to below $100\,cm^{-1}$ where a single far-IR photon carries only a fraction of the binding energy of the rare gas atoms, which is on the order of $\sim 1000\,cm^{-1}$ for Ar. Therefore, PD even of rare gas complexes in the far-IR spectral range is an MPD process.

The basic assumption behind the application of the messenger atom technique is that only the metal cluster acts as chromophore, while the weakly bound atomic or molecular ligand acts just as a messenger and does not perturb the structural properties of the cluster. This will be true for most transition metal clusters (exceptions are found for the late transition metals with completely filled *d* shells) complexed with rare gas atoms, since usually directional binding leads to significant barriers for isomerization. Indeed, in the case of cationic vanadium clusters, the influence of the rare gas on the IR spectra has been found to be negligible [95]. Experimentally, it is found that for complexes of V_n^+ with Ar, Kr or Xe, the band positions in the IR spectra are essentially identical. However, in complexes of a cluster with multiple argon atoms, slight blue shifts of the bands on the order of about $1–2\,cm^{-1}$ per Ar atom can be observed. These shifts are most likely related to the mechanism of sequential MPD. With increasing number of ligands in the complex, it becomes easier to dissociate a single Ar atom because of the decreasing binding energy per ligand. Therefore, different internal energies are required to induce the dissociation process. At higher excitations, (cross-) anharmonicities that are important in the multiple photon absorption process lead generally to a red-shift of the absorption bands and complexes with a single ligand that need a higher internal excitation to fragment will therefore exhibit the most pronounced red-shift of their absorption bands.

The vibrational properties of small metal clusters, however, can be considerably influenced by the rare gas atoms. For example, the IR-MPD spectrum of neutral silver trimers obtained by dissociation of their Ar complexes shows two bands in the $100–220\,cm^{-1}$ range and corresponds to the spectrum of Ag_3 in its $^2B_2$ ground state, although a more complicated vibronic structure can be expected to be originating from the dynamical Jahn-Teller effect in Ag_3. Here, binding of an Ar atom seems to lock Ag_3 in one of the C_{2v} structures. Additionally, the low-frequency mode of Ag_3 is observed to shift with increasing Ar coverage from $113\,cm^{-1}$ for Ag_3–Ar to about $120\,cm^{-1}$ for Ag_3–Ar_4, the value known for Ag_3 embedded in rare gas matrices [96].

4.3.3. Vanadium and niobium clusters

Mainly because of their relative ease of production and their favorable isotopic distribution, vanadium and niobium clusters have been intensively experimentally studied in the past and this has caused an extensive follow-up of theoretical investigations. Currently, both systems (in particular niobium clusters) have been developed to some of the best studied metal cluster systems by both experiment and theory. They are preeminent examples for the size dependence of physical and chemical properties, e.g., niobium clusters exhibit dramatic cluster size-dependent changes in their electronic properties or in their reactivities toward H_2 or N_2. Although several experiments, e.g., using photoelectron or optical spectroscopy, allowed for insights into the evolution of their electronic structures, the understanding of the geometric structures is still inadequate. In the following, we will discuss new insights into the structural properties of vanadium and niobium clusters obtained by application of far-IR vibrational spectroscopy with FELIX in combination with theoretical studies.

4.3.3.1. Cationic vanadium clusters For vanadium cluster cations V_n^+ in the size range of $n = 3$–23, the experimental far-IR spectra have been obtained via MPD of their argon complexes (Fig. 20). These far-IR spectra vary strongly with size and each

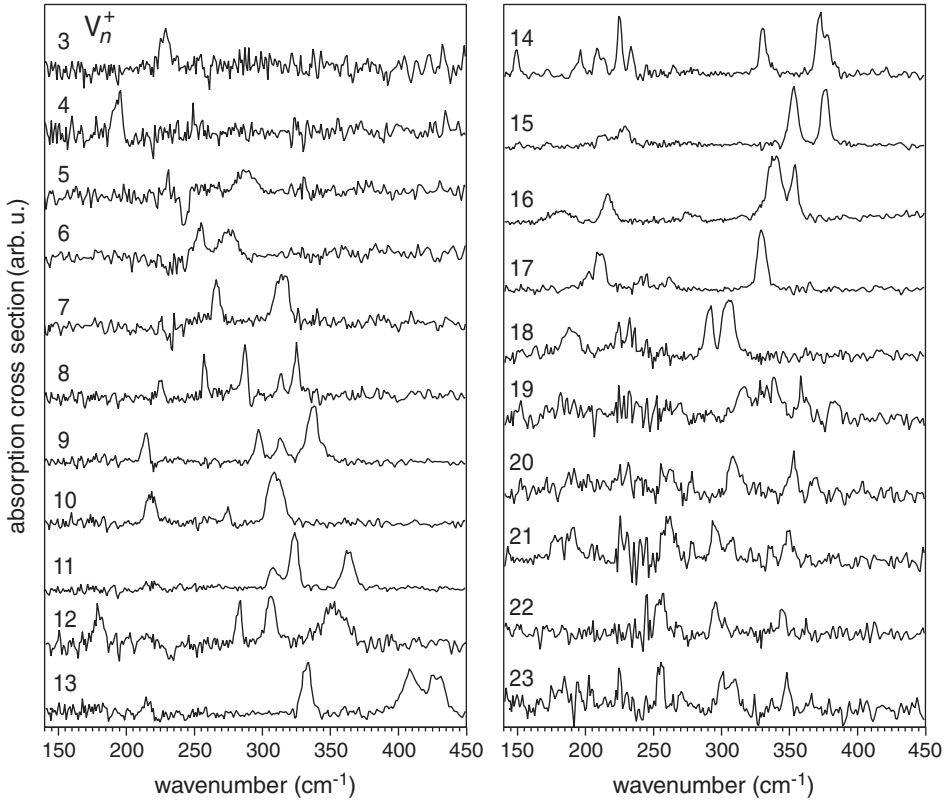

Figure 20: Far-IR MPD spectra of the argon complexes of cationic vanadium clusters. The spectra are measured in the range 140–580 cm^{-1}, but signals are only found and displayed up to 450 cm^{-1}.

cluster has its one individual "fingerprint" spectrum. Most spectra are relatively simple and contain only a few absorption bands up to the size of $n = 17$. Generally, a low number of IR active modes is a sign of high symmetry of the corresponding species. Furthermore, it indicates that the number of isomers for a given cluster size must be low, or that there is only a single isomer formed under the conditions of cluster growth. The cluster containing 14 V atoms forms somehow an exception with a more complicated spectrum that may indicate a lower symmetry.

More detailed structural information can be obtained by comparison with theory. For small vanadium cluster cations up to $n = 15$, density functional calculations have been performed employing the DMol[3] code. The PBE functional and numerical atomic orbitals have been used in these calculations. For V_8^+ the experimental IR spectrum and calculated IR spectra for the four lowest energy isomers of this cluster are compared in Fig. 21. V_8^+ is one of the smaller clusters that exhibits more details in its spectrum, but, is still small enough for accurate and reliable calculations. The isomer A with $S = 1/2$ is found to be the energetically lowest isomer. Good agreement between experimental and calculated IR spectra is achieved for isomer A and C that have the same underlying geometry, a doubly capped distorted tetragonal bipyramid. Isomer A has a doublet electronic state, while C is in a quartet state. For the higher energy isomer C, the agreement with the experimental spectrum is slightly better than

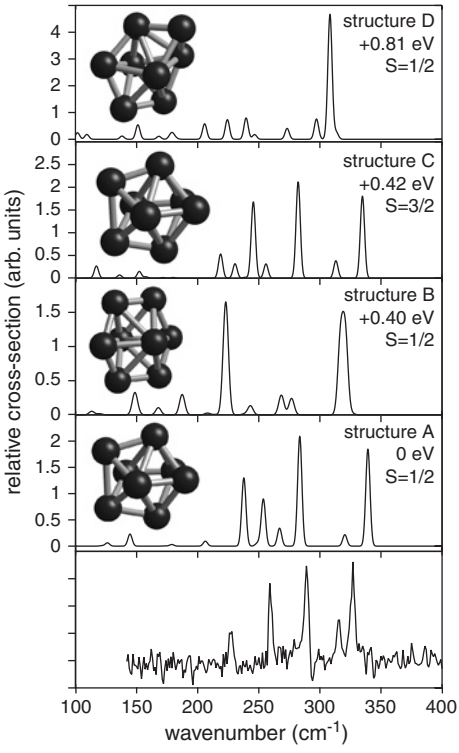

Figure 21: Comparison of the experimental IR spectrum of V_8^+ with calculated IR absorption spectra of some isomers. The calculated spectra are folded with a Gaussian line shape function of 4 cm^{-1} width (FWHM).

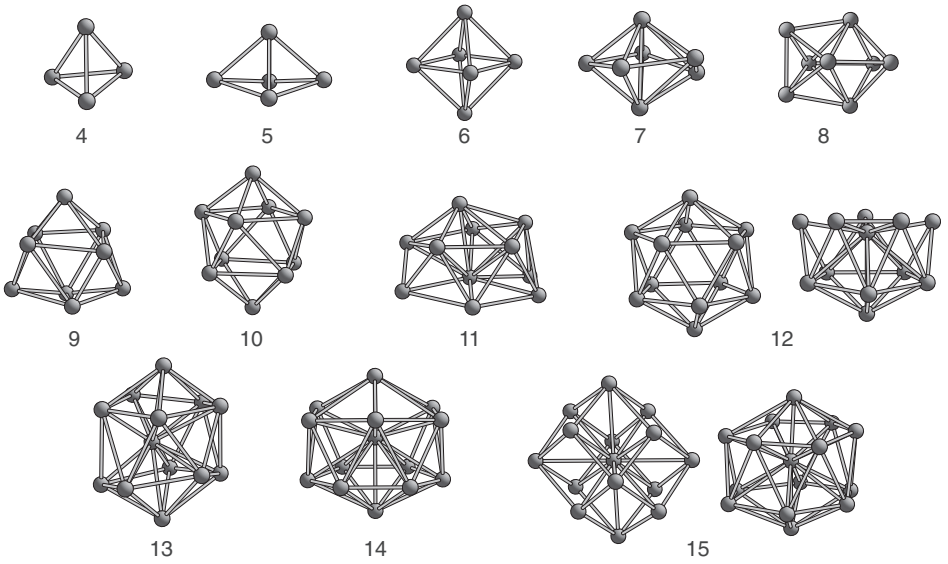

Figure 22: Geometries of cationic vanadium clusters V_n^+ obtained by comparison of the experimental far-IR spectra with spectra for different isomers from DFT calculations. For $n = 12$ and 15, a clear distinction between the isomers shown could not be made.

for the energy minimum. This could be an artifact of the DFT calculations that do not take into account the weakly bound Ar atoms. However, in test calculations on V_3Ar^+ and V_4Ar^+ no significant influence of the Ar atoms has been found. Nevertheless, for other clusters attachment of Ar atoms can reverse the energetic order of different isomeric structures (see Section 4.2.3). For the clusters containing 4–15 atoms the most probable geometric structures that are identified from the comparison of the calculated IR spectra of the isomers and the experimental spectrum for a given cluster size are shown in Fig. 22 [3, 97].

The bulk structure of vanadium is body centered cubic (bcc) with a shortest V–V distance of 2.63 Å. The two optically active phonon modes are at 165 cm^{-1} (transversal) and 230 cm^{-1} (longitudinal) [98]. All our spectra have signals in this range as well as up to a factor two higher frequency. Structural features of the small cluster can deviate significantly from elements of the *bcc* bulk structure. Whereas the distorted octahedral structure of V_6^+ or the doubly capped octahedron of V_8^+ can be considered as parts of the *bcc* structure, other cluster sizes show completely different structural motives, e.g., a triply capped trigonal prism for V_9^+ or a capped anti-cube structure for V_{10}^+. For clusters with $n = 7$, 12, and 13, the spectra even indicate structures of (slightly distorted) fivefold symmetry. With growing cluster size, however, the clusters develop properties similar to those of the bulk metal. In the electronic structure of anionic vanadium clusters similarities to the bulk have been found starting with the 13-atom cluster, where a band appears that has been assigned to a surface feature. A second bulk-like feature evolves starting with the 17-atom cluster. The interpretation of Wu et al. is that, in the range from $n = 13$ to 16, a transition from molecular-like to bulk-like behavior occurs and that already V_{17}^- possesses an inner structure similar to that of the bulk [79].

In fact, in that size range, the vibrational spectra provide consistent evidence for such a structural transition. Small clusters have all atoms on their surface, but starting with the V_{13}^+ cluster one observes the appearance of vibrational bands at comparatively high energies that are assigned by comparison with theory to vibrational modes involving motions of internal atoms. Accordingly, the transition from molecular-like to bulk-like behavior observed in the photoelectron spectra coincides with the appearance of volume atoms. Also the vibrational spectra of the larger clusters signify an approach toward bulk-like geometric structures. For instance, for V_{15}^+, four bands are observed in the IR spectrum, which goes nicely along with the number of IR-active modes in a structure of O_h symmetry. This isomer (left structure for V_{15}^+ in Fig. 22) mimics already the *bcc* structure. The nearest metal–metal distances are calculated to be 2.39 Å for V_{15}^+, significantly shorter than the atomic distances in the bulk, 2.63 Å. For smaller clusters the interatomic distances decrease even more, e.g., to a minimum distance of 2.26 Å and an average bond length of 2.41 Å in V_8^+ and finally to 1.76 Å in the dimer [97]. The lowered coordination of the atoms within the cluster with respect to the bulk leads to an increase in the bond strength, that is expressed, e.g., in a high (vibrational) bond order [84].

4.3.3.2. Isomers of neutral niobium clusters Structure determination based on the vibrational spectra can become more complicated if the cluster formation process leads to a mixture of isomers of a cluster. In the case of cationic vanadium clusters there is no conclusive evidence for coexisting isomers, except possibly for V_{12}^+ [97]. This is quite different for, e.g., niobium clusters, where the presence of isomers has been found to be quite common for neutral as well as cationic clusters in the size range of $n = 9$–19. This coexistence of different isomeric structures has been experimentally revealed mainly via the investigation of the kinetics with reactant molecules like H_2, N_2 or C_2H_4, where bi- or multiple-exponential reaction kinetics are interpreted as signatures for the presence of isomers with different reactivities [99–103].

A specific isomer can in principle be selected by making use of these differences in reactivities toward a reactant. If the unwanted isomers have a significantly higher reactivity they can be titrated away from the isomeric mixture. A following mass selection can separate the reaction products from the less reactive isomers. Another approach exploits differences in the IPs of neutral clusters. These differences can be considerable, i.e., on the order of several tenths of an eV. Using single photon ionization with tunable UV lasers it becomes possible to ionize the isomer with the lowest IP close to its ionization threshold without interference of the other isomer(s). The unwanted isomers remain in the mixture, but do not contribute to the mass spectrometric signal.

For neutral Nb_9 two isomers are known to coexist and it has been possible to obtain their isomer-specific far-IR spectra [104]. These spectra, together with a comparison of calculated spectra for different structures, are shown in Fig. 23. Incidentally, the two Nb_9 isomers have rather different IPs of 4.92 and 5.20 eV [105], which are both lowered in the Ar complexes by about 0.07 eV. Therefore, ionization with UV photons of 4.96 eV can be used to probe selectively only one isomer (iso1). At higher UV photon energies the argon complexes of all isomers are ionized and the resulting vibrational spectrum corresponds to that of the mixture of isomers. Spectral information on the isomers with higher IPs can be extracted from the spectra of the isomeric mixtures.

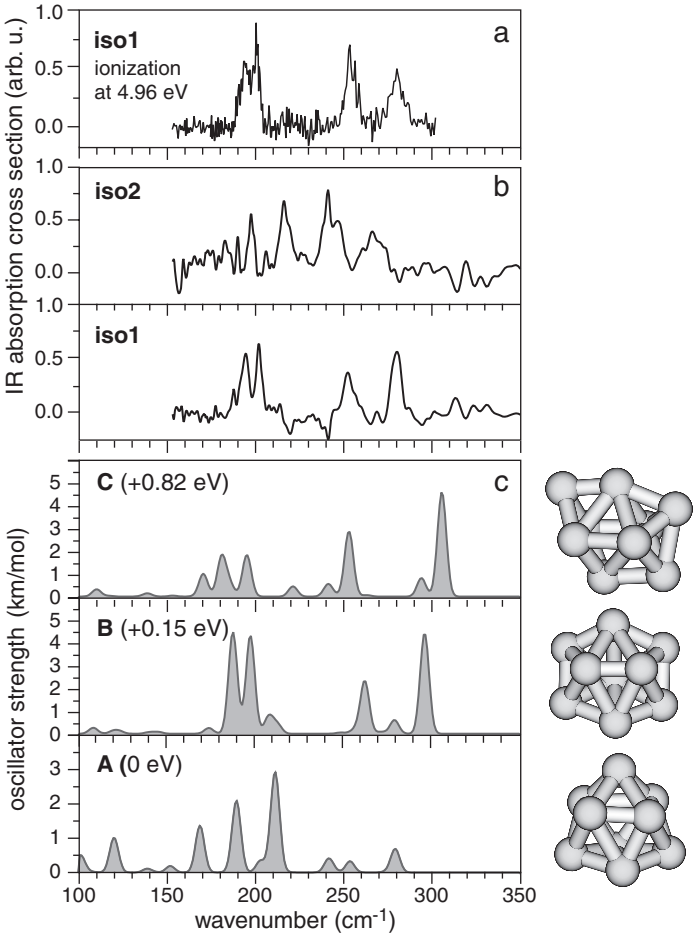

Figure 23: Isomer-specific spectra of neutral Nb_9 clusters. In (a) the spectrum of the single isomer iso1 is shown as measured via near-threshold ionization. The spectra in (b) are obtained by iterative subtractive deconvolution of the spectra of the Nb_9Ar_n complexes ($n = 1$–4). Calculated IR spectra for low energy isomers are plotted in the lowest panel (c).

A detailed analysis of the MPD spectra of the $Nb_9Ar_n^+$ complexes containing different numbers of Ar atoms n ($n = 1$–4) indicates that the spectrum of Nb_9Ar^+ is mainly dominated by one isomer, while with increasing n the second isomer becomes more abundant. This can be explained by different affinities of the cluster isomers toward the Ar atoms. These particularities allow for an independent determination of the vibrational spectra of *both* isomers via subtractive deconvolution of the spectra of the Nb_9Ar_n complexes. One of the resulting spectra nicely agrees with the spectrum obtained via selective ionization. A comparison with the calculated spectra for different low energy isomers leads to a rather definite structural assignment of isomer 1 to geometry B. This structure can be described as a non-planar hexagon with a dimer above and an atom below the hexagon. It is only 0.15 eV higher in energy than the lowest energy structure, a triply capped trigonal prism. The structural assignment for

the second isomer is less certain. The comparison of the band positions suggests that isomer 2 may have structure A, although the IR intensities do not match. Further evidence for these structural assignments is derived from the calculation of the (adiabatic) ionization energies. We find values of 5.13 eV for structure A and 4.98 eV for structure B that are in good agreement with the experimental values.

4.4. Complexes of transition metal clusters

Metal clusters, or even strongly bound clusters in general, are often discussed as models for the surfaces of bulk materials. Obviously this comparison has its limitations, since in a cluster that contains typically less than 100 atoms, all or a dominant fraction of the atoms are located on the surface and the number of volume atoms is low. For bulk material, the reverse is generally true. Additionally, the coordination of metal atoms in a cluster can be very different compared to atoms within an extended metal surface and will be usually lower and less symmetric. Nevertheless, there exist striking parallels in the bonding of chemisorbed molecules to an extended metal surface and to metal clusters. Not only the similarities between ligand-covered metal clusters and adsorbates on surfaces but also the differences, e.g., in the coupling of vibrational modes of ligands or the effect of the quasi-continuous band structure of bulk metals, have been thoroughly discussed before [106].

In a slightly modified picture, free metal clusters in the gas-phase can be viewed as models for defect sites of an imperfect metal surface. Here, the basic idea is that an isolated cluster of known size and charge state could mimic the electronic or geometric properties of a defect site that in turn could coincide with an active site for a certain catalytic reaction. Thereby, studies of gas-phase clusters can help in the understanding of the mechanism of a heterogeneous catalytic reaction. For clusters bound to a substrate, the interaction with the substrate will change the electronic structure and geometry of a cluster on a surface in comparison to the gas-phase properties. However, a comparison between free clusters having no interaction with a substrate and deposited clusters can give valuable insights into the cluster–substrate interaction. In the last part of this chapter we will show that complexes of free metal clusters can actually be used as reference systems for understanding the properties of metal clusters deposited on a substrate.

The following discussion will be mainly restricted to complexes of transition metal clusters with a single or a few ligand molecules. Those systems can be viewed as models of adsorbate molecules interacting with a metal surface at low coverage. They are a closer representation of surface adsorbates than ligand-stabilized clusters, where a dominant fraction or even all of the metal atoms are bound directly to ligand molecules. In the latter systems, the electronic and geometric structure of the metal cluster can be significantly altered through the ligand shell complicating a comparison with a (partly) covered metal surface.

4.4.1. Developments in the vibrational spectroscopy of metal cluster complexes

In the very first experiments, small metal cluster complexes have been synthesized in cryogenic matrices via co-condensation and annealing techniques and subsequently characterized by IR spectroscopy using either grating or FT-IR spectrometers. From the analysis of the concentration dependence of the spectral features, it is possible to get indications on the corresponding metal cluster sizes and the complex

stoichiometries [107]. By this means Moskovits has investigated the interaction of CO with small neutral Cu, Ni, and Pd clusters with $n \leqslant 4$ [108–110]. Later, the vibrational spectra of some transition metal dimers complexed with CO [111, 112] or ethylene [113] have been reported by Andrews. CO complexes of slightly larger clusters of gold ($n \leqslant 5$) and lead ($n \leqslant 4$) grown in an Ar matrix have been studied by Jiang and Xu [114, 115]. Matrix isolation spectroscopy of cluster complexes has been improved by performing the complex formation in the matrix with initially mass-selected metal clusters [116–118]. For intensity reasons, most of the spectroscopic characterization of cluster complexes is performed in the spectral range of the internal ligand modes only, i.e., for CO ligands between 1600 and 2200 cm^{-1}, and there is a lack of experimental data on the metal cluster modes. This, together with the usual presence of product mixtures and concomitant matrix effects, makes the assignment of spectral features to certain cluster species a challenging task and can lead to ambiguous conclusions.

The development of spectroscopic techniques that couple vibrational spectroscopy with mass spectrometric detection made it possible to ensure the identity of the species under investigation. For instance, mass-selective IR-MPD with line-tunable CO_2 lasers has been used in the past to obtain IR spectral information for some metal cluster complexes in a limited spectral range around 10 μm. A rather comprehensive overview of these studies has been given in a review on reactions of transition metal clusters by Knickelbein [119]. Although the accessible spectral range is rather limited, it includes the vibrational signatures of several relevant ligand molecules, e.g., C–O stretching or C–H deformation modes. Systems that have been investigated via IR-MPD using CO_2 lasers include, for instance, silver clusters complexed with ethylene or ethylene oxide [120], methanol or ethanol on coinage metal clusters [121–123], hydrogen dissociatively adsorbed on iron clusters [124], or ammonia complexes of silver [14, 125] or iron clusters [126]. Remarkably, in most of these cases there are no indications for qualitative changes in the ligand–cluster interaction as a function of the cluster size. A particular exception is found for complexes of gold cluster cations with methanol molecules, where the C–O stretching vibration of the adsorbed methanol changes discontinuously with cluster size. This has been related to a 2D to 3D shape transition in the size region of $n = 7$–9 [123].

The recently developed technique of embedding species in superfluid helium droplets is a new and very promising variant of matrix isolation spectroscopy [127]. Complexes can be formed via pick-up of metal atoms and molecules from the gas-phase. These species are instantaneously thermalized to the temperature of the droplet (0.37 K for ^{4}He) resulting in a stabilization of complex structures that are not necessarily the thermodynamically most stable ones. The superfluid helium interacts only very weakly with the embedded species and any excitation is followed by the evaporation of a significant number of He atoms from the droplet. Absorption of photons by embedded species can be sensitively monitored, e.g., via bolometric detection of changes in the particle flux. First examples for the vibrational spectroscopy of metal cluster complexes within He nanodroplets have been reported [128–131].

Somehow complementary to the area of metal cluster complexes is the field of the complexes of atomic metals and their ions with one or multiple ligand molecules. Gas-phase experiments on cationic metal atom complexes have been lately addressed in a review by Duncan [132]. These systems often contain weakly bound ligands and in these cases dissociation can be induced using less powerful laser systems that are

tunable throughout the IR, e.g., optical parametric oscillators (OPO) or difference frequency mixing units. Using a similar technique, Weber et al. have studied anionic complexes of coinage metal atoms, i.e., $AuCO_2^-$ and $MH_2OAr_n^-$ (M=Cu, Ag, Au; $n = 1, 2$) [133, 134]. A discussion of the large body of matrix isolation experiments on such species is beyond the scope of this chapter.

Vibrationally resolved UV photoelectron spectroscopy forms an alternative approach to obtain vibrational properties for ligands bound to anionic metal clusters. For instance, Kim et al. have investigated O_2 complexes of anionic Cu, Ag, and Au clusters [135, 136] as well as N_2 interacting with Nb or W clusters [137, 138]. The vibrational structure within the photoelectron spectra has been used to discriminate between dissociative and non-dissociative interaction of the diatomic ligands with the metal clusters.

The first demonstration of IR-MPD spectroscopy of metal cluster–ligand complexes using an FEL has been performed on $Ag_n(NH_3)_m$ complexes [139]. For this system a direct comparison to data from IR-MPD experiments using a CO_2 laser could be made. The use of the FEL allowed extending the spectral range and accessing the vibrational modes also for complexes with deuterated ammonia. This initial study has been followed by experiments to investigate the interaction of single CO molecules with clusters of the late transition metals, i.e., Co, Rh, Ni [140–142], CO, and NO complexes of cationic and anionic Au clusters [143–145], and with water complexes of cationic vanadium clusters [146].

For cationic and anionic gold clusters, saturated complexes with CO have been produced and characterized via IR-MPD spectroscopy [143, 144] (Fig. 24). For these systems it has been possible to complement the spectroscopy in the range of the internal CO stretching modes by PD experiments in the far-IR to probe the Au–C stretching and Au–CO deformation modes. Indications on the structures are derived from a comparison of the stoichiometries of the saturated complexes with the numbers of available binding sites on the possible cluster geometries. The IR spectra are used to constrain and further strengthening of these structural assignments. For the saturated cationic gold carbonyls, planar structures are found for metal cluster sizes at least

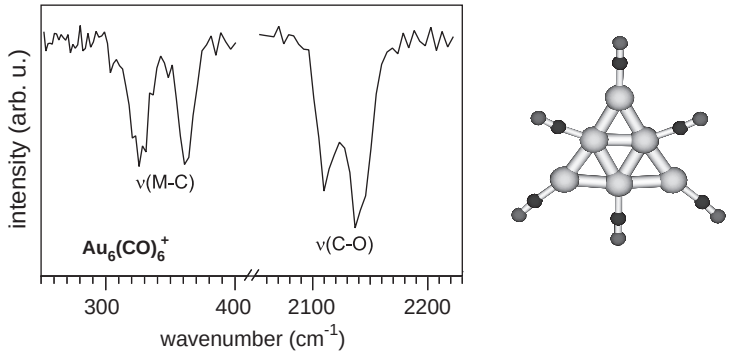

Figure 24: IR-MPD spectrum of $Au_6(CO)_6^+$ and its proposed structure. The observation of two bands in the ν(CO) range is attributed to the presence of two types of distinct binding sites in Au_6^+. An assignment of the bands in the low-frequency range of the spectrum is less unambiguous, since this range comprises both metal–ligand stretch and deformation modes.

up to $n = 7$ with the CO ligands binding only to low-coordinated gold atoms having less than five neighboring Au atoms [143].

In the following, a more focused discussion will be given on the properties of the CO complexes of rhodium clusters.

4.4.2. Effects of cluster size and charge on the binding of CO to rhodium clusters

An important aspect in the study of adsorbed CO molecules is the strong sensitivity of the frequency of the internal CO stretching vibration ν(CO) toward (i) the electron density on the metal center and (ii) the binding geometry of the CO molecule. This sensitivity, and the large oscillator strength of CO ligands that allows for vibrational spectroscopy even at very low coverage, cause the wide usage of CO adsorbates for probing the properties of metal surfaces or of finely dispersed metals via ν(CO) [147].

The bonding of CO to transition metal atoms is commonly described in terms of the Blyholder model of M←C σ donation and M→C π backbonding [148]. The two corresponding natural bond orbitals with M–C binding character for the Rh–CO complex, together with an MO scheme of the carbon monoxide molecule are depicted in Fig. 25. The backbonding is an interaction of (partially) filled M(δ) orbitals with the empty CO(2π) orbitals that are of antibonding character and relates the CO bond strength to the occupancy of the M(δ) orbitals. This leads to a dependence of the CO bond strength, and thereby the ν(CO) frequency, on the charge on the metal center.

Analogously, the interaction of a CO molecule with multiple metal atoms leads to a more efficient M→C π back donation and significant weakening of the CO bond, typically leading to a decrease of the ν(CO) frequency by 100–150 cm^{-1} per additional metal-C bond. These typical shifts in the ν(CO) frequency allow identification of the presence of CO ligands in atop (μ^1), bridging (μ^2), or capping (μ^3) configuration. A pronounced cluster size dependence in the binding geometry of CO is found for single CO molecules bound to rhodium cluster cations, neutrals, or anions (Fig. 26) [141].

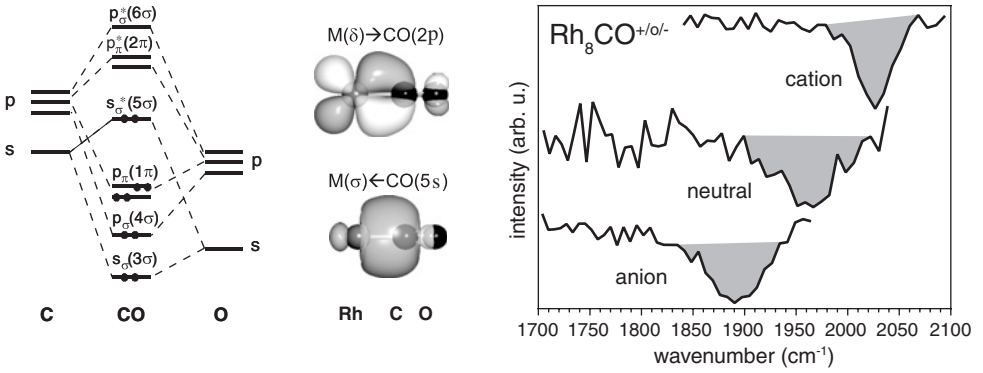

Figure 25: Left: Qualitative MO scheme of CO and plots of the natural bond orbitals in RhCO with M–C binding character. Right: Observed charge dependence of the position of the ν(CO) band for $Rh_8CO^{+/o/-}$. The influence of the ionic charge can be understood via the amount of back-donation into antibonding 2π orbitals of the CO that increases from the cation to the anion. Hence the internal CO bond weakens leading to a shift of the ν(CO) band to lower wavenumbers.

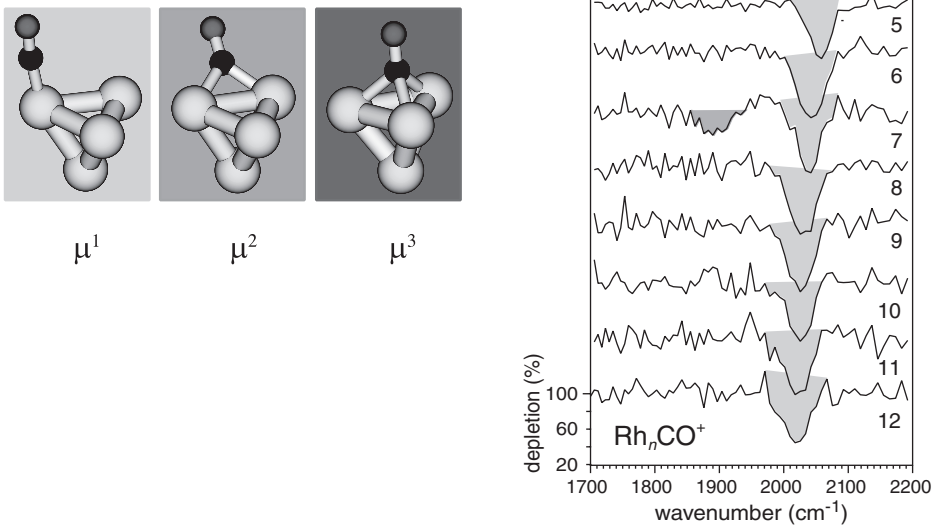

Figure 26: Left: Examples for different binding geometries of CO, coordinating to a single (μ^1), two (μ^2), or three (μ^3) metal atoms. Right: ν(CO) bands of Rh_nCO^+ complexes. Starting from $n = 5\mu^1$ binding CO is always observed, whereas for smaller clusters CO is found to bind in a μ^2 ($n = 3$) or μ^3 ($n = 4$) geometry. For $n = 7$ isomers with μ^1 and μ^2 bound CO coexist.

In the gas-phase, metal cluster complexes can be prepared in different charge states and the charge dependence of ν(CO) is directly observable (Fig. 25). The charge and cluster size dependence of ν(CO) can be simply modeled. To model the M→C π backbonding it is assumed that the occupancy $P(2\pi)$ of the CO(2π) orbital depends on the fraction of the total cluster charge z that resides on the metal atom to which the CO binds. This fraction is inversely proportional to the number of surface atoms n_S in the cluster:

$$P(2\pi) = P(2\pi)_\infty - \frac{\gamma z}{n_S} \tag{4}$$

If one includes the minor contribution $\Delta\nu_{ES}$ due to the electrostatic interaction of a charged metal cluster with the dipole of the CO molecule, this leads to a stretching frequency of

$$\nu(\mathrm{CO}) = \nu_\infty + \Delta\nu_{ES} + \frac{\gamma'}{n_S} \tag{5}$$

for CO adsorbed on a charged cluster. For large clusters, n_S is proportional to $n^{2/3}$; in small clusters one can estimate n_S by comparison with known cluster structures. More details and a more rigorous derivation of Eq. (5) are given in Ref. [142]. The experimentally determined dependence of the ν(CO) frequency in $Rh_nCO^{+/0/-}$ complexes containing up to more than 30 Rh atoms on charge and size is shown in Fig. 27. In this plot, only the data for μ^1 bound CO complexes are included. The solid lines in Fig. 27

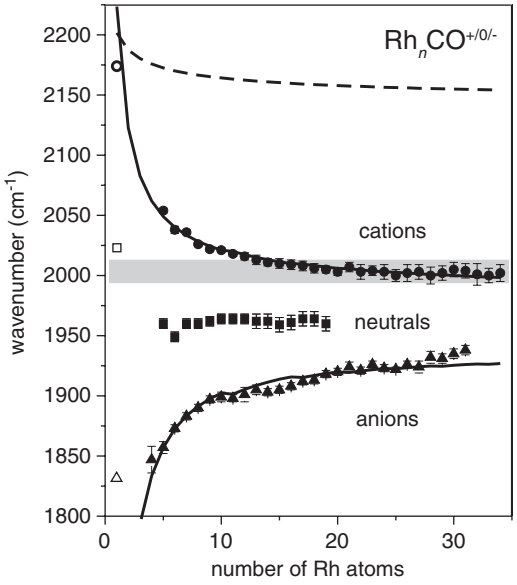

Figure 27: Size and charge dependence of the ν(CO) stretch frequency of μ^1 bound CO in the mono-carbonyl complexes of rhodium clusters. Open symbols are used for the atomic complexes (values from Ref. [156]). The grey band marks the range of the values reported for ν(CO) on rhodium surfaces.

are obtained from the model described above that accounts for the influence of a diluted charge on the amount of back-donation and that includes also the electrostatic interaction between the charge and the CO dipole, whereas the dashed line shows the electrostatic effect only. The model successfully describes the size dependence of ν(CO) for the CO complexes of rhodium, cobalt, and nickel clusters. However, in the cases of the charged clusters the asymptotic values ν_∞(CO) for $n \to \infty$ do not exactly coincide with the values for neutral clusters. This may indicate that the charge is partially localized at the binding site. Furthermore, the ν(CO) values for the neutral clusters and the asymptotic values ν_∞(CO) are significantly below the values of ν(CO) found for CO adsorbed on extended surfaces (low coverage limit). This is probably related to the lower coordination of the cluster atoms compared to an extended surface.

The vibrational data for CO adsorbed on free clusters in the gas-phase can be compared to vibrational data of CO adsorbates at clusters on a substrate to assess the electron density on the deposited metal particles. Hence, quantitative information on the charge transfer between metal cluster and substrate, e.g., from defect centers, can be derived. However, in such a comparison one has to be aware that structures of deposited clusters can be different from those in the gas-phase and that, because of a strong dependence of ν(CO) on the surface coverage, a comparison can only be made for similar coverages, i.e., at the low coverage limit. Additionally, the CO adsorption itself may induce changes in the charge distribution between metal and support [149]. For deposited Rh clusters on a highly ordered Al_2O_3 film [150] the comparison with the gas-phase data indicates a significant positive charging of the deposited clusters by about $+0.4$ to $+0.6e$ [141] (Fig. 28). Similar reasoning has been used to assess the charging of small gold clusters deposited on defect-rich or defect-free MgO substrates [144].

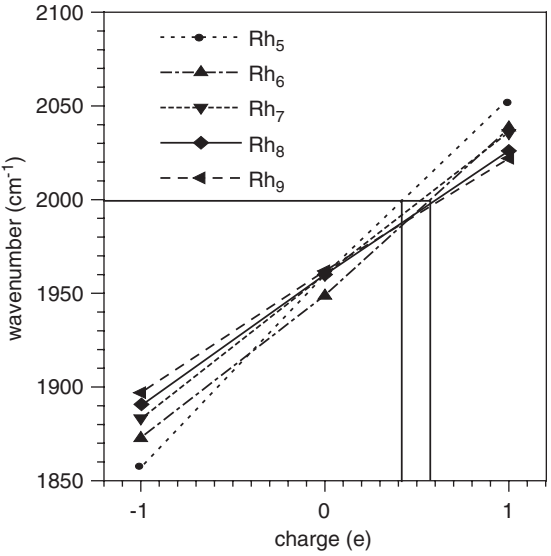

Figure 28: Effect of charge on the ν(CO) stretch frequency of μ^1 bound CO in small rhodium cluster–CO complexes. The horizontal line indicates the observed ν(CO) value of 2000 cm^{-1} for CO adsorbed on deposited clusters of similar size on highly ordered Al_2O_3 [150].

5. SUMMARY AND CONCLUSIONS

IR-REMPI and IR-MPD using the intense and tunable radiation from an IR-FEL can be applied to obtain unique spectroscopic information on mass-selected particles in molecular beams or ion traps. The new experimental data on the vibrational properties contribute to a better understanding of the physical and chemical properties of metal-containing clusters and to a better insight into the evolution of these properties with cluster size. The technique can be extended to chemically relevant cluster–adsorbate systems and enables a detailed study of the influence of the cluster structure on the chemical properties, as well as of the effect of the adsorbates on the internal cluster structure.

IR-REMPI studies are particularly useful to follow the evolution of structural properties with cluster size for larger, neutral clusters that are strongly bound. IR-MPD, on the other hand, is a more generally applicable technique to study clusters, both neutral and ionic. In combination with vibrational frequencies from electronic structure calculations IR-MPD can be used to characterize the geometric structure of individual clusters. IR-PD spectra with the highest detail are obtained using the messenger atom technique in combination with mass selection of both parent and fragment ions. However, when heavier messenger species like Ar atoms are used their perturbation in some cases is significant and has to be accounted for in the calculations.

The IR spectroscopy of metal-containing clusters remains to be one of the most active research areas at FELIX. Even though significant progress has been made in generating tunable IR laser in the mid-IR region using table top systems [151–154] in the recent years, experiments that require higher pulse energies, like IR-REMPI and IR-MPD,

and/or experiments that require photon energies below $\sim 500\,\mathrm{cm}^{-1}$ still need to be performed using an IR-FEL today. For the near future, intracavity experiments are planned at FELIX extending the upper limit for the photon flux by two orders of magnitude [155], which may allow for a whole new class of experiments. Finally, improvements in cluster production, namely with respect to increasing the control over the cluster composition and structure, will be crucial in addressing ever more specific questions related to the interplay between the cluster composition, structure, and reactivity.

NOTE

1. FELIX is located at the FOM Institute for Plasmaphysics "Rijnhuizen" in Nieuwegein, The Netherlands. For more details see http://www.rijnh.nl/n4/n3/f1234.htm.

ACKNOWLEDGMENTS

We gratefully acknowledge the contributions from all authors of the original papers, the "Stichting voor Fundamental Onderzoek der Materie (FOM)" in providing beam time on FELIX and the skillful assistance of the FELIX staff, in particular A.F.G. van der Meer and B. Redlich. This work is supported by the Collaborative Research Center 546 of the German Research Foundation DFG and the EU IHP Research Training Network (Delayed Ionization and Competing Cooling Mechanisms in Atomic Clusters).

REFERENCES

[1] Duncan M.A., Int. J. Mass Spectrom. 200 (2000) 545.
[2] Bieske E.J., Dopfer O., Chem. Rev. 100 (2000) 3963.
[3] Fielicke A., Kirilyuk A., Ratsch C., Behler J., Scheffler M., von Helden G., Meijer G., Phys. Rev. Lett. 93 (2004) 023401.
[4] Rosenbaum N.H., Owrutsky J.C., Tack L.M., Saykally R.J., J. Chem. Phys. 84 (1986) 5308.
[5] Davis S., Fárník M., Uy D., Nesbitt D.J., Chem. Phys. Lett. 344 (2001) 23.
[6] Okumura M., Yeh L.I., Lee Y.T., J. Chem. Phys. 83 (1985) 3705.
[7] Okumura M., Yeh L.I., Myers J.D., Lee Y.T., J. Chem. Phys. 85 (1986) 2328.
[8] Okumura M., Yeh L.I., Lee Y.T., J. Chem. Phys. 88 (1988) 79.
[9] Yeh L.I., Okumura M., Myers J.D., Price J.M., Lee Y.T., J. Chem. Phys. 91 (1989) 7319.
[10] Bagratashvili V.N., Letokhov V.S., Makarov A.A., Ryabov E.A., Multiple Photon Infrared Laser Photophysics and Photochemistry, Harwood Academic Publishers GmbH, Amsterdam, 1985.
[11] Buck U., J. Phys. Chem. 98 (1994) 5190.
[12] Shin S.K., Chen Y., Oh D., Wittig C., Phil. Trans. Roy. Soc. London A 332 (1990) 361.
[13] Selegue T.J., Moe N., Draves J.A., Lisy J.M., J. Chem. Phys. 96 (1992) 7268.
[14] Rayner D.M., Lian L., Athanassenas K., Collings B.A., Fournier R., Mitchell S.A., Hackett P.A., Surf. Rev. Lett. 3 (1996) 649.
[15] Knippels G.M.H., Mols R., van der Meer A.F.G., Oepts D., van Amersfoort P.W., Phys. Rev. Lett. 75 (1995) 1755.
[16] Oomens J., van Roij A.J.A., Meijer G., von Helden G., Astrophys. J. 542 (2000) 404.
[17] Oomens J., Meijer G., von Helden G., J. Phys. Chem. A 105 (2001) 8302.

[18] von Helden G., van Heijnsbergen D., Meijer G., J. Phys. Chem. A 107 (2003) 1671.
[19] Campbell E.E.B., Ulmer G., Hertel I.V., Phys. Rev. Lett. 67 (1991) 1986.
[20] Wurz P., Lykke K.R., J. Chem. Phys. 95 (1991) 7008.
[21] Wurz P., Lykke K.R., J. Phys. Chem. 96 (1992) 10129.
[22] Amrein A., Simpson R., Hackett P., J. Chem. Phys. 95 (1991) 1781.
[23] von Helden G., Holleman I., Knippels G.M.H., van der Meer A.F.G., Meijer G., Phys. Rev. Lett. 79 (1997) 5234.
[24] van Heijnsbergen D., von Helden G., Duncan M.A., van Roij A.J.A., Meijer G., Phys. Rev. Lett. 83 (1999) 4983.
[25] von Helden G., Kirilyuk A., van Heijnsbergen D., Sartakov B., Duncan M.A., Meijer G., Chem. Phys. 262 (2000) 31.
[26] Oomens J., Sartakov B.G., Meijer G., von Helden G., Int. J. Mass Spectrom. 254 (2006) 1.
[27] Bekkerman A., Kolodney E., von Helden G., Sartakov B., van Heijnsbergen D., Meijer G., J. Chem. Phys. 124 (2006) 184312.
[28] Baer T., Hase W.L., Unimolecular Reaction Dynamics, Oxford University Press, Oxford, 1996.
[29] Knippels G.M.H., Van Werkhoven G.H.C., Haselhoff E.H., Faatz B., Oepts D., Van Amersfoort P.W., Nucl. Instrum. Methods A 358 (1995) 308.
[30] Oepts D., van der Meer A.F.G., van Amersfoort P.W., Infrared Phys. Technol. 36 (1995) 297.
[31] Asmis K.R., Brümmer M., Kaposta C., Santambrogio G., von Helden G., Meijer G., Rademann K., Wöste L., Phys. Chem. Chem. Phys. 4 (2002) 1101.
[32] Dietz T.G., Duncan M.A., Powers D.E., Smalley R.E., J. Chem. Phys. 74 (1981) 6511.
[33] Ledoux M.J., Pham-Huu C., Chianelli R.R., Curr. Opin. Solid State Mater. Sci. 1 (1996) 96.
[34] Claridge J.B., York A.P.E., Brungs A.J., Marquez-Alvarez C., Sloan J., Tsang S.C., Green M.L.H., J. Catal. 180 (1998) 85.
[35] Ganesan R., Lee J.S., Angew. Chem. Int. Ed. 44 (2005) 6557.
[36] Hollemann A.F., Wiberg N., Lehrbuch der Anorganischen Chemie, 101st edition, de Gruyter, Berlin, New York, 1995.
[37] Guo B.C., Kerns K.P., Castleman A.W., Science 255 (1992) 1411.
[38] Slanina Z., Sun M.-L., Lee S.-L., THEOCHEM 334 (1995) 229.
[39] Pilgrim J.S., Duncan M.A., J. Am. Chem. Soc. 115 (1993) 9724.
[40] von Helden G., Tielens A., van Heijnsbergen D., Duncan M.A., Hony S., Waters L., Meijer G., Science 288 (2000) 313.
[41] von Helden G., van Heijnsbergen D., Duncan M.A., Meijer G., Chem. Phys. Lett. 333 (2001) 350.
[42] van Heijnsbergen D., Fielicke A., Meijer G., von Helden G., Phys. Rev. Lett. 89 (2002) Art. No. 013401, 4 pp.
[43] Dance I., J. Chem. Soc., Chem. Commun. (24) (1992) 1779.
[44] Dance I., J. Am. Chem. Soc. 118 (1996) 6309.
[45] Rohmer M.M., Benard M., Bo C., Poblet J.M., J. Am. Chem. Soc. 117 (1995) 508.
[46] Benard M., Rohmer M.M., Poblet J.M., Bo C., J. Phys. Chem. 99 (1995) 16913.
[47] Gueorguiev G.K., Pacheco J.M., Phys. Rev. Lett. 88 (2002) Art. No. 115504, 4 pp.
[48] Oshima C., Aizawa T., Wuttig M., Souda R., Otani S., Ishizawa Y., Ishida H., Terakura K., Phys. Rev. B 36 (1987) 7510.
[49] van Heijnsbergen D., von Helden G., Meijer G., Duncan M.A., J. Chem. Phys. 116 (2002) 2400.
[50] van Heijnsbergen D., Demyk K., Duncan M.A., Meijer G., von Helden G., Phys. Chem. Chem. Phys. 5 (2003) 2515.

[51] Demyk K., van Heijnsbergen D., von Helden G., Meijer G., Astron. Astrophys. 420 (2004) 547.
[52] Fielicke A., Meijer G., von Helden G., J. Am. Chem. Soc. 125 (2003) 3659.
[53] Asmis K.R., Meijer G., Brümmer M., Kaposta C., Santambrogio G., Wöste L., Sauer J., J. Chem. Phys. 120 (2004) 6461.
[54] Brümmer M., Kaposta C., Santambrogio G., Asmis K.R., J. Chem. Phys. 119 (2003) 12700.
[55] Asmis K.R., Santambrogio G., Brümmer M., Sauer J., Angew. Chem. Int. Ed. 44 (2005) 3122.
[56] Santambrogio G., Brümmer M., Wöste L., Döbler J., Sierka M., Sauer J., Meijer, G., Asmis K.R. (2006) in preparation.
[57] Gause O., Diploma thesis, Freie Universität Berlin, Berlin, 2004.
[58] Kaposta C., Ph.D. thesis, Freie Universität Berlin, Berlin, 2005.
[59] Asmis K., Sauer J., Mass Spectrom. Rev. (2006) submitted.
[60] Justes D.R., Mitric R., Moore N.A., Bonacic-Koutecký V., Castleman A.W., Jr., J. Am. Chem. Soc. 125 (2003) 6289.
[61] Calatayud M., Andrés J., Beltrán A., J. Phys. Chem. A 105 (2001) 9760.
[62] Johnson J.R.T., Panas I., Chem. Phys. 248 (1999) 161.
[63] Tepper B., Richter B., Dupuis A.C., Kuhlenbeck H., Hucho C., Schilbe P., bin Yarmo M.A., Freund H.-J., Surf. Sci. 496 (2002) 64.
[64] Vyboishchikov S.F., Sauer J., J. Phys. Chem. A 105 (2001) 8588.
[65] Brázdová V., Ganduglia-Pirovano M.V., Sauer J., Phys. Rev. B 69 (2004) 165420.
[66] Döbler J., Sauer J., private communication.
[67] Pacchioni G., Frigoli F., Ricci D., Weil J.A., Phys. Rev. B 63 (2001) 054102.
[68] Solans-Monfort X., Branchadell V., Sodupe M., Sierka M., Sauer J., J. Chem. Phys. 121 (2004) 6034.
[69] Becke A.D., Phys. Rev. A 38 (1988) 3098.
[70] Lee C., Yang W., Parr R.G., Phys. Rev. B 37 (1988) 785.
[71] Becke A.D., J. Chem. Phys. 98 (1993) 1372.
[72] Sherrill C.D., Lee M.S., Head-Gordon M., Chem. Phys. Lett. 302 (1999) 425.
[73] Sodupe M., Bertran J., Rodriguez-Santiago L., Baerends E.J., J. Phys. Chem. A 103 (1999) 166.
[74] Janssens E., Santambrogio G., Brümmer M., Wöste L., Lievens P., Sauer J., Meijer G., Asmis K.R., Phys. Rev. Lett. 96 (2006) 233401.
[75] Feyel S., Schröder D., Schwarz H., J. Phys. Chem. A 110 (2006) 2647.
[76] Riley S.J., J. Non-Cryst. Solids 205–207 (1996) 781.
[77] Häkkinen H., Yoon B., Landman U., Li X., Zhai H.-J., Wang L.-S., J. Phys. Chem. A 107 (2003) 6168.
[78] Kietzmann H., Morenzin J., Bechthold P.S., Ganteför G., Eberhardt W., Yang D.-S., Hackett P.A., Fournier R., Pang T., Chen C., Phys. Rev. Lett. 77 (1996) 4528.
[79] Wu H., Desai S.R., Wang L.-S., Phys. Rev. Lett. 77 (1996) 2436.
[80] Weis P., Int. J. Mass Spectrom. 245 (2005) 1.
[81] Schooss D., Blom M.N., Parks J.H., Issendorff B.v., Haberland H., Kappes M.M., Nano Lett. 5 (2005) 1972.
[82] Issendorff B.v., Cheshnovski O., Annu. Rev. Phys. Chem. 56 (2005) 549.
[83] Brockhouse B., Rev. Mod. Phys. 67 (1995) 735.
[84] Lombardi J.R., Davis B., Chem. Rev. 102 (2002) 2431.
[85] Baker M.D., Ozin G.A., Godber J., J. Phys. Chem. 89 (1985) 305.
[86] Shriver D.F. and Cooper III, C.B., in: Advances in Infrared and Raman Spectroscopy. R.J.H. Clark, R.E. Hester (eds), Heyden, London, Vol. 6, 1980, p. 127.

[87] Cotton F.A., Walton R.A., Multiple Bonds Between Metal Atoms, 2nd edition, Clarendon, London, 1993.
[88] Morse M.D., Hopkins J.B., Langridge-Smith P.R.R., Smalley R.E., J. Chem. Phys. 79 (1983) 5316.
[89] Knickelbein M.B., J. Chem. Phys. 100 (1994) 4729.
[90] Jarrold M.F., Creegan K., Int. J. Mass Spectrom. Ion Processes 102 (1990) 161.
[91] Bréchignac C., Cahuzac P., Carlier F., Leygnier J., Chem. Phys. Lett. 164 (1989) 433.
[92] Ray U., Jarrold M.F., Bower J.E., Kraus J.S., Chem. Phys. Lett. 159 (1989) 221.
[93] Wang C.R.C., Pollack S., Cameron D., Kappes M.M., J. Chem. Phys. 93 (1990) 3787.
[94] Armentrout P.B., Annu. Rev. Phys. Chem. 52 (2001) 423.
[95] Fielicke A., von Helden G., Meijer G., Eur. Phys. J. D 34 (2005) 83.
[96] Fielicke A., Rabin I., Meijer G., J. Phys. Chem. A 110 (2006) 8060.
[97] Ratsch C., Fielicke A., Kirilyuk A., Behler J., von Helden G., Meijer G., Scheffler M., J. Chem. Phys. 122 (2005) 124302.
[98] Sears V.F., Svensson E.C., Powell B.M., Can. J. Phys. 73 (1995) 726.
[99] Zakin M.R., Brickman R.O., Cox D.M., Kaldor A., J. Chem. Phys. 88 (1988) 3555.
[100] Hamrick Y., Taylor S., Lemire G.W., Fu Z.-W., Shui J.-C., Morse M.D., J. Chem. Phys. 88 (1988) 4095.
[101] Bérces A., Hackett P.A., Lian L., Mitchell S.A., Rayner D.M., J. Chem. Phys. 108 (1998) 5476.
[102] Berg C., Schindler T., Kantlehner M., Niedner-Schatteburg G., Bondybey V.E., Chem. Phys. 262 (2000) 143.
[103] Elkind J.L., Weiss F.D., Alford J.M., Laaksonen R.T., Smalley R.E., J. Chem. Phys. 88 (1988) 5215.
[104] Fielicke A., Ratsch C., von Helden G., Meijer G., J. Chem. Phys. 122 (2005) 091105.
[105] Knickelbein M.B., Yang S., J. Chem. Phys. 93 (1990) 1476.
[106] Moskovits M., J. Mol. Catal. 82 (1993) 195.
[107] Moskovits M., Acc. Chem. Res. 12 (1979) 229.
[108] Moskovits M., Hulse J.E., J. Phys. Chem. 81 (1977) 2004.
[109] Moskovits M., Hulse J.E., Surf. Sci. 61 (1976) 302.
[110] Hülse J.E., Moskovits M., Surf. Sci. 57 (1976) 125.
[111] Tremblay B., Manceron L., Gutsev G.L., Andrews L., J. Chem. Phys. 107 (2002) 8479.
[112] Tremblay B., Gutsev G., Manceron L., Andrews L., J. Phys. Chem. A 106 (2002) 10525.
[113] Wang X., Andrews L., J. Phys. Chem. A 107 (2003) 337.
[114] Jiang L., Xu Q., J. Chem. Phys. 122 (2005) 034505.
[115] Jiang L., Xu Q., J. Phys. Chem. A 109 (2005) 1026.
[116] Fedrigo S., Haslett T.L., Moskovits M., J. Am. Chem. Soc. 118 (1996) 5083.
[117] Haslett T.L., Fedrigo S., Bosnick K., Moskovits M., Duarte H.A., Salahub D., J. Am. Chem. Soc. 122 (2000) 6039.
[118] Fedrigo S., Haslett T.L., Moskovits M., Z. Phys. D 40 (1997) 99.
[119] Knickelbein M.B., Annu. Rev. Phys. Chem. 50 (1999) 79.
[120] Koretsky G.M., Knickelbein M.B., J. Chem. Phys. 107 (1997) 10555.
[121] Knickelbein M.B., Koretsky G.M., J. Phys. Chem. A 102 (1998) 580.
[122] Koretsky G.M., Knickelbein M.B., Rousseau R., Marx D., J. Phys. Chem. A 105 (2001) 11197.
[123] Dietrich G., Krückeberg S., Lützenkirchen K., Schweikhard L., Walther C., J. Chem. Phys. 112 (2000) 752.
[124] Knickelbein M.B., Koretsky G.M., Jackson K.A., Pederson M.R., Hajnal Z., J. Chem. Phys. 109 (1998) 10692.
[125] Rayner D.M., Lian L., Fournier R., Mitchell S.A., Hackett P.A., Phys. Rev. Lett. 74 (1995) 2070.

[126] Jackson K.A., Knickelbein M., Koretsky G., Srinivas S., Chem. Phys. 262 (2000) 41.
[127] Toennies J.P., Vilesov A.F., Angew. Chem. Int. Ed. 43 (2004) 2622.
[128] Nauta K., Moore D.T., Stiles P.L., Miller R.E., Science 292 (2001) 481.
[129] Stiles P.L., Miller R.E., J. Phys. Chem. A 110 (2006) 5620.
[130] Stiles P.L., Miller R.E., J. Phys. Chem. A 110 (2006) 10225; DOI: 10.1021/jp063187a.
[131] Stiles P.L., Moore D.T., Miller R.E., J. Chem. Phys. 131 (2004) 3130.
[132] Duncan M.A., Int. Rev. Phys. Chem. 22 (2003) 407.
[133] Boese A.D., Schneider H., Glöß A.N., Weber J.M., J. Chem. Phys. 122 (2005) 154301.
[134] Schneider H., Boese A.D., Weber J.M., J. Chem. Phys. 123 (2005) 084307.
[135] Kim Y.D., Int. J. Mass Spectrom. 238 (2004) 17.
[136] von Gynz-Rekowski F., Bertram N., Ganteför G., Kim Y.D., J. Phys. Chem. B 108 (2004) 18916.
[137] Kim Y.D., Ganteför G., Chem. Phys. Lett. 382 (2003) 644.
[138] Kim Y.D., Stolcic D., Fischer M., Ganteför G., J. Chem. Phys. 119 (2003) 10307.
[139] Simard B., Dénommée S., Rayner D.M., van Heijnsbergen D., Meijer G., von Helden G., Chem. Phys. Lett. 357 (2002) 195.
[140] Fielicke A., von Helden G., Meijer G., Simard B., Dénommée S., Rayner D.M., J. Am. Chem. Soc. 125 (2003) 11184.
[141] Fielicke A., von Helden G., Meijer G., Pedersen D.B., Simard B., Rayner D.M., J. Phys. Chem. B 108 (2004) 14591.
[142] Fielicke A., von Helden G., Meijer G., Pedersen D.B., Simard B., Rayner D.M., J. Chem. Phys. 124 (2006) 194305.
[143] Fielicke A., von Helden G., Meijer G., Pedersen D.B., Simard B., Rayner D.M., J. Am. Chem. Soc. 127 (2005) 8416.
[144] Fielicke A., von Helden G., Meijer G., Simard B., Rayner D.M., J. Phys. Chem. B 109 (2005) 23935.
[145] Fielicke A., von Helden G., Meijer G., Simard B., Rayner D.M., Phys. Chem. Chem. Phys. 7 (2005) 3906.
[146] Jaeger T.D., Fielicke A., von Helden G., Meijer G., Duncan M.A., Chem. Phys. Lett. 392 (2004) 409.
[147] Sheppard N., Nguyen T.T., in: Advances in Infrared and Raman Spectroscopy. R.E. Hester, R.J.H. Clark (eds), Heyden, London, Vol. 5, 1978, p. 67.
[148] Blyholder G., J. Phys. Chem. 68 (1964) 2772.
[149] Sterrer M., Yulikov M., Risse T., Freund H.-J., Carrasco J., Illas F., Valentin C.D., Giordano L., Pacchioni G., Angew. Chem. Int. Ed. 45 (2006) 2633.
[150] Frank M., Bäumer M., Kühnemuth R., Freund H.-J., J. Phys. Chem. B 105 (2001) 8569.
[151] Bosenberg W.R., Guyer D.R., J. Opt. Soc. Am. B: Opt. Phys. 10 (1993) 1716.
[152] Raffy J., Debuisschert T., Pocholle J.P., Papuchon M., Appl. Opt. 33 (1994) 985.
[153] Gerhards M., Opt. Commun. 241 (2004) 493.
[154] Kuyanov K.E., Momose T., Vilesov A.F., Appl. Opt. 43 (2004) 6023.
[155] Militsyn B.L., von Helden G., Meijer G.J.M., van der Meer A.F.G., Nucl. Instrum. Methods A 507 (2003) 494.
[156] Zhou M., Andrews L., J. Am. Chem. Soc. 121 (1999) 9171.

This page intentionally left blank

Chapter 9

Trapped ion electron diffraction: structural evolution of silver and gold clusters

Joel H. Parks* **and Xiaopeng Xing**

Rowland Institute at Harvard, Cambridge, MA 02142, USA

> "In order for physics to be useful to other sciences in a theoretical way, other than in the invention of instruments, the science in question must supply to the physicist a description of the object in the physicist's language …… In order for physical theory to be of any use, we must know where the atoms are located."
>
> R.P. Feynman

1. INTRODUCTION

The size-dependent evolutions of the structures and physical and chemical properties of finite nanoscale materials aggregates have been the subjects of continuing basic and applied research interests. The study of small metal clusters has made extensive contributions to understanding the size-dependent, many-body character of nanoscale physics and chemistry. Metal clusters provide the unique opportunity to extend this research to determine how properties evolve as the number of atoms in the cluster increases. Important examples which have increased our appreciation of the different forms in which size dependence is manifest include measurements and calculations of metal cluster melting [1, 2], the transition of planar to three-dimensional (3D) structures [3, 4] and the reactivity of gold cluster nanocatalysts [5, 6].

Structure determination is one of the outstanding challenges of cluster science, and it has been approached in several ways. Direct structural determination via analysis of diffraction measurements is most desirable. However, such a methodology was not practiced because of technical difficulties, and consequently, one resorted to indirect methods, mostly through theoretical analysis of photoelectron spectroscopic (PES) data [7–10]. Diffraction measurements provide the only direct comparison with theoretical calculations insofar as the patterns are the Fourier transform of the pair correlation function, and thus are directly related to atomic positions. Electron diffraction probes the interference of electron scattering between all pairs of atoms, and thus intrinsically depends on the specific position of every atom in the structure.

The Chemical Physics of Solid Surfaces, Volume 12
ISSN: 1571-0785
DOI: 10.1016/S1571-0785(07)12009-5

*Corresponding author.
E-mail: parks@rowland.harvard.edu

We remark that the term ''direct structural determination method'' is used here to signify a method that is based on a diffraction process, and to distinguish such method from those that while measuring properties that are structure-sensitive (for example, electron spectroscopy) are not based on scattering and/or diffraction from the atomic constituents. This does not imply that in a direct structural determination method further analysis of the data, including comparisons between the measured diffraction patterns and those calculated for theoretically optimized structures, is not required in order to fully determine the atomic arrangement. In fact, it will be shown in Section 3 that each cluster size requires the calculation of 6–10 low-energy isomers to ensure a correlation between diffraction data and calculated low-energy structures is achieved.

Trapped ion electron diffraction (TIED) is a technique which was developed in our laboratory in 1999 to provide a direct measurement of the dependence of cluster structure on size and temperature. Debye first proposed gas-phase diffraction measurements in 1915 [11] and performed X-ray diffraction of carbon tetrachloride in 1929 [12]. In 1930, Wierl performed gas-phase diffraction using mono-energetic electron beams [13] providing increased sensitivity and greatly reduced exposure times. Electron diffraction measurements were initially performed [14–17] on neutral cluster beams emitted by supersonic expansion sources with broad cluster size distributions and uncertain internal energy distributions. Since the total beam flux was required for diffraction measurements, the uncertainties in cluster size and internal energy prevented an unambiguous interpretation of electron diffraction patterns. An exception to these limitations was the diffraction measurements on neutral beams of C_{60} and C_{70} clusters [18]. Clearly, such beam diffraction experiments were not capable of rigorously investigating the size dependence of cluster structures.

Storing cluster ions in a quadrupole ion trap [19] provided a capability to take advantage of cluster source technologies to avoid the shortcomings of beam measurements. As demonstrated initially for C_{60}^+ clusters [20], the ion trap enables one to accumulate size-selected clusters, collisionally relax the vibrational energy distribution and expose the clusters to an electron beam for a sufficient time to perform electron diffraction measurements. This can lead to a more controlled investigation of quantum size effects which serve to probe the structural transitions as the clusters evolve from molecular to bulk behavior. Diffraction techniques have been shown to be particularly sensitive to the measurement of size-dependent changes in structural symmetry for $(CsI)_nCs^+$ clusters, $30 \leqslant n \leqslant 39$ [21]. Quite recently, TIED measurements of mass-selected metal clusters have observed changes in local order of Ag_n^+, $36 \leqslant n \leqslant 46$, 55 [22], and structural transitions in Au_n^-, $11 \leqslant n \leqslant 24$ [23].

This chapter presents a description of the research performed in our laboratory to develop TIED methods and its application to measurements of structural transitions in metal clusters. It is beyond the scope to treat the apparatus and techniques of gas-phase diffraction, quadrupole ion traps, cluster sources and ion beams in detail; however, the unique role of each technology will be described. Similarly, theoretical calculations of cluster structural isomers performed by our collaborators will not be discussed in depth, but ample references will be included. Section 2 will present TIED experimental methods and analysis, and diffraction results obtained for silver clusters and gold clusters will be reviewed in Section 3.

2. METHODS OF TRAPPED ION ELECTRON DIFFRACTION

2.1. Diffraction apparatus

The TIED diffraction apparatus described in this section represents our current measurement technology which includes many improvements since the first measurements [20]. The current measurement capability and source stability allow experiments to study metal clusters over the size range of 10–100 atoms at temperatures between 90 and 600 K. Design of the TIED apparatus considered the constraints introduced by cluster sources and the requirements necessary to study clusters of a specific size and vibrational temperature. Cluster sources emit a beam composed of a distribution of cluster sizes and internal energies. The quadrupole ion trap was chosen as a technology which enabled the accumulation of size-selected clusters, the ability to relax the vibrational energy distribution via collisions with a background gas, and to store the size-selected clusters in a small cloud for an adequate time to perform electron diffraction measurements. The reliability and utility of TIED depends on avoiding the deleterious effects of inelastic scattering, minimizing the background electron scattering, achieving and maintaining alignment of the electron beam, designing cluster sources with sufficient stability to take data over $\geqslant 4$ h and an understanding of the operation and limitations of ion traps. An overall schematic of the diffraction apparatus is shown in Fig. 1, identifying the primary components including cluster

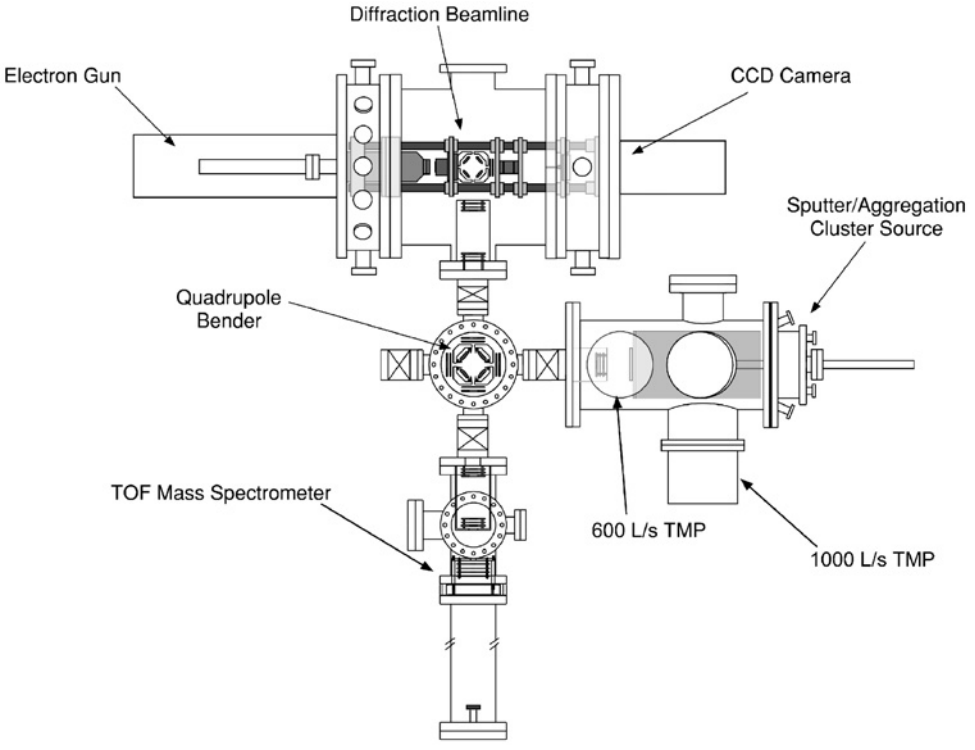

Figure 1: The electron diffraction instrument consists of three main components: the UHV chamber housing the diffraction beamline, the TOFMS and the sputter-aggregation cluster source.

source, time-of-flight mass spectrometer (TOFMS), electron gun, UHV trap chamber and charge-coupled device (CCD) camera.

2.1.1. Cluster ion and diffraction beamlines

Several different cluster ion sources have been used depending on the particular cluster materials being studied. For neutral beam diffraction measurements, an effusive C_{60} beam was emitted by a Knudsen oven, and for trapped C_{60}^+ measurements [20], ions were loaded into the trap by in situ ionization with a low-energy electron gun. Cluster ions of $(CsI)_nCs^+$ [21] were produced by a gas aggregation source [24] in which ions are produced by a current-stabilized discharge above the aperture of the CsI oven. The metal cluster source for Ag_n^+ [22] and Au_n^- [23] includes a liquid nitrogen cooled aggregation tube enclosing a magnetron sputter discharge similar to that designed by the Haberland group [25].

In the current apparatus configuration shown in Fig. 1, the cluster ion beam emitted by the source enters an electrostatic quadrupole bender [26] which directs the beam either to a TOFMS or to the diffraction beamline. The 1 m TOFMS accelerates the deflected ions parallel to the axis using a McLaren [27] lens design. The TOFMS has sufficient resolution to optimize the cluster source parameters so that ion beam intensity can be peaked within a cluster size range of interest. The optimized beam is then deflected towards the diffraction beamline to load ions into the trap.

The individual components of the diffraction beamline apparatus are shown schematically in Fig. 2. All beamline components are fabricated from non-magnetic materials (copper, titanium, ceramics) where possible and a μ-metal^{TM} shield eliminates

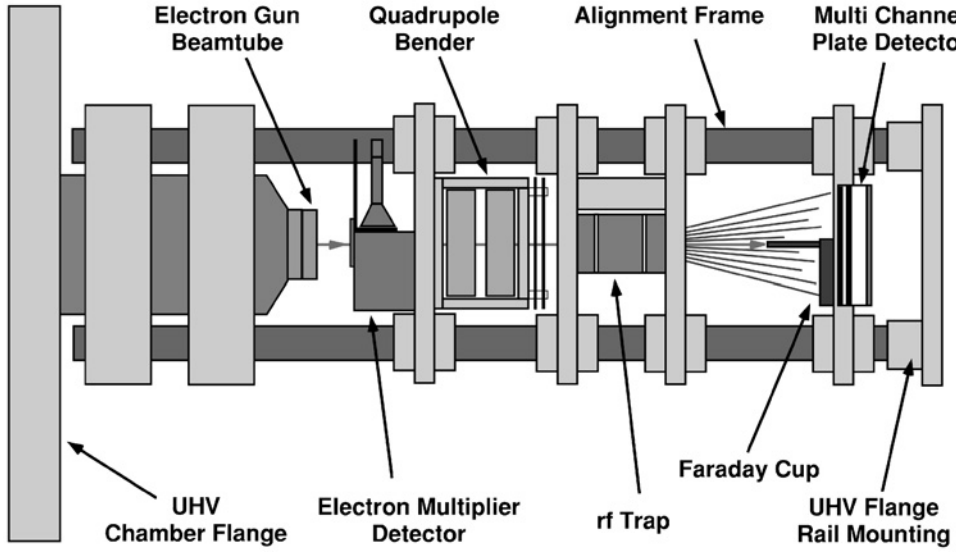

Figure 2: Components of the diffraction beamline mounted on rods to maintain a cylindrical symmetry around the electron beam axis. The e-beam passes through the trapped ion cloud producing scattered electrons indicated by off-axis lines. The primary beam enters the Faraday cup and scattered electrons strike a multi-channel plate detector producing the diffraction pattern on a phosphor screen. This screen is imaged by a CCD camera mounted external to the UHV chamber.

stray earth magnetic fields over the entire diffraction beamline to eliminate misalignment of the electron beam. As shown in Fig. 2, the small bender (ABB Extrel), channeltron ion detector (Burle Electrooptics), ion trap, Faraday cup and microchannel plate (MCP)/phosphor screen detector (Burle Electrooptics) are all mounted on a structure composed of three 12.5 mm diameter titanium rods to maintain cylindrical symmetry around the electron beam axis. The detection distance from the trap center to the microchannel plate surface can be varied from ~8 to 12 cm. The three alignment rods are fitted to the electron gun structure and are maintained parallel to the e-beam by mounting the far end to the chamber flange as shown in Fig. 2.

2.1.2. Electron background

The electron gun (Kimball Physics) provides a near collimated e-beam having a current of i_{eb}~0.6–1 μA and electron energy of 40.0 keV. The e-beam traverses the trap through apertures in the grounded endcap electrodes and is gently focused into the Faraday cup. Considerable care is taken to design these apertures to avoid scattering from the e-beam and also X-rays emitted by the gun. The e-beam alignment procedure images the beam through all components and then positions the Faraday cup to minimize detected background scattering. The Faraday cup is mounted on an X–Y translator to facilitate alignment. A primary effort during development of the TIED technique was directed towards minimizing the background electron scattering. The small number of trapped cluster ions and their low density (~10^7 cm^{-3}) results in a low rate of elastic scattering relative to the incident electron beam current (~10^{-9}), which makes the design and positioning of each component critically important. The lowest background electron scattering achieved was $i_{e\text{-back}}/i_{eb} \sim 3 \times 10^{-8}$, which was measured by counting the rate of single electron events ($i_{e\text{-back}}$) detected at reduced e-beam current (i_{eb}~2 nA). This low level of background scattering was achieved by fabricating the Faraday cup in the form of a graphite tube of ~3 cm length and ~1 mm inner diameter. This design maximized the conversion of high-energy electrons to X-rays, which were then absorbed in the walls. The dominant noise contributions were from high-energy background electrons scattered from apertures and scattering from residual gases in the UHV chamber. The UHV chamber achieves a base pressure of ~10^{-9} Torr and the pressure during diffraction measurements is $\leqslant 10^{-8}$ Torr.

2.1.3. Ion trap data sequence

The ion trap design and operation is described more completely elsewhere [19]. The ion trap operates at an rf of 300 kHz with an endcap electrode spacing of 1 cm. Cluster ions are loaded into the trap by passing the cluster beam through a second electrostatic bender (ABB Extrel) which directs the ions into the trap through an aperture in the grounded endcap electrode. The enhanced loading efficiency [28] produced by this configuration generates ion clouds of ~10^4 ions. The ions are trapped in the presence of ~10^{-3} Torr He gas, which serves to relax the clusters into stable trajectories. Figure 3 shows a TOF mass spectrum for Au_n^- clusters and several mass spectra of trapped clusters obtained by resonantly ejecting the cluster ions into the channeltron ion detector shown in Fig. 2. Efficient mass selection of a single size from the broad range of cluster sizes entering the trap from the source, Fig. 3a, is achieved by first applying SWIFT resonant excitation [29, 30] during ion loading to trap a narrow range of ~4 cluster sizes shown in Fig. 3b. This reduces the ion–ion interactions

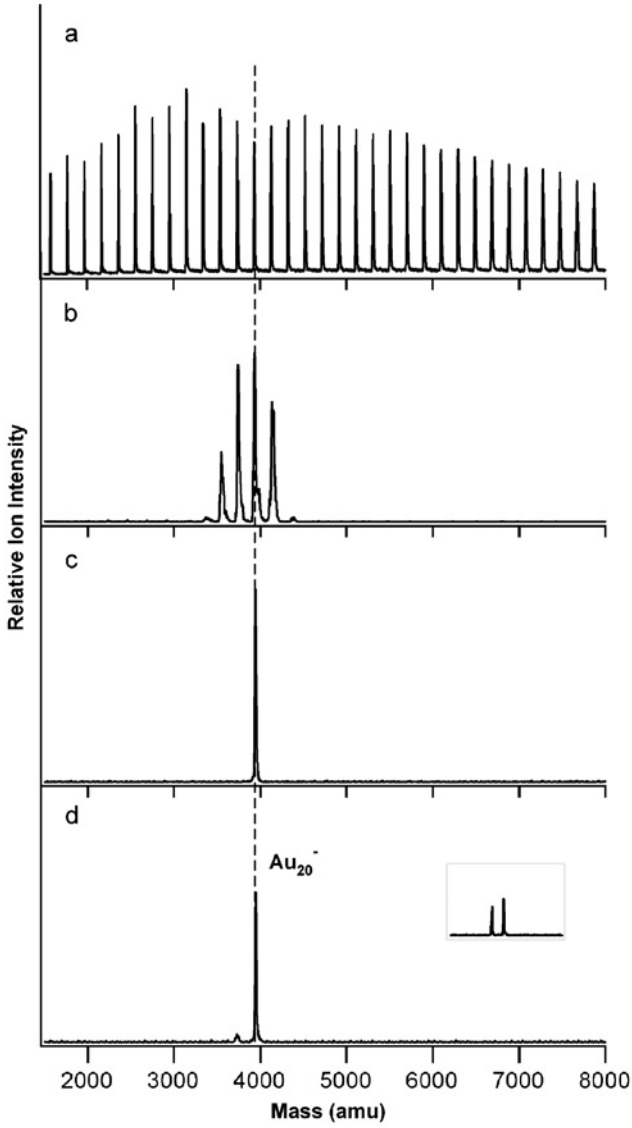

Figure 3: Mass spectra displaying (a) the detected TOF spectrum of cluster masses emitted by the source, (b) trapped cluster spectrum obtained by broadband SWIFT excitation and (c) subsequent isolation of a single cluster mass using narrowband SWIFT excitation. In this example, gold anions of size $n = 20$ (dashed line) have been isolated. The spectrum in (d) is obtained after annealing with optimum excitation and the inset indicates the result of excessive excitation amplitude.

sufficiently to allow a second SWIFT excitation to reproducibly isolate the single mass of interest as in Fig. 3c.

Storing the clusters for $\sim$5 sec in He gas at pressure $\sim 10^{-3}$ Torr thermalizes the cluster vibrational and translational energies at the gas temperature [31]. The gas temperature is set by channeling the gas through the trap super structure which is

heated and held at a constant temperature by ceramic heaters or cooled directly by flowing liquid nitrogen. After evacuating the He background, the relaxed ion cloud is held at the trap parameter $q_z = 0.5$ during the diffractive exposure. At this q_z value, the ion cloud dimension is comparable to the e-beam diameter so that the overlapped ion cloud volume includes a large fraction of the ions. For the current trap design, ion–ion interactions for cluster numbers significantly greater than $\sim 10^4$ expand the beam, reducing density and cloud overlap with the e-beam.

Annealing the trapped clusters increases the probability that the resulting structure has been relaxed to that of the lowest-energy isomer. We have found, however, that the degree to which annealing helps depends on the cluster material. Annealing has been performed by applying an external rf field ($V_{0\text{–}p} \sim 0.2$ V) for ~100 msec resonant with the ion motion frequency to excite translational motion, which heats the clusters by translational to vibrational (T-V) transfer in collisions with a background Ne gas ($\sim 10^{-3}$ Torr). After annealing, the cluster ensemble is cooled to the He gas temperature over ~3–5 sec. Clusters prepared in this way minimize the effects of source parameters on the measured cluster structure. Figure 3d shows the mass spectrum after annealing Au_{20}^- for optimum excitation amplitude producing cluster heating with negligible dissociation. The mass spectrum inset in Fig. 3d displays ~50% dissociation resulting from excessive heating.

A low-level SWIFT excitation is maintained during the diffraction exposure to eliminate possible fragments or multiply charged species produced by e-beam inelastic processes. This assures that the diffraction pattern is the result of the selected parent cluster ion. To identify these inelastic scattering processes, mass spectra were obtained after cluster exposure to the e-beam. Figure 4 shows mass spectra of trapped Au_n^- and Au_n^+ clusters before and after e-beam exposure for several sizes. The primary inelastic process for Au_n^- is loss of the attached electron and for Au_n^+ multiple ionization dominates. The rate of both inelastic processes increases with increasing cluster size. The fast electron interacts primarily with the electronic states of the cluster and that dissociation or fragmentation which can arise from vibrational excitation is not observed. Experiments have shown no evidence of the presence of cluster heating via these inelastic interactions. As a result of the loss of parent ions during the diffraction exposure by these inelastic processes, each diffraction exposure is limited to ~10–20 sec after which the trap is reloaded with a fresh ion cloud. A second identical trap sequence is taken immediately after the cluster exposure with the source electrostatically shuttered to record a detector background. To summarize, each diffraction cycle is composed of ion loading, mass selection, vibrational relaxation, annealing, e-beam exposure, ion ejection and a second identical sequence to record a detector background. In a typical experimental run over ~4–5 h, the diffraction pattern is collected for ~300–400 cycles representing an average of over ~$3\text{–}4 \times 10^6$ mass-selected clusters.

2.1.4. Detection

The diffracted electrons are detected by a 25 mm diameter image quality MCP chevron detector which forms an image on the phosphor screen coupled to the MCP through a fiberoptic plate. A CCD camera (Photometrics) external to the UHV chamber images the pattern on the CCD pixel array (512×512). The front plate of the MCP chevron is biased with ~–350 V to suppress detection of low-energy electrons formed by the e-beam. The diffraction pattern is in the form of Debye–Scherrer rings similar to

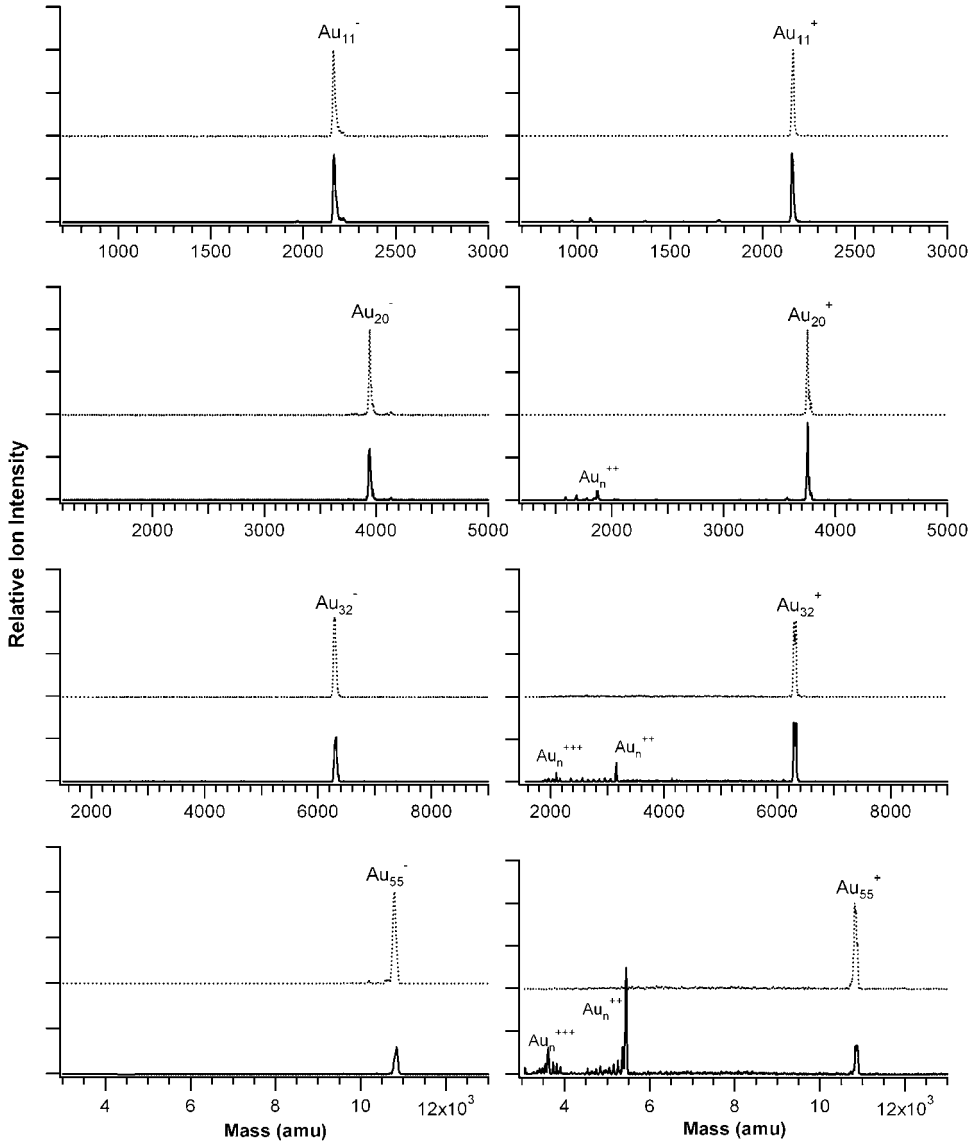

Figure 4: Mass spectra displaying the effect of inelastic electron scattering for selected gold cluster anions and cations of various sizes. Upper mass spectra (dashed lines) show the trapped ion mass before e-beam exposure. The lower mass spectra are obtained after exposure.

powder diffraction as a result of the orientational and spatial disorder of the trapped cluster ions. The trapped ion cloud dimensions and 2 mm endcap aperture allow detection of scattered electrons with a maximum scattering angle of ± 6–9° depending on the detector–trap distance.

The individual pixelated CCD images obtained for each diffraction cycle form two 16-bit unsigned arrays, a cluster diffraction image and a background image without clusters present. A difference image is obtained by subtracting the cluster and

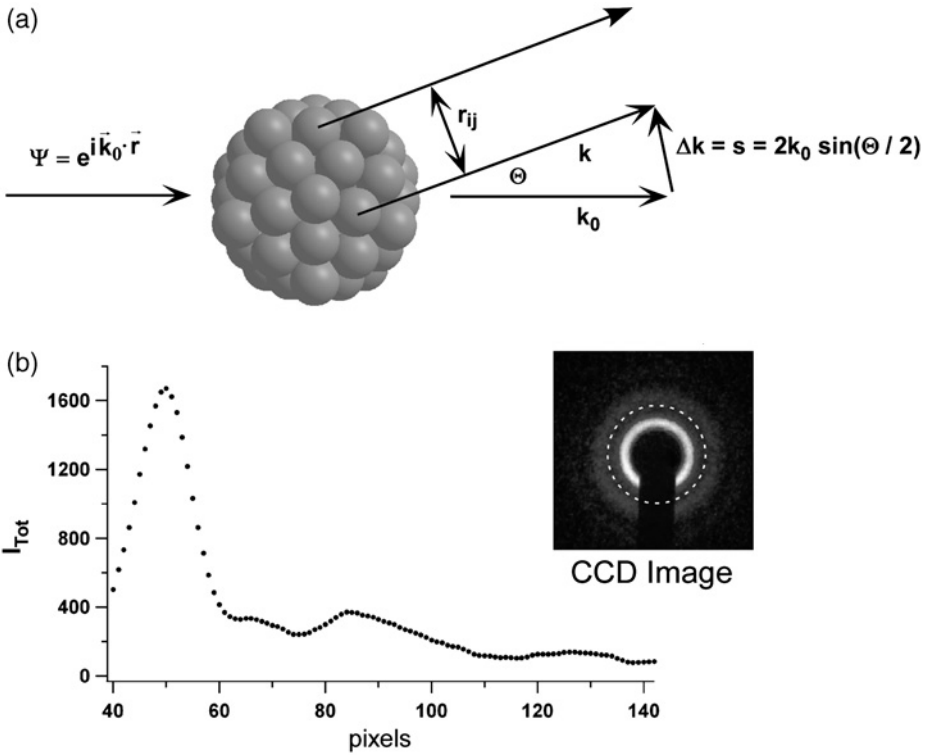

Figure 5: (a) Schematic of the electron-cluster scattering geometry, identifying terms appearing in Eqs. (1) and (3). (b) The total scattering intensity vs. pixels is extracted from the CCD image by integrating about successive rings centered on the diffraction pattern (dashed) and separated by 1 pixel.

background images and is stored for averaging. The average of these difference images (32 bit signed) displays the diffraction pattern used for cluster structure analysis as shown in Fig. 5. Although the difference image subtracts the electron background, the statistical fluctuations of the background remain and determine the signal-to-noise ratio, which is proportional to $Nn\sigma_e i_{eb}\sqrt{t}$. Here N is the number of clusters, n the number of atoms per cluster, σ_e the elastic scattering cross-section, i_{eb} the e-beam current and t the total exposure time. The decrease in signal-to-noise ratio for larger scattering angles, θ, results from the rapid decrease in the scattering cross-section, $\sigma_e \sim 1/(\sin\,\theta/2)^4$.

2.2. Diffraction data

2.2.1. Diffraction analysis

This section briefly reviews gas-phase diffraction analysis and its application to fitting cluster data to theoretical structures [32–35]. The experimental data are fit to the total scattering intensity calculated from theoretical isomer structures to determine which isomer yields the best fit. This intensity, I_{total}, is approximated by a sum of the independent scattering, I_{indep}, from each cluster atom and molecular scattering, I_{molec}, resulting from the interference of elastic scattering from atomic pairs. Multiple scattering processes do not contribute significantly for clusters in the size range of

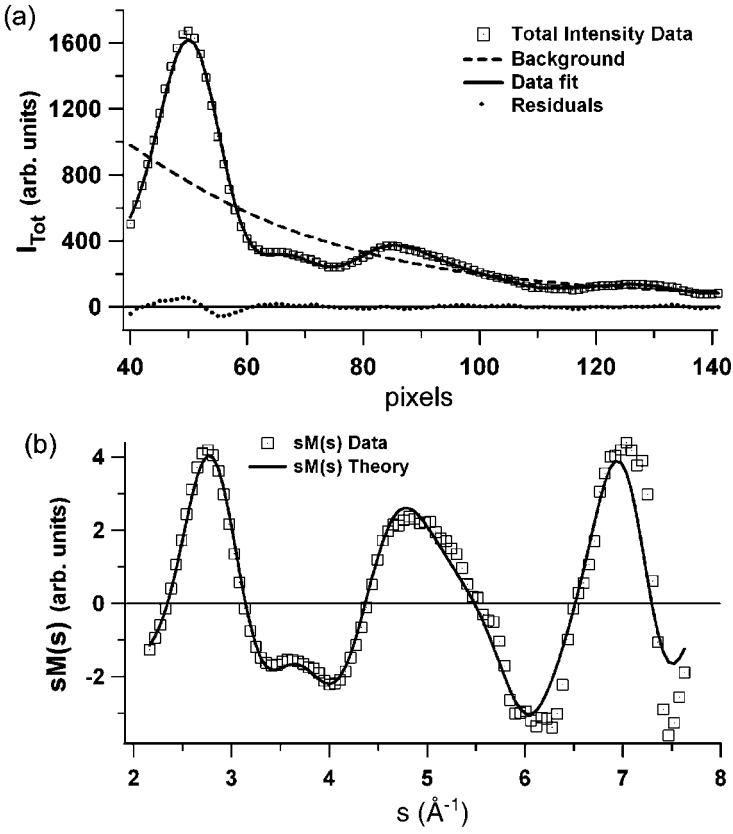

Figure 6: (a) An example fit of Eq. (1) to the total intensity data of Ag_{55}^{+}, (b) comparison of the reduced molecular scattering data, sM(s), to the theoretical scattering defined by Eq. (3) for the calculated structure of Ag_{55}^{+}.

10–100 atoms and materials of interest. The data fitting analysis is shown schematically in Figs. 5 and 6.

The total elastic scattering from a cluster having N atoms with pair separations r_{ij} can be expressed by

$$I_{\mathrm{Tot}}^{\mathrm{Theo}}(s) = I_{\mathrm{indep}}^{\mathrm{Theo}} + I_{\mathrm{molec}}^{\mathrm{Theo}} = f_{\mathrm{B}}^{2}(s)\left\{ N + d\sum_{i,j}^{N} \frac{\sin\ sr_{ij}}{sr_{ij}} \mathrm{e}^{-\langle l_{ij}^{2}\rangle s^{2}/2} \right\} \tag{1}$$

The data reduction extracts the molecular scattering contribution from the total scattering intensity by approximating the independent scattering contribution with a polynomial:

$$I_{\mathrm{indep}}^{\mathrm{Theo}} = N f_{\mathrm{B}}^{2}(s) = N f_{\mathrm{at}}^{2}(s) \cdot \mathrm{poly}(s) \tag{2}$$

where f_{at} is the atomic scattering amplitude and s the momentum transfer. The momentum transfer is related to the scattering angle, θ, by $s = (4\pi/\lambda_{\mathrm{B}})\sin(\theta/2)$, as shown in Fig. 5a, where the incident momentum is $k_0 = 2\pi/\lambda_{\mathrm{B}}$, and $\lambda_{\mathrm{B}} = 0.06$ Å is the de Broglie wavelength for 40 keV electron energy. As shown in Fig. 5b, the total

scattering intensity vs. CCD pixel value is extracted from the data by averaging the intensity pattern over successive rings of CCD pixels centered on the pattern and concentric with the e-beam axis. Pixel values are related to s by a scaling factor s_c which is determined by the fit. The polynomial function contains terms up to s^3 and is slowly varying relative to the molecular scattering variations. The parameter d accounts for effects which might degrade the molecular scattering contribution such as finite resolution of the experimental ring pattern and is usually close to unity.

The molecular scattering contribution contains an exponential factor to estimate the effects of temperature on the cluster structure. The mean squared vibrational amplitude, $\langle l_{ij}^2 \rangle$, is derived in the harmonic oscillator approximation [32] to estimate atomic vibrations and corresponds to the Debye–Waller factor associated with the scattering of phonon modes in solids. In Eq. (3), the mean square vibrational amplitude can be approximated by, $\langle l_{ij}^2 \rangle \approx L^2$ [32], in which the single parameter, L, represents an average over all atom pairs in the cluster. We have also used molecular dynamics (MD) simulations [36] to include vibrational effects in the theoretical structures. The DFT structures are used to initialize the simulations which are performed at the experiment temperature. A theoretical diffraction pattern, sM(s), was derived for each isomer from an average of the patterns calculated for $\sim 10^3$ atomic configurations determined by these simulations. The accuracy of this method to represent the effect of temperature on cluster structure clearly depends on the pseudopotential employed by the simulation. We have used this method only to represent cluster structures at temperatures of $\sim$120 K at which anharmonic effects are not expected to contribute significantly.

The reduced molecular scattering defined by

$$\mathrm{sM}_{\mathrm{Theo}}(s) \equiv s\left[\frac{I_{\mathrm{Tot}}^{\mathrm{Theo}} - Nf_{\mathrm{B}}^2}{Nf_{\mathrm{B}}^2}\right] = s\frac{d}{N}\sum_{i,j}^{N}\frac{\sin\, sr_{ij}}{sr_{ij}}\mathrm{e}^{-\langle l_{ij}^2\rangle s^2/2} \tag{3}$$

is useful to interpret diffraction patterns, since this form does not depend on absolute intensities or approximations in the theoretical calculation of f_{at}. The reduced molecular scattering eliminates the large dynamical range of the total scattering, allowing the details of the diffraction interference structure to be observed and compared with experiment.

2.2.2. Data fitting methods

The fitting analysis of diffraction data to theoretical structures has been carried out by two equivalent methods. The total intensity in Eq. (1) can be fit to $I_{\mathrm{Tot}}^{\mathrm{Exp}}$ by varying d, s_c, L and the polynomial coefficients to minimize $\chi^2 = \sum_i [I_{\mathrm{Tot}\,i}^{\mathrm{Theo}} - I_{\mathrm{Tot}\,i}^{\mathrm{Exp}}]^2/\sigma_i^2$. Here the sum is over all data points and σ_i is the standard deviation of the ith pixel ring intensity. The result of such a weighted fit for Ag_{55}^+ is shown in Fig. 6a, which displays the intensity fit, residuals and the resulting background, f_{B}. Figure 6b compares the reduced molecular intensity determined from the theoretical structure and the corresponding experimental $\mathrm{sM}_{\mathrm{exp}}(s)$ derived from the total intensity data by calculating:

$$\mathrm{sM}_{\mathrm{Exp}}(s) \equiv s\left[\frac{I_{\mathrm{Tot}}^{\mathrm{Exp}} - Nf_{\mathrm{B}}^2}{Nf_{\mathrm{B}}^2}\right] \tag{4}$$

using the background f_B determined by the total intensity fit. This method seems to do well for larger clusters for which the S/N is sufficient to determine the background polynomial with minimum uncertainty over the entire data range.

A second fitting procedure can be performed by initially estimating the background polynomial by fitting Nf_B^2 to the total intensity data. The reduced molecular intensity given by Eq. (3) is then calculated for each s value and this sM(s) data fit to Eq. (2) by varying d, s_c and L. A new background is then determined by fixing d, s_c and L in Eq. (2) to calculate a new background by varying the polynomial coefficients. This iterative procedure is extended until the fit converges. The difference between these two procedures is that fitting to the reduced molecular scattering involves varying fit parameters over a significantly reduced dynamic range. This procedure seems to determine better-fits for smaller clusters for which the S/N is minimal at the higher s values where the background cannot be determined with sufficient accuracy. It is important to mention that these fitting procedures are primarily used to identify the specific, calculated structural isomer which yields the best fit to the diffraction data. It has been found that the structural isomer identified in this way is independent of which fitting procedure is applied.

There are cases for which a physical model might include several low-energy isomer structures. The theoretical model of the diffraction pattern was then composed of a sum of isomer contributions representing an ensemble of trapped clusters composed of a mixture of isomer structures. The fitting procedure varied the fractional contribution of each isomer structure in the sM(s) model to optimize the fit to experimental patterns.

The weighted R-value [37] is calculated to characterize the goodness-of-fit between the theoretical, $sM_{Theo}(s)$, and experimental, $sM_{Exp}(s)$, and is defined by

$$R = \left[\frac{\sum_i w_i (sM_i^{Theo} - sM_i^{Exp})^2}{\sum_i w_i (sM_i^{Exp})^2} \right]^{1/2} \tag{5}$$

The sums are over all pixel rings, and the weighting factors are given by $w_i = 1/\sigma_i^2$. The data for each cluster size were fit to all theoretical isomer structures calculated for that size. These fits were performed with both fit procedures described above and in each case the same isomer structure was identified as the best fit with weighted R-values in the range of 0.07–0.15.

3. STRUCTURAL TRANSITIONS IN METAL CLUSTERS

3.1. Silver cluster cations

The first measurements of mass-selected metal clusters by TIED methods investigated the development of silver cluster cation structures over the size range 36–55 atoms. This range was chosen to gain a better understanding of how cluster structures evolve through intermediate sizes to achieve ''magic number'' structures composed of closed electronic or atomic shells. This size range includes two such closings, an octahedral atomic shell closing at Ag_{38}^+ and an icosahedral atomic shell closing at Ag_{55}^+. These measurements [22] have indicated an evolution from short-range order among nearest neighbors having fivefold symmetry to a global order having icosahedral symmetry at

$n = 55$. A unique structure is observed at $n = 38$, which exhibits a distortion of fcc symmetry characterized by local order having fivefold symmetry.

3.1.1. Experimental results

The total scattering data for all sizes studied are displayed in Fig. 7. The total scattering intensity data in the range $s \approx 3.5$–$4\,\text{Å}^{-1}$ are observed to change with cluster size although the overall characteristics are very similar. These changes will be shown to be consistent with an evolution of structures from those exhibiting local order having fivefold symmetry to a structure having global order with icosahedral symmetry at Ag_{55}^{+}.

The reduced molecular scattering intensity, sM(s), extracted using an approximate background fit is shown in Fig. 8 for each cluster size. The diffraction data shown in Fig. 8 were obtained for unannealed clusters. The peak positions and the positions on the s axis at which the data have zero values (zero crossings) are observed in Fig. 8 to be nearly identical for each cluster size, suggesting a similar symmetry dominates in this size range. The diffraction patterns in Fig. 8 display a shoulder on the second positive peak near $s \sim 5\,\text{Å}^{-1}$, which has been identified with the presence of fivefold symmetry [38, 39]. The upper panel in Fig. 9 defines the ratio, s_2/s_1, of the s values corresponding to the first two positive diffraction peaks as well as the ratio s_{sh}/s_1 of s values for the shoulder on the second peak and the first positive peak. The value of these ratios were obtained from the sM(s) data in Fig. 8 for each cluster size and are

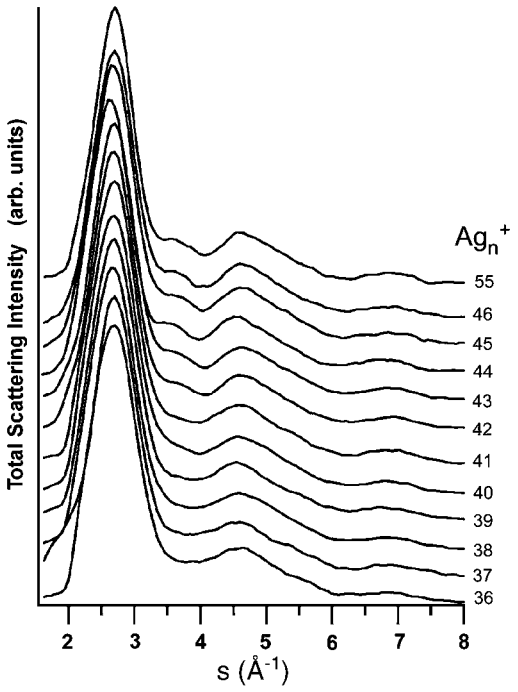

Figure 7: The total scattering intensity vs. s (Å^{-1}) is shown for all silver cluster sizes $n = 36$–46 and 55.

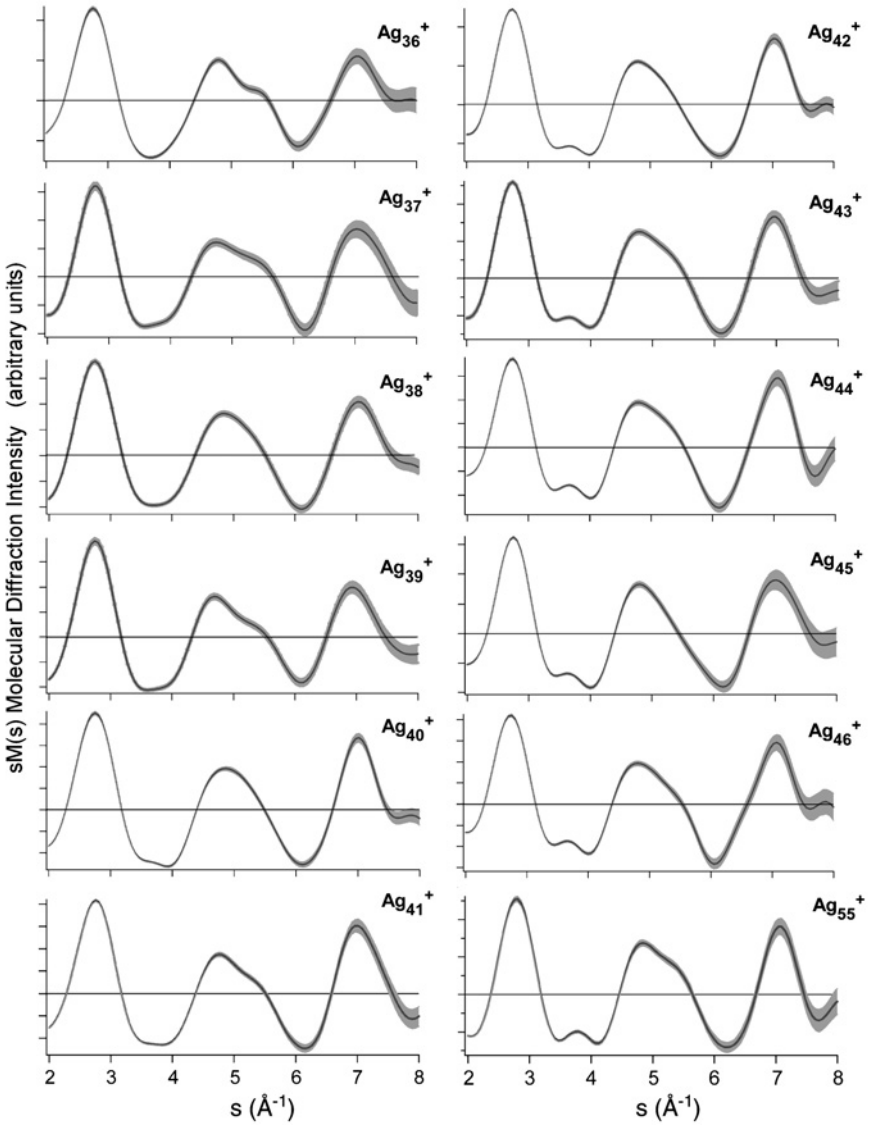

Figure 8: Experimental reduced molecular intensity sM(s) vs. s (Å^{-1}) is displayed for silver cluster sizes $n = 36$–46 and 55. The experimental data (black line) and uncertainty ($\pm 1\sigma$, gray band) are shown for each cluster size.

shown in the lower panel of Fig. 9. The average values of ratios $s_2/s_1 = 1.73 \pm 0.02$ and $s_{sh}/s_1 = 1.93 \pm 0.03$ are in excellent agreement with those calculated for a structure having global icosahedral symmetry [39], for which $s_2/s_1 = 1.71$ and $s_{sh}/s_1 = 2.04$. The doublet structure in the first negative peak near $s \sim 3.8\,\text{Å}^{-1}$ is also characteristic of fivefold symmetry (as shown, for example, in C_{60}^{+} diffraction [20]) and is observed in Fig. 8 to become better resolved with increasing size. These changes in doublet

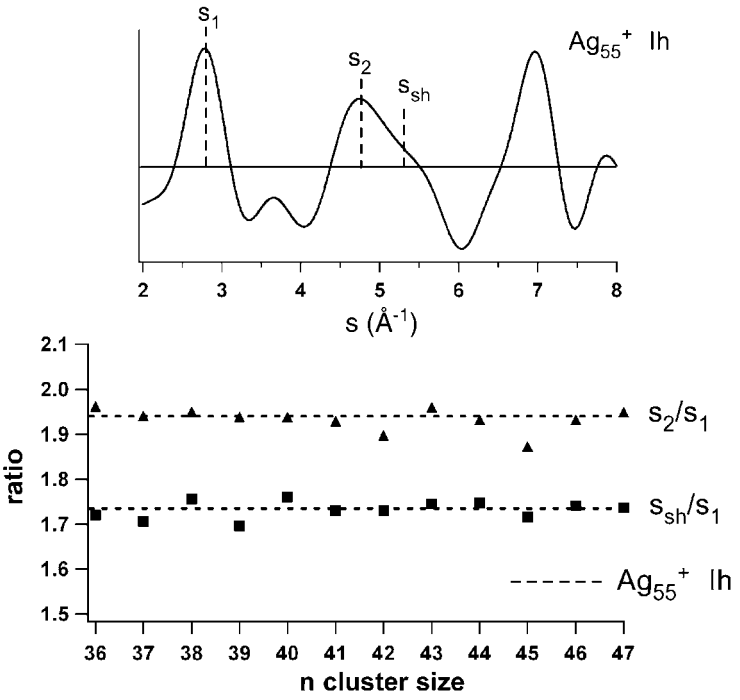

Figure 9: Ratios of peak positions (s_1, s_2) and shoulder (s_{sh}) indicated in the upper panel are obtained from sM(s) data displayed in Fig. 8. These data are compared with the ratios obtained for Ag_{55}^{+} having Ih symmetry indicated by dashed lines.

structure can be shown analytically to arise from increased interference as the fraction of Ag atoms having fivefold coordination increases.

3.1.2. Analysis and discussion

The presence of fivefold symmetry is clearly indicated by the diffraction patterns of Ag_n^+ clusters throughout the size range. Diffraction data were compared with theoretical calculations of molecular diffraction patterns for cluster sizes $n = 36$–39, 43 and 55 to understand how this symmetry is related to cluster structures. Structures for silver clusters were calculated by the research groups of Garzón and Michaelian at the Universidad Nacional Autónoma de México. For each size, a genetic algorithm [40] incorporating a many-body model potential [41] was used to perform a broad search of the structural phase space to identify an ensemble of the low-energy isomers occurring with high frequency. The structures of ~6–10 lowest-energy isomers corresponding to minima of the potential energy landscape were further optimized by generalized gradient approximation (GGA) density functional calculations [42]. These calculations identified only two cluster sizes which possessed an isomer characterized by a global symmetry: truncated octahedral (fcc) at $n = 38$ and icosahedral (Ih) at $n = 55$, consistent with previous semi-empirical calculations [43, 44]. The calculated structures of all other isomers exhibited some degree of global asymmetry or disorder. The analysis of Ag_n^+ included vibrational effects in the theoretical structures by using the DFT structures to initialize MD simulations [36] performed at the experiment

temperature of 120 K. A theoretical diffraction pattern, sM(s), was derived for each isomer from an average of atomic configurations determined by these simulations.

For structures lacking a global symmetry, it is highly desirable to assign a semi-quantitative measure to enable comparison and classification. The short-range order parameters, Q_l, were originally formulated for this purpose to describe metallic glasses and supercooled liquids [45]. These parameters were previously applied to characterize cluster structures derived from Monte Carlo calculations of a 38-atom Lennard-Jones cluster [46]. The short-range order parameter is formed from a set of spherical harmonics associated with every bond joining an atom to its nearest neighbors. The definition of the order parameter is

$$Q_l = \left(\frac{4\pi}{2l+1} \sum_{m=-l}^{l} |\bar{Q}_{lm}|^2 \right)^{1/2} \tag{6}$$

where

$$\bar{Q}_{lm} = \frac{1}{N_b} \sum_{r_{ij} < r_0} Y_{lm}(\theta_{ij}, \varphi_{ij}) \tag{7}$$

Here N_b is the number of bonds having a length r_{ij} less than a nearest neighbor criterion r_0, and the Y_{lm} is a spherical harmonic with θ_{ij} and φ_{ij} – the polar and azimuthal angles of the bond direction with respect to an arbitrary coordinate system. After performing the sum over m, the Q_l parameters become independent of the coordinate system used to define θ_{ij} and φ_{ij}. The nearest neighbor separation, $r_0 = 3.5$ Å, was used for silver clusters.

The order parameter for $l = 6$ indicates the importance of icosahedral symmetry [45] and is used here as a measure of the degree that fivefold symmetry is present in a cluster structure. Figure 10 displays the results of calculating Q_6 for all isomers calculated for each cluster size. The value $Q_6 = 0.104$ was calculated for the lowest-energy isomer of

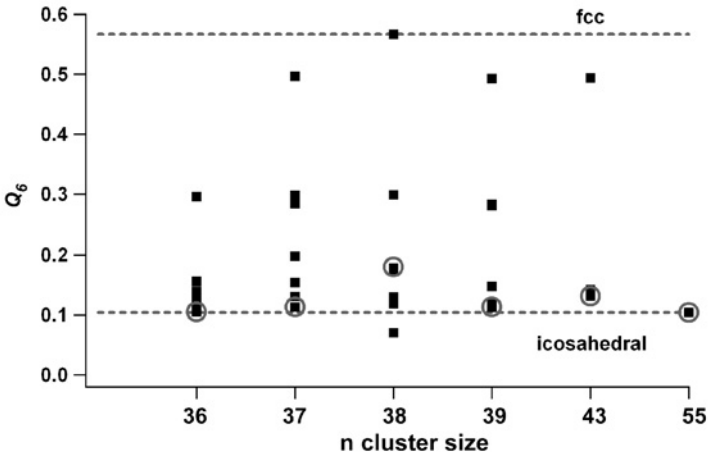

Figure 10: The calculated Q_6 short-range order parameters are shown for all isomer structures (black squares) for each cluster size. Q_6 values for the best-fit structures are circled. The Q_6 values for fcc and icosahedral symmetries are indicated by dashed lines.

$n = 55$, which displayed global order having icosahedral symmetry and is shown in Fig. 10 by the upper dashed line. The average value of Q_6 for 72% of all the calculated isomers was $\langle Q_6 \rangle = 0.13 \pm 0.03$, indicating the general presence of structures characterized by local order having fivefold symmetry. Perhaps a more important result of this analysis is that $\langle Q_6 \rangle = 0.11 \pm 0.01$ for the best-fit structures of $n = 36$, 37, 39 and 43 indicated by circles in Fig. 10. The value $Q_6 = 0.57$ found for the lowest-energy isomer of $n = 38$ is identical to the value of Q_6 calculated for fcc symmetry indicated by the upper dashed line in Fig. 10. However, the best-fit isomer structure of $n = 38$ has $Q_6 = 0.18$, which is consistent with the mixed symmetry discussed further below. This short-range order analysis of the calculated structures is in general agreement with the data analysis described by Fig. 9. These analyses suggest that the presence of local order having fivefold symmetry is a unifying characteristic of these cluster structures.

The comparison of diffraction data with patterns calculated from several low-energy isomer structures is shown in Figs. 11–13. Annealing the clusters did not change the

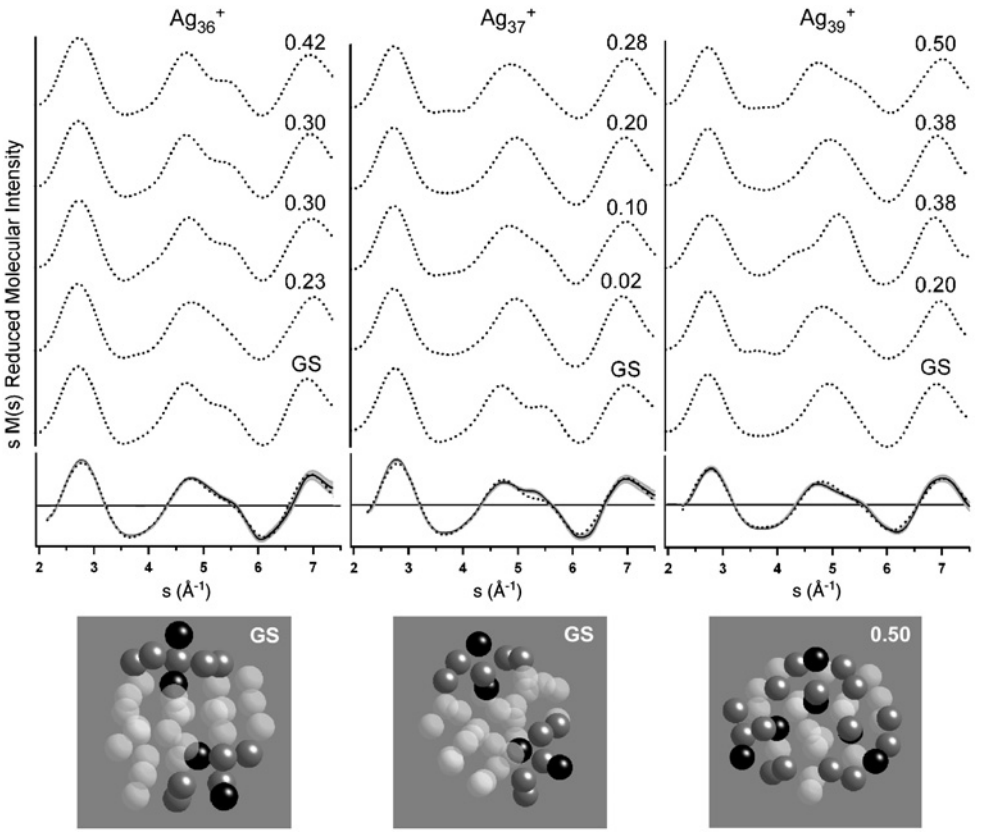

Figure 11: Calculated isomer diffraction patterns of sM(s) vs. s (Å^{-1}) for structures of Ag_n^+ clusters with $n = 36$, 37 and 39 are shown (dotted curves). The energy (in eV) of the isomer above the ground state (GS) is shown to the right of each isomer diffraction pattern. The experimental diffraction sM(s) (black curve) along with the best-fit isomer (dotted curve) is shown in the bottom panel. The gray shading shows the data uncertainty $\pm\sigma$. The best-fit isomer structure is shown to the right of each fit. Local order in each fit structure is indicated by black and gray atoms.

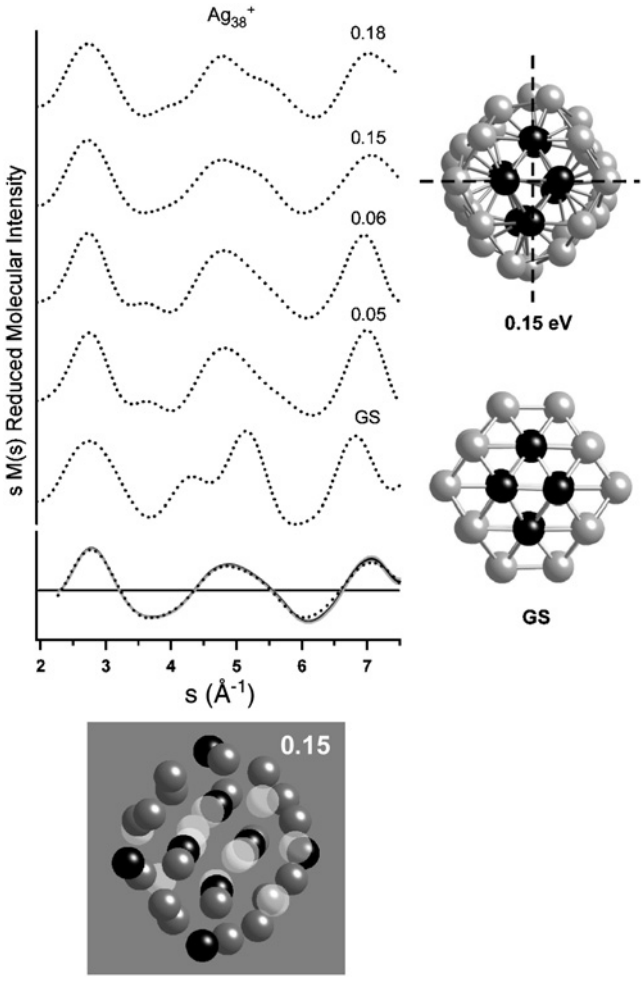

Figure 12: Similar to Fig. 11 for diffraction data and isomer structures for Ag_n^+ clusters with $n = 38$.

isomer structure that best fit the data, consequently the data presented here are for unannealed clusters. In the bottom panel, the experimental data are overlayed with the calculated sM(s) for the isomer structure producing the best fit. The best-fit structure for each size is shown beneath the plots. The fit uncertainty ($\pm 1\sigma$) shown in gray includes the standard deviations of the raw data and of the background added in quadrature. The quality of these fits indicates close agreement between the data and theoretical structures, for which R-values were in the range 0.09–0.12. It is important to point out that only a single isomer made a significant contribution to the fits for sizes $n = 36$, 39, 43 and 55. A marginally better-fit was obtained for $n = 37$ by including a second isomer contributing ~30% to the isomer mixture.

One of the more important elements of the fitting algorithm is a self-consistent determination of the normalized background scattering, $\langle f_B/N \rangle$. The convergence of successive model fits for each isomer yields a refined background consistent with the

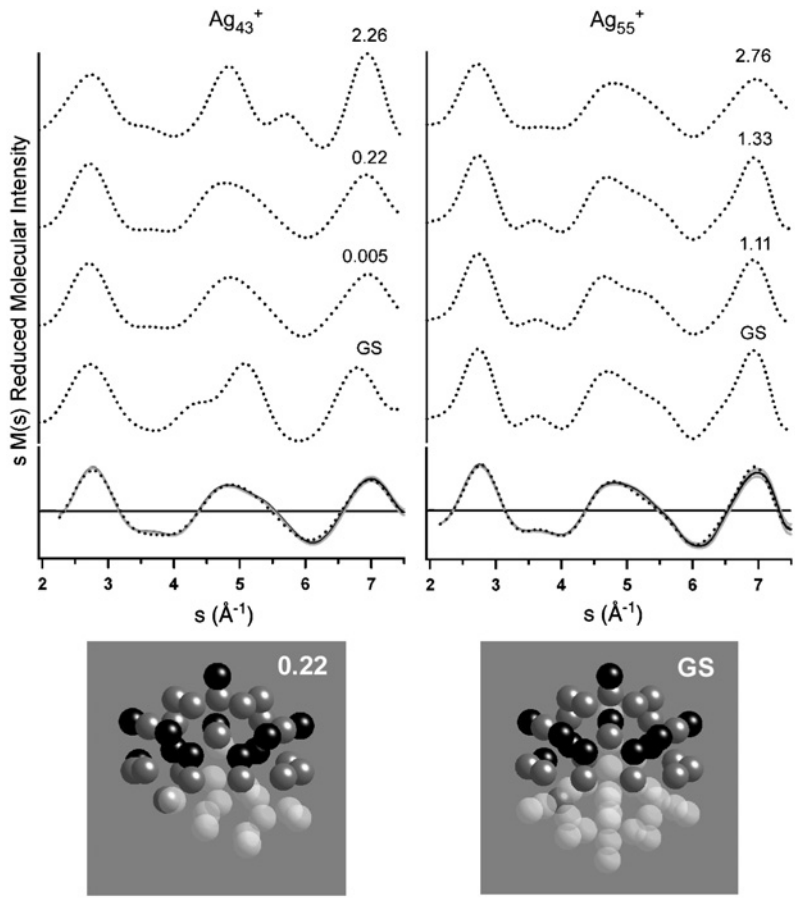

Figure 13: Similar to Fig. 11 for diffraction data and isomer structures for Ag_n^+ clusters with $n = 43$ and 55.

optimum theoretical model. Performing these fits independently for each cluster size yields a set of background curves. It is important to point out that these background curves are expected to be very similar for all Ag cluster sizes. A master curve of $\langle f_B/N \rangle$ vs. s formed by averaging the individual background curves is shown in Fig. 14 and indicates that estimates of the scattering background are identical to within a standard deviation of $\pm 9.7\%$. This result ensures that the background extracted from each total scattering data set did not contribute to the evolving structure observed in the sM(s) patterns.

3.1.2.1. Ag_{36}^+, Ag_{37}^+ and Ag_{39}^+ The best fits of diffraction data for these three cluster sizes are shown in Fig. 11 to correspond to structures dominated by local order having fivefold symmetry. Images of these structures shown at the bottom of Fig. 11 display a few of these locally ordered regions for each size. Note that the local order in the form of pentagonal bipyramids is primarily found among nearest neighbors residing on the outer surface of the cluster structure. The fivefold symmetry maximizes the number of nearest neighbor contacts yet can avoid the strain this symmetry normally introduces

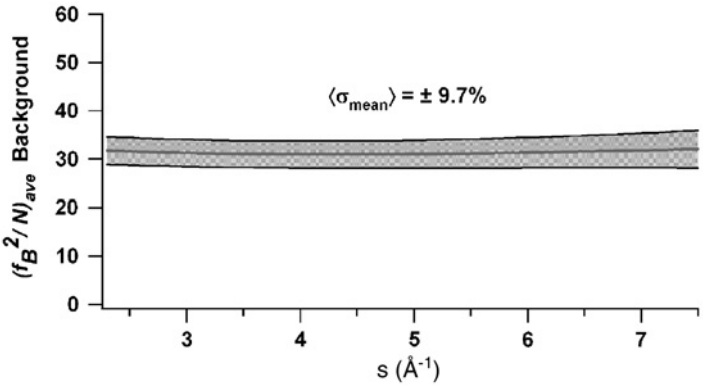

Figure 14: The scattering background averaged over all Ag_n^+ fits, $\langle f_B/N\rangle_n$, is plotted vs. s (Å^{-1}). The grey shading indicates the background uncertainty ($\pm 1\sigma$) and the average uncertainty is indicated as $\langle\sigma_{mean}\rangle = \pm 9.7\%$.

as a result of the overall structural dissymmetry [47]. It is not clear why the calculated isomers only qualitatively describe the data obtained for Ag_{37}^+ in the region near $s = 5$ Å^{-1}, although the zero crossings and relative peak intensities are reproduced by the calculated structure. The rapid variation in sM(s) near $s = 5$ Å^{-1} is observed only in the data for $n = 37$, and it is possible that calculations have simply not identified the correct structure.

3.1.2.2. Ag_{38}^+ Once again, the best-fit structure shows local order having fivefold symmetry concentrated in surface regions similar to the structures calculated for $n = 36$, 37 and 39. However, the best-fit structure at 0.15 eV above the ground state displays clear evidence of the remnants of fcc symmetry for atoms within the outer shell. The best-fit structure for $n = 38$ shown to the right in Fig. 12 includes four slightly distorted inner atomic rows of 14 atoms. These correspond to the inner row structure of the truncated octahedral calculated for the $n = 38$ ground state (shown for comparison in Fig. 12) having fcc symmetry. This interesting mixture of symmetries arising at the octahedral shell closing probably is a result of the inherent structural stability associated with such "magic numbers". This can account for the slight divergence of the Q_6 value from the icosahedral limit displayed in Fig. 10. A similar situation was observed in diffraction measurements for $(CsI)_nCs^+$ clusters at the bcc shell closing size of $n = 32$ [21]. The overall cluster structure displays a longer-range inversion symmetry about planes indicated by the dashed lines in Fig. 12.

3.1.2.3. Ag_{43}^+ and Ag_{55}^+ The calculated best-fit structure for $n = 43$ shown at the bottom of Fig. 13 exhibits an ordered atomic arrangement similar to that of $n = 55$ over a large fraction of the 43 atoms. This accounts for the similarity observed in the 55 and 43 sM(s) patterns shown in Fig. 8. At $n = 55$, global order having icosahedral Ih symmetry is observed characterizing the closed-shell structure. The global order observed for $n = 55$ is consistent with a high-symmetry structure indicated by PES [48] and also has been verified by TIED measurements performed in the Kappes group [49].

3.1.3. Summary

In summary, the present diffraction measurements have observed the structural evolution of Ag_n^+ in the range $n = 36$–55. In the region $n < 55$, we have found that local order having fivefold symmetry dominates the cluster structures. Similar sM(s) patterns were observed in recent TIED measurements performed in the Kappes group [50]. With the exception of $n = 38$, which exhibits mixed fivefold-fcc symmetries, the Q_6 order parameters calculated for the best-fit isomer structures show negligible size dependence. This indicates that the number of local fivefold symmetry sites within these structures is increasing with size leading up to the closed atomic structure at $n = 55$ having global order.

The local fivefold symmetry does not result from the decoration of an inner icosahedral core of 13 atoms having Ih symmetry. Not a single isomer calculated for cluster sizes below $n = 55$, comprising a total of ~40 DFT optimized cluster structures, contains an icosahedral core. The local order in these calculated structures becomes apparent only after an order analysis of the cluster structure.

A question which motivates further measurements is whether the evolving character of Ag_n^+ structures derives from the closed-shell Ih symmetry of $n = 55$, or does local fivefold symmetry more generally arises in the structures of metal clusters? Investigations of disordered metal structures including metallic glasses and supercooled metal melts have observed [51, 52] and analyzed [39, 45] the presence of short-range order characterized by fivefold symmetry. Perhaps it is not surprising that these diffraction measurements have also observed such local symmetry in the structures of small metal clusters.

3.2. Gold cluster anions

We recently completed the first direct structural determination of gold structures, achieved through joint diffraction measurements and density functional calculations of gold cluster anions in the size range $11 \leqslant n \leqslant 24$ [23]. Through these investigations, we identify specific isomer structures and follow the remarkable structural transitions among different symmetries and forms. Our analysis shows clear evidence of a planar (2D) to 3D transition over the range $n = 12$–14, caged structures for $n = 16$ and 17, culminating in a tetrahedral structure at $n = 20$ and the appearance of a highly symmetric tube-like structure at $n = 24$. These results are in general agreement with those obtained through recent indirect (PES/DFT) studies [10].

3.2.1. Experimental results

The total scattering data for all Au_n^- sizes are displayed in Fig. 15. The total scattering intensity data in the range $s \approx 3.5$–$4\,\text{Å}^{-1}$ change with cluster size. The molecular scattering intensity, sM(s), extracted by the data analysis is shown in Fig. 16 for each cluster size. The diffraction data shown in Fig. 16 were obtained for annealed clusters, which were found to be necessary to obtain reproducible diffraction data. The diffraction patterns in Fig. 16 show that the second positive peak near $s \sim 5\,\text{Å}^{-1}$ changes significantly within this cluster size range. This peakshape and the relative peak amplitudes will be shown to be the dominant characteristics identifying the transitions between the various structural motifs identified within the size range $n = 11$–24.

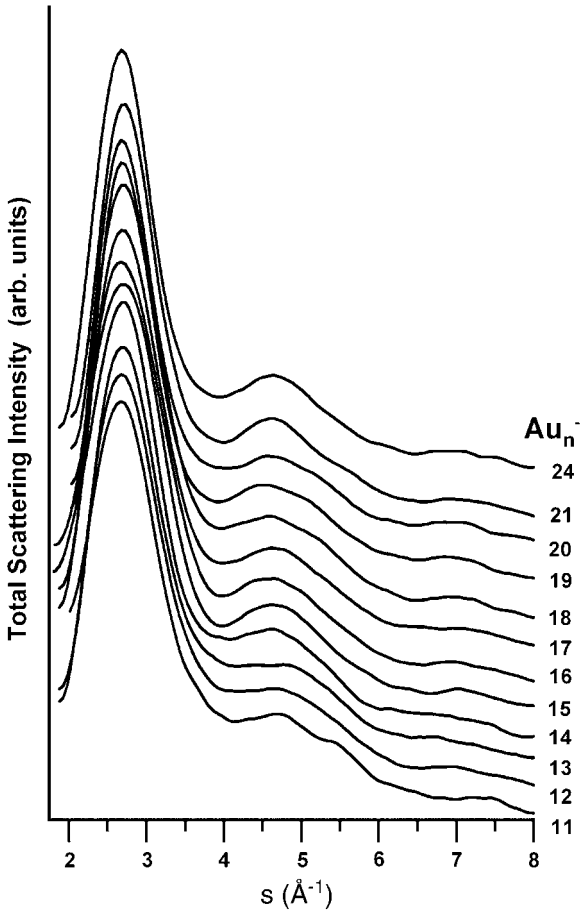

Figure 15: The total scattering intensity vs. s (Å^{-1}) is shown for all Au_n^- cluster sizes $n = 11$–21 and 24.

3.2.2. Analysis and discussion

The comparisons of diffraction data for annealed clusters with calculated structural isomers are shown in Figs. 17 and 18. For each cluster size, sM(s) patterns are calculated for each isomer structure. At the bottom, the experimental data are compared with the calculated sM(s) for the isomer structure producing the best fit. The experimental uncertainty shown includes only the standard deviations of the raw data. In several cases, the best fit diffraction pattern was derived by summing two patterns calculated for different isomeric structures. This sum of isomer contributions is assumed to represent an ensemble of trapped clusters composed of these structures. The fitting procedure varied the fractional contribution of each isomer structure in the sM(s) model to optimize the fit to the experimental patterns. The best-fit isomer structure(s) is shown at the lower right for each cluster size.

Structures for gold clusters were calculated by Landman and Yoon at the Georgia Institute of Technology. The electronic and geometric structures of the gold cluster

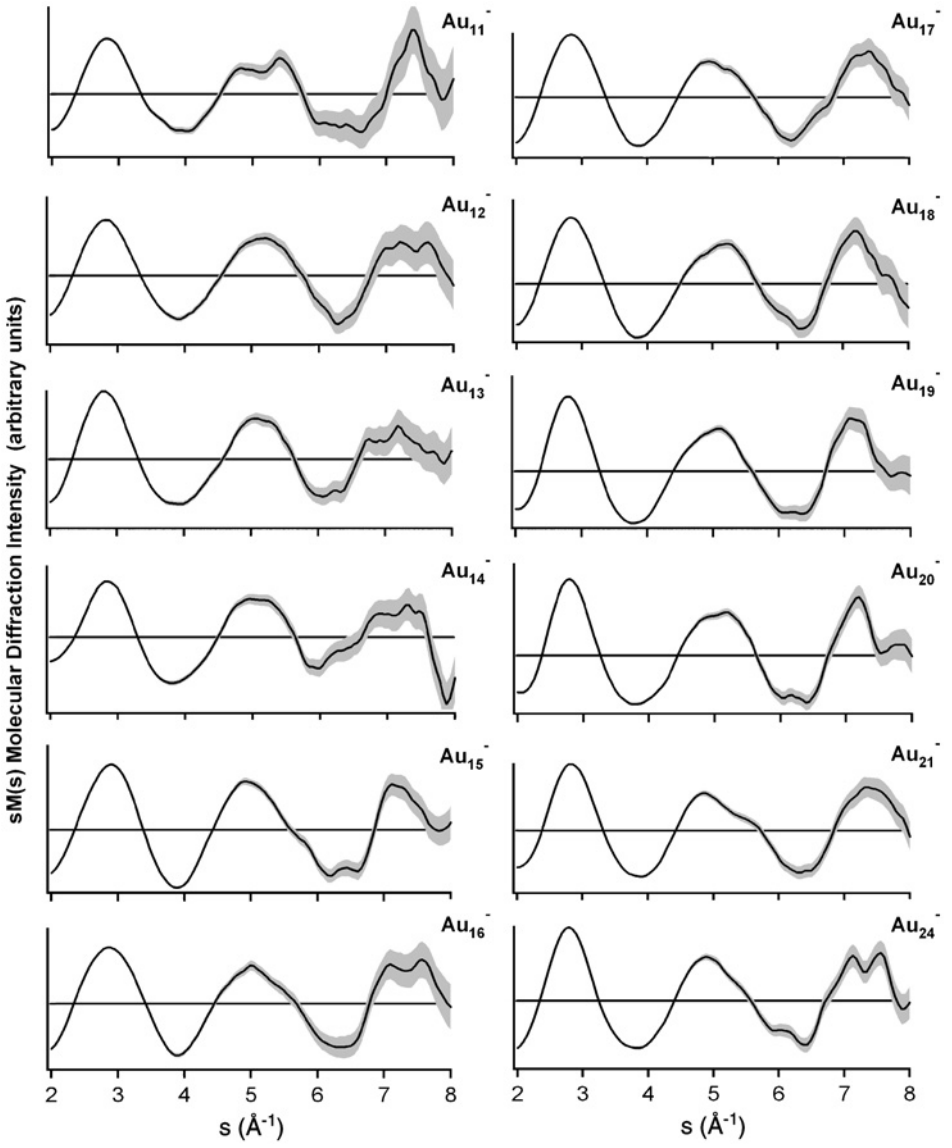

Figure 16: Experimental reduced molecular intensity sM(s) vs. s (Å^{-1}) is displayed for Au_n^- cluster sizes $n = 11$–21 and 24. The experimental data (black line) and uncertainty ($\pm 1\sigma$, gray band) are shown for each cluster size.

anions were obtained through the use of the Born–Oppenheimer (BO) local spin-density-functional (LSD) MD simulation method (BO-LSD-MD) [53], which was used as a tool for structural optimization via energy minimization using a conjugate-gradient-like technique. In the calculations, norm-conserving scalar relativistic pseudopotentials [54] were employed for the $5d^{10}6s^1$ valence electrons of the gold atom, within the generalized gradient approximation (PBE/GGA) [55]. The Kohn–Sham

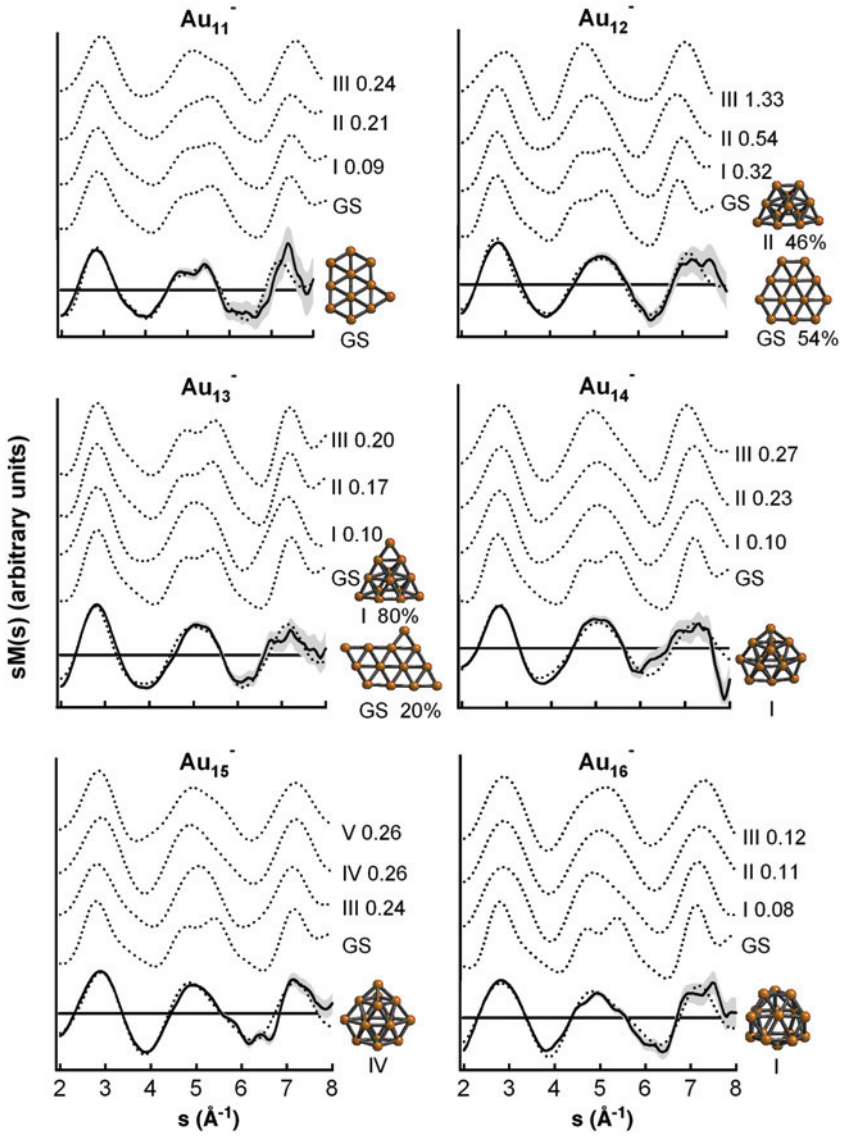

Figure 17: Calculated isomer diffraction patterns of sM(s) vs. s (Å^{-1}) for structures of Au_n^- clusters with $11 \leqslant n \leqslant 16$ are shown (dotted curves). The energy (in eV) of the isomer above the ground state (GS) is shown to the right of each isomer diffraction pattern. The experimental diffraction sM(s) (black curve) along with the best-fit isomer (dotted curve) is shown in the bottom panel. The gray shading shows the data uncertainty $\pm\sigma$. The best-fit isomer structure is shown to the right of each fit.

(KS) orbitals were expanded in a plane-wave basis with a 62 Ry kinetic energy cutoff. This approach has been used in numerous occasions previously and its feasibility and accuracy for gold has been well documented [4, 56, 57]. The BO-LSD-MD method is particularly suited for studies of finite charged systems because it does not employ a supercell (periodic replication of the atoms), thus allowing for accurate determination

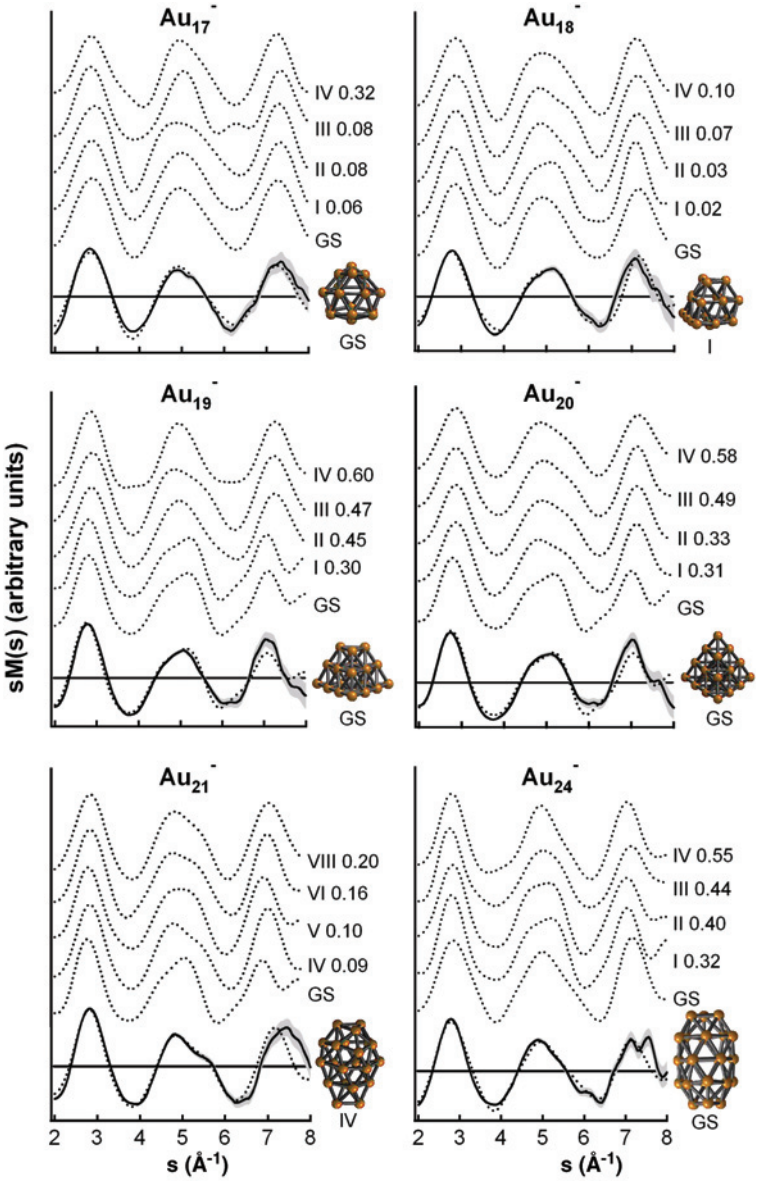

Figure 18: Similar to Fig. 1 for diffraction data and isomer structures for Au_n^- clusters with $17 \leqslant n \leqslant 21$ and $n = 24$.

of the total energy of both charged and neutral systems. All the clusters were relaxed fully without any symmetry constraints. A large number of initial structural candidates were used, but here we report only the few energetically low-lying isomers for each size, which are important in interpreting the experimental data.

The data for each cluster size were fit to all theoretical isomer structures calculated for that size. These fits were performed with the two different algorithms discussed in

Section 2.2.2 and in each case the same isomer structure was identified as the best fit with weighted *R*-values [37] in the range of 0.07–0.15. In the cluster size range on which we focus in this study, the signal-to-noise ratio in the displayed diffraction patterns degrades after $s \sim 7\,\text{Å}^{-1}$ and rapidly varying structure is a consequence of noise fluctuations and should be disregarded.

3.2.2.1. Au_{11}^-–Au_{15}^- In Fig. 17 we display calculated diffraction patterns for selected low-energy structures and the best fits for clusters in the size range Au_n^- $11 \leqslant n \leqslant 15$. Anionic gold clusters in this range have been the subject of theoretical [4, 58] and experimental [3] discoveries identifying the presence of large planar clusters. Experimental evidence for a transition from planar to 3D structures has been observed in measurements of cluster ion mobility [3] at $n = 12$ and photoelectron spectra [8] at $n = 13$. As indicated in Fig. 17, theory predicts many low-lying isomers within ~0.3 eV for each cluster size. In cases for which the diffraction patterns do not clearly differentiate a particular structural isomer, ion mobility [3] and/or photoelectron measurements [8] can help to identify the most probable structure. Although different cluster sources can introduce uncertainty in the isomer distribution, it is nevertheless interesting to note cases in which the different measurements agree or are clearly inconsistent.

The Au_{11}^- diffraction pattern appears to be most consistent with the two lowest-energy 2D isomers. The mobility measurement identifies the ground-state structure (marked as 11G in Fig. 17). The Au_{12}^- diffraction pattern is best fit by a cluster ensemble composed of a mixture of two isomers: 54% planar ground state and 46% of 12II, which is the lowest 3D isomer. Both ion mobility and photoelectron measurements indicate an isomer mixture. This size appears to be the first departure from pure planar structure. The best fit of the Au_{13}^- diffraction data also appears to arise from a mixture of structural isomers: 20% planar ground state and 80% of 13I (the lowest-energy 3D structure). Ion mobility observes a non-planar structure and also suggests the 3D isomer 13I, whereas the photoelectron results indicate the presence of an isomer mixture. For Au_{14}^-, there is no evidence of a planar structure and the diffraction pattern is best fit by a single isomer, the lowest-energy 3D structure 14I, in agreement with both mobility and photoelectron data. The diffraction pattern for Au_{15}^- is best fit by the higher lying isomer 15VI. The theoretical pattern is unique among the eight isomer patterns calculated for Au_{15}^- providing support for this assignment (isomers II and III not shown). The photoelectron spectra suggest a mixture of the 15III and 15V isomers, which is inconsistent with the diffraction result. In summary, the above patterns depict a transition with cluster size from planar to 3D structures. The smooth nature of the transition is reflected by the occurrence of sets of closely-spaced-in-energy isomers for cluster sizes in the transition region ($n = 12$–14).

3.2.2.2. Au_{16}^-–Au_{21}^- Calculated diffraction patterns for selected low-energy structures and the best fits for clusters in the size range Au_n^- $16 \leqslant n \leqslant 21$ are shown at the bottom of Fig. 17 ($n = 16$) and in Fig. 18. The diffraction pattern for Au_{16}^- is uniquely fit by the cage structure isomer 16I lying 0.08 eV above the 2D ground state. Evidence for this cage structure has recently been observed in photoelectron measurements [9]. The diffraction pattern for Au_{17}^- is fit equally well by the ground-state cage structure and a second low-energy isomer separated by only 0.06 eV. However, the photoelectron

results [9] prefer the ground-state cage structure. The diffraction pattern for Au_{18}^- is best fit by the isomer 18I that lies only 0.02 eV above the ground state. The theoretical diffraction pattern for this fit is unique among the six isomer diffraction patterns calculated for Au_{18}^-, providing strong evidence for assigning the 18I structure. The photoelectron spectra suggest a mixture of the ground state and the 18IV isomer which is inconsistent with the diffraction result.

The diffraction patterns observed for clusters in the size range $n = 18$–20 all exhibit a shoulder on the left side of the second peak, which is evidence for the presence of fcc symmetry (which is the bulk gold structure). This symmetry has been identified [7] for the tetrahedral structure of the Au_{20}^- ground state which gives the best fit to the diffraction pattern. The diffraction pattern for Au_{19}^- is also fit by a similar tetrahedral structure (the ground-state structure 19G) in which a single vertex atom is missing. The structure for Au_{18}^-, 18I, which provides the best fit with the diffraction data is also related to the tetrahedral structure with atoms missing at two vertices and slight atomic displacements. However, with the addition of a single atom, that is for Au_{21}^-, the observed diffraction pattern changes in a radical fashion. Although there are several low-energy structures for Au_{21}^-, which display the presence of fcc symmetry, the best-fit structure is found to be isomer 21IV, an elongated cage.

3.2.2.3. Au_{24}^- Figure 18 displays the calculated diffraction patterns for the low-energy structures of Au_{24}^- that present evidence for the emergence of an empty single wall tube-like structure [59]. Indeed, the best-fit structure is found to be the highly symmetric ground-state isomer, 24G, whose structure (shown in Fig. 19) is composed of three stacked six-member rings with the center one being hexagonal (green) and the other two having threefold symmetry (red). The outer six-member rings are each capped by a three-atom triangle (yellow) as shown in Fig. 19a. The commonality between the Au_{24}^- and Au_{16}^- structures is also shown in Fig. 19b, where we note that both these low-energy structures contain 12 atoms with fivefold coordination and 12 (4 for Au_{16}^-) atoms with sixfold coordination. Figure 19b also indicates that the tubular structure of Au_{24}^- may be viewed as obtained from the 16I isomeric structure Au_{16}^- by replacing the bottom capping atom in the latter by a six-member ring, which is then capped by a triangle. The diffraction patterns for $n = 16$ (Fig. 17) and 24 (Fig. 18) are essentially identical and unique among all the patterns derived from the calculated isomers, both exhibiting a triangular second peak, which supports the structural assignments.

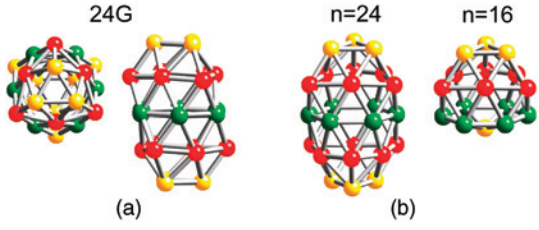

Figure 19: (a) The structure for $n = 24$ is shown in end-on and perspective views to emphasize the symmetry and planar aspects of the structure. (b) A comparison of the structures of gold cluster anions with $n = 24$ and 16 atoms are shown.

3.2.3. Summary

A series of unique structural transitions in gold anion clusters throughout the size range of $n = 11$–24 atoms has been observed. The identification of these structures has been accomplished through direct structural determination – that is, the comparison of electron diffraction data from trapped clusters with density functional calculations of structural isomers for each cluster size. These transitions exhibit changes in form and symmetry evolving from planar species at $n = 11$ to hollow cages, and finally to a highly symmetric, tube-like structure at $n = 24$ observed in these diffraction measurements for the first time.

The rich array of size-dependent structural motifs described in this study is specific to gold clusters, and it is likely to originate from the relativistically enhanced s–d hybridization of gold bonding orbitals [4]. The determination of these cluster structures, achieved here through joint electron diffraction measurements and first-principles calculations, adds to the published plethora of gold structures [3, 4, 7–10, 56–59]. Most importantly, the determination of these cluster structures is essential to an understanding of the size-dependent evolution of cluster properties, for example, assisting a more complete understanding of the mechanisms that control the chemical reactivity and catalytic activity of gold clusters [60].

4. OUTLOOK

The TIED technology and analysis have been developed to a level that measurements of cluster diffraction can be performed reliably and reproducibly. The several technical interfaces between cluster source and ion trap, electron beam and diffraction beamline components, and ion trap and scattered electron detection have stable, workable solutions, which allow continuous operation over the long times required to accrue diffraction data. Experiments are somewhat lengthy, ~4 h, but the computer technology to control these interfaces and perform data acquisition is robust and requires relatively little tuning over these run times. It is encouraging that our instrument and the instrument built in the Kappes group reproduces measurements for similar clusters. This technology will continue to be extended to improve the S/N in order to measure clusters composed of lower atomic mass atoms and smaller size clusters and to reduce experimental run times.

TIED measurements have been successfully extended to the measurement of metal cluster structures. The technique exhibits sufficient sensitivity to identify the presence of both local and global symmetries. The theorists have been exceptionally helpful to supply the structure calculations, which together with TIED measurements form the necessary combination to identify the evolution of structure with increasing cluster size. The measurements on Ag_n^+ and Au_n^- clusters have reinforced several conclusions. Although the metal cluster calculations provide many low-energy structural isomers, it is remarkable that the best fits with data usually identify a single, or at most two, isomer structure independent of fitting procedure. The experimental identification of the unique, highly symmetric structure calculated for Au_{24}^- and its similarity with the structure for Au_{16}^- are some of the more striking examples of TIED capability. In cases for which the best fit cannot differentiate between similar isomer structures, the diffraction pattern still serves the purpose to identify symmetries that are clearly absent.

There are several important areas of cluster physics and chemistry for which TIED measurements may lead to a deeper understanding. Nanocatalysis is a growing field with the possibilities to increase reactivity and perhaps reaction specificity. It would be particularly helpful to be able to identify the relationship, or correlation between structure and reactivity for gas-phase clusters. In this case, the utility of diffraction data to identify the calculated isomer structure of a gas-phase reactant may allow such a correlation to be discerned and related to catalytic processes. The temperature dependence of metal clusters is a property which has been investigated experimentally by measurements of cluster dissociation, mobility and calorimetry. However, the possibility to directly identify the change in cluster structure vs. temperature can be accomplished by diffraction measurements. This will surely lead to one of the more interesting combinations of TIED technology and theoretical calculation in the near future.

ACKNOWLEDGMENTS

It is a great pleasure to identify the group of postdoctoral fellows who have contributed to the development of the TIED science and technology. In order of their tenure in my laboratory, they are Douglas Cameron, Mathias Maier-Borst, Stefan Kruekeberg, Detlef Schooss, Rongbin Huang and Xi Li in addition to my co-author Xiaopeng Xing. It is difficult to imagine the success we have experienced without the broad accomplishment and creative efforts of these individuals. I enjoyed them as colleagues and as friends. Last but not least, I acknowledge fruitful discussions with Mordechai Rokni who helped to originate the ideas leading to TIED, and to Abraham Szöke for conversations leading to a clearer view of the issues involved.

I also thank my Rowland Institute colleagues Michael Burns and Frans Spaepen for many helpful conversations and advice regarding analysis and interpretation of diffraction measurements. Although the theoretical contributions of my collaborators in this work has been mentioned above, Uzi Landman's physical insight and clarity are greatly appreciated, and the suggestions and encouragement of Ignacio Garzón and Karo Michaelian were particularly helpful.

This research was supported by the Department of Energy (DOE) under Grant No.DE-FG02-01ER45921.

REFERENCES

[1] Haberland H., Hippler T., Donges J., Kostko O., Schmidt M., von Issendorff B., Phys. Rev. Lett. 94 (2005) 035701.
[2] Cleveland C.L., Leudtke W.D., Landman U., Phys. Rev. Lett. 81 (1998) 2036.
[3] Furche F., Ahlrichs R., Weis P., Jacob C., Gilb S., Bierweiler T., Kappes M.M., J. Chem. Phys. 117 (2002) 6982.
[4] Häkkinen H., Moseler M., Landman U., Phys. Rev. Lett. 89 (2002) 33401.
[5] Heiz U., Sanchez A., Abbet S., Schneider W.-D., J. Am. Chem. Soc. 121 (1999) 3214.
[6] Sanchez A., Abbet S., Heiz U., Schneider W.-D., Häkkinen H., Barnett R.N., Landman U., J. Phys. Chem. A 103 (1999) 9573.
[7] Li J., Li X., Zhai H.-J., Wang L.-S., Science 299 (2003) 864.
[8] Häkkinen H., Yoon B., Landman U., Li X., Zhai H.-J., Wang L.-S., J. Phys. Chem. A 107 (2003) 6168.

[9] Bulusu S., Li X., Wang L.-S., Zeng X.C., Proc. Natl. Acad. Sci. 103 (2006) 8326.
[10] Yoon B., Koskinen P., Huber B., Kostko O., von Issendorf B., Häkkinen H., Moseler M., Landman U., Chem. Phys. Chem. 8 (2007).
[11] Debye P., Ann. Phys. 46 (1915) 809.
[12] Debye P., Bewilogua L., Ehrhardt F., Phys. Z. 30 (1929) 84; Debye P., Phys. Z. 31 (1930) 419.
[13] Mark H., Wierl R., Naturwissenschaften 18 (1930) 205; Wierl R., Ann. Phys. 8 (1931) 521.
[14] De Boer B.G., Stein G.D., Surf. Sci. 106 (1981) 84; Yokozeki A., Stein G., J. Appl. Phys. 49 (1978) 2224.
[15] Farges J., Feraudy M.F., Raoult B., Torchet G., Surf. Sci. 106 (1981) 95; Farges J., Raoult B., Torchet G., J. Chem. Phys. 59 (1973) 3454.
[16] Hovick J.W., Bartell L.S., J. Phys. Chem. B 102 (1998) 534; Bartell L.S., Chem. Rev. 86 (1986) 491.
[17] Reinhard D., Hall B.D., Ugarte D., Monot R., Phys. Rev. B 58 (1998) 4917; Reinhard D., Hall B.D., Berthoud P., Valkealahti S., Monot R., Phys. Rev. B 55 (1997) 7868.
[18] Hedberg K., Hedberg L., Bethune D.S., Donald S., Brown C.A., Dorn H.C., Johnson R.D., de Vries M., Science 254 (1991) 410; Hedberg K., Hedberg L., Bühl M., Bethune D.S., Brown C.A., Johnson R.D., J. Am. Chem. Soc. 119 (1997) 5314.
[19] Parks J.H., Pollack S., Hill W., J. Chem. Phys. 101 (1994) 6666; Parks J.H., Szöke A., J. Chem. Phys. 103 (1995) 1422.
[20] Maier-Borst M., Cameron D.B., Rokni M., Parks J.H., Phys. Rev. A 59 (1999) R3162.
[21] Krückeberg S., Schooss D., Maier-Borst M., Parks J.H., Phys. Rev. Lett. 85 (2000) 4494.
[22] Xing X., Danell R.M., Garzón I.L., Michaelian K., Blom M.N., Burns M.M., Parks J.H., Phys. Rev. B 72 (2005) 081405R.
[23] Xing X., Yoon B., Landman U., Parks J.H., Phys. Rev. B 74 (2006) 165423.
[24] Maier-Borst M., Dissertation, Universität Konstanz, 1997.
[25] von Issendorff B., Haberland H., private communication.
[26] Heiz U., Vanolli F., Trento L., Schneider W.-D., Rev. Sci. Instrum. 68 (1997) 1986.
[27] Wiley W.C., McLaren I.H., Rev. Sci. Instrum. 26 (1955) 1150.
[28] Quarmby S.T., Yost R.A., Int. J. Mass Spectrom. 190/191 (1999) 81.
[29] Guan S., Marshall A.G., Int. J. Mass Spectrom. Ion Processes 157/158 (1996) 5; Marshall A.G., Wang T.-C.L., Ricca T.L., J. Am. Chem. Soc. 107 (1985) 7893.
[30] Julian R.K., Jr., Cooks R.G., Anal. Chem. 58 (1993) 14; Soni M.H., Cooks R.G., Anal. Chem. 66 (1994) 2488.
[31] Asano K.G., Goeringer D.E., McLuckey S.A., Int. J. Mass Spectrom. 185/186/187 (1999) 207.
[32] Bartell L.S., Kohl D.A., Carroll B.L., Gavin R.M., Jr., J. Chem. Phys. 42 (1965) 3079; Kuchitsu K., Bartell L.S., J. Chem. Phys. 35 (1961) 1945; Bartell L.S., J. Chem. Phys. 23 (1955) 1219.
[33] D'Antonio P., George C., Lowrey A.H., Karle J., J. Chem. Phys. 55 (1971) 1071.
[34] Hargittai I., Hargittai M. (eds), Stereochemical Applications of Gas-Phase Electron Diffraction, VCH, New York, 1988; (and references therein).
[35] Davis M.I., Electron Diffraction in Gases, Marcel Dekker, New York, 1971.
[36] Zhong W., Cai Y., Tománek D., Phys. Rev. B 46 (1992) 8099.
[37] Prince E., in: The Rietveld Method, R.A. Young (ed.), Oxford University Press, Oxford, 1995, p. 43.
[38] Kelton K.F., Lee G.W., Gangopadhyay A.K., Hyers R.W., Rathz T.J., Rogers J.R., Robinson M.B., Robinson D.S., Phys. Rev. Lett. 90 (2003) 195504.
[39] Sachdev S., Nelson D.R., Phys. Rev. Lett. 53 (1984) 1947.
[40] Michaelian K., Chem. Phys. Lett. 293 (1998) 202.
[41] Rosato V., Guillope M., Legrand B., Philos. Mag. A 59 (1989) 321.

[42] Fernández E.M., Soler J.M., Garzón I.L., Balbás L.C., Phys. Rev. B 70 (2004) 165403.
[43] Michaelian K., Rendón N., Garzón I.L., Phys. Rev. B 60 (1999) 2000.
[44] Baletto F., Rapallo A., Rossi G., Ferrando R., Phys. Rev. B 69 (2004) 235421.
[45] Steinhardt P.J., Nelson D.R., Ronchetti M., Phys. Rev. B 28 (1983) 784; Nelson D.R. and Spaepen F., in: Solid State Physics. F. Seitz, D. Turnbull (eds), Academic Press, Boston, 42, 1989, p. 1.
[46] Doye J.P.K., Miller M.A., Wales D.J., J. Chem. Phys. 110 (1999) 6896.
[47] Wales D.J., Science 271 (1996) 925.
[48] Häkkinen H., Moseler M., Kostko O., Morgner N., Hoffmann M.A., Issendorff B.v., Phys. Rev. Lett. 93 (2004) 093401.
[49] Schooss D., Blom M.N., Parks J.H., Issendorff B.v., Haberland H., Kappes M.M., Nano Lett 5 (2005) 1972.
[50] Blom M.N., Schooss D., Stairs J., Kappes M.M., J. Chem. Phys. 124 (2006) 244308.
[51] Schenk T., Holland-Moritz D., Simonet V., Bellissent R., Herlach D.M., Phys. Rev. Lett. 89 (2002) 75507.
[52] Kelton K.F., Lee G.W., Gangopadhyay A.K., Hyers R.W., Rathz T.J., Rogers J.R., Robinson M.B., Robinson D.S., Phys. Rev. Lett. 90 (2003) 195504.
[53] Barnett R.N., Landman U., Phys. Rev. B 48 (1993) 2081.
[54] Troullier N., Martins J.L., Phys. Rev. B 43 (1991) 1993.
[55] Perdew J.P., Burke K., Ernzerhof M., Phys. Rev. Lett. 77 (1996) 3865.
[56] Häkkinen H., Landman U., Phys. Rev. B 62 (2000) R2287.
[57] Häkkinen H., Landman U., J. Am. Chem. Soc. 123 (2001) 9704.
[58] Gilb S., Ph.D. thesis, University of Karslruhe, 2001.
[59] Recently, tube-like structures were predicted (Fa W., Dong J., J. Chem. Phys. 124 (2006) 114310–114314) for Au_{26} to Au_{28} neutral clusters with atoms having fivefold and sixfold coordination. However, there is no experimental evidence for these structures. We also note that supported single-shell gold nanowires exhibiting a tube-like helical structure have been reported in an electron microscope study (Oshima Y., Onga A., Takayanagi K., Phys. Rev. Lett. 91 (2003) 205503–205514). There appears to be no relationship between the nanowire structure, nor the structure predicted for Au_{26} with the structure determined here for Au_{24}^-.
[60] Heiz U., Landman U. (eds), Nanocatalysis, Springer, Berlin, 2006.

This page intentionally left blank

Chapter 10

Superatoms: building blocks of new materials

A.W. Castleman, Jr.[a,*] and S.N. Khanna[b]

[a]Departments of Chemistry and Physics, Pennsylvania State University, University Park, PA 16802, USA

[b]Department of Physics, Virginia Commonwealth University, Richmond, VA 23284, USA

1. INTRODUCTION

Materials found in nature generally have atoms or molecules as the elementary building units. Depending on the physical conditions such as density, and thermodynamic parameters such as temperature and pressure, these primitive building units arrange in different patterns and forms. For example, carbon forms graphite, diamond and amorphous carbon structures. The properties of these diverse arrangements are, however, very different, indicating that the same building blocks, arranged differently, can lead to diverse material characteristics. One also observes that although the molecules are built from atoms, the properties of molecular solids can be completely different from those of elemental solids of constituent atoms. After all, the properties of table salt are totally unlike those of pure sodium or chlorine. One of the principal objectives of the research on atomic clusters is to incorporate both these principles into creating novel architectures, where designer clusters serve as the elementary blocks. Since the properties of clusters can be controlled by size and composition, and since the properties of assemblies are governed by the overlying architecture of elementary motifs, such arrangements offer the unprecedented ability to design materials with tailored properties [1–11].

It is important to highlight that while isolated clusters are themselves stable, the cluster assemblies do not always constitute most stable forms of matter. Consequently, their existence cannot be foreseen in the conventional ways, such as stability in binary phase diagrams. The existence of non-equilibrium phases is, however, not without precedence. After all, amorphous metals obtained by fast quenching of liquid metals, while metastable, form practical materials [12]. While the most stable form of carbon is graphite, diamonds have existed forever. In the field of cluster assemblies, the

The Chemical Physics of Solid Surfaces, Volume 12
ISSN: 1571-0785
DOI: 10.1016/S1571-0785(07)12010-1

*Corresponding author.
E-mail: awc@psu.edu

fullerides consisting of C_{60} clusters joined by alkali atoms are now routinely generated [13] by vaporizing metal and carbon. Met-Cars consisting of 20-atom cages composed of 8 transition metal atoms and 12 carbon atoms have been assembled in films [14, 15]. While all these metastable materials are useful solids, their synthesis does require unconventional methods: ones that circumvent nature's path to thermodynamically stable forms of matter. The journey to these unconventional materials offering the possibility of tuning physical, chemical, electronic, magnetic and optical properties [5, 6] therefore begins by identifying the prospective cluster building blocks that have interesting behaviours and maintain their identity in assemblies. The concept of superatoms [16–18] not only aims at identifying such species but also provides a general framework for classification of the potential cluster species into groups.

We begin by briefly reviewing some earlier work on clusters that relates to the development of the concept. In 1984, Walter Knight and co-workers [19] generated sodium clusters by vaporizing the sodium and passing the vapour through a supersonic nozzle. A mass spectra of the generated clusters showed that clusters containing 2, 8, 18, 20, 40, 58… atoms were more prominent than other sizes (Fig. 1). These numbers were called magic numbers and experiments on other alkali metals revealed similar magic species, indicating that they were not specific to sodium. Since alkali atoms are monovalent, the prominence in the mass spectra could be due to either the electronic counts or other features such as special geometries at these sizes. That the observed phenomenon is primarily electronic was indicated by experiments that showed a drop in ionization potential at sizes corresponding to electronic count one above the magic species [20], and low values of electronic affinities at the magic sizes. Further experiments on the dissociation of clusters showed that the magic sizes were the favoured fragmentation products [21, 22] and that it required more energy to fragment magic species. All these observations indicated that (1) the magic clusters are very stable species and (2) their stability is probably rooted in electronic counts. Knight and co-workers also proposed [20] that the stability of magic clusters could be understood within a simple jellium picture. Since the concept of superatoms relies on the electronic structure and electron counts, we now consider this model in detail.

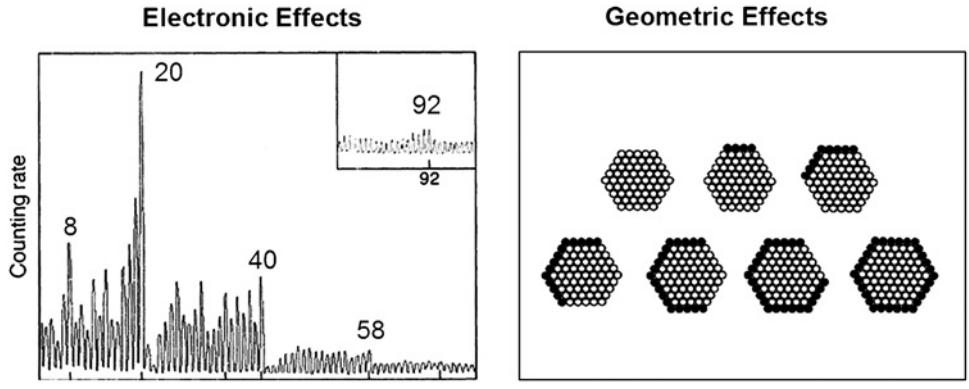

Figure 1: Global features determining the stability of metal clusters.

2. JELLIUM: TENETS, ELECTRON COUNTS AND ENERGETIC STABILITY

The electronic structure of simple metals is usually described within a simple picture where the valence electrons form a nearly free electron gas weakly perturbed by the potential generated by the ionic cores. In fact, the ionic potential is usually replaced by a pseudo-potential that is much weaker and whose lowest eigen states correspond to the valence states. Apart from simplifying electronic structure calculations, the replacement allows use of perturbation theories to describe the electronic structure and transport. Another pragmatic and simpler approximation along these lines is the jellium model where one ignores the lattice structure of the ionic cores altogether and replaces them by a uniform positive background. Ekardt [23] and Knight and co-workers [20] proposed a similar model for clusters where the cluster was replaced by a spherically symmetric potential well, with the positive charge density being uniform inside the sphere and zero outside. The electronic levels in such a potential well are characterized by a radial and angular momentum quantum numbers n and l, respectively, similar to the case of atoms. (Note that the potential has a different radial dependence in atoms and it leads to different combinations of n and l.) As in atoms, the magnetic quantum number takes values from $-l, -l+1, \ldots, 0, \ldots l-1, l$ and the spin quantum number takes the two values of $\pm 1/2$. In Fig. 2 we schematically show the one-electron levels in an H atom and those in a spherical jellium (the energy levels in the two systems are not inferred to be the same).

Note the ordering $1s^2\ 1p^6\ 1d^{10}\ 2s^2\ 1f^{14}\ 2p^6 \ldots$ compared to $1s^2\ 2s^2\ 2p^6\ 3s^2\ 3p^6\ 3d^{10} \ldots$ for the H atom. Fairly similar ordering of levels (except for higher energy levels) is obtained for harmonic, intermediate and square well forms of potential [20]. Inclusion of electron exchange correlation effects can be pursued by solving density functional equations for the background positive charge distribution. Theoretical studies [24] show that the electronic shell structure is maintained, even though the spacing between the shells can depend on the shape of the potential. The key message is that the electronic shell structure is a generic property of the confined nearly free electron gas. It is known that atomic and molecular systems with filled electronic shells and large gaps in the excitation spectrum exhibit enhanced stability. It was therefore natural to examine if the origin of magic numbers is rooted in the electronic shell structure. It was pointed out that the stable sizes at 2, 8, 18, 20, 34, 40,… indeed correspond to the electron counts that lead to filled electronic shells. The stability of clusters could thus be linked to the filling of the electronic shells.

3. CLUSTER STABILITY, ELECTRONIC MARKERS AND SUPERATOMS

While the electronic shell structure governs the stability at small sizes, experiments at larger sizes brought about another component to the stability. It was found that the clusters containing a few hundred atoms exhibited another set of magic numbers. As an example, Martin and co-workers [25] generated calcium clusters containing up to around 5000 atoms. The observed mass spectrum was characterized by a recurring set of 20 peaks. More interestingly, each complete set was found to correspond to the formation of one complete icosahedral shell of atoms with the set of 20 peaks each corresponding to completion on one of the triangular faces of the growing icosahedral

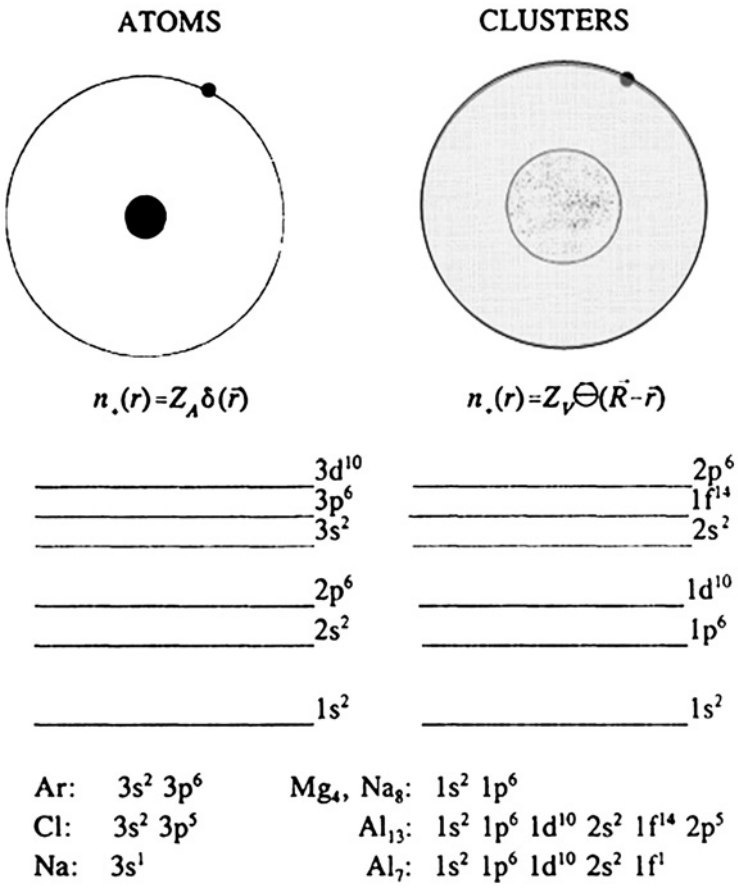

Figure 2: Energy levels in atoms and clusters.

shell. Their experiments indicated that at large sizes the stability is dominated by the geometrical compactness of the clusters. Combined with the electronic origin of magic numbers at small sizes, the indication was that the stability of a cluster has an electronic and a geometric component. While the electronic effects dominate at small sizes, the geometric compactness dominates at large sizes. This led Khanna and Jena [16] to propose that it should be possible to design very stable clusters by combining electronic and geometric factors. To prove their assertion, they carried out theoretical studies on Al_{13} and $Al_{12}C$ clusters, which have geometrically compact structures, to investigate the effect of electron count on the stability. Since Al_{13} has 39 electrons while $Al_{12}C$ has 40 electrons, they argued that the replacement of an Al in Al_{13} by C should enhance the stability. The theoretical studies indeed predicted an increase in binding energy by 4.4 eV. They argued that by combining electronic and geometric factors, it should thus be possible to design very stable species that could serve as the building blocks of new materials.

The existence of the electronic shells in a nearly free electron gas and their role in governing the stability raised the question whether stable clusters exhibit electronic

features much in the same way as atoms. Consider the case of Al that is trivalent. An Al_{13} cluster has 39 valence electrons and would correspond to the level structure $1s^2$ $1p^6$ $1d^{10}$ $2s^2$ $1f^{14}$ $2p^5$ with one hole in the valence 2p shell. Does it have commonality with halogen atoms that also have a missing electron in their outer p-shell? Will filling of this hole lead to inert gas behaviour? Castleman and co-workers [26] examined the reactivity of Al_n^- with oxygen in a flow reactor to examine the inert behaviour of Al_{13}^- and related species. While the details of their work are presented later, their studies really confirmed that although most clusters are etched away by oxygen, species such as Al_{13}^-, Al_{23}^- and Al_{37}^- remained intact. All these sizes correspond to magic numbers and correspond to systems with filled electronic shells much in the same way as inert gas atoms. This was an intriguing finding in view of the fact that bulk aluminium surfaces are highly susceptible to etching by oxygen. More importantly, the findings demonstrated that the electronic bands in clusters exhibit the same chemistry as atoms in the periodic chart.

The possibility of designing stable species by combining electronic and geometric features and the demonstration that the chemical features of the clusters have commonality with atoms in the periodic table were remarkable findings. The stage was set for SUPERATOMS, fairly stable species with well-defined chemical markers, mimicking atoms of the periodic table and holding potential for making novel cluster motifs and eventually cluster assembled materials [17, 27–32].

4. ADDING A THIRD DIMENSION TO THE PERIODIC TABLE

The findings that the stable species can be formed by varying size and the chemical significance of the electronic shells in the confined nearly free electron gas opened the possibility that superatoms mimicking atoms in the periodic table and constituting a third dimension to the periodic table could be synthesized. The designing and studying the properties of superatoms is an active subject in our groups, pursued in depth through a combination of experiment and first principles theory.

4.1. Rare-gas mimics: creating a closed-shell system

Our initial and key finding was that the Jellium model could be used to predict which species may be stable against reactive destruction based on their closed-shell electronic character. Al_{13}^- became the model based on which other species were discovered [17, 29, 30, 33]. In terms of the Jellium model, this aluminium species is a closed-shell 40-electron system that behaves as a rare-gas mimic; indeed in its ground state it has been found to be totally inert against etching by oxygen, as have other related closed-shell species such as Al_{23}^- and Al_{37}^-. By contrast, proximate species of higher mass readily undergo etching, which proceeds until a size is reached that forms these closed-shell clusters as terminal products. This is evident in Fig. 3, which shows the mass spectra of the unreacted and reacted aluminium clusters. The upper panel in the figure shows a typical nascent distribution, while the effects of increased etching are seen in the lower two panels. Not only are the magic peaks resistant to etching by oxygen, but they also are formed at the expense of the higher order unstable clusters that become successively etched. The experimental results, in combination with theoretical calculations, showed that Al_{13}^- is totally unreactive with oxygen and behaves effectively as a

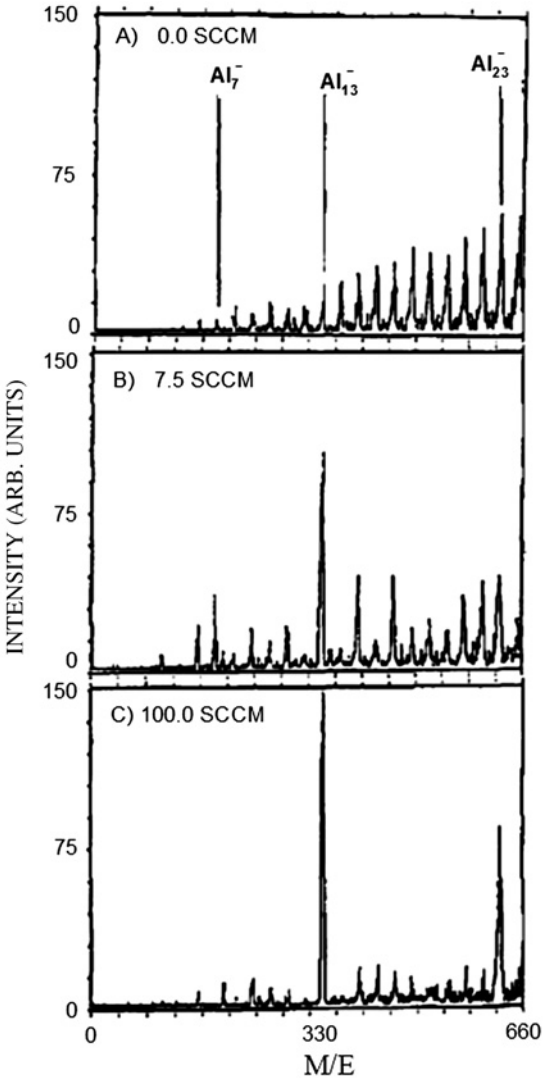

Figure 3: Oxygen etching of aluminium clusters. Adapted from Ref. [9].

rare-gas mimic in accord with its closed electronic nature. These findings raised the question: if one species could mimic an atom, were there others?

4.2. Superhalogen character

During the course of studying the reactivity of aluminium clusters, the entire comprehensive concept of superatoms suddenly unfolded. As mentioned before, an Al_{13} has an electronic configuration of $1s^2\ 1p^6\ 1d^{10}\ 2s^2\ 1f^{14}\ 2p^5$ with one hole in the valence 2p shell. This is similar to the case of halogen atoms that also have five electrons in

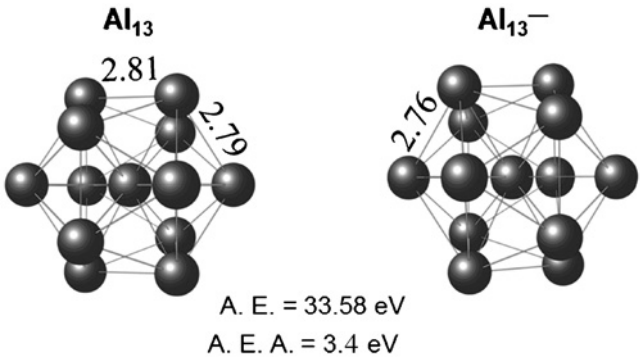

Figure 4: Geometries of Al_{13} and Al_{13}^- clusters. Bond lengths are marked in Å. A.E. is the atomization energy and A.E.A. is the adiabatic electron affinity.

their valence p-shell. It was therefore tempting to probe if the properties of Al_{13} were similar to those of a halogen atom. Theoretical studies by Khanna and Jena [16] indicated that the cluster indeed had a high vertical electron affinity of around 3.7 eV that is more than the known values of 3.36 eV for Br and 3.62 eV for Cl. Figure 4 shows the ground-state geometry of neutral Al_{13} and Al_{13}^- along with its atomization energy and a calculated adiabatic electron affinity of 3.4 eV. Experimental studies [34, 35] confirmed the theoretical prediction placing the vertical electron affinity to be 3.75 eV and an adiabatic electron affinity to be 3.57 eV.

The superhalogen nature of Al_{13} became particularly enlightening during our recent studies on its reactions with HI [17]. In particular, a very prominent species comprising $Al_{13}I^-$ was detected to readily form. Theoretical studies revealed that the extra electron charge was mostly localized at the aluminium cluster leaving the Al_{13} core almost intact as in Al_{13}^-. This suggested an analogy to stable halogen dimer anions. In view of its electron affinity, Al_{13} is somewhere between a bromine and a chlorine. Consequently, $Al_{13}I^-$ is a mimic of the well-known ions, BrI^- and ClI^-. Hence, the aluminium cluster is indicated to be behaving as a superhalogen. This finding was remarkable as it showed that groups of aluminium atoms can display behaviours reminiscent of halogen atoms.

However, the aforementioned is not the only evidence for this halogen-like nature of Al_{13}. Further studies [29, 33] with I_2 in place of HI led to even more unexpected results. $Al_{13}I_2$ was found to be a prominent species, again with an analogy to well-known halogen species, namely BrI_2^- or ClI_2^-. The theoretically deduced charge distribution is shown in Fig. 5. Again note that the aluminium 13-mer retains its integrity, and functions as a superhalogen.

The biggest surprise came in studies made with high iodine concentrations (see Fig. 6). A multiple iodine sequence was first observed which, when etched with oxygen, revealed a stable distribution of iodized aluminium species, reminiscent of the polyhalide series well known in the condensed phase [29]. The dramatic odd–even intensity distributions seen in the figure are characteristics found in the condensed phase, and similar to expectations for XI_n^- anions that are very stable for n = odd, where X is also a halogen. One major difference compared to the condensed phase is the fact that the theoretical

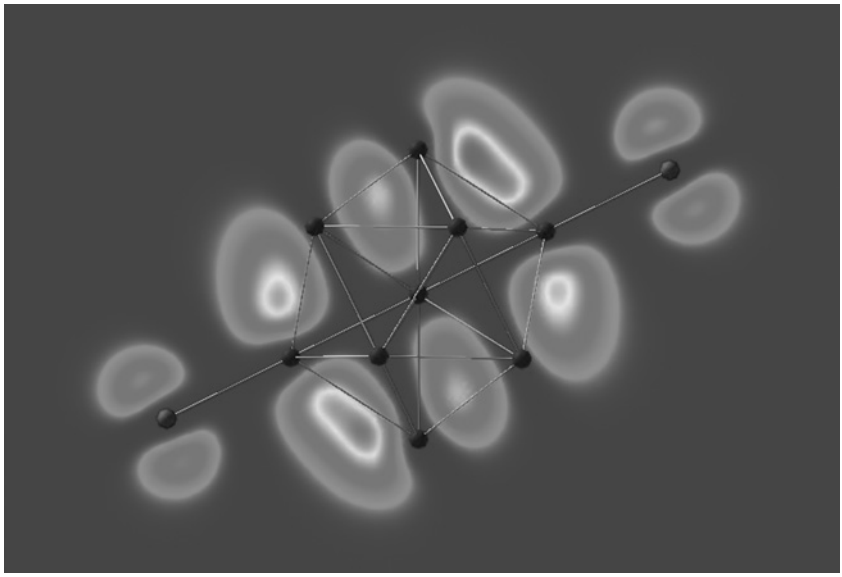

Figure 5: Charge density of the highest occupied molecular orbital in $Al_{13}I_2^-$. Adapted from Ref. [33].

findings confirmed that the halogen atoms are individually bonded to the aluminium cluster–halogen mimic, and not as molecular iodine chains as in the case of polyiodides in the condensed phase.

Theoretical studies have also been performed to investigate the possibility of combining Al_{13} with alkali atoms in order to build analogues of salts using superhalogens instead of halogen atoms. Studies on $Al_{13}K$ indeed showed [9] that a stable molecule can be formed that is bound by ionic forces much in the same way as alkali halides. Figure 7 shows the ground-state geometry of $Al_{13}K$ that places the K at a hollow site on the surface of Al_{13}. The structure of Al_{13} was found to remain almost intact during the formation of the molecule. Following the theoretical prediction, Bowen and coworkers [36] have recently synthesized this molecule in gas-phase experiments. Their measurements of the electron affinity and negative ion photoelectron spectra show that the cluster has all the hallmarks of a molecule bound by ionic forces, thus confirming the theoretical prediction.

4.3. An alkaline earth-like system

Another surprising finding was that of a second cluster series, this one involving Al_{14} as a core, with bound iodine atoms in an even–odd series with an exactly opposite odd–even trend to that seen for $Al_{13}I_n^-$. These species are also evident in Fig. 6. A significant aspect is that the series commences with $Al_{14}I_m^-$, $m = 3$. Observation of the experimental trends and theoretical results shows that the aluminium core has taken on a valence of two character, revealing the formation of a cluster mimic of alkaline earth metal (see Fig. 8). With the calculated charge distribution, the remaining aluminium core effectively takes on a 40-electron closed shell-like character.

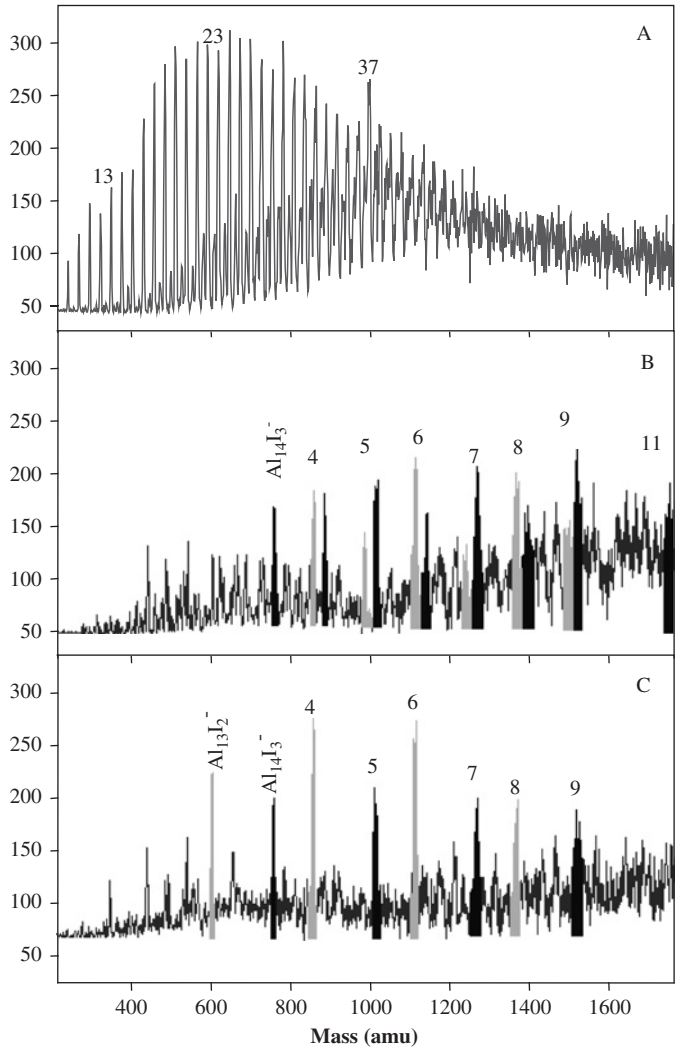

Figure 6: Mass spectra of (A) Al_n^- clusters, (B) Al with I_2, and (C) Al with I_2 and etched by O_2. Adapted from Ref. [29].

4.4. Multivalence character

Further evidence for the validity and broad applicability of the superatom concept comes from a recent observation that there are other cluster compositions which display multivalent character, showing, for example, that combinations of Al_7 with other atoms and molecules give rise to closed shells of 18, 20 and 22 electrons having concomitant variations in valences. Some examples include bonding of the anion to carbon, which gives rise to an 18-electron system. The prominent 7-mer cation is a 20-electron species, while the bare anion has 22-electron character, and bonding to two halogens gives rise to a 20-electron superatom as well [37].

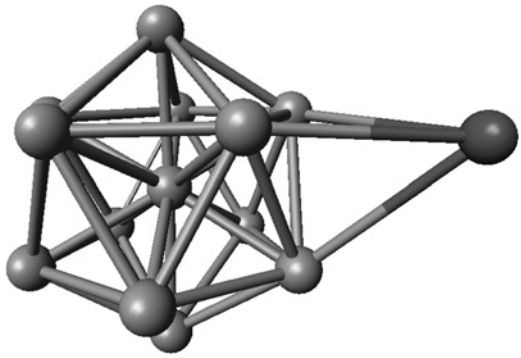

Figure 7: Ground-state geometry of $Al_{13}K$. Note that K occupies a hollow site on the Al_{13} icosahedron.

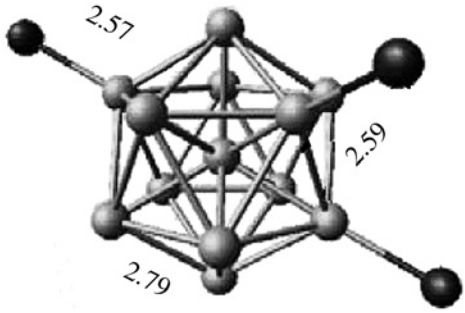

Figure 8: Ground-state structure of an $Al_{14}I_3^-$ cluster.

There seems no limit in the ability to derive a full table of element mimics employing the superatom concept.

5. INFLUENCING PROPERTIES: CREATION OF ACTIVE SITES AND EFFECTS ON REACTIVITY

As we further considered the implications of the cluster distributions shown in Fig. 6, another interesting fact became evident. The odd–even intensity variations seen for the polyiodides of the aluminium-13 and aluminium-14 species were evident in the nascent spectra and became enhanced as the oxygen etchants were progressively added. This suggested that alternate clusters were particularly unstable and, with respect to oxidation, more reactive. The reasons were revealed through theoretical calculations of iodized aluminium clusters equivalent to those in Fig. 6, showing that the clusters reactive towards oxygen in each group (odd numbers of iodine for the aluminium 13-mers and even numbers in the case of aluminium 14-mers) had particularly large electronic charge distributions suggesting the existence of active sites responsible for the enhanced reactivity, hence leading to the odd–even distributions found (see Fig. 9).

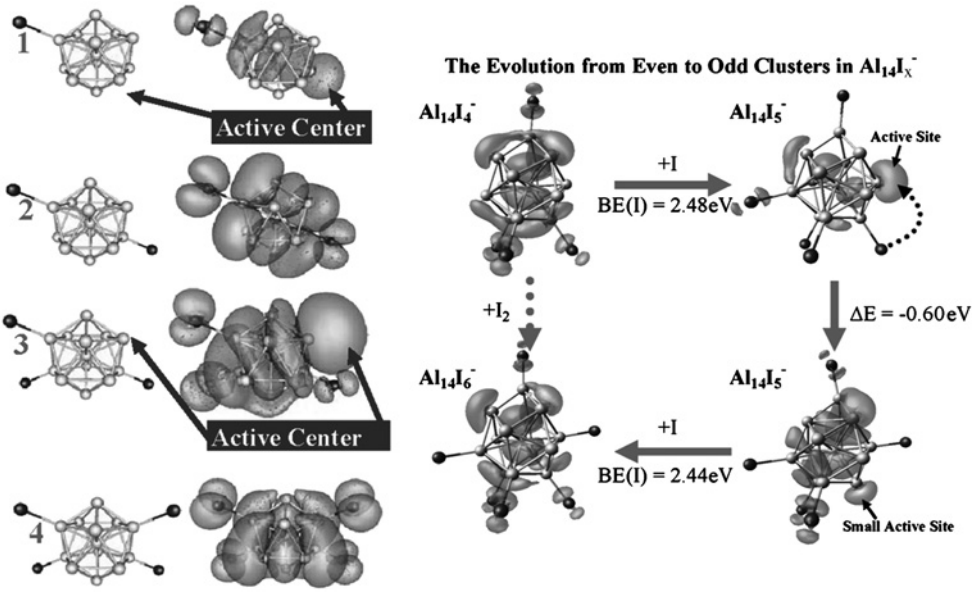

Figure 9: Active sites on iodized Al_{13} and Al_{14}. The left side shows the creation and occupation of active sites around an Al_{13} cluster. The panel on the right shows similar behaviour for Al_{14} clusters.

In order to obtain further evidence of this effect, experiments were conducted in a flow tube reactor to investigate the reactions of aluminium clusters with methyl iodide. The findings revealed that for nascent aluminium clusters, there was only a limited, very slow reaction unless very high concentrations of methyl iodide were employed. Significantly, as is evident from Fig. 10, upon iodizing aluminium clusters, reactions with CH_3I became much more facile.

One of the most promising prospects is that, through cluster assembly, one may design nanoscale materials with preselected properties. In this context, a very active subject of research comprises work in the area of catalysis where efforts have been made to find systems whose selectivity and efficiency can be tailored. Whether this can be accomplished via an appropriate assembly of superatoms has not been established, but some of these recent combined theoretical predictions and related experimental findings seem to be promising, especially from these results showing that reactive sites can be created on certain cluster species in the superatom framework.

6. ESTABLISHING THE CONCEPT OF EMPLOYING SUPERATOMS IN PRODUCING NANOSCALE MATERIALS FORMATION

6.1. Arsenic–potassium cluster materials as an example

The findings outlined in the foregoing sections show that there is great promise offered by the concept of using the assembly of superatoms to develop new nanoscale materials of tailored properties. But the question remained: will it be possible to realize the promise, in practice? Recently we achieved the first directed cluster assembly employing

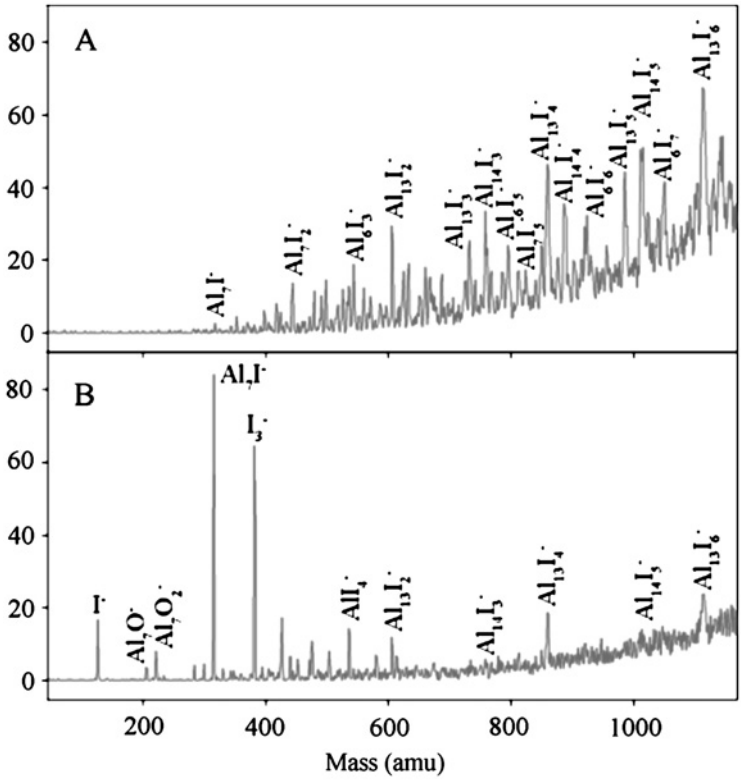

Figure 10: (A, B) Reactions of nascent and iodized aluminium clusters with CH_3I.

a combination of gas-phase cluster studies, first principles theory and synthetic chemical approaches. Theoretical studies led to the prediction that certain cluster species should be particularly abundant. The gas-phase cluster, As_7K_3 (see Fig. 11) was found to be one of the prominent species in the arsenic–potassium system revealed by ablation–photoionization experiments. The theory pointed to a possibility of forming a structure involving the assembly of six such units as shown in Fig. 12. Further theoretical considerations showed that it was the most viable building block in the identified series, subsequently established to be a composition representing one island of stability in varying compositions in the As–K system (see Fig. 13). As discussed in detail elsewhere [38], the system was assembled using synthetic chemistry methods, with the theoretically predicted structure being confirmed by X-ray diffraction.

We believe this to be the first example of the formation of cluster assembled materials following a protocol involving the search for clusters predicted theoretically to have the required electronic attributes to be stable in order to serve as building blocks, and to have appropriate islands of stability that they can be synthesized into extended materials. This new approach offers an exciting new avenue to pursue in the quest for ways to tailor the design of nanoscale materials of desired properties, from the ''bottom up''.

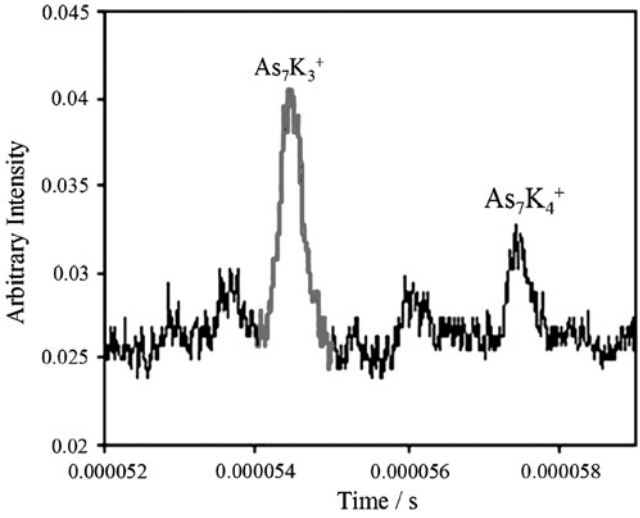

Figure 11: Mass spectrum of As_xK_y.

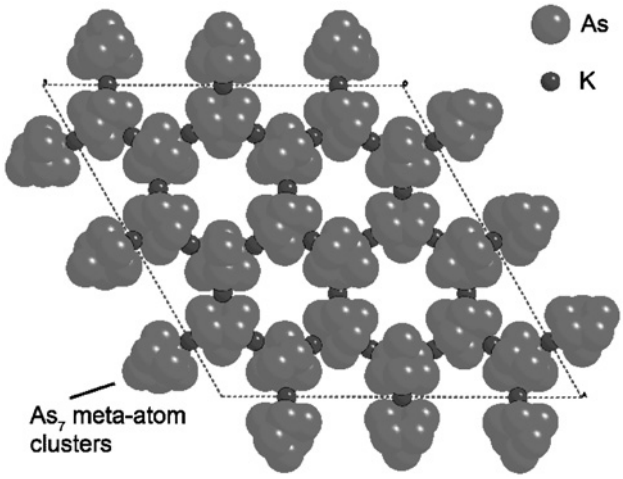

Figure 12: Schematic diagram showing a cluster assembled solid built of As_7 and K units.

7. IMPLICATIONS OF CLUSTER SCIENCE TO MATERIAL AND SURFACE PROPERTIES

7.1. Promising approaches

In the discussions above we have mainly focussed on aluminium and arsenic clusters. However, the concept can easily be extended to a wide class of systems including clusters of semiconducting elements. Note that the electronic levels in semiconducting clusters cannot be described within a simple framework of a confined free electron gas.

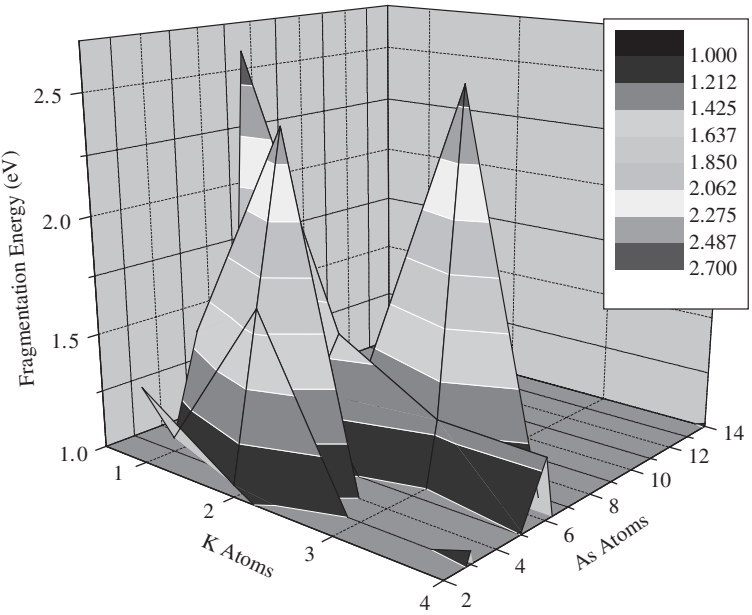

Figure 13: Fragmentation energy of K_xAs_y where $x = 1, 4$; $y = 1$–14.

The extension of the superatom concept, therefore, will involve the development of alternate classes of guiding principles to determine stable species and different electronic markers for their classification. To give an example, we have recently looked at metal semiconductor clusters [39, 40] composed of a silicon cage containing an endohedral metal atom. In Fig. 14 we show the geometrical structure of an $Si_{12}Cr$ cluster. Each Si atom in the cluster is bonded to three other surface Si atoms and the metal atom at the centre. We recently suggested that if the electronic manifold could be decomposed into Si–Si bonds and the Si–metal manifolds, the system may be looked upon as an outside silicon cage encapsulating a nearly free electron gas formed by selected silicon electrons and the valence electrons of the metal. The stability and electronic properties of such a system are governed by a dual principle where each Si bonded to a metal atom donates an electron to the valence pool. The clusters, where (1) Si atoms are fourfold coordinated and (2) the total number of valence electrons obtained by summing one electron from each Si site coordinated to the metal atom including the valence electrons of the metal attain 18 and 20, exhibit enhanced stability. Deviations from these numbers lead to changes in the electronic properties much in the same way as for the confined nearly free electron gas for metal clusters (Fig. 2).

Unlike bulk matter composed of atoms, the cluster materials formed through superatoms will be marked by the intra- and inter-cluster length scales leading to novel classes of materials with unique electronic, magnetic, chemical and optical characteristics. The electronic bands in ordinary solids are formed by the broadening of the electronic levels caused by the overlap of the atomic orbitals. In cluster solids, the

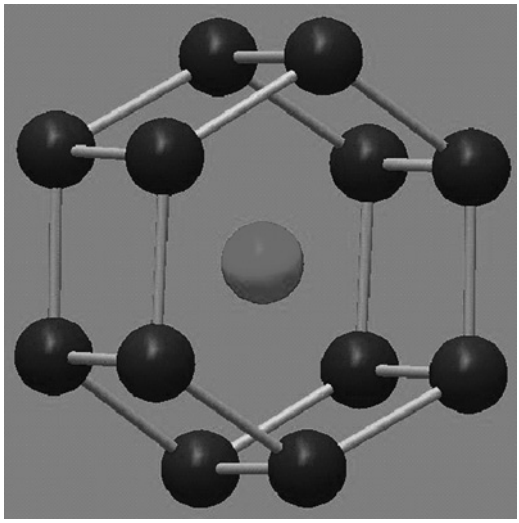

Figure 14: Ground-state geometry of an $Si_{12}Cr$ cluster. A Cr atom is at the centre sandwiched between hexagons of Si atoms. Adapted from Ref. [39].

electronic shells of individual superatoms will be broadened by their interaction. Since it is desirable to reduce interaction between superatoms to maintain identity, the cluster assemblies will be marked by narrow bands carrying the imprints of individual clusters. The vibrational frequencies in clusters are often higher than those in solids. The superatom assemblies will offer the possibility of low-frequency inter-cluster modes combined with high-frequency intra-cluster modes. The assemblies are also likely to offer new versatility in the area of electronic transport that is expected to be highly anisotropic.

There may also be magnetic effects that can find value in the materials area. Clusters of conventional magnetic materials exhibit higher magnetic moments per atom due to reduced coordination of the surface sites. In cluster assemblies it will be ideal to maintain selected magnetic features of individual clusters by tuning the coupling between individual clusters. The developments in the area of molecular magnets are already demonstrating the novelties that can be attained.

7.2. Potential pitfalls in extending concepts

While studies on small clusters can serve to bridge the gap between atoms and solids, it is important to reiterate the fact that clusters are not pieces of bulk matter with a large surface to volume ratio. A case in point is the recent report on the chlorination of the Al_{13}^- as a model reaction for the oxidation of bulk surfaces. These studies followed the earlier work by Bergeron et al. [27], who had shown that an Al_{13}^- would be susceptible to etching by Cl since AlCl molecule has a high binding energy of 5.30 eV that is larger than the 4.65 eV required to remove an Al atom from Al_{13}^-. In these studies, Burgert et al. [41] exposed hot Al_{13}^- clusters to chlorine under conditions when there are only few collisions, thus creating conditions under which the clusters cannot become

thermalized. The researchers found that the cluster progressively lost Al atoms, eventually resulting in the fragment Al_7^-. The authors argued that since the topology of an Al_{13}^- cluster with one central Al atom surrounded by 12 outer Al atoms is similar to the close packing of Al atoms in the bulk Al, studies on this cluster might exemplify the etching of bulk aluminium surfaces. It is important to underscore that such reasoning is flawed since the electronic structure of Al_{13}^- is marked by an electronic shell closure leading to a large HOMO–LUMO gap while bulk Al is a metal. Indeed, as our extensive studies have shown, Al_{13}^- does not oxidize in the presence of oxygen even though many other aluminium clusters do. Moreover, bulk aluminium does oxidize in the presence of oxygen, a reaction that is only impeded in the case of the bulk due to the formation of an oxide coating at the surface. Clearly, Al_{13}^- is not a model of a surface!

On a more fundamental note, such reasonings ignore the fundamental fact that clusters constitute a new phase of matter with novel behaviours distinct from the individual atom or bulk. For example, clusters of non-magnetic solids can be magnetic [42, 43], the reactivity can change by orders of magnitude by just the addition of a single atom, the optical properties change discontinuously with size and so on. This is important since the entire development of superatoms and their application rely on the novelty of behaviours and properties emerging in reduced sizes. The prospects of developing new materials through the assembly of superatoms is a highly promising avenue to explore, and we can expect many new developments in this field in the future.

ACKNOWLEDGMENTS

We gratefully acknowledge funding by the United States Air Force Office of Scientific Research, Grant #FA9550-04-1-0066, the U.S. Department of the Army through a MURI Grant #W911NF-06-1-0280, the Department of Energy, Grant #DE-DE-FG02-02ER46009 and the Department of Energy, Grant #DE-FG02-92ER14258.

Particular thanks go to various people in our groups: Denis E. Bergeron, recent Ph.D., Kevin M. Davis, Mark Merritt, Sam J. Peppernick, Patrick Roach. SNK gratefully acknowledges funding by the United States Air Force Office of Scientific Research, Grant #FA9550-05-1-0186 and is grateful to VCU for a study/research leave.

REFERENCES

[1] Khanna S.N., Castleman A.W., Jr. (eds), Quantum Phenomena in Clusters and Nanostructures, Springer, New York, 2003.
[2] Anderson H.H. (ed.), Small Particles and Inorganic Clusters, Springer, New York, 1997.
[3] Sattler K. (ed.), Cluster Assembled Materials, Trans Tech Publications, Switzerland, 1996.
[4] Jena P., Khanna S.N., Rao B.K. (eds), Clusters and Nano-Assemblies, World Scientific, New Jersey, 2003.
[5] Xie R.-H., Bryant G.W., Zhao J., Kar T., Smith V.H., Phys. Rev. B 71 (2005) 125422.
[6] Serrano-Guisan S., Domenicantonio G.D., Abid M., Abid J.-P., Hillenkamp M., Gravier L., Ansermet J.-P., Felix C., Nat. Mater. 5 (2006) 730.
[7] Cui L.-F., Huang X., Wang L.-M., Zubarev D.Y., Boldyrev A.I., Li J., Wang L.-S., J. Am. Chem. Soc. 128 (2006) 8390.
[8] Kesanli B., Fettinger J., Eichhorn B., J. Am. Chem. Soc. 125 (2003) 7367.
[9] Khanna S.N., Jena P., Phys. Rev. B 51 (1995) 13705.

[10] Cui L.-F., Huang X., Wang L.-M., Zubarev D.Y., Boldyrev A.I., Li J., Wang L.-S., J. Am. Chem. Soc. 128 (2006) 8390.
[11] Morisato T., Jones N.O., Khanna S.N., Kawazoe Y., Comp. Mat. Sci. 35 (2006) 366.
[12] Kovalenko N.P., Krasny Y.P., Krey U. (eds), Physics of Amorphous Metals, John Wiley Publications, New York, 2001.
[13] Haddon R.C., Hebard A.F., Rosseinsky M.J., Murphy D.W., Duclos S.J., Lyons K.B., Miller B., Rosamilia J.M., Fleming R.M., Kortan A.R., Glarum S.H., Makhija A.V., Muller A.J., Eick R.H., Zahurak S.M., Tycko R., Dabbagh G., Thiel F.A., Nature 350 (1991) 320.
[14] Guo B.C., Kerns K.P., Castleman A.W., Jr., Science 255 (1992) 1411.
[15] Davis K.M., Peppernick S.J., Castleman A.W., Jr., J. Chem. Phys. 124 (2006) 164304.
[16] Khanna S.N., Jena P., Phys. Rev. Lett. 69 (1992) 1664; Shinohara H., Rep. Prog. Phys. 63 (2000) 843.
[17] Bergeron D.E., Castleman A.W., Jr., Morisato T., Khanna S.N., Science 304 (2004) 84.
[18] Bergeron D.E., Castleman A.W., Jr., Jones N.O., Khanna S.N., Nano Lett. 4 (2004) 261.
[19] Knight W.D., Clememger K., de Heer W.A., Saunders W.A., Chou M.Y., Cohen M.L., Phys. Rev. Lett. 52 (1984) 2141.
[20] de Heer W.A., Knight W.D., Chou M.Y., Cohen M.L., Solid State Phys. 40 (1987) 93.
[21] Nonose S., Tanaka H., Mizuno T., Kim N.J., Someda K., Kondow T., J. Chem. Phys. 105 (1996) 9167.
[22] Brechignac C., Cahuzac Ph., Carlier F., de Frutos M., Barnett R.N., Landman U., Phys. Rev. Lett. 72 (1994) 1636.
[23] Ekardt W., Phys. Rev. B 29 (1984) 1558.
[24] Alonso J.A., Balbas L.C., Top. Curr. Chem. 182 (1996) 119.
[25] Martin T.P., Bergmann T., Gohlich H., Lange T., Chem. Phys. Lett. 172 (1990) 209.
[26] Leuchtner R.E., Harms A.C., Castleman A.W., Jr., J. Chem. Phys. 91 (1989) 2753.
[27] Bergeron D.E., Castleman A.W., Jr., Jones N.O., Khanna S.N., J. Chem. Phys. 121 (2004) 10456.
[28] Bergeron D.E., Ph.D. Thesis, The Pennsylvania State University, August 2004.
[29] Bergeron D.E., Roach P.J., Castleman A.W., Jr., Jones N.O., Khanna S.N., Science 307 (2005) 231.
[30] Bergeron D.E., Roach P.J., Castleman A.W., Jr., Jones N.O., Reveles J.U., Khanna S.N., J. Am. Chem. Soc. 127 (2005) 16048.
[31] Han Y.-K., Jung J., J. Chem. Phys. 121 (2004) 8500.
[32] Han Y.-K., Jung J., J. Chem. Phys. 123 (2005) 101102.
[33] Jones N.O., Khanna S.N., Bergeron D.E., Roach P.J., Castleman A.W., Jr., J. Chem. Phys. 124 (2006) 154311.
[34] Cha C.-Y., Ganteför G., Eberhardt W., J. Chem. Phys. 100 (1994) 995.
[35] Li X., Wang L.-S., Phys. Rev. B 65 (2000) 153404.
[36] Zheng W.-J., Thomas O.C., Lippa T.P., Xu S.-J., Bowen K.H., J. Chem. Phys. 124 (2006) 144304.
[37] Reveles J.U., Khanna S.N., Roach P.J., Castleman A.W., Jr., Proc. Natl. Acad. Sci. USA 103 (2006) 18405.
[38] Castleman A.W., Jr., Khanna S.N., Sen A., Reber A.C., Davis K.M., Peppernick S.J., Ugrinov A., Merritt M.D., From Designer Clusters to Synthetic Crystalline Nano-Assemblies (in preparation).
[39] Khanna S.N., Rao B.K., Jena P., Phys. Rev. Lett. 89 (2002) 016803.
[40] Reveles J.U., Khanna S.N., Phys. Rev. B 74 (2006) 035435.
[41] Burgert R., Schnokel H., Olzmann M., Bowen K.H., Angew. Chem. Int. Ed. 45 (2006) 1476.
[42] Reddy B.V., Khanna S.N., Dunlap B.I., Phys. Rev. Lett. 70 (1993) 3323.
[43] Cox A.J., Louderback J.G., Bloomfield L.A., Phys. Rev. Lett. 71 (1993) 923.

This page intentionally left blank

Chapter 11

Magnetic properties of 2D islands on single-crystal metal surfaces

H. Brune* **and S. Rusponi**

Institut de Physique des Nanostructures, Ecole Polytechnique Fédérale de Lausanne (EPFL), CH-1015 Lausanne, Switzerland

1. INTRODUCTION

Exploring the ultimate density limits of magnetic information storage, whether on computer hard disks or in MRAMs (magnetic random access memories), requires elaborate tuning of the preferred (easy) magnetization axis, of the magnetic anisotropy energy (MAE), and of the magnetic moment in the units used to store a bit. These units are single-domain particles (with diameter $d < 20$ nm) where the magnetic moments of all atoms are ferromagnetically aligned [1] to form the overall magnetic moment of the particle **M**, also called the macrospin. The preferred orientations of **M**, and the anisotropy energy barriers $\boldsymbol{K}$ separating them, are given by the delicate balance between several competing energies. These are the magnetocrystalline bulk anisotropy, its surface and step counterparts, and the shape anisotropy or demagnetizing energy resulting from the interaction of **M** with its own dipolar stray field.

The resulting overall anisotropy energy defines the stability of the magnetization direction against thermal excitation, and therefore the minimum particle size for which non-volatile information storage may be achieved (at 300 K this requires $K = 1.2$ eV). However, unraveling the origin of anisotropy is far from trivial due to the competition between these energies [2]. A further key parameter is the modulus of **M**: M defining not only the dipolar stray field used to read and write, but also mediating interactions between adjacent bits. These interactions are minimized for out-of-plane magnetization and therefore uniaxial out-of-plane systems are best suited to explore the ultimate density limit of magnetic recording [3, 4].

Current studies attempting to identify the origin of magnetic anisotropy, and the density limit with which one may ultimately place magnetic particles without appreciable interactions, mainly deal with two model systems. These are colloids or three-dimensional (3D) nanoparticles, and 2D nanostructures created by molecular-beam epitaxy at single-crystal surfaces. For colloidal particles, remarkable progress has been

The Chemical Physics of Solid Surfaces, Volume 12
ISSN: 1571-0785
DOI: 10.1016/S1571-0785(07)12011-3

*Corresponding author.
E-mail: harald.brune@epfl.ch

achieved in monodispersity [5], their self-assembly into 2D superlattices [6, 7], and in the accomplished anisotropy energies per constituent atom [8, 9].

Despite their promising properties for applications, 3D nanoparticles present several difficulties. Although the magnetic properties of a single particle can be addressed [10], it is almost impossible to study the morphology of the particle in conjunction with its magnetism. The particles frequently have a few atomic layers of oxide at their surface, which are not ferromagnetic [11]. This causes uncertainties in the morphology of the ferromagnetically ordered particle core. Owing to these difficulties, no general view on the origin of anisotropy in nanoparticles has yet evolved. The anisotropy has either been attributed mainly to the volume [12] or surface [10] contribution of the crystalline lattice, or to shape anisotropy caused by eccentricities of the magnetic core [11]. A second difficulty is the out-of-plane alignment of the easy magnetization axes in colloidal monolayers. An individual particle can have several easy magnetization axes. In addition, the deposited particles are randomly oriented and therefore their axes point into random directions [13]. However, every in-plane component of the magnetization leads to undesired dipolar interactions. Attempts of applying out-of-plane magnetic fields during deposition piles up the particles by dipolar interactions and thereby inhibits formation of ordered monolayers [8]. A third difficulty is coalescence between adjacent particles upon annealing. This equally leads to high blocking temperatures and is often difficult to discern from the desired coercivity increase in the individual particles by change of their crystalline structure [12].

2D nanostructures at surfaces are optimally suited to address the origin of anisotropy, and also to explore density limits of non-interacting magnetic units. The anisotropy imposed by the substrate makes them uniaxial, for example oriented out-of-plane. The size and spatial uniformity achieved by self-assembly techniques [14–16] are comparable to those of colloids. Under ultrahigh vacuum conditions, there is no oxide shell and all constituent atoms are ferromagnetically ordered. Thus, the particle morphology contributing to the magnetic signal is accessible at the atomic scale and can be related to the magnetic properties measured in situ with integrating techniques.

Inspired by these advantages, and by the technological relevance of the questions raised above, many fundamental studies have been carried out on the magnetic properties of 2D islands on single-crystal metal surfaces. These studies use epitaxial growth and are therefore complementary to studies depositing magnetic clusters from the gas phase [17]. For general overviews of magnetic nanostructures and their technical applications, we refer to Refs. [1, 18–20]. We focus here in particular on experiments which try to establish an atomic scale understanding of the contribution of the individual constituent atoms to the magnetic properties of the overall island. One of the key experimental techniques is scanning tunneling microscopy (STM), either used to characterize the morphology of the island ensemble or to infer magnetic information on individual islands using spin-polarized (SP) tips. Magnetic properties such as spin and orbital moments, as well as anisotropy energies, are inferred by established spatially integrating techniques, such as magneto-optical Kerr effect (MOKE) and X-ray magnetic circular dichroism (XMCD).

We begin our chapter with a discussion of the temperature-induced transition from the blocked to the superparamagnetic state, followed by disappearance of magnetic order once the islands Curie temperature is reached. The mechanism of thermally activated magnetization reversal is still a non-trivial issue due to the difficulty to

characterize the transition state of the island either by experiment or theory. We discuss examples of coherent rotation and domain-wall nucleation, as well as curling. Section 3 takes Co islands on Pt(1 1 1) as an example to show the different contribution of step vs. surface atoms to the magnetic anisotropy. This system also demonstrates the non-triviality of magnetization reversal as it shows a transition from coherent rotation for small and compact islands to domain-wall nucleation upon a critical diameter which is for ramified islands in the range of 150 Å. We discuss self-assembly of magnetic island superlattices in Section 4. In the same section, we discuss the magnetic properties of superlattices. The first example are Co double-layer islands on an Au(7 8 8) surface which presently is the highest density of uniaxial out-of-plane particles with no dipolar interactions and most homogeneous magnetic moments and anisotropies. However, its blocking temperature is with 50 K too small to become technically relevant. The second example is Co pillars realized by sequential deposition of Co and Au onto Au(1 1 1). This system can be grown such as to be blocked at 300 K, however, it suffers from dipolar interactions. The island shape favors in-plane magnetization, nevertheless the islands are out-of-plane magnetized due to the magnetocrystalline anisotropy imposed by the substrate. The substrate role is addressed in Section 5 for individual magnetic adatoms on alkali surfaces showing different degrees of hybridization and revealing the ground state electron configuration. The evolution of orbital moment and anisotropy energy as function of lateral coordination is addressed for Co adatoms and small islands on Pt(1 1 1). Section 6 is devoted to spin-polarized STM measurements reporting spin-polarized surface states on Gd islands on W(1 1 0), unusually high tunnel magneto-resistance values for Co/Pt(1 1 1)–Cr/W tip junctions, and contrast inversion for Co islands on Cu(1 1 1) and Cr-coated W tips. Finally, we summarize and give future perspectives in the conclusions.

2. MAGNETIZATION VS. TEMPERATURE

The temperature evolution of the magnetic moment $M(T)$ of a nanoparticle shows three distinct regimes whose boundaries are the Curie temperature T_C and the blocking temperature T_b. These temperatures are the macroscopic signature of two atomic interaction energies. The first is the exchange interaction J, which leads to a magnetic moment of the nanoparticle for ferromagnetic alignment of the spins of adjacent atoms. The second is the spin–orbit interaction inducing coupling of the electron spins to the crystal field. This gives rise to magnetocrystalline anisotropy leading to the everyday experience that magnets are magnetized along preferential directions (easy axes). Besides magnetocrystalline anisotropy, there are several other sources of anisotropy, for instance magnetostriction, shape, and surface anisotropy. The resulting overall anisotropy is referred to as MAE K.

Briefly, the magnitude of $M(T)$ is determined by the exchange energy and the atomic moments, while the direction of $M(T)$ is determined by the MAE. Typical orders of magnitude are 1–20 meV/atom for J and 0.1–1 meV/atom for K. With increasing temperature, T_b marks the boundary between the blocking region, where the MAE keeps the magnetization direction parallel to the easy axis, and the superparamagnetic region, in which the nanoparticle can continually reverse its magnetization direction due to thermal excitation. T_C marks the boundary between the superparamagnetic

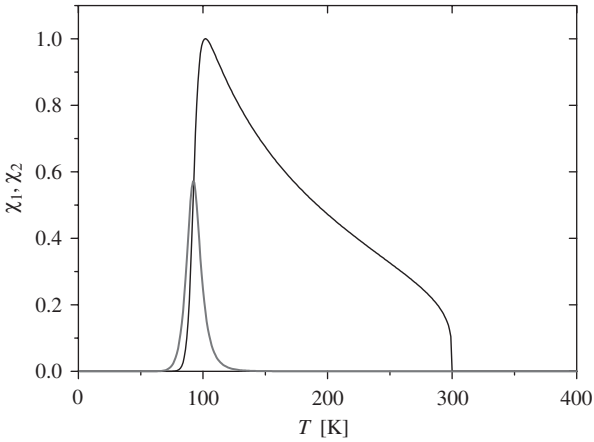

Figure 1: Temperature dependence of the zero-field susceptibility of a single particle. The black and gray curve represents the real and imaginary part of the susceptibility, respectively.

region and the paramagnetic region in which the thermal excitation breaks the parallel alignment of spins inside the particles.

This evolution is displayed by the temperature diagram of the zero-field susceptibility for a single-domain nanoparticle having a single easy magnetization axis (Fig. 1). Let us consider the nanoparticle in the blocked state with its magnetic moment aligned to the easy axis. In the absence of external magnetic field ($H = 0$), the spin *up* and spin *down* states are separated by an energy barrier $E(K)$ which is a function of the MAE K. Independently, on the details of the landscape shape of this energy barrier, the thermally activated magnetization reversal rate follows the Arrhenius law $\nu = \nu_0 \exp(-E/k_B T)$. The relaxation time τ is given by $\tau = \tau_0 \exp(E/k_B T)$, with $\tau_0 = \nu^{-1}$. The barrier is readily overcome if $T > T_b = E/k_B \ln(1/\omega\tau_0)$, where ω is related to the observation time $t = 2\pi/\omega$. In the case of Fig. 1, ω is the sweep frequency of the external magnetic field used to measure the susceptibility. T_b is the blocking temperature, defined by the temperature where the ensemble reaches half of its thermodynamic equilibrium susceptibility χ_{eq}. For $T > T_b$, the particles are superparamagnetic, and $\chi(T) = \chi_{eq}(T)$. For $T < T_b$, the particles are blocked in a fixed magnetization state (up or down), and hence $\chi(T) = 0$. For $T \approx T_b$, the system is determined by the kinetics of barrier crossing which depends on the actual shape of the energy barrier. Up to now, the overall magnetic moment $M(T)$ of the nanoparticle was assumed to be temperature independent which is equivalent to assuming an infinite Curie temperature. A more realistic description is obtained when introducing the temperature dependence of the magnetic moment in order to take into account that at $T = T_C$ the thermal energy overcomes the exchange energy causing the breaking of the ferromagnetic order in the island. For a uniaxial nanoparticle, a natural choice is given by the exact expression for the temperature dependence of the magnetization of a Ising lattice. For example, in the case of a plane triangular Ising lattice, it reads $M(T) = [(w(T)+1)^3/(w(T)-1)^3]^{1/8}[(w(T)-3)/(w(T)+3)]^{1/8}$, where $w(T) = \exp(4J/T)$ and $T_C = 4J/\ln 3$ [21]. This results in an abrupt drop of the real part of the susceptibility ($\chi_1(T)$) to zero at $T = T_C$ (Fig. 1).

It is instructive to move a step further in the understanding of the magnetization reversal problem. Three mechanisms are possible for the magnetization switching: coherent rotation, domain-wall nucleation with subsequent wall propagation, and curling. The thermal switching by coherent rotation was theoretically investigated by Neel [23] and Brown [24]. They assumed uniaxial MAE and single-domain magnetization, i.e., at any time during the reversal process the spin and orbital moments of the constituent atoms are ferromagnetically aligned to form a single magnetization vector, the nanoparticle macrospin $\boldsymbol{M}$. The energy diagram of this macrospin in an external magnetic field $\boldsymbol{H}$ is described by $E = K \sin^2 \theta - \boldsymbol{MH}$ with two minima, corresponding to the *up* and *down* orientation of $\boldsymbol{M}$, separated by the cluster's MAE K at zero field (θ is the angle between surface normal and $\boldsymbol{M}$). The anisotropy energy at zero field is the energy $K = E(90^\circ)$, associated with the in-plane configuration forming the transition state that has to be overcome during magnetization reversal. The crossing rate of the MAE barrier is described, in the limit of small external field, by the Arrhenius expression $v = v_0 \exp((-K + HM)/k_B T)$ with $v_0 \sim 10^{10}\,\mathrm{s}^{-1}$ [22]. The temperature dependence of the switching field can also be calculated and it was experimentally measured by Wernsdorfer et al. [22] for individual ellipsoidal cobalt nanoparticles having a diameter of 25 ± 5 nm (Fig. 2).

The thermally activated magnetization reversal by domain-wall nucleation and displacement was theoretically investigated by Braun for the 1D problem, or equivalently for elongated particles (particles with an in-plane aspect ratio larger than 1:10) [26–28]. Braun demonstrated that the excitation (or nucleus) with the lowest energy is an untwisted domain-wall pair and once this nucleus has formed the magnetization can reverse without further expense in energy. The nucleation barrier is proportional to the particle vertical cross-section S_z and in the limit of small field ($H < 2K/M$) reads $E = 8S_z\sqrt{JK}$, where K includes contributions of crystalline and shape anisotropies. One defines a critical length L_{cr} by comparing the previous energy with the energy required for the coherent magnetization rotation, which, for a uniform MAE

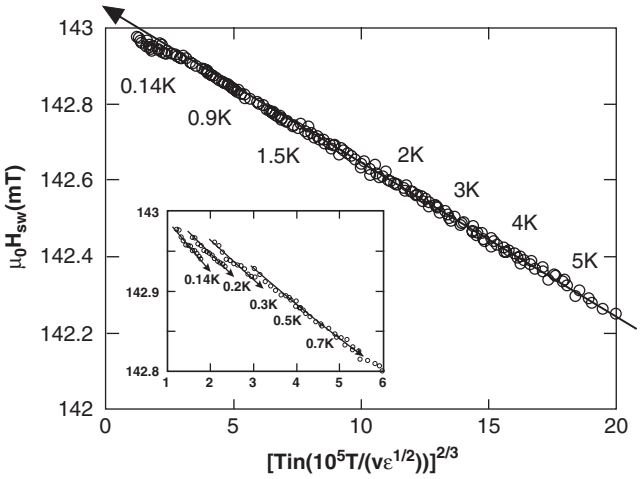

Figure 2: Scaling plot of the mean switching field H_{sw} for field sweeping rates between 0.01 and 120 mT/s and temperatures between 0.14 and 5.0 K. After Ref. [22].

distribution, reads $E = S_z L_{cr} K$, giving $L_{cr} = 8\sqrt{J/K}$. Actually, for very elongated particles $L \gg L_{cr}$, the particle ends behave independently and at finite temperature, due to the thermal fluctuations, magnetization reversal by nucleation of a reversed domain at one particle end becomes energetically favorable [29–31]. In this case, the nucleation barrier $E = 4S_z\sqrt{JK}$ is half the value calculated for the untwisted domain-wall pair case and the critical length reads $L_{cr} = 4\sqrt{J/K}$ and $L_{cr} \approx 5\sqrt{J/\mu_0 M^2}$ for the two limiting cases of $\mu_0 M^2 \ll K$ [29] and $\mu_0 M^2 \gg K$ [32], respectively.

Experimental evidence of a shape-dependent switching behavior has been reported for one monolayer thick perpendicularly magnetized Fe islands on Mo(1 1 0). Spin polarized-STM measurements (SP-STM) recording thermal switching rates of individual islands containing some hundreds atoms suggested that elongated particles (with a maximum aspect ratio of 1:4) switch faster than equally sized compact islands [25]. The authors report a critical length of $L_{cr} = 9.1 \pm 0.3$ nm (Fig. 3).

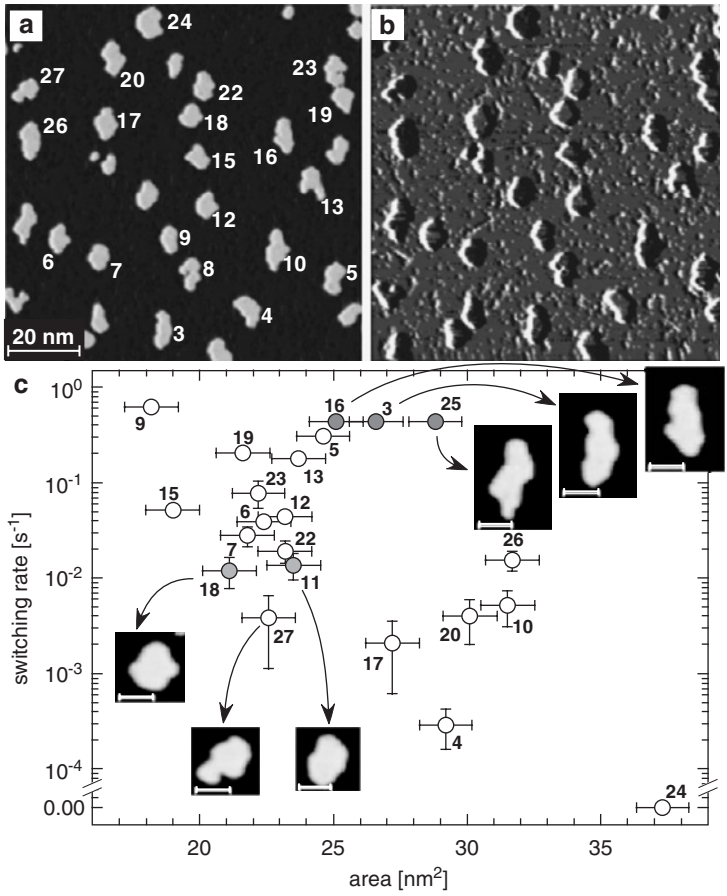

Figure 3: (a) Topography and (b) magnetic dI/dV signal of Fe islands on Mo(1 1 0). (c) Plot of the switching rate vs. the area of individual islands. The scatter of the switching rate points to a shape-dependent crossover from coherent rotation of compact Fe islands shorter than $L_{cr} \approx 9$ nm toward nucleation and expansion of reversed domains in elongated islands. (Insets) Topography of selected Fe islands (scale bar: 5 nm) [25].

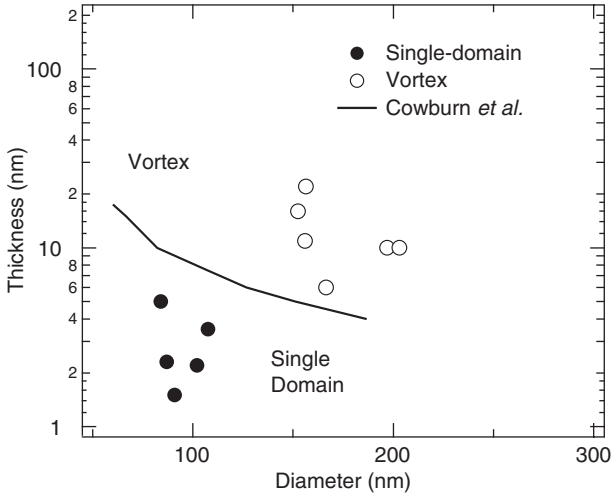

Figure 4: A phase diagram of magnetic states for different diameters and thicknesses of the Fe islands on W(0 0 1). Solid and open circles show the single domain and vortex state, respectively. The solid line is the dividing line following calculations by Cowburn et al. [33]. After Ref. [34].

Finally, the third reversal mode consists in the incoherent reversal by curling or vortex formation. This mode is in general unlikely in truly 2D nanostructures since the critical length for the turnover from coherent rotation to curling in an oblate spheroid quickly increases as the spheroid thickness is reduced [35]. For example, using bulk values for J and M, Skomski [36] evaluated a critical length of about 400 nm for a perpendicularly magnetized one monolayer thick Co film (one monolayer, ML, is defined as a coverage corresponding to the density of substrate surface atoms). Experimentally, SP-STM measurements of in-plane magnetized Fe islands on W(0 0 1) with a thickness of a few nanometers demonstrated that the single-domain state is stable for lateral sizes up to 200 nm [34] (Fig. 4).

3. Co ISLANDS ON Pt(1 1 1): MAE AND REVERSAL MECHANISM

In a 3D magnetic crystal, the magnetic anisotropy and the preferred directions of magnetization are related to the crystal axes by the quantum-mechanical spin–orbit interaction. As the dimension of a magnetic sample is reduced, for example in ultrathin (a few ML thick) films, e.g., used in the latest hard-disk read heads, the shape anisotropy caused by the magnetic stray fields outside the sample gains of importance. This anisotropy favors alignment of the magnetization along the film plane. Other energies that have their source in the electronic structure can be even more important. The reduced number of nearest neighbors of atoms at the surface of a thin film or at the edge of a nanostructure leads to more atomic-like electronic properties. 2D nanostructures created and analyzed under well-defined conditions (UHV, STM, and in situ magnetic characterization) represent an ideal prototype system to investigate the role of the different anisotropy energies, the reversal mechanism, and the contributions made by the differently coordinated constituent atoms.

3.1. Transition from blocking to superparamagnetic

With atomic beam epitaxy, several island morphologies can be produced by controlling the growth parameters [37]. The ramified islands in Fig. 5a are formed upon deposition at 130 K due to limited mobility of atoms along the island edge. Annealing of these islands to 300 K activates edge mobility yielding compact islands without much coarsening (see Fig. 5b). Further annealing to 340 K converts the monolayer-high islands of Fig. 5b into double-layer islands represented in Fig. 5c. This mutation is caused by the surface and interface free energies favoring atoms climbing up onto the second layer and thereby reducing, with respect to Pt(1 1 1)/vacuum, the more costly Co/vacuum and Co/Pt interfaces by a factor of 2.

The island size and perimeter distributions were obtained from a statistical ensemble of about 1000 islands imaged by STM for each sample. The size distributions are normalized to yield unit area under the curves. As expected, the size distribution of the ramified islands is very well reproduced by the theoretical curve obtained by kinetic Monte-Carlo simulations and by nucleation theory taking into account the random island spacing [38] (asymmetric bell curve, non-zero when $s \to 0$). The mean sizes for the three samples are: $S_r = 1000 \pm 600$, $S_c = 1200 \pm 700$, and $S_b = 5000 \pm 1500$ atoms. The nonlinear relationship between the island area and perimeter length (see insets) gives each of the two distributions its characteristic shape, thus enabling to disentangle the different role played by inner and edge atoms.

The magnetic behavior was characterized by measuring the temperature dependence of the zero-field susceptibility with MOKE. Independent of island shapes and sizes, a MOKE signal was observed only in polar configuration demonstrating an out-of-plane magnetization easy axis. The $\chi(T)$ curves were measured as the field derivative of the Kerr intensity with the external field sweeping around zero with frequency $\omega = 0.1$–$100\ s^{-1}$ and an amplitude of 100 Oe. This amplitude is motivated by a trade-off between signal-to-noise and the linearity of the superparamagnetic $M(H)$ curves. In our case, they are linear up to much higher fields (linear response theory gives the upper field limit as $MH \ll k_B T$). All the $\chi_1(T)$ curves present the same characteristic behavior shown in Fig. 1.

We first consider fits of the experimental data assuming magnetization reversal by coherent rotation. MOKE is a spatially integrating method (the laser spot size was about $1\ mm^2$) reporting the properties of the island ensemble. Accordingly, we sum over all islands, taking their size and perimeter distribution into account. The $\chi(T)$ function for a given island is obtained as follows. The kinetics of barrier crossing and therefore the residence time in the spin up and spin down states is described by master equations. In the limit of small fields one can linearize these equations and multiply with the equilibrium susceptibility to obtain the following analytical expression for the in-phase (real) and out-of-phase (imaginary) part of the zero-field susceptibility ($\chi = \chi_1 + i\chi_2$):

$$\chi_1(\omega, T) = \chi_{eq}(T) \frac{1}{1 + \omega^2 \tau^2} \tag{1}$$

$$\chi_2(\omega, T) = \chi_{eq}(T) \frac{\omega \tau}{1 + \omega^2 \tau^2} \tag{2}$$

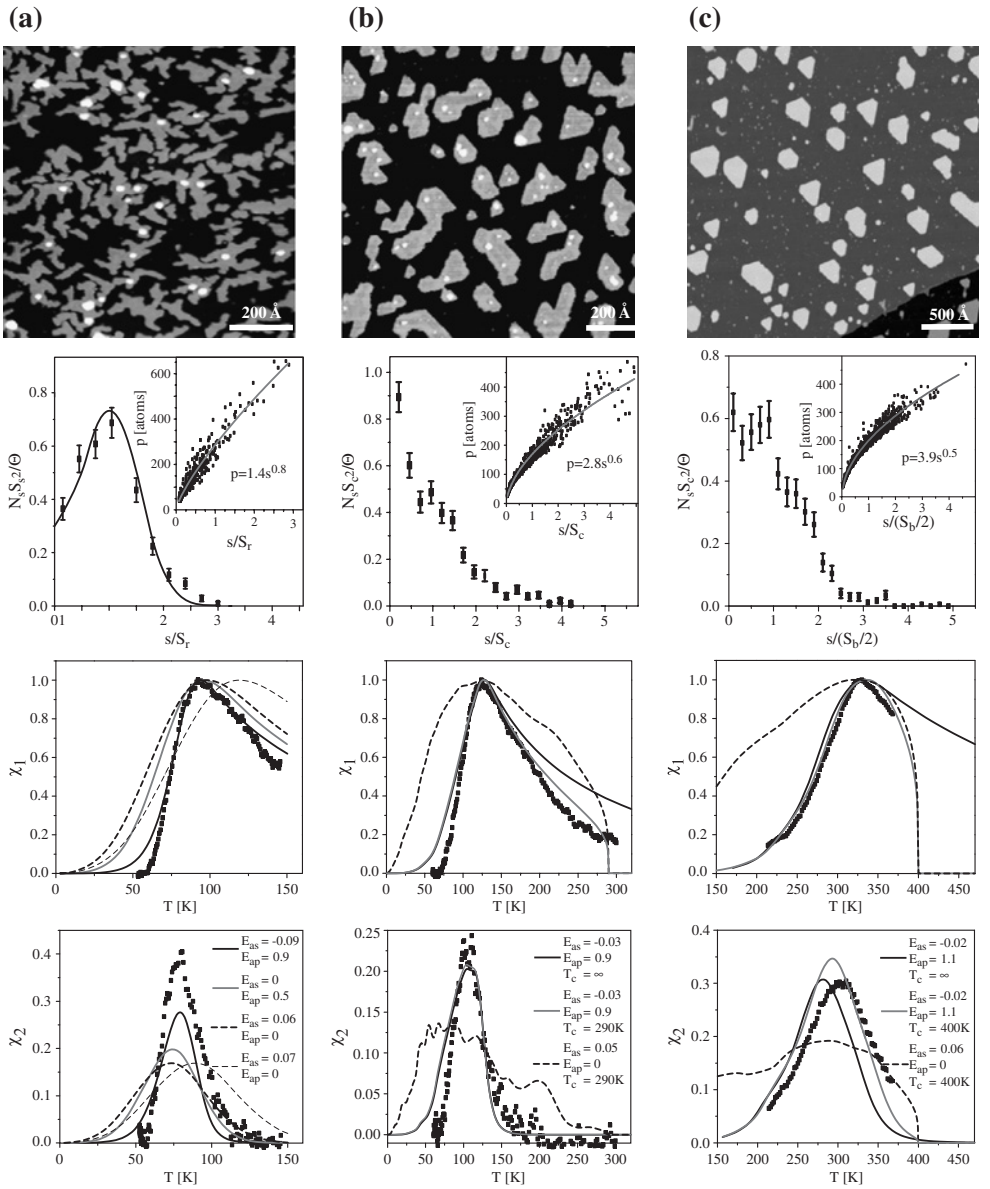

Figure 5: STM images, size s and perimeter p distributions, real ($\chi_1(T)$) and imaginary ($\chi_2(T)$) susceptibility curves for three different island shapes: ramified monolayer (column a), compact monolayer (column b), and bilayer (column c). S is the average island size, and N_s the density of islands of size s, the Co coverage is the same for the three morphologies ($\Theta = 0.4$ ML). In the size and perimeter distribution figures, the black and gray curves represent the best fits according to the text. In the susceptibility graphs, the various curves represent the fits according to the values for the MAE of inner (E^{as}) and edge atoms (E^{ap}) shown in the legends. The MAE values are given in meV/atom.

where $\tau = 1/\nu_0 \exp(K/k_B T)$ [39]. χ_{eq} is the zero-field susceptibility at thermodynamic equilibrium given by [40, 41]

$$\chi_{eq}(T) = M^2 \left[\frac{\exp(K/k_B T)}{\sqrt{\pi K k_B T}\,\mathrm{Erfi}(\sqrt{K/k_B T})} - \frac{1}{2K} \right] \tag{3}$$

This equation takes into account the fluctuations of the magnetization around the energy minima. The blocking temperature T_b is defined by $\omega\tau(T_b) = 1$. Its expression and the transition width are given by $T_b = K/k_B \ln(1/\omega\tau_0)$ and $\Delta T_b = k_B T_b^2/\ K \approx T_b/30$, respectively.

For $T < T_b$, the particle is blocked in a fixed magnetization state (*up* or *down*), hence $\chi(T) = 0$ (blocked region). For $T \approx T_b$, the crossing over the MAE barrier is thermally activated and the magnetic state of the particle is determined by the kinetics of barrier crossing (activation region). This is reflected in a peak both in the $\chi_1(T)$ and in the $\chi_2(T)$ curves. Finally, for $T > T_b$, the particle is superparamagnetic, and $\chi(T) = \chi_{eq} \propto 1/T$ (superparamagnetic region). For comparison, Fig. 6 shows the infinite anisotropy limit, leading to a two-state system (Ising model, see dashed short curves in main figure and inset), and the vanishing anisotropy limit, characterized by an occupation of all orientations of M (Langevin model, long dashed curves). With increasing temperature, χ_{eq} goes from one limit to the other and therefore its decay is slightly steeper than the $1/T$ behavior characterizing the two limiting cases. It is seen that the Ising model is a good approximation for $\chi(T)$ if $T_b < T < 2T_b$, whereas the Langevin model may only be used for very high temperatures.

The origin of M and K is revealed by testing different assumptions to compute these values for a given island with size s and perimeter p. In order to keep the fitting to a single parameter, we assume that M is simply given by the number of constituent atoms times their moment m, $M = sm$. This assumption is justified because m varies by much less than 20% for the size range of interest [42]. m was determined by measuring the magnetization curve of compact islands at $T > T_b$. Figure 7 shows the typical superparamagnetic reversible S-shaped curve. The magnetization reaches 0.6 of its saturation value at the experimentally available field of ± 500 Oe. With the Ising model, which is a good approximation just above T_b, we obtain the gray curve yielding $m = 2.1 \pm 0.2\,\mu_B$ per atom. This value is in very good agreement with the one expected from taking the sum of the calculated Co spin moment [43] $m_{Co,S} = 1.8\,\mu_B$, its measured orbital moment [44] $m_{Co,L} = 0.2\,\mu_B$, and the measured polarization of Pt at its interface with Co amounting to [45] $m_{Pt} = 0.2\,\mu_B$. We note that already for the moments the size distribution and obviously the correct models are crucial. Assuming an ensemble of particles all having the average size would give $m = 3.0 \pm 0.2\,\mu_B$ per atom and erroneously using the Langevin model would yield $m = 6 \pm 1\,\mu_B$ per atom. Note also that M respectively m enter as scaling factor on the vertical axis. This implies that the reference measurement on a fully saturated monolayer sample was essential to measure m, however, it also implies that errors on M do not affect the shape of $\chi(T)$ which is used to determine the MAE K. Conclusions reached below on K are independent of the exact value of m.

The MAE of a particle strongly depends on the coordination of the constituent atoms [16, 46–48]. Therefore, the natural choice for the expression of the MAE is $K = sE^{as} + pE^{ap}$, where E^{as} and E^{ap} are the contribution of highly coordinated (inner)

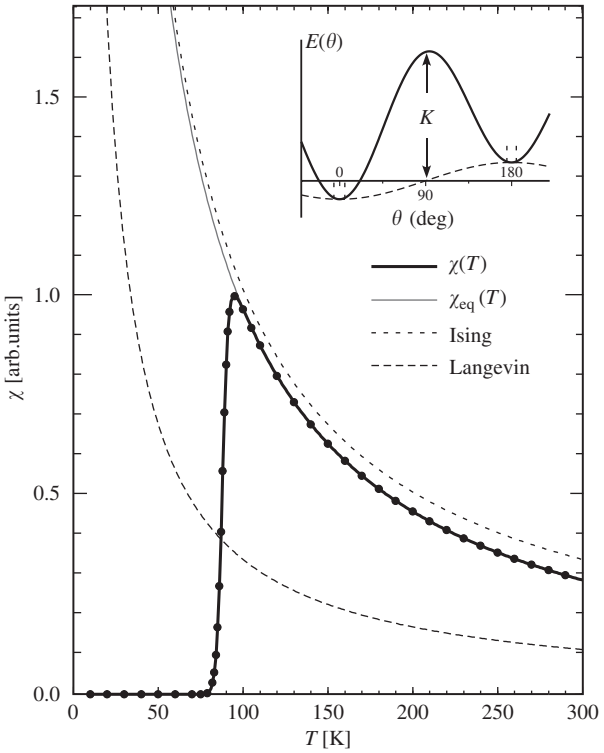

Figure 6: Zero-field magnetic susceptibility $\chi(T)$ for a magnetic island with out-of-plane easy axis. Different models are compared for $K = 200\,\text{meV}$, $M = 3150\,\mu_B = 182\,\text{meV/T}$ corresponding to islands with 1500 Co atoms triangular field sweep with $\omega = 0.3\,\text{Hz}$. The analytical model ($\chi(T)$, thick full curve) perfectly describes the blocking to superparamagnetic transition as seen by comparison with the numerical calculation (circles). The equilibrium zero-field susceptibility, χ_{eq}, is shown as a thin gray curve. (Inset) Energy of a uniaxial monodomain particle as a function of the orientation of M with respect to an out-of-plane external field H in the Ising model (two states: up and down), in the Langevin model (continuum of states, no anisotropy, E is given by Zeemann energy HM), and in the full model incorporating the anisotropy energy K. $\chi(T)$ derived from the Ising and Langevin models are shown in the main figure for comparison.

and low coordinated (edge) atoms, respectively. By simultaneously fitting the $\chi_1(T)$ and $\chi_2(T)$ curves the following magnetic anisotropy energies per atom are obtained for the three island morphologies:

- ramified: $E^{ap} = 0.9\,\text{meV}$, $E^{as} = -0.09\,\text{meV}$
- compact: $E^{ap} = 0.9\,\text{meV}$, $E^{as} = -0.03\,\text{meV}$
- bilayer: $E^{ap} = 1.0\,\text{meV}$, $E^{as} = -0.02\,\text{meV}$

with an error of $\pm 0.1\,\text{meV}$ ($\pm 0.2\,\text{meV}$ in the case of bilayer islands) on E^{ap} and $\pm 0.003\,\text{meV}$ on E^{as}.

The value $E^{ap} \approx 1\,\text{meV/atom}$ associated to edge atoms, having on average four in-plane neighbors, compares well with the MAE/atom measured by means of XMCD in small Co clusters on Pt(1 1 1) with a size of 7–10 atoms, where the lateral coordination

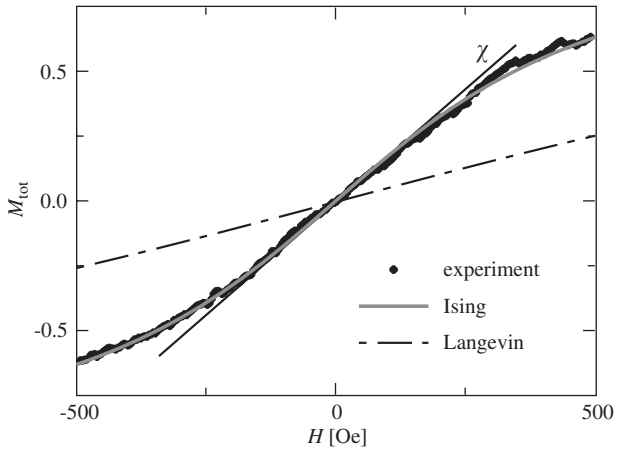

Figure 7: Magnetization (M_{tot}) of the sample shown in Fig. 5b as a function of out-of plane field. $T = 150$ K, triangular field sweep with $\omega = 0.6$ Hz. M_{tot} is normalized to the Kerr signal obtained for saturation of a single monolayer film, taking the coverage of 0.4 ML into account. The Ising fit is shown as a gray line and yields $m = 2.1\ \mu_B$ when taking the size distribution into account. The dash dotted line is the Langevin model with this value.

of the majority of the constituent atoms is comparable [46] (see Section 5). It is also in good agreement with the value of 0.8 ± 0.1 meV/atom observed for Co islands on Au(7 8 8) [16], and with the estimate of 1.0 ± 0.3 meV/atom derived from Ref. [48] for Co islands on Au(1 1 1). For the bilayer islands, this value seems high since the first layer perimeter atoms are higher coordinated and therefore expected to have lower anisotropy than the second layer step atoms. The larger error in the estimation is not due to deficiencies in the fit procedure but is due to the fact that nominally identical samples actually show different T_b. Possible causes are the different strain affecting border atoms in mono- and bi-layer islands [47] modifying the local density of states or different relaxation of the tensile stress taking place during the annealing procedure.

The predominant role played by the border atoms in determining the MAE is also directly pointed out by the shape of the $\chi_2(T)$ curves. An MAE proportional to the island size would result in a much broader $\chi_2(T)$ curve with respect to the measured one (Fig. 5). This directly follows from geometrical considerations since in 2D the island size has a distribution twice as wide as the one of the perimeter. By comparing with 3D colloid particles, where the MAE distribution is always larger than the one of the size [5, 11], this also means that arrays of 2D nanoparticles grown by MBE may achieve narrower MAE distribution than anticipated on the basis of the size distribution alone [16] (see Section 4).

The previous analysis was focused on the temperature range centered around the peak of the $\chi(T)$ curves containing the information about the MAE distribution of the samples. Nevertheless, it is instructive to get a closer look to the high-temperature region where a faster than predicted decrease of $\chi_1(T)$ is observed both for compact and bilayer islands. In the previous discussion, $M(T)$ was assumed to be temperature independent. Removing this assumption and assuming $M(T) = [(w(T)+1)^3/(w(T)-1)^3]^{1/8}[(w(T)-3)/(w(T)+3)]^{1/8}$, where $w(T) = \exp(T_C/T \ln 3)$, which is the exact expression for the temperature dependence of the magnetization of a plane

triangular Ising lattice [21], gives a better fit. In the case of compact islands, the fit gives $T_C = 290 \pm 10$ K. The absence of the abrupt drop of the susceptibility signal at $T = T_C$ can probably be ascribed to the island morphology. Some small second layer clusters in fact decorate the compact islands. Because T_C strongly depends on coordination, these second layer nuclei can locally increase the island T_C explaining the weak signal still visible around the estimated Curie temperature.

In the case of bilayer islands, the best fit gives $T_C = 400 \pm 10$ K. This value agrees with the following theoretical estimation. The Curie temperature of ultra-thin films is expected to depend on the film thickness n following the relationship [49] $1 - T_C(n)/T_C(\infty) = A - (n-1)/2N_0$, where N_0 is the range of spin–spin interaction and A is a constant taking into account the non-zero Curie temperature of the monolayer film (from the monolayer data one calculates $A = 0.79$). In the case of Co, the range of the spin–spin interactions has been calculated [50] to be $N_0 = 9$–10, which gives $T_C(2) = 370$–450 K. The experimental check of this value is difficult because annealing at temperatures slightly higher than about 380 K produces irreversible change of the $\chi(T)$ curves which tend to flatten while the island morphology stays unchanged. A similar onset temperature was recently measured by Robach et al. [51] who observed a 6 ML Co film on Pt(1 1 1) to reverse its magnetization from in-plane to out-of-plane following a brief annealing to about 375 K. By analyzing the magnetic crystal truncation rods of the Pt surface, the authors found the origin of the observed change of the film MAE in the site exchange between interfacial Co and Pt atoms. They also estimated the exchange to affect only $4 \pm 1\%$ of the interfacial Co monolayer. This interfacial exchange could be responsible for the evolution of the magnetism observed for annealing temperature higher than about 400 K. The partial Co/Pt exchange will likely produce a widening of the island MAE distribution which is seen as a widening and flattening of the $\chi(T)$ curves.

Before turning to alternative mechanisms of magnetization reversal, we briefly discuss the effect of mutual dipolar interactions. Looking at the agreement between experimental and calculated data for $\chi_1(T)$ in the superparamagnetic regime, showing the steeper than $1/T$ decrease, suggests absence of such interactions since their presence would considerably flatten this decrease [52]. The absence of interactions can be also rationalized by simply comparing the switching field H_{sw} of a given island with the stray field H_{stray} created by all other neighbors. The worst case is obtained assuming all the macrospins of the neighbors to be aligned. Considering an ensemble of monodisperse compact monolayer particles with $M = S_c \mu_{Co} = 146$ meV/T ($K \approx 120$ meV) one gets $\mu_0 H_{stray} \approx 1 \times 10^{-2}$ T (Eq. (4) of Ref. [53]). The temperature dependence of the switching field is given by $H_{sw} = H_0(1 - \sqrt{T/T_b})$ [54], where $\mu_0 H_0 = 2K/M = 1.6$ T. It is easily seen that dipolar interactions affect the islands behavior only when $0.99\, T_b < T < T_b$.

3.2. Magnetization reversal

The previous discussion assumed magnetization reversal by coherent rotation. However, Section 2 showed an example where 2D nanostructures reversed their magnetization by domain-wall nucleation. The size decides which of the two reversal processes is energetically favored. Magnetization reversal takes place by coherent rotation if the island diameter is smaller than L_{cr}, otherwise wall nucleation and subsequent motion costs less energy. In order to estimate the critical length for Co/Pt(1 1 1), we note that

the mean MAE value is $K \leqslant 0.15\,\mathrm{meV/atom} = 1.5\,\mathrm{MJ/m^3}$, assuming an identical contribution of all the atoms forming the islands [39]. This implies $K \geqslant \mu_0 M^2$ which is unfortunately just in-between the two limiting cases $\mu_0 M^2 \ll K$ and $\mu_0 M^2 \gg K$ which can be treated analytically. Evaluation of L_{cr} for the Co particles in the two cases gives 8 and 10 nm, respectively.

A more realistic evaluation of the critical length L_{cr} was obtained by performing micromagnetic calculations of the magnetization reversal process in absence of thermal excitation. The calculations employed the widely used OOMMF program which calculates the motion of the magnetization vector following the Landau–Lifshitz–Gilbert equation under the effect of a local field taking into account the exchange and dipole–dipole interaction, and uniaxial anisotropy energy [55]. We considered rectangular islands, however, rounding of the corners did not affect the results. The height (z) was set to 2.5 Å (1 ML) and the width (y) and length (x) were varied in order to see the effect of the island elongation on the magnetization reversal mechanism. The initial magnetization was assumed to be saturated ($m = 1.4\,\mathrm{MA/m} \approx 2.1\,\mu_B/\mathrm{atom}$) and canted respect to z by an angle of $\theta = 182^\circ$. This angle corresponds to the maximum possible misalignment between surface normal and magnetic field and allows convergence of the micromagnetic calculation with reduced magnetic fields ($\mu_0 H < 2K/M$) applied along z. The exchange stiffness was assumed to be $J = 10^{-11}\,\mathrm{J/m} = 16\,\mathrm{meV/atom}$ [56, 57] and $K = 0.15\,\mathrm{meV/atom} = 1.5\,\mathrm{MJ/m^3}$ following the experimental value.

In Fig. 8, the spatial distribution of the island magnetization is shown for different island dimensions. The snapshots are taken when the total z component of the magnetization $M_z = 0$. Clearly, the magnetization reversal proceeds by nucleation and displacement of an untwisted domain-wall pair for the longer islands, while the favorite mechanism is coherent rotation for the shorter ones, the critical length being $L_{cr} \geqslant 30\,\mathrm{nm}$. The micromagnetic calculations also extend the validity limits of the

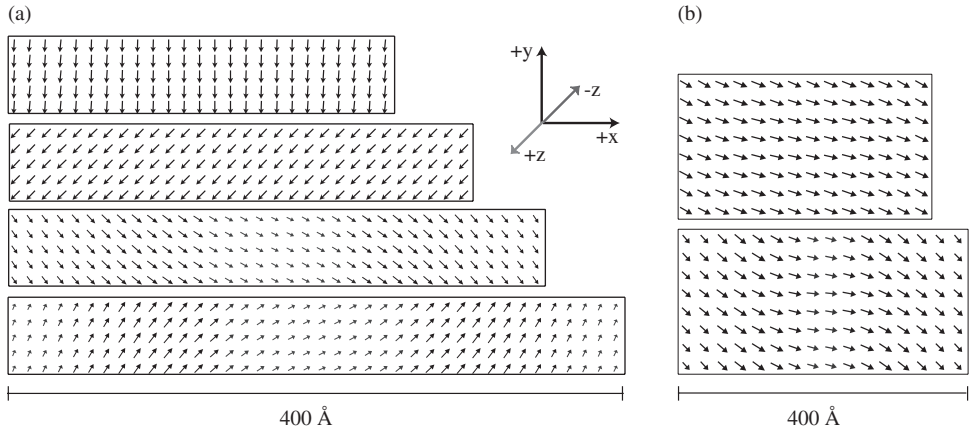

Figure 8: Micromagnetic calculations of the island magnetization. The snapshots show the magnetization distribution corresponding to a vanishing value of the total z-component of the magnetization ($M_z = 0$, $J = 10^{-11}\,\mathrm{J/m} = 16\,\mathrm{meV/atom}$, $m \approx 1.4\,\mathrm{MA/m} \approx 2.1\,\mu_B/\mathrm{atom}$, $K = 0.15\,\mathrm{meV/atom} = 1.5\,\mathrm{MJ/m^3}$). The MAE is assumed uniaxial along z. The damping coefficient was $\alpha = 0.1$ and the vertical field was $B_Z = 0.9\,\mathrm{T}$. The islands were discretized by cuboids with a lateral size of 2.5 Å. The island height was set to 2.5 Å. The width (y) was fixed to 50 Å (a) and 200 Å (b).

analytical theory by supporting the independence of L_{cr} on the island aspect ratio (Fig. 8). This means that the magnetization reversal proceeds by wall nucleation and displacement as soon as at least one of the in-plane island dimensions becomes longer than L_{cr}. We note that the critical length strongly depends on the exchange stiffness which in turn depends on the island thickness. The value used in the simulations was measured for an 8 ML thick film, and it could be smaller for 1 ML [25, 57]. For example, one gets $L_{cr} \geqslant 20$nm nm for $J = 5 \times 10^{-12}$ J/m = 8 meV/atom. By assuming the energy barrier for nucleation at the particle end being half the one required for nucleation in the particle center, the micromagnetic simulations roughly estimated $L_{cr} \geqslant 15$nm. Considering for example the sample in Fig. 5b, the islands have lengths smaller than 20 nm with only a minor fraction having lengths up to 30 nm.This suggests that reversal by coherent rotation of the magnetization is a good approximation and that, eventually, only a negligible fraction of the islands may reverse their magnetization by domain-wall nucleation and displacement. Evidently, all simulations and analytical models of this discussion assume a homogeneous distribution of K, and the experimental [46, 58] and theoretical [47] evidence of a significant increase of K with reduced coordination is not taken into account.

As a parallel check we note that the energy barrier for nucleation of domain walls may be assumed proportional to the island section. A rough estimation of the distribution of island sections is given by the distribution of the area-to-perimeter ratios. By fitting the $\chi(T)$ curves assuming the energy barrier for switching $E = s/p\ E_{sec}$, where $E_{sec} \propto 4\sqrt{JK}$, instead of $K = sE^{as} + pE^{ap}$, gives in general a slightly worse agreement with the experimental data, with the exception of the ramified islands (Fig. 9).

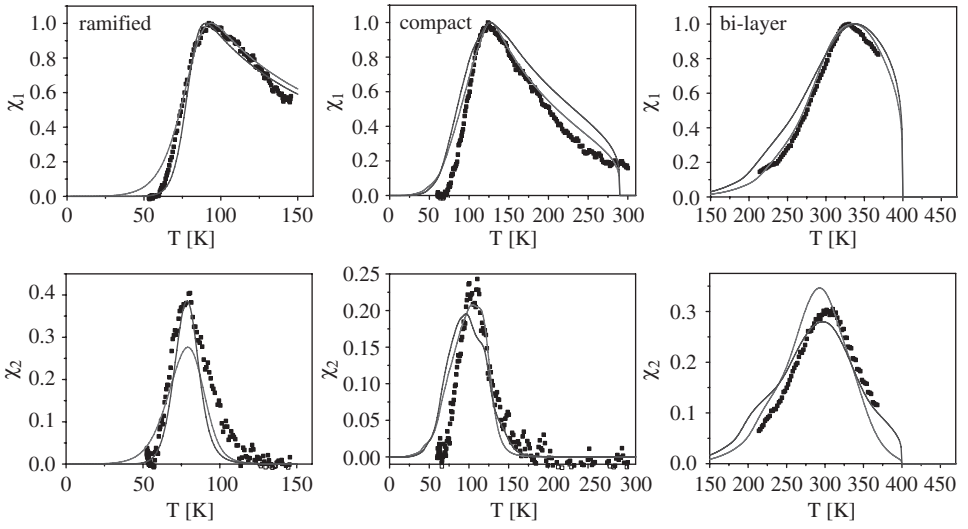

Figure 9: The experimental $\chi_1(T)$ and $\chi_2(T)$ curves measured for the three island shapes (ramified monolayer, compact monolayer, and bilayer) shown in Fig. 5. The black and gray curves represent the best fits assuming $E = s/p\ E_{sec}$ and $K = sE^{as} + pE^{ap}$, respectively.

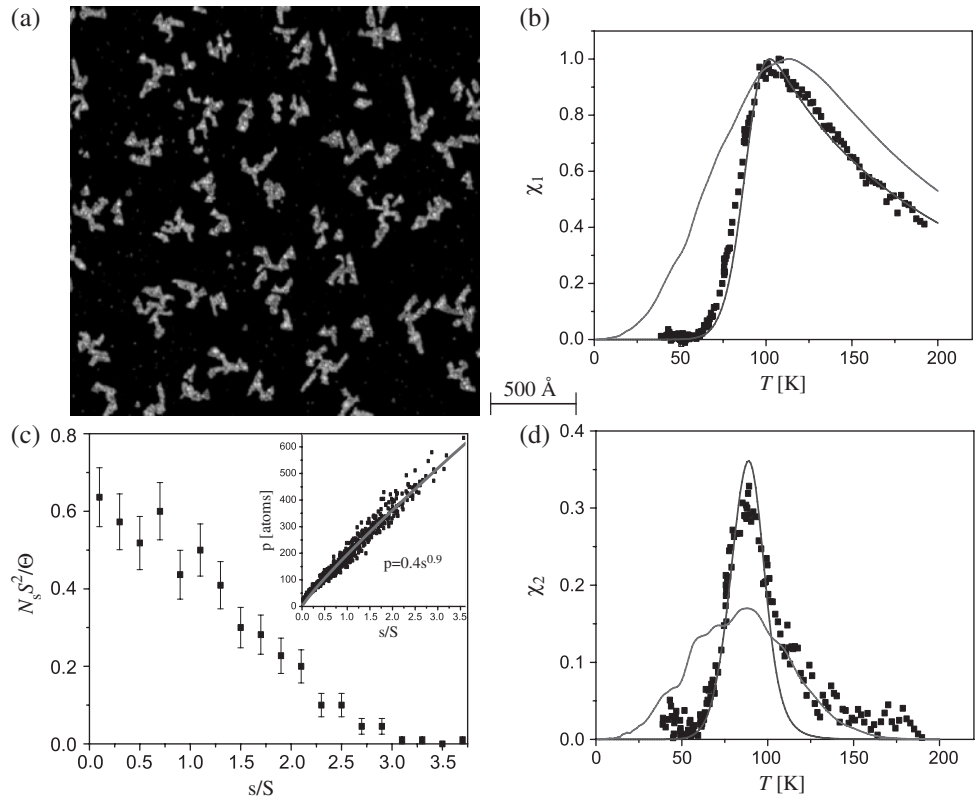

Figure 10: (a) STM image, (c) size s and perimeter p distribution, (b) real $\chi_1(T)$, and (d) imaginary $\chi_2(T)$ susceptibility for Co islands purposely grown to have a mean lateral size longer than 150 Å. The mean size is $S = 1100 \pm 800$ atoms. The black and gray curves represent the best fits assuming $E = s/p\ E_{\mathrm{sec}}$ and $K = sE^{as} + pE^{ap}$, respectively ($\Theta = 0.08$ ML, $T_{\mathrm{dep}} = 150$ K, subsequent addition of $\Theta = 0.08$ ML at $T_{\mathrm{dep}} = 250$K).

To test where a transition to domain-wall nucleation possibly takes place for Co/Pt(1 1 1), we purposely chose growth conditions increasing the island length ($L \geqslant 15$ nm). Figure 10 shows that for this morphology a model assuming domain nucleation and motion nicely reproduces the experimental data points, whereas the fit assuming $K = sE^{as} + pE^{ap}$ gives an erroneous temperature dependence of $\chi(T)$. The proportionality constant in $E_{\mathrm{sec}} \propto 4\sqrt{JK}$, which depends on the actual island shape, can be roughly estimated by comparing the values of the island mean section and of the ratio s/p measured by STM on a set of islands. By doing so and taking the fit value of E_{sec} one estimates $JK = 2.0 \pm 0.5\,\mathrm{meV}^2/\mathrm{atom}^2$, in good agreement with the value $JK = 2.4\,\mathrm{meV}^2/\mathrm{atom}^2$ assumed in the previous discussion. Altogether, this strongly suggests a transition from coherent rotation to domain-wall nucleation and motion for Co/Pt(1 1 1) at a critical length of $L_{\mathrm{cr}} \approx 15$ nm.

3.3. Tailoring the magnetism of 2D nanoparticles

The finding of different contributions of step and surface atoms to the magnetic anisotropy opens new possibilities to separately tune the MAE and magnetic moment of

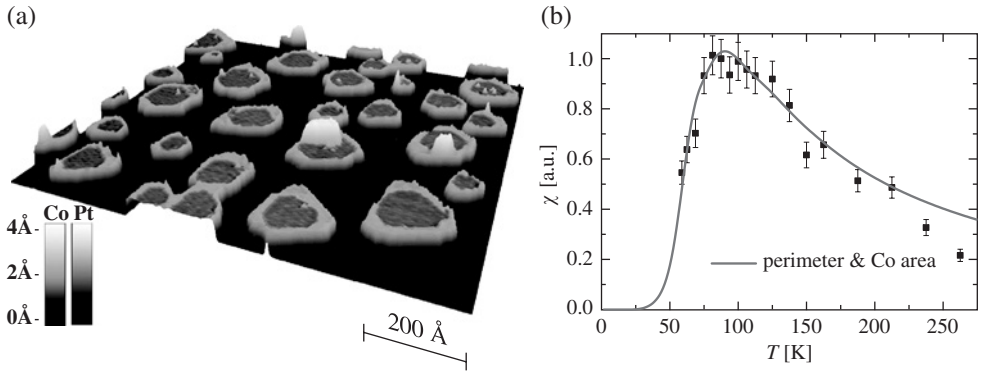

Figure 11: Tailoring magnetic properties in bi-metallic islands: (a) 3D view of an STM image of one monolayer high islands with Pt core and an approximately 3 atom wide Co shell (deposition of 0.2 ML Pt at 130 K and annealing to 760 K generates the quasi hexagonal non-magnetic core; subsequent deposition of 0.2 ML Co at 220 K creates the Co rim). In the STM topographs, Co can be discerned from Pt by its 0.3 Å larger apparent height which was used as color code; (b) $\chi(T)$ reveals that the Co-rim Pt-core islands have the same anisotropy as the pure Co islands with equal perimeter length [39].

nanostructures. The idea was exemplified by producing bi-metallic one monolayer high islands with a non-magnetic core (Pt), surrounded by a few atoms-wide magnetic rim (Co) (see Fig. 11a). The growth conditions took care that the rim is at least two atoms wide in order to increase the exchange-coupling energy and thus enforce long-range ferromagnetic order. In monatomic Co chains, where the chain atoms have only two magnetic neighbors, ferromagnetic order has been reported to extend only over 15 atoms at 45 K [59]. It is seen from Fig. 11b that keeping the MAE per edge atom fixed to the value inferred above for the pure Co islands perfectly reproduces the switching behavior. The bi-metallic islands have identical anisotropy as their equally shaped pure Co counterparts; however, they have a much smaller over-all moment due to their non-magnetic core, and thus reduced dipolar interactions. Many other examples where coordination and interfaces are employed to tailor K and M are currently under investigation.

3.4. Oxidation effect on the island MAE

Due to their reduced dimensions, small magnetic particles created by metal epitaxy at surfaces are very sensitive to pollution, in particular to oxidation. The effect of oxidation on the magnetic properties can be quite complex. Since oxidation generally starts at the low coordinated sites, partial oxidation may provide helpful insight into the origin of magnetic properties, such as magnetic anisotropy. Generally, oxidation degrades the magnetic properties, for instance it has been reported to reduce the anisotropy [60]. However, in particular systems it may dramatically increase the anisotropy, e.g., due to exchange coupling with an antiferromagnetic CoO shell [61]. STM images show clearly that the oxidation process begins at the island edge for Co/Pt(1 1 1) (Fig. 12). With increasing oxygen exposure, the dislocation pattern characteristic of clean Co is progressively replaced by a superstructure with a periodicity of 10 ± 1 Å. An oxygen dose of only 0.3 Langmuir is sufficient for the superstructure to cover the entire surface of small islands, whereas clean Co patches remain only in the center of the largest islands (Fig. 12c).

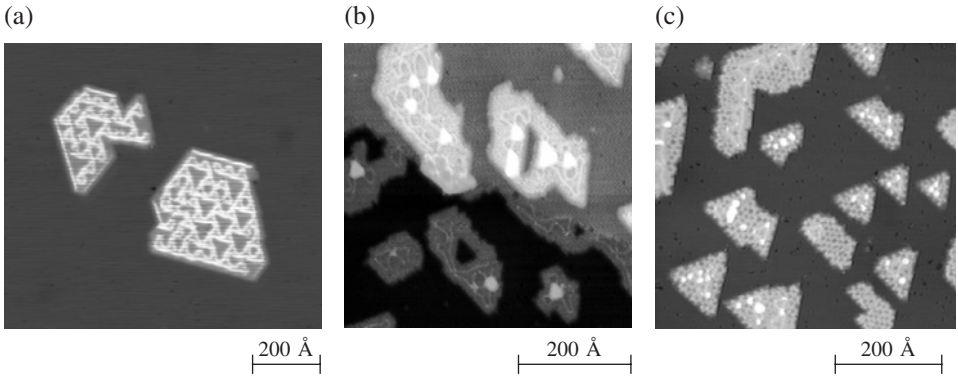

Figure 12: (a) STM image of one monolayer high pure cobalt islands on Pt(1 1 1) showing a triangular pattern of partial surface dislocations appearing bright and marking Co atoms adsorbed on bridge sites. (b) STM image of Co islands after the exposure to 0.05 Langmuir (L) O_2 showing selective oxygen adsorption starting at the steps removing the partials. (c) STM image of Co islands after exposure to 0.3 Langmuir of O_2. Only a small fraction of the larger islands have still the native strain relief pattern in their center, the remaining Co covered surface is transformed into an oxygen-induced 3×3 structure [58].

MOKE measurements show that partial oxidation modifies the temperature dependence of $\chi(T)$ in two ways. The temperature at which the maximum occurs is reduced, and the maximum taken on by $\chi_1(T)$ increases (Fig. 13a). This apparently strange effect can be understood with the help of a qualitative argument. The island MAE K strongly depends on the perimeter atoms. Thus, for a very small amount of oxygen, for which only the island edge is oxygen covered due to the selective adsorption at step sites [62], the anisotropy strongly drops. The island magnetic moment is less sensitive to oxidation and decreases proportionally to the oxidized fraction of the island. As can be seen from Fig. 13, this model also holds quantitatively [58]. It also explains the oxygen-induced compression of the MAE distribution reflected by the observed compression of the $\chi_2(T)$ curves.

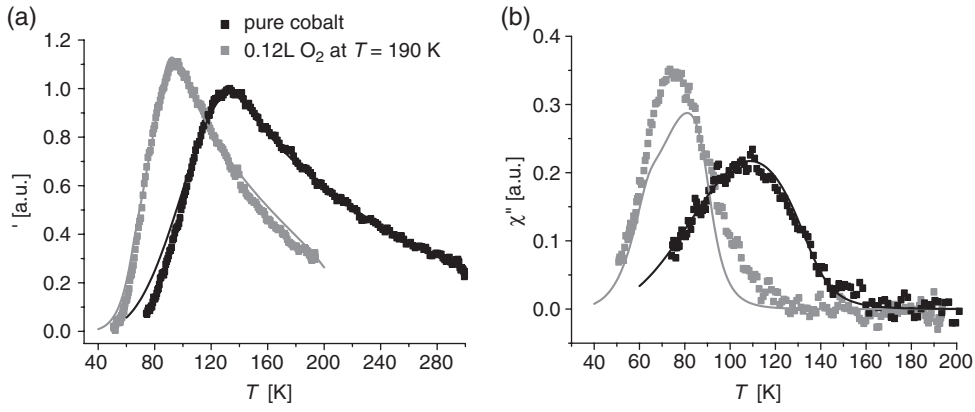

Figure 13: In-phase zero-field susceptibility (a) and out-of-phase zero-field susceptibility (b) as a function of temperature for pure and oxidized cobalt islands [58].

4. SUPERLATTICES OF UNIAXIAL MONODOMAIN ISLANDS

The bit density on magnetic hard disks has been increasing at a constant pace for many years [4]. This development creates technological challenges, such as reliable reading and writing of the bits; however, it also prompts the question after the fundamental ultimate density limit of magnetic recording. This question can be addressed by studying model systems consisting of periodically arranged ferromagnetic monodomain particles each of them potentially storing one bit. Ideally, the particles should have out-of-plane magnetic anisotropy since this minimizes mutual dipolar interactions. In order to achieve the required uniform write fields and read signals, the particles have to be uniaxial and the distributions of moments M and magnetic anisotropy energies K have to be narrow.

Several approaches have been used for the creation of such model systems. Examples are 2D superlattices of size-uniform 3D nanoparticles produced by colloidal chemistry or by precipitation [63], uniform shells with well-aligned easy magnetization axes [64] were produced by deposition onto superlattices of polystyrene particles, and self-assembly of equidistant 2D islands during atomic vapor epitaxy onto single-crystal template surfaces has led to the most uniform magnetic properties at the highest densities [16]. However, none of these approaches has so far led to the desired model system. The 3D nanoparticles will be a very promising material, once uniaxial particles with aligned out-of-plane easy axes can be achieved. The approach based on colloid lithography [65] has to be extended to smaller sizes, and self-assembly onto template surfaces has to be extended to bi-metallic and slightly larger particles in order to achieve blocking temperatures above 300 K. In the following, we present the results so far achieved with the latter approach.

4.1. Self-assembly of equidistant islands

The stress resulting from lattice mismatch in heteroepitaxial systems, and from missing bonds of the surface atoms often leads to weakly incommensurate surface layers. On close-packed surfaces, these layers have surface partial dislocations (domain walls) marking transitions between fcc- and hcp-stacking domains. These dislocations can be well localized, or extend over many lattice sites giving rise to smooth stacking transitions as in moiré patterns. The dislocations order into regular patterns due to the long-range repulsive interactions which for metals are mediated by elastic deformations extending far into the substrate. The density of dislocations is given by the achieved strain relief and can be adjusted in heteroepitaxial systems by the misfit between film and substrate elements. Examples for periodic dislocation patterns are the herringbone ($\sqrt{3} \times 22$) reconstruction of Au(1 1 1) [66], moiré patterns [67], or dislocation networks [68, 69] observed for metallic multilayers. For many systems, the surface partial dislocations represent strongly repulsive line defects for diffusing adatoms [70–72]. Their influence on nucleation can go as far as to drive the most perfect layer-by-layer growth yet observed [73]. However, they can also create sites with preferential incorporation of the deposited species [74]. Independent of the exact mechanism, the combination of ordered dislocations and their strong influence on adatom diffusion can often be employed to grow periodic arrays of almost monodisperse islands [37].

Concerning the magnetic properties of such superlattices, the most studied system is Co on Au(1 1 1) [42, 48, 75, 76]. We therefore discuss first nucleation at the elbows of

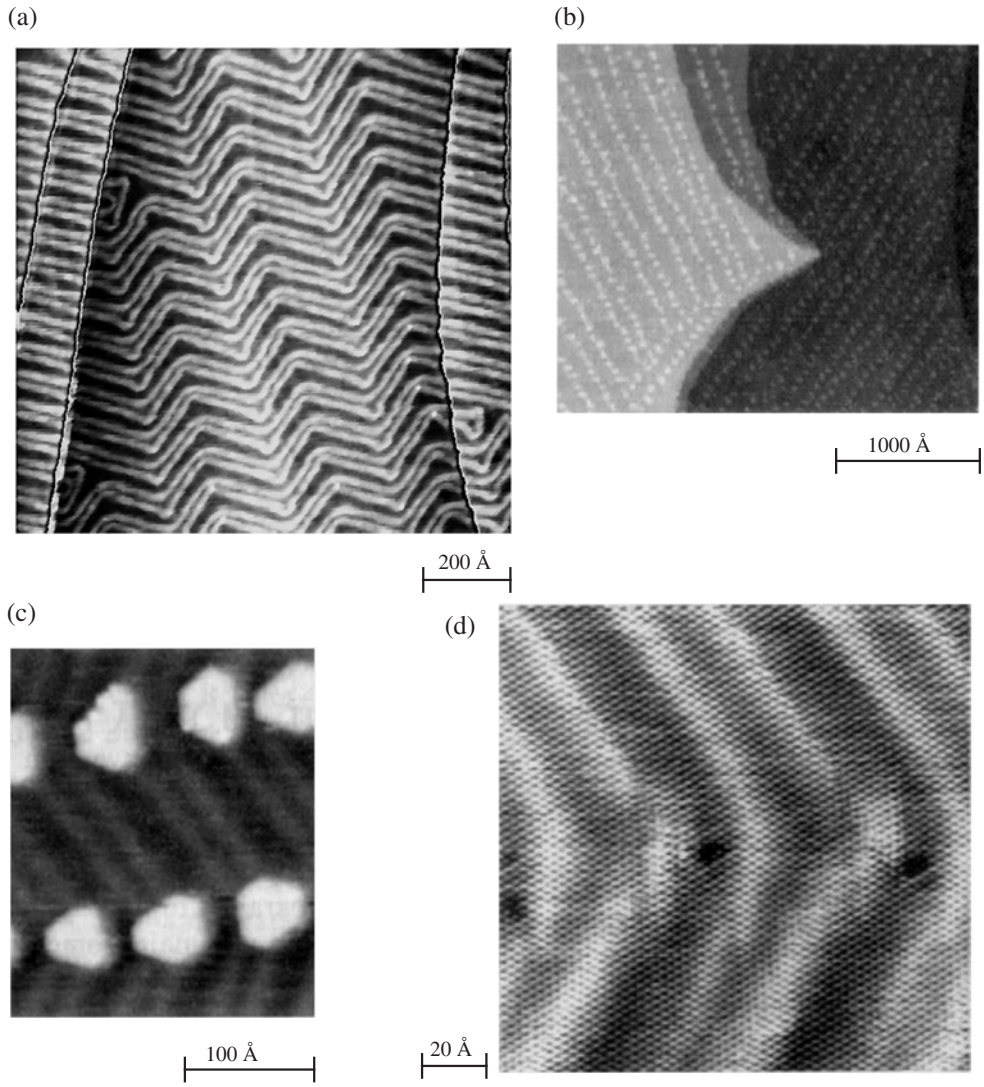

Figure 14: (a) STM image of the herringbone pattern characterizing the mesoscopic order of the Au(1 1 1)–($\sqrt{3} \times 22$) reconstruction [66]. (b) Ni nucleation on that surface at room temperature takes place at the elbows of the reconstruction ($\theta = 0.11$ ML) leading to Ni islands aligned in rows along the $\langle 1\ 1\ \overline{2} \rangle$-directions. (c) $\theta = 0.14$ ML [77]. (d) Site-selective incorporation of Ni into the first Au monolayer is revealed by deposition at 350 K giving access to the embedded Ni islands ($\theta = 0.002$ ML) [74].

the Au(1 1 1)–($\sqrt{3} \times 22$) reconstruction. Figure 14a shows the clean Au(1 1 1) surface with the $\langle 1\ 1\ \overline{2} \rangle$-oriented partial dislocations which are imaged 0.20 Å higher than fcc-areas and therefore appear bright. Stress relief is unidirectional in the ($\sqrt{3} \times 22$) unit cell. Along $\langle 1\ \overline{1}\ 0 \rangle$ there are 23 surface atoms on 22 bulk atoms, corresponding to a 4.3% compression, while the atomic distances remain the bulk value along $\langle 1\ 1\ \overline{2} \rangle$. To achieve overall isotropic surface stress, a well-ordered mesoscopic pattern of two domains with alternating orientation of $\pm 120^\circ$ evolves on large terraces. Deposition

of Ni at room temperature leads to monolayer high Ni islands lined up along the elbows of the herringbone reconstruction pattern (Fig. 14b and c).

Ordered nucleation was initially believed to be caused by diffusing Ni adatoms being attracted toward the dislocation elbows by a higher binding energy there [77]. Due to the present knowledge, however, order results from site-selective exchange of Ni atoms with Au surface atoms [74]. The exchange is localized at the elbows where a close-packed atomic row terminates, giving rise to Au atoms with reduced lateral coordination which are especially susceptible to exchange or incorporation processes. The embedded Ni clusters, comprising four to five atoms each, are clearly detected as depressions in Fig. 14d. The site-selective exchange is followed by preferential nucleation of Ni adislands on top of substitutional Ni islands. Very similar order has also been found for Co [78, 79], Fe [80, 81], and Rh [82]. The mechanism is believed for all these systems to be identical to the one of Ni. The argument given by Meyer et al. is that the elements Ni, Co, Fe, and Rh have a larger surface free energy and heat of sublimation than Au [74]. In line with this argument, ordering is absent for elements with lower values of these quantities such as Ag [83] and Al [72]. However, Al/Au(1 1 1) exhibits exchange at $T > 245\,\mathrm{K}$ [84, 85], showing the limits of this prediction solely based on bulk quantities.

Ordering by site-selective exchange is specific to Au(1 1 1) and related vicinal surfaces, and to elements of the periodic table exhibiting exchange on these surfaces. A more general approach relying on pure adatom diffusion on dislocation networks has been suggested [14]. Dislocations may confine adatoms by their repulsion to the unit cell into which they are deposited leading to the nucleation of exactly one island per unit cell. The repulsion of adatoms extends over some lattice sites avoiding nucleation close to the dislocation which would result in their overgrowth and create bridges between neighboring cells. In addition, fcc- and hcp-domains often have different adatom binding energies leading to one preferential nucleation site within each unit cell. Therefore, the potential energy surface seen by the diffusing adatom has a global minimum per supercell from which it goes smoothly upwards toward the edges. A similar distribution of binding energies may be realized on moiré patterns, one recent example being Ir/graphene/Ir(1 1 1) [86].

For ideal confinement, the size distribution is determined by the statistics of deposition into the unit cells. The probability of finding k atoms deposited within a unit cell with a size of n substrate lattice sites is a binomial distribution $P(k) = \binom{n}{k} p^k q^{n-k}$. This distribution has a standard deviation of $\sigma = \sqrt{q/np}$, where $p = \theta$ denotes the coverage in ML units, and $q = 1–p$. For Ag nucleation on 2MLAg/Pt(1 1 1)–(25×25), the measured size distribution was with $\sigma = 0.20$ wider than $\sigma = 0.12$ expected for ideal confinement at the coverage $p = 0.10$ and cell size $n = 625$ [14, 87]. Under ideal conditions, size distributions as narrow as $\sigma = 0.04$ are expected ($\theta = 0.50$, $n = 625$) but await experimental confirmation.

For magnetic elements, one often finds exchange or incorporation at random sites destroying order and therefore requiring careful choice of the template. While Co and Fe did exchange down to 50 K on 2MLAg/Pt(1 1 1)–(25×25), a template consisting of 2MLCu/Pt(1 1 1)–(13×13) [89] enabled the growth of ordered arrays of triangular monolayer high Fe and Co islands (see Fig. 15). Cu(1 1 1) is unstable upon exchange with Co down to 170 K [90], therefore low deposition temperatures had to be used. This led to the formation of three small clusters per unit cell which were subsequently

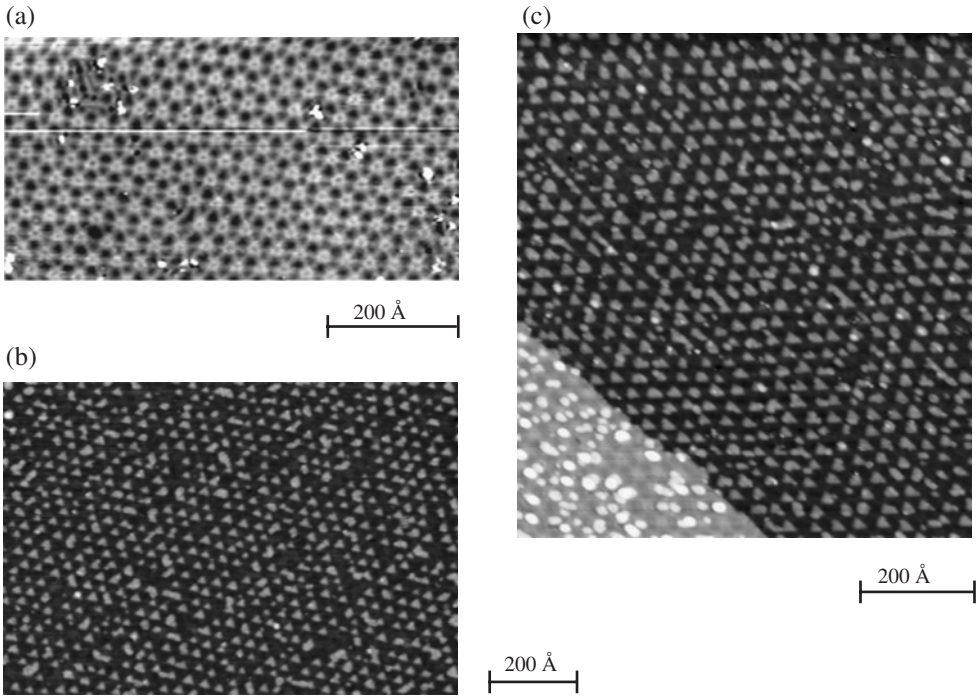

Figure 15: (a) STM image of the (13×13) dislocation network of 2 ML Cu on Pt(1 1 1) [88]. (b) Periodic arrangement of trigonal monolayer Fe islands formed by deposition at $T_{dep} = 100\,K$ and annealing at $T_{ann} = 250\,K$ onto the surface shown in (a) ($\theta = 0.10\,ML$) [14, 88]. (c) Triangular Co islands obtained on 2MLCu/Pt(1 1 1)–(13×13) ($\theta = 0.10\,ML$, $T_{dep} = 90\,K$, $T_{ann} = 200\,K$) [88].

transferred by gentle annealing into a single triangular island. From the surface free energies, Cu tends to cover Co and also Fe. Very different degrees of intermixing have been reported for Co/Cu(1 1 1). Early studies report etching of Cu for room temperature deposition of Co [91] and coexistence of both elements in islands [92]. Embedding of 3 ML high Co islands by one layer into Cu(1 1 1) upon deposition at 150 K [90], and entire capping of Co with Cu upon annealing to only 300 K have been reported [90, 93]. More recent studies investigating the electronic structure and therefore being very sensitive to intermixing are contradictory on the degree of intermixing. Pure Co adlayer islands for deposition at 290 K and subsequent rapid cooling, and intermixing upon deposition at 345 K are reported [94], while Co islands created at 300 K are reported to be surrounded by a few atoms wide Cu seam, independent of the speed with which the sample is quenched to low T [95]. Therefore, it is not excluded that a small fraction of the islands shown in Fig. 15 consists of Cu, even though the STM images show no direct evidence of this.

The preceding examples use templates exhibiting phase shifts between subsequent terraces. The last example uses Au(1 1 1) vicinal surfaces and thereby enables phase-coherent lattices over the entire crystal since atomic steps are used as nucleation sites. For appropriate orientation of the miscut, these surfaces exhibit energetically stable B-steps ({1 1 1}-microfacets) which, for not too small miscuts, are equidistant over the entire crystal due to elastic repulsions [96]. The (1 1 1)-oriented terraces exhibit the

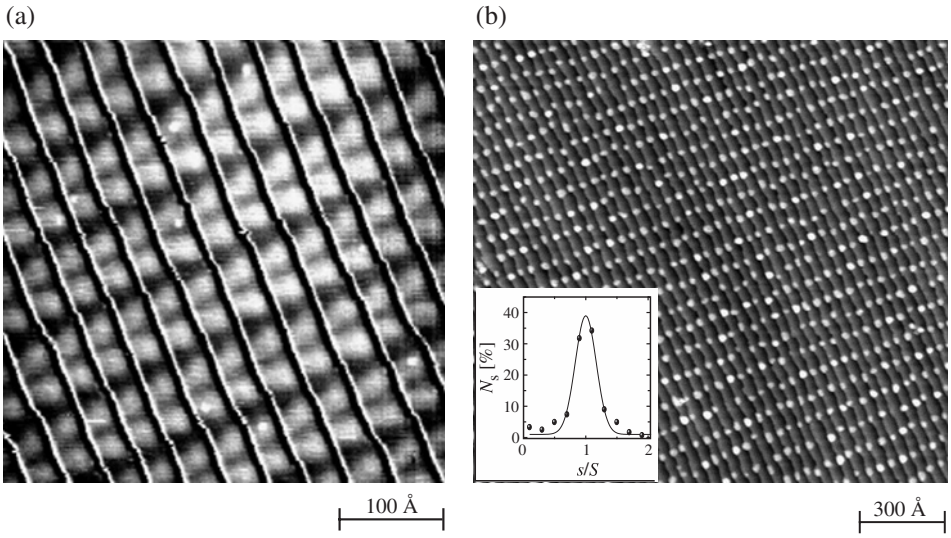

Figure 16: (a) STM image of the Au(7 8 8) surface. The corrugation due to the terrace levels has been subtracted in order to enhance the reconstruction lines [97]. (b) STM image showing 0.2 ML Co deposited on Au(7 8 8) at 130 K and annealed to 300 K. Co forms bilayer islands organized into a phase-coherent superlattice with a unit cell of 3.5 nm × 7.0 nm, corresponding to a density of 26 Tera-islands/in.^{2} (Inset) Size distribution with mean island size $S = 70$ atoms and $\mathrm{HWHM}_s = 14$ atoms; N_s denotes the abundance of islands with size s [16].

($\sqrt{3} \times 22$) reconstruction with domain walls running perpendicular to the step edges and being aligned from terrace to terrace (see Fig. 16a for the case of Au(7 8 8)).

Nucleation of Co takes place at the crossing of the domain walls and the steps [96, 97]. Figure 16b shows a typical pattern of double-layer Co islands obtained by depositing $\theta = 0.2$ ML Co onto Au(7 8 8) at 130 K and subsequent annealing to 300 K. This two-step process significantly increases the degree of order [96] with respect to direct deposition at 300 K [97]. The island size distribution in the inset of Fig. 16 is well reproduced by a Gaussian fit with $\sigma = 20\%$ which is close to the best value obtained for colloid particles. Comparing the Arrhenius representation of the island density with kinetic Monte-Carlo simulations including traps and exchange (insertion) yielded perfect agreement between simulation and experiment for trap energy $E_{\mathrm{trap}} = 0.28$ eV and a barrier for insertion $E_{\mathrm{ins}} = 0.78$ eV, compared with a diffusion barrier of $E_{\mathrm{m}} = 0.120 \pm 0.002$ eV [98].

However, Au vicinal surfaces present difficulties in growing bi-metallic islands due to exchange and incorporation. The ideal template, with a period of 50–100 Å, inducing magnetocrystalline out-of-plane anisotropy, and enabling annealing of the magnetic islands without intermixing, has yet to be discovered. We close by noting a few other templates which might be worse further investigation [99]. Moiré structures [100, 101] are quite promising since they can also be formed by thin sulfide [102], oxide [103], or nitride [104] films which are chemically more stable than metal surfaces. Very uniform cluster arrays were obtained for V [105] and Pd [106] on $Al_2O_3/Ni_3Al(1\,1\,1)$–($\sqrt{67} \times \sqrt{67}$)$R48^\circ$, while so far the clusters with magnetic elements, such as Fe, are less well ordered on this template [107]. While the lattice constant of the template is

normally a fixed number given by the misfit of overlayer and substrate, the lattice constant of 2D alloy layers is a function of their composition and generally given by Vegard's law. This enables growth of templates with adjustable supercell size, as has been shown for Au_xNi_{1-x} layers on Ni(1 1 1) [100]. Also, buffer layer assisted growth [108], where the metal atoms are evaporated onto an inert gas buffer which is subsequently desorbed, is a very promising approach since it enables formation of 3D clusters which may then land onto the surface. Monodisperse 3D clusters can be produced by combining cluster source with energy filter and mass selection [109]. These clusters can be soft-landed onto metal surfaces preventing fragmentation and/or incorporation into the substrate [110]. The latter two techniques produce size uniform but randomly spaced clusters. Uniform spacing may possibly be achieved by using these techniques on template surfaces.

4.2. Uniform magnetic properties of Co islands on Au(7 8 8)

The magnetic properties of the lattice shown in Fig. 16b were characterized by XMCD and MOKE. The spin (m_S) and orbital (m_L) moments of the Co atoms in the 2D islands have been determined by means of XMCD for a superlattice with a coverage of $\theta = 0.35$ ML, leading to a mean size of 120 atoms per island. Figure 17a shows the X-ray absorption spectroscopy (XAS) data for both helicities recorded under normal incidence at the Co $L_{2,3}$ absorption edges (2p to 3d transitions) and at a magnetic field of 5 T saturating the sample. From the resulting XMCD spectrum, m_S and m_L can be derived by means of the sum rules [111, 112]. The angular dependence of m_L is displayed in Fig. 17c and shows that the sample easy axis is within the error bars the

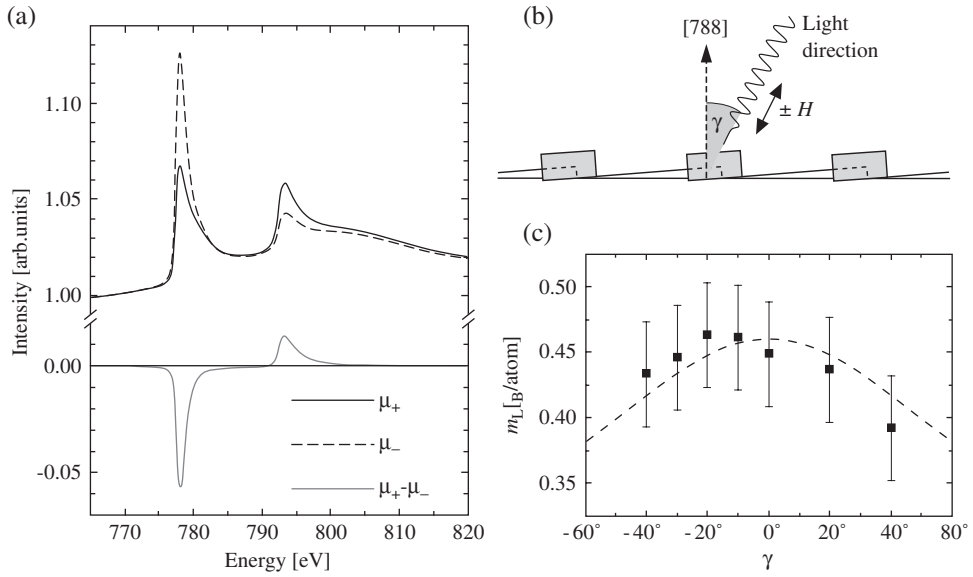

Figure 17: (a) XAS spectra for 0.35 ML Co on Au(7 8 8) taken at normal incidence ($\gamma = 0°$, $T = 10$ K, $B = 5$ T, $B_{sat} = 2.5$ T). μ_+ and μ_- are spectra recorded with left and right circularly polarized light, the difference is the XCMD signal. (b) Magnetic field and incident beam are parallel and form an angle γ with the surface normal. (c) Orbital moment m_L as a function of γ. The line corresponds to the fit with Eq. (4). After Ref. [16].

surface normal, in agreement with the results for Co islands on Au(1 1 1) [42, 48]. The data suggest a slightly canted easy axis since the highest m_L value is found at $\gamma \simeq -15^\circ$. This is expected due to the fact that the Co islands are attached to substrate steps [113] which breaks the symmetry in the direction perpendicular to the steps. However, for simplicity and since the data do not provide significant support for a slight canting we assume the easy axis to be out-of-plane. The perpendicular and parallel component of the orbital moment, $m_{L,\perp}$ and $m_{L,\parallel}$, are therefore given by

$$m_L(\gamma) = m_{L,\perp} + (m_{L,\parallel} - m_{L,\perp})\sin^2(\gamma) \tag{4}$$

This gives $m_{L,\perp} = (0.46 \pm 0.05)\,\mu_B$ and $m_{L,\parallel}$–$m_{L,\perp} = (0.11 \pm 0.01)\,\mu_B$. Applying the sum rules and the formalism described in Refs. [111, 112, 114], a spin moment of $m_S = (1.7 \pm 0.1)\,\mu_B$ per Co atom was found, close to the bulk value [115]).

The MAE distribution of the Co islands was determined by considering a superlattice of slightly larger islands created by repeating the deposition and annealing sequence previously described in coverage steps of at most 0.3 ML. This procedure allows a linear increase of the island size preserving a narrow size distribution until the onset of coalescence ($HWHM_s = 32\%$ for a coverage of $\theta = 0.75$ ML (see Figs. 18a and b). The zero-field susceptibility $\chi(T)$, shown in Fig. 18c, has a sharp peak at $T_b = 50$ K marking the transition from the blocked state to the superparamagnetic one. This transition takes place in a narrow temperature window of about 15 K, indicative of a very narrow MAE distribution. A fit with Eq. (1) taking into account the real size and perimeter length distributions, measured by analyzing the geometry of more than 2000 islands acquired by STM, and assuming $K = pE^{ap}$ and $M = sm_{Co}$ with $m_{Co} = m_L + m_S = 2.2\,\mu_B$ reproduces the experimental data very well with $E^{ap} = 0.8 \pm 0.1$ meV/atom.

A consistency check of the MOKE and XMCD measurements was done by comparing the islands MAE measured with both techniques. The mean island size of the sample studied with XMCD is $s = 120$ atoms, with $p = 55$ atoms situated at the rim. Therefore, $M = 264\,\mu_B$ and from MOKE $K = pE^{ap} = 44 \pm 5$ meV. The anisotropy of m_L, measured by XMCD, is linked to the magnetocrystalline anisotropy energy per atom, E_{MC}, by [42, 116–118]

$$E_{MC} = -\alpha \frac{\xi}{4\mu_B}(m_{L,||} - m_{L,\perp}) \tag{5}$$

with $\xi = 70$ meV, the Co spin–orbit coupling constant [42], and α accounting for the fact that the exchange splitting is generally smaller than the width of the band [114, 118]. Since MOKE determines the total anisotropy $K = E_{MC} + E_{shape}$, the shape anisotropy has to be subtracted. Assuming circular island geometry one estimates $E_{shape} = -0.08$ meV/atom, favoring in-plane magnetization, which yields an MOKE value of $E_{MC} = 0.45 \pm 0.04$ meV/atom. This value meets the one estimated with XMCD assuming $\alpha = 0.23 \pm 0.02$ in agreement with previously reported estimates of $\alpha = 0.2$ [117].

Figure 18d shows the particles MAE distribution derived from the perimeter length distribution and the value of E^{ap}. Similar to the size distribution, the K distribution has a Gaussian shape. However, its HWHM is with 17% almost a factor of 2 smaller than the size distribution having 32%. This is explained by the MAE assumed to be given by the perimeter length, which in 2D has a distribution half as wide as the one of the size. The second remarkable feature is that the value of 17% is less than half of the

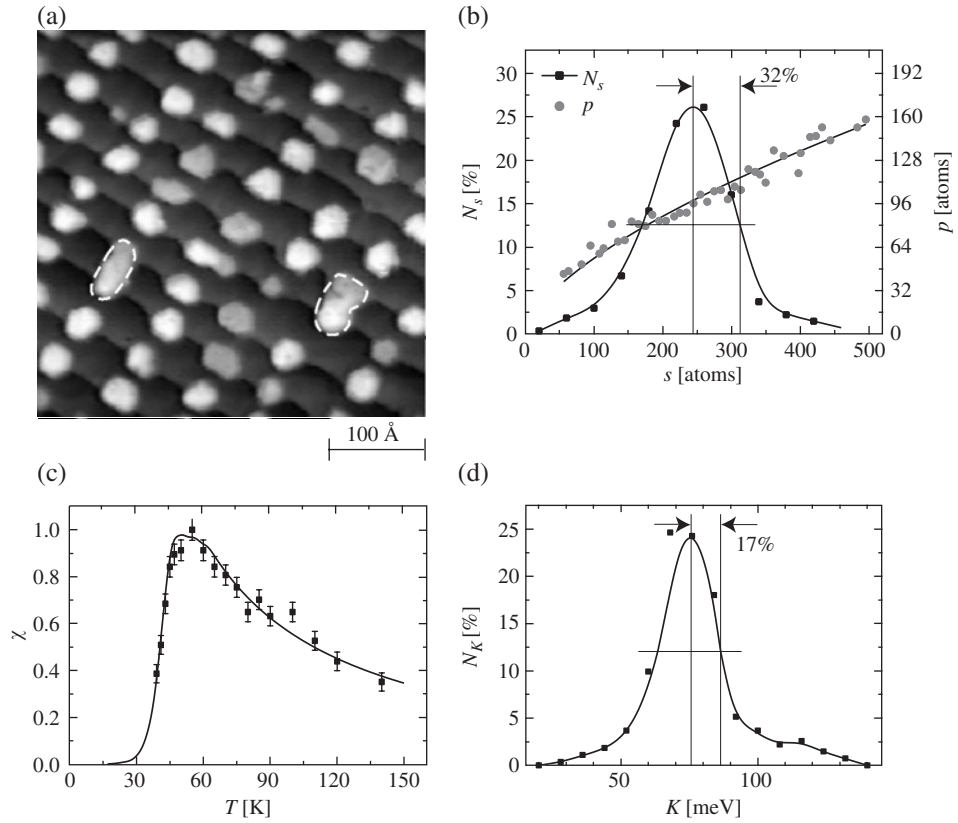

Figure 18: (a) STM image showing the surface morphology for a Co coverage of $\theta = 0.75$ ML. Coalesced islands are encircled by dashed white lines. (b) Size and perimeter length distribution. (c) $\chi(T)$, the solid line represents the fit calculated by assuming K to originate from the perimeter atoms. (d) MAE distribution used to fit $\chi(T)$ in (c) [16].

best result so far achieved for colloid particles [5]. For the 3D colloid particles, the nonuniformity at the surface and the competition between several causes of anisotropy, such as faceting, strain, or shape anisotropy, may give rise to several easy axes per particle. In addition, these axes are randomly oriented from one particle to the next leading to dipolar interactions, which altogether explains the relatively wide anisotropy energy distribution [11]. Figure 18 shows that ordered arrays of uniaxial out-of-plane nanostructures grown by MBE may achieve much more narrow MAE distributions than anticipated based on the size distribution alone [16].

The system is also characterized by negligible dipolar interactions between the islands. Similar to the case of Co/Pt(1 1 1) discussed above, one can exclude interactions in looking at the decay of $\chi(T)$ above T_b. This decay is steeper than $1/T$ as expected for a non-interacting uniaxial system. A second independent evidence for the absence of interactions was derived by growing a sample with a bimodal size distribution due to the coexistence of noncoalesced and coalesced Co islands. For this sample, $\chi(T)$ was reported to display a clear double peak which is only possible if the macrospins of the two island sizes can fluctuate individually [16]. Similar estimations than above of the

stray field of all other islands acting onto a given island suggest that the islands moment can be increased by a factor of 10 still not giving rise to interactions. This is very promising since it theoretically enables an increase of T_b by a factor of 10 and thus realization of a superlattice of uniaxial out-of-plane particles which are blocked up to above room temperature.

4.3. Array of room temperature blocked nanoparticles: Co pillars on Au(1 1 1)

The Co dots on Au(7 8 8) show very good uniformity of the spatial and magnetic properties; however, their blocking temperature of about 50 K is too low to present a model system relevant for applications. A step forward in the direction of producing a long-range ordered array of room temperature blocked nanoparticles was accomplished by Fruchart et al. [41, 119]. The authors succeeded in fabricating vertical self-assembled Co pillars on Au(1 1 1) which increases the size of the Co islands usually grown on Au(1 1 1) and with it their MAE, while keeping the in-plane periodicity unaltered.

The surface morphology following the pillar growth sequence is shown in Fig. 19. As a first step, 0.2 ML Co are deposited on Au(1 1 1) at 300 K which produces 2 ML high Co islands located at the elbows of the herringbone reconstruction. Subsequently, the surface is covered with the amount of Au necessary to fill the space between the islands and to complete 4 ML above the substrate. During this deposition step, the temperature is raised from 425 to 475 K. The distance between bulk hcp Co(0 0 0 1) layers is with 2.05 Å smaller than the one of Au(1 1 1) (2.35 Å). In agreement with this

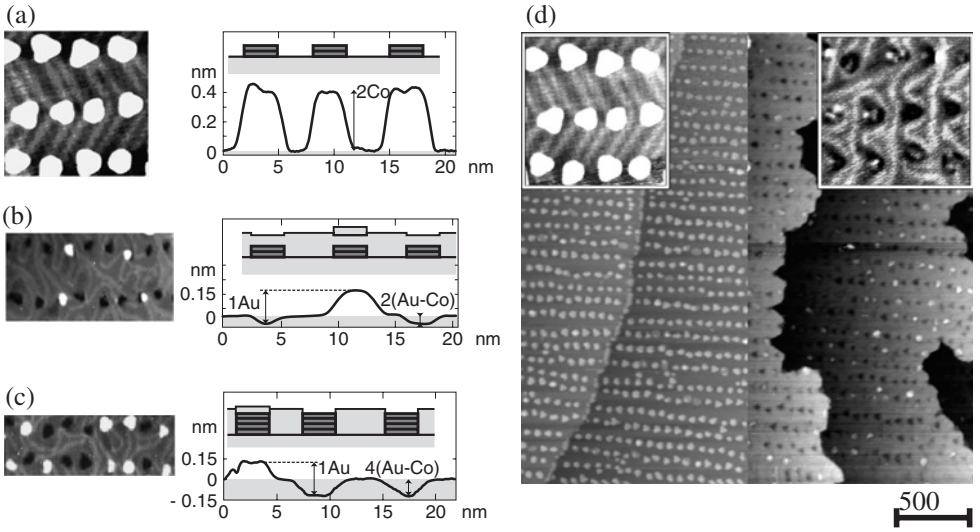

Figure 19: Pillar-growth illustrated by STM views of the uppermost surface layer. For steps (a)–(c) right panels show the surface profile in STM line scans and a schematic sample cross-section. (a) 0.2 ML Co deposited onto Au(1 1 1) at 300 K leads to 2 ML high islands located at the elbows of the Au(1 1 1)–($\sqrt{3} \times 22$) reconstruction (image size 250×250 Å^2). (b) After deposition of Au up to completion of four atomic layers (600×350 Å^2). (c) After deposition of the second layer of Co dots (600×250 Å^2), (d) STM image of ordered 2 ML high Co islands (left) and pillars grown by deposition of 10 Co/Au bilayers (right, different area). Insets show enlargements revealing the Au reconstruction [41, 119].

geometrical consideration, the buried islands appear as an array of 0.6 Å deep hollows (Fig. 19b). As a third step, 0.2 ML of Co are deposited at 500 K. This is the amount of Co needed to increase the height of the previous Co islands by 2 ML. The newly deposited Co atoms displace the Au and go on top of the buried dots, as can be inferred from Fig. 19c. The array now displays hollows and islands. The hollows are about 1.2 Å deep, i.e., four times the difference of layer spacing between Co and Au, suggesting that the dots are now indeed four atomic layers high.

This implies a double-layer place-exchange between deposited Co atoms and Au atoms covering the buried Co dots from the previous layer. Subsequently, the amount of Au required to complete a smooth fifth layer is deposited at 500 K. The situation is then similar to that after step two. Starting from this point and maintaining the temperature at 500 K, the sequence can be repeated and preserves order up to 16 cycles (Fig. 19d). This is consistent with the fabrication of continuous pillars of nearly pure Co on Au(1 1 1) with an aspect ratio of about 2:1 (height over diameter). For 80 Å high pillars, a blocking temperature of 300 K was reported [119]. However, the temperature dependence of the remanent magnetization suggested magnetic interactions between adjacent pillars, which could contribute to the observed high blocking temperature.

5. MAE AND MAGNETIC MOMENT OF SINGLE ATOMS

In the previous sections, we discussed examples demonstrating the link between magnetic properties and atomic coordination. Moving from bulk ferromagnets to the edge atoms of 2D islands deposited on low-index single-crystal metal surfaces may increase the MAE from a few tens of μeV/atom to 1 meV/atom. This trend is expected to continue moving from small islands, where the lateral coordination is still 2–6 down to single adatoms. Recent experiments [46] confirmed calculations predicting magnetic anisotropies of the order of 10 meV/atom [120, 121], i.e., 10^3 times larger than bulk anisotropies.

Adatoms due to their zero lateral coordination are predicted to have spin and orbital magnetic moments in-between those of bulk compounds and free atoms [120, 122]. Gas-phase transition metal (TM) atoms possess large m_S and m_L, according to Hunds rules, which are due to intra-atomic Coulomb interactions. In a solid, electron delocalization and crystal field effects compete with these interactions, causing a substantial decrease of m_S and partial or total quenching of m_L. Such effects have been predicted to be strongly reduced in TM impurities at non-magnetic surfaces owing to the decreased coordination [120], with implications also for the appearance of significant magnetic anisotropy. TM clusters in the gas phase have shown a strong dependence of the total magnetic moment ($m_S + m_L$) on the particle size [123, 124].

In the first part of this section, we discuss the XMCD results of Co adatoms and small islands on Pt(1 1 1), giving hard experimental numbers on K, m_L, and m_S, for single adatoms up to islands of 40 atoms. We then turn to Fe, Co, and Ni adatoms on K thin films showing different degrees of hybridization revealing the electronic ground state configuration.

5.1. Single Co atoms and small islands on Pt(1 1 1)

Single atoms and small islands have been created by statistical and kinetically controlled growth of Co on Pt(1 1 1) [37]. The Co/Pt system was chosen in order to

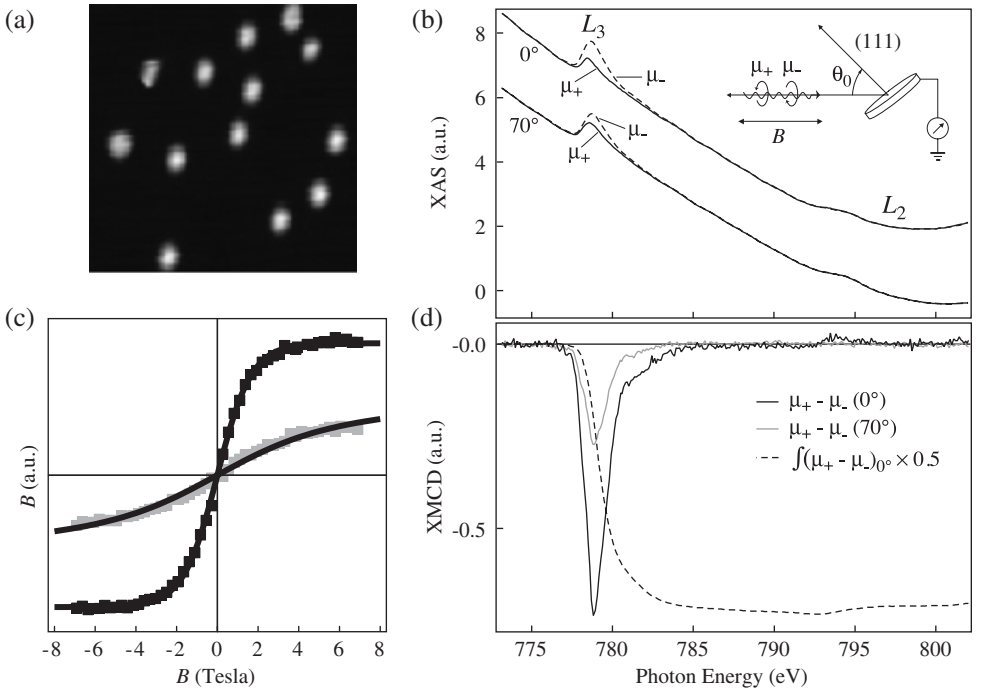

Figure 20: (a) STM image of isolated Co adatoms on Pt(1 1 1) ($\theta = 0.010$ ML, 85×85 Å). (b) $L_{3,2}$ XAS spectra of sample shown in (a) ($T = 5.5 \pm 0.5$ K, $B = 7$ T). (c) Magnetization curves at $\theta_0 = 0°$ (black symbols) and $\theta_0 = 70°$ (gray symbols) ($T = 5.5$ K). (d) XMCD spectra ($\mu_+ - \mu_-$) obtained for $\theta_0 = 0$ and 70°. The dashed line is the integrated XMCD at $\theta_0 = 0°$ [46].

maximize the MAE effects, since hcp-Co presents the largest MAE among 3d ferromagnetic elements (0.045 meV/atom compared with, e.g., 0.005 meV/atom for Fe). In addition, CoPt alloying in the bulk-ordered $L1_0$ phase results in an MAE increase up to 0.8 meV/Co atom [125], owing to the strong spin–orbit coupling of the Pt 5d states. Figure 20a shows an STM image of isolated Co adatoms obtained by depositing 0.01 ML at $T = 5.5$ K, for which thermal surface diffusion is completely inhibited. Figure 20b shows the XAS spectra of the Co $L_{2,3}$ edges using left and right circularly polarized light in the total electron yield mode. The XMCD signal (Fig. 20d) is the difference between the XAS spectra recorded for parallel (μ_+) and anti-parallel (μ_-) alignment of the photon helicity with respect to the applied field B. Fields of up to 7 T were used to magnetize the sample. For $\theta_0 = 0°$ field and light are along the surface normal, for 70° the sample is strongly tilted as shown in the inset of Fig. 20b. The spectra at $\theta_0 = 70°$ have been normalized to the $(\mu_+ + \mu_-)$–L_3 intensity at $\theta_0 = 0°$ in order to eliminate the dependence of the electron yield on the sample orientation.

The XAS spectra show relatively weak absorption features compared with the Pt background due to the extremely low concentration of Co adatoms. However, the XMCD signal is very large relative to the total Co absorption signal, indicating the presence of strong magnetic moments localized at the Co atoms. Two magnetic properties are characteristic of the single Co adatoms. First, the vanishing intensity of the XMCD at the L_2 edge indicates unusually strong orbital magnetism. Second, the large

difference between the in-plane and out-of-plane $M(B)$ curves (Fig. 20c) reveals an extraordinary MAE. According to the XMCD sum rules [111, 112, 115], $m_L = 1.1 \pm 0.1\ \mu_B$/atom is measured along to the easy axis ($\theta_0 = 0^\circ$) [46]. This value is smaller than $3\ \mu_B$ of a gas-phase Co atom, but much higher than in bulk, where m_L is usually reduced to 0.1–0.2 μ_B owing to the hybridization of the d-states. The explanation lies with the reduced coordination of an isolated atom adsorbed on top of a flat surface, favoring d-electron localization and thus the survival of atomic-like character in the 3d orbitals. The presence of such a large orbital magnetization has significant consequences for the magnetic anisotropy.

The MAE E_a was determined by measuring the component of the adatom magnetization parallel to B, with B applied along the surface normal and tilted to it by $\theta_0 = 70^\circ$. The data points in Fig. 20c represent the peak of the L_3 XMCD intensity at 778.6 eV divided by the pre-edge intensity at 775 eV as a function of B, which corresponds to a good approximation to $M(B)$. The difference between the $\theta_0 = 0^\circ$ and $\theta_0 = 70^\circ$ curves is consistent with the XAS-normalized XMCD spectra. The solid lines are Langevin fits to the data assuming uniaxial anisotropy yielding $E_a = 9.3 \pm 1.6$ meV/atom, which is an exceptionally large value [46]. Typical systems with high MAE are $SmCo_5$ ($E_a = 1.8$ meV/Co atom [125]), Co/Pt, Co/Au multilayers ($E_a \approx 0.3$ meV/Co atom [44, 117]), and 1D Co atomic chains ($E_a = 2.0$ meV/Co atom [59]). Different effects combine in establishing the magnitude of the MAE for the Co adatoms. The reduced coordination leads to 3d-electron localization (band narrowing), which augments the spin–orbit energy due to increases in the local density of states near the Fermi level and the orbital and spin magnetic moment [116, 126].

The influence of the atomic coordination on the MAE and m_L is revealed by measurements on small 2D islands. Figure 21 reports m_L and E_a as a function of n for Co_n/Pt(1 1 1). The smaller n, the larger are the m_L and E_a dependences on changes of the cluster size. Particles with $n = 3$ and 4 atoms have m_L reduced to 0.78 ± 0.05 and $0.59 \pm 0.05\ \mu_B$/atom, respectively. One-atom variations of the particle size cause significant reductions of E_a: for $n = 3$ atoms, $E_a = 3.3 \pm 0.4$ meV/atom, only about 30%

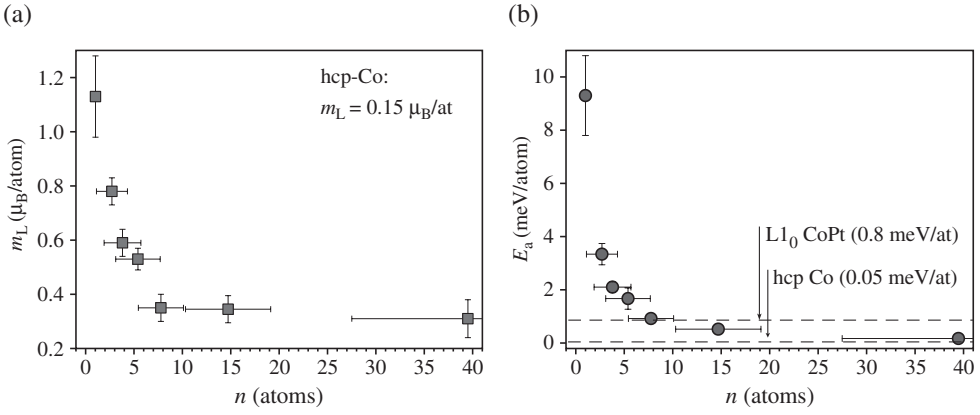

Figure 21: (a) m_L and (b) E_a as a function of average island size n for Co_n/Pt(1 1 1). For comparison, the dashed lines show E_a of the L_{10} CoPt alloy and hcp-Co, respectively. The error bars on the horizontal scale represent the standard deviation of the size distribution as determined by STM [46].

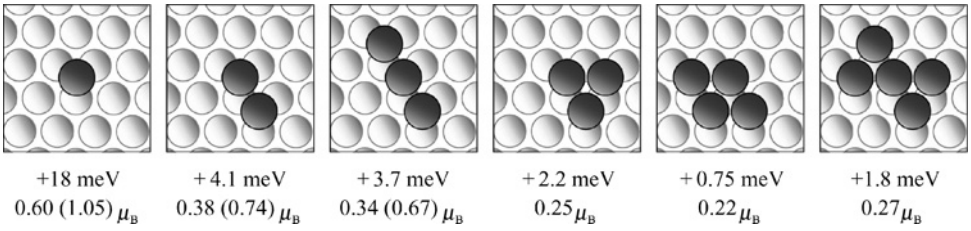

Figure 22: Ab initio calculations of E_a and m_L for Co/Pt(1 1 1) using the spin-polarized-relativistic Korringa–Kohn–Rostocker Greens function method in the spin-density approximation [46]. The Co atoms are on fcc sites. The m_L values in brackets have been computed within the orbital polarization scheme with a 50% reduced Racah parameter. The reported values are averages over all constituent atoms, atoms at different sites within the islands may well have relevant differences in E_a and m_L (see Ref. [127]).

of the single adatom value. Ab initio calculations show that the atomic coordination rather than the absolute particle size is the key to determine m_L and E_a [46, 127] (see Fig. 22). In the experiment, different shapes coexist for each cluster size and the size distribution has a finite width. This makes impossible discerning anisotropies of, e.g., elongated from triangular trimers, having according to the calculations 3.7 and 2.2 meV/atom, respectively.

Comparison between Fig. 21a and b also demonstrates the correlation between m_L and E_a, as expected from a perturbative treatment of the spin–orbit interaction. According to Bruno [116] and van der Laan [126] E_a is directly related to the anisotropy of m_L, and in TM atoms with more than half-filled d-shells the easy axis is the direction where m_L is maximum. In the experiment, the incomplete saturation of the magnetization close to the direction of the hard axis (Fig. 20c) does not allow a precise estimate of the m_L anisotropy via the XMCD sum rule for the orbital moment. However, it is clear that a large m_L anisotropy, hence large E_a values, can be observed only if m_L itself is large, thus explaining the observed correlation between E_a and m_L reported in Fig. 21. In addition to the large orbital moment of Co, the magnetization induced in the substrate creates additional MAE due to the strong spin–orbit coupling of the Pt 5d-states, an effect common to CoPt compounds [128]. The effect of the interaction with the substrate is well revealed by the quite different magnetic properties observed for Co adatoms on alkali metal films, for example K. In contrast to Pt, the outer electronic shell of K has *s*-character, i.e. $L = 0$. In this case the spin–orbit interaction is expected to be absent.

5.2. Magnetic impurities on alkali metals

The degree of hybridization of the electronic states of magnetic adatoms or of very small islands with the substrate determines to which extent the magnetic properties are described by discrete values of the magnetization or by a continuum of values, as in classical magnets. The magnetization as a function of external field under equilibrium conditions is in the first case described by the Brillouin function in the latter by the Langevin function. The fact that the Langevin function had to be used for Co/Pt(1 1 1) suggests that the Co moments behave as classical magnetization vectors emerged in an anisotropy potential energy surface created by the substrate lattice. It is anticipated that under these conditions magnetization reversal takes place by crossing of the

anisotropy barrier, and not by tunneling, as e.g. observed for single molecule magnets which couple less strongly to their environment [129]. Similarly, single adatoms on metal surfaces covered by a few monolayer thick oxide films are expected to have less hybridization, to preserve more of their atomic electronic structure and consequently to show stronger effects of quantization of the magnetic moment [130].

The differences of hybridization and electronic ground state configuration become apparent when comparing different magnetic adatoms on different metal hosts. We discuss XAS and XMCD data probing the local electronic and magnetic structure of Fe, Co, and Ni impurities deposited on K and Na films [131]. K and Na films were evaporated onto a clean Cu(1 1 1) substrate. Transition metals were subsequently deposited in minute quantities, 0.002–0.015 ML, at $T = 10\,\mathrm{K}$ in order to obtain isolated impurities. XAS at the $L_{2,3}$ edges was performed in total electron yield mode using circularly polarized light with 99% polarization in magnetic fields up to $B = \pm 7\,\mathrm{T}$ with the sample at $T = 10\,\mathrm{K}$.

Figure 23 shows the XAS and XMCD spectra recorded for Fe, Co, and Ni impurities deposited on a K film. The XAS spectra present narrow multiplet structures which are not observed for single Co atoms on Pt(1 1 1). This is a clear indication of a strong localization of the 3d electrons on the transition metal impurities. The multiplet structure serves as a sensitive fingerprint of the electronic ground state configuration which can be determined by comparison of the experimental spectra with those calculated by atomic multiplet theory. The spectra shown as insets correspond to the $3d^n \rightarrow 2p^5 3d^{n+1}$ transitions calculated in zero crystal field with an atomic value for the spin–orbit splitting. The comparison of experiment and theory allows unambiguous determination of the respective ground states, i.e., d^7 ($^4F_{9/2}$) for Fe, d^8 ($^3F_4$) for Co, and d^9 ($^2D_{5/2}$) for Ni. These correspond to a magnetic moment $m = g_J \mu_B \sqrt{J(J+1)}$ (here J denotes the generalized angular momentum and not the magnetic exchange

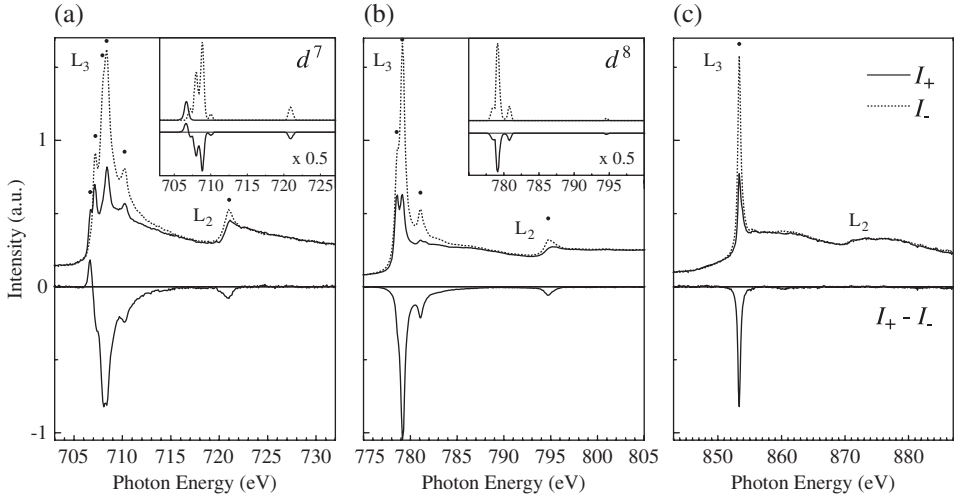

Figure 23: XAS and XMCD spectra of the $L_{2,3}$ edges recorded with parallel (solid line) and anti-parallel (dashed line) alignment of the light helicity with respect to the field direction. (a) 0.015 ML Fe, (b) 0.015 ML Co, and (c) 0.004 ML Ni deposited on K films. The insets of (a) and (b) show the corresponding calculated spectra [132] for atomic d^7 and d^8 configurations [131].

energy as above) of about 6.6 μ_B for Fe, 5.6 μ_B for Co, and 3.6 μ_B for Ni. These values are sensibly higher than the bulk values of 2.2 μ_B, 1.7 μ_B, and 0.6 μ_B, respectively. Another interesting feature is represented by the XMCD at the L_2 edge which has opposite sign with respect to bulk spectra for Fe and Co, whereas it is zero for Ni. The last observation is understood from the ground state configuration d^9 which does not allow L_2 edge transitions, corresponding to the $J = 5/2 \rightarrow J = 1/2$ excitation which is forbidden by the dipole selection rule [133].

6. SPATIALLY RESOLVED MEASUREMENTS OF SPIN POLARIZATION OF MAGNETIC ISLANDS

Magnetic random access memories (MRAMs) will possibly replace our current dynamic random access memories (DRAM) due to their shorter access time, and to the fact that they are non-volatile [134]. A typical MRAM architecture consists of an array of magnetic cells, each consisting of two ferromagnetic layers separated by an insulating barrier. The cells can be designed so that the magnetic moments of the two layers can be parallel or anti-parallel. These states allow a bit of information to be stored. The magnetization of one electrode of the spin-valve is pinned by exchange bias [135], while the orientation of the magnetization of the free layer is controlled by magnetic fields generated by electrical currents. The state of the cells is read by the tunnel magnetoresistance (TMR). In recent literature, the TMR is defined as $(R_a - R_p)/R_p$, with R_a and R_p being the junction resistance for anti-parallel and parallel magnetization of the two ferromagnets, respectively.

MRAMs began to be considered seriously when two groups reported TMR values of 10% at room temperature [136, 137]. The breakthrough was achieved by using amorphous aluminum oxide barriers to make pin-hole-free tunnel barriers. Calculations suggested that much higher values of TMR could be realized by using crystalline rather than amorphous barriers [138, 139]. It was predicted that tunneling through crystalline barriers of materials depends strongly on the symmetry of the wave functions at the Fermi energy. It turns out that the states with the most symmetric wave functions can get through certain barriers much more easily than states with lower symmetry. Some ferromagnetic materials, for example, body-centered-cubic (bcc) Fe, FeCo, and Co, have the property that the high-symmetry state is present for the electrons with majority spin but not for minority electrons. When the moments are parallel, the high-symmetry majority electrons can get through the barrier and enter the electrode on the other side. When the moments are anti-parallel, the high-symmetry majority electrons in one electrode can get through the barrier, but they cannot enter the electrode on the other side unless there is a scattering event that breaks the symmetry. Experimentally, very large values of TMR at room temperature have recently been reported. By using molecular beam epitaxy to produce crystalline interfaces, TMRs of 220 and 410% have been observed with Fe(1 0 0)/MgO(1 0 0)/Fe(1 0 0) [140] and Co(1 0 0)/MgO(1 0 0)/Co(1 0 0) [141] magnetic tunneling junctions.

Nanoparticles could play a leading role in the development of future MRAMs. When magnetic nanoclusters are deposited on a non-magnetic substrate charge transfer, multiple electronic scattering and interference phenomena generally govern the electronic and the magnetic properties of the combined system. For example, surface states of non-magnetic noble metal substrates, such as Cu(1 1 1), turn spin polarized

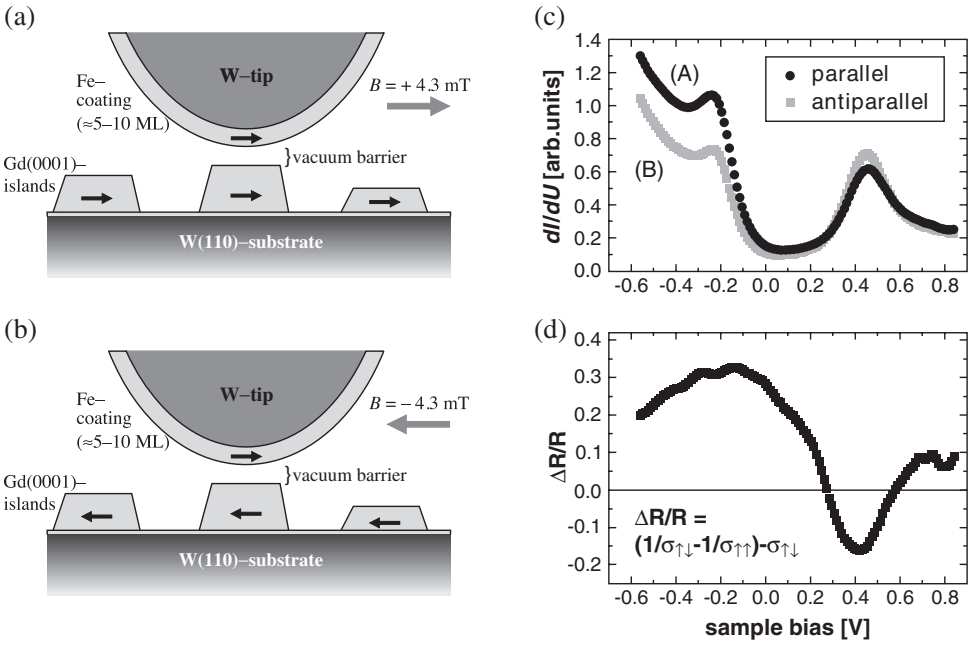

Figure 24: (a) and (b) Schematic drawing of the experimental setup for measuring the vacuum TMR between an Fe-coated W tip and a Gd(0 0 0 1) island on W(1 1 0). (c) Tunnel conductance dI/dV for parallel and anti-parallel alignment of tip and sample magnetization ($T = 70$ K). (d) Resistance changes as function of bias voltage [142].

and attain a different character when Co nanoislands are added to the substrate surface [94, 95]. Such spin-polarized surface states (SP-SS) can serve as spin-transport channels across the vacuum barrier to or from another magnetic material, an issue which is of central importance for spintronic applications based on spin-polarized tunneling. STM experiments by Wiesendanger et al. indicate that TMR is maximized by tunneling to a SP-SS [142]. The experimental situation is schematically depicted in Fig. 24. An Fe-coated W tip, prepared by in situ thin-film deposition in a UHV system containing a variable-temperature STM, is positioned above a Gd(0 0 0 1) island grown on a W(1 1 0) substrate. Gd islands of a few 100 nm diameter exhibit a very low coercivity on the order of 11 mT. Therefore, an external field of a few mT applied in the sample plane was found to be sufficient for switching the magnetization direction of the Gd islands while leaving the magnetization state of the Fe coated tip unaffected. With the feedback loop open, the bias voltage V was ramped between –0.6 and 0.8 V and the differential conductance dI/dV(V) was measured. This signal is approximately proportional to the LDOS at the position of the tip.

Figure 24c shows two conductance curves corresponding to the experimental situations depicted in Fig. 24a and b. Pronounced maxima are observed in both spectra at $V_1 = -0.2$ V and $V_2 = 0.45$ V corresponding to the energies of the two spin components of an exchange-split d_z^2 surface state of Gd(0 0 0 1). The asymmetry between spectrum (A) and (B) is due to the spin-valve effect enhancing the conductance for the surface-state spin component being parallel to the majority spin states of the tip and

reducing it for the anti-parallel component. The resistance change as function of bias voltage is plotted in Fig. 24d. It reaches 31% (TMR = 45%) for the filled and 13% for the empty part of the two spin components of the exchange-split surface state.

TMR values up to 850% were reported for STM tunnel junctions formed by out-of-plane magnetized ferromagnetic bilayer Co islands on Pt(1 1 1) and an anti-ferromagnetic Cr-coated W-tip [143]. Co double-layer islands were created by deposition of 0.40 ML on the Pt(1 1 1) substrate held at 130 K and subsequent annealing to 340 K [39]. The –9.4% misfit between Co and Pt leads to partial dislocations in the first layer [58], whereas in double-layer islands the stress is relieved by a moiré structure [144, 145], see the superstructure on-top of the islands in Fig. 25a. When imaged with a Cr-coated W-tip, in addition to the corrugation of the moiré, one clearly discerns two island species by an apparent height difference (see Fig. 25b). This contrast is magnetic since it is only obtained with magnetic tips (either Cr-coated W-tips, or NiMn bulk-tips), and it vanishes above the island blocking temperature of $T_b = 180$ K, independently determined by means of MOKE measurements [39]. The MOKE measurements also reveal out-of-plane magnetization in agreement with the fact that spin

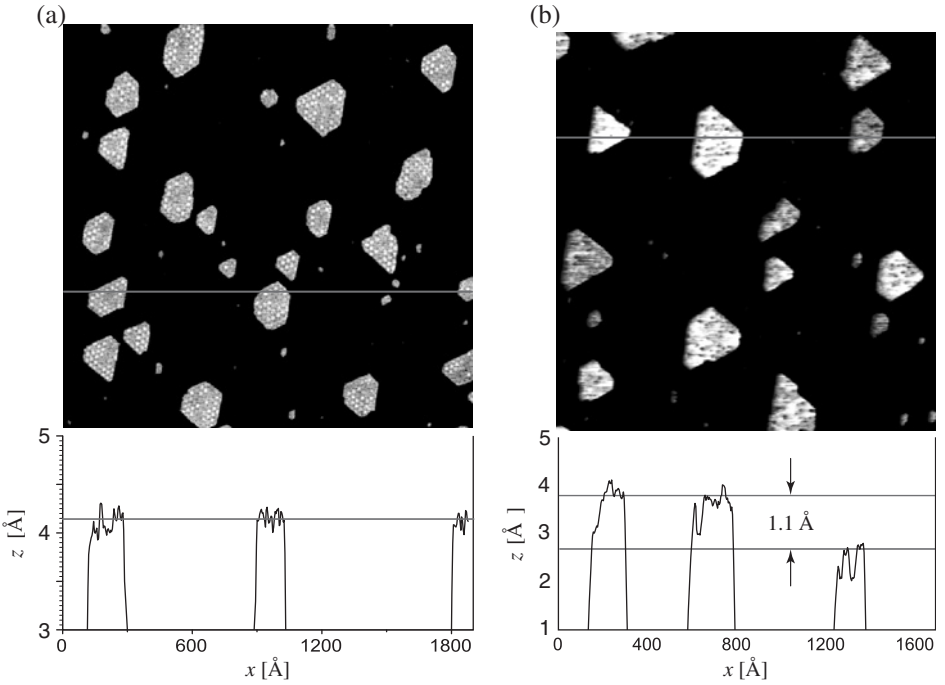

Figure 25: (a) Constant current STM image of double-layer Co islands recorded with a bare W tip. The moiré structure has an apparent height corrugation of 0.30 ± 0.03 Å ($T_{sample} = 140$ K, $V_t = -0.2$ V and $I_t = 1.0$ nA). (Bottom panel) Constant current profile obtained by averaging over ± 5 line scans around the marked position. All islands appear with identical heights irrespective of their magnetization (absence of spin contrast). (b) Constant current STM image of double-layer Co islands recorded with a Cr-coated W tip ($T_{sample} = 140$ K, $T_{tip} \approx 280$ K, $V_t = -0.2$ V, $I_t = 0.3$ nA). (Bottom) Averaged (± 5 lines) line scan at the indicated position revealing a surprisingly high difference of 1.1 ± 0.1 Å in the apparent height of islands with opposite magnetization [143, 147].

contrast is only observed with a Cr coating thickness of 20–40 ML reported to give out-of-plane polarization of the tip [146]. The magnetic contrast typically amounts to $\Delta z = 0.20 \pm 0.05$ Å, but occasionally values as high as $\Delta z = 1.1 \pm 0.1$ Å were also measured (see Fig. 25b). The contrast in apparent height can be converted into a TMR-value as follows:

$$\Delta R/R = \frac{R_a - R_p}{R_p} = \frac{I_p}{I_a} - 1 = \exp(A\sqrt{\phi}\Delta z) - 1 \tag{6}$$

where ϕ is the average over the work-functions of tip and sample and $A = 2\sqrt{2m_e/h^2} = 1.025\ \mathrm{eV}^{-1/2}\ \mathrm{Å}^{-1}$. Assuming a typical value of $\phi = 4$ eV yields TMR values of $\Delta R/R = 50 \pm 15\%$ for $\Delta z = 0.2$ Å and $\Delta R/R = 850 \pm 200\%$ for $\Delta z = 1.1$ Å, respectively.

The junction polarization is derived from the magnetic contrast by

$$P = P_t P_S = \frac{I_p - I_a}{I_p + I_a} = \frac{\exp(A\sqrt{\phi}\Delta z) - 1}{\exp(A\sqrt{\phi}\Delta z) + 1} \tag{7}$$

One finds $P = 0.20 \pm 0.05$ and 0.80 ± 0.04 for $\Delta z = 0.20 \pm 0.05$ Å and $\Delta z = 1.1 \pm 0.1$ Å, respectively. $P = 0.20 \pm 0.05$ is comparable with polarization values reported between Co(0 0 0 1) surfaces and amorphous Co-based alloy tips [148]. However, 80% polarization of the tunnel barrier implies a polarization of the Co islands of at least 80%, about two times larger than the value determined by Andreev reflection for Co bulk [149, 150]. This can be rationalized by the low dimensionality of the islands increasing the density of states at the Fermi level, or by k-selective tunneling leading to a higher polarization than the state averaged value. The strong polarization of the tip, which must have been close to 100% in this experiment, can possibly be caused by chemisorbed species at the tip apex.

Recently, a theoretical work suggested the modulation and control of the spin-polarized surface states based on an appropriate design of the nanostructure geometry, such as the size of the islands [151]. The idea consists in the spatial and energetic tuning of the spin polarization of islands by means of quantum confinement. Figure 26 reports the result of calculations for equilateral triangular islands of Co on Cu(1 1 1).

This prediction was experimentally confirmed by Pietzsch et al. by using a low-temperature STM with a Cr-coated W-tip [152]. Figures 27a and b show $\mathrm{d}I/\mathrm{d}V$ maps at bias voltages allowing to observe the standing wave patterns on both the Cu substrate and on the Co islands. The contrasts between islands are due to their magnetization being oriented either up or down, that is, parallel or anti-parallel to the tip magnetization. The contrast inversion between (a) and (b) is not caused by a magnetization reversal of either tip or sample, but is the result of contributions to the LDOS from states of opposite spin, their relative weights depending on the applied bias. The chromium at the tip has an electronic structure dominated by minority spin states near the Fermi level [153], allowing a very effective tunneling between tip and sample minority states for parallel magnetization of both electrodes. The bias voltage of Fig. 27a has been chosen in a range where the main contribution to the sample LDOS comes from the dispersive majority spin state which is responsible for the

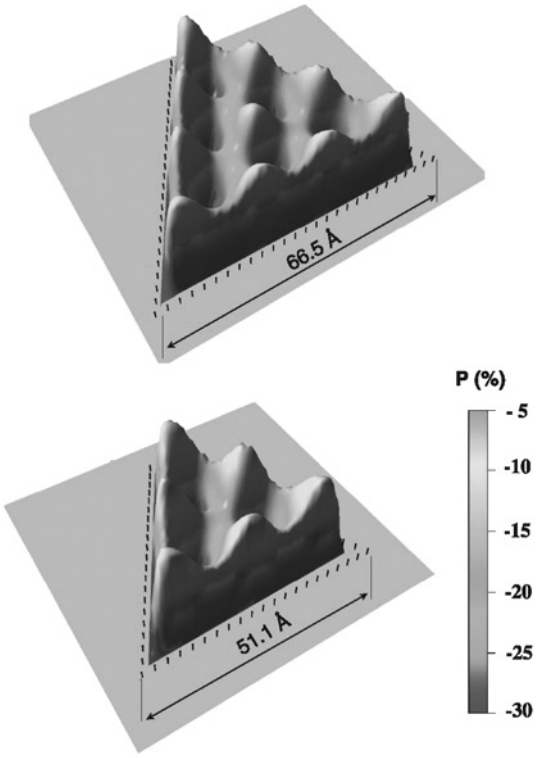

Figure 26: Spin polarization of surface-state electrons on triangular Co islands on Cu(1 1 1); calculations are performed for $E = 0.5\,\text{eV}$ above E_F [151].

standing wave pattern. Therefore, the islands exhibit inverted contrast for energies higher than about –0.065 eV.

In a narrow energy window between 0.18 and 0.43 eV above the Fermi level, the islands return to normal spin contrast as shown in Fig. 27b. In this interval an unoccupied localized minority spin d-state outweighs the majority band. Figure 27c also shows the effect of electron confinement, manifest in the evolution of the standing wave periods as a function of bias voltage. The inset of Fig. 27c allows for a comparison of the dispersive behavior of the Co islands and the Cu substrate. Both data sets were fitted (solid lines) assuming a 2D free electron gas, confined for Co but not for Cu. While the Cu values match the fit parabola very well, the Co data display a steplike structure. The effect of SP-SS on the Co patterns is displayed in Fig. 27d showing $\mathrm{d}I/\mathrm{d}V$ profiles taken along lines as indicated in Fig. 27a for bias voltages being representative for ranges of inverse, balanced, and normal spin contrast. In each case, the standing wave amplitude is found to be significantly larger on the anti-parallel island, regardless of the sign of the bias-dependent spin-polarization. The amplitude ratios of the parallel and anti-parallel case are 0.49, 0.40, and 0.32 at the respective voltages. Qualitatively, this behavior is explained as follows. Because the tip has an effective negative SP within the energy range relevant for the standing wave observation, tunneling into the oscillatory majority surface state band is not very efficient for the parallel configuration. By contrast, in anti-parallel magnetized islands,

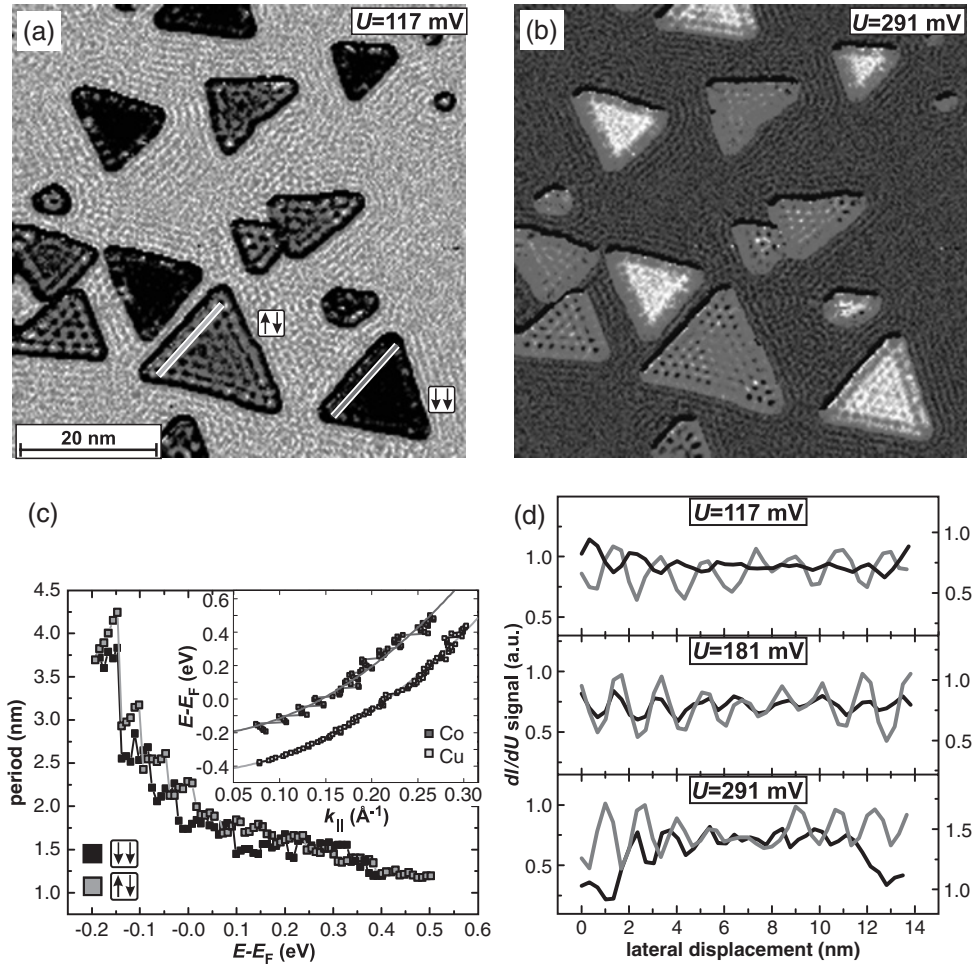

Figure 27: Co islands on Cu(111) ($\theta = 0.6$ ML, $T = 14$ K). (a) and (b) $\mathrm{d}I/\mathrm{d}V$ maps at indicated bias voltages showing standing wave patterns on Cu substrate and Co islands. Arrows indicate parallel ($\uparrow\uparrow$) or anti-parallel ($\uparrow\downarrow$) magnetization of islands and tip. (c) Standing wave periods on Co islands as a function of bias voltage. (Inset) E–E_F vs. $k_{\|}$ for Co and Cu. (d) $\mathrm{d}I/\mathrm{d}V$ profiles taken along lines indicated in (a). Regardless of the bias voltage, the standing wave amplitude is larger on the anti-parallel island [152].

the role of minority and majority spins is exchanged with respect to the tip. As a consequence, the oscillatory state in anti-parallel islands has the matching spin character for an effective tunneling of the excess tip minority spin electrons, resulting in an enhanced scattering amplitude. Only delocalized sample majority electrons take part in the LDOS oscillations while localized minority d-like electrons do not. Still, the net balance of contributions from majority and minority states to the sample LDOS determines the overall contrast between the islands which may be normal or inverted (or balanced at the point of sign inversion), depending on the bias voltage; the standing wave pattern is then superimposed onto this background signal.

The experimental data did not reveal any spin-induced modification of the Cu oscillation pattern in the immediate vicinity of oppositely magnetized Co islands.

However, a remarkable feature was found in the island rims. The spin character of the rim state is opposite to that exhibited by the island at the corresponding energy, emphasizing that the spin polarization, on a lateral scale of a few angstroms, may not only change its magnitude but also its sign, depending on the electronic states involved.

7. CONCLUSIONS AND OUTLOOK

Experiments of small well-defined magnetic islands have significantly improved our understanding of orbital magnetism. Orbital moments and anisotropy energies have been determined for Co/Pt(1 1 1) as function of island size from single atoms up to large islands. They reveal a direct link between preserved orbital moments in low-coordinated atoms and their high anisotropy. From thin film studies these effects were anticipated, however, the order of magnitude of the anisotropies was a surprise. Co step atoms reach anisotropies of very hard magnetic alloys and Co adatoms have 10 times higher values. This implies blocking temperatures of Co monomers of $T_b = 4.3\,\mathrm{K}$ ($K = 9.3\,\mathrm{meV}$), while due to the steep decrease of anisotropy with increasing coordination a Co heptamer has $T_b = 3.2\,\mathrm{K}$ ($K = 7\,\mathrm{meV}$). By contrast, due to the different moments, the coercitive field of monomers ($m = 5\,\mu_B$) is 32 T, while the one of heptamer ($m = 21\,\mu_B$) is 6 T.

For larger islands, the mechanism of thermal magnetization reversal has been seen to vary from system to system. As anticipated, compact islands show coherent rotation up to larger sizes than ramified ones. Also, the Curie temperatures of the first are larger than for the latter. The transition between the two reversal modes can be calculated knowing the exchange stiffness J, which is only known for bulk and films of several ML thickness. Therefore, SP-STM measurements of the width of domain walls in monolayer films are very valuable.

SP-STM has been developed as a reliable tool for the determination of spin-polarization and tunnel magneto-resistance of junctions with 2D islands. However, de-convolution of tip and sample polarizations remains a challenge and one has to rely on calculations. SP-STM may also be used in the future to locally check whether the above-mentioned blocking temperatures are indeed characterizing individual islands. This is worthwhile since thermal magnetization reversal may take place along a direction of M which has not been explored in the XMCD measurements of K. Whether single magnetic atoms or small islands behave a classical moment or have quantized orientations of M, and under which conditions they reverse by thermally activated barrier crossing or by tunneling depends on the interaction with the substrate and is expected to vary from metals to insulators.

Although progress has been made, the self-assembly of regular lattices of uniaxial out-of-plane islands with $T_b = 350\,\mathrm{K}$, absence of dipolar interactions, and narrow distributions of K and M continues to be a challenge. New promising template surfaces have been discovered possibly enabling also the growth of superlattices of bi-metallic particles. Bi-metallic islands promise to have higher anisotropies for given size and therefore will be interesting to investigate again by combination of atomic scale and spatially integrating techniques. At the end, one would like to grow upstanding pillars since then also the shape anisotropy favors out-of-plane easy axis and the pillars can reach high blocking temperatures while taking only little space in the sample plane.

REFERENCES

[1] Chou S.Y., IEEE Proc. 85 (1997) 652.
[2] Harris J., Awschalom D., Phys. World 12 (1999) 19.
[3] Albrecht M., Rettner C., Moser A., Best M., Terris B., Appl. Phys. Lett. 81 (2002) 2875.
[4] Plumer M.L., van Ek J., Weller D. (eds), The Physics of Ultra-High-Density Magnetic Recording, Springer Series in Surface Sciences, Vol. 41, Springer, Berlin, 2001.
[5] Woods S.I., Kirtley J.R., Sun S., Koch R.H., Phys. Rev. Lett. 87 (2001) 137205.
[6] Petit C., Taleb A., Pileni M., Adv. Mater. 10 (1998) 259.
[7] Puntes V., Krishnan J., Appl. Phys. Lett. 78 (1999) 2187.
[8] Petit C., Rusponi S., Brune H., J. Appl. Phys. 95 (2004) 4251.
[9] Antoniak C., Lindner J., Spasova M., Sudfeld D., Acet M., Farle M., Fauth K., Wiedwald U., Boyen H.G., Ziemann P., Wilhelm F., Rogalev A., Sun S. Phys. Rev. Lett 97 (2006) 117201.
[10] Jamet M., Wernsdorfer W., Thirion C., Mailly D., Dupuis V., Mélinon P., Pérez A., Phys. Rev. Lett. 86 (2001) 4676.
[11] Held G.A., Grinstein G., Doyle H., Sun S., Murray C.B., Phys. Rev. B 64 (2001) 012408.
[12] Sun S., Murray C., Weller D., Folks L., Moser A., Science 287 (2000) 1989.
[13] Black C.T., Murray C.B., Sandstrom R.L., Sun S., Science 290 (2000) 1131.
[14] Brune H., Giovannini M., Bromann K., Kern K., Nature 394 (1998) 451.
[15] Repain V., Baudot G., Ellmer H., Rousset S., Europhys. Lett. 58 (2002) 730.
[16] Weiss N., Cren T., Epple M., Rusponi S., Baudot G., Rohart S., Tejeda A., Repain V., Rousset S., Ohresser P., Scheurer F., Bencok P., Brune H., Phys. Rev. Lett. 95 (2005) 157204.
[17] Bansmann J., Baker S.H., Binns C., Blackman J.A., Bucher J.P., Dorantes-Dávila J., Dupuis V., Favre L., Kechrakos D., Kleibert A., Meiwes-Broer K.H., Pastor G.M., Perez A., Toulemonde O., Trohidou K.N., Tuaillon J., Xie Y., Surf. Sci. Rep. 56 (2005) 189.
[18] Himpsel F.J., Ortega J.E., Mankey G.J., Willis R.F., Adv. Phys. 47 (1998) 511.
[19] Hopster H., Oepen H.P. (eds), Magnetic Microscopy of Nanostructures, Nanoscience and Technology, Springer, Berlin, 2005.
[20] Sellmyer D.J., Skomski R. (eds), Advanced Magnetic Nanostructures, Springer, 2006.
[21] Bell G.M., Lavis D.A., Statistical Mechanics of Lattice Models, Vol. 1, Ellis Horwood Limited, Chichester, 1989.
[22] Wernsdorfer W., Orozco E.B., Hasselbach K., Benoit A., Barbara B., Demoncy N., Loiseau A., Pascard H., Mailly D., Phys. Rev. Lett. 78 (1997) 1791.
[23] Neel I., Ann. Geophys. 5 (1949) 99.
[24] Brown W., Phys. Rev. 130 (1963) 1677.
[25] Bode M., Pietzsch O., Kubetzka A., Wiesendanger R., Phys. Rev. Lett. 92 (2004) 067201.
[26] Braun H.-B., Phys. Rev. Lett. 71 (1993) 3557.
[27] Braun H.-B., Phys. Rev. B 50 (1994) 16485.
[28] Braun H.-B., Phys. Rev. B 50 (1994) 16501.
[29] Braun H.-B., J. Appl. Phys. 85 (1999) 6172.
[30] Brown G., Novotny M.A., Rikvold P.A., Phys. Rev. B 64 (2001) 134422.
[31] Forster H., Bertram N., Wang X., Dittrich R., Schrefl T., J. Magn. Magn. Mater. 267 (2003) 69.
[32] Khapikov A.F., J. Appl. Phys. 89 (2001) 7454.
[33] Cowburn R., Koltsov D., Adeyeye A., Welland M., Phys. Rev. Lett. 83 (1999) 1042.
[34] Yamasaki A., Wulfhekel W., Hertel R., Suga S., Kirschner J., Phys. Rev. Lett. 91 (2003) 127201.
[35] Aharoni A., Introduction to the Theory of Ferromagnetism, International Series of Monographs on Physics, Vol. 93, Oxford Science Publications, 1996.

[36] Skomski R., Oepen H.-P., Kirschner J., Phys. Rev. B 58 (1998) 3223.
[37] Brune H., Surf. Sci. Rep. 31 (1998) 121.
[38] Evans J.W., Bartelt M.C., Phys. Rev. B 63 (2001) 235408.
[39] Rusponi S., Cren T., Weiss N., Epple M., Buluschek P., Claude L., Brune H., Nat. Mater. 2 (2003) 546.
[40] Chantrell R.W., Ayoub N.Y., Popplewell J., J. Magn. Magn. Mater. 53 (1985) 199.
[41] Fruchart O., Jubert P.O., Meyer C., Klaua M., Barthel J., Kirschner J., J. Magn. Magn. Mater. 239 (2002) 224.
[42] Koide T., Miyauchi H., Okamoto J., Shidara T., Fujimori A., Fukutani H., Amemiya K., Takeshita H., Yuasa S., Katayama T., Suzuki Y., Phys. Rev. Lett. 87 (2001) 257201.
[43] Wu R., Li C., Freeman A.J., J. Magn. Magn. Mater. 99 (1991) 71.
[44] Nakajima N., Koide T., Shidara T., Miyauchi H., Fukutani H., Fujimori A., Iio K., Katayama T., Nyvlt M., Suzuki Y., Phys. Rev. Lett. 81 (1998) 5229.
[45] Ferrer S., Alvarez J., Lundgren E., Torrelles X., Fajardo P., Boscherini F., Phys. Rev. B 56 (1997) 9848.
[46] Gambardella P., Rusponi S., Veronese M., Dhesi S.S., Grazioli C., Dallmeyer A., Cabria I., Zeller R., Dederichs P.H., Kern K., Carbone C., Brune H., Science 300 (2003) 1130.
[47] Pick C., Stepanyuk V.S., Baranov A.N., Hergert W., Bruno P., Phys. Rev. B 68 (2003) 104410.
[48] Dürr H.A., Dhesi S.S., Dudzik E., Knabben D., Laan G.v.d., Goedkoop J.B., Hillebrecht F.U., Phys. Rev. B 59 (1999) R701.
[49] Zhang R., Willis R., Phys. Rev. Lett. 86 (2001) 2665.
[50] Frota-Pessôa S., Muniz R., Kudrnovsky J., Phys. Rev. B 62 (2000) 5293.
[51] Robach O., Quiros C., Steadman P., Peters K.F., Lundgren E., Alvarez J., Isern H., Ferrer S., Phys. Rev. B 65 (2002) 054423.
[52] Chantrell R.W., Walmsley N., Gore J., Maylin M., Phys. Rev. B 63 (2001) 024410.
[53] Haginoya C., Heike S., Ishibashi M., Nakamura K., Koike K., Yoshimura T., Yamamoto Y., Hirayama Y., J. Appl. Phys. 85 (1999) 8327.
[54] Sharrock M.P., IEEE Trans. Mag. 26 (1990) 193.
[55] We used the OOMMF program, release 1.1 beta 2 (http://math.nist.gov/oommf/).
[56] Schilfgaarde M.v., Antropov V.P., J. Appl. Phys. 85 (1999) 4827.
[57] Etzkorn M., Anil Kumar P.S., Tang W., Zhang Y., Kirschner J., Phys. Rev. B 72 (2005) 184420.
[58] Cren T., Rusponi S., Weiss N., Epple M., Brune H., J. Phys. Chem. B 108 (2004) 14685.
[59] Gambardella P., Dallmeyer A., Maiti K., Malagoli M., Eberhardt W., Kern K., Carbone C., Nature 416 (2002) 301.
[60] Hill T., Mozaffari-Afshar M., Schmidt J., Risse T., Freund H.J., Surf. Sci. 429 (1999) 246.
[61] Skumryev V., Stoyanov S., Zhang Y., Hadjipanayis G., Givord D., Nogués J., Nature 423 (2003) 850.
[62] Gambardella P., Šljivančanin Ž., Hammer B., Blanc M., Khunke K., Kern K., Phys. Rev. Lett 87 (2001) 056103.
[63] Petit C., Taleb A., Pileni M.P., J. Phys. Chem. B 103 (1999) 1805.
[64] Albrecht M., Hu G., Guhr I.L., Ulbrich T.C., Boneberg J., Leiderer P., Schatz G., Nat. Mater. 4 (2005) 203.
[65] Boneberg J., Burmeister F., Schafle C., Leiderer P., Reim D., Fery A., Herminghaus S., Langmuir 13 (1997) 7080.
[66] Barth J.V., Brune H., Ertl G., Behm R.J., Phys. Rev. B 42 (1990) 9307.
[67] Brune H., Kern K., in: Growth and Properties of Ultrathin Epitaxial Layers, D.A. King, D.P. Woodruff (eds.), Vol. 8 of The Chemical Physics of Solid Surfaces and Heterogeneous Catalysis, Elsevier Science, Amsterdam, 1997, p. 149.
[68] Brune H., Röder H., Boragno C., Kern K., Phys. Rev. B 49 (1994) 2997.

[69] Günther C., Vrijmoeth J., Hwang R.Q., Behm R.J., Phys. Rev. Lett. 74 (1995) 754.
[70] Brune H., Bromann K., Röder H., Kern K., Jacobsen J., Stoltze P., Jacobsen K., Nørskov J., Phys. Rev. B 52 (1995) R14380.
[71] Meyer J.A., Schmid P., Behm R.J., Phys. Rev. Lett. 74 (1995) 3864.
[72] Fischer B., Brune H., Fricke A., Barth J.V., Kern K., Phys. Rev. Lett. 82 (1999) 1732.
[73] Michely T., Hohage M., Esch S., Comsa G., Surf. Sci. 349 (1996) L89.
[74] Meyer J.A., Baikie J.D., Kopatzki E., Behm R.J., Surf. Sci. 365 (1996) L647.
[75] Takeshita H., Suzuki Y., Akinaga H., Mizutani W., Ando K., Katayama T., Itoh A., Tanaka K., J. Magn. Magn. Mater. 165 (1997) 38.
[76] Padovani S., Chado I., Scheurer F., Bucher J.P., Phys. Rev. B. 59 (1999) 11887.
[77] Chambliss D.D., Wilson R.J., Chiang S., Phys. Rev. Lett. 66 (1991) 1721.
[78] Voigtländer B., Meyer G., Amer N.M., Phys. Rev. B 44 (1991) 10354.
[79] Padovani S., Molinàs-Mata P., Scheurer F., Bucher J.P., Appl. Phys. A 66 (1998) 1199.
[80] Voigtländer B., Meyer G., Amer N.M., Surf. Sci. 255 (1991) L529.
[81] Stroscio J.A., Pierce D.T., Dragoset R.A., First P.N., J. Vac. Sci. Technol. A 10 (1992) 1981.
[82] Altman E.I., Colton R.J., Surf. Sci. 304 (1994) L400.
[83] Chambliss D.D., Wilson R.J., J. Vac. Sci. Technol. B 9 (1991) 928.
[84] Krzyzowski M.A., Ph.D. thesis, Bonn, 1995.
[85] Fischer B., Barth J.V., Fricke A., Nedelmann L., Kern K., Surf. Sci. 389 (1997) 366.
[86] N'Diaye A., Bleikamp S., Feibelman P.J., Michely T., Phys. Rev. Lett. 97 (2006) 215501.
[87] Bromann K., Giovannini M., Brune H., Kern K., Eur. Phys. J. D 9 (1999) 25.
[88] Giovannini M., Metallic Thin Layers and Nanostructures: Fabrication and Characterization, Ph.D. thesis, EPFL, 2000.
[89] Holst B., Hohlen M., Wandelt K., Allison W., Surf. Sci. 377–379 (1997) 891.
[90] Pedersen M.Ø., Bönicke I.A., Lægsgaard E., Stensgaard I., Ruban A., Nørskov J.K., Besenbacher F., Surf. Sci. 387 (1997) 86.
[91] Figuera J.d.l., Prieto J.E., Ocal C., Miranda R., Phys. Rev. B 47 (1993) 13043.
[92] Figuera J.d.a., Prieto J.E., Kostka G., Müller S., Ocal C., Miranda R., Heinz K., Surf. Sci. 349 (1996) L139.
[93] Rabe A., Memmel N., Steltenpohl A., Fauster T., Phys. Rev. Lett. 73 (1994) 2728.
[94] Diekhöner L., Schneider M.A., Baranov A.N., Stepanyuk V.S., Bruno P., Kern K., Phys. Rev. Lett. 90 (2003) 236801.
[95] Pietzsch O., Kubetzka A., Bode M., Wiesendanger R., Phys. Rev. Lett. 92 (2004) 057202.
[96] Repain V., Baudot G., Ellmer H., Rousset S., Europhys. Lett. 58 (2002) 730.
[97] Repain V., Baudot G., Ellmer H., Rousset S., Mater. Sci. Eng. B 96 (2002) 178.
[98] Rohart S., Baudot G., Repain V., Girard Y., Rousset S., Bulou H., Goyhenex C., Proville L., Surf. Sci. 559 (2004) 47.
[99] Brune H., in: Properties of Single Organic Molecules on Crystal Surfaces, F. Rosei, P. Grütter, W. Hofer (eds.), Springer, New York, 2006, p. 247.
[100] Besenbacher F., Nielsen L.P., Sprunger P.T., in: Growth and Properties of Ultrathin Epitaxial Layers, D.A. King, D.P. Woodruff (eds), Vol. 8 of The Chemical Physics of Solid Surfaces and Heterogeneous Catalysis, Elsevier Science, Amsterdam, 1997, p. 207.
[101] Böhringer M., Jiang Q., Berndt R., Schneider W.D., Zegenhagen J., Surf. Sci. 367 (1996) 245.
[102] Wiederholt T., Brune H., Wintterlin J., Behm R.J., Ertl G., Surf. Sci. 324 (1995) 91.
[103] Degen S., Krupski A., Kralj M., Langner A., Becker C., Sokolowski M., Wandelt K., Surf. Sci. 576 (2005) L57.
[104] Corso M., Auwärter W., Muntwiler M., Tamai A., Greber T., Osterwalder J., Science 303 (2004) 217.
[105] Becker C., Rosenhahn A., Wiltner A., Bergmann K.v., Schneider J., Pervan P., Milun M., Kralj M., Wandelt K., New J. Phys. 4 (2002) 75.

[106] Degen S., Becker C., Wandelt K., Faraday Discuss 125 (2004) 343.
[107] Lehnert A., Krupski A., Degen S., Franke K., Decker R., Rusponi S., Kralj M., Becker C., Brune H., Wandelt K., Surf. Sci. 600 (2006) 1804.
[108] Weaver J.H., Waddill G.D., Science 251 (1991) 1444.
[109] Vandoni G., Félix C., Monot R., Buttet J., Harbich W., Chem. Phys. Lett. 229 (1994) 51.
[110] Bromann K., Félix C., Brune H., Harbich W., Monot R., Buttet J., Kern K., Science 274 (1996) 956.
[111] Thole B., Carra P., Sette F., van der Laan G., Phys. Rev. Lett. 68 (1992) 1943.
[112] Carra P., Thole B., Altarelli M., Wang X., Phys. Rev. Lett. 70 (1993) 694.
[113] Gambardella P., Dallmeyer A., Maiti K., Malagoli M., Rusponi S., Ohresser P., Eberhardt W., Carbone C., Kern K., Phys. Rev. Lett. 93 (2004) 077203.
[114] Ohresser P., Brookes N.B., Padovani S., Scheurer F., Bulou H., Phys. Rev. B 64 (2001) 104429.
[115] Chen C., Ydzerda Y., Lin H.-J., Smith N.V., Meigs G., Chaban E., Ho G.H., Pellegrin E., Sette F., Phys. Rev. Lett. 75 (1995) 152.
[116] Bruno P., Phys. Rev. B 39 (1989) 865.
[117] Weller D., Stöhr J., Nakajima R., Carl A., Samant M.G., Chappert C., Mégy R., Beauvillain P., Veillet P., Held G.A., Phys. Rev. Lett. 75 (1995) 3752.
[118] Stöhr J., J. Magn. Magn. Mater. 200 (1999) 470.
[119] Fruchart O., Klaua M., Barthel J., Kirschner J., Phys. Rev. Lett. 83 (1999) 2769.
[120] Nonas B., Cabria I., Zeller R., Dederichs P.H., Huhne T., Ebert H., Phys. Rev. Lett. 86 (2001) 2146.
[121] Félix-Medina R., Guirado-López R., Dorantes-Dávila J., Pastor G.M., J. Appl. Phys. 87 (2000) 4894.
[122] Wildberger K., Stepanyuk V.S., Lang P., Zeller R., Dederichs P.H., Phys. Rev. Lett. 75 (1995) 509.
[123] Billas I.M.L., Châtelain A., Heer W.A.d., Science 265 (1994) 1682.
[124] Apsel S.E., Emmert J.W., Deng J., Bloomfield L.A., Phys. Rev. Lett. 76 (1996) 1441.
[125] Weller D., Moser A., IEEE Trans. Mag. 35 (1999) 4423.
[126] van der Laan G., J. Phys.: Condens. Matter 10 (1998) 3239.
[127] Lazarovits B., Szunyogh L., Weinberger P., Phys. Rev. B 67 (2003) 024415.
[128] Solovyev I.V., Dederichs P.H., Mertig I., Phys. Rev. B 52 (1995) 13419.
[129] Mishra A., Wernsdorfer W., Abboud K.A., Christou G., J. Am. Chem. Soc. 126 (2004) 15648.
[130] Hirjibehedin C.F., Lutz C.P., Heinrich A.J., Science 312 (2006) 1021.
[131] Gambardella P., Dhesi S.S., Gardonio S., Grazioli C., Ohresser P., Carbone C., Phys. Rev. Lett. 88 (2002) 047202.
[132] van der Laan G., Thole B.T., Phys. Rev. B 43 (1991) 13401.
[133] van der Laan G., Thole B.T., Phys. Rev. B 42 (1990) 6670.
[134] Gallagher W.J., Parkin S.P., IBM J. Res. Dev. 50 (2006) 5.
[135] Parkin S.S.P., Xin J., Kaiser C., Panchula A., Roche K., Samant M., IEEE Proc 91 (2003) 661.
[136] Moodera J.S., Kinder L.R., Wong T.M., Meservey R., Phys. Rev. Lett. 74 (1995) 3273.
[137] Miyazaki T., Tezuka N., J. Magn. Magn. Mater. 139 (1995) L231.
[138] Butler W.H., Zhang X.-G., Schulthess T.C., MacLaren J.M., Phys. Rev. B 63 (2001) 054416.
[139] Mathon J., Umerski A., Phys. Rev. B 63 (2001) 220403.
[140] Parkin S.S.P., Kaiser C., Panchula A., Rice P.M., Hughes B., Samant M., Yang S.H., Nat. Mater. 3 (2004) 862–867.
[141] Yuasa S., Fukushima A., Kubota H., Suzuki Y., Ando K., Appl. Phys. Lett. 89 (2006) 042505.

[142] Wiesendanger R., Bode M., Getzlaff M., Appl. Phys. Lett. 75 (1999) 124.
[143] Rusponi S., Weiss N., Cren T., Epple M., Brune H., Appl. Phys. Lett. 87 (2005) 162514.
[144] Grütter P., Dürig U.T., Phys. Rev. B 49 (1994) 2021.
[145] Lundgren E., Stanka B., Schmid M., Varga P., Phys. Rev. B 62 (2000) 2843.
[146] Kubetzka A., Bode M., Pietzsch O., Wiesendanger R., Phys. Rev. Lett. 88 (2002) 057201.
[147] Brune H., e-J. Surf. Sci. Nanotechnol. 4 (2006) 478.
[148] Ding H.F., Wulfhekel W., Henk J., Bruno P., Kirschner J., Phys. Rev. Lett. 90 (2003) 116603.
[149] Soulen R.J., Jr., Byers J.M., Osofsky M.S., Nadgorny B., Ambrose T., Cheng S.F., Broussard P.R., Tanaka C.T., Nowak J., Moodera J.S., Barry A., Coey J.M.D., Science 282 (1998) 85.
[150] Upadhyay S.K., Palanisami A., Louie R.N., Buhrman R.A., Phys. Rev. Lett. 81 (1998) 3247.
[151] Niebergall L., Stepanyuk V.S., Berakdar J., Bruno P., Phys. Rev. Lett. 96 (2006) 127204.
[152] Pietzsch O., Okatov S., Kubetzka A., Bode M., Heinze S., Lichtenstein A., Wiesendanger R., Phys. Rev. Lett. 96 (2006) 237203.
[153] Rau C., Eichner S., Phys. Rev. Lett. 47 (1981) 939.

Chapter 12

Electronic structure and magnetic properties of small deposited transition metal clusters

Wilfried Wurth* **and Michael Martins**

Universität Hamburg, Institut für Experimentalphysik, Luruper Chaussee 149, D-22761 Hamburg, Germany

1. INTRODUCTION

Small clusters are intriguing systems because their physical and chemical properties lie somewhere in between the properties of their atomic or molecular constituents and the respective bulk solids. For larger clusters, specific physical quantities typically emerge as a smooth function of the size of the clusters. This evolution is often a result of the changes in the average coordination of the constituents as a function of cluster size. If the cluster size gets comparable to or smaller than the wavelength of the electrons which determine the physical properties, we enter the regime where quantum size effects become important. In this size regime the evolution of physical quantities becomes less predictable, and typically adding or removing a single atom or molecule from a cluster may result in very significant changes (as schematically illustrated in Fig. 1). However, small clusters have the advantage that they present tractable systems for sophisticated high-level theoretical treatments. Hence, small clusters are an ideal playground for the test of theoretical models against experimental results.

Clusters represent prototypical nanosystems since their size is in the range of a few nm or less. Their physical properties can potentially be tailored for specific applications. Ideally this should be possible by simply changing the size of the clusters. In practice for technological applications, clusters have to be either deposited on a substrate, embedded in a matrix, or covered individually by protective layers so that the interaction of the clusters with the respective environment plays a very important role for their properties.

In this contribution we will concentrate on the electronic structure and the magnetic properties of small transition metal clusters in contact with metal surfaces. We will focus on the discussion of results which have been obtained in our group in recent years with X-ray spectroscopic techniques making use of tunable high-brilliance,

The Chemical Physics of Solid Surfaces, Volume 12
ISSN: 1571-0785
DOI: 10.1016/S1571-0785(07)12012-5

*Corresponding author.
E-mail: wilfried.wurth@desy.de

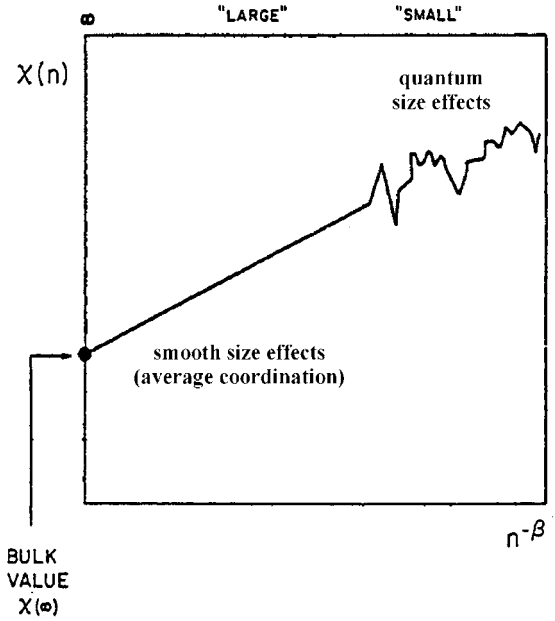

Figure 1: The figure illustrates the typical evolution of a physical quantity ($\chi(n)$) as a function of cluster size (n number of cluster constituents).

variable polarization soft X-ray sources at modern storage rings. Hence, the main examples will be iron and chromium clusters in the size range below 15 atoms in contact with ferromagnetic surfaces such as nickel and iron. Before discussing these results, findings for free transition metal clusters will be briefly reviewed to set the stage for the discussion of the supported clusters. Also, here we will present only a small subset of the results which are published in the literature. The examples we took are chosen to illustrate certain features which are also important for the discussion of the supported clusters and are by no means complete.

2. DISCUSSION

2.1. Small isolated transition metal cluster

In this section we will present a few selected experimental results for gas-phase transition metal clusters to highlight some important aspects of their electronic structure and magnetic properties which are of relevance for the following discussion of the supported clusters. For the discussion of the theoretical models of free cluster magnetism we defer to the chapter by Gustavo Pastor.

2.1.1. Electronic structure

The detailed investigation of the electronic structure of small isolated clusters has so far been limited to spectroscopic studies of the outermost electronic levels. For small clusters in the size range below 100 atoms, a detailed investigation of the electronic

structure is only sensible for a size-selected cluster sample since in this regime every atom counts. Since size-selected cluster beams with this mass resolution are very dilute targets, a measurement of the electronic structure in a photoemission experiment is only possible using a powerful laser as a light source. However, the typical laser sources available have photon energies below 10 eV, which then limits these studies to the outermost electronic levels and is the reason why so far photoemission studies on small isolated clusters have been performed almost exclusively on anions.

An important aspect which is also highly relevant for magnetism is the degree of localization of the outermost electronic wavefunctions. This localization changes when we go from a single atom via a more molecule-like small cluster to bigger solid-like clusters. While in the single atom electrons are of course highly localized and Coulomb and exchange interaction of the electrons determine their energies, for the bigger entities the possibility to lower the kinetic energy by delocalization becomes more and more important. It has been shown for the s- and p-derived states that already for quite small clusters, the electronic wavefunctions are in fact delocalized over the whole cluster.

For the discussion of the magnetic properties of 3d and 4d transition metal clusters, the behavior of the transition metal d-states is essential. In a very simple tight-binding picture which can be used to a first approximation for d-electrons, the degree of localization, i.e., the bandwidth of the transition metal d-states will depend on the probability for an electron to hop to a nearest-neighbor site and the average coordination of the atoms. Hence we expect an increasing delocalization when the cluster size is increased. However, due to the fact that the hopping probability is quite small, the d-levels remain very localized [1] for many systems. To fully understand the changes in localization of the d-states, s-d-hybridization effects have to be included. These effects are indeed observed to have become more important with increasing cluster size using high-resolution photoelectron spectroscopy. In these studies it has been shown that s-d-hybridization sets in for Ni-clusters with roughly $n > 10$ [1–4], Co-clusters in the size range above 20 atoms [3–5], and Fe-clusters roughly above 25 atoms [6]. For Cr-clusters, a more complicated pattern showing even–odd alternations has been observed which results from a particularly strong Cr-dimer bond as a structural subunit [7]. Although here these distinct features disappear above roughly $n = 25$. For the 4d clusters only results for Pd have been reported, where the tendency for stronger delocalization is observed in a similar size range as that for Ni [1].

To conclude this subsection, from the detailed photoemission results it is obvious that transition metal clusters with a size below 20–30 atoms should exhibit particularly interesting magnetic properties due to the strong localization of the d-electrons.

2.1.2. Magnetic properties

The appearance or absence of magnetism for transition metal solids is very often discussed in the framework of the Stoner model for itinerant magnetism. In this model, it is assumed that the relevant d-electron states form bands due to d-d and s,p-d hybridization. The question whether there is a net spin moment of the d-electrons depends on the competition between the gain in exchange energy due to spin polarization and the increase in kinetic energy which results from such a spin polarization. In the Stoner model, this results in the Stoner criterion that magnetism is only observed if the product of $g(E_F) \cdot I > 1$, where $g(E_F)$ is the density of states at the Fermi-level and I an atomic exchange integral. Indeed, within this model only Fe, Co, and Ni

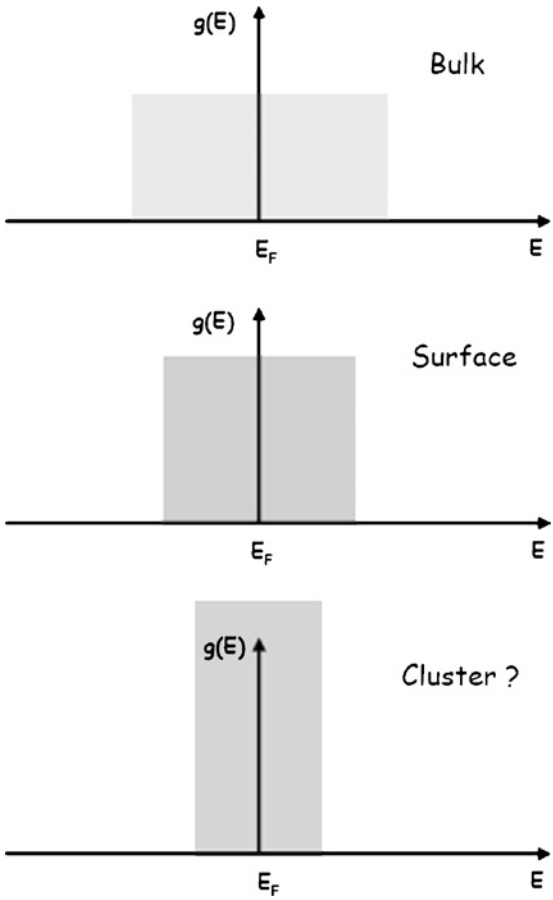

Figure 2: The figure illustrates the expected changes in the band structure as a function of atomic coordination when going from bulk solids to surfaces and clusters.

turn out to be magnetic. It is obvious that a decrease in bandwidth as a result of decreased atomic coordination will result in a higher density of states at the Fermi-level (as depicted in Fig. 2) and hence an increased tendency to magnetism.

This is indeed what is observed in experimental and theoretical studies of the magnetism of isolated clusters. Experimentally, the magnetic moments of gas-phase clusters are studied in Stern–Gerlach experiments, where a cluster beam enters an inhomogeneous magnetic field, and the force resulting from the interaction of the magnetic moments and the field gradient leads to a deflection of the beam. From the size of the deflection one can calculate the size of the total magnetic moment of the cluster. However, it turns out that this analysis is by no means straightforward (see Refs. [8, 9] for a recent discussion).

Firstly, small clusters with a net magnetic moment per individual atom and a ferromagnetic exchange interaction between the atomic moments are typically superparamagnetic, i.e., they behave like a paramagnet with a large magnetic moment given by the sum of the atomic moments. The large total moment results from the fact that

the ferromagnetic interaction leads to single domain particles (for small particles, introduction of domain walls to minimize the magnetic energy would cost too much exchange energy). However, at finite temperatures above the so-called blocking temperature this domain has no preferred orientation with respect to the symmetry axes of the particle since the magnetic anisotropy energy is too small to lead to a fixed orientation.

Secondly, in the Stern–Gerlach experiments typically only a deflection of the cluster beam in the direction of increasing magnetic field is observed fundamentally different from the atomic case. This indicates that the clusters in the beam apparently relax to the magnetic ground state. In order to conserve energy and angular momentum, this has to be related to coupling between spin and rotations. Recently, it was proposed that there is no thermal relaxation process involved since cold clusters show the same behavior [9]. The authors instead invoke an adiabatic transition with increasing magnetic field due to avoided crossings in the energy diagram of the Zeeman levels as a result of spin-rotation coupling. The Langevin-like behavior is then explained as an ensemble average over different clusters in the beam.

Independent of a detailed understanding of the relaxation process involved the Langevin function has been successfully used to determine the magnetic moments per atom for size-selected cluster beams. For the 3d transition metals investigated (Co, Fe, Ni, and Mn), in all cases an increase of the total magnetic moment per atom is observed with decreasing cluster size [10–25]. While in the size regime between roughly 50 and 700 atoms a gradual decrease in the magnetic moments per atom is observed, which can be attributed to a smooth transition from surface coordination to bulk coordination, below 50 atoms a rapid increase of the magnetic moments and large oscillations with cluster size are also found. Obviously, here the details of the electronic and geometric structures play an important role for a detailed understanding of the magnetic properties. In similar experiments, quite large magnetic moments have even been observed for 4d transition metal Rh-clusters in the size range below 20 atoms [26], while for Ru- and Pd-clusters non-magnetic behavior has been found [27].

To summarize this subsection, enhanced magnetic moments are found for small transition metal clusters. A detailed analysis in terms of a separation of spin and orbital moments and an analysis of anisotropy energies as a function of size have so far not been possible for free metal clusters.

2.2. Small supported transition metal cluster

In the following we will discuss experimental results obtained for small size-selected metal clusters deposited on single crystal surfaces. We will also cite theoretical results directly related to the experiments. However, for a detailed discussion of the theory of magnetism of deposited clusters we again defer to the chapter by Gustavo Pastor.

2.2.1. Electronic structure

So far there have been only very limited attempts to study the evolution of the electronic structure of size-selected small transition metal clusters supported on a surface. Pioneering photoemission experiments on Pt, Au, and Pd clusters on silica and on Ag(1 1 0) have shown that it is very difficult to obtain a clear picture of the size dependence of the valence electronic structure [28–34]. The problems are associated with the large background from the underlying substrate which has to be subtracted

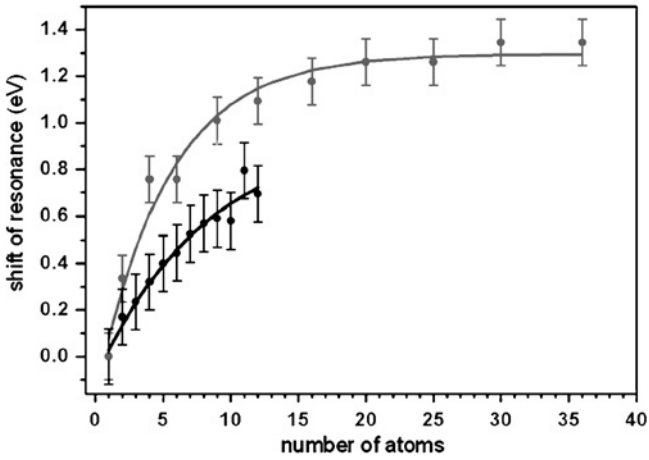

Figure 3: The shift of the Cr-L_3 resonance position for Cr-cluster on Fe with respect to the value for the adsorbed Cr-atom is shown as a function of the number of cluster atoms. The upper curve shows calculated results, while the lower curve shows experimental results.

and with the difficult interpretation of shifts in energy which could be a result of changes in the ground-state properties and/or in the excited-state properties.

We have recently investigated the size-dependence of the X-ray absorption resonances resulting from transitions from the spin-orbit split 2p-levels to the unoccupied 3d-states for size-selected Cr-clusters deposited on ultrathin Fe films grown epitaxially on a Cu(1 0 0)-surface [35]. The observed shifts in the resonance position with increasing cluster size are depicted in Fig. 3 together with calculated values obtained using FEFF to theoretically model the X-ray absorption spectra [36]. For the calculation the substrate was modeled using a large Fe-cluster, and for the Cr-clusters planar clusters were assumed in agreement with theoretical predictions for the respective most stable structures [37].

Experiment and calculations show a similar trend, i.e., a monotonous shift toward larger transition energies, which appears to saturate for larger clusters. The experimental results are in good agreement with similar results obtained previously for Cr-clusters on an Ru(0 0 1)-surface [38]. The calculations show that the observed shifts are directly related to the coordination of the cluster atoms and hence can be interpreted as a result of the increasing delocalization of the d-electrons with increasing cluster size.

To summarize, detailed knowledge about the electronic structure of small size-selected metal clusters is still lacking due to experimental difficulties to obtain high-resolution photoemission results. However, the results obtained so far appear to indicate that delocalization of the d-electronic states occurs in a similar size regime as that for free clusters.

2.2.2. Magnetic properties

In this subsection we will discuss results obtained on the magnetic properties of small deposited transition metal clusters. In contrast to the results for the free clusters, all the results for the deposited clusters have been obtained using X-ray magnetic circular

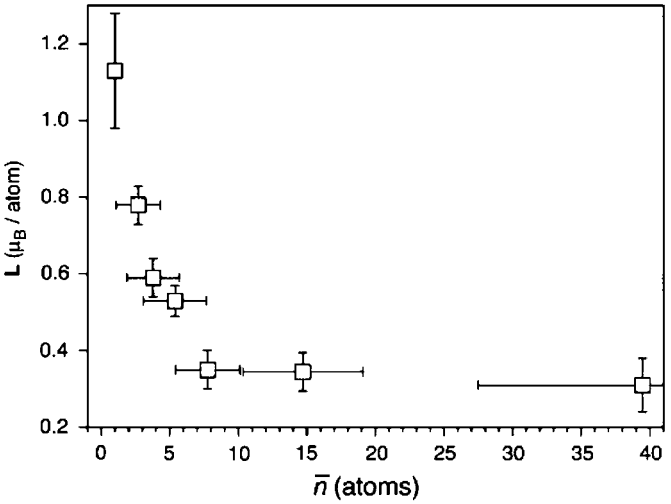

Figure 4: Orbital magnetic moments vs. number of cluster atoms for Co on Pt(1 1 1). Note that the bars given for the number of atoms do not represent error bars, but rather are a result of the statistical nature of the deposition process (adapted from Ref. [41], with permission from Science).

dichroism (XMCD) at third generation storage ring facilities, which provide highly brilliant soft X-ray radiation with variable polarization. In an XMCD experiment, one measures the resonant X-ray absorption cross-section for a spin-orbit split core level with right and left circular polarized light. It has been demonstrated that the difference between right and left circular absorption, i.e., the dichroism spectrum can be used for element-specific magnetometry. Using sum rules derived from considerations on atomic absorption spectra, one can even deduce spin and orbital moments separately from the dichroism signal [39, 40].

Figure 4 shows results for the variation of the orbital magnetic moments obtained with XMCD experiments for Co-clusters on Pt(1 1 1) [41].

In contrast to the results discussed below, these experiments have been performed on clusters which were grown epitaxially as a result of deposition of individual Co-atoms. Consequently, the clusters are not single-sized but a statistical distribution of cluster sizes is present on the surface. In the experiment, a tremendous increase of the orbital moments with decreasing cluster size is found. The changes in spin magnetic moment per atom are much smaller. The authors have been able to show that this increase in orbital moment per atom correlates well with an increase in magnetic anisotropy energy per atom. While calculations in the size range from one to five atoms are not able to reproduce the large orbital moments quantitatively, they do however obtain similar trends and the large increase in anisotropy energy. These results are particularly interesting since large anisotropy energies per atom would imply that medium-size clusters could be ferromagnetic even above 100 K provided the magnetic anisotropy energy would be equally high for these clusters.

While the Co experiments were performed on transition metal clusters on a non-magnetic Pt-surface and hence had to be performed in a high external magnetic field to align the cluster moments, we have recently studied size-selected clusters on ferro-magnetic substrates which are permanently magnetized prior to deposition. For these

experiments we have built a UHV-compatible cluster source which can produce a mono-sized cluster beam of sufficient intensity to be able to prepare size-selected cluster on a clean single crystal surface [42]. Since we deposit mass-selected clusters we have to make sure that the clusters stay intact upon deposition. We avoid fragmentation upon impact by using a soft-landing scheme [43, 44] where the clusters are deposited in an Ar-matrix of a thickness of ten layers, which is then desorbed prior to the experiment. To prevent agglomeration of the deposited clusters by atom diffusion or due to overlap resulting from the statistical distribution of clusters on the surface, we use an equivalent atom coverage below 0.03 monolayer and keep the substrate temperature around 20 K.

In the first series of experiments we have investigated Fe-clusters on an Ni(1 0 0)-surface [45, 46].

Figure 5 shows in the top part experimental results for the spin magnetic moments per d-hole as a function of cluster size for the size range from two to nine cluster

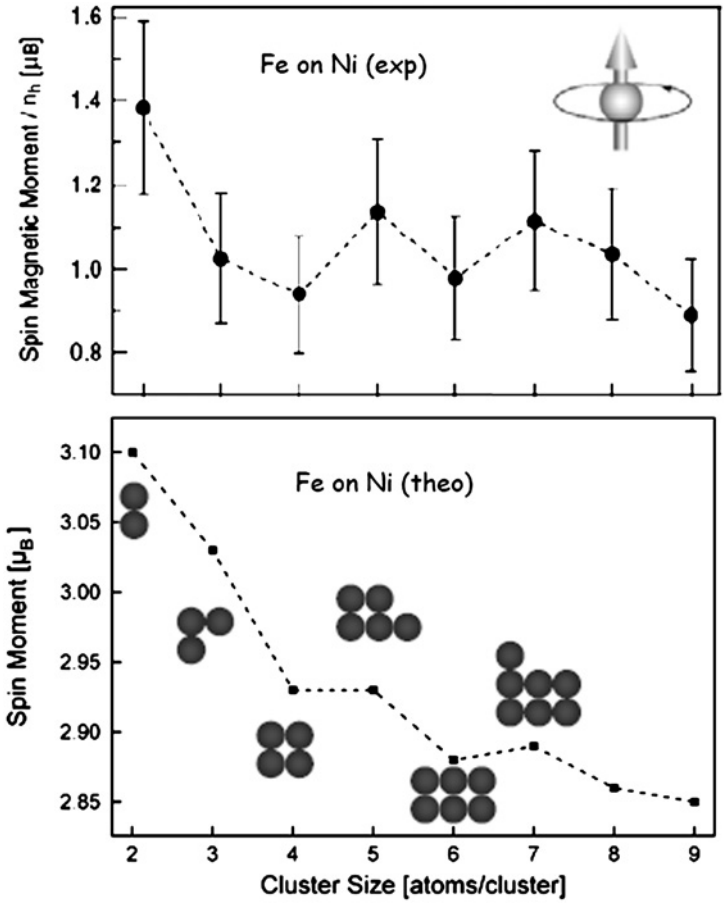

Figure 5: Spin magnetic moments for Fe-clusters with size *n* supported on an Ni(1 0 0)-surface. The top part shows experimental results (spin moments/d-hole) [46], while the bottom part shows the calculated results (spin moments/atom) for the depicted configurations [47].

atoms. Besides a general trend of a decreasing spin moment as a function of increasing cluster size, small oscillations are observed which lead to relative minima for cluster size Fe_4 and Fe_6 and respective relative maxima for the cluster sizes Fe_5 and Fe_7. In the bottom part, calculated spin moments per atom are presented [47] (similar values have been obtained in a different study [48]). The calculated values which are obtained for the cluster structures depicted in the figure follow the same general trend of a decrease of the spin moment per atom with increasing cluster size. Also, the small oscillations observed in the experiment are qualitatively reproduced in the theoretical results. A good comparison of the absolute values is difficult since in the experimental determination of the effective spin moments $S_{\text{eff}} = S + 7T_z$, a contribution from the anisotropy of the charge distribution $7T_z$ is hidden which is not known a priori. Taking into account the number of d-holes from the calculations $n_d \simeq 3.4$ [48] and the calculated spin moments, we would arrive at a value of $7T_z \sim -0.8$ per atom for the trimer and the larger clusters. While this value is below the value found for single atoms on alkali surfaces [49] the dimer value of $7T_z \sim -1.7$ per atom would be much higher, indicating that in this case other effects like structural relaxation of the substrate might play an important role. The trends observed for the spin magnetic moments, and especially the tendency to show small odd–even oscillations can very well be understood in a model assuming a linear dependence of the spin magnetic moments per atom on the intracluster coordination of the atoms [47]. The maxima observed for Fe_5 and Fe_7 are then easily explained because in going from the tetramer and the hexamer to the pentamer and the heptamer, respectively, a singly coordinated atom is added. As a consequence, the average spin moment per atom is higher than that for the compact (magic) structures.

A particular strength of the XMCD spectroscopy is the possibility to disentangle spin and orbital magnetic moments. Figure 6 shows the orbital magnetic moments as a function of cluster size for the Fe-clusters on the Ni(1 0 0)-surface.

The size of the average orbital moment is roughly $0.5\mu_B$ per atom, which is much higher than the bulk ($m_l = 0.05\mu_B$) or the surface value ($m_l \sim 0.1\mu_B$) for iron. In contrast to the observations for the spin moment, the experimental results show a

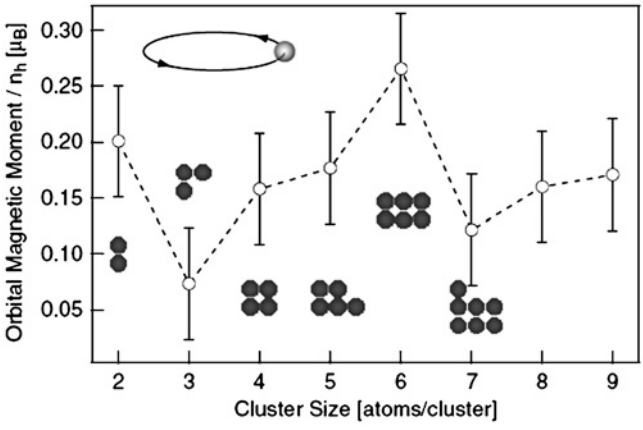

Figure 6: Experimentally determined orbital magnetic moments for Fe-clusters with size n supported on an Ni(1 0 0)-surface [46].

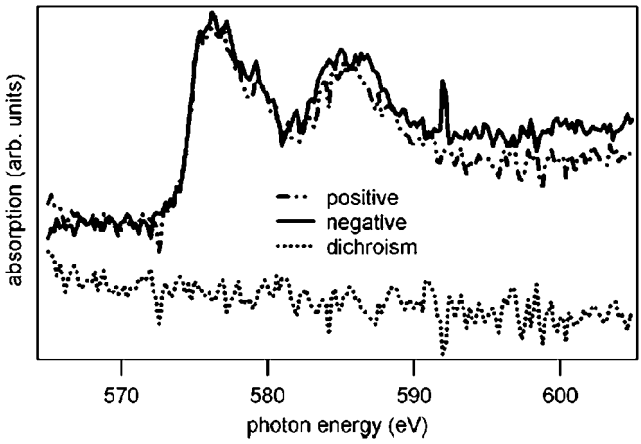

Figure 7: The figure shows the X-ray absorption spectra at the Cr $L_{2,3}$-edge obtained for Cr-dimers on Ni(1 0 0) for right and left circular polarized light and the resulting dichroism spectrum.

large variation of the orbital moment when a single atom is added or subtracted from a particular cluster. Surprisingly, the lowest values are found for the trimer and the heptamer, while the hexamer shows the highest orbital moment. This is counter-intuitive since one would expect that the orbital moment is particularly large if the atomic coordination is small, similar to what is observed for the spin moment. However, this seems not to be the case since the hexamer, for example, is a compact cluster with a higher average coordination of the cluster atoms than the trimer or the heptamer. To explain these findings is also theoretically challenging. It is very difficult to get accurate results for the orbital moments in the calculations since here a good description of correlation effects is extremely important.

Recently, we have started to look at the magnetic properties of Cr-clusters deposited on Ni- and Fe-substrates. Surprisingly, we do not find an XMCD signal for the Cr-atoms, -dimers, or –trimers on Ni. The XMCD results at the Cr $L_{2,3}$-edge for the Cr-dimers on Ni(1 0 0) are shown in Fig. 7.

The absence of a dichroic signal for the dimer can be explained when we consider the fact that we have an anti-ferromagnetic intracluster exchange coupling between Cr-atoms, which for an isolated dimer of course leads to a zero total magnetic moment and consequently to a vanishing dichroic signal. For the deposited cluster, we have to take into account the cluster–substrate exchange coupling as well. In the case of Cr deposited on Ni, this coupling is anti-ferromagnetic as well. Already for the deposited dimer this will lead to spin frustration and one could envision that consequently non-collinear spin structures should appear. However, calculations show [50] that the energetically most favorable state for the Cr-dimer is a collinear state where the dimer shows an anti-ferromagnetic intracluster coupling and a ferromagnetic coupling of one of the dimer atoms to the substrate while the second dimer atom is coupled anti-ferromagnetically to the underlying Ni-moments. This situation is depicted in Fig. 8.

The calculations show that this arrangement is only stable if the two Cr-atoms sit in nearest-neighbor sites on the surface. As soon as the distance between the two dimer

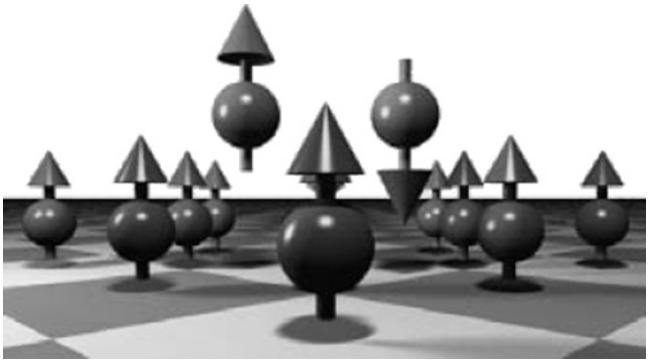

Figure 8: The cartoon shows the orientation of the spin magnetic moments for the ground state of a Cr-dimer on an Ni(1 0 0) substrate [50].

atoms is increased, they will both couple anti-ferromagnetically to the Ni-spins and consequently the chromium spins will be oriented parallel. This is illustrated in Fig. 9.

This behavior is a result of the fact that the intracluster exchange coupling is stronger than the cluster–substrate coupling.

While this explains well the experimental results for the dimer, theory so far disagrees with experiment on the spin structure of the trimer and the coupling of the spin of the single atom to the underlying Ni-substrate. Theory [50] predicts that the trimer also prefers a collinear state where the Cr-atoms on nearest-neighbor sites are coupled anti-ferromagnetically. This leads to a net total magnetic moment of the Cr-trimer,

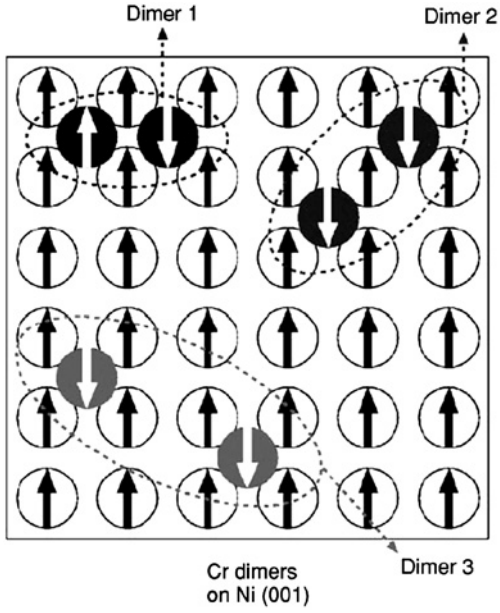

Figure 9: The cartoon illustrates the changes in the orientation of the Cr-dimer spins as a function of the distance of the dimer atoms [50].

which is in contrast to our experimental finding. The absence of the dichroic signal for the trimer implies a non-collinear arrangement where the spins of the Cr-atoms are actually tilted strongly with respect to the surface normal since the experimental geometry – magnetization and photon helicity parallel to the surface normal – is sensitive to the projection of the magnetic moments on the surface normal only.

Even more disturbing is the absence of a dichroic signal for the single atom in the experiment. It is quite clear from the calculations that the anti-ferromagnetically coupled state of the single Cr-atom to the Ni-substrate is energetically more stable. However, the experimental results seem to imply that the magnetic moments of the Cr-atoms may actually be fluctuating between the ferromagnetically and the anti-ferromagnetically coupled state.

When we change to Cr-clusters deposited on ultrathin iron films epitaxially grown on a Cu(1 0 0)-surface, the situation is totally different. Here we observe a strong dichroic signal for Cr-clusters in the size range from two to thirteen atoms. Figure 10 shows the X-ray absorption spectra for left and right circular polarization and the resulting dichroism signal at the Fe $L_{2,3}$- and the Cr $L_{2,3}$-edge for Cr_3-clusters on Fe.

From the sign change of the dichroism signal – positive at the L_3-resonance and negative at the L_2-resonance for the Fe-substrate and vice versa for the Cr-cluster – we can immediately conclude that the coupling between Cr_3-cluster and Fe-substrate is anti-ferromagnetic. A detailed analysis of the evolution of the spin moment as a function of cluster size reveals, however, a decrease of the spin magnetic moment [51] by a factor of 4 from the atom to the Cr_{13}-cluster. This decrease is an order of magnitude larger than the observed decrease for Fe-clusters on Ni (see above). Therefore, this cannot be a consequence of delocalization (average atomic coordination), but has to be related to significant changes in spin structures. Theoretical investigations, using the full-potential Korringa–Kohn–Rostoker Green function method with the possibility to treat non-collinear magnetism, have revealed that in the case of Cr-clusters on Fe the competition of intracluster exchange interaction and cluster–substrate exchange interaction leads indeed to complicated spin structures. In contrast to the situation for Cr-clusters on Ni, for Cr on Fe the cluster–substrate exchange interaction is stronger than the intracluster exchange interaction. As a consequence for the dimer, the cluster atoms prefer anti-ferromagnetic coupling to the substrate even so this implies ferromagnetic order between the two Cr-atoms. However, starting with the trimer non-collinear spin structures result from spin frustration. The calculated projections of the spin moments on the surface normal agree quite well with the experimental findings up to the pentamer which is the largest cluster calculated [51]. Recent non-collinear tight-binding calculations [52] also show that non-collinear spin structures are the preferred ground state for Cr-clusters on Fe. However, the details of the spin arrangements and the resulting spin moments appear to be different for the two different theoretical models.

The complicated spin structures observed for anti-ferromagnetic clusters coupled to ferromagnetic substrates which result from the competing interactions might actually also have interesting implications for the understanding of the interface phenomena responsible for the exchange-bias effect.

To summarize, XMCD studies on deposited transition metal clusters are a powerful tool for a detailed understanding of the complex magnetic properties of these clusters.

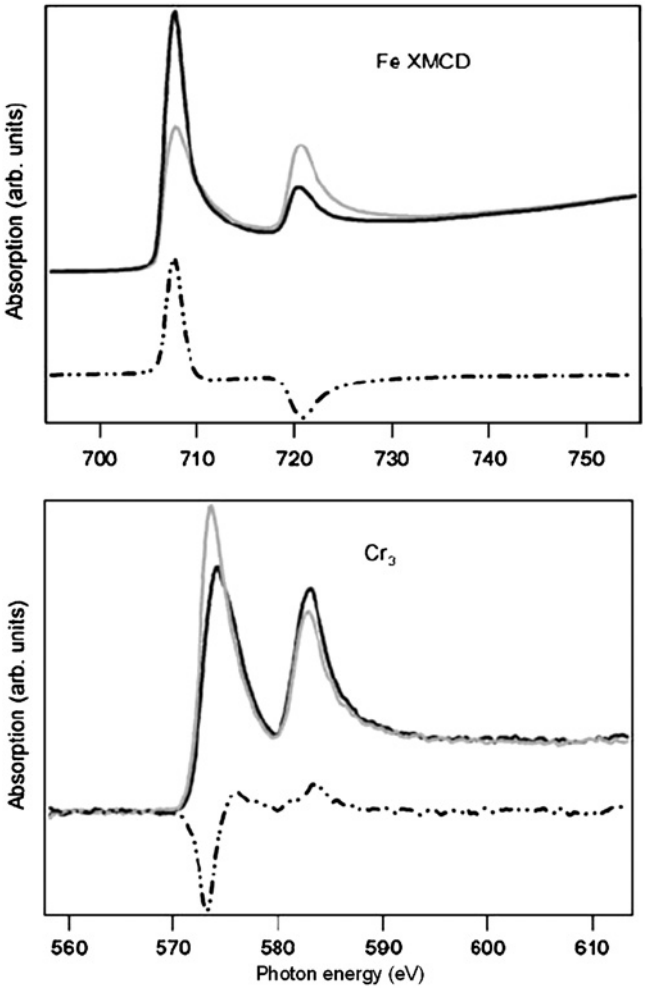

Figure 10: X-ray absorption spectra for left and right circular polarization and resulting dichroism spectra (dash-dotted lines) for Cr_3-clusters supported on Fe. The top part shows the dichroism signal from the Fe substrate at the Fe $L_{2,3}$-edge, while the bottom part depicts the dichroism signal obtained at the Cr-$L_{2,3}$-edge.

3. SUMMARY

In the discussion above, we have tried to exemplify the very intriguing properties of small deposited transition metal clusters in the size range below 20 atoms. In this size range, fundamental aspects of the evolution of magnetic moments from the atom to the surface or bulk values can be studied. Furthermore, in this size range competing exchange interactions lead to the formation of complex spin structures for the clusters which involve quite often also a rearrangement of the spins in the first layer of the substrate. Ferromagnetic clusters show a strong enhancement of the spin magnetic moments and an even stronger enhancement of the orbital magnetic moments with decreasing cluster size.

It is important to stress that to understand magnetic properties of size-selected clusters in contact with surfaces in detail requires experiments which determine spin and orbital moments as a function of the number of cluster atoms. In this size regime every atom counts, therefore mono-sized clusters have to be investigated. Since the geometrical structure of the clusters has a profound impact on the magnetic properties, it would be highly desirable to obtain information about structural properties of small metal clusters on surfaces.

For the understanding of the evolution of the magnetic properties and especially the complex spin structures involved, strong theoretical support is absolutely necessary.

For the future, we envision that high-field studies of magnetic properties for clusters in contact with non-magnetic surfaces in the weak-coupling limit will increase. Of course, it is also highly interesting to study deposited 4d transition metal clusters where theory predicts large magnetic moments for a number of different systems. We have in fact started first experiments on Ru-cluster with some quite surprising preliminary results.

ACKNOWLEDGMENTS

The experimental results from our group presented here have been obtained by a group of excellent Ph.D. and diploma students, Leif Glaser, Oliver Heisterkamp, Uta Langenbuch, Tobias Lau, and Matthias Reif. Interpretation of the results would not have been possible without the important contributions and the very fruitful collaboration with our colleagues from theory, Samir Lounis, P. Mavropoulos and Stefan Blügel (Jülich), Sven Bornemann, Jan Minar, and Hubert Ebert (München).

We gratefully acknowledge financial support by the BMBF (05 KS4GUB/6) and the DFG through the collaborative research center SFB 668 and the priority program SPP 1153.

REFERENCES

[1] Gantefor G., Eberhardt W., Phys. Rev. Lett. 76 (1996) 4975.
[2] Liu S.R., Zhai H.J., Wang L.S., J. Chem. Phys. 117 (2002) 9758.
[3] Liu S.R., Zhai H.J., Wang L.S., Phys. Rev. B 65 (2002) 113401.
[4] Morenzin J., Kietzmann H., Bechthold P.S., Gantefor G., Eberhardt W., Pure Appl. Chem. 72 (2000) 2149.
[5] Liu S.R., Zhai H.J., Wang L.S., Phys. Rev. B. 6415 15 (2001) 153402.
[6] Wang L.S., Li X., Zhang H.F., Chem. Phys. 262 (2000) 53.
[7] Wang L.S., Wu H.B., Cheng H.S., Phys. Rev. B. 55 (1997) 12884.
[8] Knickelbein M.B., J. Chem. Phys. 121 (2004) 5281.
[9] Xu X.S., Yin S.Y., Moro R., de Heer W.A., Phys. Rev. Lett. 95 (2005) 237209.
[10] Deheer W.A., Milani P., Chatelain A., Z. Phys. Chem. 169 (1990) 63.
[11] Deheer W., Milani P., Chatelain A., Z. Phys. D: At., Mol. Clusters 19 (1991) 241.
[12] Deheer W.A., Becker J.A., Billas I.M.L., Milani P., Chatelain A., Int. J. Mod. Phys. B 6 (1992) 3733.
[13] Bucher J.P., Douglass D.C., Bloomfield L.A., Phys. Rev. Lett. 66 (1991) 3052.
[14] Bucher J.P., Bloomfield L.A., Int. J. Mod. Phys. B 7 (1993) 1079.
[15] Billas I.M.L., Becker J.A., Deheer W.A., Z. Phys. D: At., Mol. Clusters 26 (1993) 325.
[16] Billas I.M.L., Chatelain A., Deheer W.A., Science 265 (1994) 1682.

[17] Billas I.M.L., Chatelain A., deHeer W.A., Surf. Rev. Lett. 3 (1996) 429.
[18] Hirt A., Gerion D., Billas I.M.L., Chatelain A., deHeer W.A., Z. Phys. D: At., Mol. Clusters 40 (1997) 160.
[19] Billas I.M.L., Chatelain A., deHeer W.A., J. Magn. Magn. Mater. 168 (1997) 64.
[20] Knickelbein M.B., Phys. Rev. Lett. 86 (2001) 5255.
[21] Knickelbein M.B., Chem. Phys. Lett. 353 (2002) 221.
[22] Knickelbein M.B., Phys. Rev. B 70 (2004) 014424.
[23] Knickelbein M.B., J. Chem. Phys. 116 (2002) 9703.
[24] Douglass D.C., Cox A.J., Bucher J.P., Bloomfield L.A., Phys. Rev. B 47 (1993) 12874.
[25] Apsel S.E., Emmert J.W., Deng J., Bloomfield L.A., Phys. Rev. Lett. 76 (1996) 1441.
[26] Cox A.J., Louderback J.G., Bloomfield L.A., Phys. Rev. Lett. 71 (1993) 923.
[27] Cox A.J., Louderback J.G., Apsel S.E., Bloomfield L.A., Phys. Rev. B 49 (1994) 12295.
[28] Eberhardt W., Fayet P., Cox D.M., Fu Z., Kaldor A., Sherwood R., Sondericker D., Phys. Rev. Lett. 64 (1990) 780.
[29] Cox D.M., Eberhardt W., Fayet P., Fu Z., Kessler B., Sherwood R.D., Sondericker D., Kaldor A., Z. Phys. D: At., Mol. Clusters 20 (1991) 385.
[30] Roy H.V., Boschung J., Fayet P., Patthey F., Schneider W.D., Z. Phys. D: At., Mol. Clusters 26 (1993) 252.
[31] Roy H.V., Boschung J., Fayet P., Patthey F., Schneider W.D., Int. J. Mod. Phys. B 7 (1993) 556.
[32] Roy H.V., Fayet P., Patthey F., Schneider W.D., Delley B., Massobrio C., Phys. Rev. B 49 (1994) 5611.
[33] Roy H.V., Patthey F., Fayet P., Schneider W.D., Delley B., Surf. Rev. Lett. 3 (1996) 943.
[34] Schneider W.D., Roy H.V., Fayet P., Patthey F., Delley B., Massobrio C., Cluster Assembled Mater 232 (1996) 51.
[35] Reif M., Glaser L., Martins M., Wurth W., Phys. Rev. B 72 (2005) 155405.
[36] Rehr J.J., Albers R.C., Rev. Mod. Phys. 72 (2000) 621.
[37] Zhuang J., Sun Z.H., Zhang W.H., Zhuang M., Ning X.J., Liu L., Li Y.F., Phys. Rev. B 69 (2004) 165421.
[38] Lau J.T., Achleitner A., Wurth W., Chem. Phys. Lett. 317 (2000) 269.
[39] Schutz G., Wagner W., Wilhelm W., Kienle P., Zeller R., Frahm R., Materlik G., Phys. Rev. Lett. 58 (1987) 737.
[40] van der Laan G., J. Electron. Spectrosc. Relat. Phenom. 103 (1999) 859.
[41] Gambardella P., Rusponi S., Veronese M., Dhesi S.S., Grazioli C., Dallmeyer A., Cabria I., Zeller R., Dederichs P.H., Kern K., Carbone C., Brune H., Science 300 (2003) 1130.
[42] Lau J.T., Achleitner A., Ehrke H.U., Langenbuch U., Reif M., Wurth W., Rev. Sci. Instrum. 76 (2005) 063902.
[43] Cheng H.P., Landman U., J. Phys. Chem. 98 (1994) 3527.
[44] Lau J.T., Wurth W., Ehrke H.U., Achleitner A., J. Low Temp. Phys. 29 (2003) 223.
[45] Lau J.T., Fohlisch A., Nietubyc R., Reif M., Wurth W., Phys. Rev. Lett. 89 (2002) 57202.
[46] Lau J.T., Fohlisch A., Martins M., Nietubyc R., Reif M., Wurth W., New J. Phys. 4 (2002) 98.1.
[47] Mavropoulos P., Lounis S., Zeller R., Blügel S., Appl. Phys. Mater. Sci. Process. 82 (2006) 103.
[48] Martinez E., Longo R.C., Robles R., Vega A., Gallego L.J., Phys. Rev. B 71 (2005) 165425.
[49] Gambardella P., Dhesi S.S., Gardonio S., Grazioli C., Ohresser P., Carbone C., Phys. Rev. Lett. 88 (2002) 047202.
[50] Lounis S., Mavropoulos P., Dederichs P.H., Blügel S., Phys. Rev. B 72 (2005) 224437.
[51] Lounis S., Reif M., Mavropoulos P., Glaser L., Dederichs P.H., Martins M., Blügel S., Wurth W., cond-mat/0608048 (2006).
[52] Robles R., Nordstrom L., Phys. Rev. B 74 (2006) 094403.

This page intentionally left blank

Chapter 13

Magnetic properties of deposited and embedded clusters

C. Binns*

Department of Physics and Astronomy, University of Leicester, University Road, Leicester LE1 7RH, UK

1. INTRODUCTION

Over the last few years, there has been a growing interest in the magnetic behaviour of clusters from a wide range of scientific disciplines. Magnetism in systems where the magnetic electrons are confined within a few atomic spacings is not as well understood as in either the atomic or the bulk regimes. This increase in interest has coincided with the development of technologies that can manufacture tightly controlled magnetic nanostructures including quantum dots, monolayers, self-organised islands, quantum wires and deposited clusters. Undoubtedly, much of the enthusiasm comes from a growing realisation of the enormous potential of magnetic nanostructures in the formation of high-performance magnetic materials and devices.

The interest extends beyond the boundaries of mainstream physics and chemistry as magnetic clusters and nanoparticles have an important part to play in natural systems in a diverse variety of environments. An example is the MV-1 bacterium that manufactures nanoparticles of magnetite arranged in chains to maintain alignment with the earth's magnetic field [1]. Similar magnetite chains discovered in meteorites from Mars are considered to be the strongest evidence for the previous existence of extra-terrestrial bacteria [2]. Recent studies of mixed ferritin and magnetite nanoparticles reveal a similar magnetic behaviour to human brain tissue [3]. It has also been suggested that magnetic clusters play a crucial role in seeding the condensation of the interstellar medium to form free-floating planets [4].

This article will review the recent research on magnetic structures produced by forming clusters in the gas phase and depositing them on surfaces or embedding them in matrices. Due to the tight size control achievable, this has proved itself to be a powerful technique to produce and study clusters in a range of environments and to produce new materials. Over two decades ago, based on earlier work at Karlsruhe on cryogenic free jet expansions [5], the technology to produce beams of gas phase, size-selected metal clusters was developed [6]. In the case of magnetic particles, this

The Chemical Physics of Solid Surfaces, Volume 12
ISSN: 1571-0785
DOI: 10.1016/S1571-0785(07)12013-7

*Corresponding author.
E-mail: cb12@leicester.ac.uk

afforded the wonderful opportunity to study how magnetism in matter develops as a substance is built atom-by-atom from the monomer. Magnetism is well understood at the limiting scales of atoms and the bulk but in particles containing a few to a few thousand atoms (1–5 nm diameter), the magnetic behaviour depends on size and can change significantly with the addition or removal of a single atom.

For particles smaller than about 5 nm, either as free clusters or supported on a surface, the fundamental spin and orbital moments per atom can be substantially different to the bulk value as can the spin ordering within the clusters. This was originally discovered by magnetic deflection experiments using gradient magnetic fields applied to free clusters in flight [7, 8]. Thus, it was found that ferromagnetic 3d transition metal clusters have enhanced total moments [7–12], clusters of the paramagnetic metal rhodium become magnetic at sizes smaller than about 60 atoms [13] and ferrimagnetism was discovered in clusters of the antiferromagnetic metal Mn [14].

In addition to changes in the fundamental atomic moments and their spin ordering, there are important other size effects. Ferromagnetic clusters of the size discussed in this chapter (smaller than 10 nm diameter) are single-domain particles, that is, systems in which it is energetically unfavourable to form a domain boundary. These have held enormous fascination since the classic work of Stoner and Wohlfarth [15] and Néel [16] over half a century ago. The particles, notwithstanding complications such as canted spins at the surface [17–20], can be considered as giant moments of exchange-coupled atomic spins. At temperatures much lower than those required to perturb the internal alignment of the atomic magnetic moments, the particle moment as a whole can fluctuate over the anisotropy barrier separating different spin directions at time-scales varying from nanoseconds to eons. At low temperatures, there is interest in the possibility of the tunnelling of the magnetisation vector through the barrier – one of the few examples of macroscopic quantum tunnelling [21–23].

At $T = 0\,\mathrm{K}$, reversing the direction of the cluster magnetisation requires an external field to drive the magnetisation vector across the anisotropy boundary KV separating different magnetic alignments, where K is the anisotropy constant and V is the particle volume. At elevated temperatures when $kT \gg KV$, the anisotropy barrier becomes unimportant but the external field must compete with thermal fluctuations of the moment. In general, when a saturating field is removed from a particle (or an assembly) at temperature, T, the magnetisation decays with a relaxation rate, τ, that can be expressed by the Arrhenius relationship:

$$\frac{1}{\tau} = f_0 \exp\left(\frac{-KV}{k_\mathrm{B}T}\right) \tag{1}$$

where f_0 is the natural gyromagnetic frequency of the particles. For volumes typical in deposited transition metal clusters, observations must be done at cryogenic temperatures ($\leqslant 5\,\mathrm{K}$) for the magnetic relaxation to be slower than measurement times using dc magnetometry. At room temperature, the thermal energy $k_\mathrm{B}T$ is much greater than the anisotropy energy of each particle so that all magnetisation directions are almost energetically equal. The magnetisation of an assembly of N clusters in a field H is then described by the classical Langevin function:

$$M = N\mu_\mathrm{tot}\left[\coth\left(\frac{\mu_\mathrm{tot}H}{k_\mathrm{B}T}\right) - \frac{k_\mathrm{B}T}{\mu_\mathrm{tot}H}\right] = N\mu_\mathrm{tot}L(x) \tag{2}$$

where μ_{tot} is the magnetic moment of each cluster and $x = H\mu_{tot}/k_B T$. This can be several hundred atomic spins and so, unlike isolated atoms where very low temperatures or very high fields are required to achieve saturation, assemblies of clusters can be saturated easily. The temperature at which half the cluster moments have relaxed during the time of a measurement is known as the blocking temperature, T_B, and only a narrow temperature region around T_B separates, essentially, permanently frozen moments from superparamagnetic behaviour. The quest to find deposited clusters smaller than 5 nm in which T_B is above room temperature is an important challenge for future generations of magnetic recording technology.

It is now known that isolated clusters maintain a significant enhancement of the magnetic moment per atom after they have been deposited on a surface [24–26] or embedded in a matrix [27]. As the flux from cluster sources has steadily improved [28, 29], the field has evolved to consider not just isolated clusters but films up to several micrometres thick built out of the pre-formed clusters. As shown schematically in Fig. 1, these can be deposited in conjunction with a vapour of another material to form a granular material of the particles embedded in a matrix [30]. This affords independent control over the grain size and volume fraction and it is even possible to affect some control over the cluster shape by adjusting the impact energy on the surface [31]. The flexibility of control increases further if the clusters are functionalised in the gas phase by making them out of more than one material [32–34] or as core–shell particles, for example, by a controlled oxidation [35, 36]. One can also modify the deposited films by post-processing, such as heating or oxidation [37] and depositing onto patterned substrates allows the formation of ordered assemblies of magnetic dots [38].

Another important characteristic of films produced by the co-deposition technique is that the clusters maintain their identity in a matrix of a material that alloys with that of the particles [39] enabling the production of nanoscale *granular* mixtures of *miscible* materials. This is not possible by any other fabrication technique. The degree of

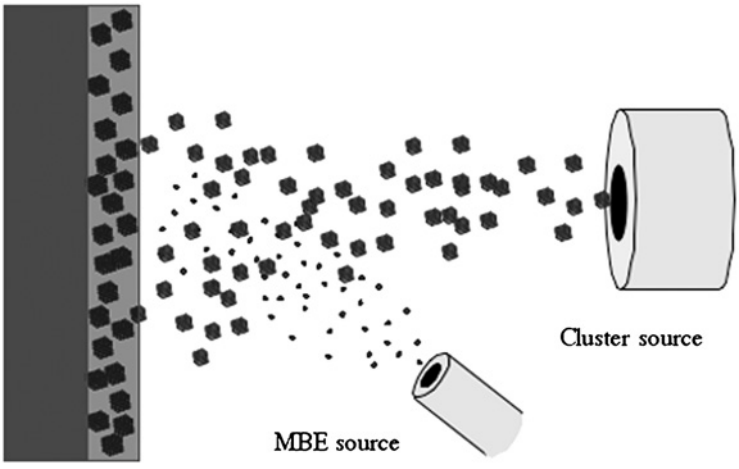

Figure 1: Formation of a cluster-assembled film by co-deposition of gas-phase clusters and an atomic vapour from a conventional deposition source.

control over the nanostructure one achieves with cluster deposition enables one to optimise the magnetic performance of films for particular applications. Examples include maximising the giant magnetoresistance (GMR) of nanogranular films by embedding size-selected magnetic clusters in non-magnetic matrices [40, 41] or maximising the saturation magnetisation in granular Fe–Co films produced by embedding Fe clusters in Co matrices or vice versa. It has been shown that this way it may be possible to achieve a magnetisation that exceeds the Slater–Pauling limit [42, 43].

In all such industrial applications, the required cluster volume fraction is high – near the percolation threshold or higher – so there are strong interactions between the clusters. Understanding the detailed nature of the cluster interactions has therefore become increasingly important. Inter-particle interactions produce a rich variety of magnetic configurations resulting from competing energy terms. The dipolar interaction introduces frustration as it is impossible to obtain an optimum alignment for every particle. In addition, there is frustration resulting from the competition between the inter-particle dipolar and exchange terms and the intra-particle anisotropy energy (magnetocrystalline, shape, magnetoelastic, etc.) that requires the magnetisation vector to be aligned along specific axes in each particle.

Although the metallurgy of cluster-deposited films would appear trivial, this is superficial, as the reality is a rich complexity of structure and magnetic behaviour. For example, the atomic structure is not always known even for the particles in the gas phase. When they are embedded in matrices, the structure and morphology is modified and becomes dependent on the matrix material. At very low volume fractions, nanoparticle assemblies are superparamagnetic but as the volume fraction is increased, contact between the nanoparticles produces a strong exchange interaction and the effective particle size increases. Although the nature of the interfaces, for example, the degree of intermixing, is a largely open question, the effective increase in particle size is clearly seen in the magnetic behaviour. These agglomerates interact via dipolar forces and the assembly no longer follows a simple superparamagnetic magnetisation. When the volume fraction is increased beyond the percolation threshold, the frustration between the nanoscale random anisotropy and the exchange interaction produces spin-glass-like behaviour and a significant magnetic softening. Pure cluster films, even though they are composed of a single element, have a different magnetic behaviour to conventional thin films produced by depositing atoms. For example, they do not form domains but minimise the magnetostatic term by having a magnetisation that smoothly changes orientation with position [44].

For free clusters in the gas phase, up to now, the only specific magnetic probe available has been Stern–Gerlach deflection measurements, which can determine the total magnetic moment as a function of the number of atoms. However, if the clusters are deposited on to a substrate in sufficiently good vacuum to remain pristine, a whole raft of extra in situ experiments developed by surface scientists opens up allowing the determination of the electronic properties and structure. In addition, the orbital and spin magnetic moments per atom can be measured independently using X-ray magnetic circular dichroism (XMCD). It also becomes possible to accumulate a sufficient density on a surface to 'switch on' inter-cluster interactions so that the effect of these on the magnetic behaviour can be determined. Section 2 summarises recent work on deposited clusters on various substrates including non-magnetic and magnetic materials. Section 3 discusses the structural and magnetic behaviour of embedded clusters

in various matrices produced by co-deposition as in Fig. 1. This type of sample allows ex situ measurements so that conventional magnetometry becomes possible. New considerations here are changes in structure induced by the matrix material and electronic and magnetic interactions with the matrix. Finally, Section 4 describes some possible technological applications of materials produced by depositing clusters.

2. DEPOSITED CLUSTERS

2.1. Morphology of films produced by depositing clusters

In general, the morphology of cluster-deposited films depends on both the cluster and substrate materials and the kinetic energy of the incident clusters. Within the soft landing regime (<0.1 eV per atom), the film topography varies from a random paving by individual clusters, when diffusion is limited, to large ramified islands composed of clusters when the cluster diffusion is significant. In the case of some simple metals, for clusters below a certain size, complete liquid-drop-like coalescence occurs to produce large particles. Case studies of all these different growth modes have been reported by several groups [45–49] and the data have been analysed using the deposition–diffusion–aggregation (DDA) model [49]. Changes in growth mode have been demonstrated as a function of cluster deposition energy [50] and of the density of substrate defects [48].

In the case of transition metal clusters like Fe or Co, only the random paving type of growth appears to occur. An example is shown in Fig. 2, which displays an in situ scanning tunnelling microscope (STM) image of Fe clusters deposited onto Si(1 1 1) in ultra-high vacuum (UHV). Although not every type of substrate has been studied by direct imaging techniques, the magnetic data to be presented in later sections show that at low cluster densities the behaviour is consistent with a collection of isolated particles with the same size as those deposited. This is true for a wide range of substrates including highly oriented pyrolitic graphite (HOPG), organic materials and various metals, so it is reasonable to assume that films produced by depositing magnetic transition metal clusters always grow as a random paving by the nanoparticles. The magnetic data also indicate that the anisotropy axes are randomly oriented, so it appears

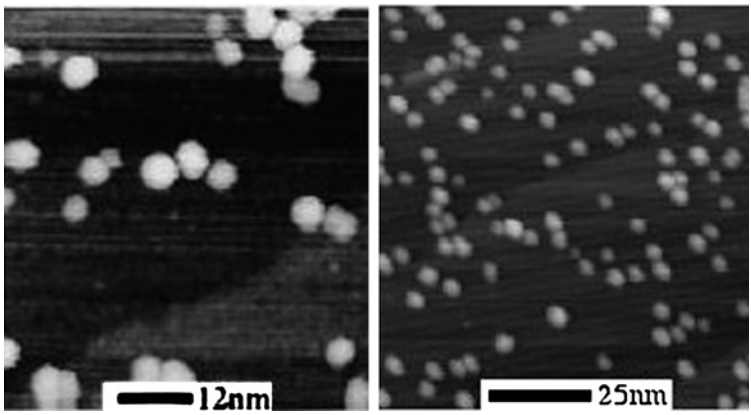

Figure 2: In situ STM images from Fe clusters deposited onto an Si(1 1 1) substrate showing a random paving morphology.

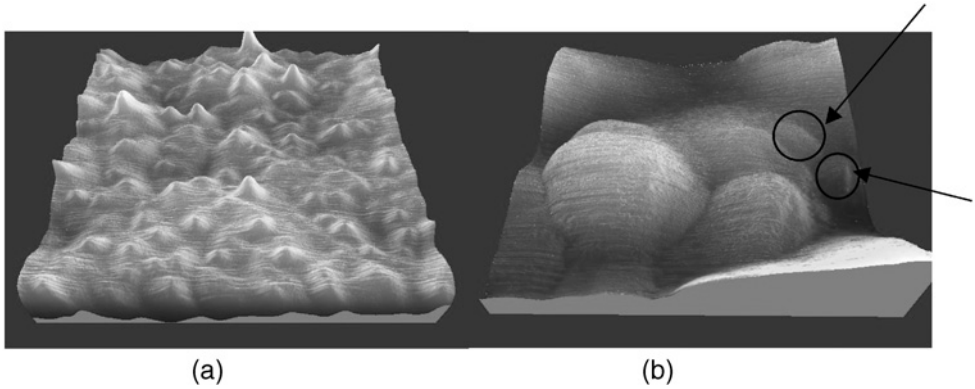

Figure 3: (a) Non-contact AFM image (900×900 nm) of 40 nm thick film of Fe clusters with a mean diameter of 2 nm deposited on Si and capped with a 3 nm thick film of amorphous carbon for removal from the UHV system. (b) High-resolution (50×50 nm) image of the sample in (a) showing features with the size of the individual deposited particles (after accounting for tip convolution). Reproduced with permission from Ref. [43].

that films grow by clusters landing with a random orientation of their crystallographic axes at random positions on the substrate, where they stick.

In thick cluster films in which there are many layers of the deposited clusters, the effective particle size, as indicated by the magnetic data, is much larger than a single deposited cluster. Large area AFM images, such as the one shown in Fig. 3a, obtained from a 40 nm thick film of deposited Fe clusters on Si also appear to indicate large feature sizes. Recent high-resolution images obtained in non-contact mode however (Fig. 3b) indicate that the individual deposited clusters can still be made out within the larger-scale morphology. Thus, the deposited particles, when they are in contact, are exchange-coupled and behave magnetically as larger particles but the crystalline orientation still changes randomly on the length scale of a single deposited cluster ($\sim$2–3 nm).

2.2. Magnetic measurements based on dichroism

The most powerful techniques for studying the magnetic behaviour of deposited clusters are based on dichroism, that is, a dependence of X-ray absorption or photoemission intensity on the relative alignment between the sample magnetisation and photon polarisation. XMCD involves, in the case of transition metals, measurement of the difference in L-edge X-ray absorption spectra obtained using circularly polarised X-rays with their angular momentum parallel or antiparallel to the sample magnetisation. The orbital (m_L) and spin (m_S) contributions to the total magnetic moment can be determined independently and (in heterogeneous systems) for each element by applying magnetooptical sum rules to the absorption spectra [51, 52]. The experimental geometry, along with a typical pair of L-edge absorption spectra and their difference from a sample of Fe clusters on HOPG [25], is shown in Fig. 4a.

More precisely, the technique measures the quantities: $\langle L_z \rangle$ and $\langle S_z + 7T_z \rangle$ per valence band hole, n_h, where $\langle L_z \rangle$ and $\langle S_z \rangle$ are the expectation values of the z (static) components of the orbital and spin angular momenta of the atoms and $\langle T_z \rangle$ is the

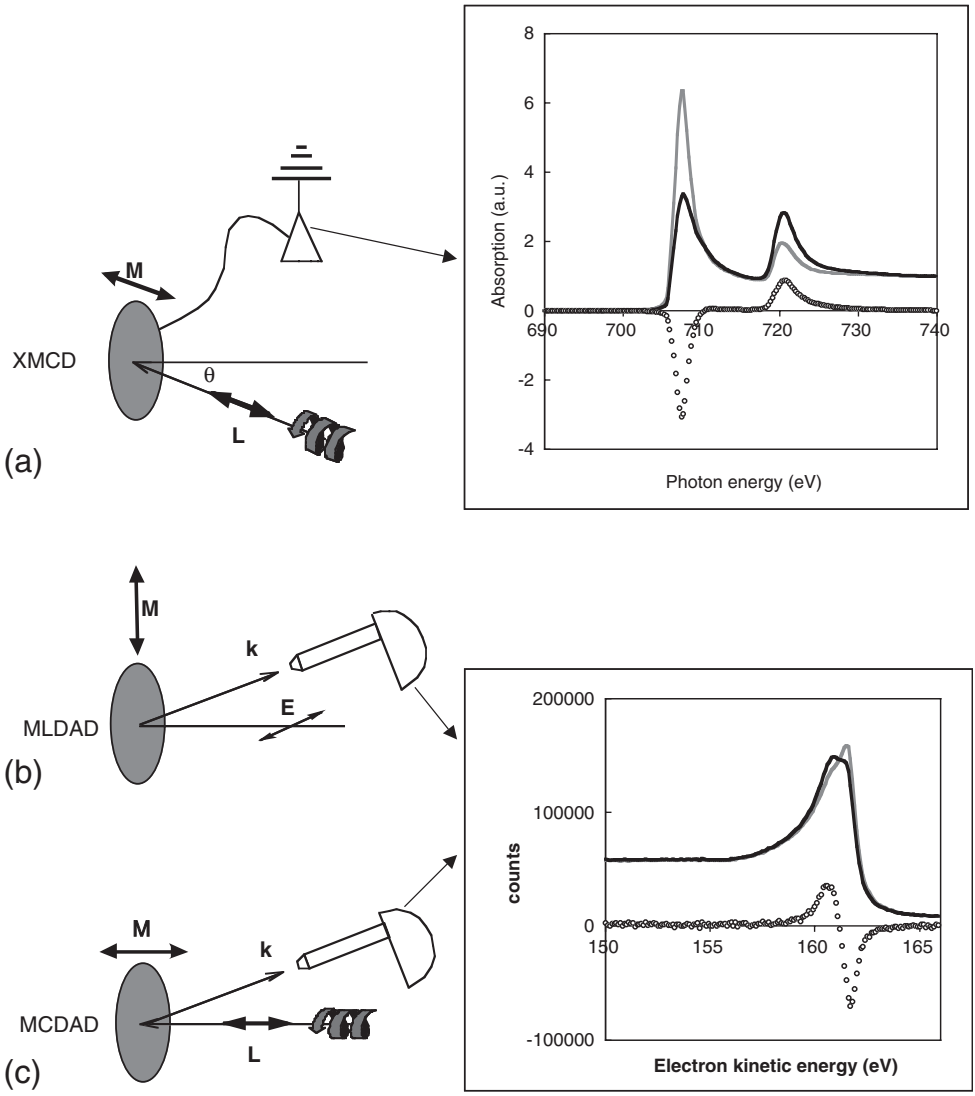

Figure 4: (a) Standard geometry of the XMCD measurement, which measures the difference in *L*-edge absorption between parallel and antiparallel alignment of the magnetisation vector and photon angular momentum. The magnetic field is applied along the direction of the photon beam and at a variable angle, θ, relative to the sample normal. The inset shows the *L*-edge absorption and XMCD from a film of Fe clusters on HOPG [25]. (b) MLDAD measures the difference in the 3p photoemission spectra (from 3d transition metals) taken with linearly polarised XUV light on reversing the magnetisation in the sample plane and perpendicular to the photon polarisation vector. (c) MCDAD measures the difference in the 3p photoemission spectra taken with circularly polarised XUV light on reversing the magnetisation along the direction of the photon angular momentum. The inset shows MLDAD from an Fe film grown on CoSi [59].

expectation value of the magnetic dipole operator given by

$$T = \frac{1}{2}[\mathbf{S} - 3\hat{\mathbf{r}}(\hat{\mathbf{r}} \cdot \mathbf{S})] \tag{3}$$

This term averages to zero over all directions and does not contribute to the measured magnetisation in conventional magnetic measurements but since the X-rays sample a directional cut through the atomic electron density, the term must be included in the sum rule. It can be eliminated, yielding the pure spin moment, by averaging measurements over all X-ray incidence angles, making a single measurement on a polycrystalline sample or, for samples with rotational symmetry about the substrate normal, making a single measurement at the 'magic' angle of 54.7° ($= \arctan\sqrt{2}$) [53, 54]. The number of valence band holes can be determined by measuring the integrated (white line) L-edge absorption strength, which is proportional to n_h, of a thick film of the same material in situ and comparing it to that of the clusters. One of the powerful attributes of XMCD is that, since it derives from an X-ray absorption edge, it is element-specific, thus it can determine, separately, the orbital and spin moments localised in different magnetic elements in heterogeneous systems, as demonstrated in Fig. 5.

The only sources that emit a sufficiently high flux of circularly polarised X-rays to study nanostructures by XMCD are synchrotron storage rings. These produce circularly polarised radiation of helicity either above or below the orbit plane of the electrons and also from insertion devices such as helical undulators [55].

Dichroism is also observed in the 3p angle-resolved photoemission spectra of 3d transition metals taken with linearly or circularly polarised light with the geometries shown in Fig. 4b and c. The techniques measure the difference in the spectra in response to reversing the alignment between the in-plane sample magnetisation and

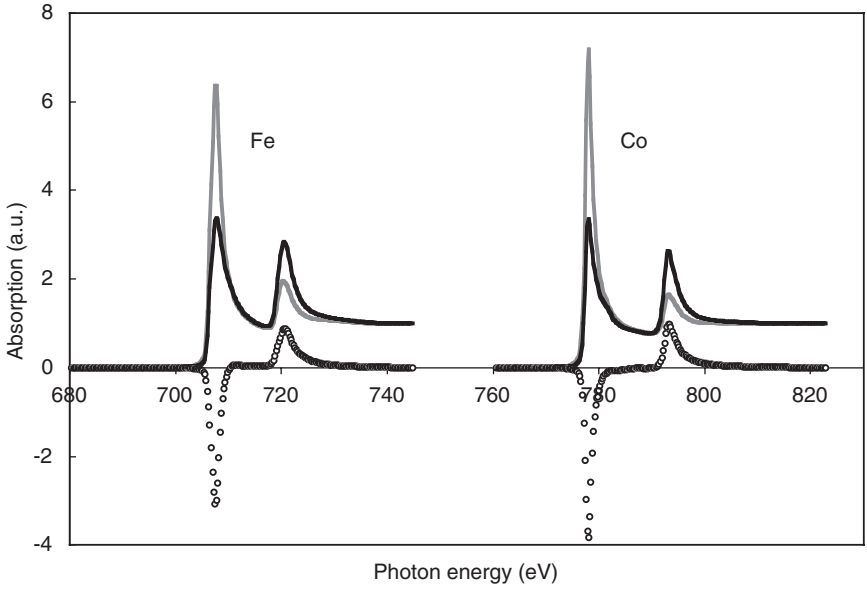

Figure 5: L-edge absorption and XMCD measurements from Fe clusters coated with Co.

the linear polarisation of the XUV light (MLDAD [56]) or between the out-of-plane sample magnetisation and angular momentum of circularly polarised light (MCDAD [57]). Since angle-resolved photoemission spectra must be collected in zero field, the techniques are, in general, restricted to measuring remanence, but they are surface sensitive and capable of measuring sub-monolayer quantities of material. Also, it is possible to deposit clusters onto a magnetic substrate whose remanence keeps the clusters magnetised [58]. In fact, the exchange interaction between a clean magnetic substrate and deposited clusters is equivalent to a large applied field [59] but still allows photoemission measurements. As with XMCD, a synchrotron source must be used to provide the polarised XUV radiation and endstations at which light of variable polarisation is available can be fitted with movable magnetising coils allowing both geometries to be combined in a single experiment. This enables the comparison of in-plane and out-of-plane magnetisation.

2.3. Magnetism in exposed clusters

In this section, the behaviour of magnetic clusters deposited on a surface and left exposed to vacuum will be considered. Working in this regime requires that the cluster deposition must be carried out in situ and the measurements performed in very good UHV conditions ($\sim 10^{-11}$ mbar) to avoid contamination of the clusters. In the case of free clusters, some gas adsorption on the clusters can be tolerated as the mass-separation can distinguish the clean clusters from those with gas molecules attached. In deposited samples, most in situ magnetic measurements have been done with spatially averaged techniques such as XMCD that measure the entire cluster assembly and are unable to discriminate between the behaviour of clean and contaminated clusters. There are, however, several experimental advantages in studying adsorbed clusters, for example, it is possible to exert accurate control over the cluster temperature down to low cryogenic values allowing the magnetically blocked state to be observed. In addition, structural techniques such as X-ray diffraction, STM and TEM can be used as well as more powerful magnetic probes such as XMCD, which is able to determine the spin and orbital components of the total moment. Finally, the interactions between the clusters can be studied by accumulating a sufficient density on the surface.

2.3.1. Isolated elemental clusters

A natural starting point in describing adsorbed clusters is to review measurements carried out at very low coverages to determine the behaviour of the isolated particles. An important question to address is whether the enhanced magnetic moments observed in free transition metal clusters are retained if the cluster is adsorbed on a surface. The earliest reported studies of isolated and exposed magnetic clusters deposited from the gas phase onto surfaces in UHV were of size-selected 2.5 nm (700-atom) Mn clusters at very low coverages on HOPG substrates [60, 61]. Photoelectron spectroscopy using synchrotron radiation was used to probe shallow core levels and showed changes in the lineshape of the Mn 3s photoemission spectra that were consistent with an increased magnetic moment of the atoms in the cluster estimated at about 20% larger than the bulk value. The experiment was insensitive to the spin configuration.

More recently, the powerful XMCD technique has been utilised in deposited cluster experiments and while addressing the magnitude of the moment, it is also possible to

obtain information on the separate contributions of the spin and orbital components. To gain some understanding of the effect of the interaction with the substrate, it is useful to consider results from isolated atoms of Fe, Co and Ni adsorbed on K and Na films obtained by Gambardella et al. [62]. They studied films with coverages as low as 0.2% of a monolayer and used the most accurately measured quantity obtainable by the XMCD technique, that is, the ratio:

$$R = \frac{\langle L_z \rangle}{2\langle S_z \rangle + 7\langle T_z \rangle} \tag{4}$$

to determine how 'atomic-like' the adsorbed atoms were. The valence state of each element was determined by modelling the shape of the $L_{2,3}$ absorption edge and was found to be d^7 for Fe, d^8 for Co and d^9 for Ni. Knowing this, the quantities in Eq. (4) can be obtained by Hund's rules and the atomic value of R (R_{atom}) compared with the measured one (R_{exp}). The ratio $R_{\text{exp}}/R_{\text{atom}}$ was found to be 100%, 89% and 63% for Ni, Co and Fe, respectively, that is Ni has the same moments as in a free atom with the same valence, while Co and Fe show a 10% and 37% decrease, respectively. The reductions are due to a partial quenching of the orbital moment, but even in the case of Fe the quenching is much less than in isolated Fe impurities embedded in a bulk host.

Mass-selected Fe_N clusters with sizes $N = 2$–9 adsorbed, at the dilute limit, on Ni thin film substrates have been studied by Lau et al. [63]. For such small clusters, it is important to ensure a soft-landing, and this was achieved by depositing the clusters, decelerated to 2 eV/atom, onto Ar multilayers that were physisorbed at 15 K on the substrate. These were then removed by flash heating to 100 K. Substantial increases in the orbital-to-spin ratio and the spin and orbital moments per valence band hole relative to the bulk were observed, but the uncertainty in n_{h} and the $\langle T_z \rangle$ term meant that absolute values were not given. Larger clusters in the size range 180–690 atoms deposited at low coverage on graphite were studied using XMCD by Baker et al. [64]. In this study, the vale of n_h was obtained by comparing the total Fe $L_{2,3}$ absorption cross-section of the clusters with that of a thick conventional film deposited in situ and was found to be the same within experimental uncertainty. Thus, n_{h} could be taken as the bulk value of 3.39 [65]. In addition, the $\langle T_z \rangle$ term was obtained by measuring the dichroism as a function of the incident angle of the X-rays so absolute values of the magnetic moments were obtained and the total moment was found to be about 10% greater than the bulk value with about half of this enhancement coming from an increased orbital contribution.

The different datasets for adsorbed Fe atoms [62], small Fe_N ($N = 1$–9) clusters [63] and larger Fe_N ($N = 180$–690) clusters [64] can be compared directly by plotting the orbital ($\langle L_z \rangle$) and spin ($\langle S_z \rangle$) angular momenta per valence band hole, n_{h}, as is done in Fig. 6. For the adsorbed Fe atoms on K, the valence state was identified as d^7 so $n_{\text{h}} = 3$ [62]. The orbital and spin moments for the isolated atoms shown in Fig. 5 were derived from the published R value, described above, assuming that most of the reduction in R is due to a partial quenching of the orbital moment. For the small clusters, the published data for the orbital component is $\langle L_z \rangle / n_{\text{h}}$, which can be entered directly on the plot. The spin term is given as $\langle S_z \rangle + 7/2\langle T_z \rangle$ and the pure spin component has been extracted assuming that $\langle T_z \rangle$ is the average of the value in isolated atoms ($-1/7$) and that in the larger deposited clusters ($-0.11/7$) [64]. The $\langle L_z \rangle / n_{\text{h}}$ and $\langle S_z \rangle / n_{\text{h}}$ values

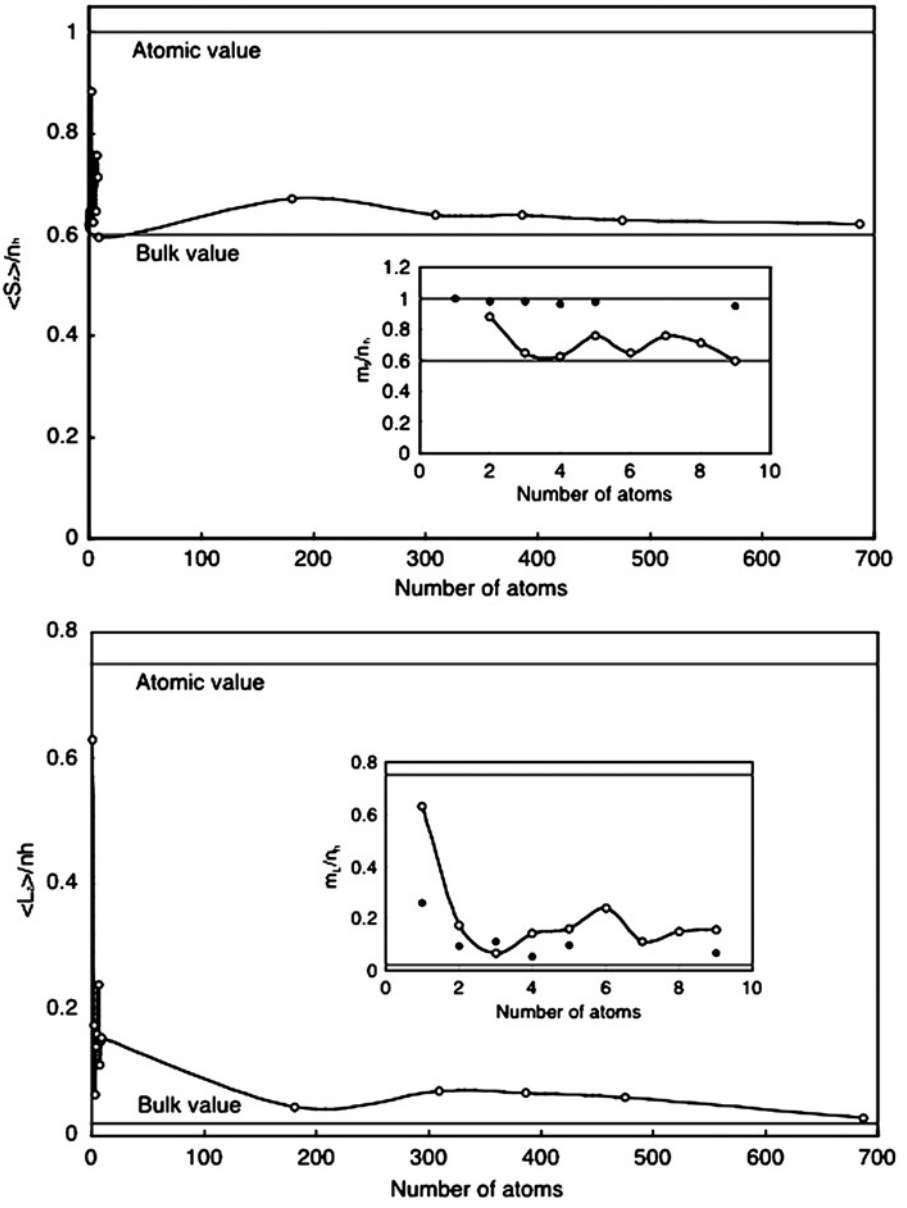

Figure 6: Angular momentum values $\langle S_z \rangle$ and $\langle L_z \rangle$ per valence band hole, n_h measured by XMCD for Fe_N clusters as a function of N, the number of atoms in the cluster, adsorbed on various substrates (open circles). Fe_1/K data from Gambardella et al. [62], Fe_2–Fe_9/Ni data from Lau et al. [63] and Fe_{180}–Fe_{690}/HOPG data from Baker et al. [64]. The insets show the small cluster region in more detail. The filled circles are the $\langle S_z \rangle$ and $\langle L_z \rangle$ values per valence band hole calculated by Lazarovits et al. [66].

for the larger clusters were obtained from the published orbital and spin magnetic moments and dividing by the value of n_h (3.39) measured during the experiment. The results of a relativistic calculation of the orbital and spin moments in small Fe clusters adsorbed on Ag(1 0 0) surfaces [66] are also shown in Fig. 6. The calculation for the spin moment tends to overestimate the values but, apart from the monomer, the calculated orbital moment agrees well with the measured values.

Whatever the inaccuracies in the assumptions made in the comparison of the different datasets and notwithstanding the different substrates used in the experiments, some general conclusions can be drawn from Fig. 6 about the size-dependent magnetic behaviour of supported Fe clusters. Both the orbital and spin components decrease rapidly with cluster size and with only three atoms/cluster values close to the bulk value are found for both $\langle L_z\rangle/n_h$ and $\langle S_z\rangle/n_h$. This is different to the behaviour of free Fe clusters in which moments close to the atomic limit were found up to $N = 12$ [10]. There is evidence for short- and long-period oscillations in both moments as a function of size. Over a wide size range, the total magnetic moment is about 10% larger than the bulk with about half of the enhancement coming from the orbital moment. The adsorbed cluster moments converge with the bulk values for $N \geqslant 700$, as observed in free clusters [7].

It would seem that for sizes larger than 700 atoms (2.5 nm), the cluster magnetic moments have converged with those of bulk Fe. This does not rule out novel effects for larger sizes, for example in interacting cluster films, the consequence of having a nanoscale grain structure, even at the 10 nm scale (~50,000 atoms), is a profound change in the way the film magnetises in an external field (see Section 3). Even the properties of isolated clusters show interesting effects at larger sizes however. According to recent measurements by Bansmann and Kleibert [67], the orbital moment rises again for larger cluster sizes (Fig. 7) and looked at over a broad size range of 0.2–10.75 nm (2–55,000 atoms) it appears to go through a series of oscillations.

This behaviour could indicate structural changes in the supported particles. In clusters the bulk cohesive energy must be balanced against the surface energy and the increasing dominance of the surface term as the cluster size decreases means that it is possible to set up highly strained structures in order to minimise the surface energy. For materials with a close-packed atomic structure, generally one expects there to be a transition from a close-packed to an icosahedral structure below some critical size, with possibly an intervening decahedral structure [68]. In the case of bcc materials like Fe, a further transition from the bcc to the fcc phase is also expected at some larger size.

This may be what is indicated in Fig. 7. Larger supported Fe clusters such as those studied by Bansmann and Kleibert [67] are bcc as verified by TEM imaging of individual particles with sizes in the range 4–10 nm [69, 70]. In the intermediate size range, Baker et al. [71] showed, using extended X-ray absorption fine structure (EXAFS) that Fe clusters embedded in amorphous carbon are a mixture of fcc and bcc phases. As discussed in Section 3, embedded clusters show a structure that very much depends on epitaxy with the matrix material, but if the matrix is amorphous carbon then it is likely that the cluster structure is the same as clusters adsorbed on HOPG. It is tempting, therefore, to associate the oscillatory structure of Fig. 7 to a transition from a bcc to an fcc phase at around 700 atoms (2.5 nm) followed by a transition from the close-packed to another phase below about 100 atoms. In free clusters, this small cluster structure would be icosahedral but for supported clusters there are other

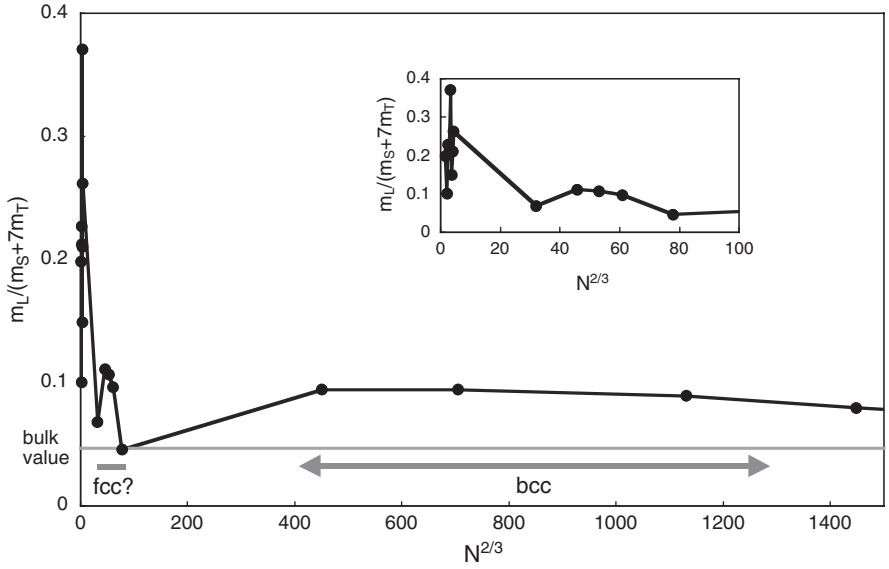

Figure 7: $m_L/(m_S+7m_T)$ ratio for Fe clusters over an extended size range (2–55,000 atoms) obtained by combining the data from Lau et al. [63], Baker et al. [64] and Bansmann and Kleibert [67]. The data are plotted as a function of $N^{2/3}$, which is proportional to the number of surface atoms.

possible morphologies including flat 2D islands. In this regime, large changes in the orbital moment are observed when incrementing the cluster size by a single atom.

An uncertainty in the above analysis is that Fig. 7 presents data from Fe clusters on different substrates (Ni, HOPG and Co) and this may affect the variation of the element-specific moments. Measurements were carried out by Bansmann et al. [72] on large (5–12 nm) Co clusters deposited on Ni(1 1 1) and Fe(1 1 0) substrates. For Co clusters supported on Fe substrates, the measured orbital and spin moments are close to the bulk values, whereas on Ni substrates they are slightly reduced. Interestingly, Co is expected to stay in the close-packed phase throughout the large-size regime through to small clusters so one would not expect the large particle 'hump' in the orbital moment observed for Fe in Fig. 7.

The Rostock group also carried out a study using XMCD of the orbital and spin moments in exposed 7.5 nm diameter FeCo alloy clusters produced by an arc cluster ion source (ACIS) employing an FeCo alloy target [73, 74] and deposited in situ onto an Ni(1 1 1)/W(1 1 0) substrate. The data were recorded in remanence after magnetisation with an external magnet and since the Ni films have a remanence that is nearly 100% of saturation, the exchange coupling with the Fe–Co clusters at the surface ensures that the clusters were saturated, as required for a sum rule analysis of the magnetic moments. Figure 8 shows the photoabsorption spectra of the two alloy metals involved, Fe and Co. It is seen that the dichroism has the same sign for the spectra demonstrating the ferromagnetic coupling between the elements. The figure also illustrates nicely the element specificity of the technique that yields the magnetic moments per atom of each element.

A sum rule analysis of the optical absorption data reveals enhanced spin and orbital moments in both constituents (Fe and Co). These are listed in Table 1 and compared

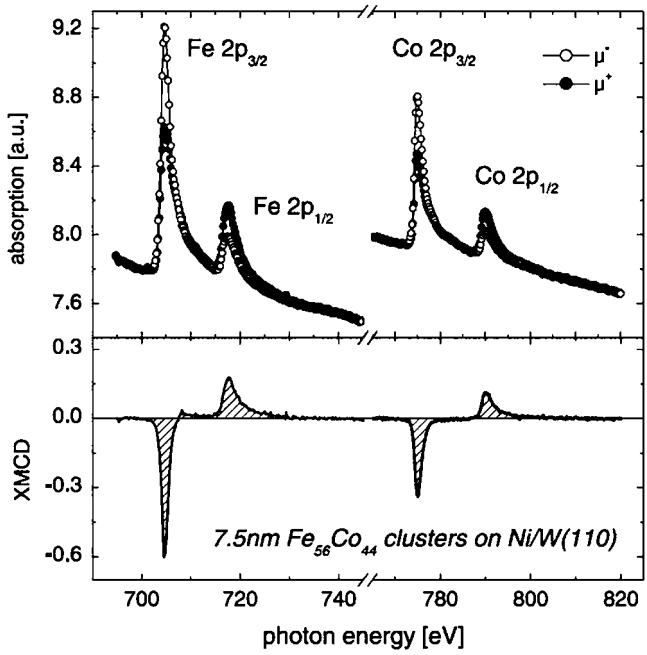

Figure 8: Upper part: photoabsorption spectra of 7.5 nm Fe–Co particles deposited on a Ni(1 1 1) film on W(1 1 0) taken in remanence with circularly polarised radiation for opposite magnetisation directions μ^+ and μ^-. Lower part: corresponding XMCD data (intensity differences). Reproduced with permission from Ref. [67].

with the bulk values. The Fe moments in the alloy particles agree with calculated values for the $Fe_{50}Co_{50}$ bulk [75], whereas the Co moments exceed the calculated values by about 15% (spin moment) and 50% for the orbital moment. Note that the estimated uncertainty in the experimental values is about 10%. The increased magnetic moment in bulk Fe–Co alloys can be understood by the increased spin polarisation due to the degree of band filling within a rigid band model.

When assuming a homogenous mixture of Fe and Co in these relatively large particles (~7.5 nm diameter), it is likely that the behaviour is similar to the bulk. However, even for a 7.5 nm particle, an additional perturbation arises due to the fact that ~40% of the atoms are on the two outermost surface atomic layers in which increased orbital moments are expected. Although it is known that calculations in general underestimate the orbital moment, the data indicate that there is some

Table 1: Magnetic moments of pure Fe, Co, and 7.5 nm $Fe_{56}Co_{44}$ alloy clusters deposited onto Ni/W(1 1 0) [73].

	Co			Fe			Average μ/atom (μ_B)
	m_L (μ_B)	m_S (μ_B)	m_T (μ_B)	m_L (μ_B)	m_S (μ_B)	m_T (μ_B)	
$Fe_{56}Co_{44}$	0.21	2.00	2.21	0.10	2.30	2.40	2.32
Fe, Co bulk	0.15	1.55	1.70	0.09	2.00	2.09	–

The corresponding bulk values have been taken from Ref. [75].

additional enhancement arising from the high surface-to-volume fraction in nanoparticles. This is in accord with the observation of an enhanced orbital moment in large Fe clusters shown in Fig. 7.

As the particles get smaller, the bulk interpretation becomes less applicable. Recent ab initio theoretical studies of very small Fe_mCo_n clusters, where $m+n \leqslant 6$ [76] and $m+n = 5$, 13 [77], showed that the moment per atom increases monotonically as a function of the Fe content rather than going through a peak as observed in the Slater–Pauling curve. It was also shown in the case of five-atom Fe_mCo_n [76] clusters that the moment is enhanced relative to pure Fe clusters of the same size due to structural changes induced by including Co.

2.3.2. The effect of cluster–cluster interactions of exposed clusters on surfaces

In an experiment studying clusters deposited in situ onto substrates, observing the effect of a changing inter-cluster interactions is a simple matter of varying the coverage. Figure 9 shows how the value of m_L, obtained by XMCD measurements in 400-atom Fe clusters (2.1 nm diameter) deposited on graphite, varies with cluster coverage. The coverage is expressed as the equivalent thickness in Å of a continuous layer and so on this scale 12.5 Å corresponds to a densely packed hexagonal cluster monolayer and 7.5 Å is the equivalent thickness for the two-dimensional percolation threshold. A significant drop in the measured value of m_L occurs and converges with the bulk value as the monolayer is approached. It is clear that as the clusters come into contact the enhancement in the orbital moment is lost. This is expected following the calculations of Guirado-Lopez et al. [78] who showed that the orbital moment enhancement in transition metal clusters in this size range is confined to the surface layers with the interior of the cluster showing a bulk-like quenching. Thus, as surface

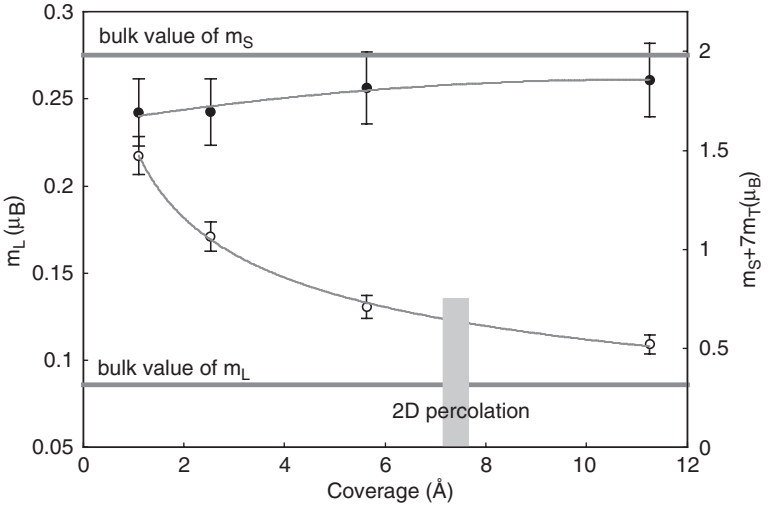

Figure 9: Values of m_L (open circles) and $m_S + 7m_T$ (filled circles) obtained by normal incidence XMCD from un-filtered Fe clusters (mean size = 400 atoms) on HOPG as a function of cluster coverage measured as an equivalent film thickness. A close-packed monolayer corresponds to approximately 12.5 Å film thickness and the percolation threshold would occur at around 7.5 Å. The bulk values of orbital and spin moments measured by XMCD are indicated. Reproduced with permission from Ref. [24].

atoms come into contact with those of neighbouring clusters and adopt high co-ordination sites, the quenching of the orbital moment will extend to the surface. A similar result was observed by Bansmann and Kleibert who demonstrated, using XMCD, a decay of the orbital moment with coverage in large 9 nm diameter (~32,000 atom) Fe clusters deposited on Co/W(1 1 0) substrates [73].

The apparent small change in the spin moment observed in Fig. 9 is a consequence of a changing value of the dipole moment m_T (Eq. (3)) as the coverage is increased. This term produces a variation of the 'effective' spin moment measured by XMCD as a function of the measurement angle with respect to the surface normal. It is expected to be insignificant in bulk systems in which there is a highly symmetric distribution of the spin moment but in isolated 690-atom clusters it was estimated to have a magnitude of $0.012\mu_B$ [64] and oriented opposite to the spin moment. Thus, as the cluster coverage increases and the system becomes more 'bulk-like', the decreasing dipole moment will appear as a small increase in the effective spin moment. This effect masks any variation in the true spin moment (as would be measured by another technique) as a function of coverage. Evidence for an enhanced spin moment in a thick film of clusters comes from a study using MLDAD of Fe clusters deposited on vitrovac (an amorphous CoSi alloy) substrates [59]. Figure 10 shows the normalised MLDAD signals from a 50 Å thick layer of 260-atom Fe clusters and a similar thickness Fe MBE film, both deposited in situ. It is clear that there is a 5% increase in the

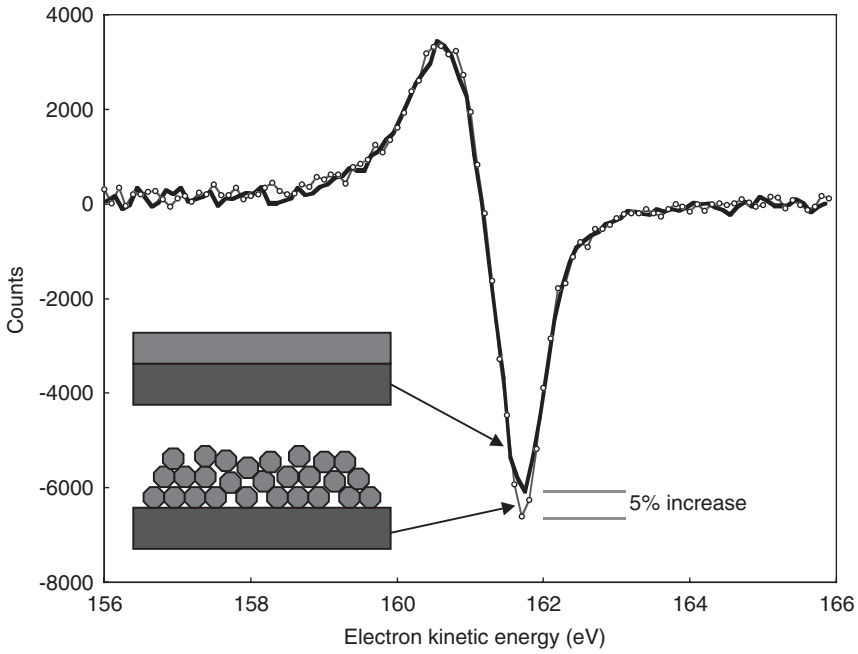

Figure 10: A comparison of the MLDAD signal (see Fig. 2) from a thick layer (50 Å) of Fe clusters containing ~260 atoms on vitrovac (thin curve with open circles) with a similar-thickness MBE-grown Fe film on vitrovac (thick curve). Both films are magnetically saturated in both directions by the exchange field at the interface and it is observed that the MLDAD signal is 5% higher in the cluster film. Reproduced with permission from Ref. [59].

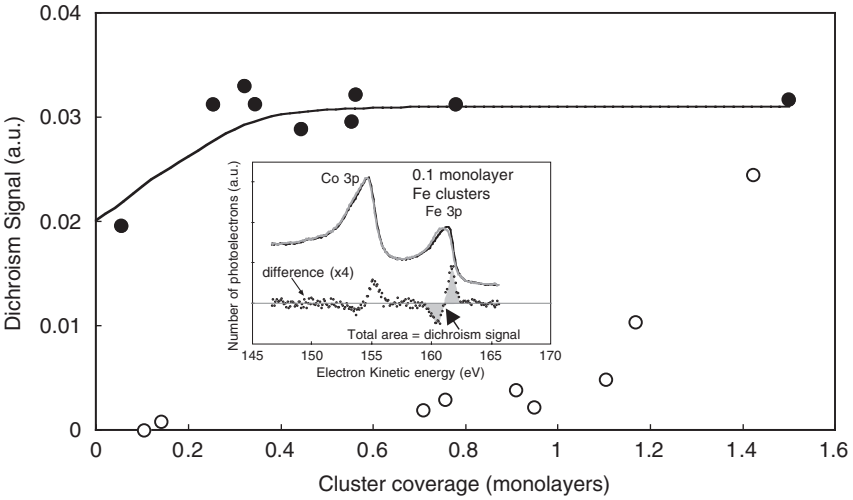

Figure 11: Strength of the MLDAD dichroism signal, normalised to the Fe 3p peak intensity, as a function of coverage for deposition of 141-atom Fe clusters on magnetic vitrovac substrates and 400-atom Fe clusters on non-magnetic Cu and HOPG substrates [79] (open circles). The solid line shows an MC simulation of the magnetisation in growing superparamagnetic cluster islands in the interface exchange field of the vitrovac as a function of coverage (see text). The inset shows a photoemission and dichroism spectrum for both directions of sample magnetisation indicating how the total dichroism signal is obtained. Reproduced with permission from Ref. [59].

dichorism from the cluster film indicating an increased spin moment even in a dense assembly.

The same study determined the strength of the exchange interaction between a deposited magnetic cluster and a magnetic substrate. Figure 11 shows the MLDAD dichroism signal, obtained by taking the total area within the dichroism spectrum (inset) divided by the Fe 3p intensity, as a function of coverage of 141-atom Fe clusters deposited onto a magnetic vitrovac substrate [59] (filled circles). The magnetic saturation of the cluster films is observed and there is a significant magnetisation of the isolated clusters at very low coverage. This is the magnetisation of the isolated superparamagnetic clusters exposed to the magnetic field at the vitrovac surface. The effect of the ferromagnetic substrate is demonstrated by comparing the data to previously reported MLDAD measurements [79] from Fe clusters deposited in situ onto HOPG surfaces at 40 K. Antiparallel saturating fields have been applied to these clusters prior to taking spectra, but at low coverage, despite the lower temperature, the superparamagnetism in the supported clusters returns the magnetisation to zero until the coverage reaches a complete monolayer and the film becomes ferromagnetic.

For the clusters on the magnetic substrate, the effective field, B, acting on them at the lowest coverage, at which they can be assumed to be the isolated clusters is given by inserting their magnetisation (relative to saturation) and a temperature of 300 K into Eq. (2). This gives an effective field of about 4 T. A more rigorous procedure uses a Monte Carlo (MC) simulation to obtain the average island size as a function of coverage and (assuming that the larger islands remain superparamagnetic) obtains the expected magnetisation at each coverage. The solid line in Fig. 11 shows the best fit

through the data optimised by adjusting B as the single parameter, which confirms an effective field of 4 T acting on the clusters in contact with the vitrovac. This is the average field within the clusters and is clearly much larger than the dipolar fringing field above the vitrovac, whose internal field at saturation is about 1 T. Its source is the molecular field due to the exchange interaction between the particles in direct atomic contact with the vitrovac surface. The molecular field can be assumed to decay exponentially with height above the surface with a characteristic exchange length, l_{ex}, of about 3 Å, as shown schematically in Fig. 12. The average field within a cluster with a diameter d is given by

$$B_{av} = B_{ex}\frac{l_{ex}}{d}\left(1 - \exp\left(\frac{d}{l_{ex}}\right)\right) \tag{5}$$

where B_{ex} is the effective field due to exchange at the contact point of the clusters on the vitrovac. Thus, to obtain a mean field of 4 T requires an interface exchange field of ~20 T. This is about 50 times smaller than the molecular field in bulk Fe but is of the same order of magnitude as the exchange coupling between neighbouring Fe clusters [80].

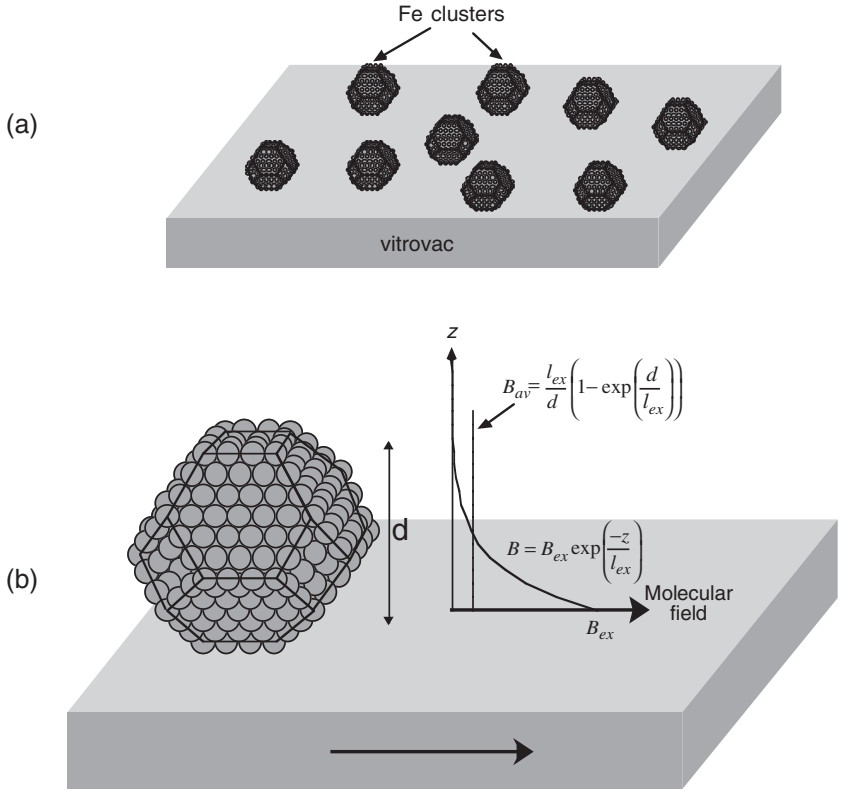

Figure 12: (a) Schematic diagram of Fe clusters deposited on vitrovac. (b) Schematic of the molecular field within Fe clusters adsorbed on vitrovac due to the exchange interaction at the contact point between the clusters and the substrate. Reproduced from Ref. [59] with permission from IOP Journals on 6 Jan. 2007.

Magnetism has only been studied experimentally in deposited 3d transition metal clusters so far but ab initio calculations of the spin moment in small 4d metal clusters with different geometries on Ag(1 0 0) were carried out by Wildberger et al. [81]. While they found a permanent moment in dimers for elements between Mo and Rh in the periodic table, magnetism was less favoured as the cluster size increased. In the case of the largest clusters studied, i.e. nine-atom flat islands, only Ru and Rh had stable moments. The Rh moment was $0.6\mu_B$, which compares with $0.8\mu_B$ measured in nine-atom free Rh clusters [13].

3. EMBEDDED NANOPARTICLE ASSEMBLIES

Section 2 focused on in situ experiments on magnetic clusters deposited on surface and exposed to vacuum. In this section, the behaviour of assemblies of nanoparticles embedded in solid matrices will be summarised. The films include deposited clusters coated in situ with other materials and films produced by the co-deposition technique (Fig. 1) that can be removed from the vacuum system for ex situ measurements. This opens a wide variety of possible measurements including conventional magnetometry. In addition, the choice of the material of the embedding matrix is an extra parameter to modify the behaviour of the magnetic nanoparticles. The discussion will include isolated cluster behaviour in very dilute assemblies, higher densities in which there is significant interaction through to pure cluster films several layers thick deposited with no matrix. These nanostructured magnetic materials show magnetisation behaviour that is different to similar thickness conventional films.

3.1. Atomic structure of embedded clusters

Numerous high-resolution TEM studies of transition metals have been carried out (see Ref. [82] and references within). Examples of images of isolated Co and Fe clusters embedded in amorphous carbon (a-C) from the gas phase are shown in Fig. 13. The Fe particle (Fig. 13a) has a dodecahedral shape and an atomic bcc structure while the Co

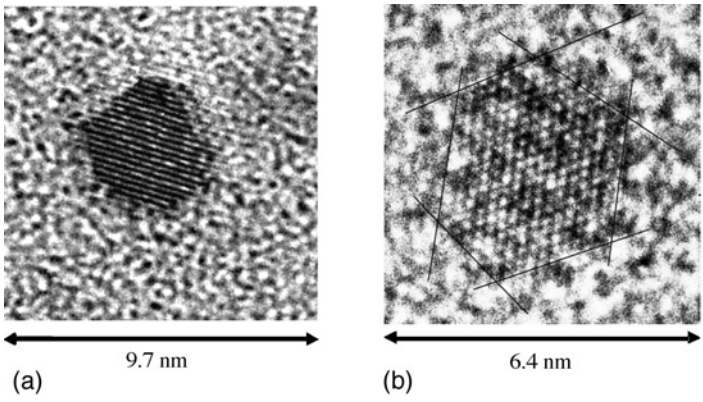

Figure 13: High-resolution TEM images of (a) an isolated bcc Fe cluster and (b) an isolated fcc Co cluster embedded in amorphous carbon. The dodecahedral and truncated octahedral shapes, respectively, are consistent with the minimum energy morphologies predicted by Wulff's constructions [83]. Reproduced from Ref. [43] with permission from IOP Journals on 6 Jan. 2007.

Table 2: Structural parameters of Fe clusters embedded in various matrices.

Matrix Material Containing Fe Clusters	Volume Fraction (%)	r_1 (Å)	r_2 (Å)	R_3 (Å)	r_4 (Å)	Structure of Fe Clusters
Silver	5	2.49±0.01	2.85±0.01	4.10±0.01	4.79±0.01	Bulk bcc
	40	2.49±0.01	2.85±0.01	4.08±0.02	4.77±0.01	structure
Copper	6	2.53±0.02	3.57±0.02	4.43±0.02	5.28±0.02	γ-Fe fcc structure with slightly reduced lattice parameter
Amorphous carbon	4	2.49±0.01	2.56±0.02			Mixture of bcc and fcc phases
	40	2.46±0.01	2.57±0.01			
Cobalt	9	2.49±0.02	2.84±0.02	4.06±0.02	4.78±0.02	Bulk bcc structure
Bulk bcc Fe		2.49	2.87	4.06	4.76	

particle (Fig. 13b) is a truncated octahedron and has an fcc atomic structure. The shapes of both particles are consistent with the minimum energy morphologies predicted by Wulff's construction [83].

Amorphous carbon matrices, which are highly transparent to energetic electrons, are useful for obtaining TEM images but are not very interesting for technological applications where generally the nanoparticles are embedded, by co-deposition, within a metal film. For clusters in general matrices, EXAFS measurements are a powerful method of obtaining atomic structures. They yield inter-atomic distances out to fourth nearest neighbours between different chemical combinations of atoms. Table 2 shows the results of an EXAFS study, using the SRS at Daresbury Laboratory [71], of samples of Fe nanoparticles embedded in various matrices with a range of volume fractions using the co-deposition technique (Fig. 1). The particle size distribution was log-normal with a median diameter of 1.85 nm (280) atoms. An interesting picture emerges, that is, the atomic structure of the Fe nanoparticles is determined by epitaxy with the matrix material. Thus, the Fe structure is found to be bcc in Ag and Co matrices, where there is a close lattice match between the Fe bcc and Ag or Co close-packed lattice and becomes fcc in Cu in which the γ-fcc Fe lattice is well matched to the Cu fcc structure. The structure of the isolated clusters does not change if the volume fraction is increased to beyond the percolation threshold. In a-C matrices where the clusters have no epitaxial relationship with the matrix, the Fe particles are found in both the fcc and bcc phases. It is tempting to associate the smallest clusters in the size distribution with the more closely packed fcc phase and the larger clusters with the bcc phase as discussed in Section 2. It is likely that the atomic structure of the Fe clusters in the a-C matrix is the same as when they are in the gas phase. Films of Fe clusters embedded in Co are an important material for the production of high-moment films as reported in Section 4.2.

The measurements were also carried out for Co clusters with a similar size distribution embedded in Ag and Fe matrices [39] and the results of the analysis are shown in Table 3. The Co clusters in Ag show a close-packed structure but the measurements were unable to distinguish between the fcc and hcp phases. A significant result is that

Table 3: Structural parameters of Co clusters embedded in Ag and Fe matrices.

Matrix Material Containing Co Clusters	Volume Fraction (%)	r_1 (Å)	r_2 (Å)	r_3 (Å)	r_4 (Å)	Structure of Co Clusters
Silver	5	2.49 ± 0.02	3.49 ± 0.02	4.04 ± 0.02	4.36 ± 0.02	Close-packed hcp or fcc
Iron	7	2.45 ± 0.02	2.86 ± 0.02	4.06 ± 0.02	4.73 ± 0.02	Bcc Fe structure

Table 4: Coordination numbers of Co-atoms in a cluster consisting of an fcc-truncated octahedron embedded in a matrix M.

Type of the Co–M Interface for a Co-Cluster Model Embedded in a Matrix M	$N_{\text{Co–Co}}$ (Total = Core + Disturbed)	$N_{\text{Co–M}}$ (Total)
Epitaxy Co–M with an abrupt interface	$10.6 = 10.6 + 0$	1.4
One diffuse layer at the Co–M interface	$8.8 = 6.5 + 2.3$	3.2
Two diffuse layers at the Co–M interface	$6.5 = 2.9 + 3.6$	5.5
Three diffuse layers at the Co–M interface	$4.6 = 1.6 + 3$	7.4

The size of the cluster considered in this case is 3.4 nm (1289 atoms, $m = 5$ layers). For clusters of this size, the coordination numbers predicted for the formation of 0, 1, 2 or 3 intermixed CoM layers are shown.

the Co clusters embedded in Fe have the bcc structure, which has important implications for its magnetic behaviour. In general, the interface of clusters embedded in the noble metals was sharp with some evidence for intermixing in the case of transition metal matrices. Even for these small clusters in a miscible transition metal matrix, however, there always remains a pure elemental cluster core. This justifies the assertion in Section 1 that the cluster/atom co-deposition technique is able to produce nanogranular mixtures of miscible metals.

An EXAFS study carried out at the LURE synchrotron on isolated Co clusters embedded in metal matrices including Ag, Pt and Nb focused on the degree of intermixing at the cluster/matrix boundary [84, 85]. Table 4 shows the predicted Co–Co and Co–matrix coordination numbers for isolated Co particles in metal matrices with different degrees of intermixing at the Co–matrix interface. It was assumed that the Co clusters had a mean diameter of 3.4 nm (1289 atoms), which is the same size as the particle shown in the TEM image of Fig. 13b. For all the matrices, the Co atomic structure was found to be close-packed but fcc rather than the bulk hcp structure. The Co–Co coordination includes the core (dense Co) part and the 'disturbed', i.e. more diffuse Co with a larger separation in the case where interfacial mixing occurs. The measured values of $N_{\text{Co–Co}}$ and $N_{\text{Co–M}}$, where M is Ag, Pt or Nb, are shown in Table 5 and comparison with Table 4 reveals that the interface is sharp with no intermixing in the case of Co clusters embedded in Ag matrices but that there are one and two mixed atomic layers in Pt and Nb matrices, respectively.

3.2. In situ studies of Co-coated Fe clusters

Edmonds et al. [25] carried out an XMCD study of dilute assemblies of Fe clusters deposited on HOPG and coated with Co films in situ. They showed that the combined films consist of flat Co islands with embedded Fe clusters and whereas the exposed Fe

Table 5: Coordination numbers of Co atoms in different matrices, N_{Co-M} (M = Ag, Pt or Nb) as deduced from the fits to the EXAFS spectra.

Sample	N_{Co-Co} (Total = Core + Disturbed)	N_{Co-M} (Total)	Degree of Intermixing at Interface
Co-clusters/Ag-matrix	11	1	Sharp interface
Co-clusters/Pt-matrix	9.6	2.4	1 atomic layer mixed
Co-clusters/Nb-matrix	7	5	2 atomic layers mixed

clusters prior to coating appeared to be magnetically isotropic (see Fig. 14), the coated clusters showed a strong in-plane anisotropy. It was assumed that this arose from the shape anisotropy of the Co islands and was superimposed on the Fe clusters, which were exchange-coupled to the Co. The orbital (Fig. 15a) and spin (Fig. 15b) moments localised on the Fe clusters could be extracted due to the chemical specificity of XMCD. The orbital moment loses the sharp variation with cluster size seen in the exposed clusters, which may be due to a suppression of the bcc–fcc transition expected in the exposed clusters. As shown in Section 3.1, epitaxy with the Co matrix maintains the Fe clusters in the bcc phase. Nevertheless, the orbital moment stays significantly enhanced relative to the bulk value. The spin moment, shown in Fig. 15b, is increased following the Co coating by about $0.2\mu_B$ at all cluster sizes investigated. Note that the comparison between the exposed and Co-coated Fe clusters in Fig. 15b is made for data taken at the 'magic' angle (54.7°) so that the dipole term should be zero in both sets of data. Figure 15c shows the measured size-dependent spin moment compared with the tight-binding calculation by Xie and Blackman [86] for free Co-coated Fe clusters, with a composition of Fe_NCo_{1021-N}. In order to carry out the comparison,

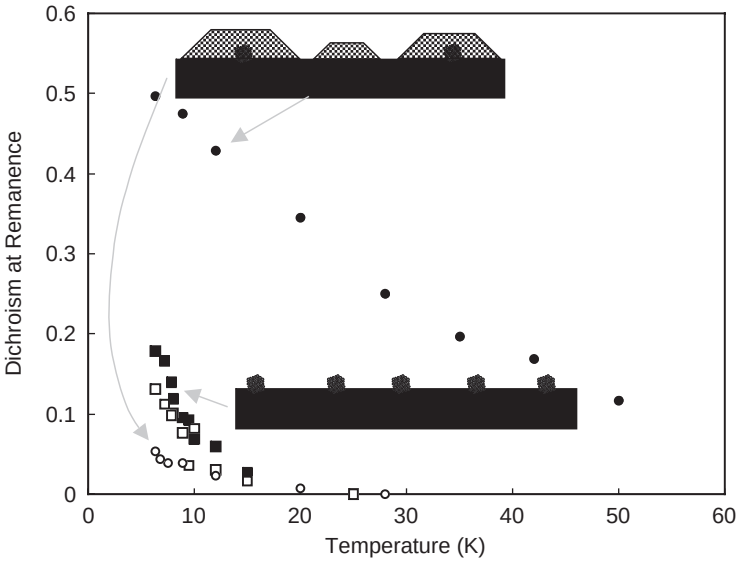

Figure 14: Ratio of remanent to saturation magnetisation measured from the Fe $L_{3,2}$ XMCD spectra signal vs. sample temperature of the exposed (squares) and Co-capped (circles) Fe clusters. Out-of-plane measurements are denoted by open symbols and in-plane by filled symbols. Reproduced from Ref. [25] with permission.

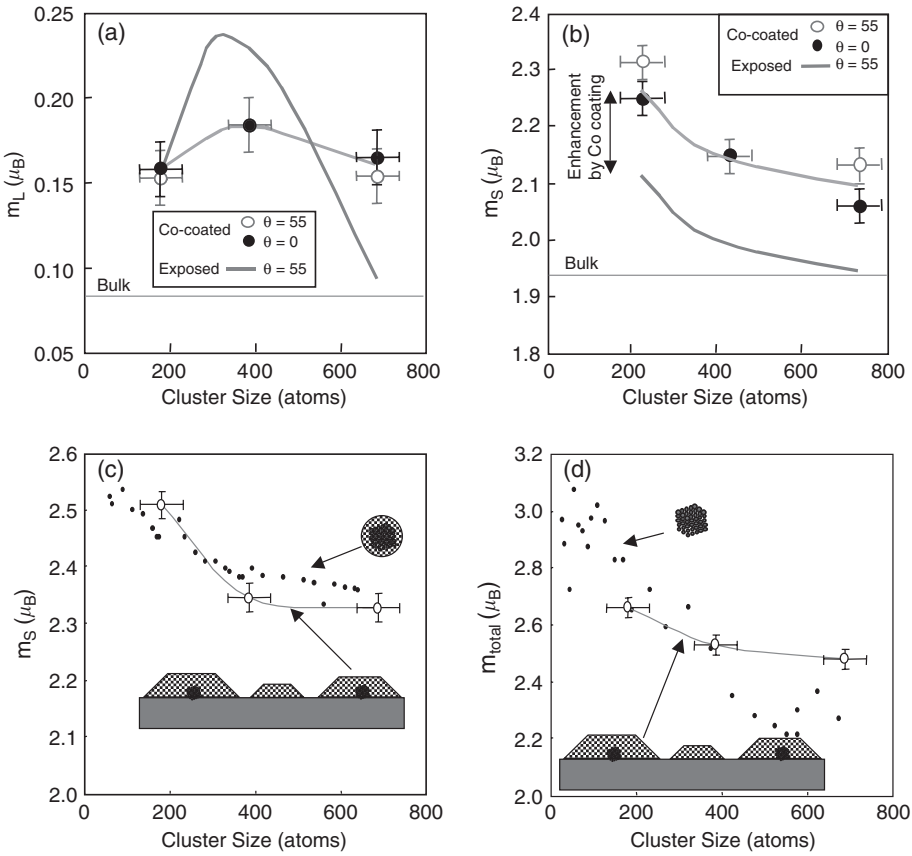

Figure 15: (a) Orbital moment of the Fe atoms in Co-capped Fe clusters on HOPG as a function of cluster size (circles). For comparison, the orbital moment measured in the exposed clusters is also shown (thick line). The sharp variation is washed out but the orbital moment remains significantly enhanced relative to the bulk value. (b) Spin moment of the Fe atoms in Co-capped Fe clusters on HOPG as a function of cluster size (circles). For comparison, the spin moment measured from the exposed clusters is shown (thick line) and it is seen that the Co-coating induces a similar increase in the spin moment over the whole size range. Note that the value of the spin moment is the one derived from the spectra taken at the 'magic' angle (55°) at which the dipole contribution goes to zero. (c) Spin moment of the Fe atoms in Co-coated Fe clusters as a function of size compared to the calculation by Xie and Blackman [86] for free Fe_NCo_{1021-N} clusters. Note that the experimental data has been shifted by a correction for a known systematic error in the measured XMCD moment (see text). (d) Total (orbital + spin) moment of the Fe atoms in Co-coated Fe clusters as a function of size compared to the measured values in free clusters from Stern–Gerlach deflection measurements [7].

a correction of $0.15\mu_B$ was added to the measured spin moment to account for a systematic error in the value given by applying the XMCD sum rules [87]. This arises from the insensitivity of the sum rules, based on dichroism in the 2p–3d transition, to any spin polarisation in the transition metal 4s states. With this correction in place, the agreement with the calculation is good over the whole size range. As shown in Fig. 15d, over a significant fraction of the size range investigated, the total magnetic moment per atom in the Co-coated Fe clusters, obtained by adding the spin and orbital moments measured by XMCD, is as large as in free Fe clusters.

3.3. Magnetometry of isolated Fe and Co clusters in Ag matrices

To explain the magnetic properties of dense interacting assemblies of nanoparticles embedded in matrices, which are the materials with technological applications, it is important to understand the behaviour of the isolated clusters within the same matrix. This can be probed by magnetometry measurements in dilute (1–2% volume fraction) assemblies of magnetic clusters embedded in non-magnetic matrices prepared by co-depositing the clusters and the matrix as in Fig. 1.

Figure 16a shows in-plane magnetic isotherms in the temperature range 50–300 K (symbols) from an assembly of un-filtered Fe clusters embedded in Ag with a volume fraction of 1% (Fe_1Ag_{99}) by the co-deposition technique (Fig. 1) [80, 88]. The upper left inset shows the same data plotted vs. H/T and it is evident that the magnetisation isotherms scaled thus follow a universal curve. This feature, the lack of hysteresis and the observation that the fitted particle size, assuming the curves are Langevin functions, is independent of temperature are the three criteria to be satisfied for confidence that the samples are superparamagnetic [80].

Since the assembly displays ideal superparamagnetism in the range 50–300 K, the size distribution of the clusters can be obtained by fitting a set of Langevin functions to every isotherm. Each fitted Langevin function has a different argument (particle size) and the set of fitting variables are the amplitudes of the functions. Ten size bins were used in the range 0.5–8 nm and the average amplitude as a function of particle size, obtained by fitting the data at all temperatures, is shown in the bottom inset in Fig. 16a. The calculated magnetisation curves are displayed as lines and the fit is excellent in every case. The size distribution is the usual asymmetric shape and has been fitted to a log-normal distribution of particle diameters, d:

$$f(d) \propto \exp\left(-\frac{((\mathrm{In}\, d) - \mu)^2}{2\sigma^2}\right) \tag{6}$$

where μ and σ in Eq. (6) are respectively the mean and standard deviation of $\ln d$ and are treated as fitting variables. The most probable diameter is thus $\exp(\mu)$ and, as pointed out by O'Grady and Bradbury [89], the standard deviation of particle diameters, σ_d, is given from the fitted values of μ and σ by

$$\sigma_d = \exp\left(\mu + \frac{\sigma^2}{2}\right)(\exp(\sigma^2) - 1)^{1/2} \tag{7}$$

Fitting Eq. (6) to the measured size distribution (bottom inset in Fig. 16a) yields a most probable diameter of 2.57 nm with a standard deviation of particle diameters, from Eq. (7), of $\sigma_d = 1.03$. The median diameter, d_m, obtained by finding the value of d at which the integral of the distribution given by Eq. (1) is equal on either side of d_m, is 3.0 nm.This is taken as the representative size for further analysis. The size distribution thus obtained by magnetometry is similar to that obtained by direct STM imaging of deposited cluster films produced by the same cluster source [80] confirming that the clusters are isolated in the film.

As shown in Fig. 16b, at 2 K the magnetic isotherm of the Fe_1Ag_{99} sample develops hysteresis showing that some of the clusters within the size distribution are magnetically blocked with the proportion depending on the symmetry of the anisotropy. As demonstrated by Jamet et al. [70], for embedded Fe nanoparticles of about the

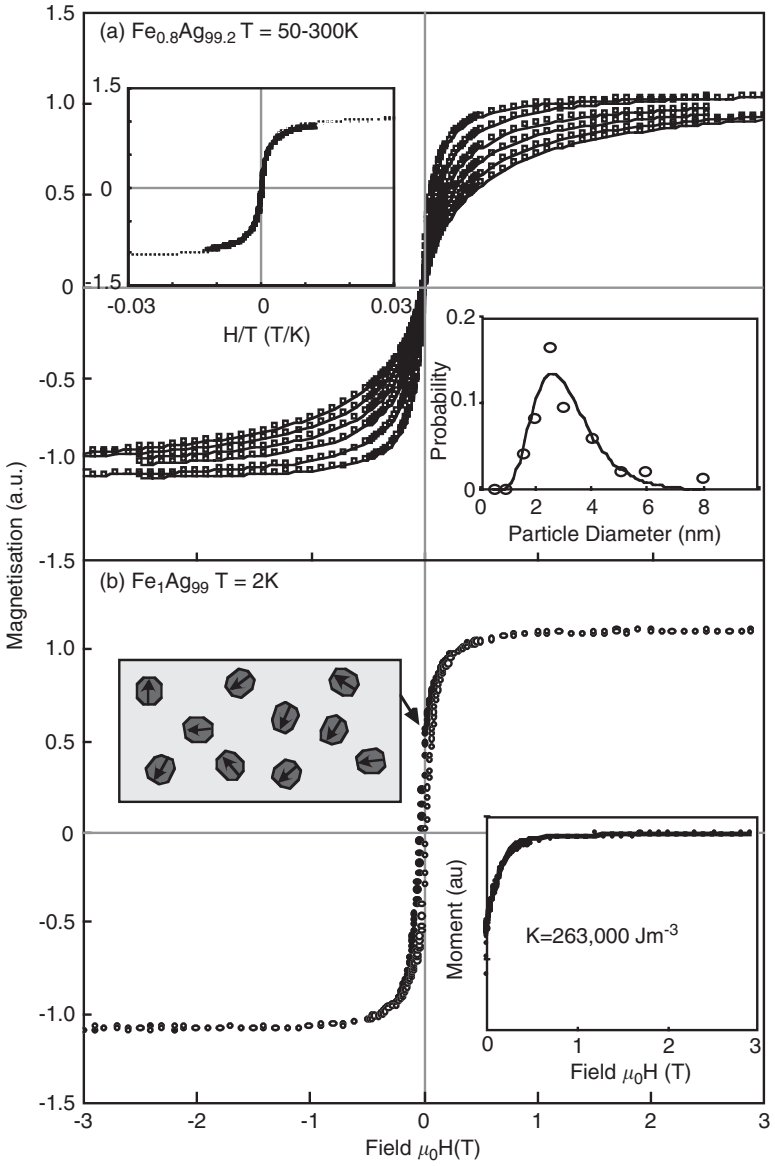

Figure 16: Magnetisation isotherms in the range 50–300 K of an Fe_1Ag_{99} cluster-assembled film (open squares) compared to fits by Langevin functions (line) with a size distribution represented by 10 size bins in the range 0.5–8 nm. The lower inset shows the average probability of each bin for the optimum fit to curves at temperatures >50 K (open circles) and the corresponding log-normal distribution (line) fitted by Eq. (6). The fit gives a most probable diameter of 2.57 nm and a standard deviation of particle diameters, from Eq. (7), of 1.03. The upper left inset shows the magnetisation data plotted vs. H/T, demonstrating the universal scaling expected for a superparamagnetic assembly. (b) In-plane magnetisation isotherms at 2 K of Fe_1Ag_{99} sample: (full circles) field sweeping down and (open circles) field sweeping up. The lower right inset shows the decay from saturation (full circles) compared to a calculation (line) assuming a random distribution of uniaxial anisotropy axes (Eq. (8)). The best-fit anisotropy constant is displayed in the inset. The upper left inset shows schematically the random orientation direction averaged over a hemisphere giving 50% remanence. Reproduced from Ref. [43] with permission from IOP Journals on 6 Jan. 2007.

same size, because of the high surface-to-volume ratio (~40% of the atoms are on the surface layer) these small particles are dominated by surface anisotropy. Cubic anisotropy or any symmetry higher than uniaxial would only occur in clusters containing magic numbers of atoms. According to Xie and Blackman [90], adding a few atoms to one of the facets is sufficient to induce uniaxial anisotropy. There are only a few magic numbers in the entire size distribution and so the vast majority of the clusters are expected to show uniaxial anisotropy. Even in the case of magic numbers, the process of depositing and embedding the clusters may induce stresses that lower the symmetry of the anisotropy. The remanence, M_r, of an assembly of blocked particles with uniaxial anisotropy is $M_r/M_s = 0.5$ if the directions of the anisotropy axes are randomly distributed over three dimensions and $M_r/M_s = 0.71$ if they are distributed over two dimensions in the plane of the applied field. The measured remanence is just below 0.5 and thus closest to the case for uniaxial anisotropy axes randomly distributed over 3D. The slight discrepancy is either due to the smallest clusters in the distribution remaining unblocked at 2 K or, more interestingly, to canted surface moments at zero field as predicted by calculations on small (~1 nm) bcc and fcc Fe nanoparticles [91] and measured for larger (~20 nm) cubic Fe particles [92]. For particles with a uniaxial anisotropy randomly oriented in 3D, the magnetisation between saturation and remanence is obtained at each field by minimising over all alignments of the anisotropy axes, the intra-particle energies:

$$E_\phi = KV \sin^2(\theta - \phi) - \mu \mathrm{B} \cos \phi \tag{8}$$

Here K is the anisotropy constant, V is the particle volume, μ is the particle magnetic moment and θ and ϕ are the angles between the applied field and the anisotropy axis and particle magnetisation, respectively. The inset in Fig. 16b compares the curve, calculated thus, with the data and it is evident that this simple model reproduces the data accurately. So in zero field, the system is a collection of static, randomly aligned cluster giant moments each pointing along the local anisotropy axis. The anisotropy constant is a parameter of the fit and optimises at $K = 2.63 \times 10^5\,\mathrm{J\,m^{-3}}$ (~3 meV/atom). Note that this includes all anisotropy terms including the surface, magnetocrystalline, shape and stress contributions. A previous measurement with the applied field perpendicular to the film plane revealed similar behaviour with a slightly higher anisotropy constant [88], which was attributed to a degree of 'flattening' of the clusters on landing.

Magnetic isotherms from a Co_2Ag_{98} cluster-assembled film in the temperature range 50–300 K are shown in Fig. 17a (symbols) along with the Langevin fits using the procedure described above (lines) [88]. In this case, as seen in the upper left inset, a departure from the H/T scaling and thus ideal superparamagnetism is observed only below 150 K, which is attributed to a higher anisotropy of the Co clusters (see below). Thus, the basic assumption of superparamagnetism, that is, a nearly isotropic magnetic moment, will require a higher temperature to be realised. The size distribution can be obtained by Langevin fits as described above but restricted to the data obtained at $T \geqslant 150$ K. The result along with the fitted log-normal distribution (Eq. (6)) is shown in the lower inset in Fig. 17a. Applying the same analysis as for the Fe clusters gives a most probable Co particle diameter of 2.51 nm and a standard deviation of diameters (Eq. (7)) of 0.90. In this case the median diameter is 2.8 nm.

The low temperature isotherms from the isolated Co clusters in Ag are shown in Fig. 17b and again a remanence of slightly less than 50% is found. As discussed earlier

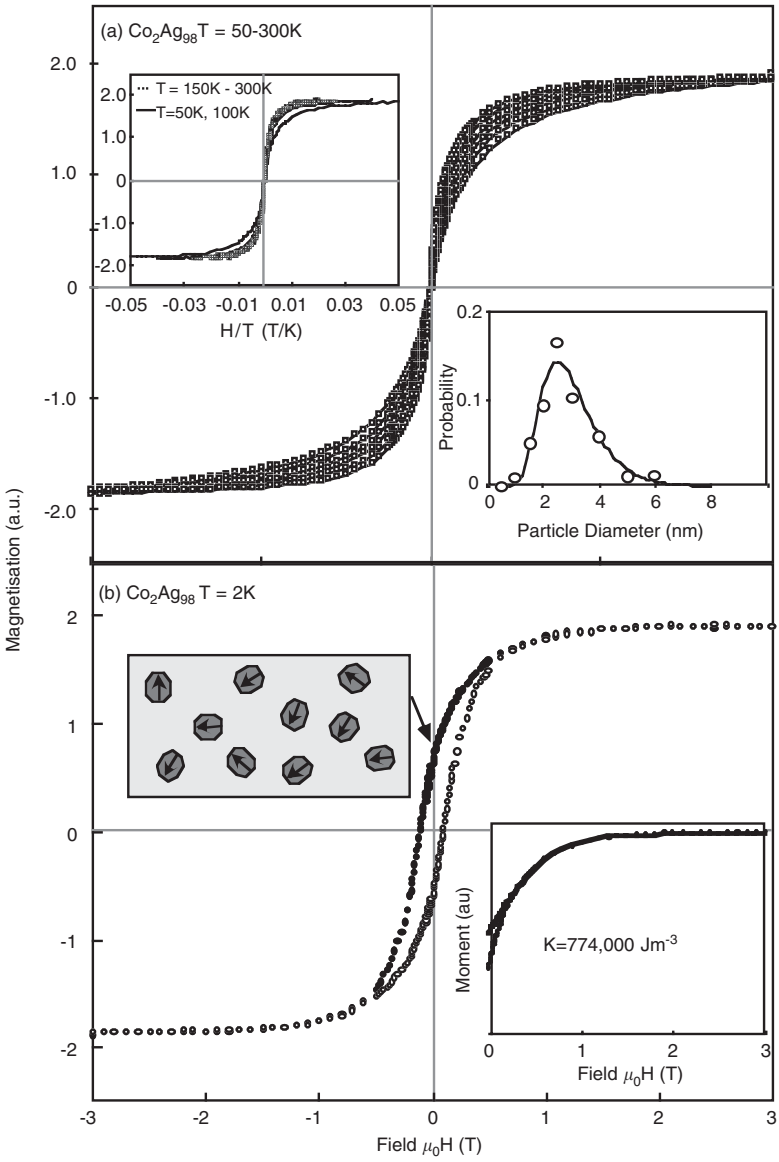

Figure 17: Magnetisation isotherms in the range 50–300 K of a Co_2Ag_{98} cluster-assembled film (open squares) compared to fits by Langevin functions (line) with a size distribution represented by 10 size bins in the range 0.5–8 nm. The lower inset shows the average probability of each bin for the optimum fit to curves at temperatures >150 K (open circles) and the corresponding log-normal distribution (line) fitted by Eq. (6). The fit gives a most probable diameter of 2.51 nm and a standard deviation of particle diameters, from Eq. (7), of 0.90. The upper left inset shows the magnetisation data plotted vs. H/T. In this case, unlike Fe, the 50 and 100 K isotherms do not follow the universal H/T scaling, indicating a departure from ideal superparamagnetism below 150 K. (b) In-plane magnetisation isotherms at 2 K of Co_2Ag_{98} sample: (full circles) field sweeping down and (open circles) field sweeping up. The lower right inset shows the decay from saturation (full circles) compared to a calculation (line) assuming a random distribution of uniaxial anisotropy axes (Eq. (8)). The best-fit anisotropy constant is displayed in the inset. The upper left inset shows schematically the random orientation direction averaged over a hemisphere giving 50% remanence. Reproduced from Ref. [43] with permission from IOP Journals on 6 Jan. 2007.

for Fe clusters, Co nanoparticles are also expected to show a uniaxial anisotropy and the remanence indicates that the clusters are randomly oriented over 3D. The approach to saturation can thus be modelled using Eq. (7) and this is compared to the data in the inset in Fig. 17b. The anisotropy constant that optimises the fit is about three times larger than that found in the Fe cluster assembly, which explains why higher temperatures are required to observe ideal superparamagnetism in Co cluster assemblies.

3.4. Monte Carlo model of nanoparticle assemblies

The behaviour of these and higher-density particle assembles (Section 3.5) was modelled by an MC simulation developed to describe the behaviour of cluster-assembled films [80]. It considers N identical spherical magnetic particles with a diameter D and volume V_0 inside a cubic box of edge length L. As dictated by the experimental results, the single-domain particles are assumed to have a randomly oriented uniaxial anisotropy. The particles interact via long-range dipolar forces and short-range exchange forces, these only being included between neighbouring particles in contact. The total energy of the system is the sum of particle magnetic energies:

$$E_i = -\sum_i \varepsilon_i$$

in which the energy of the ith particle is

$$\varepsilon_i = h(\hat{\mathbf{S}}_i \cdot \hat{\mathbf{H}}) + k(\hat{\mathbf{S}}_i \cdot \hat{\mathbf{e}}_i)^2 + g\sum_j \frac{3(\hat{\mathbf{S}}_i \cdot \hat{\mathbf{R}}_{ij})(\hat{\mathbf{S}}_i \cdot \hat{\mathbf{R}}_{ij}) - (\hat{\mathbf{S}}_i \cdot \hat{\mathbf{S}}_j)}{R_{ij}^3} + J\sum_j (\hat{\mathbf{S}}_i \cdot \hat{\mathbf{S}}_j) \qquad (9)$$

where $\hat{\mathbf{S}}_i$ and $\hat{\mathbf{e}}_i$ are unit vectors in the directions of the magnetic moment (spin) and anisotropy axis of the ith particle and $\hat{\mathbf{R}}_{ij} \cdot \mathbf{D}$ is the centre-to-centre distance between the particles. The energy parameters entering Eq. (4) are the Zeeman energy, μH, where $\mu = M_s V_0$; the dipolar energy, $g = \mu_0 \mu^2 / 4\pi D^3$; the anisotropy energy, $k = KV_0$; and the effective exchange energy, J. The anisotropy parameter can be obtained from the fits to the experimental magnetisation curves as described in the previous section and the exchange energy can be obtained by fitting the measured approach to saturation as described in Section 3.6. The equilibrium magnetic configuration of the system at a certain temperature and applied field is obtained by an MC simulation using the Metropolis algorithm [93]. The model predicts a percolation threshold at a volume fraction of 29% and that the dilute limit extends up to about 5%, where the probability of particles in contact is small. The intermediate volume fraction regime covers the range 5–25%. In all simulations it was assumed that the morphology of the Fe clusters does not change with volume fraction.

The simulation was tested for a dilute Fe_1Ag_{99} nanoparticle assembly similar to the one shown in Fig. 16 using the corresponding fitted anisotropy (in this case $2.41 \times 10^5\,\mathrm{J\,m^{-3}}$). At such a low volume fraction, the exchange parameter does not have a significant effect as the probability of finding two particles in contact is very low. The calculated full magnetisation curve using the MC model is compared with the experimental data curve obtained at 2 K (i.e. below the blocking temperature) in Fig. 18 (top curve). It is observed that the model describes the data reasonably well and gives a good estimate of the coercive field (0.02 T). The main discrepancy is the loss of hysteresis at a lower field than observed in the data. This is attributed to the

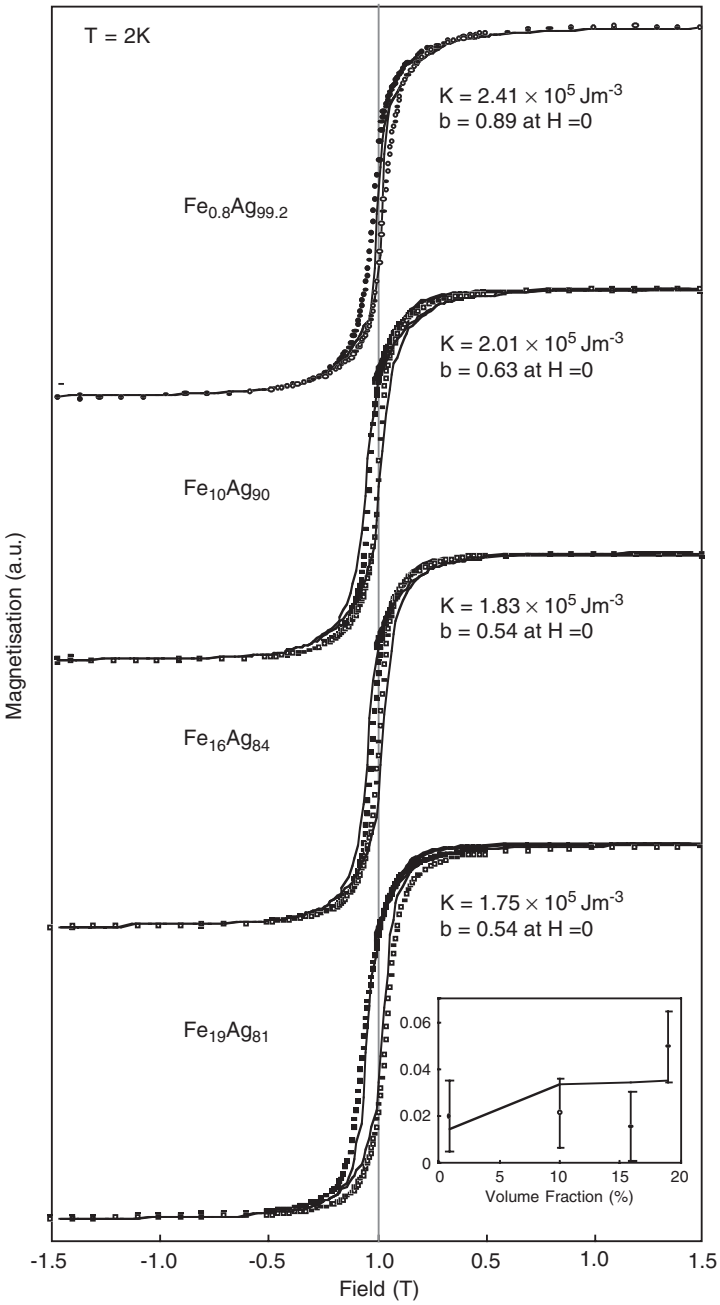

Figure 18: Isotherms at 2 K from samples with intermediate volume fractions below the percolation threshold. The symbols are the measured data and the thick lines are fits between saturation and remanence using Eq. (8) with the optimal value of the anisotropy constant shown. The thin solid lines are the MC simulations for the full isotherms with the predicted value of b (Eq. (10)) at remanence shown. The inset compares the values of H_c obtained from the measurements and the MC simulation. Reproduced from Ref. [43] with permission from IOP Journals on 6 Jan. 2007.

model describing each particle by a single average spin whereas for isolated particles the surface spins need a higher field than the core to saturate because of the enhanced surface anisotropy. As shown in Section 3.5, at higher concentrations where the inter-particle interactions are dominant the surface contribution is less important and the model gives even better agreement.

3.5. Evolution of magnetic behaviour with nanoparticle volume fraction below the percolation threshold

The volume fraction in a cluster-assembled film for a given particle size can be adjusted simply by changing the relative deposition rates of the clusters and matrix material. The evolution of the magnetisation curves at 300 K as a function of volume fraction for films containing 3 nm diameter Fe nanoparticles in Ag matrices is shown in Fig. 19 for volume fractions below the percolation threshold. The most noticeable feature is the increase in the low-field susceptibility as the cluster density increases. This is characteristic of larger particles and indeed it is possible to get good fits using Langevin functions with a higher supermoment than in the dilute film. It is, however,

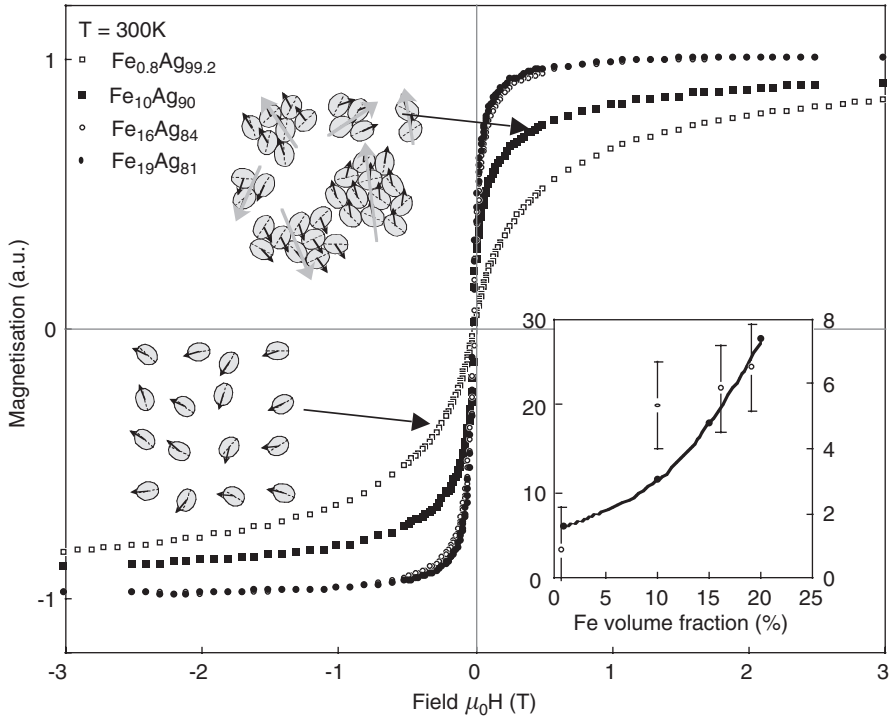

Figure 19: Magnetisation isotherms at 300 K of films of Fe clusters embedded in Ag as a function of volume fractions below the percolation threshold. The lower right inset compares the measured initial susceptibility with that calculated by the MC simulation as a function of volume fraction (note the different scales). The left insets are schematic representations of the assemblies of particles, which are shown elongated to represent the observed uniaxial anisotropy. At the lowest volume fraction, the magnetisation is superparamagnetic, while at the higher volume fractions the assembly consists of exchange-coupled aggregates that interact with each other via dipolar forces (see text). Reproduced from Ref. [43] with permission from IOP Journals on 6 Jan. 2007.

erroneous to treat these films as superparamagnetic with a volume-fraction-dependent cluster size. The magnetic isotherms do not scale with H/T and Langevin fits to these curves give an optimum particle size that depends on the temperature of the fit. As pointed out by Allia et al. [94] both these features violate the criteria for superparamagnetism.

The MC model can be applied to these samples but for comparisons at room temperature it is important to point out that "time" in the model is measured in Monte Carlo steps (MCS). The simulations applied in this case extend to 10^4 MCS per spin, which approximately corresponds to an observation time of 10^{-7} sec [93]. Comparing the measured and simulated data is thus similar to comparing measurements with widely different time scales, for example, dc magnetometry and Mössbauer spectroscopy. However, the MC simulation, because it mimics the role of thermal fluctuations, reproduces qualitatively the trend of the experimental data. The trend in the initial susceptibility as the volume fraction changes for the experimental data is plotted in the inset in Fig. 19 and compared with the prediction from the MC model. It is seen that there is qualitative agreement with the model. Theoretical modelling [95] and measurements [94] show that, without exchange, dipolar forces decrease the low-field susceptibility emphasising the importance of including exchange interactions to explain the behaviour of these samples.

The magnetic isotherms of the same samples as in Fig. 19 measured at 2 K are shown in Fig. 18. In each case, the demagnetisation from saturation is still well described using Eq. (8) (thick solid lines in Fig. 18) and the remanence is close to 50% indicating that at 2 K in zero field the moments are frozen along randomly oriented axes averaged over 2π steradians in the direction of the most recent saturation. Here, however, the moments do not belong to individual deposited nanoparticles but to exchange-coupled aggregates of the nanoparticles. These are the relevant magnetic particles in samples with volume fractions between 5% and the percolation threshold. As before, a remanence of 50% indicates that the anisotropy of the aggregates is uniaxial. The magnitude of the anisotropy of the aggregates, obtained by the fit to the data using Eq. (8) is lower in the $Fe_{10}Ag_{90}$ film than that found in the isolated clusters and decreases with increasing density of clusters. This is expected due to an averaging of the individual cluster anisotropies to produce a resultant value along the anisotropy axis of the whole aggregate. In addition, a real decrease in the intra-cluster magnetocrystalline anisotropy may be expected as a result of a decreasing orbital moment with density as shown by previous XMCD measurements on exposed Fe clusters on graphite [36] and as described in Section 2.3.2.

The complete magnetisation curves obtained using the MC model as a function of volume fraction are indicated in Fig. 18 by the thin solid lines. The anisotropy value used was that of the isolated clusters (Fig. 16b) as is appropriate. If the model is working correctly, it should itself predict the reduction of anisotropy of the aggregates due to the random orientation of the constituent nanoparticles. The good-fit to the data indicates that this is the case. This also implies that the decreasing anisotropy constant in the films is due mostly to the averaging effect and not due to the measured reduction of the orbital moment. This is not surprising since the orbital moment will affect only the magnetocrystalline term and it is clear that this is a minor component. The relatively small contribution of the magnetocrystalline term to the anisotropy of embedded clusters has been confirmed recently by direct micro-SQUID measurements

of the switching field of individual nanoparticles [70]. The simulation also gives a good estimate of the coercive field and predicts the experimental observation of a slight increase with increasing Fe volume fraction. The large error bars for the experimentally determined values of H_c are due to uncertainties in the removal of the background slope from the raw data. The variation of H_c with volume fraction is due to the different character of the dipolar interactions in the system well below and close to the blocking temperature. For $T \ll T_b$, H_c is predicted to decrease with increasing volume fraction, while for $T \sim T_b$ it will increase. This is clearly the regime found in these samples. More fundamentally, it is evident that H_c is modified by interactions, as it is observed to increase despite a decreasing anisotropy constant in the aggregates. This would be a contradiction in a non-interacting system.

The increased exchange coupling due to aggregation is indicated by the MC simulation via the global parameter:

$$b = \frac{1}{N} \sum_i \hat{\mathbf{S}}_i \cdot \hat{\mathbf{e}}_i \tag{10}$$

that is, the fraction of projected moments along the local easy axes. A value of 1 indicates complete decoupling of clusters so that all moments are along local easy axes and 0.5 will be found in the case where all neighbouring moments are aligned co-linearly by exchange. The values of b obtained from the MC simulations shown in Fig. 18 are indicated beside each magnetisation curve. For the dilute cluster film (Fig. 16) it is found that $b = 0.89$ at $H = 0$ and $T = 2\,\mathrm{K}$ but drops to 0.63 in the $Fe_{10}Ag_{90}$ sample and drops further towards the exchange-coupled limit as the Fe cluster volume fraction increases. Note that this reduction in b indicates an increasing proportion of the deposited nanoparticles contained in exchange-coupled aggregates, whose total moments are randomly oriented in zero field. This is consistent with the observation of an approximately 50% remanence in both the measured data and the MC simulations.

An analysis of the magnetisation curve at 10% volume fraction was carried out [80] using a model proposed by Allia et al. [94] consisting of a Curie–Weiss-like extension to the Langevin function to represent dipolar coupling. It showed that the morphology of the assembly consists of exchange-coupled aggregates, containing an average of about six particles, interacting via dipolar forces. The different morphologies at 1% and 10% volume fractions are shown schematically in the left insets in Fig. 19.

3.6. Pure cluster films

Beyond the percolation threshold, a cluster-assembled film becomes a single ferromagnetic infinite cluster with a complex morphology and simple phenomenological models are not applicable. In this section, we explore the behaviour of the extreme case, that is, films of pure deposited clusters with no matrix. It is clear from looking at images such as the one shown in Fig. 3b that, although the film is ferromagnetic, the ground-state configuration of spins will be different from that in a film made by depositing atoms. For example, MFM images of cluster-assembled films do not show domains with clear boundaries in the conventional sense but a seemingly random patchwork arising from a continuously varying magnetic direction with a correlation length larger than a single deposited cluster [44] (see Fig. 22).

The previous section showed that the clusters and their anisotropy axes are randomly oriented in the assembly so it is appropriate to apply a random anisotropy (RA)

model developed by several authors in the last two decades [96–100]. In this approach, the magnetic ground state in a granular film is determined by the relative strength of a random anisotropy field:

$$H_r = \frac{2K_r}{M_s} \tag{11}$$

and an exchange field:

$$H_{ex} = \frac{2A}{M_s R_a^2} \tag{12}$$

Here, K_r is the (randomly oriented) anisotropy of the grains, M_s is their saturation magnetisation, A is the exchange constant for the interaction between the grains and R_a is the nanometre-scale region over which the local anisotropy axis is correlated, i.e. the characteristic grain size. The relative strength of the fields is given by the dimensionless parameter:

$$\lambda_r = \frac{H_r}{H_{ex}} \tag{13}$$

The model was originally developed to describe amorphous films in which a local, randomly oriented, anisotropy is due to local atomic order. It is even better suited to providing a description of the magnetisation in cluster-assembled films in which the distance R_a over which an anisotropy axis is correlated is well defined (i.e. the particle diameter). For $\lambda_r > 1$, the magnetic correlation length at zero field is R_a, and the magnetic vector in each particle points along the local intra-particle anisotropy axis ($b = 1$). Note that in an arrow representation this state would be identical to that in isolated non-interacting particles at absolute zero. With increasing inter-particle exchange (or decreasing intra-particle anisotropy), the configuration becomes a correlated super-spin glass (CSSG) in which the magnetisation vector in neighbouring particles is nearly aligned ($b \sim 0.5$) but the random deviation of the moments from perfect alignment produces a smooth rotation of the magnetisation throughout the system with a magnetic correlation length that is a factor $1/\lambda_r^2$ larger than the particle diameter. The difference between the two states is illustrated in Fig. 20.

The RA model has been used successfully to analyse the data in several ex situ magnetometry studies of cluster-assembled films [101–104] in which the films were capped by protective non-magnetic layers for removal from the deposition chamber. More recently, a system developed to allow transfer of a film directly into a vibrating sample magnetometer (VSM) in UHV conditions has enabled the study of exposed films without the protective non-magnetic capping layer [80, 88]. Here, a case study of pure Fe and Co cluster films capped with Ag and analysed using the RA model is presented. The particle sizes are the same as in the samples used to obtain isolated particle data shown in Figs. 16 and 17, that is, 3.0 and 2.8 nm diameter for the Fe and Co clusters, respectively. Thus, the magnetic behaviour of the isolated and strongly interacting nanoparticles can be compared directly.

In a film whose ground state is a CSSG, the RA model predicts an approach to magnetic saturation that depends on the dimensionality of the film [100]. In two

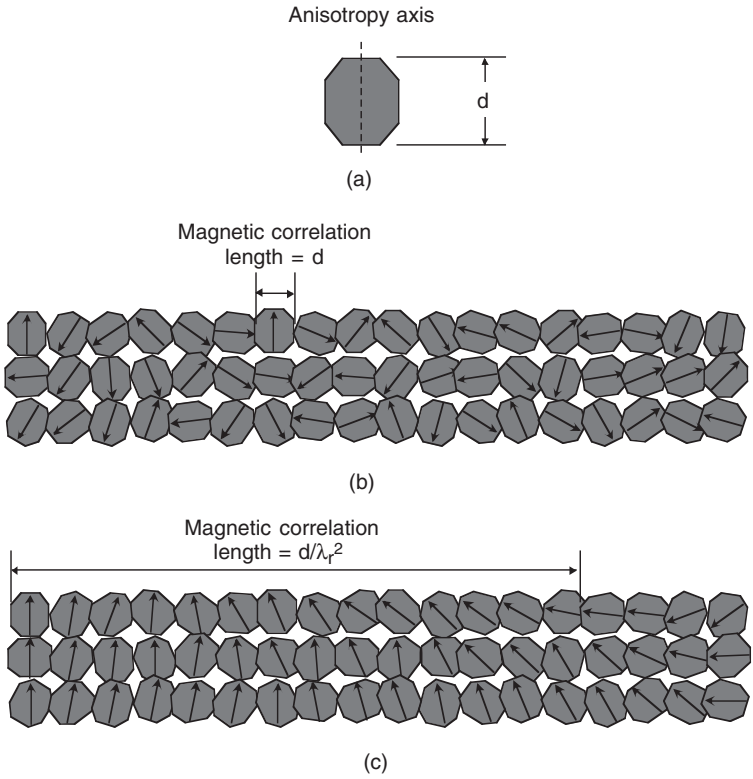

Figure 20: (a) Schematic representation of a magnetic nanoparticle with a uniaxial anisotropy axis (represented by a slight elongation); (b and c) a stack of particles with randomly oriented anisotropy axes. In (b) $\lambda_r \geqslant 1$ and the magnetisation vector points along the local anisotropy axis so the magnetic correlation length is a single particle diameter. In (c) $\lambda_r < 1$ and the magnetic vectors are nearly aligned. The random perturbation from perfect alignment results in a finite magnetic correlation length that is a factor $1/\lambda_r^2$ larger than a single particle. Reproduced from Ref. [43] with permission from IOP Journals on 6 Jan. 2007.

dimensions the magnetisation follows:

$$M = M_s\left(1 - \frac{1}{32}\frac{\lambda_r^2}{\sqrt{h_{ex}}}\int_0^\infty dx\ C(x)x^2K_1[x\sqrt{h_{ex}}]\right) \tag{14}$$

and in three dimensions:

$$M = M_s\left(1 - \frac{1}{30}\frac{\lambda_r^2}{\sqrt{h_{ex}}}\int_0^\infty dx\ C(x)x^2\ \exp[x\sqrt{h_{ex}}]\right) \tag{15}$$

In Eqs. (14) and (15), $h_{ex} = H/H_{ex}$, K_1 is the modified Hankel function and $C(x)$ is the correlation function for the anisotropy axes with x in units of R_a. In a cluster-assembled film with mono-sized clusters, $C(x)$ can be taken to be a simple step function with a cut-off at $x = 1$.

Figure 21 shows the approach to saturation for a 5 nm thick film of deposited Fe nanoparticles and a 20 nm thick film of deposited Co nanoparticles. The RA model curves were calculated using Eq. (14) for the Fe cluster film, which was only two

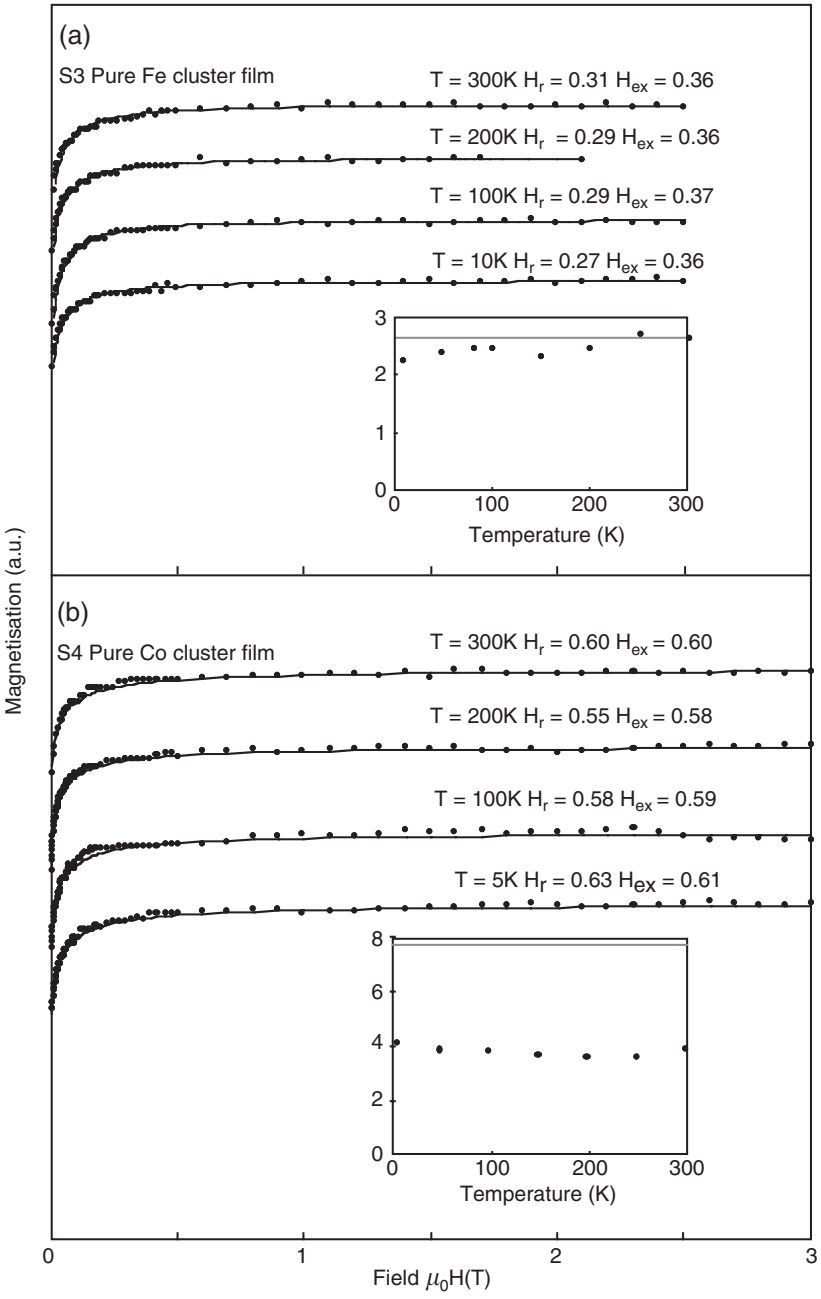

Figure 21: (a) Approach to saturation of a 5 nm thick pure Fe cluster (3.0 nm diameter) film for temperatures in the range 10–300 K (full circles) compared to a calculation using the RA model with the parameters shown (line). The inset shows the variation of the random anisotropy (evaluated from H_r and Eq. (11)) with temperature (full circles). The grey line shows the value for the isolated clusters. (b) As (a) but for a 20 nm thick pure Co cluster (2.8 nm diameter) film sample [88]. Reproduced from Ref. [88] with permission from IOP Journals on 6 Jan. 2007.

cluster layers thick and Eq. (15) for the thicker Co cluster film. It is observed that in both cases the values of H_{ex} and H_r change little with temperature, which is just confirmation of the observation that the shape of the curves appears to be independent of temperature. The value of the random anisotropy, K_r, obtained from H_r and Eq. (11) is shown in the insets and compared with the values for the isolated clusters. For the Fe cluster film, the random anisotropy is close to the isolated cluster value whereas for the Co cluster film it is significantly smaller. The exchange fields are ≈ 0.36 and ≈ 0.6 T for the Fe and Co cluster films, respectively, corresponding to an exchange constant (from Eq. (12)) of $A \approx 3 \times 10^{-12}$ J m^{-1} for both films, which is much less than the bulk value as would be expected. Crudely, one would expect a bulk-like exchange coupling only between atoms in contact at the interface between the particles, so averaged over the whole clusters, treated as 'giant atoms', it is much smaller. It appears from the value of A that of the order of 1 atom in 10 within the nanoparticle are exchange-coupled to atoms on neighbouring particles. For both the Fe and Co nanoparticle assemblies, the exchange energy is about 170 meV per pair. This is similar to the value found in a two-dimensional assembly of Co nanoparticles on Si(0 0 1) prepared colloidally after removal of the ligand and oxide shells [105].

For both films the value of λ_r is close to 1, indicating that the magnetic configuration is close to the crossover between a simple spin glass, in which each cluster moment is aligned randomly in zero field, and the CSSG state. This crossover was directly observed in a 150 Å thick film of 3 nm diameter Fe nanoparticles [80]. The approach to saturation was fitted using the RA model as described above and it was found that with decreasing temperature the value of λ_r increased. For temperatures below 50 K it became greater than 1 and for the same temperature range the approach to saturation no longer followed the CSSG curve. This was attributed to a crossover from the CSSG to the simple spin glass configuration.

Recently, the stray magnetic field at the surface of a pure Co cluster film was imaged using MFM [44]. Figure 22 shows the results for a 375 nm thick film produced by depositing 8 nm diameter Co nanoparticles, and it is observed that the stray field is a random patchwork as would be expected at the surface of a CSSG. By comparing directly the feature size in the MFM and the topographic image it was found that

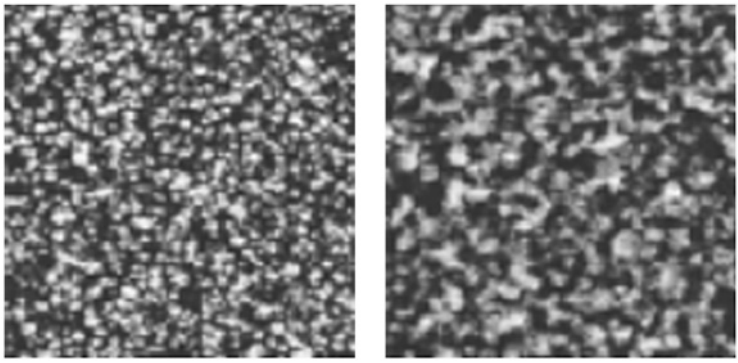

Figure 22: Topography and phase images of a 375 nm thick film of 8 nm diameter Co clusters deposited on Si(1 0 0). The scan size is 5000 nm [44]. Reproduced from Ref. [44] with permission from Phys. Rev. B on 6 Jan. 2007.

$\lambda_r \sim 0.67$, i.e. close to the value found in the films of smaller Co clusters described above. In this particular study the Co particles had a thin native oxide layer producing a ferromagnetic/antiferromagnetic core–shell system with an exchange bias of 0.5 T at low temperature after field-cooling. The room temperature data, however, showed soft magnetic behaviour characteristic of a CSSG, showing the formation of this state even in the case where the exchange interaction between the nanoparticles is complicated by an intervening antiferromagnetic layer.

Loffler et al. [101, 102] also used the RA model to analyse magnetometry data from deposited gas-phase Fe and Ni clusters with sizes in the range 10–20 nm. They modified the deposited size distribution by post-deposition annealing of the films [101] so that the study could be carried out as a function of particle size. The RA model produced good fits to the approach to saturation of the film magnetisation, though in this case the fitted value of λ_r was 2. Although this is higher than the value at which a transition to a simple spin glass should occur, the critical value of λ_r is influenced by a number of factors including the distribution on anisotropy axes, which may not be truly random.

The same group used small-angle neutron scattering to study the magnetic correlations in dense assemblies of Fe, Co and Ni clusters deposited from the gas phase [102]. Again they annealed the samples to modify the average grain size in situ and discovered that the magnetic correlation length in Fe went through a minimum when the grains size equals the bulk domain wall width. They analysed their data using an extension of the RA model taking into account domain wall formation within grains. In fact even in the films composed of small (3 nm) nanoparticles described above, the assumption that the magnetisation direction changes only at the interfaces (Fig. 20c) is an idealisation and a more realistic model would have to include some curling of the magnetisation within the grains.

Summarising the results presented for the 3 nm Fe particles embedded in Ag as a function of volume fraction, perfect superparamagnetism is observed only at very low volume fractions. For a large range of intermediate volume fractions, the film can be considered to be exchange-coupled agglomerates of clusters (super-clusters) that interact with each other via dipolar forces as shown schematically in Fig. 19. The magnetic behaviour in this region has been described as 'interacting superparamagnetism' [94]. At the high volume fraction end, the cluster films form a CSSG and show magnetically soft behaviour. At low temperatures and low volume fractions the system consists of isolated blocked particles, while at high volume fractions there is evidence that it forms a simple spin glass [80].

4. APPLICATIONS OF CLUSTER-ASSEMBLED FILMS

The technology of cluster deposition has made great strides in the last decade, leading to higher fluxes, better size selection, and methods for functionalising the clusters in the gas phase prior to deposition. It is now possible to produce thick ($\sim$1 μm) films of clusters over large areas in relatively short times, leading to the possibility of producing materials on an industrial scale. Producing films from pre-formed clusters is more complicated than conventional thin-film deposition techniques such as CVD or MBE but there are significant advantages. One is the high degree of control over the film properties resulting from the tight size-selection of the clusters and the ability to

independently vary the size of the deposited particles and their volume fraction. Another is the possibility of producing nanogranular mixtures of miscible material like Fe and Co. There are many possible technological uses but in this section two case studies of applications of magnetic cluster assemblies that take advantage of the flexibility of the film nanostructure will be presented.

4.1. Giant magnetoresistance

Ever since the discovery, in 1992, of GMR in granular films consisting of magnetic nanoparticles in a non-magnetic matrix [106, 107], the origin of the effect has provoked much attention [108]. Although multilayer films in spin-valve structures have reached a very high level of performance in hard disk read heads, the GMR effect in nanogranular materials remains of interest both fundamentally and for high-field applications. Throughout this chapter, the 'controllability' of the cluster/atom deposition technique in terms of particle size and volume fraction has been emphasised. It should therefore be possible, using this method, to optimise GMR performance in terms of the total resistance change between saturated and field-off states. The first measurement of GMR in a nanogranular material produced by depositing clusters and a non-magnetic matrix was reported in 1997 [40].

A central issue in the production of granular films by cluster assembly is the effective size distribution of the embedded grains. Although the original clusters have a tight size distribution (even without mass selection) at the volume fractions required for high GMR performance, as shown in Section 3.5, the magnetic grains consist of several of the deposited clusters exchange-coupled to behave, magnetically, as single particles. It was also shown that the exchange-coupled aggregates interact via dipolar forces. In order to understand the variation of GMR with nanoparticle volume fraction, it is useful to compare the experimental data with the MC model that was used to analyse the magnetisation data from cluster-assembled films.

Figure 23 shows the relative resistance change vs. applied field curves for two different volume fractions of Fe clusters embedded in Ag (circles). Also plotted are fitted curves using the model of Zhang and Levy (lines) [109] showing good agreement for volume fractions up to the percolation threshold. The increasing GMR with volume fraction is evident in the figure but if the volume fraction is pushed higher the magnitude of the GMR decreases again.

Even without inter-particle interactions, the GMR amplitude is expected to decrease at volume fractions above the percolation threshold as the clusters form a continuous network. The optimum volume fraction has been shown to be a result of the competition between the increasing number of magnetic centres that enhance the effect and the increase in the average grain size that suppresses it [110]. There is an additional reduction due to inter-particle interactions as is evident from the MC model. Figure 24 shows that including the inter-particle dipolar interaction produces a suppression of the peak GMR response as a result of an increasing magnetic alignment. The difference in spin-dependent valence electron scattering between the field on and field off states required for GMR is thus reduced.

The occurrence of an optimum volume fraction for GMR performance is demonstrated clearly in Fig. 25a showing the maximum relative resistance change measured as a function of volume fraction for Fe and Co clusters embedded in Ag. In both cases, there is an optimum value but this is higher in the case of Co clusters. From the

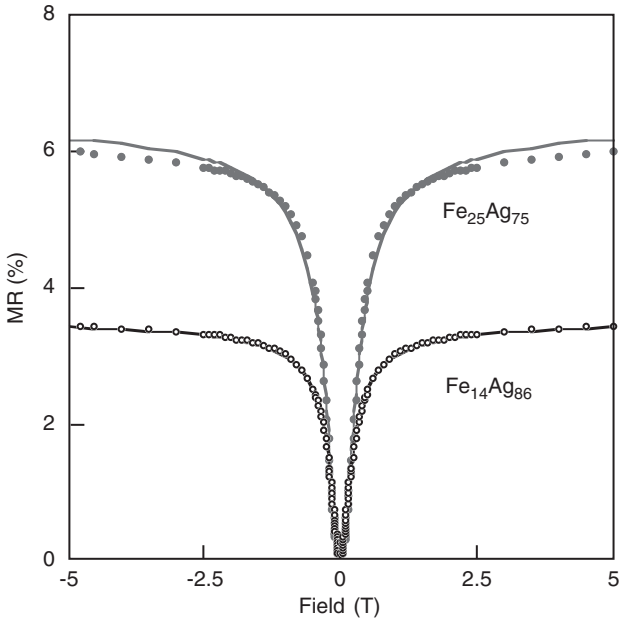

Figure 23: Resistance change (defined by $[R(H)-R(0)]/R(0)_{max}$) at room temperature for Fe clusters embedded in Ag at two different volume fractions (circles). The lines are fits using the model of Zhang and Levy [109]. Reproduced from Ref. [43] with permission from IOP Journals on 6 Jan. 2007.

previous discussion the reason for this can be identified. As shown in Section 3.3, Co clusters embedded in Ag have a much higher anisotropy than Fe clusters. This increased anisotropy maintains the magnetisation of the Co clusters along the (randomly oriented) local anisotropy axis against a stronger dipolar interaction between the clusters. This remains true when the relevant magnetic particles are exchange-coupled agglomerates of the deposited Co clusters. The dipolar interaction between Co particles (isolated clusters or agglomerates) is also weaker than between Fe clusters due to their lower spin moment. Thus, the Co clusters can be packed to a higher density before the dipolar interactions start to degrade GMR performance. This shifts the GMR peak to a higher volume fraction and thus also to a higher value. This behaviour is reproduced by the MC model as shown in Fig. 25b for interacting and non-interacting clusters, which, in the limit, can be taken to represent the case of Fe and Co clusters. The model predicts a higher resistance change than is observed however.

4.2. High moment soft films

The possibility of producing materials whose magnetisation exceeds the Slater–Pauling limit of 2.45 T (in $Fe_{70}Co_{30}$ alloy) by using cluster assembly was first suggested by measurements of enhanced magnetic moments in free Fe, Co and Ni clusters containing less than 600 atoms [7]. The XMCD results from Co-coated Fe clusters presented in Section 2 showed that it is possible to produce a magnetic moment in the coated particles that is as high as in a free Fe cluster. This suggests that depositing Fe clusters in conjunction with a Co matrix as in Fig. 1 could lead to films with a high-saturation magnetisation, possibly exceeding 2.45 T.

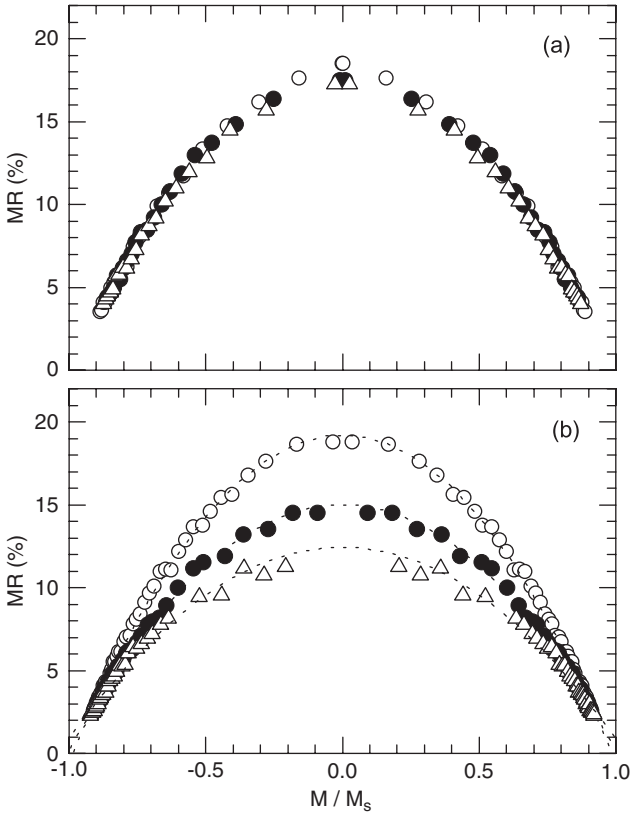

Figure 24: GMR vs. sample magnetisation for (a) a monodisperse sample and (b) a polydisperse sample. For both samples the volume fraction is 25%. Open circles are non-interacting anisotropic clusters, closed circles are interacting anisotropic clusters and triangles are interacting isotropic clusters. The dotted lines are fitted parabolas. Reproduced from Ref. [43] with permission from IOP Journals on 6 Jan. 2007.

Verifying this possibility using size-selected nanoparticles is far from trivial. To begin with XMCD measurements can be performed on tiny amounts of material (~0.1 Å equivalent film thicknesses) and so depositing a suitable sample with tight mass selection is not a problem. To produce enough material using size-selected clusters to get an accurate moment determination using a conventional magnetometer such as a VSM requires very long deposition times with normal cluster sources. Using a much more sensitive SQUID magnetometer is not helpful since this also amplifies the substrate (background) signal. To get a high-precision measurement requires enough magnetic material to produce a bigger ferromagnetic signal than the diamagnetic or paramagnetic background from the substrate, which in practise means a film ~500 Å thick. The other technical problem is that there is no reliable high-precision measurement of the amount of material deposited on a thin film.

In a recent study [111], the technical hurdles were overcome by using aerodynamic lensing [112] to produce a high flux of particles of about the right size and producing large numbers of samples so that averaging could be carried out. The amount of material in the samples was determined by calibrating a quartz oscillator thickness

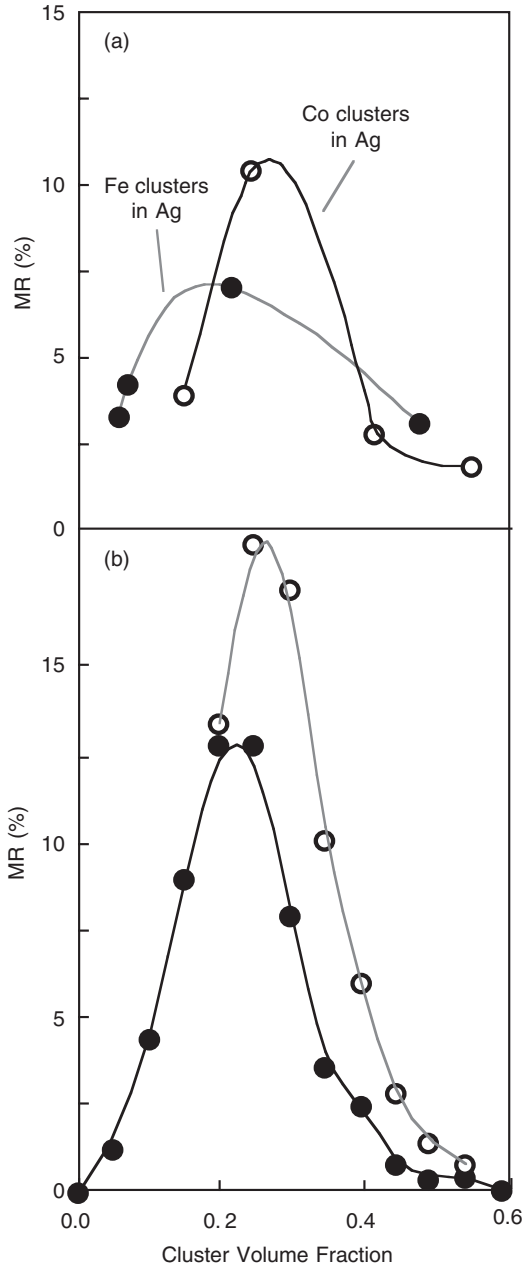

Figure 25: (a) Resistance change (defined by $[R(H)-R(0)]/R(0)_{max}$) at 2 K vs. volume fraction for Fe clusters in Ag (filled circles) and Co clusters in Ag (open circles). (b) Dependence of GMR on magnetic particle concentration predicted by the MC model. Open circles are non-interacting anisotropic clusters and closed circles are interacting anisotropic clusters. The percolation threshold is at a volume fraction of 0.3. Reproduced from Ref. [43] with permission from IOP Journals on 6 Jan. 2007.

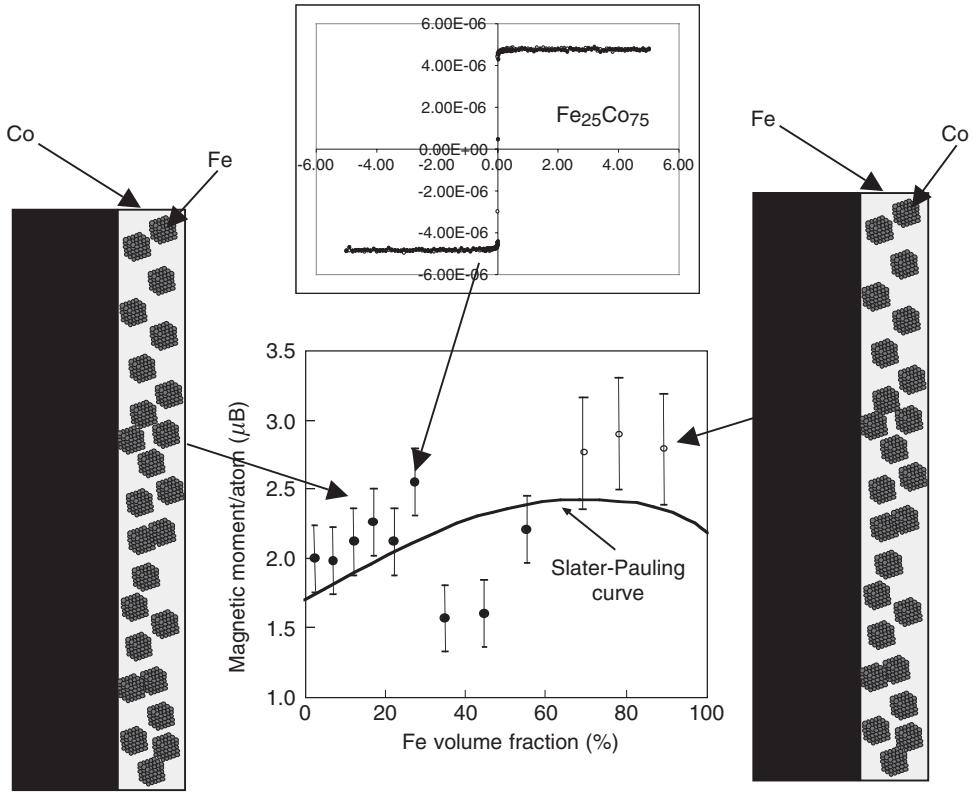

Figure 26: Magnetic moment per atom in films of Fe clusters (mean size 150 atoms) embedded in Co matrices as a function of Fe volume fraction (filled circles). The amount of Fe was determined using a quartz oscillator calibrated using pure Fe and pure Co films. The black line is the Slater–Pauling curve for conventional FeCo alloys. The open circles show some measured values obtained by swapping materials, i.e. Co clusters embedded in Fe matrices. The magnetisation curve obtained from the $Fe_{25}Co_{75}$ mixture is shown and demonstrates the magnetic softness of these nanostructured films.

monitor using the magnetic signal in a VSM. Figure 26 shows the measured magnetisation per atom as a function of volume fraction for Fe nanoparticles containing about 150 atoms in a Co matrix (filled circles). The Slater–Pauling (SP) curve for homogenous Fe–Co alloys is shown for comparison. It is clear that at low Fe volume fractions, the cluster-assembled film has a higher magnetisation per atom, but at the percolation threshold a drastic reduction to well below the SP curve occurs. This is predictable since above the percolation threshold the film can be considered to be a phase-separated mixture of Fe and Co so the moment will be a weighted average of the bulk Fe and Co values. Recent calculations by Bergman et al. using a relativistic first-principles real-space density functional theory [113] were able to model this complex system and they found enhanced spin and orbital moments on the Fe clusters but the Co moments remained close to the bulk value. The model did indicate that clustering always produced a lower moment than the homogenous alloy but this does not agree with the experimental data, which indicates a higher moment in the cluster-assembled film than the homogenous alloy up to the percolation threshold. One possible reason is

Table 6: Calculated moments of Co clusters in Fe shells and vice versa.

Cluster	Co			Fe			Average μ/atom (μ_B)
	m_L (μ_B)	m_S (μ_B)	m_T (μ_B)	m_L (μ_B)	m_S (μ_B)	m_T (μ_B)	
$Co_{339}Fe_{302}$	0.13	1.74	1.87	0.13	2.74	2.87	2.34
$Fe_{339}Co_{302}$	0.22	1.79	2.01	0.10	2.38	2.48	2.26

that the EXAFS data (Section 3.1) indicate some inter-mixing at the boundary between transition metal clusters and transition metal matrices. As shown by Xie and Blackman [86], this tends to increase the spin moment in the Fe to a higher value than in the case of an abrupt interface. More recently, a new calculation by Bergman showed that the largest moments are to be expected in the case of Fe clusters embedded in an FeCo alloy [114], which is similar to the case of Fe clusters in pure Co but with a mixed interface.

In a film with densely packed nanoparticles, the matrix itself will be in a nanogranular form and so in principle one can make the nanogranular Fe–Co by having either material deposited as nanoparticles. If the materials are swapped, that is Co nanoparticles are embedded in an Fe matrix (open circles in Fig. 26), the high Fe volume fraction end of the granular mixture can be investigated. The measured magnetisation at this end of the curve could well exceed the SP maximum but the large error bars prevent a confident assertion of this point. In addition, even embedded cluster films will probably not achieve 100% of the bulk density and the actual porosity of the embedded cluster films is not known. In Section 3.1 it was shown that Co clusters in Fe matrices have the bcc structure and the more open atomic structure may well produce an extra enhancement in the magnetisation of the Co nanoparticles. A recent tight-binding calculation (Table 6) of core–shell FeCo nanoparticles with a bcc structure containing 339 atoms in the core and 302 atoms (two monolayers) in the shell indicates that the moment is higher if the Co is the core material [115]. As shown in Section 3.6, the nanostructured morphology makes cluster-assembled materials magnetically soft and this is illustrated by the magnetisation curve of the $Fe_{25}Co_{75}$ mixture shown in Fig. 26.

5. CONCLUSIONS AND SUMMARY

This chapter has described the structure and magnetic properties of pre-formed gas-phase magnetic clusters deposited on surfaces and embedded in matrices by co-deposition with an atomic vapour. Isolated Fe and Co clusters deposited on substrates in UHV and left exposed show enhancements in their orbital and spin magnetic moments. In some cases, enhancements are observed in the orbital moment even for very large clusters containing ~50,000 atoms. The variation in the orbital moment of exposed Fe clusters on surfaces suggests a bcc–fcc transition at a few hundred atoms and a transition to a non-fcc phase for very small clusters. Coating exposed Fe clusters with Co in situ produce a total magnetic moment localised on the Fe atoms as large as in free Fe clusters of the same size. As the surface coverage of clusters is increased to a dense monolayer, the orbital moment is observed to drop towards its bulk value though there is evidence that an enhanced spin moment is maintained.

Structural studies of clusters embedded in matrices by co-deposition show that the atomic structure depends on the matrix material and appears to be dominated by epitaxy with the matrix. Thus, Fe clusters in Ag matrices are found to have the bcc structure, while in Cu the Fe clusters adopt the fcc phase. Similarly, Co clusters can be produced in the bcc or close-packed phase by choosing a suitable matrix material. When embedded in amorphous carbon, the clusters structure becomes more dependent on the intrinsic cluster energy terms and is probably the same as in free clusters.

It has been shown that the interface between the clusters and matrix can be sharp for noble metal matrices but some degree of intermixing occurs for transition metal matrices. Even for highly miscible materials such as Fe and Co, however, the cluster deposition technique still produces pure metal cluster cores. The cluster/vapour co-deposition technique is thus able to produce nanogranular versions of alloys.

Very low volume fractions of clusters embedded in non-magnetic matrices demonstrate perfect superparamagnetism but for volume fractions above $\sim$5% the effect of interactions is observed. As the volume fraction increases up to the percolation threshold, the cluster assembly consists of exchange-coupled aggregates of increasing size that interact with each other via dipolar forces. The overall effect is a magnetic softening of the film magnetisation. For pure cluster films, the behaviour becomes characteristic of a CSSG, which is very soft magnetically.

Magnetic thin films produced by the co-deposition technique have very flexible properties and by varying the size and volume fraction of the nanoparticles, which can be done independently, it is possible to exercise a great deal of control over the magnetisation behaviour of the materials. This flexibility coupled with the ability to produce nanogranular mixtures of miscible metals could lead to new high-performance materials such as soft magnetic films whose magnetisation exceeds the Slater–Pauling limit. It is likely that deposition of gas-phase clusters will be used in an industrial application within a few years.

REFERENCES

[1] Dunin-Borkowski R.E., McCartney M.R., Posfai M., Frankel R.B., Bazylinski D.A., Buseck P.R., Eur. J. Mineral. 13 (2001) 671.
[2] Thomas-Keprta K.L., Clemett C.J., Bazylinski D.A., Kirschvink J.L., McKay D.S., Wentworth S.J., Vali H., Gibson E.K., McKay M.F., Romanek C.S., Proc. Natl. Acad. Sci. USA 98 (2001) 2164.
[3] Brem F., Tiefenauer L., Fink A., Dobson J., Hirt A.M., Phys. Rev. B 73 (2006) 224427.
[4] Nübold H., Glassmeier K.-H., Icarus 144 (2000) 149.
[5] Gspann J., Surf. Sci. 106 (1981) 219.
[6] Sattler K., Mühlback J., Recknagel E., Phys. Rev. Lett. 45 (1980) 821.
[7] Billas I.M.L., Becker J.A., Châtelain A., de Heer W.A., Phys. Rev. Lett. 71 (1993) 4067.
[8] Douglass D.C., Cox A.J., Bucher J.P., Bloomfield L.A., Phys. Rev. B 47 (1993) 12874.
[9] Knickelbein M.B., J. Chem. Phys. 116 (2002) 9703.
[10] Knickelbein M.B., Chem. Phys. Lett. 353 (2002) 221.
[11] Knickelbein M.B., J. Chem. Phys. 115 (2001) 1983.
[12] Apsel S.E., Emmert J.W., Deng J., Bloomfield L.A., Phys. Rev. Lett. 76 (1996) 1441.
[13] Cox A.J., Louderback J.G., Apsel S.E., Bloomfield L.A., Phys. Rev. B 49 (1994) 12295.
[14] Knickelbein M.B., Phys. Rev. Lett. 86 (2001) 5255.
[15] Stoner E.C., Wohlfarth E.P., Philos. Trans. R. Soc. Lond. A 240 (1948) 599.

[16] Néel L., Ann. Geophys. 5 (1949) 99.
[17] Respaud M., J. Appl. Phys. 86 (1999) 556.
[18] Postnikov A.V., Entel P., Soler J.M., Eur. Phys. J. D 25 (2003) 261.
[19] Theil Kuhn L., Geim A.K., Lok J.G.S., Hedegård P., Ylänen K., Jensen J.B., Johnson E., Lindelof P.E., Eur. Phys. J. D 10 (2000) 259.
[20] Fujima N., Eur. Phys. J. D 16 (2001) 185.
[21] Chudnovsky E.M., Friedman J.R., Phys. Rev. Lett. 85 (2000) 5206.
[22] Barbara B., Chiorescu I., Giraud R., Jansen A.G.M., Caneschi A., J. Phys. Soc. Jpn. 69 (2000) 383.
[23] Barbara B., Thomas L., Lionti F., Chiorescu I., Sulpice A., J. Magn. Magn. Mater. 200 (1999) 167.
[24] Edmonds K.W., Binns C., Baker S.H., Thornton S.C., Norris C., Goedkoop J.B., Finazzi M., Brookes N.B., Phys. Rev. B 60 (1999) 472.
[25] Edmonds K.W., Binns C., Baker S.H., Maher M.J., Thornton S.C., Tjernberg O., Brookes N.B., J. Magn. Magn. Mater. 231 (2001) 113.
[26] Edmonds K.W., Binns C., Baker S.H., Maher M.J., Thornton S.C., Tjernberg O., Brookes N.B., J. Magn. Magn. Mater. 220 (2000) 25.
[27] Eastham D.A., Kirkman I.W., J. Phys.: Condens. Matter 12 (2000) L525.
[28] Piseri P., Tafreshi H.V., Milani P., Curr. Opin. Solid State Mater. Sci. 8 (2004) 195.
[29] Milani P., Iannotta S., Cluster Beam Synthesis of Nanostructured Materials, Springer, Berlin, 1999.
[30] Perez A., Melinon P., Dupuis V., Jensen P., Prevel B., Tuaillon J., Bardotti L., Martet C., Treilleux M., Broyer M., Pellarin M., Vaille J.L., Palpant B., Lerme J., J. Phys. D: Appl. Phys. 30 (1997) 709.
[31] Haberland H., Insepov Z., Moseler M., Phys. Rev. B 51 (1995) 11061.
[32] Getzlaff M., Kleibert A., Methling R.P., Bansmann J., Meiwes-Broer K.-H., Surf. Sci. 566 (2004) 332.
[33] Rousset J.L., Aires F.J.C.S., Sekhar B.R., Mélinon P., Prevel B., Pellarin M., J. Phys. Chem. B 104 (2000) 5430.
[34] Dupuis V., Favre L., Stanescu S., Tuaillon-Combes J., Bernstein E., Perez A., J. Phys.: Condens. Matter 16 (2004) S2231.
[35] Peng D.L., Sumiyama K., Hihara T., Yamamuro S., Konno T.J., Phys. Rev. B 61 (2000) 3103.
[36] Fauth K., Goering E., Schutz G., Kuhn L.T., J. Appl. Phys. 96 (2004) 399.
[37] Kholmanov I.N., Barborini E., Vinati S., Piseri P., Podesta A., Ducati C., Lenardi C., Milani P., Nanotechnology 14 (2003) 1168.
[38] Perez A., Bardotti L., Prevel B., Jensen M. Treilleux P., Melinon P., Gierak J., Faini G., Mailly D., New J. Phys. 4 (2002) 76.
[39] Baker S.H., Roy M., Louch S., Binns C., J. Phys.: Condens. Matter 18 (2006) 2385.
[40] Parent F., Tuaillon J., Stern L.B., Dupuis V., Prevel B., Perez A., Melinon P., Guiraud G., Morel R., Barthelemy A., Fert A., Phys. Rev. B 55 (1997) 3683.
[41] Binns C., Edmonds K.W., Baker S.H., Maher M.J., Thornton S.C., Upward M.D., Scripta Mater 44 (2001) 1303.
[42] Binns C., Louch S., Baker S.H., Edmonds K.W., Maher M.J., Thornton S.C., IEEE Trans. Magn. 38 (2002) 141.
[43] Binns C., Trohidou K.N., Bansmann J., Baker S.H., Blackman J.A., Bucher J.-P., Kechrakos D., Kleibert A., Louch S., Meiwes-Broer K.-H., Pastor G.M., Perez A., Xie Y., J. Phys. D: Appl. Phys. 38 (2005) R357.
[44] Koch S.A., Palasantzas G., Vystavel T., De Hosson Th.M., Binns C., Louch S., Phys. Rev. B 71 (2005) 085410.

[45] Vandamme N., Janssens E., Vanhoutte F., Lievens P., Van Haesendonck C., J. Phys.: Condens. Matter 15 (2003) S2983.
[46] Bardotti L., Prével B., Mélinon P., Perez A., Hou Q., Hou M., Phys. Rev. B 62 (2000) 2835.
[47] Bardotti L., Prevel B., Treilleux M., Melinon P., Perez A., Appl. Surf. Sci. 164 (2000) 52.
[48] Yoon B., Akulin V.M., Cahuzac Ph., Carlier F., De Frutos M., Masson A., Mory C., Colliex C., Bréchignac C., Surf. Sci. 443 (1999) 76.
[49] Bardotti L., Jensen P., Horeau A., Treilleux M., Cabaud B., Phys. Rev. Lett. 74 (1995) 4694.
[50] Carroll S.J., Pratontep S., Streun M., Palmer R.E., Hobday S., Smith R., J. Chem. Phys. 113 (2000) 772.
[51] Thole B.T., Carra P., Sette F., van der Laan G., Phys. Rev. 68 (1992) 1943.
[52] Carra P., Thole B.T., Altarelli M., Wang X., Phys. Rev. Lett. 70 (1993) 694.
[53] Stöhr J., König H., Phys. Rev. Lett. 75 (1995) 3748.
[54] van der Laan G., Phys. Rev. B 57 (1998) 5250.
[55] Elleaume P., J. Synchroton Radiat. 1 (1994) 19.
[56] Panaccione G., Sirotti F., Rossi G., Solid State Commun. 113 (2000) 373.
[57] van der Laan G., Phys. Rev. B 51 (1995) 240.
[58] Sirotti F., Girlando S., Prieto P., Floreano L., Panaccione G., Rossi G., Phys. Rev. B 61 (2000) R9221.
[59] Binns C., Sirotti F., Cruguel H., Baker S.H., Prieto P., Bellierand J.D., Thornton S.C., J. Phys.: Condens. Matter 15 (2003) 4287.
[60] Binns C., Baker S.H., Keen A.M., Norris C., Mozley S.N., Solid State Commun. 99 (1996) 353.
[61] Keen A.M., Binns C., Baker S.H., Mozley S., Norris C., Thornton S.C., Surf. Sci. 352–354 (1996) 715.
[62] Gambardella P., Dhesi S.S., Gardonio S., Grazioli C., Ohresser P., Carbone C., Phys. Rev. Lett. 88 (2002) 047202.
[63] Lau J.T., Frölisch A., Nietubyć R., Reif M., Wurth W., Phys. Rev. Lett. 89 (2002) 057201.
[64] Baker S.H., Binns C., Edmonds K.W., Maher M.J., Thornton S.C., Louch S., Dhesi S.S., J. Magn. Magn. Mater. 247 (2002) 19.
[65] Chen C.T., Idzerda Y.U., Lin H.-J., Smith N.V., Meigs G., Chaban E., Ho G.H., Pellegrin E., Sette F., Phys. Rev. Lett. 75 (1995) 152.
[66] Lazarovits B., Szunyogh L., Weinberger P., Phys. Rev. B 65 (2002) 104441.
[67] Bansmann J., Kleibert A., Appl. Phys. A 80 (2005) 957.
[68] Baletto F., Ferrando R., Rev. Mod. Phys. 77 (2005) 371.
[69] Vystavel T., Palasantzas G., Koch S.A., De Hosson J.Th.M., Appl. Phys. Lett. 82 (2003) 197.
[70] Jamet M., Wernsdorfer W., Thirion C., Dupuis V., Mélinon P., Pérez A., Mailly D., Phys. Rev. B 69 (2004) 024401.
[71] Baker S.H., Roy M., Gurman S.J., Louch S., Bleloch A., Binns C., J. Phys.: Condens. Matter 16 (2004) 7813.
[72] Bansmann J., Getzlaff M., Kleibert A., Bulut F., Gebhardt R.K., Meiwes-Broer K.H., Appl. Phys. A 82 (2006) 73.
[73] Bansmann J., Kleibert A., Appl. Phys. A 80 (2005) 957.
[74] Getzlaff M., Kleibert A., Methling R., Bansmann J., Meiwes-Broer K.-H., Surf. Sci. 566–568 (2004) 332.
[75] Ebert H., Battocletti M., Solid State Commun. 98 (1996) 785.
[76] Mpourmakis G., Fourmakis G.E., Andriotis A.N., Menon M., Phys. Rev. B 72 (2005) 104417.

[77] Kortus J., Baruah T., Pederson M.R., Ashman C., Khanna S.N., Appl. Phys. Lett. 80 (2002) 4193.
[78] Guirado-Lopez R.A., Dorantes-Davila J., Pastor G.M., Phys. Rev. Lett. 90 (2003) 226402.
[79] Edmonds K.W., Binns C., Baker S.H., Thornton S.C., Finetti P., J. Appl. Phys. 88 (2000) 3414.
[80] Binns C., Maher M.J., Pankhurst Q.A., Kechrakos D., Trohidou K.N., Phys. Rev. B 66 (2002) 184413.
[81] Wildberger K., Stepanyuk V.S., Lang P., Zeller R., Dederichs P.H., Phys. Rev. Lett. 75 (1995) 509.
[82] Yacaman M.J., Ascenio J.A., Liu H.B., Gardea-Torresday J., J. Vac. Sci. Technol. 19 (2001) 1091.
[83] Van Hardeveld R., Hartog F., Surf. Sci. 15 (1969) 189.
[84] Negrier M., Tuaillon-Combes J., Dupuis V., Melinon P., Perez A., Traverse A., Philos. Mag. A 81 (2001) 2855.
[85] Jamet M., Dupuis V., Melinon P., Guiraud G., Perez A., Wernsdorfer W., Traverse A., Baguenard B., Phys. Rev. B 62 (2000) 493.
[86] Xie Y., Blackman J.A., Phys. Rev. B 66 (2002) 085410.
[87] Binns C., Baker S.H., Louch S., Sirotti F., Cruguel H., Prieto P., Thornton S.C., Bellier J.D., Appl. Surf. Sci. 226 (2004) 249.
[88] Binns C., Maher M.J., New J. Phys. 4 (2002) 85.1.
[89] O'Grady K., Bradbury A., J. Magn. Magn. Mater. 39 (1983) 91.
[90] Xie Y., Blackman J.A., J. Phys.: Condens. Matter 16 (2004) 3163.
[91] Postnikov A.V., Entel P., Soler J.M., Eur. Phys. J. D 25 (2003) 261.
[92] Theil Kuhn L., Geim A.K., Lok J.G.S., Hedegård P., Ylänen K., Jensen J.B., Johnson E., Lindelof P.E., Eur. Phys. J. D 10 (2000) 259.
[93] Dimitrov D.A., Wysin G.M., Phys. Rev. B 54 (1996) 9237.
[94] Allia P., Coisson M., Tiberto P., Vinai F., Knobel M., Novak M.A., Nunes W.C., Phys. Rev. B 64 (2001) 144420.
[95] Kechrakos D., Trohidou K.N., Phys. Rev. B 62 (2000) 3941.
[96] Chudnovsky E.M., J. Magn. Magn. Mater. 40 (1983) 21.
[97] Chudnovsky E.M., Saslow W.M., Serota R., Phys. Rev. B. 33 (1986) 251.
[98] Saslow W.M., Phys. Rev. B. 35 (1987) 3454.
[99] Chudnovsky E.M., J. Appl. Phys. 64 (1988) 5770.
[100] Chudnovsky, E. M., in: The Magnetism of Amorphous Metals and Alloys, J.A. Fernandez-Baca, W.-Y. Ching, (eds), Springer Series in Solid-State Sciences, Vol. 80, World Scientific, Singapore, 1995.
[101] Loffler J.F., Meier J.P., Doudin B., Ansermet J.-P., Wagner W., Phys. Rev. B 57 (1998) 2915.
[102] Loffler J.F., Braun H.-B., Wagner W., Phys. Rev. Lett. 85 (2000) 1990.
[103] Thomas L., Tuaillon J., Perez J.P., Dupuis V., Perez A., Barbara B., J. Magn. Magn. Mater. 140 (1995) 437.
[104] Perez J.P., Dupuis V., Tuaillon J., Perez A., Paillard V., Melinon P., Treilleux M., Thomas L., Barbara B., Bouchet-Fabre B., J. Magn. Magn. Mater. 145 (1995) 74.
[105] Wiedwald U., Cerchez M., Farle M., Fauth K., Schütz G., Zürn K., Boyen H.-G., Ziemann P., Phys. Rev. B 70 (2004) 214412.
[106] Berkowitz A.E., Mitchell J.R., Carey M.J., Young A.P., Zhang S., Spada F.E., Parker F., Hutten A., Thomas G., Phys. Rev. Lett. 68 (1992) 3745.
[107] Xiao J.Q., Jiang J.S., Chien C.L., Phys. Rev. Lett. 68 (1992) 3749.
[108] Tsymbal E.Y., Pettifor D.G., Solid State Phys. 56 (2001) 113.
[109] Zhang S.F., Levy P.M., J. Appl. Phys. 73 (1993) 5315.

[110] Kechrakos D., Trohidou K.N., Recent Res. Dev. Phys. 4 (2003) 287.
[111] Louch S., Ph.D. thesis, University of Leicester, 2005.
[112] Di Fonzo F., Gidwani A., Fan M.H., Neumann D., Iordanoglou D.I., Heberlein J.V.R., McMurry P.H., Girshick S.L., Appl. Phys. Lett. 77 (2000) 910.
[113] Bergman A., Holmström E., Niklasson A.M.N., Nordström L., Frota-Pesôa S., Eriksson O., Phys. Rev. B 70 (2004) 174446.
[114] Bergman A., Eriksson O., unpublished.
[115] Xie Y., Blackman J.A., unpublished.

Chapter 14

Theory of magnetic clusters and nanostructures at surfaces

G.M. Pastor[a,*] and J. Dorantes-Dávila[b]

[a]Institut für Theoretische Physik, Universität Kassel, Heinrich Plett Str. 40, D-34132 Kassel, Germany

[b]Instituto de Física, Universidad Autónoma de San Luis Potosí, Alvaro Obregón 64, 78000 San Luis Potosí, Mexico

1. INTRODUCTION

Atomic clusters, small particles, and the nanostructures derived from them constitute a vast research area with multiple subfields and a truly interdisciplinary character. One of the most interesting and challenging subjects in nanoscopic physics is the study of many-body phenomena. On the one side, one would like to identify the effects that are specific to small particles and that differentiate them from molecules and condensed matter. On the other side, one would like to understand how the physical properties are modified in the finite-size regime as a function of size, composition, and local atomic environment, particularly in order to link the behavior of atoms and solids. From the cluster perspective, the latter can be regarded as the limits of a much richer and often quite complex dependence as a function of the number of atoms. One may in general distinguish a small-size or microscopic regime, where the changes of the physical properties with size are very strong, a large-size or mesoscopic regime, where statistical and scaling concepts apply, and in between a more or less extended crossover region.

Cluster magnetism is a problem of central importance in this context. During past decades, most of the experimental and theoretical studies in the field have been concerned with transition-metal (TM) clusters, which motivate remarkable fundamental and technological interests. One of the main goals of these investigations is to understand how the magnetic behavior evolves as the valence electrons of an isolated atom start to delocalize throughout the cluster and how the itinerant magnetism characteristic of TM solids is achieved. In this case, the hybridization among the *d* shells and the resulting *d*-band formation plays a dominant role. Consequently, electronic-structure contributions such as size, geometry, and composition dependence leading to band narrowing, local environment, and proximity effects have attracted considerable attention [1–3].

The Chemical Physics of Solid Surfaces, Volume 12
ISSN: 1571-0785
DOI: 10.1016/S1571-0785(07)12014-9

*Corresponding author.
E-mail: gustavo.pastor@irsamc.ups-tlse.fr

Two of the main characteristics of a magnetic material are the ground-state magnetic moments and the magnetic anisotropy energy (MAE). The former determines the saturation magnetization and the latter measures the stability of the magnetization direction with respect to external fields or temperature fluctuations. These properties play a central role in technological applications (e.g., high-density recording media, memory devices, or spin electronics) and are very sensitive to electron correlation effects and to the size, dimensionality, and composition of the system. Experiments on clusters and nanoparticles of TM elements have revealed a variety of remarkable effects not only in the gas or environment-free phase but also when deposited on surfaces or embedded in a matrix.

From the point of view of theory, recent methodological and technical developments have opened the way to an increasing number of systematic first principles calculations on magnetic nanostructures by using density-functional methods [4–8]. Still, numerous problems such as the determination of finite-temperature properties or the magneto-anisotropic behavior of low-symmetry systems remain a theoretical challenge. Therefore, the development of simpler yet reliable electronic models remains crucial in order to boost the progress in this field. Local approaches to electronic structure theory have proven to be particularly successful in this context, since they allow to relate in a transparent way the electronic and magnetic properties to the specific local environment of the atoms [9, 10]. The derived information is thus complementary to first principles studies, which are often limited by small size or translational symmetry restrictions.

The purpose of this chapter is to review recent developments on the theory of magnetic clusters and nanostructures giving emphasis to the properties of transition metals. The large variety of experimental methods of cluster production and nanostructure formation motivates the study of different physical situations, namely, free clusters, individual nano-objects embedded in matrices or deposited on surfaces, and nanostructures made of ensembles of interacting particles. It is one of our goals to identify their common features and specific behaviors. The remainder of the chapter is organized as follows. In Section 2, we recall the theoretical background and approximations used in the calculation of ground-state properties like spin and orbital moments, magnetic order, and anisotropy energies. The applications of the method are given in Sections 3–5 and include free and embedded clusters, binary alloy particles, as well as clusters deposited on surfaces. In Section 6, the theory is extended to finite temperatures in the framework of a functional integral formalism. The environment dependence of spin fluctuation energies and magnetization curves is analyzed in the case of free clusters and thin films. Electron correlation effects beyond mean-field approximation are discussed in Section 7 by considering two particularly relevant problems: the interplay between electron correlations, magnetism and cluster structure, and the Kondo screening of magnetic impurities in small metallic particles. Finally, we conclude in Section 8 by pointing out some interesting future research directions.

2. GROUND-STATE THEORY

In this section, we briefly recall the electronic models relevant for describing the magnetic properties of TM nanoparticles and nanostructures at surfaces. The main

properties of experimental and technological interest – for example, the spin and orbital moments, magnetic order, and anisotropy energies – are mathematically related to the microscopic magnitudes that characterize the cluster electronic structure such as the Coulomb and spin–orbit interactions, local densities of states, and spin-density distribution. This theoretical framework is used in subsequent sections to analyze the size and structural dependence of the magnetic properties of nanostructures in order to discuss the electronic origin of several experimental observations. The extension of the theory to finite temperatures is outlined in Section 6.1. A rigorous treatment of electron correlation effects is presented in Section 7.

2.1. Model Hamiltonians and mean-field approximation

We consider the non-relativistic Schrödinger equation for the valence electrons and expand the field operator $\hat{\psi}_\sigma(r) = \sum_{i\alpha} \phi_{i\alpha}(r)\hat{c}_{i\alpha\sigma}$ for spin σ in a set of orbitals $\phi_{i\alpha}(r)$ centered at each atom i, where α refers to the different s, p, and d orbitals. The Hamiltonian can be written as $H = \hat{H}_0 + \hat{V}$, where

$$H_0 = \sum_{\substack{i\alpha \\ j\beta}} t_{ij}^{\alpha\beta} \hat{c}_{i\alpha\sigma}^{\dagger} \hat{c}_{j\beta\sigma} \tag{1}$$

takes into account the single-particle hybridizations and

$$\hat{V} = \frac{1}{2} \sum_{\sigma\sigma'} \sum_{ijkl} \sum_{\alpha\beta\gamma\delta} V_{ijkl}^{\alpha\beta\gamma\delta} \hat{c}_{i\alpha\sigma}^{\dagger} \hat{c}_{j\beta\sigma'}^{\dagger} \hat{c}_{k\gamma\sigma'} \hat{c}_{l\delta\sigma} \tag{2}$$

is the electron–electron interaction. The transfer or hopping integrals $t_{ij}^{\alpha\beta}$ correspond to single-electron transitions between the orbital β at atom j and the orbital α at atom i. $\varepsilon_{i\alpha}^0 = t_{ii}^{\alpha\alpha}$ stands for the single-particle energy level of the orbital $i\alpha$. The Coulomb integrals $V_{ijkl}^{\alpha\beta\gamma\delta}$ represent transitions of a pair of electrons from the orbitals $k\gamma$ and $l\delta$ to the orbitals $i\alpha$ and $j\beta$.

The intra-atomic terms in $\hat{V}$ are the dominant ones for the magnetic properties. As already discussed, they are responsible for the Hund-rule correlations that lead to the formation of local magnetic moments in an open d shell. Therefore, in first approximation, we may treat explicitly only the intra-atomic Coulomb terms ($i = j = k = l$) by including the interatomic Coulomb contributions as a mean-field correction to the single-particle potential and hopping integrals. In this way, the interatomic terms screen quite efficiently the potential generated by the ions beyond the 1st or 2nd nearest neighbor shell. An explicit treatment of interatomic contributions becomes important for heterogeneous clusters, such as TM oxides, where important site-dependent charge transfers occur.

The Coulomb integrals $V_{ijkl}^{\alpha\beta\gamma\delta}$ are approximately proportional to the product of the overlap between $\phi_{i\alpha}$ and $\phi_{l\delta}$, and between $\phi_{j\beta}$ and $\phi_{k\gamma}$. Thus, the interaction Hamiltonian may be simplified by retaining explicitly only the terms involving at most two different orbitals, namely, the direct terms having $i\alpha = l\delta$ and $j\beta = k\gamma$, and the exchange terms having $i\alpha = k\gamma$ and $j\beta = l\delta$ (two-center approximation). Thus, the interaction term takes the form

$$\hat{H}_C = \frac{1}{2} \sum_{i\alpha\beta\sigma} [U_{\alpha\beta} \hat{n}_{i\alpha\sigma} \hat{n}_{i\beta\bar{\sigma}} + (U_{\alpha\beta} - J_{\alpha\beta}) \hat{n}_{i\alpha\sigma} \hat{n}_{i\beta\sigma}] - \frac{1}{2} \sum_{i,\alpha\neq\beta} J_{\alpha\beta} (\hat{s}_{i\alpha}^{+} \hat{s}_{i\beta}^{-} + \hat{s}_{i\alpha}^{-} \hat{s}_{i\beta}^{+}) \tag{3}$$

where $\hat{n}_{i\alpha\sigma}$ is the number operator and $\hat{s}^{+}_{i\alpha} = \hat{c}^{\dagger}_{i\alpha\uparrow}\hat{c}_{i\alpha\downarrow}$ the spin-1/2 raising operator $[\hat{s}^{-}_{i\alpha} = (\hat{s}^{+}_{i\alpha})^{\dagger}]$. $U_{\alpha\beta} = V^{\alpha\beta\beta\alpha}_{iiii}$ and $J_{\alpha\beta} = V^{\alpha\beta\alpha\beta}_{iiii}$ refer, respectively, to the direct and exchange Coulomb integrals between the orbitals α and β of atom i. For homogeneous clusters, they are independent of i. $U_{\alpha\beta}$ acts irrespectively of the electrons' spin and controls charge transfers among the different orbitals. $J_{\alpha\beta}$ is responsible for Hund's first rule in the atom and for the formation of spin moments. Finally, the orbital dependence of $U_{\alpha\beta}$ and $J_{\alpha\beta}$ tends to stabilize the formation of orbital moments and leads to Hund's second rule in atoms [11]. With present computer facilities, it is possible to perform mean-field ground-state calculations on small clusters using complex multiband models that treat all s, p, and d valence electrons explicitly (e.g., Hartree–Fock or density-functional theory in the local spin-density approximation). The situation changes completely when electron correlation effects or finite-temperature properties are explicitly addressed. In this case, it is necessary to simplify the valence-electron dynamics further by focusing on the d orbitals responsible for magnetism. Comparative studies between *spd* and d models at $T = 0$ show, as expected, that the magnetic properties of TM systems are largely dominated by the d valence electrons. Therefore, one often restricts α and β in Eqs. (1) and (3) to the $3d$ states.

In the mean-field approximation, the fluctuations of the correlation term are neglected and the Hamiltonian is given by

$$H = \sum_{i\alpha\sigma} \varepsilon_{i\alpha\sigma}\hat{n}_{i\alpha\sigma} + \sum_{\substack{i\neq j \\ \alpha\beta\sigma}} t^{\alpha\beta}_{ij}\hat{c}^{\dagger}_{i\alpha\sigma}\hat{c}_{j\beta\sigma} \tag{4}$$

with

$$\varepsilon_{i\alpha\sigma} = \varepsilon^{0}_{i\alpha} + \sum_{\beta}\left(U_{\alpha\beta} - \frac{J_{\alpha\beta}}{2}\right)\nu_{i\beta} - \frac{\sigma}{2}\sum_{\beta} J_{\alpha\beta}\mu_{i\beta} \tag{5}$$

Here, $\nu_{i\beta} = \langle\hat{n}_{i\beta\uparrow}\rangle + \langle\hat{n}_{i\beta\downarrow}\rangle$ and $\mu_{i\beta} = \langle\hat{n}_{i\beta\uparrow}\rangle - \langle\hat{n}_{i\beta\downarrow}\rangle$ refer, respectively, to the average occupation and spin polarization of orbital $i\beta$ ($\sigma = \pm 1$). Notice that we have assumed here for simplicity that the magnetic moments are collinear (i.e., $\langle s^{+}_{i\alpha}\rangle = 0$, $\forall\, i\alpha$). The collinear state is always a self-consistent solution since, in the absence of spin–orbit interactions, the eigenstates of H are products of spin-up and spin-down states when $\langle s^{+}_{i\alpha}\rangle = 0$. However, it is sometimes possible to find lower-energy solutions having non-collinear arrangements of the local spin polarizations. This is the case when magnetic frustrations are present, for example, in antiferromagnetic (AF) compact clusters or at the interfaces between ferromagnetic (FM) and AF materials (see Refs. [12–15]).

The average occupation numbers $\langle\hat{n}_{i\alpha\sigma}\rangle$ are determined self-consistently from

$$\langle\hat{n}_{i\alpha\sigma}\rangle = \int_{-\infty}^{\varepsilon_F} \rho_{i\alpha\sigma}(\varepsilon)\,\mathrm{d}\varepsilon$$

where

$$\rho_{i\alpha\sigma}(\varepsilon) = -\frac{1}{\pi}\mathrm{Im}\{\mathrm{G}_{i\alpha\sigma,i\alpha\sigma}(\varepsilon)\}$$

is the local density of states (LDOS) per spin orbital and $\mathrm{G}_{i\alpha\sigma,i\alpha\sigma}(\varepsilon)$ the local Green's function $[\hat{G} = (\varepsilon - H)^{-1}]$. A particularly efficient way of determining $\rho_{i\alpha\sigma}(\varepsilon)$ in systems

lacking translational symmetry (free and deposited clusters, surfaces, thin films, etc.) is the Haydock–Heine–Kelly's recursion method [16], which expresses $G_{i\alpha\sigma,i\alpha\sigma}(\varepsilon)$ as a local expansion around each atom i of the cluster. This local approach is physically very appealing since it stresses the role of the local environment as a function of size and composition, or as we move from the interior to the surface of the cluster.

2.2. Relativistic corrections

In non-relativistic (NR) quantum mechanics, the total spin operator $\vec{S} = \sum_i \vec{S}_i$ commutes with the Hamiltonian operator and therefore the direction of the magnetization relative to the cluster structure plays no role in the electronic properties. Thus, in the absence of an external magnetic field, the NR ground-state and excited-state energies are independent of the direction of the magnetization. However, the electronic and magnetic properties of real ferromagnets do depend to some extent on the orientation of the magnetization with respect to the crystal structure and to the external shape of the system. This is a consequence of relativistic corrections to the single-electron dynamics (Dirac equation) and to the electron–electron interaction (Breit interaction) (see, for instance, Ref. [17]). The leading contributions are of second order in the ratio v/c between the velocity of the electrons and the velocity of light.

The relativistic corrections to the electron–electron interaction have two origins. First, the electrons are *moving* charges and therefore each electron interacts with the magnetic field generated by the current and by the spins of the other electrons. Second, the electromagnetic interactions are mediated by photons which travel at the speed of light and are thus affected by retardation effects. In the Hartree approximation to the Breit interaction, the magnetic dipole–dipole energy E_{DD} is given in terms of the magnetization density $\vec{m}(r) = \langle \hat{\vec{m}}(r) \rangle$ [17, 18]. For transition metals, E_{DD} may be obtained as the sum of the dipole–dipole interactions between the local magnetic moments $\vec{\mu}_i$ at each atom i:

$$E_{DD} = \frac{\mu_B^2}{2} \sum_{i \neq j} \left[\frac{\vec{\mu}_i \cdot \vec{\mu}_j}{R_{ij}^3} - 3 \frac{(\vec{R}_{ij} \cdot \vec{\mu}_i)(\vec{R}_{ij} \cdot \vec{\mu}_j)}{R_{ij}^5} \right] \tag{6}$$

The dipole–dipole interaction energy between pairs of local moments is very small even at nearest neighbor (NN) distances ($E_{DD} \simeq 3 \times 10^{-6}$ eV for $R_0 \simeq 2.5$ Å and $\mu \simeq 1\mu_B$). However, E_{DD} decreases slowly as a function of distance ($E_{DD} \sim 1/R_{ij}^3$) and the summation over pairs ij converges very slowly. Therefore, E_{DD} depends on the shape of the nanoparticle or nanostructure.

The other relativistic corrections to the Schrödinger equation come from the single-electron dynamics which is given by the Dirac equation. The non-relativistic limit of the Dirac equation including the terms up to the order $(v/c)^2$ is the Pauli Hamiltonian [17]

$$H_{\text{Pauli}} = H_{\text{NR}} + H_{\text{SR}} + H_{\text{SO}} \tag{7}$$

One distinguishes, on the one side, the non-relativistic (Schrödinger) term H_{NR} and the scalar relativistic corrections H_{SR}, usually included in the external (pseudo)potential that defines the hopping integrals [see Eq. (1)]. On the other side, one finds the spin–orbit interactions

$$H_{\text{SO}} = \frac{\hbar^2}{2m^2c^2r} \frac{\partial V}{\partial r} \vec{\ell} \cdot \vec{s} = \alpha(r)\, \vec{\ell} \cdot \vec{s} \tag{8}$$

which are qualitatively important since they modify the symmetry of the wave function [19]. The spin–orbit coupling represents the interaction of the magnetic moment of the electron with the magnetic field that results from the electronic motion relative to the lattice potential $V(r)$. Since the electric field is strongest close to the nuclei, the spin–orbit (SO) effects are most important for the heaviest elements and for the most localized orbitals (core-electron states and d or f valence orbitals). For the d-electrons in transition metals, it is a good approximation to consider only the intra-atomic terms. Thus, H_{SO} may be expressed as

$$H_{\mathrm{SO}} = -\sum_{i,\alpha\sigma,\beta\sigma'} \xi_i \, (\vec{L}_i \cdot \vec{S}_i)_{\alpha\sigma,\beta\sigma'} \, \hat{c}^{+}_{i\alpha\sigma} \hat{c}_{i\beta\sigma'} \tag{9}$$

where ξ_i is the SO coupling constant at atom i (e.g., $\xi_i = \xi_{\mathrm{Co}}$ or ξ_{Pd}, $\xi_i > 0$), and $(\vec{L}_i \cdot \vec{S}_i)_{\alpha\sigma,\beta\sigma'}$ are the matrix elements of $\vec{\ell} \cdot \vec{s}$ among the d states, that couple the up and down spin manifolds, depending on the relative orientation of the magnetization with respect to the lattice structure.

The redistributions of the spin-polarized electronic density which follow the specific local environment of different atoms are crucial for the properties of itinerant electrons in nanostructures. Since the SO interactions are very sensitive to the details of the electronic spectrum, the properties related to SO interactions (e.g., orbital moments and MAEs) depend significantly on the spin-density distribution and on the variables that define it. For this reason, it is meaningful to perform accurate self-consistent calculations for each orientation of the magnetization and in particular to derive the MAE in a non-perturbative fashion as difference between electronic energies. In the following, a self-consistent tight-binding approach is considered, as extended to include SO interactions [3]. The Hamiltonian is given by $H = H_0 + H_C + H_{\mathrm{SO}}$, where the interatomic hopping term H_0 and the Coulomb interaction term H_C are the same as in Eqs. (1) and (3), and the SO coupling term H_{SO} is given by Eq. (9). The average d-electron occupation at site i,

$$n(i) = \sum_{\alpha} (\langle \hat{n}_{i\alpha\uparrow} \rangle + \langle \hat{n}_{i\alpha\downarrow} \rangle) \tag{10}$$

and the local spin magnetic moment,

$$\langle S_{i\delta} \rangle = \frac{1}{2} \sum_{\alpha} (\langle \hat{n}_{i\alpha\uparrow} \rangle - \langle \hat{n}_{i\alpha\downarrow} \rangle) \tag{11}$$

are calculated self-consistently by integrating the LDOS $\rho^{\delta}_{i\alpha\sigma}(\varepsilon)$ up to the Fermi energy ε_F. Since $\rho^{\delta}_{i\alpha\sigma}$ depends on the magnetization direction δ, it is determined by performing independent self-consistent calculations for each orientation of $\vec{M}$. In this way, the effects of hybridization, Coulomb, and SO interactions are treated on the same footing.

Once self-consistency is achieved, the average local orbital moments $\langle L_{i\delta} \rangle$ at atom i along the magnetization direction δ are calculated from

$$\langle L_{i\delta} \rangle = \sum_{\sigma} \sum_{m=-2}^{2} \int_{-\infty}^{\varepsilon_F} m \, \rho^{\delta}_{im\sigma}(\varepsilon) \, \mathrm{d}\varepsilon \tag{12}$$

where m indicates the magnetic quantum number. For simplicity, the quantization axis of the orbital momentum is here taken to be the same as the spin-quantization axis. The other components of $\langle \vec{L}_i \rangle$ can be obtained in an analogous way by rotating the

orbital quantization direction. The cluster average of $\langle L_\delta \rangle = (\sum_{i=1}^{N} \langle L_{i\delta} \rangle)/N$ can be compared with the outcome of X-ray magnetic circular dichroism (XMCD) experiments [20–25].

The electronic energy $E_\delta = \Sigma_i E_\delta(i)$ can be written as the sum of local contributions

$$E_\delta(i) = \sum_{\alpha\sigma} \left[\int_{-\infty}^{\varepsilon_F} \varepsilon \, \rho_{i\alpha\sigma}^{\delta}(\varepsilon) \, \mathrm{d}\varepsilon - E_{i\alpha\sigma}^{\mathrm{dc}} \right] \tag{13}$$

corresponding to the different atoms i of the deposited cluster and its environment. Here, $E_{i\alpha\sigma}^{\mathrm{dc}} = (1/2)\Delta\varepsilon_{i\sigma}\langle \hat{n}_{i\alpha\sigma} \rangle$ stands for the double-counting correction. The MAE is defined as the change $\Delta E_{\gamma\delta}$ in the electronic energy associated to a change in the orientation of the magnetization from the direction δ to the direction γ. In the case of deposited clusters, one usually considers the direction $\delta = z$ perpendicular to the surface and two directions within the surface plane: $\gamma = x$ along an NN bond and $\gamma = y$ perpendicular to $\hat{x}$. Thus, positive (negative) values of the off-plane anisotropy energy $\Delta E_{xz} = E_x - E_z$ indicate a perpendicular easy (hard) axis. Taking advantage of the local formulation, one may express $\Delta E_{\gamma\delta} = \Sigma_i \, \Delta E_{\gamma\delta}(i)$ as a sum of atom-resolved contributions

$$\Delta E_{\gamma\delta}(i) = E_\gamma(i) - E_\delta(i) \tag{14}$$

where $E_\delta(i)$ and $E_\gamma(i)$ are given by Eq. (13). Thus, the magneto-anisotropic properties can be related to the various local atomic environments. Notice that the calculation of ΔE as difference of E_δ's is a non-perturbative approach that includes in particular the effects of spin-density redistributions resulting from SO interactions. This requires a very precise determination of E_δ and of the self-consistent equations, since $\Delta E_{\gamma\delta}$ is usually a small quantity of the order of a meV.

A simple physical picture for the MAE and its relation to the orbital moments can be derived for homogeneous systems in the limit of saturated magnetic moments with large exchange splitting $\varepsilon_{id\uparrow} - \varepsilon_{id\downarrow} = J\mu$ [26]. In this case, at lowest-order perturbation theory, we may neglect the terms that mix spin-up and spin-down states. Thus, $H_{\mathrm{SO}} \simeq (\xi/2)\sum_i (\hat{l}_{iz\uparrow} - \hat{l}_{iz\downarrow})$ can be regarded as a magnetic field acting on the orbital moment $\hat{\ell}_{iz\sigma}$. Moreover, $\langle H_{\mathrm{SO}} \rangle / N_{\mathrm{a}} = (\xi/2)\ (\langle L_{z\uparrow} \rangle - \langle L_{z\downarrow} \rangle)$, where $\langle L_{z\sigma} \rangle$ is the average orbital moment per atom. Taking the up spins as the majority ones, we have $\langle L_{z\downarrow} \rangle \simeq 0$ for $n_d < 5$, and $\langle L_{z\uparrow} \rangle \simeq 0$ for $n_d > 5$, which implies that $\langle H_{\mathrm{SO}} \rangle N_{\mathrm{a}} \simeq \pm(\xi/2)\langle L_z \rangle$ with the $+(-)$ sign corresponding to $n_d < 5$ ($n_d > 5$). As in the atom, antiparallel (parallel) alignment of $\langle L_z \rangle$ and $\langle S_z \rangle$ is favored for $n_d < 5$ ($n_d > 5$). Under the previous assumptions, the anisotropy of the energy $\Delta E_{\gamma\delta}$ is proportional to the anisotropy of the orbital moments $\Delta L_{\gamma\delta} = \langle L_\gamma \rangle - \langle L_\delta \rangle$ and the lowest-energy magnetization direction (easy axis) is the one yielding the largest orbital moment. Qualitatively, one may say that in order to minimize the energy, the spin magnetization is "turned" to the direction yielding the largest $|\langle \vec{L} \rangle|$. It should be, however, recalled that a simple proportionality relation between $\Delta E_{\gamma\delta}$ and $\Delta L_{\gamma\delta}$ is not strictly valid in general. Fully self-consistent calculations have in fact revealed a number of exceptions, particularly when the spin moments are not saturated or when the anisotropy of the orbital moments is small [27, 28].

3. FREE AND EMBEDDED CLUSTERS

3.1. Simple trends as a function of coordination number

The lowest-order local approximation to $\rho_{i\alpha\sigma}(\varepsilon)$ is the second-order approximation which is obtained by taking into account only the contributions to $G_{i\alpha\sigma,i\alpha\sigma}(\varepsilon)$ from the nearest neighbors of atom i. Dropping the orbital dependence ($U_{\alpha\beta} = U$, $J_{\alpha\beta} = J$) and averaging over α one obtains

$$\rho_{i\sigma}^{(2)}(\varepsilon) = \frac{10}{\pi w_i}\left\{1 - \frac{(\varepsilon - \varepsilon_{i\sigma})^2}{w_i^2}\right\}^{1/2} \tag{15}$$

where $w_i^2 = (z_i/z_b)w_b^2$ is the second moment of the local DOS. $w_i = w_b\sqrt{z_i/z_b}$ plays the role of an effective local band-width that depends on the local coordination number z_i at the cluster atom i. z_b refers to the coordination number in the bulk ($z_b = 12$ for a face-centered cubic (FCC) lattice, for example) and w_b to the bulk band-width. Except close to the band edges, the reduction of local coordination number results in a reduction of the local effective band-width and thus in an enhanced paramagnetic density of states $\rho_{i0}(\varepsilon_F)$ at the Fermi energy.

The resulting self-consistent magnetic moments are given in Fig. 1. This very simple approximation already explains qualitatively various major trends in low-dimensional TM magnetism:

(i) The local spin magnetic moments μ_i increase as the local coordination number decreases since the kinetic (promotion) energy involved in the formation of local moments is smaller for larger $\rho_{i\sigma}(\varepsilon)$ (Stoner's criterion). Thus, surface atoms have larger spin-moments than the atoms inside the cluster. In addition, the enhancement of $\langle S_{iz}\rangle$ is more important at open surfaces than at closed ones [10, 29].

(ii) The average spin moment per atom $\bar{\mu}_N$ of an N-atom cluster increases with decreasing N since $\langle z_i\rangle$ decreases. Moreover, the enhancement of $\bar{\mu}_N$ originates at the cluster surface where z_i is smallest.

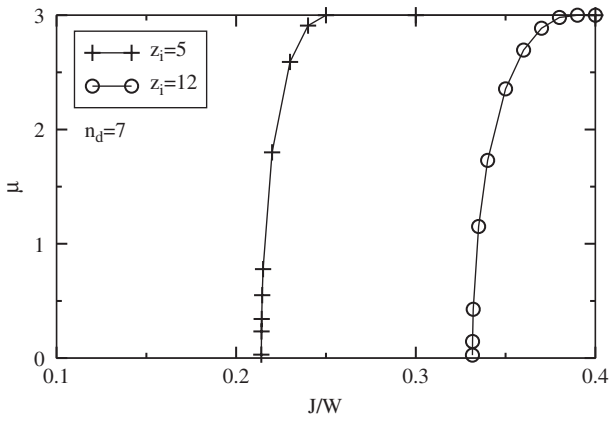

Figure 1: Self-consistent magnetic moments as a function of J/w_b as obtained by using the second-moment approximation to the local density of states [3].

(iii) Bond-length contraction results in a reduction of μ_i and $\bar{\mu}_N$ since for shorter interatomic distances, the hopping integrals and thus w_b increase.
(iv) It is in principle possible that TMs which are non-magnetic in the bulk could develop non-vanishing magnetizations if the system dimensions are reduced. This has been observed experimentally in the case of Rh_N clusters [30, 31]. For specific quantitative calculations on Rh_N, see Refs. [32–37].

It is clear that such a simple structureless LDOS cannot explain many other important properties. Equation (15) fails to reproduce that in clusters $\bar{\mu}_N$ can only take discrete values due to the discreteness of the electronic spectrum in a finite system. The same holds for the changes in the local spin moments observed even for atoms having a complete NN shell below the cluster surface. Equation (15) is also unable to distinguish between different magnetic orders which may depend on the cluster structure, as obtained, for example, in body-centered cubic (BCC) and FCC Fe clusters [38]. These are just a few examples. Nevertheless, despite these drawbacks, the second moment approximation remains an illustrative start point for a more rigorous analysis of cluster magnetic properties from a local perspective. A detailed review of theoretical studies on clusters may be found, for instance, in Ref. [3] and references therein.

3.2. Magnetic clusters in matrices

The magnetic properties of embedded clusters can be significantly modified by the interactions with the matrix if the hybridizations are strong. This is often the case for metallic substrates, particularly when the magnetic behavior of the cluster and the matrix are very different. For example, very strong effects have been found in Co or Fe clusters embedded in Nb (non-magnetic), or in Cr (antiferromagnetic) [39, 40]. In the latter case, one observes that if the size of the embedded Fe cluster is small, the magnetic order *within* the Fe cluster is antiferromagnetic with strongly reduced local magnetic moments $\mu(i)$. In other words, very small Fe clusters adopt the magnetic order induced by the spin-density wave of the Cr matrix. This contrasts with the behavior observed for free clusters which show ferromagnetic order and $\mu(i) > \mu_b$. For larger Fe_N in Cr ($N \geqslant 6$), one observes the expected transition from antiferromagnetic to ferromagnetic order within Fe_N. However, close to the interface with the matrix, the $\mu(i)$ remain significantly smaller than μ_b. The magnetic moments of the Fe atoms are very sensitive to the local chemical environment. In fact, $\langle S_{iz} \rangle_{Fe}$ is found to be roughly proportional to the number of Fe atoms $z_{Fe}(i)$ found in the first NN shell of atom *i*. Moreover, the average magnetization per atom is always smaller than μ_b(Fe) due to the contributions of interface Fe atoms. The trend is thus opposite to that of free clusters or infinite surfaces. Similarly, strong effects are observed in the case of Co clusters in Nb, where the magnetic moments of the Co atoms at the Co–Nb interface are simply quenched due to strong hybridizations with the environment.

The magnetic behavior of clusters of antiferromagnetic and non-magnetic materials like Cr and V also show very interesting proximity effects when they are embedded in ferromagnetic matrices [40]. As a representative example, Fig. 2 shows the spatial distribution of the local moments $\mu(i)$ of Cr_N clusters in bulk Fe. A similar behavior is found in the case of V_N clusters in Fe. One observes that at the interface, the magnetic coupling between cluster and matrix local moments is antiferromagnetic. Moreover, the $\mu(i)$ of Cr and V atoms are enhanced considerably by the presence of Fe atoms in

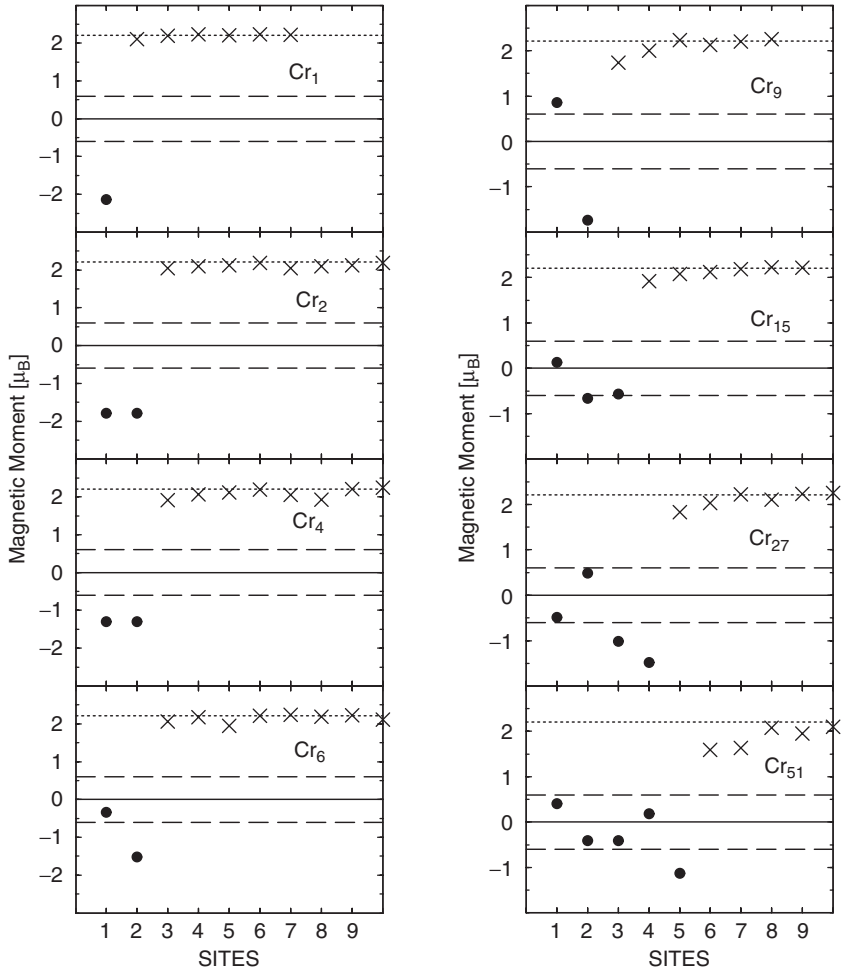

Figure 2: Local magnetic moments $\mu(i)$ for Cr_N clusters embedded in Fe as a function of *i*. Dots (crosses) correspond to Cr (Fe) atoms. The non-equivalent atomic sites *i* are ordered by increasing distance to the center of the cluster.

their first NN shell. In contrast, the $\mu(i)$ at Fe atoms close to the cluster usually tend to be reduced, although in a few cases a slight enhancement of the Fe moments is found (about 5%). The ferromagnetic order of the matrix is never altered by the embedded cluster even close to the interface. However, there are appreciable variations of the $\mu(i)$ at Fe atoms, which converge rather slowly to the Fe-bulk moment as the distance to the cluster increases. Remarkably, for very small sizes ($N \leqslant 6$), the magnetic order *within the cluster* is ferromagnetic like, with the cluster moments being antiparallel to the magnetization of the Fe matrix. This is a consequence of the strong tendency to antiferromagnetic NN coupling between Cr and Fe and between V and Fe, since in this size range all cluster atoms are at the interface. For larger sizes ($N \geqslant 9$), the magnetic order within the cluster changes to antiferromagnetic like. The local magnetic moments $\mu(i)$ of the cluster remain enhanced at the interface with the matrix. For

Cr_N, one finds antiferromagnetic alternations of $\mu(i)$ with nearly constant $|\mu(i)|$ at the interior of the cluster, while in the case of large V_N clusters $|\mu(i)|$ decreases rapidly as we move from the interface to the cluster center.

The electronic densities of states (DOS) of Cr_N and V_N embedded in Fe reflect very clearly the size-dependent changes of the magnetic order within the cluster and the proximity effects. For instance, for $N = 2$ the cluster DOS is qualitatively similar to the DOS of bulk Fe, besides the fact that minority and majority spins are interchanged (AF coupling at the interface). Only for larger sizes like Cr_{51} and V_{51}, the main features of the corresponding bulk DOS (Cr or V) start to develop.

Let us point out that, in contrast to magnetic matrices, inert matrices or colloidal solutions have a relatively weak effect on the electronic structure of the nanoparticles. In these cases, the properties of embedded clusters often resemble those of free clusters in many respects. A particularly interesting situation is found in clusters on surfaces which experience both the reduction of the local coordination number, as free clusters, and the cluster–substrate interactions, as embedded clusters. A variety of remarkable magnetic behaviors result from these competing effects. The subject is of major current interest and shall be discussed in some detail in the following sections.

3.3. Magnetic anisotropy of small clusters

Table 1 shows results for the MAE of small Fe clusters with different structures and interatomic distances [27]. The main general trends may be summarized as follows:

(i) The MAE is much larger in small clusters than in the corresponding crystalline solids. In fact, the anisotropy energy ΔE is often even larger than in thin films. For instance, $\Delta E \sim 4$–5 meV is a typical value for clusters (see Table 1). This is in agreement with experiments on free clusters and supported Fe nanoparticles [41].

(ii) ΔE depends much more sensitively than the spin moments on the geometrical structure of the cluster. Indeed, changes of sign in ΔE are found as a function of the interatomic distance d even in situations where the magnetic moments are nearly saturated and therefore do not depend on the cluster structure.

Table 1: Size and structural dependence of the MAE of Fe_N clusters [27].

N	Structure	ΔE ($d/d_b = 1.05$)	ΔE ($d/d_b = 1.00$)	ΔE ($d/d_b = 0.90$)
3	(a)	5.13 (1.43)	5.30 (−1.01)	−0.11 (−0.10)
	(b)	2.01	1.69	1.25
4	(c)	5.02 (−0.48)	5.21 (−0.59)	−1.03 (−0.11)
	(d)	0.30 (−0.12)	0.27 (−0.12)	0.33 (0.31)
5	(e)	0.29 (−1.01)	0.28 (−0.82)	−0.10 (−0.75)
	(f)	1.09 (−0.01)	0.88 (−0.03)	−0.07 (0.04)
6	(g)	−1.25 (−0.76)	−1.12 (−0.62)	0.33 (0.29)
	(h)	4.66 (0.04)	4.82 (−0.02)	−0.07 (−0.23)
7	(i)	1.78 (0.40)	1.91 (0.09)	2.22 (0.30)
	(j)	4.32 (−0.03)	4.52 (−0.02)	−0.39 (0.00)

The off-plane MAE $\Delta E = E_x - E_z$ and the in-plane MAE $\Delta E = E_x - E_y$ (results in brackets) are given in meV for different values of the interatomic bond-length d (d_b = bulk NN distance). Different structures are considered for each cluster size: (a) triangle, (b) chain, (c) square, (d) rhombus, (e) trust, (f) square pyramid, (g) triangle, (h) square bipyramid, (i) hexagon, and (j) pentagonal bipyramid (see Ref. [27]).

(iii) The magnetic energy surface of low-symmetry clusters is in general quite complex. In particular, the in-plane MAEs are often found to be very important. In some cases, they are even larger than the usually considered off-plane anisotropy. The in-plane MAE is of course largest for low-symmetry structures and decreases, though not monotonically, as the angle between non-equivalent x and y directions decreases. Experiments support these conclusions.

The strong sensitivity of the magnetic anisotropy on the details of electronic structure and the trends for different transition metals are illustrated by calculations as a function of the d-band filling n_d. In Fig. 3, the MAE ΔE_{xz} and the anisotropy $\Delta L_{zx} = \langle L_z \rangle - \langle L_x \rangle$ of the average orbital moments are reported for a sevenatom TM cluster with a pentagonal bipyramid structure. The considered magnetization directions are $\delta = z$, along the principal C_5 symmetry axis of the cluster, and $\delta = x$, which is perpendicular to z and to one of the nearest neighbor bonds in the pentagonal ring [28]. One observes strong oscillations and changes of sign of the MAE which indicate changes in the easy axis. These are related to the energy-level structure around ε_F and to the details of the SO mixing. The resulting changes in the electronic energy depend on the explicit form of H_{SO} and therefore on the direction of the magnetization.

The anisotropy of the average orbital moments $\Delta L_{zx} = \langle L_z \rangle - \langle L_x \rangle$ shows very similar trends as ΔE_{xz} with the most stable direction being in general the one that yields the largest $\langle L_\delta \rangle$, as predicted by perturbation theory [26]. Moreover, notice that the local orbital magnetic moments $\langle L_{i\delta} \rangle$, the corresponding anisotropies $\Delta L_{zx}(i) = \langle L_{iz} \rangle - \langle L_{ix} \rangle$, and the site-resolved contributions $\Delta E_{zx}(i)$ to the MAE, are very sensitive to the local environment showing even changes of sign as a function of i. A similar behavior is found for other clusters and band-fillings [27, 28]. A more detailed discussion on the role of orbital magnetism in magnetic clusters is presented in the following section.

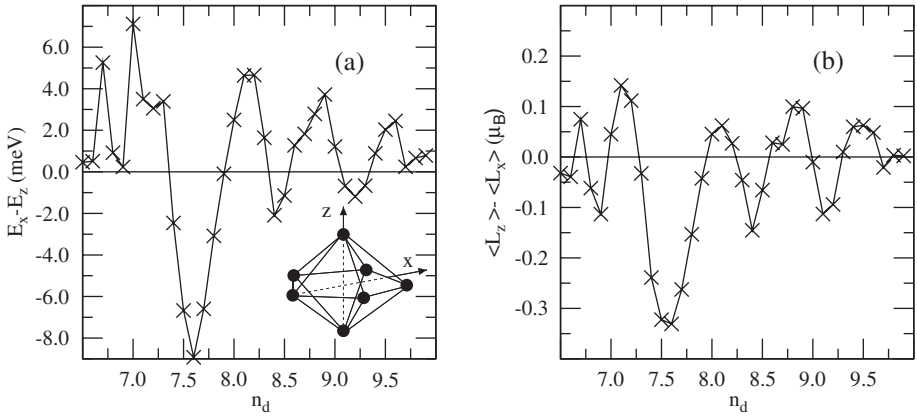

Figure 3: (a) Magnetic anisotropy energy per atom $\Delta E_{xz} = E_x - E_z$ and (b) anisotropy of the orbital magnetic moments per atom $\Delta L_{zx} = \langle L_z \rangle - \langle L_x \rangle$ in a seven-atom cluster as a function of d-band filling n_d. The cluster structure and magnetization directions are illustrated in the inset of (a).

3.4. Size-dependent enhancement of orbital magnetism

In atoms, Hund's rules predict maximum orbital angular moment L compatible with maximum spin multiplicity, while in TM solids, electron delocalization and band formation result in an almost complete quenching of $\langle L\rangle$. Such intrinsic differences between atomic and bulk behaviors are characteristic of systems developing itinerant-electron magnetism. Consequently, investigations of orbital magnetism in TM clusters – in the way from the atom to the solid – should reveal novel size-dependent phenomena that are important both from a fundamental standpoint and in view of applications of cluster-based magnetic nanostructures. These general considerations already indicate that $\langle L\rangle$ should be very sensitive to the local environment of the atoms. Indeed, recent experiments on chains [42, 43] and clusters at surfaces [20–23] show that $\langle L\rangle$ is typically a factor 2–5 larger than in the corresponding solids. Calculations on small supported clusters confirm these conclusions [4, 5]. Moreover, a size-dependent enhancement of $\langle L\rangle$ should have direct consequences on the results for the average magnetic moments per atom and on the comparison between theory and experiment [44–46]. It is therefore important to understand the dependence of orbital magnetism on variables like size, structure, local atomic environment, and d-band filling.

In order to analyze the crossover from atomic L to bulk-like quenching of $\langle L\rangle$ with increasing size, we focus first of all on Ni_N clusters. Besides its experimental relevance, Ni is a very interesting system since the differences between atomic and bulk orbital moments are dramatic ($L = L_a = 2\mu_B$ in the atomic s^1d^9 configuration, and $\langle L\rangle = L_b = 0.05\mu_B$ in the solid). In addition, the spin moments in Ni_N are the smallest among the ferromagnetic $3d$ TMs, and therefore the contribution of $\langle L\rangle$ to the total magnetic moment $\langle\vec{M}\rangle = 2\langle\vec{S}\rangle + \langle\vec{L}\rangle$ is expected to be particularly significant. In Fig. 4, results [47] are given for the average orbital moment per atom $\langle L_\delta\rangle = [\sum_{i=1}^{N} L_\delta(i)]/N$ of Ni_N with $N \leqslant 165$, having FCC or icosahedral-like geometries. Low-symmetry structures and two-dimensional (2D) islands are also considered. These are representative of different local symmetries and shapes and allow to quantify the role of cluster structure on orbital magnetism. On the one hand, we observe that the reduction of system size causes a remarkable enhancement of $\langle L_\delta\rangle$ with respect to the solid. Values about 6–8 times larger than $L_b = 0.05\mu_B$ are not uncommon. On the other hand, comparison with the atomic result $L_a = 2\mu_B$ shows that the largest part of the quenching of L takes place already at the smallest clusters, as soon as full rotational symmetry is lost. For example, for Ni_3 (triangle) we obtain $\langle L_z\rangle = 0.47\mu_B$, and for Ni_4 (rhombus) $\langle L_z\rangle = 0.35\mu_B$. Concerning the size dependence, one observes that $\langle L_\delta\rangle$ decreases with increasing N showing some oscillations as bulk-like quenching is approached (see Fig. 4). Notice that an important enhancement of $\langle L_\delta\rangle$, about 100%, is still present even for the largest considered sizes (e.g., $\langle L_\delta\rangle/L_b = 1.8$ for $N = 165$). In smaller clusters, $\langle L_\delta\rangle/L_b$ ranges from $\langle L_\delta\rangle/L_b \simeq 3$ for $N = 50$–80, to $\langle L_\delta\rangle/L_b \simeq 5$ for $N = 10$–20. Already at this stage, one concludes that orbital magnetism is the source of an important contribution to the size-dependent magnetic properties of Ni clusters.

In Fig. 4, results are also given for icosahedral clusters having $N \leqslant 55$ atoms. $\langle L_\delta\rangle$ decreases with increasing N in a similar way as for the FCC geometries. Nevertheless, the fivefold symmetric structures yield in general significantly larger $\langle L_\delta\rangle$ than the cubic symmetric ones. The results for $N \geqslant 13$ concern mainly highly symmetric structures with nearly spherical shape and closed NN shells. Clusters with lower symmetry usually present a very rich size dependence, particularly when the

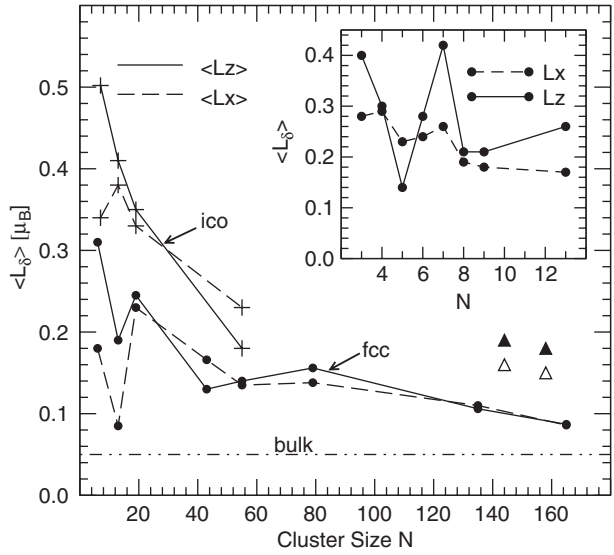

Figure 4: Average orbital magnetic moment per atom $\langle L_\delta \rangle$ of Ni_N clusters with FCC-like (dots) and icosahedral-like structures (crosses) [3]. The magnetization direction δ is a principal C_n symmetry axis ($\delta = z$) or an NN bond perpendicular to z ($\delta = x$). Full (open) triangles refer to coin-like bilayer clusters with perpendicular (in-plane) magnetization. Results for small clusters are given in the inset.

proportion of surface atoms is large. This is illustrated by the results for $N \leqslant 13$ given in the inset, which correspond to optimized geometries derived from ab initio calculations [48–50].

Structural changes may also affect the convergence to bulk-like quenching for large N, particularly for clusters on surfaces, whose shape can be experimentally tuned at least to some extent by changing the landing or growth conditions [20–23, 42]. This is illustrated by the results for two-layer-thick coin-like Ni_N, which are indicated by the triangles in Fig. 4 ($N = 144$ and 158). For these 2D islands, $\langle L_\delta \rangle$ is much larger than for 3D FCC clusters of comparable size. The enhancement with respect to L_b is here about a factor 3. Similar trends are found for other TMs, in qualitative agreement with recent experiments on Fe and Co particles [1, 20–24]. Structure and shape can have a strong influence on the quantitative value of the orbital moments in TM nanoparticles, even though the main trends are not affected significantly by the precise geometry.

From the solid state perspective, the enhancement of $\langle L_\delta \rangle$ can be qualitatively understood as the result of the following major contributions that are related to the changes in the local environment of the atoms:

(i) The reduction of local coordination number with decreasing N causes an increase of the local spin polarizations $\langle S_{i\delta} \rangle$ which induces larger orbital moments by means of the spin–orbit interactions.
(ii) The orbital dependence of the intra-atomic Coulomb interactions favors the occupation of high m states thereby amplifying the enhancement of $\langle L_\delta \rangle$. Although this contribution is quantitatively important, typically 30–40% of the

value of $\langle L_\delta \rangle$, it does affect significantly the trends as a function of size and structure.

(iii) The presence of degeneracies in the single-particle spectrum allows a more effective spin–orbit mixing that enhances $\langle L_{i\delta} \rangle$ even in situations where $\langle S_{i\delta} \rangle$ is saturated.

Qualitatively, the size-dependent magnetic moments are determined by the competition between the kinetic energy, which favors electron delocalization and small moments, and the Coulomb interactions, which tend to suppress charge fluctuations and lead to Hund rules. Thus, low-spin and quenched-L states become comparatively less stable than high-spin and enhanced-L states as N is reduced. Notice, moreover, that the changes in $\langle S_{i\delta} \rangle$ and $\langle L_{i\delta} \rangle$ involve different energy scales. Therefore, the occupations of the different m orbitals may vary without altering the spin polarizations (e.g., compare icosahedral and FCC clusters in Fig. 4). Finally, one also observes less predictable effects related to the details of the electronic structure and its dependence on cluster geometry, like the presence of high-symmetry axes or changes in bond-length.

The environment dependence of the local orbital moments $L_\delta(i)$ provides further insight on the enhancement of $\langle L_\delta \rangle$ in small clusters, and on the development of bulk-like quenching for large N. One observes that $\langle L_{i\delta} \rangle$ generally increases with i, showing some oscillations as we move from the center to the surface of the cluster. Therefore, the enhancement of $\langle L_\delta \rangle$ is driven by the surface, as it is the case for the spin moments [3]. A similar behavior is found for icosahedral geometries. For small N (e.g., $N = 19$ and 55), the enhancement of $\langle L_{i\delta} \rangle$ concerns practically all atoms, including those with a complete NN shell. For larger sizes ($N \geqslant 135$), bulk-like quenching starts to set in at the interior of the cluster, leaving significantly enhanced orbital moments only at a few outermost shells. As expected, one approaches the behavior found for TM surfaces, where the enhanced $\langle L_{i\delta} \rangle$ are restricted to a few uppermost layers. A droplet model, i.e., $(\langle L_\delta \rangle - L_b) \propto N^{-1/3}$, is in fact a good first approximation for $N \geqslant 150$–200, although the convergence to L_b remains rather slow. The fact that $\langle L_{i\delta} \rangle \simeq L_b$ for inner atoms indicates that cubic point-group symmetry, absent in all atoms except the central one, is not essential for reaching nearly bulk-like quenching. Instead, the recovery of a bulk-like local atomic environment seems a more appropriate interpretation.

The contribution of the orbital moments – that in Ni align parallel to the spin moments – increases the value of the total magnetic moment $\bar{\mu}_N = \langle L \rangle + 2\langle S \rangle$ predicted by theory, thereby improving the agreement with experiment. In fact, despite some quantitative differences among the results obtained by different groups, available spin-only calculations yield ground-state spin magnetizations that underestimate systematically the experimental $\bar{\mu}_N$ by about 0.3–$0.6\mu_B$ for $N \leqslant 13$ [48–50]. The largest part of this discrepancy is removed by including the enhanced orbital contributions, thereby resolving the previous controversy on this subject. The remaining differences, about $(0.1$–$0.2)\mu_B$, are not far from the estimated experimental uncertainties. This could also be related to correlation effects, which should favor electron localization leading to more atomic-like orbital moments and possibly to a further enhancement of $\langle L_\delta \rangle$.

The trends for other TMs can be inferred from Fig. 5, where $\langle L_\delta \rangle$ of a pentagonal bipyramid is given as a function of d-band filling n_d. $\langle L_\delta \rangle$ increases approximately linearly with increasing number of d holes, as we move from Ni ($n_d \simeq 9$) to Fe ($n_d \simeq 7$).

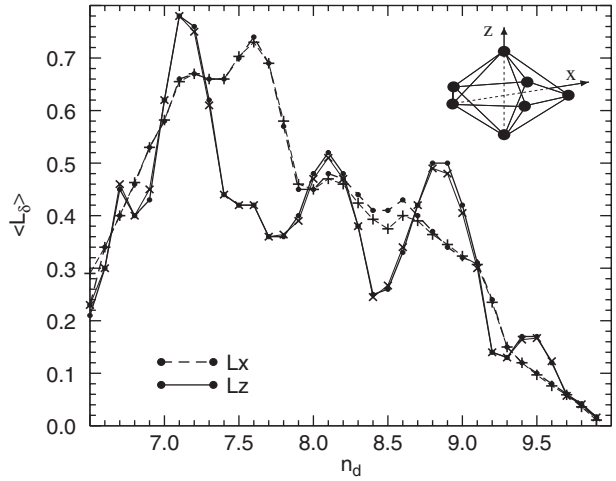

Figure 5: Average orbital moment per atom $\langle L_\delta \rangle$ in a seven-atom TM cluster as a function of d-band filling n_d. The structure and magnetization directions δ are illustrated.

Notice that the orbital moment per d hole $\langle L_\delta \rangle/(10-n_d) \simeq (0.25-0.3)\mu_B$ is quite close to recent experimental results on Fe_N clusters ($N \leqslant 9$) deposited on Ni/Cu(0 0 1) [22]. In addition, one observes oscillations and changes of sign of the anisotropy $\Delta L = L_z - L_x$, which are associated to changes in the occupations of molecular states k with different orbital moments $\langle l \rangle_k$. This is consistent with previously observed oscillations of the MAE as a function of n_d [27]. One concludes that the size-dependent enhancement of $\langle L_\delta \rangle$ is important for all magnetic TM clusters.

4. BINARY ALLOY CLUSTERS

Binary metallic clusters formed with a magnetic 3d TM and a 4d or 5d element, which are non-magnetic in bulk but have a strong magnetic susceptibility like Pd, Pt, or Rh, provide an effective way to combine the large magnetic moments of the 3d elements with an enhancement of the MAE due to the large spin–orbit coupling at the 4d or 5d orbitals. The purpose of this section is to discuss theoretical results on the spin moments, orbital moments, and MAE of CoRh clusters which are representative of this kind of binary clusters. Special attention will be given to the role of structure, size, and composition on the magnetic properties, and to the comparison with available experiments. Recently, Co–Rh nanoparticles (1–2 nm) have been synthesized by decomposition of organometallic precursors in mild conditions of pressure and temperature in the presence of a polymer [51]. The measurements show that the average magnetic moment per Co atom is about $2.38\mu_B$ for a Co concentration $x_{Co} \simeq 0.5$. This value is much larger than the average magnetic moment in CoRh bulk alloys of similar concentration.

4.1. Structure and spin moments of Co_NRh_M clusters

The interplay between structural, chemical, and magnetic properties of small free Co_MRh_N ($N+M \leqslant 13$) has been studied by Dennler et al. [52, 53]. Calculations of the

cohesive energy, structure, and spin moments have been performed by solving the spin-polarized self-consistent Kohn–Sham equations in the framework of a plane-wave basis treating core-electron effects within the projector-augmented wave approximation [54, 55]. All cluster structures were optimized by relaxing fully the atomic positions without symmetry constraints until the forces F_i, on each atom i are vanishing (typically $|F_i| \leqslant 0.01$–$0.02\,\text{eV/Å}$). This was done for each relevant value of the z component of the total spin moment S_z. In this way, the interplay between magnetism and ground-state structure was quantified. Several initial geometrical configurations corresponding to different cluster topologies were considered in order to detect nearby isomers.

Representative results [52, 53] for $Co_M Rh_N$ with $N + M = 7$ atoms are presented in Fig. 6. One observes a monotonous decrease of the cohesive energy as we go from the pure Rh_7 to pure Co_7, in agreement with the lower cohesive energy of bulk Co compared with bulk Rh. The most stable structures are in general 3D ($N \geqslant 4$) with planar isomers found at nearby energies. All studied CoRh clusters are magnetic with average spin moment per atom μ and local spin moments $\mu(i)$ that are often a factor 2 larger than those of macroscopic crystals or alloys with similar concentrations. Moreover, one observes that $\bar{\mu}_N$ and $\mu(i)$ tend to increase with increasing fraction of Co atoms. In some cases, the replacement of just one Rh atom by Co can lead to a remarkable global spin polarization and enhancement of the total cluster moment, which goes well beyond the individual contribution of the replaced atom.

From a local standpoint, one observes that the magnetic moments of Co atoms are not significantly affected by the Rh concentration even if the latter is increased beyond 50%. The presence of Rh does not reduce the Co moments, which contrasts with the important reduction of Co moments observed in some macroscopic CoRh alloys. This is probably a consequence of the extremely reduced coordination number in these small clusters. From the point of view of Rh, the presence of Co atoms in the cluster results in a remarkable increase of the local moments and in a larger stability of magnetism. From these results, one concludes that small CoRh clusters are magnetic with average magnetic moments per atom that are significantly larger than those of bulk alloys of similar concentrations. For a given cluster size, $\bar{\mu}_N$ increases with increasing x_{Co}. The most stable isomers are usually not the most magnetic ones.

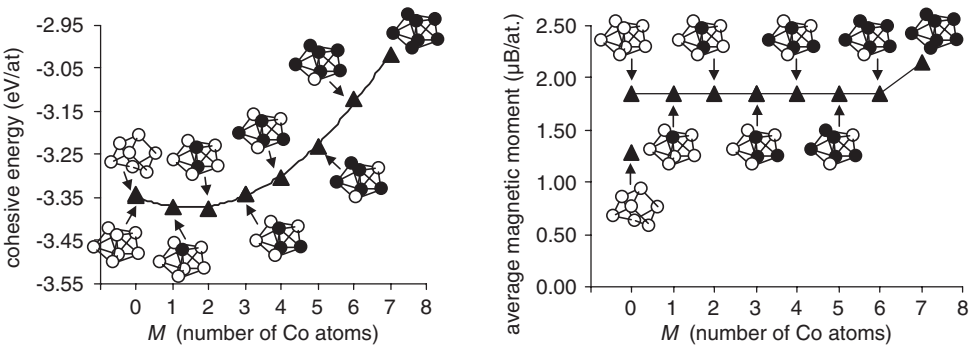

Figure 6: Cohesive energy and average magnetic moment per atom of $Co_M Rh_N$ clusters having $M + N = 7$ atoms as a function of Co concentration [52, 53].

4.2. Orbital moments and magnetic anisotropy energy

Recently, Muñoz-Navia et al. calculated the spin moments, orbital moments, and MAE of large Co_MRh_N clusters [56]. In Table 2, results are given for the magnetic moments and MAE of Co_NRh_M. An FCC-like spherical cluster with $N+M=43$ atoms is considered as a representative example, which is formed by a central atom and its successive shells of NNs. This corresponds to a $Co_{19}(Rh_{19})$ core covered with an $Rh_{24}(Co_{24})$ shell. The relevant directions of the magnetization are $\delta = z$ which is a principal C_4 symmetry axis of the cluster, $\delta = x$ which points along an NN bond perpendicular to z, and $\delta = xy$ which connects the central atom with one of the vertices in the xy plane. For each considered cluster, the lowest energy direction or easy axis is indicated. For the sake of comparison, results are also shown for Co_{19} and Co_{43}. As expected, the total magnetic moment per atom $\langle M\rangle_T/(N+M)$ decreases with decreasing Co concentration, $x_{Co} = N/(N+M)$ (i.e., increasing Rh concentration). For example, $\langle M\rangle_T/(N+M) = 1.98\mu_B$ in Co_{43} ($x_{Co} = 1.0$), $\langle M\rangle_T/(N+M) = 1.40\mu_B$ in $Rh_{19}Co_{24}$ ($x_{Co} = 0.56$ with an Rh_{19} core), and $\langle M\rangle_T/(N+M) = 0.80\mu_B$ in $Co_{19}Rh_{24}$ ($x_{Co} = 0.44$ with a Co_{19} core). Notice the particularly small value of $\langle M\rangle_T$ in the case of a Co core, in contrast to the clusters with Rh core which still preserve a significant magnetization. This is mainly due to two effects: the larger NN bond-length in the Rh core, which enhances the magnetic moments particularly at Rh atoms, and the orbital contribution $\langle L\rangle_{Co}/N = 0.47\mu_B$ of the Co surface atoms. The importance of the induced magnetic moments at the Rh atoms is more clearly seen by considering, as in Ref. [51], the average total magnetic moment per Co atom, which is given by $\langle M\rangle_T/N$. In the previous 43–atom examples, one has $\langle M\rangle_T/N = 1.98\mu_B$ for $x_{Co} = 1.00$ and $\langle M\rangle_T/N = 2.51\mu_B$ for $x_{Co} = 0.56$, which indicates that the Rh contribution is significant ($\langle M\rangle_{Rh}/M \simeq 0.68\mu_B$ in $Rh_{19}Co_{24}$). The fact that $\langle M\rangle_T/N$ increases with decreasing x_{Co} shows that, upon alloying with Rh, the Co atoms preserve the largest part of the magnetic moments they have in the pure Co case and that the induced moments at the Rh atoms are significant enough to override an eventual reduction of the Co contributions. A similar behavior has been found in spin-density-functional calculations on small clusters [53].

Recent experimental results on the NN bond-lengths and magnetic moments in Co–Rh clusters [51, 57] and the comparison with available theoretical calculations

Table 2: Average magnetic moments (in μ_B) and lowest-energy magnetization direction δ (easy axis) of Co–Rh clusters.

Cluster	$\frac{\langle M\rangle_T}{N+M}$	$\frac{\langle M\rangle_T}{N}$	$\frac{\langle L\rangle_T}{N+M}$	$\frac{\langle L\rangle_{Rh}}{2\langle S\rangle_{Rh}}$	δ
Co_{19}	2.02	2.02	0.33		xy
Co_{43}	1.98	1.98	0.29		x
$Co_{19}Rh_{24}$	0.80	1.44	0.06	0.07	z
$Rh_{19}Co_{24}$	1.40	2.51	0.30	0.14	x
$Rh_{19}Co_{60}$	1.65	2.17	0.26	0.09	z
$Rh_{19}Co_{68}$	1.76	2.25	0.35	0.08	x
$Rh_{19}Co_{66}$	1.71	2.20	0.30	0.10	xy
$Rh_{139}Co_{182}$	1.18	2.08	0.19	0.07	z

For given N and M, Co_NRh_M refers to an FCC-like cluster with a Co_N core covered by M Rh atoms, while in Rh_MCo_N the core is Rh and the outer shells are Co. $\delta = z$ is a principal C_4 symmetry axis of the cluster, $\delta = x$ is perpendicular to z and along a nearest neighbor bond, and $\delta = xy$ points from the central atom to one of the vertices in the xy plane.

suggest that these binary clusters are likely to have an Rh core with Co rich outer layers. In fact, the measurements of NN bond-lengths yield values that are very similar to that of bulk Rh [57]. Moreover, the measured magnetic moments per Co atom in the size range $N+M = 200$–400 is $\langle M\rangle_T^{\text{expt}}/N \simeq 2.3\mu_B$ for $x_{\text{Co}} \simeq 0.5$ [51]. These are much larger than the theoretical values obtained for a Co-rich core but consistent with the calculations for an Rh-rich core, eventually with some degree of mixing at the interface. Furthermore, there is direct experimental evidence for the existence of an induced moment at the Rh atoms as observed in XMCD measurements [58]. This is in qualitative agreement with the orbital-to-spin ratios obtained in our calculations which amount to $\langle L\rangle_{\text{Rh}}/2\langle S\rangle_{\text{Rh}} = 0.07$–$0.14$ for $N+M = 43$. Results on larger clusters in the experimentally relevant size range ($N + M \simeq 300$ atoms) confirm these conclusions [56].

The effects of structure and shape have been investigated by considering spherical-like and octahedral FCC clusters having $N+M = 79$, 85, and 87 atoms (see Table 2). In these cases, the dependence of the magnetic moments on Co concentration is qualitatively similar to what has been already discussed for smaller sizes. Comparing the spherical-like clusters, one observes somewhat larger $\langle S\rangle_T$ and $\langle L\rangle_T$ for $N+M = 87$ than for $N+M = 79$. This is mainly due to the larger orbital-moment contribution of the low-coordinated Co surface atoms which constitute the outermost shell for $N+M = 87$. The same kind of local enhancement of $\langle L_{i\delta}\rangle$ is also found at the corners of the octahedral structure. Interesting symmetry effects are observed by comparing the MAE of spherical and octahedral clusters. In particular in the latter case, full vectorial calculations as a function of both polar and azimuthal magnetization angles reveal a rich magneto-anisotropic energy surface with an easy axis $\delta = xy$ along the diagonal of the xy square [56].

The environment dependence of the local moments provides further insight on the magnetic behavior and on the proximity effects resulting from alloying and interface mixing [56]. Figure 7 shows results for $\langle L_{jz}\rangle$, $2\langle S_{jz}\rangle$ and $\langle M_{jz}\rangle = 2\langle S_{jz}\rangle + \langle L_{jz}\rangle$ in an FCC spherical-like cluster which is formed by an Rh_{79} core surrounded by surface Co shells including some degree of mixing at the Co–Rh interface. One observes that both $\langle L_{jz}\rangle$ and $2\langle S_{jz}\rangle$ generally increase with j, showing some oscillations as we move from the center to the surface of the cluster. Notice that the magnetic moments at the Rh atoms at the center of the cluster are antiparallel to the majority spins. This tendency to an antiferromagnetic-like order is characteristic of systems showing weak magnetism. A similar behavior is observed in pure Rh_M clusters across the size-dependent transition from a ferromagnetic to a paramagnetic state which occurs for $M \approx 50$ [34]. On the other side, particularly large positive values of $\langle L_{jz}\rangle$ and $2\langle S_{jz}\rangle$ are found at the interface of Rh atoms (e.g., $j = 8$ and $j = 11$). As a result, the average Rh contribution to $\langle M\rangle_T$ is positive. For these sizes, it amounts to about 20% of the total cluster moment and is thus responsible for the experimentally observed enhancement of the average moment per Co atom ($\langle M\rangle_{\text{Rh}}/\text{M} \simeq 0.25\mu_B$ for $N+M = 321$). These calculations show the dominant role of the Co–Rh interfaces and of the resulting proximity effects.

Alloy clusters open interesting possibilities of tailoring the magnetic behavior as a function of size and relative concentrations. As already discussed, the magnetic moment per Co atom increases for given size when Co atoms are replaced by Rh. However, except for the very small sizes ($M \leqslant 50$) where Rh_M is magnetic on its own,

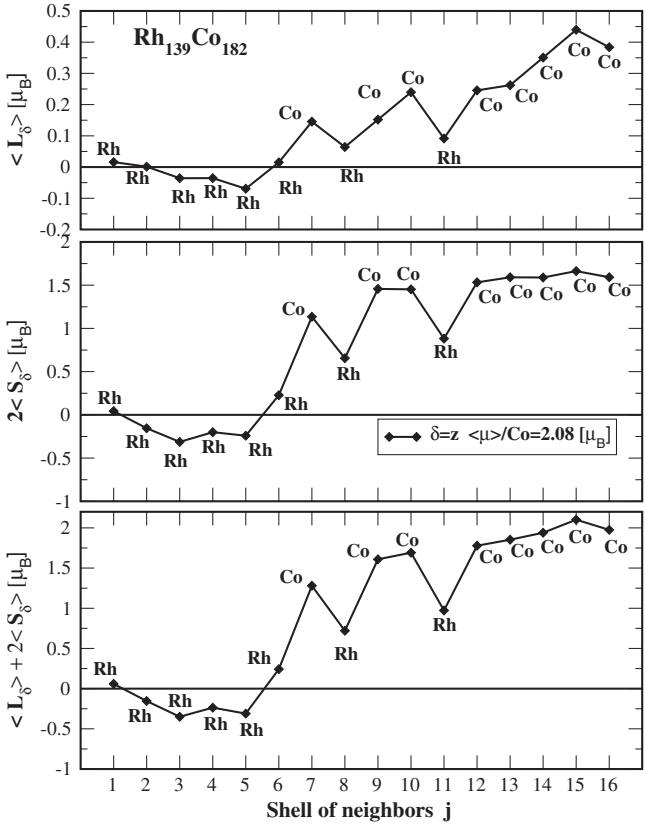

Figure 7: Local magnetic moments in FCC-like $Co_{139}Rh_{182}$: orbital contribution $\langle L_{jz}\rangle$, spin contribution $2\langle S_{jz}\rangle$, and total moment $\langle M_{jz}\rangle = 2\langle S_{jz}\rangle + \langle L_{jz}\rangle$. The cluster is formed by an Rh core surrounded by surface Co shells including some degree of mixing at the Co–Rh interface. The chemical composition, which is assumed to be the same within the shell, is indicated for each j. The results refer to the average at each NN shell j ordered by increasing distance to the central atom $j = 1$. The magnetization direction is along the easy axis $\delta = z$. The lines are a guide to the eye.

one observes that $\langle M\rangle_T/N$ in Co_NRh_M starts to decrease if $x_{Co} = N/(N+M)$ is reduced beyond a certain threshold. In this Rh-rich limit, the Co content in the cluster is not large enough to stabilize a significant net magnetization of the Rh atoms and ferromagnetic order breaks down. Let us recall that pure Rh_M is not magnetic in the experimentally relevant size range of about 300 atoms. In this case, $\langle M\rangle_T/N$ shows a maximum as a function of x_{Co}. Actually, a similar situation is known to occur in bulk Co–Rh alloys. However, recent calculations on alloy clusters [56] reveal an interesting new size-dependent effect which shifts the maximum in magnetic moment from $x_{Co} \simeq 0.5$ in the bulk to $x_{Co} \simeq 0.75$ at least for $N+M \leqslant 500$. All the magnetic properties are affected by this non-monotonous behavior. In particular, the MAE follows in general a similar trend and it can thus be optimized as a function of composition, which has an obvious importance for potential technological applications.

In conclusion, CoRh clusters show a variety of interesting properties as a function of size, structure, and composition, which deserve further systematic experimental and

theoretical studies. Remarkable surface and interface effects are also expected for other 3*d*–4*d* finite-size alloys. In this context, CoPd clusters appear to be very promising, particularly concerning magnetic anisotropy, since the Co–Pd interfaces have already revealed remarkable effect in the context of bulk alloys, thin films, and deposited clusters.

5. FERROMAGNETIC CLUSTERS ON HIGHLY POLARIZABLE SUBSTRATES

Significant progress is being achieved on the production and characterization of clusters embedded in matrices or deposited on surfaces, films made out of clusters, and auto-organized nanostructures by following different experimental routes [20–24, 42, 59–70]. On the one side, submonolayer structures are produced by methods originally developed in the context of surface physics, for example, atomic manipulation using scanning tunnel microscopy, diffusion controlled aggregation, or molecular beam epitaxy [63–65, 71]. On the other side, cluster assembled magnetic materials are created by applying methods like low-energy cluster-beam deposition on surfaces, which originally derive from research on size-selected cluster beams [21, 22, 59, 61, 68, 72]. These experimental studies, particularly from the latter point of view, emphasize the importance of extending our present theoretical understanding on free clusters to situations where the clusters are in contact with a macroscopic environment. A systematic comparison between the properties of free and deposited particles appears therefore as a fundamental step toward the characterization of the specific properties of these nanostructured materials.

Several theoretical studies have already been concerned with the spin moments, orbital moments, and MAE of Fe and Co clusters on noble metal substrates like Cu, Ag, and Au surfaces [4–6, 73]. A variety of interesting magnetic behaviors have been revealed as a result of the competition between the reduction of local coordination numbers and the interactions with the substrate. The purpose of this section is to discuss the magnetic and electronic properties of ferromagnetic clusters on highly polarizable TM substrates. Co_N clusters on Pd(1 1 1) are expected to be particularly interesting due to the strong magnetic susceptibility of Pd and since the Co–Pd interfaces are known to show a remarkably rich magneto-anisotropic behavior [74, 75]. It is therefore very appealing, from both fundamental and technological standpoints, to investigate the possibility of tailoring the magnetic anisotropy of Co nanostructures on Pd in order to stabilize perpendicular magnetizations, which could be useful in high-density recording and memory devices [76, 77].

5.1. Spin and orbital moments of Co_N clusters on Pd(1 1 1)

Table 3 summarizes results for the average magnetic moments per Co atom derived from self-consistent tight-binding calculations on Co_N clusters deposited on the Pd(1 1 1) surface. First of all, one observes that the total magnetic moments per Co atom M_{δ_0} of the deposited clusters are remarkably large for all the considered structures ($N \leqslant 13$). The most important M_{δ_0} are found for the 1D monoatomic chains (structure (e)). In this case, M_{δ_0} appears to depend very weakly on N in the considered size range: $M_x = 2.65$, 2.62, and $2.61\mu_B$ for $N = 3$, 7, and 13, respectively. Moreover,

Table 3: Magnetic properties of Co_N clusters on Pd(1 1 1).

N	Structure	$2\langle S_z\rangle$	$\langle L_x\rangle$	$\langle L_y\rangle$	$\langle L_z\rangle$	M_{δ_0}	δ_0
3	(a)	2.17	0.44	0.44	0.40	2.61	y
		[1.69]	[0.42]	[0.40]	[0.36]	[2.11]	[x]
	(e)	2.15	0.50	0.50	0.40	2.65	X
		[1.69]	[1.36]		[1.00]	[3.05]	[x]
4	(b)	2.12	0.40	0.38	0.37	2.49	z
		[1.69]	[0.54]	[0.60]	[0.40]	[2.23]	[y]
	(e)	2.17	0.49	0.38	0.50	2.67	x
		[1.69]	[0.85]		[0.69]	[2.54]	[x]
7	(c)	2.10	0.35		0.30	2.40	z
		[1.69]	[0.64]		[0.29]	[2.33]	[x]
	(e)	2.16	0.46	0.45	0.38	2.62	x
		[1.69]	[0.83]		[0.63]	[2.52]	[x]
13	(d)	2.09	0.34		0.31	2.40	z
		[1.69]	[0.48]		[0.35]	[2.17]	[x]
	(e)	2.15	0.46		0.37	2.61	x
		[1.68]	[0.86]		[0.56]	[2.54]	[x]
	(f)	2.07	0.35	0.33	0.30	2.37	z
		[1.69]	[0.59]		[0.38]	[2.28]	[x]

The averages per Co atom of the spin moment $2\langle S_z\rangle$, orbital moments $\langle L_\delta\rangle$ for $\delta = x$, y, and z, and total magnetic moment $M_{\delta_0} = 2\langle S_{\delta_0}\rangle + \langle L_{\delta_0}\rangle$ for the easy axis δ_0 are given in Bohr magnetons. The structures and magnetization directions are illustrated in Fig. 8. The results given in the first line refer to deposited clusters including the contributions of the Pd atoms at the Co–Pd interface and the results in square brackets to free Co_N having the same structure as the deposited clusters.

the results for the 13–atom chain are actually not far from the infinite-length limit, for which $M_x = 2.56\mu_B$ is obtained. 2D-like clusters show somewhat smaller magnetic moments than the monoatomic chains. Here, M_{δ_0} decreases moderately with increasing N as one approaches the 2D Co monolayer on Pd(1 1 1): $M_y = 2.61\mu_B$ for the triangle, $M_z = 2.49\mu_B$ for the rhombus, $M_x = 2.40\mu_B$ for the hexagon, and $M_x = 2.32\mu_B$ for the infinite monolayer. Comparison with the results for free clusters shows that cluster–substrate interactions yield a significant enhancement of the magnetic moments per Co atom.

The average spin and orbital moments reported in Table 3 show that the magnetization $M_\delta = (2\langle S_\delta\rangle) + \langle L_\delta\rangle)/N$ of Co_N on Pd(1 1 1) is mainly the result of three physically distinct effects. The first and leading contribution comes, as expected, from the spin moments at the Co atoms $i = 1$–N for which we obtain nearly saturated values $2\langle S_z\rangle_{Co}) = (1.66{-}1.69)\mu_B$. These depend very weakly on size and structure, and are only slightly smaller than in the corresponding free clusters. The Co spin moments constitute about 63% of the total magnetization per Co atom in the monoatomic chains, and about 64–70% in the 2D islands ($N \leqslant 13$).

The second important contribution to M_δ are the spin moments induced at the Pd atoms of the Co–Pd interface that amount to $(0.43$–$0.51)\mu_B$, depending on the cluster size and structure. This corresponds to approximately 22% of the spin polarization per Co atom, and 19% of the total moment (see Table 3). The induced spin moments are responsible for the most part of the above-discussed enhancement of M_δ in deposited clusters as compared with the free-standing case. A more detailed analysis of the local magnetic moments at the Co–Pd interface, given in Section 5.3, allows to

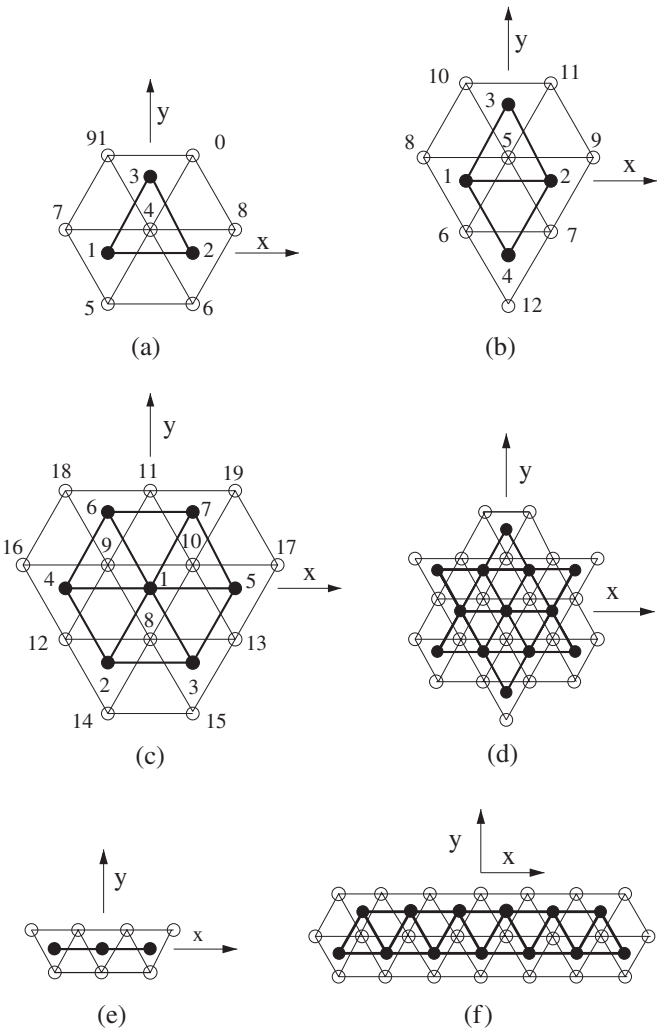

Figure 8: Illustration of the structures and magnetization directions considered in the calculations on Co_N clusters deposited on Pd(1 1 1). The z direction is perpendicular to the xy surface plane. Open (filled) circles refer to Pd (Co) atoms. The numbers label the different atomic sites i.

derive simple rules that relate the changes in the induced moments as a function of cluster size and geometry with the local environments of the Pd atoms.

The orbital magnetic moments $\langle L_\delta \rangle$ are the third main piece of the calculated magnetization. $\langle L_\delta \rangle$ is essentially parallel to the spin moment, as corresponds to elements having a d-shell which is more than half filled. Thus, they add to $\langle S_\delta \rangle$ representing about 15–19% of M_δ. One observes that $\langle L_\delta \rangle$ is in general quite sensitive to the size and geometry of the cluster and to the direction δ of the magnetization. For example, 1D clusters usually develop larger orbital moments than 2D clusters of the same size, which in both cases tend to decrease with increasing N. Notice, moreover, that the anisotropy of $\langle L_\delta \rangle$ is far more important than the one of the spin moments. This anticipates a

strong environment dependence of the MAE due to the spin–orbit interactions. As in the case of the spin polarization, the largest part of the orbital moments comes from the Co atoms (values in curved brackets). Still, the Pd contributions, (10–25)% of $\langle L_\delta \rangle$ depending on the particular cluster and δ, are not negligible (see Table 3). It is also interesting to remark that the average orbital moments at the Co atoms are significantly enhanced as compared with the corresponding bulk moment $\langle L_\delta \rangle$ (Co-bulk) $\simeq 0.13\mu_B$. A similar effect has already been observed for Co films on Pd(1 1 1) [75], as well as in free and deposited TM clusters [4–6, 47]. Quantitatively, the calculated Co orbital moments along the easy axis δ_0 are $\langle L_{\delta_0} \rangle = (0.3\text{–}0.5)\mu_B$, which corresponds to about $(0.15\text{–}0.2)\mu_B$ per d hole, a value which is somewhat smaller, though not far from the one observed in experiments on small Fe clusters deposited on Ni [22]. Comparison with the results for free clusters (given in square brackets) shows that the hybridizations with the substrate often lead to a reduction of the Co orbital moments. In the case of monoatomic chains, the effect is particularly strong and has been interpreted as a consequence of the loss of 1D character [78]. In fact, a similar strong reduction of $\langle L_\delta \rangle$ is also observed when one compares monoatomic and biatomic chains. For example, for $N = 13$, the Co moment changes from $\langle L_x \rangle = 0.42\mu_B$ in the deposited monoatomic chain (structure (e)) to $\langle L_x \rangle = 0.29\mu_B$ in the biatomic chain (structure (f)) which is already not far from our result for the 2D monolayer, namely, $\langle L_x \rangle = 0.23\mu_B$. Similar trends have been observed in experiments on Co chains of various widths grown at the steps of the Pt(9 9 7) surface [42].

5.2. Magnetic anisotropy energy and spin reorientations

The interactions between magnetic adatoms and metallic substrates often lead to redistributions of the spin-polarized density and to changes in the electronic structure which affect sensitively the spin–orbit energies. In order to quantify these effects, it is interesting to compare the off-plane MAEs $\Delta E_{xz} = E_x - E_z$ and $\Delta E_{yz} = E_y - E_z$, and the in-plane MAE $\Delta E_{xy} = E_x - E_y$ of Co_N clusters deposited on Pd(1 1 1) with the corresponding results for free clusters having the same structure as the deposited ones. The monoatomic free-standing chains show an in-line easy axis with remarkably large MAEs per Co atom [$\Delta E_{xz} < 0$ with $|\Delta E_{xz}| = (6.2 - 20)$ meV]. In the case of deposited chains, the interaction with the substrate does not modify the easy axis but reduces by an order of magnitude the absolute value of the MAEs [79]. This is consistent with the reduction of the orbital moments discussed in the previous section.

The 2D clusters and biatomic chains yield $\Delta E_{xz} < 0$ in the free-standing geometry, which implies that the easy axis is in-plane. The absolute values of the MAEs are much larger than the typical results found in thin films and at surfaces, which are of the order of (0.1–1.0) meV. These anisotropy energies are somewhat smaller than in the 1D chains, though mostly of the same order of magnitude [$|\Delta E_{xz}| = (0.88\text{–}12)$ meV]. As in the 1D case, the largest part of the enhanced MAEs is lost after deposition on Pd ($|\Delta E_{xz}| = (0.05\text{–}0.70)$ meV). Nevertheless, in the 2D clusters, the effects of the interaction with the substrate are qualitatively different since most 2D Co_N/Pd(1 1 1) present a stable off-plane magnetization direction [80]. This remarkable magnetization reorientation is the result of two main contributions: the changes in the electronic structure of the Co clusters due to cluster–substrate hybridizations, and the anisotropy of the spin–orbit energy at the Pd atoms of the Co–Pd interface, which carry small induced magnetic moments. Moreover, this effect appears to be a characteristic of the

2D like clusters, since the biatomic chain shows a perpendicular easy axis while the monoatomic chain remains in-line. A detailed analysis of the various local MAEs $\Delta E_{xz}(i)$, presented in Section 5.3, indicates that the interface between Co and Pd plays a dominant role in the magneto-anisotropic behavior of the deposited clusters, as already observed in thin Co films on Pd(1 1 1) [75]. Cluster–substrate hybridizations are therefore crucial for the magneto-anisotropic behavior of magnetic islands deposited on metallic substrates.

Concerning the size dependence of the MAE of 2D clusters, we would like to point out that the calculated easy axis of the 2D Co monolayer on Pd(1 1 1) is within the surface plane, as observed in experiment [74]. This is in part due to the dipole–dipole energy that is non-negligible in the case of extended films and that always favor an in-plane magnetization. Moreover, the in-plane direction is further stabilized by the magneto-crystalline anisotropy energy ΔE_{xz} resulting from SO interactions, which is negative for the 2D monolayer, though rather small. Consequently, a transition from off-plane to in-plane easy axis should be expected to occur in single-layer Co_N as a function of the island size. Moreover, it could be possible that at intermediate sizes the clusters show tilted magnetization with canted easy axes, as already observed in 2D Co–Pd nanostructures [75].

5.3. Local environment dependence

The local formulation given in Section 2 can be exploited to express most relevant magnetic properties as a sum of contributions corresponding to the different atoms i of the cluster and its surroundings. In this way, the observed magnetic behavior of the deposited clusters can be related to the specific local atomic environments. As an example, we consider the hexagonal Co_7 cluster on Pd(1 1 1).

Table 4 reports the corresponding local spin moments $2\langle S_{iz}\rangle$, local orbital moments $\langle L_{i\delta}\rangle$ for $\delta = x, y$, and z, and total local moments $\mu_{i\delta_0} = 2\langle S_{i\delta_0}\rangle + \langle L_{i\delta_0}\rangle$ along the easy axis $\delta_0 = z$. The labeling of atomic sites is shown in Fig. 8c.

The local spin moments $\langle S_{iz}\rangle$ at the Co atoms are nearly saturated, and therefore they are quite independent of i and of the particular size or structure of the Co_N cluster. In contrast, the $\langle S_{iz}\rangle$ induced at the Pd atoms show a very interesting environment

Table 4: Local magnetic properties of an hexagonal Co_7 cluster deposited on Pd(1 1 1).

i	$2\langle S_{iz}\rangle$	$\langle L_{ix}\rangle$	$\langle L_{iz}\rangle$	μ_{iz}	$\Delta E_{xz}(i)$
1	1.67	0.19	0.17	1.84	0.74
2–3	1.67	0.31	0.26	1.93	−0.70
4–5	1.67	0.27	0.26	1.93	−0.20
6–7	1.67	0.34	0.26	1.93	−0.80
8	0.33	0.04	0.03	0.36	−0.24
9–10	0.33	0.04	0.03	0.36	−0.19
11	0.27	0.02	0.04	0.31	1.00
12–13	0.27	0.04	0.04	0.31	1.28
14–15	0.19	0.03	0.03	0.22	0.48
16–17	0.19	0.03	0.03	0.22	−0.03
18–19	0.19	0.03	0.03	0.22	0.39
Average	2.10	0.35	0.30	2.40	0.28

The spin moments $2\langle S_{iz}\rangle$, orbital moments $\langle L_{i\delta}\rangle$ for $\delta = x$ and z, and total magnetic moments $\mu_{iz} = 2\langle S_{iz}\rangle + \langle L_{iz}\rangle$ along the easy axis z are given in Bohr magnetons for the different atomic sites i as labeled in Fig. 8c. The corresponding local magneto-crystalline anisotropy energies $\Delta E_{xz}(i) = E_x(i) - E_z(i)$ are given in meV (see Eqs. (13) and (14)).

dependence. In fact, $(S_{iz})_{\mathrm{Pd}}$ appears to be approximately determined by the number of Co atoms z_i that are NNs of the Pd atom i. For $z_i = 3$ ($i = 8$–10 in the hexagon) one obtains $2\langle S_{iz}\rangle = 0.33\mu_B$, for $z_i = 2$ ($i = 11$–13) $2\langle S_{iz}\rangle = 0.27\mu_B$, and for $z_i = 1$ ($i = 14$–19) $2\langle S_{iz}\rangle = 0.19\mu_B$ (see Table 4 and Fig. 8). Similarly, strong correlations between local magnetic moments and the immediate chemical environment of the atoms have been already observed in magnetic alloys and thin films which involve, like the present case, non-saturated magnetic moments (e.g., Fe–Al alloys or Fe–Co overlayers) [9, 10, 29]. It should be moreover noted that for these small clusters, the number of Pd atoms at the Co–Pd interface is roughly twice the number of Co atoms. Therefore, the induced Pd moments yield a sizeable contribution to the average magnetic moment per Co atom (see Table 3). In this context, one should observe that relaxations of the cluster structure or atomic rearrangements at the cluster–substrate interface often modify the magnetic properties, particularly if the relevant local atomic environments change significantly. For instance, in the case of cluster burrowing [81], one expects that the total spin polarization of the Pd host should increase, since the number of Pd atoms in contact with the Co cluster increases.

The local orbital moments $\langle L_{i\delta}\rangle$ at the Co atoms are typically a factor 2–3 larger than in bulk-Co and in addition show a very interesting environment dependence. One observes that the magnetization direction yielding the largest $\langle L_{i\delta}\rangle$ is very often different for different atoms i. Moreover, the important difference in local coordination number between the central atom $i = 1$ and the outer atoms $i = 2$–7 results in a different degree of quenching of $\langle L_{i\delta}\rangle$, the higher coordinated central atom having a smaller orbital moment than the lower coordinated outer ones. For the Pd atoms at the Co–Pd interface, the orbital moments are far less important in absolute values ($\langle L_{i\delta}\rangle = (0.01$–$0.04)\mu_B$), although they still represent about 10–15% of the total Pd moments.

The local anisotropy energies $\Delta E_{\delta\gamma}(i) = E_\delta(i) - E_\gamma(i)$ allow us to analyze the microscopic origin of the perpendicular magnetization in 2D Co_N on Pd(1 1 1) [80]. The results given in Table 4 show that it is mostly Pd, and not Co, which defines the positive sign of ΔE_{xz} and thus the perpendicular orientation of the magnetization. For example in the hexagon, $\Delta E_{xz}(i) < 0$ for $i = 2$–7 while only $\Delta E_{xz}(1) > 0$. The Pd atoms close to Co_N cannot be regarded as a mere source of modifications in the electronic structure of Co_N but rather as important magnetic components on their own. In fact, they carry non-vanishing-induced magnetic moments and, as 4*d* elements, are subject to significant spin–orbit couplings ($\xi_{\mathrm{pd}} \simeq 2\xi_{\mathrm{Co}}$) [26]. It is therefore reasonable that they contribute to ΔE_{xz} and to the overall MAE of the system. Note that $\Delta E_{xz}(i)$ of the Pd atoms is of the same order of magnitude as in the Co atoms, often even larger at Pd (see Table 4). In fact, if one would ignore the Pd contributions to the MAE, the easy axis would be in-plane. The same occurs if the induced magnetic moments or the SO interactions at the Pd atoms are neglected. The central role of the substrate Pd atoms on the MAE is thereby demonstrated. This also confirms the importance of treating the redistributions of the spin-polarized density and the spin–orbit interactions at the same electronic level.

The present discussion should encourage the development of new experimental works as well as further theoretical improvements. For example, it would be worthwhile to investigate more systematically the dependence of the magnetic properties on the geometry of the cluster and its immediate environment. This would be relevant in

particular for the comparison with experiment, since the morphology of the nanoparticles can be tuned, at least to some extent, by changing the growth and deposition conditions or by subsequent annealing [21, 59–61, 63–65, 71, 81]. The well-known sensitivity of TM magnetism to the specific local atomic environments should lead to a wide variety of interesting behaviors. Moreover, recent experimental and theoretical studies have revealed remarkable spin-reorientation transitions and spin-canted phases at Co–Pd and Co–Pt film interfaces [74, 75, 82]. Therefore, it is reasonable to expect similar phenomena in the case of Co clusters on Pd or Pt surfaces, which deserve detailed investigations both from a fundamental standpoint and in view of applications. The magnetic reorientation transitions along the crossover from 1D to 2D nanostructures have been investigated in Ref. [83].

6. FINITE-TEMPERATURE MAGNETIC PROPERTIES

From Stern–Gerlach deflection measurement on size-selected cluster beams, it is possible to derive results on the average magnetization per atom $\bar{\mu}_N(T)$ of isolated clusters as a function of the nozzle temperature T. Remarkable temperature dependences of $\bar{\mu}_N$ have been reported, which depend significantly on the considered TM [44–46, 84, 85]. In Ni_N, the magnetization curves are qualitatively similar to the bulk, except of course for an important finite-size broadening of the transition around the cluster "Curie" temperature T_C [45, 46]. Experiments on Co_N show that $\bar{\mu}_N(T)$ is about $0.1–0.5\mu_B$ larger than the bulk magnetization $M(T)$ for $50 \leqslant N \leqslant 600$ and $100\,\mathrm{K} \leqslant T \leqslant 1000\,\mathrm{K}$ [45]. Moreover, at low temperatures, $100\,\mathrm{K} \leqslant T \leqslant 500\,\mathrm{K}$, the magnetization per atom is found to increase slightly with T. This is an unexpected effect that is not observed in the solid. In Fe clusters, the temperature dependence is qualitatively different from that of Ni or Co clusters. For $250 \leqslant N \leqslant 600$ one observes a rapid, almost linear decrease of $\bar{\mu}_N(T)$ with increasing T ($T \leqslant 500$–$600\,\mathrm{K}$). For $T \geqslant 300\,\mathrm{K}$, $\bar{\mu}_N(T)$ is smaller than the bulk $M(T)$, even though at $T = 0$ it was larger (T_C(Fe-bulk) $= 1043\,\mathrm{K}$). As the cluster size increases ($250 \leqslant N \leqslant 600$) $\bar{\mu}_N(T)$ decreases further making the difference between cluster and bulk magnetizations even larger [45]. One expects that the trend should change for larger Fe clusters, although no experimental evidence seems to be available so far.

From a theoretical standpoint, very little is still known about cluster magnetism at finite temperatures [86, 87]. This is remarkable since a correct description of the temperature dependence of the magnetic properties is crucial for understanding the physics of the underlying many-body problem as well as for controlling the behavior of magnetic clusters in view of technological applications. The trends in the size dependence of finite temperature properties – for example, the cluster "Curie" temperature $T_C(N)$, which measures the stability of the magnetic order within the cluster – seem difficult to infer a priori. On the one side, taking into account the enhancement of the local magnetic moments μ_l^0 at $T = 0$ and of the d-level exchange splittings $\Delta\varepsilon_{Xl}^d = \varepsilon_{l\downarrow}^d - \varepsilon_{l\uparrow}^d$, one could expect that $T_C(N)$ should be larger and that the FM order should be more stable in small clusters than in the bulk. However, on the other side, the local coordination numbers are smaller at the cluster surface and therefore it should be energetically easier to disorder the local magnetic moments in a cluster by flipping or canting them. If the latter effect dominates, $T_C(N)$ would tend to decrease with decreasing N. Moreover, recent model calculations indicate that changes or fluctuations in the cluster structure

may also affect significantly the temperature dependence of the magnetization, in particular for systems like Fe_N and Rh_N which show a remarkable structural dependence of the magnetic properties already at $T = 0$ [88–90]. Reliable conclusions on cluster and nanostructure magnetism at finite T should be derived from an electronic theory that takes into account both the fluctuations of the magnetic moments and the itinerant character of the *d*-electron states [86, 87]. Simple spin models, for example based on the Heisenberg or Ising model, are not expected to be very predictive, unless they incorporate the electronic effects responsible for the size dependence of the local magnetic moments and of their interactions. In fact, studies of itinerant magnetism at surfaces have already shown that the effective exchange interactions J_{lm} between NN moments $\mu_l\mu_m$ depend strongly on the local environment of sites l and m [91].

6.1. Functional integral theory

The finite-temperature magnetic properties of clusters have been investigated by extending the functional-integral formalism developed by Hubbard and Hasegawa for periodic solids [92–94] to the case of finite systems with arbitrary symmetry [86]. The many-body interaction H_I is rewritten as

$$H_I = \sum_l \left(\frac{U}{2} \hat{N}_l^2 - J \hat{S}_{lz}^2 \right) \tag{16}$$

where $\hat{N}_l = \sum_{\alpha\sigma} \hat{n}_{l\alpha\sigma}$ is the number operator at atom l and $\hat{S}_{lz} = (1/2)\sum_\alpha (\hat{n}_{l\alpha\uparrow} - \hat{n}_{l\alpha\downarrow})$ is the z component of the local spin operator. For simplicity, we have neglected the orbital dependence of the Coulomb integrals so that the interaction parameters are given by $U = \overline{U_{\alpha\beta}} - \overline{J_{\alpha\beta}}/2$ and $J = \overline{J_{\alpha\beta}}$. Note that Eq. (16) includes the self-interaction terms $(U - J)\hat{n}_{l\alpha\sigma}^2/2 = (U - J)\hat{n}_{l\alpha\sigma}/2$ which are canceled out by redefining the *d*-energy levels as $\varepsilon_l^0 - (U - J)/2$.

For the calculation of the canonical partition function Q, the quadratic terms in Eq. (16) are linearized by means of a two-field Hubbard–Stratonovich transformation within the static approximation. Thus, a charge field η_l and an exchange field ξ_l are introduced at each cluster site l, which describe the finite-temperature fluctuations of the *d*-electron energy levels and local exchange splittings, respectively. Since we are mainly interested in the magnetic properties and since $J \ll U$, it is reasonable to neglect the thermal fluctuations of the charge fields η_l. Thus, for each exchange-field configuration $\vec{\xi}$, we set η_l equal to the saddle point of the free energy $F(\vec{\xi}, \vec{\eta})$ associated to the field configuration $\vec{\xi} = (\xi_1, \ldots, \xi_N)$ and $\vec{\eta} = (\eta_1, \ldots, \eta_N)$. This is given by $i\eta_l = v_l = \langle \hat{N}_l \rangle'$ which physically means that the charge distribution $v_l = \langle \hat{N}_l \rangle'$ is calculated self-consistently for each $\vec{\xi}$. The partition function is then given by

$$Q \propto \int \mathrm{d}\vec{\xi}\, Q'(\vec{\xi}) \tag{17}$$

where

$$Q'(\vec{\xi}) = \exp\{-\beta F(\vec{\xi})\} \tag{18}$$

$$Q'(\vec{\xi}) = \exp\left\{ \frac{\beta}{2} \sum_l \left(U v_l^2 - \frac{J}{2} \xi_l^2 \right) \right\} \mathrm{Tr}[\exp\{-\beta \hat{H}'\}] \tag{19}$$

depends only on the exchange variables ξ_l that describe the relevant fluctuations of the spin degrees of freedom. Thus, $F(\vec{\xi})$ represents the free energy associated to the exchange-field configuration $\vec{\xi}$. Notice that the v_l are implicit functions of $\vec{\xi}$ [86].

The static approximation is exact in the atomic limit ($t_{lm}^{\alpha\beta} = 0, \forall l \neq m$) where no fluctuations are present, and in the non-interacting limit ($U = J = 0$). For non-trivial cases, $\hat{H}'$ describes the dynamics of the d electrons as if they were independent particles moving in a random alloy with energy levels $\varepsilon'_{l\sigma}$ given by

$$\varepsilon'_{l\sigma} = \varepsilon_l^0 + U v_l - \sigma \frac{J}{2} \xi_l \tag{20}$$

The thermodynamic properties of the system are obtained as a statistical average over all possible distributions of the energy levels $\varepsilon'_{l\sigma}$ throughout the cluster. For $T \to 0$, the dominating field configuration $(\vec{\xi}^{\,0}, \vec{\eta}^{\,0})$ corresponds to the saddle point in the free energy $F(\vec{\xi}, \vec{\eta})$. This is determined from the self-consistent equations

$$\left.\frac{\partial F}{\partial \xi_l}\right|_0 = \frac{J}{2}(\xi_l^0 - 2\langle \hat{S}_{lz} \rangle') = 0 \tag{21}$$

and

$$\left.\frac{\partial F}{\partial \eta_l}\right|_0 = U(\eta_l^0 + i\langle \hat{N}_l \rangle') = 0 \tag{22}$$

where $\langle \ldots \rangle'$ indicates average with respect to the ground state of H'. Replacing Eqs. (21) and (22) in Eq. (20) yields the known mean-field approximation to the energy levels $\varepsilon'_{l\sigma}$ [38]. Consequently, the present approach is the natural finite-temperature extension of the self-consistent tight-binding theory presented in Section 2.1 for the ground state.

The integrand $\exp\{-\beta F(\vec{\xi})\}$ of Eq. (17) is proportional to the probability $P(\vec{\xi})$ for a given $\vec{\xi}$. The thermodynamic properties are obtained by averaging over all possible $\vec{\xi}$ with $\exp\{-\beta F(\vec{\xi})\}$ as weighting factor. For example, the local spin magnetization at atom l is given by

$$\mu_l(T) = \frac{1}{Q} \int \mathrm{d}\vec{\xi} \exp\left\{ -\frac{\beta}{2} \sum_l \left(U \overline{\eta}_l^2 + \frac{J}{2} \xi_l^2 \right) \right\} \mathrm{Tr}[2\hat{S}_l^z \exp\{-\beta \hat{H}'\}] \tag{23}$$

$$\mu_l(T) = \frac{1}{Q} \int \mathrm{d}\vec{\xi}\, 2\langle S_{lz} \rangle' \, \mathrm{e}^{-\beta F'(\vec{\xi})} \tag{24}$$

where $\langle S_{lz} \rangle'$ is the average spin moment corresponding to the effective single-particle Hamiltonian H', which depends on the fluctuating $\vec{\xi}$. For clusters, the statistical average in Eq. (24) can be performed by Monte Carlo sampling. As in any finite-system calculation, the restriction $\Sigma_l \xi_l \geqslant 0$ – or equivalently positive values of the total cluster moment – must be applied to avoid trivially vanishing results for the average magnetization due to time-inversion symmetry. This corresponds to the experimental situation where the cluster moment is aligned along an external magnetic field. The cluster magnetization per atom $\overline{\mu}_N = \sum_l \mu_l(T)/N$ is then obtained as the average of the local magnetizations [86, 95]. For solids or extended nanostructures, the average is approximated by using the theory of random alloys and effective medium approaches

like the virtual crystal approximation (VCA) or the coherent potential approximation (CPA) [96].

The free-energy difference

$$\Delta F(\vec{\xi}) = F(\vec{\xi}) - F(\vec{\xi}^{\,0}) \tag{25}$$

with respect to the minimum or ground-state value $F(\vec{\xi}^{\,0})$ determines the probability that the exchange-field fluctuation $\Delta\vec{\xi} = \vec{\xi} - \vec{\xi}^{\,0}$ is realized at a given T. $\Delta F(\vec{\xi})$ can be regarded as the spin fluctuation energy associated to $\vec{\xi}$, since the fluctuations of $\vec{\xi}$ are responsible for the fluctuations of the spin moments $\langle S_{lz}\rangle'$. Taking into account that $\partial F/\partial\xi_l = J(\xi_l - 2\langle\hat{S}_{lz}\rangle')/2$ and integrating Eq. (24) by parts one obtains

$$\mu_l(T) = \frac{1}{Q}\int \mathrm{d}\vec{\xi}\ \xi_l\ \mathrm{e}^{-\beta F(\vec{\xi})} \tag{26}$$

Thus, the temperature-dependent local spin magnetization is equal to the average of the local exchange field. Eq. (26) justifies the intuitive association between the fluctuations of the local moment $\mu_l = 2\langle\hat{S}_{lz}\rangle'$ at atom l and those of the exchange field ξ_l. A local free energy $F_l(\xi)$ can be obtained by averaging over all possible values of ξ_m for $m \neq l$ [86].

6.2. Spin fluctuation energies in clusters

In clusters and other non-periodic systems, it is very interesting to analyze the spin fluctuation energies $\Delta F(\vec{\xi})$ from a local point of view and to clarify the relation between the local contributions to $\Delta F(\vec{\xi})$ and the temperature dependence of the spin moments μ_l. A first insight on the magnetic behavior of 3d transition-metal clusters at $T > 0$ can be obtained by considering the low-temperature limit of $\Delta F(\vec{\xi})$ by setting $\xi_m = \xi_m^0$ for $m \neq l$ (see Eq. (21)). The local free-energy difference

$$\Delta F_l(\xi) = F(\xi_l = \xi, \xi_m = \xi_m^0) - F(\vec{\xi} = \vec{\xi}^{\,0}) \tag{27}$$

with $\xi_l^0 = \mu_l^0$ being the local moment of atom l at $T = 0$, represents the energy involved in an exchange-field fluctuation at atom l above the Hartree–Fock ground state. $\Delta F_l(\xi)$ determines the probability of the fluctuation $\Delta\xi = \xi - \xi_l^0$ and thus conditions the stability of the ground-state magnetic order within the cluster at finite T. Comparing the $\Delta F_l(\xi)$ for different sizes and for different atoms l within the cluster provides useful information on the stability of the local magnetizations and its environment dependence. In particular, this allows us to identify the atoms which trigger the decrease of the magnetization at low T.

Recent studies in Fe and Ni clusters show that $\Delta F_l(\xi) > 0$ for all $\xi \neq \mu_l^0$ which implies, as expected, that in these clusters the FM order is stable at low temperatures. For very small Fe clusters (e.g., Fe_2 and Fe_4), $F_l(\xi)$ shows two minima located at the exchange fields $\xi^+ = \mu_l^0$ and $\xi^- \simeq -\mu_l^0$. This indicates that the dominant magnetic excitations are flips of the magnetic moments keeping their amplitude approximately constant. At finite T, the probability distribution $P_l(\xi) \propto \exp\{-\beta\Delta F_l(\xi)\}$ has two maxima at ξ^+ and ξ^-. It is therefore more probable to find $\xi \simeq -\mu_l^0$ than $\xi \simeq 0$. For somewhat larger clusters (e.g., Fe_6 and Fe_9), $F_l(\xi)$ shows two minima for the lowest coordinated atoms, where the local magnetic moments μ_l^0 are largest. In these cases, only moderate or small fluctuations $\Delta\xi = \xi - \mu_l^0$ are possible with an excitation energy $\Delta F_l(\xi)$ smaller than the energy $\Delta F_l(\xi^-) = F_l(\xi^-) - F_l(\xi^+)$ required to flip the local

moment. In contrast, for the most coordinated atoms which have smaller μ_l^0 (e.g., the central atom in BCC-like Fe_9), one usually observes a single minimum in $F_l(\xi)$, which implies that the fluctuations of the amplitude of the local moments dominate.

The fact that the atoms having the smallest local coordination numbers z_l show such a Heisenberg- or Ising-like behavior is not surprising. On the one side, the kinetic-energy loss ΔE_K caused by flipping a local magnetic moment ($\xi \simeq \mu_l^0 \rightarrow \xi \simeq -\mu_l^0$) decreases with decreasing z_l, since the perturbation introduced by flipping ξ_l is in general less important when l has a small number of neighbors, and since the contribution of atom l to E_K is approximately proportional to $\sqrt{z_l}$ (second moment approximation). On the other side, the exchange energy $\Delta E_X = (J/4)\sum_l \mu_l^2$ is basically a local property which is much less affected by the change of sign of ξ. Thus, when z_l is reduced, the local character is enhanced and it becomes energetically more favorable to have $\xi \simeq -\mu_l^0$ than $\xi \simeq 0$. At this point one may anticipate that at finite T, when statistically some of the fields ξ_m at NNs of l have negative values, $F_l(\xi)$ should tend to develop a second minimum close to $\xi^- \simeq -\mu_l^0$. Such a behavior has already been observed in bulk and thin-film calculations [92, 93, 96].

$\Delta F_l(\xi)$ depends strongly on the local environment of the different atoms within the cluster, as illustrated by the results for Fe_{15} shown in Fig. 9. One observes that the FM order is particularly stable at the outermost shell $l = 3$. The larger spin-flip energy

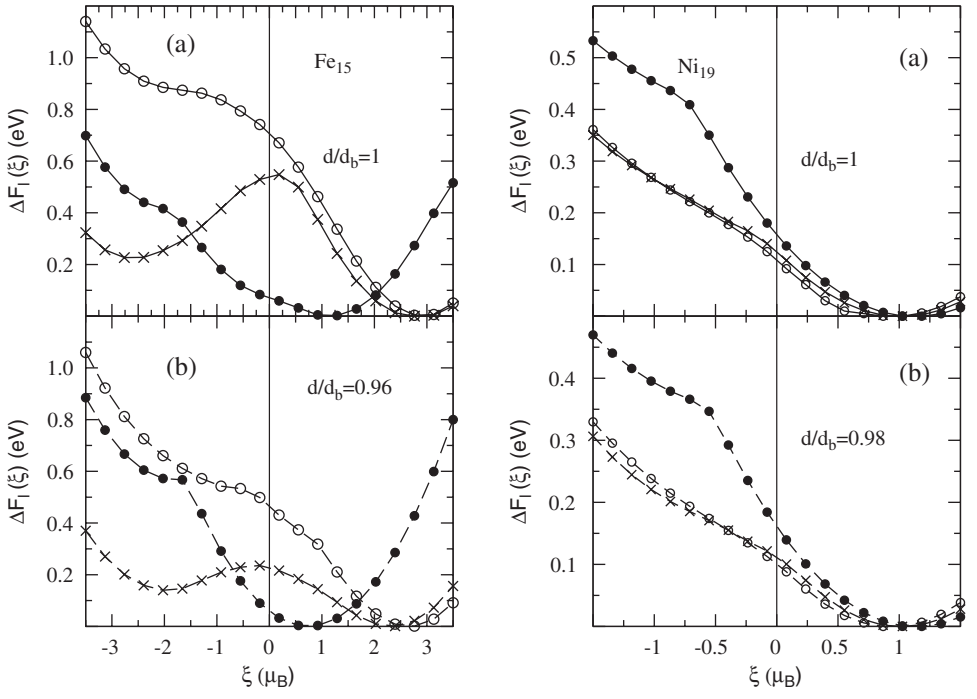

Figure 9: Local spin-fluctuation energy $\Delta F_l(\xi) = F_l(\xi) - F_l(\xi_l^0)$ as a function of the exchange field ξ at different atoms l of Fe_{15} with BCC-like structure (left) and of Ni_{19} with FCC-like structure (right). Dots refer to the central atom ($l = 1$), crosses to the first NN shell ($l = 2$), and open circles to the outermost shell ($l = 3$). Results are given for (a) bulk NN distance $d/d_b = 1$ and (b) relaxed NN distance.

$\Delta F_3(-\xi_3^0)$ is favored by the larger local moment μ_3^0 found at these atoms, which in this case compensates the reduction of local coordination number z_l at the cluster surface (for $l = 3$ there are four first NNs and one second NN). However, notice that this trend is not always followed. For example, the atoms at the second shell (crosses in Fig. 9) show a much smaller $\Delta F_l(-\xi_l^0)$, despite having similar μ_l^0 and similar z_l as the atoms in the outermost shell (for $l = 2$ there are four first NNs and three second NNs).

The quantitative values of the spin fluctuation energies are strongly affected by changes in the interatomic distances. For example, bond-length contractions – a typical result of geometry optimization – shift the positions of the minima at ξ_l^0 to smaller absolute values, in accordance with the reduction of the local magnetic moments at $T = 0$. Moreover, one finds significant reductions of the free energy $\Delta F_l(-\xi_l^0) = F_l(-\xi_l^0) - F_l(\xi_l^0)$ required to flip a local magnetic moment (cf. Fig. 9a and b). Similar reductions of the "Curie" temperature $T_C(N)$ are expected to occur upon bond-length contraction, since in first approximation $T_C(N)$ should be proportional to $\langle \Delta F_l(-\xi_l^0) \rangle_l$. Conversely, if the NN distances are expanded one first obtains an enhancement of the local moments μ_l^0 as well as an increase of the local spin-fluctuation energies. At the same time, a more pronounced double-minimum is found in $\Delta F_l(\xi)$, particularly at the cluster surface, which is characteristic of the localized regime. In addition, at large distances, the atomic moments tend to decouple and the spin fluctuations energies decrease.

In contrast to Fe clusters, the dominant spin excitations in Ni_N involve mainly amplitude fluctuations of the local exchange fields around the Hartree–Fock moments. This is characterized by a single-minimum in $\Delta F_l(\xi)$ as shown in Fig. 9 for Ni_{19}. The same type of behavior is also observed in the case of bulk Ni. This is probably due to the fact that the magnetic moments at $T = 0$ are much smaller in Ni than in Fe. Let us recall that $\Delta F_l(\xi)$ also shows a single minimum in Fe_N when the local moments at $T = 0$ are small (e.g., at the central atom in Fe_{15}). Only in Ni_2 one observes that negative values of $\xi \simeq -\mu_l^0$ are, if not more probable, at least as probable as $\xi = 0$. The dimer behavior can be interpreted as an enhancement of the local character of the spin fluctuation in very small Ni clusters due to the strong reduction of the local coordination number and of the kinetic energy of the d electrons.

As in the case of Fe, $\Delta F_l(\xi)$ in Ni clusters depends strongly on the size N and on the atomic position l, which let us expect interesting changes in the temperature-dependent properties. Moreover, one observes that bond-length contractions ($d < d_b$) usually result in a reduction of $\Delta F_l(\xi)$ even if μ_l^0 remains essentially unchanged. Comparing surface and inner atoms, it is interesting to point out that the spin-fluctuation energies are in general smaller at the cluster surface, i.e., as the local coordination number is smaller (see Fig. 9). Thus, one expects that in Ni clusters the surface atoms should drive the decrease of the average magnetization per atom as T increases.

The previous results illustrate the strong sensitivity of the finite temperature magnetic properties of 3d TM clusters to the local environment of the atoms. $\Delta F_l(\xi)$ is actually much more sensitive to size and structure than the magnetic moments at $T = 0$. The effect is most clear in small clusters where the local magnetic moments are nearly saturated, and therefore depend weakly on the site l or on precise cluster geometry. This suggests that temperature-induced structural changes could also play a role on the magnetic behavior at finite T. In fact, as will be discussed in Section 7.3, exact diagonalization studies within the single-band Hubbard model have revealed the

importance of structural changes and structural fluctuations to the temperature dependence of the magnetic properties of clusters [88–90]. Comparing results for different l, one finds that the spin-flip energy $\Delta F_l(-\xi_l^0)$ does not scale simply with the local coordination number z_l. Therefore, the effective exchange couplings between local magnetic moments cannot be transferred straightforwardly from one environment to another. Electronic structure effects due to the itinerant character of the d electrons are therefore important, as already found at the surfaces of macroscopic TMs [91].

6.3. Short-range magnetic order in transition-metal clusters

The single-site spin-fluctuations considered in the previous section ignore short-range magnetic correlations among the local magnetic moments. In the framework of the functional-integral formalism, short-range magnetic order (SRMO) manifests itself as correlations between the exchange fields at neighboring sites. For example, in the FM case, $\langle \xi_l \xi_m \rangle > \langle \xi_l \rangle \langle \xi_m \rangle$ for NN atoms i and j. One is interested in the size dependence of the temperature $T_{\mathrm{SR}}(N)$ above which thermal fluctuations destroy the short-range correlations between the local magnetic moments, for example, between NN μ_l. A significant degree of SRMO is observed in the bulk and near the surfaces of Fe, Co, and Ni [91, 97, 98]. This holds even for $T > T_C$, i.e., after the average magnetization $M(T)$ vanishes ($T_{\mathrm{SR}}(b) > T_C(b)$). For small clusters having a radius R smaller than the range of SRMO, it is no longer possible to increase the entropy without destroying the energetically favorable local magnetic correlations.

The degree of SRMO actually depends on the details of the electronic structure and on cluster size. Nevertheless, a simple phenomenological relation can be derived between the low- and high-temperature values of the magnetization per atom of an N-atom cluster, namely, $\bar{\mu}_N(T=0)$ and $\bar{\mu}_N(T > T_C)$ [99]. Let us characterize the degree of SRMO by the number of atoms v involved in an SRMO domain. The average magnetization per atom at $T > T_{\mathrm{C}}(N)$ is then approximately given by

$$\bar{\mu}_N(T > T_{\mathrm{C}}) \simeq \bar{\mu}_N^0 \sqrt{\frac{v}{N}} \tag{28}$$

which represents the average $\sqrt{\langle \mu^2 \rangle}$ of N/v randomly oriented SRMO domains, each carrying a magnetic moment $v\mu_N^0$ where $\mu_N^0 = \bar{\mu}_N(T=0)$. By varying v we may go from the disordered-local-moment regime, where $v = 1$ and SRMO is negligible, to the limit where v and N are comparable and SRMO dominates ($T_C \to T_{\mathrm{SR}}$). A first estimate of the actual value of v is provided by bulk and surface results [91, 97, 98]. For bulk Fe, Haines et al. [97] have retrieved a range of SRMO near T_C up to the next nearest neighbors which corresponds to $v \simeq 15$. Similar values are obtained in calculations of SRMO in Fe bulk and Fe surfaces [91]. For Ni, the SRMO is generally expected to be stronger than for Fe [98].

As shown in Table 5, the comparison between experiment and the results derived from Eq. (28) neglecting SRMO (i.e., with $v = 1$) is very poor. This rules out the disorder-local-moment picture for Fe and Ni clusters, as it is already known to be the case for the bulk and near surfaces [91, 97, 98]. On the contrary, the results including SRMO are in very good agreement with experiment for both Fe_N, with $v = 15$, and Ni_N, with $v = 19$–43. This provides a clear evidence for the existence of SRMO in these clusters above $T_C(N)$ and is also consistent with known surface and bulk properties of

Table 5: Average magnetization per atom $\bar{\mu}_N$ (in μ_B) of Fe_N and Ni_N clusters at high temperatures ($T > T_C(N)$) as obtained from Eq. (28) where v refers to the size of the SRMO domains.

	N	$\bar{\mu}_N(v=1)$	$\bar{\mu}_N(v=v_{SR})$	$\bar{\mu}_N$(expt)
Fe_N	50–60	0.47–0.38	1.61–1.48	1.6 ± 0.2
	82–92	0.33–0.31	1.26–1.20	1.2 ± 0.2
	120–140	0.27–0.25	1.05–0.97	0.9 ± 0.1
	250–290	0.16–0.15	0.63–0.59	0.4 ± 0.05
	500–600	0.10–0.09	0.38–0.36	0.4 ± 0.05
Ni_N	140–160	0.06–0.05	0.39–0.24	0.36 ± 0.16
	200–240	0.05–0.04	0.33–0.20	0.24 ± 0.16
	550–600	0.03–0.02	0.17–0.11	0.11 ± 0.08

For Fe $v_{SR} = 15$ and for Ni $v_{SR} = 19$–43. The experimental results are estimated from Ref. [44].

itinerant magnetism. Eq. (28) can also be used to infer the degree of SRMO in clusters from the experimental results for $\bar{\mu}_N(T=0)$ and $\bar{\mu}_N(T > T_C)$ [44]. For example, assuming that v is independent of N, one obtains $v = 13$–15 for Fe_N ($25 \leqslant N \leqslant 700$). A more detailed analysis of Eq. (28) shows that these values of v are not overestimated [99]. In fact, the degree of SRMO in the clusters could be somewhat larger than in the corresponding solids, possibly as a consequence of the enhancement of the local magnetic moments and exchange splittings. One concludes that SRMO plays a significant role in the finite-temperature behavior of magnetic TM clusters and that it should be taken into account in the interpretation of experiments as well as in theoretical developments.

6.4. Environment dependence of the magnetization curves

The purpose of this section is to discuss the interplay between local environment and the stability of ferromagnetism at finite temperatures by reviewing recent calculations on the local magnetization curves $M_l(T)$ in small Fe clusters and ultrathin films. In Fig. 10, results are given for the layer-resolved magnetization curves $M_l(T)$ of a five-layer BCC (0 0 1) Fe film as obtained by using the single-site VCA [96]. For the sake of comparison, the corresponding bulk magnetization curve is also shown. At low temperatures, the surface layers ($l = 1$) show a rapid linear decrease of $M_1(T)$, which is quite different from the behavior at inner layers. This indicates that the spin-fluctuation energies are lower at the surface despite the larger ground-state moments. A similar linear decrease of $M(T)$ has been found in experiments and previous calculations [100–103]. At the inner layers ($l = 2$ and 3) the ground-state magnetization $M_l(0)$ and the temperature dependence of $M_l(T)$ are similar to the bulk. In fact, for $l = 2$ and 3, $M_l(T)$ scales with the ground moment $M_l(0)$. This is not the case for $l = 1$ since in this case the reduction of the spin-fluctuation energies dominates in front of the enhancement of the local moments. A similar behavior is found for a free-standing Fe having a reduced interatomic distance $d/d_{bulk} = 0.87$ [96].

The Curie temperature of the five-layer film is only 5% lower than the bulk one. This appears to be the result of compensations between the contributions of surface and inner layers, where the latter dominate the magnetic behavior of the film as a whole. On the one side, the surface layers show a very rapid decrease of $M_1(T)$ that seems to point to a significantly smaller T_C than in the bulk. And on the other side, the ferromagnetic order is more stable at the inner layers which have a complete NN shell

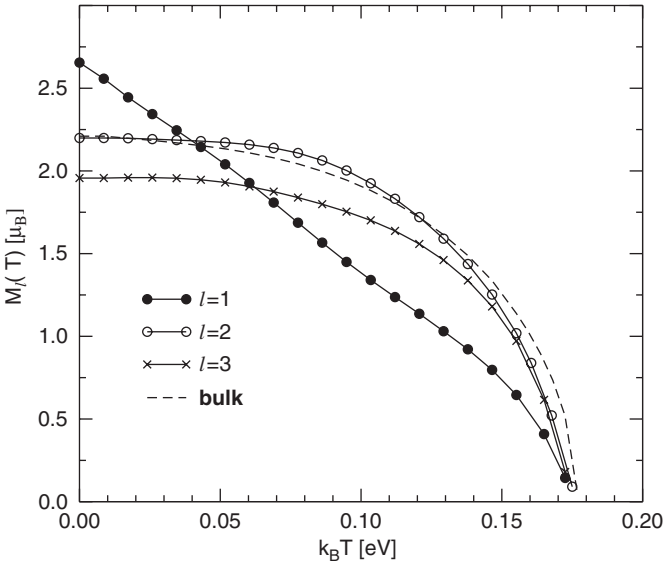

Figure 10: Layer magnetization $M_l(T)$ of a five-layer BCC (0 0 1) Fe film calculated in the VCA. $l = 1$ (dots) refers to the surface layers, $l = 2$ (open circles) to the layers below the surface, and $l = 3$ (crosses) to the central layer. The dashed curve is the corresponding bulk result.

($l = 2$ and 3). Finally, close to T_C, the coupling between inner and surface layers tends to stabilize the magnetization.

The finite-temperature magnetic properties of nanostructures have also been investigated by varying systematically the NN distance d in ultrathin Fe films around the bulk value d_b and for some relevant substrates. In this way, the interplay between kinetic and Coulomb energies can be explored, since shorter NN distances yield larger d-band widths which correspond to larger coordination numbers. A remarkable non-monotonous dependence of the magnetization curves on d/d_b has been observed which can be interpreted in terms of the changes in the local magnetic moments and in the spin-fluctuation energies $\Delta F_l(\xi)$ [96]. In this context, it is particularly interesting to compare the role of the local environment on the ground state and finite temperature properties and to establish correlations between them. Figure 11 summarizes results for the magnetization $M_l(0)$ at $T = 0$ and for the Curie temperature T_C of Fe monolayers as a function of d/d_b, as obtained by using the VCA and CPA. One observes that the ground-state moment grows rapidly with increasing d as the density of states at the Fermi energy increases, in agreement with Stoner's theory. At some point, $M_l(0)$ reaches the saturation value $M_{\text{sat}} = 10 - n_d$ beyond which $M_l(0)$ is independent of d. The Curie temperature, which measures the stability of ferromagnetism at finite T, shows a much more interesting non-monotonous behavior that can be qualitatively interpreted in terms of a mean-field Heisenberg model for the atomic spins. In this framework $k_B T_C \simeq z J_H M_l(0)^2/3$, where z is the coordination number, J_H is the effective Heisenberg coupling between NN spins, and $M_l(0)$ is the $T = 0$ moment. Three different regimes can be distinguished. First, for $0.87 \leqslant d/d_b \leqslant 0.91$ T_C increases due to the increase of the local moments and the associated enhancement of the exchange splitting $\Delta\varepsilon_x^d$ (see Fig. 11a and b). In this range, $M_l(0)$ and $\Delta\varepsilon_x^d$ increase

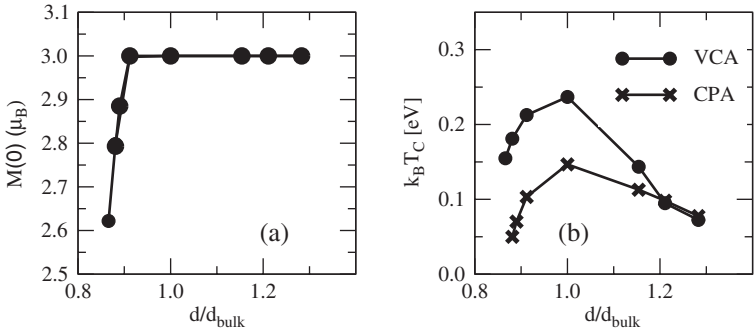

Figure 11: (a) Ground-state magnetization $M(0)$ and (b) Curie temperature T_C of a BCC (0 0 1) Fe monolayer as a function of the nearest neighbor distance d. Dots (crosses) refer to VCA (CPA) results.

significantly which dominates over the effects of the reduction of the NN hoppings on the magnetic order. In fact, the effective Heisenberg coupling $J_H \simeq 3k_B T_C/[zM_l(0)^2]$ increases with d, for example in the CPA, from $J_H \simeq 4.5$ meV$/\mu_B^2$ for $d/d_{\text{bulk}} = 0.88$ to $J_H \simeq 8.3$ meV$/\mu_B^2$ for $d/d_{\text{bulk}} = 0.91$. The subtle effects of itinerant magnetism become even more evident for $0.9 < d/d_{\text{bulk}} \leqslant 1$ where $M_l(0)$ is constant and still T_C increases. Notice that in this range, the mean-field exchange splitting at $T = 0$ is also constant so that the enhancement of T_C must be ascribed to changes in the electronic structure in the presence of spin fluctuations (random alloy). Finally, for $d/d_{\text{bulk}} > 1$, the behavior changes and the effective J_H decreases with increasing d. In this case, the electronic hoppings and the kinetic energy of the electrons are small and the spin fluctuations have a more localized character. Consequently, as d increases the spin-fluctuation energies decrease, since the perturbations introduced by disorder are less significant. In summary, the distance dependence of the finite-temperature properties are the result of a subtle competition between localized and itinerant aspects of magnetism. Interesting phenomena can also be expected as a function of other variables like cluster size and local coordination number, which also affect the relative importance of kinetic and Coulomb contributions.

In the case of a finite system as a cluster, the average quantities which give useful information about the magnetic order are the root mean square of the magnetization $\overline{M}_z(T) = 2\langle(\Sigma_i S_{iz})^2\rangle^{1/2}$ and the pair correlation functions $C_{ij}(T) = 4\langle S_{iz} S_{jz}\rangle$ between the local magnetic moments at atoms i and j. These are determined by integration over all the exchange fields at each atom i by using Monte Carlo methods [104]. The convergence of the thermal average can be significantly improved by performing in parallel several simulations for different temperatures (parallel tempering) [95].

In Fig. 12, representative results are given for $\overline{M}_z(T)$ and $C_{ij}(T)$ of Fe_6 having a bipyramid structure (see inset). One observes that at low temperatures the average magnetic moment per atom $\bar{\mu}_N(T) = \overline{M}_z(T)/N$ is saturated ($\bar{\mu}_N(T \to 0) \simeq 3.0\mu_B$), while at high temperatures $\bar{\mu}_N(T \to \infty)$ approaches the value expected for a magnetically disordered state [105]. Starting from low temperatures, $\bar{\mu}_N$ decreases since the local magnetic moments in the cluster fluctuate. The stability of ferromagnetic order within the cluster can be characterized by the temperature $T_C(N)$ corresponding to the inflexion point in $\bar{\mu}_N(T)$. This can be regarded as the precursor of the critical point associated to the Curie temperature in bulk ferromagnets. From Fig. 12, the

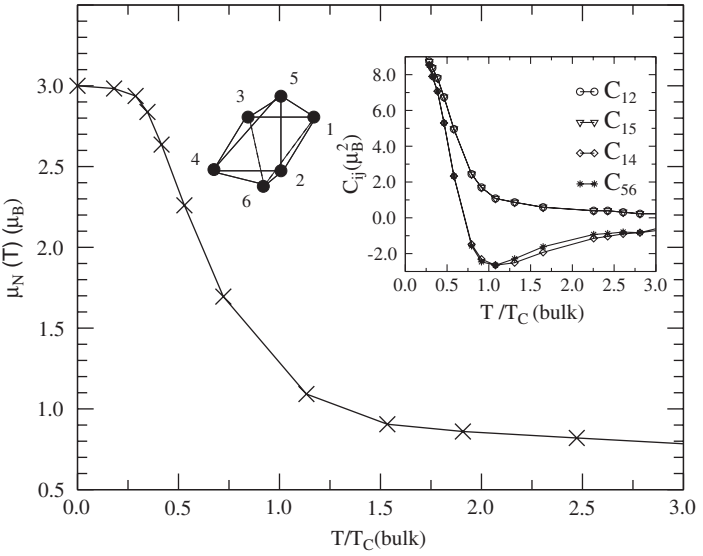

Figure 12: Temperature dependence of the magnetization $\mu_N(T)$ for Fe_6. The geometry of the cluster and the pair correlation functions C_{ij} are shown in the inset.

temperature at which the inflexion point occurs is $T_C(6)/T_C(\text{bulk}) \simeq 0.72$, which is significantly smaller than the bulk Curie temperature calculated with the same model.

In order to gain further insight on the temperature dependence of $\bar{\mu}_N$ and its interplay with the local environment, we report in the inset of Fig. 12 the pair-correlation functions C_{ij} between the local moments. The indices i and j corresponding to the atomic sites are indicated in the illustration of the cluster structure (see inset). Notice the rapid decrease of C_{ij} with temperature and the different qualitative behaviors of C_{12} and C_{15} on the one side, and of C_{14} and C_{56} on the other side. In the latter case, there is a range of temperatures for which the magnetic couplings between the pair sites 14 and 56 is antiferromagnetic like, i.e., $C_{ij} < 0$ for $T/T_C(\text{bulk}) \geqslant 0.7$. This explains qualitatively the fast decrease of $\mu_N(T)$ with increasing T.

The previous discussion illustrates the remarkable non-monotonous dependence of the magnetization curves as a function of the positions of the atoms within the nanostructure or as a function of interatomic distances. These trends can be correlated, at least qualitatively, with the environment dependence of the electronic structure of itinerant d electrons and with the resulting changes in the ground-state magnetic moments and spin-fluctuation energies. Nevertheless, several important aspects of the problem still remain to be addressed. For example, non-collinear magnetic order and fluctuations of vector exchange fields are likely to affect the magnetization curves and probably reduce the calculated values of T_C. The effects of interfaces with non-magnetic substrates are expected to be important, particularly in the case of small clusters deposited on surfaces. They should be incorporated in order to achieve a more realistic comparison with experiment. It would also be very interesting to extend the model Hamiltonian in order to include spin–orbit interactions that are responsible for magnetic anisotropy and for spin reorientation transitions as a function of temperature and structure [75, 106–108]. Finally, it remains a major challenge to improve on

the treatment of electronic correlations which are expected to become increasingly important as the system dimensions decrease. This problem is addressed in the following section.

7. ELECTRON CORRELATION EFFECTS IN MAGNETIC CLUSTERS

The mean-field results discussed in previous sections, either at $T = 0$ or in the framework of the static approximation at finite temperatures, have revealed a variety of very interesting magnetic behaviors of clusters and nanostructures in good agreement with experimental observations. Nevertheless, in order to achieve a profound understanding of nanostructure magnetism, it is necessary to go beyond mean-field approximations and to improve on the treatment of electron correlations. The many-body phenomena underlying the magnetic properties of nanostructures are not only important from a fundamental point of view, but they are likely to be crucial in investigations of more delicate properties such as photoemission spectra, time-dependent properties, or finite temperature effects, particularly in connection with magnetic anisotropy. Consequently, it is worthwhile to extend the studies of cluster magnetism by including charge and spin fluctuations explicitly.

The simultaneous determination of electron correlation effects, magnetism, and cluster geometry is a very difficult task. Therefore, most theoretical studies performed so far have dealed with only part of these aspects of the problem at a time. An explicit ab initio treatment of electron correlations has been severely hampered by the localized character of the atomic-like $3d$ orbitals, and by the complicated dependence of the magnetic moments and magnetic order on cluster geometry. The mean-field approximation discussed in Section 2.1 could be in principle improved systematically, for example, by treating the residual interactions by perturbation methods or by using Gutzwiller or Jastrow variational *Ansätze* [109, 110]. However, a general implementation of such calculations for TM clusters would be very demanding, particularly if the structure is arbitrary, i.e., lacking of any symmetry. In Sections 7.1–7.4, we review theoretical results on the structural, electronic, and magnetic properties of clusters, which were obtained by considering simple many-body model Hamiltonians and exact diagonalization methods. Thus, a rigorous solution of the many-body problem is achieved which contains enough complexity to be able to shed light on the physics of real systems.

7.1. Hubbard clusters

The magnetic behavior of itinerant electrons is known to be very sensitive to the details of the electronic structure, the cluster structure, and the local environment of the atoms. It is therefore of considerable interest to investigate the interplay between electron correlations, magnetism and cluster structure, and the resulting stability of cluster ferromagnetism with respect to structural changes and electronic excitations. In order to study this problem, one may simplify the model given by Eqs. (1)–(3) by dropping the d-band degeneracy. One obtains then the single-band Hubbard Hamiltonian [111]

$$H = -t \sum_{\langle i,j \rangle,\sigma} \hat{c}^{\dagger}_{i\sigma} \hat{c}_{j\sigma} + U \sum_{i} \hat{n}_{i\uparrow} \hat{n}_{i\downarrow} \tag{29}$$

where $\hat{c}^{\dagger}_{i\sigma}(\hat{c}_{i\sigma})$ refers to the creation (annihilation) operator for an electron at site i with spin σ, and $\hat{n}_{i\sigma} = \hat{c}^{\dagger}_{i\sigma}\hat{c}_{i\sigma}$ to the corresponding number operator. The first term is the kinetic-energy operator, which describes electronic hoppings between NN sites i and j leading to electron delocalization and bond formation ($t>0$). The second term takes into account the intra-atomic Coulomb repulsion, which is the dominant contribution from the electron–electron interaction ($U>0$) [1 1 1]. At low energies, the electronic properties result from a delicate balance between the tendency to delocalize the valence electrons in order to reduce their kinetic energy, and the effect of the Coulomb repulsions associated to local charge fluctuations. The relative importance of these contributions depends strongly on the electron density or number of electrons v, on the total spin S and on the ratio U/t.

The Hubbard model for small clusters can be solved numerically by expanding its eigenfunctions $|\Psi_l\rangle = \Sigma_m \alpha_{lm}|\Phi_m\rangle$ in a complete set of basis states $|\Phi_m\rangle = [\Pi_{i\sigma}(\hat{c}^{\dagger}_{i\sigma})^{n^m_{i\sigma}}]|vac\rangle$ which have definite occupation numbers $n^m_{i\sigma}$ at all orbitals $i\sigma$ ($\hat{n}_{i\sigma}|\Phi_m\rangle = n^m_{i\sigma}|\Phi_m\rangle$ with $n^m_{i\sigma} = 0$ or 1). The values of $n^m_{i\sigma}$ satisfy the conservation of the number of electrons $v = v_{\uparrow} + v_{\downarrow}$ and of the z component of the total spin $S_z = (v_{\uparrow} - v_{\downarrow})/2$, where $v_{\sigma} = \Sigma_i n^m_{i\sigma}$. Taking into account all possible electronic configurations may imply a considerable numerical effort which in practice sets a drastic limit to the size of the clusters under study. For example, at half-band filling and minimal S_z, the dimension of the Hilbert space $D = \binom{N}{v_{\uparrow}}\binom{N}{v_{\downarrow}}$ is $D = 853776$, 2944656, and 11778624, for $N = 12$, 13, and 14, respectively. For not too large clusters, the expansion coefficients α_{lm} corresponding to the ground state ($l = 0$) and low-lying excited states are determined by sparse-matrix diagonalization procedures such as the Lanczos iterative method [112]. Several ground-state properties can be calculated in terms of the coefficients α_{lm} of the eigenstate $|\Psi_l\rangle$ by simple operations on the basis states $|\Phi_m\rangle$, for example, the spin-density distribution

$$\langle \hat{n}_{i\sigma}\rangle_l = \sum_m |\alpha_{lm}|^2 \, n^m_{i\sigma} \tag{30}$$

the density correlation functions

$$\langle \hat{n}_{i\sigma}\hat{n}_{j\sigma'}\rangle_l = \sum_m |\alpha_{lm}|^2 \, n^m_{i\sigma} n^m_{j\sigma'} \tag{31}$$

and the spin correlation functions

$$\langle \hat{S}^z_i \hat{S}^z_j\rangle_l = \frac{1}{4}\sum_m |\alpha_{lm}|^2 \, (n^m_{i\uparrow} - n^m_{i\downarrow})(n^m_{j\uparrow} - n^m_{j\downarrow}) \tag{32}$$

In this way, the underlying electron correlation problem is solved exactly within a full many-body scheme.

In order to perform the ground-state geometry optimization, or the sampling of different structures at finite T, it should be noted that in the Hubbard model only the topological aspect of the structure is relevant for the electronic properties. Defining the cluster structure is equivalent to defining for each atom i those atoms j which are connected to i by a hopping element t. This implies that the set of all possible non-equivalent cluster structures is a subset of the set of *graphs* with N vertices [113]. For example, for $N = 3$ there are two different graphs (triangle and linear chain) and for

$N = 4$ these are six (tetrahedron, rhombus, square, star, etc.). Taking into account only NN hoppings with fixed bond-length results in a discretization of the configurational space. Geometry optimizations and samplings at finite T can be performed within the graph space. In order to generate all possible graphs one considers the adjacency matrix A, which contains all the information to define a graph ($A_{ij} = 1$ if i and j are NNs and $A_{ij} = 0$ otherwise). An efficient storage and handling of A on a computer is achieved by writing it as an integer number [89]. For the study of clusters, we must consider only those graphs which can be represented as a true *structure* in space. Therefore, a *graph* is acceptable as a cluster *structure* if a set of atomic coordinates $\vec{R}_i$ exists ($i = 1,\ldots,N$), such that the interatomic distances R_{ij} satisfy the conditions $R_{ij} = R_0$ if the sites i and j are connected in the graph (i.e., if $A_{ij} = 1$), and $R_{ij} > R_0$ otherwise (i.e., if $A_{ij} = 0$). Notice that the number of graphs n_g, i.e., the number of site configurations to be considered, increases extremely rapidly with the number of atoms N.

7.2. Ground-state structure and total spin

The most stable structure and the corresponding ground-state spin S have been determined systematically as a function of U/t and v [89]. The main conclusions and trends derived from these calculations for $N \leqslant 8$ are summarized below.

For low electron or hole concentration (i.e., $v/N \leqslant 0.4$–0.6 and $2 - v/N \leqslant 0.3$–0.6), the optimal cluster structure is independent of U/t, i.e., the structure which yields the minimal kinetic energy (uncorrelated limit) remains the most stable one, irrespectively of the strength of the Coulomb interactions. Moreover, no magnetic transitions are observed: the ground state is always a singlet or a doublet. For low carrier concentration, the Coulomb interactions are very efficiently suppressed by the correlations, so that the magnetic and geometric structure of the clusters are dominated by the kinetic energy term.

For small v, the structures are compact having maximal average coordination number $\bar{z}(t_{ij} = -t < 0)$. These are all substructures of the icosahedron which maximize the number of *triangular* loops. In contrast, for large v (small $v_h = 2N - v$) open structures are found. In particular for $v_h = 2$ we obtain bipartite structures, which have the largest possible number of *square* loops. This can be qualitatively understood in terms of the single-particle spectrum. In the first case (small v) the largest stability is obtained for the largest band-width for bonding (negative-energy) states ($\varepsilon_b \leqslant -\bar{z}t$), while in the second case (small v_h) it is obtained for the largest band-width for antibonding (positive-energy) states, i.e., for the most compact bipartite structure.

A much more interesting interplay between electronic correlations, magnetism, and cluster structure is observed around half-band filling (i.e., $|v/N - 1| \leqslant 0.2 - 0.4$) where several structural transitions are found as a function of U/t. Starting from the uncorrelated structures ($U = 0$) one observes that as U is increased, first one or more of the weakest cluster bonds are broken. These structural changes occur for $U/t \simeq 1 - 4$ and are most often seen for $v < N$, since in this case the $U = 0$ structures are more compact. As U is further increased ($U/t > 5$–6), it becomes energetically more advantageous to create new bonds. Higher coordination gives the strongly correlated electrons more possibilities for performing a mutually avoiding motion that lowers the kinetic energy.

The structural changes at larger U are often accompanied by strong changes in the magnetic behavior. They are actually driven by magnetism [114]. For half-band filling

($v = N$), the optimal structures show minimal total spin S and strong antiferromagnetic correlations. None of the structures having a (unsaturated) ferromagnetic ground state [115] were found to be the most stable ones for any value of U/t. The optimal antiferromagnetic structures are *non-bipartite*. For instance, the rhombus is more stable than the square for $N = v = 4$. The bonds that would be frustrated in a static picture of antiferromagnetism yield an appreciable energy lowering when quantum fluctuations are taken into account. Therefore, Hubbard clusters with one electron per site and large U/t can be best seen as frustrated quantum antiferromagnets.

For all studied cluster sizes ($N \leqslant 8$), the most stable structures show ferromagnetism for $v = N+1$ and large U (typically $U/t > 4$–14). This is in agreement with Nagaoka's theorem [116]. For the smaller clusters, i.e., $N = 3$, 4, and 6, this is the only case where the optimal structures are ferromagnetic. However, for larger clusters, ferromagnetism extends more and more throughout the (U/t)–(v/N) phase diagram. Clusters with $N = 7$ ($N = 8$) are ferromagnetic for $v = 4$, 6, 8, and 10 ($v = 9$–12). The tendency toward ferromagnetism is much stronger above half-band filling than below. This is qualitatively in agreement with experiments on 3*d*-TM clusters. In fact, the magnetic moments per atom μ in V and Cr clusters are very small if not zero ($\mu < 0.6$–$0.8\mu_B$) [117], while Fe and Co clusters show large magnetizations [44, 45, 118].

It is important to remark that the appearance of ferromagnetism is much less frequent than what one would expect from mean-field Hartree–Fock arguments (i.e., Stoner criterion). This reflects the importance of correlations in low-dimensional systems [114, 119]. It should be however noted that the Hubbard model for clusters probably exaggerates the effects of quantum fluctuations, since it is one of the most extremely low-dimensional systems one can consider. Improvements on the model, either by including several bands or non-local interactions, should tend to weaken such strong fluctuation effects.

Hubbard clusters are in accordance with nature in a further interesting aspect. While the number of possible site configurations or graphs n_g increases exponentially with the number of atoms N, the number of structures n_o which are optimal for some value of the parameters U/t and v/N remains a handful. For example, for $N = 7$ (8), $n_g = 853$ (11117) while $n_o = 18$ (23). As the cluster size increases, some growth patterns start to dominate and the same or very similar structures cover larger and larger regions of the phase diagrams. The situation tends to what one observes in the macroscopic limit (solid state) where – regardless of the infinite number of topologically different atomic arrangements – the equilibrium lattice structures of the elements are only a few (FCC, HCP, BCC, etc.).

7.3. Spin excitations and structural fluctuations at finite temperatures

The finite-temperature properties are derived from the canonical partition function

$$Z = \sum_g \sum_l \mathrm{e}^{-\beta\varepsilon_l(g)} \tag{33}$$

over electronic and structural degrees of freedom. In particular, the average total spin $\langle S \rangle$ is obtained from

$$\langle \hat{S}^2 \rangle = \frac{3}{Z} \sum_g \sum_l \langle \hat{S}_z^2 \rangle \, \mathrm{e}^{-\beta\varepsilon_l(g)} \tag{34}$$

In Eqs. (33) and (34), $\varepsilon_l(g)$ stands for the energy of the lth eigenstate corresponding to a cluster structure or geometry g. $\beta = 1/k_B T$, where T is the temperature of the cluster source that defines the macroscopic thermal bath with which the small clusters are in equilibrium before expansion. Thermal average refers then to the ensemble of clusters in the beam. Keeping v and N fixed (canonical ensemble) corresponds to the experimental situation in charge and size-selected beams [44]. In order to sample all relevant cluster geometries we recall that in the Hubbard model only the topological aspect of the structure is relevant to the electronic properties. Taking into account, only NN hoppings with fixed bond-lengths results in a discretization of the configurational space so that the sampling of cluster geometries can be performed within graph space (see Section 7.1).

Figure 13 shows a representative example of the temperature dependence of the average total magnetic moment $\langle S\rangle$ in small Hubbard clusters ($\langle S\rangle(\langle S\rangle + 1) = \langle \hat{S}^2\rangle$). For large U/t (saturated FM ground state), $\langle S\rangle$ decreases monotonically with increasing T tending to a remnant value $\langle S\rangle_\infty > 0$ at high temperatures ($T/t \geqslant 1$) that corresponds to an equally probable occupation of all electronic states within the first Hubbard band ($k_B T \ll U$). In the present case, $\langle S\rangle_\infty = 1.5$. The classical analogue of $\langle S\rangle_\infty$ is the average of N random spins which does not vanish in a finite system ($\langle \mu_\infty\rangle = \mu_0/\sqrt{N}$) [99]. The difference $\langle S\rangle - \langle S\rangle_\infty$ is a measure of the importance of short-range magnetic order (see Section 6.3).

For smaller values of U/t corresponding to a non-saturated FM ground state – for example, $S = 3/2$ for $U/t = 16$ – a completely different, non-monotonous temperature dependence of $\langle S\rangle$ is found. Here, one observes first an increase of $\langle S\rangle$ with increasing T, for $T < 0.05t$, followed by a decrease toward the high-temperature limit $\langle S\rangle_\infty$. The increase of $\langle S\rangle$ at low T results from populating low-lying excited states which have higher S than the ground state ($E(S = 5/2) - E(S = 3/2) = 0.02t$ for $U/t = 16$). If the temperature is further increased, $\langle S\rangle$ decreases since the FM correlations are destroyed

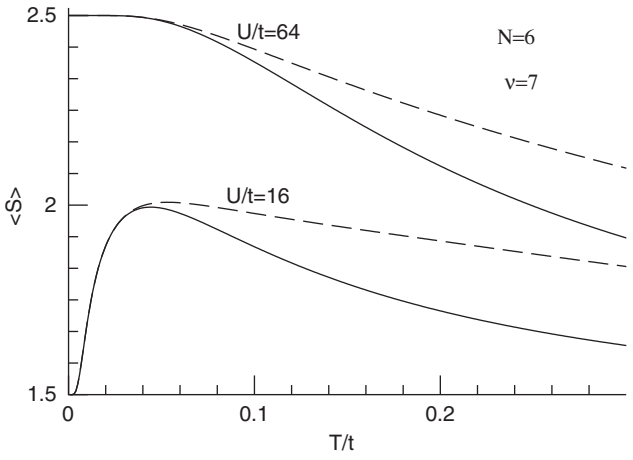

Figure 13: Temperature dependence of the average total spin $\langle S\rangle$ of clusters having $N = 6$ atoms and $v = 7$ electrons where $\langle S\rangle(\langle S\rangle + 1) = \langle \hat{S}^2\rangle$ and t refers to the hopping integral. The calculations take into account either the electronic excitations alone (dashed) or both electronic excitations and structural fluctuations (solid).

in a similar way as for $U/t = 64$. It is interesting to observe that a weak increase of the average magnetization per atom with increasing T has been experimentally observed in large Co_N clusters ($N \simeq 50 - 600$ and $T \simeq 400$) [44]. The temperature dependence of $\langle S \rangle$ in non-saturated FM clusters is very sensitive to the value of U/t. If U/t is increased beyond $U/t = 16$, the $S = 5/2$ states are stabilized with respect to the quartet and the maximum in $\langle S \rangle(T)$ shifts to lower temperatures. For sufficiently large U/t, the sextet becomes the ground state. In contrast, at smaller U/t (e.g, $U/t = 12$), the excitation energies to high-spin states increase and the low-lying excitations correspond to minimal S. Consequently, $\langle S \rangle$ decreases rapidly at low T showing eventually a minimum at intermediate T. The strong sensitivity of the spin excitation spectra on U/t reflects the importance of electron correlations to the finite temperature behavior.

The crossover from the low-temperature ferromagnetically ordered state to the high-temperature disordered state is significantly broadened by the finite size of the cluster. However, a characteristic temperature scale $T_C(N)$ may be identified above which the FM correlations are strongly reduced by thermal spin fluctuations. In contrast, the local moments $\langle \hat{S}_i^2 \rangle$ remain essentially unaffected well above T_C. Taking the inflection point in $\langle S \rangle(T)$ as a measure of $T_C(N)$ one obtains $T_C/t \simeq 0.1 - 0.2$ (see Fig. 13). This corresponds to about 1/100 of the bulk band-width W_b or to 500–600 K if parameters appropriate for TMs are used ($W_b = 16t$ for the FCC structure and $W_b = 5$–$6\,\text{eV}$ for TM d-bands). Similar conclusions are derived from the temperature dependence of the spin-correlation functions. Furthermore, the magnetic susceptibility $\chi(T)$ shows a Curie–Weiss like behavior of the form $\chi \propto 1/(T - T_C)^{-1}$ for $T > T_C = 0.15t$, and the specific heat $C_p(T)$ shows a peak at $T \simeq T_C$ due to magnetic excitations. These results can be interpreted as a precursor of a magnetic phase transition in the infinite solid [88].

The solid curves in Fig. 13 are obtained by including temperature-induced changes of structure (see Eqs. (33) and (34)). Structural fluctuations play no role at low temperatures where the ground-state structure dominates ($T/t < 0.05$). However, at higher T, they contribute to a more rapid decrease of $\langle S \rangle$. With increasing T, the average coordination $\langle z \rangle$ decreases since breaking NN bonds becomes increasingly probable. The reduction of $\langle z \rangle$ is more important for $U/t = 16$ than for $U/t = 64$ since ferromagnetism tends to stabilize the more compact structures [89]. Consequently, the effect of structural fluctuations on $\langle S \rangle(T)$ is stronger for moderate U/t, where the ground-state magnetic moments are not saturated. The reduction of $\langle S \rangle$ as a result of structural fluctuations may be qualitatively understood as follows. In open structures, the band-width for bonding (negative energy) states is smaller. Therefore, the eigenstates with maximal spin, whose energy is dominated by the minority electrons, are comparatively less stable than lower spin states. In other words, the spin-flip energy $\Delta E = E(S_{\max} - 1) - E(S_{\max})$ tends to decrease with decreasing coordination number. Thus, $\langle S \rangle(T)$ is reduced as more open structures are populated. More complex structural effects are found for other v/N and U/t. For example, one may find structures having a higher energy *and* a higher ground-state spin S than the optimal structure at $T = 0$ [89]. In such cases, taking into account structural fluctuations could tend to increase $\langle S \rangle(T)$. One concludes that structural fluctuations can play an important role in the temperature dependence of cluster magnetic properties.

7.4. Kondo screening of magnetic impurities in metal clusters

In solids, TM and RE compounds are known to present remarkable properties, such as Kondo, intermediate-valence, or heavy-fermion behavior, which are intrinsically related to the localized character of the *d* or *f* electrons and to their interactions with the conduction-band states [109, 120]. The unconventional properties of such strongly correlated systems reflect the competition between the tendency of electrons to delocalize, in order to form chemical bonds and energy bands, and the resulting local charge fluctuations, which increase the Coulomb-repulsion energy and which favor the occupation of localized states. A typical manifestation of this interplay is the presence of small energy scales in the excitation spectrum that lead to striking low-temperature properties. Clearly, the reduction of size in clusters can drastically modify and eventually suppress these phenomena, as a result of the discreteness of the energy spectrum, due to a reduction of the number of electronic states near the Fermi level, or even as a consequence of a change in the lattice structure. In the case of a magnetic impurity in a finite-size metallic environment, the formation of a Kondo singlet [121, 122] may be significantly affected if the available number of conduction-electron states at temperatures $k_B T$ lower than the mean level spacing δ_N is not enough to effectively screen the magnetic moment of the impurity.

Recently, the consequences of confinement and of the discreteness of the energy spectrum have been investigated by considering the Anderson model in idealized nanoscopic systems [123–125]. In addition, there are several other contributions that are expected to be important for the study of clusters, particularly in the small-size regime. For example, besides the usual dependence of the single-particle electronic spectrum on size and shape, one should take into account the changes in the local environment of the impurity and of the *sd* or *sf* hybridizations, which determine the degree of localization of the impurity states. Moreover, as already discussed in the previous section, the low-lying spin excitations and isomerizations are likely to involve comparable energy scales. Therefore, the contributions of geometries with different impurity positions should be treated on the same footing. A thorough optimization and sampling of cluster structures is therefore necessary in order to describe the ground-state and low-temperature properties. It is the purpose of this section to review theoretical results on the electronic, structural, and magnetic properties of small metal cluster containing magnetic impurities. These have been obtained in the framework of a real-space version of the single-impurity Anderson model [126] which is solved by exact diagonalization methods.

We consider N-atom clusters containing $N-1$ simple-metal atoms and one magnetic impurity. The model Hamiltonian is given by

$$\hat{H} = \hat{H}_s + \hat{H}_f + \hat{H}_{sf} \tag{35}$$

The first term

$$\hat{H}_s = -t_{ss} \sum_{\langle i,j\rangle,\sigma} \hat{c}^{\dagger}_{i\sigma} \hat{c}_{j\sigma} \tag{36}$$

describes the *s*-like valence-electron states of the simple-metal atoms and of the impurity by using a single-band tight-binding model. As usual, $\hat{c}^{\dagger}_{i\sigma}$ ($\hat{c}_{i\sigma}$) refers to the creation (annihilation) operator of an electron with spin σ at the *s* orbital of atom *i*, and t_{ss} to the NN *s*-electron hopping integral. Possible differences between the *s* levels

ε_s in different atoms are disregarded by setting $\varepsilon_s = 0$ both at the metal-host sites ($1 \leqslant i \leqslant N-1$) and at the impurity ($i = 0$). The second term

$$\hat{H}_f = \varepsilon_f \sum_\sigma \hat{n}_{f\sigma} + U_{ff}\hat{n}_{f\uparrow}\hat{n}_{f\downarrow} \tag{37}$$

concerns the magnetic degrees of freedom of the impurity [126]. Here $\hat{n}_{f\sigma} = \hat{f}^\dagger_\sigma \hat{f}_\sigma$ is the electron number operator of the localized *d*- or *f*-like impurity orbital, ε_f the corresponding energy level, and U_{ff} the Coulomb-repulsion integral. Orbital degeneracies are neglected for simplicity. Finally, the third term

$$\hat{H}_{sf} = V_{sf} \sum_\sigma (\hat{f}^\dagger_\sigma \hat{c}_{0\sigma} + \hat{c}^\dagger_{0\sigma}\hat{f}_\sigma) \tag{38}$$

takes into account the coupling between the localized level and the delocalized electrons by means of an intra-atomic *sf* hybridization at the impurity atom $i = 0$.

$\hat{H}$ may be written in terms of the single-particle eigenstates $\hat{a}^\dagger_k = \sum_j \alpha_{jk}\hat{c}^\dagger_j$ of $\hat{H}_s$ as

$$\hat{H} = \sum_{k\sigma} \varepsilon_k \hat{n}_{k\sigma} + \sum_\sigma \varepsilon_f \hat{n}_{f\sigma} + U_{ff}\hat{n}_{f\uparrow}\hat{n}_{f\downarrow} + \sum_{k\sigma} V_{kf}(\hat{f}^\dagger_\sigma \hat{a}_{k\sigma} + \hat{a}^\dagger_{k\sigma}\hat{f}_\sigma) \tag{39}$$

The *s*-electron eigenenergies are denoted by ε_k ($[\hat{H}_s, a^\dagger_{k\sigma}] = \varepsilon_k a^\dagger_{k\sigma}$) and the *kf* hybridizations by $V_{kf} = \alpha_{ik} V_{sf}$, where *i* refers to the impurity atom. Notice that ε_k and V_{kf} depend strongly on the size, cluster topology, and impurity position *i*. As we shall see, this form of the Hamiltonian is particularly useful in cases where symmetry considerations allow to reduce the number of conduction electron states that couple to the impurity.

The ground-state and excited-state properties are calculated by using exact diagonalization methods [89, 112]. In particular, the spin gap is given by

$$\Delta E = E(S = 1, 3/2) - E(S = 0, 1/2) \tag{40}$$

where $E(S)$ stands for the lowest eigenenergy of spin S. Relevant finite-temperature properties, like the specific heat

$$C = \left(\frac{\langle E^2 \rangle - \langle E \rangle^2}{k_B T^2} \right) \tag{41}$$

the zero-field magnetic susceptibility

$$\chi = \frac{\langle S_z^2 \rangle}{k_B T} \tag{42}$$

the corresponding impurity contribution

$$\chi_f = \frac{\left(\langle s_{zf}^2 \rangle + \sum_i \langle s_{zf} s_{zi} \rangle \right)}{k_B T} \tag{43}$$

and the effective impurity moment

$$\mu_f^2 = k_B T \chi_f = \langle s_{zf}^2 \rangle + \sum_i \langle s_{zf} s_{zi} \rangle \tag{44}$$

are determined in the canonical ensemble. Here the temperature T refers to the cluster source that defines the macroscopic thermal bath with which the clusters are in

equilibrium before expansion in the beam. The averages apply then to the ensemble of clusters in the beam.

For small clusters ($N \leqslant 8$), a complete geometry optimization can be performed by considering all non-equivalent cluster topologies, in analogy to previous works on the Hueckel and Hubbard models [89, 113]. Alternatively, for selected clusters having a high point-group symmetry (e.g., FCC clusters of nearly spherical shape) one may use a decoupling scheme that allows exact calculations of finite-temperature properties of relatively large clusters ($N \leqslant 80$–100). Only the conduction states k that couple with the magnetic degrees of freedom (i.e., having $V_{kf} \neq 0$) need to be included in the many-body diagonalization. The other conduction states define a single-particle problem that can be solved independently.

For the purpose of the present discussion we take $\varepsilon_s = 0$ and t_{ss} as the unit of energy, and we set $V_{sf}/t_{ss} = 0.5$, $\varepsilon_f/t_{ss} = -5$, and $U_{ff}/t_{ss} = 100$. These parameters are re presentative of the Kondo regime where the impurity moment is localized and only very small virtual charge fluctuations are possible ($n_f \simeq 1$ since $U_{ff} \gg |\varepsilon_s - \varepsilon_f| \gg |V_{sf}|$). The band filling or number of electrons v is varied in order to illustrate the role of the single-particle electronic structure (e.g., even–odd effects). Otherwise, we focus on neutral systems which have one electron per orbital, i.e., $v = N+1$ where N is the number of atoms.

In solids, the magnetic behavior of impurities and in particular the Kondo temperature are known to depend crucially on the conduction-electron density of states at the Fermi level [121, 122]. It is therefore very interesting to discuss if a similar analysis applies to the finite-size version of this effect. For even v the ground state is in general a singlet and $\Delta E = E(1) - E(0)$ is of the same order, though somewhat smaller, as the singlet–triplet gap $\Delta E_0 = 2V_{sf}^2/|\varepsilon_f|$ of the two-level problem ($\Delta E_0 = t_{ss}/10$ for the present parameter choice). In contrast, for odd v, $\Delta E = E(3/2) - E(1/2)$ is of the order of s-electron hopping t_{ss}, which indicates that this is essentially an electron-hole excitation within the conduction band. As a result, ΔE shows strong oscillations as a function of v [127].

The band-filling dependence of ΔE may be qualitatively understood in terms of the cluster-specific single-particle spectrum ε_k and kf hybridizations V_{kf}. For even v, the singlet–triplet gap can be obtained quite accurately from the solution of a two-level problem which is given by $\Delta E = 2V_{kf}^2/|\varepsilon_k - \varepsilon_f|$. The dependence of ΔE on the impurity position i reflects the dependence of $V_{kf} = \alpha_{ik} V_{sf}$ on i. As will be discussed below, these small singlet–triplet gaps can be interpreted as a finite-size equivalent of the Kondo effect. The situation changes for odd v since the highest occupied s-electron state is fully occupied in the lowest-energy configurations. The sf hybridization may only promote the impurity electron to higher s levels, which are empty for both spin directions. Therefore, the impurity spin remains unchanged after such a charge fluctuation: either $s_{zf} = 1/2$ or $s_{zf} = -1/2$. The first $S = 3/2$ state corresponds then to the creation of an electron-hole pair in the conduction-band spectrum. Consequently, the excitation energy is of the order of t_{ss} and the dependence on the impurity position is very weak.

An interesting interplay has been observed between cluster topology, impurity position, and magnetic behavior. The energy changes associated to different impurity positions are relatively small, often smaller than the magnetic excitations. Larger isomerization energies are found when the topology of the cluster changes. This

suggests that at finite temperatures some structural transitions should coexist with the lowest electronic or magnetic excitations. An analogous effect has also been observed in Hubbard clusters (see Section 7.3) [89]. Similar trends hold at higher excitation energies, where one finds a multitude of isomers with very similar stability.

In Figs. 14 and 15, results are given for the temperature dependence of the effective impurity moment μ_f^2, the magnetic susceptibility χ, and the specific heat C. The most stable clusters having $N = 5$ atoms and $v = 6$ electrons are considered. The statistical averages were calculated in the canonical ensemble by considering each cluster structure separately for all T. The effective impurity moment μ_f shows very clearly the consequences of the low-energy Kondo-like excitations. For the most stable structures having a singlet ground state (isomers $i = 1$–4), μ_f vanishes at $T = 0$ due to the screening of the impurity by the conduction electrons. The impurity moment fluctuates between up and down directions keeping strong AF correlations with the conduction s states. For very low T, one obtains $\langle s_{zf}^2 \rangle = 1/4$ and $\sum_i \langle s_{zf} s_{zi} \rangle = -1/4$ so that the screening of the impurity magnetic moment is complete (see Eq. (44)). In contrast, the clusters lacking of singlet formation (e.g., isomer $i = 5$) show an unscreened moment $\mu_f^2 = 1/4$ down to $T = 0$ since $\Delta E = 0$. As T increases and T approaches $\Delta E(i)/k_B$, the AF spin correlations of the singlet ground state ($i = 1$–4) are progressively destroyed by thermal fluctuations across the singlet–triplet gap. Consequently, an exponentially activated increase of μ_f is observed which depends on the impurity position i. For $k_B T \gg \Delta E(i)$, $\sum_i \langle s_{zf} s_{zi} \rangle \to 0$. At this point ($k_B T \simeq 10 \Delta E$ in Fig. 14), the impurity moment is completely uncoupled from the conduction states and $\mu_f^2 \simeq 1/4$ for all i. The Kondo clusters ($i = 1$–4) join the behavior of the unscreened ones ($i = 5$). Notice that in the Kondo limit, where the f-level ε_f is well below the Fermi energy and

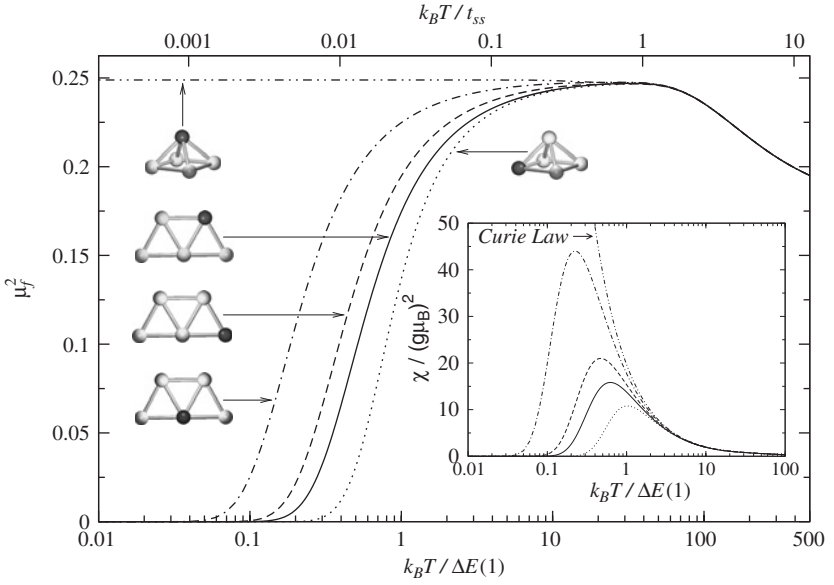

Figure 14: Temperature dependence of the effective impurity moment μ_f^2 and magnetic susceptibility χ of the most stable clusters having $N = 5$ atoms and $v = 6$ valence electrons (see Eqs. (42)–(44)). $\Delta E(1)$ stands for the singlet–triplet gap of the most stable structure.

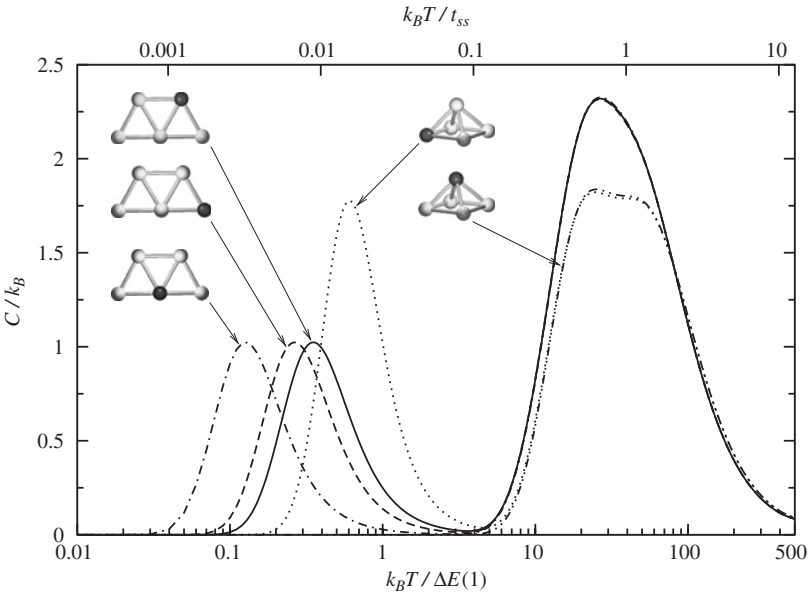

Figure 15: Temperature dependence of the specific heat C of the most stable clusters having $N = 5$ atoms and $v = 6$ valence electrons (see Eq. (41)). $\Delta E(1)$ stands for the singlet–triplet gap of the most stable structure.

U_{ff} is very large, the f-orbital occupation n_f remains very close to 1 even for $k_BT \gg \Delta E(i)$. Only at higher temperatures one starts to observe a reduction of μ_f^2, which is proportional to a decrease of n_f, due to thermally induced charge fluctuations from the impurity f level to the conduction band. This occurs for $k_BT \sim (\varepsilon_F - \varepsilon_f)$ which amounts approximately to $|\varepsilon_f| = 5t_{ss}$ for the present parameter choice. Finally, it is interesting to point out the remarkable qualitative similarities between the present results for μ_f in Anderson clusters and the far more complex physics of the Anderson impurity model in the macroscopic limit, as derived by using the renormalization group method [128].

The magnetic susceptibility of the cluster χ is shown in the inset of Fig. 14. For large T, the impurity moment fluctuates freely and a Curie-like increase of χ is observed for decreasing T. The saturation and further decrease of χ for $T < \Delta E(i)/k_B$ reflect the formation of a singlet ground state and the screening of the magnetic degree of freedom for $i = 1$–4. As expected, for $i = 5$ the Curie law holds even for $T \to 0$ as for free moments in insulators. The maximum of χ for different impurity positions scales with $\Delta E(i)$ as can be seen by comparing the various curves. In intermediate valence states a shift of the maximum to higher temperatures is found, which is consistent with a larger value of the singlet–triplet splitting $\Delta E(i)$. In this case, the magnetic response is also reduced by the increasing importance of charge fluctuations between magnetic and non-magnetic configurations.

The corresponding results for the specific heat C are shown in Fig. 15. For $i = 1$–4, one observes a low-temperature peak at $T \simeq \Delta E(i)/k_B$ that depends on the cluster geometry and impurity position i and that is a consequence of spin fluctuations. In

fact, the first peak in C occurs at approximately the same T for which χ is maximum. The cluster structures that fail to form a Kondo singlet (e.g., $i = 5$) do not show such a low-temperature peak. At higher T, one observes an increase of C and a much broader maximum that is mainly due to electron-hole excitations within the conduction states. This contribution depends somewhat on the cluster topology, i.e., on the details of the conduction electron spectrum, but is essentially independent of the impurity position in the Kondo limit. However, some coupling between spin and charge fluctuations starts to develop for parameters corresponding to intermediate valence behavior.

Summarizing, the exact diagonalization studies show that the impurity moment can be screened in the ground state as a result of strong electron correlations, in a similar way as the Kondo screening observed in the macroscopic limit. Further studies on larger clusters and other parameter regimes, particularly in order to explore the cluster intermediate-valence behavior, would be certainly worthwhile. Quantitative information about the low-energy electronic configurations of magnetic impurities in metal clusters can also be obtained in the framework of realistic electronic-structure approaches, for example, by performing first principles density-functional or explicitly correlated calculations [129, 130]. In this way, it can be shown that transition-metal impurities like Ni preserve their magnetic degree of freedom when solved in small metal clusters like Cu_N or Na_N [129]. As in the present model study, the ab initio results indicate that the most stable cluster topologies are not much affected by the presence of the impurity, and that the energy differences for different impurity positions are similar to the excitation energies between different spin multiplicities. Moreover, the correlation between cluster structure and magnetism is also found to be particularly strong.

8. CONCLUSION

The variety of physical problems reviewed in this chapter reflect part of the remarkable current activity on the theory of magnetic nanostructures and at the same time suggest interesting perspectives on future developments. A significant proportion of the discussion has been focused on analyzing the electronic and magnetic properties from a local perspective in order to correlate the observed phenomena with the local environment of the atoms in each specific nanostructure. For instance, we have followed the evolution of spin and orbital moments, magnetic order and magnetic anisotropy in pure and alloy clusters, clusters deposited on surfaces or embedded in macroscopic matrices. Understanding the microscopic origin of these cluster properties is very important for developing new magnetic materials, in particular for applications in high-density recording and memory devices. Among the most interesting candidates for tuning the magnetic behavior of nanoparticles one should mention binary-alloy clusters and clusters deposited on highly polarizable substrates, where very interesting new effects are expected including complex non-collinear magnetic order and spin-canted phases.

From a more fundamental perspective, electron correlation effects and temperature-dependent properties appear as challenging subjects where many open questions still remain to be elucidated. Methodological improvements on both theoretical and experimental methods are certainly worthwhile and necessary. For example, one would

like to understand how electron correlations affect subtle properties like spin excitation energies and magnetic anisotropy. Rigorous calculations using realistic *d*-band Hamiltonians and exact diagonalization methods on small clusters could serve as a basis for testing approximations applicable to larger systems. The analysis of the evolution of the many-body electronic structure as a function of size would also provide a more profound understanding of the spin and orbital contributions to the magnetization of nanoparticles and of the crossover from localized to itinerant magnetism as a function of size and dimensionality.

The enhancement of the local magnetic moments in low-dimensional systems and the presence of significant short-range magnetic order above the Curie temperature are two characteristics of TM magnetism which play a significant role for determining the finite temperature behavior. Moreover, as discussed in previous sections, temperature-induced changes or fluctuations of the geometrical structure can also be very important, for example, for small clusters or close to the surface of nanoparticles. The functional-integral theory reviewed in this chapter can be applied to study this problem since the fluctuations of the local magnetic moments and the itinerant character of the *d*-electron states are taken into account at the same electronic level. More systematic studies of finite-temperature properties are necessary, in particular concerning the size dependence of the cluster "Curie" temperature $T_C(N)$. Monte Carlo algorithms are an appropriate tool for performing the functional integration over exchange fields by including collective spin fluctuations beyond the usual single-site approximations. For large clusters and cluster-based nanostructures, simpler spin models with effective spin–spin interactions could be derived from the electronic calculations. This should open the way to investigations of non-adiabatic spin-relaxation processes and of the dynamics of magnetic recording within a microscopic theory.

In conclusion, the theory of magnetic nanostructures is a most challenging research area that will continue to reveal a series of novel phenomena, fascinating from a fundamental standpoint and important for technological applications.

ACKNOWLEDGMENTS

Helpful discussions with S. Dennler, R. Garibay-Alonso, J. Morillo, M. Muñoz-Navia, and J.L. Ricardo-Chávez are gratefully acknowledged. The authors would also like to thank for the kind hospitality of Laboratoire de Nanostructures, Magnétisme et Optoélectronique of Institut National des Sciences Appliquées of Toulouse, France, where most of the research reported in this paper has been performed.

REFERENCES

[1] Bansmann J., Baker S.H., Binns C., Blackman J.A., Bucher J.-P., Dorantes-Dávila J., Dupuis V., Favre L., Kechrakos D., Kleibert A., Meiwes-Broer K.-H., Pastor G.M., Perez A., Toulemonde O., Trohidou K.N., Tuaillon J., Xie Y., Surf. Sci. Rep. 56 (2005) 189.

[2] Binns C., Trohidou K.N., Bansmann J., Baker S.H., Blackman J.A., Bucher J.-P., Kechrakos D., Kleibert A., Louch S., Meiwes-Broer K.-H., Pastor G.M., Perez A., Xie Y., J. Phys. D: Appl. Phys. 38 (2005) R357.

[3] Pastor G. M., in: Atomic Clusters and Nanoparticles, Lectures Notes of the Les Houches Summer School of Theoretical Physics, C. Guet, P. Hobza, F. Spiegelman, F. David (eds), Springer, Berlin, 2001, p. 335.
[4] Nonas B., Cabria I., Zeller R., Dederichs P.H., Huhne T., Ebert H., Phys. Rev. Lett. 86 (2001) 2146.
[5] Cabria I., Nonas B., Zeller R., Dederichs P.H., Phys. Rev. B 65 (2002) 054414.
[6] Lazarovits B., Szunyogh L., Weinberger P., Phys. Rev. B 65 (2002) 104441; Lazarovits B., Szunyogh L., Weinberger P., Phys. Rev. B 67 (2003) 024415.
[7] Ebert H., Bornemann S., Minr J., Dederichs P.H., Zeller R., Cabria I., Comput. Mater. Sci. 35 (2006) 279.
[8] Stepanyuk V.S., Niebergall L., Baranov A.N., Hergert W., Bruno P., Comput. Mater. Sci. 35 (2006) 272.
[9] Heine V., in: Solid State Physics, H. Ehrenreich, F. Seitz, D. Turnbull (eds), Vol. 35, Academic Press, New York, 1980, p. 1.
[10] Falicov L.M., Somorjai G.A., Proc. Natl. Acad. Sci. USA 82 (1985) 2207.
[11] Slater J.C., Quantum Theory of Atomic Structure, Vols. I and II, McGraw-Hill, New York, 1960.
[12] Oda T., Pasquarello A., Car R., Phys. Rev. Lett. 80 (1998) 3622.
[13] Ojeda M.A., Dorantes-Dávila J., Pastor G.M., Phys. Rev. B 60 (1999) 6121; Ojeda M.A., Dorantes-Dávila J., Pastor G.M., Phys. Rev. B 60 (1999) 9122.
[14] Kohl C., Bertsch G.F., Phys. Rev. B 60 (1999) 4205.
[15] Rollmann G., Entel P., Sahoo S., Comput. Mater. Sci. 35 (2006) 275.
[16] Haydock R., in: Solid State Physics, H. Ehrenreich, F. Seitz, D. Turnbull (eds), Vol. 35, Academic Press, New York, 1980, p. 215.
[17] Strange P., Relativistic Quantum Mechanics, Cambridge University Press, Cambridge, 1998.
[18] Jansen H.J.F., Phys. Rev. B 38 (1998) 8022.
[19] Landau L.D., Lifshitz E.M., Quantum Mechanics, Vol. 3, Pergamon Press, Oxford, 1965.
[20] Binns C., Surf. Sci. Rep. 44 (2001) 1.
[21] Röhlsberger R., Bansmann J., Senz V., Jonas K.L., Bettac A., Leupold O., Rüffer R., Burkel E., Meiwes-Broer K.-H., Phys. Rev. Lett. 86 (2001) 5597.
[22] Lau J.T., Föhlisch A., Nietubyc R., Reif M., Wurth W., Phys. Rev. Lett. 89 (2002) 057201.
[23] Koide T., Miyauchi H., Okamoto J., Shidara T., Fujimori A., Fukutani H., Amemiya K., Takeshita H., Yuasa S., Katayama T., Suzuki Y., Phys. Rev. Lett. 87 (2001) 257201.
[24] Gambardella P., Rusponi S., Veronese M., Dhesi S.S., Grazioli C., Dallmeyer A., Cabria I., Zeller R., Dederichs P.H., Kern K., Carbone C., Brune H., Science 300 (2003) 1130.
[25] Fauth K., Gold S., Hessler M., Schneider N., Schutz G., Chem. Phys. Lett. 392 (2004) 498; Wiedwald U., Cerchez M., Farle M., Fauth K., Schutz G., Zurn K., Boyen H.G., Ziemann P., Phys. Rev. B 70 (2004) 214412.
[26] Bruno P., Magnetismus von Festkörpern und Grenzflächen, Ferienkurse des Forschungszentrums Jülich, Jülich, 1993, and references therein.
[27] Pastor G.M., Dorantes-Dávila J., Pick S., Dreyssé H., Phys. Rev. Lett. 75 (1995) 326.
[28] Nicolas G., Dorantes-Dávila J., Pastor G.M., Phys. Rev. B 74 (2006) 014415.
[29] Victora R.H., Falicov L.M., Ishida S., Phys. Rev. B 30 (1984) 3896.
[30] Cox A.J., Louderback J.G., Bloomfield L.A., Phys. Rev. Lett. 71 (1993) 923.
[31] Cox A.J., Louderback J.G., Apsel S.E., Bloomfield L.A., Phys. Rev. B 49 (1994) 12295.
[32] Galicia R., Rev. Mex. Fis. 32 (1985) 51.
[33] Reddy B.V., Khanna S.N., Dunlap B.I., Phys. Rev. Lett. 70 (1993) 3323.
[34] Villaseñor-González P., Dorantes-Dávila J., Dreyssé H., Pastor G.M., Phys. Rev. B 55 (1997) 15084.

[35] Jinlong Y., Toigo F., Kelin W., Phys. Rev. B 50 (1994) 7915.
[36] Li Z.-Q., Yu J.-Z., Ohno K., Kawazoe Y., J. Phys.: Condens. Matter 7 (1995) 47.
[37] Piveteau B., Desjonquéres M.-C., Olés A.M., Spanjaard D., Phys. Rev. B 53 (1996) 9251.
[38] Pastor G.M., Dorantes-Dávila J., Bennemann K.H., Physica B 149 (1988) 22; Pastor G.M., Dorantes-Dávila J., Bennemann K.H., Phys. Rev. B 40 (1989) 7642; Dorantes-Dávila J., Dreyssé H., Pastor G.M., Phys. Rev. B 46 (1992) 10432.
[39] Vega A., Balbás L.C., Dorantes-Dávila J., Pastor G.M., Phys. Rev. B 50 (1994) 3899.
[40] Alvarado P., Dorantes-Dávila J., Pastor G.M., Phys. Rev. B 58 (1998) 12216.
[41] Bodker F., Morup S., Linderoth S., Phys. Rev. Lett. 72 (1994) 282.
[42] Gambardella P., Dallmeyer A., Maiti K., Malagoli M.C., Eberhardt W., Kern K., Carbone C., Nature 416 (2002) 301.
[43] Gambardella P., Dallmeyer A., Maiti K., Malagoli M.C., Rusponi S., Ohresser P., Eberhardt W., Carbone C., Kern K., Phys. Rev. Lett. 93 (2004) 077203.
[44] Billas I.M.L., Becker J.A., Châtelain A., de Heer W.A., Phys. Rev. Lett. 71 (1993) 4067.
[45] Billas I.M.L., Châtelain A., de Heer W.A., Science 265 (1994) 1682.
[46] Apsel S.E., Emert J.W., Deng J., Bloomfield L.A., Phys. Rev. Lett. 76 (1996) 1441.
[47] Guirado-López R., Dorantes-Dávila J., Pastor G.M., Phys. Rev. Lett. 90 (2003) 226402.
[48] Castro M., Jamorski Ch., Salahub D., Chem. Phys. Lett. 271 (1997) 133.
[49] Reddy B.V., Nayak S.K., Khanna S.N., Rao B.K., Jena P., J. Phys. Chem. A 102 (1998) 1748.
[50] Reuse F.A., Khanna S., Eur. Phys. J. D 6 (1999) 77.
[51] Zitoun D., Respaud M., Fromen M.-C., Casanove M.J., Lecante P., Amiens C., Chaudret B., Phys. Rev. Lett. 89 (2002) 037203.
[52] Dennler S., Morillo J., Pastor G.M., Surf. Sci. 532–535 (2003) 334.
[53] Dennler S., Morillo J., Pastor G.M., J. Phys.: Condens. Matter 16 (2004) S2263.
[54] Kresse G., Hafner J., Phys. Rev. B 47 (1993) 558.
[55] Kresse G., Furthmüller J., Phys. Rev. B 47 (1996) 11169.
[56] Muñoz-Navia M., Dorantes-Dávila J., Pastor G.M., J. Phys.: Condens. Matter 16 (2004) S2251.
[57] Fromen M.-C., Lecante P., Casanove M.J., Bayle Guillemaud P., Zitoun D., Amiens C., Chaudret B., Respaud M., Benfield R.E., Phys. Rev. B 69 (2004) 235416.
[58] Respaud M., private communication.
[59] Padovani S., Chado I., Scheurer F., Bûcher J.P., Phys. Rev. B 59 (1999) 11887; Padovani S., Scheurer F., Chado I., Bucher J.P., Phys. Rev. B 61 (2000) 72.
[60] Russier V., Petit C., Legrand J., Pileni M.P., Phys. Rev. B 62 (2000) 3910; Pinna N., Maillard M., Courty A., Russier V., Pileni M.P., Phys. Rev. B 66 (2002) 045415.
[61] Jamet M., Wernsdorfer W., Thirion C., Mailly D., Dupuis V., Mélinon P., Pérez A., Phys. Rev. Lett. 86 (2001) 4676.
[62] Mirbt S., Abrikosov I.A., Johansson B., Skriver H.L., Phys. Rev. B 55 (1997) 67; Jamet M., Dupuis V., Mélinon P., Guiraud G., Pérez A., Wernsdorfer W., Traverse A., Baguenard B., Phys. Rev. B 62 (2000) 493.
[63] Eigler D.M., Schweizer E.K., Nature 344 (1990) 524.
[64] Roeder H., Hahn E., Brune H., Bucher J.P., Kern K., Nature 366 (1993) 141.
[65] Ohresser P., Brookes N.B., Padovani S., Scheurer F., Bulou H., Phys. Rev. B 64 (2001) 104429.
[66] Dürr H.A., Dhesi S.S., Dudzik E., Knabben D., van der Laan G., Goedkoop J.B., Hillebrecht F.U., Phys. Rev. B 59 (1999) R701.
[67] Luis F., Torres J.M., García L.M., Bartolomé J., Stankiewicz J., Petroff F., Fettar F., Maurice J.-L., Vaures A., Phys. Rev. B 65 (2002) 094409.
[68] Qiang Y., Sabiryanov R.F., Jaswal S.S., Liu Y., Haberland H., Sellmyer D.J., Phys. Rev. B 66 (2002) 064404.

[69] Deshmukh M.M., Kleff S., Guéron S., Bonet E., Pasupathy A.N., von Delft J., Ralph D.C., Phys. Rev. Lett. 87 (2001) 226801.
[70] Lysenko O.V., Stepanyuk V.S., Hergert W., Kirschner J., Phys. Rev. Lett. 89 (2002) 126102.
[71] Shen J., Skomski R., Klaua M., Jenniches H., Manoharan S.S., Kirschner J., Phys. Rev. B 56 (1997) 2340.
[72] See, for instance, Liz Marzán L.M., Kamat P.V. (eds), Nanoscale Materials, Kluwer Academic Publishers, Boston, 2003.
[73] Izquierdo J., Bazhanov D.I., Vega A., Stepanyuk V.S., Hergert W., Phys. Rev. B 63 (2001) 140413.
[74] Kohlhepp J., Gradmann U., J. Magn. Magn. Mater. 139 (1995) 347.
[75] Dorantes-Dávila J., Dreyssé H., Pastor G.M., Phys. Rev. Lett. 91 (2003) 197206.
[76] Heinrich B., Bland J.A.C. (eds), Ultrathin Magnetic Structures I and II, Springer, Berlin, 1994.
[77] Sun S., Murray C.B., J. Appl. Phys. 85 (1999) 4325; Sun S., Murray C.B., Weller D., Folks L., Moser A., Science 287 (2000) 1989.
[78] Dorantes-Dávila J., Pastor G.M., Phys. Rev. Lett. 81 (1998) 208.
[79] Félix-Medina R., Dorantes-Dávila J., Pastor G.M., New J. Phys. 4 (2002) 100.
[80] Félix-Medina R., Dorantes-Dávila J., Pastor G.M., Phys. Rev. B 67 (2003) 094430.
[81] See, for instance, Zimmermann C.G., Yeadon M., Nordlund K., Gibson J.M., Averback R.S., Herr U., Samwer K., Phys. Rev. Lett. 83 (1999) 1163; Padovani S., Scheurer F., Bucher J.P., Europhys. Lett. 45 (1999) 327; Lysenko O.V., Stepanyuk V.S., Hergert W., Kirschner J., Phys. Rev. Lett. 89 (2002) 126102.
[82] Lee J.W., Jeong J.R., Shin S.C., Kim J., Kim S.K., Phys. Rev. B 66 (2002) 172409.
[83] Dorantes-Dávila J., Pastor G.M., Phys. Rev. B 72 (2005) 085427.
[84] Gerion D., Hirt A., Billas I.M.L., Châtelain A., de Heer W.A., Phys. Rev. B 62 (2000) 7491.
[85] Knickelbein M.B., J. Chem. Phys. 115 (2001) 1983.
[86] Pastor G.M., Dorantes-Dávila J., Bennemann K.H., Phys. Rev. B 70 (2004) 064420.
[87] Polesya S., Sipr O., Bornemann S., Minar J., Ebert H., Europhys. Lett. 74 (2006) 1074.
[88] López-Urías F., Pastor G.M., Bennemann K.H., J. Appl. Phys. 87 (2000) 4909; López-Urías F., Pastor G.M., J. Magn. Magn. Mater. 294 (2005) e27–e31; López-Urías F., Pastor G.M., unpublished.
[89] Pastor G.M., Hirsch R., Mühlschlegel B., Phys. Rev. Lett. 72 (1994) 3879; Pastor G.M., Hirsch R., Mühlschlegel B., Phys. Rev. B 53 (1996) 10382.
[90] López-Urías F., Pastor G.M., Phys. Rev. B 59 (1998) 5223.
[91] Dorantes-Dávila J., Pastor G.M., Bennemann K.H., Solid State Commun. 59 (1986) 159; Dorantes-Dávila J., Pastor G.M., Bennemann K.H., Solid State Commun. 60 (1986) 465.
[92] Hubbard J., Phys. Rev. B 19 (1979) 2626; Hubbard J., Phys. Rev. B 20 (1979) 4584; Hasegawa H., J. Phys. Soc. Jpn. 49 (1980) 178; Hasegawa H., J. Phys. Soc. Jpn. 49 (1980) 963.
[93] Kakehashi Y., J. Phys. Soc. Jpn. 50 (1981) 2251.
[94] Moriya T. (ed.), Electron Correlation and Magnetism in Narrow-Band Systems, Springer Series in Solid State Sciences, Vol. 29, Springer, Heidelberg, 1981; Vollhardt D., Blumer N., Held K., Kollar M., Advances in Solid State Physics, Vol. 38, Vieweg Wiesbaden, 1999, p. 383.
[95] Garibay-Alonso R., Dorantes-Dávila J., Pastor G.M., unpublished.
[96] Garibay-Alonso R., Dorantes-Dávila J., Pastor G.M., Phys. Rev. B 73 (2006) 224429.
[97] Haines E.M., Clauberg R., Feder R., Phys. Rev. Lett. 54 (1985) 932.
[98] Korenman V., Frange R.E., Phys. Rev. Lett. 53 (1984) 186.
[99] Pastor G.M., Dorantes-Dávila J., Phys. Rev. B 52 (1995) 13799.

[100] Pfandzelter R., Potthoff M., Phys. Rev. B 64 (2001) 140405.
[101] Kisker E., Schröder K., Gudat W., Campagna M., Phys. Rev. B 31 (1985) 329.
[102] Kirschner J., Globl M., Dose V., Scheidt H., Phys. Rev. Lett. 53 (1984) 612; Kirschner J., Phys. Rev. B 30 (1984) 415.
[103] Hasegawa H., J. Phys. F: Metal Phys. 17 (1987) 165.
[104] Hukushima K., Nemoto K., J. Phys. Soc. Jpn. 65 (1996) 1604.
[105] Binder K., Rauch R., Wildpaner V., J. Phys. Chem. Solids 31 (1970) 391.
[106] Enders A., Peterka D., Repetto D., Lin N., Dmitriev A., Kern K., Phys. Rev. Lett. 90 (2003) 217203.
[107] Kawakami R.K., Escorcia-Aparicio E.J., Qiu Z.Q., Phys. Rev. Lett. 77 (1996) 2570; Choi H.J., Qiu Z.Q., Pearson J., Jiang J.S., Li D., Bader S.D., Phys. Rev. B 57 (1998) R12713; Kawakami R.K., Bowen M.O., Choi H.J., Escorcia-Aparicio E.J., Qiu Z.Q., Phys. Rev. B 58 (1998) R5924.
[108] Pappas D.P., Kämper K.-P., Miller B.P., Hopster H., Fowler D.E., Luntz A.C., Brundle C.R., Shen Z.-X., J. Appl. Phys. 69 (1991) 5209; Allenspach R., Bischof A., Phys. Rev. Lett. 69 (1992) 3385; Allenspach R., J. Magn. Magn. Mater. 129 (1994) 160.
[109] Fulde P., Electron Correlations in Atoms, Molecules and Solids, Springer, Berlin, 1993.
[110] Reindl S.L., Pastor G.M., Phys. Rev. B 47 (1993) 4680.
[111] Hubbard J., Proc. R. Soc. Lond. A 276 (1963) 238; Hubbard J., Proc. R. Soc. Lond. A 281 (1964) 401; Kanamori J., Prog. Theoret. Phys. 30 (1963) 275; Gutzwiller M.C., Phys. Rev. Lett. 10 (1963) 159.
[112] Lanczos C., J. Res. Nat. Bur. Stand. 45 (1950) 255; Parlett B.N., The Symmetric Eigenvalue Problem, Prentice-Hall, Englewood Cliffs, 1980; Collum J.K., Willoughby R.A., Lanczos Algorithms for Large Symmetric Eigenvalue Computations, Vol. I, Birkhäuser, Boston, 1985.
[113] Wang Y., George T.F., J. Chem. Phys. 86 (1987) 3493.
[114] Callaway J., Chen D.P., Tang R., Z. Phys. D 3 (1986) 91; Callaway J., Chen D.P., Tang R., Phys. Rev. B 35 (1987) 3705.
[115] Lieb E.H., Phys. Rev. Lett. 62 (1989) 1201.
[116] Nagaoka Y., Solid State Commun 3 (1965) 409; Thouless D.J., Proc. Phys. Soc. Lond. 86 (1965) 893; Nagaoka Y., Phys. Rev. 147 (1966) 392; Tasaki H., Phys. Rev. B 40 (1989) 9192.
[117] Douglass D.C., Bucher J.P., Bloomfield L.A., Phys. Rev. B 45 (1992) 6341.
[118] Bucher J.P., Douglass D.C., Bloomfield L.A., Phys. Rev. Lett. 66 (1991) 3052.
[119] Falicov L.M., Victora R.H., Phys. Rev. B 30 (1984) 1695; Ishii Y., Sugano S., J. Phys. Soc. Jpn. 53 (1984) 3895.
[120] Falicov L.M., Hanke W., Maple M.B. (eds), Valence Fluctuations in Solids, North-Holland, Amsterdam, 1981; Wachter P., Boppart H. (eds), Valence Instabilities, North-Holland, Amsterdam, 1982.
[121] Kondo J., Prog. Theoret. Phys. 32 (1964) 37.
[122] Hewson A.C., The Kondo Problem to Heavy Fermions, Cambridge University Press, Cambridge, 1997.
[123] Thimm W.B., Kroha J., von Delft J., Phys. Rev. Lett. 82 (1999) 2143.
[124] Schlottmann P., Philos. Mag. Lett. 81 (2001) 575.
[125] Cornaglia P.S., Balseiro C.A., Phys. Rev. B 66 (2002) 115303.
[126] Anderson P.W., Phys. Rev. 124 (1961) 41.
[127] Pastor G.M., Ann. Phys. (Leipzig) 14 (2005) 547.
[128] Krishna-Murthy H.R., Wilkins J.W., Wilson K.G., Phys. Rev. B 21 (1980) 1003; Krishna-Murthy H.R., Wilkins J.W., Wilson K.G., Phys. Rev. B 21 (1980) 1044.
[129] Ricardo-Chávez J.L., Pastor G.M., Comput. Mater. Sci. 35 (2006) 311.
[130] Suaud N., Pastor G.M., Evangelisti S., Maynau D., Chem. Phys. Lett. 378 (2003) 503.

Chapter 15

Modelling the structure and dynamics of metal nanoclusters deposited on graphite

R. Smith[a,*], S.D. Kenny[a], J.J. Belbruno[b] and R.E. Palmer[c]

[a]Department of Mathematical Sciences, Loughborough University, Loughborough, Leicestershire LE11 3TU, UK

[b]Department of Chemistry, Dartmouth College, Hanover, NH 03755, USA

[c]Nanoscale Physics Research Laboratory, School of Physics and Astronomy, The University of Birmingham, Edgbaston, Birmingham B15 2TT, UK

1. INTRODUCTION

Size-selected nanoclusters have attracted considerable interest recently because of the potential application of dispersed arrays of these clusters on surfaces. Metal clusters have application in electronics and catalysis and much experimental work has been undertaken to investigate the conditions under which the dispersed arrays of clusters can be formed. One way to form cluster arrays on surfaces is by the use of energetic cluster beams, for example Ag_N clusters can be deposited on a graphite substrate where N can be carefully controlled and ranges up to a maximum value of a few hundred [1, 2]. Gold clusters on surfaces have also been investigated [3, 4]. One of their applications is to form sites at which proteins or other organic molecules can bind suggesting the possibility of their use as nanoscale biosensors. In addition to Au and Ag, Ni clusters are also important since they have magnetic properties [5, 6], so there are a whole range of different metal nanoclusters on a substrate which have potentially interesting applications [4–12].

If the size-selected (i.e. specially chosen value of N) nanoclusters are projected towards the surface with a certain energy, then different energy deposition regimes result in different interaction processes between the cluster and the substrate. Depending on the energy, the clusters can soft-land and diffuse, pin on the surface or implant beneath. Experimental work linked to molecular dynamics (MD) computer simulations investigating metal clusters on graphite has shown that the clusters pin on the surface if a certain energy threshold E_P is surpassed [7, 8, 13]. Below E_P the clusters diffuse

The Chemical Physics of Solid Surfaces, Volume 12
ISSN: 1571-0785
DOI: 10.1016/S1571-0785(07)12015-0

*Corresponding author.
E-mail: r.smith@lboro.ac.uk

across the surface with high mobility and aggregate at defects. If the energy is increased further above E_P then the clusters implant below the surface [9–11].

Theoretical methods can be used to predict many of the experimentally observed features of cluster interactions with surfaces. This is not just important from a fundamental physics point of view but is also useful in helping to design nanostructures with certain prespecified properties. In addition, the atomistic simulations can be invoked to derive general principles which can be used as a guide in the design of experiments or the manufacture of nanocluster arrays. In this chapter, we discuss what has so far been achieved by atomistic computer simulation and where such methods might be further developed in the future. These ideas will be used to describe the physics of what happens during the energetic collision of the clusters with the surface as the energy of impact of the clusters with the surface increases. We will not discuss in depth the long-time diffusive processes that can occur after this initial energetic phase. In all cases, the substrate that will be used in the model will be graphite.

In order to be able to understand the cluster–surface interactions, we will first consider the bonding of small clusters to the graphite surface. This will be investigated by using ab initio calculations to determine bond strengths and atomic arrangements and also as a guide to parameterising classical potentials for use with larger-scale simulations. Such ab initio methods are very computationally intensive and limited so far to small systems. After this, classical dynamics potential functions will be described. The determination of the geometry of the clusters before impact with the surface will then be examined using these potentials. It will be shown that for this problem a genetic algorithm (GA) outperforms many other global optimisation algorithms for calculating the minimum energy (i.e. the most stable) configurations. Next, classical MD simulations will investigate the energetic interactions themselves. With this combination of approaches the whole energy regime can be investigated from soft landings where the cluster either sits on the surface or diffuses across, to the disintegration and implantation of the cluster below the surface as the impact energy of the cluster increases further. Finally, we discuss future prospects for this work and where the gaps can be filled to provide a complete theoretical understanding of cluster–surface interactions from the formation of the cluster through to the construction of nanostructured cluster arrays.

The work carried out to date is not a complete story and there are inevitably some gaps. Ab initio calculations are typically only possible with systems of the size of 100–200 atoms and only a few graphite layers, which means that the bonding arrangements of only small clusters can be determined. We consider here using ab initio methods for the bonding of metal clusters containing a maximum of five atoms to graphite although current computing power is such that as we write larger systems with clusters containing seven or more atoms can be considered. For application purposes, the work becomes more useful when cluster sizes are bigger than this, and impacts with clusters ranging from seven atoms up to a few hundred have been investigated experimentally. However, it is also important in studying the bonding of very small clusters to understand the basic physics and chemistry involved. The MD simulations are carried out on systems that are typically 1000 or more times larger than those considered in the ab initio study and with clusters that are the same size as those used in experiments. The interaction potentials used in the MD modelling do not always give results that agree with the ab initio predictions for the bonding

arrangements and even the MD simulations described here only examine the collisional phase of the interaction of the cluster with the substrate and do not consider the diffusive processes responsible for the long-time evolution of the clusters on the substrate. The collisional phase of the cluster–surface interactions is, however, well described. In addition, techniques are becoming available that will allow classical potential functions to be constructed that lie closer to the ab initio results. There are also other methods being developed that will allow the examination of the long-time evolution more easily. These are directions for future research in this field. Bearing these provisos in mind, there are still many useful examples where the modelling can help guide and explain experimental results. Modelling can be used to explain the bonding arrangements, experimentally observed pinning thresholds and implantation depths, deriving some general principles to help explain the cluster–substrate interactions in the different energy regimes.

2. AB INITIO CALCULATIONS OF THE INTERACTION OF SMALL METAL CLUSTERS WITH GRAPHITE

In this section, the bonding of Ag and Au adatoms and dimers to graphite is considered using ab initio density functional theory (DFT) calculations. This is interesting not only to have a more accurate understanding of how the small clusters attach to the surfaces but also so that the calculations can be used to determine parameters for classical potential energy functions. Here we describe the application of DFT for small Au and Ag clusters bonded to graphite.

2.1. Computational methodology

All DFT calculations were carried out using the programme PLATO [14]. This is a DFT code in which the Kohn–Sham eigenvectors are expanded in numeric atomic-like orbitals with a finite range. Pseudopotentials (and the exchange and correlation functional) are taken from the relativistic, separable, dual-space Gaussian scheme of Hartwigsen et al. [15]. Integrals for orbital overlap, kinetic energy, one- and two-centre neutral potential terms, non-local pseudopotential and ion–ion interactions are calculated and tabulated prior to use and interpolated during calculations. All other integrals are calculated numerically on an atom-centred mesh. Forces are obtained by differentiation of the total energy. Careful effort is made in locating the optimised parameters for the orbitals. In order to obtain the correct triangular structure for an isolated Au_3 cluster, for example, orbitals from Au, Au^{2+} and Au^{4+} should be included, supplemented by higher orbital angular momentum orbitals (resulting in a triple numeric plus polarisation basis set). The orbitals are forced to go to zero at a selected cut-off radius, the equivalent of confining the atom to a square well. In principle, there are three degrees of freedom available to optimise the orbitals; the charges on the ions, the cut-off radius and a smoothing distance. The charges are predefined and the smoothing distance is kept to the minimum value needed to have the orbitals and their derivatives go to zero smoothly at the cut-off radius. The cut-off radius is chosen so as to optimise the orbitals. The supercell for static optimisation contained a $4 \times 4 \times 1$ primitive cell for adatoms, Au_2 and Au_3 and a $5 \times 5 \times 1$ primitive cell for Au_4 and Au_5 to minimise the coupling between cells. A four-layer slab was used for atoms and dimers. For larger clusters, a two-atomic layer slab was employed.

In these cases, relative energies were unchanged by the addition of a third layer in the slab. All slabs were decorated with vacuum regions of 20 a.u. above and below. The local density approximation (LDA) was used throughout. The LDA provides better agreement, with respect to experimental values, bond lengths and harmonic frequencies, while overestimating the bond energies. The generalised gradient approximation (GGA) results in the opposite behaviour. The true calculated parameters lie somewhere between the LDA and GGA results. Both methods have difficulties in the description of weak interactions. The problem with the LDA is with the interlayer attraction in graphite, while the GGA underestimates the metal–adsorbate interaction. It is clear that issues are presented by either method, but since our conclusions involve relative results, the LDA is preferable since it provides a better adsorbate-graphite description. The energy and maximum force (in any direction) are converged to within 0.00001 Ryd and 0.0005 Ryd/a_0, where a_0 is the Bohr radius, for optimisation. For further details of the calculations the reader is referred to Refs. [16–18].

2.2. The structure of small isolated Au clusters

The structures for the small Au clusters are first calculated. For a gold dimer, PLATO returns a binding energy of 2.86 eV and a bond length of 2.53 Å, in good agreement with the experimental data of $\approx$2.61 eV and 2.47 Å. The ab initio calculations show that the Au_N minimum energy configurations for $N = 3$–6 are all planar in agreement with previous DFT results. Experimental results for these clusters, with the exception of the trimer, are not yet available. The DFT results are the structures shown on the left hand side of Fig. 1. The first non-planar structure is the symmetric seven-atom cluster. The structures shown on the right hand side of Fig. 1 are the minimum energy configurations calculated using a classical potential description. This potential will be described in more detail in the next section. The Au_3 and Au_7 clusters give the same minimum energy structure for both cases. The minimum energies for the structures are given in Table 1. The results highlight the inadequacies of the empirical potential for Au in that it both predicts too high cohesive energies for the very small clusters and also requires that the close-packed configurations have the lowest energy. The empirical silver potential used in this work represents the energetics better but still favours close-packed configurations.

2.3. Bonding of the clusters to the surface

Since the focus of this report is the interactions of adsorbates with surface, it is important that the calculations present a realistic prediction of the observed surface structure. The suitability of the PLATO formalism for graphite has been examined. The surface contraction, defined as the decrease in the distance between the top and second layers, was found to be 0.12 Å, a value greater than the experimental result, 0.05 Å. This discrepancy between computational and experimental results is attributed to the known DFT difficulty with weak interactions, such as the interlayer attraction in graphite. The layout of the atoms in the graphite surface along with a definition of the potential bonding sites is shown in Fig. 2.

For all adsorbates, we have calculated the binding energy at various points along the path between α- and β-sites along the ⟨110⟩ direction. The path is shown in Fig. 2. The adsorbate does not sit flat on the surface and the closest atom below the metal adatom is dragged slightly out of the surface by the binding. We distinguish here between the

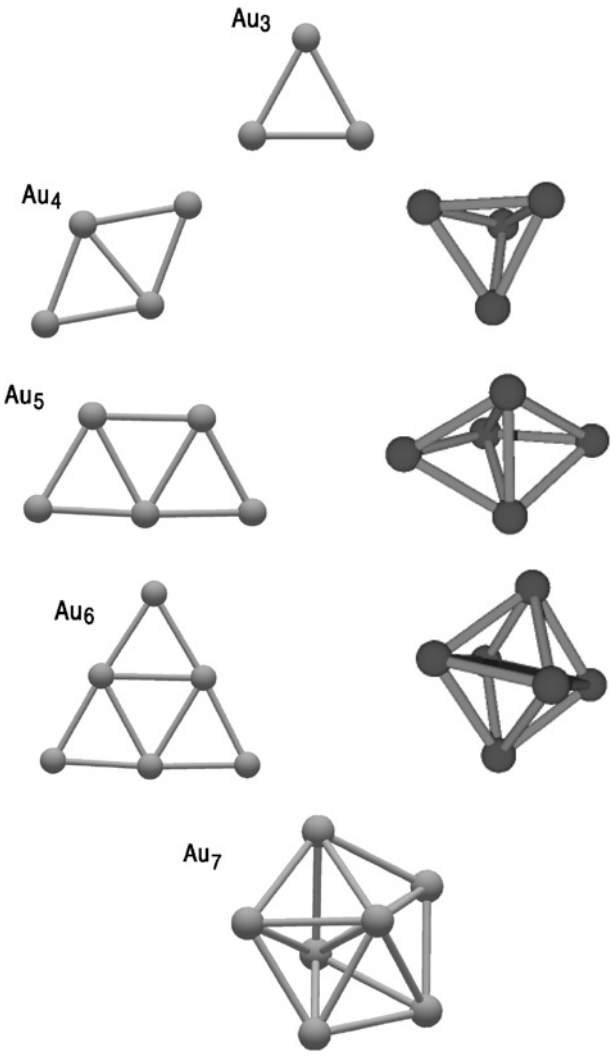

Figure 1: The minimum energy configurations of the small Au clusters calculated using PLATO (left images) and classical potentials (right series of images).

Table 1: Minimum energies E_N for the small Au clusters calculated by ab initio and classical potentials.

Size	Ab Initio (eV)	Classical (eV)
2	−2.86	−4.09
3	−4.61	−7.26
4	−8.01	−10.68
5	−10.84	−13.89
6	−14.63	−17.33
7	−16.94	−20.45

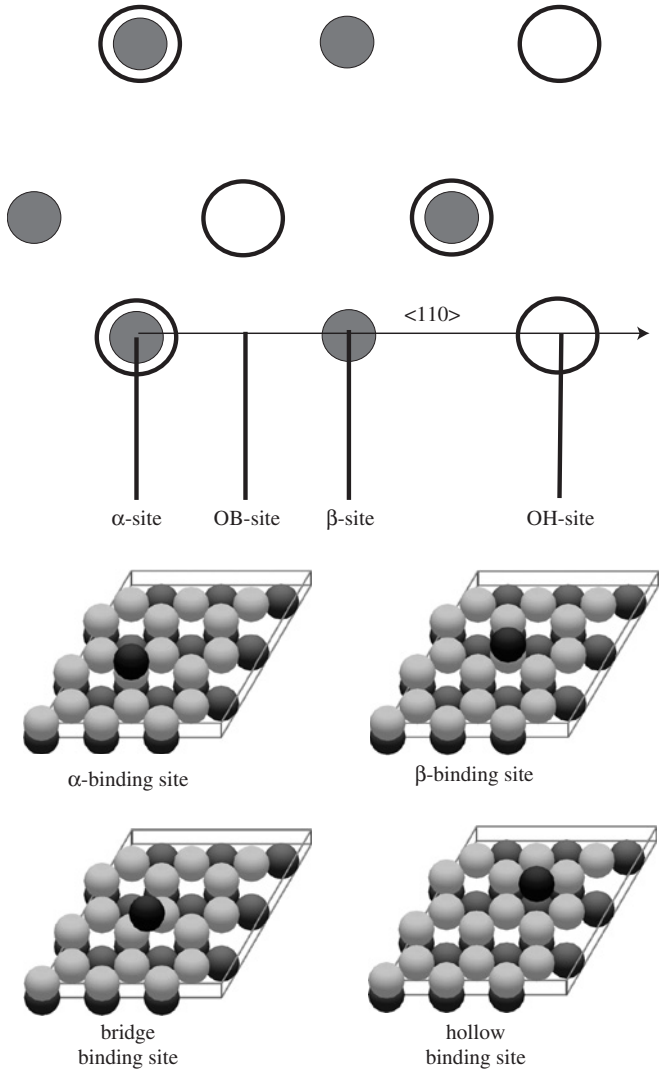

Figure 2: Layout of the graphite surface together with a description of the bonding sites considered for the adatom and dimer.

binding energy and the adsorption energy, both of which are the same for the adatom but differ for the small clusters. For the dimer, for example, the binding energy, E_B, is calculated as the dissociative energy of the dimer from the surface, E(system) – E(graphite) – 2E(atom), while the explicit dimer adsorption energy, E_A, is given as E(system) – E(graphite) – E(isolated dimer). The latter quantity assumes that the dimer bond energy on the surface is identical to its value in the gas phase. In Table 2, we focus on E_A values.

Results in Table 2 show that the β-sites are slightly preferred for both Ag and Au adatoms, but the differences in binding energy between various sites are not significant. The energy difference between the β-site and the over-hole (OH) site, the least

Table 2: Adsorption energies of the small Ag and Au clusters with the graphite surface along ⟨110⟩.

Site	Au Atom (eV)	Au Dimer (eV)	Au Trimer (eV)	Au Tetramer (eV)	Ag Atom (eV)	Ag Dimer (eV)
α	0.662	1.129	1.32	1.28	0.430	0.513
β	0.674	1.137	1.36	1.32	0.439	0.511
Bridge (OB)	0.654	1.154	1.36	1.32	0.434	0.523
Hollow (OH)	0.512	0.919	1.21	0.97	0.392	0.552

The lowest-energy gold dimer position is when the dimer axis is aligned near to the surface normal. The results for the Au trimer and tetramer are for vertically oriented planar clusters which are the lowest-energy configurations with the exception of the α-site for the Au trimer. In this case, a configuration with the trimer parallel to the surface is 0.02 eV more favourable at 1.34 eV [18]. The heights of the metal above the surface is 2.53 and 2.61 Å for the Ag adatom and dimer, respectively. The Au clusters vary in height between 2.79 Å for Au_2 and 2.31 Å for Au_4.

well bound of the binding sites, is only 0.05 eV for Ag and 0.16 eV for Au. This indicates that the energy landscape for the adatoms on the graphite surface is very flat. Such low barriers are an indication that diffusion over the surface would readily occur. The binding energies for the Au adatom and the dimer and the energy differences between the sites are larger than for the corresponding Ag values indicating that the gold adatoms and dimers are slightly less mobile than the silver ones [16]. Nonetheless, assuming a typical attempt frequency of 10^{13} for surface processes, the bonding energy differences between the various sites along the ⟨110⟩ direction would indicate a hop time of around 10^{-10} sec. This is inconsistent with the experimental results which indicate a longer hop time of a few minutes [19] suggesting a larger energy barrier between sites. This is therefore an area for future clarification.

Seven different configurations of silver dimers adsorbed on graphite were studied. Table 2 shows that the most favoured site is in agreement with the adatom case, since for the adsorption at the site labeled 'over-hollow', the centre of a dimer bond is situated at that point and the two silver atoms lie close to one α- and one β-site each. The dimer adsorption energy for all sites is approximately 0.5 eV. The surface binding energy per atom is approximately 0.25 eV, less than that for single adatoms. The maximum energy difference between possible binding sites is even smaller than that for the adatom sites. This implies that the dimers should be at least as mobile over the graphite surface as the adatoms. Experimentally, the observation of dimers was a rare event, which is consistent with a mobile adsorbed species that is almost free to move over the surface and eventually aggregates into the experimentally observed islands. When compared with single adatoms, dimers reside at a higher distance above the surface ($\approx$2.6 vs. $\approx$3.0 Å, for atoms and dimers, respectively, at β-binding sites). The two atoms of Ag_2 are not at the same height if they encounter different surroundings, as they generally do. The top layer of graphite is deformed to some extent by the adsorption process, but the second layer of the graphite is seldom disturbed at all. For the Au adatoms on graphite, the results indicate that, energetically, β-binding sites are the most favoured and hollow sites are the least favoured binding positions. This is in agreement with the scanning tunnelling microscope (STM) observation [19] that a gold adatom was typically located near a β-site and never observed over a hollow. While the energy differences among the α-, β- and bridge sites are small, the hollow site is significantly less favoured. The binding energies for gold adatoms are systematically larger than those for silver adatoms. The energy differences along this direction of the

surface are also greater for gold than for silver atoms. Decreased mobility was observed in the STM for gold, relative to silver adatoms [11]. Two other differences between silver and gold adatoms are computationally observed. Gold atoms are negatively charged when bound at any site, whereas silver adatoms are positively charged. Larger surface deformation in the region close to the metal adatom is induced by gold in comparison to silver.

PLATO has also been applied to the adsorption of gold dimers on the graphite surface. Binding configurations of a dimer initially oriented parallel to the surface, analogous to the silver dimer clusters, were studied. The most energetically favoured parallel case locates the two gold atoms close to one α- and one β-site, in agreement with the adatom results indicating a slight preference for over-atom binding sites. When compared to gold adatoms, dimers bind at a higher distance above the surface ($\approx$2.5 vs. $\approx$2.8 Å, for atoms and dimers, respectively, at β-binding sites). Since the two atoms encounter different surroundings, they are not necessarily expected to be located at the same height. Dimers over α- and β-sites feature a significant angle (see Fig. 3), while dimers for other binding sites are nearly parallel to the surface plane.

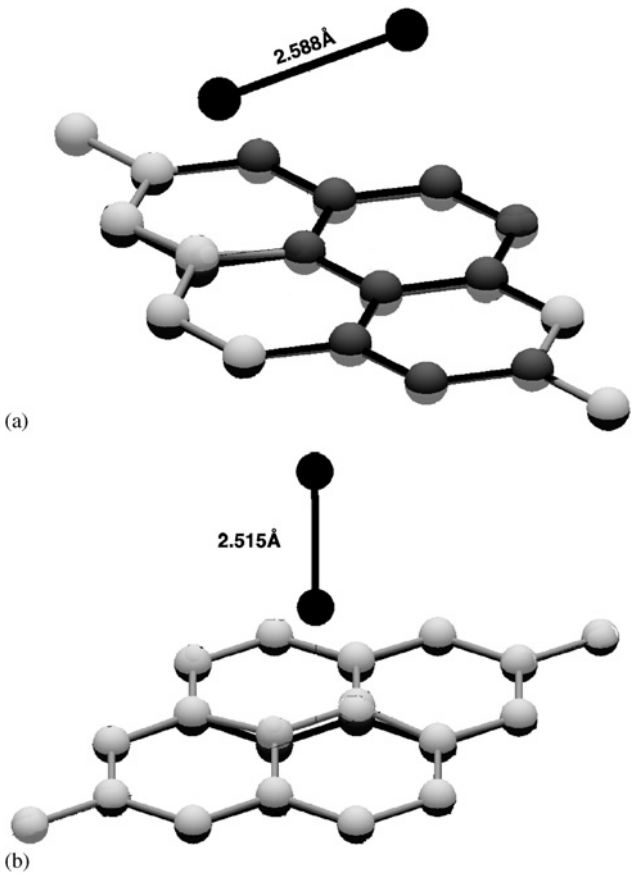

Figure 3: Two positions of the Au dimer on the graphite surface: (a) the Au dimer over an α-site and (b) the Au dimer over the bridge site.

The bond length of the dimers does not significantly vary with binding site. This implies that the internal interaction in the dimers is stronger than the dimer–surface interaction. This is also implied from the definition of adsorption energy of the dimer which is less than the sum of the binding energy for two single atoms.

The gold dimer may alternatively be oriented with the internuclear axis perpendicular, or nearly so, to the graphite surface (as shown in Fig. 3). The adsorption energies, calculated as E_A, are systematically larger than those for the parallel cases. At all binding sites, the optimised dimers are nearly perpendicular to the surface. A dimer over a hollow site is not stable and is expected to relax quickly to a position over one of the other three sites. One may draw the energy landscape of perpendicular dimers along the ⟨110⟩ direction. This landscape indicates that the dimer should be more mobile than the adatom. Relativistic effects could be a factor in the gold dimer preference for perpendicular orientations.

The interesting binding predicted for the adatoms and dimers of gold and silver points to consideration of larger clusters on the graphite surface. Energetics and configurations on graphite surfaces for Au_N ($N = 3$–5) were investigated using the density functional approach previously described. Isolated gold trimers have shown a small and energetically almost insignificant (50 meV) computational preference for triangular, D_{3h}, rather than linear, $D_{\infty h}$, configurations in good agreement with the reported experimental results. The small difference in the energies of the two conformers, however, could easily be affected by the interaction of an adsorbed trimer with the surface. Both triangular and linear forms were optimised first in an orientation parallel to the surface. The trimers and the surface were allowed to relax simultaneously during the structural optimisation. It was found that, contrary to the isolated trimers, the parallel, linear configurations consistently and regardless of the specific type of binding site, had significantly greater surface adsorption energy (1.35 eV) in comparison with parallel triangular structures (0.92 eV). The optimised over β-binding site structure shown in Figure 4 is an example of the results from this set of calculations. The starting geometry provided Au–Au bonds with a bond length equal to the surface lattice distance, but the optimisation resulted in changes so that the final bond length is much closer to that found in the isolated trimer. This relaxation was an indication that the gold–gold interaction was greater than the gold–graphite interaction. The gold trimers induced a surface polarisation and surface deformation. Gold atoms over β-sites drag up the underneath and nearby carbon atoms, but gold atoms over hollow or α-sites tend to depress the surface. The carbon atoms were displaced as much as 0.05 Å in height, but in-plane motion was limited to less than one-tenth of that.

Each gold atom in the linear cases was initially set over carbon atoms at the same height above the surface, but the unconstrained optimisation resulted in distortion of the linear shape. The final vertex angles for the cases of over adjacent β- and α-sites were 161° and 167°, respectively (see Fig. 4). The terminal gold atoms were closer to the surface and acquired a greater negative charge (–0.19e) than the central atoms (−0.10e). An optimisation involving an isosceles triangle geometry parallel to the surface was also attempted. During optimisation, the central gold atom had much greater range of motion than the terminal atoms and the trimer tended to evolve slowly to the nearly linear case with atoms over all β-sites. The motion of the gold atoms was along –C–C– bonds. The final energy of the system was nearly identical to that of the parallel, linear case. We noted earlier that gold dimers preferred a normal

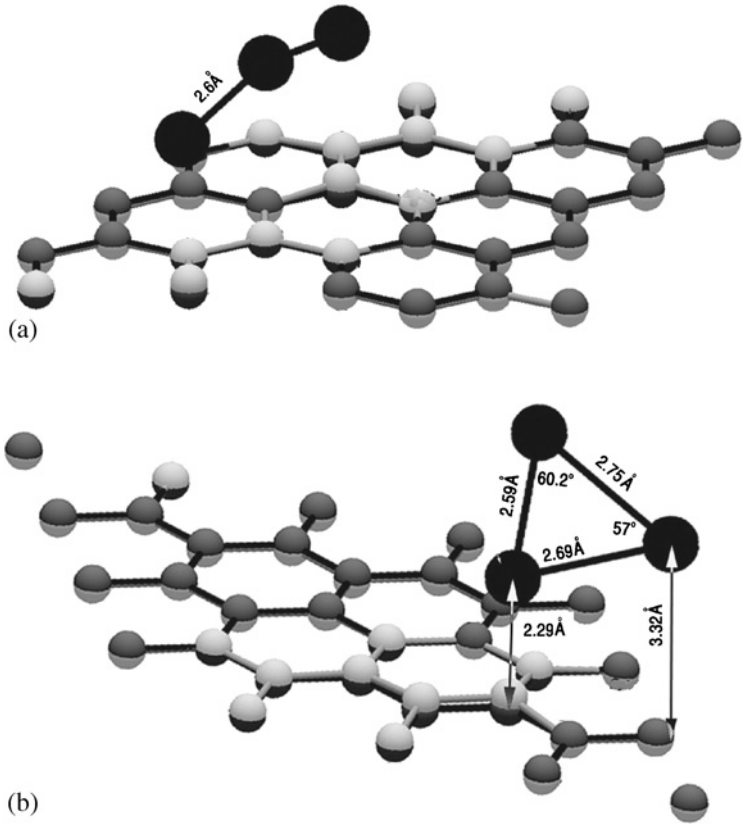

Figure 4: Two positions of the Au trimer on the graphite surface: (a) the linear trimer over a β-site and (b) the triangular trimer located initially over the β-site.

(to the surface) orientation. This result led to a test of such vertical orientations for the gold trimers. Figure 4 shows one such conformation over a β-site for a triangular gold trimer. With the exception of the unstable over-hollow site conformation, the adsorption energies for these orientations were approximately identical to those for the parallel linear cases. The carbon atom directly below the gold was significantly raised above the surface.

The similarities among the adsorption energies for the trimer configurations reflected the fact that the internal interactions of gold clusters dominated the metal–surface interaction. However, the insignificant difference between the linear and triangular geometry for an isolated cluster, 0.05 eV, and the nearly 0.4 eV energy differences observed on the surface indicated that, even though small, the cluster–surface interaction was important. This small cluster–surface interaction directed both the cluster geometry and the orientation of the cluster on the surface. The effect observed for the trimer on graphite points out the need for high accuracy methods in cluster–surface calculations.

The cluster movement from one binding site to another may be thought of as occurring through movement of the gold atoms along C–C bonds. There is some

literature precedent for vertically oriented clusters. Au_3 was previously reported to prefer a vertical orientation on the $TiO_2(1\,0\,1)$ surface. On $TiO_2(1\,0\,1)$, the trimer adsorption involved two gold atoms and two surface oxygen atoms. This difference in the two adsorption structures is most certainly reflective of the different structural and electronic properties of the surfaces. Graphite surfaces are flat and involve covalently bonded atoms, while $TiO_2(1\,0\,1)$ is ionic and the oxygen atoms protrude from the surface.

Moving on to Au_4, a single linear configuration was examined, because the adsorption energy for the linear conformer was significantly smaller (0.4 vs. 1.3 eV) than for non-linear cases; a reflection of the relative importance of the gold–gold vs. the gold–graphite interaction. The linear geometry was also unfavourable for isolated clusters. A square conformer of Au_4, oriented parallel to the surface had the smallest binding energy of all of the geometries examined. The preferred cluster geometry, as observed in the isolated cluster and shown in Fig. 5, was based on a rhomboid or diamond structure. This geometry supports a central gold–gold bond, allowing greater stability in comparison to the other possible structures. The data indicated that a vertical orientation of the diamond-shaped tetramer was preferred over a parallel configuration, but to a lesser extent than in the case of the trimers. The repulsive Pauli interaction for a parallel tetramer is greater than that for a vertically oriented molecule and the energy released upon binding to the surface is not sufficient to overcome this repulsion in the parallel case. This effect caused the tetramer in the parallel configuration to lie a considerably greater distance from the surface than for the vertical structure.

The optimised tetramer structure over a β-site on the graphite surface is shown in Fig. 5. These adsorbed tetramers had a stable planar structure, slightly distorted from that of the isolated cluster. The inner bond was approximately 12° from the normal to the surface. The carbon atom directly below the cluster was deformed away from the surface and was significantly negatively charged. For the deposited tetramers, the two bonds closest to the surface were elongated (2.70 and 2.74 Å), while the bonds distant

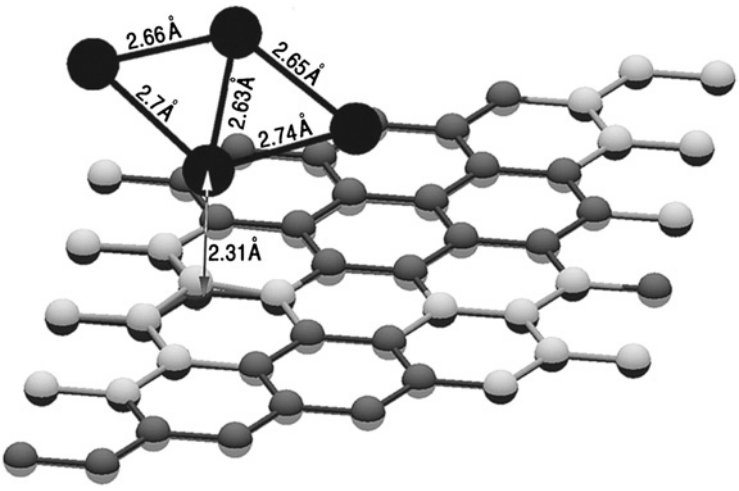

Figure 5: The position of the Au tetramer on the graphite surface initially over a β-site.

from the surfaces were contracted (2.66 and 2.65 Å). The closest gold atom was 2.31 Å above the surface. For a diamond-shaped Au_4 cluster oriented parallel to the surface, the four atoms do not remain in a plane; the terminal atoms were slightly raised from planarity. In this case, the Au_4 cluster depressed the surface. The inner bond was relatively shorter than the others. Here, the two terminal atoms were closer to the surface; the two carbon atoms below were raised above the surface and the central bond, parallel to surface, was longer than the terminal bonds by 0.15 Å.

Three cases of adsorbed gold pentamers were optimised. Preliminary testing indicated that vertical orientations were disfavoured; the results focussed on parallel orientations of the pentamer. When the planar pentamer was deposited so that all of the gold atoms were approximately over β-sites, the minimum energy was attained (see Fig. 6). This optimised structure maximises the number of metal–metal bonds and leads to greater stabilisation of the molecule. The nearly over β-sites orientation was approximately isoenergetic (within 80 meV) with that in which the gold atoms were nearly above α-sites. The direct interaction with the carbon atoms appears to be maximised by either configuration.

When the cluster interacted with the surface, the planar geometry of the Au_5 molecule was distorted. The centre atom remained at a greater distance from the surface than the remainder of the cluster. The bond lengths of the deposited pentamer were only slightly distorted from those of the free molecule. This pyramidal structure was a local minimum for isolated pentamers. The result that the parallel pentamer configurations were more stable than vertical orientations is consistent with the trend that was observed for smaller clusters. The preference for a vertical arrangement is strongest for dimers and decreases as the cluster size increases to Au_4. The increased number of gold–graphite interactions provides sufficient energy to overcome the Pauli repulsion at the surface. A square pyramidal structure was approximately 0.6 eV higher in energy.

In summary, therefore, we have performed a detailed investigation of the bonding arrangements of small clusters on graphite. There is some agreement with the limited experimental work in the literature but for application purposes larger clusters need to be studied. Expanding computational power will soon allow the investigation of larger clusters using ab initio methods, thus allowing a closer link to the applications. In the

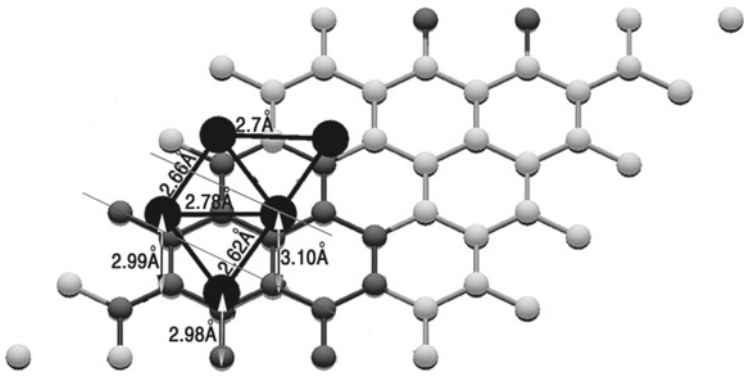

Figure 6: The position of the Au plane pentamer on the graphite surface initially over a β-site.

meantime, larger-scale dynamical simulations have been carried out using classical potentials and this work is now described in the following sections.

3. INTERACTION POTENTIALS

To model the energetic interaction of the metal atoms with graphite, classical potential energy functions are required as ab initio calculations are not yet feasible with current computing power for the number of atoms required to model keV cluster interactions with graphite. We used the same type of parameterisation for all three metal atoms types in the study, i.e. Ag, Au and Ni. This was a many-body embedded-atom potential function developed by Ackland et al. [20] and fit to bulk metal structures and not to close nuclear interactions. As a result, we splined the metal–metal potential to the two-body Ziegler–Biersack–Littmark (ZBL) screened Coulomb potential [21] for high interaction energies so that for small interatomic separation the potential was entirely determined by the ZBL part. The splining function was taken as an exponential of a cubic so that the potential and the forces are continuous at the splining points. The covalent C–C interaction for the graphite substrate was modelled by a many-body Brenner [22, 23] potential, also splined in the same way to the ZBL potential, while an additional long-range Lennard-Jones potential [24] between atoms that are not linked through a series of covalent bonds was employed to take into account the van der Waals interaction between graphite layers. This means that no two atoms in the same graphite layer interact through van der Waals forces.

The Ag–C, Au–C and Ni–C interactions were modelled by a pairwise Morse interaction potential. For Ag and Au, this potential was fitted so that the binding energy of atoms to the surface was as close as possible to that determined by the ab initio calculations described in the previous section. For the Ni–C interactions no ab initio calculations have been carried out and so the same pairwise Morse form for the bonding of the Ni atoms to the surface was chosen as for the Au atoms. As with the metal–metal interactions, splining to the ZBL potential was carried out so that close encounters could be more accurately simulated. The parameters for the Morse functions are given in Ref. [6]. Some earlier work used another potential to model Ag–C interactions [7] but the ab initio calculations found that this previous parameterisation overestimated the binding energy of the Ag adatom and dimer by about a factor of 2. Such an increase in the binding energy was found slightly to reduce the pinning threshold of clusters.

Although the parameters for the metal–carbon interactions were chosen as closely as possible to fit the ab initio binding energies, it is not possible to do this exactly with a pair potential and there are consequently some differences in the behaviour. The Ackland metal potentials also predict different behaviour in some cases. Two of these differences are highlighted here and have the same origin in that both the Ackland metal potentials and the Morse metal–carbon potentials are such that they prefer the atoms to arrange themselves in a close-packed formation. As already discussed, Fig. 1 shows that the ab initio minimum energy configurations for Au_N, $N = 4$–6 are all planar, whereas the Ackland potential gives three-dimensional structures. The cluster containing seven atoms has the same configuration for both and consists of five atoms arranged in a regular pentagonal structure with the other two atoms placed symmetrically above and below the pentagon. All faces of the seven

atom polyhedron are equilateral triangles. Although ab initio calculations for larger structures have not been carried out by us, it would be expected that the geometries determined by both approaches would be in better agreement as the cluster geometries become closer to the bulk configuration. Although the Ackland Au potential overestimates the binding energy of the clusters compared to ab initio calculations, the Ag potential gives values that lie much closer. For example, the Au dimer calculated using PLATO gives a binding energy of 2.86 eV and a bond length of 2.53 Å, whereas the Ackland potential gives 4.09 eV and 2.83 Å, respectively. For Ag PLATO gives 2.48 eV and 2.53 Å, whereas Ackland gives 2.53 eV and 2.52 Å with much better agreement.

Another illustration of the difference between the ab initio calculations and those from the empirical potential comes from the position of the adatom on the surface. To determine the interaction potential for the metal–C interactions, it was necessary to fit the Morse parameters in an appropriate way; however, it was not possible to capture all of the complete details of the interaction. It was possible to match the optimum height above the graphite surface for the adatom but for both Ag and Au the pair potential gave the over-hole site as the preferred minimum configuration rather than the β-site predicted by the ab initio calculations. The bridge site was also marginally preferred to the β-site. In both cases, this is as a result of the pair potential preferring the atom to attain the close-packed structure.

4. THE DETERMINATION OF CLUSTER GEOMETRIES

It would be expected that the structural arrangement of the atoms that make up a size-selected cluster should depend on the physical process by which the clusters are formed. There are many examples where the preparation conditions have a pronounced influence on the size of the cluster or molecule that forms during the condensation process or the form of the crystal structure for bulk materials, where, for example, rapidly quenched materials can take a different structure than materials quenched over longer times. In most of the experiments carried out in conjunction with our theoretical investigation, the clusters were formed by the condensation of ions and atoms sputtered from a silver target which condense by collision with inert gas atoms. Nucleation ceases after passage through a nozzle [8]. Size selection was carried out by the differential deflection of the charged clusters containing different numbers of atoms, in an electric field. The condensation process in the nozzle is complex and occurs over time scales that are much longer than those of atomic vibrations. Even assuming a good model for the force fields between all the objects involved in the condensation process, the integration time step for the dynamical system that represents the interactions is so small in comparison to the condensation time that a model of this process is not used. Instead, we assume that the clusters containing N atoms arrange themselves in the structure corresponding to their minimum energy configuration. Once the energy of interaction between the particles is known, the problem of determining the cluster structure is reduced to that of a global optimisation problem, i.e. determine the coordinates in space of the N atoms that minimise the interaction energy of the N atoms. This is a problem with $3N - 6$ degrees of freedom. (The -6 comes from the fact that the first atom can be fixed at the origin,

the second can be arranged along one of the cartesian coordinate axes and the third atom can be restricted to lie in the plane of the other 2.)

A recent investigation [25] has compared a number of different global optimisation algorithms for determining these minimum energy structures. The algorithms considered are multilevel single linkage (MSL) [26], topographical multilevel single linkage (TMSL) [27], topographical differential evolution (TDE) [28] and a genetic algorithm (GA) [29]. All are iteration (or generation)-based algorithms. Of these algorithms, MSL and TMSL have a similar algorithmic structure. They generate random points from the search space per iteration. On the other hand, TDE and GA do not generate random points per iteration. They maintain a set (population set) of candidate solutions (points in the search space), the size of which does not vary with iteration. They are known as population-based algorithms. Although they do not generate random points per iteration, they create new points, known as the children, using some genetic operators such as crossover and mutation. Newly created children in an iteration replace bad parents (bad candidate solutions) in the population set. Initial points in the population set are generated randomly within the search space. In all the test cases, the GA outperformed the other algorithms both in terms of the function evaluations required to determine the minimum energy structure and in the value of the minimum energy. The GA is described in detail in Refs. [25, 29]. Basically, to determine the minimum energy configuration of N atoms, it involves taking a parent population of M random arrangements of the N atoms, cutting each in two, randomly exchanging the halves and relaxing the produced child structures using a quasi-Newton method. Occasionally, a mutation is introduced. The best from the population of the parent and child structures are maintained and the process repeated. The advantage of the GA compared to a black box global optimisation approach is that it is physically based and uses the idea that an already existing cluster of atoms can be rearranged with knowledge of the configurations of other clusters. This evolution strategy, together with the relatively small number of candidate clusters required, gives it a considerable advantage over the MSL and TDE methods.

The convergence of the GA is only partially dependent on the symmetry of the cluster. For example, one might expect that symmetric clusters would be determined quickly by the GA compared to non-symmetric clusters. This is in fact only partially the case. Numerical experiments carried out for Ag clusters with atoms ranging from 35 to 40 show that the number of generations required to determine the minimum energy structure for the symmetric (the outer surface of 38-atom cluster takes the shape of a truncated octahedron) 38-atom cluster is not out of line with its neighbours. The results are shown in Table 3. Figure 7 shows the structure of the 38-atom cluster after one generation of the GA and its final optimised truncated octahedron structure. Although with any optimisation algorithm, one can never be certain that the global optimum has been reached, the minimum energy values given in Table 3 are in line with what would be expected. It is worth noting that because of the large number of nearby local minima that the convergence requires a large number of generations to fine-tune. For example, for the 40-atom cluster an energy value of –100.27 eV was obtained after 486 generations of the algorithm. It took a further 641 generations to reduce the energy by 0.02 eV to the final value.

Table 3: Minimum energies of Ag clusters with sizes close to the 38 atom symmetric configuration, calculated using the Ackland potential.

	Number of Atoms in Cluster					
	35	36	37	38	39	40
Number of iterations to convergence	118	384	811	487	709	1127
Cluster potential energy (−eV)	86.70	89.55	92.34	95.40	97.78	100.29
Energy per atom (−eV)	2.477	2.488	2.496	2.510	2.507	2.507

The GA was run for 1500 generations and the generation number for which the final lowest energy value was obtained is given in the second row. The population size was 40 and the initial population was generated by randomly arranging 40 sets of atoms in a cube of side 11 Å. Note that the energy per atom for the symmetric 38-atom cluster is larger in magnitude than for the adjacent clusters.

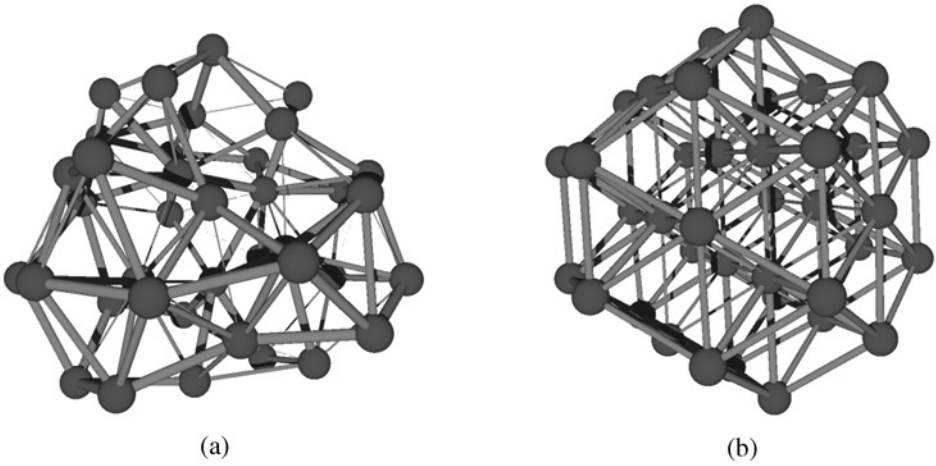

Figure 7: (a) The geometry of the lowest-energy 38-atom cluster in the population after one generation of the GA starting from 30 random arrangements of atoms in space. (b) The final truncated octahedron structure after 487 generations.

5. MOLECULAR DYNAMICS METHODOLOGY

MD simulations were carried out first to determine the pinning thresholds of the clusters on the surface and then as the energy of impact is increased to determine their implantation depths. To model the dynamic interaction of a cluster with the substrate, the cluster was first placed above the substrate outside the potential interaction range. The internal kinetic energy of the cluster could be varied but most simulations were carried out with internal kinetic energy before impact corresponding to a temperature of 300 K. MD simulations are always a compromise between speed of the calculation and the choice of a realistic system size or integration time. Numerical experiments are therefore carried out to determine an optimal substrate size to use in the simulations and the length of time for which the collision process is followed. It was found by numerical experiment that pinning thresholds could be determined without influence of the boundary conditions if a system of size 180 Å × 180 Å with nine graphite layers was chosen [6]. This size was found to be sufficient for modelling the impact of clusters

containing up to 200 atoms impacting with an energy up to 2.5 keV in that increasing the numbers of atoms beyond this did not change the calculated pinning thresholds. The carbon atoms at the vertical edges were fixed and adjacent atoms undergo a damped force to prevent lattice displacement waves reflecting back into the impact zone. These waves are quite strong and can displace the surface layers by several Å. They propagate in a hexagonal manner from the impact point [30] and can affect the pinning of the cluster if the reflected waves are strong. Such clearly visible surface ripples only occur in layered structures such as graphite. To determine the implantation depths of the clusters whose impact energy varies up to 5 keV, it was necessary to increase the depth of the target to 16 layers and to save on computing time the area of the target was less than that used for the pinning thresholds [11]. The collisional process was typically followed for up to 10 psec. For both the pinning and the implantation calculations, integration was carried out using a variable time-step [31] which increases as the maximum kinetic energy of any particle in the collision decreases. Some simulations were followed for up to 12 psec to check that collisional process was truly over. Atomic motion can certainly occur after this time but this is as a result of diffusive rather than collisional processes.

6. PINNING CLUSTERS ON SURFACES

Arrays of size-selected clusters on surfaces have many applications and one way to accomplish the deposition of such arrays is by direct use of an energetic cluster beam rather than by chemical methods. If such a cluster beam is used then it is important to know the physics of how the interaction takes place. The ab initio calculations for the small metal clusters have shown that whereas the binding energy of the clusters to the surface (see Table 2) is sufficient to prevent most clusters from 'evaporating' at room temperature, the energy barriers for diffusion across the surface are very small. Unpinned clusters would diffuse at room temperature and eventually find defects in the surface to which they would bind. Thus, if the energy of the beam is sufficient to induce a surface defect but not so large as to destroy the cluster, then pinning would occur. A key aspect then is to determine what the energy threshold E_P is for pinning the clusters.

The metal clusters under consideration are all comprised of atoms from metals that adopt the fcc close-packed structure in the bulk, namely Ag, Ni and Au, so that the main difference in the energetic interactions ought to be as a result of the different cluster masses. In order to determine the pinning thresholds, for each cluster size, the cluster energy was increased in steps of 25 eV until a permanent defect in the substrate was observed. Only one cluster orientation and impact point was considered in generating the results since test calculations showed that the effect of impact point and orientation for large clusters affected the results by at most ± 25 eV. Because the calculations were only carried out in increments of 25 eV, a finer uncertainty cannot be determined without further calculations.

Since the atomic spacing for Ag and Au atoms is similar, the main differences between the computed results for Ag and Au should be due mostly to the different masses of the impacting clusters. The mass ratio between Ni and Ag is similar to that between Ag and Au, so differences between the Ni and Ag results compared to the Ag

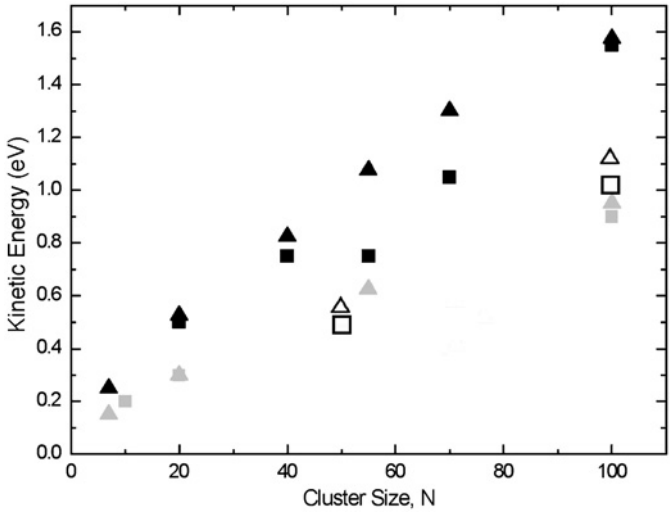

Figure 8: The pinning energy thresholds for Au (dark symbols), Ag (open symbols) and Ni (grey symbols) clusters. The square symbols are the experimental results and the triangles the MD. There is an uncertainty of about ± 25 eV in the MD results dependent on the precise impact point and cluster orientation.

and Au data should be due to the different cluster sizes. All simulations were for normally incident clusters.

The level of agreement between the experimental pinning thresholds obtained from STM after deposition at different energies and those obtained from the MD simulations, as shown in Fig. 8, is remarkably good overall. Generally, there is also a slight over-prediction of the value of E_P compared to experiment. Although the curves are shown as passing through the origin, it is meaningless to consider very small clusters since for one to three atoms the impact point becomes important and it is then necessary to run a representative set of trajectories to determine average behaviour. In fact, pinning in the surface for small clusters, from $N = 1$ to ≈ 5, becomes a less common occurrence than implantation beneath (if the energy is too large), reflection or entrapment in the surface binding potential without pinning (for smaller energies).

The simulations also show a variety of detailed atomic processes leading to the formation of a surface defect and hence the pinning of the cluster. One mechanism is when at least one C atom in surface layer under the cluster is knocked into an interstitial position between the first and second layers and replaced by a cluster atom [7]. Although this is a common mechanism, some other mechanisms were also observed. In some cases, a first layer C atom could be knocked into an adatom position above the surface. In another example, a cluster atom could become trapped between the first two graphite layers which themselves remained broadly intact. A final mechanism involves the formation of a 'crease' in the surface where two or more surface C atoms begin to form bonds with corresponding second layer atoms while retaining their first layer neighbours. The length of the bond between atoms in the first layer and second layer is longer than that between those in the first layer at around 2 Å, so this appears to be an intermediate stage towards an sp^3-bonded configuration induced by the local momentum transfer to the substrate.

It is interesting to examine in detail the energy required to induce these processes. As a background, the formation energy of a vacancy in graphite, E_{VF}, has been determined experimentally as about 7.0 eV [32]. Reported values of the interstitial formation energy are somewhat smaller, lying between 5.5 and 7.0 eV [33]. However, the amount of energy required to be imparted to a stationary C atom in a lattice at rest, to remove it permanently from its lattice site (the displacement energy threshold E_D) is 33 eV [24].

6.1. A simple model for the pinning thresholds

A simple relationship for the pinning thresholds as a function of cluster size can be determined based on a binary elastic collision model, treating the impacting cluster as a single object. If we assume that, at the moment of impact, we have a 'heavy' body (the cluster) colliding with a light body (the recoil carbon atoms in the top layer that lie under the cluster), then from conservation of energy and momentum for an elastic collision, the energy transferred to the recoil carbon atoms, E_{Tr}, is given by

$$E_{Tr} \approx 4\frac{N_C M_C E_P}{N M_{Clus}} \tag{1}$$

where M_C is the mass of the carbon atom, N_C the number of carbon atoms set into motion by the impact and M_{Clus} the mass of the cluster atoms. If a certain value of E_{Tr} is to be surpassed before a C atom displaces, then E_P can be determined. The original assumption was that only one C atom was set in motion [5, 8], so that $N_C = 1$ and then $E_P \propto N$.

However, analysis of the MD simulations shows that the cluster sets in motion a number of atoms simultaneously so if we assume the worst case that these are all atoms in the first layer lying under the cluster, then $N_c \propto N^{2/3}$ and then $E_p \approx N^{1/3}$. We might, therefore, expect a dependence of E_P with N that was somewhere between these two extreme cases.

A log plot of E_P against N gives $E_P \propto N^s$, with $s \approx 0.6$, for the Ag, Au and Ni data. This lies within the expected range of $1/3 < s < 1$. The above formula also predicts that $E_P \propto M_{Clus}$ when cluster atoms have the same atomic spacing. Since Au and Ag have approximately the same lattice constant, the proportionality should then hold. Indeed, if we consider the 55-atom cluster with the calculated values of E_P to be 600 [8] and 1075 eV for Ag and Au, respectively, the ratio of these threshold energies is 1.79, whereas the mass ratio is 1.84 which agrees very well. However, the pinning thresholds for Ni are only slightly less than those for Ag, despite the mass ratio being 1.83, almost the same as that between Au and Ag. In this case, the Ni lattice spacing is 14% smaller than for Ag, so that for Ni clusters the energy density deposited in the surface is more concentrated and fewer surface atoms are set in motion. The optimisation process shows that the Ni and Au clusters of equivalent size have the same morphology before impact. They also have similar cohesive energies so the differences between the values of E_P are mainly due to the smaller lattice constant for Ni and the heavier mass of the Au cluster.

In order to determine the value of E_{Tr} from the simulations, the kinetic energy of the atoms in the graphite lattice was monitored so that a value for each atom could be determined. This shows that for the Au cluster impacts the maximum kinetic energy of a substrate C atom occurs between 100 and 200 fsec after the cluster impact with the

surface. The maximum kinetic energy transferred to an atom was found to vary between 4.75 and 6.25 eV irrespective of cluster size in the range $N = 7$–100, but dependent on the impact position and orientation. These values are similar to the vacancy or interstitial formation energies reported above. Since, the MD simulations show that a number of atoms lying under the cluster are set in motion simultaneously. The result is that surface defects can form without an atom having to attain anything approaching the energy of E_D.

The morphology of the Ni, Ag and Au deposited clusters, 10 psec after impact at energies corresponding to the pinning thresholds, is shown in Fig. 9. These simulations show that the Au clusters are more spread out after impact while the Ni clusters are more compact. The Ag clusters lie somewhat between. In fact some fragmentation of the Au clusters takes place. The small fragments are not pinned but trapped in the surface binding potential and would be expected to diffuse over the surface and recombine because of small energy barriers.

Although some caution is required in interpreting height data from experiment due to tip convolution, electronic and oxide effects, the heights of the clusters in the simulation are in general agreement with the ambient STM measurements obtained from sampling a range of clusters on the surface [5]. The measurements show that the most commonly observed cluster height for the Au_{55} cluster at 1.15 keV is that of a single adatom layer, whereas for a Ni_{250} cluster deposited at 1.8 keV, the most common height is three layers above the surface. The images shown in Fig. 9 confirm the general observation that Ni clusters are higher whereas Au clusters are spread out.

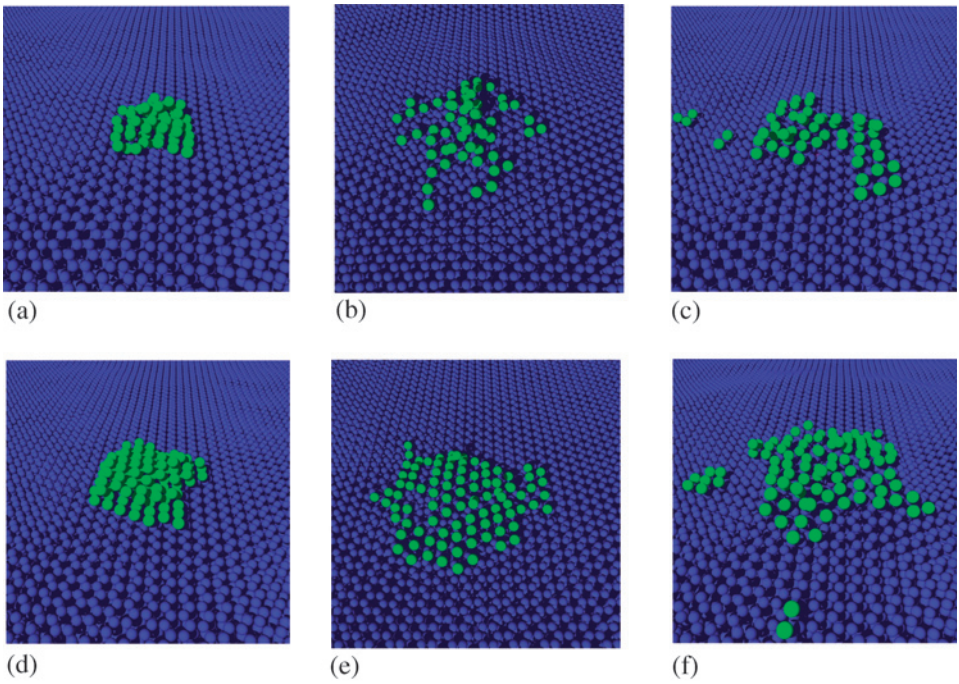

Figure 9: Images of the pinned clusters on the graphite surface: (a) 55-atom Ni cluster, (b) 55-atom Ag cluster, (c) 55-atom Au cluster, (d) 100-atom Ni cluster, (e) 100-atom Ag cluster and (f) 100-atom Au cluster.

Both the Ni_{55} and Ni_{100} clusters are quite compact with up to four layers of Ni atoms whereas there are only a few second layer adatoms for the corresponding Au clusters.

In summary, the pinning energy threshold E_P varies with cluster size scaling with N^s, where $s \approx 0.6$. Comparison of different kinds of clusters indicates there is also a dependence of the pinning thresholds on the cluster mass with the heavier clusters requiring a larger energy to pin. The extra momentum required for the heavier clusters means that they are less compact after pinning and cover a bigger surface area than the lighter materials. This observation is in agreement with experiment STM measurements.

The modelling is also consistent with other experimental observations. The binding energy for small clusters, calculated by ab initio methods, is very similar at different sites on the defect-free surface and it would be expected that the same would apply for larger clusters. Thus, unpinned clusters would be highly mobile and diffuse to surface defects. Below the threshold for pinning, STM images of large areas of the graphite surface show no clusters.

7. LOW-ENERGY CLUSTER IMPLANTATION

In addition to the manufacture of nanostructured cluster arrays on surfaces, cluster implantation beneath the surface also has potential application. Unlike implantation by single ions, in graphite clusters can create an open tunnel at the bottom of which lie the original cluster atoms [34, 35]. This could lead to catalytic applications with enhanced thermal stability. In other cases, cluster beams could be used in silicon technology for shallow implantation applications by reducing the spreading of a beam due to space charge effects [36]. In this section, we consider the fate of Ag_N clusters impacting at slightly higher energies than used for pinning so that the clusters implant below the surface. The energy range considered varies between ~0.5 and 15 keV depending on the cluster size.

The implantation of Ag clusters into graphite is a good example of a case where theory can be used to guide experiment and even help refine the experimental technique. To investigate experimentally the depths to which Ag_7 clusters implanted into graphite, a negative-ion beam source was used [10, 34]. The flux was chosen low enough so that pits caused by individual cluster impacts were separated sufficiently that they could be imaged in the STM. The depth of the pits was measured using the STM tip. However, the tip was too wide to fit into the hole and so an oxidising etching process was used initially at a temperature of 650° for times of up to 5 min, to increase the lateral width of the damaged region so that the tip could be inserted into the hole and the depth measured. Figure 10 shows the comparison between the MD simulations and the first experimental results for 5 keV Ag_7 implantation at normal incidence into graphite. The experimental results measure the depth of the hole and the simulation results the position of the implanted ions. It can be seen from Fig. 10 that the most likely damage depth determined by MD is always about three monolayers deeper than the experimental results. Further experiments conducted by oxidation and annealing at different temperatures confirmed that the high temperature annealing induced a recovery in the damaged layers at the bottom of the hole where the ions had implanted. However, at the lower temperatures the oxidation process took a much longer time to complete. By using the results of the simulations we were able to

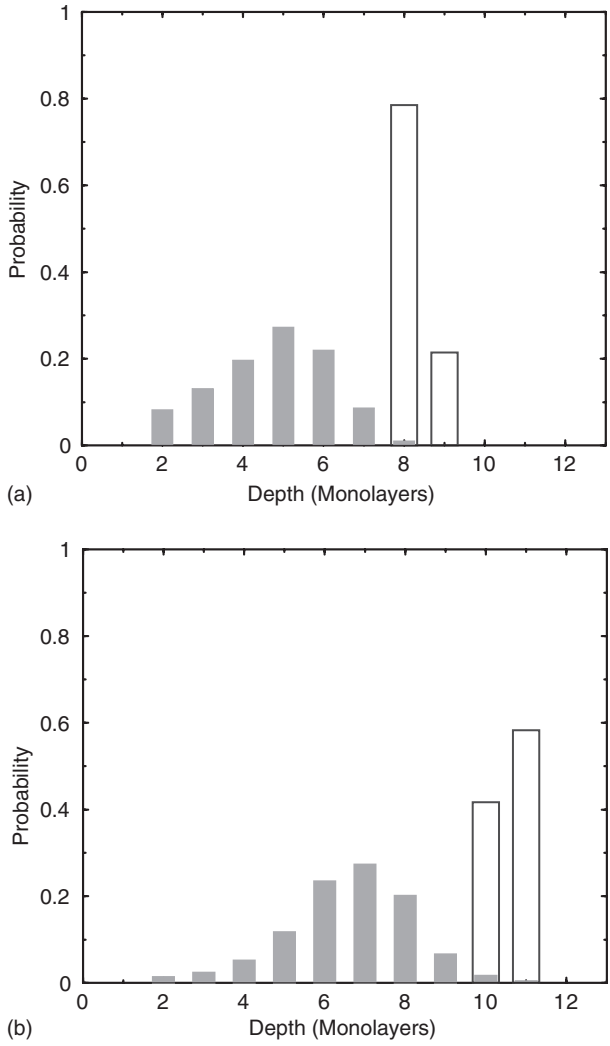

Figure 10: A comparison between the 'raw' experimental data and the predictions of the MD simulations for (a) 3 keV Ag_7 impacts at normal incidence on graphite and (b) 5 keV. The shaded bars are the experimental data and the unshaded the MD results.

determine that the peak depth of damage induced by the cluster before annealing could be determined from the experimental Gaussian depth profiles as corresponding to two standard deviations greater than the measured peak after annealing [11].

For a given energy, there is a difference in behaviour between the small clusters and the larger clusters as they pass through the graphite layers, since the smaller clusters travel much faster, see Figs. 11 and 12. It will be shown that this leads to different scaling laws where the implantation depth changes from a linear dependence on energy for large slow clusters to a linear dependence on velocity for small faster clusters. Figure 13 illustrates the slowing down process of both an Ag_7 and Ag_{50} incident normally with an energy of 5 keV on graphite, in (a) the z velocity of the centre of

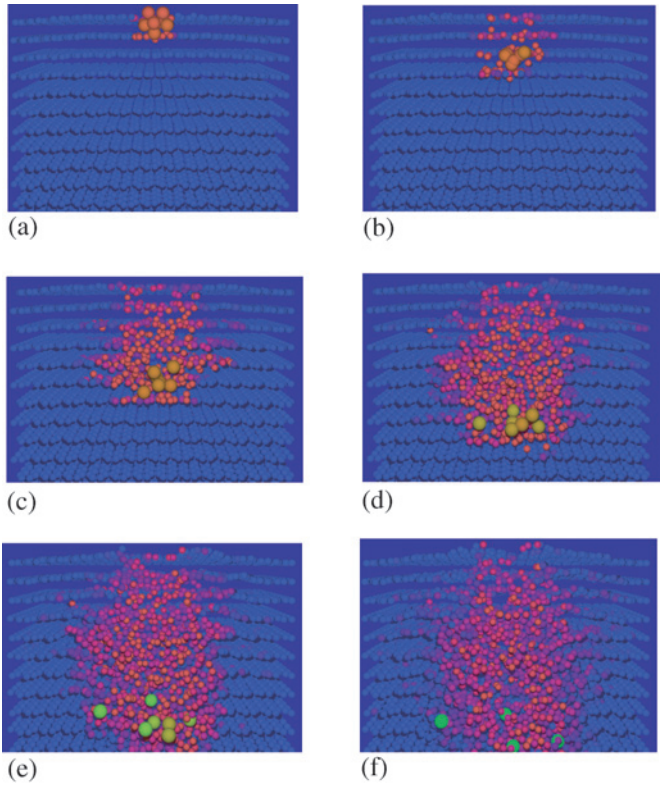

Figure 11: Snapshots of the position of the Ag_7 cluster as it implants into the graphite surface over the first 0.5 psec of its trajectory.

mass, υ_z (normal to the surface) of the cluster is plotted against the implantation depth z. The z coordinate is measured with respect to the first graphite layer. The diagram clearly shows that the cluster approaches the surface with a constant velocity before slowing down in such a manner that $d\upsilon_z/dz = \text{const}$, until the end of the range is reached. In Fig. 13b the kinetic energy K_z associated with υ_z of the Ag_{50} cluster is plotted as a function of depth. In this case $dK_z/dz = \text{const}$, until the end of the range. Figure 13c shows a comparison between the implantation depths of the Ag_7 cluster and the cluster velocity before impact. The upper abscissa value of 0.4 Å fsec^{-1} corresponds to an energy of about 6.3 keV. It can be seen that there is a linear dependence on implantation depth with cluster velocity over this energy range for the Ag_7 cluster. In Fig. 13d the implantation depth for the Ag_{50} cluster is plotted as a function of the initial energy of the cluster. Here, for small energies there is an approximately linear dependence of depth with energy, which changes to a dependence more akin to that for the Ag_7 cluster as the energy increases.

This difference in behaviour can also be understood by comparing snapshots of cross-sections through the graphite substrate as the cluster penetrates. Figures 11 and 12 compare these cross-sections for the case of an Ag_7 cluster incident at 5 keV (714.3 eV per atom) with the impact of a 200-atom cluster at 5 keV (25.0 eV per atom). At the start of the implantation process, the Ag_7 cluster breaks through the first

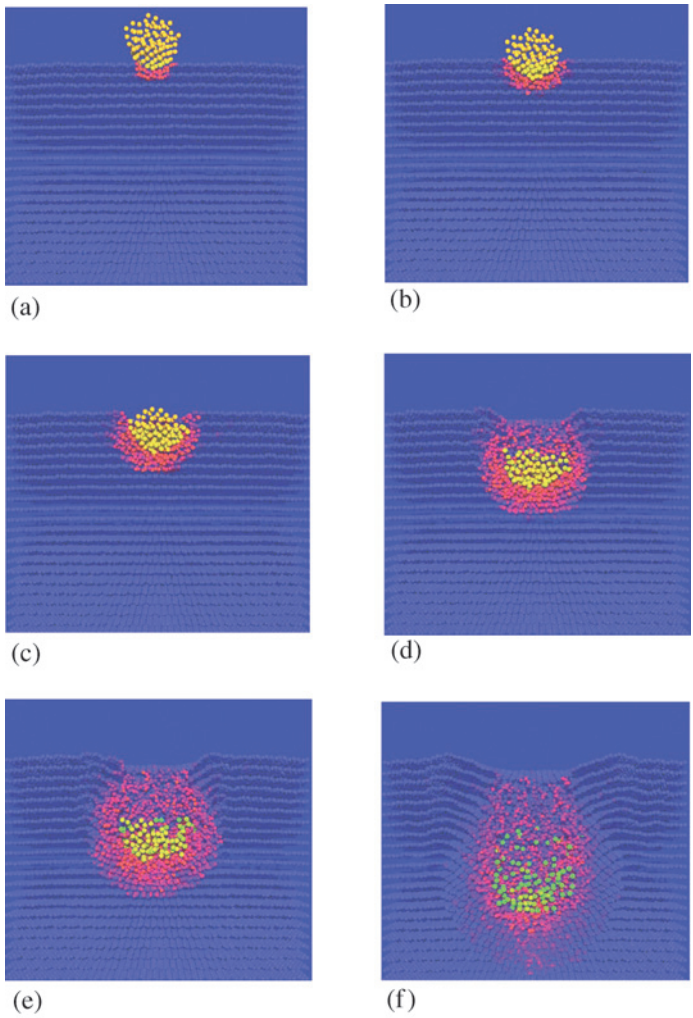

Figure 12: Snapshots of the position of the Ag_{200} cluster as it implants into the graphite surface over the first 0.5 psec of its trajectory.

graphite layer and reaches the next layer before any carbon atom sets in motion by the collision with the first layer. The Ag_{200} cluster, on the other hand, first causes the graphite layer to bend rather than the cluster passing through and breaking bonds. It then pushes the carbon atoms in the graphite layer ahead of the cluster so that they interact with the next layer before the cluster atoms. It is this basic difference in the form of the collision cascade that leads in the first case to the linear decrease in the cluster velocity with depth and in the second case to a constant stopping power for the cluster.

The regime where the implantation depth is proportional to the energy is valid for clusters of size 20–200 and energies up to about 100 eV per atom. This is shown in Figure 14. Although the linear dependence with impact energy is apparent for each

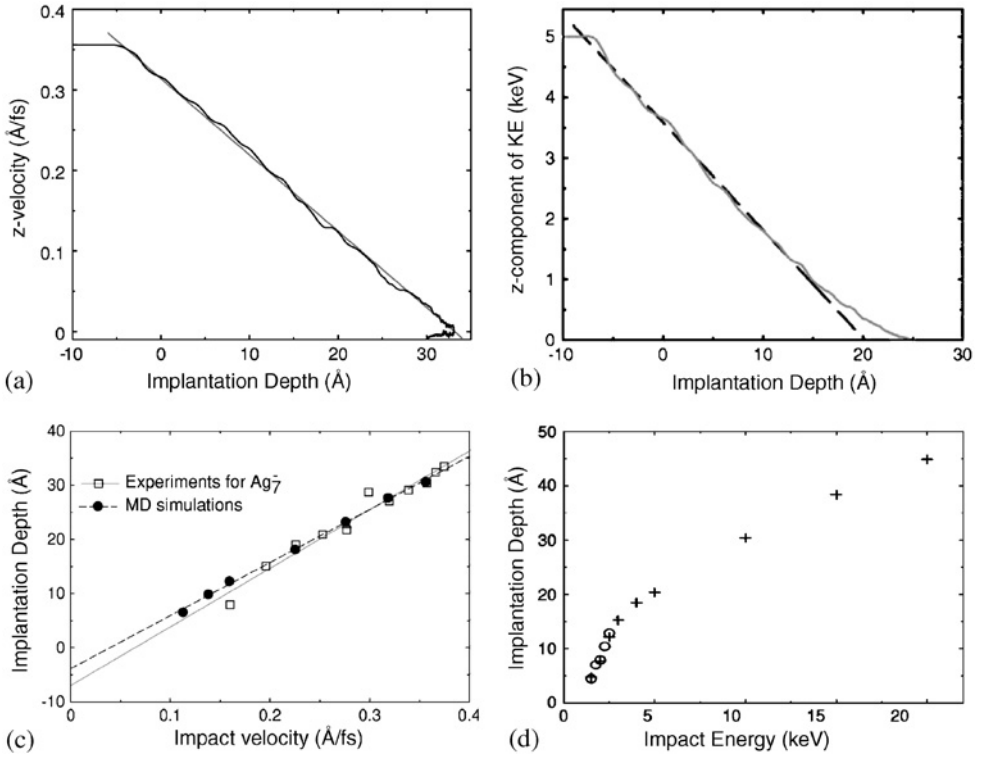

Figure 13: (a) The velocity component, perpendicular to the surface, v_z, of the centre of mass of the Ag_7 cluster incident normally on graphite at an energy of 5 keV plotted as a function of depth (z). Note the linear decrease in velocity as the cluster slows down and comes to rest at a depth of around 3 nm. (b) The kinetic energy, K_z, associated with v_z, for the Ag_{50} cluster incident normally on graphite at an energy of 5 keV plotted as a function of depth (z). Note the linear decrease in K_z for most of the range as the cluster slows down and comes to rest at a depth of around 2.5 nm. (c) The implantation depth of the Ag_{50} cluster plotted as a function of impact velocity. Note the linear dependence. The experimental data is taken from the upper end of the distribution after annealing as discussed in the text. (d) The implantation depth of the Ag_{50} cluster plotted as a function of impact energy.

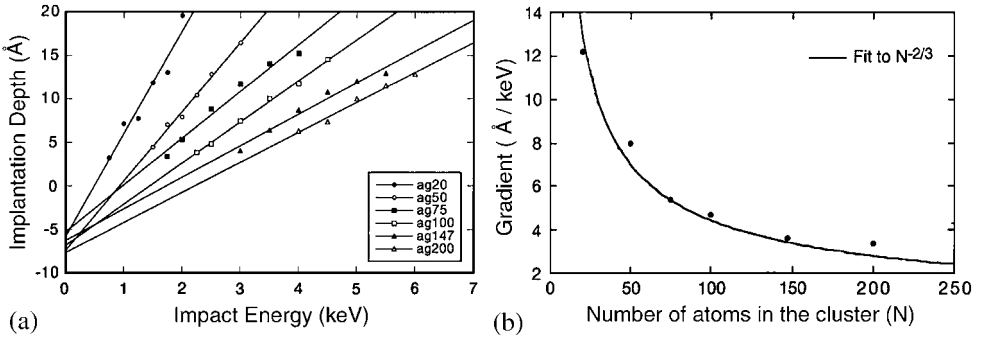

Figure 14: (a) The implantation depth plotted as a function of the impact energy for the large 'slow' clusters showing a linear scaling with depth. (b) The dependence of the gradient in (a) on the cluster size (N).

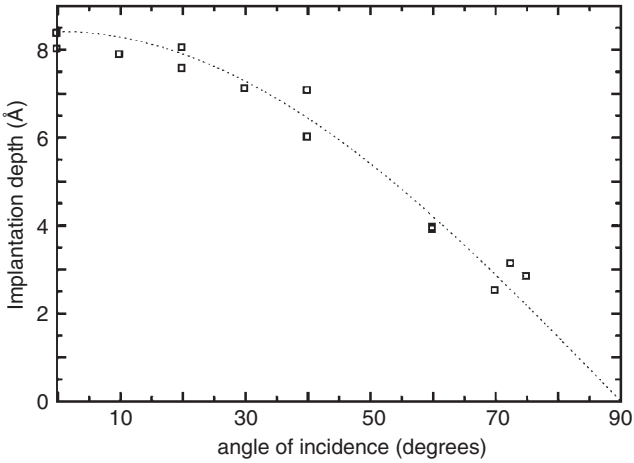

Figure 15: The relationship between the implantation depth and the incidence angle for Ag_{25} cluster impacts at 3 keV. The dotted line is a cosine curve.

cluster size, the gradients of the lines shown in Fig. 14a are all different. Figure 14b shows a plot of the gradients of these lines vs. the cluster size N. The data fit well to an $N^{-2/3}$ scaling, meaning that the implantation depth $D \propto E/N^{2/3}$. The explanation for this is given in Ref. [10], namely that the energy E expended before the cluster comes to rest is proportional to number of carbon atoms with which the cluster collides, i.e. linearly dependent on the product of the implantation depth D and the cross-sectional area of the cluster $kN^{2/3}$ for some constant k. Rewriting this last relation gives the result $D \propto E/N^{2/3}$.

In addition to normal incidence clusters, the variation of implantation depth with incidence angle can also be investigated. Several simulations were performed projecting a 3 keV Ag_{25} cluster onto the centre of a $50 \times 50 \times 36\,\text{Å}^3$ graphite slab. This graphite lattice contained 12 layers, which were more than enough to slow down the 3 keV cluster. Different angles of incidence were considered. Figure 15 shows that the variation is cosine-like for angles up to about $\sim 75^\circ$. The number of silver atoms deposited on the actual surface itself increased with incidence angle (measured relative to the normal) up to $\sim 75^\circ$. For higher angles, no silver atom was implanted inside the surface. At these oblique incidences, the cluster footprint on the surface is also more spread out and takes an approximately elliptical shape as would be expected by a direct projection of the cluster cross-section.

In summary, therefore, implantation of size-selected energetic clusters with graphite have shown good agreement with experiment, helped to guide experiment and also allowed explanations of the physical processes involved through the use of simple dynamical models.

8. CONCLUSION AND FUTURE PROSPECTS

Ab initio calculations have been carried out to determine the bonding arrangements of small clusters both as stand-alone systems and also bonded to a graphite surface. The

small cluster energies and bond lengths were in good agreement with experiment but so far there is no experimental data to confirm the predictions of all the cluster arrangements on the surface. Larger cluster minimum energy structures could be determined by a novel GA approach. Classical MD simulations have been carried out to investigate both the pinning of size-selected clusters on the graphite surface and the implantation of metal clusters below the surface. The pinning energy thresholds have also been shown to be in good agreement with experiment as were the implantation depths and indeed helped to guide the experimental technique. In addition, some simple formulae could be established to predict pinning thresholds and implantation depths.

There are of course some gaps in the story. Only small systems have so far been analysed with the ab initio methodology. In addition, we have not examined the bonding of the clusters to surface defects by ab initio methods. Computing power is rapidly becoming available that will make investigations of larger clusters possible, so this is certainly an area where future advances seem certain. The classical potentials used in the MD methodology also have their origins in the 1980s. They are not always consistent with the predictions of the ab initio models. Thus, MD simulations are demanding better potentials to describe the bonding of the atoms. The reason that they work so well for the pinning and implantation studies is that the physical processes are dominated by collisions between atoms and not by bonding. The existing classical potentials are very good for describing collisions between atoms. The 'attractive' part of the classical potential description could be better described by fitting to ab initio data. This is a topic of current research and the use of neural networks to fit such potential energy surfaces seems to bear some promise [37]. Another area which requires further study concerns the processes involved with diffusion of clusters over the surface. This requires a different approach than a direct time integration using MD since a typical MD time step is of the order of 10^{-15} sec and diffusive processes take place over much longer time scales. To determine the diffusion rates, it is necessary to evaluate all the various transitions that a cluster on a surface may undergo. This involves determining the heights of all the saddle points surrounding the local minimum on the potential energy surface in which the cluster is currently situated. A useful method for determining these saddle points is the dimer method [38] which can also be used in conjunction with a kinetic Monte Carlo approach to model diffusion [39]. Finally, of course there are potentially many different applications of clusters on surfaces, many different surfaces that can be investigated and many different types of cluster, in fact enough systems to keep both modellers and experimentalists happy for some years to come.

REFERENCES

[1] Carroll S.J., Weibel P., von Issendorff B., Kuipers L., Palmer R.E., J. Phys.: Condens. Matter 8 (1996) L617.
[2] Carroll S.J., Seeger K., Palmer R.E., Appl. Phys. Lett. 72 (1998) 305.
[3] Palmer R.E., Pratontep S., Boyen H.-G., Nat. Mater. 2 (2003) 443.
[4] Leung C., Xirouchaki C., Berovic N., Palmer R.E., Adv. Mater. 16 (2004) 223.
[5] Di Vece M., Palomba S., Palmer R.E., Phys. Rev. B 72 (2005) 073407.

[6] Smith R., Nock C., Kenny S.D., Belbruno J.J., DiVece M., Palomba S., Palmer R.E., Phys. Rev. B 73 (2006) 125429.
[7] Carroll S.J., Nellist P.D., Palmer R.E., Hobday S., Smith R., Phys. Rev. Lett. 84 (2000) 2654.
[8] Carroll S.J., Pratontep S., Streun M., Palmer R.E., Hobday S., Smith R., J. Chem. Phys. 113 (2000) 7723.
[9] Pratontep S., Preece P., Xirouchaki C., Palmer R.E., Sanz-Navarro C.F., Kenny S.D., Smith R., Phys. Rev. Lett. 90 (2003) 055503.
[10] Kenny D.J., Palmer R.E., Sanz-Navarro C.F., Smith R., J. Phys.: Condens. Matter 14 (2002) L185.
[11] Sanz-Navarro C.F., Smith R., Kenny D.J., Pratontep S., Palmer R.E., Phys. Rev. B 65 (2002) 165420.
[12] Prisco U., Leung C., Xirouchaki C., Jones C.H., Heath J.K., Palmer R.E., J. R. Soc. Interface 2 (2005) 169.
[13] Smith R., Kenny S.D., Sanz-Navarro C.F., Belbruno J.J., J. Phys.: Condens. Matter 15 (2003) S3153.
[14] Kenny S.D., Horsfield A.P., Fujitani H., Phys. Rev. B 62 (2000) 4899.
[15] Hartwigsen C., Goedecker S., Hutter J., Phys. Rev. B 58 (1998) 3641.
[16] Wang G.M., BelBruno J., Kenny S.D., Smith R., Surf. Sci. 541 (2003) 91.
[17] Wang G.M., BelBruno J.J., Kenny S.D., Smith R., Phys. Rev. B 69 (2004) 195412.
[18] Wang G.M., BelBruno J., Kenny S.D., Smith R., Surf. Sci. 576 (2005) 107.
[19] Ganz E., Sattler K., Clarke J., Surf. Sci. 219 (1989) 33.
[20] Ackland G.J., Tichy G., Vitek V., Finnis M.W., Philos. Mag. A 56 (1987) 735.
[21] Ziegler J.F., Biersack J.P., Littmark U., The Stopping and Range of Ions in Solids, Pergamon, New York, 1985.
[22] Brenner D.W., Phys. Rev. B 42 (1990) 9458.
[23] Brenner D.W., Phys. Rev. B 46 (1992) 1948.
[24] Smith R., Beardmore K.M., Thin Solid Films 272 (1996) 255.
[25] Ali M.M., Smith R., Hobday S., Comput. Phys. Commun. 175 (2006) 451.
[26] Rinnooy Kan A.H.G., Timmer G.T., Math. Program. 39 (1987) 57.
[27] Ali M.M., Storey C., J. Global Optim. 5 (1994) 349.
[28] Ali M., Törn A., in: Optimisation in Computational Chemistry and Molecular Biology: Local and Global Approaches, A. Floudas, M. Pardalos (eds), Kluwer Academic Publisher, Dordrecht, The Netherlands, 2000, pp. 287–300.
[29] Hobday S., Smith R., J. R. Soc. Chem. Faraday Trans. 93 (1997) 3919.
[30] Smith R., Webb R.P., Proc. R. Soc. A 441 (1993) 495.
[31] Smith R., Atom and Ion Collisions in Solids and at Surfaces, Cambridge University Press, Cambridge, 1997.
[32] Kushmerick J.G., Kelly K.F., Rust H.P., Halas N.J., Weiss P.S., J. Phys. Chem. B 103 (1999) 1619.
[33] Heggie M., private communication, 2005.
[34] Kenny D.J., Palmer R.E., Sanz-Navarro C.F., Smith R., Eur. Phys. J. D 16 (2001) 115.
[35] Carroll S.J., Nellist P.D., Palmer R.E., Hobday S., Smith R., Phys. Rev. Lett. 84 (2000) 2654.
[36] Smith R., Shaw M., Webb R.P., Foad M., J. Appl. Phys. 83 (1998) 1348.
[37] Bholoa A., Kenny S.D., Smith R., Nucl. Instrum. Methods B, (2007), doi:10.1016/j.nimb.2006.11.040.
[38] Henkelman G., Jonsson H., J. Chem. Phys. 111 (1999) 7101.
[39] Gordon S., Smith R., Kenny S.D., Phys. Rev. B 72 (2005) 214104.

INDEX